Macromolecules

Perspective

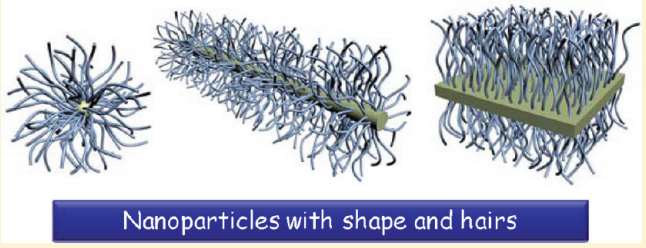
pubs.acs.org/Macromolecules

Shaped Hairy Polymer Nanoobjects

Yongming Chen*

Laboratory of Polymer Physics and Chemistry, Institute of Chemistry, The Chinese Academy of Sciences, Beijing 100190, China

ABSTRACT: Shaped hairy polymer nanoobjects are defined as a kind of polymeric particles with persistent geometric shape and densely tethered polymer hairs. Their size, at least in one dimension, should not exceed 100 nm. Components of the nanoobjects are mainly organic polymers, and therefore, they exhibit viscoelasticity and stimuli responsibility in general. Namely, they are soft nanomatter, greatly differing from those stiff and rigid inorganic nanoparticles. While spherical polymeric nanoparticles have been studied intensively, much less attention has been paid to those nonspherical hairy polymer nanoparticles like cylindrical and lamellar ones. The reasons are because fabrication of the shaped soft nanoparticles is still difficult and also less information has been known about the shape-induced properties, especially in biomedical application. In recent years, scientists are realizing that the shape of nanoparticles does matter to their properties of plasma circulation in mice and cell uptake, revealing a nearly unexplored area. In this Perspective, the author would like to focus on these soft nanoobjects with shapes and tethered polymeric hairs by introducing how to shape them, to densely tether polymer hairs, and why the hair and the shape are important.



1. INTRODUCTION

Polymer nanoparticles are very important materials, exhibiting many fantastic applications including delivering drugs, loading catalysts, medical diagnosing and imaging, and improving performances of polymer materials as nanofillers. It is well-known that the size and the surface character are very important factors to influence the properties of nanoparticles. However, most of the properties and applications of nanoparticles were obtained from spherical ones. Much less is known on how the shape of nanoparticles matters. Another important issue of polymer nanoparticles is their surface structure. When they are densely grafted with polymer chains, the hairlike polymers not only supply a forestlike soft shell to isolate their cores from surroundings but also interact with environments and carry functions, which do not occur with bald polymer particles. The issue of polymer hairs on polymeric nanoparticles also has not attracted enough attention. This Perspective would like to draw attention to these polymeric nanoparticles with geometric shapes and densely polymeric hairs.

If polymer nanoparticles have different shapes besides sphere, they are regarded as the polymer nanoobjects (PNOs). Namely, the PNOs should have a persistent shape in geometry that is stabilized by either chemical linkage or strong physical interaction. Basic shapes of the PNOs include sphere, cylinder or worm, and lamella or sheet. When cylinders are used as building blocks, star shaped and cyclic shaped PNOs can be obtained. In order to distinguish from the micrometer-sized particles which may be generated by microfabrication, at least one dimension of these PNOs is in the range of tens to one hundred nanometers, and thus these nanomaterials are more suitable made by bottom-up approaches. Because of the size and the persistent morphology, the PNOs can be visualized by microscopic techniques like electron microscopy and atom force microcopy, and therefore, their morphologies can be easily analyzed. When polymer hairs are densely tethered, the shaped PNOs have a core/shell structure.

It needs to mention that the PNOs should differ from the shaped inorganic nanoparticles that have been extensively studied. In general, the PNOs of polymer nature hold the properties of organic polymer materials, i.e., viscoelasticity and deformability. By external stimuli, they show responsive properties by changing composition, chemical property, size, and even shape. Because of solvation of polymer segments, they are soluble or dispersible in solvents and show concentration-dependent viscosity. They can be easily functionalized since they are composed of organic monomeric units. As a contrast, in general, inorganic nanoparticles are stiff and rigid, i.e., not deformable, unlikely to exhibit stimuli-responsive properties, and also easily forming precipitates in solvents. Therefore, hairy PNOs are *soft nanomatter with shapes*.

In this Perspective, I would like to focus on the *shaped PNOs including spheres, cylinders, and sheets from which well-defined polymer hairs are densely tethered*. The cores that govern the shape can be either single polymer chains or organic nanogel networks which endow the shaped PNOs with flexibility and thus deformability, which may be very important to exhibit more useful properties. The length scale is limited to tens to hundred nanometers because on one hand it is not easy to reach through top-down approaches and on the other hand it is close to the nature occurred items like proteins, shaped viruses, and DNAs. Schematic presentation of basic hairy PNOs is demonstrated in

Received: July 1, 2011
Revised: January 9, 2012
Published: January 27, 2012

 © 2012 American Chemical Society dx.doi.org/10.1021/ma201495m | *Macromolecules* 2012, 45, 2619–2631

Figure 1. These PNOs with characteristics of densely attached polymer chains can be regarded as the molecular brushes of

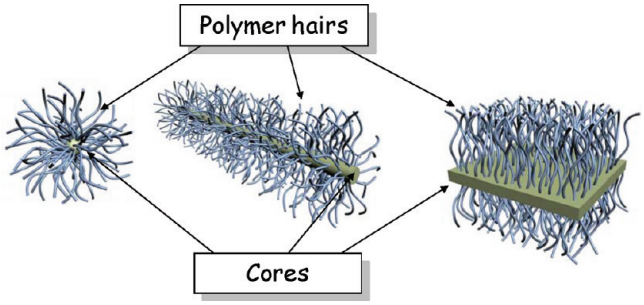


Figure 1. Cartoon presentation of core/shell PNOs of different geometric shapes.

different morphology. In following sections I will introduce how to prepare these hairy PNOs, how to control their shape, and how the shape and hairs matter in properties and potential application.

2. PREPARATION OF SPHERICAL PNOS

In order to give a full shape diagram, spherical hairy PNOs are briefly introduced. There are many different spherical PNOs with tethered polymer hairs, and they have been studied extensively. They mainly include spherical polymer brushes with a nanogel core tethered with many arms and spherical block copolymer micelles with a fixed core. Thus, the cores of spherical PNOs can be nanogels either preformed[1] or *in situ* formed[2−4] and the cross-linked cores of block copolymer aggregates.[5] In addition, preformed giant dendritic polymers may be applied as the core to graft polymer hairs.[6] The cores not only supply a support for polymer hairs to tether from but also exhibit functions. The hair structure is also important in terms of their properties and functions. Dependent upon how polymers are tethered, spherical PNOs can include homo-type, core/shell-type, hetero-type, and Janus-type as shown in Figure 2.

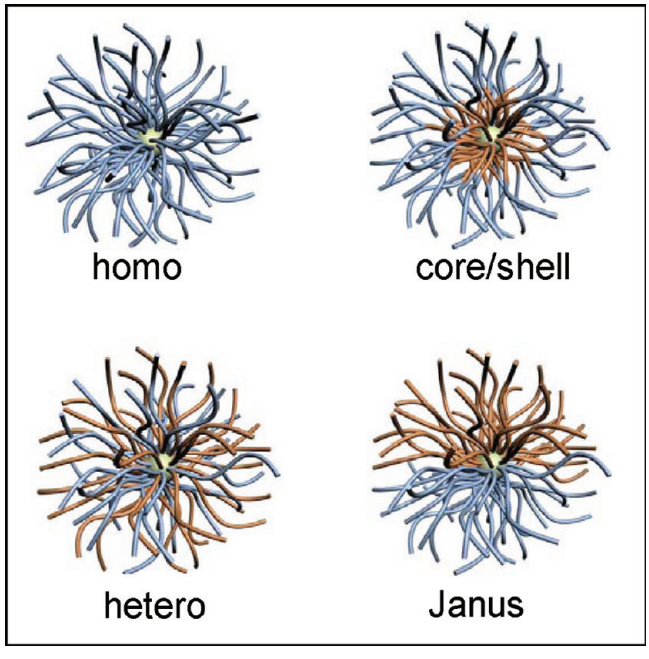


Figure 2. Cartoon presentation of types of spherical PNOs categorized by hair structures.

2.1. Spherical Polymer Brushes. When a large amount of linear polymer segments is covalently coupled to a nanocore, spherical brushes are obtained. Star polymers that densely bear a lot of arms can be also regarded as spherical polymer brushes.[7] If the tethering density is high, neighboring polymer hairs repel each other and thus are stretched. Particle size covers a range from 20 to 100 nm (even larger) dependent upon core size, arm length, and density.[1] One of the ways to synthesize spherical brushes is by the grafting-from approach, of which the polymer arms are formed by radiating grafting polymerization from a core with many initiating functionalities using controlled polymerization (as shown in Figure 3A). By this way, initiating

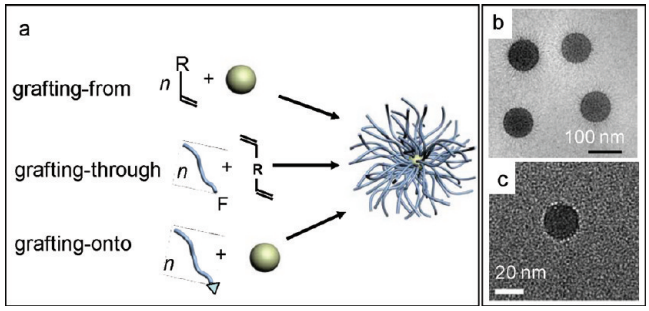


Figure 3. (a) Grafting chemistry to prepare hairy spherical PNOs. (b) Cryo-TEM of spherical polyelectrolyte brushes (cesium counterions) by the grafting-from approach. (Reproduced and adapted from ref 11.) (c) Star polymers by the grafting-through approach. (Reproduced and adapted from ref 12. Copyright 2009 Wiley-VCH Verlag GmbH & Co. KGaA.)

groups for graft polymerization are introduced first onto the surfaces of either nanoparticles[8,9] or nanosize hyperbranched molecules.[6] Under the optimized condition, the obtained PNOs are well-controlled in terms of size distribution, hair composition, and length. However, since the controlled radical polymerization is normally applied, interparticle coupling due to radical−radical termination occurs easily. Therefore, the polymerization should be conducted under a high feed ratio of monomers to initiating groups and terminated at very low monomer conversion when radical polymerization is applied. Also, such particles have been prepared by photoemulsion polymerization.[10] Figure 3B gives a TEM image of thus produced PNOs densely grafted with poly(styrenesulfonate) polyelectrolytes.[11] Stretched polymer hairs tethered onto polystyrene (PS) colloids are clearly observed by cryo-TEM.

The grafting-through approach, also called as arm-first, has been applied to prepare the star polymers with microgel cores, i.e., hairy spherical PNOs (Figure 3), for a long time. By this way, the preformed linear polymers terminated with an initiating group initiate the polymerization of divinyl monomers to form cross-linked nanogels as cores *in situ*. With shorter arm precursors and more divinyl cross-linkers, the nanoobjects would have more arms and larger nanogel cores.[7] Figure 3c shows a star polymer obtained by this approach, and one may observe a nice spherical shape ca. 23 nm in diameter.[12] Normally the spherical PNOs obtained by this means are poorly controlled due to uncontrolled star−star coupling. Recently, Gao et al. have prepared star polymers with high molecular weight and narrow size distribution by copolymerization of macromonomers and divinyl monomers initiated with small initiators under atom radical transfer polymerization (ATRP). Star−star radical coupling was reduced due to the low concentration

dx.doi.org/10.1021/ma201495m | *Macromolecules* 2012, 45, 2619−2631

of initiators.[2] Pan et al. prepared spherical polymers with narrow size dispersion by the grafting-through approach, but a poor solvent of the early formed cores was used.[3,4] Thus, a polymerization-induced micellization was involved which restricted star−star radical coupling. The star polymer particles with ca. 220 of arms and of 50 nm in diameter were obtained. Also, spherical polymer brushes may be prepared by the grafting-onto approach, i.e., coupling preformed polymers onto the surface of cores-to-be (Figure 3a). But less attention has been paid to this approach due to concern of low grafting efficiency.

Beside the homopolymers being tethered, grafting chemistry like the grafting-from approach is applied to graft block copolymers onto the preformed nanogels by sequential polymerization to obtain core/shell-type hairy PNOs (Figure 2). Heterotype PNOs bearing different hairs can be obtained by grafting-from approach which needs a state-of-art strategy for modifying the surface of colloids with different initiating species and then conducting different graft polymerization successively.[13] Also, this type of PNOs can be prepared by a combination of first grafting-through and then grafting-from methods.[14]

2.2. Core Fixed Block Copolymer Aggregates. Self-assembly of block copolymers forms micellar nanoparticles of various structures in selective solvents and generates microphase-separated ordered bulk materials. As demonstrated in Figure 4a,

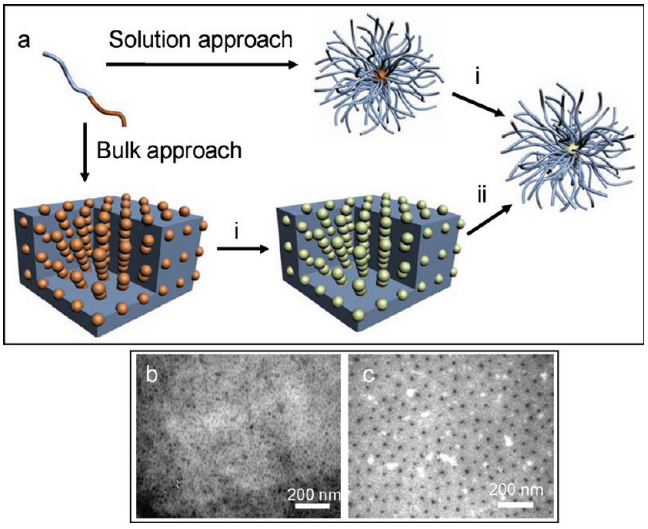


Figure 4. (a) Preparation of spherical PNOs by fixation cores of block copolymer self-assembly in solution and bulk (conditions: (i) cross-link, (ii) disperse in solvent). TEM images of (b) microtomed slice of bulk PTEPM-*b*-PS and (c) its dispersed spherical PNOs in THF (data obtained according ref 23).

the simplest aggregates from solution approach are core/shell starlike micelles. Hairy PNOs may be obtained easily by chemically cross-linking cores of the preformed spherical micelles. The first example was reported by Liu et al., who applied polystyrene-*b*-poly(2-cinnamoylethyl methacrylate) (PS-*b*-PCEMA) that self-assembles into star and crew-cut micelles with PCEMA cores in solutions.[15] When UV irradiation is subjected, the PCEMA cores are cross-linked by [2 + 2] cyclization of cinnamyl units, and hairy spherical nanoobjects are obtained. Recently, water-soluble poly(ethylene oxide) (PEO) hairy nanospheres with polysilsesquioxane network cores in uniform size have been obtained by self-assembly of PEO-*b*-poly[3-(trimethoxysilyl)propyl methacrylate] (PEO-*b*-PTMPM) in water and then gelation of cores.[16] In general, the size of such spherical PNOs is in the range 20−100 nm attributing to packing block copolymer molecules in a nanospace. The number of hairs per PNO can reach a few hundred which are governed by the aggregation number of block copolymer precursors. Such cross-linking strategy has been applied to fix the morphologies other block copolymer self-assemblies like vesicles.[5,17] More complex spheres with heterohairs can be obtained using the triblock copolymers with cross-linkable middle segments[18,19] or mixed different diblock copolymers to form the micelles with two kinds of polymer chains as corona.[20,21] When the cores are cross-linked, two incompatible hairs are microphase-separated and a patchy surface is formed.

Moreover, bulk microphase-separated block copolymers have been used to generate the spherical PNOs efficiently (Figure 4a). By cross-linking spherical microdomains of block copolymer bulk materials and then dispersing in a solvent of non-cross-linked phases, hairy spherical polymers can be obtained easily. Ishizu and Fukutomi prepared poly(4-vinylpyridine)-*b*-polystyrene (P4VP-*b*-PS) block copolymer films in which the P4VP segments formed spheres dispersed in continuous PS microdomains.[22] When the specimen was exposed to a vapor of 1,4-dibromobutane, the P4VP cores were cross-linked while the PS segments remained intact. Dispersing the films in an organic solvent, the PS hairy nanospheres with cross-linked cores were thus obtained. Chen et al. have applied poly[3-(triethoxysilyl)-propyl methacrylate]-*b*-PS (PTEPM-*b*-PS) and PTEPM-*b*-P2VP block copolymers that may form the bulk spherical structure to prepare hairy PNOs.[23,24] Simply by exposing the microphase separated materials to an atmosphere of hydrochloric acid, the isolated PTEPM spherical domains were gelated and the PS,[23] also P2VP,[24] hairy PNOs were obtained. Also, the block copolymers of poly(glycidol methacrylate) (PGMA) bearing epoxy in every repeating units have been developed and an atmosphere of amines may induce cross-linking of the PGMA cores.[25] This chemistry is versatile to functionalize the cores of PNOs by using functionalized amines and reactivity of epoxy. Relatively to the solution approach, the above bulk approach is more efficient for production of spherical PNOs since no solvent is needed during self-assembling process.

Bulk block copolymer approach is suitable to fabricate PNOs with different polymer hairs tethered on different surface of a core, namely Janus-type hairy spheres (Figure 2) that may be difficult to prepare by either grafting chemistry or block copolymers in solution. In this case, a triblock copolymer with middle block as core-forming segment that forms certain microdomain structure has to be applied. Ishizu et al. prepared Janus hairy spheres through cross-linking the P2VP cores which located at the lamellar interfaces of PS and poly(butyl methacrylate) (PBMA) of microphase-separated PS-*b*-P2VP-*b*-PBMA and dispersing in a solvent.[26] Similarly, Müller et al. cross-linked the polybutadiene (PB) cores of bulk PS-*b*-PB-*b*-PMMA by either S_2Cl_2 or AIBN to get the Janus spherical PNOs.[27] By further hydrolysis of PMMA faces, amphiphilic Janus-type PNOs were obtained.[28]

3. CYLINDRICAL PNOS

Cylinder with large ratio of length/diameter is the simplest nonspherical shape. Figure 5 shows the types of such one-dimensional PNOs depending structure of polymer hairs. Herein cylindrical molecular brushes and block copolymer cylinders are introduced. Similarly to the cases of spherical PNOs, grafting approach and self-assembly approach are applied to prepare the hairy cylinders.

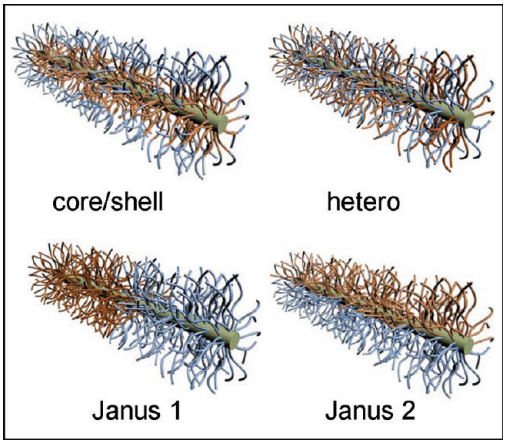


Figure 5. Cartoon presentation of cylindrical PNOs with different hairy structures.

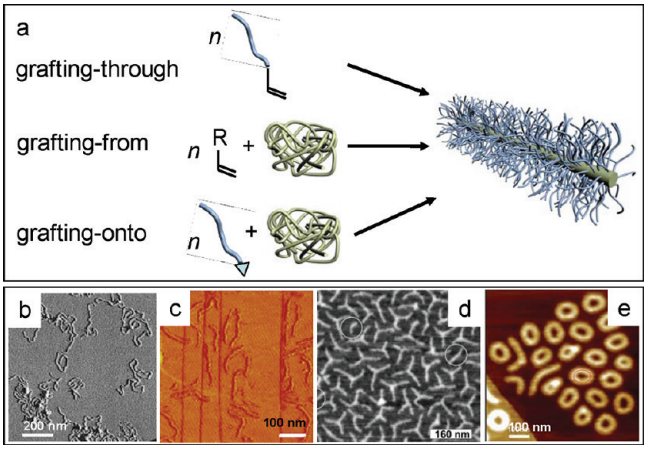


Figure 6. (a) Synthesis of wormlike molecular brushes by grafting chemistry. (b–e) Selected AFM images of different shaped brushes. [(b–d) Reproduced and adapted from refs 31, 37, and 52. (e) Reproduced and adapted from ref 53. Copyright 2008 American Association for the Advancement of Science.]

3.1. Cylindrical Molecular Brushes. This is a kind of single molecular nanoobjects of cylindrical shape. In this case, bulky linear polymers are grafted onto a long polymer main chain in a density that neighboring polymer branches feel crowding and repel each other. As a result, the backbone chains are forced to elongate and the extent is mainly governed by steric hindrance of the bulky side polymer segments and grafting density (detail status may refer to a review article[29]). It needs to mention in this article that the backbone should have a degree of polymerization of at least a few hundred in order to give large length/width ratio (l/d), i.e., to show one-dimensional shape. Otherwise, the brushes with low length/width ratio are more like symmetric star polymers. For a polymer chain with degree of polymerization over 1000, the contour length of molecular brushes easily reaches several hundred nanometers. When the backbones are obtained by a controlled polymerization, the length of molecular brush is controlled, which is important to study the size induced properties. The diameter is dependent by the size and tethering density of side chains, and normally it is a few tens of nanometers. When the grafting density is fixed, the size of side chains governs the stiffness of molecular cylinders as revealed by the in-depth study from Schmidt et al.[30−32] It is indicated that when the side PS chains change molecular weight from 700 to 5000, the persistence length increases from 13 to 100 nm.[30] It may become stiffer if the side chains grow further.[33] Therefore, molecular cylindrical PNOs exhibit a tunable stiffness.

Cylindrical molecular brushes are prepared by grafting approaches which are similar to these of spherical brushes, but long polymer backbones become the cores (Figure 6a). Among them, the grafting-through approach, i.e., polymerization of macromonomers, has been mainly applied for synthesizing molecular brushes.[30−32,34,35] However, selecting polymerization chemistry is critical to get long molecular worms due to the hindrance of bulk polymer segments to the chain propagation reaction of polymerizable groups. In practice, it has been demonstrated that conventional radical polymerization of vinyl macromonomers may produce very long wormlike molecular brushes even for the macromonomers with molecular weight as high as 5 kDa.[30] Figure 6b shows an AFM image of molecular brushes obtained by radical polymerization of macromonomers.[31] The composition of homobrushes by this way is very uniform since each repeating unit along the backbone bears a side polymer chain. However, the length of backbones is not controllable due to the intrinsic drawbacks of radical polymerization and removal of the unreacted macromonomers is tedious sometimes. Controlled radical polymerization of macromonomers has been explored in order to control the brush axial length. Unfortunately, it is hard to obtain molecular brushes with high enough degree of polymerization of backbone. Recently, ring-opening metathesis polymerization (ROMP) of macromonomers has been applied to obtain wormlike molecular brushes and has been proven to be an efficient way to control formation of molecular brushes.[36,37] The norbornene-terminated polymers were homopolymerized using high efficient Grubb's catalysts, which showed fast initiation, high reactivity, and tolerance of functional groups. The polymerization of norbornene macromonomers bearing polylactide (PLA) of high molecular weight (4.3 kDa) at a ratio of monomer to initiator of 1160 underwent nearly quantitatively and gave wormlike PNOs with molecular weight as high as 13 000 kDa with low distribution.[36] Figure 6c shows AFM image of controlled cylindrical brushes reported by Grubbs et al.[37]

Attributing to development of controlled radical polymerization which is tolerable to functional monomers, the grafting-from approach has been widely applied to synthesize wormlike molecular brushes.[38] Different from the above way, the initiating groups are introduced after formation of backbones by postmodification, and then controlled radical polymerization is conducted to graft side polymers. Since the preformed backbones can be prepared by controlled polymerization like anionic polymerization, the length of brushes can be easily tailored, which is very important for studying properties. However, this approach has been suffered from problems like low grafting efficiency[39] and radical–radical coupling, which decrease the uniformity of molecular brushes. It needs to optimize the condition to enhance grafting efficiency to improve the uniformity of brushes.[40]

Relative to the above two approaches, the grafting-onto approach by coupling polymers onto a backbone is studied much less, challenged by low coupling efficiency. Matyjaszewski et al. have studied formation of molecular brushes using click chemistry.[41] A series of azido-terminated polymers were reacted with the polymethacrylates whose repeating units were modified with pentynoate units catalyzed by copper complex. It was found that the thin and short PEO (750 Da) demonstrated the highest grafting density (ca. 88%) only at a highly excessive PEO feed,

dx.doi.org/10.1021/ma201495m | Macromolecules 2012, 45, 2619–2631

whereas other polymers from vinyl monomers were grafted at much lower density.

These three approaches of grafting chemistry have been applied to prepare the brushes with block copolymers as side chains, i.e., core/shell type PNOs in Figure 5.[34,41,42] Moreover, the grafting-through approach has been applied to prepare heterotype[35,43] and Janus 1-type block PNOs[43−46] shown in Figure 5. Chen et al. combined grafting-through and grafting-from methods to prepare hybridized brushes tethered with alternating dendrons and polyacrylates.[47] While side chain length and branch composition have been studied extensively, the density control is less concerned. It has been explored to radically polymerize the macromonomers bearing two chains to increase the density of grafted chains.[48] However, this approach faced a high steric hindrance of macromonomers to polymerize into long molecular worms. This problem seems to have been overcome by ROMP, and it was indicated by Bowden et al. that the molecular brushes with two PLA branches per norbornene unit were synthesized by corresponding bulky macromonomers in the presence of the Grubbs' second generation catalyst.[36] As a contrast, well-defined loose brushes were obtained more easily. Deng et al. have prepared the backbones first by alternating radical copolymerization of styrene and *N*-[2-(2-bromoisobutyryloxy)ethyl]maleimide whose initiating sites along the backbone were "diluted" in a controlled way.[49] Then polyacrylate branches were grafted to give the more flexible brushes.

When bulky dendritic wedges, instead of linear polymers, are grafted, the so-called dendronized polymers may also show wormlike morphology. Their synthesis and morphologies are similar to the molecular brushes, and the details can be found in the latest feature article.[50] Owing to stepwise synthesis of dendrons, the dendronized polymers may have a better controlled structure.[51]

3.2. Starlike and Cyclic PNOs. Persistent wormlike molecular brushes may be used as the building blocks to fabricate the PNOs with different geometric shapes. When polymer side chains are densely grafted from coil star polymers, the thin arms are stiffened and thickened. Thus, the PNOs with visualized starlike shape by AFM can be obtained. Matyjaszewski et al. prepared the shaped PNOs with three or four arms by ATRP grafting from coil star polymer precursors.[52] As revealed in Figure 6d, the arm number can be counted from the AFM image of molecular PNOs and the defects of star polymers can be visualized directly.

Cyclic PNOs may be obtained using molecular brushes, too. Schappacher and Deffieux coupled polystyryllithium and/or polyisoprenyllithium onto a cyclic poly(chloroethyl vinyl ether) with the degree of polymerization of 870.[53] The obtained donut ringlike PNOs had a circumference of around 210 nm as shown by AFM (Figure 6e). It is interesting that heterografted cyclic brushes in selective solvent of one branches self-assembled into a hollow column with diameter of individual nanorings. Also by conducting first ring-expansion methathesis polymerization (REMP) to get cyclic polymer precursors and then grafting PEG chains, PEGylated cyclic PNOs have been synthesized.[54] Applying REMP of dendritic macromonomers, i.e., the grafting-through approach, Frechét et al. obtained uniform small cyclic PNOs with diameters of 35−40 nm.[55] Moreover, Grubbs et al. have applied REMP of ω-norbornenyl macromonomers to prepare giant cyclic molecular brushes with DP of backbones as high as 3000.[56]

3.3. Cylindrical PNOs by Block Copolymers. The above molecular brushes are prepared by stepwise synthesis and, therefore, in principle their size and composition can be tailor-made in the molecular level. However, on the other hand, the synthesis is tedious, and it is difficult to obtain PNOs in large amounts for application development. Also challenged by synthesis of backbones, it is unlikely to prepare very long cylindrical PNOs. These problems definitely limit their practical application. Spontaneous self-assembly of block copolymers can be more efficiently to produce cylindrical PNOs with larger size scale. When block copolymers self-assemble into wormlike micelles, chemically cross-linking the cores of aggregates can generate robust cylindrical PNOs with densely tethered polymer coronas. This type of PNOs is similar to the wormlike molecular brushes in morphological characteristics, but they may be very long. Also, their core is thicker since the core is cross-linked cylindrical microdomain instead of thin linear single polymer chain. Moreover, the hairs that come from un-cross-linked segments can be longer than that of molecular brushes, meaning that whole cylinder has a much thicker cross section. For example, the cylinders from self-assembled PS_{1250}-*b*-$PCEMA_{158}$ block copolymers have a cross-linked PCEM core of diameter to be ca. 30 nm and an external diameter to be ca. 80 nm.[57] Herein the cross-linked core contributes cylinder stiffness, and by changing condition the cross-linking densities may be tuned.[57−59]

In principle, the block copolymers that may self-assemble into wormlike micelles can be applied to prepare the stable PNOs with cross-linked cores. The first work was presented by Liu et al. using PS-*b*-PCEMA in a selective solvent of PS to form cylindrical micelles.[60] UV-irradiated cross-linking PCEMA cores gave PS hairy cylindrical PNOs. Also, Bates et al. reported that certain PEO-*b*-PB forms giant cylindrical micelles of length in at least several micrometers in water.[61] The main advantage of this approach is its facile formation of very long core/shell nanofibers which are impossible by the molecular brush approach. Though the principle is simple, few reports via this solution approach to prepare cylindrical nanoobjects have been found. It is attributed to the requirements that have to be matched to produce the cylindrical PNOs; i.e., the block copolymers may form wormlike micelles in solution, and also the core segments can be stabilized. Suitable block copolymers for such purpose are still very few due to a narrow window of block copolymer composition to form fibril micelles. Thus, it is still a challenge to rational synthesize cylindrical PNOs through cross-linking fibril block copolymer aggregates in a solution.

Relative to the solution approach, bulk microphase separation of block copolymers is a more generalized strategy to obtain cylindrical PNOs as revealed in Figure 7a. The reason is that the block copolymers form hexagonally packed cylinders in a relatively wide range of component window, and no solvent interaction needs to consider. Therefore, one may rationally design the block copolymers with reactive segments to form cylinder cores and produce cylindrical PNOs in a large amount via bulk path. Liu et al. reported formation of cylindrical PNOs by using microphase-separated PS-*b*-PCEMA upon exposure to UV irradiation.[62] By further dispersing in THF, uniform polymer fibers of ca. 60 nm in diameter and several micrometers in length were obtained. Figure 7b shows the cylindrical PNOs by cross-linking polyisoprene cylindrical cores of bulk PS-*b*-PI with S_2Cl_2.[63] Chen et al. obtained cylindrical PNOs by gelating the PTEPM cores of bulk hexagonally packed cylinders from PTEPM-*b*-PS[23] and PTEPM-*b*-P2VP.[24] Thus, obtained PNOs had polysilsesquioxane cores, and therefore, they are organic/inorganic hybridized one-dimensional PNOs. Figure 7c shows the cylindrical PNOs of PTEPM-*b*-P2VP been protonated in

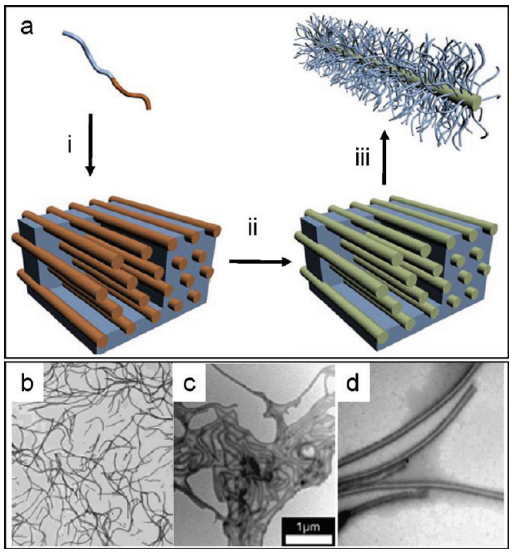


Figure 7. (a) Cylindrical PNO preparation via bulk block copolymer approach [conditions: (i) bulk microphase separation; (ii) cross-link certain domains; (iii) disperse in solvent]. Selected TEM images of cylindrical PNOs from (b) PS-*b*-PI and (c) PTEPM-*b*-P2VP. (Reproduced and adapted from refs 63 and 24.) (d) PS-*b*-PTEMP-*b*-P2VP. (Reproduced and adapted from ref 68. Copyright 2010 Elsevier Ltd.)

acidic water.[24] Similar hybrid fibrils were also obtained by using bulk PI-*b*-PEO in the presence of (3-glycidyloxypropyl)trimethoxysilane and aluminum *sec*-butoxide. The metal alkoxides were enriched into the cylindrical PEO cores, and after the gelation cross-linking, PI hairy cylinders with ceramic cores were prepared.[64] Qin et al. have developed the PGMA-*b*-P*t*BA system which is more flexible to functionalize the cores of cylinders by using epoxy chemistry.[25] Above examples via bulk microphase separation and dispersing in solution demonstrated that the cylindrical PNOs can be facilely produced. Since no solvents are needed during self-assembling process, this procedure is more efficiently and environmental friendly in addition to the rational design.

It should be mentioned that the shape of cylinders is inherited from its bulk cylindrical microphase structure which is thermodynamically stable. When it is dispersed in a solvent of the non-cross-linked segments, the densely tethered polymer hairs are highly solvated, and as a result, the neighboring hairs should repel each other to induce tension. But the shape of cylinders still remains unchanged due to the stabilized cores by cross-linking. Thus, the chemically cross-linking is important to keep the shape. However, the stabilization can also be supplied by physical interaction if it is strong enough. It is known that polymer chains below glass transition temperature (T_g) are frozen and unlike to reorganize. Recently, Qin et al. applied the block copolymers who have a high-T_g segment to generate cylindrical PNOs.[65] The key is to disperse the cylindrical microdomain structured P*t*BA-*b*-PS in methanol, which is a good solvent of polyacrylate shells but a bad solvent of PS cores and at mild room temperature. Though strong interaction between methanol and polyacrylate hairs occurs, the cylindrical shape is kept by the frozen PS cores, i.e., nonchemical stabilization. When the temperature was brought to reflux, the cylinders were switched into spherical PNOs, supporting a kinetically stabilized structure.

As revealed above, simple hairy cylindrical PNOs are obtained from diblock copolymers. The PNOs with a complex structure, like tubes and Janus cylinders, can be prepared by applying triblock copolymers. For example, Liu et al. reported that in methanol PI-*b*-PCEMA-*b*-P*t*BA formed cylindrical micelles followed by fixation PCEMA middle shells.[66] Then the PI cores were removed by ozonolysis to give hairy nanotubular PNOs. Similarly, bulk PBMA-*b*-PCEMA-*b*-P*t*BA microphase-separated into cylindrical structure with P*t*BA cores and PCEMA shells dispersed in the PBMA matrix.[67] After cross-linking PCEMA middle layers, the nanofibers with inward tethered P*t*BA and then poly(acrylic acid) thereof were obtained. Moreover, fine fibril structure with P2VP functional cores (TEM image shown in Figure 7d) was obtained from PS-*b*-PTEMP-*b*-P2VP triblock copolymers.[68] Other interesting structure is Janus 2-type cylinders (in Figure 5) with two polymer hairs being tethered along two halves of cylinders along longitudinal direction that were prepared by cross-linking the PB cylinders of lamellae/cylinder phase of PS-*b*-PB-*b*-PMMA.[69]

Unfortunately, there is one instinct disadvantage in the block copolymer approach. Though the diameter of such PNO is very uniform, the length is unlikely controlled due to the characters of molecular self-assembly. Recently, it is demonstrated that growth of wormlike micelles of block copolymers can be controlled by using crystallizable polymer segments and a controlled condition.[70,71] This achievement on "living" molecular self-assembly may give a hint to control the length of cylindrical PNOs from block copolymers.

4. SHEETLIKE PNOS

This is a kind of PNOs with a layered core from which polymer chains are tethered along two faces, and Figure 8a shows homo-,

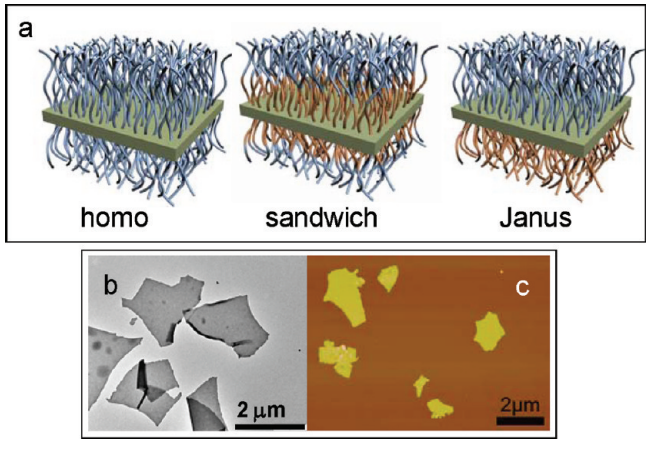


Figure 8. (a) Type of sheetlike PNOs by bulk block copolymer approach. (b) TEM image of homotype. (Reproduced and adapted from ref 25.) (c) AFM image of sandwich-type sheets. (Reproduced and adapted from ref 81. Copyright 2009 The Royal Society of Chemistry.)

sandwich- and Janus-type PNOs. Therefore, this is two-dimensional PNO as an analogue of spherical and cylindrical ones. However, its preparation by grafting chemistry with two-dimensional backbone is still very challenging. This is because the synthesis of two-dimensional polymers with one monomer unit thick is very difficult.[72−74] Also, other two-dimensional thin nanomaterials that can be applied for grafting polymer hairs are scarcely found except graphenes and clays. Therefore, it is still not imaginable to prepare two-dimensional hairy PNOs by the

ways to get cylindrical molecular brushes. A feasible choice can be fixing the preformed molecular self-assemblies with two-dimensional morphology. But the reports on formation of disclike/sheetlike self-assemblies in solution are scarcely found. Examples include disks from bolaamphiphiles,[75] coil−rod−coil triblock copolymers,[76] coil−coil diblock copolymers with a perfluoropolymer segment,[77] PAA-*b*-PMA-*b*-PS triblock copolymers in the presence of diamines,[78] supramolecular block copolymers,[79] and diblock copolymers with one crystallizable segment.[80] These examples demonstrate that stable disklike PNOs can be obtained by directly cross-linking their cores. Actually, Lee et al.[76] and Wooley et al.[78] have chemically fixed disks either by cores or corona. However, apparently these researches unlikely become a generalized procedure to get disk or sheetlike hairy PNOs.

As a contrast, alternating packed lamellae are the most common structure of bulk microphase separation of symmetric diblock copolymers. Chemically cross-linking certain layers and dispersing in a solvent may generate giant hairy sheets, just like the hairy cylinders introduced in previous section. Since each periodic length composed of two diblock copolymer chains packed back-to-back, the thickness of individual sheets roughly accords to the length scale of two block copolymer chains. They are composed of a gelated middle layer with both faces attached with densely polymer hairs originated from the uncross-linked segments. Recently, Chen et al. have carried out this procedure in several systems for producing hairy sheets. The block copolymers like PTEPM-*b*-PS,[23] PTEPM-*b*-P2VP,[24] and P*t*BA-*b*-PGMA[25] as well as P*t*BA-*b*-PS[65] in certain composition microphase-separated into highly ordered lamellar materials. After inducing gelation in PTEPM or PGMA layers, PS, P2VP, and P*t*BA hairy nanosheets were obtained easily. Therefore, the bulk approach using block copolymers can be a generalized and also facile procedure to produce hairy sheetlike PNOs. The thickness of sheets, ranging from 20 to 100 nm in general, is very uniform owing to highly ordered polymer packing. The size of sheet in plane may easily reach several micrometers, and it may be broken into small pieces by a violent condition like sonication. However, because of a randomly fracturing by mechanical force, the shape and the contour length along sheet dimension are unfortunately uncontrollable.

In terms of structure, diblock copolymer precursors generate the PNOs with homogeneous hairs while the triblock copolymers may be used to prepare the sheets with complex hairs and also cores. When triblock copolymers PTEPM-*b*-PS-*b*-P2VP were applied, sandwich-type hairy sheets (Figure 8c) composed of a cross-linked PTEPM middle layer with PS-*b*-P2VP tethered along its both faces were prepared.[81] To form Janus-type sheets, one has to apply triblock copolymers with a cross-linkable middle segment.[68,82,83] Müller et al. applied the PS-*b*-PB-*b*-PBMA triblock copolymers and Janus-type sheets with one face covered with PS and another face with PBMA were prepared by cross-linking the PB middle domains.[82]

5. HAIR AND SHAPE INDUCED PROPERTIES AND APPLICATION

Understanding the polymer hairs and the shape induced properties is very important for application of these soft hairy PNOs. It is well-known that the shape of nanoparticles is very important for material science. For example, the properties of polymer composites being filled with a small amount of exfoliated fibrous carbon nanotubes and sheetlike clays may be changed dramatically. However, nearly all these shaped nanoparticles are blended into the matrix either directly or with modified surface polarity. The reports on how the polymer hairs matter for composites are found very less.[84,85] In this part the author features the researches that may elucidate how the polymer hairs and the shape to influence the properties of PNOs. Also, potential applications of hairy PNOs are commented.

5.1. Tethered Polymer Hairs Are Important. Densely tethering linear polymer chains is an instinct character of the PNOs that are concerned in this Perspective. Since they are grafted outward, they definitely exhibit important roles during interaction with their environment. Polymer hairs may help the nanoparticles to disperse entropically favorably in a polymer matrix. Though being widely applied as fillers to reinforce polymer structural materials, nanoparticles without tethered polymer hairs are entropically unfavorable when they are blended with a polymer matrix. It has been reported that the densely tethered PS chains may help the spherical nanoparticles to overcome depletion demixing effect and to form homogeneous dispersed nanocomposites in a PS matrix.[84] Several parameters like length and density of polymer hairs may influence mixing result, which is very important for understanding properties of polymer nanocomposite materials.[86] As explained in Figure 9a, depletion is suppressed completely

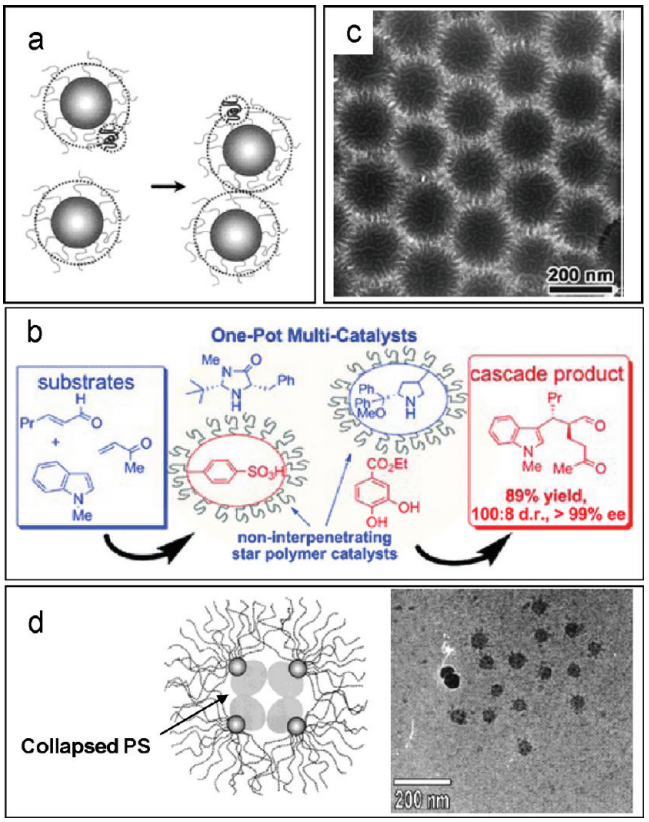


Figure 9. Polymer hairs of PNOs playing functions (a) to suppress depletion mixing of hairy colloids in a polymer matrix, (b) to isolate different incompatible cores, (c) to microphase-separate on surface of cores, and (d) to induce organization. (Images were reproduced and adapted from refs 84, 89, 90, and 28, respectively.)

when the PS hairs are longer than the PS chains of matrix.[84] The polymer hairs on a hard nanosphere may not only allow a complete miscibility even at a very high blending volume but also lead to solidification of composite materials.[85] Moreover,

dx.doi.org/10.1021/ma201495m | *Macromolecules* 2012, 45, 2619−2631

polymer hairs may feel environmental difference and induce dramatic phase separation of whole PNOs.[6,87] When the temperature-sensitive polymers, poly(oligo(ethylene glycol) methacrylate)s, were grafted onto a dendritic polyethylene nanoparticle, the core/shell PNOs showed sharp phase transition with a tunable thermosensitivity.[6]

The tethered chains may play a function to isolate different nanoparticles, i.e., cores, which have chemically incompatible functions in solution. In cascade reactions, sequential reactions are catalyzed by different catalysts like acid and base that cannot occur in a same reactor due to the intrinsic neutralization reaction between two catalytic sites. However, when the nanoparticles functionalized with sulfonic acid groups and amines were densely tethered with polymer hairs, the cascade reactions, first acid-catalyzed hydrolysis, and then amine-catalyzed Baylis−Hillman reaction occurred in the same flask, supplying a new concept for conducting cascade reactions in an environmental friendly way.[88,89]

In terms of the tethered hair structure, either randomly (hetero-type) or area selected tethered (Janus-type) polymer hairs may endow the PNOs with interesting properties. Zhao et al. grafted mixed PBA and PS chains on the surface of silica nanospheres.[13] Since two tethered polymers are incompatible, they microphase-separated to form nanopatterns along the particle surface (Figure 9c).[90] Moreover, the amphiphilicity of different tethered polymer hairs induced self-assembling of Janus-type spherical PNOs[27] in selective solvents to give giant micelles, as shown in Figure 9d.[28] The same Janus PNOs have been applied as stabilizers of emulsion polymerization to generate very uniform colloids.[91] Therefore, shaped PNOs with different tethering polymer hairs may be used as building blocks being organized into superstructures.

Furthermore, polymer hairs own a large number of chain terminals which equal to the number of tethered hairs. For a spherical PNO, the number of terminals ranges from tens to hundreds. But for a cylindrical PNO, the branch terminals easily reach thousands or more. Because of repulsion of neighboring chains, the terminal ends are located along the surfaces of hairy PNOs. Therefore, they are more accessible to the environments in application when functionalities are introduced.[92] Another aspect of functionalities is the repeating units of polymer hairs which are in huge number. In principle, these terminals and repeat functionalities may be useful.

The above introduction has revealed the importance of polymer hairs of PNOs in material science. Actually, the polymer hairy surfaces of nanomaterials are far from known, especially for the nanoparticles applied for biomedicine application. The structure of tethered polymer chains may greatly influence the fate of nanoparticles in biomedical systems like cellular uptake.[93,94] It was found that internalization efficiency of cells to hairy gold nanoparticles was governed by the properties of densely tethered polymers. The efficiency increased obviously from neutral, negative charged, and positive charged polymers. Also, the hair length is important. It was found that the blood half-time of gold nanoparticles with size of ca. 17 nm increased obviously from 4 to 30 to 51 h when the molecular weight of tethered PEG chains changed from 2K to 5K to 10K.[95]

5.2. Shape Matters. *Shape Transformation.* The PNOs that composed of organic polymer cores and coronas are soft—a character distinguished them from those stiff inorganic and organic crystalline nanoparticles. It has been already known that spherical polymer particles can be stimuli-responded by changing size and phase behavior dependent upon their structure.[87,96] As a contrast, much less attention has been paid to the PNOs of nonspherical shapes. Actually changing shape as responding of external stimuli is more interesting for soft shaped PNOs. So far, stimuli-responsive cylindrical molecular brushes have been studied mostly.[97] For example, Schmidt et al. reported that wormlike molecular brushes with poly(*N*-isopropylacrylamide) (PNIPAM) side chains which are temperature sensitive may transform into compact spherical objects when temperature is above the LCST of PNIPAM.[98] Figure 10a shows the AFM images of brush shapes

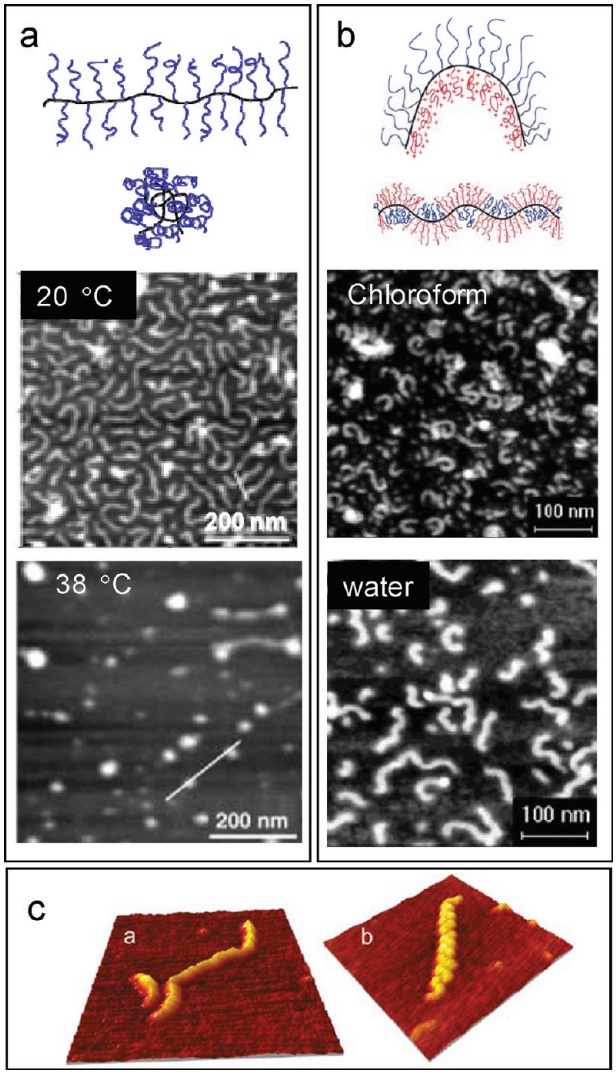


Figure 10. Shape changeable cylindrical PNOs. (a) Worm-global transformation stimulated by changing temperature. (Reproduced and adapted from ref 98. Copyright 2004 Wiley-VCH Verlag GmbH & Co. KGaA.) (b) Intramolecular phase separation induced by solvent. (Reproduced and adapted from ref 35.) (c) Worm-helix transformation from polylysine brush (left) to its complex with SDS (right). (Reproduced and adapted from ref 99.)

at different temperature. Also, molecular brushes randomly grafted with P2VP and PMMA (hetero-type in Figure 5) exhibit horseshoes or meander-like morphologies when spin-cast from different solvents. As shown in Figure 10b, intramolecular microphase separation between neighboring side chains in different solvents demonstrates different shapes.[35] The shape transformation from simple wormlike to helical cylinders can be also

dx.doi.org/10.1021/ma201495m | *Macromolecules* 2012, 45, 2619−2631

induced by adding sodium dodecyl sulfate (SDS) to molecular brushes with polylysine branches (Figure 10c).[99]

Shaped PNOs as Soft Assembling Blocks. As building blocks with persistent shapes in nanoscale, well-defined PNOs exhibit distinct self-assembling properties. It is known that hairy spherical polymer nanoparticles may form ordered gels above the critical concentration. But such materials are isotropic due to the symmetric shape of nanoparticles. As a contrast, the PNOs with asymmetric geometric shape may form anisotropic ordered soft materials. Formation of lyotropic liquid-crystalline phase was found in several cylindrical PNOs above critical concentration not only from molecular brushes[100,101] but also from block copolymer PNOs.[57,71] Also with help of a flow field, the wormlike brushes may form epitaxial ordered pattern on surface of the highly oriented pyrolytic graphite.[102]

Solution self-assembly of Janus-type PNOs of spheres,[28] sheets,[83] and cylinders[103] from block copolymers has been studied by Müller and his colleagues. The self-assembly of these PNOs is remarkable since the aggregation number can be precisely controlled and even visualized in some cases. For example, in a selective solvent, three or four Janus 2-type cylinders bearing PMMA and PS coronas self-assembled along axial direction to form superfibers (Figure 11a).[103] Cylindrical PNOs in

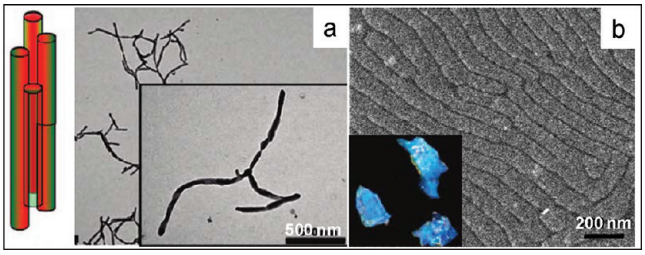


Figure 11. TEM images of (a) solution self-assembly of Janus 2-type cylindrical PNOs. (Reproduced and adapted from ref 103.) (b) Microtomed slice of bulk lamellar microphase structure of Janus 1-type cylindrical PNOs (inset is optical image of sample). (Reproduced and adapted from ref 106.)

other forms have been studied. In a selective solution of the coil segment of brush-*b*-PS PNOs, supermicelles aggregated from four to five molecular objects were visualized by morphological study using AFM.[104] By chemical reaction, Liu et al. organized two different tubular block copolymer PNOs with amino and carboxylic terminals, respectively, by amide linkages into giant block coPNOs of cylindrical shape.[105]

Bulk microphase separation of block cobrushes has been reported recently.[43,44,106] Rzayev has demonstrated that the brush block copolymer (PLA brush)-*b*-(PS brush) (Janus 1-type cylindrical PNOs) at bulk had a lamellar structure with spacing period as large as 160 nm (Figure 11b).[106] A similar Janus cylinders tethered with PLA and PBA also formed lamellae with periodic length more than 100 nm in bulk.[43] Attributing to such a large ordered structure, these bulk materials demonstrated a blue (inset in Figure 11b) or green color appearance due to reflecting certain wavelength light by larger ordered structure, implying application as photonic crystalline materials. These examples demonstrate that the large building blocks from PNOs may be applied to develop the materials with properties that are difficult to get from tranditional coil polymers. The asymmetric brush block copolymers, (PLA brush)-*b*-(PS brush), have given cylindrical bulk structure with polylactide brush as discontinuous phase.[107] After removing PLA domains, porous materials with the pore size larger than that of conventional coil block copolymers can be obtained.

Templating and Aligning Inorganic Particles. Spherical polymer particles like micelles have been used for stabilizing inorganic functional symmetric nanoparticles which may also be obtained by many other ways. However, formation of nonspherical inorganic particles or alignment of functional particles normally needs a nonspherical template. Cylindrical PNOs like core/shell molecular brushes have become nice candidates for this purpose.[108] For example, Schmidt et al. utilized molecular brushes with P2VP cores to align gold nanoparticles and to form gold nanowires as shown in Figure 12a.[34] Müller et al.

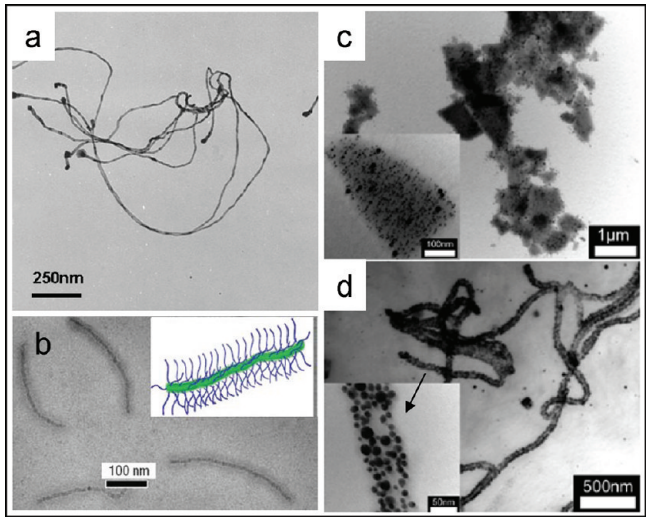


Figure 12. TEM images of (a) gold wires (reproduced and adapted from ref 34) and (b) water-soluble silica wires (reproduced and adapted from ref 101. Copyright 2008 Macmillan Publishers Limited) by core/shell brushes, aligned gold clusters by the P2VP hairs tethered along (c) sheetlike and (d) cylindrical PNOs (reproduced and adapted from ref 24).

prepared core/shell brushes whose internal segments were PTMPM. By inducing gelation to the PTMPM cores, water-soluble organic/inorganic hybrid wires with controlled length inheriting from molecular brushes can be obtained (Figure 12b).[101] When molecular brushes had triblock copolymer side chains with PTMPM as the middle block to gelate the middle shells, water-soluble organo-silica hairy tubes were prepared.[109] The cylindrical PNOs by block copolymer approach have been explored to support functional inorganic nanoparticles. For examples, Liu et al. have filled the tubular PNOs with inorganic clusters of Fe_2O_3, Pd, and Pd/Ni alloy.[67,110,111] In these cases, the functional compartments to load inorganic species are located inside the cores of molecular templates. Chen et al. have applied the P2VP hairs outward tethered onto cores of spherical, cylindrical, and sheetlike shapes to support gold nanoparticles. As shown in Figure 12c,d, tremendous Au nanoparticles were captured by the P2VP hairy-shaped PNOs. Moreover, the P2VP hairs with supported nanoparticles still exhibited pH stimuli sensitivity.[24] Therefore, the tethered P2VP chain forests can not only capture inorganic nanoparticles but also demonstrate pH sensitivity.

Shape Illumining Medical Application. Like block copolymer micelles and vesicles, the spherical PNOs have exhibited great potentials of biomedical application in drug delivery and imaging. Superior to block copolymer micelles, the PNOs with chemically stable cores do not have deaggregation problem,

which is important during transportation of loaded drugs. However, the importance of shaped PNOs in biomedicine application is far from simply to behave as a carrier. Recently, researchers have realized that the shapes of micro/nanoparticles matter greatly, which had been neglected for a long time. Thus, rapidly increasing attention to the relation of particle shape and properties of bionanomaterials is paid.[112] The shape induced properties were stimulated by an observation of the phagocytosis of elliptical disks.[113] It was found that the internalization by macrophages became very fast if the contact area occurred at the edge of microdiscs to the cell membrane. However, the particle was unlikely to be internalized if the contact occurred at its low curvature area. Thus, shaping nanoparticles may be another way to show target endocytosis, and Figure 13a shows the spherical

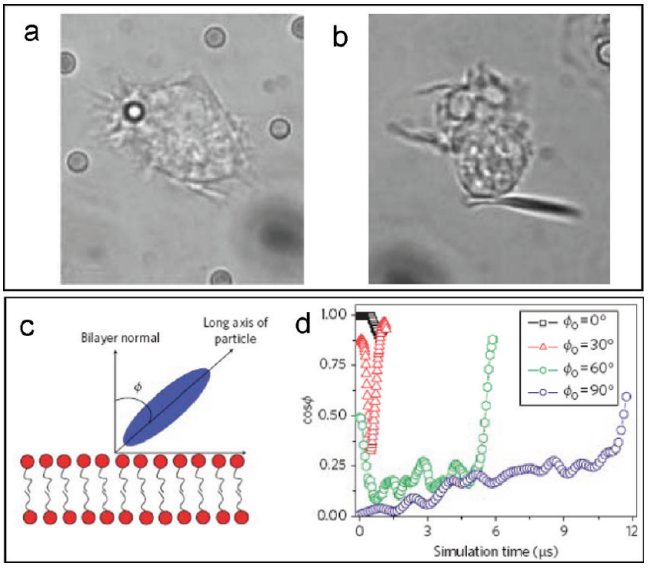


Figure 13. Snap images from microscopy video of (a) spherical PS objects (diameter: 3 μm) were taken by alveolar macrophage in 2 min whereas (b) ellipsoid microobjects escaped. (Reproduced and adapted from ref 114. Copyright 2008 Springer Science.) (c) Initial orientation angle ϕ of long axis of ellipsoid and bilayer and (d) time of penetration process related with ϕ. (Reproduced and adapted from ref 118. Copyright 2010 Macmillan Publishers Limited.)

particles were captured by macrophages whereas the nonspherical analogues escaped.[114] Also, the shape effect was observed by Gratton et al. that the HeLa cells preferred to internalize the rodlike microparticles.[115]

The above remarkable observations were obtained from microparticles, which seems beyond the concern of this paper. But sporadic reports on the cases of nanoparticles are appearing, which certainly will further push research to understand shaped nanoparticles in biomedical application. Disher et al. have studied pharmacological behaviors of cylindrical micelles of amphiphilic block copolymers (filomicelles) compared with spherical analogues.[116] It was found that the long filomicelles exhibited 10 times longer plasma circulation relatively to the spherical one. Also, the longer filomicelles showed different uptake behavior in flow or static condition. Please note that the filomicelle has a core/shell structure which is similar to the cylindrical PNOs introduced in this article. Another example that showed shape-dependent properties was given by Herrmann et al.[117] Uptake efficiency of rodlike nanoparticles made from DNA−PPO block copolymers by Coca-2 cells was 12 times higher than that of the spherical counterparts. The phenomena related with shape have been confirmed by a recent study on the translocation of various shaped nanoparticles crossing lipid bilayers using computer simulation.[118] As shown in Figure 13b, the authors revealed that a nanoellipsoid, half-lengths of three axes were 1.6 × 3.2 × 6.4 nm, took much less time to cross a bilayer vertically than horizontally, according to the experimental observation in spite of different length scale.[113,115] Though the reason is far from known and still no more reports can be found, the shape of nanoparticles does matter.

Furthermore, shaped polymer nanoparticles have exhibited several advantages in pharmaceutical application. Attributing to their semiflexible conformation and small cross-sectional area, long core/shell filomicelles showed excellent penetration feature relatively to the block polymer vesicles in networks of polymer hydrogels[119] and could reach the tumor stroma.[120] Also, the PEG-*b*-PCL worms demonstrated higher drug-loading capacity to hydrophobically trapping paclitaxel and the maximum tolerated dose doubled to the case of spherical ones, which are important to reveal a better tumor shrinkage effect.[121] Johnson et al. have prepared PEGylated molecular brushes by ROMP, and every repeating unit had a pre-positioned azide group. Then anticancer drugs like doxorubicin were coupled the inside of brushes via photocleavable linkages.[122,123] By UV stimuli, free doxorubicin drugs were released from molecular brushes and exhibited cancer cell toxicity. Therefore, one-dimensional fibril nanoparticles are revealing amazing application that may not find from its spherical counterparts.

6. SUMMARY AND OUTLOOK

The PNOs with attached polymer hairs represent a special kind of polymer nanomaterial. As material objects, they exhibit different shapes like sphere, cylinder, and sheet. As introduced in this Perspective, they have been prepared through strategies of either grafting chemistry or block copolymer self-assembly. The former way is suitable to obtain spherical and wormlike PNOs in smaller size range. By prelocating functionalities, grafting chemistry, and postmodification, such PNOs may have a precisely controlled structure in molecular level in terms of size, arm structure, composition, and surface functionalities. The PNOs from block copolymer self-assembly, especially in bulk, can be more rationally designed and produced. Three basic shapes can be obtained easily by bulk microphase-separated block copolymers of different composition. The polymer hairs are inherited from the unfixed blocks, and thus no grafting chemistry is needed. Therefore, it is suitable to prepare a series of PNOs with different shapes for studying shape induced properties. Moreover the PNOs with Janus hairs and multicompartments can be easily obtained by using triblock copolymers. Though the shape library cannot compare with the cases by top-down microfabrication,[124] the hairy PNOs by bottom-up approach are demonstrating uncompetitive advantages in control of object composition in molecular level and size in nanometer scale.

With rapidly increased attention drawn by the interest in shapes induced properties, more effort should be paid to challenge synthesis of the PNOs with precisely controlled shape and size as well as composition. It may include the following aspects: (1) *Size and size distribution control:* As objects, size and size distribution are very important for understanding their properties. Size distribution is more crucial for self-assembly of PNOs in a more precise way. The size of PNOs, especially those nonspherical ones, should be controlled from tens to

hundreds and even thousands of nanometers. While the size of hairy PNOs can be tuned by changing core size and hair length, the size distribution control for polymer brushes relies on the controlled polymerization. No matter whether prepared by grafting chemistry or self-assembly approaches, spherical PNOs with very low size distribution can be easily obtained. However, even though the backbones can be formed by controlled polymerization, cylindrical polymer brushes by grafting chemistry still show some distribution in length as exampled in Figure 6c,d. In terms of the cylindrical and sheetlike PNOs by block copolymer approach, it is impossible to control their size distribution so far. Conducting a suitable microfabrication from top-down to the self-assembled structures should be a choice. (2) *Simple and efficient synthesis:* The shaped PNOs have a complex core/shell structure and their synthesis is still not an easy work, especially when application is considered. Thus, the methodologies to obtain nonspherical PNOs rationally and facilely are desperately needed. So far it seems that the ROMP of macromonomers is the most efficient way to prepare wormlike PNOs with controlled chain length, low size distribution, and high monomer conversion. Also, the bulk block copolymer approach is very simple to shape PNOs rationally though it is unlikely to control of size along axial direction. (3) *Functionalization:* So far, few reports can be found on functionalization of the PNOs according to the application. Through state-of-art design, the PNOs should be functionalized at the core and surface. Recently, Chen et al. have applied a strategy of co-self-assembly of PTEPM block copolymers with silane coupling agents to functionalize the cores of PNOs with different shapes from the same block copolymer family.[125] In addition to tune microphase structure, the blended silanes bearing functional groups can be enriched and fused into PTEPM domains by cross-linking.

In terms of properties, the functions of polymer hairs and shapes in some aspects have been summarized above, and it shows that the both do matter. Dependent upon the progress of synthesis, the tailor-made PNOs remain to stimulate the research for their unique properties in following aspects. (1) *Precise self-assembly using PNOs*: Provided that the shape, size, and composition could be controlled, precisely assembling PNOs into highly ordered and even complicated structures in nano-, micro-, and macro-scale would be expected. Moreover, the PNOs may be assembled into individual fine structures by manipulation with aid of AFM tips. Since the building block is deformable, the superassemblies would exhibit smart properties. (2) *Mimicking functions of natural shaped particles*: At least in morphology, the PNOs may match with some nanoparticles in biosystems like shaped viruses and DNA regarding the size, shape, flexibility, and surface functionalizability. These features allow scientists to explore how these factors influence their behaviors in order to mimic the functions of those biological items in some aspects. (3) *Properties for biomedical application:* With precisely tailor-made PNOs, a deep understanding the behaviors of PNOs in protein interaction, cell internalization and selection, plasma circulation, and organ distribution will become possible. It will be very important to design novel delivery systems for therapeutic and diagnosis application by tuning shapes and size. (4) *Shape and hairs induced application in material sciences:* Depth understanding how shape and hairs matter the properties of materials in application is still ongoing. The observation of the hairy spheres that may be completely miscible with polymer matrix[85] will stimulate to explore the case of nonspherical nanoobjects.[126]

The development of the shaped PNOs will be driven by properties. The hairy spherical PNOs have already exhibited amazing application in various areas. For example, the PNOs from core cross-linked block copolymers may be functionalized with fluorescent dyes[127,128] and with suparamegnetic γ-Fe_2O_3[129,130] for potential biomedicine applications and may greatly reduce friction of lubricant base oil.[131] While some properties like templating, organizing, and stimuli-responsive shape change are straightforward to design and fulfill, those properties like the behaviors related with biomedicine application are still very limited and even may be not predictable. Thus, it will be more attractive to stimulate researchers to uncover new phenomena of shaped hairy PNOs.

AUTHOR INFORMATION

Corresponding Author

*E-mail: ymchen@iccas.ac.cn.

Biography



Yongming Chen received his Master degree in 1990 from Northwest University at Xi'an in the area of coordination chemistry of rare earths. In 1993, he obtained his Ph.D. from the Institute of Polymer Chemistry, Nankai University in Tianjin, for work on molecular recognition of polymers with Professor B. L. He. From 1994 to 1998, Dr. Chen was Postdoctoral Researcher and later Research Assistant at the Institute of Chemistry, CAS in Beijing, working with Professor F. Xi on dendrimer chemistry. He spent the period 1998−2001 as Postdoctoral Researcher in Germany: first at the Institute of Organic Chemistry and Macromolecular Chemistry II, University of Düsseldorf, working with Professor G. Wulff and later at the Institute of Physical Chemistry, University of Mainz, working with Professor M. Schmidt. Since 2001, Chen is Professor at the Institute of Chemistry of the CAS. Professor Chen's research interests are in the areas of controlled polymerization and synthesis of well-defined polymers, self-assembly, and polymer properties. He also serves as associate editor of *Polymer* journal since 2007 and editorial advisory board of *Macromolecules* since 2011.

ACKNOWLEDGMENTS

This work is supported by the Natural Science Foundation of China (No. 21090350, 21090353, and 50973119).

REFERENCES

(1) Zhao, B.; Zhu, L. *Macromolecules* **2009**, *42*, 9369−9383.
(2) Gao, H. F.; Ohno, S.; Matyjaszewski, K. *J. Am. Chem. Soc.* **2006**, *128*, 15111−15113.
(3) Zheng, G. H.; Pan, C. Y. *Macromolecules* **2006**, *39*, 95−102.

(4) Wan, W. M.; Pan, C. Y. *Macromolecules* **2007**, *40*, 8897−8905.
(5) Chen, Y. M.; Du, J. Z.; Xiong, M.; Zhang, K.; Zhu, H. *Macromol. Rapid Commun.* **2006**, *27*, 741−750.
(6) Sun, G. B.; Guan, Z. B. *Macromolecules* **2010**, *43*, 9668−9673.
(7) Gao, H. F.; Matyjaszewski, K. *Prog. Polym. Sci.* **2009**, *34*, 317−350.
(8) Pyun, J.; Matyjaszewski, K.; Kowalewski, T.; Savin, D.; Patterson, G.; Kickelbick, G.; Huesing, N. *J. Am. Chem. Soc.* **2001**, *123*, 9445−9446.
(9) Li, C. M.; Schmidt, M.; Chen, Y. M. *Abstr. Pap. Am. Chem. Soc.* **2003**, *225*, 511−512.
(10) Guo, X.; Weiss, A.; Ballauff, M. *Macromolecules* **1999**, *32*, 6043−6046.
(11) Wittemann, A.; Drechsler, M.; Talmon, Y.; Ballauff, M. *J. Am. Chem. Soc.* **2005**, *127*, 9688−9689.
(12) Goh, T. K.; Tan, J. F.; Guntari, S. N.; Satoh, K.; Blencowe, A.; Kamigaito, M.; Qiao, G. G. *Angew. Chem., Int. Ed.* **2009**, *48*, 8707−8711.
(13) Zhao, B.; Zhu, L. *J. Am. Chem. Soc.* **2006**, *128*, 4574−4575.
(14) Du, J. Z.; Chen, Y. M. *Macromolecules* **2004**, *37*, 3588−3594.
(15) Guo, A.; Liu, G. J.; Tao, J. *Macromolecules* **1996**, *29*, 2487−2493.
(16) Du, J. Z.; Chen, Y. M. *Macromol. Rapid Commun.* **2005**, *26*, 491−494.
(17) Du, J. Z.; Chen, Y. M. *Macromolecules* **2004**, *37*, 5710−5716.
(18) Hoppenbrouwers, E.; Li, Z.; Liu, G. J. *Macromolecules* **2003**, *36*, 876−881.
(19) Njikang, G.; Han, D. H.; Wang, J.; Liu, G. J. *Macromolecules* **2008**, *41*, 9727−9735.
(20) Hu, J. W.; Liu, G. J. *Macromolecules* **2005**, *38*, 8058−8065.
(21) Zheng, R. H.; Liu, G. J.; Yan, X. H. *J. Am. Chem. Soc.* **2005**, *127*, 15358−15359.
(22) Ishizu, K.; Fukutomi, T. *J. Polym. Sci., Part C: Polym. Lett.* **1988**, *26*, 281−286.
(23) Zhang, K.; Gao, L.; Chen, Y. M. *Macromolecules* **2007**, *40*, 5916−5922.
(24) Zhang, K.; Gao, L.; Chen, Y. *Macromolecules* **2008**, *41*, 1800−1807.
(25) Qin, J. L.; Jiang, X. B.; Gao, L.; Chen, Y. M.; Xi, F. *Macromolecules* **2010**, *43*, 8094−8100.
(26) Saito, R.; Fujita, A.; Ichimura, A.; Ishizu, K. *J. Polym. Sci., Part A: Polym. Chem.* **2000**, *38*, 2091−2097.
(27) Erhardt, R.; Boker, A.; Zettl, H.; Kaya, H.; Pyckhout-Hintzen, W.; Krausch, G.; Abetz, V.; Müller, A. H. E. *Macromolecules* **2001**, *34*, 1069−1075.
(28) Erhardt, R.; Zhang, M. F.; Boker, A.; Zettl, H.; Abetz, C.; Frederik, P.; Krausch, G.; Abetz, V.; Müller, A. H. E. *J. Am. Chem. Soc.* **2003**, *125*, 3260−3267.
(29) Sheiko, S. S.; Sumerlin, B. S.; Matyjaszewski, K. *Prog. Polym. Sci.* **2008**, *33*, 759−785.
(30) Wintermantel, M.; Gerle, M.; Fischer, K.; Schmidt, M.; Wataoka, I.; Urakawa, H.; Kajiwara, K.; Tsukahara, Y. *Macromolecules* **1996**, *29*, 978−983.
(31) Gerle, M.; Fischer, K.; Roos, S.; Müller, A. H. E.; Schmidt, M.; Sheiko, S. S.; Prokhorova, S.; Moller, M. *Macromolecules* **1999**, *32*, 2629−2637.
(32) Zhang, B.; Grohn, F.; Pedersen, J. S.; Fischer, K.; Schmidt, M. *Macromolecules* **2006**, *39*, 8440−8450.
(33) Sheiko, S. S.; Sun, F. C.; Randall, A.; Shirvanyants, D.; Rubinstein, M.; Lee, H.; Matyjaszewski, K. *Nature* **2006**, *440*, 191−194.
(34) Djalali, R.; Li, S. Y.; Schmidt, M. *Macromolecules* **2002**, *35*, 4282−4288.
(35) Stephan, T.; Muth, S.; Schmidt, M. *Macromolecules* **2002**, *35*, 9857−9860.
(36) Jha, S.; Dutta, S.; Bowden, N. B. *Macromolecules* **2004**, *37*, 4365−4374.
(37) Xia, Y.; Kornfield, J. A.; Grubbs, R. H. *Macromolecules* **2009**, *42*, 3761−3766.
(38) Beers, K. L.; Gaynor, S. G.; Matyjaszewski, K.; Sheiko, S. S.; Möller, M. *Macromolecules* **1998**, *31*, 9413−9415.
(39) Neugebauer, D.; Sumerlin, B. S.; Matyjaszewski, K.; Goodhart, B.; Sheiko, S. S. *Polymer* **2004**, *45*, 8173−8179.
(40) Sumerlin, B. S.; Neugebauer, D.; Matyjaszewski, K. *Macromolecules* **2005**, *38*, 702−708.
(41) Gao, H. F.; Matyjaszewski, K. *J. Am. Chem. Soc.* **2007**, *129*, 6633−6639.
(42) Cheng, G. L.; Böker, A.; Zhang, M. F.; Krausch, G.; Müller, A. H. E. *Macromolecules* **2001**, *34*, 6883−6888.
(43) Xia, Y.; Olsen, B. D.; Kornfield, J. A.; Grubbs, R. H. *J. Am. Chem. Soc.* **2009**, *131*, 18525−18532.
(44) Runge, M. B.; Bowden, N. B. *J. Am. Chem. Soc.* **2007**, *129*, 10551−10560.
(45) Runge, M. B.; Dutta, S.; Bowden, N. B. *Macromolecules* **2006**, *39*, 498−508.
(46) Li, Z.; Ma, J.; Cheng, C.; Zhang, K.; Wooley, K. L. *Macromolecules* **2010**, *43*, 1182−1184.
(47) Zhang, Y.; Li, X. K.; Deng, G. H.; Chen, Y. M. *Macromol. Chem. Phys.* **2006**, *207*, 1394−1403.
(48) Deng, G. H.; Chen, Y. M. *J. Polym. Sci., Part A: Polym. Chem.* **2004**, *42*, 3887−3896.
(49) Deng, G. H.; Chen, Y. M. *J. Polym. Sci., Part A: Polym. Chem.* **2009**, *47*, 5527−5533.
(50) Chen, Y. M.; Xiong, X. Q. *Chem. Commun.* **2010**, *46*, 5049−5060.
(51) Zhang, B. Z.; Wepf, R.; Fischer, K.; Schmidt, M.; Besse, S.; Lindner, P.; King, B. T.; Sigel, R.; Schurtenberger, P.; Talmon, Y.; Ding, Y.; Kröger, M.; Halperin, A.; Schlüter, A. D. *Angew. Chem., Int. Ed.* **2011**, *50*, 737−740.
(52) Matyjaszewski, K.; Qin, S. H.; Boyce, J. R.; Shirvanyants, D.; Sheiko, S. S. *Macromolecules* **2003**, *36*, 1843−1849.
(53) Schappacher, M.; Deffieux, A. *Science* **2008**, *319*, 1512−1515.
(54) Zhang, K.; Lackey, M. A.; Wu, Y.; Tew, G. N. *J. Am. Chem. Soc.* **2011**, *133*, 6906−6909.
(55) Boydston, A. J.; Holcombe, T. W.; Unruh, D. A.; Fréchet, J. M. J.; Grubbs, R. H. *J. Am. Chem. Soc.* **2009**, *131*, 5388−5389.
(56) Xia, Y.; Boydston, A. J.; Grubbs, R. H. *Angew. Chem., Int. Ed.* **2011**, *50*, 5882−5885.
(57) Liu, G. J.; Ding, J. F.; Qiao, L. J.; Guo, A.; Dymov, B. P.; Gleeson, J. T.; Hashimoto, T.; Saijo, K. *Chem.—Eur. J.* **1999**, *5*, 2740−2749.
(58) Liu, G. J.; Li, Z.; Yan, X. H. *Polymer* **2003**, *44*, 7721−7727.
(59) Yan, X. H.; Liu, G. J. *Langmuir* **2004**, *20*, 4677−4683.
(60) Tao, J.; Stewart, S.; Liu, G. J.; Yang, M. L. *Macromolecules* **1997**, *30*, 2738−2745.
(61) Won, Y. Y.; Davis, H. T.; Bates, F. S. *Science* **1999**, *283*, 960−963.
(62) Liu, G. J.; Qiao, L. J.; Guo, A. *Macromolecules* **1996**, *29*, 5508−5510.
(63) Liu, G. J.; Yan, X. H.; Duncan, S. *Macromolecules* **2002**, *35*, 9788−9793.
(64) Ulrich, R.; De Chesne, A.; Templin, M.; Wiesner, U. *Adv. Mater.* **1999**, *11*, 141−146.
(65) Qin, J. L.; Chen, Y. M.; Yan, D. D.; Xi, F. *Macromolecules* **2010**, *43*, 10652−10658.
(66) Stewart, S.; Liu, G. *Angew. Chem., Int. Ed.* **2000**, *39*, 340−344.
(67) Yan, X. H.; Liu, G. J.; Liu, F. T.; Tang, B. Z.; Peng, H.; Pakhomov, A. B.; Wong, C. Y. *Angew. Chem., Int. Ed.* **2001**, *40*, 3593−3596.
(68) Zhang, K.; Gao, L.; Chen, Y. M. *Polymer* **2010**, *51*, 2809−2817.
(69) Liu, Y. F.; Abetz, V.; Müller, A. H. E. *Macromolecules* **2003**, *36*, 7894−7898.
(70) Wang, X. S.; Guerin, G.; Wang, H.; Wang, Y. S.; Manners, I.; Winnik, M. A. *Science* **2007**, *317*, 644−647.
(71) Gilroy, J. B.; Gadt, T.; Whittell, G. R.; Chabanne, L.; Mitchels, J. M.; Richardson, R. M.; Winnik, M. A.; Manners, I. *Nature Chem.* **2010**, *2*, 566−570.

(72) Sakamoto, J.; van Heijst, J.; Lukin, O.; Schlüter, A. D. *Angew. Chem., Int. Ed.* **2009**, *48*, 1030−1069.
(73) Bauer, T.; Zheng, Z. K.; Renn, A.; Enning, R.; Stemmer, A.; Sakamoto, J.; Schlüter, A. D. *Angew. Chem., Int. Ed.* **2011**, *50*, 7879−7884.
(74) Wang, J. L.; Li, X. P.; Lu, X. C.; Hsieh, I.-F.; Cao, Y.; Moorefield, C. N.; Wesdemiotis, C.; Cheng, S. Z. D.; Newkome, G. R. *J. Am. Chem. Soc.* **2011**, *133*, 11450−11453.
(75) Song, B.; Wang, Z. Q.; Chen, S. L.; Zhang, X.; Fu, Y.; Smet, M.; Dehaen, W. *Angew. Chem., Int. Ed.* **2005**, *44*, 4731−4735.
(76) Jin, L. Y.; Ahn, J. H.; Lee, M. *J. Am. Chem. Soc.* **2004**, *126*, 12208−12209.
(77) Edmonds, W. F.; Li, Z. B.; Hillmyer, M. A.; Lodge, T. P. *Macromolecules* **2006**, *39*, 4526−4530.
(78) Li, Z. B.; Chen, Z. Y.; Cui, H. G.; Hales, K.; Qi, K.; Wooley, K. L.; Pochan, D. J. *Langmuir* **2005**, *21*, 7533−7539.
(79) Ren, L. X.; Ke, F. Y.; Chen, Y. M.; Liang, D. H.; Huang, J. *Macromolecules* **2008**, *41*, 5295−5300.
(80) Yin, L.; Hillmyer, M. A. *Macromolecules* **2011**, *44*, 3021−3028.
(81) Zhang, K.; Gao, L.; Zhang, C.; Chen, Y. M. *J. Mater. Chem.* **2009**, *19*, 3482−3489.
(82) Walther, A.; Andre, X.; Drechsler, M.; Abetz, V.; Müller, A. H. E. *J. Am. Chem. Soc.* **2007**, *129*, 6187−6198.
(83) Walther, A.; Drechsler, M.; Müller, A. H. E. *Soft Matter* **2009**, *5*, 385−390.
(84) Lindenblatt, G.; Schartl, W.; Pakula, T.; Schmidt, M. *Macromolecules* **2000**, *33*, 9340−9347.
(85) Fischer, S.; Salcher, A.; Kornowski, A.; Weller, H.; Förster, S. *Angew. Chem., Int. Ed.* **2011**, *50*, 7811−7814.
(86) Yezek, L.; Schartl, W.; Chen, Y. M.; Gohr, K.; Schmidt, M. *Macromolecules* **2003**, *36*, 4226−4235.
(87) Cayre, O. J.; Chagneux, N.; Biggs, S. *Soft Matter* **2011**, *7*, 2211−2234.
(88) Helms, B.; Guillaudeu, S. J.; Xie, Y.; McMurdo, M.; Hawker, C. J.; Fréchet, J. M. J. *Angew. Chem., Int. Ed.* **2005**, *44*, 6384−6387.
(89) Chi, Y. G.; Scroggins, S. T.; Fréchet, J. M. J. *J. Am. Chem. Soc.* **2008**, *130*, 6322−6323.
(90) Zhu, L.; Zhao, B. *J. Phys. Chem. B* **2008**, *112*, 11529−11536.
(91) Walther, A.; Hoffmann, M.; Müller, A. H. E. *Angew. Chem., Int. Ed.* **2008**, *47*, 711−714.
(92) Bencherif, S. A.; Gao, H.; Srinivasan, A.; Siegwart, D. J.; Hollinger, J. O.; Washburn, N. R.; Matyjaszewski, K. *Biomacromolecules* **2009**, *10*, 1795−1803.
(93) Liang, M.; Lin, I. C.; Whittaker, M. R.; Minchin, R. F.; Monteiro, M. J.; Toth, I. *ACS Nano* **2010**, *4*, 403−413.
(94) Deng, Z. J.; Liang, M. T.; Monteiro, M.; Toth, I.; Minchin, R. F. *Nature Nanotechnol.* **2011**, *6*, 39−44.
(95) Perrault, S. D.; Walkey, C.; Jennings, T.; Fischer, H. C.; Chan, W. C. W. *Nano Lett.* **2009**, *9*, 1909−1915.
(96) Hu, J. M.; Liu, S. Y. *Macromolecules* **2010**, *43*, 8315−8330.
(97) Lee, H. I.; Pietrasik, J.; Sheiko, S. S.; Matyjaszewski, K. *Prog. Polym. Sci.* **2010**, *35*, 24−44.
(98) Li, C. M.; Gunari, N.; Fischer, K.; Janshoff, A.; Schmidt, M. *Angew. Chem., Int. Ed.* **2004**, *43*, 1101−1104.
(99) Cong, Y.; Gunari, N.; Zhang, B.; Janshoff, A.; Schmidt, M. *Langmuir* **2009**, *25*, 6392−6397.
(100) Wintermantel, M.; Fischer, K.; Gerle, M.; Ries, R.; Schmidt, M.; Kajiwara, K.; Urakawa, H.; Wataoka, I. *Angew. Chem., Int. Ed.* **1995**, *34*, 1472−1474.
(101) Yuan, J. Y.; Xu, Y. Y.; Walther, A.; Bolisetty, S.; Schumacher, M.; Schmalz, H.; Ballauff, M.; Müller, A. H. E. *Nature Mater.* **2008**, *7*, 718−722.
(102) Xu, H.; Sheiko, S. S.; Shirvanyants, D.; Rubinstein, M.; Beers, K. L.; Matyjaszewski, K. *Langmuir* **2006**, *22*, 1254−1259.
(103) Walther, A.; Drechsler, M.; Rosenfeldt, S.; Harnau, L.; Ballauff, M.; Abetz, V.; Müller, A. H. E. *J. Am. Chem. Soc.* **2009**, *131*, 4720−4728.
(104) Khelfallah, N.; Gunari, N.; Fischer, K.; Gkogkas, G.; Hadjichristidis, N.; Schmidt, M. *Macromol. Rapid Commun.* **2005**, *26*, 1693−1697.
(105) Yan, X. H.; Liu, G. J.; Li, Z. *J. Am. Chem. Soc.* **2004**, *126*, 10059−10066.
(106) Rzayev, J. *Macromolecules* **2009**, *42*, 2135−2141.
(107) Bolton, L.; Bailey, T. S.; Rzayev, J. *Nano Lett.* **2011**, *11*, 998−1001.
(108) Yuan, J. Y.; Müller, A. H. E. *Polymer* **2010**, *51*, 4015−4036.
(109) Mullner, M.; Yuan, J. Y.; Weiss, S.; Walther, A.; Fortsch, M.; Drechsler, M.; Müller, A. H. E. *J. Am. Chem. Soc.* **2010**, *132*, 16587−16592.
(110) Li, Z.; Liu, G. J. *Langmuir* **2003**, *19*, 10480−10486.
(111) Yan, X. H.; Liu, G. J.; Haeussler, M.; Tang, B. Z. *Chem. Mater.* **2005**, *17*, 6053−6059.
(112) Mitragotri, S.; Lahann, J. *Nature Mater.* **2009**, *8*, 15−23.
(113) Champion, J. A.; Mitragotri, S. *Proc. Natl. Acad. Sci. U. S. A.* **2006**, *103*, 4930−4934.
(114) Champion, J. A.; Mitragotri, S. *Pharm. Res.* **2009**, *26*, 244−249.
(115) Gratton, S. E. A.; Ropp, P. A.; Pohlhaus, P. D.; Luft, J. C.; Madden, V. J.; Napier, M. E.; DeSimone, J. M. *Proc. Natl. Acad. Sci. U. S. A.* **2008**, *105*, 11613−11618.
(116) Geng, Y.; Dalhaimer, P.; Cai, S. S.; Tsai, R.; Tewari, M.; Minko, T.; Discher, D. E. *Nature Nanotechnol.* **2007**, *2*, 249−255.
(117) Alemdaroglu, F. E.; Alemdaroglu, N. C.; Langguth, P.; Herrmann, A. *Macromol. Rapid Commun.* **2008**, *29*, 326−329.
(118) Yang, K.; Ma, Y. Q. *Nature Nanotechnol.* **2010**, *5*, 579−583.
(119) Kim, Y.; Dalhaimer, P.; Christian, D. A.; Discher, D. E. *Nanotechnology* **2005**, *16*, S484−S491.
(120) Christian, D. A.; Cai, S. S.; Garbuzenko, O. B.; Harada, T.; Zajac, A. L.; Minko, T.; Discher, D. E. *Mol. Pharmaceutics* **2009**, *6*, 1343−1352.
(121) Cai, S. S.; Vijayan, K.; Cheng, D.; Lima, E. M.; Discher, D. E. *Pharm. Res.* **2007**, *24*, 2099−2109.
(122) Johnson, J. A.; Lu, Y. Y.; Burts, A. O.; Xia, Y.; Durrell, A. C.; Tirrell, D. A.; Grubbs, R. H. *Macromolecules* **2010**, *43*, 10326−10335.
(123) Johnson, J. A.; Lu, Y. Y.; Burts, A. O.; Lim, Y.-H.; Finn, M. G.; Koberstein, J. T.; Turro, N. J.; Tirrell, D. A.; Grubbs, R. H. *J. Am. Chem. Soc.* **2011**, *133*, 559−566.
(124) Petros, R. A.; DeSimone, J. M. *Nat. Rev. Drug Discovery* **2010**, *9*, 615−627.
(125) Gao, L.; Zhang, K.; Chen, Y. M. *Polymer* **2011**, *51*, 3681−3686.
(126) Liu, J.; Thompson, Z. J.; Sue, H. J.; Bates, F. S.; Hillmyer, M. A.; Dettloff, M.; Jacob, G.; Verghese, N.; Pham, H. *Macromolecules* **2010**, *43*, 7238−7243.
(127) Li, Z.; Liu, G. J.; Law, S. J.; Sells, T. *Biomacromolecules* **2002**, *3*, 984−990.
(128) Qiu, X. P.; Liu, G. J. *Polymer* **2004**, *45*, 7203−7211.
(129) Liu, G. J.; Yang, H. S.; Zhou, J. Y. *Biomacromolecules* **2005**, *6*, 1280−1288.
(130) Zhou, Z. H.; Liu, G. J.; Hong, L. Z. *Biomacromolecules* **2011**, *12*, 813−823.
(131) Zheng, R. H.; Liu, G. J.; Devlin, M.; Hux, K.; Jao, T. C. *Tribol. Trans.* **2010**, *53*, 97−107.

Macromolecules

Article

pubs.acs.org/Macromolecules

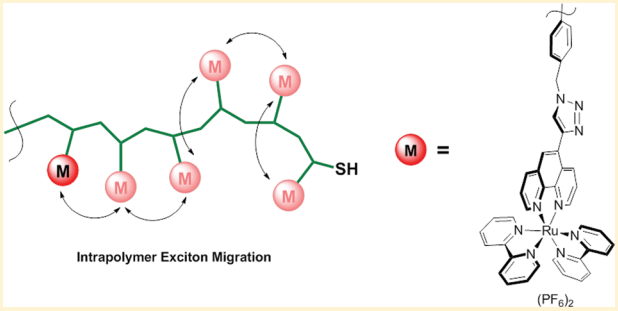
Light Harvesting Arrays of Polypyridine Ruthenium(II) Chromophores Prepared by Reversible Addition−Fragmentation Chain Transfer Polymerization

Yali Sun, Zhuo Chen, Egle Puodziukynaite, Dustin M. Jenkins, John R. Reynolds, and Kirk S. Schanze*

Department of Chemistry and Center for Macromolecular Science and Engineering, University of Florida, Gainesville, Florida 32611, United States

Supporting Information

ABSTRACT: Polystyrene-based polymers that feature pendant Ru(II) polypyridine chromophores have been prepared by using reversible addition−fragmentation chain transfer (RAFT) polymerization combined with the azide−alkyne click reaction. RAFT polymerization was effected using 4-chloromethylstyrene to afford functional polymers with M_n values of 3300 and 8600 g/mol with low polydispersity. Reaction of the resulting poly(4-chloromethylstyrene)s with azide ion afforded the corresponding poly(4-azidomethylstyrene)s, which were further reacted in an azide−alkyne click reaction with (5-ethynyl-1,10-phenanthroline)-bis(2,2-bipyridine)ruthenium(II) to afford the chromophore loaded polymers. The reactions were followed by using nuclear magnetic resonance and infrared spectroscopy, and the results suggest that the click reactions lead to nearly quantitative functionalization of the azidomethyl functional polymers. The photophysical and electrochemical properties of the Ru functional polymers were characterized in solution. Emission quantum yield and lifetime studies reveal that the metal-to-ligand charge transfer excited state is quenched in the polymers relative to a model Ru complex chromophore. This finding indicates that the thiol end-group on the polymers that arises from the thiocarbonylthio RAFT chain transfer agent is able to quench the MLCT state, presumably by a charge transfer mechanism. Stern−Volmer quenching studies show that the polymers are quenched with very high efficiency by negatively charged ions compared to model systems, revealing amplified quenching takes place.



INTRODUCTION

Polymeric chromophore systems of interest for light harvesting applications and fundamental studies of energy (exciton) transport have attracted considerable attention over the past two decades due to their potential for employment in photosensitization, catalysis and photoenergy conversion.[1−16]

As part of a coordinated effort within the Solar Fuels Energy Frontier Research Center,[17] our interest lies in developing light harvesting metallopolymer chromophore assemblies with controlled structures for use in artificial photosynthesis and solar fuel cells (Scheme 1). Ruthenium(II) polypyridine complexes have been widely investigated from a fundamental standpoint,[18] as well as for application in artificial photosynthesis, dye-sensitized photovoltaic cells, and sensors owing to their robust and tunable photochemical, photophysical and electrochemical properties.[19−25]

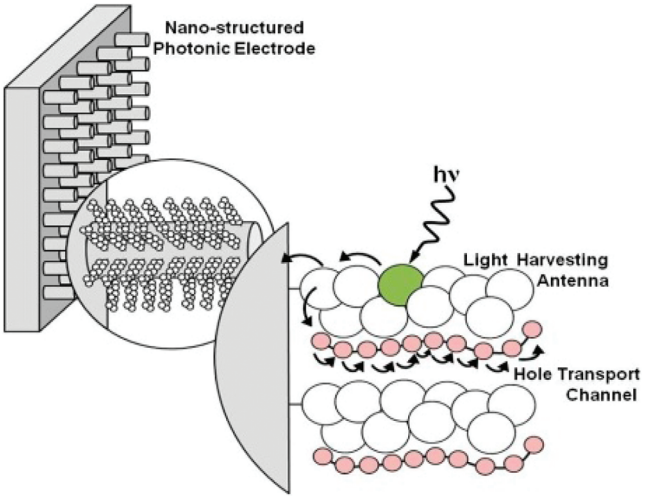
Metallopolymer structures resulting from the incorporation of ruthenium(II) polypyridine pendant moieties into a polystyrene scaffold can function as a light-harvesting antenna system, producing a polymeric array with a combination of beneficial properties such as high optical cross section, excellent photostability, luminescence, long excited state lifetime, and efficient charge and/or exciton transport over nanoscale distances.

Several groups have previously investigated the synthesis, photophysical and electrochemical properties of polymers that feature pendant metal complexes.[6,7,10,26,27] These studies provided insight concerning the mechanism and dynamics of charge/exciton transport in polymeric chromophore assemblies featuring long-lived triplet metal to ligand charge transfer (MLCT) excited states. Specifically, Meyer, Papanikolas and co-workers reported on a series of copolymers consisting of a styrene backbone having Ru(II) and Os(II) pendants linked to the polymer via ether or amide functionalities.[6,7,10] Studies of the amide-linked polymers involved a combined approach utilizing experimental photoluminescence studies and Monte Carlo simulations and concluded that MLCT excitons are transported along the chains efficiently by a site-to-site hopping mechanism with a time constant falling between 1−4 ns.[6,10] Additionally, our group reported the photophysics and luminescence quenching of a series of copolymers that contained a conjugated poly(phenylene ethynylene) backbone derivatized with pendant Ru(II) and Os(II) polypyridine chromophores.[12] These polymers exhibited an amplified

Received: December 28, 2011
Revised: February 12, 2012
Published: March 5, 2012

ACS Publications © 2012 American Chemical Society

Scheme 1. Illustration of functional metallopolymer assemblies with controlled pattern adsorbed on photonic electrode. Reproduced from ref 17 with permission. Copyright Springer 2011.



quenching effect,[28−30] which was interpreted as evidence for exciton transport within the polymers via the conjugated polymer backbone and/or by self-exchange hopping between adjacent metal complex chromophores. Dendritic chromphore arrays have also been studied, and the quenching dynamics of $[Ru(bpy)_3]^{2+}$-pendant poly(amidoamine) (PAMAM) dendrimers exhibit a structural dependency.[31,32] In addition, electrostatic attraction between the positively charged dendrimers and negatively charged quenchers results in larger Stern−Volmer quenching constants (K_{sv}) when compared to the small molecule reference complex $[Ru(bpy)_3]^{2+}$.

Reversible addition−fragmentation chain transfer (RAFT) polymerization allows construction of polymers with well-defined molecular weights and lower molecular weight polydispersity (PDI) compared to traditional free radical polymerization methods.[33−39] Additionally, due to monomer functional group tolerance, polymers can be prepared with specific chemical functionalities allowing for further functionalization, such as reactions that fall within the scope of "click chemistry". The azide−alkyne Huisgen cycloaddition is a prototypical "click chemistry" reaction, well-known for its high yield and straight-forward product purification.[40−44] This "click" reaction proceeds under mild reaction conditions at room temperature, and consequently is not expected to affect the polymer backbone, degree of cross-linking, or structure of the chromophore units such as the polypyridine ruthenium complexes that are the focus of this work.

Herein, we present the synthesis of a novel polymer system consisting of a polystyrene backbone, fabricated by RAFT polymerization, functionalized with pendant (phen)-$Ru^{II}(bpy)_2^{2+}$ complex units attached via the phenanthroline ligand to the polymer backbone by the azide−alkyne Huisgen cycloaddition click reaction (phen =1,10-phenanthroline and bpy =2,2′-bipyridine). Two different narrow polydispersity polymers were prepared by RAFT polymerization of 4-chloromethylstyrene leading to polymers containing *ca.* 20 and 50 repeat units; the chloromethyl groups were converted to azidomethyl residues via a postpolymerization substitution reaction followed by the azide−alkyne click reaction used to attach (phen)$Ru^{II}(bpy)_2^{2+}$ units to each polystyrene repeat unit. The photophysical and electrochemical properties of the Ru−polypyridine units were preserved in the polymer, and evidence was found for exciton migration to the thiol (−RSH) functionality at the end of the polymer chains. The aforementioned "amplified quenching" effect was also discovered to be present and has been elucidated with studies involving oppositely charged ionic quenchers.

EXPERIMENTAL SECTION

General. All solvents and chemicals used for synthesis were reagent grade and used as received from commercial suppliers without further purification unless noted. All organic solvents used for photophysical and quenching studies were HPLC grade. Deionized water was obtained using a Millipore purification system. 1,10-Phenanthroline (phen) and 4-vinylbenzyl chloride (4-VBC) were purchased from Fisher Scientific. Copper(I) iodide, sulfuric acid, fuming 20% as free SO_3, 2,2′-azobis(isobutyronitrile) (AIBN), *N*,*N*,*N*′,*N*′,*N*″-pentamethyldiethylenetriamine (PMDETA), ammonium hexafluorophosphate and tetrabutylammonium hexafluorophosphate ((TBA)PF_6) were purchased from Aldrich Chemical Co. Bromine, trimethylsilylacetylene, and bis(triphenylphosphine)palladium(II) dichloride ($Pd(PPh_3)_2Cl_2$) were obtained from Acros, GFS Chemicals, and Strem Chemicals, respectively. AIBN and (TBA)PF_6 were recrystallized twice from ethanol and dried in vacuum before being used as initiator and supporting electrolyte, respectively. The syntheses of 5-bromo-1,10-phenanthroline (5-Brphen),[45] benzyl azide,[46] cis-$Ru(bpy)_2Cl_2{\cdot}2H_2O$,[47] and 2-cyanoprop-2-yl 1-dithionaphthalate (CPDN)[48] were carried out according to the published procedures. The structural characterization of the new compounds was confirmed by ^1H and ^{13}C NMR, electrospray-time-of-flight (ESI−TOF) mass spectrometry, Fourier transform infrared spectroscopy (FTIR) and/or elemental analysis.

Characterization and Physical Measurement. ^1H NMR and ^{13}C NMR spectra were recorded on a Varian VXR 300 or Mercury-300 spectrometer, and all chemical shifts are referenced to the residual solvent signals, 7.26 ppm in $CDCl_3$, 1.94 ppm in CD_3CN and 3.31 ppm in CD_3OD, respectively. ESI-TOF mass spectra were measured by an Agilent 6210 TOF-MS spectrometer. The FT-IR spectra were obtained as KBr disks with a Perkin-Elmer Spectrum One FT-IR spectrometer at a resolution of 0.5 cm^{-1}. Elemental analysis was performed on an Eager 200. Gel permeation chromatography (GPC) analyses were carried out on a system comprised of a Rainin Dynamax SD-200 pump and a Beckman Instruments Spectroflow 757 absorbance detector.

All photophysical experiments were conducted using 1 cm^2 square quartz cuvettes fitted with a serum cap. All samples were prepared as optically dilute solutions in HPLC grade organic solvents or deionized water. The sample solutions were deaerated with argon gas for 30 min for organic solution and 90 min for aqueous solution prior to photopysical measurements except for UV−visible absorption. Steady-state UV−visible electronic absorption spectra in solution were measured on a Varian-Cary 50 Bio UV−visible spectrophotometer. Steady-state emission spectra, corrected for instrument response, were recorded on a spectrofluorometer from Photon Technology International (PTI). Photoluminescence lifetimes were obtained by using a single photon counting Fluo Time 100 (Picoquant) fluorescence lifetime spectrometer and excitation was provided using a PDL 800-B picosecond pulsed diode laser operating at 370 nm. The excited-state lifetimes were obtained from exponential fit of all wavelength emission transients in FluoFit software with goodness-of-fit determined by visual inspection of the residuals. Emission quantum yields, Φ_{em}, were measured in optically dilute (absorbance <0.1) methanol or acetonitrile solutions at RT relative to $[Ru(bpy)_3]Cl_2$ in air saturated H_2O, where Φ_{em} is 0.0379 in air-saturated water vs in degassed water reported as 0.055.[49]

Electrochemistry was performed in spectrophotometric grade acetonitrile solutions containing 0.1 M tetrabutylammonium hexfluorophosphate ((TBA)PF_6) as the supporting electrolyte using a single-compartment three-electrode cell with a platinum flag as the counter electrode, a non-aqueous Ag/Ag^+ electrode calibrated vs Fc/

dx.doi.org/10.1021/ma202804u | *Macromolecules* 2012, 45, 2632−2642

Fc^+ in 0.1 M (TBA)PF_6 aceonitrile solutions ($E_{1/2}(Fc/Fc^+)$ = 0.14 V vs Ag/Ag^+) as a reference electrode, and a platinum disk (0.02 cm^2) as the working electrode. An EG&G Princeton Applied Research model 273A potentiostat/galvanostat was used under the control of Corrware II software from Scribner and Associates. All electrochemical measurements were carried out in an argon-filled drybox (Vacuum Atmosphere). All $E_{1/2}$ values were calculated from (E_{pa} + E_{pc})/2, and were converted to $E_{1/2}$ vs saturated calomel electrode (SCE) using $E_{1/2}(Fc/Fc^+)$ = +395.6 mV vs SCE.

Synthesis. *5-Ethynyl-1,10-phenanthroline (5-CC-phen).* Pd$(PPh_3)_2Cl_2$ (62.5 mg, 0.0975 mmol, 10 mol %) and copper(I) iodide (20.75 mg, 0.1075 mmol, 11 mol %) were added to a deaerated solution of 5-bromo-1,10-phenanthroline (250 mg, 0.975 mmol) in 30 mL of THF and 10 mL of diisopropylamine. The resulting mixture was degassed by gently bubbling with argon for 30 min. Subsequently, trimethylsilylacetylene (~0.2 mL, 1.5 mmol) was added to the mixture, which was stirred at ambient temperature for 24 h to produce a black-brown colored mixture. After the reaction finished, the solvent was evaporated under vacuo and the residue was dissolved in 20 mL of methanol. An aqueous KCN solution of 10 mL (50 mg/10 mL of H_2O) was added to the solution, which was sonicated for 1 h at room temperature. After that, most of the solvent was evaporated. The residual solution was extracted with dichloromethane. The organic layers were collected, and the solvent was evaporated under vacuo. The crude product was chromatographed on silica gel using CH_2Cl_2/methanol (95/5) as the eluent to give the compound in beige color (140 mg, 70% yield). ^{1}H NMR (300 MHz, $CDCl_3$), δ: 9.22 (m, 2H), 8.76 (dd, J_1 = 1.8 Hz, J_2 = 8.4 Hz, 1H), 8.22 (dd, J_1 = 1.8 Hz, J_2 = 8.1 Hz, 1H), 8.09 (s, 1H), 7.73 (m, 1H), 7.66 (m, 1H), 3.56 (s, 1H). ESI–MS (TOF): m/z 205.07 ($[M + H]^+$), 409.14 ($[2M + H]^+$).

*[Ru(bpy)$_2$(5-CC-phen)](PF$_6$)$_2$ (**1**).* A mixture of 5-CC-phen (140 mg, 0.686 mmol) and *cis*-Ru$(bpy)_2Cl_2\cdot 2H_2O$ (364 mg, 0.70 mmol) in 30 mL of EtOH/H_2O (1:1) was refluxed under argon in the dark overnight to give a clear red solution. After cooling to room temperature, most of the solvent was removed by rotary evaporation. Then, an excess of saturated aqueous NH_4PF_6 solution was added dropwise to the aqueous residue under vigorous stirring to produce a precipitate which was collected on a sintered glass crucible by suction filtration. The final product was washed three times with water and diethyl ether. The crude product was purified by column chromatography on silica with acetonitrile and water (85: 15, v/v) with 0–0.2% saturated aqueous KNO_3 solution as eluent to obtain the compound in red color (560 mg, 90% yield). ^{1}H NMR (300 MHz, CD_3CN), δ: 8.86 (dd, J_1 = 1.5 Hz, J_2 = 8.4 Hz, 1H,), 8.5 (m, 6H), 8.08 (m, 4H), 8.98 (m 2H), 7.80 (m, 3H), 7.76 (m, 1H), 7.52 (ddm, J_1 = 1.8 Hz, J_2 = 12 Hz, 2H), 7.44 (tm, J = 6 Hz, 2H), 7.21 (m, 2H), 4.13 (s, 1H). ^{13}C NMR (75 MHz, CD_3CN), δ: 157.31, 157.03, 153.37, 153.14, 152.10, 152.07, 152.05, 147.65, 147.64, 137.99, 137.86, 136.65, 135.11, 132.85, 130.92, 130.34, 127.64, 127.51, 126.67, 126.63, 124.35, 124.27, 120.64, 86.66, 78.06. ESI–MS (TOF): m/z 309.05 ($[M - 2PF_6]^{2+}$), 763.07 ($[M - PF_6]^+$).

*[Ru(bpy)$_2$(5-benzyl-triazole-phen)](PF$_6$)$_2$ (**2**).* A mixture of benzyl azide (3.27 mg, 0.024 mmol) and $[Ru(bpy)_2(5\text{-CC-phen})](PF_6)_2$ (21.8 mg, 0.024 mmol), CuBr (3.44 mg, 0.024 mmol), PMDETA (4.16 mg, 0.024 mmol) in 0.5 mL of DMF was degassed under argon for 40 min. Then the mixture was stirred at ambient temperature for 48 h. After the reaction was complete, a large amount of ether was added to obtain a precipitate, which was collected by centrifugation. The crude product was dissolved in acetonitrile, an insoluble impurity was separated by centrifuge, and the acetonitrile solution was evaporated by rotary evaporation. This dissolve-precipitation process was repeated for several times until any insoluble material was completely removed. Finally, the target compound was precipitated in diethyl ether (23 mg, 92% yield). ^{1}H NMR (300 MHz, CD_3CN), δ: 9.36 (dd, J_1 = 0.9 Hz, J_2 = 8.7 Hz, 1H), 8.53 (m, 6H), 8.10 (m, 4H), 7.99 (m, 2H), 7.85 (d, J = 5.7 Hz, 2H), 7.76 (m, 2H), 5.57 (m, 2H), 7.44 (m, 8H), 7.22 (m, 2H), 5.73 (s, 2H). ^{13}C NMR (75 MHz, CD_3CN), δ: 158.80, 158.32, 153.86, 153.30, 139.19, 139.07, 138.01, 137.35, 130.39, 129.96, 129.56, 128.88, 128.76, 127.70, 127.37, 126.13, 125.60, 55.29. ESI–MS (TOF): m/z 375.59 ($[M - 2PF_6]^{2+}$), 896.14 ($[M - PF_6]^+$).

Poly(4-vinylbenzyl chloride) (PVBC, DP = 20). To a 10 mL Schlenk tube with a stirring bar was added 4-vinylbenzyl chloride (4.10 g, 26.86 mmol), CPDN (146.0 mg, 0.54 mmol), and AIBN (22.0 mg, 0.13 mmol). The solution was deoxygenated by bubbling argon for 30 min. Then the flask was immersed in an oil bath which was maintained at 80 °C for 8 h. Subsequently, the flask was put in an ice bath to quench the polymerization reaction. The crude polymer was dissolved in THF, and the solution was dropwise added to methanol to produce a solid precipitate. This dissolve–precipitation process was repeated three times to obtain the final polymer as a pink powder (2.10 g, 50% yield). ^{1}H NMR (300 MHz, $CDCl_3$), δ: 6.75–7.4 (sb, 2H,), 6.25–6.75 (sb, 2H), 4.52 (sb, 2H), 1.45–2.0 (mb, 2H). GPC: M_n ~ 3100 g/mol, PDI = 1.12.

Poly(4-vinylbenzyl chloride) (PVBC, DP = 50). The title compound was synthesized following the synthetic procedure for PVBC, DP = 20, except 4-vinylbenzyl chloride (4.10 g, 26.86 mmol), CPDN (73.0 mg, 0.27 mmol), and AIBN (5.5 mg, 0.0325 mmol) were used, and the reaction time was extended to 16 h. The product PVBC, DP~50 (1.20 g) was obtained with the conversion yield of 29.2%. GPC: M_n ~ 8600 g/mol, PDI = 1.21.

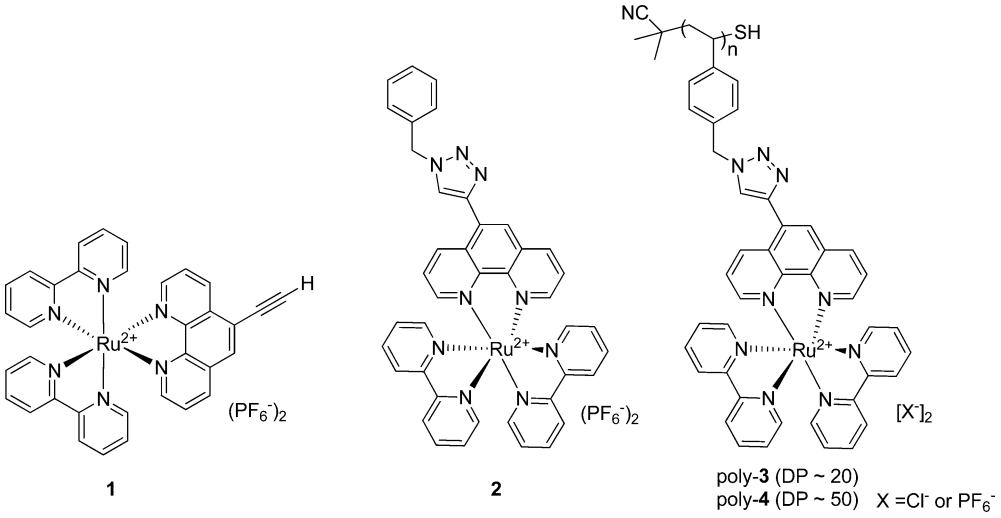
Poly(4-vinylbenzyl azide) (PVBA, DP = 20). A solution of PVBC (1.0 g, 6.58 mmol of polymer repeat units) and NaN_3 (1.26 g, 19.4 mmol) in DMF (100 mL) was stirred at room temperature for 24 h. (*Caution! Sodium azide is highly toxic and presents a severe explosion risk when shocked, heated, or treated with acid.*) Then the polymer was precipitated from methanol. This dissolve-precipitation process was repeated three times. The final product was dried in vacuo for 24 h to obtain the product as a white powder (0.85 g, 90% yield). ^{1}H NMR (300 MHz, $CDCl_3$), δ: 6.75–7.4 (sb, 2H,), 6.25–6.75 (sb, 2H), 4.27 (sb, 2H), 1.45–2.0 (mb, 2H). GPC: M_n ~ 3000 g/mol, PDI = 1.11.

Poly(4-vinylbenzyl azide) (PVBA, DP = 50). The title compound was synthesized following the synthetic procedure for PVBA, DP = 20. The product PVBA, DP ~ 50 was obtained with the conversion yield of 97% (0.92 g). GPC: M_n ~ 8900 g/mol, PDI = 1.27.

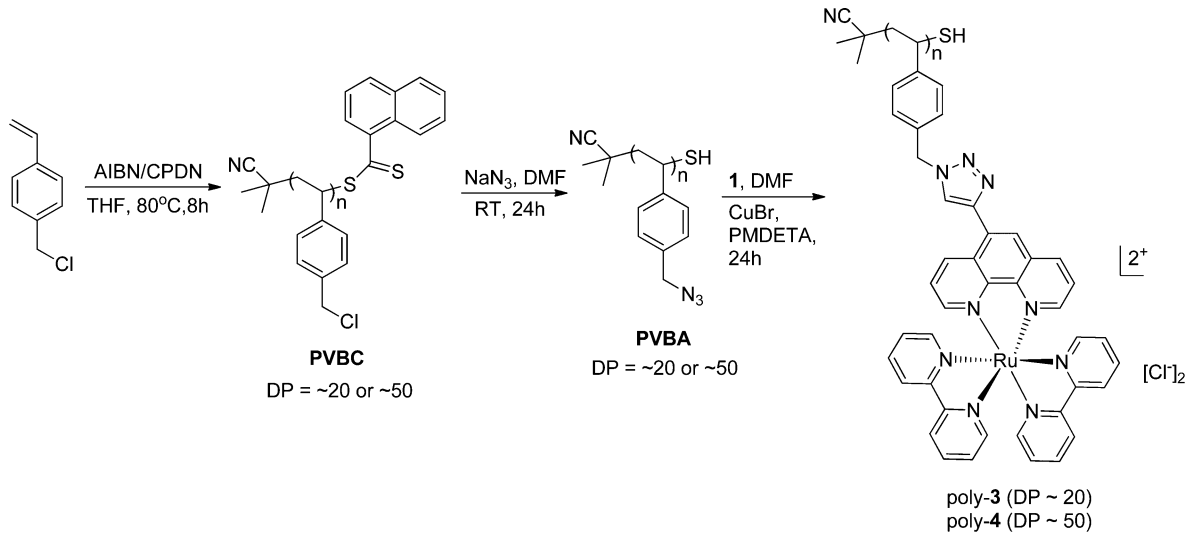
*Poly-**3**.* A solution of PVBA (17.5 mg, 0.11 mmol) and **1** (110 mg, 0.12 mmol) in DMF (~3 mL) in a small vial was degassed with argon for 30 min. Subsequently, copper(I) bromide (17.2 mg, 0.12 mmol) and PMEDTA (20.8 mg, 0.12 mmol) were added. The mixture was stirred at ambient temperature for 44 h under argon atmosphere protection. After the reaction was complete, a large amount of ethanol was added to produce a precipitate. Then the majority of liquid was removed by decanting with a pipet, and the residual solid was rinsed with ethanol several times. The crude product was dissolved in acetone in a centrifuge tube. After centrifugation, the insoluble impurity was precipated to the bottom of the tube; the clear acetone supernatant solution was decanted into a round-bottom flask, and the solvent was removed by rotary evaporation. This dissolve–centrifuge–evaporation procedure was repeated three times. Finally, the polymer product was metathesized to the chloride salt by precipitation of an acetone solution of the PF_6^- salt from a saturated tetrabutylammonium chloride/acetone solution. The chloride salt of the polymer was dissolved in water and purified by dialysis with a membrane with MWCO = 12–14 kDa. The product poly-**3** was obtained with the conversion yield of 36% (36 mg). ^{1}H NMR (300 MHz, CD_3CN), δ: 7–9 ppm (mb), 5.56 (sb). Anal. Calcd for $C_{864}H_{667}F_{240}N_{181}P_{40}Ru_{20}S$ (n ~ 20): C, 48.41; H, 3.14, N, 11.83. Found: C, 45.84; H, 3.06; N, 10.13.

*Poly-**4**.* The title compound was synthesized following the synthetic procedure for poly-**3**, only except PVBA (DP ~ 50) (17.5 mg, 0.11 mmol) was used. The product poly-**4** was obtained with the conversion yield of 50% (50 mg). Anal. Calcd for $C_{2199}H_{1702}F_{600}N_{466}P_{100}Ru_{50}S$ (n ~ 55): C, 48.69; H, 3.17, N, 12.04. Found: C, 51.36; H, 4.10; N, 11.65.

Chart 1



Scheme 2



RESULTS AND DISCUSSION

Synthesis and Characterization of Ru-Pendant Polystyrenes. The chemical structures of the ruthenium complexes and the chromophore loaded polymers that were the focus of the investigation are shown in Chart 1. Complex **1** is a synthetic intermediate having a terminal acetylene group at the 5-position of phenanthroline ligand. Complex **2**, containing the same trizole functionality as the pendant chromophores, serves as a model complex for the polymers with regard to photophysical, electrochemical and emission quenching properties. Polymers poly-**3** and poly-**4** feature a polystyrene backbone with approximately 20 and 50 pendant ruthenium light harvesting units per polymer chain, respectively.

The ruthenium functionalized polymers were synthesized by the sequence shown in Scheme 2. In this approach, 4-vinylbenzyl chloride (4-VBC) was chosen as the monomer due to the stability of the chloromethyl substituent with respect to the RAFT polymerization conditions. It is quantitatively converted to the azidomethyl group in a post polymerization substitution reaction. RAFT polymerization of 4-VBC afforded a chloromethyl-substituted polystyrene (PVBC), which displayed an off-white (faint pink) color attributed to the dithioester end group introduced by the chain transfer reagent CPDN.

By adjustment of the reaction conditions and stoichiometry, two samples of PVBC were prepared with M_n of 3100 g/mol (DP ~ 20) and 8600 g/mol (DP ~ 50); both samples exhibited low polydispersity. Subsequent to polymerization, the PVBC samples were converted to the corresponding azidomethyl-subsituted polymers (PVBA) by treatment with sodium azide. GPC analysis of the PVBA samples revealed that the chloromethyl to azidomethyl conversion resulted in little change of the M_n and PDI of the samples. Additionally, the faint pink color characteristic of the PVBC samples was lost during the azide treatment, and the product PVBA samples were colorless (white). As outlined below, the photophysical properties of the polymers are sensitive to the nature of the end-group, and therefore we explored this effect in more detail. UV−visible absorption spectroscopy shows that the absorption band with λ_{max} ~ 320 nm that arises from the naphthalene dithioate unit disappears upon conversion of PVBC to PVBA (Supporting Information, Figure S1). We believe that the loss of this transition signals that the naphthalene dithioate unit is cleaved to a thiol (R−SH) end group during the reaction with

dx.doi.org/10.1021/ma202804u | Macromolecules 2012, 45, 2632−2642

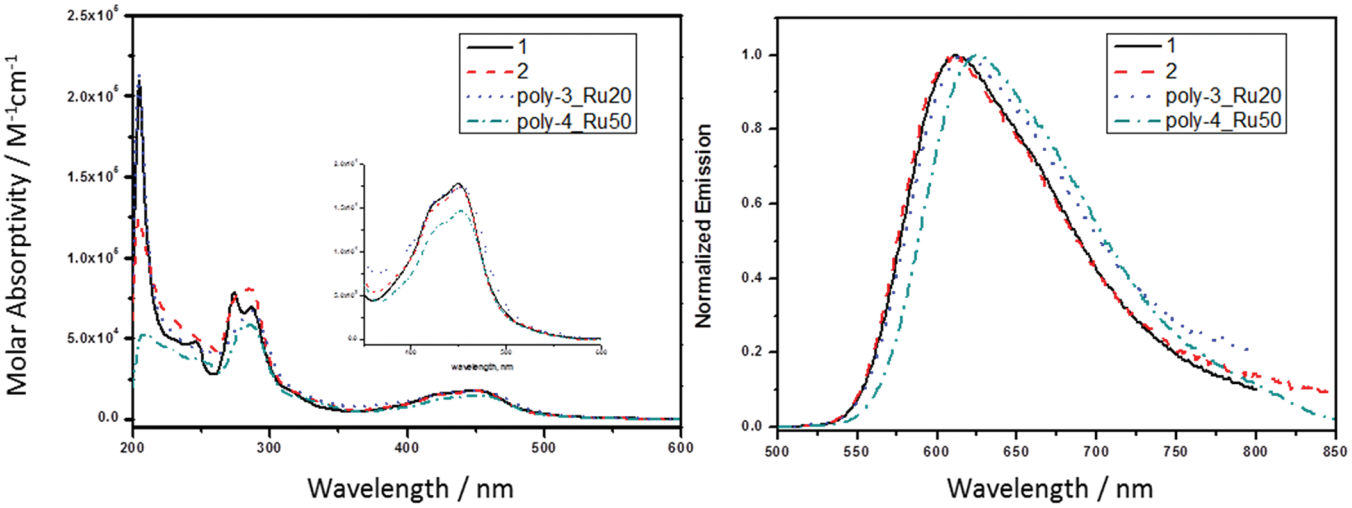


Figure 1. Ground state absorption (left) and emission (right) spectra of **1** (——), **2** (---), poly-**3** (···), and poly-**4** (-·-·-) in CH_3OH solution. Molar absorptivity values for the polymers are determined based on the polymer repeat unit concentration.

azide. Thus, as shown in Scheme 2, it is believed that for PVBA samples and the corresponding Ru-pendant polymers the polymer end groups are thiols, R−SH.

The transformation from PVBC to PVBA was monitored by ^{1}H NMR and FT-IR (Figures S2 and S5 in Supporting Information). Quantitative transformation was demonstrated by the complete loss of the resonance at 4.52 ppm for the benzylic $-CH_2Cl$ group in PVBC coupled with the appearance of a peak at 4.27 ppm due to the $-CH_2N_3$ methylene (Figure S2, Supporting Information). A strong band was observed in the infrared spectrum of PVBA at 2090 cm^{-1} which was not in the spectrum of PVBC; this feature arises from the unsymmetrical stretching mode of the azide unit.[50] As noted above, comparative GPC analysis of the PVBC and PVBA samples (Figure S5 in Supporting Information) concluded that there was not a significant difference in M_n or PDI values for the two systems, indicating that the polymer backbone was not affected by the substitution reaction.

The ruthenium-containing polymers (poly-**3** and poly-**4**) were obtained by grafting the (5-CC-phen)$Ru^{II}(bpy)_2^{2+}$ complex **1** onto the polystyrene backbone via a "click" reaction between the azide functionality of PVBA and the terminal alkyne unit in **1**. The polymers were prepared as chloride salts which were soluble in water, methanol and DMF; portions of the materials were converted, via counterion metathesis, to the hexafluorophosphate salts, which were soluble in acetone, acetonitrile and DMF. Note that the solubility of the polymers parallels that of the Ru(II) monomer complexes. The infrared spectrum of poly-**3** (DP ∼ 20) revealed that the band due to the azide stretch at ∼2100 cm^{-1} was completely absent (Figure S4, Supporting Information), indicating that the click reaction was essentially quantitative. By contrast for poly-**4** (DP ∼ 50) there was a small residual peak at ∼2100 cm^{-1} suggesting that in this system there was a small amount of unreacted residual azidomethylstyrene repeats remaining after the click reaction.

The ^{1}H NMR spectra of the ruthenium-grafted polymers was dominated by the resonances due to the phenanthroline and bipyridine ligands (Figure S3, Supporting Information) in the aromatic region. The resonances were very broad, and additionally the signals for the polystyrene backbone, and the benzylic methylene group attached to the triazole ring could not be discerned. These features are likely due to the fact that the ruthenium-functionalized polymers adopt a relatively rigid structure and the signals are broad due to the low conformational mobility of the polymer backbone in solution. Moreover, the characteristic resonance for the benzylic methylene group was broad and slightly shifted upfield to 5.56 ppm relative its position in model complex **2** where it appeared at 5.73 ppm.

Absorption and Photoluminescence Spectroscopy. The electronic absorption spectra of the ruthenium complexes and polymers were recorded at room temperature in deaerated methanol solution (Figure 1). All four chromophores displayed similar spectra which are characteristic of the ruthenium(II) polypyridyl complexes. Specifically, they each featured strong absorption bands in the UV region with maxima at ∼280 and 205 nm due to intraligand $\pi-\pi^*$ transitions, along with a moderately intense transition (∼1.5−1.7 × 10^4 M^{-1} cm^{-1}) in the visible region with λ_{max} ∼ 450 nm arising from dπ(Ru) to π^*(ligand) metal-to-ligand charge transfer (MLCT).[18,51] Note that the polystyrene backbone did not significantly contribute to absorption in the UV region because the phenyl-localized transitions are orbitally forbidden and therefore relatively weak compared to the transitions localized on the metal complex chromophores.

Steady-state emission spectra were measured in deaerated methanol solutions at room temperature upon 450 nm excitation. Each complex and polymer featured a broad and moderately intense luminescence with a corrected maximum at λ_{max} ∼ 610−620 nm arising from the ruthenium-localized MLCT excited state. Interestingly, the emission from the polymers was red-shifted relative to that of the model complex **2**. Specifically, for poly-**3** (DP ∼ 20), the maximum is shifted by 7 nm, and for poly-**4** (DP ∼ 50), the λ_{max} was red-shifted by 12 nm compared to the band maximum for complexes **1** and **2**. This result shows that the red-shift depends on the polymer chain length, with a greater shift occurring for the longer polymer. Despite the shift in maximum, the band shape of the MLCT emission from the polymers is essentially identical to that for the monomeric complexes. The similarity of the emission spectral bandshapes and relatively small shifts in emission maxima indicate that attachment to the polymer backbone does not significantly influence the emissive excited state of the pendent ruthenium chromophores. The shift in band maxima for the polymers may arise from the

dx.doi.org/10.1021/ma202804u | Macromolecules 2012, 45, 2632−2642

Table 1. Photophysical and Electrochemical properties of Complexes and Polymers[a]

compounds	absorption λ_{max} (nm) ($\varepsilon/10^4$ M^{-1} cm^{-1}) $\pi-\pi^*$	absorption λ_{max} (nm) ($\varepsilon/10^4$ M^{-1} cm^{-1}) $d\pi-\pi^*$	λ_{em}/nm	τ/ns (α)[b]	ϕ_{em}	$E_{1/2}^{ox}$/V	$E_{1/2}^{red}$/V
1	287 (6.95) 274 (7.82)	448 (1.78)	612	CH_3OH: 961 ns ACN: 1.30 μs	0.080	1.31	−1.21
2	286 (8.09) 287 (7.92)	450 (1.75)	612	CH_3OH: 947 ns ACN: 1.02 μs	0.108	1.29	−1.28, −1.50, −1.76
poly-**3**	287 (6.71)	452 (1.75)	619	τ_1 = 83 (0.71) τ_2 = 419 (0.29) $\langle\tau\rangle$ = 122	0.023	N/A	N/A
poly-**4**	286 (5.84)	452 (1.47)	624	τ_1 = 123 (0.45) τ_2 = 524 (0.55) $\langle\tau\rangle$ = 288	0.031	N/A	N/A
poly-**3** (PF_6^-)[c]	287 (6.07)	451 (1.64)	623	τ_1 = 132 (0.44) τ_2 = 814 (0.56) $\langle\tau\rangle$ = 456	0.009	1.33	−1.51, −1.81

[a]Measured in CH_3OH solution unless indicated otherwise. Electrochemical potentials determined by cyclic voltammetry with Pt working electrode in acetonitrile solution containing 0.1 M (TBA)PF_6, scan rate of 100 mV/s, using ferrocene/ferrocenium (Fc/Fc^+) as an external standard. Listed potentials are corrected to be relative to saturated calomel electrode (SCE). [b]$\langle\tau\rangle$ is median lifetime calculated as $\langle\tau\rangle = \sum\alpha_i\tau_i$. [c]Measured in acetonitrile (ACN) solution.

heterogeneity in the microenvironment experienced by the individual chromophores in the polymeric arrays.

Quantum yields and decay lifetimes for the MLCT emission for the two complexes and the two polymers are listed in Table 1. Several points are of interest regarding this data. First, the emission quantum yields and lifetimes for the model complexes **1** and **2** were similar to one another, and are typical for Ru-polypyridine complexes such as $Ru(bpy)_3^{2+}$.[18] From this we conclude that the ethynyl and triazole substituents on the phenanthroline ligand do not affect the radiative and nonradiative decay dynamics of the MLCT state. Second, the emission quantum yields for the polymer samples were markedly lower than for the monomer complexes, with ϕ_{em} = 2.3 and 3.1%, for poly-**3** and poly-**4**, respectively. Concurrently it was also observed that the emission decays for the polymers were biphasic, and exhibited a substantially faster decay profile compared to the models (note the significantly lower $\langle\tau\rangle$ values). Another important point to be discussed further below is the fact that the emission lifetime and yield were lower for poly-**3** than for poly-**4**, suggesting that the quenching pathway may be enhanced at lower DP.

The reduced emission yields and lifetimes for the polymer samples revealed that the rate of nonradiative decay was enhanced in these materials. In previous studies by Meyer and co-workers of a set of polystyrene-based polymers that featured pendant Ru−polypyridine complex chromophores, it was found that the MLCT emission decay was biphasic;[52] however the overall emission yield was not substantially lower compared to that of monomer models. This work shows that incorporating the complexes into a polystyrene array does not in and of itself lead to quenching of the MLCT state (e.g., via self-quenching due to high local chromophore concentration). Thus, other factors must be considered in order to explain quenching observed for poly-**3** and poly-**4**. Two possible origins for the MLCT quenching can be hypothesized: (1) quenching by residual benzyl azide units ($ArCH_2N_3$) that reside in the polymer due to incomplete click reaction conversion or (2) quenching by the thiol (R−SH) end-groups on the polymer chains.

In order to explore these possible quenching pathways, bimolecular (Stern−Volmer) emission quenching experiments were carried out using the model complex **2**. Quenching of the MLCT emission by benzyl azide in CH_3CN solution was examined first, and the results showed no measurable quenching even up to 80 mM quencher concentration (Figure S7, Supporting Information). This result indicates that the quenching in the polymers was not due to residual benzyl azide repeat units. Next was examined the quenching of **2** by dodecanethiol (n-$C_{12}H_{25}$−SH), and here the results revealed moderately efficient quenching with $K_{SV} \sim 1 \times 10^2$ M^{-1}, corresponding to $k_q \sim 1 \times 10^8$ M^{-1} s^{-1}. This finding is consistent with previous studies showing that excited state RuL_3^{2+} is quenched by alkanethiols via reductive electron transfer.[53] Together, the results strongly suggest that the enhanced nonradiative decay pathway occurring in the poly-**3** and poly-**4** is due to MLCT quenching by the thiol end-groups on the polystyrene chains. As noted above, this conclusion is consistent with the finding that the quenching is more efficient in the shorter polymer, where in this case the average distance between the thiol end-group and the pendant chromophores is lower. Furthermore, the fact that the end group is able to effect such efficient quenching strongly suggests that there is energy migration along the polymer chains via a self-exchange hopping mechanism.[10] It is also interesting to note that previous studies have reported the fluorescence of dyes attached to polymers obtained by RAFT are strongly quenched by the end-group.[54−57]

Electrochemistry. The electrochemical properties of the polymers and model complexes were probed using cyclic voltammetry. The studies were carried out on **1**, **2**, and poly-**3** in acetonitrile solution with 0.1 M (TBA)PF_6 as a supporting electrolyte; poly-**3** was studied as the PF_6^- salt to allow for better solubility in the electrolyte solution. The results are listed in Table 1 and the voltammograms for **2** and poly-**3** are compared in Figure 2 (all potentials listed relative to SCE). The two model complexes and the polymer all featured a reversible anodic wave at ∼1.30 V which is attributed to the Ru(II/III) couple. The model complexes featured three clearly resolved, reversible cathodic waves at ca. −1.28, −1.50, and −1.76 V

dx.doi.org/10.1021/ma202804u | Macromolecules 2012, 45, 2632−2642

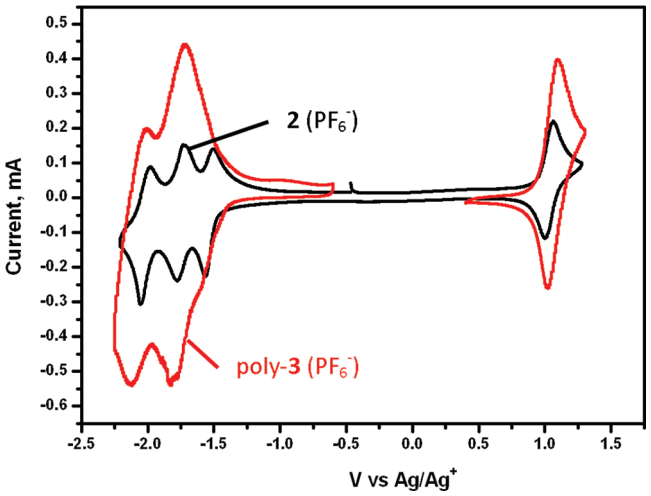


Figure 2. Cyclic voltammetry of **2** and poly-**3** (PF_6^- salts) at a platinum button working electrode in acetonitrile solution containing 0.1 M (TBA)PF_6 with a scan rate of 50 mV/s and ferrocene/ferrocenium (Fc/Fc^+) as an external standard.

resulting from sequential one-electron reduction of the phenanthroline and two bipyridine ligands. By contrast, poly-**3** showed only two resolved cathodic waves. The first wave, which exhibited a significantly larger current, occurred at ca. −1.51 V, and the second wave fell at ca. −1.81 V. The reason for the more complex cathodic electrochemistry of poly-**3** is likely due to heterogeneity in the individual ruthenium sites in the polymer which results in heterogeneous broadening in the electrochemical potential for the reductive processes. Nevertheless, the overall electrochemical response of the polymer retained the characteristics of the units, demonstrating that the polymeric nature of the system did not lead to a significant difference in the ability of the individual sites to undergo redox processes.

Amplified Emission Quenching. A number of previous investigations have studied the amplified quenching effect when chromophoric polyelectrolytes are quenched by oppositely charged quencher ions.[28,58−60] Amplified quenching has been shown to occur when a chromophoric polyelectrolyte exhibits a substantially larger Stern−Volmer quenching constant (K_{SV}) compared to a monomeric model chromophore. This process has been attributed to two main factors:[61] (1) ion-pairing between the (oppositely) charged quencher ion and repeat units in the polyelectrolyte chain effectively increases the local concentration of the quencher ion, and possibly more important, (2) the fact that excitons in the polychromophore are able to undergo rapid diffusive transport along the polymer chain, in effect increasing the effective sphere of action of the quencher ion. Although most studies have focused on π-conjugated polyelectrolytes, there is also substantial evidence that amplified quenching occurs in nonconjugated polyelectrolytes with pendant chromophores.[62]

Since poly-**3** and poly-**4** are polycations due to the dipositive charge of the Ru(II) pendant chromophores, it was undertaken to explore whether these systems would exhibit an amplified quenching effect in the presence of anionic quencher ions. Given the observation of efficient quenching by the thiol end-groups, which suggests that energy transport is active, it was anticipated that amplified quenching would be observed. In the course of this work 9,10-anthraquinone-2,6-disulfonate (AQS) and ferrocyanide, $Fe(CN)_6^{4-}$, were used as the quenchers, and the K_{SV} values for quenching of poly-**3** and poly-**4** were compared with the monomer model complex **2**.

Figure 3 illustrates the results of a typical quenching study where poly-**3** (polymer repeat unit concentration 10 μM) was

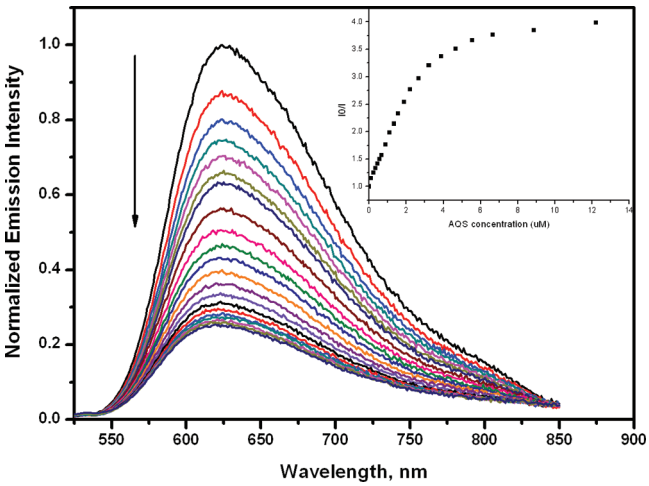


Figure 3. Phosphorescence quenching of poly-**3** (c = 10 μM) by AQS (c = 1−14 μM) in degassed aqueous solution. Inset illustrates the Stern−Volmer plot (I^o/I vs [AQS]) of the data constructed by monitoring the emission intensity at 625 nm.

quenched by addition of AQS. As can be seen, the quenching of the emission was very efficient, with 50% quenching observed upon addition of ca. 1.1 μM AQS. Note that this concentration corresponds to ∼9:1 ratio of Ru chromophores to each AQS quencher ion. In this system the Stern−Volmer plot was approximately linear until ∼80% of the initial emission intensity was quenched; however, beyond this the quenching levels off, indicating that in this system there were some ruthenium sites that were not quenched efficiently. A linear fit to the quenching data at low AQS concentration (c < 2 μM) afforded $K_{SV} \sim 8.75 \times 10^5$ M^{-1}. When poly-**3** was quenched with $Fe(CN)_6^{4-}$, a similar K_{SV} value was obtained (Table 2). Interestingly, when

Table 2. Stern−Volmer Quenching Constants[a]

compound or polymer	AQS[b]	AQS[c]	$Fe(CN)_6^{4-}$
2	6.3×10^4		
poly-**3**	8.7×10^5	3.8×10^5	8.0×10^5
poly-**4**	2.9×10^6	2.0×10^6	

[a]Quenching constants (K_{SV}) determined from linear region of Stern−Volmer plots in units of M^{-1}, measurements in H_2O. [b]Determined from quenching of steady state emission. [c]Determined from time-resolved emission decay using median lifetimes, $\langle\tau\rangle$.

the longer chain polymer poly-**4** was quenched with AQS, the efficiency was substantially larger, with $K_{SV} \sim 2.9 \times 10^6$ M^{-1}.

The Stern−Volmer plots for quenching of poly-**3**, poly-**4**, and model complex **2** by AQS are compared in Figure 4, and the Stern−Volmer constants are listed in Table 2. Of note is the fact that the quenching of the model complex was considerably less efficient than for the polymers; this result clearly reveals that there is significant amplification of the quenching response in both of the polymers, with a ∼10-fold amplification for poly-**3** and ∼50-fold amplification for poly-**4**.

In order to further probe the mechanism of quenching, emission lifetime studies were carried out to probe the effect of

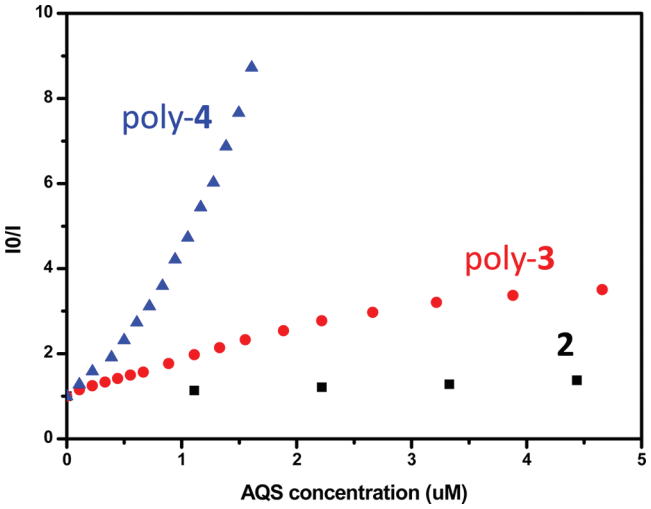


Figure 4. Stern–Volmer plots for emission quenching of **2**, poly-**3**, and poly-**4** with AQS (λ_{ex} = 450 nm, λ_{em} = 625 nm).

AQS concentration on the excited state decay kinetics. The decays were monitored at the emission maximum for each polymer as a function of AQS concentration, and the results are shown in Figure 5. As can be seen from this data, addition of AQS had a profound effect on the decay kinetics; for each polymer the emission decay rate increased upon addition of a low concentration of AQS. In every case the emission decays were modeled with a biexponential function, and Stern–Volmer plots were constructed using the median lifetimes $\langle\tau\rangle$ computed from the biexponential fitting parameters. For poly-**3** and poly-**4** linear fits of these lifetime SV plots afforded values that were slightly smaller than those obtained from steady-state quenching (Table 2). Nonetheless, the lifetime quenching was efficient for both polymers, indicating a significant component of quenching occurred via a dynamic mechanism.

DISCUSSION

Here we describe a novel approach to the synthesis of polymeric chromophores consisting of a polystyrene backbone functionalized with pendant ruthenium–polypyridine units. The backbone was prepared via the RAFT polymerization method, affording chloromethyl-substituted polystyrenes with narrow polydispersity and controlled chain length. Conversion of the chloromethyl substituents to azidomethyl was effected post-polymerization, after which the $(phen)Ru(bpy)_2^{2+}$ units were tethered to the backbone via the azide–alkyne click reaction. The resulting polymers exhibited the photophysical and electrochemical response characteristic of the metal complex chromophores with some important differences, discussed below.

Previous work has been carried out to synthesize and characterize the photophysics of polymers with nonconjugated backbones such as polystyrene or poly(methyl methacrylate) functionalized with pendant metal complex chromophores. The best studied examples are those reported by Meyer, Papanikolas, and co-workers, which relied on anionic polymerization to construct the polystyrene, followed by coupling of the Ru–polypyridine units via active-ester mediated amide bond formation.[9,10] Examples of copolymers constructed by RAFT or ATRP methods featuring pendant Ir(III) and Ru(II) pendant chromophores were reported by Schubert and co-workers.[26,27] By comparsion with this previous work, the RAFT-click methodology reported here has advantages and disadvantages. In particular, the RAFT method is easier to implement compared with the amide-linked polymers that are constructed by anionic polymerization. Anionic polymerization must be carried out using rigorously dry solvents and under inert atmosphere; by comparison RAFT is a less sensitive methodology and is considerably more tolerant to various functional groups. The systems reported by Schubert and co-workers relied upon ester linkages to attach the pendant chromophores to the polymer backbone. While this chemistry is versatile, the ester linkages may suffer from hydrolytic instability, especially if the polymers are used in applications with acidic or basic metal–oxide interfaces. The click reaction used in the present context affords a triazole "linker" that is robust and thermally stable under a variety of solution conditions.

Another key advantage of the RAFT technology is that it provides a straightforward avenue to the construction of multiblock polymers.[33] However, in the context of the present work, cleavage of the thiocarbonylthio end group that occurs during the conversion of PVBC to PVBA precludes polymer chain extension of PVBA or the ruthenium functional polymers.

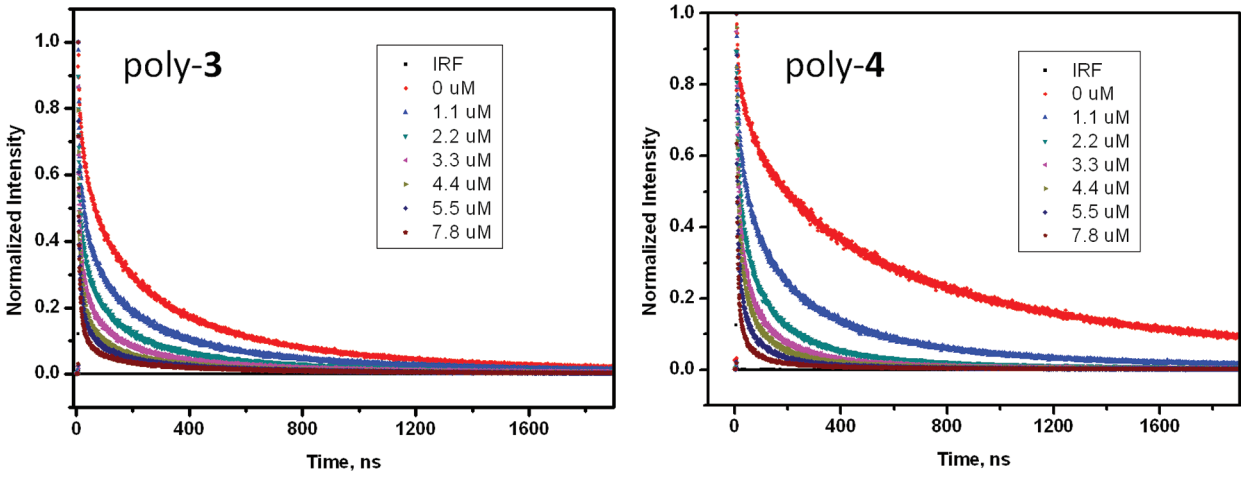
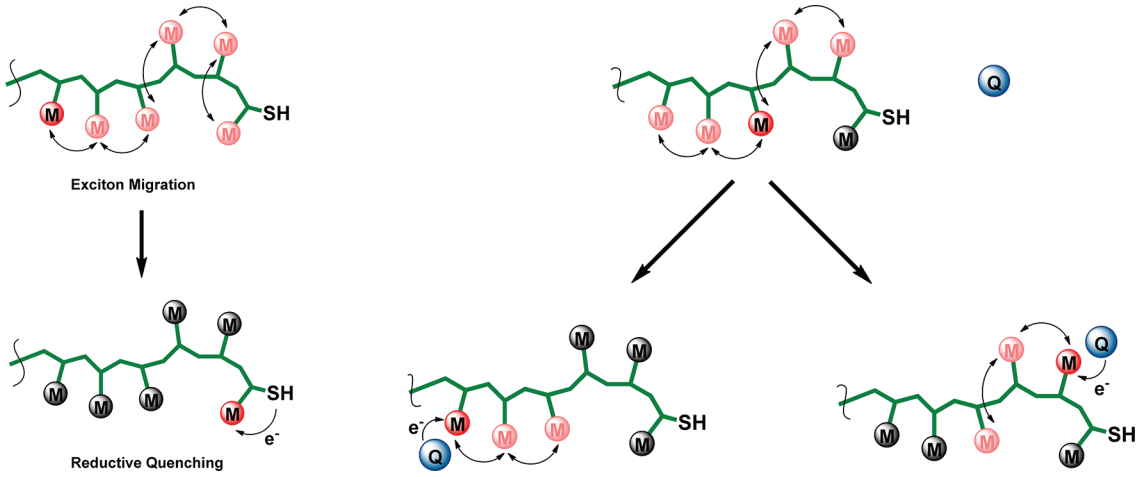


Figure 5. Normalized emission decays of poly-**3** (left) and poly-**4** (right) (c = 32 μM) at various concentrations of AQS quencher in aqueous solution (see inset for AQS concentrations). Excitation at 370 nm with detection at 600 nm.

dx.doi.org/10.1021/ma202804u | *Macromolecules* 2012, 45, 2632–2642

Scheme 3. Proposed Energy Transfer Mechanisms



Thus, construction of a multiblock polymer would require chain extension of PVBC prior to the chloromethyl to azide conversion step.

Despite its clear advantages, the RAFT method has one fundamental disadvantage—the end-group which results from the thiocarbonylthio chain transfer agent (CTA) is an effective quencher of the MLCT excited state. As noted above, other groups have reported that the end groups resulting from the RAFT CTA quench excited states.[54−57] A detailed study that examined quenching of a fluorescent coumarin dye by four different thiocarbonylthio CTAs revealed that in each case quenching was moderately efficient, and the authors postulated the mechanism involved reversible formation of an exciplex.[54] In poly-**3** and poly-**4** the available evidence suggested the synthetic sequence affords a thiol (R-SH) end group, and bimolecular quenching studies confirmed that alkanethiols are moderately efficient quenchers of the ruthenium MLCT excited state, presumably via reductive electron transfer quenching.[63] The end-group quenching process is a disadvantage for the RAFT polymers, as it complicates their photophysics, and results in polymers with reduced excited state lifetime and emission quantum efficiency compared to the monomeric chromophores.

One important aspect of this study was to explore whether the MLCT exciton undergoes diffusive transport among the $(phen)Ru(bpy)_2^{2+}$ chromophores within a polymer chain. Previous results gave evidence for exciton transport in polystyrene pendant ruthenium polymers with site to site hopping times in the range of <5 ns.[6,10] The results presented here indicate that a similar process is active in poly-**3** and poly-**4**: (1) Quenching of the exciton by the polymer end group is remarkably efficient, given that one would expect the quenching to occur only when the excited complex is in close proximity to the end-group (e.g., <10 Å). (2) The polymers exhibited "amplified quenching" with amplification factors of 10- and 50-fold for poly-**3** and poly-**4**, respectively, relative to model complex **2**.

Scheme 3 provides qualitative models for the mechanism of end-group quenching and amplified quenching by anionic quencher ions, indicating how MLCT exciton transport may play a role. First, for the end-group quenching process, the exciton must be in close proximity to the end-group for quenching to occur. Thus, excitons that are produced by photoexcitation distal on a polymer chain relative to the end group must be transported via a random walk process along the chain to arrive at a chromophore which is in proximity to the end-group. The fact that the MLCT decay rate was considerably faster for poly-**3** (DP 20) compared to poly-**4** (DP 50) suggests that the diffusion length of the exciton is ∼20 polymer repeat units.

The mechanism of amplified quenching is more complicated, and the possibility that both MLCT exciton and quencher ion diffusion along the polyelectrolyte chain may occur makes it difficult to draw a definitive conclusion as to which is more important to the effect. The Stern−Volmer quenching data for poly-**3** and poly-**4** by AQS and $Fe(CN)_6^{4-}$ revealed that the MLCT state was quenched efficiently (>50% quenching) even when the quencher ions were present at much lower concentration compared to the polymer repeat units (10:1 PRU to quencher). This result showed that during the lifetime of the MLCT state the exciton and quencher come into close proximity for quenching when the quencher is present at concentrations 10-fold less than the repeat units. Moreover, the emission lifetime studies (Figure 5) reveal that the quenching process is dynamic, and from this it is inferred that either the quencher ion is able to diffuse to the exciton, or the exciton is able to diffuse to the quencher with a rate that is competitive with excited state decay. The question is whether quencher ion diffusion or exciton diffusion is the dominant dynamic process. Experimental and theoretical studies of counterions in dilute polyelectrolyte solutions conclude that the ions are predominantly in close proximity to the polyelectrolyte chains.[64,65] However, recent molecular dynamics simulations and experiments suggest that counterions exchange rapidly (∼1 ns) between being closely bound and "territorial" (e.g., within the electrostatic field of the polyelectrolyte, but not specifically associated with a monomer ionic site).[65] If this is the case, it is likely that a quencher ion can diffuse along a polyelectrolyte chain on a time scale that is competitive with decay of the MLCT exciton by rapidly exchanging between individual monomer sites via the "territorial" state. Thus, at this point we can only suggest that both exciton diffusion along the chain, combined with the close proximity and rapid diffusion of the quencher ion along the polyelectrolye chain contribute to the amplified quenching effect.

dx.doi.org/10.1021/ma202804u | *Macromolecules* 2012, 45, 2632−2642

SUMMARY AND OUTLOOK

A set of two polystyrenes functionalized with (phen)Ru(bpy)$_2^{2+}$ chromophores on each repeat unit have been prepared by a synthetic methodology invoving RAFT polymerization to create the backbone, combined with dipolar cycloaddition "click" chemistry to attach the chromophores. The polymers exhibit the optical and electrochemical response characteristic of the ruthenium chromophores, except that excited state quenching is observed which is attributed to the end-group resulting from the thiocarbonylthio chain transfer agent. Evidence for transport of the MLCT exciton among the chromophores is provided from the end-group quenching results. The chromophore loaded polymers serve as efficient light harvesting arrays, with a single polystyrene chain that contains 20 chromophores exhibiting molar absorptivity in excess of 350 000 M^{-1} cm^{-1}. Studies in progress seek to extend controlled radical polymerization methods to prepare polychromophores that are end-functionalized with carboxylic- or phosphonic acid anchoring groups. These polymers will be adsorbed to metal-oxide surfaces to allow for investigation of light-harvesting and charge transfer at semiconductor interfaces.

ASSOCIATED CONTENT

Supporting Information

UV absorption spectra of PVBC and PVBA, ^{1}H NMR spectra of metal complexes and polymers, infrared spectra and gel permeation chromatograms of PVBC and PVBA, and emission quenching of **2** by benzyl azide and $C_{12}H_{25}SH$. This material is available free via the Internet at http://pubs.acs.org.

AUTHOR INFORMATION

Corresponding Author

*E-mail: kschanze@chem.ufl.edu.

Notes

The authors declare no competing financial interest.

ACKNOWLEDGMENTS

This research was supported as part of the UNC EFRC: Solar Fuels and Next Generation Photovoltaics, an Energy Frontier Research Center funded by the U.S. Department of Energy, Office of Science, Office of Basic Energy Sciences under Award Number DE-SC0001011.

REFERENCES

(1) Guillet, J. *Polymer Photophysics and Photochemistry*; Cambridge University Press: Cambridge, U.K., 1985.
(2) Webber, S. E. *Chem. Rev.* **1990**, *90*, 1469−1482.
(3) Baxter, S. M.; Jones, W. E.; Danielson, E.; Worl, L. A.; Younathan, J.; Strouse, G. F.; Meyer, T. J. *Coord. Chem. Rev.* **1991**, *111*, 47−71.
(4) Stoessel, S. J.; Stille, J. K. *Macromolecules* **1992**, *25*, 1832−1837.
(5) Jones, W. E.; Watkins, D. M.; Fox, M. A. *Chem. Eng. News* **1993**, *71*, 38−48.
(6) Dupray, L. M.; Devenney, M.; Striplin, D. R.; Meyer, T. J. *J. Am. Chem. Soc.* **1997**, *119*, 10243−10244.
(7) Fleming, C. N.; Dupray, L. M.; Papanikolas, J. M.; Meyer, T. J. *J. Phys. Chem. A* **2002**, *106*, 2328−2334.
(8) Fleming, C. N.; Brennaman, M. K.; Papanikolas, J. M.; Meyer, T. J. *Dalton Trans.* **2009**, 3903−3910.
(9) Friesen, D. A.; Kajita, T.; Danielson, E.; Meyer, T. J. *Inorg. Chem.* **1998**, *37*, 2756−2762.
(10) Fleming, C. N.; Maxwell, K. A.; DeSimone, J. M.; Meyer, T. J.; Papanikolas, J. M. *J. Am. Chem. Soc.* **2001**, *123*, 10336−10347.
(11) Hjelm, J.; Constable, E. C.; Figgemeier, E.; Hagfeldt, A.; Handel, R.; Housecroft, C. E.; Mukhtar, E.; Schofield, E. *Chem. Commun.* **2002**, 284−285.
(12) Liu, Y.; Jiang, S.; Schanze, K. S. *Chem. Commun.* **2003**, 650−651.
(13) Walters, K. A.; Trouillet, L.; Guillerez, S.; Schanze, K. S. *Inorg. Chem.* **2000**, *39*, 5496−5509.
(14) Peng, Z.; Gharavi, A. R.; Yu, L. *J. Am. Chem. Soc.* **1997**, *119*, 4622−4632.
(15) Wu, X.; Fraser, F. C. *Macromolecules* **2000**, *33*, 4053−4060.
(16) Serin, J.; Schultze, X.; Adronov, A.; Fréchet, J. M. J. *Macromolecules* **2002**, *35*, 5396−5404.
(17) Meyer, T. J.; Papanikolas, J. M.; Heyer, C. M. *Catal. Lett.* **2011**, *141*, 1−7.
(18) Juris, A.; Balzani, V.; Barigelletti, F.; Campagna, S.; Belser, P.; Von Zelewski, A. *Coord. Chem. Rev.* **1988**, *84*, 85−277.
(19) Meyer, T. J. *Acc. Chem. Res.* **1989**, *22*, 163−170.
(20) Campagna, S.; Puntoriero, F.; Nastasi, F.; Bergamini, G.; Balzani, V. *Top. Curr. Chem.* **2007**, *280*, 117.
(21) Hagfeldt, A.; Boschloo, G.; Sun, L.; Kloo, L.; Pettersson, H. *Chem. Rev.* **2010**, *110*, 6595−6663.
(22) Borisov, S. M.; Wolfbeis, O. S. *Chem. Rev.* **2008**, *108*, 423−461.
(23) Sassolas, A.; Leca-Bouvier, B. D.; Blum, L. J. *Chem. Rev.* **2008**, *108*, 109−139.
(24) Sauvage, J. P.; Collin, J. P.; Chambron, J. C.; Guillerez, S.; Coudret, C.; Balzani, V.; Barigelletti, F.; Cola, L. D.; Flamigni, L. *Chem. Rev.* **1994**, *94*, 993−1019.
(25) Szaciłowski, K.; Macyk, W.; Drzewiecka-Matuszek, A.; Brindell, M.; Stochel, G. *Chem. Rev.* **2005**, *105*, 2647−2694.
(26) Happ, B.; Friebe, C.; Winter, A.; Hager, M. D. *Eur. Polym. J.* **2009**, *45*, 3433−3441.
(27) Ulbricht, C.; Becer, C. R.; Winter, A.; Schubert, U. S. *Macromol. Rapid Commun.* **2010**, *31*, 827−833.
(28) Tan, C.; Pinto, M. R.; Schanze, K. S. *Chem. Commun.* **2002**, 446.
(29) Zhou, Q.; Swager, T. M. *J. Am. Chem. Soc.* **1995**, *117*, 12593−12602.
(30) Chen, L. H.; McBranch, D. W.; Wang, H. L.; Helgeson, R.; Wudl, F.; Whitten, D. G. *Proc. Natl. Acad. Sci. U.S.A.* **1999**, *96*, 12287−12292.
(31) Glazier, S.; Barron, J. A.; Morales, N.; Ruschak, A. M.; Houston, P. L.; Abruña, H. D. *Macromolecules* **2003**, *36*, 1272−1278.
(32) Glazier, S.; Barron, J. A.; Houston, P. L.; Abruña, H. D. *J. Phys. Chem. B* **2002**, *106*, 9993−10003.
(33) Chiefari, J.; Chong, Y. K.; Ercole, F.; Krstina, J.; Jeffery, J.; Roshan, Le, T. P. T.; Mayadunne, R. T. A.; Meijs, G. F.; Moad, C. L.; Moad, G.; Rizzardo, E.; Thang, S. H. *Macromolecules* **1998**, *31*, 5559−5562.
(34) Moad, G.; Rizzardo, E.; Thang, S. H. *Aust. J. Chem.* **2006**, *59*, 669−692.
(35) Barner-Kowollik, C.; Perrier, S. *J. Polym. Sci. A: Poly. Chem.* **2008**, *46*, 5715−5723.
(36) Braunecker, W. A.; Matyjaszewski, K. *Prog. Polym. Sci.* **2007**, *32*, 93−146.
(37) Moad, G.; Rizzardo, E.; Thang, S. H. *Acc. Chem. Res.* **2008**, *41*, 1133−1142.
(38) McCormick, C. L.; Sumerlin, B. S.; Lokitz, B. S.; Stempka, J. E. *Soft Matter* **2008**, *4*, 1760−1773.
(39) Moad, G.; Chen, M.; Haussler, M.; Postma, A.; Rizzardo, E.; Thang, S. H. *Polym. Chem.* **2011**, *2*, 492−519.
(40) Huisgen, R. *Pure Appl. Chem.* **1989**, *61*, 613−628.
(41) Huisgen, R.; Szeimies, G.; Moebius, L. *Chem. Ber.* **1967**, *100*, 2494−2507.
(42) Rostovtsev, V. V.; Green, L. G.; Fokin, V. V.; Sharpless, K. B. *Angew. Chem., Int. Ed.* **2002**, *41*, 2596−2599.
(43) Bastide, J.; Hamelin, J.; Texier, F.; Ven, V. Q. *Bull. Soc. Chim. Fr.* **1973**, 2555−2579.
(44) Bastide, J.; Hamelin, J.; Texier, F.; Ven, V. Q. *Bull. Soc. Chim. Fr.* **1973**, 2871−2887.

(45) Hissler, M.; Connick, W. B.; Geiger, D. K.; McGarrah, J. E.; Lipa, D.; Lachicotte, R. J.; Eisenberg, R. *Inorg. Chem.* **2000**, *39*, 447−457.
(46) Alvarez, S. G.; Alvarez, M. T. *Synthesis* **1997**, 413−414.
(47) Sullivan, B. P.; Salmon, D. J.; Meyer, T. J. *Inorg. Chem.* **1978**, *17*, 3334−3341.
(48) Zhu, J.; Zhu, X.; Cheng, Z.; Lu, J.; Liu, F. *Polymer* **2002**, *43*, 7037−7042.
(49) Harriman, A. *J. Chem. Soc., Chem. Commun.* **1977**, 777−778.
(50) Lieber, E.; Rao, C. N. R.; Chao, T. S.; Hoffman, C. W. W. *Anal. Chem.* **1957**, *29*, 916−918.
(51) The molar absorptivity values are determined based on the polymer repeat unit concentration, where a single repeat is a polystyrene unit with a pendant ruthenium chromophore.
(52) Dupray, L. M.; Meyer, T. J. *Inorg. Chem.* **1996**, *35*, 6299−6307.
(53) Miyashita, T.; Hasegawa, Y.; Matsuda, M. *Langmuir* **1991**, *7*, 1491−1494.
(54) Farinha, J. P. S.; Relógio, P.; Charreyre, M.; Prazeres, T. J. V.; Martinho, J. M. G. *Macromolecules* **2007**, *40*, 4680−4690.
(55) Chen, M.; Ghiggino, K. P.; Mau, A. W. H.; Rizzardo, E.; Sasse, W. H. F.; Thang, S. H.; Wilson, G. J. *Macromolecules* **2004**, *37*, 5479−5481.
(56) Chen, M.; Ghiggino, K. P.; Mau, A. W. H.; Sasse, W. H. F.; Thang, S. H.; Wilson, G. J. *Macromolecules* **2005**, *38*, 3475−3481.
(57) Chen, M.; Ghiggino, K. P.; Launikonis, A.; Mau, A. W. H.; Rizzardo, E.; Sasse, W. H. F.; Thang, S. H.; Wilson, G. J. *J. Mater. Chem.* **2003**, *13*, 2696−2700.
(58) Harrison, B. S.; Ramey, M. B.; Reynolds, J. R.; Schanze, D. S. *J. Am. Chem. Soc.* **2000**, *122*, 8561−8562.
(59) Wang, J.; Wang, D. L.; Miller, E. K.; Moses, D.; Bazan, G. C.; Heeger, A. J. *Macromolecules* **2000**, *33*, 5153−5158.
(60) Tan, C.; Atas, E.; Müller, J. G.; Pinto, M. R.; Kleiman, V. D.; Schanze, K. S. *J. Am. Chem. Soc.* **2004**, *126*, 13685−13694.
(61) Jiang, H.; Taranekar, P.; Reynolds, J. R.; Schanze, K. S. *Angew. Chem., Int. Ed. Engl.* **2009**, *48*, 4300−4316.
(62) Lu, L. D.; Helgeson, R.; Jones, R. M.; McBranch, D.; Whitten, D. *J. Am. Chem. Soc.* **2002**, *124*, 483−488.
(63) Nanosecond transient absorption spectroscopy was carried out on poly-**3** in an effort to observe the products of reductive quenching by the end group (e.g., (phen)Ru(bpy)$_2^+$). The only observed transient absorption was due to the MLCT excited state, with no evidence for the formation of a long-lived intermediate that could be assigned to the quenching product. This negative result does not rule out reductive quenching, because it is quite likely that the return electron transfer step is rapid.
(64) Chang, R.; Yethiraj, A. *J. Chem. Phys.* **2002**, *116*, 5284−5298.
(65) Prabhu, V. M. *Curr. Opin. Colloid Interface Sci.* **2005**, *10*, 2−8.

Macromolecules

Article

pubs.acs.org/Macromolecules

Influence of Tetra(ethylene glycol) (EG_4) Substitution at the Loop Region on the Intramolecular DNA *i*-Motif

Yuhe Yang,[†] Yawei Sun,[‡] Yang Yang,[‡] Yongzheng Xing,[†,‡] Tao Zhang,[§] Zeming Wang,[∥] Zhongqiang Yang,*[,†] and Dongsheng Liu*[,†]

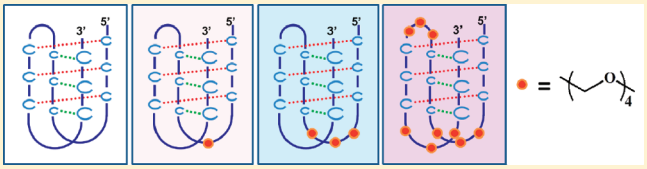
[†]Key Laboratory of Organic Optoelectronics & Molecular Engineering of the Ministry of Education, Department of Chemistry, Tsinghua University, Beijing 100084, China

[‡]National Center for Nanoscience and Technology, Beijing 100190, China

[§]Department of Chemistry, Renmin University of China, Beijing 100872, China

[∥]Department of Chemistry, University of Science and Technology of China, Hefei 230026, China

ABSTRACT: In this research, we employed tetra(ethylene glycol) (EG_4) to substitute bases at the loop region of the intramolecular DNA *i*-motif formed by $(CCCTAA)_3CCC$, and systematically studied the influence of such nonbase components on the stability and conformation of the formed structures by circular dichroism (CD), UV−vis spectroscopy and gel electrophoresis. We found that with all loop bases substituted, the *i*-motif structure can still form. The stability of the *i*-motif generally got weaker with the increase of the substitution number. Substitution at different positions might lead to different topologies. The findings above demonstrate that bases at the loop region play an important role on the stability and topology of the intramolecular DNA *i*-motif.



INTRODUCTION

i-motif is a four-stranded DNA structure formed by C-rich oligodeoxynucleotides (ODNs), a part of well-known human telomere.[1−8] *i*-motif, associating with G-quadruplex,[9] plays an important role in aging, cancer[10,11] and gene expression regulation.[12,13] Therefore, many efforts have been made to understand its detailed structure and intercalation topology. In 1993, Gehring and Leroy revealed that hemiprotonated base C forms a Hoogsteen base pair ($C{\cdot}C^+$), which leads to a parallel-stranded duplex. Such two duplexes in an antiparallel orientation associate into a quadruplex under slightly acidic condition.[1] The following studies found that *i*-motif can also be formed inter- or intramolecularly other than formed by four DNA strands.[14]

Owing to the inherent property and pH responsiveness, DNA *i*-motif have been employed in many applications. For example, DNA *i*-motif was used as basic building blocks to form 1-D extended nanowires based on non-Watson−Crick base pairing,[15] not only DNA, but also DNA_2−RNA_2 *i*-motif, and RNA_2−PNA_2 *i*-motif have also been formed with the potential of a building block for structural RNA nanotechnology.[16,17] More recently, a new type of DNA hydrogel was constructed from three-armed DNA nanostructures through the formation of intermolecular *i*-motif structures, furthermore, it can be reversibly switched between sol and gel state upon pH changes.[18] With the help of DNA *i*-motif, it is possible to construct DNA nanomachines,[19,20] and the key role of driving such nanomachines is the pH responsiveness of *i*-motif structure.[21] Other noncontact stimuli (e.g., electricity, light) were also utilized to trigger the pH responsiveness,[22,23] and allow DNA nanostructures to be integrated into devices, thus performing more complex tasks. It has shown that the *i*-motif structure is influenced by many factors, including pH, ion strength, temperature, molecular crowding, sequence length and composition, etc.[8,24−26] However, the influence of loop sequences on the intramolecular *i*-motif is underexplored.[27] Herein, we introduce a nonbase component, tetraethylene glycol (EG_4), at the loop region and study its influence on the DNA *i*-motif.

EXPERIMENTAL SECTION

Materials. All chemicals were purchased from Aldrich. The organic solvents were dried according to published methods. THF was distilled from sodium under N_2 immediately prior to use. Water used in all experiments was Millipore Milli-Q deionized (15.6 MΩ cm).

As shown in Figure 1, the tetra(ethylene glycol) (EG_4) was introduced into the loop region of the ODNs via the phosphoramidite process according to the literature.[28]

Synthesis of 12-*O*-Dimethoxytrityltetraethylene Glycol (1). A solution of dimethoxytrityl chloride (DMT-Cl, 7.45 g, 22 mmol), tetra(ethylene glycol) (3.88 g, 20 mmol) in pyridine (2 mL), and CH_2C1_2 (150 mL) was mixed and stirred at 0 °C overnight. The organic phase was extracted with 5% of aqueous $NaHCO_3$ (2 × 25 mL) then with water. The organic phase was dried over Na_2SO_4, filtered then evaporated. The compound was purified by column chromatography (CH_2Cl_2/methanol as eluant, 50:1, v/v).

Synthesis of 12-*O*-Dimethoxytrityltetraethylene Glycol-1-[(2-cyanoethyl)-(*N*,*N*-diisopropyl)]phosphoramidite (2). The

Received: February 1, 2012
Revised: March 1, 2012
Published: March 13, 2012

 © 2012 American Chemical Society

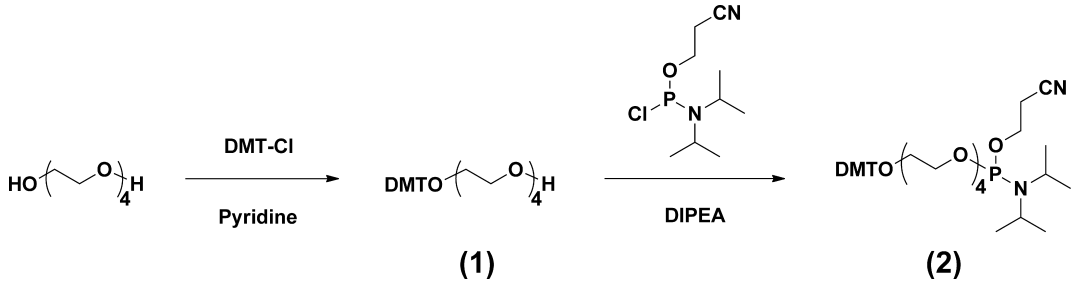
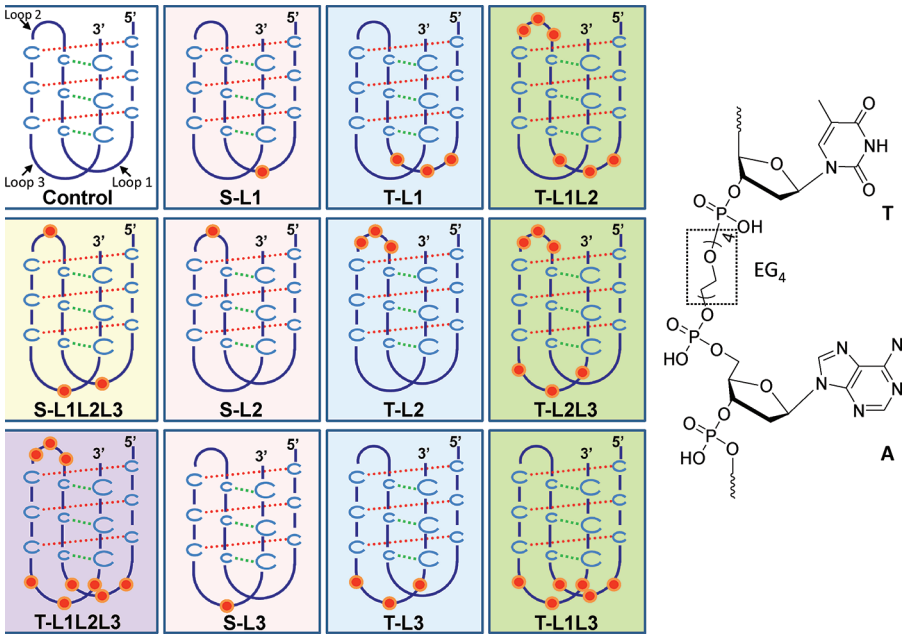


Figure 1. Synthetic route of 12-*O*-dimethoxytrityltetraethylene glycol (**1**) and 12-*O*-dimethoxytrityltetraethylene glycol-1-[(2-cyanoethyl)-(*N*,*N*-diisopropyl)]-phosphoramidite (**2**).

Scheme 1. (A) Schematic Illustration of EG_4 Modified ODNs;[a] (B) Illustration of the Molecular Structures of EG_4 Modified ODN



[a]Each orange ball stands for one EG_4 unit.

compound (**1**) obtained above (2.2 g, 4.4 mmol) was kept under vacuum overnight then dissolved in CH_2C1_2 (10 mL) containing *N*,*N*-diisopropylethylamine (DIPEA, 1.1 g, 8.8 mmol). 2-Cyanoethyl diisopropyichlorophosphite (PAM-Cl, 1.3 g, 5.3 mmol) was added under nitrogen atmosphere with stirring. After 30 min, the mixture was poured into 50 mL of ethyl acetate and extracted with 10% of aqueous $NaHCO_3$ (2 × 80 mL) then water. The organic phase was dried over Na_2SO_4, filtered then evaporated. The compound was purified by column chromatography (CH_2Cl_2/THF/Et_3N as eluant, 50:49:1, v/v/v).

Synthesis of ODNs Modified with EG_4. The syntheses were conducted automatically on an Applied Biosystems 394 DNA Synthesizer, then purified by denatured polyacrylamide gel electrophoresis (20% polyacrylamide, 1 × TBE (Tris−borate−EDTA), 7 M urea) and desalted by C18 columns purchased from Glen Research. The molecular weights of the purified ODNs were determined by BIFLEX III MALDI−TOF mass spectroscopy. Modified ODNs strand concentration was determined by Varian Cary 100 UV−vis spectrometer at 260 nm, in a pH 8.0 buffer. The single strand extinction coefficient was calculated from mononucleotide and dinucleotide data of a nearest-neighbor approximation.[29]

Gel Electrophoresis Analysis. The purity of EG_4 modified ODNs were checked by 15% denatured PAGE at a concentration of 40 μM in pH 8.0 TBE buffer at room temperature. To verify whether the EG_4 modified ODNs can form secondary structures, the samples were slowly annealed from 95 °C to room temperature and then incubated at 4 °C overnight in 100 MES buffer (pH 5.0). After the sample was loaded on a native 15% polyacrylamide gel, the gel electrophoresis was run at 4 °C. All gels were stained by Stains All and then analyzed on a Beijing Sage Creation phosphorimager instrument.

Circular Dichroism (CD) Spectra. The ODN samples were dissolved in 100 mM MES buffer (pH 5.0) to get a concentration of 2 μM, heated to 95 °C for 5 min, and gently cooled to room temperature. The CD spectra were collected on an Applied Photophysics Chirascan Spectropolarimeter, the determination was carried out at the range of 220−320 nm at room temperature in a 1.0 cm length cell. The reported spectra correspond to the average of at least three scans. The scan of the buffer alone was used as a control and subtracted from the average scan for each sample. CD melting curves were measured at 289 nm, and the temperature was scanned at a heating rate of 1 °C/min. The melting point (T_m) was obtained from the peak of the corresponding differential melting curve.

RESULTS AND DISCUSSION

Design of EG_4 Modified ODNs. In this paper, we studied the influence of loop region on the formation of *i*-motif structure, in particular, when the base at loop region was replaced by nonbase unit, tetra(ethylene glycol) (EG_4), which locally destroys the base stacking,[14] thus loosens the interaction between bases, meanwhile, the charge density keeps unchanged as the phosphate part still remains after the modification.

dx.doi.org/10.1021/ma300230q | *Macromolecules* 2012, 45, 2643−2647

Scheme 1 shows the design of EG_4 modified ODNs, including (i) unmodified ODNs (as control); (ii) modified ODNs with one or three EG_4 at one, two or three loops. The structure includes 3 loops as indicated in the left top image: the loop near the 5′ end, in the middle, and near the 3′ end were named as loop 1, loop 2, and loop 3, respectively. We adopted the following convention for all the ODNs: the letter S indicates single substitution, which refers to base A at the middle of one loop substituted with EG_4 and the letter T indicates triple substitution where all three bases in one loop were substituted. L1, L2, and L3 represent the loop positions of the EG_4 unit. For example, T-L1L3 represents three EG_4 units substituted by three bases at loop 1 and 3, and no replacement at loop 2.

Synthesis and Characterization of ODNs. In order to introduce EG_4 into the loop region of the ODNs, the conventional phosphoramidite process was conducted.[28] In a typical experiment, as shown in Figure 1, EG_4 was first modified with DMT to get compound (1) and then reacted with PAM-Cl to obtain compound (2). Normally, automatic synthesizer uses acetonitrile (ACN) as solvent, in case of compound (2), which has good solubility in ACN, therefore, it is possible to treat compound (2) as a common base to synthesize modified ODNs directly. The position of EG_4 at loop region could be programmed by automatic synthesizer. The yield of the modified ODNs was over 90%, and this synthetic method provides a general guidance on inserting functional groups into DNA.

In order to characterize EG_4 modified ODNs, the MALDI-TOF mass spectroscopy was conducted, see Table 1. It is shown that the observed molecular weight has a good agreement with the calculated value and the error was below 0.4%, indicating EG_4 modified ODNs were successfully synthesized.

Table 1. Summary of Molecular Weights of EG_4 Modified ODNs

name	sequence (5′-3′)[a]	calcd [g/mol]	found [g/mol]	error (%)
control	CCC TAA CCC TAA CCC TAA CCC	6200	6207	0.11
S-L1	CCC T*A CCC TAA CCC TAA CCC	6152	6148	0.07
S-L2	CCC TAA CCC T*A CCC TAA CCC	6152	6150	0.03
S-L3	CCC TAA CCC TAA CCC T*A CCC	6152	6151	0.02
S-L1L2L3	CCC T*A CCC T*A CCC T*A CCC	6056	6036	0.33
T-L1	CCC *** CCC TAA CCC TAA CCC	6038	6044	0.10
T-L2	CCC TAA CCC *** CCC TAA CCC	6038	6039	0.02
T-L3	CCC TAA CCC TAA CCC *** CCC	6038	6042	0.07
T-L1L2	CCC *** CCC *** CCC TAA CCC	5876	5882	0.10
T-L2L3	CCC TAA CCC *** CCC *** CCC	5876	5880	0.07
T-L1L3	CCC *** CCC TAA CCC *** CCC	5876	5884	0.14
T-L1L2L3	CCC *** CCC *** CCC *** CCC	5714	5720	0.11

[a]An asterisk stands for one EG_4 unit.

We also carried out denaturing gel electrophoresis to confirm the purity of EG_4 modified ODNs. As shown in Figure 2A, all modified ODNs had a clean single band, indicating the synthesis was efficient and the product was pure, this

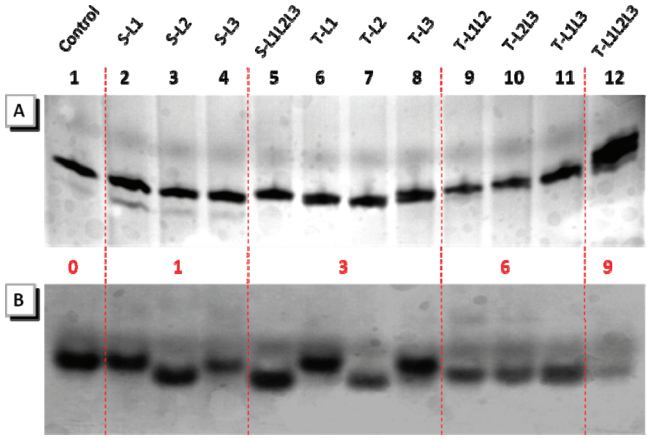


Figure 2. (A) Denaturing gel electrophoresis of EG_4 modified ODNs at pH 8.0. (B) Native gel electrophoresis of EG_4 modified ODNs at pH 5.0. The red number in the middle represents the substitution number of EG_4 unit.

observation, when combined with the result from mass spectroscopy in Table 1, giving further evidence that the EG_4 modified ODNs with high purity were indeed obtained.

Formation of *i*-Motif Sturcture. We sought to determine if the modification of EG_4 influences the formation of intramolecular *i*-motif, and CD spectra and native gel electrophoresis at pH 5.0 were employed.

As shown in Figure 3, the black line represents the unmodified sequence, with a positive peak at 289 nm, a negative peak at 258 nm and a crossover at 273 nm, which are characteristic peaks of $C{\cdot}C^+$ pairs,[30] indicating intramolecular *i*-

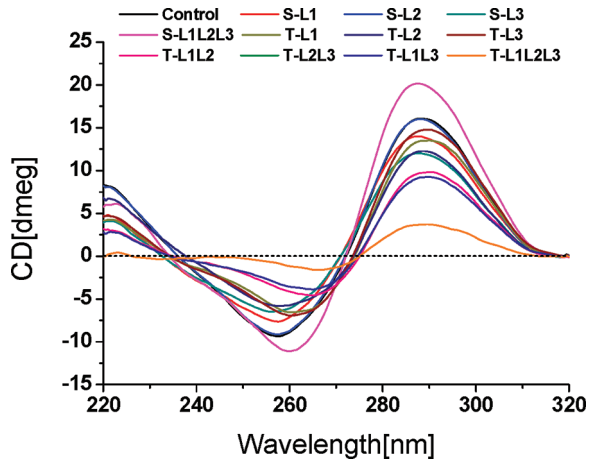


Figure 3. CD spectra of EG_4 modified ODNs at pH 5.0.

motif structure was formed at pH 5.0.[31] It is observed that after bases at different loop regions were substituted with different numbers of EG_4, the positive peaks still appeared around 289 nm, at a range of 288−291 nm, and the negative peaks and crossovers also showed a similar behavior; therefore, it is concluded that the *i*-motif structure still formed with EG_4 modified ODNs.

dx.doi.org/10.1021/ma300230q | *Macromolecules* 2012, 45, 2643−2647

Stability Influenced by EG_4 Substitution. The stability of the intramolecular *i*-motif structures formed by 12 sequences derived from $(CCCTAA)_3CCC$ by substitution of the TAA loops with EG_4 spacer is investigated. We sought to examine the melting point (T_m) of ODNs by CD, and evaluate the influence of different substitution numbers and positions of EG_4 on the stability of modified ODNs.

Five typical sequences with substitution numbers of 0, 1, 3, 6, and 9 were chosen, as shown on the top of Figure 4, based on the following rules: unmodified ODN was used as control; S-L1 contained 1 EG_4 unit at the middle of loop 1; T-L1 contained 3 EG_4 units at loop 1; T-L1L2 contained 6 EG_4 units, one triple substitution at loop 1 and another at loop 2; T-L1L2L3 contained 9 EG_4 units, showing that all bases at all loop regions were replaced. The CD melting curve in Figure 4 showed a clear trend that with the increase of substitution number from 0, 1, 3, and 6 to 9, the T_m continuously decreased from 64.9 to 61.7, 58.2, 49.3, and 45.4 °C, respectively, indicating that substitution of EG_4 at the loop region disturbed the stability of DNA *i*-motif. This might be attributed to the break of, such as $\pi-\pi$ stacking between loop bases in case of single substitution, the stacking between base A and $C{\cdot}C^+$ and the base stacking between A·T base pair and $C{\cdot}C^+$,[14] the latter two in particular for the case of triple substitution.

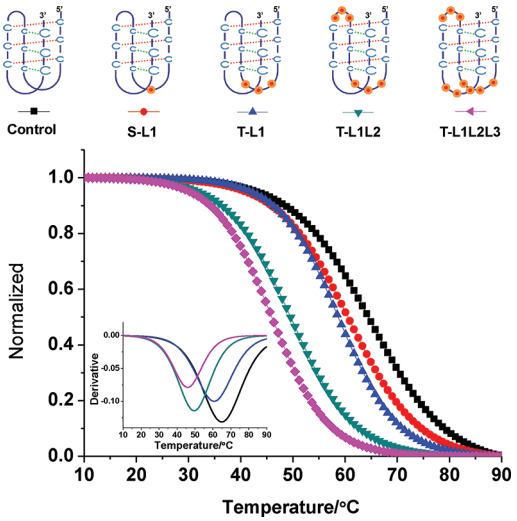


Figure 4. CD melting curves of EG_4 modified ODNs at pH 5.0.

In order to further investigate the influence of both substitution numbers and positions on the stability of modified ODNs, we characterized all T_m by CD and the results are listed in Table 2. We examined single substitution as shown in the second column of Scheme 1, S-L1, S-L2, and S-L3, and their corresponding T_m were 61.7, 64.9, and 62.2 °C, respectively, showing a relatively small difference from the control sequence (T_m = 64.9 °C). Note that the influence of single substitution at loop 2 on T_m is smaller than that at loop 1 and loop 3, this will be further discussed in triple substitution section. Moreover, when three discrete bases at the middle of all loops were substituted, S-L1L2L3, shown on the left of the second row in Scheme 1, its T_m was 62.5 °C, which is only 2.4 °C lower than the control, suggesting that single substitution has little influence on the stability of the system. The preservation of the stability indicates that single substitution of EG_4 is a feasible option of adding functional groups in DNA *i*-motif.

Table 2. Summary of T_m of EG_4 Modified ODNs

name	number of EG_4	T_m (±0.5 °C)
control	0	64.9
S-L1	1	61.7
S-L2	1	64.9
S-L3	1	62.2
S-L1L2L3	3	62.5
T-L1	3	58.2
T-L2	3	58.8
T-L3	3	56.9
T-L1L2	6	49.3
T-L2L3	6	50.7
T-L1L3	6	52.2
T-L1L2L3	9	45.4

Next, we looked into the triple substitution at loop regions. Triple substitution at one loop was shown in the third column of Scheme 1, corresponding to T-L1, T-L2, and T-L3, their T_m decreased to 58.2, 58.8, and 56.9 °C, respectively. Such reduction was not only attributed to the disruption of $\pi-\pi$ stacking between loop bases as that occurred in single substitution, but also the stacking between A·T base pair and its adjacent $C{\cdot}C^+$, which are considered to make *i*-motif highly stable.[14] The reduction of T_m became more pronounced as the number of triple substitution increased to two, shown in the last column of Scheme 1, corresponding to T-L1L2, T-L2L3, and T-L1L3, and their T_m further decreased to 49.3, 50.7, and 52.2 °C, respectively, which has a good agreement with our explanation above. Note that the EG_4 substitution at loop 2 showed less decrease on T_m comparing to that at other two loops. This effect has the same trend as that in the single substitution, suggesting that either single or triple substitution at loop 2 has less influence on T_m than that at loop 1 and 3. Finally as all bases at all loop regions were substituted, shown on the bottom left of Scheme 1, T-L1L2L3, the T_m decreased to 45.4 °C, almost 20 °C lower than the control, this result when combined with T_m data above, suggests that in case of triple substitution, the more EG_4 units in the loop region, the lower the T_m and thus the lower the stability of the system.

We make a final observation regarding to the influence of substitution position on topology. We studied the native gel electrophoresis at pH 5.0, at which condition, it is well-known that intramolecular *i*-motif structure forms.[8] In Figure 2B, lanes 2, 3, and 4 were ODNs with single substitution, it appeared that substitution at both loop 1 and loop 3 (S-L1 and S-L3) resulted in a band position proximal to that of unmodified one (lane 1), however, the ODN modified at loop 2 (S-L2) exhibited a faster migration. Similar results were observed with the triple substitution. Both T-L1 (lane 6) and T-L3 (lane 8) had similar migration rate, but slower than T-L2 (lane 7). Since ODNs with a same number of EG_4 possess the same molecular weight and charge, the different migration rates might be caused by different topologies. It is known that loops 1 and 3 correspond to wide grooves, and loop 2 corresponds to a narrow groove, the faster migration might be attributed to the more compact structure of ODNs induced by the modification of EG_4 at the narrow groove. This provides interesting information for other DNA sequence modification designs.

■ CONCLUSION

In this work, we studied the influence of the bases at the loop region on the intramolecular *i*-motif structure of human

telomeric DNA. We discovered that though *i*-motif structure can still form, the stability and topology of EG_4 modified ODNs varied with substitution numbers and positions. In general, single substitution at all loops preserved the stability of *i*-motif, while the triple substitution of three bases at one loop resulted in a significant decrease of stability, and the more EG_4 substitutions, the less stable of the system. The substitution at the narrow groove results in a faster migration in agarose gel comparing to those at other two wide grooves, suggesting modification at different positions has different extents of influence on the topology. These results would benefit to the in-depth understanding of the folding topology of *i*-motif and their future applications in drug discovery and diagnosis.

AUTHOR INFORMATION

Corresponding Author

*E-mail: (D.L.) liudongsheng@tsinghua.edu.cn; (Z.Y.) zyang@tsinghua.edu.cn.

Notes

The authors declare no competing financial interest.

ACKNOWLEDGMENTS

The authors thank the National Basic Research Program of China (973 program, No. 2011CB935701), the National Natural Science Foundation of China (No. 21121004, 91027046, and 20974030), and the NSFC-DFG joint project TRR61 for financial support.

REFERENCES

(1) Gehring, K.; Leroy, J.; Guéron, M. *Nature* **1993**, *363*, 561−565.
(2) Leroy, J.; Gehring, K.; Kettani, A.; Guéron, M. *Biochemistry* **1993**, *32*, 6019−6031.
(3) Chen, L.; Cai, L.; Zhang, X.; Rich, A. *Biochemistry* **1994**, *33*, 13540−13546.
(4) Kang, C.; Berger, I.; Lockshin, C.; Ratliff, R.; Moyzis, R.; Rich, A. *Proc. Natl. Acad. Sci. U.S.A.* **1994**, *91*, 11636−11640.
(5) Leroy, J.; Guéron, M.; Mergny, J.; Hélène, C. *Nucleic Acids Res.* **1994**, *22*, 1600−1606.
(6) Phan, A.; Guéron, M.; Leroy, J. *J. Biol. Chem.* **2000**, *299*, 123−144.
(7) Parkinson, G.; Lee, M.; Neidle, S. *Nature* **2002**, *417*, 876−880.
(8) Mergny, J.; Lacroix, L.; Han, X.; Leroy, J.; Hélène, C. *J. Am. Chem. Soc.* **1995**, *117*, 8887−8898.
(9) Phan, A. T.; Mergny, J. *Nucleic Acids Res.* **2002**, *30*, 4618−4625.
(10) Harley, C.; Villeponteau, B. *Curr. Opin. Genet. Dev.* **1995**, *5*, 249−255.
(11) Greider, C. *Proc. Natl. Acad. Sci. U.S.A.* **1998**, *95*, 90−92.
(12) Khan, N.; Avino, A.; Tauler, R.; Gonzalez, C.; Eritja, R.; Gargallo, R. *Biochimie* **2007**, *89*, 1562−1572.
(13) del Toro, M.; Bucek, P.; Avino, A.; Jaumot, J.; Gonzalez, C.; Eritja, R.; Gargallo, R. *Biochimie* **2009**, *91*, 894−902.
(14) Guéron, M.; Leroy, J. *Curr. Opin. Struct. Biol.* **2000**, *10*, 326−331.
(15) Ghodke, H. R.; Krishnan, R.; Vignesh, K.; Kumar, G. V. P.; Narayana, C.; Krishnan, Y. *Angew. Chem., Int. Ed.* **2007**, *46*, 2646−2649.
(16) Chakraborty, S.; Modi, S.; Krishnan, Y. *Chem. Commun.* **2007**, *43*, 70−72.
(17) Chakraborty, S.; Krishnan, Y. *Biochimie* **2008**, *90*, 1088−1095.
(18) Cheng, E. J.; Xing, Y. Z.; Chen, P.; Yang, Y.; Sun, Y. W.; Zhou, D. J.; Xu, L. J.; Fan, Q. H.; Liu, D. S. *Angew. Chem., Int. Ed.* **2009**, *48*, 7660−7663.
(19) Liu, H. J.; Liu, D. S. *Chem. Commun.* **2009**, *45*, 2625−2636.
(20) Liu, D.; Cheng, E.; Yang, Z. *NPG Asia Mater.* **2011**, *3*, 109−114.
(21) Liu, D. S.; Balasubramanian, S. *Angew. Chem., Int. Ed.* **2003**, *42*, 5734−5736.
(22) Liu, H. J.; Xu, Y.; Li, F. Y.; Yang, Y.; Wang, W. X.; Song, Y. L.; Liu, D. S. *Angew. Chem., Int. Ed.* **2007**, *46*, 2515−2517.
(23) Yang, Y.; Liu, G.; Liu, H. J.; Li, D.; Fan, C. H.; Liu, D. S. *Nano Lett.* **2010**, *10*, 1393−1397.
(24) Miyoshi, D.; Matsumura, S.; Li, W.; Sugimoto, N. *Nucleosides Nucleotides Nucleic Acids* **2003**, *22*, 203−221.
(25) Kaushik, M.; Suehl, N.; Marky, L. *Biophys. Chem.* **2007**, *126*, 154−164.
(26) Guedin, A.; De Cian, A.; Gros, J.; Lacroix, L.; Mergny, J. *Biochimie* **2008**, *90*, 686−696.
(27) Nonin, S.; Phan, A.; Leroy, J. *Structure* **1997**, *5*, 1231−1247.
(28) Durand, M.; Chevrie, K.; Chassignol, M.; Thuong, N.; Maurizot, J. *Nucleic Acids Res.* **1990**, *18*, 6353−6359.
(29) Richards, E. *Handbook of Biochemistry and Molecular Biology: Nucleic Acids*, 3rd ed.; CRC Press: Cleveland, OH, 1975; Vol. *1*, pp 596−603.
(30) Edwards, E.; Patrick, M.; Ratliff, R.; Gray, D. *Biochemistry* **1990**, *29*, 828−836.
(31) Kanehara, H.; Mizuguchi, M.; Tajima, K.; Kanaori, K.; Makino, K. *Biochemistry* **1997**, *36*, 1790−1797.

Macromolecules

Article

pubs.acs.org/Macromolecules

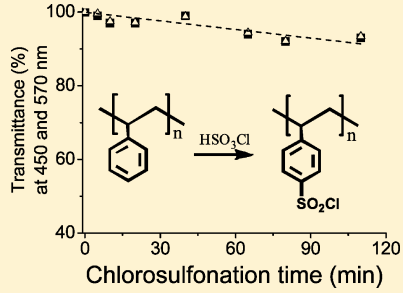
Transparent Polystyrene Substrates with Controllable Surface Chlorosulfonation: Stable, Versatile, and Water-Compatible Precursors for Functionalization

Anselmo del Prado,[†] Nerea Briz,[‡] Rodrigo Navarro,[†] Mónica Pérez,[†] Alberto Gallardo,[†] and Helmut Reinecke*[,†]

[†]Institute of Polymer Science and Technology (ICTP-CSIC), Juan de la Cierva 3, E-28006 Madrid, Spain

[‡]Tecnalia, Mikeletegi Pasealekua, 2 Parque Tecnológico, E-20009 San Sebastián, Spain

ABSTRACT: A simple and economic method is presented that allows the preparation of transparent polystyrene (PS) substrates activated with chlorosulfonyl groups. Chlorosulfonation has been analyzed by ATR-FTIR. Linear PS chains with different degrees of chlorosulfonation have been synthesized as model compounds in order to analyze the modification quantitatively. After chlorosulfonation the activated surfaces can be quantitatively converted in aqueous solution at room temperature to sulfo or sulfonazide groups or react with bifunctional aliphatic amines of different length via formation of sulfonamide linkages. In this way, surfaces with a huge variety of functionalities like amines, carboxylic or sulfonic groups, sulfonazides, esters, etc. may be obtained in a selective way controlling their density at the surface. In all cases, functional surfaces with excellent optical transparency are obtained. Aminated surfaces have successfully been probed for ELISA assays.



INTRODUCTION

Polystyrene is one of the most used polymer materials in the bioanalytical sector because it has excellent optical clarity, is easy to mold and relatively inexpensive. Slides and multiple-well plates from this material have gained widespread acceptance in part because pipetting, washing, and signal detection are easily automated.

A significant drawback of this polymer is its hydrophobic nature to which cells and other biomaterials have difficulty attaching. To overcome this problem, PS is often modified by chemical or physical methods. Typical surface treatments of polystyrene use corona discharge and chemical vapor deposition as well as gas phase ozonation under irradiation of UV light.[1,2] Other conventional methods used to modify polystyrene surfaces with amino groups are plasma polymerization of allylamine or plasma treatments in the presence of N_2 or NH_3.[3] A disadvantage of this type of physical surface modification techniques is the lack of selectivity and control of the reactions and usually a large number of different functional groups are created on the surface. This problem may be circumvented when wet-chemical surface treatments are used. A suitable reaction for the preparation of preactivated PS is the classical chlorosulfonation of aromatic rings using chlorosulfonic acid. This reaction on PS is being carried out for more than 50 years and many applications of the obtained products have been studied. In numerous work,[4−15] chlorosulfonation and subsequent sulfonamidation is carried out on cross-linked PS beads or PS in powder. In a patent from 1968, chlorosulfonation has been tried for the first time on PS surfaces using a hexane−HSO_3Cl emulsion.[16] However, nowadays it is known that this medium does not lead to chlorosulfonated surfaces but rather to the formation of SO_3H groups. Furthermore, the reactive solution is deactivated after short time as chlorosulfonation of the alkane cosolvent takes place as a secondary reaction. In fact, the first successful chlorosulfonation of plane transparent PS surfaces has been described very recently by Bicak et al.[17] who used this reaction for an improved metal deposition of copper on PS substrates. Because of the aim followed in this work the authors used relatively harsh reaction conditions that lead to the loss of transparency of the substrates and strongly opaque surfaces were obtained.

In the present work, we show for the first time the feasibility of obtaining "transparent" chlorosulfonated PS substrates. The method described here allows a facile control of the extension of chlorosulfonation on the surface, where up to 100% of the present aromatic rings may be activated. The activated surface is stable and water compatible. The utility of this activated material for subsequent functionalizations with amine or carboxylic groups maintaining the transparency of the substrates is demonstrated. Transparency is an indispensable condition for the subsequent use of the material in bioanalytical assays.

Received: February 10, 2012
Revised: March 8, 2012
Published: March 19, 2012

 © 2012 American Chemical Society dx.doi.org/10.1021/ma300283d | *Macromolecules* 2012, 45, 2648−2653

EXPERIMENTAL PART

Materials. Transparent polystyrene sheets of 1 mm thickness and a surface of 8.0 cm × 2.5 cm were purchased from Resopal S.A., Madrid, Spain. Chlorosulfonic acid, concentrated sulfuric acid, Orange II, Toluidine blue O, α,ω-aminoacids, alifactic diamines, styrene, and sodium *p*-vinylphenylsulfonate were purchased from Sigma-Aldrich. Chlorosulfonic acid was distilled under reduced pressure prior to use.

96-well plates of PS from Sarstedt and the interleukin 6 detection ELISA set from eBioscience were used for the ELISA experiments

Methods. *Chlorosulfonation of PS Substrates.* In a thermostatable reactor reactangular transparent PS samples (dimensions 2.5 × 8.0 × 0.1 cm^3) or multiple-well plates are brought in contact with freshly distilled chlorosulfonic acid at temperatures between −15 and 0 °C. At different time intervals, the sample is taken with Teflon coated tweezers, washed for 15 s in cold (0 °C) concentrated sulfuric acid and finally for 30 s in an ice/water mixture. Then the samples are dried at ambient temperature.

Functionalization of PS Substrates. In a thermostatable reactor reactangular chlorosulfonated PS substrates with different amounts of chlorosulfonyl groups are immersed in aqueous solutions of α,ω-functionalized amines of different concentrations at temperatures between 0° and 70 °C. At different time intervals the samples are taken out, washed with warm (40 °C) water and dried at ambient temperature.

a. Synthesis of Chlorosulfonated PS by Polymerization. Preparation of Monomer (S-SO_2Cl).[18] A 15 g sample of sodium *p*-vinylbenzenesulfonate is suspended in 70 mL of *N*,*N*-dimethylformamide (DMF). The suspension is cooled to 0 °C and 30 mL of thionyl chloride are added dropwise. After the addition a pale yellow solution is obtained. The mixture is stirred for further 24 h at room temperature and then poured into ice. The organic phase is extracted twice with 100 mL of diethyl ether and dried with $MgSO_4$. Finally the solvent is eliminated and the crude product purified by chromatography using silica gel and CH_2Cl_2 as the eluent. Yield 85%.

b. Preparation of Homopolymer (PS-SO_2Cl). The desired polymer is obtained by classical radical polymerization in a 1 M solution of toluene using as the initiator AIBN (azobis(diisobutyronitrile)) in a 0.015 molar concentration. The polymerization is carried out at 60 °C for 48 h. The formed polymer precipitates during the polymerization and is isolated by filtration, washed twice with hexane, and dried as a fine white powder.

c. Preparation of Copolymers. Copolymers between 4-vinylbenzenesulfonyl chloride and styrene of different compositions are prepared in analogous conditions to those used in the homopolymerization. The obtained copolymers are precipitated in hexane−ether (1:1) and purified by three cycles of solubilization/precipitation in THF/hexane−ether.

Bioanalytical Application, ELISA Assay. Interleukin 6 (IL6) ELISA set (eBioscience) was used to evaluate the bioanalytical application of the modified surfaces. Previously, the new aminated plates were exposed to glutaraldehyde pretreatment (10% of glutaraldehyde solution for 20 minutes) to facilitate the covalent bond to the antibody. Then, the recommended protocol given in the ELISA set was carried out on new modified surfaces and a reference surface.

Characterization of Modified Substrates. ATR-FTIR measurements are carried out using an FTIR spectrometer Spectrum One of Perkin-Elmer equipped with a single reflection ATR device using as internal reflection elements diamond/ZnSe. This setup allows studying the samples with a penetration depth of around 2 μm.

To determine quantitatively the relative degree of modification of the functionalized films the bands at 1450 and 1370 cm^{-1} are used that correspond to the polymeric main chains of PS and the O═S═O valence bond of the SO_2Cl groups, respectively.

H NMR spectra of the compounds were recorded at 25 °C on a 300 MHz Varian spectrometer operating at 300 MHz using deuterated acetone or deuterated dimethyl sulfoxide as the solvent.

Colorimetric Determination. For the determination of amine (primary, secondary, and ternary) concentration at the surfaces a method described by P. Hamerli et al.[19] has been used: samples were immersed into a 500 mmol/L Acid Orange II (AO) solution dissolved in water with pH 3, set by HCl. After overnight shaking for at least12 h at room temperature, samples were washed twice with the acidic water. In order to dissolve the adsorbed AO, they were shaken for 15 min at room temperature in water with pH 12, set by NaOH. The AO concentration (which is similar to the amine concentration of the surfaces) of the solution was colorimetrically determined with an optical spectrometer at 485 nm.

Carboxylic groups were determined by an analogue procedure using Toluidine Blue O (TBO) as the dye. Its concentration after extraction from the surface is determined by measuring the absorbance at 697 nm.

AFM. Data about the surface roughness of the simples has been obtained using the atomic force microscope NANOSCOPE A/M-AFM-2 1556EX from Digital Instruments in tapping mode.

RESULTS AND DISCUSSION

Preparation. The main aim of this work is to prepare transparent PS substrates selectively functionalized with chlorosulfonyl (−SO_2Cl) groups. The challenge in the modification reaction between chlorosulfonic acid and transparent PS materials is to control the extremely high reactivity of this acid and overcome the problem of washing the surfaces after modification has taken place without loosing the transparency of the polymeric material. For this washing procedure a medium must be chosen that has to be a solvent for the acid, should not give a strong exothermic reaction with it and should neither interact with polystyrene as its surface would loose smoothness and transparency. Apolar organic solvents do usually interact with polymers and are furthermore immiscible with chlorosulfonic acid. On the other hand, most of the polar media like water or alcohols react violently when brought in contact with the acid. For this reason, we have carried out a two-step cleaning procedure using cold concentrated sulfuric acid in the first step and a water/ice mixture in the second one. The samples can then be dried and analyzed with respect to the achieved content of functional groups, transparency and surface reactivity.

The chemical analysis of the modified surfaces was carried out by ATR-FTIR spectroscopy. A series of spectra of PS samples exposed to chlorosulfonic acid for different periods of time is shown in Figure 1b. The IR spectrum of unmodified PS (Figure 1a) shows mainly three significant bands in the studied range: two at 1600 and 1490 cm^{-1} corresponding to the

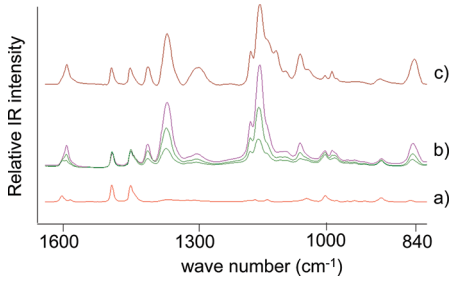


Figure 1. ATR-FTIR spectra in the range of 1650−800 cm^{-1} of (a) a pure PS film (yellow), (b) films modified for 10 min (green), 20 min (red), and 40 min (violet) with chlorosulfonic acid at −10 °C and (c) poly(styrene-*co*-4-vinylbenzenesulfonyl chloride) 50:50. Spectra are normalized with respect to the band at 1450 cm^{-1}.

dx.doi.org/10.1021/ma300283d | *Macromolecules* 2012, 45, 2648−2653

aromatic rings, and one at 1450 cm^{-1} proceeding from the C−H deformation of the polymeric alkyl main chain.

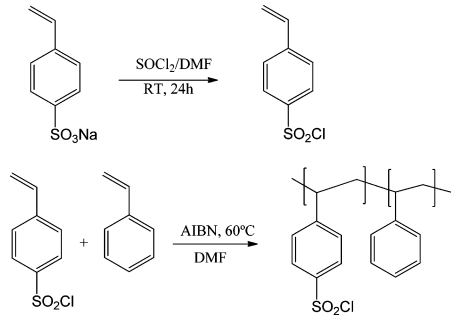
Upon chlorosulfonation, the IR spectrum changes significantly and new strong bands due to symmetric (1370 cm^{-1}) and asymmetric O═S═O valence bonds (1170 cm^{-1}) proceeding from the chlorosulfonyl group can be observed. Furthermore, a new band arises at 830 cm^{-1} due to the formation of *para*-substituted aromatic rings. After normalization of the spectra with respect to the band at 1450 cm^{-1} that is not affected by the modification reaction and remains constant, a relative conversion for the chlorosulfonation reaction can be determined using the increase of the band intensity at 1370 cm^{-1}.

The preparation of linear PS model compounds with different chlorosulfonation degrees has been faced in order to create a calibration curve and obtain absolute values for the degree of modification of the functionalized PS surfaces. Two approaches have been tried: the first one consisted in the chemical modification of PS in solution and the second one in a bottom-up approach by copolymerization of styrene and 4-vinylbenzenesulfonyl chloride.

Chlorosulfonation of PS in solution was not successful, because even under highly diluted conditions and low reaction temperatures cross-linked products were obtained that did not allow analysis by conventional H NMR. Probably, the electrophilic aromatic substitution with chlorosulfonyl groups takes place via activated transition states (like radicals) that recombine with radicals from other chains. The impossibility to obtain soluble chlorosulfonated PS in this way had also been observed by other authors.[17]

An alternative way to prepare model systems for chemically modified PS substrates is a bottom-up approach copolymerizing styrene with chlorosulfonated styrene monomer (Scheme 1).

Scheme 1. Synthesis of 4-Vinylbenzenesulfonyl Chloride and Its Copolymerization with Styrene



The latter compound is obtained by chlorination of commercially available sodium p-vinylbenzenesulfonate (see details in the Experimental Part).

The chemical structure of these copolymers and the percentage of sulfonyl chloride moieties have been checked by H NMR.

The ATR-FTIR-spectrum of poly(styrene-*co*-4-vinylbenzenesulfonyl chloride) 50:50 is compared in Figure 1 with the spectra of chemically modified PS substrates. One can see that the spectra of 1b and 1c are virtually identical showing that the structures of chlorosulfonated surfaces and model compounds are very similar. The IR-band intensity at 1370 cm^{-1} of model copolymers of different compositions were measured and used for calibration of the band intensities.

Figure 2 shows the degree of modification of chlorosulfonated PS surfaces as a function of reaction time for three

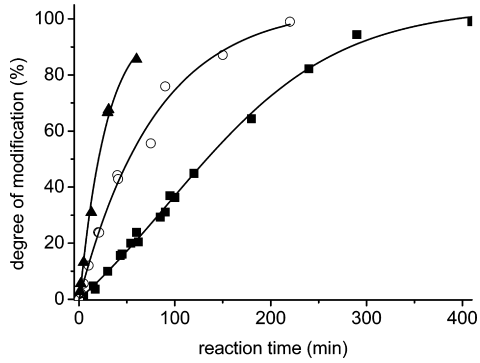


Figure 2. Degree of modification as a function of the chlorosulfonation time of PS at −10 (■), 0 (○), and +10 °C (▲).

different temperatures. According to this data even at the lowest temperature (−10 °C) complete conversion of all aromatic groups present in the subsurface area detectable by ATR takes place.

Surface Properties. One of the most important reasons for using PS in many bioanalytical assays like ELISA, is its excellent transparency necessary for the optical detection of for example color intensities. We have measured the transmittance of chlorosulfonated PS substrates as a function of the time samples had been exposed at −10 °C to the chlorosulfonating agent. The test has been carried out using two different wavelengths typically used in ELISA assays. As can be seen in Figure 3, the transmittance is independent of the wavelength

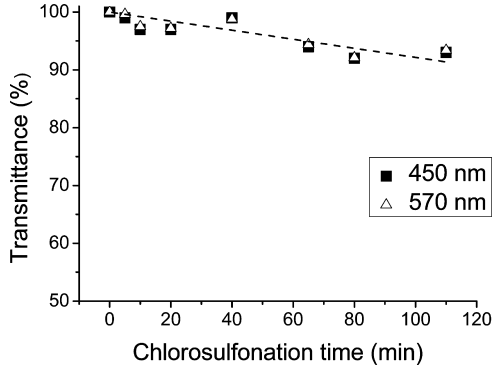


Figure 3. Transmittance of PS substrates as a function of chlorosulfonation time.

and decreases slowly and linearly with the time of functionalization. Even after 2 h of exposition to the acid the transparency of the substrate is maintained to more than 90%. The reasons for these excellent optical properties are on the one hand the high selectivity of the chlorosulfonation reaction at low temperatures and on the other hand the washing procedure in cold sulfuric acid and ice/water that eliminates the chlorosulfonic acid from the surface without producing a strongly exothermic reaction.

In order to analyze the surface morphology of chlorosulfonated PS substrates and study to which extent the surface roughness is influenced by the treatment with the modifier solution AFM images of pure and modified PS samples were recorded. These images together with the corresponding

dx.doi.org/10.1021/ma300283d | *Macromolecules* 2012, 45, 2648−2653

roughness profile obtained from AFM are shown in Figure 4. AFM images of both probes are qualitatively similar. The

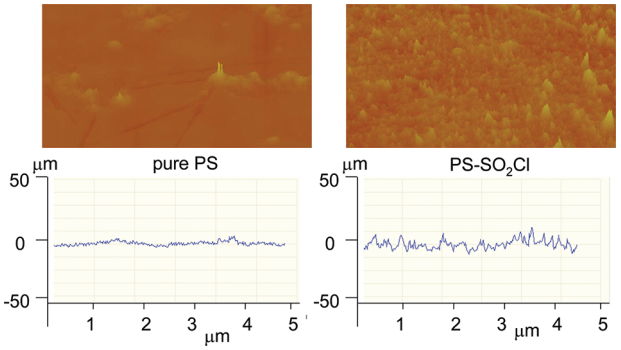


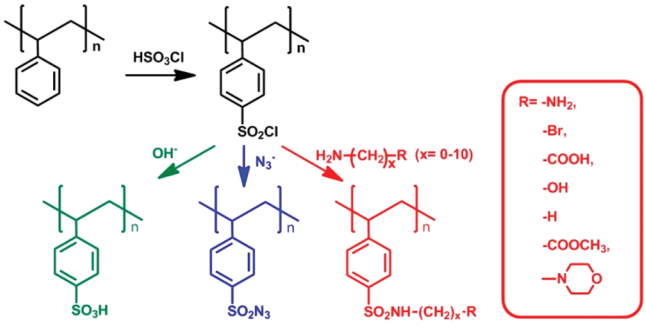
Figure 4. AFM images and corresponding roughness profile of a PS surface before and after modification for 10 min with chlorosulfonic acid at −10 °C.

characteristic surface roughness parameter R_q slightly increases from 1.8 to 2.6 μm when the surfaces are exposed to the acid. However, this increase in roughness does hardly affect the transparency of the samples.

Reactivity. Chlorosulfonated PS samples are stable and can be stored for long periods of time under ambient conditions without loosing their activity. FTIR-ATR analysis shows that freshly prepared samples and substrates stored for one year at room temperature in air exhibit identical spectra and reactivities toward nucleophiles. This is in contrast to many plasma modified materials that have generally to be used within a few months because they loose their activity due to reorientation processes of the functional groups on the surface.

The chemical reactivity of the activated surfaces has been tested exposing them in aqueous solution at room temperature to different nucleophiles that are shown in Scheme 2. Reactions

Scheme 2. Preparation of Functionalized PS Substrates



of the reactive groups with these nucleophiles have been followed by FTIR-ATR. Figure 5 shows that the chorosulfonyl moieties can be easily converted quantitatively to SO_3H groups when immersing the substrates in aqueous solution of pH = 11. The corresponding $-SO_3H$ bands indicated by black arrows appear at 1013, 1029, and 1127 cm^{-1} (spectrum c) while the band at 1370 cm^{-1} has completely disappeared and the second SO_2Cl band at 1170 cm^{-1} has broadened. The resulting spectrum in this case is very similar to that of pure commercial PS-SO_3H. It should be mentioned that the surfaces after this reaction remain as transparent as before.

Of further interest, is the fact that the hydrolysis of chlorosulfonyl groups that works very well at basic pH is

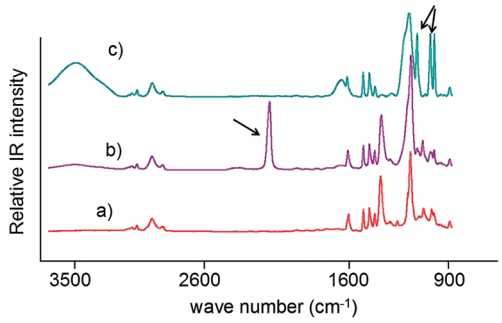


Figure 5. Polystyrene substrate modified with (a) SO_2Cl groups, (b) SO_2N_3 groups, and (c) SO_3H groups.

slow under neutral or acidic conditions. This allows carrying out modification reactions with other nucleophiles in water without the uncontrolled formation of sulfo moieties. In fact, immersion of the chlorosulfonated substrates into an aqueous sodium azide solution leads selectively to the formation of sulfonazide bonds as indicated by the formation of a strong band at 2132 cm^{-1} corresponding to the N_3^- units on the surface (spectrum b in Figure 5) while no peaks corresponding to SO_3H groups are observed. Also in this case the transparency of the samples is maintained.

Of special interest is the reaction of chlorosulfonated PS surfaces with bifunctional aliphatic amines allowing the amine group the linkage to the surface while the second functionality remains available for further reactions. In this way PS substrates with free amine, carboxylic, hydroxyl, halogen, morpholine, or ester groups can be prepared controlling their surface density. The number of functional groups on the surface is in all cases predetermined by the number of chlorosulfonic groups created previously. A further advantage of this approach of surface functionalization is the possibility to choose the appropriate length of the alkyl spacer x of the modifier. The possibility to vary this length is of special interest when biomolecules of demanding geometry shall be linked to the substrate.

Particularly interesting for bioanalytical assays are surfaces with amine and carboxy groups which may form covalent links to proteins or other biomolecules. In Figure 6 the change of the FTIR-ATR spectrum of chorosulfonated PS is shown when the substrate is immersed for 20 min in an aqueous solution of an aliphatic diamine (for example propane diamine): the

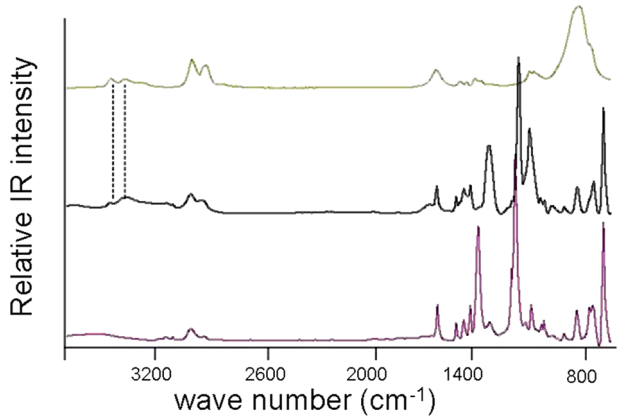


Figure 6. IR spectra of PS-SO_2Cl sample before (violet) and after (black) the amination reaction with propane diamine. For comparison the IR spectra of pure propane diamine is also shown (yellow).

dx.doi.org/10.1021/ma300283d | Macromolecules 2012, 45, 2648−2653

symmetric O═S═O band at 1370 cm^{-1} disappears completely and appears at 1315 cm^{-1} in the sulfonamide compound; the asymmetric O═S═O band at 1170 cm^{-1} is slightly shifted to 1152 cm^{-1}. Additionally new bands appear at 1094 cm^{-1} due to C−N valence bonds and at 3368 and 3279 cm^{-1} which proceed from associated and nonassociated N−H valence bonds respectively (broken lines).

In an analogue way carboxylated surfaces can be obtained reacting chlorosulfonated PS substrates in aqueous solutions with α,ω-aminoacids (for example β-alanine). Also in this case the characteristic shift from both SO_2Cl bands at 1370 and 1170 cm^{-1} to lower wave numbers is observed upon the formation of SO_2NH-units (Figure 7). Furthermore, a strong

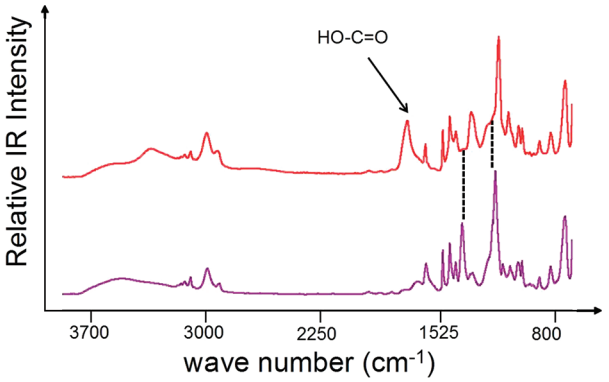


Figure 7. IR spectra of PS-SO_2Cl sample before (violet) and after (red) the carboxylation step using β-alanine.

carbonyl band appears at 1726 cm^{-1} and a broad carboxylic O−H valence bond around 3300 cm^{-1}. It has to be emphasized that the carboxylation reaction should be carried out at a pH that corresponds to the pK_s of the amine group. At lower pH the concentration of free active amine groups is reduced due to salt formation with the carboxy protons and at higher pH hydrolysis of SO_2Cl to SO_3H units may take place as a secondary reaction.

The number of available functional groups on the surface has been determined by colorimetry using Orange II for amine groups and Toluidine O for COOH groups. The method consists in the reversible formation of a salt complex between the functional group and a dye. When the complex is formed on the surface, excess dye can be washed off. Then the adhered dye is extracted by immersing the substrate in a known volume of basic water for amine groups and acidic solution for acid groups. Finally the dye concentration can be determined photometrically. In the case of aminated surfaces one detects between 2 and 10 nmol/cm^2 functional groups, in the case of carboxylated substrates between 50 and 400 nmol/cm^2 what is around 1−3 orders of magnitude larger than the amount in commercial plasma functionalized PS substrates. The difference in the functionalities density of aminated and carboxylated surfaces is probably due to different penetration depths of the corresponding dyes used in the colorimetric determination. A detailed study of this phenomenon is actually in progress.

ELISA. An ethylendiamine modified multiplate was studied for its bionalytical application as ELISA substrate. Because of the fact that the aldheyde groups react satisfactorily with amine groups of antibodies a glutaraldehyde treatment is applied on the aminated surface. The immunoassay was performed in the gluatraldehyde-ethylendiamine modified surface and in the reference ELISA set plate.

A standard curve with different concentrations of IL6 in the new surface is carried out to study the viability of the system. In Figure 8, the standard curve of the new modified multiplate is

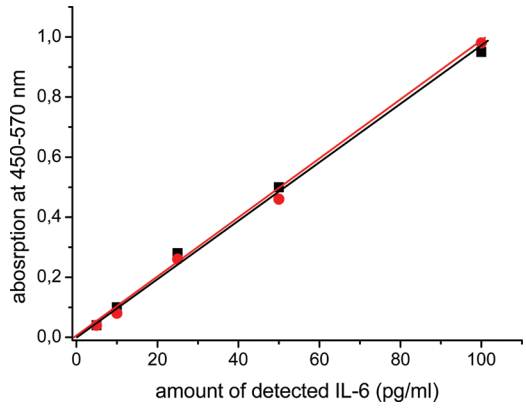


Figure 8. Standard curves for the determination of human IL-6 using ethylendiamine modified plate (black) and reference ELISA set plate (red).

presented and compared with the standard curve of the ELISA set multiplate. Obtained data result in similar curves showing that the new modified multiplate has the same high efficiency than the reference ELISA set multiplate.

According to the specifications of the IL6 ELISA set, whose detection limits are established in the range of 2−200 pg/mL, the sensitivity of the new modified multiplate is studied introducing a sample of 2 pg/mL of IL6. Using the standard curve previously obtained, the system quantified 2.08 pg/mL (DS 0.19, n = 5) demonstrating a sensitivity similar to the reference ELISA set multiplate and the potential applicability of the new surface for ELISA assays.

■ CONCLUSIONS

PS substrates can be activated by a simple and economic wet-chemical treatment in chlorosulfonic acid at low temperatures providing the surface selectively with a tunable number of chlorosulfonic groups that can be used to create or anchor a great variety of functional groups or biomolecules to the surface without loosing its transparency. The preactivated chlorosulfonated substrates are hydrolytically stable in ambient conditions and can be stored for months without loosing their activity. Surfaces homogeneously covered with a required number of amine or carboxylic groups may be created in a simple, cheap and reproducible way. The first ELISA assays carried out with 96-well polystyrene plates aminated according to the method presented here have shown that these materials can be used as an alternative to conventional materials.

■ AUTHOR INFORMATION

Corresponding Author

*Telephone: 34-91-5622900. Fax: 34-91-5644853.

Notes

The authors declare no competing financial interest.

■ REFERENCES

(1) Gonzalez-Vergara, E.; Vincent, J. B. *J. Mol. Recognit.* **1996**, *9−5/6*, 558.

(2) Bacquet, M.; Salunkhe, M.; Caze, C. *React. Polym.* **1991**, *16−1*, 61.
(3) Salunkhe, M. M.; Mane, R. B.; Kanade, A. S. *Eur. Polym. J.* **1991**, *27−6*, 461.
(4) Herweh, J.; Poshkus, A. US3709844, 1973.
(5) Klefenz, H.; Sanner, A.; Tschang, C. J. US 4,235,973, 1980.
(6) Imbert-Laurenceau, E. I.; Berger, M. C.; Pavon-Djavid, G.; Jouan, A.; Migonney, V. *Polymer* **2005**, *46*, 1277.
(7) Senkal, B. F.; Tekin, E. T.; Yavuz, E. *Polym. Adv. Technol.* **2009**, *20−3*, 308.
(8) Gutch, P. K.; Srivastava, R. K.; Sekhar, K. *J. Appl. Polym. Sci.* **2008**, *107−6*, 4109.
(9) Senkal, B. F.; Bildik, F.; Yavuz, E.; Sarac, A. *React. Funct. Polym.* **2007**, *67−12*, 1471.
(10) Bicak, N.; Gazi, M.; Galli, G.; Chiellini, E. *J. Polym. Sci., Part A: Polym. Chem.* **2006**, *44−23*, 6708.
(11) Senkal, B. F.; Yavuz, E. *Polym. Adv. Technol.* **2006**, *17−11/12*, 928.
(12) Bulbul Sonmez, H.; Senkal, B. F.; Sherrington, D. C.; Bicak, N. *React. Funct. Polym.* **2003**, *55−1*, 1.
(13) Biçak, N.; Şenkal, B. F. *J. Appl. Polym. Sci.* **1998**, *68−13*, 2113.
(14) Rabia, I.; Zerouk, J. E.; Mekhalif, S. *Polym. Adv. Technol.* **1998**, *9*, 107.
(15) Chu, V. P.; Tarcha, P. J. *J. Appl. Polym. Sci.* **1987**, *34−5*, 1917.
(16) Sherwood, A. E. GB 1100712, 1968.
(17) Bicak, N.; Karagoz, B. *Surf. Coatings Technol.* **2008**, *202*, 1581.
(18) Kamogawa, H.; Kanzawa, A.; Kadoya, M.; Nayto, T.; Nanasawa, M. *Bull. Chem. Soc. Jpn.* **1983**, *56*, 762.
(19) Hamerli, P.; Weigel, T.; Groth, T.; Paul, D. *Biomaterials* **2003**, *24*, 3989.

Macromolecules

Article

pubs.acs.org/Macromolecules

Hydride Transfer Ring-Opening Polymerization of a Cyclic Oligomethylhydrosiloxane. Route to a Polymer of Closed Multicyclic Structure

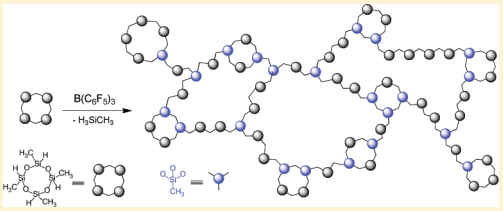
Julian Chojnowski,*[,†] Jan Kurjata,[†] Witold Fortuniak,[†] Slawomir Rubinsztajn,[‡] and Barbara Trzebicka[§]

[†]Center of Molecular and Macromolecular Studies, Polish Academy of Sciences, Sienkiewicza 112, 94-011 Łódź Poland

[‡]Global Research Center, General Electric Company, 1 Research Circle, Niskayuna, Schenectady, New York 12309, United States

[§]Center of Polymers and Carbon Materials, Polish Academy of Sciences, M. Skłodowskiej Curie 34, 41-819 Zabrze, Poland

ABSTRACT: The ring-opening polymerization of 2,4,6,8-tetramethyltetrahydro-cyclotetrasiloxane, D^H_4, in the presence of tris(pentafluorophenyl)-borane, $B(C_6F_5)_3$, has been studied in dilute toluene solution. The mechanism of this polymerization was investigated. The initiation and propagation steps are the $B(C_6F_5)_3$ catalyzed ring-opening of D^H_4 by the SiH group resulting in its addition to a growing chain, which occurs with hydride ion transfer to the chain end. Since there are multiple SiH groups present in the monomer, the formed polymer has extensive branching. Although the bulk polymerization leads to gel formation at an early stage of the process, no gelation is observed when the reaction is performed in 10 wt % solution in toluene. This unexpected observation is due to two reaction features. First, an extensive cyclization occurs leading to a closed multicyclic polymer structure. Second, the initiation leads to the formation of very reactive $-OSiMeH_2$ chain end, which is the real propagation center. Branching does not occur in the propagation but in the initiation and termination steps. Gaseous $MeSiH_3$ is released in the latter step.



INTRODUCTION

Tris(pentafluorophenyl)borane, $B(C_6F_5)_3$, readily catalyzes the transfer of hydride ions from silicon to organic compounds. Thus, it is often used as a catalyst in the reduction of organic compounds by hydrosilanes.[1−3] This borane is also a very active catalyst for hydride transfer reactions in organosilicon chemistry, which lead to the formation of siloxane or silylether bonds.[4−7] Kawakami used $B(C_6F_5)_3$ to promote the polycondensation of hydrosilane with silanols.[8,9] It is also a very effective catalyst for the dehydrocarbon polycondensation of hydrosilanes with alkoxysilanes,[4,10−17] as well as a promoter of metathesis reactions between hydrosilane groups and alkoxysilane[4] and metathetic dismutation reactions of oligohydrosiloxanes.[18] The hydride transfer from silicon promoted by $B(C_6F_5)_3$ is also the main step in a new class of ring-opening polymerization reactions of cyclic siloxanes,[19] which is proposed here to be named the hydride transfer polymerization reaction. In the hydride transfer ring-opening polymerization (ROP) of cyclic siloxanes the monomer ring is opened by SiH with the assistance of $B(C_6F_5)_3$. Concurrently the new siloxane bond is formed, which links the opened monomer to the polymer chain while the hydride ion is transferred to the polymer chain end, eq 1.[19]



(1)

It should be noted that the hydride transfer polymerization is different than the classical cationic polymerization initiated by protic or Lewis acids, which occurs according to a quite different mechanism. $B(C_6F_5)_3$ is known as a fairly strong Lewis acid, which when activated by a protic compound, is used as an initiator for the cationic polymerization of olefin monomers such as methoxystyrene.[20−22] Being activated by a protic molecule, it is also able to open a siloxane bond.[23] The hydride transfer polymerization occurs in the absence of protic compounds but it requires the presence of a silyl hydride, which initiates the polymerization. Tris(pentafluorophenyl)-borane plays the role of the catalyst in this polymerization.[19]

The hydride transfer polymerization of cyclic siloxanes is accompanied by hydrosiloxane metathetic processes and is limited to strained ring monomers such as hexamethylcyclotrisiloxane, (D_3).[19] If the siloxane bond is in an unstrained cyclic molecule, such as octamethylcyclotetrasiloxane (D_4), it is not cleaved by the SiH-$B(C_6F_5)_3$ system at room temperature. However, the opening of siloxane bonds may occur when hydrogen is bonded to a silicon atom of the SiOSi group.[18] An even more active system is one in which both silicon atoms bear hydrogen. This was observed in rapid metathetic dismutation of 1,1,3,3-tetramethyldisiloxane in the presence of $B(C_6F_5)_3$.[18] It was thus interesting to investigate the behavior of an unstrained cyclosiloxane having SiH groups exclusively. Such a compound could also be the monomer in the hydride transfer polymerization. It would not require the

Received: December 12, 2011
Revised: February 22, 2012
Published: March 7, 2012

ACS Publications © 2012 American Chemical Society

Si−H initiator since the polymerization would be initiated by the monomer itself. This thought prompted an investigation of the polymerization of 2,4,6,8-tetramethylcyclotetrasiloxane (D^H_4) initiated by $B(C_6F_5)_3$. The cationic polymerization of D^H_4 initiated by a strong protic acid was the subject of previous research.[24−27] This polymerization leads to linear poly(hydromethylsiloxane). However, D^H_4 is a polyfunctional monomer in the hydride transfer polymerization so branching and cross-linking is expected when its polymerization is promoted by $B(C_6F_5)_3$.

EXPERIMENTAL SECTION

Materials. 2,4,6,8-Tetramethylcyclotetrasiloxane (D^H_4) reagent grade product of ABCR (Germany) was kept over calcium hydride and distilled. Purity was checked by gas chromatography and was above 98%. Toluene (POCH, Polskie Odczynnki Chemiczne) was shaken with H_2SO_4, washed with water, then with a sodium carbonate solution, again with water, dried over $MgSO_4$, distilled over P_2O_5 and distilled again from sodium. The catalyst was reagent grade tris(pentafluorophenyl)borane (Aldrich) with a reported purity of 95% and was use without further purification.

Analytical Methods. Gas chromatography analyses were performed using a Hewlett-Packard HP 6890 chromatograph equipped with a thermal conductivity detector and a HP1 capillary column l = 30 m, d = 0.53 mm. Typical conditions were as follows: helium carrier gas flow rate 5 mL/min, detector temperature 250 °C, injector temperature 250 °C, and column programmed for 3 min at 40 °C isotherm, from 40 to 240 °C at a rate of 10 °C/min and 10−15 min at 240 °C isotherm; *n*-dodecane was used as the internal standard.

MALDI TOF spectra were recorded on a Voyager Elite spectrometer equipped with a N_2 laser operating at 337 nm in linear mode. Dithronal was used as the matrix and NaI as the cationizing agent.

SEC measurements were performed in THF at 35 °C using a differential refractive index detector Δn-2010 RI WGE Dr. Bures. The column set from Polymer Standard Service (PSS) contained four SDV columns (5 μm): 1×10^5 Å, 1×10^3 Å and two 1×10^2 Å. Apparent molar masses were calculated based on polystyrene calibration using the WinGPC Unity software from PSS. The molar masses of the samples taken at 50% monomer conversion were measured with an LDC analytical RefractoMonitor equipped with two Phenogel columns covering the molar mass range 10^2−10^5 and a refractive index detector. Toluene was used as the solvent with polystyrene as the standard.

^{1}H NMR spectra were recorded on a Bruker DRX 500 operating system at 500 MHz. ^{29}Si NMR were recorded on the same instrument working at 99.6 MHz in the inverse gate pulse sequence mode with a relaxation delay of 3 s, scan number 10 K, time domain 65 K and a 90 deg pulse 15.00. The $Cr(acac)_3$ complex was added as a relaxation reagent.

Polymerization of D^H_4 and Kinetic Studies. Polymerizations were performed in a 50 mL Schlenk flask equipped with a magnetic stirrer and a three-way stopcock through which argon was flowed. Substrate, catalyst, GC standard and solvent were introduced through this stopcock by means of a precision Hamilton syringe with a long needle. Samples were withdrawn at various time intervals and neutralized upon the addition of 4-ethylpyridine and subjected to GC analysis. *n*-Dodecane was used as the GC standard. The polymerizations were performed at room temperature (23 °C). The polymeric product was precipitated three times from toluene solution upon addition of methanol. The polymer was subjected to NMR, SEC and MALDI TOF analysis. ^{1}H NMR, δ in ppm: 0.15−0.18, 0.18−0.22, br s, SiC**H**$_3$; 4.74, br s Si**H**. ^{29}Si NMR, δ in ppm: −33.0 − (−36.5), br m, HCH_3**Si**O; −53 − (−58), −62 − (−67), br m CH_3**Si**$O_{1.5}$. An example of experiments used for kinetic studies is given as follows: The reactor was purged with nitrogen and charged with D^H_4 (1.23 g, 5.1×10^{-3} mol), toluene (10.6 g, 12.3 mL) and *n*-dodecane (0.43 g, 2.53×10^{-3} mol). The zero-time sample was withdrawn by means of a Hamilton syringe. Catalyst $B(C_6F_5)_3$ (3.1×10^{-3} g, 6.1×10^{-6} mol) in a toluene solution was introduced by a Hamilton precision syringe. The subsequent samples were withdrawn at timed intervals and introduced to an Eppendorfer vessel containing an excess of 4-ethylpyridine. The time of the introduction of the sample to the quencher solution was considered as the zero time of the reaction. The samples were analyzed by gas chromatography.

Trapping of Volatile Product. D^H_4 (2 mL, 1.98 g) was placed in a glass reactor equipped with a bubbler through which nitrogen gas was flowing and an outlet connected with an NMR tube by means of a Teflon pipe. The outlet of the pipe was placed deep under the surface of deuterated chloroform, which was in the tube. $B(C_6F_5)_3$ (40 μL of a 0.05×10^{-2} M solution in toluene) was introduced into the reactor. The evolution of a gaseous product was observed, immediately, which together with vapors of toluene and monomer was carried out by the stream of nitrogen to the NMR tube where they were partly absorbed by chloroform. After 5 min of reaction time, the formation of gel was observed. The evolution of the volatile product continued after the gelation of the reaction mixture. After 15 min of reaction time, tube was taken out, closed tightly with a Teflon stopper and inserted into the NMR spectrometer. ^{29}Si NMR spectrum of products trapped in $CDCl_3$ showed a singlet signal at δ = −63.90 ppm. A triplet of D^H_4 was also observed. There was no other silicon resonance seen in the spectrum. This new signal corresponded to the resonance of methyltrihydrosilane Me**Si**H_3 for which −64.86 ppm had been found by Fritz and Arnason.[28] This structure was fully confirmed by ^{1}H NMR spectrum which yields a quartet assigned to CH_3Si**H**$_3$ centered at δ = 3.52 ppm, J_{H-H} = 4.60 Hz and a quartet of C**H**$_3SiH_3$ centered at δ = 0.18 ppm, which were both exactly the same as those obtained in the simulated spectrum of methyltrihydrosilane by ACD/ChemSketch software.

RESULTS AND DISCUSSION

Reaction Features. Tris(pentafluorophenyl)borane (TPFPB) is considered to be a fairly strong Lewis acid.[29] In the presence of this Lewis acid the classical cationic ring-opening polymerization of tetramethylcyclotetrasiloxane (D_4) did not proceed with noticeable rate at room temperature. The behavior of 2,4,6,8-tetrahydro-tetramethylcyclotetrasiloxane (D^H_4) was found to be quite different. The addition of the 10^{-3} mol/L of $(C_6F_5)_3B$ to neat D^H_4, i.e. 0.005 g of the borane to 10 g of the monomer, resulted in relatively rapid formation of gel. Such behavior could be expected as D^H_4 has four potential reactive centers for the initiation of the hydride transfer polymerization. In addition, the open polymer chain has multiple potential centers for subsequent hydride transfer reactions which could lead to branching and cross-linking of the polymer product. In contrast to the polymerization in bulk, when the reaction was carried out in a dilute solution in inert solvent such as 10 wt % of D^H_4 solution in toluene, and when a similar concentration of $(C_6F_5)_3B$, i.e., 10^{-3} mol/L was used, the reaction proceeded at room temperature with a moderate rate and gel was not formed even after a longer reaction time. Higher cyclic oligomers D^H_5 and D^H_6 were detected by GC−MS and the isolated polymer had a molar mass of $M_n = 3 \times 10^3$ at about 50% monomer conversion. The ^{29}Si NMR analysis revealed that its chain was mostly composed of MeHSiO units. These observations were convincing proof that the hydride transfer ring-opening polymerization dominated over processes leading to branching and cross-linking, at least in the early stage of this reaction.

The conversion of monomer was monitored by sampling and gas chromatography analysis. The monomer conversion−time dependencies at various concentrations of the borane catalyst are shown in Figure 1. The striking feature of this polymerization is that it proceeded to the full conversion of monomer. Its cyclic homologues, which were transiently formed as a result of backbiting, see Figure 2A, were fully consumed in the late

dx.doi.org/10.1021/ma202687u | Macromolecules 2012, 45, 2654−2661

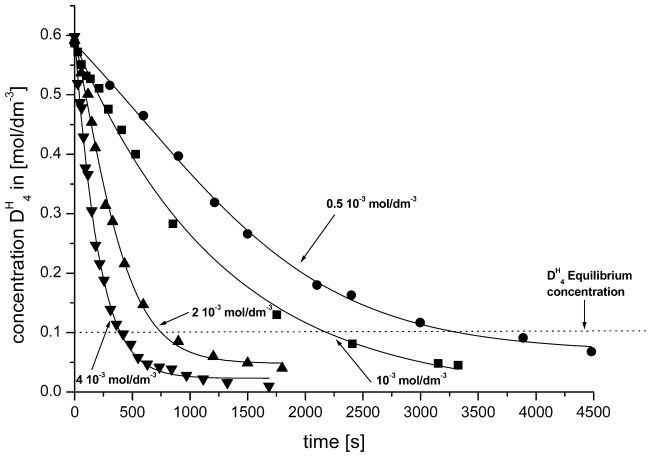


Figure 1. Monomer conversion–time dependences of D^H_4 polymerization in 10 wt % solution in toluene at 23 °C at various concentrations of $B(C_6F_5)_3$.

stages of this polymerization (Figure 2B). The ring-opening polymerization (ROP) of unstrained cyclic siloxanes, such as

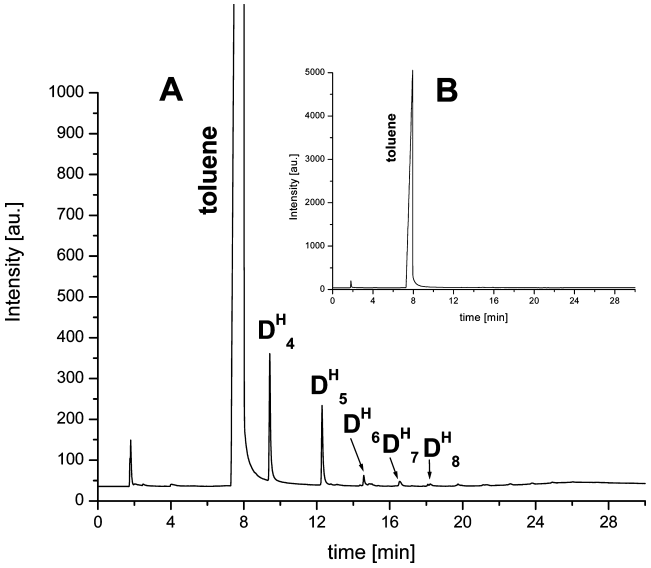


Figure 2. Gas chromatogram of the polymerization system of D^H_4 in 10 wt % solution in toluene at 23 °C: (A) quenched at the moment when D^H_4 was at its equilibrium concentration in classical ROP and (B) quenched after a longer reaction time.

D^H_4, is an entropy driven process which is reversible. In classical cationic or anionic ROP of D^H_4 the concentration of the monomer and cyclic oligomers cannot drop below their equilibrium values, which for D^H_4 is known to be about 0.1 mol/L[30] and is independent of temperature and initial monomer concentration. The decrease of the monomer concentration below this limit means that the reaction takes a course which is different from that of classical ROP of cyclic siloxanes. Another feature of this polymerization is that the polymer formation is accompanied by the evolution of a volatile gaseous product. It was produced even after all monomer had been consumed, thus indicating that the formation of the volatile product was related to a process leading to a transformation of the formed polymer. A slow increase in the viscosity of the reaction mixture was also observed in this late period of the reaction. A branching process of the polymer occurred as shown by ^{29}Si NMR, see below, which was accompanied by an increase in its molar mass and the formation of a volatile product. However, when the initial monomer concentration was 10 wt %, the gel was not formed even though the reaction was allowed to proceed for a long time.

The polymerization in its initial period is well approximated by the first order kinetic law, and the external order in catalyst is first order as well. The apparent catalytic constant was 0.46 dm^3 mol^{-1} s^{-1} at 23 °C.[31]

Analysis of the Volatile Product. Elucidation of a rational polymerization mechanism first requires knowing the structure of the volatile product formed. The polymerization was performed in a concentrated toluene solution of D^H_4 under conditions close to that in the bulk. Nitrogen gas was bubbled through the reactor sweeping away the gaseous product formed together with vapors of the solvent and monomer. The volatile products were partially trapped in an NMR tube filled with $CDCl_3$. The ^{29}Si NMR and ^{1}H NMR spectra of the trapped compounds are shown in Figure 3, parts A and B. Inspection of

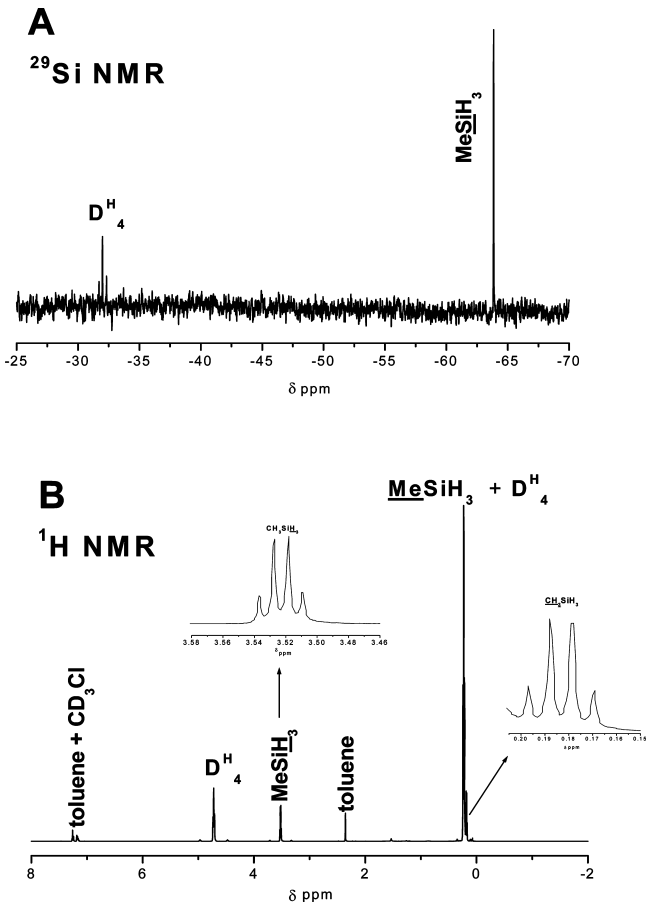


Figure 3. (A) ^{29}Si NMR spectra and (B) ^{1}H NMR spectra of products trapped in $CDCl_3$ from N_2 gas stream bubbled through the polymerization mixture of D^H_4.

the spectra revealed that the mixture, besides containing toluene and monomer, also contained the volatile methyltrihydrosilane CH_3SiH_3.

Characterization of Polymer. The isolated polymer product was analyzed by ^{1}H and ^{29}Si NMR and by SEC. The NMR spectra are shown in Figures 4 and 5. The analysis proved that the polymer chain is composed of two kinds of units:

dx.doi.org/10.1021/ma202687u | Macromolecules 2012, 45, 2654–2661

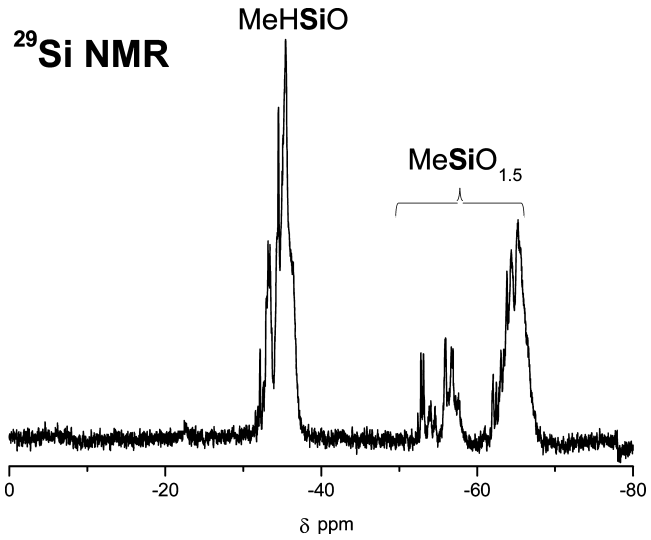


Figure 4. ^{29}Si NMR spectrum of the polymer product isolated from the polymerization system of D^H_4 in 10 w% solution catalyzed by $(C_6F_5)_3B$, 1.00 × 10^{-3} mol/L, at 23 °C, quenched after 2 h.

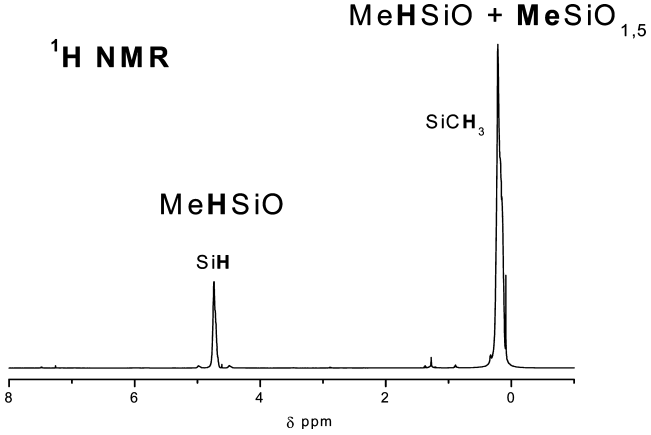
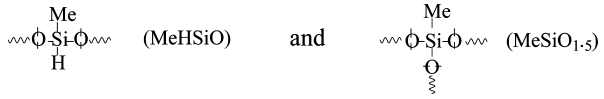


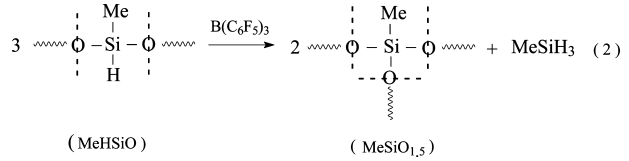
Figure 5. ^{1}H NMR spectrum of the polymer product isolated from the polymerization system of D^H_4 in 10 wt % solution in toluene catalyzed by $(C_6F_5)_3B$, 1.00 × 10^{-3} mol/L, at 23 °C, quenched after 1 h.



The former is a chain extending unit while the latter is a branching unit. The spectra did not show any pendant chain-end units.

In a separate experiment, the reaction was carried out under the same conditions, as used in the kinetic experiment described above represented by the curve marked with squares in Figure 1. Samples were withdrawn after various times and the polymer product was isolated and subjected to NMR and SEC analysis. Results are listed in Table 1. The process was followed over a period much longer than was required to reach the equilibrium concentration of D^H_4 was achieved. Although only molar masses of polymers are apparent, determined with the use of a polystyrene calibration curve, their increase with the reaction time accompanied by significant increase in dispersities is indubitable (see also Figure 6). The percentages of both units, MeHSiO, and $MeSiO_{1.5}$, were calculated by ^{1}H and ^{29}Si NMR, which permitted determination of the branching of the polymer product in the subsequently drawn samples. Results are listed in Table 1. The degree of branching was characterized by comparison of the contribution of linear and branched units to the structure of the polymer. The method for calculating the degree of branching used for classical hyperbranched polymers,[32] was not used as it does not fit this type of polymerization mechanism.

The results indicate that in the initial stage of polymerization, the linear units dominate the polymer structure. At 50% of the monomer conversion, one branching point corresponds to about 10 linear MeHSiO units. The branching became more prominent at a higher monomer conversion. When the concentration of the monomer fell to 8% of its initial concentration, which occurred after 1 h, the number of linear units was only twice as large as that of the branched units. This point may be recognized as the end of the monomer polymerization since its concentration was well below its cyclic monomer−linear chain equilibrium concentration. Further reaction led mostly to a conversion of the linear MeHSiO units into the branched $MeSiO_{1.5}$ units, which caused a further decrease in the monomer concentration. The reaction proceeds according to a simplified eq 2 and must lead to a strong restructuring of the siloxane chain.



The analysis of the polymer, when the reaction was quenched after 24 h, showed that the three-way-bonded branching unit strongly prevails over the two bonded linear unit as the respective number ratio is 3:1. It could be predicted that polymer gelation would occur at a much earlier stage in reaction 2. However, the polymer after 24 h of reaction time was still soluble even though its molar mass has grown as shown in Table 1. The only explanation for the unusual behavior of this system is that the formation of cyclic structures dominates the pattern of the polymerization in its later stage.

Confirmation of the validity of proposed reaction 2 and important information about the mechanism of the polymerization of D^H_4 initiated by $B(C_6F_5)_3$ are provided in the results of a MALDI TOF study. The spectrum of the polymer isolated from the reaction system after the monomer concentration decreased below its chain-ring equilibrium value is shown in Figure 7. The peaks correspond well to the molar mass of the combination of numbers of MeHSiO and $MeSiO_{1.5}$ units, which are labeled above the signals. This result is not only consistent with a process that proceeds according to eq 2, but it also suggests that other structural units are not present in the macromolecule chain nor do they appear at its termini. The only explanation for this observation is that cyclic structures occupy chain ends or the whole molecule has a cyclic structure. The mechanism of this polymerization must also explain another strange feature of the MALDI TOF spectrum of the polymer. It shows that the number of $MeSiO_{1.5}$ units in the macromolecule is always even, i.e., 2, 4, 6, 8, ... Signals corresponding to macromolecules having odd number of branching units are not detected.

Reaction Mechanism. The classical cationic polymerization of octamethylcyclotetrasiloxane (D_4) initiated by $B(C_6F_5)_3$ does not proceed at a measurable rate under the

dx.doi.org/10.1021/ma202687u | Macromolecules 2012, 45, 2654−2661

Table 1. Characteristics of Polymer Products Isolated from the Polymerization System of D^H_4 in 10 wt % Solution in Toluene, Catalyzed by $(C_6F_5)_3B$, 1.00 × 10^{-3} mol/L, at 23 °C, after Various Reaction Times

reaction time, h	monomer conversion %	molar mass[a] M_n × 10^{-3}	molar mass[a] M_w × 10^{-3}	dispersity M_w/M_n	MeHSiO units, %	$MeSiO_{1.5}$ units, %
0.25	50	2.5[b]	4.6[b]	1.8[b]	90.3	9.7
1	92	3.0	7.7	2.6	72.2	27.8
2	99	2.9	17.1	6.0	51.6	48.4
6	100	5.7	64.0	11.2	42.9	57.1
24	100	9.3	95.3	10.3	25.2	74.8

[a]These are apparent molar masses measured by SEC with RI detection and calculated with polystyrene calibration. Since the polymers have branched structures their absolute molar masses could be higher than the values obtained basing on calibration with linear polystyrene. [b]Measured on an LDC Analytical Refractomonitor with RI detector.

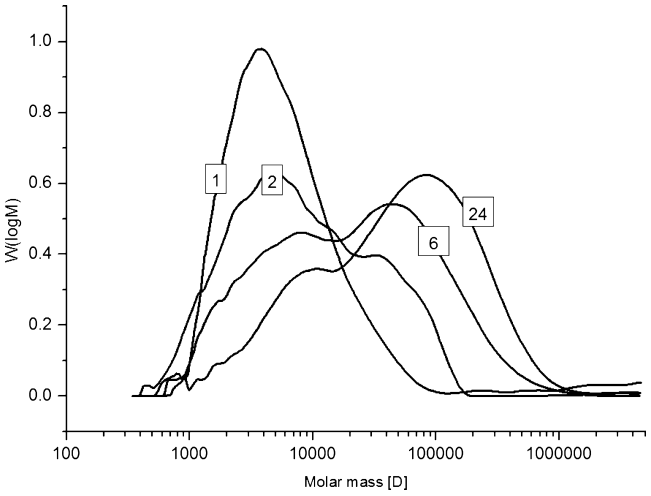


Figure 6. SEC curves of the polymer product isolated from the polymerization system of D^H_4 in 10 wt % toluene solution catalyzed by $(C_6F_5)_3B$, 1.00 × 10^{-3} mol/L, at 23 °C, after 1, 2, 6, and 24 h.

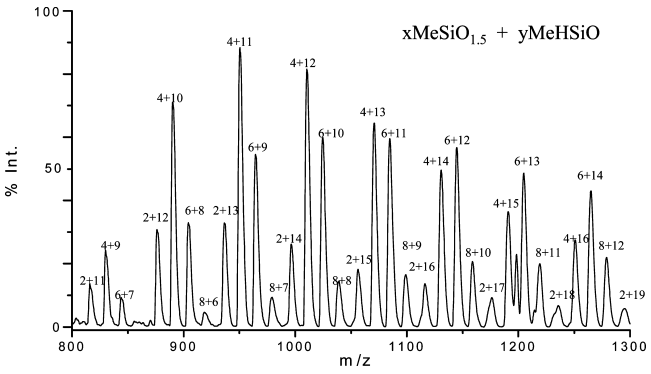
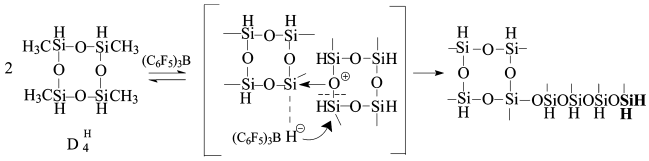


Figure 7. MALDI TOF spectrogram of the polymer product isolated from the polymerization system of D^H_4 in 10 wt % toluene solution catalyzed by $(C_6F_5)_3B$, 1.00 × 10^{-3} mol/L, at 23 °C, quenched after 1 h. Peaks are marked by the sum of the number of branching units $xMeSiO_{1.5}$ and chain extending units yMeHSiO which corresponds to the m/z value at the peak maximum.

conditions used in this study. The observed relatively fast polymerization of D^H_4, which occurred in the presence of $B(C_6F_5)_3$, must be explained by a nonclassical cationic mechanism related to the presence of the SiH groups in the cyclic monomer. The mechanism must also explain the formation of $MeSiO_{1.5}$ units and the evolution of $MeSiH_3$ as well as the extensive cyclization of the polymer formed. A general scheme of the polymerization, which is in agreement with the experimental results and with results of earlier research,[18,19] is shown in Scheme 1 and all of the steps of this process are discussed below:

Initiation. It was shown elsewhere that the hydride transfer mediated by $B(C_6F_5)_3$ may lead to the opening and reformation of the siloxane bond if the silicon atom is also bonded to hydrogen.[18] It is worth recalling that this process occurs particularly readily if both silicon atoms of the disiloxane unit bear hydrogen. It was shown that the rate of $HMe_2SiOSiMe_2H$ disproportionation catalyzed by $B(C_6F_5)_3$ is higher than that of $Me_3SiOSiMe_2H$ by about 2 orders of magnitude.[19] The ring-opening of D_3 occurs also much faster by $HMe_2SiOSiMe_2H$ than by $Me_3SiOSiMe_2H$. It is thus conceivable that the D^H_4 ring is opened by another D^H_4 molecule in the presence of $B(C_6F_5)_3$ and, in this way, the hydride transfer polymerization of D^H_4 is initiated according to eq 3.



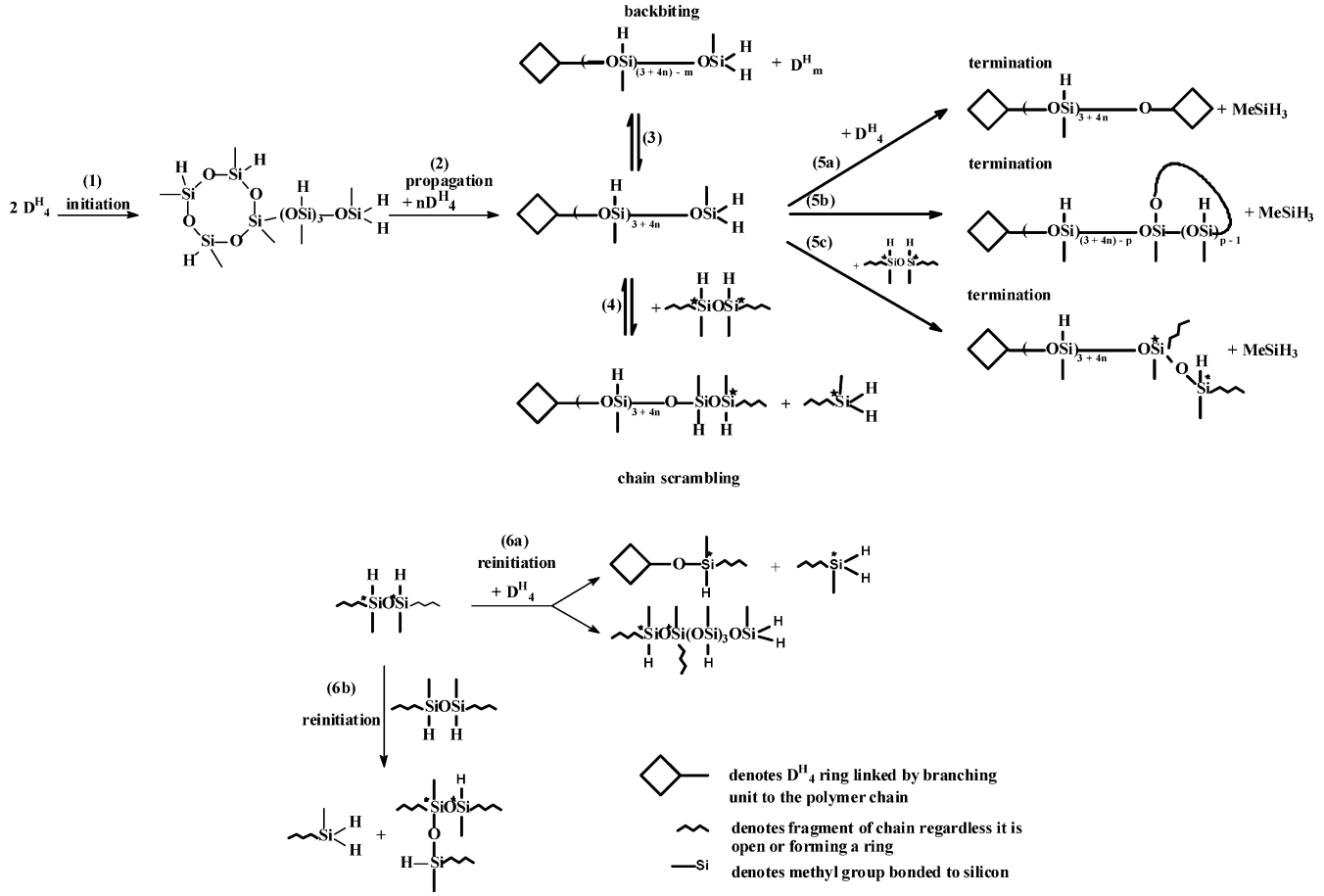
(3)

The mechanism of this reaction is analogous to those of the metathesis of 1,1,3,3-tetramethydisiloxane[18] and condensation of alkoxysilane with hydrosilane.[4] The hydride ion is transferred from the monomer to the borane with the formation of a bicyclic oxonium ion intermediate by the addition of another monomer molecule to a vacant silicon. Then an H^- is transferred to the silicon atom of the added monomer leading to the opening of its ring. The formed $OSiMeH_2$ end unit is very reactive toward hydride transfer and may be considered as an active propagation center, eq 3. It was demonstrated in our earlier studies[19] that the ring-opening of the D_3 in the presence of $B(C_6F_5)_3$ proceeded more rapidly with $PhMeSiH_2$ than with $PhMe_2SiH$ by a factor of 300. This suggests that linear propagation dominates over branching and cross-linking. A silicon atom bearing two hydrogen atoms reacts with the siloxane bonds under catalysis by $B(C_6F_5)_3$ much more rapidly than a silicon atom having only one hydrogen bonded to it. The initiation reaction leads to the transformation of one MeHSiO unit into a branching $MeSiO_{1.5}$ unit. It also leaves the eight membered ring structure at the beginning of the initiated chain, which is connected to the chain by the branching unit as illustrated in eq 3.

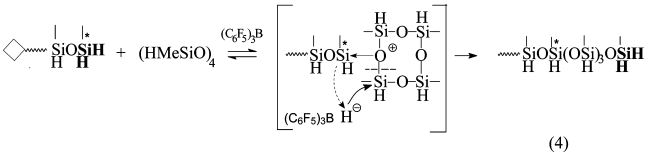
Propagation. The active propagation center $-OSiMeH_2$ forms an oxonium salt with the monomer and the borane in the propagation step. The oxonium salt decomposes upon monomer ring-opening. The ring-opened monomer is added to

dx.doi.org/10.1021/ma202687u | Macromolecules 2012, 45, 2654–2661

Scheme 1. Ring-Opening Polymerization of 2,4,6,8-Tetramethylcyclotetrasiloxane, D^H_4, in the Presence of $B(C_6F_5)_3$



a growing polymer end while the hydride ion is transferred to the chain end thus regenerating the active propagation center, eq 4.

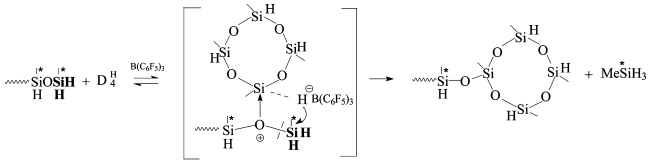


(4)

The propagation is reversible since the propagation center may form the oxonium ion intermediate with a siloxane unit in its polymer chain. This backbiting process may lead to a series of cyclics homologues of D^H_4 (reaction 3 in Scheme 1). If the analogous reaction occurs intermolecularly it leads to a chain transfer, which causes chain scrambling as shown in reaction 4 in Scheme 1.

Termination. The important feature of this reaction is the chain termination in which the $OSiMeH_2$ active propagation center is transformed to volatile $MeSiH_3$. This reaction occurs when the oxonium ion intermediate is formed by hydride transfer from an OSiMeH unit in the monomer or polymer to the active propagating center $OSiMeH_2$, reactions 5abc in Scheme 1. The termination which occurs as a result of the reaction of $OSiMeH_2$ with monomer is shown in eq 5.

$MeSiH_3$ is cleaved from the active center and the remaining oxygen is used to form a bond with vacant silicon. The termination on polymer takes an analogous path. If the chain termination takes place with the participation of monomer,



(5)

then the monomer ring is added to the chain end through the formation of a $MeSiO_{1.5}$ unit, as shown in eq 5 and reaction 5a in Scheme 1. When the chain is terminated by the reaction with the MeHSiO unit within its own chain, then a ring is formed (Scheme 1 reaction 5b). An intermolecular reaction of this type leads to branching or cross-linking (Scheme 1 reaction 5c). The low initial concentration of monomer is crucial to obtaining soluble polymer product.

Most probably, the methylsilane byproduct, $MeSiH_3$ could reversibly reinitiate a new chain forming two active propagation centers ($OSiMeH_2$), but it is volatile and escapes from the reaction system.

Reinitiation. The formation of the propagating center $OSiMeH_2$ also occurs as a result of reactions between monomer and polymer chain, as shown in reaction 6a of Scheme 1. In this case, either a new chain is grafted from the polymer chain or the chain is cleaved into two parts. One of them closes the monomer ring through its $MeSiO_{1.5}$ unit and the other gains the propagating $OSiMeH_2$ end.

Still other reinitiation reactions may occur either intra- or intermolecularly between two MeHSiO polymer chain units as shown in eq 6b of Scheme 1. These reactions dominate in the

dx.doi.org/10.1021/ma202687u | *Macromolecules* 2012, 45, 2654−2661

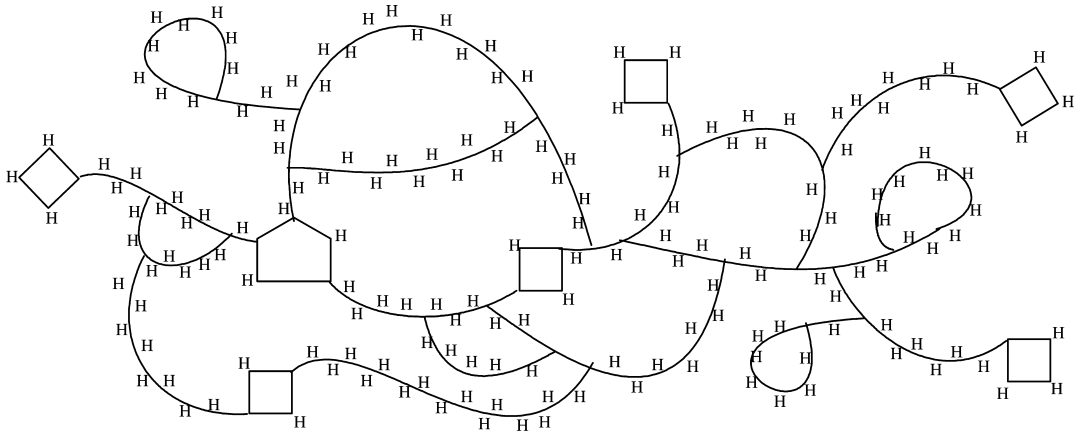


Figure 8. Schematic representation of the macromolecule of the polymer formed in the hydride transfer polymerization of D^H_4 catalyzed by $(C_6F_5)_3B$ in a dilute solution of an inert solvent at an early stage in the reaction.

second slow stage of the process. They occur much more slowly than the D^H_4 polymerization.

Since the process is performed in a dilute solution, the intramolecular reactions strongly dominate. They lead to the extensive formation of loops, so that the resulting macromolecule has a multicyclic structure schematically presented in Figure 8. The intermolecular reactions are manifested in the increase in molar mass of the polymer. This may gain importance when a formed rigid, multicyclic macromolecule is less susceptible to intramolecular reactions than to intermolecular chain extension.

Each of the initiation and termination reactions results in the conversion of one MeHSiO unit into one $MeSiO_{1.5}$ unit, which decreases the rates of monomer reformation and monomer analogues formation in depolymerization processes (reaction 3 of Scheme 1). This is the reason for the disappearance of the monomer and cyclic oligomers from the reaction system shown in Figure 2B. Reactions 6a and 6b (Scheme 1) also result in the formation of the $OSiMeH_2$ chain ends. As mentioned previously, the $OSiMeH_2$ group is very reactive in both the propagation and termination steps so its stationary concentration in the reaction system, particularly in the second stage of the reaction, should be at a low level.

Each of the initiation and reinitiation steps, reactions 1, 6a, and 6b in Scheme 1, lead to the formation of one $MeSiO_{1.5}$ unit and one $OSiMeH_2$ terminal group. Each of the termination reactions 5a, 5b and 5c in Scheme 1 similarly give rise to the formation of one $MeSiO_{1.5}$ unit, but lead to the disappearance of one $OSiMeH_2$ terminus. The even number of the $MeSiO_{1.5}$ units found by MALDI-TOF indicates that the number of initiation and reinitiation turns is equal to the number of the termination acts. It may be further concluded that the $OSiMeH_2$ group is not present in the final polymer product at measurable concentrations which is consistent with NMR spectroscopic analysis. The only possible open chain end-group for the investigated polymer is $-OSiMeH_2$. Lack of the $-OSiMeH_2$ group in the final polymer strongly indicates that the formed macromolecule is built from various size cyclic structures. The polymerization of D^H_4 in the presence of $B(C_6F_5)_3$ is a good example of three-dimensional addition polymerization leading to closed multicyclic structures free of pendant chain ends. Such structures have so far been obtained by equifunctional polycondensation of multifunctional monomers under ideal reaction conditions.[33,34] A polysiloxane with polycyclic structure was generated by the hydrolytic coupling of a cyclic methylhydrosiloxane, but the polymer was insoluble and contained some quantity of silanol groups.[35]

CONCLUSIONS

D^H_4 undergoes ring-opening polymerization initiated by $B(C_6F_5)_3$. The polymerization proceeds according to a nonclassical mechanism, which may be classified as hydride transfer ring-opening polymerization.

The $-OSiMeH_2$ chain end is the active propagating center, but its stationary concentration in the polymerization system is very small.

The polymerization occurs with the transformation of linear MeHSiO units into branching $MeSiO_{1.5}$ units, which takes place in initiation and termination steps. Volatile $MeSiH_3$ forms as a byproduct in the termination step. Cyclic structure formation dominates in the products of the polymerization.

Gel formation may be avoided by performing the polymerization in dilute solution in an inert solvent. The polymerization of 10 wt % solution of D^H_4 in toluene leads to full conversion of monomer into soluble polymer.

The macromolecule formed has a nearly perfect multicyclic structure composed of small rings originating from the monomer and its homologues as well as larger macrocycles of various sizes. This easily synthesized soluble polymer having many reactive SiH groups may be used as a core starting material for the synthesis of more complex multifunctional polymer structures.

AUTHOR INFORMATION

Notes

The authors declare no competing financial interest.

ACKNOWLEDGMENTS

The authors are grateful to the Center of Molecular and Macromolecular Studies of the Polish Academy of Sciences in Łódź Poland for the financial support of this research. The authors are indebted to Mary Krenceski Ph.D. from Momentive Performance Materials and to David Simone Ph.D. and Matthew Butts Ph.D. from General Electric GRC for the language improvement of this paper.

REFERENCES

(1) Piers, W. E. *Adv. Organomet. Chem.* **2005**, *52*, 1.
(2) Gevorgian, V.; Rubin, M.; Benson, S.; Liu, X.; Yamamoto, Y. *J. Org. Chem.* **2000**, *65*, 6179.
(3) Berkefeld, A.; Piers, W. E.; Parvez, M. *J. Am. Chem. Soc.* **2010**, *132*, 10660.
(4) Chojnowski, J.; Rubinsztajn, S.; Cella, J.; Fortuniak, W.; Cypryk, M.; Kurjata, J.; Kaźmierski, K. *Organometallics* **2005**, *24*, 6077.

(5) Chojnowski, J.; Rubinsztajn, S.; Fortuniak, W.; Kurjata, J. *Macromolecules* **2008**, *41*, 7352.
(6) Brook, M. A.; Grande, J. B.; Ganachaud, F. Silicon Polymers. *Adv. Polym. Sci.* **2011**, *235*, 161.
(7) Cella, J.; Rubinsztajn, S. *Macromolecules* **2008**, *41*, 6965.
(8) Zhou, D. Q.; Kawakami, Y. *Macromolecules* **2006**, *38*, 6902.
(9) Kawakami, Y.; Kakihana, Y.; Ooi, O.; Oishi, M.; Suzuki, K.; Shinke, S.; Uenishi, K. *Polym. Int.* **2009**, *58*, 279.
(10) Rubinsztajn, S.; Cella, J. *Macromolecules* **2005**, *38*, 1061.
(11) Kurjata, J.; Fortuniak, W.; Rubinsztajn, S.; Chojnowski, J. *Eur. Polym. J.* **2009**, *45*, 3372.
(12) Grande, J. B.; Thompson, D. B.; Gonzaga, F.; Brook, M. A. *Chem. Commun.* **2010**, *46*, 4988.
(13) Grande, J. B.; Gonzaga, F.; Brook, M. A. *Dalton Trans.* **2010**, *39*, 9369.
(14) Thompson, D. B.; Brook, M. A. *J. Am. Chem. Soc.* **2008**, *130*, 32.
(15) Chen, X. J.; Cui, Y. D.; Yin, G. Q.; Liao, L. W.; Hu, W. B. *Chin. J. Polym. Sci.* **2008**, *26*, 481.
(16) Xunjun, C.; Yingde, C.; Guoqiang, Y.; Liewen, L. *J. Appl. Polym. Sci.* **2007**, *106*, 1007.
(17) Wakabayashi, R.; Kawahara, K.; Kuroda, K. *Angew. Chem., Int. Ed.* **2010**, *49*, 5273.
(18) Chojnowski, J.; Fortuniak, W.; Kurjata, J.; Rubinsztajn, S.; Cella, J. *Macromolecules* **2006**, *39*, 3802.
(19) Chojnowski, J.; Rubinsztajn, S.; Fortuniak, W.; Kurjata, J. *J. Inorg. Organomet. Polym. Mat.* **2007**, *17*, 173.
(20) Vergnaud, J.; Sarazin, Y.; Strub, H.; Carpentier, J. F. *Eur. Polym. J.* **2010**, *46*, 1093.
(21) Kostjuk, S. V.; Radchenko, A. V.; Ganachaud, F. *Macromolecules* **2007**, *40*, 482.
(22) Radchenko, A. V.; Kostjuk, S. V.; Vasilenko I.V.; Ganachaud, F.; Kaputsky, F. N.; Guillaneuf, Y. *J.Polym. Sci., Part A: Polym Chem.* **2008**, *46*, 6928.
(23) Longuet, C.; Joly-Duhamel, C.; Ganachaud, F. *Macromol. Chem. Phys.* **2007**, *208*, 1883.
(24) Graczyk, T.; Lasocki, Z. *Bull. Acad. Polon. Sci.* **1978**, *26*, 917.
(25) Graczyk, T.; Lasocki, Z. *Bull. Acad. Polon. Sci.* **1979**, *27*, 185.
(26) Gupta, S. P.; Moreau, M.; Masure, M.; Sigwalt, P. *Eur. Polym. J.* **1993**, *29*, 15.
(27) Palaprat, G.; Ganachaud, F.; Mauzac, M.; Hemery, P. *Polymer* **2005**, *46*, 11213.
(28) Fritz, G.; Arnason, I. *Z. Anorg. Allg. Chem.* **1976**, *419*, 213.
(29) Jacobsen, H.; Berke, H.; Döring, S.; Kehr, G.; Erker, G.; Fröhlich, R.; Meyer, O. *Organometallics* **1999**, *18*, 1724.
(30) Beevers, M. J.; Semlyen, J. A. *Polymer* **1972**, *13*, 385.
(31) CH_3SiH_3, which is byproduct of this process, may reinitiate the polymerization. This possible reinitiation is out of control in this study. Since the polymerization is carried out in an open system this gaseous product (bp −57 °C) is supposed to escape from the polymerization solution. However, its small stationary concentration in this system may affect the polymerization rate.
(32) Frey, H.; Hölter, D. *Acta Polym.* **1999**, *50*, 67.
(33) Kricheldorf, H. R. *Acc. Chem. Res.* **2009**, *42*, 981.
(34) Kricheldorf, H. R. *J. Polym, Sci., Part A: Polym. Chem.* **2009**, *47*, 1971.
(35) Kurian, P.; Kennedy, J. P.; Kisluik, A.; Sokolov, A. *J. Polym. Sci., Part A: Polym. Chem.* **2002**, *40*, 1285.

Macromolecules

Article

pubs.acs.org/Macromolecules

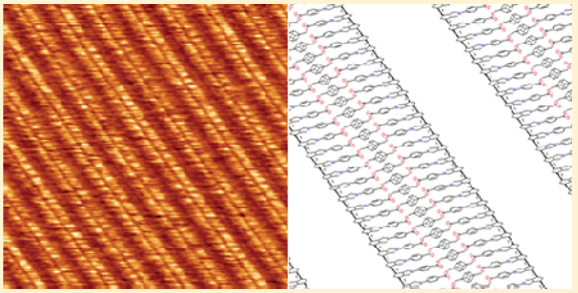
Polynorbornene-Based Double-Stranded Ladderphanes with Cubane, Cuneane, Tricyclooctadiene, and Cyclooctatetraene Linkers

Nai-Hua Yeh, Chih-Wei Chen, Shern-Long Lee, Hung-Jen Wu, Chun-hsien Chen,* and Tien-Yau Luh*

Department of Chemistry, National Taiwan University, Taipei, Taiwan 106

Supporting Information

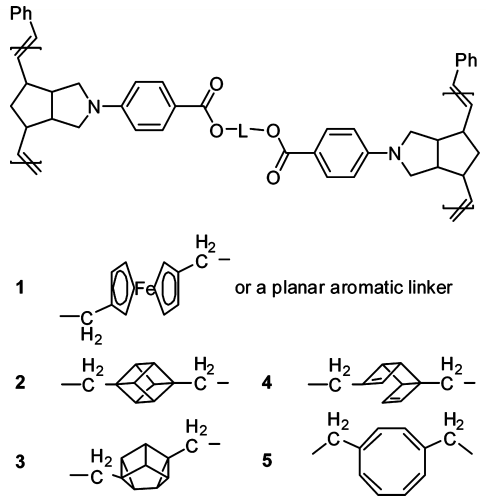
ABSTRACT: Double-stranded ladderphanes **2**, **3**, and **5** having cubane, cuneane, and cyclooctatetraene linkers are synthesized by ring-opening metathesis polymerization (ROMP) of the corresponding bisnorbornene monomers **10**, **11**, and **13**, respectively. Attempts to polymerize the corresponding tricyclooctadiene-linked bisnorbornene **12** are not successful, starting monomer being recovered. Polymer with this tricyclic diene linker **4** is obtained from the rhodium-catalyzed isomerization of **2**. The scanning tunneling microscopic (STM) image of **2** shows an ordered pattern on the graphite surface by self-assembly.



INTRODUCTION

Cubane represents one of the most fascinating molecules not only for its unique structural feature but also for other potential applications.[1] Cubane skeleton, although highly strained, exhibits extraordinary stability under various conditions. Incorporation of cubane moiety into oligomers and polymers has been sporadically explored.[2−6] Thus, [*n*]cubylcubanes and oligocubyl rods are synthesized from the treatment of diiodocubane or diiodooligocubyl with *tert*-butyllithium.[1b,2] Polymerization of bishomoallylcubane by cross-metathesis gives the corresponding oligomers with six to seven repeat units.[3] In addition to polyamides[4] and polyacrylates,[5] cubane-containing polynorbornenes are obtained by the ring-opening metathesis polymerization (ROMP) of the corresponding diastereomeric mixture of exo- and endo-norbornene esters.[6] Incorporation of valence isomers of cubane (such as substituted cuneane or tricycle[4.2.0.0^{2,5}]octadiene) other than a cyclooctatetraene derivative[5] into a polymer has not been explored.

We recently reported a series of symmetrical[7] and unsymmetrical[8] double-stranded polynorbornene-based ladderphanes **1** having a range of different rigid aromatic or organometallic linkers.[9] Related disulfide-based ladderphanes have recently been disclosed.[10] Like a DNA molecule, the aromatic linkers in these ladderphanes are cofacially aligned, and the corresponding single-stranded polynorbornenes can undergo replication generating a daughter polymer.[7−9] Each of the monomeric unit in **1** spans about 5−6 Å.[7−9,11] The smallest possible dimensions of cylindrical 1,4-disubstituted cubane derivatives and related substituted C_8H_6-valence isomers such as cuneane, *syn*-tricycle[4.2.0.0^{2,5}]octadiene, or cyclooctatetraene are no more than 3.8 Å.[12] It is envisaged that a cubane derivative and related valence isomers can fit into this space and, therefore, could be used as linkers for double-stranded ladderphanes. In this paper, we wish to report the synthesis and characterization of a range of double-stranded polybisnorbornenes **2**−**5** using cubane and its valence isomers as linkers.



RESULTS AND DISCUSSION

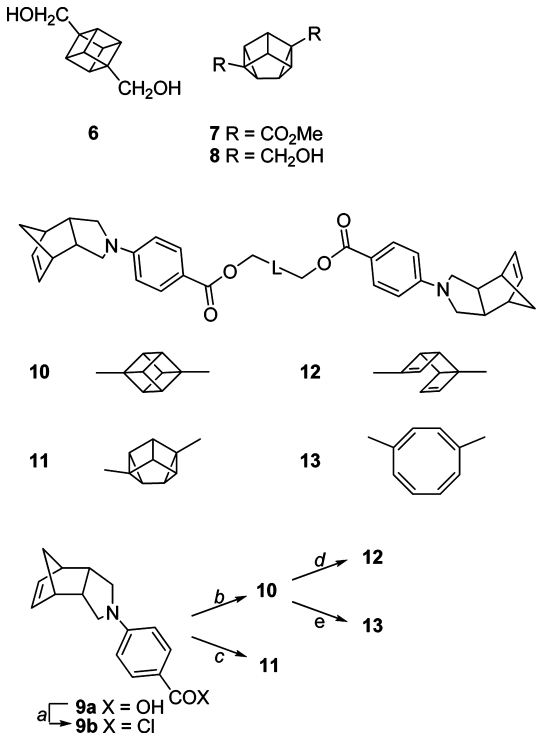
Cubanedicarbinol **6** was synthesized according to literature procedures.[13] Reduction of dimethyl 2,6-cuneanedicarboxylate **7**[12c,14] by LAH gave 75% yield of **8**. Diol **6** was allowed to react with acid chloride **9b** in the presence of Et_3N to afford the corresponding monomer **10** in 73% yield (Scheme 1). In a similar manner, monomer **11** was prepared. Treatment of **10** with 5 mol % $[Rh(NBD)Cl]_2$ in $CHCl_3$−toluene at rt gave the corresponding tricyclooctadiene derivative **12** in 75% yield.[15] When the reaction was carried at refluxing temperature, cyclooctatetraene-linked bisnorbornene **13** was obtained in 70% yield (Scheme 1).[5,15b]

ROMP of **10** with 20 mol % of the first generation of the Grubbs catalyst (G-I) gave the corresponding polymer **2** in

Received: January 4, 2012
Revised: March 2, 2012
Published: March 13, 2012

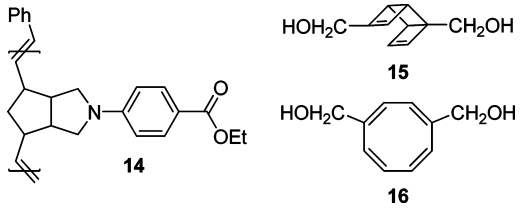
ACS Publications © 2012 American Chemical Society

Scheme 1. Synthesis of Monomers 10−13[a]



[a]Reagents and conditions: (a) $(COCl)_2$, (b) **6**, Et_3N, 73%; (c) **8**, pyridine, 67%; (d) $[Rh(NBD)Cl]_2$, $CHCl_3$−toluene, rt, 75%; (e) $[Rh(NBD)Cl]_2$, $CHCl_3$−toluene, reflux, 70%.

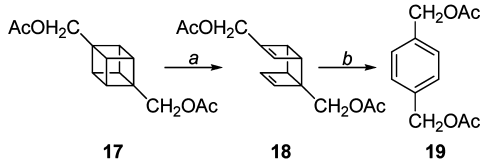
90% yield (M_n = 6000, PDI = 1.3, degree of polymerization [DP] = 9). The absorption for the protons on cubane linker in **2** in the ^1H NMR spectrum appears as a broad peak centered at δ 3.86 ppm. The corresponding carbon signal in the ^{13}C NMR spectrum of **2** exhibits at δ 44.5 ppm, in addition to the quarternary carbons at δ 57.0 ppm. Ethanolysis of **2** with NaOEt in EtOH and DCM gave **6** in 54% yield in addition to single-stranded polynorbornene **14a**[11b] in 65% yield (M_n = 2900, PDI = 1.2, DP = 10). A similar degree of polymerization between **2** and **14** indicates that **2** would be a double-stranded ladderphane.



In a similar manner, ROMP of **11** under similar conditions using 12 mol % of the G-I catalyst gave **3** in 83% yield (M_n = 10 200, PDI = 1.8, DP = 16). Four of the six cuneane protons in **2** appear at δ 2.20−2.55 ppm. Ethanolysis of **3** gave **14** in 74% yield (M_n = 4300, PDI = 1.3, DP = 17) and diol **8** (85%). These results suggest that cuneane skeleton is also stable under the ROMP conditions. A similar degree of polymerization between **3** and **14b** supports the double-stranded nature of **3**.

Attempts to polymerize **12** with G-I catalyst were unsuccessful. Upon mixing of **12** and 20 mol % of the G-I catalyst, the DCM solution turned red immediately. After stirring for 1 h, starting **12** was recovered in 80% yield. Cyclobutene is more strained than 2-norbornene,[16] and cyclobutene derivatives are known to undergo ROMP upon treatment with a variety of metal−carbene catalysts.[17] Indeed, tricyclooctadiene has been used as a cross-linking agent for olefin metathesis polymerization.[18] It seems likely that the ruthenium catalyst may interact preferentially with the double bonds in tricyclooctadiene moiety in **12**. A DCM solution of **18**, prepared from **17**, was allowed to react with 1 equiv of G-I catalyst at rt for 1 h (Scheme 2). α,α'-Diacetoxyl-*p*-xylene **19**

Scheme 2. Reaction of 18 with G-I Catalyst[a]



[a]Reagents and conditions: (a) $[Rh(NBD)Cl]_2$, $CHCl_3$−toluene, rt, %; (b) G-I catalyst (1 equiv), $CDCl_3$, %.

was obtained in 58% yield. An extrusion of a C_2H_2 moiety from tricyclooctadiene scaffold may take place. The discrepancy between this work and literature results with parent tricyclooctadiene[18] is striking. Presumably, the presence of substituents in **18** may lead to different selectivity, although the actual mode of the reaction remains unclear at this stage. It is worthy to note that a stoichiometric amount of G-I catalyst was required for this transformation. Accordingly, 80% recovery of **12** from the reaction with 20 mol % of G-I described above is understandable.

Since tricyclooctadiene linker is obtained by rhodium-catalyzed ring-opening reaction,[15] it is envisaged that polymer **2** might also undergo similar ring-opening reaction. Thus, treatment of **2** with 5 mol % $[Rh(NBD)Cl]_2$ in $CHCl_3$−toluene at rt gave **4** in 85% yield (M_n = 6100, PDI = 1.3, DP = 9). The three olefinic protons in the tricyclooctadiene linker in **4** appears at δ 6.1 ppm as a broad peak in the ^1H NMR spectrum. The corresponding carbon signals in the ^{13}C NMR spectrum emerge at 128.6, 135.3 (two types of carbon), and 144.6 ppm. Ethanolysis of **4** under the same conditions as described above gave diol **15** and **14c** (M_n = 2700, PDI = 1.2, DP = 9) in 48% and 60%, respectively.

As described above, monomer **13** was obtained from the thermolysis of **10** in the presence of the rhodium catalyst. Similar thermal treatment of **4** in the presence of $[Rh(NBD)Cl]_2$ in refluxing toluene−$CHCl_3$ mixed solvent,[5,15b] however, resulted in the recovery of **4** in essentially quantitative yield.[19]

Polymer **5** (M_n = 6500, PDI = 1.3, DP = 10) was obtained in 87% yield from the ROMP of **13** with G-I catalyst. The ^1H NMR of **5** shows broad peaks at δ 5.8−6.1 ppm attributed to the olefinic protons of the cyclooctatetraene linkers. Ethanolysis of **5** under the same conditions as described above gave diol **16** and **14d** (M_n = 3200, PDI = 1.3, DP = 11) in 50% and 68%, respectively. It is worthy to note that cyclooctatetraene moiety in **13** were stable under these conditions.[20]

Thermal Gravimetric Analyses (TGA) of 2−5. Relatively speaking, polymers **2**−**5** were quite thermally stable. The temperatures with 5% weight loss for **2**, **3**, **4**, and **5** were 244, 299, 276, and 304 °C, respectively, as revealed by TGA measurements. The DSC studies, however, indicate that none of these ladderphanes exhibit glass transition temperatures.[21]

Scanning Tunneling Microscopic Images. The scanning tunneling microscopy (STM) image of **2** shows a well-aligned

dx.doi.org/10.1021/ma300027k | *Macromolecules* 2012, 45, 2662−2667

motif on highly ordered pyrolytic graphite (HOPG) surface.[22] The brighter and darker parts of the lamellae can be ascribed to the aromatic cores and cubane parts of **2**, respectvely, due to the magnitude of conductance. The apparent width of each stripe (from the bright spot of one stripe to the bright spot of the adjacent stripe) shown in Figure 1 is about 2.9 nm, which is

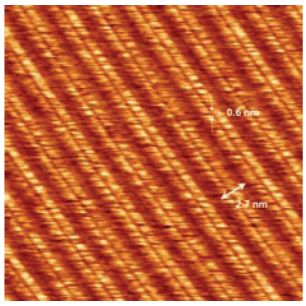


Figure 1. STM images of **2** on H. Imaging conditions of E_{bias}, $i_{tunneling}$, and image size: 0.68 V, 174 pA, and 22 × 22 nm.

consistent with the estimated width for **2** (ca. 2.6 nm[23]) plus van der Waals spacing. In addition, the two adjacent monomeric units in **2** are separated by ∼0.6 nm, which would match nicely to the span for each of the monomric unit in polynorbornene-based ladderphanes.[7−10] As shown in Figure 1, a dark line is present in the center along the longitudinal axis of the polymer separating each stripe into two symmetrical parts. Presumably, the cubane moiety, which is nonconductive, would occupy at the center aligned coherently along the polymeric axis. Like those of double-stranded ladderphanes,[7−9,24a] the present result indicates that the assembly of the polymeric molecules **2** may also exhibit $\pi-\pi$ attractions between end groups (vinyl and styryl) along longitudinal axis of the polymers and van der Waals interactions between the neighboring polymeric backbones.

CONCLUSION

In summary, we have demonstrated the first polynorbornene-based double-stranded ladderphanes with nonaromatic linkers. Cubane and three other C_8H_6 valence isomeric linkers in these polymers **2**−**5** are stable under the polymerization conditions. The present results suggest that double-stranded ladderphanes can be easily accessible by the G-I-catalyzed ROMP protocol, as long as a rigid linker with a span less than 6 Å[11a] is used to connect two norbornene moieties fused with endo-*N*-arylpyrrolidine ring. These ladderphanes are coherently aligned on the HOPG surface to form an ordered pattern by self-assembly as depicted in Figure 1. This phenomenon now appears to be a general feature in these polynorbornene-based ladderphanes.

EXPERIMENTAL SECTION

General. Melting points were measured with Fargo MP-1D melting point apparatus and not calibrated. ^{1}H and ^{13}C NMR spectra were recorded on a Varian 400 Unity Plus or a Bruker Advance-400 MHz FT-NMR spectrometer (400 MHz) using $CDCl_3$ as solvent at ambient temperature. The chemical shift of $CDCl_3$ was calibrated at 7.26 ppm in ^{1}H NMR spectra and 77.0 ppm in ^{13}C NMR. Infrared spectra (IR) were obtained by using Thermo Nicolet Avatar 360 ESP FT-IR spectrometer and configured with EZ OMNIC software. High-resolution mass spectroscopy was obtained by using a Jeol-JMS-700 mass spectrometer using the FAB method with a 3-nitrobenzyl alcohol matrix, an Applied Biosystems 4800 Proteomics Analyzer (Applied Biosystem, Foster City) using the MALDI method equipped with an Nd/YAG laser (335 nm) operating at a repetition rate of 200 Hz, or a Waters LCT Premier XE (Waters Corp., Manchester, UK) using the ESI method withdual ionization ESCi (ESI/APCi) source options. GPC was performed on a Waters GPC instrument equipped with Waters 1515 HPLC pump using Waters 2487 absorbance detector. Polymer (∼0.5 mg) in THF (0.1 mL) was filtered through a 0.5 μm filter, and 20 μL of the sample was injected into Shodex KF-G, Styragel HR2, Styragel HR3, and Styragel HR4 columns (7.8 × 300 mm) were with oven temperature at 40 °C using standard polystyrene samples (1.84×10^5−996 Da) for calibration. THF was used as the eluent (flow rate = 1.0 mL min^{-1}). Waters Empower HPLC/GPC network software was used for data analyses. Thermogravimetry analysis (TGA) measurements were performed on a Dynamic Q500 thermogravimetric analyzer in conjunction with TA Instruments 5100 system at a scan rate of 10 °C/min under a nitrogen atmosphere. Differential scanning calorimetry (DSC) measurements were performed on a LT-Modulate DSC 2920 instrument in conjunction with the TA Instruments 5100 system at a scan rate of 10 °C/min under a nitrogen atmosphere.

2,6-Bis(hydroxymethyl)cuneane (8). Under N_2, to a suspension of LAH (250 mg, 6.59 mmol) in THF (20 mL) at 0 °C was added dropwise a solution of dimethyl 2,6-cuneanedicarboxylate **7**[12c,14] (250 mg, 1.14 mmol) in THF (20 mL), and the mixture was stirred for 12 h. The reaction was quenched by 10% NaOH (1.0 mL). The mixture was filtered and evaporated in vacuo to afford the residue, which was purified by flash column chromatography (silica gel, EA) to afford **8** as a white solid (140 mg, 75%): mp 83−84 °C. ^{1}H NMR (400 MHz, $CDCl_3$): δ 1.15−1.22 (br, 2 H), 2.25−2.28 (m, 2 H), 2.35−2.40 (m, 2 H), 2.74−2.77(m, 2 H), 3.60 (d, J = 12.0 Hz, 2 H), 3.69 (d, J = 12.0 Hz, 2 H); ^{13}C NMR (100 MHz, $CDCl_3$) δ 34.3, 35.1, 39.4, 48.3, 62.5. IR (KBr): ν 3419, 1635, 1011 cm^{-1}. HRMS (FAB) (M^+): calcd for $C_{10}H_{12}O_2$ 164.0837; found 164.0834.

Monomer 10. Under N_2, to a solution of 1,4-bis(hydoxymethyl)-cubane[13] **6** (328 mg, 2 mmol) and Et_3N (600 mg, 6 mmol) in DCM (60 mL) at 0 °C was added a solution of **9b** freshly prepared from the corresponding carboxyl acid[7] (1.1 g, 4.1 mmol) in DCM (50 mL). The mixture was gradually warmed to rt and stirred for 10 h, poured into water (100 mL), and extracted with DCM (100 mL × 2). The organic layer was washed with brine (100 mL × 2), dried ($MgSO_4$), filtered, and evaporated in vacuo. The residue was chromatographed on silica gel (DCM) to afford **10** (932 mg, 73%); mp 246−248 °C. ^{1}H NMR (400 MHz, $CDCl_3$): δ 1.53 (d, J = 8.4 Hz, 2 H), 1.63 (d, J = 8.4 Hz, 2 H), 2.96−3.00 (m, 8 H), 3.09−3.11 (m, 4 H), 3.28−3.33 (m, 4 H), 3.87 (s, 6 H), 4.42 (s, 4 H), 6.17 (s, 4 H), 6.39 (d, J = 8.8 Hz, 4 H), 7.86 (d, J = 8.8 Hz, 4 H). ^{13}C NMR (100 MHz, $CDCl_3$): δ 44.5, 45.4, 46.6, 50.5, 52.1, 57.1, 64.5, 110.9, 0.6, 131.1, 135.8, 150.4, 167.3. IR (KBr): ν 3058, 2965, 2848, 1698, 1605, 1524, 1473, 1378, 1271, 1177, 1104, 970, 828, 768 cm^{-1}. HRMS (MALDI) (M + H^+): calcd for $C_{42}H_{43}N_2O_4$ 639.3223; found 639.3240.

Monomer 11. To a solution of acyl chloride **9b** which was fresh prepared from corresponding carboxyl acid[7] (300 mg, 1.18 mmol) in pyridine (20 mL) was added a solution of **8** (100 mg, 0.61 mmol) in pyridine (20 mL), and the mixture was refluxed for 12 h. Water (250 mL) and DCM (250 mL) were added. The organic layer was washed with brine (100 mL), dried ($MgSO_4$), filtered, and evaporated in vacuo to afford the residue which was chromatographed on silica gel (DCM/EA = 30/1) to afford **11** as a white solid (261 mg, 67%); mp 190 °C (dec.). ^{1}H NMR (400 MHz, $CDCl_3$): δ 1.52 (d, J = 8.2 Hz, 2 H), 1.62 (t, J = 8.2 Hz, 2 H), 2.33−2.36 (m, 2 H), 2.40−2.42 (m, 2 H), 2.69−2.71 (m, 2 H), 2.94−3.05 (m, 8 H), 3.05−3.10 (m, 4 H), 3.25−3.32(m, 4 H), 4.23 (d, J = 12.0 Hz, 2 H), 4.33 (t, J = 12.0 Hz, 2 H), 6.16 (s, 4 H), 6.38 (d, J = 8.4 Hz, 4 H), 7.85 (t, J = 8.4 Hz, 4 H). ^{13}C NMR (100 MHz, $CDCl_3$): δ 34.7, 36.1, 40.3, 45.0, 45.5, 46.7, 50.5, 52.1, 63.8, 110.7, 116.5, 131.1, 135.6, 150.1, 166.9. IR (KBr): ν 3050, 2964, 2933, 2847, 1697, 1605, 1523, 1474, 1379, 1273, 1178, 1098, 969, 830, 769, 725 cm^{-1}. HRMS (FAB) (M + H^+): calcd for $C_{42}H_{43}N_2O_4$ 639.3223; found 639.3219.

Monomer 12. A solution of **10** (300 mg, 0.47 mmol) and $[Rh(NBD)Cl]_2$ (10.8 mg, 0.023 mmol)[5,15] in anhydrous toluene and

$CHCl_3$ (4/1, 40 mL) was stirred for 24 h at rt. The solvent was removed in vacuo, and the residue was chromatographed on silica gel (DCM) to afford **12** (225 mg, 75%); mp 178−179 °C. ^{1}H NMR (400 MHz, $CDCl_3$): δ 1.53 (d, J = 8 Hz, 2 H), 1.63 (d, J = 8 Hz, 2 H), 2.90−3.00 (m, 9 H), 3.09−3.15 (m, 5 H), 3.21−3.40 (m, 5 H), 4.35 (d, J = 11.2 Hz, 1 H), 4.46 (d, J = 11.2 Hz, 1 H), 4.67 (ABq, J = 13.6 Hz, 2 H), 6.01 (s, 1 H), 6.05−6.12 (m, 2 H), 6.16 (s, 4 H), 6.38 (d, J = 8.8 Hz, 4 H), 7.86 (d, J = 8.8 Hz, 4 H). ^{13}C NMR (100 MHz, $CDCl_3$): δ 37.0, 37.2, 41.1, 45.4, 46.6, 50.3, 50.4, 52.1, 60.9, 65.1, 110.9, 116.2, 130.6, 131.3, 135.3, 135.8, 136.4, 144.7, 150.4, 166.7, 167.1. IR (KBr): ν 2961, 2863, 2349, 2317, 1701, 1604, 1523, 1484, 1474, 1379, 1272,1179, 1098, 970, 827, 768, 632 cm^{-1}. HRMS (MALDI) (M + Na^+): calcd for $C_{42}H_{42}N_2O_4Na$ 661.3043; found 661.3072.

Monomer 13. A solution of **10** (300 mg, 0.47 mmol) and $[Rh(NBD)Cl]_2$ (10.8 mg, 0.023 mmol)[5,15b] in anhydrous toluene and $CHCl_3$ (19/1, 40 mL) was refluxed for 24 h, cooled to rt, and the solvent was removed in vacuo. The residue was chromatographed on silica gel (DCM) to afford **13** (210 mg, 70%); mp 197−198 °C. ^{1}H NMR (400 MHz, $CDCl_3$): δ 1.53 (d, J = 8.4 Hz, 2 H), 1.63 (d, J = 8.4 Hz, 2 H), 2.95−3.00 (m, 8 H), 3.09−3.10 (m, 4 H), 3.29−3.30 (m, 4 H), 4.69 (s, 4 H), 5.85−5.97 (m, 6 H), 6.16 (s, 4 H), 6.37 (d, J = 8.8 Hz, 4 H), 7.86 (d, J = 8.8 Hz, 4 H). ^{13}C NMR (100 MHz, $CDCl_3$): δ 45.4, 46.6, 50.4, 52.1, 66.3, 66.4, 110.9, 116.1, 128.5, 128.7, 131.2, 131.3, 132.3, 132.8, 135.8, 139.1, 139.2, 150.5, 166.6. IR (KBr): ν 3058, 2961, 2856, 1695, 1604, 1522, 1475, 1384, 1265, 1173, 1088, 884, 825, 767 cm^{-1}. HRMS (MALDI) (M + Na^+): calcd for $C_{42}H_{42}N_2O_4Na$ 661.3043; found 661.3053.

General Procedure for the ROMP of 10, 11, and 13. Under N_2, a solution of monomer and G-I catalyst (12−20 mol %) in DCM was stirred for 1 h at rt. Ethyl vinyl ether (2 mL) was then added, and the mixture was stirred for 10 min. The resulting solution was concentrated, the resulting DCM solution was added to EA, and the precipitate was collected to give the corresponding polymer.

*Polymer **2** (White Solid, 135 mg, 90%).* ^{1}H NMR (400 MHz, $CDCl_3$): δ 1.20−1.55 (br, 2 H), 1.60−2.05 (br, 2 H), 2.50−3.05 (br, 8 H), 3.05−3.40 (br, 8 H), 3.60−4.05 (br, 6 H), 4.20−4.60 (br, 4 H), 5.20−5.60 (br, 4 H), 6.40−6.80 (br, 4 H), 7.65−8.05 (br, 4 H). ^{13}C NMR (400 MHz, $CDCl_3$): δ 46.6, 49.8, 57.1, 64.6, 111.5, 117.4, 125.9, 128.4, 131.1, 131.2, 150.8, 166.7. IR (KBr): ν 2961, 2935, 2854, 1702, 1605, 1521, 1478, 1378, 1269, 1179, 1096, 963, 827, 766 cm^{-1}. GPC (THF): M_n = 6000, PDI = 1.3.

*Polymer **3** (White Solid, 332 mg, 83%).* ^{1}H NMR (400 MHz, $CDCl_3$): δ 1.20−1.50 (br, 2 H), 1.75−2.05 (br, 2 H), 2.20−2.55 (br, 4 H), 2.55−3.60 (br, 18 H), 3.80−4.80 (br, 4 H), 4.95−5.80 (br, 4 H, including vinyl end group), 6.30−6.75 (br, 4 H), 7.20−7.40 (phenyl end group), 7.85−8.15 (br, 4 H). ^{13}C NMR (100 MHz, $CDCl_3$): δ 33.8, 34.6, 36.0, 39.6, 40.3, 43.3, 44.8, 49.6, 63.8, 111.5, 117.5, 126.0, 128.6, 131.3, 151.0, 166.7. IR (KBr): ν 3047, 2932, 2852, 1698, 1605, 1522, 1479, 1381, 1273, 1180, 1101, 960, 769 cm^{-1}. GPC (THF): M_n = 10 200, PDI = 1.8.

*Polymer **5** (White Solid, 131 mg, 87%).* ^{1}H NMR (400 MHz, $CDCl_3$): δ 1.22−1.54 (br, 2 H), 1.68−2.03 (br, 2 H), 2.50−3.05 (br, 8 H), 3.05−3.54 (br, 8 H), 4.25−4.60 (br, 4 H), 5.20−5.65 (br, 4 H), 5.73−6.05 (br, 6 H), 6.36−6.80 (br, 4 H), 7.70−8.05 (br, 4 H). ^{13}C NMR (100 MHz, $CDCl_3$): δ 36.4, 36.7, 45.4, 46.6, 49.6, 66.5, 111.7, 117.2, 126.1, 128.6, 131.5, 132.5, 132.9, 139.2, 151.1, 166.5. IR (KBr): ν 2936, 2853, 1703, 1604, 1527, 1478, 1380, 1271, 1179, 1096, 965, 825, 767 cm^{-1}. GPC (THF): M_n = 6500, PDI = 1.3.

*Polymer **4**.* A solution of polymer **2** (150 mg, 0.23 mmol) and $[Rh(NBD)Cl]_2$ (5.4 mg, 0.012 mmol)[5,15] in anhydrous toluene and $CHCl_3$ (19/1, 40 mL) was stirred for 24 h at rt. The resulting solution was concentrated, the resulting DCM solution was added to MeOH, and the precipitate was collected to give **4** as a white solid (128 mg, 85%). ^{1}H NMR (400 MHz, $CDCl_3$): δ 1.30−1.50 (br, 2 H), 1.65−2.05 (br, 2 H), 2.43−3.50 (br, 19 H), 4.05−4.80 (br, 4 H), 5.20−5.55 (br, 4 H), 5.80−6.15 (br, 3 H), 6.30−6.60 (br, 4 H), 7.70−8.05 (br, 4 H). ^{13}C NMR (100 MHz, $CDCl_3$): δ 36.8, 37.3, 41.1, 44.7, 46.3, 49.9, 61.0, 65.2, 111.7, 117.2, 126.0, 128.6, 131.3, 135.3, 135.9, 144.5, 151.1, 166.6, 167.0. IR (KBr): ν 3024, 2936, 2853, 1710, 1604, 1521, 1478, 1384, 1277, 1178, 1094, 1070, 826, 766 cm^{-1}. GPC (THF): M_n = 6100, PDI = 1.3.

General Procedure of Ethanolysis of Polymers 2−5. Under N_2, to a solution of polymer **2** (0.14−0.15 mmol) in DCM (20 mL) was added NaOEt solution (3 mL) which was freshly prepared from Na (9.0 g, 0.391 mmol) dissolved in (100 mL) was stirred at rt for 48 h. Water (100 mL) and DCM (100 mL) were added. The organic layer was separated and washed with brine and dried with $MgSO_4$. The resulting solution was concentrated, and the resulting DCM solution was added to MeOH and the precipitate was collected by centrifuge to give afford the polymer **14** as a white solid. ^{1}H NMR (400 MHz, $CDCl_3$): δ 1.30−1.37 (br, 4 H), 1.80−1.83 (br, 1 H), 2.62−2.78 (br, 2 H), 2.80−3.10 (br, 2 H), 3.10−3.30 (br, 4 H), 4.20−4.35 (br, 2H), 5.30−5.50 (br, 2 H), 6.42−6.60 (br, 2 H), 7.81−7.88 (br, 2 H). ^{13}C NMR (100 MHz, $CDCl_3$): δ 14.5, 35.6, 36.2, 44.6, 44.7, 44.9, 46.5, 46.7, 46.9, 49.5, 60.1, 111.4, 117.4, 131.2, 131.7, 132.0, 150.8, 167.0. The supernatant was evaporated in vacuo, and the residue was chromatographed on silica gel (EA) to afford the diol linker.

***14a** (65%, White Solid).* M_n = 2900, PDI = 1.2, and **6** (white solid, 54%).[13]

***14b** (74%, White Solid).* M_n = 4800, PDI = 1.3, and **8** (white solid, 85%).

***14c** (60%, White Solid).* M_n = 2700, PDI = 1.2, and **15** as a colorless liquid (12.3 mg, 48%). ^{1}H NMR (400 MHz, $CDCl_3$): δ 1.50−1.55 (br, 2H), 2.70−2.78 (m, 1 H), 3.01−3.05 (m, 1 H), 3.10−3.18 (m, 1 H), 3.72 (d, J = 11.2 Hz, 1 H), 3.82 (d, J = 11.2 Hz, 1 H), 4.05 (ABq, J = 14.4 Hz, 2 H), 6.03 (t, J = 2.8 Hz, 2 H), 6.14 (t, J = 2.4 Hz, 1 H). ^{13}C NMR (100 MHz, $CDCl_3$): δ 36.3, 36.4, 40.4, 53.2, 60.6, 64.3, 128.3, 135.8, 136.6, 148.8. IR (KBr): ν 3351, 2958, 2924, 2854, 1463, 1269, 1017 cm^{-1}. HRMS (ESI, M − H^+): calcd for $C_{10}H_{11}O_2$ 163.0759; found 163.0768.

***14d** (68%, White Solid).* M_n = 3200, PDI = 1.3, and **16** as a colorless liquid (11.6 mg, 50%). ^{1}H NMR (400 MHz, $CDCl_3$): δ 1.30−1.35 (br, 2H), 4.05 (d, J = 6.8 Hz, 4H), 5.81−5.90 (m, 4H), 5.94−6.00 (m, 2H). ^{13}C NMR (100 MHz, $CDCl_3$): δ 66.3, 126.8, 127.8, 131.4, 131.5, 133.0, 133.2, 143.2. IR (KBr): ν 3371, 2924, 2853 1641, 1461, 1269, 1037 cm^{-1}. HRMS (FAB): calcd for $C_{10}H_{12}O_2$: 164.0837; found: 164.0839.

1,4-Bis(acetoxymethyl)tricyclooctadiene (18). A solution of **17**[14] (100 mg, 0.40 mmol) and $[Rh(NBD)Cl]_2$ (9.2 mg, 0.02 mmol)[5,15] in anhydrous toluene and $CHCl_3$ (4/1, 40 mL) was stirred at rt for 24 h. The solvent was removed in vacuo, and the residue was chromatographed on silica gel (DCM) to afford **18** (70 mg, 70%). ^{1}H NMR (400 MHz, $CDCl_3$): δ 2.02 (s, 3 H), 2.04 (s, 3 H), 2.74−2.76 (m, 1 H), 2.96−3.00 (m, 1 H), 3.09−3.13 (m, 1 H), 4.13 (d, J = 11.5 Hz, 1 H), 4.24 (d, J = 11.5 Hz, 1 H), 4.43 (ABq, J = 14.1 Hz, 2 H), 5.93 (d, J = 2.4 Hz, 1 H), 6.00−6.03 (m, 2 H). ^{13}C NMR (100 MHz, $CDCl_3$): δ 20.7, 20.8, 36.8, 36.9, 40.9, 49.7, 61.1, 65.4, 130.9, 135.0, 136.3, 143.9, 170.6, 171.2. IR (KBr): ν 3095, 3034, 2964, 2878, 2360, 2337, 1741, 1437, 1377, 1231, 1030 cm^{-1}. HRMS (ESI): calcd for $C_{14}H_{16}O_4Na$ 271.0946; found 271.0945.

Reaction of 18 with G-I Catalyst. Under N_2, a solution of **18** (12.4 mg, 0.05 mmol) and G-I catalyst (41.1 mg, 0.05 mmol) in $CDCl_3$ in an NMR tube was allowed to stand at rt. The reaction was monitored by the NMR spectroscopy.[21] After 1 h, ethyl vinyl ether (2 mL) was added, and the mixture was allowed to stand for 10 min. The solvent was then removed in vacuo, and the residue was chromatographed on silica gel (DCM) to afford **19**[25] (6.4 mg, 58%). ^{1}H NMR (400 MHz, $CDCl_3$): δ 2.09 (s, 6 H), 5.09 (s, 4 H), 7.35 (s, 4 H). ^{13}C NMR (100 MHz, $CDCl_3$): δ 20.8, 65.8, 128.3, 135.9, 170.6.

STM Imaging. The samples for imaging were prepared by placing a 10 μL aliquot consisting of **2** in 1-phenyloctane on HOPG (highly orientated pyrolytic graphite, Advanced Ceramics, ZYH grade) with a micropipet. To acquired stable images, samples were subjected to a shear flow[7c,24] which packs molecules together into a 2D close-packed motif. The STM imaging was performed with a PicoScan controller (4500, Agilent Technologies) at room temperature, and the STM probes were commercially available Pt/Ir tips (PT, Nanotips, Veeco Metrology Group/Digital Instruments). Typical imaging conditions of

dx.doi.org/10.1021/ma300027k | *Macromolecules* 2012, 45, 2662−2667

bias voltage and tunneling current ranged from 0.50 to 0.9 V and from 30 to 100 pA, respectively.

■ ASSOCIATED CONTENT

Supporting Information

^{1}H and ^{13}C NMR spectra for all new compounds and the GPC, TGA, and DSC results for polymers. This material is available free of charge via the Internet at http://pubs.acs.org.

■ AUTHOR INFORMATION

Notes

The authors declare no competing financial interest.

■ ACKNOWLEDGMENTS

We thank the National Science Council and the National Taiwan University for support.

■ REFERENCES

(1) For reviews, see: (a) Griffin, G. W.; Marchand, A. P. *Chem. Rev.* **1989**, *89*, 997−1010. (b) Eaton, P. E. *Angew. Chem., Int. Ed.* **1992**, *31*, 1421−1436. (c) Higuchi, H.; Ueda, I. In *Carbocyclic Cage Compounds*; Osawa, E., Yonemitsu, O., Eds.; Wiley-VCH: New York, 1992; pp 217−247. (d) Bashir-Hashemi, A.; Higuchi, H. In *The Chemistry of Cyclobutanes*; Rappoport, Z., Liebman, J. F., Eds.; Wiley: New York, 2005; pp 873−921. (e) Hopf, H. In *The Chemistry of Cyclobutanes*; Rappoport, Z., Liebman, J. F., Eds.; Wiley: New York, 2005; pp 1061−1109.

(2) Eaton, P. E.; Pramod, K.; Emrick, T.; Gilardi, R. *J. Am. Chem. Soc.* **1999**, *121*, 4111−4123.

(3) Chauvin, Y.; Saussine, L. *Macromolecules* **1996**, *29*, 1163−1166.

(4) (a) Kakuchi, T.; Hirahata, W.; Yano, S.; Kaga, H. *Polym. Bull. (Berlin)* **1997**, *38*, 651−655. (b) Mahkam, M.; Sanjani, N. S. *Polym. Int.* **2000**, *49*, 260−264.

(5) McGonagle, A. E.; Savage, G. P. *Aust. J. Chem.* **2009**, *62*, 145−149.

(6) Priefer, R.; Nguyen, S.; Farrell, P. G.; Harpp, D. N. *Macromolecules* **2003**, *36*, 5435−5436.

(7) (a) Yang, H.-C.; Lin, S.-Y.; Yang, H.-c.; Lin, C.-L.; Tsai, L.; Huang, S.-L.; Chen, I-W. P.; Chen, C.-h.; Jin, B.-Y.; Luh, T.-Y. *Angew. Chem., Int. Ed.* **2006**, *45*, 726−730. (b) Yang, H.-C.; Lin, S.-M.; Liu, Y.-H.; Wang, Y.; Chen, M.-M.; Sheu, H.-S.; Tsou, D.-L.; Lin, C.-H.; Luh, T.-Y. *J. Organomet. Chem.* **2006**, *691*, 3196−3200. (c) Yang, H.-C.; Lee, S.-L.; Chen, C.-h.; Lin, N.-T.; Yang, H.-C.; Jin, B.-Y.; Luh, T.-Y. *Chem. Commun.* **2008**, 6158−6160. (d) Chou, C.-M.; Lee, S.-L.; Chen, C.-H.; Biju, A. T.; Wang, H.-W.; Wu, Y.-L.; Zhang, G.-F.; Yang, K.-W.; Lim, T.-S.; Huang, M.-J.; Tsai, P.-Y.; Lin, K.-C.; Huang, S.-L.; Chen, C.-h.; Luh, T.-Y. *J. Am. Chem. Soc.* **2009**, *131*, 12579−12585. (e) Lin, N.-T.; Lee, S.-L.; Yu, J.-Y.; Chen, C.-h.; Huang, S.-L.; Luh, T.-Y. *Macromolecules* **2009**, *42*, 6986−6991. (f) Yang, K.-W.; Xu, J.; Chen, C.-H.; Huang, H.-H.; Yu, T. J.-Y.; Lim, T.-S.; Chen, C.-h.; Luh, T.-Y. *Macromolecules* **2010**, *43*, 5188−5194. (g) Chen, C.-W.; Chang, H.-Y.; Lee, S. L.; Hsu, I.-J.; Lee, J.-J.; Chen, C.-h.; Luh, T.-Y. *Macromolecules* **2010**, *43*, 8741−8746. (h) Wang, H.-W.; Chen, C.-H.; Lim, T.-S.; Huang, S.-L.; Luh, T.-Y. *Chem.—Asian J.* **2011**, *6*, 524−533.

(8) (a) Lin, N.-T.; Lin, S.-Y.; Lee, S.-L.; Chen, C.-h.; Hsu, C.-H.; Hwang, L.-P.; Xie, Z.-Y.; Chen, C.-H.; Huang, S.-L.; Luh, T.-Y. *Angew. Chem., Int. Ed.* **2007**, *46*, 4481−4485. (b) Ke, Y.-Z.; Lee, S.-L.; Chen, C.-h.; Luh, T.-Y. *Chem.—Asian J.* **2011**, *6*, 1748−1751.

(9) For reviews, see: (a) Luh, T.-Y.; Yang, H.-C.; Lin, N.-T.; Lin, S.-Y.; Lee, S.-L.; Chen, C.-h. *Pure Appl. Chem.* **2008**, *80*, 819−829. (b) Luh, T.-Y. *Pure Appl. Chem.* **2012**, *84*, 000.

(10) (a) Sakai, N.; Lista, M.; Kel, O.; Sakurai, S.; Emery, D.; Mareda, J.; Vauthey, E.; Matile, S. *J. Am. Chem. Soc.* **2011**, *133*, 15224−15227. (b) Lista, M.; Areephong, J.; Sakai, N.; Matile, S. *J. Am. Chem. Soc.* **2011**, *133*, 15228−15231. (c) Sakai, N.; Matile, S. *J. Am. Chem. Soc.* **2011**, *133*, 18542−18545.

(11) (a) Lin, W.-Y.; Murugesh, M. G.; Sudhakar, S.; Yang, H.-C.; Tai, H.-C.; Chang, C.-S.; Liu, Y.-H.; Wang, Y.; Chen, I-W. P.; Chen, C.-h.; Luh, T.-Y. *Chem.—Eur. J.* **2006**, *12*, 324−330. (b) Lin, W.-Y.; Wang, H.-W.; Liu, Z.-C.; Xu, J.; Chen, C.-W.; Yang, Y.-C.; Huang, S.-L.; Yang, H.-C.; Luh, T.-Y. *Chem.—Asian J.* **2007**, *2*, 764−774.

(12) (a) Fleischer, E. B. *J. Am. Chem. Soc.* **1964**, *86*, 3889−3890. (b) Yufit, D. S.; Struchkov, Yu. T.; Eremenko, L. T. *Russ. Chem. Bull.* **1993**, *42*, 1152−1155. (c) Roux, M. V.; Davalos, J. Z.; Jimenez, P.; Notario, R.; Castano, O.; Chickos, J. S.; Hanshaw, W.; Zhao, H.; Rath, N.; Liebman, J. F.; Farivar, B. S.; Bashir-Hashemi, A. *J. Org. Chem.* **2005**, *70*, 5461−5470. (d) Zakharov, V. V.; Bugaeva, G. P.; Ivanova, M. E.; Romanova, L. B.; Eremenko, L. T.; Nefedov, S. E.; Eremenko, I. L. *Russ. Chem. Bull.* **1998**, *47*, 1349−1552.

(13) (a) Eaton, P. E.; Cole, T. W. Jr. *J. Am. Chem. Soc.* **1964**, *86*, 962−964. (b) Chapman, N. B.; Key, N. B.; Toyne, K.-J. *J. Org. Chem.* **1970**, *35*, 3860−3867. (c) Eaton, P. E.; Yip, Y. C. *J. Am. Chem. Soc.* **1991**, *113*, 7692−7697.

(14) Cassar, L.; Eaton, P. E.; Halpern, J. *J. Am. Chem. Soc.* **1970**, *92*, 6366−6368.

(15) (a) Cassar, L.; Eaton, P. E.; Halpern, J. *J. Am. Chem. Soc.* **1970**, *92*, 3515−3518. (b) Eaton, P. E.; Galoppini, E.; Gilard, R. *J. Am. Chem. Soc.* **1994**, *116*, 7588−7596.

(16) Greenberg, A.; Liebman, J. F. *Strained Organic Molecules*; Academic Press: New York, 1978; p 94.

(17) (a) Wu, Z.; Grubbs, R. H. *Macromolecules* **1994**, *27*, 6700−76703. (b) Perrott, M. G.; Novak, B. M. *Macromolecules* **1996**, *29*, 1817−1823. (c) Maughon, B. R.; Grubbs, R. H. *Macromolecules* **1997**, *30*, 3459−3469. (d) Weck, M.; Maughon, B. R.; Mohr, B.; Grubbs, R. H. *Polym. Prepr. (Am. Chem. Soc., Div. Polym. Chem.)* **1996**, *37*, 587−588. (e) Weck, M.; Mohr, B.; Maughon, B. R.; Grubbs, R. H. *Macromolecules* **1997**, *30*, 6430−6437. (f) Thorn-Csanyi, E. *NATO ASI Ser., Ser. C* **1998**, *506*, 117−137. (g) Charvet, R.; Novak, B. M. *Macromolecules* **2001**, *34*, 7680−7685. (h) Charvet, R. A.; Novak, B. M. *Polym. Prepr. (Am. Chem. Soc., Div. Polym. Chem.)* **2001**, *42*, 496−497. (f) Charvet, R.; Novak, B. M. *Polym. Prepr. (Am. Chem. Soc., Div. Polym. Chem.)* **2002**, *43*, 728−729. (i) Charvet, R.; Novak, B. M. *Macromolecules* **2004**, *37*, 8808−8811. (j) Lapinte, V.; de Frémont, P.; Montembault, V.; Fontaine, L. *Macromol. Chem. Phys.* **2004**, *205*, 1238−1245. (k) Morandi, G.; Montembault, V.; Pascual, S.; Legoupy, S.; Fontaine, L. *Macromolecules* **2006**, *39*, 2732−2735. (l) Song, A.; Parker, K. A.; Sampson, N. S. *J. Am. Chem. Soc.* **2009**, *131*, 3444−3445. (m) Morandi, G.; Pascual, S.; Montembault, V.; Legoupy, S.; Delorme, N.; Fontaine, L. *Macromolecules* **2009**, *42*, 6927−6931. (n) Song, A.; Lee, J. C.; Parker, K. A.; Sampson, N. S. *J. Am. Chem. Soc.* **2010**, *132*, 10513−10520. (o) Song, A.; Parker, K. A.; Sampson, N. S. *Org. Lett.* **2010**, *12*, 3729−3731. (p) Lee, K. S.; Choi, T.-L. *Org. Lett.* **2011**, *13*, 3908−3911.

(18) Coleman, C. G.; McCarthy, T. J. *Polym. Prepr. (Am. Chem. Soc., Div. Polym. Chem.)* **1988**, *29*, 283−284.

(19) Presumably, the rigid skeleton of polymer **4** may retard ring-opening process of tricyclooctadiene moieties.

(20) Cyclooctatetraene is known to be stable with G-I catalyst (cf.: Scherman, O. A.; Rutenberg, I. M.; Grubbs, R. H. *J. Am. Chem. Soc.* **2003**, *125*, 8515−8522).

(21) The details are described in the Supporting Information.

(22) The assembly could be commensurate with the lattice structure of the underlying graphite. The corrugation of the polymer backbone is parallel to one of the unit-cell vectors of HOPG. However, the following factors could also be used to illustrate the ordered pattern in Figure 1. They are (1) attractive $\pi-\pi$ interactions between the termini of neighboring polymers, (2) lateral van der Waals interactions between the polymer backbones, and (3) the shear force excerted on the arrangment of polymers during sample preparation for STM imaging. These factors, along with molecule−substrate interactions, would facilitate the ordered assembly of **2**.

(23) The distance was estimated based on the X-ray structures of 1,4-cubanedimethanol (ref 12d) and bisnorbornene and related monomers (refs 7b and 11a).

(24) (a) Lee, S.-L.; Lin, N.-T.; Liao, W.-C.; Chen, C.-h.; Yang, H.-C.; Luh, T.-Y. *Chem.—Eur. J.* **2009**, *15*, 11594−11600. (b) Lee, S.-L.; Chi, C.-Y. J.; Huang, M.-J.; Chen, C.-h.; Li, C.-W.; Pati, K.; Liu, R.-S. *J. Am. Chem. Soc.* **2008**, *130*, 10454−10455.
(25) (a) Gaefke, G.; Enkelmann, V.; Höger, S. *Synthesis* **2006**, *121*, 2971−2973. (b) Arlette, S.-C.; Marcel, H. *Magn. Reson. Chem.* **1981**, *17*, 227−231.

Macromolecules

Article

pubs.acs.org/Macromolecules

Thermosensitive Biodegradable Homopolymer of Trimethylene Carbonate Derivative at Body Temperature

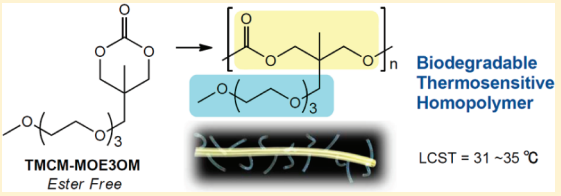
Hiroharu Ajiro,[†,‡] Yoshikazu Takahashi,[‡] and Mitsuru Akashi*[,†,‡]

[†]The Center for Advanced Medical Engineering and Informatics, Osaka University, 2-2, Yamada-oka, Suita, Osaka 565-0871, Japan

[‡]Department of Applied Chemistry, Graduate School of Engineering, Osaka University, 2-1 Yamada-oka, Suita, Osaka 565-0871, Japan

Supporting Information

ABSTRACT: A thermosensitive biodegradable homopolymer with a lower critical solution temperature (LCST) at body temperature was developed, with a poly(trimethylene carbonate) (PTMC) backbone and oligoethylene glycol (OEG). The novel monomer was designed by the direct connection of OEG into trimethylene carbonate (TMC), and no other functional groups exist in the polymer structure. Such a well-defined monomer unit contributed to its homogeneous characteristics. Three units of ethylene glycol in the TMC derivative resulted in a water-soluble nature at room temperature, and the solution became cloudy at higher temperatures. The LCST ranged from 31 to 35 °C and was influenced by the molecular weight and polymer concentration. Four units of ethylene glycol, however, increased the LCST temperature to 72 °C. It is noteworthy that the present characteristics, thermosensitivity at body temperature, biodegradablility, and a well-defined homopolymer structure, are promising for biomedical applications as an essential material.



INTRODUCTION

A large number of studies have been performed on thermosensitive synthetic polymers. Poly(*N*-isopropylacrylamide) (PNIPAm)[1,2] is one of the most intensively studied polymers[3−5] and possesses a LCST at 32 °C. PNIPAm was widely examined as a biomaterial[6,7] because its LCST was near body temperature. Other than PNIPAm and its derivatives, poly(*N*-vinylisobutylamide) (PNVIBA),[8,9] a poly(methyl methacrylate) (PMMA) derivative with oligoethylene glycol (OEG),[10] and a poly(vinyl ether) derivative with OEG[11−14] have been reported as thermosensitive synthetic homopolymers. These polymers exhibit two main features: a "well-defined structure" due to the homopolymer with clear monomer units and a "non-biodegradable characteristic" with the responsive temperature near body temperature. Referring to PNIPAm, many applications would be expected once any novel biodegradable homopolymer possessing a LCST at body temperature is discovered because the precise structure would usually have well-defined characteristics. However, to our knowledge, there is no such synthetic polymer thus far probably because it is necessary to have very a fine balance between hydrophilicity and hydrophobicity in the monomer structure.

In general, copolymerization approaches with a combination of hydrophobic and hydrophilic moieties have been developed for thermosensitive polymers as a material, such as various copolymers of PNIPAM using poly(trimethylene carbonate) (PTMC),[15] poly(methacrylic acid),[16] poly(propylacrylic acid),[17] and poly(vinylpyrrolidone),[18] and by introducing different moieties using radical polyaddition[19] or macromonomer initiation[20] approaches. Except for PNIPAM copolymers, poly(ethylene glycol) (PEG)[21] has been abundantly employed, combined with poly(organophosphazenes),[22] polyacrylate derivatives,[23] and poly(3-hydroxyalkanoate),[24] as well as other original chemical structures like poly(amidoamine) dendrimers,[25] poly[(vinylamine)-*co*-*N*-vinylisobutyramide],[26] and poly[(*N*-vinylamide)-*co*-(vinyl acetate)].[27] Some of these copolymers are fully biodegradable for the purposes of biomedical applications, such as poly(lactide)-*co*-poly(ethylene glycol).[28]

On the other hand, aliphatic polycarbonate has received attention as a biodegradable polymer, and novel polymers have been developed. For example, the alternating copolymerization of limonene oxide and carbon dioxide has been achieved with a specific single site catalyst.[29] PTMC is also known as a biodegradable synthetic polymer and has been actually used as a biomedical material in suture thread, taking advantage of its soft characteristics.[30−32] Recently, research on novel PTMC derivatives and copolymers for biomaterial use has attracted attention, due to the organic catalyst system reported by Waymouth, Hedrick, and co-workers in 2007.[33,34] Furthermore, micelle[35] and polymersome[36,37] preparations have predominantly been investigated as drug delivery systems by using copolymers with PTMC and hydrophilic polymers or by using trimethylene carbonate (TMC) derivatives with a protected carboxylic acid group at the side chain, such as 5-methyl-5-benzyloxycarbonyl-1,3-dioxan-2-one[38−40] and 3-chloropropyl 5-methyl-2-oxo-1,3-dioxane-5-carboxylate.[41] Moreover, temperature responsiveness was achieved with PTMC derivatives by

Received: January 24, 2012
Revised: March 6, 2012
Published: March 19, 2012

 © 2012 American Chemical Society

introducing a PEG domain into the block copolymer[42,43] and into the side chain along the polymer main chain.[44] Such thermosensitive PTMC derivatives are based on the copolymer structure, bearing both hydrophilic and hydrophobic regions in the polymer main chain separately (Figure 1a). Their polymer designs are excellent for the creation of nanomaterials, such as micelle and lamellar structures, which need domain separation. However, we were interested in the synthesis of a novel thermosensitive biodegradable homopolymer as an essential material (Figure 1b). Thus, we chose the monomer design from three possible strategies to modify PTMC, which are a macroinitiator,[35,42,43,45] polymer reaction,[38−41] and monomer synthesis.[40,44,46−48]

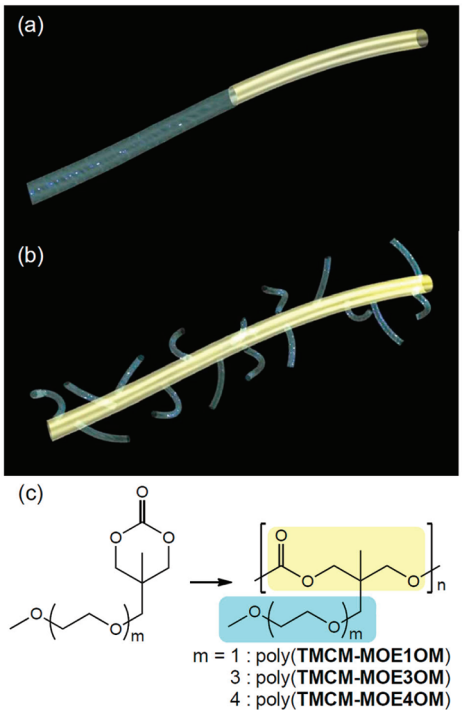


Figure 1. Schematic illustration and chemical structure of polymers. The model of block copolymer with hydrophilic and hydrophobic domains (a), the model of homopolymer composed of hydrophilic and hydrophobic parts (b), and the chemical structures of novel trimethylene carbonate derivatives and their polymerization (c).

In this study, novel TMC derivatives, composed of different units of OEG groups directly connected into the TMC backbone were synthesized, and the turbidities of their polymers in water against temperature were examined (Scheme 1). In these screening tests, we discovered a novel thermosensitive biodegradable homopolymer that possessed a LCST at 33 °C. Herein we report this series of TMC derivatives and their polymerization (Figure 1c).

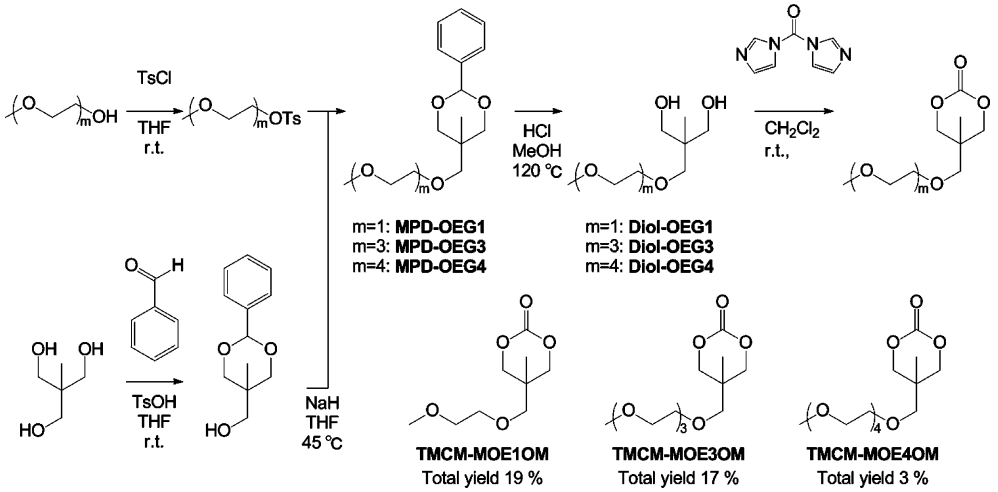
EXPERIMENTAL SECTION

Materials. Methoxyethanol, triethylene glycol monomethyl ether, tetraethylene glycol monomethyl ether, *p*-toluenesulfonyl chloride, benzaldehyde, *p*-toluenesulfonic acid, 2-methyoxyethyl *p*-toluenesulfonate, sodium hydride in oil (20 wt %), 1,1′-carbonyldiimidazole (CDI), benzyl alcohol, 1,8-diazabicyclo[5.4.0]undec-7-ene (DBU), and trimethylolethane were purchased from Tokyo Chemical Industry Co., Ltd., Japan. Anhydrous dimethylformamide (DMF) was purchased from Aldrich. Tetrahydrofuran (THF) and dichloromethane (CH_2Cl_2) for synthesis and polymerization solvents were distilled with calcium hydride before use.

Tosylation of Oligoethylene Glycol Monomethyl Ether. The tosylation of oligoethylene glycol monomethyl ether was performed according to previous reports.[49] The typical procedure was described for 2-{2-(2-methoxyethoxy)ethoxy}ethyl tosylate as follows: 21 mL of triethylene glycol monomethyl ether (131 mmol) was dissolved in an aqueous NaOH solution (5 mol/L, 40 mL) and kept at 0 °C. A *p*-toluenesulfonyl chloride (25 g, 131 mmol) solution in THF (120 mL) was slowly added into the mixture and stirred for 22 h. The reaction mixture was extracted with CH_2Cl_2 and NaCl(aq) to recover the 2-{2-(2-methoxyethoxy)ethoxy}ethyl tosyleate (40.2 g, yield 96%). The same procedure for the synthesis of 2-[2-{2-(2-methoxyethoxy)-ethoxy}ethoxy]ethyl tosylate as per 2-{2-(2-methoxyethoxy)ethoxy}-ethyl tosyleate was carried out, except that tetraethylene glycol monomethyl ether was used instead of triethylene glycol monomethyl ether (40.1 g, yield 92%)

Synthesis of 5-Hydroxymethyl-5-methyl-2-phenyl-1,3-dioxane (HMPD). Protection of the diol moiety of trimethylolethane was achieved according to previous reports.[48] Trimethylolethane (24.7 g, 205 mmol) was added into anhydrous THF (480 mL) in the flask and stirred to dissolve. Benzaldehyde (25 mL, 247 mmol) was slowly introduced by a dropping funnel, and the mixture was stirred for 16 h at room temperature. The reaction was stopped by adding 0.38 mL of aqueous ammonium solution (28%) for neutralization. The reaction

Scheme 1. Syntheses of Novel Trimethylene Carbonate Derivatives



dx.doi.org/10.1021/ma300183t | *Macromolecules* 2012, 45, 2668−2674

mixture was evaporated to remove the THF and extracted by CH_2Cl_2 and NaCl(aq) to collect the organic layer (32.2 g, yield 75%).

Synthesis of 5-(2-Methoxyethoxymethyl)-5-methyl-2-phenyl-1,3-dioxane (MPD-OEG1). Sixty percent sodium hydride in oil (5.03 g, 126 mmol) was placed in a three-necked flask under nitrogen and washed by anhydrous THF (10 mL) three times. Anhydrous DMF (14 mL) and anhydrous THF (70 mL) were combined in the flask, and HMPD (20.5 g, 98.5 mmol) was introduced with stirring at 60 °C for 5 h. Next, 2-methyoxyethyl *p*-toluenesulfonate (25 g, 109 mmol) was introduced under a nitrogen atmosphere with stirring at 60 °C for 14 h. The reaction mixture was then extracted by CH_2Cl_2 and NaCl(aq) to collect the organic layer. The crude mixture was purified by silica gel column chromatography to obtain 18.7 g of MPD-OEG1 (70.3 mmol, yield 71%). ^{1}H NMR ($CDCl_3$, 400 MHz) δ:0.82 (s, 3H, CH_3C), 3.39 (s,3H, CH_3O), 3.55−3.58 (m, 2H, OCH_2CH_2O), 3.61 (d, 2H, J = 11.7 Hz, CCH_2OCPh), 3.66−3.68 (m, 2H, OCH_2CH_2O), 3.72 (s, 2H, OCH_2C), 4.06 (d, 2H, J = 11.7 Hz, CCH_2OCPh), 5.42 (s, 1H, $CHPh$), 7.36 −7.48 (m, 5H, Ph). FT-IR (cm^{-1}): 2850, 1454, 1387, 1358, 1311, 1208, 1095. CI-MS: m/z = 267 ($[M + 1]^+$).

Synthesis of 5-[2-{2-(2-Methoxyethoxy)ethoxy}-ethoxymethyl]-5-methyl-2-phenyl-1,3-dioxane (MPD-OEG3). The same procedure as per the MPD-OEG1 synthesis was repeated, except that 2-{2-(2-methoxyethoxy)ethoxy}ethyl tosyleate (20.0 g, 60.2 mmol) was used instead of 2-methyoxyethyl *p*-toluenesulfonate. The crude mixture was purified by silica gel column chromatography using hexane/ethyl acetate (1/2, v/v). A total of 19.3 g of MPD-OEG3 was obtained at R_f = 0.62 (52.4 mmol, yield 87%). ^{1}H NMR ($CDCl_3$, 400 MHz) δ: 0.81 (s, 3H, CH_3C), 3.37 (s, 3H, CH_3O), 3.53−3.71 (m, 16H, OCH_2H_2O, OCH_2CCH_3), 4.05 (d, 2H, J = 11.7 Hz, OCH_2CCH_3), 5.41 (s, 1H, $CHPh$), 7.33−7.49 (m, 5H, Ph). FT-IR (cm^{-1}): 2860, 1454, 1387, 1208, 1097, 1025. FAB-MS: m/z = 355 ($[M + 1]^+$).

Synthesis of 5-(2-[2-{2-(2-Methoxyethoxy)ethoxy}ethoxy]-ethoxymethyl)-5-methyl-2-phenyl-1,3-dioxane (MPD-OEG4). The same procedure as per the MPD-OEG1 synthesis was repeated, except that 2-[2-{2-(2-methoxyethoxy)ethoxy}ethoxy]ethyl tosylate (11.5 g, 55.2 mmol) was used instead of 2-methyoxyethyl *p*-toluenesulfonate. A total of 15.2 g of MPD-OEG4 was obtained (38.1 mmol, yield 69%). ^{1}H NMR ($CDCl_3$, 400 MHz) δ: 0.81 (s, 3H, CH_3C), 3.37 (s, 3H, CH_3O), 3.53−3.74 (m, 20H, OCH_2H_2O, OCH_2CCH_3), 4.06 (d, 2H, J = 11.7 Hz, OCH_2CCH_3), 5.41 (s, 1H, $CHPh$), 7.33−7.49 (m, 5H, Ph). FT-IR (cm^{-1}): 2861, 1454, 1387, 1208, 1097, 1025, 970. CI-MS: m/z = 399 ($[M + 1]^+$).

Synthesis of 2-(2-Methoxyethoxymethyl)-2-methylpropan-diol (Diol-OEG1). According to the previous literature,[46] the diol deprotection of MPD-OEG1 (18.7 g, 70.3 mmol) was achieved by refluxing in MeOH (70 mL) and 5 M HCl(aq) (70 mL) at 110 °C for 8 h. The reaction mixture was extracted by CH_2Cl_2 and ultrapure water to collect the aqueous layer. The crude mixture was then purified by distillation to obtain 6.46 g of Diol-OEG1 (36.3 mmol, yield 52%). ^{1}H NMR (D_2O, 400 MHz) δ:0.89 (s, 3H, CH_3C), 3.41 (s, 3H, CH_3O), 3.44 (s, 2H, OCH_2CCH_3), 3.51 (s, 4H, CH_2OH), 3.66−3.68 (m, 4H, OCH_2CH_2O). FT-IR (cm^{-1}): 3332, 2877, 1455, 1358, 1088, 1033. CI-MS: m/z = 179 ($[M + 1]^+$).

Synthesis of 2-[2-{2-(2-Methoxyethoxy)ethoxy}-ethoxymethyl]-2-methylpropan-diol (Diol-OEG3). The same procedure as per the Diol-OEG1 synthesis was repeated except that MPD-OEG3 (19.3 g, 52.4 mmol) was used instead of MPD-OEG1. A total of 10.5 g of Diol-OEG3 was obtained (37.4 mmol, yield 71%). ^{1}H NMR ($CDCl_3$, 400 MHz) δ: 0.79 (s, 3H, CH_3C), 3.39 (s, 3H, CH_3O), 3.52−3.74 (m, 18H, OCH_2CCH_3, OCH_2CH_2O). FT-IR (cm^{-1}): 3323, 2880, 1456, 1350, 1079, 1024. CI-MS: m/z = 267 ($[M + 1]^+$).

Synthesis of 2-(2-[2-{2-(2-Methoxyethoxy)ethoxy}ethoxy]-ethoxymethyl)-2-methylpropan-diol (Diol-OEG4). The same procedure as per the Diol-OEG1 synthesis was repeated, except that MPD-OEG4 (15.2 g, 38.2 mmol) was used instead of MPD-OEG1. A total of 7.30 g of Diol-OEG4 was obtained (23.5 mmol, yield 62%). ^{1}H NMR ($CDCl_3$, 400 MHz) δ: 0.75 (s, 3H, CH_3C), 3.38 (s, 3H, CH_3O), 3.53−3.74 (m, 22H, OCH_2CCH_3, OCH_2CH_2O). FT-IR (cm^{-1}): 2873, 1455, 1350, 1297, 1092, 1037, FAB-MS: $[M + 1]^+$ = 311.

Synthesis of 5-(2-Methoxyethyoxymethyl)-5-methyl-1,3-dioxa-2-one (TMCM-MOE1OM). Under a nitrogen atmosphere, 6.46 g (36.3 mmol) of Diol-OEG1 was placed in a three-necked flask and dissolved in anhydrous CH_2Cl_2 (25 mL) with molecular sieve 4A (MS4A) powder and stirring at room temperature for 3 h. A 160 mL aliquot of 0.4 M CDI solution in CH_2Cl_2 (40 mmol) was introduced into the mixture, and stirring was maintained at room temperature for 20 h. After filtration and evaporation, the crude mixture was purified by silicagel chromatography to obtain 3.9 g of the novel monomer TMCM-MOE1OM (19.1 mmol, yield 53%). ^{1}H NMR ($CDCl_3$, 400 MHz) δ: 1.10 (s, 3H, CH_3C), 3.37 (s, 3H, CH_3O), 3.45 (s, 2H, OCH_2CCH_3), 3.52−3.54 (m, 2H, OCH_2CH_2O), 3.60−3.62 (m, 2H, OCH_2CH_2O), 4.08 (d, 2H, J = 10.9 Hz, O═$COCH_2$), 4.36 (d, 2H, J = 10.9 Hz, O═$COCH_2$). FT-IR (cm^{-1}): 2875, 1745, 1473, 1401, 1175, 1107, 1090. Anal. Calcd for $C_9H_{16}O_5$: C, 52.93; H, 7.90; O, 39.17. Found: C, 52.78; H, 7.72, O, 39.50. CI-MS: m/z = 205 ($[M + 1]^+$).

Synthesis of 5-[2-{2-(2-Methoxyethoxy)ethyoxy}-ethoxymethyl]-5-methyl-1,3-dioxa-2-one (TMCM-MOE3OM). The same procedure as per the TMCM-MOE1OM synthesis was repeated, except that Diol-OEG3 (10.5 g, 37.4 mmol) was used instead of Diol-OEG1. A total of 3.84 g of the novel monomer TMCM-MOE3OM was obtained (12.5 mmol, yield 34%). ^{1}H NMR ($CDCl_3$, 400 MHz) δ: 0.94 (s, 3H, CH_3C), 3.38 (s, 3H, CH_3O), 3.45 (s, 2H, OCH_2CCH_3), 3.54−3.66 (m, 12H, OCH_2CH_2O), 4.07 (d, 2H, J = 10.8 Hz, O═$COCH_2$), 4.36 (d, 2H, J = 10.8 Hz, O═$COCH_2$). FT-IR (cm^{-1}): 2871, 1748, 1472, 1401, 1174, 1105. Anal. Calcd for $C_{13}H_{24}O_7$: C, 53.42; H, 8.22; O, 38.36. Found: C, 52.94; H, 9.05, O, 38.01. CI-MS: m/z = 293 ($[M + 1]^+$).

Synthesis of 5-(2-[2-{2-(2-Methoxyethoxy)ethyoxy}ethoxy]-ethyoxymethyl)-5-methyl-1,3-dioxa-2-one (TMCM-MOE4OM). The same procedure as per the TMCM-MOE1OM synthesis was repeated, except that Diol-OEG4 (7.30 g, 23.5 mmol) was used instead of Diol-OEG1. A total of 1.29 g of the novel monomer TMCM-MOE4OM was obtained (3.76 mmol, yield 16%). ^{1}H NMR ($CDCl_3$, 400 MHz) δ: 1.09 (s, 3H, CH_3C), 3.38 (s, 3H, CH_3O), 3.45 (s, 2H, OCH_2CCH_3), 3.54−3.66 (m, 16H, OCH_2CH_2O), 4.07 (d, 2H, J = 10.8 Hz, O═$COCH_2$), 4.36 (d, 2H, J = 10.8 Hz, O═$COCH_2$). FT-IR (cm^{-1}): 2870,1747, 1472, 1402, 1176, 1104. Anal. Calcd for $C_{15}H_{28}O_8$: C, 53.57; H, 8.33; O, 38.10. Found: C, 52.66; H, 8.48, O, 38.86. CI-MS: m/z = 337 ($[M + 1]^+$).

Polymerization. Polymerization of TMC derivatives were achieved by the literature.[33] A typical polymerization procedure was described for TMCM-MOE1OM. In the three-necked flask, 0.5 g of TMCM-MOE1OM (2.45 mmol) was dissolved in about 5 mL of anhydrous CH_2Cl_2 with CaH_2 to stir for overnight. Using a cannula with glass filter to remove CaH_2, the monomer solution was transferred to the other flask with a three-way cock, and the solvent CH_2Cl_2 was evaporated under reduced pressure. Then, the required amount of anhydrous CH_2Cl_2 under nitrogen atmosphere was introduced. Into the monomer solution, 0.6 mL of benzyl alcohol (0.049 mmol) solution in CH_2Cl_2 as initiator and 0.6 mL of DBU (0.049 mmol) solution in CH_2Cl_2 as catalyst were added to start the polymerization at room temperature for 8 h. The reaction was stop by adding small portion of acetic acid, and then the reaction mixture was poured into a large amount of hexane/2-propanol (9/1, v/v). The product was recovered by decantation and centrifugation and dried under vacuum (73% yield).

Measurements. ^{1}H NMR and ^{13}C NMR spectra were measured by a JEOL JNM-GSX400 system. Attenuated total reflection (ATR) IR spectra were obtained with a Spectrum 100 FT-IR spectrometer (Perkin-Elmer). The interferograms were coadded 64 times and Fourier-transformed at a resolution of 4 cm^{-1}. The number-average molecular weights and their distribution were measured by gel permeation chromatography. A Tosoh System HLC-8120GPC was used with PMMA standards at 40 °C. Two commercial columns (TSKgel SuperH4000 and TSKgel GMH_{XL}) were connected in series and tetrahydrofuran was used as an eluent. The mass spectra were measured on a JEOL JSM-700 mass spectrometer for novel monomers. MALDI-TOF/MS were measured with a Bruker Autoflex

dx.doi.org/10.1021/ma300183t | *Macromolecules* 2012, 45, 2668−2674

Table 1. Polymerization of TMC Derivatives[a]

entry	monomer	[monomer]/[initiator]	conc (mol/L)	time (h)	yield[b] (%)	M_n[c] × 10^3	PDI[c]
1	TMCM-MOE1OM	50	1.44	8	73	2.5	1.06
2	TMCM-MOE3OM	50	0.80	8	72	0.96	1.42
3[d]	TMCM-MOE3OM	100	0.73	36	60	7.4	1.28
4	TMCM-MOE3OM	300	1.98	36	97	11	1.36
5	TMCM-MOE4OM	200	0.74	36	16	2.3	1.41

[a]Initiator = benzyl alcohol. Catalyst = DBU. [Initiator]/[Cat.] = 1.0. Solvent = CH_2Cl_2. Monomer = 0.5 g. [b]Hexane/isopropanol (9/1, v/v) insoluble-part. [c]Determined by SEC by PMMA standard in THF. [d]Monomer = 0.3 g.

III. LCST was measured by the JASCO V-550 ETC-505S and JSSCO V-550 ETC-505T system.

RESULTS AND DISCUSSION

During the design of the monomer structure for the biodegradable thermosensitive homopolymer, we selected OEG as the thermosensitive parts according to the literature.[7,10,14,28−30] As the polymer main chain, a PTMC backbone was believed to be suitable because it contains no ester groups which might cause inflammation due to increased acidity upon degradation. For the same reason, we avoided ester groups[24−27] to join the OEG to the TMC in the monomer structure (Figure 1c), although it is a convenient functional group for converting polymer characteristics. In this manner, the novel TMC derivatives, TMCM-MOE1OM, TMCM-MOE3OM, and TMCM-MOE4OM were designed and synthesized, in order to control their thermosensitive characteristics by the length of the OEG units. Trimethylolethane was employed as the starting material, and five steps were required for the synthesis. Carbonylation reaction with diol[50] was confirmed by Fourier transform infrared (FT-IR) spectra (Supporting Information, Figure S1). The detailed monomer synthesis procedures and analyses are described in the Supporting Information.

The results of the polymerization are summarized in Table 1. The polymerization in CH_2Cl_2 at 25 °C was achieved with benzyl alcohol as the initiator and DBU as the catalyst.[33] When compared to the polymerization of TMCM-MOE1OM, the number-average molecular weight (M_n) of poly(TMCM-MOE3OM) tended to decrease under dilute concentrations (Table 1, entries 1 and 2) as determined by size exclusion chromatography (SEC). By changing the ratio of the [monomer]/[initiator] and the concentration over a long reaction time, a larger M_n for poly(TMCM-MOE3OM)s was obtained, although they were still smaller than the theoretical values (Table 1, entries 3 and 4). One of the possible explanations for this discrepancy is a substituent effect in the monomer structure by a reverse reaction during the equilibrium polymerization.[51] Alternatively, the OEG units near the growing chain end might affect the polymerizability at the closed position because a much lower M_n value was observed in the polymerization of TMCM-MOE4OM bearing the longest OEG units.

Figure 2 shows the SEC traces of poly(TMCM-MOE3OM)s with different M_ns (Table 1, entries 2−4). When the ratio of the [monomer]/[initiator] was 50, the amount of DBU required increased work due to the same amount of DBU used as the initiator. This amount of DBU could attenuate a living polymerization system or cause polymer degradation, thus resulting in a broad polydispersity index (PDI) and the possible aggregation of species at high M_w values (Figure 2a). On the other hand, the PDI became narrow with a smaller amount of

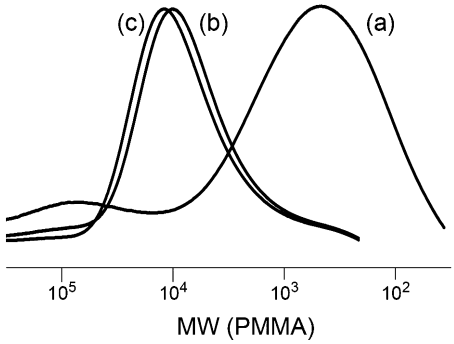


Figure 2. SEC charts of poly(TMCM-MOE3OM)s obtained with [monomer]/[initiator] = 50 (Table 1, entry 2) (a), 100 (Table 1, entry 3) (b), and 300 (Table 1, entry 4) (c).

DBU, and the order of the M_w conformed to the theoretical values (Figure 2b,c). In order to examine the polymer model, various SEC standards and solvents were examined, whereas the values were listed with the PMMA standards. For example, the M_n was estimated as 5500, 4900, and 4500 in the case of poly(TMCM-MOE3OM) in chloroform with PMMA, PEG, and polystyrene standards (Table 1, entry 3). An estimation of the M_n by ^{1}H NMR on the basis of the phenyl groups of the initiator resulted in larger values than the theoretical values, whereas matrix-assisted laser desorption ionization/time-of-flight mass spectroscopy (MALDI-TOF/MS) did not detect higher molecular weight species (Supporting Information, Figure S2). The M_n of some PTMC copolymers, which were obtained with the DBU system, were analyzed by ^{1}H NMR using protons from the macroinitiator[52] and the aromatic group in the initiator.[53] The estimation of the M_n by ^{1}H NMR with the initiator group was not in good agreement with the results from SEC in this study, and hence the possibility of a secondary initiation cannot be excluded. Further systematic studies under various polymerization conditions would make the mechanism clearer. In any case, the polymers were successfully recovered as a hexane/isopropanol (9/1, v/v) insoluble part as a highly sticky liquid.

Figure 3 shows the ^{1}H NMR spectra of the monomers and their polymers. The splitting spectral pattern of the monomers around 4.2 ppm (Figure 3a,c,e), which was based on their ring structures, became a single peak after polymerization (Figure 3b,d,f), thus confirming that the ring-opening polymerization had occurred. The peaks between 3 and 4 ppm corresponded to the OEG groups, and the methyl protons in the polymer main chain appeared at around 1 ppm, together with a split peak around 0.9 ppm, in all polymers. Considering the amount of methyl groups, the split peak at around 0.9 ppm should be assigned as part of the methyl group. Because of the low M_n of the polymers, the split peak at around 0.9 ppm could be a

dx.doi.org/10.1021/ma300183t | Macromolecules 2012, 45, 2668−2674

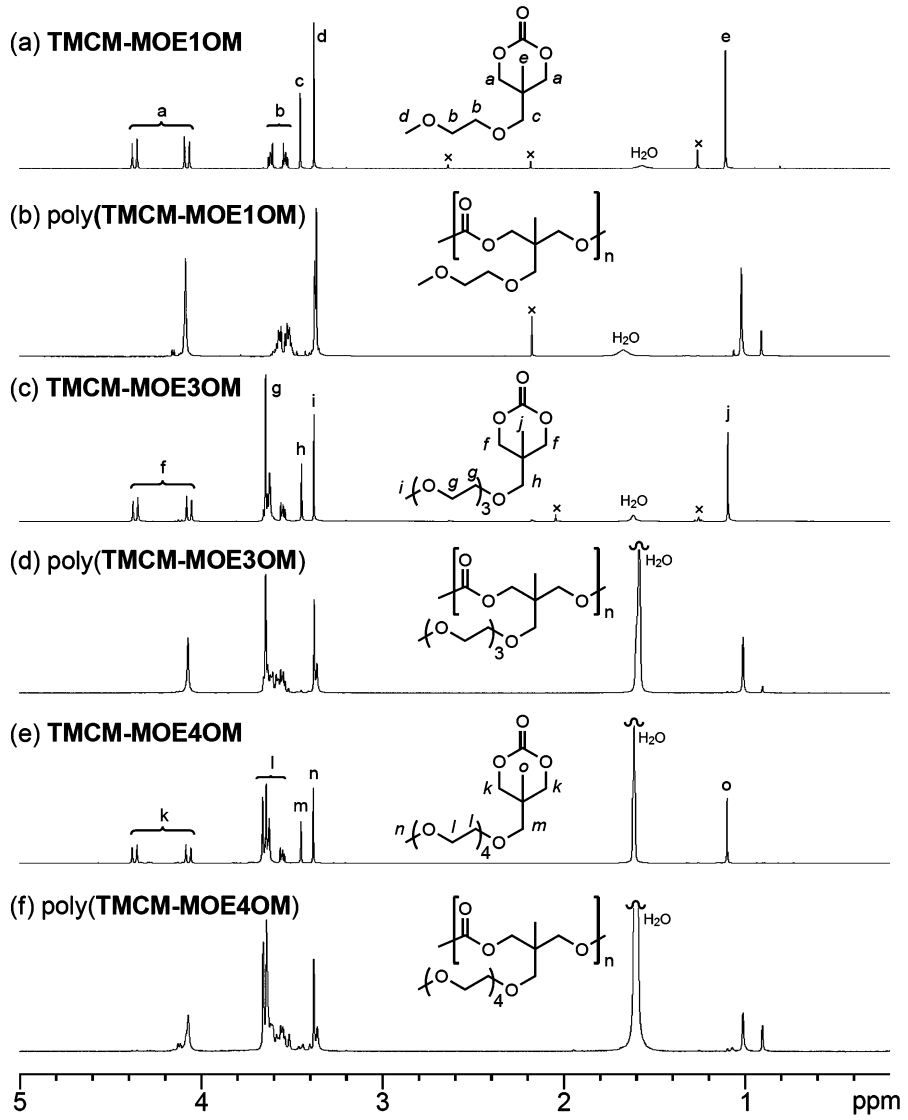


Figure 3. [1]H NMR spectra of monomer TMCM-MOE1OM (a), poly(TMCM-MOE1OM) (b), TMCM-MOE3OM (c), poly(TMCM-MOE3OM) (d), TMCM-MOE4OM (e), and poly(TMCM-MOE4OM) (f).

hydroxyl group terminated species, which was recognized in the precursor.

It is known that PTMC is insoluble in methanol, and thus the hydrophilicity of poly(TMCM-MOE1OM) was confirmed by being soluble in methanol as well as acetone and ethanol (Supporting Information, Table S1). Poly(TMCM-MOE3OM) and poly(TMCM-MOE4OM) were even soluble in water at 25 °C, and therefore the thermosensitivities of the polymers were measured by their turbidity.

The results of the light transmittance of the poly(TMCM-MOE3OM) and poly(TMCM-MOE4OM) solutions in ultrapure water against temperature are depicted in Figure 4. The LCST of poly(TMCM-MOE3OM) with a 960 M_n was 43 °C during the heating process, and this value decreased slightly during the cooling process (Figure 4a, closed squares). On the other hand, poly(TMCM-MOE3OM) with M_n values of 7400 and 11 000 showed LCST values at 33 °C (Figure 4a, closed triangles and closed circles). Given that a 960 M_n is low and that there may possibly be a hydroxyl group at the polymer chain end, the result of 43 °C should be ascribed to the slightly increased hydrophilicity effect. This is also supported by the LCST of poly(TMCM-MOE4OM) with the increased hydrophilicity due to the longer OEG units; the LCST was 72 °C at a 2300 M_n (Figure 4a, open squares), showing improved solubility in water. Therefore, it was determined that the true LCST of poly(TMCM-MOE3OM) originated from the polymer main chain and was 33 °C near body temperature. Poly(TMCM-MOE3OM) is a promising novel thermosensitive biodegradable homopolymer with a similar essential polymer structure as PNIPAm.

Finally, the concentration effect was examined with poly(TMCM-MOE3OM) in comparison to Figure 4a, which was set at 2.0 mg/mL. The lower concentrations of 1.0 and 0.5 mg/mL broadened the transition behaviors and increased the LCST temperatures to 34 and 35 °C, respectively. In contrast, the higher concentrations of 4.0 and 8.0 mg/mL resulted in values of 32 and 31 °C. No more concentrated solution could be prepared. Obviously, the LCST was influenced by the polymer concentration, suggesting a coacervate structure rather than a coil−globule transition. At the same time, differential scanning calorimetry (DSC) analysis indicated a very small endothermic peak at 33 °C (Supporting Information, Figure S3). The

dx.doi.org/10.1021/ma300183t | *Macromolecules* 2012, 45, 2668−2674

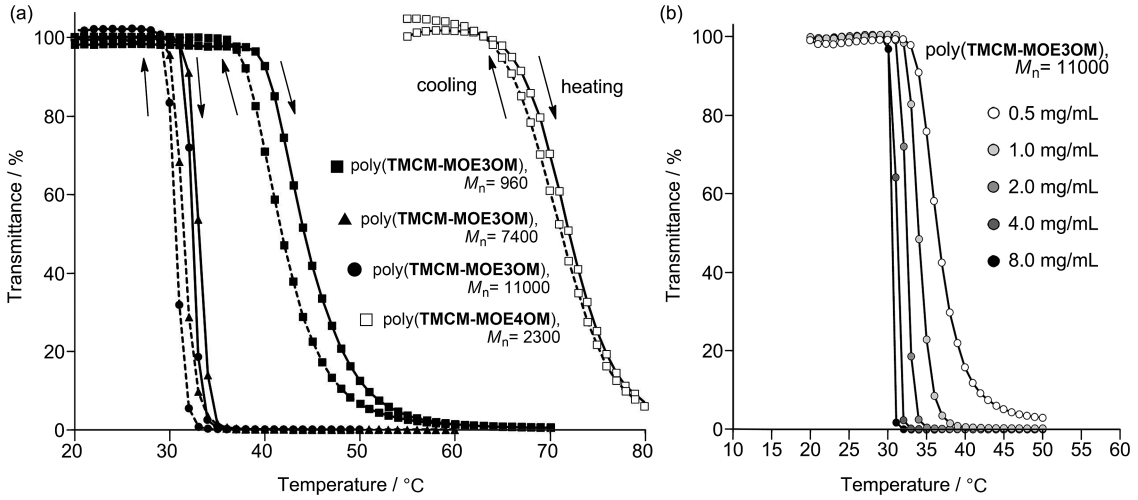


Figure 4. Transmittance vs temperature plots of poly(TMCM-MOE3OM) and poly(TMCM-MOE4OM) solutions in water at 2.0 mg/mL in heating and cooling processes (a). Closed square: poly(TMCM-MOE3OM) with 960 of M_n. Closed triangle: poly(TMCM-MOE3OM) with 7400 of M_n. Closed circle: poly(TMCM-MOE3OM) with 11 000 of M_n. Open square: poly(TMCM-MOE4OM) with 2300 of M_n. Transmittance vs temperature plots of poly(TMCM-MOE3OM) solution with 7400 of M_n with 0.5, 1.0, 2.0, 4.0, and 8.0 mg/mL (b).

enthalpy was estimated as 2.20 J/g in the region from 30 to 45 °C, using a 2 °C/min heating process with 4.7 mg of poly(TMCM-MOE3OM). Direct observation of the cloudy suspension was also performed by microscopy, revealing a phase separation (Supporting Information, Figure S4). At present, poly(TMCM-MOE3OM) itself is a highly viscous liquid, and the synthesis of higher M_n of poly(TMCM-MOE3OM)s is currently underway.

■ CONCLUSIONS

In conclusion, a novel thermosensitive biodegradable homopolymer with a LCST at body temperature was prepared with a PTMC backbone and OEG units. The polymer was constructed from a repeating well-defined monomer structure without the inclusion of any ester groups, which generate acidic compounds during degradation. Although poly(TMCM-MOE1OM) was insoluble, poly(TMCM-MOE3OM) and poly(TMCM-MOE4OM) were soluble in water at 25 °C, showing a LCST. Poly(TMCM-MOE3OM) was a highly viscous liquid below a M_n of 11 000, and its LCST in water ranged from 31 and 35 °C, depending on the concentration. The LCST of poly(TMCM-MOE4OM) appeared at 72 °C and differed greatly from poly(TMCM-MOE3OM). We believe that poly(TMCM-MOE3OM) is promising as an essential polymer material for various biomedical applications.

■ ASSOCIATED CONTENT

Ⓢ Supporting Information

FT-IR spectra of monomers. MALDI/TOF-MS of polymers; solubility test; DSC analysis of poly(TMCM-MOE3OM); microscope observation of poly(TMCM-MOE3OM) in water; photos of poly(TMCM-MOE3OM). This material is available free of charge via the Internet at http://pubs.acs.org.

■ AUTHOR INFORMATION

Corresponding Author

*E-mail akashi@chem.eng.osaka-u.ac.jp; Ph +81-6-6879-7356; Fax +81-6-6879-7359.

Notes

The authors declare no competing financial interest.

■ ACKNOWLEDGMENTS

The authors are grateful to the fruitful discussion with Drs. T. Kida, M. Matsusaki, and T. Akagi. The authors are also grateful to MDs. K. Yamamoto and S. Nanto. This work was partly supported by a Grant-in-Aid for Young Scientists (B) No. 21750220.

■ REFERENCES

(1) Pelton, R. *Adv. Colloid Interface Sci.* **2000**, *85*, 1−33.
(2) Kikuchi, A.; Okano, T. *Prog. Polym. Sci.* **2002**, *27*, 1165−1193.
(3) Winnik, F. M. *Macromolecules* **1990**, *23*, 233−242.
(4) Ringsdorf, H.; Simon, J.; Winnik, F. M. *Macromolecules* **1992**, *25*, 7306.
(5) Bokias, G.; Staikos, G.; Iliopoulos, I. *Polymer* **2000**, *41*, 7399−7405.
(6) Dube, D.; Francis, M.; Leroux, J.-C.; Winnik, F. M. *Bioconjugate Chem.* **2002**, *13*, 685−692.
(7) Garbern, J. C.; Hoffman, A. S.; Stayton, P. S. *Biomacromolecules* **2010**, *11*, 1833−1839.
(8) Suwa, K.; Wada, Y.; Kikunaga, Y.; Morishita, K.; Kishida, A.; Akashi, M. *J. Polym. Sci., Part A: Polym. Chem.* **1997**, *35*, 1763−1768.
(9) Yamamoto, K.; Serizawa, T.; Muraoka, Y.; Akashi, M. *Macromolecules* **2001**, *34*, 8014−8020.
(10) Han, S.; Hagiwara, M.; Ishizone, T. *Macromolecules* **2003**, *36*, 8312−8319.
(11) Kono, K.; Murakami, T.; Yoshida, T.; Haba, Y.; Kanaoka, S.; Takagishi, T.; Aoshima, S. *Bioconjugate Chem.* **2005**, *16*, 1367−1374.
(12) Aoshima, S.; Kanaoka, S. *Adv. Polym. Sci.* **2008**, *210*, 169−208.
(13) Sugihara, S.; Kanaoka, S.; Aoshima, S. *Macromolecules* **2005**, *38*, 1919−1927.
(14) Sugihara, S.; Kanaoka, S.; Aoshima, S. *Macromolecules* **2004**, *37*, 1711−1719.
(15) Lee, R.; Chen, W.-H. *React. Funct. Polym.* **2011**, *71*, 455−462.
(16) Brazel, C. S.; Peppas, N. A. *Macromolecules* **1995**, *28*, 8016−8020.
(17) Yin, X.; Hoffman, A. S.; Stayton, P. S. *Biomacromolecules* **2006**, *7*, 1381−1385.
(18) Siu, M.; He, Ch.; Wu, C. *Macromolecules* **2003**, *36*, 6588−6592.
(19) Mizutani, M.; Satoh, K.; Kamigaito, M. *Macromolecules* **2011**, *44*, 2382−2386.
(20) Alli, S.; Alli, A.; Hazer, H. *J. Appl. Polym. Sci.* **2012**, *124*, 536−548.

(21) Lutz, J.-F.; Akdemir, O.; Hoth, A. *J. Am. Chem. Soc.* **2006**, *128*, 13046−13047.
(22) Song, S.-C.; Lee, S. B.; Jin, J.-I.; Sohn, Y. S. *Macromolecules* **1999**, *32*, 2188−2193.
(23) Qiao, Z.-Y.; Du, F.-S.; Zhang, R.; Liang, D.-H.; Li, Z.-C. *Macromolecules* **2010**, *43*, 6485−6494.
(24) Hazer, B.; Lenz, R. W.; Cakmakli, B.; Borcakli, M.; Kocer, H. *Macromol. Chem. Phys.* **1999**, *200*, 1903−1907.
(25) Haba, Y.; Kojima, C.; Harada, A.; Kono, K. *Macromolecules* **2006**, *39*, 7451−7453.
(26) Yamamoto, K.; Serizawa, T.; Muraoka, Y.; Akashi, M. *J. Polym. Sci., Part A: Polym. Chem.* **2000**, *38*, 3674−3681.
(27) Yamamoto, K.; Serizawa, T.; Akashi, M. *Macromol. Chem. Phys.* **2003**, *204*, 1027−1033.
(28) Jeong, B.; Bae, Y. H.; Lee, D. S.; Kim, S. W. *Nature* **1997**, *388*, 860−862.
(29) Byrne, C. M.; Allen, S. D.; Lobkovsky, E. B.; Coates, G. W. *J. Am. Chem. Soc.* **2004**, *126*, 11404−11405.
(30) Cheng, S.-X.; Miao, Z.-M.; Wang, L.-S.; Zhuo, R.-X. *Macromol. Rapid Commun.* **2003**, *24*, 1066−1069.
(31) Kashio, M.; Sugizaki, T.; Tanaka, Y.; Yamamoto, S.; Moriya, O.; Nishikubo, T. *Polym. J.* **2011**, *43*, 525−530.
(32) Danquah, M.; Fujiwara, T.; Hahato, R. I. *Biomaterials* **2010**, *31*, 2358−2370.
(33) Nederberg, F.; Lohmeijer, B. G. G.; Leibfarth, F.; Pratt, R. C.; Choi, J.; Dove, A. T.; Waymouth, R. M.; Hedrick, J. L. *Biomacromolecules* **2007**, *8*, 153−160.
(34) Coulembier, O.; Sanders, D. P.; Nelson, A.; Hollenbeck, A. N.; Horn, H. W.; Rice, J. E.; Fujiwara, M.; Dubois, P.; Hedrick, J. L. *Angew. Chem., Int. Ed.* **2009**, *48*, 5170−5173.
(35) Zhang, H.-H.; Huang, Z.-Q.; Sun, B.-W.; Guo, J.-X.; Wang, J.-L.; Chen, Y.-Q. *J. Polym. Sci., Part A: Polym. Chem.* **2008**, *46*, 8131−8140.
(36) Sanson, C.; Schatz, C.; Meins, J.-F. L.; Brulet, A.; Soum, A.; Lecommandoux, S. *Langmuir* **2010**, *26*, 2751−2760.
(37) Sanson, C.; Schatz, C.; Meins, J.-F. L.; Soum, A.; Thevenot, J.; Garanger, E.; Lexommandoux, S. *J. Controlled Release* **2010**, *147*, 428−435.
(38) Seow, W. Y.; Yang, Y. Y. *J. Controlled Release* **2009**, *139*, 40−47.
(39) Lu, J.; Shoichet, M. S. *Macromolecules* **2010**, *43*, 4943−4953.
(40) Li, F.; Danquah, M.; Mahato, R. I. *Biomacromolecules* **2010**, *11*, 2610−2620.
(41) Nederberg, F.; Zhang, Y.; Tan, J. P. K; Xu, K.; Wang, H.; Yang, C.; Gao, S.; Guo, X. D.; Fukushima, K.; Li, L.; Hedrik, J. L.; Yang, Y.-Y. *Nat. Chem.* **2011**, *3*, 409−414.
(42) Zhang, Z.; Gripma, D. W.; Feijen, J. *J. Controlled Release* **2006**, *112*, 57−63.
(43) Kim, S. Y.; Kim, H. J.; Lee, K. E.; Han, S. S.; Sohn, Y. S.; Jeong, B. *Macromolecules* **2007**, *40*, 5519−5525.
(44) Kim, S. H.; Tan, J. P. K; Fukushima, K.; Nederberg, F.; Yang, Y. Y.; Waymoutgh, R. M.; Hedrick, J. L. *Biomaterials* **2011**, *32*, 5505−5514.
(45) Watanabe, J.; Kotera, H.; Akashi, M. *Macromolecules* **2007**, *40*, 8731−8736.
(46) Wang, X.-L.; Zhuo, R.-X.; Liu, L.-J.; He, F.; Liu, G. *J. Polym. Sci., Part A: Polym. Chem.* **2002**, *40*, 70−75.
(47) Sanders, D. P.; Fukushima, K.; Coady, D. J.; Nelson, A.; Fujiwara, M.; Yasumoto, M.; Hedrick, J. L. *J. Am. Chem. Soc.* **2010**, *132*, 14724−14726.
(48) Chen, W.; Yang, H.; Wang, R.; Cheng, R.; Meng, F.; Wei, W.; Zhong, Z. *Macromolecules* **2010**, *43*, 201−207.
(49) Lin, X.; Li, W.; Zhang, J.; Sun, H.; Yan, Y.; Wu, L. *Langmuir* **2010**, *26*, 13201−13209.
(50) Davies, S. G.; Roberts, P. M.; Stephenson, P. T.; Storr, H. R.; Thomson, J. E. *Tetrahedron* **2009**, *65*, 8283−8296.
(51) Matsuo, J.; Aoki, K.; Sanda, F.; Endo, T. *Macromolecules* **1998**, *31*, 4432−4438.
(52) Lee, A. L. Z.; Venkataraman, S.; Sirat, S. B. M.; Gao, S.; Hedrick, J. L. *Biomaterials* **2012**, *33*, 1921−1928.
(53) Qiao, Y.; Yang, C.; Coady, D. J.; Ong, Z. Y.; Hedrick, J. L.; Yang, Y. Y. *Biomaterials* **2012**, *33*, 1146−1153.

Macromolecules

Article

pubs.acs.org/Macromolecules

Mechanistic Pathway for the Formation of Radial Polystyrenes Using Diacyl Chloride

Santosh Kumar,[†,⊥,§] Priyank N. Shah,[†,§] Seonyoung Ahn,[#] Woon Sung Hwang,[‡] Ik Kyung Sung,[‡] Shailesh R. Shah,[∥] C. N. Murthy,[⊥] Taihyun Chang,[#] and Jae-Suk Lee[†,*]

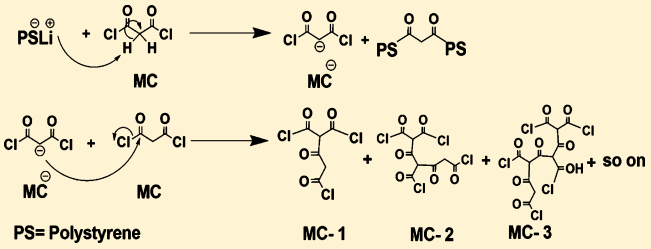
[†]Department of Nanobio Materials and Electronics, School of Materials Science and Engineering, Gwangju Institute of Science and Technology (GIST), 123 Cheomdan-gwagiro (Oryong-dong), Buk-gu, Gwangju, 500-712, Korea

[‡]R&D Center, Kolon Industries, Inc., Chemical Organization 294 Gajwa-dong, Seo-gu, Incheon-si 404-815, Korea

[⊥]Applied Chemistry Department, Faculty of Technology & Engineering, and [∥]Department of Chemistry, Faculty of Science, The M.S. University of Baroda, Vadodara 390 002, India

[#]Department of Chemistry and Division of Advanced Materials Science, Pohang University of Science and Technology (POSTECH), Pohang, 790784, Korea

ABSTRACT: An efficient and useful synthetic route for the synthesis of linear and star polystyrenes (PS) is described, employing living anionic polymerization to link living polystyryl anions to inexpensive and readily available malonyl chloride and other coupling agents with higher functionality that were generated *in situ* at room temperature. The polymers prepared in this way were analyzed and characterized by size-exclusion chromatography (SEC), temperature gradient interaction chromatography (TGIC) and matrix-assisted laser desorption/ionization time-of-flight mass spectrometry (MALDI−TOF MS). It was observed that with the increase in molecular weight of the living PS, the number of arms and weight fraction of higher arm polymers decrease significantly.



INTRODUCTION

With increasing importance of hyperbranched polymers such as dendrimers synthesis and high resolution analysis of these polymers has become pertinent and have attractive much attention in recent years.[1−3] Star polymers exhibit unique and interesting properties and also have important applications[4−8] that differ from those of the corresponding linear polymers. Recently, we reported the synthesis of three different block copolymers: the di-, tri-, and star-block polymers of polystyrene-*b*-polyisoprene (SI).[9] A simple bifunctional coupling agent, malonyl chloride (MC), for the synthesis of block copolymers while controlling the molecular weights and weight fractions, employing living anionic polymerization, was demonstrated. It was envisaged that this strategy can be extended to the synthesis of polymers with a higher number of arms. With a lead from our previous findings, here in we report the experimental evidence and in-depth investigation of the mechanism using state-of-the-art analytical techniques resulting in the realization of our hypothesis through the synthesis of star polystyrenes (PSs). Synthesis of PSs has been achieved by linking living polystyryl anions with various *in situ* generated coupling agents from (MC) at room temperature.

Size-exclusion chromatography (SEC) is the most widely used method for the separation of polymers by their molecular weights.[10,11] However, SEC separates the polymers relative to their hydrodynamic chain size, and it has been most successful in the analysis of linear homopolymers, in which a relatively simple correlation exists between the molecular weight and the hydrodynamic size. The resolution in SEC is not as good for branched polymers as linear polymers because the hydrodynamic chain size does not increase with the molecular weight as significantly as with linear polymers. For a more rigorous characterization of branched polymers, interaction chromatography (IC) is preferred and shows much higher resolution.[12−16] Mass spectrometry (MS) is a valuable technique for the analysis and identification of low molecular weight polymers with different end groups. Matrix-assisted laser desorption/ionization time-of-flight mass spectrometry (MALDI−TOF MS) has made the analysis of these low molecular weight polymers possible for a wide variety of polymers that have rarely been directly analyzed by mass spectrometric methods.[17−20] This soft ionization method has become the most widely used MS technique in polymer analyses because it is applicable to a greater variety of synthetic polymers than any other MS method leading to simple spectra, displaying only singly charged quasi-molecular ions with little or no fragmentation.[21−24] The present study on the new star polystyrenes utilizes MALDI−TOF MS for the structure elucidation and end-group analysis of star polystyrenes synthesized by living anionic polymerization. The intricate details revealed by this analysis elucidate the mechanism of

Received: January 30, 2012
Revised: February 29, 2012
Published: March 19, 2012

ACS Publications © 2012 American Chemical Society

Table 1. Selected Data for the Weight Fraction, (Wt. Fr.) Molecular Weight (M_n) and Polydispersity Index (M_w/M_n) of Various Armed Polystyrene Using *sec*-Butyllithium (*s*-BuLi) as an Initiator and Malonyl Chloride (MC) as a Coupling Agent at Room Temperature

	wt. fr., %[a] (M_n/PDI)[b]					
sample	1 arm	2 arm	3 arm	4 arm	5 arm	higher, %
C1	37.3	21.1	24.2	7.1	6.3	4.0
	(2.0K/1.01)	(4.3K/1.02)	(6.4K/1.04)	(8.9K/1.07)	(10.5K/1.02)	–
C2	42.1	21.2	23.3	5.9	4.6	2.8
	(4.3K/1.02)	(8.6K/1.05)	(12.6K/1.05)	(17.1K/1.05)	(23.4K/1.06)	–
C3	44.4	20.1	22.9	5.1	5.6	1.8
	(7.0K/1.03)	(14.9K/1.03)	(22.9K/1.02)	(30.9K/1.04)	(34.5K/1.03)	–
C4	47.4	20.1	23.5	4.4	3.4	1.3
	(18.3K/1.02)	(35.1K/1.01)	(54.1K/1.03)	(74.6K/1.02)	–	–
C5	52.9	19.3	22.3	4.0	1.5	
	(53.0K/1.01)	(105K/1.03)	(150K/1.02)	(217K/1.01)	–	–
C6	60.8	20.7	16.3	2.2	–	–
	(92.0K/1.05)	(180K/1.04)	(280K/1.07)	–		

[a]Weight fractions were calculated using reversed phase temperature gradient interaction chromatography (RP-TGIC). [b]Number-average molecular weight, M_n, and the polydispersity index, M_w/M_n was measured by size-exclusion chromatography multiangle laser light scattering (SEC-MALLS) after the fractionation of each samples.

polymer formation and contribute to a greater understanding of both the polymerization process and the end-functionalization mechanisms.

There are a few reports on the synthesis of star-shaped polystyrenes with the help of bifunctional coupling agents such as 4-(chlorodimethylsilyl)styrene (CDMSS)[25,26] and divinylbenzene (DVB)[27−31] employing living anionic polymerization. Synthesis of CDMSS is not easy, requires several steps, stringent conditions and also results in low yields. The use of DVB as a coupling agent has its own disadvantages.[32,33] Its reaction with low-molecular-mass organolithium compounds (e.g., *n*- and *s*-BuLi) is extremely difficult to control. Even at nearly equimolar DVB: initiator ratios, large aggregates are formed in the system. The polydispersity (structural heterogeneity) of such systems is quite high. In comparison, our methodology employed here is a highly valuable tool even for the synthesis of a variety of star-shaped block copolymers at once as was observed with the living polystyrene-*b*-polyisoprenyl anion.[9] The effect of chain length on the number of arms formed in the star-shaped PS has also been studied. We found that longer chains (with molecular weights ranging from 2.0K to 92.0K) formed fewer arms in the star-shaped polymers, as explained below. In the present communication, we investigated this mechanism for the first time and confirmed our hypothesis regarding the synthesis of star polystyrene by linking living polystyryl anions to the coupling agents produced from a simple bifunctional coupling agent, MC at room temperature.

EXPERIMENTAL SECTION

Materials. The styrene monomer (Aldrich, 99%) was passed through activated alumina, washed with an aqueous solution of sodium hydroxide and then with distilled water to remove inhibitors, dried over calcium hydride and vacuum distilled under reduced pressure. Malonyl chloride (Aldrich, 97%) was dried over calcium hydride, vacuum distilled, diluted with toluene, and sealed in glass ampules equipped with break-seals. Toluene (Aldrich, 99%) was purified using a standard high-vacuum technique described elsewhere.[34,35] *sec*-Butyllithium (*s*-BuLi) (Aldrich, 1.6 M in hexane), calcium hydride (Junsei, 95%), *n*-butyllithium (Aldrich 1.6 M in hexane) and 1,1-diphenylethylene (Aldrich, 97%) were used as received without further purification.

Polymerization. Samples C1−C6 were synthesized in a specially fabricated glass apparatus with break-seals under high-vacuum conditions (10^{-6} Torr). The synthesis of sample C1 (1:0.5 molar ratio of initiator to coupling agent) is described as an example of a typical anionic polymerization. The homopolymerization of styrene (0.790 g, 7.65 mmol) was initiated by the addition of *sec*-butyl lithium (*s*-BuLi, 0.024 g, 0.399 mmol) at room temperature using toluene as the polymerization solvent. The color of the reaction mixture turned a deep red-orange that indicated the formation of the living polystyryl anion.[13] After allowing this reaction to proceed for 2 h, malonyl chloride (0.028 g, 0.197 mmol). was introduced to the living polystyryl anion and was allowed to react for 1 h. The reaction was terminated by the addition of methanol, and the resulting mixture was poured into a large amount of methanol to ensure complete precipitation. The precipitated polymer was filtered and dried. It was then dissolved in benzene and freeze-dried. A similar procedure was followed for samples C2−C6 using a similar ratio of initiator to coupling agent and varying the concentration of the initiator relative to the monomer.

Characterization. *RP-TGIC Analysis.* For the separation by reverse-phase temperature gradient interaction chromatography (RP-TGIC), a C18 bonded silica column (Nucleosil, 500 Å pore, 250 mm × 2.1 mm i.d., 7-μm particle size) was used. The mobile phase was a mixture of CH_2Cl_2 and CH_3CN (58/42, v/v, Samchun, HPLC grade) with a flow rate of 0.25 mL/min. The column temperature was controlled by circulating water from a bath/circulator (Haake, C25P) through a homemade column jacket. The polymer sample was dissolved in the elution solvent (2 mg/mL), and the injection volume was 100 μL. TGIC chromatograms were recorded with a UV absorption detector (Younglin, UV 730D) at a wavelength of 260 nm.

SEC Analysis. For the SEC analysis of the fractionated samples, two mixed bed columns (Polymer Lab. Mixed C, 300 × 8.0 mm i.d.) were used. SEC chromatograms were recorded with multiangle laser light scattering (Wyatt, mini-DAWN TREOS) and a refractive index detector (Shodex, RI-101) using tetrahydrofuran (THF) (Samchun, HPLC grade) as the mobile phase. The polymer samples were dissolved in THF, the injection volume was 100 μL, and the flow rate of the mobile phase was 0.8 mL/min. The column temperature was maintained at 40 °C using a column oven (Eppendorf, TC-50).

MALDI−TOF Analysis. For the MALDI−TOF MS measurements, a Bruker Reflex III mass spectrometer was used. The spectrometer was equipped with a nitrogen laser (λ = 337 nm), a pulsed ion extraction, and a reflector. Polymer solutions were prepared in THF at a concentration of 5 mg/mL. The matrix, 1,8-dihydroxy-9(10*H*)-anthracenone (dithranol, Aldrich, 97%), was dissolved in THF at a concentration of

dx.doi.org/10.1021/ma3002142 | *Macromolecules* 2012, 45, 2675−2681

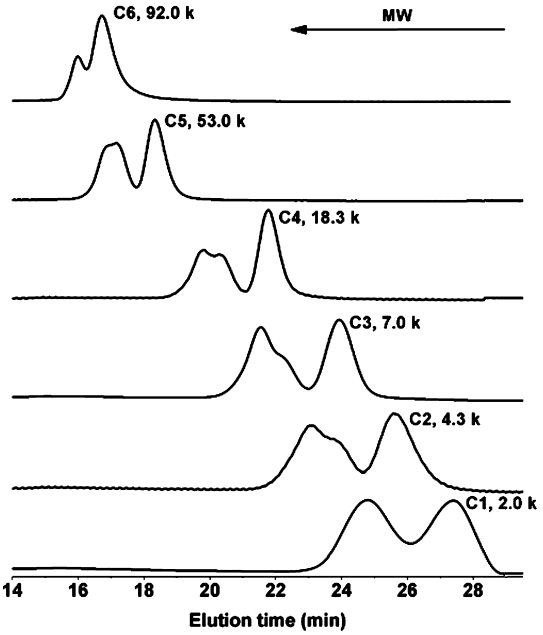


Figure 1. Size-exclusion chromatography (SEC) chromatograms of samples C1−C6, showing the effect of increasing molecular weight (MW) of the PS precursor. *Note*: The molecular weight of the precursor (PS having one arm) is also shown.

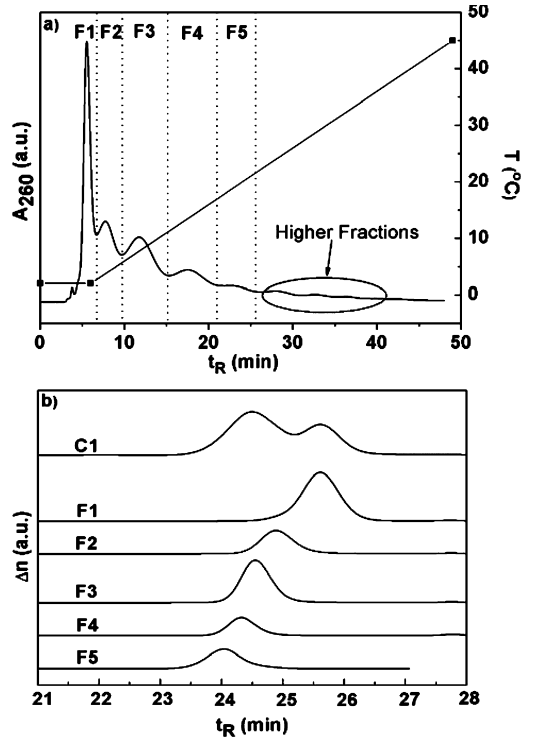
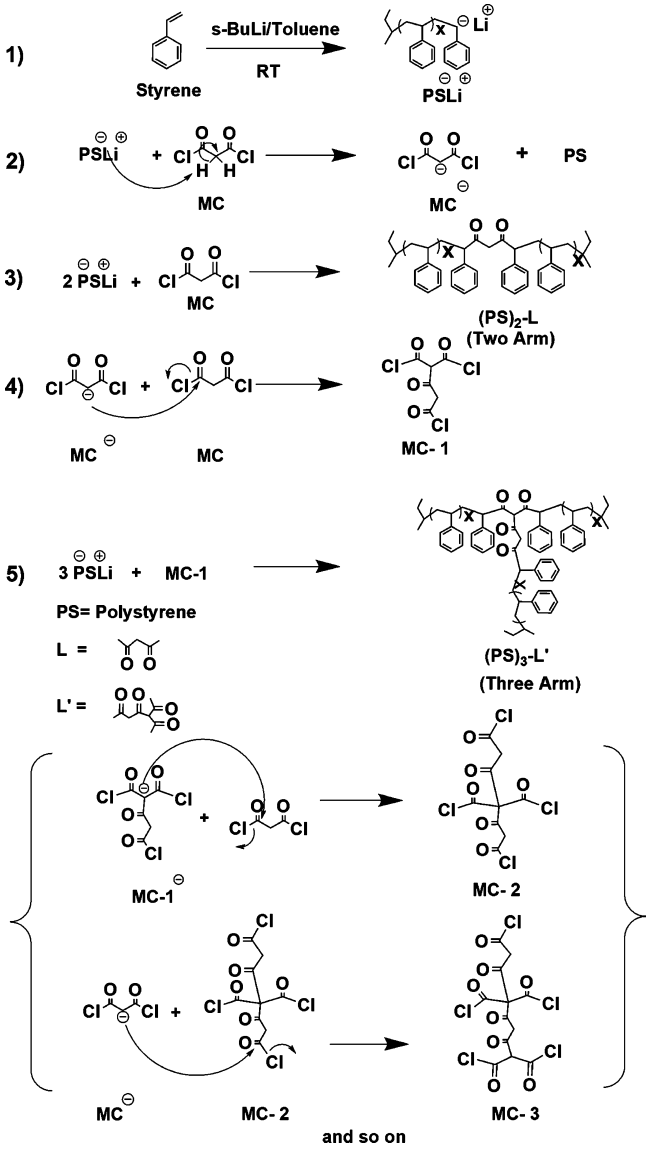


Figure 2. (a) TGIC curves obtained from sample C1, F1−F5 showing its fractionation (dotted lines): column, C18 bonded silica, 100 Å, 250 × 4.6 mm; eluent, CH_2Cl_2/CH_3CN (55/45, v/v); flow rate, 0.5 mL/min. Some minor products (up to 4%) of PS having six or more arms are marked with a circle. (b) Size-exclusion chromatography (SEC) curves obtained from sample C1 and the SEC curves of five temperature gradient interaction chromatography (TGIC) fractions (F1−F5) after the fractionation of sample C1.

20 mg/mL. A 5 μL aliquot of the polymer solution was mixed with 50 μL of the matrix solution and 1.5 μL of a silver trifluoroacetate

Scheme 1. Mechanism of Formation of Various Armed Star Polystyrene from Malonyl Chloride and *in Situ* Generated Multifunctional Coupling Agents



(Aldrich, 98%) solution (1 mg/mL) in THF. A 0.5-μL portion of the final solution was deposited onto a sample target plate and allowed to dry in air at room temperature.

RESULTS AND DISCUSSION

The synthesis of the star-shaped polystyrene was achieved through the anion-initiated polymerization of styrene by the addition of MC to the living polystyryl anions. This reaction sequence resulted in a mixture of five or more armed polystyrenes, depending upon the molecular weight of the living polystyryl anion. The living anionic polymerizations were performed using a 1:0.5 molar ratio of initiator to coupling agent and by varying the concentration of the initiator relative to the monomer in samples C1−C6. The experiments resulted in mixtures of star-shaped PS that had a varying number of arms with controlled molecular weights and relatively low PDIs (1.01−1.09) (Table 1) with nearly a 100% yield in each case. The extent of the linking reaction decreases as the molecular weight of the parent polymeric chain increases from C1−C6.

dx.doi.org/10.1021/ma3002142 | *Macromolecules* 2012, 45, 2675−2681

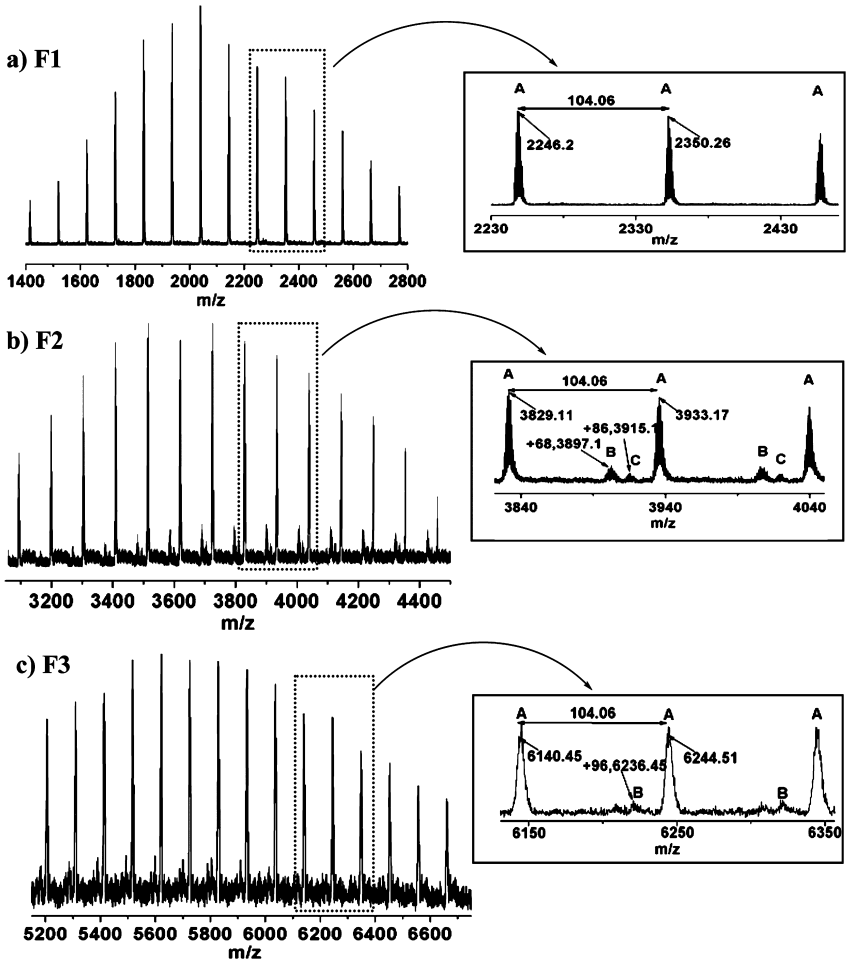


Figure 3. Matrix-assisted laser desorption/ionization time-of flight mass spectrometry (MALDI−TOF MS) spectra of only the F1−F3 fractions separated from sample C1. (a) MALDI−TOF mass spectrum of one arm, F1. Inset: magnification of the m/z 20-mer and 22-mer peaks of the desired product, $Bu(C_8H_8)_{20}H(Ag^+)$. (b) MALDI−TOF mass spectrum of two-arm fraction F2. Inset: magnification of the m/z 34-mer and 36-mer peaks of the desired product, $2Bu(C_8H_8)_{34}C_3H_2O_2(Ag^+)$, (c) MALDI−TOF mass spectrum of three-armed fraction F3. Inset: magnification of the m/z 55-mer and 57-mer peaks of the desired product, $Bu_3(C_8H_8)_{55}C_6H_3O_4(Ag^+)$.

The molecular weights (M_n) of the polymers were determined by SEC-MALLS (Table 1) after separating them with a RP-TGIC technique.[9,19,20,36]

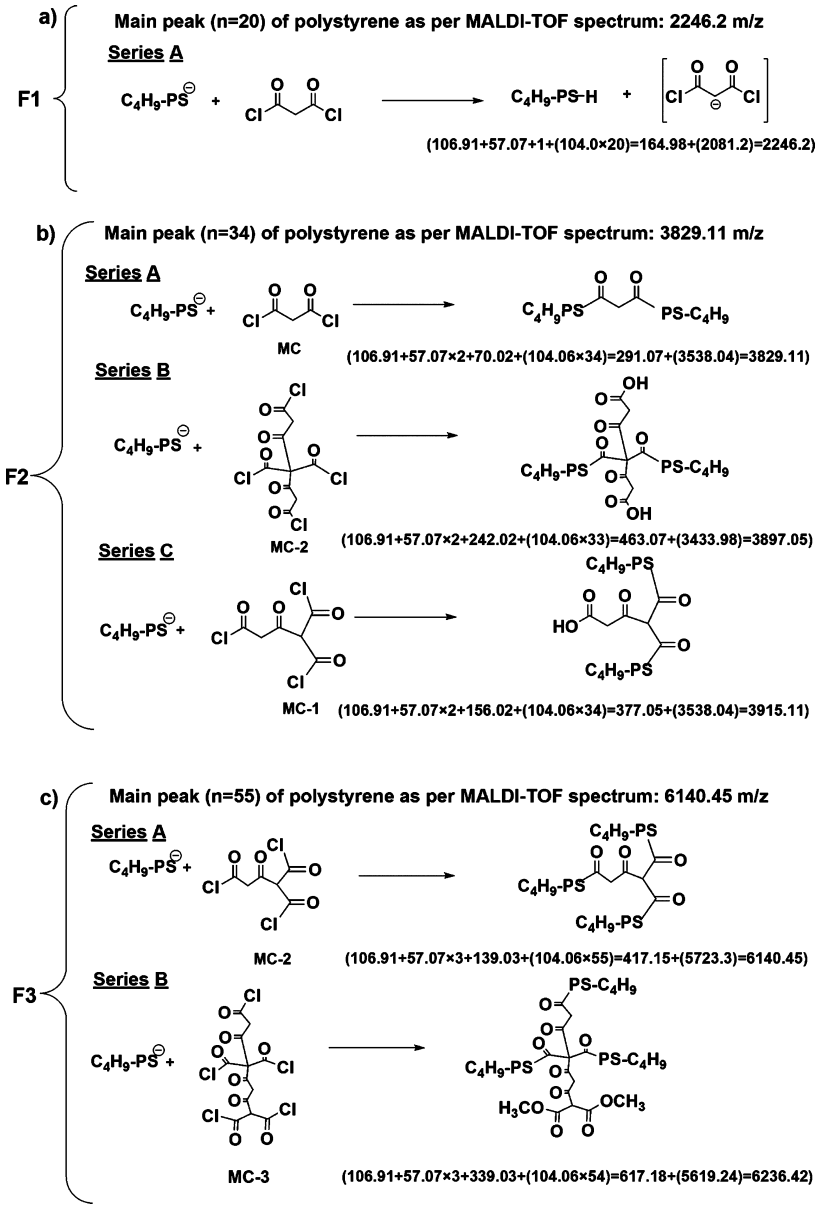
Figure 1 depicts the SEC chromatograms of the six star-shaped PSs prepared with PS anions of different molecular weights. The chromatograms clearly show that the samples are complex mixtures of the star-shaped PS with a varying number of arms. To further investigate the constituents in the PS mixtures that we prepared, sample C1 was used as a representative example. The resulting polystyrenes, after being subjected to the RP-TGIC analysis, indicated that the formation of the anion (MC^-) was dominant over the coupling, leading to the three-armed polymer via the trifunctional coupling agent MC-1, which was generated *in situ* because of the acidity of the methylene hydrogens of MC.[9]

Figure 2a displays the RP-TGIC chromatograms of C1. These chromatograms show three to five distinct peaks for the homopolystyrene. In addition higher-armed star polymers are clearly observed as minor products (up to 4%) and are marked with a circle in Figure 2a. Under RP-TGIC conditions, the retention of the polymer species increases as its absolute molecular weight increases. Therefore, the elution sequence under these conditions contains 2-, 3-, 4-, and 5-armed star polystyrene. To identify the species that correspond to each elution peak, RP-TGIC elution peaks of C1 were fractionated, as marked with dotted vertical lines in Figure 2a. The weight fractions of each fraction were calculated and listed in Table 1. Figure 2b depicts the individual SEC chromatogram of C1 and its RP-TGIC fractions, F1−F5. The absolute molecular weight can be measured more easily by SEC than RP-TGIC since a single solvent is used in SEC while a mixed solvent is used in the TGIC separation.[37] Their individual SEC values (Table 1) indicate that the molecular weights of the each TGIC peak increases 2-, 3-, 4-, and 5-fold indicating that they corresponds to two arm, three arm, four arm and five arm star-shaped polystyrenes. As can be seen from the results included in Table 1, the reactivity of living polystyryl anions remains same in all cases but the number of arms and their weight fractions decrease gradually from C1−C6. It is also depicted in the table that as the molecular weight increases the number of arms decreases which is due to the steric hindrance generated by bulkier polystyryl chains inhibiting the living polystyryl anions to approach for further substitution.

Scheme 1 depicts the mechanistic path leading to the concurrent synthesis of various armed star polystyrenes. The proposed mechanism shows the *in situ* generation of the new coupling agents (MC-1, MC-2, MC-3, etc.) and the results from the novel synthesis of the three-, four-, and five armed

dx.doi.org/10.1021/ma3002142 | *Macromolecules* 2012, 45, 2675−2681

Scheme 2. Structure Elucidation of One (F1), Two (F2), and Three Arm (F3) Fractions from Sample C1



polystyrenes. As shown in step 2, with the introduction of MC into the living polystyryl anions, the living anion abstracts an acidic proton from the active methylene group of MC, forming a new resonance-stabilized anion (MC^-) and terminating the living polymer to give PS. At the same time, the coupling agent (MC) undergoes a substitution reaction at both ends to form the linear two-armed PS (step 3). The anion MC^- further reacts with another molecule of the coupling agent MC in a nucleophilic substitution reaction that leads to the coupled malonyl chloride (MC-1, step 4). The reaction of the living polystyryl anion with the *in situ* generated trifunctional coupling agent MC-1 leads to the synthesis of the three-armed polystyrene (Step 5). Furthermore, the living MC^- also react with the newly formed MC-1 (or a new anion from MC-1 may react with MC) to give MC-2 as a new coupling agent, which leads to the formation of the four-armed polystyrene. Similarly MC^- can also react with MC-2 to form a five-armed coupling agent MC-3 in a similar reaction sequence that gives higher branched polystyrene. The proposed mechanism satisfactorily explains the simultaneous formation of all the observed products, and the investigations are well supported by the TGIC and MALDI−TOF analyses discussed hereafter.

To further investigate the mechanism (Scheme 1), the MALDI−TOF analysis of each fraction was conducted. The analysis was performed for the first three fractions that were obtained from sample C1. Structural elucidation was also performed for the first three fractions, F1−F3. The latter fractions were not analyzed because the resolution becomes poor for high molecular weight polymers using this technique.[38,39] The expanded trace of the mass spectrum of F1 is shown in Figure 3a. The spectrum contains a major distribution A (inset), whose m/z values correspond to the Ag^+ adducts of the PS oligomers with a *sec*-butyl end group $[(C_4H_9)(C_8H_8)_nH(Ag^+)]$. For example, the 20-mer of this distribution is expected to produce a signal at m/z = 57.12 (C_4H_9) + 20 × 104.06 (20 × C_8H_8) + 1 (H) + 106.91 (Ag^+) = 2246.2 (Scheme 2a).

For the two arm fraction (F2), all the oligomers were also detected as Ag-cationized ions. The expanded trace of the mass

dx.doi.org/10.1021/ma3002142 | *Macromolecules* 2012, 45, 2675−2681

spectrum of F2 is shown in Figure 3b. The spectrum contains a major distribution A (inset), whose m/z values correspond to the Ag^+ adducts of the PS oligomers with two *sec*-butyl end groups $[(C_4H_9)_2(C_8H_8)_nC_3H_2O_2(Ag+)]$. For example, the 34-mer of this distribution is expected to produce a signal at m/z = 2 × 57.12 (C_4H_9) + 34 × 104.06 (34 × C_8H_8) + 70 ($C_3H_2O_2$) + 106.91 (Ag^+) = 3829.11 (Scheme 2b). There are two additional unexpected minor products, which result in series B and C. The oligomers of series B and series C appear at m/z values that are 68 and 86 Da greater than those of the A oligomers (Scheme 2b). These minor products must form because of the different termination modes of the four branched MC-2 and three branched MC-1 coupling agents that did not completely react, as shown in Scheme 2b.

Figure 3c shows the MALDI−TOF mass spectrum of the three arm fraction (F3) of sample C1. The major product series A (inset) results from the expected termination of the completely reacted coupling agent MC-1 that is generated *in situ*. (Scheme 2c) viz. $Bu_3(C_8H_8)_nC_6H_3O_4(Ag^+)$. The 55-mer of this distribution is expected to produce a signal at m/z = 3 × 57.12 (3 × C_4H_9) + 55 × 104.06 (55 × C_8H_8) + 140.06 ($C_6H_3O_4$) + 106.91 (Ag^+) = 6140.45. The oligomers of series B appear at m/z values that are 96 Da greater (6236.45) than those of the polymers A and result from a different termination of the half-reacted coupling agent MC-3 (Scheme 2c).

CONCLUSIONS

A novel, inexpensive and readily available coupling agent has been employed in an anionic polymerization at room temperature, leading to the concurrent synthesis of star polystyrenes with a varying numbers of arms. As the molecular weight of the polymeric chains increases, the number of arms decreases. This trend is due to the steric hindrance which inhibits the approach of the living polystyryl anion to the bulky polymeric chains and prevents the formation of multiple arms. This case study demonstrates that MALDI−TOF MS is a sensitive and reliable probe for the detailed analysis of the polymer coupling reactions. This characterization tool can be used for the quantitative determination of the end groups of similarly sized oligomers. The analysis of the products from novel coupling reactions by MALDI−TOF MS provides fast, accurate and detailed insight into the corresponding end group structures. This strategy may prove to be highly valuable in the synthesis of various star-block copolymers by applying the living anionic polymerization technique. Work in this area is in progress.

AUTHOR INFORMATION

Corresponding Author

*Telephone: +82 62 970 2306. Fax: +82 62 970 2304. E-mail: jslee@gist.ac.kr.

Author Contributions

§Both of these authors have contributed equally to the manuscript.

Notes

The authors declare no competing financial interest.

ACKNOWLEDGMENTS

This work was supported by the Program for Integrated Molecular System (PIMS, GIST), World Class University (WCU) (R31-2008-000-10026-0) program at GIST. This research was financially supported by the Ministry of Knowledge Economy (MKE), Korea Institute for Advancement of Technology (KIAT) through the Inter-ER Cooperation Projects. T.C. acknowledges the supports from NRF via the NRL (R0A-2007-000-20125-0), SRC (R11-2008-052-03002), and WCU (R31-2008-000-10059-0) programs.

REFERENCES

(1) Roovers, J.; Comanita, B. *Adv. Polym. Sci.* **1999**, *142*, 179−228.
(2) Inoue, K. *Prog. Polym. Sci.* **2000**, *25*, 453−571.
(3) Vogtle, F.; Gestermann, S.; Hesse, R.; Schwierz, H.; Windisch, B. *Prog. Polym. Sci.* **2000**, *25*, 987−1041.
(4) Bywater, S. *Adv. Polym. Sci.* **1979**, *30*, 89−116.
(5) Roovers, J. *Encyclopedia of Polymer Science and Engineering*, 2nd ed.; Kroschwitz, J. I., Ed.; Wiley-Interscience: New York, 1985; p 478.
(6) Hsieh, H. L.; Quirk, R. P. *Anionic Polymerization: Principles and Applications*; Marcel Dekker: New York, 1996; p 333.
(7) Grest, G. S.; Fetters, L. J.; Huang, J. S.; Richter, D. *Adv. Chem. Phys.* **1996**, *94*, 67−163.
(8) Hirao, T.; Yoo, H. S.; Ozama, Y.; Abou El-Magd, A.; Sugiyama, K.; Hirao, A. *J. Inorg. Organomet. Polym.* **2010**, *20*, 445−456.
(9) Kumar, S.; Shah, P. N.; Kang, B. G.; Min, J. K.; Hwang, W. S.; Sung, I. K.; Shah, S. R.; Murthy, C. N.; Ahn, S.; Chang, T.; Lee, J. S. *J. Polym. Sci., Part A: Polym. Chem.* **2010**, *48*, 2636−2641.
(10) Yau, W. W.; Kirkland, J. J.; Bly, D. D. *Modern Size-Exclusion Liquid Chromatography, Practice of Gel Permeation and Gel Filtration Chromatography*; John Wiley & Sons: New York, 1979.
(11) Mori, S.; Barth, H. G. *Size Exclusion Chromatography*; Springer-Verlag: New York, 1999.
(12) Chang, T. *Adv. Polym. Sci.* **2003**, *163*, 1−60.
(13) Lee, H. C.; Chang, T.; Harville, S.; Mays, J. W. *Macromolecules* **1998**, *31*, 690−694.
(14) Lee, H. C.; Lee, W.; Chang, T.; Yoon, J. S.; Frater, D. J.; Mays, J. W. *Macromolecules* **1998**, *31*, 4114−4119.
(15) Perny, S.; Allgaier, J.; Cho, D.; Lee, W.; Chang, T. *Macromolecules* **2001**, *34*, 5408−5415.
(16) Choi, H.; Im, K.; Chang, T. *Macromol. Res* **2012**, *20*, 101−105.
(17) Tanaka, K.; Waki, H.; Ido, Y.; Akita, S.; Yoshida, Y.; Yoshida, T. *Rapid Commun. Mass Spectrom.* **1988**, *2*, 151−153.
(18) Karas, M.; Hillenkamp, F. *Anal. Chem.* **1988**, *60*, 2299−2301.
(19) Chang, T. *J. Polym. Sci., Part B: Polym. Phys.* **2005**, *43*, 1591−1607.
(20) Park, S.; Park, I.; Ryu, C. Y.; Chang, T. *J. Am. Chem. Soc.* **2004**, *126*, 8906−8907.
(21) Pasch, H.; Schrepp, W. *MALDI−TOF Mass Spectrometry of Polymers*; Springer: Berlin, 2003.
(22) Arnould, M. A.; Polce, M. J.; Quirk, R. P.; Wesdemiotis, C. *Int. J. Mass Spectrom.* **2004**, *238*, 245−255.
(23) Morelle, W.; Michalski, J. C. *Curr. Anal. Chem.* **2005**, *1*, 29−57.
(24) Hong, J.; Cho, D.; Chang, T.; Shim, W. S.; Lee, D. S. *Macromol. Res.* **2003**, *11*, 341−346.
(25) Knauss, D. M.; Al-Muallem, H. A.; Huang, T.; Wu, D. T. *Macromolecules* **2000**, *33*, 3557−3568.
(26) Im, K.; Kim, Y.; Chang, T.; Lee, K.; Choi, N. *J. Chromatogr. A* **2006**, *1103*, 235−242.
(27) Worsfold, D. J. *Macromolecules* **1970**, *3*, 514−517.
(28) Kohler, A.; Zilliox, J. G.; Rempp, P.; Polacek, J.; Koessler, I. *Eur. Polym. J.* **1972**, *8*, 627−639.
(29) Eschwey, H.; Burchard, W. *Polymer* **1975**, *16*, 180−184.
(30) Iiohles, A.; Polacek, J.; Koessler, I.; Zilliox, J. G.; Rempp, P. *Eur Polym. J.* **1972**, *8*, 627−639.
(31) Young, R. N.; Fetters, L. J. *Macromolecules* **1978**, *11*, 899−904.
(32) Vinogradova, L. V. *Russ. J. Appl. Chem.* **2010**, *83*, 351−378.
(33) Hadjichristidis, N. *J. Polym. Sci., Part A: Polym. Chem.* **1999**, *37*, 857−871.
(34) Hadjichristidis, N.; Iatrou, H.; Pispas, S.; Pitsikalis, M. *J. Polym. Sci., Part A: Polym. Chem.* **2000**, *38*, 3211−3234.

(35) Shah, P. N.; Min, J. K.; Kim, H. J.; Park, S. Y.; Lee, J. S. *Macromolecules* **2011**, *44*, 7917−7925.
(36) Park, S.; Chang, T. *Macromolecules* **2006**, *39*, 3466−3468.
(37) Lee, W.; Park, S.; Chang, T. *Anal. Chem.* **2001**, *73*, 3884−3889.
(38) Rader, H. J.; Schrepp, W. *Acta Polym.* **1998**, *49*, 272−293.
(39) Thomson, B.; Suddaby, K.; Rudin, A.; Lajoie, G. *Eur. Polym. J.* **1996**, *32*, 239−256.

Macromolecules

Article

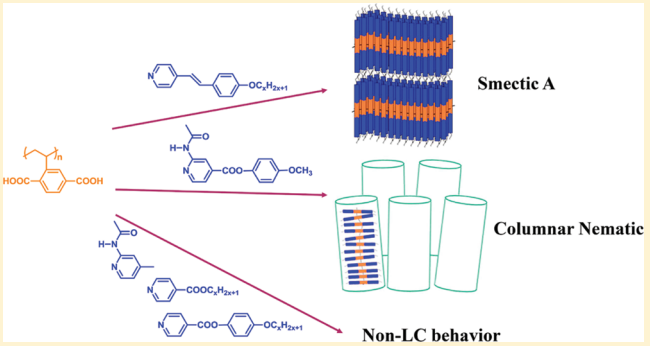
pubs.acs.org/Macromolecules

Synthesis and Characterization of Mesogen-Jacketed Liquid Crystalline Polymers through Hydrogen-Bonding

Yiding Xu, Wei Qu, Qian Yang, Jukuan Zheng, Zhihao Shen,* Xinghe Fan,* and Qifeng Zhou

Beijing National Laboratory for Molecular Sciences, Key Laboratory of Polymer Chemistry and Physics of Ministry of Education, College of Chemistry and Molecular Engineering, Peking University, Beijing 100871, China

ABSTRACT: In an attempt to construct mesogen-jacketed liquid crystalline polymers through noncovalent interactions, poly(2-vinylbenzene-1,4-dioic acid) and five series of pyridine derivatives were synthesized as hydrogen-bonding donor and acceptors, respectively. The structures of the compounds were confirmed by ^{1}H NMR, FT-IR, and gel permeation chromatography. A series of complexes with the same degree of polymerization and polydispersity were obtained by mixing the hydrogen-bonding donor and acceptors. The hydrogen-bonds were confirmed by FT-IR spectra. We found that the rigidity and structures of pyridine derivatives and the strength of the hydrogen-bonding all influenced the liquid crystalline behaviors of the resulting complexes. Smectic A and columnar nematic phases were observed in complexes PPANCx and PPANNEC, respectively.



INTRODUCTION

Liquid crystalline polymers (LCPs) have received much attention because of their potential applications, such as nonlinear optic devices and engineering plastics.[1] Mesogen-jacketed liquid crystalline polymers (MJLCPs) are side-chain LCPs with a very short spacer or no spacer between the backbone and laterally attached bulky side groups, which are often mesogens.[2,3] Various liquid crystalline (LC) phases, such as columnar nematic, hexagonal columnar, rectangular columnar, smectic A, and smectic C, have been observed, resulting from a small change in chemical structures of MJLCPs.[4] In addition, the molecular weight also plays an important role in the phase behavior of MJLCPs.

So far, most of MJLCPs have been synthesized by polymerizing small molecules which contain vinyl groups. Thus, synthesis of monomers is one of the most important and difficult parts in researching MJLCPs. Because of the differences of polymerizability of monomers, it is difficult to obtain MJLCPs with similar DP and PDI values. To further investigate the relationship between polymer liquid crystalline phase and side-group structure, we prefer to have MJLCPs with the same degree of polymerization via noncovalent interactions between a polymer containing the basic part of MJLCPs and different small molecules.

As one of the key interaction in aggregation in nature, hydrogen-bonding (H-bonding) is widely used in building LCPs. Since the first report of the supramolecular side-chain polymer containing a hydrogen-bonded (H-bonded) mesogenic core,[5] the design and preparation of supramolecular LCPs built through H-bonding have attracted much attention. Main-chain, side-chain, and network supramolecular LCPs have been prepared through H-bonding.[5−9] In a recent research on MJLCPs, H-bonding between side groups leads to the smectic packing.[10] On the other hand, as another important type of noncovalent interactions, electrostatic interaction has been utilized to obtain lamellar structures in ionic complexes between MJLCPs and surfactants.[11]

In this work, a new series of MJLCPs containing H-bonding in their side groups were designed. Herein, poly(2-vinylbenzene-1,4-dioic acid) (PPA) was used as the H-bonding donor and several pyridine derivatives as the acceptors. As shown in Chart 1, H-bonded mesogens were directly attached to the polymer backbone laterally. Smectic phases and a columnar nematic phase were observed in three of the complexes. The results demonstrated that H-bonding with bond energy much smaller than those of covalent bonds were also stable enough to built MJLCPs.

EXPERIMENTAL METHODS

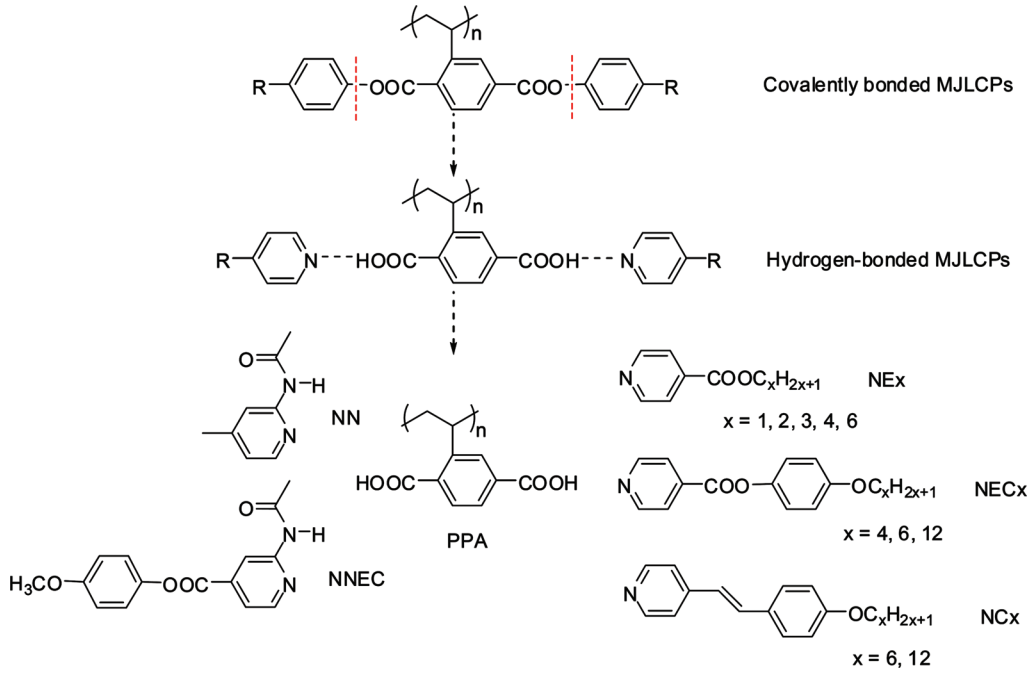
Materials. 2-Vinylbenzene-1,4-dioic acid,[12] 4-(4′-hydroxy)-styrylpyridine,[13] 4-alkoxyphenol,[14] and 4-(4′-alkoxy)styrylpyridine[15,20] were prepared according to the literature. Benzoyl peroxide (BPO) was purified by recrystallization from chloroform/methanol. Tetrahydrofuran (THF) was refluxed over sodium under argon and distilled out before use. *N*,*N*-Dimethylformamide (DMF) was refluxed over potassium hydroxide and distilled out before use. Chlorobenzene was washed by H_2SO_4, distilled water, $NaHCO_3$, and distilled water separately, refluxed over CaH_2, and distilled before use. All other reagents were used as received from commercial sources.

Characterization Methods. All of the characterization methods, such as ^{1}H NMR spectrometry, FT-IR spectroscopy, gel permeation chromatography (GPC), mass spectrometry (MS), thermogravimetric

Received: December 20, 2011
Revised: February 29, 2012
Published: March 16, 2012

ACS Publications © 2012 American Chemical Society

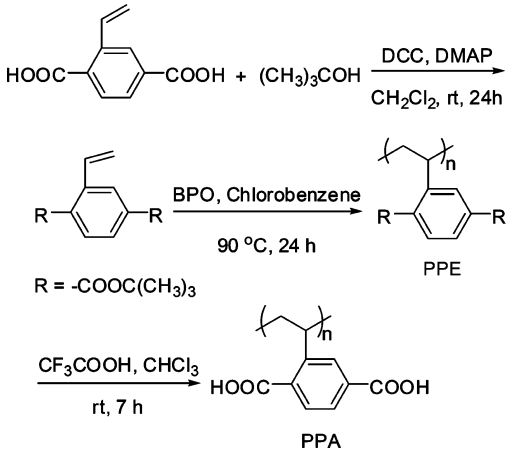
Chart 1. Chemical Structures of H-Bonded MJLCPs



analysis (TGA), differential scanning calorimetry (DSC), one-dimensional wide-angle X-ray diffraction (1D WAXD), polarized light microscopy (PLM), and small-angle X-ray scattering (SAXS), used in this study were similar to those reported previously.[16,17]

Synthesis of Poly(2-vinylbenzene-1,4-dioic acid) (PPA). The synthetic routes of poly(2-vinylbenzene-1,4-dioic acid) are depicted in Scheme 1. The experimental details are described below in three steps.

Scheme 1. Synthetic Routes of PPA



1. Synthesis of Di-tert-butyl-2-vinylbenzene-1,4-dioate. 2-Vinylbenzene-1,4-dioic acid (9.60 g, 50 mmol), 2-methylpropan-2-ol (17.50 g, 0.20 mol), *N*,*N*-dimethylpyridin-4-amine (DMAP, 0.60 g, 5.0 mmol), *N*,*N*′-dicyclohexyl carbodiimide (DCC, 30.90 g, 0.15 mol), and 200 mL of dried dichloromethane were added into a 500 mL round-bottomed flask. The mixture was stirred at ambient temperature for 24 h. After the floating solid was filtrated off and the solvent was evaporated under reduced pressure, the crude product was purified by silica gel column chromatography with dichloromethane as the eluent to obtain the monomer as a light yellow liquid. Yield: 60%. ^{1}H NMR (300 MHz, δ, ppm, $CDCl_3$): 1.61 (s, 18H), 5.37–5.43 (d, 1H), 5.69–5.78 (d, 1H), 7.31–7.45 (q, 1H), 7.78–7.92 (m, 2H), 8.17 (s, 1H).

2. Polymerization. The polymer, poly(di-*tert*-butyl-2-vinylbenzene-1,4-dioate) (PPE), was obtained by conventional solution radical polymerization.[21] The monomer (4.56 g, 30 mmol), 1.00 mL of chlorobenzene solution of 0.05 M BPO, 15 mL of chlorobenzene, and a magnetic stir bar were added into a polymerization tube. After three freeze–pump–thaw cycles, the tube was sealed off under vacuum. Polymerization was carried out at 90 °C for 12 h. The tube was then opened, and the reaction mixture was diluted with THF. The resultant polymer was precipitated and washed with methanol. After redissolved in THF and reprecipitated in methanol, the polymer was dried to a constant weight. Yield: 55%.

3. Synthesis of Poly(2-vinylbenzene-1,4-dioic acid). A polymer sample of 1.56 g was dissolved in 50 mL of chloroform. Then 15 mL of trifluoroacetic acid was slowly added at the temperature of an ice/water bath. The solution was further stirred at ambient temperature for 24 h. After the removal of the solvent under reduced pressure, the residue was washed with ethyl ether for three times to obtain the product as a white powder. Yield: 95%.

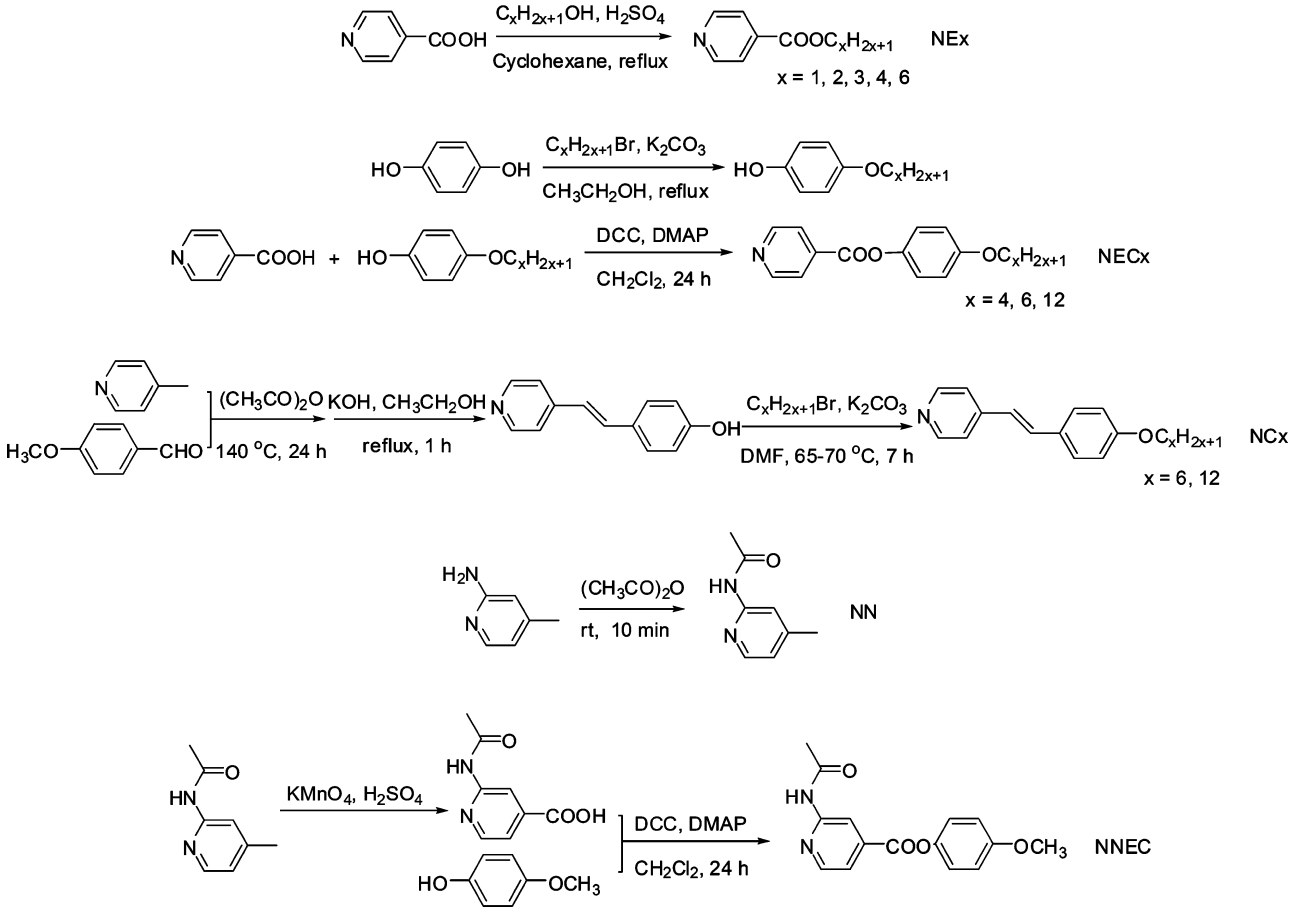
Synthesis of Pyridine Derivatives. The synthetic routes of five series of pyridine derivatives are depicted in Scheme 2. The experimental details are described below using ethyl isonicotinate (NE_2), 4-(dodecyloxy)phenyl isonicotinate (NEC_{12}), 4-(4′-hexanoxy)styrylpyridine (NC_6), 2-*N*-acetylamino-4-methylpyridine (NN), and 4-(methoxy)phenyl 2-*N*-acetylaminoisonicotinate (NNEC) as examples.

1. Synthesis of Ethyl Isonicotinate (NE_2). A mixture of isonicotinic acid (1.23 g, 10 mmol), 20 mL of ethanol, and 0.5 mL of H_2SO_4 were fluxed for 12 h in a 100 mL round-bottomed flask. After ethanol was evaporated under reduced pressure, about 20 mL of Na_2CO_3 solution (1 M) was added into the mixture. Then the mixture was extracted with ether. After evaporation of the solvent, the product was obtained as a colorless liquid. Yield: 90%. ^{1}H NMR (300 MHz, δ, ppm, $CDCl_3$): 1.46–1.55 (t, 3H), 4.35–4.50 (q, 2H), 7.80–7.90 (d, 2H), 8.75–8.85 (d, 2H).

2. Synthesis of 4-(Dodecyloxy)phenyl Isonicotinate (NEC_{12}). Isonicotinic acid (1.23 g, 10 mmol), 4-dodecyloxyphenol (1.35 g, 5.0 mmol), DCC (6.20 g, 30 mmol), DMAP (0.12 g, 1.0 mmol), and 50 mL of dichloromethane were mixed in a 100 mL round-bottomed flask, and the mixture was stirred for 24 h at ambient temperature. The precipitate was filtered off and washed with dichloromethane for several times. After the evaporation of the solvent, the crude product was purified via silica gel column chromatography with ethyl acetate as the eluent to obtain 4-(dodecyloxy)phenyl isonicotinate as a white

dx.doi.org/10.1021/ma202742k | Macromolecules 2012, 45, 2682–2689

Scheme 2. Synthetic Routes of Pyridine Derivatives



solid. Yield: 55%. ^{1}H NMR (300 MHz, δ, ppm, $CDCl_3$): 0.95−1.00 (t, 3H), 1.20−1.80 (m, 20H), 3.95−4.00 (t, 2H), 6.88−6.94 (d, 2H), 7.08−7.17 (d, 2H), 7.88−7.97 (d, 2H), 8.83−8.90 (d, 2H). EI−MS: M/z = 383. Anal. Calcd Ffor $C_{24}H_{33}NO_3$: C, 75.16; H, 8.67; N, 3.65; Found: C, 75.33; H, 8.73; N, 3.71.

3. Synthesis of 4-(4′-Hexanoxy)styrylpyridine (NC$_6$). 4-(4′-Hydroxy)stilbazole (1.97 g, 10 mmol), 1-bromohexane (0.85 g, 5.2 mmol), K_2CO_3 (1.39 g, 10 mmol), and 50 mL of DMF were added into a round-bottomed flask, and the mixture was stirred at 65−70 °C for 7 h. After cooled, the reaction mixture was poured into excess ice/water with intense stirring. The precipitate was washed with water and purified by silica gel column chromatography with ethyl acetate as the eluent to obtain 4-(4′-hexanoxy) styrylpyridine as a light yellow solid. Yield: 65%. ^{1}H NMR (300 MHz, δ, ppm, $CDCl_3$): 0.86−0.90 (t, 3H), 1.20−1.60 (m, 6H), 1.75−1.84 (m, 2H), 3.92−4.00 (t, 2H), 6.80−7.50 (m, 8H), 8.54−8.59 (d, 2H). EI−MS: M/z = 281. Anal. Calcd for $C_{19}H_{23}NO$: C, 81.10; H, 8.24; N, 4.98; Found: C, 81.63; H, 8.65; N, 5.34.

4. Synthesis of 2-N-Acetylamino-4-methylpyridine (NN). 2-Amino-4-methylpyridine (3.31 g, 30 mmol) and about 15 mL of acetic anhydride were added into a 100 mL round-bottomed flask, and the mixture was stirred at 80 °C for 10 min. The reaction mixture was poured into excess $NaHCO_3$ solution with intense stirring. Then the solution was extracted with dichloromethane for three times. After evaporation of the solvent, the product was obtained as a white solid. Yield: 98%. ^{1}H NMR (300 MHz, δ, ppm, $CDCl_3$): 2.18 (s, 3H), 2.37 (s, 3H), 6.86−6.88 (d, 1H), 8.09 (s, 1H), 8.10−8.12 (d, 1H), 8.97 (s, 1H). EI−MS: M/z = 150. Anal. Calcd for $C_8H_{10}N_2O$: C, 63.98; H, 6.71; N, 18.65; Found: C, 63.90; H, 6.75; N, 18.54.

5. Synthesis of 4-(Methoxy) Phenyl 2-N-Acetylaminoisonicotinate (NNEC). NN (12.10 g, 81 mmol) and 14.5 g of $KMnO_4$ were dissolved in 500 mL of water. After stirred for 15 min, 15 mL of 98% H_2SO_4 was added into the solution, and the mixture was heated at 80 °C for 8 h. After cooled, the precipitate was filtered off. An aqueous solution of Na_2CO_3 was added until the pH of the reaction solution reached 10. The solution was then extracted with ethyl acetate twice. The aqueous phase was concentrated and acidized with HCl. The crude product 2-*N*-acetylamino isonicotinic acid was obtained as a white solid. Yield: 15%.

Crude 2-*N*-acetylamino isonicotinic acid (2.05 g), 4-methoxyphenol (2.50 g, 20 mmol), DCC (6.25 g, 30 mmol), DMAP (0.12 g, 1.0 mmol), and 30 mL of dried dichloromethane were added into a 100 mL round-bottomed flask, and the mixture was stirred at ambient temperature for 48 h. The precipitate was filtered off and washed with dichloromethane for several times. After evaporation of the solvent, the crude product was purified via silica gel column chromatography with ethyl acetate as the eluent to obtain 4-(methoxy) phenyl 2-*N*-acetylamino-isonicotinate as a white solid. Yield: 30%. ^{1}H NMR (300 MHz, δ, ppm, $CDCl_3$): 2.36 (s, 3H), 3.83 (s, 3H), 6.91−6.96 (d, 2H), 7.11−7.16 (d, 2H), 7.72−7.76 (d, 1H), 8.21 (s, 1H), 8.44−8.47 (d, 1H), 8.89 (s, 1H). EI−MS: M/z = 286. Anal. Calcd For $C_{15}H_{14}N_2O_4$: C, 62.93; H, 4.93; N, 9.79; Found: C, 63.10; H, 4.88; N, 9.81.

Preparation of H-Bonded Complexes. The H-bonding donor and acceptor with equal molar pyridine moieties and −COOH moieties were dissolved in DMF, and the solvent was removed by slow evaporation. The complexes were then dried under reduced pressure.

RESULTS AND DISCUSSION

Synthesis and Characterization of the H-Bonding Donor. The structures of the monomer and PPE were confirmed by ^{1}H NMR. As shown in parts a and b of Figure 1, the signals of the vinyl group in the monomer at 5.4, 5.7, and 7.3 ppm in Figure 1a completely disappeared in Figure 1b, indicating the

dx.doi.org/10.1021/ma202742k | Macromolecules 2012, 45, 2682−2689

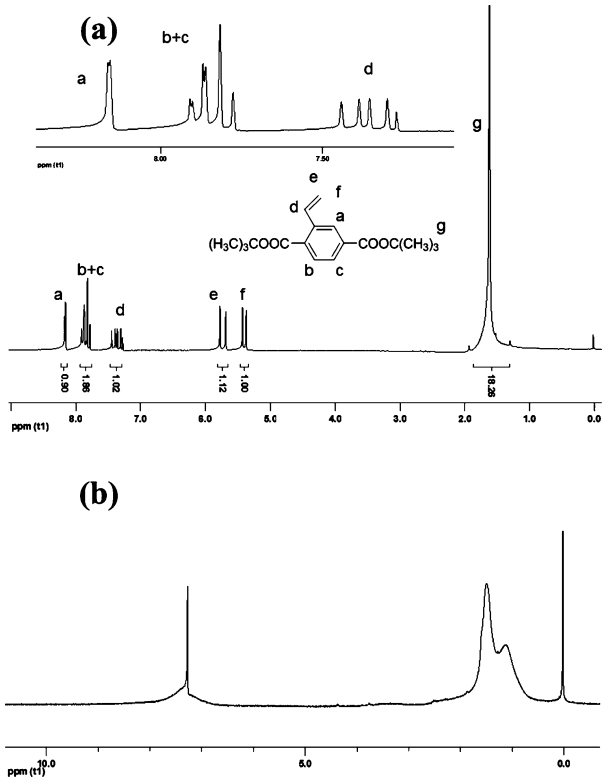


Figure 1. [1]H NMR spectra of the monomer (a, with the inset showing the partially magnified image) and PPE (b).

successful polymerization (in Figure 1b, the signals of benzene ring were partially shielded by the large *tert*-butyl moieties).

Because of the poor solubility of PPA in THF, its molecular weight (91×10^3 g/mol) and polydispersity index (1.46) were calculated from those of PPE. FT-IR experiments were carried out to confirm the deprotection reaction. As shown in Figure 2,

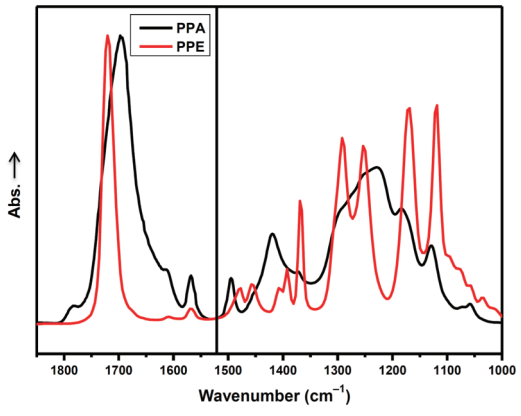


Figure 2. FT-IR spectra of PPE and PPA.

the C═O band of the polymer at 1720 cm^{-1} shifted to 1695 cm^{-1}, indicating that $-COOC(CH_3)_3$ changed to $-COOH$. In addition, the broad band between 3000 and 3700 cm^{-1} also confirmed the existence of $-COOH$ groups.

TGA measurements showed that the temperature of 1% weight loss of PPA was about 180 °C under a nitrogen atmosphere, which was lower than those of some similar MJLCPs reported previously,[4] mainly because of the high density of carboxylic acid in the side groups of the polymer. The DSC experiment of PPA was performed under a nitrogen atmosphere at the heating and cooling rates of 10 °C/min. No thermal transitions were observed during both the heating and cooling processes.

Characterizations of H-Bonded Complexes. *PPANEx.* The complexes of PPANEx showed poorer thermal stability than the other four series of complexes probably because all NEx were volatile liquids. The FT-IR spectrum of $PPANE_6$ is shown in Figure 3. The absorption bands at 1940 and 2550 cm^{-1} were

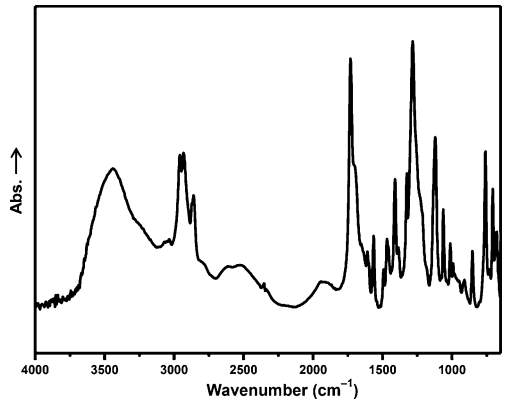


Figure 3. FT-IR spectrum of $PPANE_6$.

indicative of strong H-bonding between carboxylic acid of PPA and the pyridine group of NE_6.[5,18] No further studies were carried out due to the poor stability of these complexes.

PPANECx. The second series of H-bonding acceptors NECx containing two rings were designed and synthesized in order to increase the stability of the complexes. As expected, the temperatures at 1% weight loss of PPANECx were about 180 °C (mainly due to the weight loss of the PPA moieties), which were much higher than those of PPANEx. DSC experiments were carried out to study the thermal behaviors of NECx and PPANECx. As shown in Figure 4a, a melting peak with an onset temperature of 80 °C and a crystallization peak with an onset temperature of 43 °C were observed during the heating and cooling processes of NEC_4, respectively. For the $PPANEC_4$ complex, there was an endothermic process with a peak temperature of 70 °C during the second heating process (Figure 4b), indicating that not all NEC_4 complexed with PPA. The crystallization of NEC_4 during first cooling was disturbed by the partially H-bonded structure, which led to the lack of an exothermic peak. In the variable-temperature 1D WAXD experiments, diffraction peaks in the high-angle region ($2\theta > 20$ °C) also confirmed the existence of macrophase separation.

PPANCx. The FT-IR spectrum of $PPANC_6$ is shown in Figure 5. The carbonyl band of PPANC6 appeared at 1705 cm^{-1}, which had a 8 cm^{-1} shift compared with that of PPA, indicating that the H-bonding between the pyridine moiety and the acid moiety was weaker than that between two acid moieties.[19] The bands at 1950 and 2550 cm^{-1} also confirmed the existence of H-bonding.

DSC experiments were also carried out to study the miscibility between the H-bonding donor and acceptors. As shown in Figure 6, there were two endothermic peaks and two exothermic peaks during the heating and cooling processes of NC_6, as reported in literature.[20] However, no transition peaks were observed in the DSC curves of PPA and $PPANC_6$, indicating the formation of a H-bonded complex.

dx.doi.org/10.1021/ma202742k | *Macromolecules* 2012, 45, 2682−2689

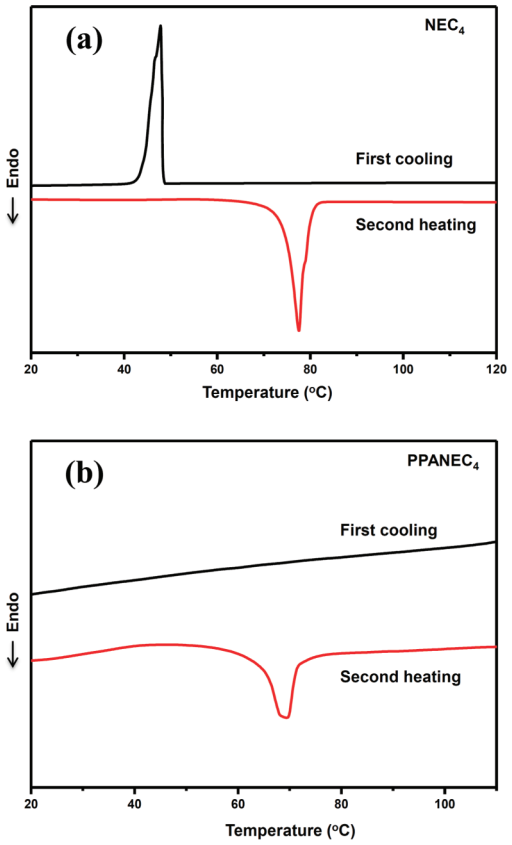


Figure 4. DSC thermograms of NEC_4 (a) and $PPANEC_4$ (b) at the heating and cooling rates of 10 °C/min under a nitrogen atmosphere.

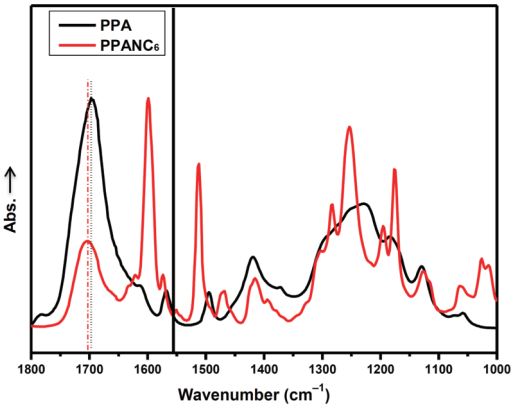


Figure 5. FT-IR spectra of PPA and $PPANC_6$.

PLM experiments during heating and cooling were carried out to study the LC behavior of $PPANC_6$ (Figure 7). The sample did not show birefringence during the heating progress. When the temperature reached 90 °C in the cooling process, birefringence was observed, although there were no endothermic peaks in the DSC curve.

One-dimensional WAXD was used to further study the phase structure of the complex. Only an amorphous high-angle halo was observed during the heating process (Figure 8a), indicating that no nanoscale ordered structure was formed. A diffraction peak at a 2θ of 3.98° (d = 2.22 nm) appeared when the sample was cooled to 130 °C (Figure 8b). There were no diffraction peaks during the cooling process of NC_6, and 130 °C was much higher than the isotropic-LC transition temperature of NC_6.

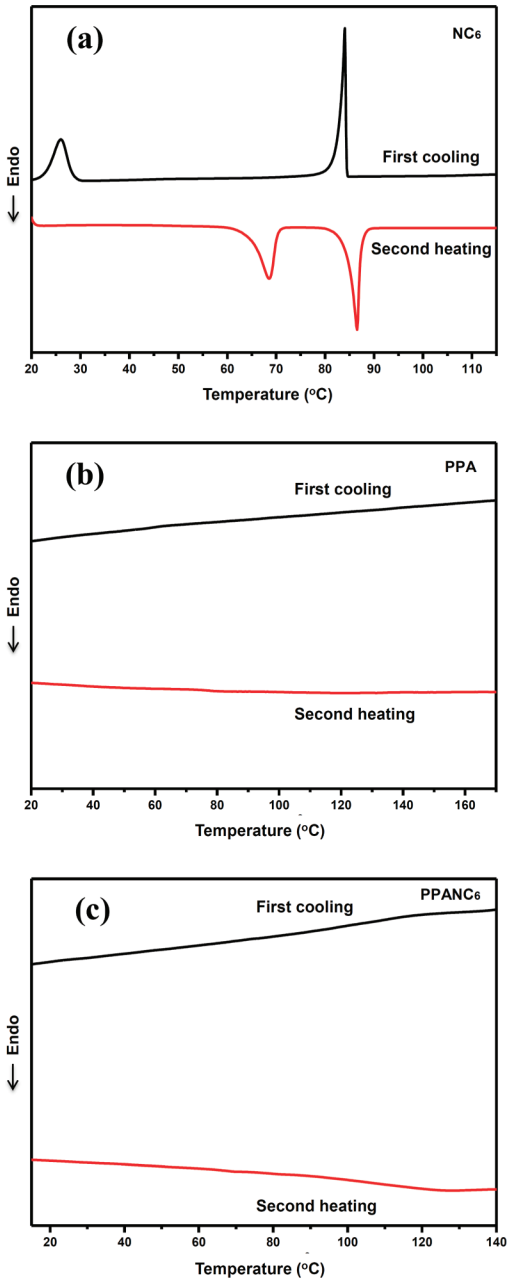


Figure 6. DSC thermograms of NC_6 (a), PPA (b), and $PPANC_6$ (c) at the heating and cooling rates of 10 °C/min under a nitrogen atmosphere.

Therefore, the ordered structure could be attributed to the H-bonded complex. Because the d-spacing (2.22 nm) was close to half of the calculated length (4.60 nm) of the side group of the complex, we presumed that there might be a diffraction peak at an even lower angle. After the cooling process of 1D WAXD, SAXS experiments were employed to confirm this conjecture. As shown in Figure 9, two peaks with q values of 1.36 and 2.88 nm^{-1} were observed. The ratio of the scattering vectors of these two peaks was approximately 1:2, indicating a smectic packing of $PPANC_6$. The d-spacing of the first diffraction peak was 4.62 nm, which was close to the calculated side-group length of the H-bonded complex. Thus, the structure of $PPANC_6$ could be smectic A (Figure 10). Similar to $PPANC_6$, two peaks with a scattering vector ratio of 1:2 were also observed in the SAXS experiment of $PPANC_{12}$ (Figure 9), and the structure of

dx.doi.org/10.1021/ma202742k | Macromolecules 2012, 45, 2682–2689

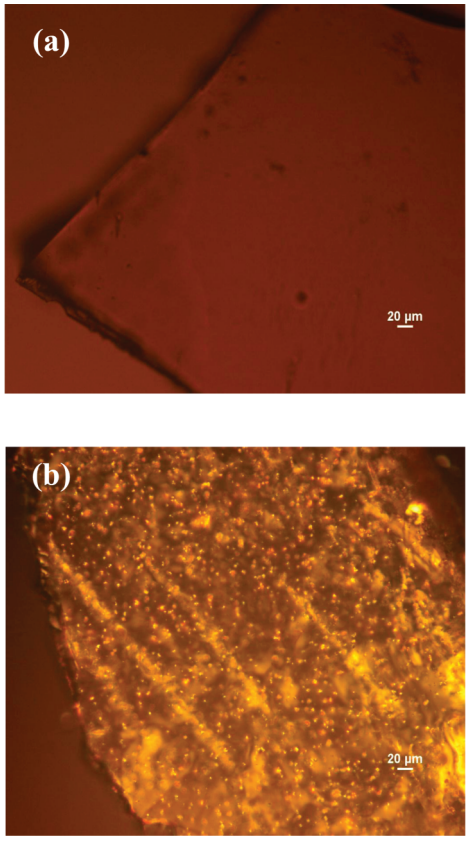


Figure 7. PLM images of $PPNC_6$ taken at 140 (a) and 60 °C (b) during cooling.

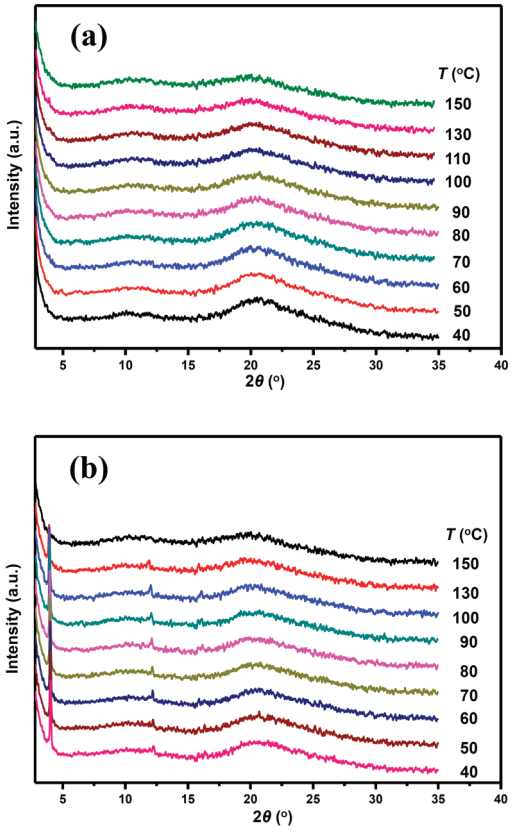


Figure 8. 1D WAXD patterns of $PPANC_6$ during the first heating (a) and the subsequent cooling (b) processes.

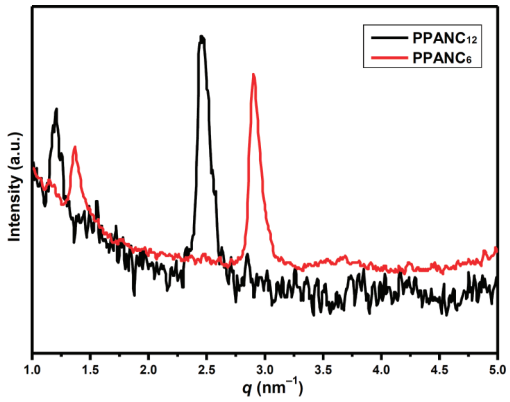


Figure 9. SAXS patterns of $PPANC_6$ and $PPANC_{12}$ after the cooling process of 1D WAXD.

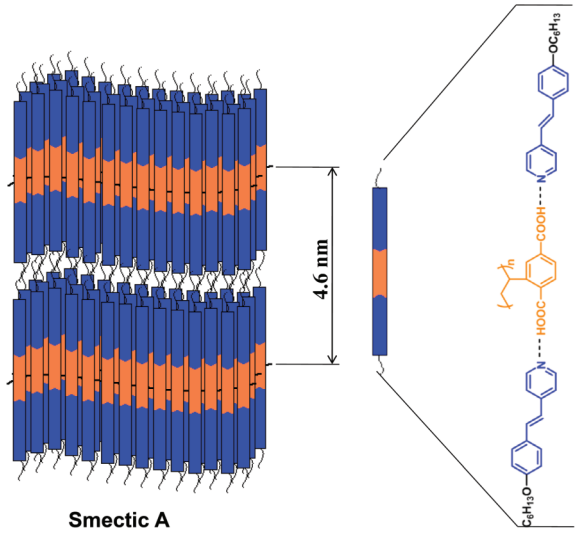


Figure 10. Schematic drawing of the smectic packing of $PPANC_6$.

$PPANC_{12}$ could also be smectic A also because the *d*-spacing of the first diffraction peak was close to the calculated length of the side group in this complex.

PPANN. 2-*N*-Acetylamino-4-methylpyridine, which was able to form a double H-bonding with the pyridine moiety, was designed to study the relationship between the self-assembled structure and the H-bonding strength. Similar to $PPANC_6$, PPANN did not show any transition peaks during the heating and cooling processes in DSC curves (Figure 11). PLM and 1D WAXD were also carried out. However, no LC behavior was observed. The lack of liquid crystallinity of this complex might be because the volume of the H-bonded side group was not large enough to induce the "jacketing" effect.

PPANNEC. NNEC, which had a larger volume than NN, was designed to prove our conjecture. Similar to NC_6 and NN, NNEC showed good miscibility with the H-bonding donor. 1D WAXD experiments were employed to study the LC behavior of the complex. As shown in Figure 12, there was only a scattering halo in the low-angle region ($2\theta < 5°$) at 40 °C. A diffraction peak at a 2θ of 2.53° developed, and the intensity increased during the heating process, indicating that a nanoscale ordered structure was formed. The diffraction peak retained its intensity during the cooling process similar to some other MJLCPs reported previously. No higher-order diffraction peaks were observed during the heating and cooling processes.

dx.doi.org/10.1021/ma202742k | *Macromolecules* 2012, 45, 2682–2689

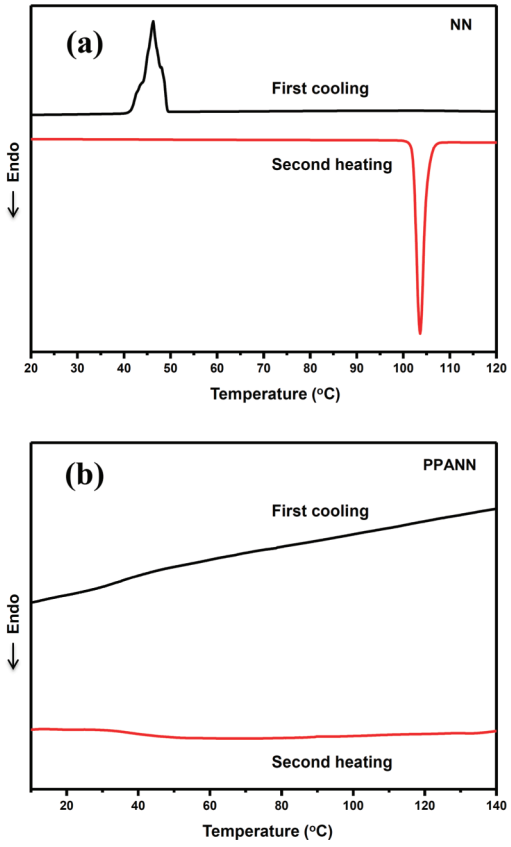


Figure 11. DSC thermograms of NN (a) and PPANN (b) at the heating and cooling rates of 10 °C/min under a nitrogen atmosphere.

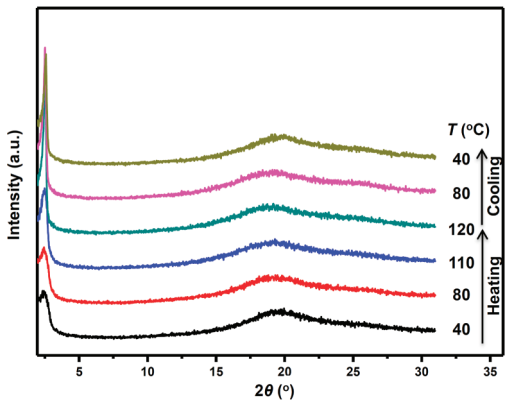


Figure 12. 1D WAXD patterns of PPANNEC during the first heating and the subsequent cooling processes.

On the basis of the position of the diffraction peak, the *d*-spacing was calculated to be 3.48 nm, which was close to the calculated length (3.30 nm) of the side group of the H-bonded complex. Therefore, the phase structure of PPANNEC could be columnar nematic (Figure 13).

The LC behaviors of the pyridine derivatives and their H-bonded complexes are concluded in Table 1. NEx, NECx, and NCx were able to form a single H-bonding with −COOH. However, only PPANCx exhibited liquid crystallinity, indicating that the rigidity of pyridine derivatives played an important role in the packing of the H-bonded complexes. Comparing the LC behaviors of PPANECx, PPANN, and PPANNEC, only PPANNEC exhibited liquid crystallinity, which indicated that the H-bonding strength was also important in the packing of the complexes (noting

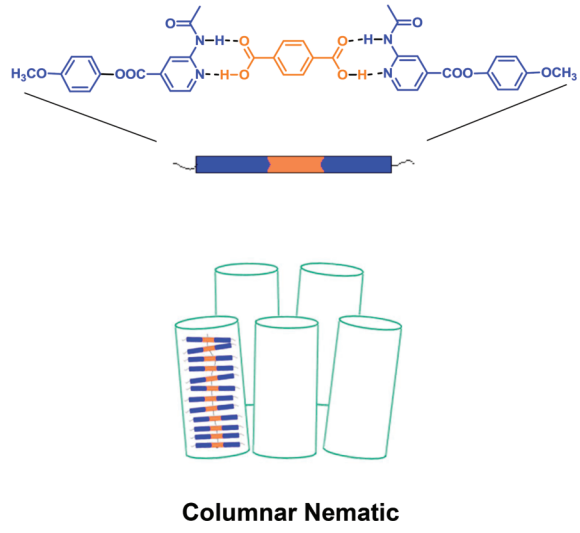


Figure 13. Schematic drawing of the columnar nematic packing of PPANNEC.

Table 1. LC Behaviors of Pyridine Derivatives and Their Complexes with PPA

pyridine derivative	LC behavior	complex	LC behavior
NEx	no	PPANEx	*a*
NECx	no	PPANECx	*a*
NCx	yes	PPANCx	smectic A
NN	no	PPANN	no
NNEC	no	PPANNEC	columnar nematic

[a]The complex was not stable or showed macrophase separation.

that NNEC had a similar H-bonding acceptor moiety as that of NN and similar rigidity as that of NEC).

CONCLUSION

In summary, we obtained MJLCPs with noncovalent side groups. Poly(2-vinylbenzene-1,4-dioic acid) and five series of pyridine derivatives were synthesized as H-bonding donor and acceptors, respectively. The H-bonded complexes, which had the same DP and PDI values, were studied using FT-IR, DSC, PLM, 1D WAXD, and SAXS techniques. PPANEx showed weaker stability than other four series of complexes. Macrophase separation was observed in PPANECx. PPANN did not exhibit LC phase behavior upon heating and cooling. Smectic A and columnar nematic structures were observed for PPANCx and PPCNNEC. Both the rigidity and the structure of the pyridine derivatives, as well as the strength of H-bonding, affected the liquid crystalline behavior of the complexes. This work paved a way to synthesizing MJLCPs with H-bonding. Currently using other noncovalent interactions to build MJLCPs is also in progress.

AUTHOR INFORMATION

Corresponding Author

*E-mail: (X.F.) fanxh@pku.edu.cn; (Z.S.) zshen@pku.edu.cn.

Notes

The authors declare no competing financial interest.

ACKNOWLEDGMENTS

This research was supported by the National Natural Science Foundation of China (Grants 21134001, 20974002, and 20990232).

REFERENCES

(1) Blumstein, A. *Polymeric Liquid Crystals*; Plenum Press: New York, 1985.
(2) Zhou, Q. F.; Li, H. M.; Feng, X. D. *Macromolecules* **1987**, *20*, 233.
(3) Zhou, Q. F.; Zhou, X. L.; Wen, Z. Q. *Macromolecules* **1989**, *22*, 491.
(4) Chen, X. F.; Shen, Z. H.; Wan, X. H.; Fan, X. H.; Chen, E. Q.; Ma, Y. G.; Zhou, Q. F. *Chem. Soc. Rev.* **2010**, *39*, 3072.
(5) Kato, T.; Kihara, H.; Uryu, T.; Fujishima, A.; Fréchet, J. M. J. *Macromolecules* **1992**, *25*, 6836.
(6) Kato, T.; Mizoshita, N.; Kishimoto, K. *Angew. Chem., Int. Ed.* **2006**, *45*, 38.
(7) Fouquey, C.; Lehn, J. M.; Levelut, A. M. *Adv. Mater.* **1990**, *2*, 254.
(8) Kihara, H.; Kato, T.; Uryu, T.; Fréchet, J. M. J. *Chem. Mater.* **1996**, *8*, 961.
(9) Kato, T.; Ihata, O.; Ujiie, S.; Tokita, M.; Watanabe, J. *Macromolecules* **1998**, *31*, 3551.
(10) Cheng, Y. H.; Chen, W. P.; Shen, Z. H.; Fan, X. H.; Zhu, M. F.; Zhou, Q. F. *Macromolecules* **2011**, *44*, 1429.
(11) Cheng, Y. H.; Chen, W. P.; Zheng, C.; Qu, W.; Wu, H.; Shen, Z. H.; Liang, D.; Fan, X. H.; Zhu, M. F.; Zhou, Q. F. *Macromolecules* **2011**, *44*, 3973.
(12) Zhang, D.; Liu, Y. X.; Wan, X. H.; Zhou, Q. F. *Macromolecules* **1999**, *32*, 5183.
(13) Koopmans, C.; Ritter, H. *J. Am. Chem. Soc.* **2007**, *129*, 3502.
(14) Zhang, H.; Yu, Z.; Wan, X.; Zhou, Q. F.; Woo, E. M. *Polymer* **2002**, *43*, 2357.
(15) Kato, T.; Kihara, H.; Ujiie, S.; Uryu, T.; Fréchet, J. M. J. *Macromolecules* **1996**, *29*, 8734.
(16) Gao, L. C.; Zhang, C. L.; Liu, X.; Fan, X. H.; Wu, Y. X.; Chen, X. F.; Shen, Z. H.; Zhou, Q. F. *Soft Matter* **2008**, *4*, 1230.
(17) Xu, Y. D.; Yang, Q.; Shen, Z. H.; Chen, X. F.; Fan, X. H.; Zhou, Q. F. *Macromolecules* **2009**, *42*, 2542.
(18) Xu, J. W.; Toh, C. L.; Liu, X. M.; Wang, S. F.; He, C. B.; Lu, X. H. *Macromolecules* **2005**, *38*, 1684.
(19) Lee, J. Y.; Painter, P. C.; Coleman, M. M. *Macromolecules* **1988**, *21*, 954.
(20) Bruce, D. W.; Dunmur, D. A.; Lalinde, E.; Maitlis, P. M.; Styring, P. *Liq. Cryst.* **1988**, *3*, 385.
(21) Xu, Y. D.; Shen, Z. H.; Fan, X. H.; Zhou, Q. F. *Acta Polym. Sin.* **2011**, *9*, 1053.

Macromolecules

Article

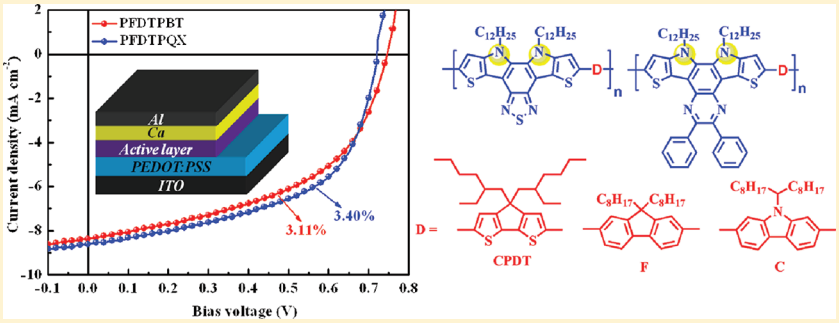
pubs.acs.org/Macromolecules

Synthesis, Photophysical and Photovoltaic Properties of Conjugated Polymers Containing Fused Donor−Acceptor Dithienopyrrolobenzothiadiazole and Dithienopyrroloquinoxaline Arenes

Yen-Ju Cheng,* Yu-Ju Ho, Chiu-Hsiang Chen, Wei-Shun Kao, Cheng-En Wu, So-Lin Hsu, and Chain-Shu Hsu

Department of Applied Chemistry, National Chiao Tung University 1001 Ta Hsueh Road, Hsin-Chu, 30010 Taiwan

Supporting Information



ABSTRACT: We have developed two nitrogen-bridged pentacyclic donor−acceptor dithienopyrrolobenzothiadiazole (**DTPBT**) and dithienopyrroloquinoxaline (**DTPQX**) arenes where the two outer electron-rich thiophene moieties are covalently fastened with the central electron-deficient benzothiadiazole and quinoxaline cores by two nitrogen bridges. These rigid and coplanar **DTPBT** and **DTPQX** building blocks were copolymerized with fluorene (F), carbazole (C) and cyclopentadithiophene (**CPDT**) units via Suzuki or Stille coupling polymerization to afford six new alternating copolymers **PFDTPBT**, **PCDTPBT**, **PCPDTDTPBT**, **PFDTPQX**, **PCDTPQX** and **PCPDTDTPQX**, respectively. The nitrogen bridges not only planarize the structure to induce stronger intermolecular $\pi-\pi$ interaction but also play an important role in determining the electronic and photophysical properties of the polymers. The device based on **PFDTPQX**/$PC_{71}BM$ (1:4, w/w) exhibited a open-circuit voltage (V_{oc}) of 0.72 V, a short-circuit current (J_{sc}) of 8.62 mA/cm^2 and a FF of 0.55 leading to a decent power conversion efficiency (PCE) of 3.40% due to the lower-lying HOMO energy level, and the highest hole-mobility of **PFDTPQX**.

INTRODUCTION

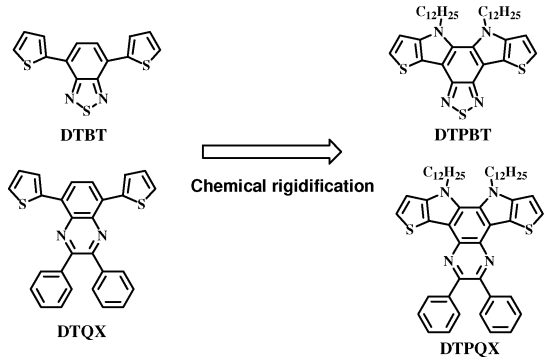
In recent years, all-solution processed polymer solar cells (PSCs) have attracted tremendous academic and industrial interests. To realize low-cost, lightweight, large-area and flexible photovoltaic devices,[1] p-type photoactive conjugated polymer materials play the most important role in boosting high efficiency of PSCs.[2] An ideal p-type conjugated polymer should simultaneously possess low optical band gap (LBG) with strong extinction coefficient to harvest more solar photons and excellent hole mobility for efficient charge transport. Conjugating an electron-rich donor (D) unit with an electron-deficient acceptor (A) unit in an alternating arrangement is the most widely used strategy to produce a low band gap (LBG) polymer.[3] On the other hand, forced planarization by covalently locking neighboring aromatic units is an effective approach to reduce the band gap, because the parallel p-orbital interactions can facilitate π-electron delocalization and elongate effective conjugation length.[4] Furthermore, rigid structures can reduce the rotational disorder around interannular single bonds to lower the reorganization energy, which is beneficial to improve charge mobility.[5] As a result, considerable research effort has been devoted to the development of electron-rich donors having coplanar ladder-type heteroarenes.[6] The D−A polymers based on a series of fascinating fused structures have achieved high-performance solar cells. We envisaged that forced planarization by covalently fastening adjacent electron-rich donor and electron-deficient acceptor units into a coplanar fused D−A assembly may strengthen the electronic interactions between the donor and the acceptor units in a D−A copolymer, leading to more interesting molecular properties.[7] Surprisingly, conjugated polymers consisting of D−A fused moieties are rare in the literatures owing to the challenging synthesis to prepare fused D−A monomer precursor. The benzothiadiazole (BT) and quinoxaline (QX) units are regarded as the superb

Received: December 21, 2011
Revised: February 15, 2012
Published: March 6, 2012

 © 2012 American Chemical Society dx.doi.org/10.1021/ma202764v | *Macromolecules* 2012, 45, 2690−2698

acceptors due to their moderate electron affinity and planar structure.[8] Consequently, nonfused D−A−D structures, 4,7-di(thiophen-2-yl)benzothiadiazole (**DTBT**) or 4,7-di-(thiophen-2-yl)quinoxaline (**DTQX**) units, are the most commonly used components in the D−A polymers for PSCs applications (Scheme 1).[9]

Scheme 1. Chemical Structure of Nonfused DTBT and DTQX Units and Fused DTPBT and DTPQX Units

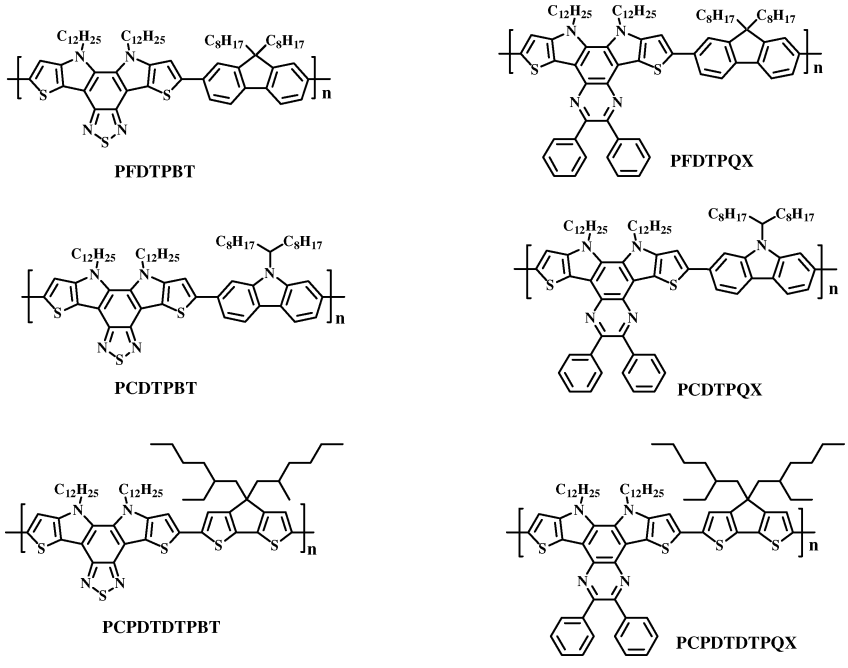


It is of great interest to planarize the **DTBT** structure by connecting 3-positons of the two outer thiophenes with the 5 and 6-positions of the central benzothiadiazole core via two bridging atoms. For this purpose, we have successfully developed a nitrogen-bridged D−A−D dithienopyrrolobenzothiadiazole (**DTPBT**) unit where two pyrrole units are embedded into a multifused pentacyclic structure (Scheme 1).[10] The **DTPBT** structure can be further chemically converted to another new fused D−A−D dithienopyrroloquinoxaline (**DTPQX**) structure. The dibromo-**DTPBT** and dibromo-**DTPQX** monomers were copolymerized with fluorene (F) and carbazole (C) and cyclopentadithiophene (CPDT) donor units, respectively, to prepare six alternating D−A fused conjugated copolymers, poly(fluorene-*co*-dithienopyrrolobenzothiadiazole) **PFDTPBT**, poly(carbazole-*co*-dithienopyrrolobenzothiadiazole) **PCDTPBT**, poly(cyclopentadithiophene-*co*-dithienopyrrolobenzothiadiazole) **PCPDTDTPBT**, poly(fluorene-*co*-dithienopyrroloquinoxaline) **PFDTPQX**, poly(carbazole-*co*-dithienopyrroloquinoxaline) **PCDTPQX** and poly(cyclopentadithiophene -*co*-dithienopyrroloquinoxaline) **PCPDTDTPQX** (Scheme 2). The thermal, photophysical and electrochemical properties of these polymers have been characterized and the nitrogen-bridged effect was carefully investigated. Preliminary tests of the photovoltaic performance based on these polymers show promise for solar cell applications.

RESULTS AND DISCUSSION

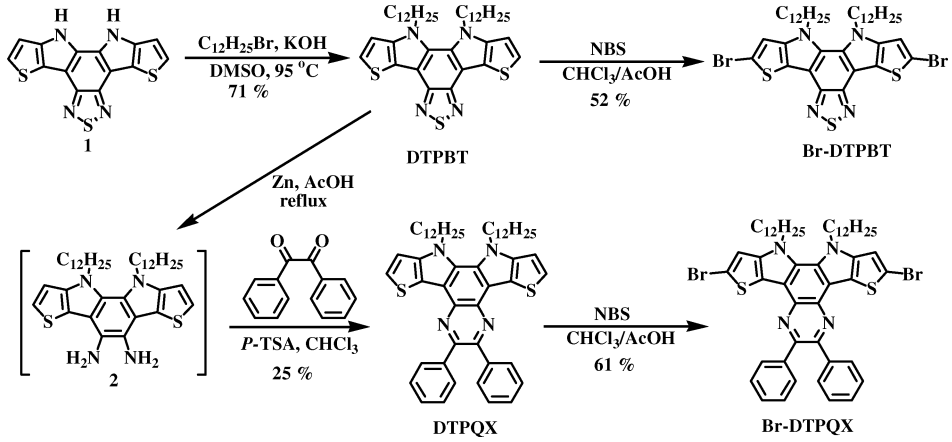
Synthesis. The synthesis of the monomers **Br-DTPBT** and **Br-DTPQX** is depicted in Scheme 3. *N*-alkylation of compound **1** resulted in the formation of **DTPBT**. NBS bromination of **DTPBT** regioselectively occurred at 5-positions of the thienyl moieties to yield the brominated monomer **Br-DTPBT**. Reduction of the thiadiazole moiety in **DTPBT** by Zn/AcOH generated the corresponding diamine intermediate **2** which underwent condensation with benzil to yield dithienopyrroloquinoxaline **DTPQX**. Again, bromination of **DTPQX** selectively occurred at 5-positions of the thienyl moieties to obtain **Br-DTPQX** in 61% yield. With **Br-DTPBT** monomer in hand, the copolymers **PFDTPBT**, **PCDTPBT** and **PCPDTDTPBT** were prepared by reacting **Br-DTPBT** with 2,7-bis(4′,4′,5′,5′-tetramethyl-1′,3′,2′-dioxaborolane-2′-yl)-9,9-dioctylfluorene (**F**) and 2,7-bis(4′,4′,5′,5′-tetramethyl-1′,3′,2′-dioxaborolan-2′-yl)-*N*-9″-heptadecanylcarbazole (**C**) using Suzuki polymerization and 2,6-di(trimethyltin)-4,4-diethylhexylcyclopenta[2,1-*b*:3,4-*b*′]dithiophene (**CPDT**) via Stille polymerization (Scheme 4). In a similar manner, the copolymers **PFDTPQX**, **PCDTPQX**, and **PCPDTDTPQX** were also synthesized by using **Br-DTPQX** as the monomer (Scheme 4). All the polymerization

Scheme 2. Chemical Structures of Polymers PFDTPBT, PCDTPBT, PCPDTDTPBT, PFDTPQX, PCDTPQX, and PCPDTDTPQX

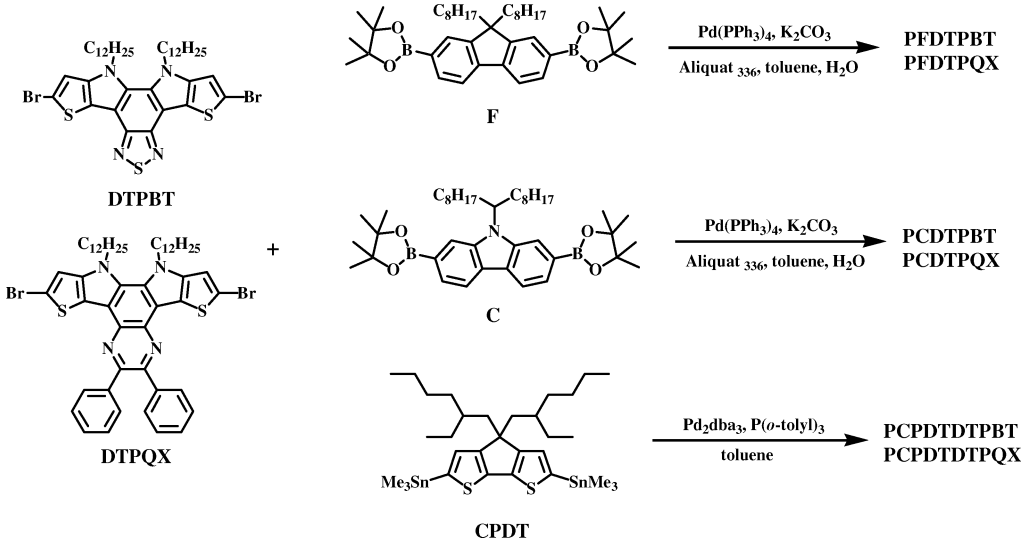


dx.doi.org/10.1021/ma202764v | *Macromolecules* 2012, 45, 2690−2698

Scheme 3. Synthesis of Br−DTPBT and Br−DTPQX Monomer



Scheme 4. Suzuki and Stille Polymerization Toward PFDTPBT, PCDTPBT, PCPDTDTPBT, PFDTPQX, PCDTPQX, and PCPDTDTPQX



reactions were refluxed for 72 h to produce the polymers with reasonably high molecular weights (M_n) ranging from 17 to 34 kDa (Table 1). All of the monomers and corresponding copolymers were fully characterized by NMR spectra (see Supporting Information). The nitrogen bridges allows for introducing aliphatic side chains to promote solubility of the resultant conjugated polymers in common organic solvents, such as chloroform, toluene, chlorobenzene and 1,2-dichlorobenzene.

Table 1. Molecular Weights, Polydispersity Index and Thermal Properties of Polymers

copolymer	M_w[a]	M_n[a]	PDI[a]	T_d (°C)[b]
PFDTPBT	55 000	20 000	2.70	397
PCDTPBT	121 000	27 000	4.47	393
PCPDTDTPBT	58 500	23 400	2.50	388
PFDTPQX	70 000	34 000	2.17	415
PCDTPQX	50 900	30 200	1.68	428
PCPDTDTPQX	36 100	17 000	2.10	408

[a]Molecular weights and polydispersity were determined by gel permeation chromatography (GPC) in THF using polystyrene standards. [b]Decomposition temperature (5% weight loss) measured by TGA.

Thermal Properties. Thermal properties of all copolymers were analyzed by differential scanning calorimetry (DSC) and thermal gravimetric analysis (TGA) and summarized in Table 1. The decomposition temperatures (T_d) of the polymers are located at 388−428 °C (Figure 1), demonstrating their sufficiently high thermal stability for applications of PSCs. From the DSC measurement, neither melting point nor glass transition temperatures was observed, suggesting that these copolymers tend to be amorphous (see Figure S1, Supporting Information).

Optical Properties. The absorption spectra of all studied polymers were measured in both dilute chloroform and in the thin films (Figure 2), and the correlated optical parameters were summarized in Table 2. We compared the nitrogen-bridged polymers with the corresponding nonfused **DTBT**- or **DTQX**-based polymers reported in the literatures.[11] There are several interesting and noteworthy observations. Compared to the nonfused polymers, all the *N*-bridged copolymers showed significant band-broadening from the solution state to the solid state, indicating that strong interchain $\pi-\pi$ interactions indeed takes place due to the coplanar and rigid pentacyclic structures.

dx.doi.org/10.1021/ma202764v | *Macromolecules* 2012, 45, 2690−2698

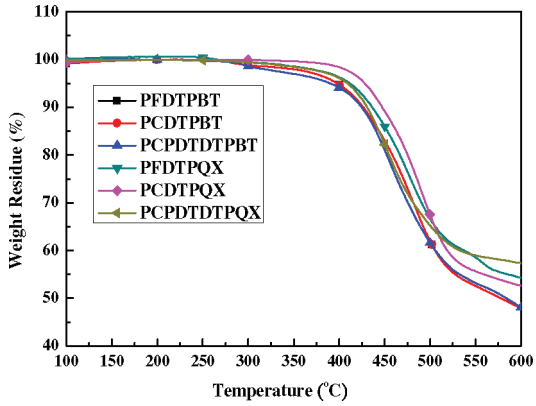


Figure 1. Thermal gravimetric analysis (TGA) measurements of the polymers with a ramping rate of 10 °C/min.

Table 2. Optical Properties of the Copolymers in the Chloroform Solution and in the Thin Film

	chloroform solution			thin film		
polymer	λ_{max} (nm)	λ_{onset} (nm)	E_g^{opt} (eV)	λ_{max} (nm)	λ_{onset} (nm)	E_g^{opt} (eV)
PFDTPBT	517	553	2.24	526	576	2.15
PCDTPBT	518	557	2.23	527	581	2.13
PCPDTDTPBT	588	635	1.95	614	700	1.77
PFDTPQX	518	551	2.25	528	566	2.19
PCDTPQX	513	553	2.24	518	570	2.18
PCPDTDTPQX	582	626	1.98	610	670	1.85

The nonfused **DTBT**-based polymers generally exhibited two distinct absorption bands. One is due to the localized $\pi-\pi$ transition and the other comes from intramolecular charge transfer absorption. However, for the *N*-bridged copolymers, the two bands are merged into a wide absorption window

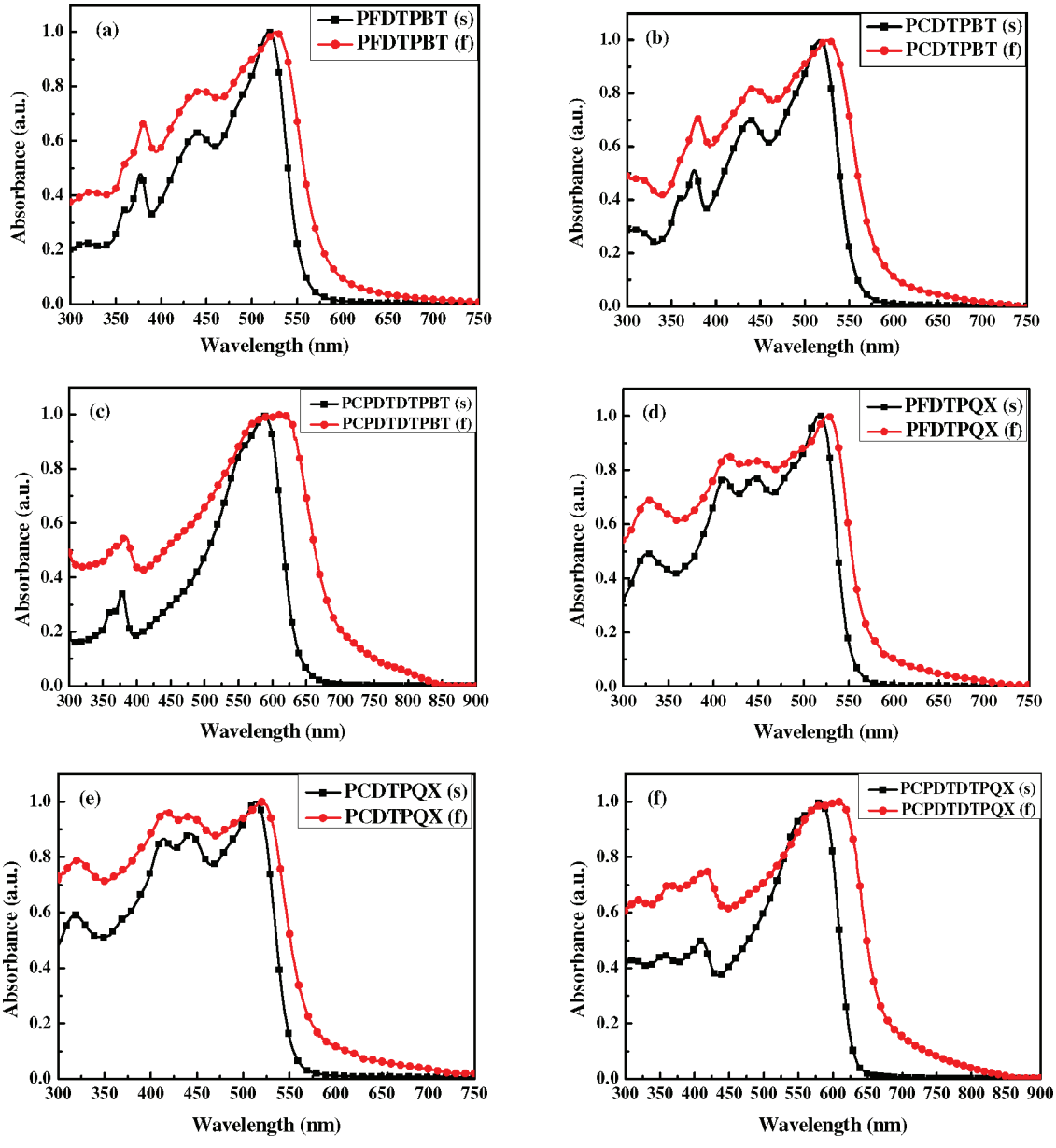


Figure 2. Normalized absorption spectra of all the polymers in the chloroform solution and the thin film.

dx.doi.org/10.1021/ma202764v | *Macromolecules* 2012, 45, 2690–2698

covering from 300 to 700 nm with several vibronic structures. Also note that *N*-bridged polymers exhibited hypsochromic-shifted absorption spectra relative to their corresponding nonfused counterparts. This phenomenon is somewhat different from what we expected previously. To gain deeper insight into the nitrogen effect, we carefully analyzed the absorption spectra of pentacylic nonfused **DTBT** and nitrogen-bridged **DTPBT** small molecules (Figure 3). **DTBT** shows a shorter

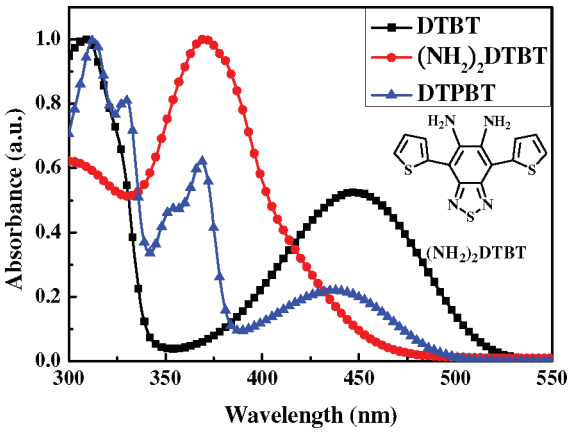


Figure 3. Normalized absorption spectra of **DTBT**, **DTPBT**, and **$(NH_2)_2$DTBT** in the toluene solution.

wavelength absorbance at 310 nm resulting from the $\pi-\pi^*$ transition of the pentacyclic units and a lower energy band at 450 nm attributed to the intramolecular charge transfer (ICT) between the thiophene units and the benzothiadiazole segment. In addition to the two typical bands observed in **DTBT**, an extra band at 368 nm was observed in the nitrogen-bridged **DTPBT** analogue. This band is highly associated with an internal charge transfer transition from a short D−π−A diaminobenzothiodiazole chromophore embedded in **DTPBT**. To confirm this hypothesis, we also synthesized an open-chain nitrogen-substituted **$(NH_2)_2$DTBT** for comparison (structure see in Figure 3). Indeed, **$(NH_2)_2$DTBT** also shows a strong absorption band at 368 nm due to the push−pull dipolar diaminobenzothiadiazole structure. Note that the ICT band at 450 nm observed in **DTPBT** is diminished in **$(NH_2)_2$DTBT**. The electronic and steric effects are responsible for the weak thiophene/BT communication in **$(NH_2)_2$DTBT**. First, the D−π−A push−pull effect decreases the electron deficiency of the BT unit. Second, the two amino groups in **$(NH_2)_2$DTBT** cause structural twisting between the BT and thiophene units. Interestingly, when the coplanarity is fastened in **DTPBT**, a ICT band at 438 nm is regained with relatively weaker intensity.

Although the electronic effect of nitrogen induces an extra absorbance at shorter wavelengths, it also attenuates the electron-accepting ability of the BT and QX units in the polymers. Therefore, the photoinduced charge transfer transition from the electron-rich units to the BT or QX units in the nitrogen-bridged polymers is shifted to higher energy. It is highly intriguing if the nitrogen bridges can be replaced by carbon bridges with more insulating character. This related research is currently underway in our lab. Furthermore, the **DTPBT**-based copolymers showed more red-shifted absorption spectra than the **DTPQX**-based copolymers, indicating that the accepting strength of **DTPBT** is slightly stronger than that of **DTPQX**. The optical band gaps (E_g^{opt}) deduced from the absorption edges of thin film spectra are in the following order: **PCPDTDTPBT** (1.77 eV) < **PCPDTDTPQX** (1.85 eV) < **PCDTPBT** (2.13 eV) < **PFDTPBT** (2.15 eV) < **PCDTPQX** (2.18 eV) < **PFDTPQX** (2.19 eV).

Electrochemical Properties. Cyclic voltammetry (CV) was employed to examine the electrochemical properties and evaluate the HOMO and LUMO levels of the polymers (Table 3 and Figure 4). All of the polymers showed stable and

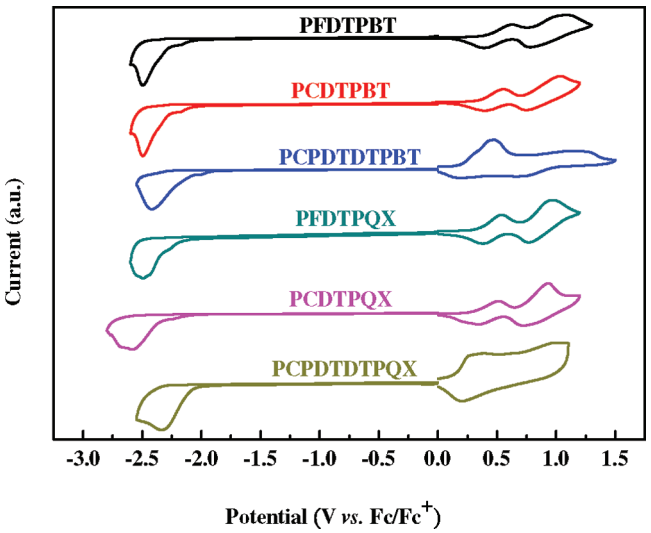


Figure 4. Cyclic voltammograms of the polymers in the thin film at a scan rate of 80 mV/s.

reversible p-doing and n-doing processes, which are important prerequisites for semiconductor materials. The HOMO energy level is estimated to be −5.11 and −5.06 eV for **PFDTPBT** and **PFDTPQX**, −5.06 and −5.02 eV for **PCDTPBT** and **PCDTPQX**, and −4.90 and −4.88 eV for **PCPDTDTPBT** and **PCPDTDTPQX**, respectively. **PCPDTDTPBT** and **PCPDTDTPQX** with higher-lying HOMO energy levels

Table 3. Electrochemical Onset Potentials and Electronic Energy Levels of the Polymers

copolymer	E_{ox}^{onset}(V)	E_{red}^{onset}(V)	HOMO[a] (eV)	LUMO^{el} [b] (eV)	LUMO^{opt} [c] (eV)	E_g^{el} (eV)
PFDTPBT	0.39	−2.08	−5.11	−2.64	−2.96	2.47
PCDTPBT	0.34	−2.05	−5.06	−2.67	−2.93	2.39
PCPDTDTPBT	0.18	−1.90	−4.90	−2.82	−3.13	2.08
PFDTPQX	0.34	−2.11	−5.06	−2.61	−2.87	2.45
PCDTPQX	0.30	−2.08	−5.02	−2.64	−2.84	2.38
PCPDTDTPQX	0.16	−2.01	−4.88	−2.71	−3.03	2.17

[a]HOMO= $-(E_{ox}^{onset} - E_{(ferrocene)}^{onset} + 4.8)$; $E_{(ferrocene)}^{onset}$ = 0.08 V. [b]LUMO= $-(E_{red}^{onset} - E_{(ferrocene)}^{onset} + 4.8)$; $E_{(ferrocene)}^{onset}$ = 0.08 V. [c]LUMO levels of the polymers were obtained from the equation LUMO = HOMO + E_g^{opt}.

dx.doi.org/10.1021/ma202764v | *Macromolecules* 2012, 45, 2690−2698

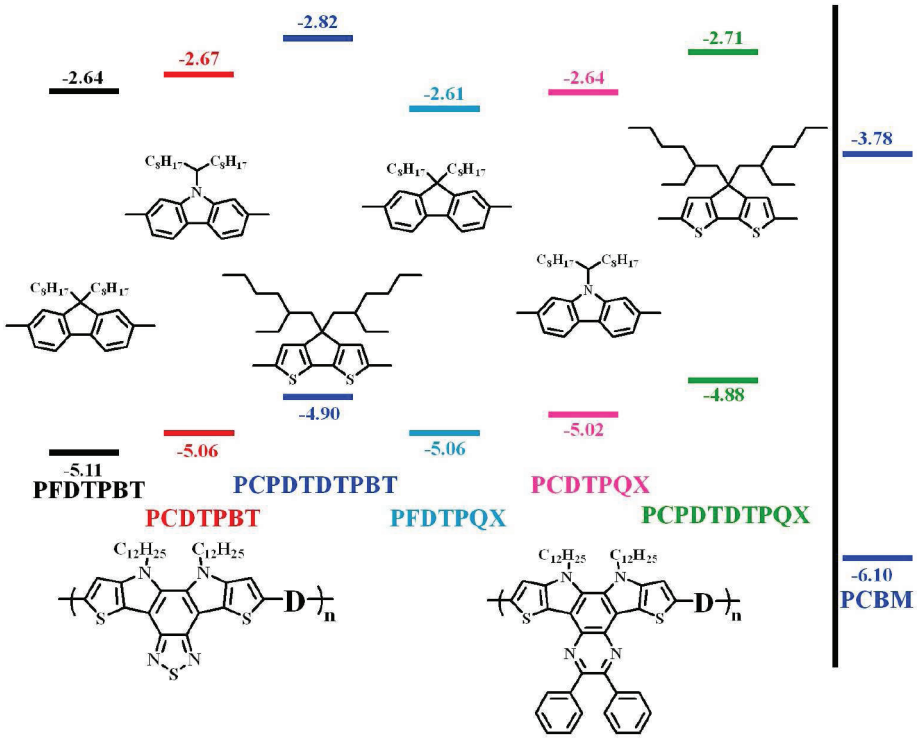


Figure 5. Energy diagram of HOMO–LUMO levels for the polymers and $PC_{71}BM$.

Table 4. Photovoltaic Characteristics

copolymer	wt % ratio of Copolymer and $PC_{71}BM$	mobility (cm^2/V s)	V_{oc} (V)	J_{sc} (mA/cm^2)	FF (%)	PCE (%)
PFDTPBT	1:3	4.7×10^{-5}	0.74	−8.37	50	3.11
PCDTPBT	1:3	1.8×10^{-5}	0.72	−7.47	47	2.54
PCPDTDTPBT	1:2	1.3×10^{-5}	0.48	−6.23	45	1.35
PFDTPQX	1:4	5.9×10^{-5}	0.72	−8.62	55	3.40
PCDTPQX	1:3	3.2×10^{-5}	0.70	−8.27	51	2.95
PCPDTDTPQX	1:3	7.8×10^{-6}	0.50	−5.64	49	1.38

should have poorer air-stability. The fluorene-based polymers exhibited a slight deeper HOMO energy levels compared to the corresponding carbazole-based polymers, while the **CPDT**-based polymers showed the highest-lying HOMO levels. On the other hand, the LUMO energy levels of these polymers are located at relatively higher-lying positions from −2.6 to −2.8 eV. This behavior is consistent with the fact that the donating effect of the nitrogen weakens the electron-accepting ability of BT and QX, thereby lifting up the LUMO energy levels of the polymers. According to the HOMO–LUMO energy difference, the band-gaps (E_g^{el}) obtained from CV measurements are greater than the corresponding optical band-gaps (E_g^{opt}), which is a phenomenon consistent with the reports in the literatures.[12] The HOMO–LUMO energy diagram of the polymers is shown in Figure 5 for comparison.

Hole-Mobility and Photovoltaic Characteristics. Bulk heterojunction PSCs were fabricated on the basis of ITO/PEDOT:PSS/polymer:$PC_{71}BM$/Ca/Al configuration and their performances were measured under 100 mW/cm^2 AM 1.5 illumination. Hole-only devices (ITO/PEDOT:PSS/polymer/Au) were also fabricated in order to estimate the hole mobilities of these polymers via space-charge limit current (SCLC) theory. The characterization data of the optimized device conditions are summarized in Table 4 and the *J*–*V* curves of these devices are shown in Figure 6. The hole mobility of the

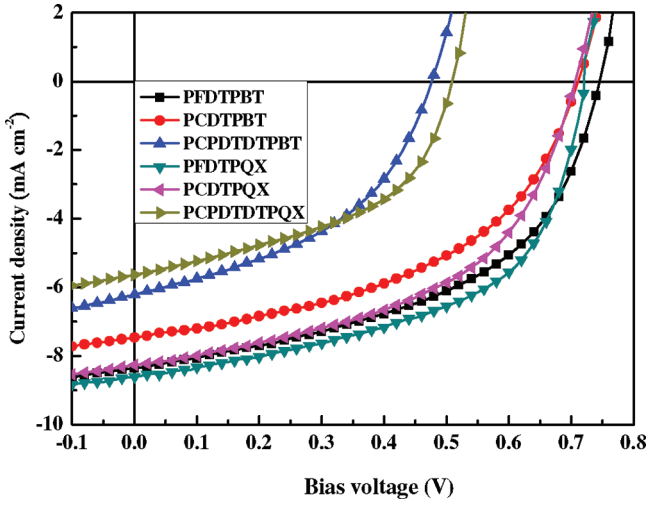


Figure 6. *J*–*V* characteristics of ITO/PEDOT:PSS/polymer:$PC_{71}BM$/Ca/Al under illumination of AM1.5, 100 mW/cm^2.

polymer follows the trend: **PCPDTDTPQX** (7.8×10^{-6} cm^2/V s) < **PCPDTDTPBT** (1.3×10^{-5} cm^2/V s) < **PCDTPBT** (1.8×10^{-5} cm^2/V s) < **PCDTPQX** (3.2×10^{-5} cm^2/V s) < **PFDTPBT** (4.7×10^{-5} cm^2/V s) < **PFDTPQX** (5.9×10^{-5} cm^2/V s). This result suggests that the **DTPQX**-based

dx.doi.org/10.1021/ma202764v | *Macromolecules* 2012, 45, 2690–2698

polymers generally have higher hole mobilites than their corresponding **DTPBT**-based polymers. The device based on the **PCPDTDTPBT**/$PC_{71}BM$ blend (1:2, w/w) exhibited a V_{oc} of 0.48 V, a J_{sc} of 6.23 mA/cm^2, a FF of 45% and a PCE of 1.35%, which is very similar to the device based on **PCPDTDTPQX**/$PC_{71}BM$ blend (1:3, w/w) (V_{oc} = 0.50 V, J_{sc} = 5.64 mA/cm^2 and a FF = 49%, PCE = 1.38%). The relatively lower V_{oc} values of the devices are mainly owing to the higher-lying HOMO values of the polymers, and the lower J_{sc} might be due to the unfavorable morphology of the active layer.[13] The device incorporating **PCDTPBT**/$PC_{71}BM$ (1:3, w/w) blend and **PCDTPQX**/$PC_{71}BM$ (1:3, w/w) blend delivered an improved PCE of 2.54% and 2.95%, respectively. This enhancement is ascribed to the **PCDTPBT** and **PCDTPQX**'s higher hole-mobilities and lower-lying HOMO values to obtain higher V_{oc}. The **PFDTPBT**/$PC_{71}BM$ (1:3, w/w) based device showed a V_{oc} of 0.74 V, a high J_{sc} of 8.37 mA/cm^2 and a FF of 50%, with a PCE of 3.11%. More encouragingly, **PFDTPQX**/$PC_{71}BM$ (1:4, w/w) based device exhibited a V_{oc} of 0.72 V, a J_{sc} of 8.62 mA/cm^2 leading to a highest PCE of 3.4%. This performance has outperformed the device based on a nonfused **PFDTQX** polymer reported in the literature.[11d]

CONCLUSIONS

We have successfully developed two novel donor−acceptor multifused **DTPBT** and **DTPQX** unit where two outer thiophene rings are covalently fastened with the central benzothiadiazole and quinoxaline rings by nitrogen bridges. These rigid and coplanar **DTPBT** and **DTPQX** building blocks were copolymerized with electron-rich donors, fluorene (**F**), carbazole (**C**), or cyclopentadithiophene (**CPDT**), via Suzuki or Stille coupling polymerization. The D−π−A diaminobenzothiodiazole and diaminoquinoxaline chromophores embedded in **DTPBT** and **DTPQX** segments induce internal charge transfer transitions upon photoexcitation, resulting in enhanced light-absorption ability in the UV region. Meanwhile, this electronic effect of nitrogen also reduces the electron-deficiency of the BT or QX acceptors. Therefore, the intramolecular charge transfer along the polymer backbones is attenuated. The optimized performance of the devices incorporating these polymers follows the trend: **PFDTPQX** > **PFDTPBT** > **PCDTPQX** > **PCDTPBT**, which is in good agreement with the trend of their hole-mobilities. The device based on **PFDTPQX**/$PC_{71}BM$ (1:4, w/w) exhibited a J_{sc} of 8.62 mA/cm^2 and a highest PCE of 3.4%. This research has gained a deep insight of the steric and electronic effects of the nitrogen bridges on the donor−acceptor fused systems, providing a useful guidance for future molecular design of conjugated polymers in PSCs applications.

EXPERIMENTAL SECTION

General Measurement and Characterization. All chemicals are purchased from Aldrich or Acros and used as received unless otherwise specified. ^{1}H and ^{13}C NMR spectra were measured using Varian 300 MHz instrument spectrometer. The molecular weight of polymers was measured by the GPC method (Viscotek VE2001GPC), and polystyrene was used as the standard (THF as the eluent). Differential scanning calorimeter (DSC) was measured on TA Q200 Instrument and thermal gravimetric analysis (TGA) was recorded on Perkin-Elmer Pyris under a nitrogen atmosphere at a heating rate of 10 °C/min. Absorption spectra were taken on a HP8453 UV−vis spectrophotometer. The electrochemical cyclic voltammetry was conducted on a Bioanalytical Systems Inc. analyzer. A carbon glass-coated with a thin polymer film was used as the working electrode and an Ag/AgCl as the reference electrode, while 0.1 M tetrabutylammonium hexafluorophosphate ($TBAPF_6$) in acetonitrile was the electrolyte. CV curves were calibrated using ferrocence as the standard, whose HOMO is set at −4.8 eV with respect to zero vacuum level. The HOMO energy levels were obtained from the equation HOMO = $-(E_{ox}^{onset} - E_{(ferrocene)}^{onset}+4.8)$ eV. The LUMO levels of polymer were obtained from the equation LUMO = $-(E_{red}^{onset} - E_{(ferrocene)}^{onset}+4.8)$ eV.

Fabrication and Characterization of BHJ Devices. ITO/glass substrates were ultrasonically cleaned sequentially in detergent, water, acetone and isopropyl alcohol. Then, the substrates were covered by a 30 nm thick layer of PEDOT:PSS (Clevios P provided by H. C. Stark) by spin coating. After annealing in air at 150 °C during 30 min, the samples were cooled down to room temperature. Polymers were dissolved in *o*-dichlorobenzene (ODCB) (0.47 wt %) and $PC_{71}BM$ (purchased from Nano-C) was added to reach the desired ratio. The solution was then heated at 110 °C and stirred overnight. Prior to deposition, the solution was filtrated through a 0.45 μm filter and the substrates were transferred in a glovebox. The photoactive layer was then spin coated at different spin coating speed in order to tune its thickness. After drying, the samples were annealed during 15 min. The detailed processing parameters (spin coating speed; annealing temperature) are shown as follows: **PFDTPBT**/$PC_{71}BM$ (1000 rpm; 130 °C), **PCDTPBT**/$PC_{71}BM$ (1000 rpm, without annealing), **PCPDTDTPBT**/$PC_{71}BM$ (700 rpm; without annealing), **PFDTPQX**/$PC_{71}BM$ (1000 rpm; without annealing), **PCDTPQX**/$PC_{71}BM$ (700 rpm; 130 °C), **PCPDTDTPQX**/$PC_{71}BM$ (700 rpm; without annealing). The cathode made of calcium (35 nm thick) and aluminum (100 nm thick) was evaporated through a shadow mask under high vacuum (<10^{-6} Torr). Each device is constituted of 4 pixels defined by an active area of 0.04 cm^2. Finally, the devices were encapsulated and *I*−*V* curves were measured in air.

Electrical Characterization under Illumination. The devices were characterized under 100 mW/cm^2 AM 1.5 simulated light measurement (Yamashita Denso solar simulator). Current−voltage (*J*−*V*) characteristics of PSC devices were obtained by a Keithley 2400 SMU. Solar illumination conforming the JIS Class AAA was provided by a SAN-EI 300W solar simulator equipped with an AM 1.5G filter. The light intensity was calibrated with a Hamamatsu S1336-5BK silicon photodiode. The performances presented here are the average of the 4 pixels of each device.

Hole-Only Devices. In order to investigate the respective hole mobility of the different copolymer films, unipolar devices have been prepared following the same procedure except that the active layer is made of pure polymer and the Ca/Al cathode is replaced by evaporated gold (40 nm). The hole mobilities were calculated according to space charge limited current theory (SCLC). The *J*−*V* curves were fitted according to the following equation:

$$J = \frac{9}{8}\varepsilon\mu\frac{V^2}{L^3}$$

Here ε is the dielectric permittivity of the polymer, μ is the hole mobility, and L is the film thickness (distance between the two electrodes).

Synthesis of DTPBT. To a suspension solution of **1** (1.00 g, 3.06 mmol), 1-bromododecane (4.58 g, 18.38 mmol) and potassium iodide (20 mg) in DMSO (100 mL) was added potassium hydroxide (2.00 g, 35.64 mmol) in one portion at 80 °C. The resulting solution was stirred for 16 h at 80 °C and then was extracted with ethyl acetate (400 mL × 3) and water (200 mL). The combined organic layer was dried over $MgSO_4$. After removal the solvent under reduced pressure, the residue was purified by column chromatography on silica gel (hexane/ethyl acetate, v/v, 10/1) to give an orange-red solid **DTPBT** (1.44 g, 71%). ^{1}H NMR ($CDCl_3$, 300 MHz): δ 7.37 (d, J = 5.1 Hz, 2 H), 7.12 (t, J = 5.1 Hz, 2 H), 4.44 (t, J = 7.5 Hz, 4 H), 1.81−1.65 (m, 4 H), 1.30−0.90 (m, 36 H), 0.80 (t, J = 6.9 Hz, 6 H). ^{13}C NMR ($CDCl_3$, 75 MHz): δ 147.5, 145.5, 132.1, 126.8, 121.2, 111.7, 110.9, 50.3, 31.9, 30.0, 29.53, 29.51, 29.4, 29.30, 29.28, 29.0, 26.5, 22.7, 14.1. MS (EI,

dx.doi.org/10.1021/ma202764v | Macromolecules 2012, 45, 2690−2698

$C_{38}H_{54}N_4S_3$): calcd, 663.06; found, 663. Anal. Calcd for $C_{38}H_{54}N_4S_3$: C, 68.83; H, 8.21; N, 8.45; Found: C, 68.93; H, 8.17; N, 8.00.

Synthesis of Br-DTPBT. To a solution of **DTPBT** (1.50 g, 2.26 mmol) in chloroform (31 mL)/acetic acid (31 mL) was added *N*-bromosuccinimide (0.85 g, 4.76 mmol) in one portion at 0 °C. The flask was wrapped with alumiunm foil and stirred for 1 h at 0 °C and then was stirred for another 1 h at room temperature. The reaction was quenched by water (100 mL). The mixture solution was extracted with dichloromathane (300 mL × 3) and water (100 mL). The combined organic layer was dried over $MgSO_4$. After removal of the solvent under reduced pressure, the residue was purified by column chromatography on silica gel (hexane/ethyl acetate, v/v, 30/1). The product was recrystallized from hexane to give an red solid **Br-BTDTP** (0.96 g, 52%). ^{1}H NMR ($CDCl_3$, 300 MHz): δ 7.20 (s, 2 H), 4.41 (t, J = 7.5 Hz, 4 H), 1.79 (t, J = 6.3 Hz, 4 H), 1.28−1.13 (m, 36 H), 0.87 (t, J = 6.9 Hz, 6 H). ^{13}C NMR ($CDCl_3$, 75 MHz): δ 147.1, 143.2, 130.9, 121.3, 115.0, 113.6, 110.8, 50.4, 31.9, 30.0, 29.6, 29.56, 29.53, 29.4, 29.3, 29.0, 26.5, 22.7, 14.1. MS (EI, $C_{38}H_{52}Br_2N_4S_3$): calcd, 820.85; found, 820. Anal. Calcd for $C_{38}H_{52}Br_2N_4S_3$: C, 55.60; H, 6.39; N, 6.83; Found: C, 55.51; H, 6.52; N, 6.87.

Synthesis of DTPQX. To a solution of **DTPBT** (1.20 g, 1.81 mmol) in acetic acid (60 mL) was added zinc powder (2.40 g, 36.71 mmol) in one portion at room temperature. The mixture solution was heated to 140 °C for 15 min. After the solution was cooled at room temperature, the solid was removed by filtration. The mixture solution was extracted with ethyl acetate (500 mL × 3) and sodium hydroxide solution until the organic layer was basic. The combined organic layer was dried over $MgSO_4$. After removal of the solvent under reduced pressure, a black liquid **2** was obtained without further purification. To a solution of **2** and benzil (0.46 g, 1.63 mmol) in chloroform (36 mL) was added catalytic *p*-TSA in one portion at room temperature. The resulting mixture was heated to 65 °C and stirred for 16 h. The reaction solution was quenched by sodium bicarbonate solution, and then extracted with dichloromethane (300 mL × 3) and water (150 mL). The combined organic layer was dried over $MgSO_4$. After removal of the solvent under reduced pressure, the residue was purified by column chromatography on silica gel (hexane/ethyl acetate, v/v, 20/1) and washed by ethanol to give a yellow solid **DTPQX**. (0.38 g, 25%). ^{1}H NMR ($CDCl_3$, 300 MHz): δ 7.78−7.81 (m, 4 H), 7.47 (d, J = 5.1 Hz, 2 H), 7.37−7.40 (m, 6 H), 7.21 (d, J = 5.1 Hz, 2 H), 4.58 (t, J = 7.5 Hz, 4 H), 1.89 (s, 4 H), 1.15−1.29 (m, 36 H), 0.86 (t, J = 6.6 Hz, 6 H). ^{13}C NMR ($CDCl_3$, 75 MHz): δ 149.3, 146.2, 140.6, 133.8, 131.9, 130.8, 128.4, 127.7, 121.0, 117.4, 111.8, 50.6, 32.2, 30.6, 29.9, 29.8, 29.71, 29.65, 29.5, 27.0, 23.0, 14.5; MS (EI, $C_{52}H_{64}N_4S_2$): calcd, 809.22; found, 809. Anal. Calcd for $C_{52}H_{64}N_4S_2$: C, 71.09; H, 6.71; N, 10.36; Found: C, 71.30; H, 6.64; N, 10.35.

Synthesis of Br-DTPQX. To a solution of **DTPQX** (0.30 g, 0.36 mmol) in chloroform (7 mL)/acetic acid (7 mL) was added *N*-bromosuccinimide (0.14 g, 0.78 mmol) in one portion at 0 °C. The flask was wrapped with alumiunm foil and stirred for 1 h at 0 °C and then was stirred for another 1 h at room temperature. The reaction was quenched by water (50 mL). The mixture solution was extracted with dichloromathane (100 mL × 3) and water (50 mL). The combined organic layer was dried over $MgSO_4$. After removal of the solvent under reduced pressure, the residue was purified by column chromatography on silica gel (hexane/ethyl acetate, v/v, 100/1). The product was recrystallized from hexane to give an red solid **Br-DTPQX** (0.22 g, 61%). ^{1}H NMR ($CDCl_3$, 300 MHz): δ 7.75−7.12 (m, 4 H), 7.28 (m, 6 H), 7.21 (s, 2 H), 4.44 (t, J = 7.5 Hz, 4 H), 1.83 (s, 4 H), 1.21−1.15 (m, 36 H), 0.86 (t, J = 6.6 Hz, 6 H). ^{13}C NMR ($CDCl_3$, 75 MHz): δ 149.3, 143.4, 139.9, 133.1, 130.3, 130.1, 128.2, 128.0, 120.6, 116.9, 114.7, 114.1, 50.2, 31.9, 30.2, 29.5, 29.4, 29.35, 29.3, 29.1, 26.5, 22.7, 14.1; MS (EI, $C_{52}H_{62}Br_2N_4S_2$): calcd, 967.01; found, 967. Anal. Calcd for $C_{52}H_{62}Br_2N_4S_2$: C, 64.59; H, 6.46; N, 5.79; Found: C, 64.37; H, 6.48; N, 6.13.

Synthesis of PFDTPBT. To a 25 mL round-bottom flask was introduced **Br-DTPBT** (100 mg, 0.12 mmol), 2,7-bis(4′,4′,5′,5′-tetramethyl-1′,3′,2′-dioxaborolane-2′-yl)-9,9-dioctylfluorene **F** (78 mg, 0.12 mmol), $Pd(PPh_3)_4$ (5.6 mg, 0.0049 mmol), K_2CO_3 (126 mg, 2.36 mmol), Aliquat336 (22 mg, 0.054 mmol), degassed toluene (7 mL), and degassed H_2O (1.5 mL). The mixture was heated to 90 °C under nitrogen gas for 72 h. Then, 4,4,5,5-tetramethyl-2-phenyl-1,3,2-dioxaborolane (6.1 mg, 0.03 mmol) was added to the mixture solution and reacted for 24 h at 90 °C. Finally, 1-bromobenzene (4.7 mg, 0.03 mmol) was added to the mixture solution and reacted for 24 h at 90 °C. The solution was added into methanol dropwise. The precipitate was collected by filtration and washed by Soxhlet extraction with methanol, acetone, and chloroform sequentially for 1 week. The Pd−thiol gel (Silicycle Inc.) was added to above chloroform solution to remove the residual Pd catalyst. After filtration and removal of the solvent, the polymer was redissolved in THF and added into methanol to reprecipitate out. The purified polymer was collected by filtration and dried under vacuum for 1 day to give a dark red solid (110 mg, 86%, M_n = 20000, PDI = 2.70). ^{1}H NMR ($CDCl_3$, 300 MHz): δ 7.90−7.60 (m, 6 H), 7.60−7.40 (m, 2 H), 4.40−7.80 (m, 4 H), 1.80−2.20 (m, 8 H), 1.50−1.00 (m, 60 H), 0.85−0.75 (m, 12 H).

Synthesis of PCDTPBT. The procedure is following the synthesis of **PFDTPBT**. **Br-DTPBT** (100 mg, 0.12 mmol), 2,7-bis(4′,4′,5′,5′-tetramethyl-1′,3′,2′-dioxaborolan-2′-yl)-*N*-9″-heptadecanylcarbazole **C** (80 mg, 0.12 mmol), $Pd(PPh_3)_4$ (5.6 mg, 0.0049 mmol), K_2CO_3 (126 mg, 2.36 mmol), Aliquat336 (22 mg, 0.054 mmol), degassed toluene (7 mL), degassed H_2O (1.5 mL), 4,4,5,5-tetramethyl-2-phenyl-1,3,2-dioxaborolane (6.1 mg, 0.03 mmol), and 1-bromobenzene (4.7 mg, 0.03 mmol). The purified polymer was collected by filtration and dried under vacuum for 1 day to give a orange-red solid (113 mg, 87%, M_n = 27000, PDI = 4.47). ^{1}H NMR ($CDCl_3$, 300 MHz): 8.20−8.05 (m, 2 H), 8.00−7.85 (m, 2 H), 7.80−7.60 (m, 4 H), 7.60−7.50 (m, 2 H), 4.80−4.40 (m, 5 H), 2.60−2.30 (m, 2 H), 2.20−1.80 (m, 2 H), 1.30−1.10 (m, 60 H), 0.90−0.75 (m, 12 H).

Synthesis of PFDTPQX. The procedure is following the synthesis of **PFDTPBT**. **Br-DTPQX** (87 mg, 0.09 mmol), 2,7-bis(4′,4′,5′,5′-tetramethyl-1′,3′,2′-dioxaborolane-2′-yl)-9,9-dioctylfluorene **F** (58.5 mg, 0.09 mmol), $Pd(PPh_3)_4$ (4.2 mg, 0.0036 mmol), K_2CO_3 (94.5 mg, 0.68 mmol), Aliquat336 (16.5 mg, 0.045 mmol), degassed toluene (5 mL), degassed H_2O (1 mL), 4,4,5,5-tetramethyl-2-phenyl-1,3,2-dioxaborolane (4.9 mg, 0.023 mmol), and 1-bromobenzene (3.7 mg, 0.023 mmol). The purified polymer was collected by filtration and dried under vacuum for 1 day to give an orange-red solid (100 mg, 93%, M_n = 34000, PDI = 2.17). ^{1}H NMR ($CDCl_3$, 300 MHz): 7.90−7.70 (m, 10 H), 7.60−7.35 (m, 8 H), 4.80−4.50 (m, 4 H), 2.15−1.80 (m, 8 H), 1.50−1.05 (m, 60 H), 0.95−0.75 (m, 12 H).

Synthesis of PCDTPQX. The procedure is following the synthesis of **PFDTPBT**. **Br-DTPQX** (100 mg, 0.10 mmol), 2,7-bis(4′,4′,5′,5′-tetramethyl-1′,3′,2′-dioxaborolan-2′-yl)-*N*-9″-heptadecanylcarbazole **C** (68 mg, 0.10 mmol), $Pd(PPh_3)_4$ (4.8 mg, 0.0041 mmol), K_2CO_3 (108 mg, 0.78 mmol), Aliquat336 (16 mg, 0.04 mmol), degassed toluene (6 mL), degassed H_2O (1 mL), 4,4,5,5-tetramethyl-2-phenyl-1,3,2-dioxaborolane (5.3 mg, 0.026 mmol), and 1-bromobenzene (4.1 mg, 0.026 mmol). The purified polymer was collected by filtration and dried under vacuum for 1 day to give an orange-red solid (119 mg, 95%, M_n = 30200, PDI = 1.68). ^{1}H NMR ($CDCl_3$, 300 MHz): 8.30−8.10 (m, 2 H), 8.00−7.65 (m, 10 H), 7.60−7.40 (m, 8 H), 4.80−4.60 (m, 1 H), 2.70−2.30 (m, 2 H), 2.20−1.80 (m, 6H), 1.40−1.00 (m, 60H), 0.90−0.75 (m, 12 H).

Synthesis of PCPDTDTPBT. To a 25 mL round-bottom flask was introduced **Br-DTPBT** (50 mg, 0.06 mmol), 2,6-di(trimethyltin)-4,4-diethylhexylcyclopenta[2,1-*b*:3,4-*b*′]dithiophene **CPDT** (44 mg, 0.06 mmol), $Pd_2(dba)_3$ (4.5 mg, 0.0049 mmol), tri(*o*-tolyl)phosphine (11.8 mg, 0.038 mmol), and dry chlorobenzene (2.2 mL). The mixture was then degassed by bubbling nitrogen for 10 min at room temperature. The round-bottom flask was placed into the microwave reactor and reacted for 45 min under 270 W. Then, tributyl(thiophen-2-yl)stannane (5.6 mg, 0.015 mmol) was added to the mixture solution and reacted for 10 min under 270 W. Finally, 2-bromothiophene (2.4 mg, 0.015 mmol) was added to the mixture solution and reacted for 10 min under 270 W. The solution was added into methanol dropwise. The precipitate was collected by filtration and washed by Soxhlet extraction with acetone, hexane, and chloroform sequentially for 1 week. The Pd-thiol gel (Silicycle Inc.) and Pd-TAAcOH were added to above chloroform solution to remove the residual Pd catalyst and Sn

metal. After filtration and removal of the solvent, the polymer was redissolved in chloroform again and added into methanol to reprecipitate out. The purified polymer was collected by filtration and dried under vacuum for 1 day to give a dark purple solid (50 mg, 78%, M_n = 23400, PDI = 2.50). ^{1}H NMR ($CDCl_3$, 300 MHz): 7.25−7.10 (m, 4 H), 4.70−4.30 (m, 4 H), 2.10−1.70 (m, 8 H), 1.30−0.90 (m, 54 H), 0.90−0.60 (m, 18 H).

Synthesis of PCPDTDTPQX. To a 25 mL round-bottom flask was introduced **Br-DTPQX** (100 mg, 0.10 mmol), 2,6-di(trimethyltin)-4,4-diethylhexylcyclopenta[2,1-*b*:3,4-*b*′]dithiophene **CPDT** (75.3 mg, 0.10 mmol), $Pd_2(dba)_3$ (7.6 mg, 0.0083 mmol), tri(*o*-tolyl)phosphine (20.1 mg, 0.066 mmol), and dry chlorobenzene (3.6 mL). The mixture was then degassed by bubbling nitrogen for 10 min at room temperature. The round-bottom flask was placed into the microwave reactor and reacted for 45 min under 270 W. Then, tributyl(thiophen-2-yl)stannane (19.2 mg, 0.026 mmol) was added to the mixture solution and reacted for 10 min under 270 W. Finally, 2-bromothiophene (8.4 mg, 0.026 mmol) was added to the mixture solution and reacted for 10 min under 270 W. The solution was added into methanol dropwise. The precipitate was collected by filtration and washed by Soxhlet extraction with acetone, hexane, and chloroform sequentially for 1 week. The Pd−thiol gel (Silicycle Inc.) and Pd-TAAcOH were added to above chloroform solution to remove the residual Pd catalyst and Sn metal. After filtration and removal of the solvent, the polymer was redissolved in chloroform again and added into methanol to reprecipitate out. The purified polymer was collected by filtration and dried under vacuum for 1 day to give a red purple solid (88 mg, 70%, M_n = 17000, PDI = 2.10). ^{1}H NMR ($CDCl_3$, 300 MHz): 8.00−7.70 (m, 4 H), 7.60−7.30 (m, 10 H), 4.80−4.30 (m, 4 H), 2.20−1.80 (m, 6 H), 2.00−1.40 (m, 52 H), 1.00−0.70 (m, 18 H).

■ ASSOCIATED CONTENT

Supporting Information

DSC measurements and ^{1}H and ^{13}C NMR spectra of all the intermediates, monomers, and corresponding copolymers. This material is available free of charge via the Internet at http://pubs.acs.org.

■ AUTHOR INFORMATION

Corresponding Author

*E-mail: yjcheng@mail.nctu.edu.tw.

Notes

The authors declare no competing financial interest.

■ ACKNOWLEDGMENTS

We thank the National Science Council and the "ATU Program" of the Ministry of Education, Taiwan, for financial support.

■ REFERENCES

(1) (a) Yu, G.; Gao, J.; Hummelen, J. C.; Wudl, F.; Heeger, A. J. *Science* **1995**, *270*, 1789. (b) Günes, S.; Neugebauer, H.; Sariciftci, N. S. *Chem. Rev.* **2007**, *107*, 1324. (c) Thompson, B. C.; Fréchet, J. M. J. *Angew. Chem., Int. Ed.* **2008**, *47*, 58.

(2) (a) Cheng, Y.-J.; Yang, S.-H.; Hsu, C.-S. *Chem. Rev.* **2009**, *109*, 5868. (b) Chen, J.; Cao, Y. *Acc. Chem. Res.* **2009**, *42*, 1709.

(3) (a) Roncali, J. *Chem. Rev.* **1997**, *97*, 173. (b) van Mullekom, H. A. M.; Vekemans, J. A. J. M.; Havinga, E. E.; Meijer, E. W. *Mater. Sci. Eng. Res.* **2001**, *32*, 1.

(4) Roncali, J. *Macromol. Rapid Commun.* **2007**, *28*, 1761 and reference therein.

(5) (a) Brédas, J. L.; Calbert, J. P.; da Silva Filho, D. A.; Cornil, J. *Proc. Natl. Acad. Sci. U.S.A.* **2002**, *99*, 5804. (b) Ando, S.; Nishida, J.-I.; Tada, H.; Inoue, Y.; Tokito, S.; Yamashita, Y. *J. Am. Chem. Soc.* **2005**, *127*, 5336.

(6) (a) Xu, C.; Wakamiya, A.; Yamaguchi, S. *J. Am. Chem. Soc.* **2005**, *127*, 1638. (b) Li, L.; Xiang, J.; Xu, C. *Org. Lett.* **2007**, *9*, 4877. (c) Bounchard, J.; Wakim, S.; Leclerc, M. *J. Org. Chem.* **2004**, *69*, 5705. (d) Cheng, Y.-J.; Wu., J.-S.; Shih, P.-I.; Chang, C.-Y.; Jwo, P.-C.; Kuo, W.-S.; Hsu, C.-S. *Chem. Mater.* **2011**, *23*, 2361. (e) Wu., J.-S.; Cheng, Y.-J.; Dubosc, M.; Hsieh, C.-H.; Chang, C.-Y.; Hsu, C.-S. *Chem. Commun.* **2010**, *46*, 3259. (f) Chen, C.-H.; Cheng, Y.-J.; Dubosc, M.; Hsieh, C.-H.; Chu, C.-C.; Hsu, C.-S. *Chem. Asian. J.* **2010**, *5*, 2483. (g) Chen, C. H.; Hsieh, C.-H.; Dubosc, M.; Cheng, Y.-J.; Hsu, C.-S. *Macromolecules* **2010**, *6973*, 697. (h) Wong, K.-T.; Chao, T.-C.; Chi, L.-C.; Chu, Y.-Y.; Balaiah, A.; Chiu, S.-F.; Liu, Y.-H.; Wang, Y. *Org. Lett.* **2006**, *8*, 5033. (i) Wang, J.-Y.; Hau, S. K.; Yip, H.-L.; Davies, J. A.; Chen, K.-S.; Zhang, Y.; Sun, Y.; Jen, A. K.-Y. *Chem. Mater.* **2011**, *23*, 765. (j) Zhang, M.; Sun, Y.; Guo, X.; Cui, C.; He, Y.; Li, Y. *Macromolecules* **2011**, *44*, 7625. (l) Forster, M.; Annan, K. O.; Scherf, U. *Macromolecules* **1999**, *32*, 3159. (k) Goldfinger, M. B.; Swager, T. M. *J. Am. Chem. Soc.* **1994**, *116*, 7895. (n) Scherf, U. *J. Mater. Chem.* **1999**, *9*, 1853. (l) Patil, S. A.; Scherf, U.; Kadashchuk, A. *Adv. Funct. Mater.* **2003**, *13*, 609. (m) Cheng, Y.-J.; Chen, C.-H.; Lin, Y.-S.; Chang, C.-Y.; Hsu, C.-S. *Chem. Mater.* **2011**, *23*, 5068. (n) Chen, C.-H.; Cheng, Y.-J.; Chang, C.-Y.; Hsu, C.-S. *Macromolecules* **2011**, *44*, 8415.

(7) (a) Guégano, X.; Kanibolotsky, A. L.; Blum, C.; Mertens, S. F. L.; Liu, S.-X.; Neels, A.; Hagemann, H.; Skabara, P. J.; Leutwyler, S.; Wandlowski, T.; Hauser, A.; Decurtins, S. *Chem.—Eur. J.* **2009**, *15*, 63. (b) Jia, C.-Y.; Liu, S.-X.; Tanner, C.; Leiggener, C.; Sanguinet, L.; Levillain, E.; Leutwyler, S.; Hauser, A.; Decurtins, S. *Chem. Commun.* **2006**, *42*, 1878. (c) Loosli, C.; Jia, C.-Y.; Liu, S.-X.; Haas, M.; Dias, M.; Levillain, E.; Neels, A.; Labat, G.; Hauser, A.; Decurtins, S. *J. Org. Chem.* **2005**, *70*, 4988. (d) Jaggi, M.; Blum, C.; Dupont, N.; Grilj, J.; Liu, S.-X.; Hauser, J.; Hauser, A.; Decurtins, S. *Org. Lett.* **2009**, *11*, 3096. (e) Balaji, G.; Shim, W. L.; Parameswaran, M.; Valiyaveettil, S. *Org. Lett.* **2009**, *11*, 4450. (f) Zhu, G.; Conner, S. E.; Zhou, X.; Shih, C.; Li, T.; Anderson, B. D.; Brooks, H. B.; Campbell, R. M.; Considine, E.; Dempsey, J. A.; Faul, M. M.; Ogg, C.; Patel, B.; Schultz, R. M.; Spencer, C. D.; Teicher, B.; Watkins, S. A. *J. Med. Chem.* **2003**, *46*, 2027. (g) Wang, H.; Shi, Q.; Lin, Y.; Fan, H.; Cheng, P.; Zhan, X.; Li, Y.; Zhu, D. *Macromolecules* **2011**, *44*, 4213.

(8) Hou, J.; Park, M.-H.; Zhang, S.; Yao, Y.; Chen, L.-M.; Li, J.-H.; Yang, Y. *Macromolecules* **2008**, *41*, 6012.

(9) (a) McNeill, C. R.; Halls, J. J. M.; Wilson, R.; Whiting, G. L.; Berkebile, S.; Ramsey, M. G.; Friend, R. H.; Greenham, N. C. *Adv. Funct. Mater.* **2008**, *18*, 2309. (b) Svensson, M.; Zhang, F.; Veenstra, S. C.; Verhees, W. J. H.; Hummelen, J. C.; Kroon, J. M.; Inganäs, O.; Andersson, M. R. *Adv. Mater.* **2003**, *15*, 988.

(10) Cheng, Y.-J.; Chen, C.-H.; Ho, Y.-J.; Chang, S.-W.; Witek, H. A.; Hsu, C.-S. *Org. Lett.* **2011**, *13*, 5484.

(11) (a) Zhang, F.; Jespersen, K. G.; Björström, C.; Svensson, M.; Andersson, M. R.; Sundström, V.; Magnusson, K.; Moons, E.; Yartsev, A.; Inganäs, O. *Adv. Funct. Mater.* **2006**, *16*, 667. (b) Blouin, N.; Michaud, A.; Leclerc, M. *Adv. Mater.* **2007**, *19*, 2295. (c) Moulé, A. J.; Tsami, A.; Bünnagel, T. W.; Forster, M.; Kronenberg, N. M.; Scharber, M.; Koppe, M.; Morana, M.; Brabec, C. J.; Meerholz, K.; Scherf, U. *Chem. Mater.* **2008**, *20*, 4045. (d) Lindgren, L. J.; Zhang, F.; Andersson, M.; Barrau, S.; Hellström, S.; Mammo, W.; Perzon, E.; Inganäs, O.; Andersson, M. R. *Chem. Mater.* **2009**, *21*, 3491. (e) Wang, E.; Hou, L.; Wang, Z.; Ma, Z.; Hellström, S.; Zhuang, W.; Zhang, F.; Inganäs, O.; Andersson, M. R. *Macromolecules* **2011**, *44*, 2067.

(12) (a) Wienk, M. M.; Kroon, J. M.; Verhees, W. J. H.; Knol, J.; Hummelen, J. C.; van Hal, P. A.; Janssen, R. A. J. *Angew. Chem., Int. Ed.* **2003**, *42*, 3371. (b) Yao, Y.; Shi, C.; Li, G.; Shrotriya, V.; Pei, Z.; Yang, Y. *Appl. Phys. Lett.* **2006**, *89*, 153507.

(13) Zhang, J.; Cai, W.; Huang, F.; Wang, E.; Zhong, C.; Liu, S.; Wang, M.; Duan, C.; Yang, T.; Cao, Y. *Macromolecules* **2011**, *44*, 894.

Macromolecules

Article

pubs.acs.org/Macromolecules

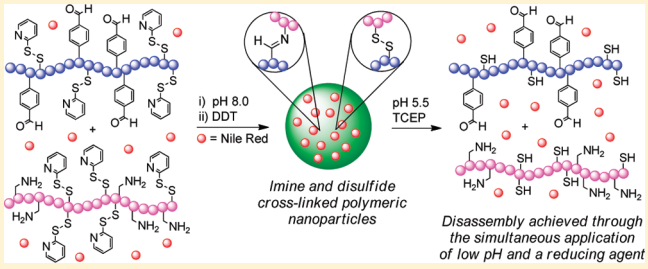
Triggering Polymeric Nanoparticle Disassembly through the Simultaneous Application of Two Different Stimuli

Alexander W. Jackson and David A. Fulton*

Chemical Nanoscience Laboratory, School of Chemistry, Bedson Building, Newcastle University, Newcastle upon Tyne NE1 7RU, United Kingdom

Supporting Information

ABSTRACT: Polymeric nanoparticles whose disassembly into their component polymer chains is triggered by the simultaneous application of two different stimuli are described. Reversible addition−fragmentation chain transfer (RAFT) polymerization was utilized to prepare acrylamide-based linear copolymers displaying pyridyl disulfide appendages and either aldehyde or amine functional groups. These copolymer chains were intermolecularly cross-linked through imine bond formation at pH 8.0 and then through disulfide bond formation to afford polymeric nanoparticles possessing hydrodynamic radii of 76 nm consisting of multiple polymer chains cross-linked through both imine and disulfide bonds. By performing the cross-linking reactions in the presence of the hydrophobic dye Nile Red, it was demonstrated that these polymeric nanoparticles could encapsulate a cargo of small hydrophobic molecules. The disassembly of the polymeric nanoparticles into their component polymer chains was accomplished by lowing the pH to 5.5 in the presence of the disulfide reducing agent tris(2-carboxyethyl)phosphine (TCEP), causing hydrolysis of the imine cross-links and cleavage of the disulfide cross-links, respectively, and demonstrating that the simultaneous application of both low pH and a reducing environment are required to trigger the disassembly process. It was shown that application of either a low pH *or* the application of the reducing agent TCEP does not trigger the disassembly of the polymeric nanoparticle as there is sufficient density of the remaining imine or disulfide cross-links which are able to maintain the structural integrity of the polymeric nanoparticle. The formation and disassembly processes of these polymeric nanoparticles was monitored by gel permeation chromatography, and the release of the dye was monitored using fluorescence spectroscopy. A 5 kDa poly(ethylene glycol) was grafted onto the polymeric nanoparticle, demonstrating the potential of these polymeric nanoparticles to undergo post-assembly functionalization.



INTRODUCTION

Polymeric nanoparticles have attracted much attention in recent years on account of their potential applications in fields such as catalysis,[1−3] imaging,[4] and drug delivery.[5−7] To increase the possible utility of polymeric nanoparticles, there has been a drive to endow these species with the abilities to undergo structural and property changes in response to the application of an external stimuli.[8] Inspired by this recent progress, we became intrigued by the possibility of developing polymeric nanoparticles which require the simultaneous application of two distinct stimuli to trigger a desired response. The ability to obtain a response by using a combination of stimuli applied simultaneously could lead to greater specificity regarding where and when events are triggered, a feature which would be highly advantageous in fields such as drug delivery. The group of Thayumanavan has developed[9] triply stimuli sensitive amphiphilic block copolymers which self-assemble into micelles possessing the abilities to encapsulate hydrophobic molecules. They have demonstrated that the kinetics of release of the encapsulated molecules from these micelles varied depending on whether single stimuli or multiple stimuli are applied, demonstrating the feasibility of combining different orthogonal triggers. Although this elegant work represents a significant advance, it is worthwhile noting that the stimuli-triggered events, namely the disassembly of the micelles and the release of their encapsulated cargo, still occur upon the application of only a single stimulus, and that the simultaneous application of stimuli changes only the rate at which events occur.

Our approach toward the development of a polymer nanoparticle requiring the simultaneous application of multiple stimuli to trigger a response was to employ reversible covalent reactions to link multiple polymer chain building blocks into polymeric nanoparticle structures, an approach which has been utilized by ourselves[10−12] and others[13−17] for the controlled formation of discrete responsive polymer nanoparticles. We choose to focus on two orthogonal reversible covalent reactions, namely the condensation of amine and aldehydes to form imines and the oxidation of thiols to form disulfides. Imine formation in aqueous solution is pH sensitive,[18] with imine formation favored at high pH and disfavored at low pH.

Received: December 17, 2011
Revised: February 17, 2012
Published: March 14, 2012

ACS Publications © 2012 American Chemical Society

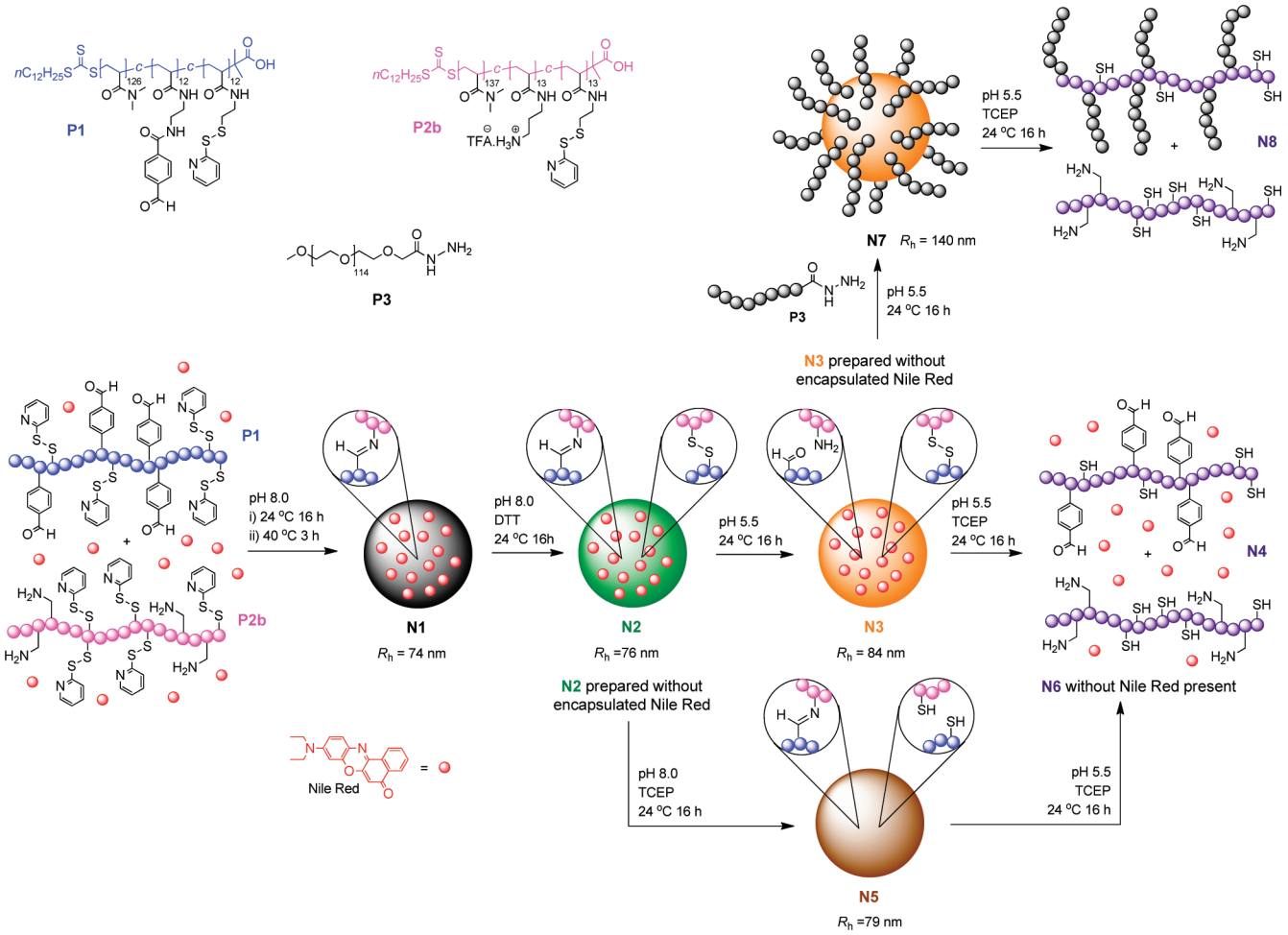


Figure 1. Polymer chains **P1** and **P2b** are cross-linked through imine bond formation in the presence of the dye Nile Red to form the polymeric nanoparticle **N1**. Further cross-linking through disulfide bond formation results in the formation of polymeric nanoparticle **N2**. Complete dissassembly of this particle is triggered through imine hydrolysis (**N3**) and then disulfide reduction to afford the component polymer chains (**N4**). Alternatively, disassembly is triggered through disulfide reduction to polymeric nanoparticle **N5** followed by hydrolysis of the imine cross-links to afford the polymeric component polymer chains **N6** (identical to **N4** except disassembly was performed in the absence of Nile Red). Functionalization of **N3** with PEG-hydrazide (**P3**) was performed to afford the PEG-decorated polymeric nanoparticle **N7**, whose disassembly into component polymers **N8** was triggered through the addition of TCEP at pH 5.5.

Consequently, it is possible to modulate the position of the imine equilibrium by changing the pH, and depending on the reaction partners, it is possible to shift the equilibrium from a near 100% yield of imine in solution to complete hydrolysis within a narrow range of ~3 pH units. The stability of the imine bond in water and the pH at which it undergoes hydrolysis can be tuned by altering the stereoelectronic characteristics of the reaction partners, in particular the carbonyl-derived part. The formation of disulfides from thiols on the other hand is a redox sensitive process, with disulfides readily reducing to thiols within a reducing environment. We envisioned that these two orthogonal reversible reactions could be used to develop a dual stimuli-responsive polymeric nanoparticle prepared from the cross-linking of multiple polymer chains through both imine and disulfide bonds, and which would require the simultaneous application of both low pH and a reducing environment to trigger its complete disassembly into its component polymer chains. A further advantage of employing reversible covalent bonds to facilitate cross-linking is that the strength of the covalent bond ensures the product assemblies possess chemical robustness, an important issue when considering possible applications. The feasibility of using reversible reactions to impart stimuli-responsive properties into polymeric nanoparticles has already been demonstrated. We have previously shown that reversible imine bond formation can be used to facilitate the formation of core cross-linked star (CCS) polymers[10,11] and discrete nanoparticles,[12] affording assemblies which are stable at pH 11 and whose disassembly can be triggered by lowering the pH to 5. The group of Thayumanavan has demonstrated[13,14] that polymer chains can be intermolecularly cross-linked through disulfide bond formation and used a redox trigger in the form of the peptide glutathione to cause their disassembly. In other work, the group of Davis and Boyer have shown[19,20] that both acetal and disulfide linkages can be incorporated into star polymers possessing pH and redox responsiveness.

In this work we show that polymer chains can be intermolecularly cross-linked using both imine and disulfide bonds and that the resulting polymeric nanoparticles can complex a cargo of hydrophobic molecules. We then show that the disassembly of these nanoparticles can be triggered using the simultaneous application of both low pH and a reducing agent, causing the release of encapsulated guest molecules. Control experiments demonstrate that the application of either

dx.doi.org/10.1021/ma202721s | *Macromolecules* 2012, 45, 2699–2708

low pH or a reducing environment does not trigger disassembly of the polymeric nanoparticles. We also demonstrate that these polymeric nanoparticles can be functionalized with a 5 kDa PEG, suggesting that the surfaces of these particles can be decorated as required for their possible eventual applications.

EXPERIMENTAL SECTION

All chemicals were purchased from Sigma-Aldrich or Alfa Aesar and were used as received without further purification. *N*,*N*′-Dimethylacrylamide was purified by vacuum distillation at 60 °C prior to use. ^{1}H and ^{13}C NMR spectra were recorded on a Bruker Advance 300 spectrometer at 300 and 75 MHz, respectively, with the residual solvent signal as an internal standard. FTIR spectroscopy was performed on a Varian 800 FTIR instrument (Varian Inc.). High-resolution mass spectrometry was performed on a Waters LCT premier mass spectrometer (Waters Inc.). Gel permeation chromatography (GPC) was conducted on a Varian ProStar instrument (Varian Inc.) equipped with a pair of PL gel 5 μm Mixed D 300 × 7.5 mm columns with guard column (Polymer Laboratories Inc.) in series, a Varian 325 UV−vis dual wavelength detector (254 nm), a Dawn Heleos II multiangle laser light scattering detector (Wyatt Technology Corp.), and a Viscotek 3580 differential RI detector. DMF (containing LiBr (1 g/L)) was used as the eluent at 0.6 mL/min. Near monodisperse methyl methacrylate standards (Agilent Technologies) were used for calibration. Data collection was performed with Galaxie software (Varian Inc.) and chromatograms analyzed with the Cirrus software (Varian Inc.) and Astra software (Wyatt Technology Corp.). Fluorescence emission spectra were recorded on a FluoroMax fluorescence spectrophotometer (SPEX) (λ = 550 nm). pH Measurements were recorded with a Hanna HI 98103 instrument that was calibrated daily with commercial buffer solutions (Sigma-Aldrich). Hydrodynamic radii (R_h) of cross-linked polymer nanoparticles in aqueous solutions were determined by dynamic light scattering (DLS). The DLS instrumentation consisted of a Malvern Instruments HPPS-ET 5002 operating at 20 °C with a 633 nm laser module. Measurements were made at a detection angle of 173° (back-scattering), and Malvern DTS 4.20 software was utilized to analyze the data. All determinations were made in duplicate.

Synthesis of Methyl-4-(dimethoxymethyl)benzoate (1).[21] A solution of 4-carboxybenzaldehyde (15.4 g, 102.6 mmol), trimethylorthoformate (32.7 g, 307.8 mmol), and concentrated H_2SO_4 (8 drops) in MeOH (100 mL) was heated under reflux conditions for 48 h. The reaction mixture was transferred to a separating funnel with saturated $NaHCO_{3(aq)}$ (100 mL). The aqueous layer was extracted with CH_2Cl_2 (3 × 150 mL). The organic extracts were combined and dried over Na_2SO_4, filtered, and evaporated to dryness to afford a crude liquid which was purified by vacuum distillation to afford the title product as a colorless liquid (19.8 g, 92%). ^{1}H NMR ($CDCl_3$): δ 3.30 (s, 6H, $CH(OCH_3)_2$), 3.89 (s, 3H, OCH_3), 5.42 (s, 1H, $CH(OCH_3)_2$), 7.51 (d, 2H, Ar, J = 8.1 Hz), 8.02 (d, 2H, Ar, J = 8.1 Hz). ^{13}C NMR ($CDCl_3$): δ 52.2, 53.0, 103.0, 127.1, 129.8, 130.8, 143.8, 167.1. FT-IR (wavenumber, cm^{-1}): 2947 (C−H), 2905 (C−H), 2834 (C−H), 1724 (C═O), 1452 (C═C), 1436 (C═C), 1410 (C═C).

Synthesis of *N*-Ethylacrylamide-2-(4-(dimethoxymethyl)-benzamide) (2). A solution of methyl-4-(dimethoxymethyl)benzoate (**1**, 6.0 g, 28.5 mmol) in 1,2-diaminoethane (100 mL) was heated under reflux for 24 h and then evaporated to dryness. The viscous yellow oil obtained was dissolved in CH_2Cl_2 (100 mL) and Et_3N (5.7 g, 56.3 mmol) added. The solution was cooled to 0 °C in an ice bath. Acryloyl chloride (2.6 g, 28.5 mmol) in CH_2Cl_2 (50 mL) was added dropwise over 30 min. The reaction was stirred overnight at room temperature and then transferred to a separating funnel with saturated $NaHCO_3$(aq) (150 mL). The aqueous layer was extracted with CH_2Cl_2 (2 × 150 mL), and the organic extracts were combined and dried over Na_2SO_4, filtered, and evaporated to dryness to afford a crude solid which was purified by column chromatography [SiO_2, EtOAc−Et_3N (95:5)] to afford the title product as a white solid (3.3 g, 40%). ^{1}H NMR ($CDCl_3$): δ 3.28 (s, 6H, $CH(OCH_3)_2$), 3.52 (m, 4H, $(CH_2)_2$), 5.37 (s, 1H, $CH(OCH_3)_2$), 5.58 (dd, 1H, J = 1.8 Hz, J = 9.9 Hz), 6.14 (dd, 1H, J = 9.9 Hz, J = 17.0 Hz), 6.23 (dd, 1H, J = 1.8 Hz, J = 17.0 Hz), 7.37 (s, 1H, NH), 7.45 (d, 2H, Ar, J = 8.1 Hz), 7.79 (d, 2H, Ar, J = 8.1 Hz), 7.84 (s, 1H, NH). ^{13}C NMR ($CDCl_3$): δ 41.3, 53.1, 103.1, 127.3, 128.2, 130.0, 131.3, 134.6, 142.1, 167.5, 168.6. FT-IR (wavenumber, cm^{-1}): 3290 (N−H), 3096 (C−H, alkene), 2947 (C−H, alkyl), 1634 (C═O), 1593 (C═O), 1448 (C═C, aromatic), 1413 (C═C, aromatic). HRMS$^+$ $C_{15}H_{21}N_2O_4$: Theoretical: 293.1501. Actual: 293.1503.

Synthesis of *N*-Ethylacrylamide-2-(4-formylbenzamide) (M1). A solution of *N*-ethylacrylamide-2-(4-(dimethoxymethyl)-benzamide) (**2**, 1.4 g, 4.8 mmol) in 1 M $HCl_{(aq)}$ (20 mL) was stirred at room temperature for 2 h and then neutralized with saturated $NaHCO_3$(aq) (100 mL). The aqueous layer was extracted with EtOAc (3 × 150 mL), and the organic extracts were combined and dried over $MgSO_4$, filtered, and evaporated to dryness to afford the title product as a white solid (1.0 g, 84%). ^{1}H NMR (DMSO-d_6): δ 3.72 (m, 4H, $(CH_2)_2$), 5.59 (dd, 1H, J = 2.5 Hz, J = 9.8 Hz), 6.09 (dd, 1H, J = 2.5 Hz, J = 17.1 Hz), 6.23 (dd, 1H, J = 9.8 Hz, J = 17.1 Hz), 7.99 (d, 2H, Ar, J = 8.4 Hz), 8.03 (d, 2H, Ar, J = 8.4 Hz), 8.23 (s, ^{1}H, NH), 8.79 (s, 1H, NH), 10.07 (s, 1H, CHO). ^{13}C NMR (DMSO-d_6): δ 38.7, 125.2, 128.3, 129.6, 132.3, 138.2, 140.1, 165.5, 166.1, 193.0. FT-IR (wavenumber, cm^{-1}): 3264 (N−H), 3091 (C−H, alkene), 2943 (C−H, alkyl), 1699 (C═O, aldehyde), 1627 (C═O, amide), 1549 (C═O, amide), 1447 (C═C, aromatic), 1414 (C═C, aromatic). HRMS$^+$ $C_{13}H_{15}N_2O_3$: Theoretical: 247.1083. Actual: 247.1085.

Synthesis of *N*-(*tert*-Butoxycarbonyl)-1,3-diaminopropane (3).[22] A solution of 1,3-diaminopropane (25.0 g, 337 mmol) in $CHCl_3$ (200 mL) was cooled to 0 °C in an ice bath. A solution of di-*tert*-butyl dicarbonate (10.5 g, 48 mmol) in $CHCl_3$ (100 mL) was added dropwise over 30 min, the reaction mixture was stirred overnight at room temperature and then filtered, and the filtrate was evaporated to dryness. Saturated $NaCl_{(aq)}$ (150 mL) was added to the clear oil obtained, and the solution was filtered to remove the bis-protected product and transferred into a separating funnel with diethyl ether (150 mL). The aqueous layer was extracted with diethyl ether (2 × 150 mL). The organic extracts were combined and dried over Na_2SO_4, filtered, and evaporated to dryness to afford the title product as a colorless liquid (6.1 g, 73%). ^{1}H NMR ($CDCl_3$): δ 1.20 (s, 2H, NH_2), 1.38 (s, 9H, $C(CH_3)_3$), 1.54 (m, 2H, CH_2−CH_2−CH_2), 2.68 (m, 2H, CH_2N), 3.14 (m, 2H, CH_2N), 5.03 (s, 1H, NH). ^{13}C NMR ($CDCl_3$): δ 28.8, 31.5, 33.9, 40.0, 79.4, 156.5. FT-IR (wavenumber, cm^{-1}): 3358 (N−H), 3308 (N−H), 2975 (C−H), 2933 (C−H), 2869 (C−H), 1687 (C═O). HRMS$^+$ $C_8H_{19}N_2O_2$: Theoretical: 175.1447. Actual: 175.1449.

Synthesis of *N*-(*tert*-Butoxycarbonyl)-propylaminoacrylamide (M2). A solution of *N*-(*tert*-butoxycarbonyl)-1,3-diaminopropane (**3**, 3.1 g, 17.8 mmol) and Et_3N (2.2 g, 21.4 mmol) in CH_2Cl_2 (75 mL) was cooled to 0 °C in an ice bath. Acryloyl chloride (1.6 g, 17.8 mmol) in CH_2Cl_2 (50 mL) was added dropwise over 30 min, and the reaction was stirred overnight at room temperature and then transferred to a separating funnel with saturated $NaHCO_{3(aq)}$ (150 mL). The aqueous layer was extracted with CH_2Cl_2 (2 × 150 mL), and the organic extracts were combined and dried over Na_2SO_4, filtered, and evaporated to dryness to afford a crude solid which was purified by column chromatography [SiO_2, hexane−EtOAc (1:1)] to afford the title product as a white solid (3.2 g, 79%). ^{1}H NMR ($CDCl_3$): δ 1.37 (s, 9H, $C(CH_3)_3$), 1.59 (m, 2H, CH_2−CH_2−CH_2), 3.10 (m, 2H, CH_2N), 3.30 (m, 2H, CH_2N), 5.27 (s, 1H, NH), 5.56 (dd, 1H, J = 1.9 Hz, J = 9.8 Hz), 6.10 (dd, 1H, J = 9.8 Hz, J = 17.0 Hz), 6.20 (dd, 1H, J = 1.9 Hz, J = 17.0 Hz), 7.02 (s, 1H, NH). ^{13}C NMR ($CDCl_3$): δ 27.8, 30.5, 36.6, 37.9, 79.6, 125.9, 131.7, 157.0, 166.4. FT-IR (wavenumber, cm^{-1}): 3230 (N−H), 3066 (C−H, alkene), 2941 (C−H, alkyl), 1686 (C═O), 1652 (C═O). HRMS$^+$ $C_{11}H_{20}N_2O_3Na$: Theoretical: 251.1372. Actual: 251.1374.

Synthesis of 2-(Pyridyldithio)ethylamine Hydrochloride (4).[23] Cysteamine hydrochloride (2.3 g, 20.2 mmol) in MeOH (20 mL) was added dropwise over 30 min to a solution of aldrithiol (8.8 g, 39.9 mmol) and acetic acid (1.6 mL) in MeOH (40 mL). The reaction was stirred overnight at room temperature then evaporated to dryness

dx.doi.org/10.1021/ma202721s | *Macromolecules* 2012, 45, 2699−2708

to afford a yellow oil, which was dissolved in MeOH (15 mL) and precipitated into to diethyl ether (300 mL). The precipitate was isolated by filtration and precipitation was repeated five times to afford the title product as a white solid (3.1 g, 69%). ^{1}H NMR (D_2O): δ 3.05 (t, 2H, J = 6.3 Hz), 3.29 (t, 2H, J = 6.3 Hz), 7.23 (m, 1H), 7.63 (m, 1H), 7.74 (m, 1H), 8.36 (m, 1H). ^{13}C NMR (D_2O): δ 34.8, 37.4, 121.7, 122.2, 138.5, 149.2, 157.2. FT-IR (wavenumber, cm^{-1}): 3131 (N−H), 2950 (C−H, alkyl), 2913 (C−H, alkyl) 1448 (C═C, aromatic), 1417 (C═C, aromatic). HRMS$^+$ $C_7H_{11}N_2S_2$: Theoretical: 187.0364. Actual: 187.0369.

Synthesis of 2-Pyridyl Disulfide Ethylacrylamide (M3). A solution of 2-(pyridyldithio)ethylamine hydrochloride (**4**, 1.9 g, 8.5 mmol) and Et_3N (1.8 g, 17.8 mmol) in $CHCl_3$ (50 mL) was cooled to 0 °C in an ice bath. To this solution acryloyl chloride (0.77 g, 8.5 mmol) in $CHCl_3$ (50 mL) was added dropwise over 30 min. The reaction mixture was stirred overnight at room temperature and then transferred to a separating funnel with H_2O (150 mL). The aqueous layer was extracted with $CHCl_3$ (2 × 100 mL), and the combined organic extracts were dried over Na_2SO_4, filtered, and evaporated to dryness to afford a crude oil which was purified by column chromatography [SiO_2, EtOAc−hexane (1:1)] to afford the title product as a white solid (1.1 g, 54%). ^{1}H NMR ($CDCl_3$): δ 2.95 (t, 2H, CH_2S, J = 5.7 Hz), 3.63, (m, 2H, CH_2N), 5.65 (dd, 1H, J = 1.7 Hz, J = 10.0 Hz), 6.15 (dd, 1H, J = 10.0 Hz, J = 17.0 Hz), 6.30 (dd, 1H, J = 1.7 Hz, J = 17.1 Hz), 7.14 (m, 1H), 7.49 (m, 1H), 7.61 (m, 1H), 8.49 (m, 1H). ^{13}C NMR ($CDCl_3$): δ 37.9, 39.4, 121.6, 126.1, 131.7, 137.2, 150.1, 159.8, 165.9. FT-IR (wavenumber, cm^{-1}): 3273 (N−H), 3048 (C−H, alkene), 2925 (C−H, alkyl), 1656 (C═O), 1446 (C═C), 1417 (C═C). HRMS$^+$ $C_{10}H_{13}N_2OS_2$: Theoretical: 241.0469. Actual: 241.0473.

Synthesis of Aldehyde/Disulfide-Functionalized Copolymer (P1). *S*-1-Dodecyl-*S*′-(α,α-dimethyl-α″-acetic acid)trithiocarbonate (DDMAT) (1 equiv, 20.7 mg, 57 μmol) and AIBN (0.2 equiv, 1.87 mg, 11.4 μmol) were added to a small Schlenk tube. *N*,*N*′-Dimethylacrylamide (160 equiv, 0.90 g, 9.12 mmol), *N*-ethylacrylamide-2-(4-formylbenzamide) (**M1**, 20 equiv, 0.28 g, 1.14 mmol), and 2-pyridyl disulfide ethylacrylamide (**M3**, 20 equiv, 0.27 g, 1.14 mmol) were then added followed by DMF (4 mL). The reaction mixture was degassed five times, and then the vessel was backfilled with N_2 and allowed to warm to room temperature. The reaction mixture was then placed in an oil bath at 70 °C, and the polymerization was quenched after 21 h. The reaction mixture was dissolved in a minimal amount of THF and added dropwise to a large excess of ice-cold diethyl ether. The polymer precipitate was then isolated by filtration, and the precipitation was repeated before drying under high vacuum. Polymer **P1** was obtained as a pale yellow solid (1.06 g). ^{1}H NMR ($CDCl_3$): δ 0.84 (br, CH_2CH_3, of the chain terminus), 1.64 (br, $CHCH_2$), 2.41 (br, $CHCH_2$), 2.87 (br, $N(CH_3)_2$), 3.46 (br, $(CH_2)_2$), 7.09 (br, Ar), 7.61 (br, Ar), 7.89 (br, Ar), 8.08 (br, Ar), 8.44 (br, Ar), 10.04 (br, CHO). The composition of **P1** can be determined by comparing the integration of the aldehyde protons of **M1** and the aromatic protons of **M3** with the integration of the $N(CH_3)_2$ protons of DMA. The monomer composition was determined to be 10.5:1:1 (DMA:**M1**:**M3**) which differs to the feed ratio, presumably due to the difference in reactivity between DMA and the monosubstituted *N*-alkylacrylamide monomers **M1** and **M3**.

Synthesis of Boc-amine/Disulfide-Functionalized Copolymer (P2a). *S*-1-Dodecyl-*S*′-(α,α-dimethyl-α″-acetic acid)-trithiocarbonate (DDMAT) (1 equiv, 24.0 mg, 66 μmol) and AIBN (0.2 equiv, 2.16 mg, 13.2 μmol) were added to a small Schlenk tube. *N*,*N*′-Dimethylacrylamide (160 equiv, 1.05 g, 10.56 mmol), *N*-(*tert*-butoxycarbonyl)-propylaminoacrylamide (**M2**, 20 eq, 0.30 g, 1.32 mmol), and 2-pyridyl-disulfide-ethylacrylamide (**M3**, 20 equiv, 0.32 g, 1.32 mmol) were then added followed by DMF (4 mL). The reaction mixture was degassed five times, and then the vessel was backfilled with N_2 and allowed to warm to room temperature. The reaction mixture was then placed in an oil bath at 70 °C, and the polymerization was quenched after 21 h. The reaction mixture was dissolved in a minimal amount of THF and added dropwise to a large excess of ice-cold diethyl ether. The polymer precipitate was then isolated by filtration, and the precipitation was repeated before drying under high vacuum. Polymer **P2a** was obtained as a pale yellow solid (1.28 g). ^{1}H NMR ($CDCl_3$): δ 0.83 (br, CH_2CH_3, of the chain terminus), 1.38 (br, $C(CH_3)_3$), 1.61 (br, $CHCH_2$), 2.42 (br, $CHCH_2$), 2.87 (br, $N(CH_3)_2$), 3.45 (br, $(CH_2)_3$), 7.10 (br, Ar), 7.61 (br, Ar), 8.45 (br, Ar). The composition of **P2a** can be determined by comparing the integration of the boc protons of **M2** and the aromatic protons of **M3** with the integration of the $N(CH_3)_2$ protons of DMA. The monomer composition was determined to be 10.5:1:1 (DMA:**M1**:**M3**) which differs from the feed ratio, presumably due to the difference in reactivity between DMA and the monosubstituted *N*-alkylacrylamide monomers **M2** and **M3**.

Synthesis of Amine/Disulfide-Functionalized Copolymer (P2b). **P2a** (1.07 g) was dissolved in $CHCl_3$ (5 mL) and TFA (5 mL) was added; the reaction mixture was left to stir for 4 h. After this time the solvent and excess TFA were removed on the rotary evaporator, and the oil obtained was dissolved in a minimal amount of $CHCl_3$ and added dropwise to a large excess of diethyl ether. The polymer precipitate was then isolated by filtration and dried under high vacuum. The polymer precipitate was then isolated by filtration, and the precipitation was repeated before drying under high vacuum. Polymer **P2b** was obtained as a pale yellow solid (0.92 g). ^{1}H NMR ($CDCl_3$): δ 0.86 (br, CH_2CH_3, of the chain terminus), 1.71 (br, $CHCH_2$), 2.44 (br, $CHCH_2$), 2.87 (br, $N(CH_3)_2$), 3.42 (br, $(CH_2)_3$), 7.11 (br, Ar), 7.63 (br, Ar), 8.44 (br, Ar).

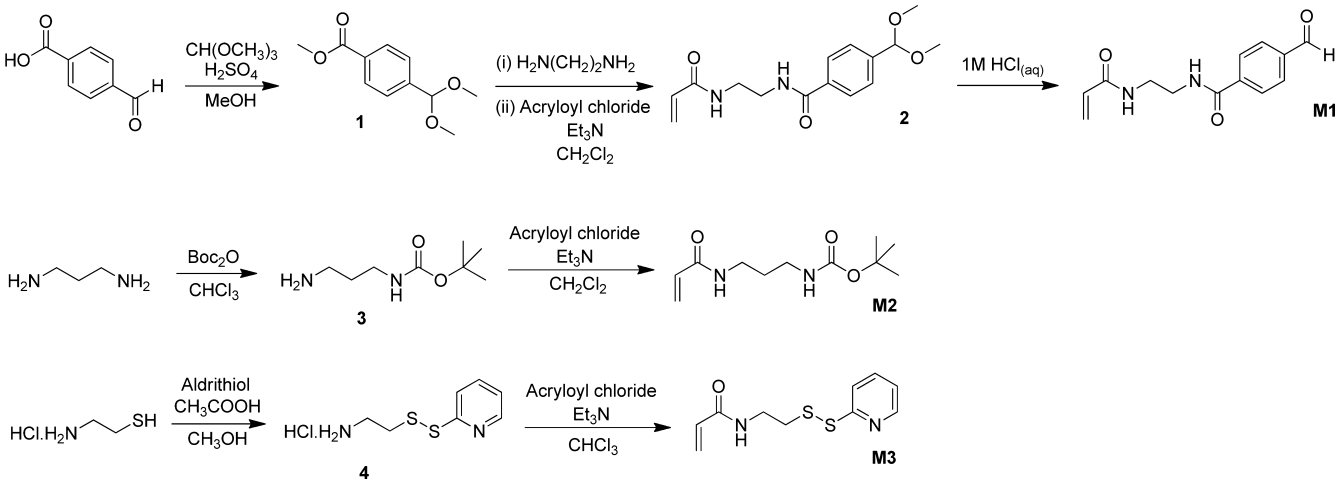
Synthesis of Hydrazide End-Functionalized Poly(ethylene glycol) (P3). Potassium *tert*-butoxide (15 equiv, 2.44 g, 21.75 mmol) in *tert*-butanol (17 mL) was added to poly(ethylene glycol) (5 kDa, 1 equiv, 7.25 g, 1.45 mmol) in toluene (90 mL). The resulting solution was purged with N_2 for 30 min before the dropwise addition of ethyl bromoacetate (27.5 equiv, 6.66 g, 39.88 mmol) over 30 min. The reaction was left to stir overnight at room temperature before filtration and evaporation to dryness. The oil obtained was dissolved in THF (30 mL) and added dropwise to a large excess of diethyl ether. The precipitation was repeated three times before the obtained precipitate was dried under high vacuum. The ethyl ester end-functionalized polymer (1 equiv, 4.45 g, 0.89 mmol) was then dissolved in methanol (70 mL), and hydrazine monohydrate (100 equiv, 4.45 g, 0.089 mol) in methanol (30 mL) was added and the reaction was left to stir overnight at room temperature. The reaction mixture was evaporated to dryness, dissolved in CH_2Cl_2 (100 mL), and transferred into a separating funnel. The organic layer was washed with H_2O (3 × 100 mL), dried with $MgSO_4$, filtered, and evaporated to dryness. The oil obtained was dissolved in THF (20 mL) and added dropwise to a large excess of diethyl ether. The precipitation was repeated three times and the precipitate obtained was dried under high vacuum. **P3** was obtained as a white solid (3.10 g). ^{1}H NMR ($CDCl_3$): δ 3.36 (br, OCH_3, of the chain terminus), 3.62 (br, $(CH_2)_2$), 4.06 (br, OCH_2CO, of the chain terminus), 8.39 (br, $CONHNH_2$, of the chain terminus).

Preparation of Imine Cross-Linked Nanoparticles (N1). Polymer **P1** (1 equiv, 43.8 mg, 2.34 μmol) and Nile Red (9.1 mg) were dissolved in THF (400 μL), to which was added H_2O (4.49 mL). Polymer **P2a** (1 equiv, 46.8 mg, 2.34 μmol) was dissolved in H_2O (4.48 mL). These two solutions were combined with rapid stirring to afford a solution with a 1 wt % concentration with respect to total copolymer building blocks. The pH was adjusted to 8.0 with small aliquots (5 μL) of 0.1 M $NaOH_{(aq)}$. The pH was adjusted to 8.0, and the reaction was left to stir for 16 h open to the atmosphere to allow the organic solvent to evaporate. After this time the reaction mixture was sealed and heated to 40 °C for 3 h. The sample was analyzed by gel permeation chromatography (GPC) and dynamic light scattering.

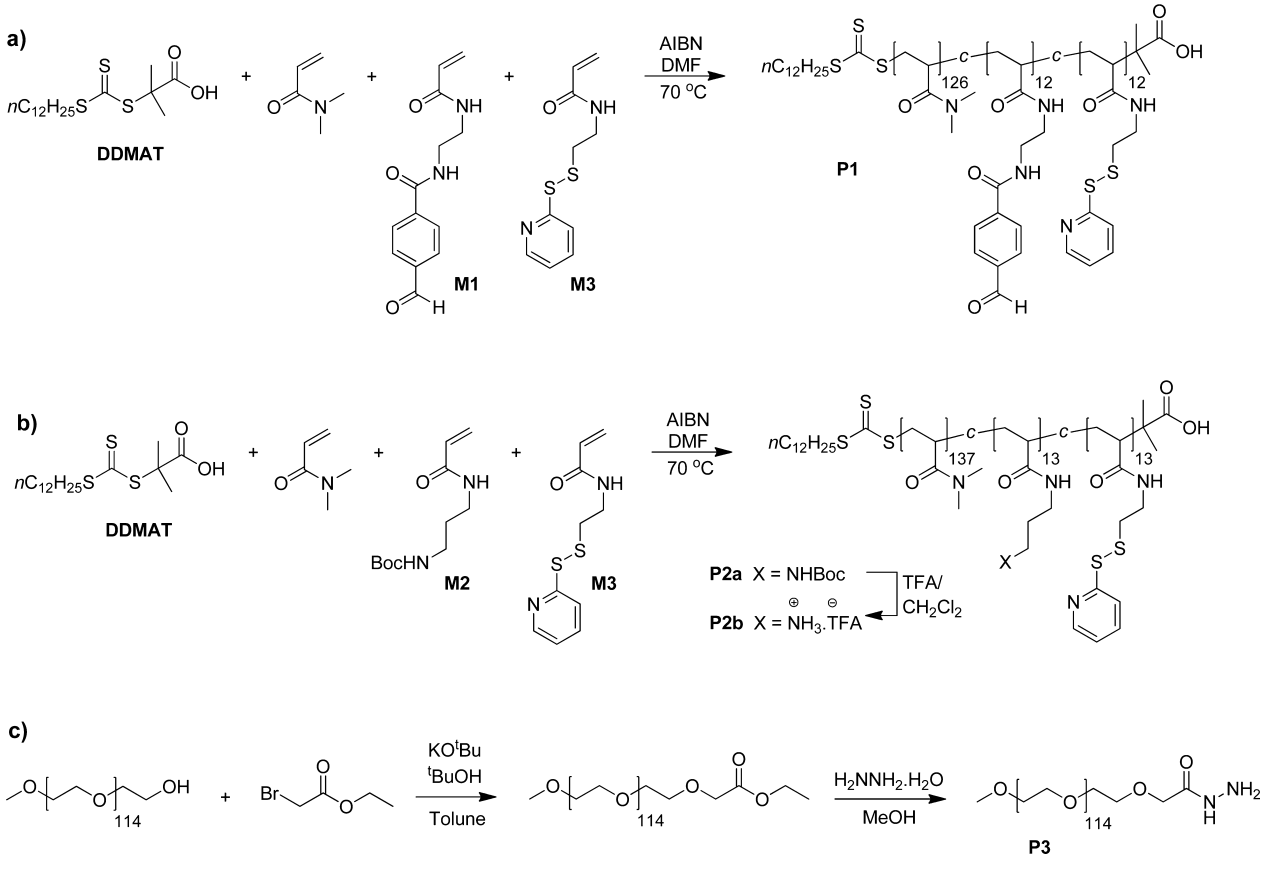
Preparation of Imine/Disulfide Cross-Linked Nanoparticles (N2). To a sample of imine cross-linked nanoparticles (**N1**, 1 wt %, pH 8.0, 7.5 mL) was added dithiothreitol (0.5 equiv per disulfide bond, 3.6 mg), and the reaction was left to stir at room temperature for 16 h. After this time the reaction mixture was filtered to remove excess Nile Red, and the reaction mixture was analyzed by GPC, fluorescence emission spectroscopy (λ = 550 nm), and dynamic light scattering.

Preparation of Disulfide Cross-Linked Nanoparticles (N3). The pH of a sample of imine/disulfide cross-linked nanoparticles (**N2**,

Scheme 1. Synthesis of Functional Acrylamide-Based Monomers (M1, M2, and M3)



Scheme 2. Synthesis of Linear Copolymer Building Blocks (a) P1 and (b) P2 and (c) Hydrazide End-Functionalized Poly(ethylene glycol) (P3)



1 wt %, pH 8.0, 6 mL) was adjusted to 5.5 with small aliquots (5 μL) of 0.1 M $HCl_{(aq)}$. The reaction was left to re-equilibrate at room temperature for 16 h before analysis by GPC, fluorescence emission spectroscopy (λ = 550 nm), and dynamic light scattering.

Disassembly of Disulfide Cross-Linked Nanoparticles (N4). To a sample of disulfide cross-linked nanoparticles (**N3**, 1 wt %, pH 5.5, 2 mL) was added TCEP (tris(2-carboxyethyl)phosphine) (5 equiv per disulfide bond, 9.0 mg). The reaction was left to stir at room temperature for 16 h, and during this time the reaction was periodically analyzed by fluorescence emission spectroscopy (λ = 550 nm). After 16 h, the reaction mixture was filtered to remove Nile Red precipitate, before analysis by GPC.

Preparation of Poly(ethylene glycol) Functionalization Nanoparticles (N5). To a sample of disulfide cross-linked nanoparticles (**N3**, 1 wt %, pH 5.5, 2 mL, prepared without Nile Red present) was added hydrazide end-functionalized poly(ethylene glycol) (**P3**, 1 equiv per aldehyde function, 31.3 mg). The reaction was left to stir at room for 16 h before analysis by GPC and dynamic light scattering.

Disassembly Poly(ethylene glycol)-Functionalized Nanoparticles (N6). To a sample of poly(ethylene glycol) functionalization disulfide cross-linked nanoparticles (**N5**, pH 5.5, 1 mL) was added TCEP (tris(2-carboxyethyl)phosphine) (5 equiv per disulfide bond, 4.5 mg). The reaction was left to stir at room for 16 h before analysis by GPC.

dx.doi.org/10.1021/ma202721s | *Macromolecules* 2012, 45, 2699–2708

Table 1. Synthesis and Characterization of Polymers P1 and P2a

polymer	chain transfer agent	monomers	initiator	time (h)	temp (°C)	solvent	M_n[a] (g mol^{-1})	M_n[b] (g mol^{-1})	M_w[b] (g mol^{-1})	D[b] (M_w/M_n)	R_h[c] (nm)
P1	DDMAT (1 equiv)	DMA (160 equiv), **M1** (20 equiv), **M3** (20 equiv)	AIBN (0.2 equiv)	21	70	DMF	18 700	14 500	20 200	1.39	4.2
P2a	DDMAT (1 equiv)	DMA (160 equiv), **M2** (20 equiv), **M3** (20 equiv)	AIBN (0.2 equiv)	21	70	DMF	20 000	16 200	24 200	1.49	4.5

[a]As determined by ^{1}H NMR spectroscopy. [b]As determined by gel permeation chromatography in DMF (0.6 mL/min) containing LiBr (1 g/L) calibrated against methyl methacrylate standards. [c]As determined by online dynamic LS measurements.

Preparation of Imine Cross-Linked Nanoparticles (N7). TCEP (5 equiv per disulfide bond, 9.0 mg) was dissolved in H_2O (0.5 mL), and the pH was adjusted to 8.0 with small aliquots (5 μL) of 0.1 M $NaOH_{(aq)}$. This was added to a sample of imine/disulfide cross-linked nanoparticles (**N2**, 1 wt %, pH 8.0, 2 mL, prepared with Nile Red present). The reaction was left stir at room temperature for 16 h before analysis by GPC and dynamic light scattering.

Disassembly of Imine Cross-Linked Nanoparticles (N8). The pH of a sample of imine cross-linked nanoparticles (**N7**, 1 wt %, pH 8.0, 6 mL) was adjusted to 5.5 with small aliquots (5 μL) of 0.1 M $HCl_{(aq)}$. The reaction was left to re-equilibrate at room temperature for 16 h before analysis by GPC and dynamic light scattering.

RESULTS AND DISCUSSION

Our first objective was to synthesize (Scheme 1) acrylamide-based monomers for the eventual preparation of linear copolymer building blocks displaying the required pendant functional groups. Monomer **M1** was prepared starting from 4-carboxybenzaldehyde, which was refluxed in the presence of trimethylorthoformate to form methyl 4-(dimethoxymethyl)-benzoate (**1**). This compound was then transformed into **2** using a two-step procedure involving reflux in ethylenediamine and then acylation of the resulting primary amine with acryloyl chloride. Hydrolysis of the dimethyl acetal function in 1 M HCl afforded the monomer **M1**. The mono-*N*-boc-protection of 1,3-diaminopropane afforded compound **3** which was acylated with acryloyl chloride to furnish the monomer **M2**. Monomer **M3** was prepared starting from cysteamine hydrochloride, which was treated with aldrithiol to introduce the pyridyl disulfide functionality within compound **4**, and then acylated by reaction with acryloyl chloride to yield the final monomer **M3**. It has been demonstrated that pyridyl disulfide-containing monomers[24,25] can be subjected to controlled living radical polymerizations, and the utility of the pyridyl disulfide functionality to prepare disulfide linkages is well-known.[26,27] All steps to prepare the monomers were synthetically straightforward and relatively high yielding, allowing their preparation on the gram scale.

Living radical polymerization methods provide access to well-defined copolymers possessing uniform molecular weights.[28−30] In particular, reversible addition−fragmentation chain transfer (RAFT) polymerization is appealing because of its versatility and experimental simplicity, and has been an incredibly useful tool to prepare building blocks for the construction of well-defined polymeric materials.[31] The RAFT chain transfer agent *S*-1-dodecyl-*S*′-(*α*,*α*-dimethyl-*α*″-acetic acid)trithiocarbonate (DDMAT)[32] was used (Scheme 2a) to mediate the copolymerization of a 1:1:8 mixture of **M1**:**M3**:DMA (*N*,*N*′-dimethylacrylamide) at 70 °C in DMF to afford the copolymer **P1**. ^{1}H NMR spectroscopy (Supporting Information Figure S4) revealed the polymer possessed a comonomer composition of 1:1:10.5 (**M1**:**M3**:DMA) and confirmed the presence of the pendant aromatic aldehyde and pyridyl disulfide functional groups. The copolymer **P2a** was also prepared (Scheme 2b) via RAFT polymerization of **M2**, **M3**, and DMA in a ratio of 1:1:8, respectively, in DMF at 70 °C. ^{1}H NMR spectroscopy (Figure S5) revealed the polymer possessed a comonomer composition of 1:1:10.5 (**M2**:**M3**:DMA) and confirmed the presence of the boc-protected alkylamine and pyridyl disulfide functional groups. Polymer **P2a** was treated with TFA/CH_2Cl_2 to afford polymer **P2b**, with ^{1}H NMR spectroscopy (Figure S6), confirming complete removal of the *N*-boc-protecting groups. Polymer **P3** was prepared (Scheme 2c) from poly(ethylene glycol) monomethyl ether (5 kDa) by treatment with excess ethyl bromoacetate to afford the ethyl ester intermediate, which after hydrazinolysis afforded the hydrazide end-functionalized poly(ethylene glycol) **P3**. Polymers **P1** and **P2a** were also characterized by GPC (Table 1 and Figure S7),[33] which confirmed monomodal distributions and acceptable polydispersity indicies. No meaningful GPC trace could be obtained from **P2b**, presumably on account of its polycationic nature, and thus its molecular weight and polydispersity index were inferred from the analysis of **P2a**.

Cross-linked nanoparticles were prepared by a two-step approach, where polymer chains were cross-linked through imine bond formation to form nanoparticle-like assemblies of polymer chains, which were then further cross-linked through the formation of disulfide bonds. Thus, copolymer **P1** and the hydrophobic dye Nile Red were dissolved in H_2O containing a minimal amount of THF to aid solubility. Copolymer **P2b** was dissolved in H_2O, and the two solutions were mixed to afford a solution with a 1 wt % concentration with respect to total copolymer building blocks and a 1:1 molar ratio of the two copolymers **P1** and **P2b**, with Nile Red present as a fine suspension (1 mg per 10 mg of copolymer). The pH of the solution was then adjusted to 8.0 with aliquots (5 μL) of 0.1 M $NaOH_{(aq)}$ and the solution left to stir at room temperature for 16 h whilst open to the atmosphere to allow the THF to evaporate. After this time the reaction was sealed and heated to 40 °C for 3 h to optimize the encapsulation of Nile Red. Gel permeation chromatography (GPC) (Figure 2a) confirmed the disappearance of the linear copolymer building blocks of retention time ∼25 min and the appearance of a peak at shorter retention time ∼17 min, confirming the presence of a high molecular weight polymeric nanoparticle (**N1**) whose constituent polymer chains are crossed-linked through the formation of imine bonds and which possesses a hydrodynamic radius of 74 nm and a PDI of 0.137 as indicated by batch dynamic light scattering (Figure 3a). The presence of a minor peak in the GPC chromatogram at retention time ∼25 min suggests all polymer chains are not incorporated into **N1**. We hypothesize that this minor species corresponds to a dimeric species formed from the cross-linking of one chain of **P1** with one chain of **P2b**, which is consistent with observations previously made by us during our studies of the cross-linking of polymers displaying multiple amine functions with polymers

dx.doi.org/10.1021/ma202721s | Macromolecules 2012, 45, 2699−2708

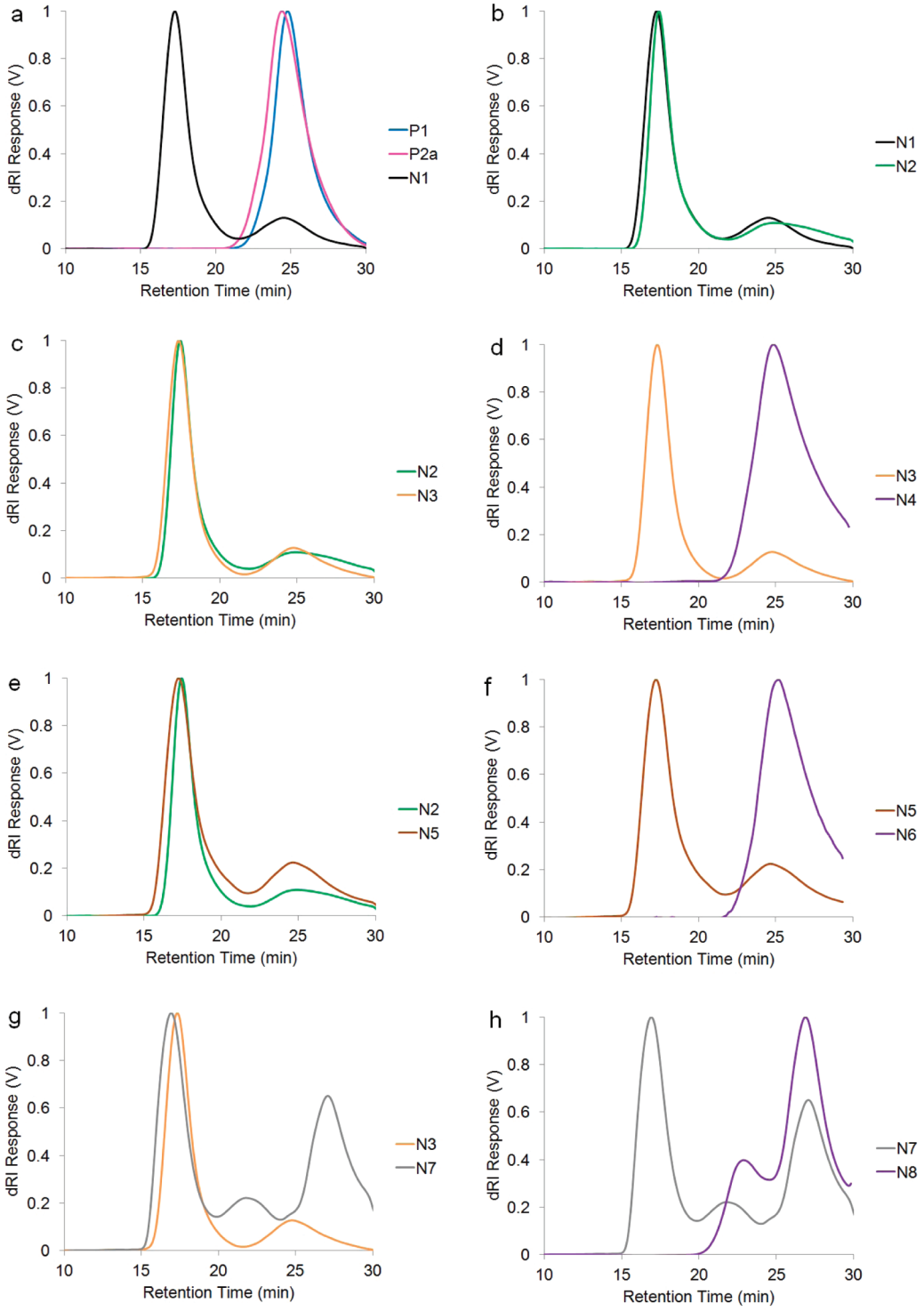


Figure 2. Differential refractive index (dRI) gel permeation chromatography (GPC) traces in DMF (0.6 mL/min, containing LiBr 1 g/L) for formation of nanoparticles (a) **N1**, (b), **N2**, (c) **N3**, (d) nanoparticle disassembly **N4**, (e) nanoparticle **N5**, (f) nanoparticle disassembly **N6**, (g) nanoparticle functionalization with PEG-hydrazide **N7**, and (h) disassembly of PEG functionalized nanoparticle **N8**.

displaying multiple aldehyde functions to form core cross-linked star polymers or nanogels.[10−12]

The polymer chains within the assembly **N1** were then further cross-linked through the formation of disulfide bonds using dithiothreitol (DTT), which was added to the reaction and left to stir at room temperature for 16 h. Under these reaction conditions DTT reduces rapidly the pendant pyridyl disulfide functional groups to the corresponding alkylthiols. Importantly, as the amount of DTT added (DTT, 0.5 equiv per pyridyl disulfide functionality) can reduce no more than half of the available pyridyl disulfide functions, those alkylthiol functions formed can then intermolecularly cross-link with remaining pyridyl disulfide functional groups through disulfide exchange. This process is driven by the formation of 2-pyridinethione, a stable and inert reaction byproduct, and the formation of highly stable 6-membered ring of the oxidized

dx.doi.org/10.1021/ma202721s | *Macromolecules* 2012, 45, 2699−2708

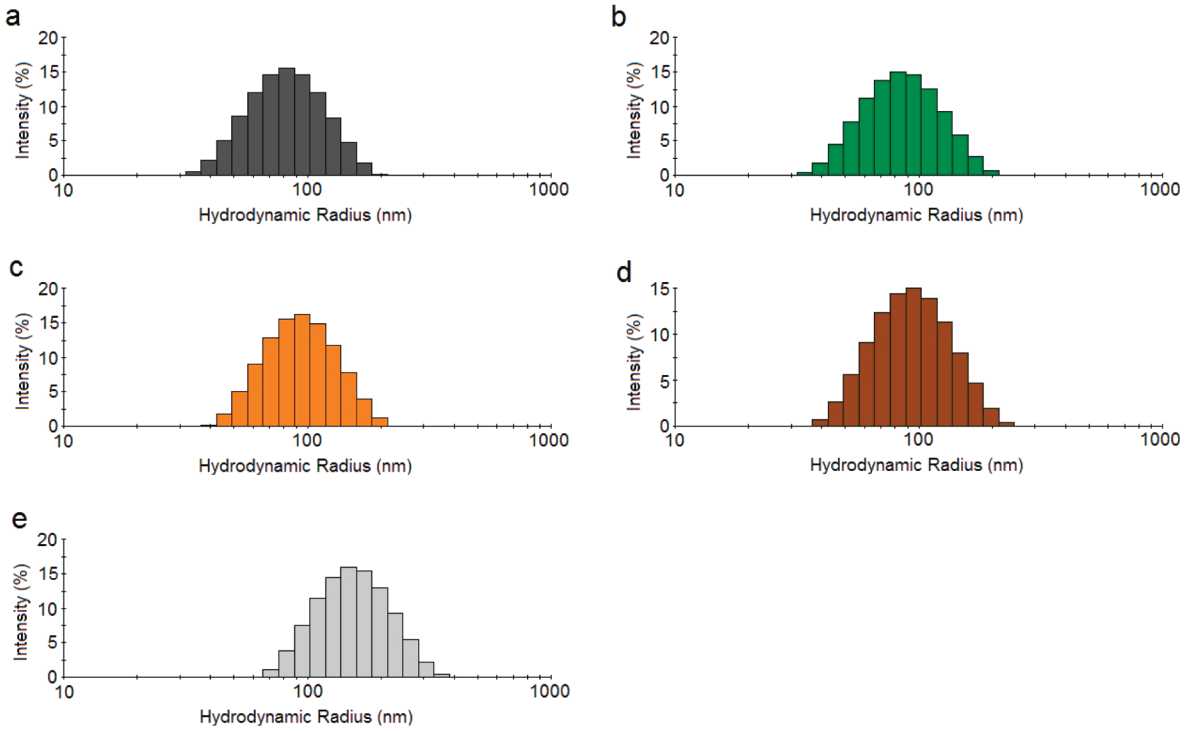


Figure 3. Histograms showing the particle size distributions of cross-linked polymeric nanoparticles (a) **N1**, (b) **N2**, (c) **N3**, (d) **N5**, and (e) **N7**, obtained from batch dynamic light scattering analysis.

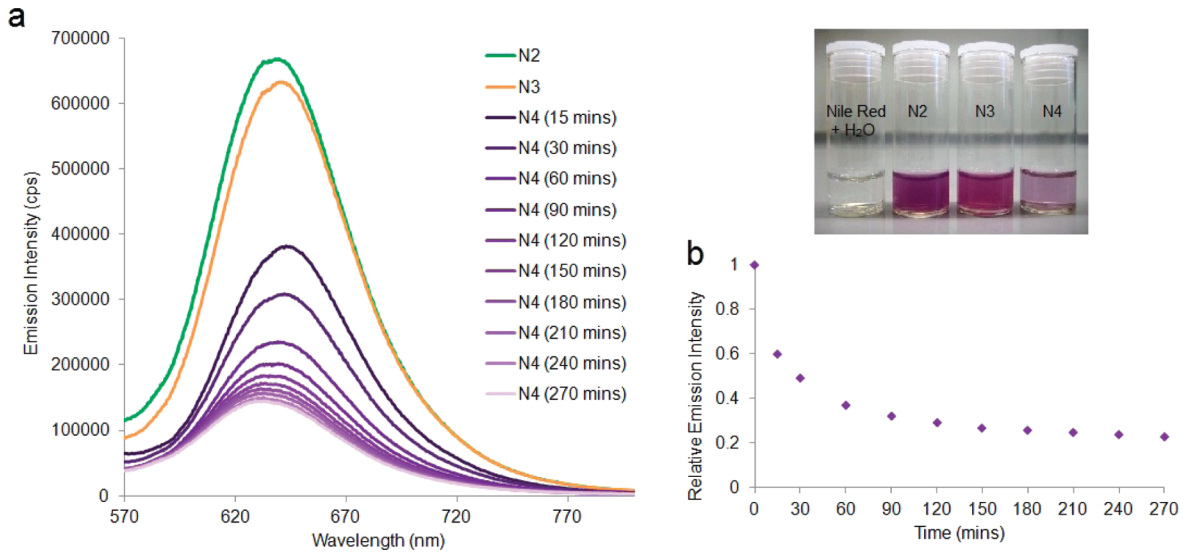


Figure 4. (a) Fluorescence emission spectra at λ_{ex} = 550 nm displaying uptake of Nile Red within **N2** (green peak) and **N3** (orange peak) and subsequent release after disassembly to **N4** (purple peaks). (b) The decrease in relative intensity plotted against time gives an insight into the kinetics of release. Photographs of solutions are also given (inset).

form of DTT.[13] The progress of this cross-linking reaction can be monitored by performing the reaction in D_2O in the absence of Nile Red while using ^1H NMR spectroscopy to observe the formation of the of 2-pyridinethione byproduct (Figure S8). It was noted during this experiment that none of the resonances associated with the aromatic moieties of copolymer **P1** can be observed, which suggests strongly that the cross-linking units are present within the interior of large polymer assemblies. GPC analysis (Figure 2b) displayed a near identical peak at retention time ~17 min corresponding to **N2**, which was revealed by batch dynamic light scattering (Figure 3b) to possess a hydrodynamic radius of 76 nm and a PDI of 0.140. The solution obtained displayed a bright red/purple color (Figure 4, inset), and fluorescence emission spectroscopy (Figure 4a) confirmed the presence of Nile Red as a result of its encapsulation within the polymeric nanoparticles.

We then performed experiments which demonstrate that the application of both low pH and a reductive environment are required to cause triggered disassembly of the polymeric nanoparticles and that application of either low pH or a reducing agent do not trigger nanoparticle disassembly. The pH of a solution of polymeric nanoparticles possessing imine and

dx.doi.org/10.1021/ma202721s | *Macromolecules* 2012, 45, 2699–2708

disulfide cross-links (**N2**) was adjusted to 5.5 with 0.1 M $HCl_{(aq)}$ aliquots (5 μL), reaction conditions which cause hydrolysis of the imine cross-links but do not affect the disulfide cross-links which are presumably present in sufficient density to maintain the structural integrity of the nanoparticle. After stirring for 16 h at room temperature, GPC analysis (Figure 2c) displayed a peak ~17 min corresponding to polymeric nanoparticle **N3**, which was shown by batch dynamic light scattering (Figure 3c) to possess a hydrodynamic radius of 84 nm and a PDI of 0.148. This observation confirms that the polymeric nanoparticle is kept intact through the disulfide cross-links even after imine hydrolysis occurs. After filtration, fluorescence emission spectroscopy (Figure 4a) displayed a slight reduction in intensity, an observation which suggests the release of a small amount (~5%) of Nile Red from the polymeric nanoparticle, presumably because the hydrolysis of the imine cross-links makes the nanoparticle more porous and reducing its ability to complex its cargo. We then applied a reductive stimulus which triggers the complete disassembly of the polymer nanoparticles. The reducing agent tris(2-carboxyethyl)phosphine (TCEP) (5 equiv per disulfide bond) was added to a solution of **N3** encapsulating a cargo of Nile Red, and the reaction was left to stir for 16 h at room temperature. TCEP is known to readily reduce disulfide bonds at both low and high pH.[34,35] GPC analysis (Figure 2d) shows the disappearance of the peak at retention time ~17 min, corresponding to the polymeric nanoparticle **N3**, and the appearance of a peak possessing a retention time of ~25 min, which corresponds to the formation of linear copolymers (**N4**). Fluorescence emission spectra were also recorded (Figure 4a) periodically, showing that the disassembly process was accompanied by a reduction in the intensity of the fluorescence associated with Nile Red which precipitated out of solution as the nanoparticle disassembled, further evidence suggesting complete disassembly. These observations suggest that the simultaneous application of both low pH and a reductive environment are required to trigger complete nanoparticle disassembly. This fluorescence experiment also gave an indication of the kinetics of the disassembly process (Figure 4b), with most of the dye being released during the first hour of the disassembly.

We then demonstrated that a reductive stimuli applied at high pH would not trigger the disassembly of the polymeric nanoparticles until low pH was also applied. A solution of nanoparticles **N2** (prepared under identical condition without Nile Red present) containing imine/disulfide cross-links was treated with TCEP at pH 8.0, reaction conditions which cause reduction of disulfide cross-links but do not affect the imine cross-links. After stirring for 16 h at room temperature, GPC analysis (Figure 2e) displayed a near identical peak at retention time ~17 min, corresponding to polymeric nanoparticle **N5**, and a minor peak at ~25 min, which is likely from a dimeric polymer assembly. Batch dynamic light scattering analysis of **N5** (Figure 3d) displayed a hydrodynamic radius of 79 nm and a PDI of 0.142. These observations confirm that the polymeric nanoparticles are kept intact through their imine cross-links after disulfide reduction occurs. Subsequent adjustment of the pH to 5.5 resulted in the complete disassembly of these polymeric nanoparticles through imine hydrolysis as confirmed by GPC analysis (Figure 2f), which displayed a peak (**N6**) at retention time ~25 min, corresponding to the presence of the component linear copolymer chains. Taken together, these experiments demonstrate that polymeric nanoparticles containing imine and disulfide cross-links require simultaneous application of both acidic pH and a reducing environment to trigger their complete disassembly.

Functional groups on or near the periphery of these polymeric nanoparticles present suitable handles to allow their further functionalization by decorating their surfaces with other potentially useful molecules and thus increasing their prospective utility. To demonstrate this possibility, we chose to adorn **N3** with a 5 kDa poly(ethylene glycol). Thus, **N3** (prepared without Nile Red present) containing disulfide cross-links and aldehyde and amine pendant functions was prepared and the hydrazide end-functionalized poly(ethylene glycol) (**P3**) (1 equiv per aldehyde) added at pH 5.5, a suitable pH to promote the formation of acylhydrazone bonds.[36] GPC analysis (Figure 2g) displayed a major peak with a decreased retention time of ~16.5 min, an observation suggesting the polymeric nanoparticle undergoes an increase in its size as a consequence of the 5 kDa PEG conjugating onto the aldehyde functions to form a new particle **N7**. This GPC chromatogram also displays excess PEG-hydrazide (~27 min) and a minor product at ~22 min, which is likely as a consequence of the conjugation of PEG onto a dimeric polymer species. Dynamic light scattering analysis (Figure 3e) of **N7** revealed a hydrodynamic radius of 140 nm and a PDI of 0.136, and we hypothesize that this large increase in hydrodynamic radius is on account of chains of **P3** incorporating both onto the periphery of the particle and into its pores, causing significant swelling. The complete disassembly of the functionalized particle **N7** was triggered by addition of TCEP (5 equiv per potential disulfide) as shown by GPC analysis (Figure 2h), which displayed (**N8**) two peaks corresponding to the excess PEG-hydrazide (~27 min) and **P1**-grafted with PEG-hydrazide (~23 min). We envisage that it should be possible to conjugate a range of polymers, or modified biomolecules, onto these polymeric nanoparticles through the formation of hydrolytically stable carbon−nitrogen double bonds such as hydrazones or oximes.

In conclusion, we have prepared polymeric nanoparticles by cross-linking component polymer chains through the formation of imine and disulfide bonds. We have exploited the orthogonal nature of these dynamic covalent reactions to show that the disassembly of the polymeric nanoparticles requires the simultaneous application of both a low pH and reducing environment. This unique dual stimuli-responsiveness makes these polymeric nanoparticles the forerunners of a new generation of "smart" delivery vehicles which may find application in e.g. the controlled intracellular delivery of high value cargos such as pharmaceuticals. It is well-known that nanoparticles can enter cells though the process of endocytosis, becoming encapsulated within endosomes which then undergo a pH drop from 7.4 to 5.5.[37,38] Upon escape from the endosome, the particles enter the cell cytosol, which is known to be a highly reducing environment relative to the blood-stream[39,40] on account of high concentrations of biological reductants such as glutathione.[41,42] The polymeric nanoparticles described here are well-placed to take advantage of the pH and redox differences between the intra- and extracellular environments, utilizing the orthogonal nature of their cross-links to ensure that their cargo is delivered in its desired locations with high levels of specificity. We hypothesize that such polymer-based drug delivery vehicles incorporating more than one dynamic covalent linkage could be manipulated to increase their abilities to target specific biological environments and are investigating this possibility.

■ ASSOCIATED CONTENT

Supporting Information

^{1}H NMR spectra of **M1**, **M2**, **M3**, **P1**, **P2a**, and **P2b**; ^{1}H NMR spectroscopy evidence of 2-pyridinethione release during **N2** formation. This material is available free of charge via the Internet at http://pubs.acs.org.

■ AUTHOR INFORMATION

Corresponding Author

*E-mail: d.a.fulton@ncl.ac.uk.

Notes

The authors declare no competing financial interest.

■ ACKNOWLEDGMENTS

Newcastle University (Studentship to A.W.J.) and One North East are gratefully thanked for support.

■ REFERENCES

(1) Terashima, T.; Kamigaito, M.; Baek, K.-Y.; Ando, T.; Sawamoto, M. *J. Am. Chem. Soc.* **2003**, *125*, 5288−5289.

(2) Helms, B.; Guillaudea, S. J.; Xie, Y.; McMurdo, M.; Hawker, C. J.; Fréchet, J. M. J. *Angew. Chem., Int. Ed.* **2005**, *44*, 6384−6387.

(3) Terashima, T.; Ouchi, M. M.; Ando, T.; Kamigaito, M.; Sawamoto, M. *Macromolecules* **2007**, *40*, 3581−3588.

(4) Fukukawa, K.; Rossin, R.; Hagooly, A.; Pressly, E.; Hunt, J.; Messmore, B.; Wooley, K.; Welch, M.; Hawker, C. J. *Biomacromolecules* **2008**, *9*, 1329−1339.

(5) Wiltshire, J. T.; Qiao, G. G. *Aust. J. Chem.* **2007**, *60*, 699−705.

(6) Oh, J. K.; Drumright, R.; Siegwart, D. J.; Matyjaszewski, K. *Prog. Polym. Sci.* **2008**, *33*, 448−477.

(7) Tyrrell, Z. L.; Shen, Y.; Radosz, M. *Prog. Polym. Sci.* **2010**, *35*, 1128−1143.

(8) (a) Spruell, J. M.; Hawker, C. J. *Chem. Sci.* **2011**, *2*, 18−26. (b) Pasparakis, G.; Vamvakaki, M. *Polym. Chem.* **2011**, *2*, 1234−1248.

(9) Klaikherd, A.; Nagamani, C.; Thayumanavan, S. *J. Am. Chem. Soc.* **2009**, *131*, 4830−4838.

(10) Jackson, A. W.; Fulton, D. A. *Chem. Commun.* **2010**, *46*, 6051−6053.

(11) Jackson, A. W.; Fulton, D. A. *Chem. Commun.* **2011**, *47*, 6807−6809.

(12) Jackson, A. W.; Stakes, C.; Fulton, D. A. *Polym. Chem.* **2011**, *2*, 2500−2511.

(13) Ryu, J.-H.; Jiwpanich, S.; Chacko, R.; Bickerton, S.; Thayumanavan, S. *J. Am. Chem. Soc.* **2010**, *132*, 8246−8247.

(14) Ryu, J.-H.; Chacko, R. T.; Jiwpanich, S.; Bickerton, S.; Babu, R. P.; Thayumanavan, S. *J. Am. Chem. Soc.* **2010**, *132*, 17227−17235.

(15) Amamoto, Y.; Higaki, Y.; Matsuda, Y.; Otsuka, H.; Takahara, A. *J. Am. Chem. Soc.* **2007**, *129*, 13298−13304.

(16) Amamoto, Y.; Kikuchi, M.; Masunaga, H.; Sasaki, S.; Otsuka, H.; Takahara, A. *Macromolecules* **2010**, *43*, 1785−1791.

(17) Higaki, Y.; Otsuka, H.; Takahara, A. *Macromolecules* **2006**, *39*, 2121−2125.

(18) Godoy-Alcántar, C.; Yatsimirsky, A. K.; Lehn, J.-M. *J. Phys. Org. Chem.* **2005**, *18*, 979−985.

(19) Syrett, J. A.; Haddleton, D. A.; Whittaker, M. R.; Davis, T. P.; Boyer, C. *Chem. Commun.* **2011**, *47*, 1449−1451.

(20) Duong, H. T. T.; Marquis, C. P.; Whittaker, M.; Davis, T. P.; Boyer, C. *Macromolecules* **2011**, *44*, 8008−8019.

(21) Crosby, I. T.; Pietersz, G. A.; Ripper, J. A. *Aust. J. Chem.* **2008**, *61*, 138−143.

(22) Boturyn, D.; Boudali, A.; Constant, J.; Defrancq, E.; Lhomme, J. *Tetrahedron* **1997**, *53*, 5485−5492.

(23) Zugates, G. T.; Anderson, D. G.; Little, S. R.; Lawhorn, I. E. B.; Langer, R. *J. Am. Chem. Soc.* **2006**, *128*, 12726−12734.

(24) Wong, L.; Boyer, C.; Jai, Z.; Zareie, H. M.; Davis, T. P.; Bulmus, V. *Biomacromolecules* **2008**, *9*, 1934−1944.

(25) Boyer, C.; Liu, J.; Wong, L.; Tippett, M.; Bulmus, V.; David, T. P. *J. Polym. Sci., Part A: Polym. Chem.* **2008**, *46*, 7207−7224.

(26) Jia, Z.; Liu, J.; Boyer, C.; Davis, T. P.; Bulmus, V. *Biomacromolecules* **2009**, *10*, 3253−3258.

(27) Boyer, C.; Liu, J.; Bulmus, V.; Davis, T. P. *Aust. J. Chem.* **2009**, *62*, 830−847.

(28) Moad, G.; Rizzardo, E.; Thang, S. H. *Aust. J. Chem.* **2005**, *58*, 379−410.

(29) Matyjaszewski, K.; Xai, J. *Chem. Rev.* **2001**, *101*, 2921−2990.

(30) Hawker, C. J.; Bosman, A. W.; Harth, E. *Chem. Rev.* **2001**, *101*, 3661−3688.

(31) Boyer, C.; Stenzel, M. H.; Davis, T. P. *J. Polym. Sci., Part A: Polym. Chem.* **2011**, *49*, 551−595.

(32) Lai, J. T.; Filla, D.; Shea, R. *Macromolecules* **2002**, *35*, 6754−6756.

(33) To avoid confusion between polydispersity indices of polymers as determined by GPC and polymer dispersity indices of polymeric nanoparticles as determined by dynamic light scattering measurements, we have chosen to use the nomenclature D for (M_w/M_n) for the former and PDI for the latter. The polydispersity measurement in dynamic light scattering is used to describe the width of the particle size distribution and is calculated by cumulants analysis of the autocorrelation function within the software of the instrument used to perform the measurements.

(34) Burns, J. A.; Butler, J. C.; Morgan, J.; Whitesides, G. M. *J. Org. Chem.* **1991**, *56*, 2648−2650.

(35) Han, J. C.; Han, G. H. *Anal. Biochem.* **1994**, *220*, 5−10.

(36) Rowan, S. J.; Cantrill, S. J.; Cousins, G. R. L.; Sanders, J. K. M.; Stoddart, J. F. *Angew. Chem., Int. Ed.* **2002**, *41*, 898−952.

(37) Schmaljohannm, D. *Adv. Drug Delivery Rev.* **2006**, *58*, 1655−1670.

(38) Bae, Y.; Fukushima, S.; Harada, A.; Kataoka, K. *Angew. Chem., Int. Ed.* **2003**, *42*, 4640−4643.

(39) Saito, G.; Swanson, J. A.; Lee, K.-D. *Adv. Drug Delivery Rev.* **2003**, *55*, 199−215.

(40) Sivakumar, S.; Bansal, V.; Cortez, C.; Chong, S.-F.; Zelikin, A. N.; Caruso, F. *Adv. Mater.* **2009**, *21*, 1820−1824.

(41) Heffernan, M.; Murthy, N. *Annu. Biomed. Eng.* **2009**, *37*, 1993−2002.

(42) Bernkop-Schnürch, A. *Adv. Drug Delivery Rev.* **2005**, *57*, 1569−1582.

Macromolecules

Article

pubs.acs.org/Macromolecules

p/n Switching of Ambipolar Bithiazole−Benzothiadiazole-Based Polymers in Photovoltaic Cells

Bijitha Balan,[†] Chakkooth Vijayakumar,[†] Akinori Saeki,*[,†,‡] Yoshiko Koizumi,[†,§] and Shu Seki*[,†]

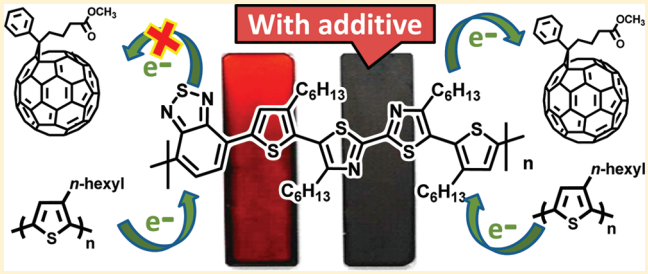
[†]Department of Applied Chemistry, Graduate School of Engineering, Osaka University, 2-1 Yamadaoka, Suita, Osaka 565-0871, Japan

[‡]PRESTO, Japan Science and Technology Agency (JST), 4-1-8 Honcho Kawaguchi, Saitama 332-0012, Japan

[§]Functional Soft Matter Research Group, RIKEN Advanced Science Institute, 2-1 Hirosawa, Wako, Saitama 351-0198, Japan

Supporting Information

ABSTRACT: Two new alternating copolymers **P1** and **P2**, of bithiazole (BT) and benzothiadiazoles (BTZ), differing in their side chain positioning at the thiophene units which sandwich the BT unit, were designed and synthesized. Both polymers exhibited broad absorption ranging from 300 to 700 nm with a narrow optical bandgap in the film state. Control over structural ordering of polymer chains was achieved in **P1** by treating with a small amount of additive (1,8-octanedithiol, ODT) as evident by a large red shift of absorption peak and also from the XRD measurements. In contrast, no such effects were observed in the case of **P2** in the presence of additive. Flash-photolysis time-resolved microwave conductivity (FP-TRMC) experiments revealed that the transient photoconductivity of **P1** is far superior to that of **P2**, which is further increased when processed with ODT. The charge carrier mobility, as determined by the space-charge-limited current (SCLC) technique, indicates that **P1** exhibits both electron and hole mobilities with a clear dominance of the latter. The charge carrier mobilities become higher and more balanced for ODT-modified **P1** films compared to that of **P1** alone. TRMC analysis revealed that the photoconductivity of **P1** reduced when blended with PCBM in the absence of additive, whereas significant enhancement was obtained in presence of additive. The blend with P3HT exhibited an increase in photoconductivity in both the presence and absence of additive. In complete accordance with the TRMC results, in the absence of additive, **P1** acted as an n-type material (P3HT as donor), whereas in presence of additive, it exhibited ambipolar nature acting as both n-type and p-type (P3HT as donor and PCBM as acceptor, respectively) material. Switching of the major charge carrier species was demonstrated simply by the presence of additive for **P1** in the present paper.



1. INTRODUCTION

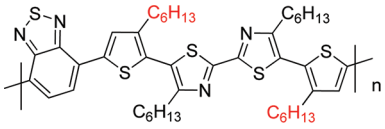
Harvesting solar energy using photovoltaic technology is considered as one of the most important ways to meet increasing global energy needs without contributing to greenhouse gases. Polymer-based bulk heterojunction (BHJ) solar cells have generated enormous interest in this context due to their potential for lightweight and flexible electronic devices through solution processes in a cost-effective way when compared to that of other renewable green energy sources.[1] An important advantage of using conjugated polymers in BHJs is that they can be structurally tailored to optimize the final device properties. Rational selection of donor (D) and acceptor (A) units and their alternate arrangement in the conjugated backbone of the polymers allow the modulation of optical bandgap and thereby electronic properties and photovoltaic performances. This D−A approach has been used in the development of a number of highly efficient organic photovoltaic (OPV) devices.[2] In order to improve the performance of polymer solar cells, many structural and morphological issues have to be addressed. For example, increasing the structural rigidity, molecular planarity, BHJ structure, optimization of processing conditions etc., plays a significant role in improving the device efficiency. Recent studies revealed that positioning of alkyl side chains attached to the conjugated backbone can play an important role in improving the photovoltaic efficiency by mainly tuning the planarity and hence the effective conjugation length and stacking of the polymer chains.[3] Similarly, the use of solvent additives such as diiodooctanes and alkanedithiols helps to control the BHJ structure and thereby improve charge separation and transport, leading to better device performance.[4]

Bithiazole (BT)-based polymers recently emerged as a new class of materials for BHJ solar cells due to its rigid, coplanar, and highly extended π-conjugated structures. However, only a limited number of BT based polymers are reported to be used in OPV devices. Because of the presence of (−C═N) imine functional group, BT acts as an acceptor and forms D−A type polymers with electron donors such as cyclopentadithiophenes, carbazoles, dithienosiloles, dithienopyrroles, thiazolothiazoles, and benzodithiophenes.[5] All these copolymers exhibit hole

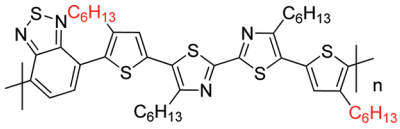
Received: December 23, 2011
Revised: February 16, 2012
Published: March 5, 2012

 © 2012 American Chemical Society dx.doi.org/10.1021/ma202778p | *Macromolecules* 2012, 45, 2709−2719

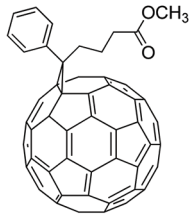
Chart 1. Structures of the Polymers (P1 and P2), PCBM, and P3HT Used in This Study



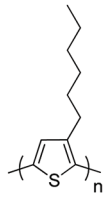
P1



P2



$PC_{60}BM$



P3HT

transport (p-type) behavior and shows excellent photovoltaic properties by mixing with n-type fullerene derivatives.

Herein we report the first example of an electron transporting (n-type) polymer **P1** based on BT for OPV applications by incorporating benzothiadiazole (BTZ) and *n*-hexylthiophene in the polymer backbone in an alternate fashion giving rise to D−A type copolymer. Interestingly, **P1** shows ambipolar (both p-type and n-type) characteristics when treated with solvent additives such as 1,8-octanedithiol (ODT). To study the effect of positioning of side chain, another polymer **P2** was synthesized consisting of same backbone but with alkyl side chains on the thiophene units occupied at a different position. Structures of **P1** and **P2** are shown in Chart 1. Regioregular poly(3-hexylthiophene) (P3HT) and [6,6]-phenyl-C_{61}-butyric acid methyl ester (PCBM) were used as p-type and n-type materials, respectively, for OPV device fabrication.

2. EXPERIMENTAL SECTION

2.1. Materials. All chemicals were purchased from Aldrich, Kanto Chemicals, TCI, or Wako and used as received. Air- and water-sensitive synthetic steps were performed in an argon atmosphere using standard Schlenk techniques.

2.2. Measurements. ^{1}H and ^{13}C NMR spectra were recorded on a 600 MHz Varian UNITY Inova spectrometer. All the chemical shifts were referenced to $(CH_3)_4Si$ (TMS; δ = 0 ppm) for ^{1}H or residual $CHCl_3$ (δ = 77 ppm) for ^{13}C. The molecular weights of the polymers were measured by gel permeation chromatography (GPC, Hitachi, L-2130, L-2350, L-2455) in tetrahydrofuran solution calibrated against polystyrene standards. Electronic absorption spectra were recorded on a JASCO V-570 spectrophotometer, and the emission spectra of the solution state were recorded on a Hitachi F-2700 spectrophotometer. Emission spectra in the film state were recorded on an II-equipped streak camera C7700 of Hamamatsu Photonics Inc. The films were excited by a third harmonic generation (THG, 355 nm) of a Nd:YAG laser (Spectra Physics Inc. INDI). Optical properties were measured in solution state and film state by using quartz cells (path length = 1 cm) and quartz plates, respectively. The film thickness was measured by a stylus surface profiler (ULVAC, Dektak 150). XRD measurements were done on a Rigaku RINT ultra X18SAXS-IP (Cu Kα: 1.5418 Å).

UV Photoelectron Spectroscopy (UPS). UPS was performed on an AC-2 of Riken Keiki Co., Ltd. For the UPS measurement, thin films of the polymers were spin-casted on an ITO-coated glass surface from *o*-dichlorobenzene (*o*-DCB) solution, and it was completely dried before mounting on the spectrometer. Photoelectrons emitted from the film were detected after illuminating the film with UV radiation. With photon energy increased with an interval of 0.1 eV, the photoelectron counts were measured.

Space-Charge-Limited Current (SCLC) Technique. The ITO glass substrate was cleaned in distilled water, tetrahydrofuran, detergent, deionized water, acetone, and isopropyl alcohol for 10 min each with ultrasonication. The dried ITO glasses were treated with UV-ozone for 30 min. PEDOT:PSS layer was cast on the ITO layer by spin-coating after passing through 0.2 μm filter. It was annealed on a hot plate at 150 °C for 30 min. An *o*-DCB solution of polymer was heated at 80 °C under stirring for at least 4 h to obtain a completely dissolved hot solution, which was filtered by using a 0.2 μm filter. The polymer layer (~100 nm) was cast on top of the PEDOT:PSS buffer layer in a nitrogen glovebox by spin-coating and allowed to evaporate the solvent slowly. The substrate was annealed on a hot plate at 150 °C for 10 min to completely remove the solvent. In hole-only or electron-only device, 100 nm Au layer or LiF (0.5 nm)/Al (100 nm) was deposited, respectively, through a shadow mask on top of the polymer layers by thermal evaporation in a vacuum chamber. The current−voltage (J−V) curves were measured using an ADCMT Corp. model 6241A. The hole or electron mobility was determined by fitting the J−V curve into the Mott−Gurney law:[6]

$$J = \frac{9}{8}\varepsilon_0\varepsilon_r\mu\frac{V^2}{L^3} \quad (1)$$

where ε_0 is the permittivity of free space, ε_r is the relative dielectric constant of the material, μ is the charge carrier (hole or electron) mobility, V is the voltage drop across the device, and L is the thickness of the polymer layer.

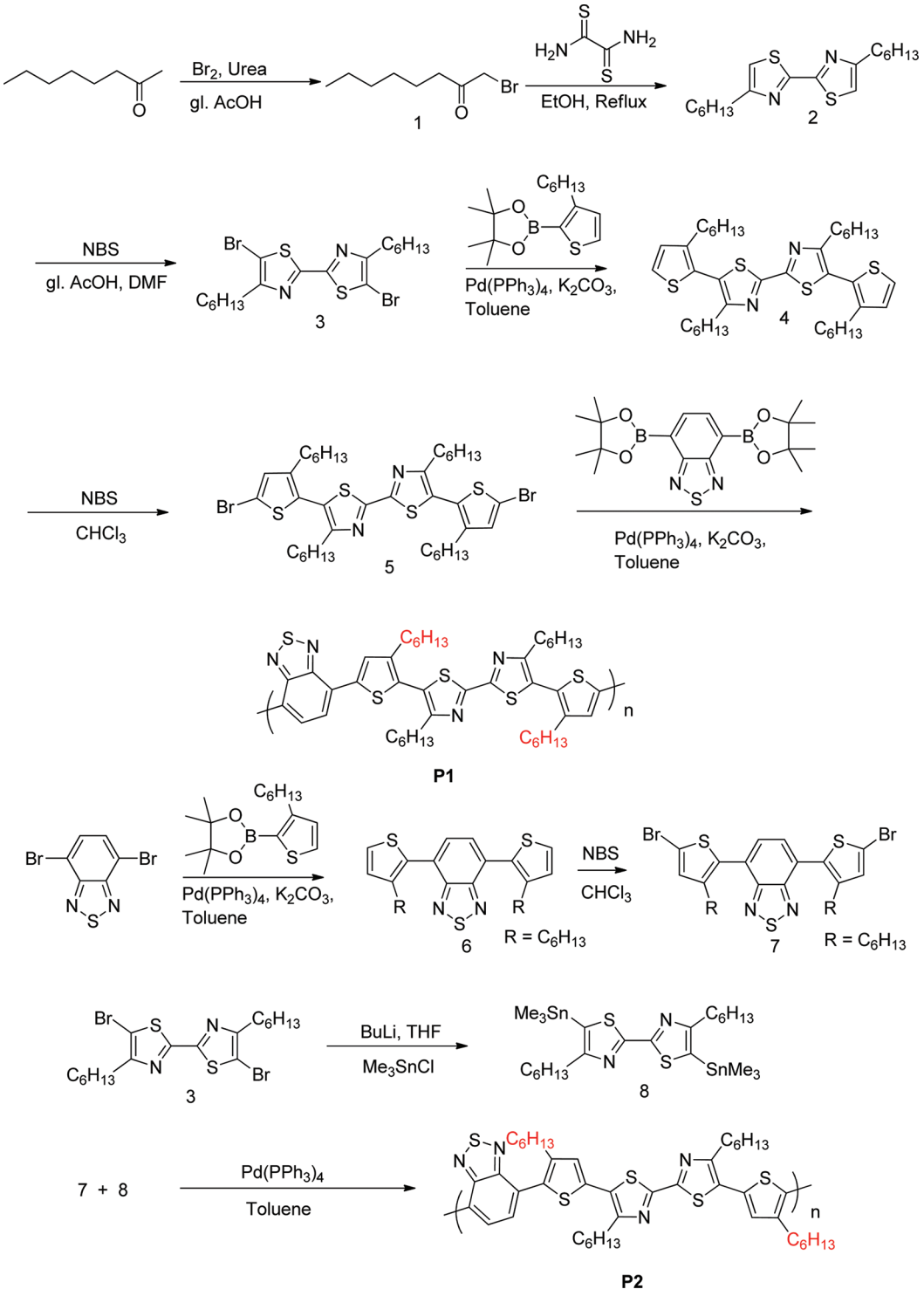
Flash-Photolysis Time-Resolved Microwave Conductivity. Transient conductivity was measured by flash-photolysis time-resolved microwave conductivity (FP-TRMC).[7] A resonant cavity was used to obtain a high degree of sensitivity in the measurement of conductivity. The resonant frequency and the microwave power were set at ~9.1 GHz and 3 mW, respectively, so that the electric field of the microwave was sufficiently small not to disturb the motion of charge carriers. The value of conductivity is converted to the product of the quantum yield (ϕ) and the sum of charge carrier mobilities ($\sum\mu$) by the equation

$$\phi\sum\mu = \frac{1}{eAI_0F_{light}}\frac{\Delta P_r}{P_r} \quad (2)$$

where e, A, I_0, F_{light}, ΔP_r, and P_r are the unit charge of a single electron, a sensitivity factor [(S/m)$^{-1}$], incident photon density of excitation laser (photons/m^2), a correction (or filling) factor (/m), change of reflected microwave power, and power of reflected microwave, respectively. The change of conductivity is equivalent with $\Delta P_r/(AP_r)$. Third harmonic generation (THG, 355 nm) of a Nd:YAG laser (Spectra Physics Inc. INDI, 5−8 ns pulse duration) was used as an

dx.doi.org/10.1021/ma202778p | *Macromolecules* 2012, 45, 2709−2719

Scheme 1. Synthetic Route Adopted for the Preparation of Monomers and Polymers



excitation source. The intensity of laser (I_0) was changed by gradient neutral density filters. The incident photon density used in the present study was 4.6×10^{15} photons cm^{-2}. The sample was set at the highest electric field in a resonant cavity. The experiments were carried out at room temperature.

Direct-Current Photoconductivity. An interdigitated comb-type gold electrode with 5 μm gaps, 40 nm height, and 2 mm width was fabricated by lithographic process was used for direct-current (dc) integration experiments. After cleaning followed by UV-ozone treatment, thin polymer film was cast on the electrode by spin-coating the *o*-DCB solution of 1 wt % polymer at 1000 rpm for 30 s. The sample was placed in a vacuum chamber, connected to the circuit and exposed to laser excitation. The applied bias was controlled by an Advantest Corp. model R8252 digital electrometer. The transient photocurrent was measured by a Tektronix digital oscilloscope equipped with termination resistance. The applied bias and incident photon density of 355 nm laser were 2×10^4 V cm^{-1} and 4.6×10^{15} photons cm^{-2}, respectively. The experiments were carried out at room temperature.

Device Fabrication and Characterization of BHJ Solar Cells. The ITO glass was precleaned in the same manner as explained for SCLC measurement and coated by a thin layer of PEDOT:PSS. 1.0 wt % *o*-

dx.doi.org/10.1021/ma202778p | *Macromolecules* 2012, 45, 2709–2719

DCB solutions of **P1** and PCBM (or P3HT) (1:1 w/w) in the absence/presence of 3 vol % ODT was heated at 80 °C under stirring for at least 3 h to obtain a completely dissolved hot solution, which was filtered by using a 0.2 μm filter. The active layer was cast on top of the PEDOT:PSS buffer layer in a nitrogen glovebox by spin-coating at 1000 rpm and transferred it into a Petri dish. After slow evaporation, the substrate was annealed on a hot plate at 150 °C for 10 min (in the case of PCBM blend, annealed at 40 °C and kept in vacuum overnight). The cathode consisting of 20 nm Ca and 100 nm Al layers was sequentially deposited through a shadow mask on top of the active layers at the rates of Ca (0.1 nm s^{-1}) and Al (0.4 nm s^{-1}) by thermal evaporation in a vacuum chamber (ca. 5×10^{-5} Pa). The device structure was ITO (120−160 nm)/PEDOT:PSS (45−60 nm)/active layer (150−200 nm)/Ca (20 nm)/Al (100 nm) with the active area of 7.1 mm^2. The current−voltage (J−V) curves were measured using an ADCMT Corp. 6241A source-measure unit under AM 1.5 G solar illumination at 100 mW cm^{-2} (1 sun) using a 300 W solar simulator of SAN-EI Corp. (model XES-301S).

Density Functional Theory (DFT). DFT calculations were performed using the Gaussian03 Rev. E.01 package. The B3LYP functions with 6-31G(d,p) basis set were used for neutral state.

2.3. Synthesis. Synthesis of monomers **1**−**3** and **6**−**8** were reported elsewhere.[5e,8] Monomers **4** and **5** and polymers **P1** and **P2** were synthesized according to Scheme 1.

Monomer **4**: Compound **3** (500 mg, 1.01 mmol, 1 equiv) and 3-hexylthiophene-2-boronic acid pinacol ester (624 mg, 2.12 mmol, 2.1 equiv) were weighed into a two-necked RB flask and dissolved in toluene (10 mL). 2 M aqueous K_2CO_3 (1.38 g in 4.9 mL water, 10 mmol, 10 equiv) and Aliquat 336 (25 mg) was added to the stirring mixture. Air was removed from the flask and filled with nitrogen by applying freeze−pump−thaw method for three times. $Pd(PPh_3)_4$ (115 mg, 0.1 mmol, 0.1 equiv) was added under N_2 counter flow and the reaction mixture was refluxed at 100 °C for 16 h. The reaction mixture was then poured into water and extracted with chloroform. The combined organic fraction was dried over Na_2SO_4 and evaporated to dryness under reduced pressure. The resulting crude product was purified by column chromatography (silica gel, 30% CH_2Cl_2−hexane) to afford monomer **4** as an yellow oil (88%). ^{1}H NMR (600 MHz, $CDCl_3$): δ 7.34 (d, J = 5.4 Hz, 2H), 6.99 (d, J = 5.4 Hz, 2H), 2.69 (t, J = 15.6 Hz, 4H), 2.55 (t, J = 15.6 Hz, 4H), 1.705 (m, 4H), 1.55 (m, 4H), 1.23−1.30 (m, 24H), 0.85 (m, 12H). ^{13}C NMR (150 MHz, $CDCl_3$): δ 160.17, 157.31, 143.39, 128.83, 126.20, 125.27, 125.20, 31.59, 31.55, 30.56, 29.68, 29.57, 29.06, 29.01, 28.89, 22.54, 14.03, 14.02.

Monomer **5**: Compound **4** (100 mg, 0.15 mmol, 1 equiv) was dissolved in a mixture of chloroform (3 mL) and glacial acetic acid (0.2 mL). *N*-Bromosuccinimide (55 mg, 0.305 mmol, 2 equiv) was added in small portions, and the reaction mixture was stirred in the dark for 2 h at room temperature. The reaction mixture was then added to water and extracted with chloroform. The crude product was purified by column chromatography (silica gel, 10% CH_2Cl_2−hexane) to afford monomer **5** as an yellow solid (80%). ^{1}H NMR (600 MHz, $CDCl_3$): δ 6.95 (s, 2H), 2.67 (t, J = 15.6 Hz, 4H), 2.47 (t, J = 15.6 Hz, 4H), 1.54−1.7 (m, 4H), 1.32−1.54 (m, 4H), 1.19−1.31 (m, 24H), 0.86 (m, 12H). ^{13}C NMR (150 MHz, $CDCl_3$): δ 160.42, 157.96, 144.32, 131.70, 126.04, 124.12, 113.01, 31.59, 31.57, 30.42, 29.71, 29.59, 29.04, 28.99, 28.91, 22.57, 22.54, 14.08, 14.05.

Polymer **P1**: Monomer **5** (114 mg, 0.12 mmol, 1 equiv), 2,1,3-benzothiadiazole-4,7-bis(boronic acid pinacol ester) (53.58 mg, 0.12 mmol, 1 equiv), and phase transfer catalyst Aliquat 336 (13 mg) were weighed to a two-necked round-bottomed flask. Dry toluene (3 mL) was added to the reaction mixture followed by 2 M aqueous solution of K_2CO_3 (0.26 mL). Air was removed from the flask and filled with nitrogen by using the freeze−thaw−pump method for three times. $Pd(PPh_3)_4$ (2.7 mg, 0.0024 mmol, 0.02 equiv) was added under N_2 counter flow, and the reaction mixture was refluxed at 100 °C. After 2 days, bromobenzene (1.2 μL, 0.012 mmol, 0.1 equiv) was added to the reaction mixture, 1 h later phenylboronic acid (1.3 mg, 0.012 mmol, 0.1 equiv) was added, and the reaction refluxed overnight to complete the end-capping reaction. The resulting polymer solution was cooled to room temperature and diluted by adding toluene (18 mL), and the polymer was precipitated by slowly adding the mixture into hexane (200 mL). The precipitates were collected by filtration and washed with hexane. The solid was dissolved in chloroform and passed through a silica column using chloroform as an eluent. The combined polymer solution was passed through Celite, concentrated, and reprecipitated in hexane. Precipitate was filtered and dried under vacuum to yield **P1** (55%). GPC: M_w = 21 200 g mol^{-1}; M_n = 14 300 g mol^{-1}; M_w/M_n = 1.4. ^{1}H NMR (600 MHz, $CDCl_3$): δ 8.08 (br, 2H), 7.90 (br, 2H), 2.82 (br, 4H), 2.66 (br, 4H), 1.78 (br, 4H), 1.65 (br, 4H), 1.26−1.38 (br, 24H), 0.86 (br, 12H).

Polymer **P1** (lower molecular weight sample): A similar procedure as the preparation of higher molecular weight sample of **P1** was adopted employing monomer **5** (100 mg, 0.105 mmol, 1 equiv), 2,1,3-benzothiadiazole-4,7-bis(boronic acid pinacol ester) (47 mg, 0.105 mmol, 1 equiv), phase transfer catalyst Aliquat 336 (10 mg), dry toluene (3 mL), 2 M aqueous solution of K_2CO_3 (0.22 mL), and $Pd(PPh_3)_4$ (2.4 mg, 0.002 mmol, 0.02 equiv). The reaction was monitored every 1 h using GPC. After 6 h the reaction was stopped by end-capping with bromobenzene (1.0 μL, 0.010 mmol, 0.1 equiv) and phenylboronic acid (1.1 mg, 0.010 mmol, 0.1 equiv) The resulting polymer solution was cooled to room temperature and diluted by adding toluene (18 mL), and the polymer was precipitated by slowly adding the mixture into hexane (200 mL). The precipitates were collected by filtration and washed with hexane. The solid was dissolved in chloroform and passed through a silica column using chloroform as an eluent. The combined polymer solution was passed through Celite, concentrated, and reprecipitated in hexane. Precipitate was filtered and dried under vacuum to yield **P1** (50%). GPC: M_w = 9500 g mol^{-1}; M_n = 5900 g mol^{-1}; M_w/M_n = 1.6. ^{1}H NMR (600 MHz, $CDCl_3$): δ 8.08 (br, 2H), 7.90 (br, 2H), 2.82 (br, 4H), 2.66 (br, 4H), 1.78−1.60 (br, 8H), 1.26−1.45 (br, 24H), 0.86 (br, 12H).

Polymer **P2**: Monomer **8** (216 mg, 0.325 mmol, 1 equiv) and monomer **9** (202 mg, 0.325 mmol, 1 equiv) were weighed to a two-necked round-bottomed flask. Dry toluene (10 mL) was added to the reaction mixture. Air was removed from the flask and filled by nitrogen by using the freeze−thaw−pump method for three times. $Pd(PPh_3)_4$ (35 mg, 0.0325 mmol, 0.1 equiv) was added under N_2 counterflow, and the reaction mixture was refluxed at 100 °C for 3 days. After 3 days bromothiophene (3 μL, 0.032 mmol, 0.1 equiv) was added to the reaction mixture, 10 h later tributyl(thiophen-2-yl)stannane (11 mg, 0.032 mmol, 0.1 equiv) was added, and the reaction refluxed overnight to complete the end-capping reaction. The resultant polymer solution was cooled to room temperature, diluted by adding toluene (20 mL), and the polymer was precipitated by slowly adding the mixture into hexane (250 mL). The precipitates were collected by filtration and washed with hexane. The solid was then dissolved in chloroform and passed through a silica column using chloroform as an eluent. The combined polymer solution was passed through Celite, concentrated, and reprecipitated in hexane. Precipitate was filtered and dried under vacuum to yield **P2** (35%). GPC: M_w = 8800 g mol^{-1}; M_n = 7300 g mol^{-1}; M_w/M_n = 1.2. ^{1}H NMR (600 MHz, $CDCl_3$): δ 7.72 (br, 2H), 7.23 (br, 2H), 3.03 (br, 4H), 2.71 (br, 4H), 1.2−1.85 (br, m, 32H), 0.85 (br, 12H).

3. RESULTS AND DISCUSSION

3.1. Synthesis and Characterization. The copolymers **P1** and **P2** were synthesized according to known or modified literature procedures as shown in Scheme 1. Standard Suzuki coupling was used for the preparation of **P1**, whereas Stille polycondensation was adopted for the synthesis of **P2**. The molecular structures of the polymers were verified by ^{1}H NMR spectra. The copolymers **P1** and **P2** have the weight-averaged molecular weight of 21 200 and 8800 with the polydispersity indices of 1.5 and 1.2, respectively, as determined by GPC against polystyrene standards in THF (Table 1). The lower molecular weight of **P2** than that of **P1** could be attributed to the poor stability of the monomer **8**[5e] from which it is prepared.

Table 1. Molecular Weights and Polydispersity Index (PDI) of Copolymers P1[a] and P2

polymers	M_w (g mol^{-1})	M_n (g mol^{-1})	PDI
P1	21200	14300	1.5
P2	8800	7300	1.2

[a]A different sample of **P1** (M_w = 9500 g mol^{-1}; PDI = 1.6) with comparable molecular weight as that of **P2** was prepared and analyzed. Details are given in the Supporting Information.

The polymers showed excellent solubility in organic solvents such as chloroform, chlorobenzene, *o*-dichlorobenzene, THF, etc. **P1** shows considerable mechanical strength when compared to that of **P2** which is clearly visible from the nature of the polymer, as it could be peeled off easily from a glass Petri dish after evaporation of the solvent forming free self-standing films, whereas **P2** was obtained as a powder (Figure 1a).

3.2. Optical Properties. The absorption spectra of copolymers **P1** and **P2** as solutions in chlorobenzene (10^{-5} M) and as thin solid films are shown in Figures 1b and 1c, respectively. The absorption spectra of **P1** in the solution state exhibits three peaks with the absorption maximum (λ_{max}) at 495 nm, whereas that of **P2** exhibits mainly two peaks in which the longer wavelength peak is broad with a blue-shifted maximum (λ_{max} = 476 nm, $\Delta\lambda$ = 19 nm) when compared to that of **P1**. Both **P1** and **P2** exhibit considerable red shift in the solid state, indicating significant planarization of the polymer main chain. However, in contrast to the solution state, **P2** exhibited more red shift ($\Delta\lambda$ = 68 nm) when compared to that of **P1** ($\Delta\lambda$ = 23 nm), although vibronic features remained the same. It should be noted that **P1** exhibits an additional shoulder in the longer wavelength region at around 680 nm, which is not observed in the case of **P2**. In an attempt to study the effect of additives and a possible improvement of the aggregation properties of polymers in the film state, a small amount (3 vol %) of 1,8-octanedithiol (ODT) was added into the solution from which the films were casted. Interestingly, the absorption maximum of **P1** film was significantly red-shifted by about 80 nm and broadened in the presence of ODT, thus improving the absorption in the visible region considerably leading to a better overlap with the solar spectrum (Figure 1b). Though it is reported that the presence of additives shift the polymer absorption by 5−10 nm,[9] such a huge red shift is a new observation. On the other hand, no red shift was observed in the absorption maximum of **P2** upon the addition of ODT (Figure 1c). These observations clearly indicate that the positioning of side chains has considerable influence on the absorption properties of **P1** and **P2** in both solution and film states.

To have a better understanding on how the positioning of alkyl side chains affects so significantly the absorption properties, calculations were performed using density-functional theory (DFT) at the B3LYP/6-31G(d,p) level. The optimized geometry of the highest occupied molecular orbitals (HOMO) and the lowest unoccupied molecular orbitals (LUMO) of the neutral states of **P1** and **P2** (two repeating units) in vacuum is shown in Figure 2. The HOMO is relatively delocalized along the conjugated backbone, whereas LUMO is localized mainly on the BTZ unit in both polymers. This indicates that the BT and thiophene units together act as electron donors and BTZ unit acts as electron acceptor in the copolymers. The dihedral angles of BT−thiophene and thiophene−BTZ units in **P1** were found to be 46.7° and 5.7°, respectively, whereas it is 3.4° and 32.4°, respectively, in the case of **P2**. The relative red shift of the absorption spectrum of these polymers in solution state or film state could be assumed to be proportional to the extend of orbital overlap and subsequent charge transfer between the donor−acceptor moieties. Since the thiophene−BTZ dihedral angle in **P1** is very small (5.7°) when compared to that of **P2** (32.4°), better orbital overlap and charge transfer between the donor−acceptor moieties occur in the former, resulting in red-shifted absorption maximum (λ_{max} = 495 nm) than that of the latter (λ_{max} = 476 nm) in solution state. In the film state, extra planarization might happen between the BT−thiophene units

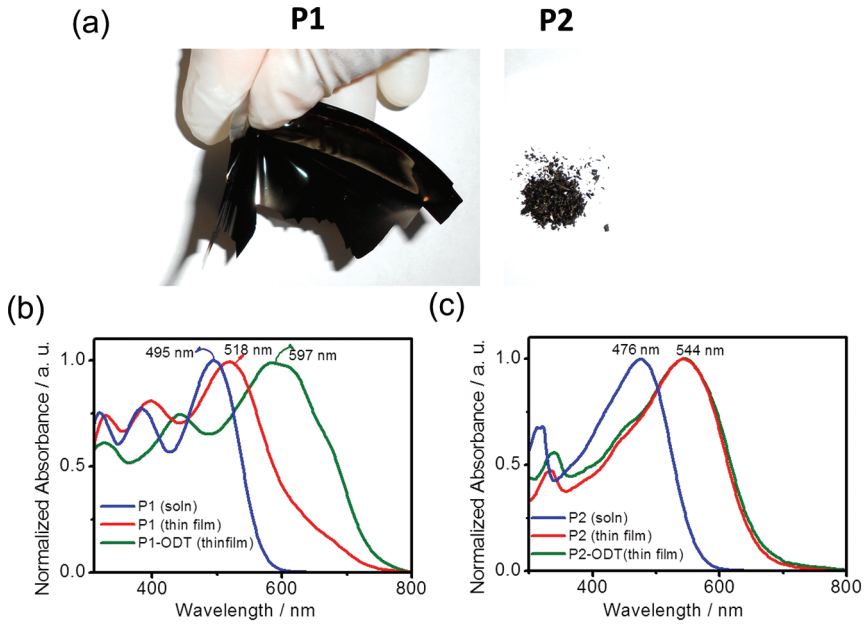


Figure 1. (a) Photographs of pristine **P1** and **P2** polymers. Normalized absorption spectra of (b) **P1** and (c) **P2** in chlorobenzene (concentration = 10^{-5} M, l = 10 mm) and in thin film states with/without processing by additive (ODT).

dx.doi.org/10.1021/ma202778p | *Macromolecules* 2012, 45, 2709−2719

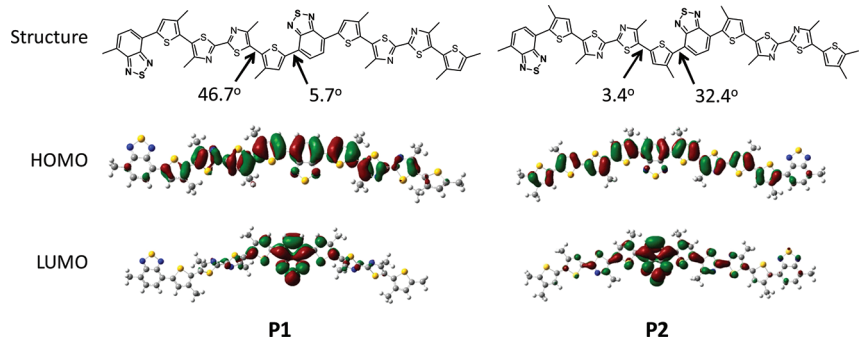
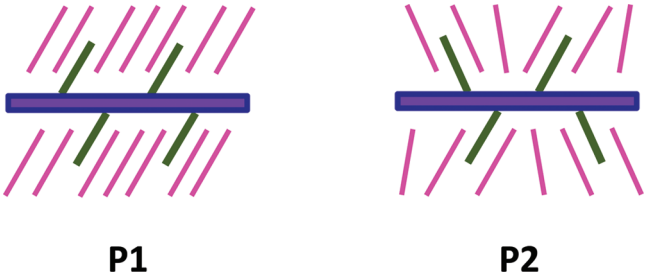


Figure 2. Energy-minimized structures of two repeating units of **P1** and **P2** (*n*-hexyl chains were replaced by methyl for simplicity) obtained by DFT calculation and the corresponding HOMO and LUMO distributions.

in **P1** as well as the thiophene–BTZ units in **P2**. Since the planarization happens between the donor–acceptor groups in **P2**, it is more effective in improving the charge transfer properties, and hence it exhibited a better red-shift (λ_{max} = 544 nm) than that of **P1** (λ_{max} = 518 nm).

It could be assumed that the alkyl chains in **P1** are oriented in one direction (as in the case of P3HT), which assists the interpolymer stacking through van der Waals interaction in a cooperative manner. On the other hand, alkyl chains in **P2** are oriented in opposite direction and may not be as effective as in the case of **P1** for assisting polymer stacking. The planarization of BT–thiophene units in **P1** in film state leads to better interactions between alkyl chains, resulting in polymer chain aggregation. This could be attributed to the observation of a shoulder band at about 680 nm in the absorption spectrum of **P1** which is absent in the case of **P2**. The additive (ODT) can effectively interact with the well-ordered alkyl side chains of **P1** than that of randomly arranged side chains of **P2**, as shown in Scheme 2, which reinforces the π-stacking between the aromatic units and van der Waals interactions between the alkyl chains in the case of former. This leads to substantial enhancement in planarity as well as the stacking of polymer chains, resulting in the broadening of the absorption spectrum and red shift in the absorption maximum (λ_{max} = 597 nm) for **P1**, whereas no such effects were observed for **P2**.

Scheme 2. Schematic Representation of Interaction of Additive ODT with P1 and P2



The optical band gaps of polymer films in the absence of ODT calculated from the absorption edges were found to be 1.64 and 1.74 eV for **P1** and **P2**, respectively. In the presence of additive, it was 1.60 eV for **P1**, showing an additive induced lowering of band gap, whereas it was unchanged for **P2**.

P1 and **P2** exhibited fluorescence emission maximum at 611 and 617 nm, respectively, in the solution state (Figure S1) and 639 and 666 nm, respectively, in the film state (Figure S2). In the film state, the fluorescence emission intensity of **P1** processed with the additive was considerably quenched compared to that of **P1** alone (Figure S2). This drop in the emission yield reiterates the strong aggregation of polymer chains in the presence of the additive, resulting in several nonradiative decay pathways for the excited states. **P2** exhibits a lower emission yield compared to that of **P1**, and no further quenching was observed in the presence of additive (Figure S2), which is in accordance with the absorption properties. The formation of aggregates of **P1** was confirmed by atomic force microscopic (AFM) experiments which revealed the presence of self-assembled aggregates with nanometer dimensions (Figure S3) in **P1**–ODT, which could benefit the charge carrier mobility (vide infra).

3.3. X-ray Diffraction. In order to get more insight into the molecular organization, X-ray diffraction analyses were performed in film state. **P1** exhibited a weak diffraction peak at 2θ = 5.23°, whereas **P2** exhibited a moderate diffraction peak at 2θ = 5.66° corresponding to the *d* spacing values of 16.9 and 15.6 Å for **P1** and **P2**, respectively (Figure 3). The *d* spacing values could be assigned to the spacing between the polymer backbone separated by the interdigitated alkyl side chains. The difference in the *d* spacing observed for **P1** and **P2** reiterates the influence of the positioning of alkyl side chains on polymer packing. The orthogonal positioning of the side chains in **P2** might be resulting in higher proximity of polymer backbones by effectively utilizing the free volume between the neighboring polymer chains. The intensity of the diffraction peak at 16.9 Å for **P1** showed nearly 6-fold increase when processed with ODT, indicating a higher ordered packing in **P1** in the presence of additive, which is in agreement with the absorption and emission properties.

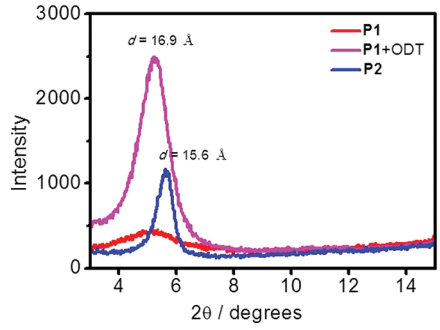


Figure 3. X-ray diffraction patterns of **P1**, **P2**, and **P1**–ODT in film state.

dx.doi.org/10.1021/ma202778p | *Macromolecules* 2012, 45, 2709–2719

3.4. Determination of Energy Levels. The HOMO levels of the polymers **P1**, **P2**, and **P1**-ODT in film state were determined as the ionization threshold energy using UV photoelectron spectroscopy (UPS) (Figure S4). The ionization threshold energy was determined from the onset of detected electrons which gave the HOMO levels of the polymers below the vacuum level in electronvolts. The LUMO levels were calculated by adding the value of band gaps in electronvolts obtained from the band-edge of UV−vis absorption of the corresponding film with the HOMO values. As listed in Table 2, both **P1** and **P2** exhibit deep-lying HOMO energy levels

Table 2. Absorption Maximum (λ_{max}), Optical Band Gap (E_g^{opt}), and HOMO and LUMO Energy Levels of P1, P1-ODT, and P2

polymers	λ_{max} (nm)	E_g^{opt} (eV)	HOMO[a] (eV)	LUMO[b] (eV)
P1	518	1.64	−5.24	−3.60
P1-ODT	597	1.60	−5.27	−3.67
P2	537	1.74	−5.53	−3.79

[a]The HOMOs of films were measured by UPS. [b]LUMO levels were obtained from the equation LUMO = HOMO + E_g^{opt}.

(−5.24 and −5.53 eV, respectively) compared to P3HT (−5.06 eV),[10] as the incorporation of electron-withdrawing BT and BTZ units into the polymer backbone is a good choice to lower the HOMO level. **P1** exhibit slightly higher HOMO and LUMO compared to that of **P2**, which again indicates that the positioning of side chain pattern also influences the band gap and HOMO−LUMO energy levels of the polymers. The higher HOMO level of **P1** suggests that the π-electrons are more delocalized in **P1** than **P2**. The ODT-modified **P1** does not differ significantly from that of **P1** in the HOMO and LUMO energy levels. This is the case giving that the change in the optical properties of **P1**-ODT from that of **P1** is mainly due to the difference in the structural order of the assembly formed.

3.5. Transient Photoconductivity of P1 and P2 by the FP-TRMC Method. The photoconductivity of the polymers **P1** and **P2** in film state were measured using the flash-photolysis time-resolved microwave conductivity (FP-TRMC) technique using a 355 nm laser as the excitation source. This electrodeless technique gives information about the short-range (nanometer scale) intrinsic charge carrier transport property and could be used to quantify the $\phi\sum\mu$ values, where ϕ is the charge carrier generation quantum yield on excitation with laser light and $\sum\mu$ is the sum of charge carrier mobilities, i.e., the sum of electron and hole mobilities (μ_e and μ_h, respectively). The photoconductivity transient obtained for **P1** is shown in Figure 4. The maximum value ($\phi\sum\mu_{max}$) is considered to

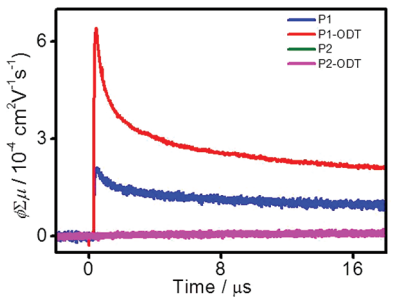


Figure 4. FP-TRMC transients of **P1** and **P2** films prepared in the presence and absence of ODT.

reflect the intrinsic charge carrier mobilities of the polymer with minimum trapping effects. The $\phi\sum\mu_{max}$ value of **P1** was found to be 2.1×10^{-4} cm^2/(V s), which increased by more than 3 times (6.5×10^{-4} cm^2/(V s)) in the films processed with 3 vol % ODT in *o*-dichlorobenzene solution. The corresponding half-lifetimes of the charge carriers ($\tau_{1/2}$) were decreased from 8.0 to 2.2 μs in the presence of additive (Table 3). In contrast, no measurable photoconductivity signals were obtained for **P2** alone or even in presence of additive (Figure 4), indicating a poor photoconductivity. This could be attributed to the low charge carrier generation as well as small charge carrier mobility of **P2**. On the other hand, better donor−acceptor orbital overlap and higher structural ordering enables efficient charge carrier generation and mobility in **P1**, which could be enhanced further in the presence of additive. The decrease in lifetime in the additive processed films could be attributed to the increase in the charge carrier mobility and subsequent acceleration in the reaction rate of bulk charge recombination.

In order to obtain the charge carrier mobility ($\sum\mu$), the value of ϕ_{max} was estimated by using direct current technique and $\sum\mu$ was obtained by dividing $\phi\sum\mu_{max}$ of TRMC measurements by ϕ_{max}. Interdigitated comb-type gold electrode with 5 μm gap was used for this analysis. The ϕ_{max} and $\sum\mu$ values obtained for **P1** and **P1**-ODT are given in Table 3. A slight decrease in the charge carrier generation quantum yield and a 5-fold increase in the charge carrier mobility were observed for **P1**-ODT compared to that of **P1** alone. Hence, the increase in the photoconductivity of **P1**-ODT compared to **P1** alone was mainly due to the increase in the charge carrier mobility rather than an increase in the charge carrier generation quantum yield.

The electron and hole mobilities of the polymer **P1** and ODT-modified **P1** in film state were measured using the space-charge-limited current (SCLC) technique, and the values are given in Table 3. (The *J*−*V* characteristics for **P1** and **P1**-ODT are given in Supporting Information Figure S5.) Both hole and electron mobilities were found to be higher in **P1**-ODT compared to that of **P1**. The hole mobility of **P1** was about 7 times higher than that of its electron mobility. In contrast, a better balance between μ_h and μ_e was seen in the films processed with ODT, in which the value of μ_h is only less than 2 times higher than that of μ_e. The better balance might have increased the rate of bulk charge recombination, leading to the decrease of charge carrier lifetimes as explained earlier. The higher value for μ_h indicates that p-type nature is predominant in both **P1** and **P1**-ODT. It must be also noted that the $\sum\mu$ values obtained from TRMC method could be comparable with many of the good organic semiconducting materials reported so far. However, the μ_h and μ_e values as estimated from SCLC measurement were relatively low. The TRMC values mainly reflect the short-range (<10 nm) conductivities where the increase in intrapolymer charge carrier mobility alone can enhance the TRMC signals significantly. On the other hand, the SCLC method reflects the long-range (>100 nm) mobility of hole and electrons where intra- and interpolymer mobilities have significant effects. So the comparison of both results revealed that **P1** exhibits good intrapolymer charge carrier mobility which enhances further in the presence of additives due to planarization of the conjugated backbone. However, this planarization was not enough to yield substantial orbital overlap between neighboring polymer chains to give high interpolymer charge carrier mobilities.

3.6. Photoconductivity of P1 and P1-ODT in the Presence of PCBM and P3HT. In order to analyze the

dx.doi.org/10.1021/ma202778p | *Macromolecules* 2012, 45, 2709−2719

Table 3. $\phi\sum\mu_{max}$, $\tau_{1/2}$, ϕ_{max}, $\sum\mu$ Values, and Hole and Electron Mobilities of P1 Films Prepared in the Absence and Presence of ODT

polymers	$\phi\sum\mu_{max}$ (10^{-4} cm^2/(V s))	$\tau_{1/2}$ (μ s)	ϕ_{max} (10^{-3})	$\sum\mu$ (cm^2/(V s))	μ_h (10^{-6} cm^2/(V s))	μ_e (10^{-6} cm^2/(V s))
P1	2.1	8.0	1.3	0.16	9.8	1.4
P1-ODT	6.5	2.2	0.97	0.67	15	9.5

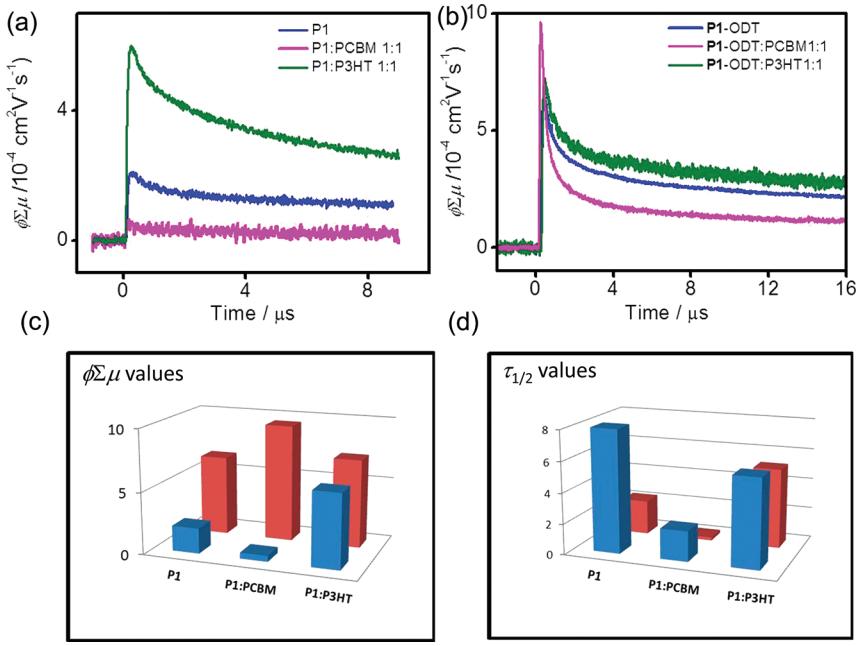


Figure 5. Comparison of the FP-TRMC transients of **P1**, **P1**:PCBM, and **P1**:P3HT films prepared in the (a) absence and (b) presence of ODT. The corresponding histograms of (c) $\phi\sum\mu_{max}$ and (d) $\tau_{1/2}$ of films prepared in the absence (blue) and presence (red) of ODT.

suitability of these materials for photovoltaic application in presence of n-type or p-type materials, TRMC analysis was carried out on **P1** and **P1-ODT** blended with PCBM or P3HT. A substantial decrease in $\phi\sum\mu$ was obtained for **P1** with increasing amounts of PCBM (20−80 wt %). In contrast, the blend films in the presence of ODT exhibited significant enhancement in $\phi\sum\mu$ value. For instance, a 1:1 blend of **P1**:PCBM processed in the absence of ODT exhibited $\phi\sum\mu$ of 0.48×10^{-4} cm^2/(V s) (about 4-fold decrease compared to that of **P1** alone), as shown in Figure 5a. On the other hand, a similar film processed with ODT showed nearly 5-fold enhancement in $\phi\sum\mu$ when compared to that of **P1** alone (Figure 5b, $\phi\sum\mu = 9.5 \times 10^{-4}$ cm^2/(V s)). We assumed that incorporation of PCBM disturbs the packing of **P1**, which is already weak in the absence of additive, leading to poor transport of charge carriers. But no such destruction happened in the presence of ODT, yielding a high photoconductivity. Mixing of **P1** with P3HT has enhanced the $\phi\sum\mu$ value (6.0×10^{-4} cm^2/(V s), Figure 5a), but processing with additives had no significant influence in this case ($\phi\sum\mu = 7.1 \times 10^{-4}$ cm^2/(V s), Figure 5b). The $\tau_{1/2}$ values were decreased in the blend films of **P1**:PCBM and **P1**:P3HT when compared to that of **P1** alone. Nearly 4-fold decrease was observed in the case of **P1**:PCBM blend (1:1 w/w), whereas less than 2-fold decrease was obtained for **P1**:P3HT blend (1:1 w/w) (Table 4). Further decrease in lifetime was observed in **P1**:PCBM films treated with ODT. On the other hand, $\tau_{1/2}$ was remained nearly same in **P1**:P3HT films processed with ODT, indicating that the additive has almost no influence on the $\phi\sum\mu_{max}$ and $\tau_{1/2}$ when **P1** is blended with P3HT.

Table 4. $\phi\sum\mu_{max}$ and $\tau_{1/2}$ Values of Polymer P1 Blended with PCBM and P3HT in the Absence and Presence of ODT

parameters	**P1**:PCBM	**P1**:P3HT	**P1**-ODT: PCBM	**P1**-ODT: P3HT
$\phi\sum\mu_{max}$ (10^{-4} cm^2/(V s))	0.48	6.0	9.5	7.1
$\tau_{1/2}$ (μs)	2.0	5.7	0.30	5.2

The annealing conditions were different in blends with PCBM and P3HT. For **P1**-ODT:PCBM blend, the films were annealed at 40 °C for 15 min and kept in vacuum overnight. Increasing the temperature above 40 °C led to a gradual decrease in the $\phi\sum\mu$ value and heating the films at 150 °C for 10 min resulted in a blue shift of about 90 nm in the absorption and also very low photoconductivity signal (Figures S7 and S8). The color of the film changed from black to red at this temperature. Such an effect is not observed in the case with P3HT even after 150 °C annealing. The absorption spectrum of pristine **P1**-ODT film did not change significantly upon thermal annealing (Figure S9). These observations suggest that at elevated temperature the small molecules of PCBM diffuse into the aggregated domains of **P1** and destruct their intermolecular π-stacking, while the entangled and high-molecular-weight P3HT polymer chains cannot migrate significantly. It is worth mentioning that the **P1**:P3HT system, i.e. all-polymer solar cell, has a high thermal stability in comparison with a conventional fullerene-based BHJ solar cells.

Blended films of **P2** with PCBM and P3HT was also prepared and analyzed. No signal was observed for films incorporated with PCBM, whereas **P2**:P3HT blends gave signals comparable to that of **P1**:P3HT. This indicates electron

dx.doi.org/10.1021/ma202778p | *Macromolecules* 2012, 45, 2709−2719

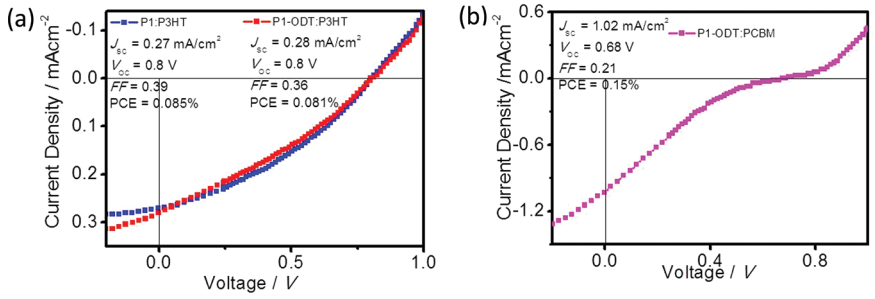


Figure 6. $J-V$ characteristics of BHJ solar cells fabricated from (a) **P1**:P3HT and **P1**-ODT:P3HT and (b) **P1**-ODT:PCBM with a 1:1 blend solution in *o*-DCB.

transfer occurs from P3HT to **P2** with good charge carrier generation quantum yield (ϕ), but $\sum\mu$ would be mainly contributed from hole mobility at the P3HT part.

3.7. Photovoltaic Properties. Since polymer **P1** exhibited both electron and hole conducting properties and the LUMO levels were positioned suitably in between that of PCBM and P3HT, photovoltaic properties of **P1** and ODT-modified **P1** were evaluated by fabricating devices with P3HT (as donor) or PCBM (as acceptor). The BHJ-type photovoltaic cells of **P1**:P3HT (1:1 w/w blend ratio) exhibited a power conversion efficiency (η) of 0.085%. The current density–voltage ($J-V$) characteristics of the solar cell measured under 100 mW cm^{-2} AM 1.5G simulated sunlight are shown in Figure 6a. It has an open-circuit voltage (V_{oc}) of 0.80 V, current density (J_{sc}) of 0.27 mA cm^{-2}, and fill factor (FF) of 0.39. The effect of additive was not much pronounced in blend with P3HT. Almost similar results were obtained for **P1**:P3HT (1:1) films processed with ODT which shows η of 0.081%, V_{oc} of 0.80 V, J_{sc} of 0.28 mA cm^{-2}, and FF of 0.36 (Figure 6a). No device response was seen in **P1** blended with PCBM probably due to the absence of bulk heterojunction structure. Interestingly, in the presence of additive, BHJ structures were formed, giving rise to photovoltaic efficiency of 0.15%, V_{oc} of 0.68 V, J_{sc} of 1.02 mA cm^{-2}, and FF of 0.21 (Figure 6b). The shape of the measured $J-V$ curve in the blend of **P1**-ODT:PCBM showed an S-kink which is due to the increase of series resistance, resulting from the imbalance or decrease in the charge carrier mobilities. This aspect is well discussed in the literature.[11] In short, polymer **P1** acted as an n-type material in the absence of additive, while it became ambipolar when treated with ODT. Interestingly the results obtained in OPV measurements were exactly in accordance with the TRMC measurements. The V_{oc} was reasonably good in the **P1**:P3HT blend, whereas it was lower for the **P1**-ODT:PCBM blend. The J_{sc} value increased considerably in the **P1**-ODT:PCBM combination compared to **P1**:P3HT. This would be due to the higher electron mobility of PCBM ($2-8 \times 10^{-3}$ cm^2/(V s))[12] than that of **P1** (see Table 3). Moreover, the additive can make better the phase segregation, leading to the improvement of J_{sc} by providing more optimal morphology for facilitating charge transport.

Attempts were made to measure the power conversion efficiency of **P2** in blends with P3HT since it gave a TRMC photoconductivity signal comparable with the **P1**:P3HT film. However, no efficiency was observed in the case of **P2**. Since the TRMC signal is mainly due to the hole mobility in P3HT part, the above observation can be explained by that although electron transfer occurs from P3HT to **P2**, the electron mobility in **P2** is too small to balance the photocurrent flow in the device.

Though the device performance fell short of the expectation, it is likely that the photovoltaic performance of this kind of copolymer can be improved if certain issues are addressed. One factor is the low value of J_{sc} observed for the polymer in blends with PCBM and P3HT. Although the additive processed films showed the absorption extending up to 800 nm, the extinction coefficient of **P1** thin film was almost 1 order lower ($\sim 4.4 \times 10^4$ cm^{-1}) when compared to that of P3HT ($\sim 2.5 \times 10^5$ cm^{-1}),[13] which is a major reason for the lowering of J_{sc}. It may also be lowered due to a lack of continuity in the polymer phase which might be caused by more than optimal intermixing of polymer with PCBM at the molecular level without good bicontinuous percolation network, resulting in hindered charge transport. Another factor is a low FF value, due to a lower and imbalanced charge carrier mobility. Another major factor contributed to the poor device performance is the lower interpolymer charge carrier mobility, as observed from SCLC measurements, which prevents the generated charge carriers reaching the electrodes.

Table 5. η, V_{OC}, J_{SC}, and FF Values of P1 and ODT-Modified P1 in Blends with PCBM and P3HT

blend films	η (%)	V_{OC} (V)	J_{SC} (mA/cm^2)	FF
P1 + P3HT (1:1)	0.085	0.80	0.27	0.39
P1-ODT + P3HT (1:1)	0.081	0.80	0.28	0.36
P1-ODT + PCBM (1:1)	0.15	0.68	1.02	0.21

Although this polymer exhibited lower photovoltaic efficiency in comparison with bithiazole-based polymers reported in the literature,[5] our work is significant due to the following reasons. The role of additives in bulk heterojunction (BHJ) devices were thought to control the aggregation and phase separation properties of fullerene derivatives, yielding an improved BHJ morphology and hence higher charge separation and photovoltaic efficiencies. But this work has unambiguously proved that the additives can significantly control the structural organization of polymer chains also, thereby improving its optical, electronic, and photovoltaic properties. More importantly, this work shows a very interesting observation of polarity (p-type or n-type) switching in the charge carrier properties of polymers exclusively controlled by the additives which is a first report of this kind as per our knowledge. In addition to that, this work clearly demonstrated that a small change in the positioning of side alkyl chains can make a drastic difference in the optical band gap, intramolecular and intermolecular charge carrier mobilities, and photovoltaic performance. It is of interest to note that our results were opposite to those of Shi et al.,[3d] where they reported that **P2**-type positioning of side alkyl

dx.doi.org/10.1021/ma202778p | *Macromolecules* 2012, 45, 2709–2719

chains in the bithiazole−benzodithiophene copolymers was superior to that of **P1**-type polymers. However, a possible question which arises may be the difference in the molecular weights of **P1** and **P2** and hence the validity of the comparison between them. In order to check this aspect, we have synthesized a lower molecular weight sample of **P1** by controlled polymerization (M_w = 9500 g mol^{-1} and PDI = 1.6) which is comparable with that of **P2** (M_w = 8800 g mol^{-1} and PDI = 1.2) and analyzed. The details are given in the Supporting Information. The absorption properties of the new sample (9.5K) in the solution state, thin film state, and additive added state were exactly same as that of the **P1** with higher molecular weight (Figure S10). Interestingly, new sample of **P1** (9.5K) also formed a free-standing film as that of old **P1** (21K). However, TRMC experiments indicated that the photoconductivities of both **P1** and **P1**-ODT exhibited lower values compared to the higher molecular weight samples (Figure S11). The $\phi\sum\mu$ value of **P1** (9.5K) was almost one-third of that of **P1** (21K) and **P1**-ODT (9.5K) was about less than half of the of **P1**-ODT (21K). The decrease in $\phi\sum\mu$ values in the lower molecular weight sample is due to decrease in both charge carrier generation quantum yield (ϕ, obtained from DC method) and mobility ($\sum\mu$) (Table S1). It seems that although the absorption properties reached saturation at a lower molecular weight, the photoconductivity properties have not reached saturation at this point. But it must be noted that no measurable photoconductivity signals were obtained for **P2** alone or even in presence of additive. Hence, it has become clear that the differences in the optoelectronic properties of **P1** and **P2** are due to the structural difference between these polymers. The comparison between **P1** polymers having different molecular weights also revealed that the molecular weight has no role on the interaction between polymer and additive.

4. CONCLUSION

We have synthesized two new conjugated D−A type copolymers **P1** and **P2** by alternating bithiazole and benzothiadiazole in which the bithiazole units are sandwiched between thiophene units. The polymers exhibited contrasting optical, electronic, and photovoltaic properties, revealing the crucial role played by the side chains on the structural ordering of conjugated polymers. These effects could be further amplified by the use of suitable additive, as evident from the improvement in absorption, photoconductivity, and charge carrier mobilities of **P1** in the presence of 1,8-octanedithiol. More importantly, the additive even induced a p/n switching in photovoltaic properties of **P1**. Thus, the present study offer chances to unveil the hidden optoelectronic properties of conjugated polymers by the control over structural ordering internally or externally for the design of novel organic optoelectronic devices.

■ ASSOCIATED CONTENT

Supporting Information

Figures showing fluorescence spectra of **P1** and **P2** in solution state and in film state, AFM images of **P1** and **P1**-ODT, photoelectron spectrum of **P1**, **P1**-ODT, and **P2** obtained by UV photoelectron spectroscopy, characteristic $J-V$ curves of **P1** and **P1**-ODT obtained from SCLC measurements, photograph showing the film surface formed by dropcasting the polymer solutions **P1**, **P1**-ODT, and **P2** in *o*-DCB, UV−vis absorption spectra and FP-TRMC transients of **P1**-ODT/PCBM blend films at different annealing temperatures and UV−vis absorption spectra of **P1**-ODT thin films at different annealing temperatures, UV−vis absorption spectra of lower molecular weight of **P1** (M_w = 9500) in the solution state, thin film state, and in the additive added state, FP-TRMC transients of **P1** (9500) films prepared in the presence and absence of ODT, $\phi\sum\mu_{max}$, $\tau_{1/2}$, ϕ_{max}, and $\sum\mu$ values of **P1** films prepared in the absence and presence of ODT, and complete ref 2h. This material is available free of charge via the Internet at http://pubs.acs.org.

■ AUTHOR INFORMATION

Corresponding Author

*E-mail: saeki@chem.eng.osaka-u.ac.jp (A.S.), seki@chem.eng.osaka-u.ac.jp (S.S.); Fax: +81-6-6879-4586; Tel: +81-6-6879-4587.

Notes

The authors declare no competing financial interest.

■ ACKNOWLEDGMENTS

This work was supported by JSPS Funding Program for Next-Generation World-Leading Researches (NEXT Program), PRESTO-JST, and KAKENHI from the MEXT Japan. The authors thank Riken Keiki Co., Ltd., for the UPS measurements.

■ REFERENCES

(1) (a) Arias, A. C.; MacKenzie, J. D.; McCulloch, I.; Rivnay, J.; Salleo, A. *Chem. Rev.* **2010**, *110*, 3−24. (b) Brabec, C. J.; Gowrisanker, S.; Halls, J. J. M.; Laird, D.; Jia, S.; Williams, S. P. *Adv. Mater.* **2010**, *22*, 3839−3856. (c) Facchetti, A. *Chem. Mater.* **2011**, *23*, 733−758.

(2) (a) Park, S. H.; Roy, A.; Beaupré, S.; Cho, S.; Coates, N.; Moon, J. S.; Moses, D.; Leclerc, M.; Lee, K.; Heeger, A. J. *Nat. Photonics* **2009**, *3*, 297−303. (b) Chen, H.-Y.; Hou, J.; Zhang, S.; Liang, Y.; Yang, G.; Yang, Y.; Yu, L.; Wu, Y.; Li, G. *Nat. Photonics* **2009**, *3*, 649−653. (c) Hou, J.; Chen, H.-Y.; Zhang, S.; Chen, R. I.; Yang, Y.; Wu, Y.; Li, G. *J. Am. Chem. Soc.* **2009**, *131*, 15586−15587. (d) Liang, Y.; Wu, Y.; Feng, D.; Tsai, S.-T.; Son, H.-J.; Li, G.; Yu, L. *J. Am. Chem. Soc.* **2009**, *131*, 56−57. (e) Liang, Y.; Feng, D.; Wu, Y.; Tsai, S.-T.; Li, G.; Ray, C.; Yu, L. *J. Am. Chem. Soc.* **2009**, *131*, 7792−7799. (f) Liang, Y.; Yu, L. *Acc. Chem. Res.* **2010**, *43*, 1227−1236. (g) Zou, Y.; Najari, A.; Berrouard, P.; Beaupré, S.; Aïch, B. R.; Tao, Y.; Leclerc, M. *J. Am. Chem. Soc.* **2010**, *132*, 5330−5331. (h) Bronstein, H.; et al. *J. Am. Chem. Soc.* **2011**, *133*, 3272−3275. (i) Chu, T.-Y.; Lu, J.; Beaupré, S.; Zhang, Y.; Pouliot, J.-R.; Wakim, S.; Zhou, J.; Leclerc, M.; Li, Z.; Ding, J.; Tao, Y. *J. Am. Chem. Soc.* **2011**, *133*, 4250−4253. (j) Zhou, H.; Yang, L.; Stuart, A. C.; Price, S. C.; Liu, S.; You, W. *Angew. Chem., Int. Ed.* **2011**, *50*, 2995−2998. (k) Wang, M.; Hu, X.; Liu, P.; Li, W.; Gong, X.; Huang, F.; Cao, Y. *J. Am. Chem. Soc.* **2011**, *133*, 9638−9641. (l) Ong, K.-H.; Lim, S.-L.; Tan, H.-S.; Wong, H.-K.; Li, J.; Ma, Z.; Moh, L. C. H.; Lim, S.-H.; de Mello, J. C.; Chen, Z.-K. *Adv. Mater.* **2011**, *23*, 1409−1413.

(3) (a) Koppe, M.; Scharber, M.; Brabec, C.; Duffy, W.; Heeney, M.; McCulloch, I. *Adv. Funct. Mater.* **2007**, *17*, 1371−1376. (b) Kline, R. J.; DeLongchamp, D. M.; Fischer, D. A.; Lin, E. K.; Richter, L. J.; Chabinyc, M. L.; Toney, M. F.; Heeney, M.; McCulloch, I. *Macromolecules* **2007**, *40*, 7960−7965. (c) Yang, L.; Zhou, H.; You., W. *J. Phys. Chem. C* **2010**, *114*, 16793−16800. (d) Shi, Q.; Fan, H.; Liu, Y.; Chen, J.; Ma, L.; Hu, W.; Shuai, Z.; Li, Y.; Zhan, X. *Macromolecules* **2011**, *44*, 4230−4240. (e) Tu, G.; Massip, S.; Oberhumer, P. M.; He, X.; Friend, R. H.; Greenham, N. C.; Huck, W. T. S. *J. Mater. Chem.* **2010**, *20*, 9231−9238. (f) Zhang, Z.-G.; Min, J.; Zhang, S.; Zhang, J.; Zhang, M.; Li, Y. *Chem. Commun.* **2011**, *47*, 9474−9476. (g) Kim, K. H.; Chung, D. S.; Park, C. E.; Choi, D. H. *Mol. Cryst. Liq. Cryst.* **2011**, *538*, 187−192. (h) Biniek, L.; Fall, S.; Chochos, C. L.; Anokhin, D. V.; Ivanov, D. A.; Leclerc, N.; Lévêque,

P.; Heiser, T. *Macromolecules* **2010**, *43*, 9779−9786. (i) Zhou, H.; Yang, L.; Xiao, S.; Liu, S.; You, W. *Macromolecules* **2010**, *43*, 811−820. (j) Lee, S.; Cho, S.; Tong, M.; Seo, J. H.; Heeger, A. *J. Polym. Sci., Part A: Polym. Chem.* **2011**, *49*, 1821−1829. (k) Shi, Q.; Fan, H.; Liu, Y.; Chen, J.; Shuai, Z.; Hu, W.; Li, Y.; Zhan, X. *J. Polym. Sci., Part A: Polym. Chem.* **2011**, *49*, 4875−4885.

(4) (a) Peet, J.; Soci, C.; Coffin, R. C.; Nguyen, T. Q.; Mikhailovsky, A.; Moses, D.; Bazan, G. C. *Appl. Phys. Lett.* **2006**, *89*, 252105. (b) Peet, J.; Kim, J. Y.; Coates, N. E.; Ma, W. L.; Moses, D.; Heeger, A. J.; Bazan, G. C. *Nat. Mater.* **2007**, *6*, 497−500. (c) Piliego, C.; Holcombe, T. W.; Douglas, J. D.; Woo, C. H.; Beaujuge, P. M.; Fréchet, J. M. J. *J. Am. Chem. Soc.* **2010**, *132*, 7595−7597. (d) Jiang, Y.; Okamoto, T.; Becerril, H. A.; Hong, S.; Tang, M. L.; Mayer, A. C.; Parmer, J. E.; McGehee, M. D.; Bao, Z. *Macromolecules* **2010**, *43*, 6361−6367. (e) Su, M.-S.; Kuo, C.-Y.; Yuan, M.-C.; Jeng, U.-S.; Su, C.-J.; Wei, K.-H. *Adv. Mater.* **2011**, *23*, 3315−3319. (f) Yao, Y.; Hou, J. H.; Xu, Z.; Li, G.; Yang, Y. *Adv. Funct. Mater.* **2008**, *18*, 1783−1789. (g) Chen, F.-C.; Tseng, H.-C.; Ko, C.-J. *Appl. Phys. Lett.* **2008**, *92*, 103316.

(5) (a) Li, K.-C.; Huang, J.-H.; Hsu, Y.-C.; Huang, P.-J.; Chu, C.-W.; Lin, J.-T.; Ho, K.-C.; Wei, K.-H.; Lin, H.-C. *Macromolecules* **2009**, *42*, 3681−3693. (b) Zhang, M.; Fan, H.; Guo, X.; He, Y.; Zhang, Z.; Min, J.; Zhang, J.; Zhao, G.; Zhan, X.; Li, Y. *Macromolecules* **2010**, *43*, 5706−5712. (c) Jung, I. H.; Yu, J.; Jeong, E.; Kim, J.; Kwon, S.; Kong, H.; Lee, K.; Woo, H. Y.; Shim, H.-K. *Chem.—Eur. J.* **2010**, *16*, 3743−3752. (d) Patra, D.; Sahu, D.; Padhy, H.; Kekuda, D.; Chu, C.-W.; Lin, H.-C. *J. Polym. Sci., Part A: Polym. Chem.* **2010**, *48*, 5479−5489. (e) Shi, Q.; Fan, H.; Liu, Y.; Hu, W.; Li, Y.; Zhan, X. *J. Phys. Chem. C* **2010**, *114*, 16843−16848. (f) Yang, M.; Peng, B.; Liu, B.; Zou, Y.; Zhou, K.; He, Y.; Pan, C.; Li, Y. *J. Phys. Chem. C* **2010**, *114*, 17989−17994. (g) Zhang, M.; Fan, H.; Guo, X.; Yang, Y.; Wang, S.; Zhang, Z.-G.; Zhang, J.; Zhan, X.; Li, Y. *J. Polym. Sci., Part A: Polym. Chem.* **2011**, *49*, 2746−2754. (h) Zhang, M.; Guo, X.; Li, Y. *Adv. Energy Mater.* **2011**, *1*, 557−560. (i) Wong, W.-Y.; Wang, X.-Z.; He, Z.; Chan, K.-K.; Djurišić, A. B.; Cheung, K.-Y.; Yip, C.-T.; Ng, A. M.-C.; Xi, Y. Y.; Mak, C. S. K.; Chan, W.-K. *J. Am. Chem. Soc.* **2010**, *129*, 14372−14380.

(6) (a) Mott, N. F.; Gurneyr, W. *Electronic Processes in Ionic Crystals*; Oxford University Press: London, 1940. (b) Blom, P. W. M.; de Jong, M. J. M.; Vleggaar, J. J. M. *Appl. Phys. Lett.* **1996**, *68*, 3308−3310. (c) Melzer, C.; Koop, E. J.; Mihailetchi, V. D.; Blom, P. W. M. *Adv. Funct. Mater.* **2004**, *14*, 865−870.

(7) (a) Saeki, A.; Fukumatsu, T.; Seki, S. *Macromolecules* **2011**, *44*, 3416−3424. (b) Saeki, A.; Tsuji, M.; Seki, S. *Adv. Energy Mater.* **2011**, *1*, 661−669.

(8) (a) Lee, J.; Jung, B.-J.; Lee, S. K.; Lee, J.-I.; Cho, H.-J.; Shim, H.-K. *J. Polym. Sci., Part A: Polym. Chem.* **2005**, *43*, 1845−1857. (b) El-Shehawy, A. A.; Abdo, N. I.; El-Barbary, A. A.; Lee, J.-S. *Eur. J. Org. Chem.* **2011**, 4841−4852.

(9) Peet, J.; Cho, N. S.; Lee, S. K.; Bazan, G. C. *Macromolecules* **2008**, *41*, 8655−8659.

(10) Chuangchote, S.; Fujita, M.; Sagawa, T.; Sakaguchi, H.; Yoshikawa, S. *ACS Appl. Mater. Interfaces* **2010**, *2*, 2995−2997.

(11) Tress, W.; Leo, K.; Riede, M. *Adv. Funct. Mater.* **2011**, *21*, 2140−2149.

(12) (a) Riedel, I.; von Hauff, E.; Parisi, J.; Martín, N.; Giacalone, F.; Dyakonov, V. *Adv. Funct. Mater.* **2005**, *15*, 1979−1987. (b) Mihailetchi, V. D.; van Duren, J. K.; Blom, P. W. M.; Hummelen, J. C.; Jassen, R. A. J.; Kroon, J. M.; Rispens, M. T.; Verhees, W. J. H.; Wienk, M. M. *Adv. Funct. Mater.* **2003**, *13*, 43−46.

(13) Kim, Y.; Cook, S.; Tuladhar, S. M.; Choulis, S. A.; Nelson, J.; Durrant, J. R.; Bradley, D. D. C.; Giles, M.; Mcculloch, I.; Ha, C.-S.; Ree, M. *Nat. Mater.* **2006**, *5*, 197−203.

Macromolecules

Article

pubs.acs.org/Macromolecules

Syndiotactic Polyallyltrimethylsilane-Based Stereoregular Diblock Copolymers: Syntheses and Self-Assembled Nanostructures

Jing-Yu Lee, Min-Ching Shiao, Fu-Yuan Tzeng, Chin-Hung Chang, Chih-Kuang Tsai, and Jing-Cherng Tsai*

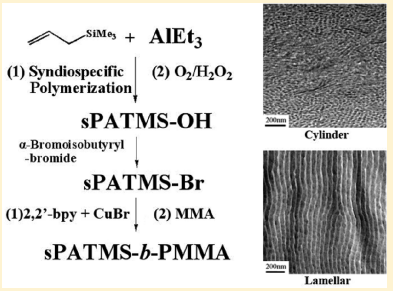
Department of Chemical Engineering, National Chung Cheng University, Chia-Yi 62142, Taiwan

Kuan-Hsin Lo, Shih-Chieh Lin, and Rong-Ming Ho*

Department of Chemical Engineering, National Tsing Hua University, Hsinchu 30013, Taiwan

Supporting Information

ABSTRACT: Structurally well-defined stereoregular diblock copolymers composed of syndiotactic polyallyltrimethylsilane (sPATMS) and poly(methyl methacrylate) (PMMA) were prepared by using an α-bromoester-terminated sPATMS macroinitiator, which was chain extended by MMA using a cuprous halide-based atom transfer radical polymerization (ATRP) system. The α-bromoester-terminated sPATMS macroinitiator was prepared via the esterfication of hydroxyl-capped sPATMS with α-bromoisobutyryl bromide. The hydroxyl-capped sPATMS was generated via a selective chain transfer reaction to triethylaluminum (TEA) during the syndiospecific polymerization of allyltrimethylsilane (ATMS) conducted in the presence of syndiospecific *ansa*-metallocene catalysts. The proposed synthetic route not only offers the high-yield production of stereoregular sPATMS-*b*-PMMA but also provides the linking of the stereoregular block (sPATMS) with PMMA through a controlled/living radical polymerization process. Moreover, the proposed method offers effective control over the block chain length, the molecular weight distribution (M_w/M_n) and the stereoregularity of sPATMS block. Thus, the self-assembly of the resultant diblock copolymers produces well-ordered nanostructures from microphase separation, as evidenced by transmission electron microscopy and small-angle X-ray scattering results.



INTRODUCTION

Self-assembly is the spontaneous association of compounds under equilibrium conditions into stable, structurally well-defined aggregates via cooperating secondary interactions (namely, noncovalent bonding forces) without human intervention.[1,2] The self-assembly of synthetic molecules, especially block copolymers (BCPs), have been comprehensively studied for their fascinating phase behaviors and tunable properties.[3] Block copolymers consist of chemically distinct polymer chains covalently linked to form a single molecule. Owing to their mutual repulsion, dissimilar blocks tend to segregate into different domains so as to self-assemble into one-, two-, or three-dimensional periodic nanostructures in the bulk state.[4] In the simplest case of noncrystalline flexible coiled diblock copolymers, various nanostructures such as spheres (S), cylinders (C), gyroid (G), and lamellae (L) can be found, depending on the relative compositions (i.e., volume fraction) between blocks, the sequence of constituted blocks and the architecture of polymer chains as well as the persistence lengths of blocks. In contrast to the formation of conventional phases from the self-assembly of noncrystalline BCPs, the competition between crystallization and microphase separation in the self-assembly of semicrystalline BCPs has attracted extensive attention because the crystallization will affect the self-assembled nanostructures and create various interesting morphologies.[5] Namely, the final morphology of semicrystalline BCPs is strongly dependent upon the experimental temperature, with respect to the order−disorder transition temperature (T_{ODT}), the crystallization temperature of the crystalline block (T_c^c), the glass transition of the amorphous block (T_g^a), and the crystallization rate.[6] As a result, well-defined nanostructures can thus be tailored by the molecular engineering of synthetic BCPs, which provides promising features for the applications of nanotechnologies.[7,8]

Silicon-containing polymers have attracted growing interests as functional materials due to their unique physical properties, including high oxygen permeability, low surface energy, high electrical resistance (insulator), thermal stability, photostability, and ease of cross-linking.[9] For the formation of self-assembled nanostructures, in particular nanostructured thin films, silicon-containing BCPs have been demonstrated to function as rigid nanopatterned templates that can be used for pattern transfer in nanoimprint lithography.[10] Despite this, studies on the self-assembly of silicon-containing BCPs have been quite limited due to the difficulty in the preparation of structurally well-defined silicon-containing BCPs.[11,12] This limits the preparation of silicon-containing BCPs for use in self-assembling studies and hampers their use in nanotechnological applications.

Received: January 5, 2012
Revised: February 28, 2012
Published: March 13, 2012

ACS Publications © 2012 American Chemical Society

We have previously conducted syntheses and self-assembling studies of propylene- and styrene-based stereoregular diblock copolymers.[13] Previous studies have demonstrated that the incorporation of stereoregular and crystallizable moieties within block copolymers enhances morphological richness and offers various morphological controls in the self-assembly processes.[14,15] The prospect of using silicon-containing stereoregular BCPs for their self-assembly studies and for use as rigid nanopatterned templates have prompted us to develop a method for their preparation, which is unable to achieve using existing methods.

Stereoregular silicon-containing polymers, including isotactic polyallytrimethylsilane (iPATMS) and syndiotactic polyallytrimethylsilane (sPATMS), have been prepared via stereospecific polymerization of allytrimethylsilane using Zieglar−Natta[16] and metallocene catalysts,[17] respectively. Nevertheless, the syntheses of stereoregular silicon-containing BCPs remain a synthetic challenge. How to achieve the connection between the silicon-containing stereoregular block and the other polymer block with high linking efficiency is essential in addition to accomplish the block length control in the construction of silicon-containing stereoregular BCPs. Methods for syntheses of α-olefin-based stereoregular BCPs with simultaneous stereoregularity, block connection and block length controls via stereospecific living polymerization of various α-olefins have been developed using stereospecific living coordination catalysts[18] or stereospecific controlled/living radical polymerization catalysts.[19] Unfortunately, silicon-containing stereoregular BCPs cannot be synthesized directly by using these stereospecific living polymerization systems as silicon-containing α-olefins (e.g., allytrimethylsilane) fail to undergo the respective stereospecific living polymerization reactions.

Another approach for the construction of silicon containing stereoregular BCPs is to conduct a selective chain transfer reaction during stereospecific polymerization of silyl group-containing α-olefins for the generation of an end-functionalized silyl group-containing stereoregular prepolymer in the first step, and then use the end-functionalized prepolymer in postpolymerization reaction for block formation. This two-step process allows for a broad variety of polymer architecture linked onto the silicon-containing stereoregular block but it needs to overcome the difficulty in the synthesis of silyl group-containing end-functionalized stereoregular prepolymer, which can only be generated via the induction of a selective chain transfer reaction during stereospecific polymerization of silyl group-containing α-olefins.[20]

Herein, silicon-containing stereoregular BCPs composed of syndiotactic polyallyltrimethylsilane (sPATMS) and poly(methyl methacrylate) (PMMA) are prepared by using an α-bromoester-terminated sPATMS macroinitiator, which is chain extended by MMA via the controlled/living radical polymerization of MMA using a cuprous halide-based ATRP process. The α-bromoester-terminated sPATMS macroinitiator is prepared via the esterfication of hydroxyl-capped sPATMS with α-bromoisobutyryl bromide. The hydroxyl-capped sPATMS can be generated by inducing a selective chain transfer reaction to triethylaluminum (TEA) during the syndiospecific polymerization of allyltrimethylsilane (ATMS) conducted in the presence of syndiospecific *ansa*-metallocene catalysts. The unique synthetic route allows the preparation of structurally well-defined silyl-containing stereoregular BCPs with good yield. The obtained silyl-containing stereoregular BCPs give a uniform chemical architecture and can self-assemble into well-ordered nanostructures, as evidenced by transmission electron microscopy (TEM) and small-angle X-ray scattering (SAXS) results.

EXPERIMENTAL SECTION

General Procedure. All reactions and manipulations were conducted under a nitrogen atmosphere using the standard Schlenk line or drybox techniques. Solvents and common reagents were commercially obtained and used either as received or purified by distillation with sodium/benzophenone. Allyltrimethylsilane (ATMS, purity >98%) and methyl methacrylate (99%) purchased from Aldrich were dried over calcium hydride and distilled under vacuum before use. Oxygen (purity >99.5%) was obtained from Matheson and were used as received. $Me_2C(Cp)(Flu)ZrCl_2$ (**I**)[21] and $Ph_2Si(Cp)(Flu)ZrCl_2$ (**II**)[22] were synthesized using methods described in the literature. The α-bromoisobutyryl bromide (98%), copper bromide (98%) and 1,10-phenanthroline (>99%) were purchased from Aldrich and used as received. Triethylaluminum (TEA, 1 M in hexane) was purchased from Aldrich and used as received. Methylaluminoxane (MAO, 14% in toluene), purchased from Albemarle, was dried under vacuum to remove residual TMA.[23] The resulting TMA-free MAO was diluted in toluene to the desired concentration before use.

Preparation of Hydroxyl-Capped sPATMS. Representative experiment (for entry 11 of Table 1): A 100 mL stainless steel reactor, equipped with a magnetic stirrer, was allowed to dry at 80 °C under vacuum. After being refilled with nitrogen, the reactor was cooled to −20 °C and then charged sequentially with 20 mL of toluene, 25.0 mmol of MAO, and 12.5 μmol of $Me_2C(Cp)(Flu)ZrCl_2$. After the reactor was allowed to stir at −20 °C for 5 min, it was charged with 8.0 mmol of TEA and then with 31.5 mmol ATMS to initiate the polymerization reaction. Polymerization was conducted at −20 °C for 24 h. The polymer solution was then treated with oxygen at a flow rate of 10 mL/min for 1 h. The solution was slowly warmed to room temperature and was then charged with H_2O_2 (5 mL, 30% in H_2O). After being stirred at room temperature for 30 min, the solution was charged with excess methanol (ca. 40 mL), which led to the deposition of the OH-capped sPATMS as a white precipitate. After isolation by filtration, the resulting polymer was purified by removing the atactic polyallytrimethylsilane via boiling acetone extraction in a Soxhlet extractor. The resulting insoluble fraction of the polymer was dried under vacuum to provide 1.64 g of OH-capped sPATMS [M_n = 15800, M_w/M_n = 1.81 by GPC (in THF at 40 °C)].

Fractionation of Hydroxyl-Capped sPATMS. On a vacuum line, 0.7 g of OH-capped sPATMS (M_n = 15800, M_w/M_n = 1.81, entry 11 of Table 1) was placed in a Soxhlet extractor and allowed to undergo Soxhlet extraction in a boiling MEK/THF mixture (5:1) for 24 h. The resulting MEK/THF solution was collected and allowed to concentrate under vacuum to 10 mL. The resulting solution was then charged with excess methanol (ca. 20 mL), which resulted in the deposition of a MEK/THF-soluble OH-capped sPATMS sample as a white precipitate. The resulting precipitate was isolated by filtration and dried under vacuum to provide 0.53 g of OH-capped sPATMS [M_n = 13300, M_w/M_n = 1.40 by GPC (in THF at 40 °C)].

Preparation of α-Bromoisobutylester-Capped sPATMS. In a 200 mL round-bottom flask, 0.35 g of OH-capped sPATMS (M_n= 13300, M_w/M_n= 1.40) was allowed to dissolve in 50 mL of toluene. The solution was then charged with excess Et_3N (ca., 1.0 mL) and then with excess α-bromoisobutyryl bromide (ca. 0.5 mL). The resulting solution was allowed to heat up to 60 °C; the esterfication reaction was conducted at 60 °C for 4 h. The reaction solution was cooled to room temperature and then charged with excess methanol (~80 mL), which led to the deposition of a sPATMS-based polymer as a pale brown precipitate. The resulting reaction product was collected through filtration, washed with methanol, and dried under high vacuum to provide 0.34 g of α-bromoisobutylester-capped sPATMS [M_n = 13500, M_w/M_n = 1.40 by GPC (in THF at 40 °C)].

Synthesis of sPATMS-*b*-PMMA. In a drybox, a 100 mL Schlenk flask equipped with a magnetic stirrer was charged sequentially with 0.26 g (0.02 mmol) of α-bromoisobutylester-capped sPATMS (M_n = 13500, M_w/M_n = 1.4), 30 mL of toluene, 5.5 μmol of copper bromide, and then 11.0 μmol of 1,10-phenanthroline.[24] The reaction vessel was capped and removed from the drybox. The reaction vessel was immersed in a oil bath and was allowed to heat up to 95 °C for 30 min for the in situ

Table 1. Preparation of End-Functionalized Stereoregular Polyallyltrimethylsilane via Selective ChainTransfer to Triethylaluminum (TEA) Mediated by Various Syndiospecific Metallocene Catalysts[h]

run	catal[a]	chain transfer agent	alkylaluminum (mmol)	temp (°C)	activity[c]	M_n[d]	PDI[d]	M_n[e] (calcd)	T_m[f] (°C)	$-\Delta H$[f] (J/g)	end group ratio(%)[g] hydroxyl	vinylidene
1	I	TEA[b]	2	20	13.03	9800	1.74	6100	250	10.6	31.4	68.6
2	I	TEA	4	20	10.51	7200	1.77	4500	248	8.5	39.4	61.6
3	I	TEA	6	20	8.47	4800	1.66	2800	244	5.6	45.4	54.6
4	I	TEA	8	20	6.24	4600	1.54	2500	238	4.4	49.2	51.8
5	I	TEA	8	40	18.42	2100	1.31	1200	250	2.8	42.8	57.2
6	I	TEA	8	0	7.72	14 800	1.70	11 200	255	18.6	63.4	36.6
7	I	TMA	8	0	4.65	16 200	1.86	13 100	249	16.7	58.4	41.8
8	I	TEA	2	−20	14.14	57 700	2.04	32 300	263	20.9	>99	-
9	I	TEA	4	−20	8.54	30 000	1.97	18 200	256	18.0	>99	-
10	I	TEA	6	−20	6.02	21 300	1.89	12 200	255	16.6	>99	-
11	I	TEA	8	−20	5.45	15 800	1.81	9800	251	10.4	>99	-
12	I	TEA	25	−20	1.95	7900	1.78	5600	248	9.9	>99	-
13	II	TEA	2	20	3.89	9800	1.65	6100	244	7.8	80.0	20.0
14	II	TEA	8	20	1.53	4400	1.53	2500	241	4.7	84.2	15.8
15	II	TEA	8	0	0.89	8600	1.65	5100	244	7.8	92.3	7.7
16	II	TMA	8	20	0.53	5100	1.81	3000	235	4.2	79.2	20.8

[a]Catalyst **I**: $Me_2C(Cp)(Flu)ZrCl_2$; Catalyst **II**: $Ph_2Si(Cp)(Flu)ZrCl_2$. [b]TEA = triethylaluminum. [c]Acticity = kg sPATMS·mol^{-1}Zr·h^{-1} [d]M_n (number-average molecular weight), M_w (weight-average molecular weight), and PDI (polydispersity, M_w/M_n) were determined by high temperature GPC (solvent, tetratydrofuran ; temperature 40 °C.). [e]M_n calculated by ^{1}H NMR. [f]T_m, (melting temperature), -ΔH(enthalpy of melting temperature) was determined by DSC. [g]The end group ratios were determined by 500 MHz ^{1}H NMR analyses (solvent, $CDCl_3$; temperature 60 °C). [h]Polymerization conditions: 30 mL of toluene; 31.5 mmol of ATMS (allyltrimethylsilane); 12.5 μmol of catalyst; 25.0 mmol of MAO; reaction time = 24 h.

generation of macroinitiator. Then, the reaction vessel was charged with 1.60 g of MMA (16.0 mmol) and allowed to undergo the chain-extension reaction at 95 °C for 24 h. The resulting solution was collected by filtration to remove insoluble copper metal complexes. The resulting polymer solution was concentrated to 15 mL via the removal of volatiles under vacuum. The resulting solution was charged with excess methanol (ca. 20 mL), which led to the deposition of the reaction product as an off-white precipitate. The resulting precipitate was isolated by filtration and allowed to undergo Soxhlet extraction with boiling cyclohexane to remove residual sPATMS. The resulting sPATMS-*b*-PMMA was dried under vacuum for 24 h to provide 1.02 g of sPATMS-*b*-PMMA [M_n = 45500, M_w/M_n = 1.29 as determined by GPC (in THF at 40 °C).

Characterization of Polymers. The molecular weight and molecular weight distribution (MWD) of synthesized polymers were determined by using GPC (Waters 2410-CALAC/GPC) with a refractive index (RI) detector and a set of U-Styragel HT columns with 10^6, 10^5, 10^4, and 10^3 Å pore sizes in series. The measurements were taken at 40 °C using THF as solvent. Polystyrene (PS) samples with narrow MWDs were used as the standards for calibration. The standards were in the range of absolute molecular weight from 980 to 2,110 000 g/mol; the *R* square of the ideal calibrated line was limited up to 0.999.

All ^{1}H and ^{13}C NMR spectra were recorded on a Bruker AV-500 NMR spectrometer. The sPATMS-based samples were dissolved in $CDCl_3$ or benzene-d_6. The recorded temperature was 60 °C.

Preparation of Bulk Samples. Bulk samples of sPATMS-*b*-PMMA BCPs were prepared by solution casting from a nonselective solvent, dichloromethane (CH_2Cl_2), at a concentration of 10 wt % sPATMS-*b*-PMMA at room temperature. After completely dissolving the polymers, the solution was filtrated through a filter with 0.45 μm pathways to remove impurities. The solution was then transferred to a vial and sealed well by aluminum foil with punch holes for the slow evaporation of the solvent. After drying, the bulk samples were further dried in a vacuum oven to remove residual solvent.

Characterization of Nanostructures. Bright-field transmission electron microscopy (TEM) images were obtained by using a JEOL JEM-2100 LaB_6 transmission electron microscope at an accelerating voltage of 200 kV. The bulk samples were sectioned at room temperature by using a Leica ultramicrotome. The microsections were collected on copper grids (100 mesh) with polyvinyl formal as a supporting membrane and covered by a thin film of carbon to protect the unstained samples from the electron damages such as shrinkage and degradation. For these silyl-containing BCPs, no staining procedure was required to enhance the mass−thickness contrast because the atomic number of silicon is obviously higher than that of carbon and oxygen. Accordingly, the sPATMS domains exhibited dark regions while the PMMA blocks appeared bright areas under TEM observations due to the intrinsic mass−thickness contrast. Small-angle X-ray scattering (SAXS) experiments were conducted at the synchrotron X-ray beamline 23A1 at the National Synchrotron Radiation Research Center (NSRRC) in Hsinchu, Taiwan.

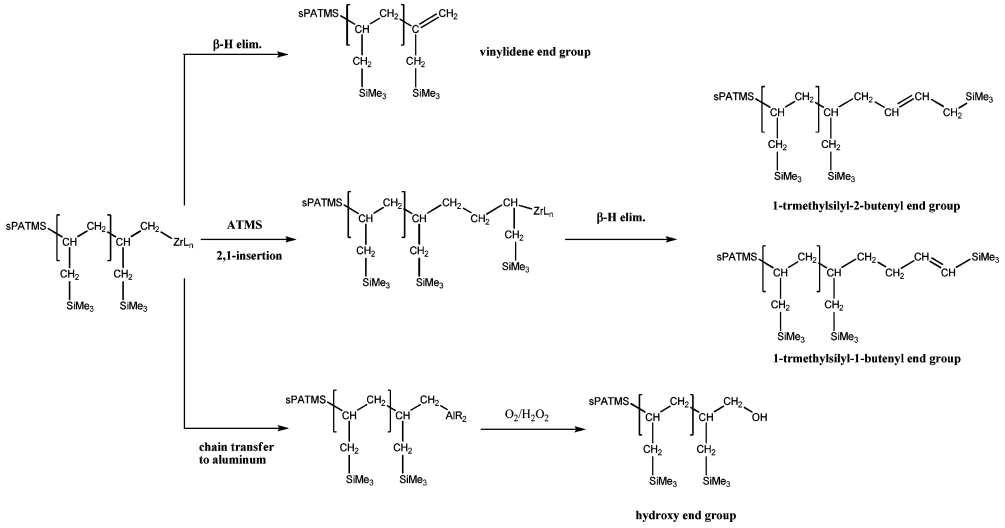
RESULTS AND DISSCUSSION

Synthesis of Hydroxyl-Capped sPATMS by Selective Chain Transfer to Alkylauminum.[25] The synthesis of OH-capped sPATMS via the selective chain transfer to alkylaluminum were investigated by syndiospecific polymerization of allyltrimethylsilane (ATMS) conducted in the presence of two *ansa*-metallocene catalysts [$(Me)_2C(Cp)(Flu)ZrCl_2$ (**I**) and $(Me)_2Si(Cp)(Flu)ZrCl_2$ (**II**)] using TEA as the chain transfer agent. The selective chain transfer reaction to TEA led to the generation of alkylaluminum-capped sPATMS as the preliminary product. After polymerization, the polymer solution was in situ treated with O_2/H_2O_2[13a,b,26] for converting the aluminum end group into a stable hydroxyl terminal group; this led to the generation of OH-capped sPATMS as the final reaction product. The resulting polymer solution was then charged with excess methanol, leading to the deposition of the ATMS-based polymer as a white precipitate, which can be isolated after filtration. The ^{1}H and ^{13}C NMR spectra of the ATMS-based polymers synthesized under these conditions were evaluated to determine the chain end structures. The results of the polymerization studies are summarized in Table 1.

There are four possible chain releasing pathways, which lead to the generation of sPATMSs with characteristic hydroxy,

dx.doi.org/10.1021/ma300034f | Macromolecules 2012, 45, 2720−2730

Scheme 1. Probable Polymer Chain End in Syndiotactic Poly(allyltrimethylsilane) Synthesis by Metallocene



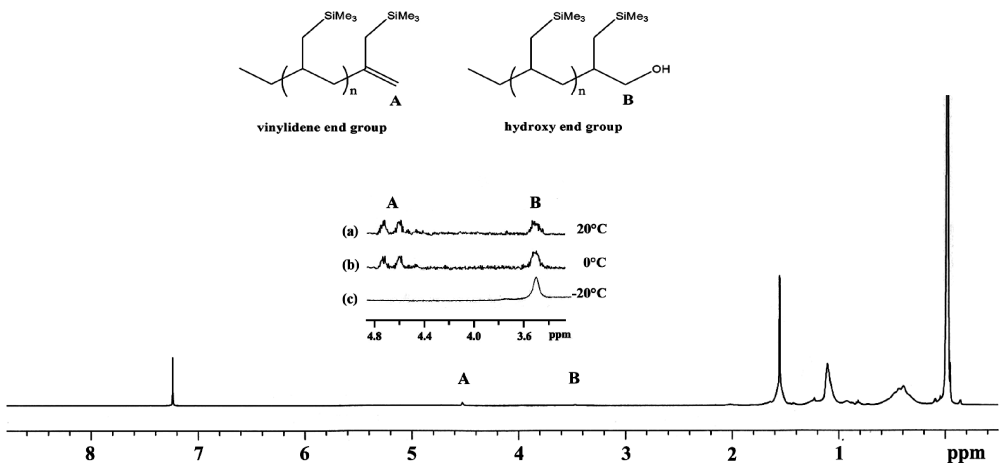


Figure 1. Expanded ^{1}H NMR (500 MHz) region of various sPATMS samples (a) M_n = 4600 g/mol, M_w/M_n = 1.54 (entry 4 of Table 1), (b) M_n = 14800 g/mol, M_w/M_n = 1.70 (entry 6 of Table 1), (c) M_n = 7900 g/mol, M_w/M_n = 1.78 (entry 12 of Table 1) (solvent, $CDCl_3$; temperature 60 °C).

vinylidene, 1-trimethylsilyl-1-butenyl, and 1-trimethylsilyl-2-butenyl end groups, respectively, as illustrated in Scheme 1. As shown in Figure 1 (entries 4, 6, and 12 of Table 1), sPATMSs with two different chain end structures, namely hydroxyl and vinylidene end groups, can be generated under these reaction conditions. The hydroxyl end group was produced from the 1,2- insertion of a terminal ATMS unit, which underwent chain transfer to aluminum to give aluminum-capped sPATMS as the preliminary reaction product; subsequently, the in situ oxidation of the resulting aluminum-capped sPATMS by the method described in the experiment section led to the generation of OH-capped sPATMS. The vinylidene chain end was generated from the 1,2-insertion of a terminal ATMS unit, which, in contrast, underwent β-hydride elimination chain transfer. It is noted that we were unable to detect the formation of 1-trimethylsilyl-1-butenyl-capped sPATMS [$(CH_3)_3Si-CH{=}CH-CH_2-CH_2-$sPATMS] and 1-trimethylsilyl-2-butenyl-capped sPATMS [$(CH_3)_3Si-CH2-CH{=}CH-CH_2-$sPATMS] generated from the 2,1-insertion of a terminal ATMS unit, which underwent subsequent β-hydride elimination transfer by abstracting methylene hydrides at the α- and γ-positions, respectively, from the terminal trimethylsilyl group. The generations of OH-capped and vinylidene-capped sPATMSs without 1-trimethylsilyl-1-butenyl-capped and 1-trimethylsilyl-2-butenyl-capped sPATMSs reveals that the insertion of ATMS follows the predominant 1,2-insertion patterns and that OH-capped sPATMS and vinylidene-capped sPATMS were generated from the 1,2-inserted terminal ATMS unit, which underwent a subsequent chain transfer reaction to TEA and the β-hydride elimination chain transfer reaction, respectively.

Although the syndiospecific ATMS polymerization conducted in the presence of these *ansa*-metallocene catalysts provides perfect regioselectivity (predominant 1,2-insertion) control, the formation of sPATMSs containing two different terminal groups (hydroxyl and vinylidene end groups; see entries 1−7 of Table 1) indicates that these catalyst systems fail to facilitate chain-end structural control through regulating chain transfer mechanisms especially when polymerization was conducted at a high polymerization temperature. The results listed in Table 1 reveal that the formation of OH-capped sPATMS via the selective chain transfer to alkylaluminums depends on the structures and concentration of chain transfer agents. As shown in entry 1−5 of Table 1, β-hydride elimination transfer (producing vinylidene-capped sPATMS) was the predominant chain releasing pathway

dx.doi.org/10.1021/ma300034f | *Macromolecules* 2012, 45, 2720−2730

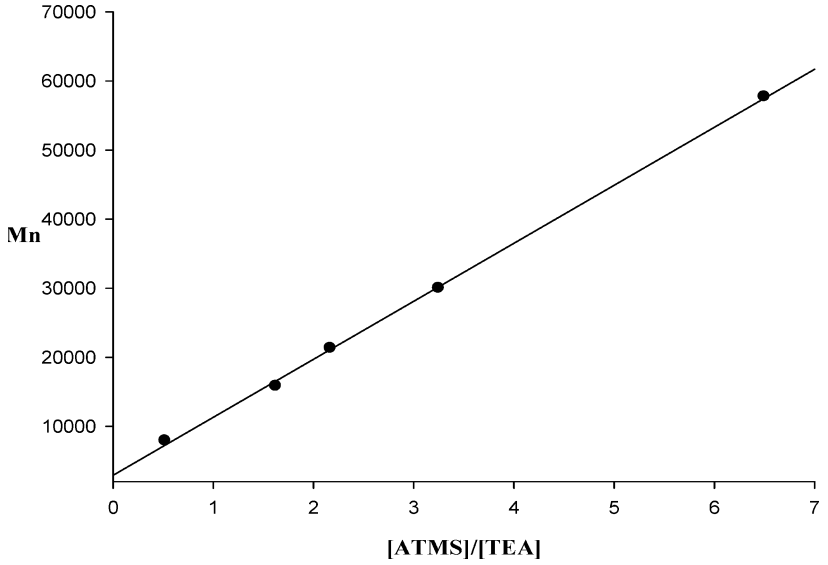


Figure 2. Plot of number-average molecular weight (M_n) of OH-capped sPATMS vs the mole ratios of [ATMS]/[TEA] (entries 8−12 of Table 1).

when polymerization was conducted at high temperature (≥20 °C). In contrast, syndiospecific ATMS polymerization conducted at low temperature (≤20 °C) shifted the chain releasing pathway from β-hydride elimination transfer to mainly the chain transfer to alkylaluminums. A comparison of entries 6−7 and 14−16 of Table 1 shows that replacing TMA with TEA led to the production of an increased amount of OH-capped sPATMS and that the amount of OH-capped sPATMS can be enhanced by increasing the concentration of trialkylaluminum in the feed. Although increasing the concentration of TEA increases the amount of OH-capped sPATMS, OH-capped sPATMS cannot be prepared as a single reaction product since these reaction conditions also generate vinylidene-capped sPATMS, which is generated through β-hydride elimination transfer, as the minor reaction product.

In order to provide pure OH-capped sPATMS for use as the end-functionalized prepolymer in the synthesis of stereoregular BCPs, syndiospecific polymerizations of ATMS at a lower temperature (−20 °C)[13b,27] were conducted to suppress the β-hydride elimination transfer for the formation of vinylidene-capped sPATMS. Entries 8−12 of Table 1 show that OH-capped sPATMS can be selectively produced as the only detectable product (by NMR analyses) at low temperature. Figure 2 shows the plot of polymer molecular weight versus [ATMS]/[TEA] by conducting the allyltrimethylsilane polymerization at −20 °C using $(Me)_2C(Cp)(Flu)ZrCl_2$ (**I**) as the catalyst and TEA as the chain transfer agent (entries 8−12). The nearly linear relationship between the molecular weight of sPATMSs and [ATMS]/[TEA] ratio indicates that chain transfer to TEA (rate constant = k_{tr}) competes with the allyltrimethylsilane chain propagation reaction. Since the degree of polymerization (X_n) follows the equation $X_n = k_p[ATMS]/k_{tr}[TEA]$, the plot in Figure 2 can be used to calculate the chain transfer constant (k_{tr}/k_p = 1/35.5) for the generation of OH-capped sPATMS by predominant chain transfer to TEA. Nevertheless, OH-capped sPATMS can be selectively generated by selective chain transfer to TEA during syndiospecific polymerization of allyltrimethylsilane conducted in the presence of syndiospecific metallocene catalysts.

End Group Analyses of Hydroxyl-Capped sPATMS. End group analyses provide detailed structural information for the resultant ATMS polymers and give direct evidence of the successful preparation of pure OH-capped sPATMS. Figure 1c shows the ^{1}H NMR spectrum (with an inset showing the expanded region and chemical shift assignments) of the OH-capped sPATMS (M_n = 7900 g/mol, M_w/M_n = 1.78; entry 12 of Table 1) isolated after the O_2/H_2O_2 treatment. As shown in the ^{1}H NMR spectrum, in addition to the four major upfield resonances (δ = 0.31, 0.42, 1.13, 1.65) corresponding to the $-CH[CH_2Si(C\mathbf{H}_3)_3]-CH_2-$, $-CH[C\mathbf{H}_2Si(CH_3)_3]-CH_2-$, $-CH[CH_2Si(CH_3)_3]-C\mathbf{H}_2-$ and $-C\mathbf{H}[CH_2Si(CH_3)_3]-CH_2-$ proton resonances of the sPATMS backbone, respectively, there is a weak downfield resonance at 3.47 ppm, which corresponds to the chain end $-CH[CH_2Si(CH_3)_3]-C\boldsymbol{H}_2-OH$ proton resonance. The detailed chemical assignments are based on the structural information on [^{13}C (DEPT 135); Figure 3] and [two-dimensional ^{1}H−^{13}C HMQC; Supporting Information] NMR spectra. These NMR spectra clearly reveal that OH-capped sPATMS prepared by selective chain transfer to TEA has a single hydroxyl terminal group, making it suitable for use as a stereoregular end-functionalized prepolymer in the construction of stereoregular BCPs. Two aliphatic chain ends, 2-(trimethylsilylmethyl)-butyl [$CH_3CH_2CH(CH_2SiMe_3)CH_2-$] (approximately 88% based on integration) and 2-(trimethylsilylmethyl)propyl [$CH_3CH(CH_2SiMe_3)CH_2-$] (approximately 12% based on integration), generated in the chain initiation steps, can be identified by ^{13}C NMR analyses (Figure 3). The [$CH_3CH_2CH(CH_2SiMe_3)CH_2-$] end group was generated in the chain initiation step by the primary insertion of allyltrimethylsilane to [Zr−Et], formed in the chain releasing step by selective chain transfer to TEA. The [$CH_3CH(CH_2SiMe_3)CH_2-$] end group was generated by the primary insertion of allyltrimethylsilane to [Zr−Me], which was formed in the chain releasing step by chain transfer to MAO.

Synthesis of Silyl-Containing Stereoregular BCPs. As demonstrated by the chain end analysis, OH-capped sPATMS prepared by the selective chain transfer route contains a single hydroxyl end group, making it suitable for use as the end-functionalized macroinitiator for the synthesis of stereoregular BCPs. Unfortunately, the OH-capped sPATMS macroinitiator prepared via the metallocene-catalyst-mediated selective chain transfer route has a broad range of molecular weight distribution, and hence is not suitable for use directly in the post block

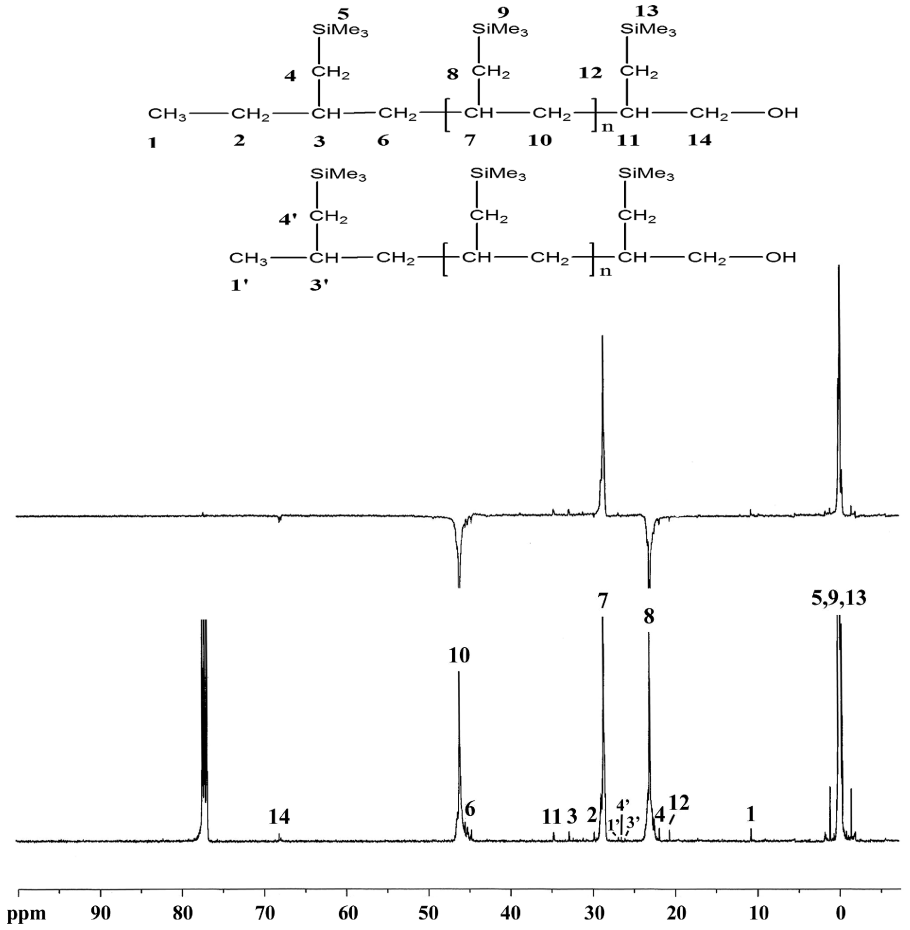


Figure 3. ^{13}C (DEPT-135) NMR (125 MHz) spectra of OH-capped sPATMS (M_n = 15800 g/mol, M_w/M_n = 1.81; entry 11 of Table 1) (solvent, $CDCl_3$; temperature 60 °C).

polymerization reaction for the preparation of structurally well-defined stereoregular BCPs. Although BCPs with relatively high polydispersity are capable of self-organizing into ordered morphologies, the broad distribution in chain length shifts the phase boundaries (relative to those of the corresponding monodisperse BCPs) and modifies the microdomain size.[28] Narrow-MWD samples of OH-capped sPATMSs are preferred for use as the end-functionalized stereoregular prepolymer for the preparation of structurally well-defined sillyl-containing stereoregular BCPs.[13b,c] Narrow-MWD samples of end-functionalized stereoregular polymers can be obtained by the fractionation of the broad-MWD product through extraction processes, as demonstrated by prior reports.[13,29] Thus, fractionation of the broad-MWD product (M_n = 15800, M_w/M_n = 1.81) by Soxhlet extractions in MEK/THF (3:1) using methods described in the Experimental Section giving a narrow-MWD sample of OH-capped sPATMS (M_n = 13100, M_w/M_n = 1.40). The hydroxyl terminal group of OH-capped sPATMS was allowed to convert into the α-bromoester end group by the reaction between the OH-capped sPATMS and α-bromoisobutyryl bromide to provide α-bromoester-terminated sPATMS with high yield. The comparison of the ^1H NMR spectra of OH-capped sPATMS (M_n = 13100 g/mol, M_w/M_n = 1.40) with that of α-bromoester-capped sPATMS (M_n = 13200 g/mol, M_w/M_n =1.40) is shown in Figure 4. The resulting α-bromoester-terminated sPATMS was in situ treated with CuBr and was chain-extended with MMA by the controlled/living radical polymerization of MMA to give sPATMS-*b*-PMMA (M_n = 42600 g/mol, M_w/M_n = 1.30)

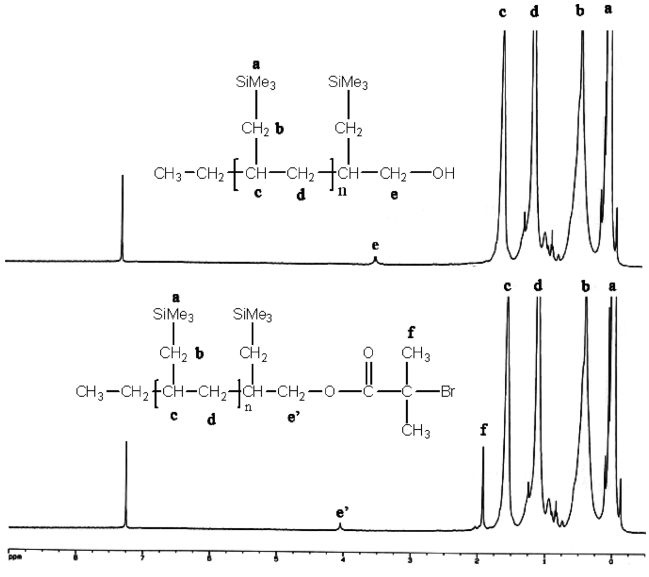
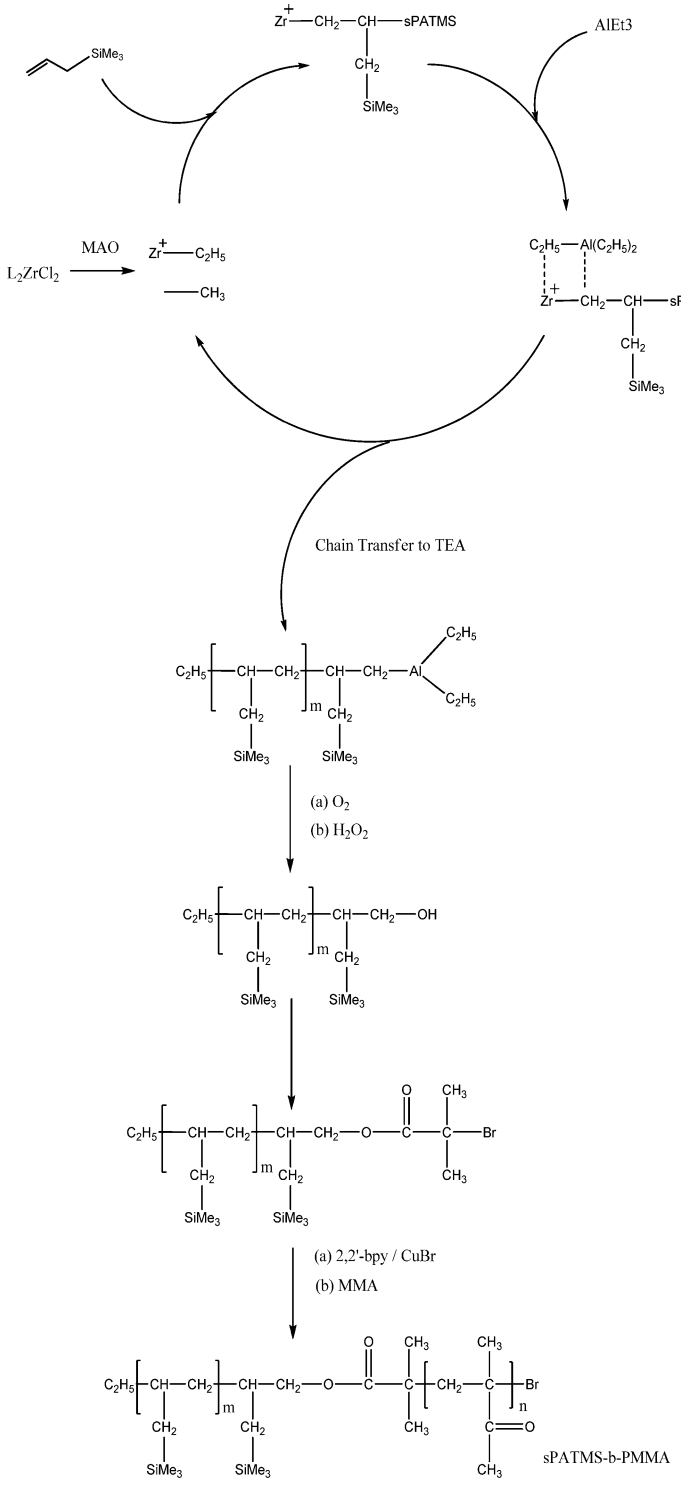


Figure 4. ^1H NMR spectra (500 MHz) of (a) OH-capped sPATMS (M_n = 13300 g/mol, M_w/M_n = 1.40), (b) Br-capped sPATMS (M_n = 13500 g/mol, M_w/M_n =1.40) (solvent, $CDCl_3$; temperature 60 °C).

as a structurally well-defined silyl-containing stereoregular diblock copolymer with a good MMA conversion ratio and high BCP yield. The detailed synthetic routes for the preparation of sPATMS-*b*-PMMA are illustrated in Scheme 2. The comparison of the GPC

dx.doi.org/10.1021/ma300034f | *Macromolecules* 2012, 45, 2720−2730

Scheme 2. Synthetic Routes for Preparations of End-Functionalized sPATMS and sPATMS-Based Stereoregular Block Copolymers



elution curves of OH-capped sPATMS with that of sPATMS-*b*-PMMA (M_n = 42600 g/mol, M_w/M_n = 1.30) is shown in Figure 5. Figures 6 show the ^{1}H NMR spectrum (with insets showing chemical shift assignments) of sPATMS-*b*-PMMA. [The ^{13}C (DEPT 135) NMR spectra can be found in Supporting Information]. The proposed synthetic route is further illustrated by the preparation of a second sPATMS-*b*-PMMA sample (M_n = 29900 g/mol, M_w/M_n = 1.24; GPC and ^{1}H NMR spectrum of this sample can be found in the Supporting Information) from the same narrow-MWD end-functionalized α-bromoester-capped sPATMS (M_n = 13500 g/mol, M_w/M_n = 1.40).

Self-Assembled Nanostructures of Stereoregular BCPs. Owing to the stereoregularity of the sPATMS block, the synthesized sPATMS-*b*-PMMA samples show semicrystalline behavior. The thermal behavior of the sPATMS-*b*-PMMA was first examined by DSC. The DSC thermograms were recorded during the second heating cycle from 0 to 270 °C with a heating rate of 10 °C/min after fast cooling by 150 °C/min

dx.doi.org/10.1021/ma300034f | *Macromolecules* 2012, 45, 2720−2730

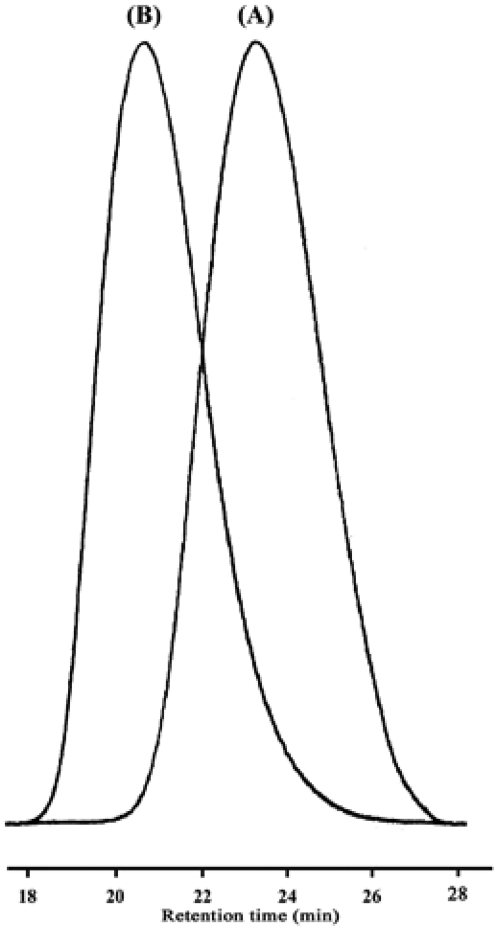


Figure 5. The GPC curves comparison between (A) OH-capped sPATMS (M_n = 13500 g/mol, M_w/M_n = 1.40), (B) sPATMS-*b*-PMMA (M_n = 45500 g/mol, M_w/M_n = 1.29) (in THF, at 40 °C).

from the melt sate of samples at 270 °C. From DSC profiles of the second heating process (Figure 7), the sPATMS-*b*-PMMA with various volume fractions of sPATMS exhibit different thermal properties. For sPATMS13-PMMA32 with a lower volume fraction of PLLA (i.e., f^{v}_{sPATMS} = 0.35), the glass transition temperatures (T_g) of sPATMS and PMMA blocks were determined as approximately 36 and 117 °C, respectively (Figure 7a). The absence of a sPATMS crystallization temperature and melting point in the high temperature region is attributed to the confinement effect for sPATMA chains restricted in the PMMA matrix. For comparison, sPATMS13-PMMA17 with a higher volume fraction of sPATMS (i.e., f^{v}_{sPATMS} = 0.51) gives glass transition temperatures of sPATMS and PMMA blocks at approximately 36 and 105 °C, respectively (Figure 7b). The slightly lower $T_{g,PMMA}$ of sPATMS13-PMMA17 than that of sPATMS13-PMMA32 is attributed to the molecular weight effect. In contrast to the amorphous behavior of sPATMS in sPATMS13-PMMA32, a small endothermic peak at 232 °C for the sPATMS melting point (T_m) can be observed in the high temperature region,[17] further confirming the confined effect on the crystallization of sPATMS chains in sPATMS13-PMMA17.

To achieve the formation of well-ordered nanostructures from the self-assembly of sPATMS-*b*-PMMA BCPs in the bulk state, the bulk samples of sPATMS-*b*-PMMA were first heated to the maximum annealing temperature, T_{max} = 270 °C, for 3 min to eliminate the sPATMS crystalline residues resulting from sample preparation. Subsequently, the thermally treated bulk samples could be obtained after rapidly cooling at a rate of 150 °C/min from the melt state at 270 °C. For sPATMS13-PMMA32 (f^{v}_{sPATMS} = 0.35), hexagonally packed cylindrical nanostuctures were observed in TEM images (Figure 8a). Owing to the higher atomic number of silicon than that of carbon and oxygen, the dark cylinders can be referred to the sPATMS microdomains and dispersed in the bright PMMA matrix under TEM observation. The self-assembled morphology can be further identified

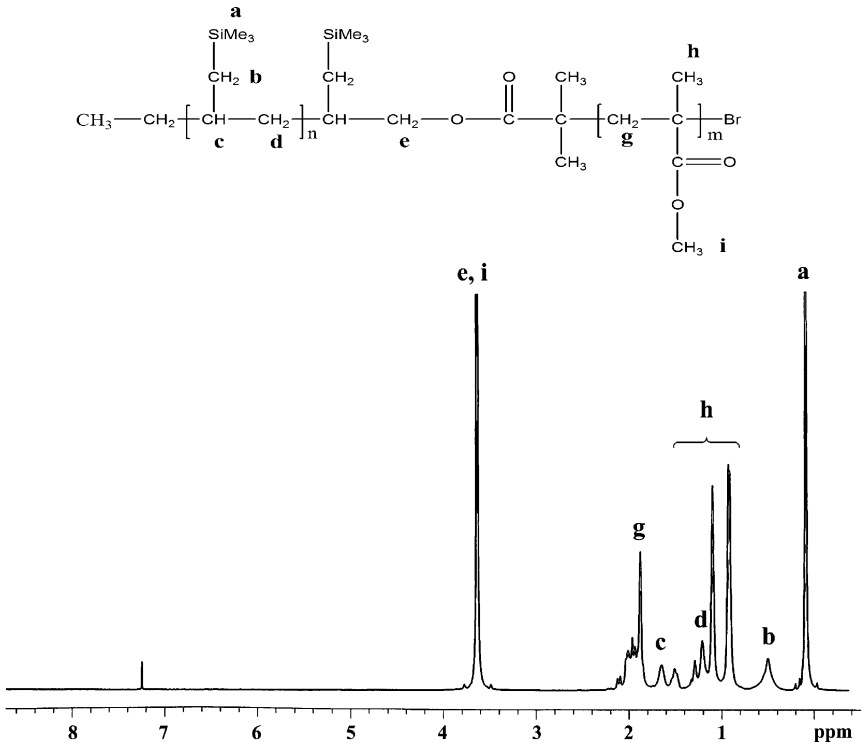


Figure 6. ^{1}H (500 Hz) NMR spectrum of sPATMS-*b*-PMMA (M_n = 45500 g/mol, M_w/M_n = 1.29, f_{sPATMS} = 0.35) (solvent, $CDCl_3$; temperature 60 °C).

dx.doi.org/10.1021/ma300034f | *Macromolecules* 2012, 45, 2720−2730

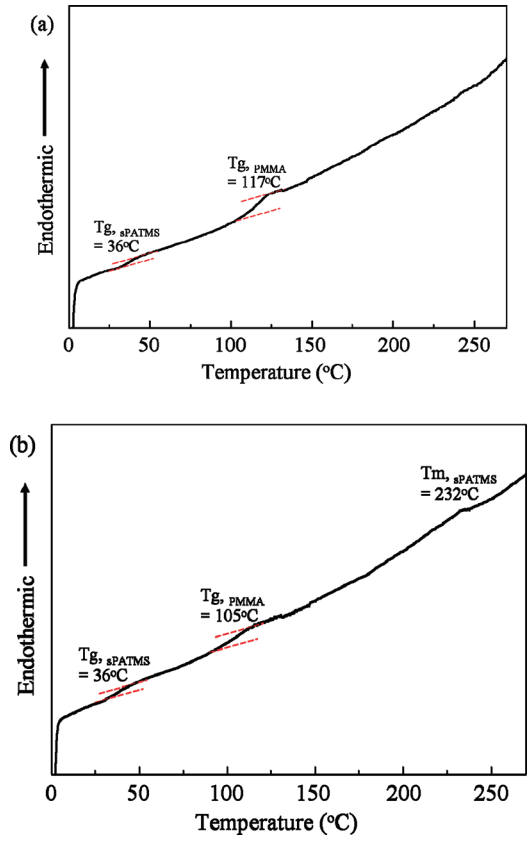


Figure 7. DSC thermograms of sPATMS–PMMA with sPATMS volume fraction of (a) 0.35 and (b) 0.51, respectively. The heating rate is 10 °C/min.

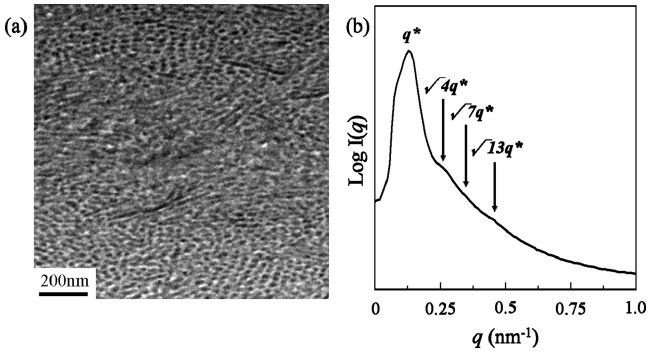


Figure 8. (a) TEM micrographs of sPATMS–PMMA (f^{v}_{sPATMS} = 0.35) block copolymer with hexagonally packed cylinder nanostructure. The microdomains of sPATMS appear dark while the PMMA microdomain displays bright. (b) Corresponding one-dimensional SAXS profile.

by SAXS experiments. Corresponding one-dimensional SAXS profile (Figure 8b) shows well-ordered reflections with peak positions at the q ratios of $1:\sqrt{4}:\sqrt{7}:\sqrt{13}$, indicating a well-ordered cylindrical phase with hexagonal packing. Using the primary peak, the d-spacing of the (100) plane was determined as 49.3 nm and the interspacing of each cylinder was then calculated as 56.9 nm. These results suggest that the crystallization temperature of sPATMS is below the order–disorder transition temperature (T_{ODT}) and the self-assembled nanostructure driven from the incompatibility of the sPATMS and PMMA blocks can be successfully developed. In contrast,

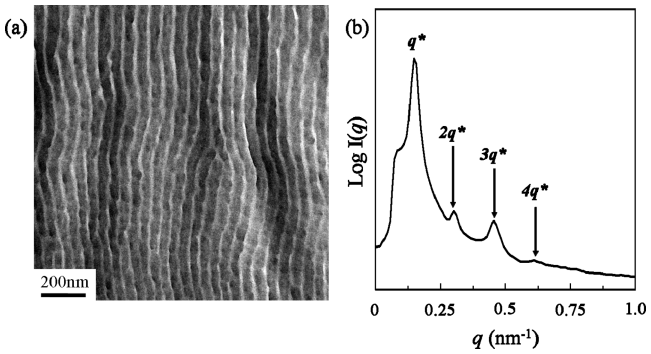


Figure 9. (a) TEM micrographs of sPATMS–PLLA (f^{v}_{PLLA} = 0.51) block copolymer with lamellar nanostructure. The microdomains of sPATMS appear dark while the PMMA microdomain displays bright. (c) Corresponding one-dimensional SAXS profile.

Figure 9a shows the lamellar nanostructure of sPATMS13-PMMA17 (f^{v}_{sPATMS} = 0.51) resulting from the self-assembly in the melt state. For SAXS experiments, the self-assembled morphology of the sPATMS-*b*-PMMA is identified as a lamellar phase according to the reflection peaks at the q ratios of 1: 2: 3: 4 (Figure 9b). The d-spacing of the (100) plane was determined as 42.9 nm from the primary peak of the reflections.

CONCLUSIONS

The preparations of structurally well-defined silyl-containing stereoregular BCPs composed of syndiotactic polytrimethylallylsilane (sPATMS) and poly(methyl methacrylate) (PMMA) through the controlled living atom transfer radical polymerization (ATRP) of methyl methacrylate using α-bromoester end-capped sPATMS for the in situ generation of CuBr-capped macroinitiator was presented. The α-bromoester end-capped sPATMS was generated via the esterification of hydroxyl-capped sPATMS with α-bromoisobutyl bromide. Hydroxyl-capped sPATMS was produced by inducing the selective chain transfer reaction to trialkylaluminum during the syndiospecific polymerization of allytrimethylsilane. This work is the first example to prepare the sily functional-moieties containing stereoregular diblock copolymers, which have a well-defined chemical architecture with uniform molecular length, and which can self-organize into the consistent morphologies, as revealed by TEM and SAXS examinations.

ASSOCIATED CONTENT

Supporting Information

^{13}C (DEPT-135) and two-dimensional ^{1}H and ^{13}C HMQC NMR spectra of α-bromoester-capped sPATMS and ^{1}H NMR spectrum and GPC curves of sPATMS-*b*-PMMA. This material is available free of charge via the Internet at http://pubs.acs.org.

AUTHOR INFORMATION

Corresponding Author

*(J.-C.T.) Telephone: 886-5-2720411 ext 33460. Fax: 886-5-2721206. E-mail: chmjct@ccu.edu.tw. (R.-M.H.) Telephone: 886-3-5738349. Fax 886-3-5715408. E-mail: rmho@mx.nthu.edu.tw.

Notes

The authors declare no competing financial interest.

■ ACKNOWLEDGMENTS

Authors would like to thank the National Science Council of Taiwan for the financial support for this research under contracts NSC-99-2221-E-194-003 and NSC-99-2120M-E-007-013.

■ REFERENCES

(1) (a) Lehn, J.-M. *Science* **1985**, *227*, 849−856. (b) Whitesides, G. M.; Grzybowski, B. *Science* **2002**, *295*, 2418−2421.

(2) (a) Lehn, J.-M. *Proc. Natl. Acad. Sci. U.S.A.* **2002**, *99*, 4763−4768. (b) Whitesides, G. M.; Boncheva, M. *Proc. Natl. Acad. Sci. U.S.A.* **2002**, *99*, 4769−4774.

(3) (a) Thomas, E. L.; Anderson, D. M.; Henkee, C. S.; Hoffman, D. *Nature* **1988**, *344*, 598−601. (b) Muthukumar, M.; Ober, C. K.; Thomas, E. L. *Science* **2002**, *277*, 1225−1232.

(4) (a) Bates, F. S.; Fredrickson, G. H. *Annu. Rev. Phys. Chem.* **1990**, *41*, 525−557. (b) Matsen, M. W.; Schick, M. *Phys. Rev. Lett.* **1994**, *72*, 2660−2663. (c) Matsen, M. W.; Bates, F. S. *Macromolecules* **1996**, *29*, 1091−1098. (d) Matsen, M. W.; Bates, F. S. *Macromolecules* **1996**, *29*, 7641−7644. (e) Bates, F. S.; Fredrickson, G. H. *Phys. Today* **1999**, *52*, 32−38.

(5) (a) Cohen, R. E.; Cheng, P.-L.; Douzinas, K.; Kofinas, P.; Berney, C. V. *Macromolecules* **1990**, *23*, 324−327. (b) Loo, Y. -L.; Register, R. A.; Ryan, A. J. *Macromolecules* **2002**, *35*, 2365−2374. (c) Ho, R.-M.; Lin, F.-H.; Tsai, C.-C.; Lin, C.-C.; Ko, B.-T.; Hsiao, B. S.; Sics, I. *Macromolecules* **2004**, *37*, 5985−5994. (d) Chen, C.-K.; Lin, S.-C.; Chiang, Y.-W.; Ho, R.-M.; Latz, B. *Macromolecules* **2010**, *43*, 7752−7758.

(6) (a) Chiang, Y.-W.; Ho, R.-M.; Ko, B.-T.; Lin, C.-C. *Angew. Chem., Int. Ed. Engl.* **2005**, *44*, 7969−7972. (b) Chiang, Y.-W.; Ho, R.-M.; Thomas, E. L.; Burger, C.; Hsiao, B. S. *Adv. Funct. Mater.* **2009**, *19*, 448−459.

(7) (a) Lin, Z.; Kim, D. H.; Wu, X.; Boosahda, L.; Stone, D.; LaRose, L.; Russell, T. P. *Adv. Mater.* **2002**, *14*, 1373−1376. (b) Qiao, Y.; Wang, D.; Buriak, J. M. *Nano Lett.* **2007**, *7*, 464−469. (c) Thurn-Albrecht, T.; Steiner, R.; DeRouchey, J.; Stafford, C. M.; Huang, E.; Bal, M.; Tuominen, M.; Hawker, C. J.; Russell, T. P. *Adv. Mater.* **2000**, *12*, 787−791. (d) Zalusky, A. S.; Olayo-Valles, R.; Taylor, C. J.; Hillmyer, M. A. *J. Am. Chem. Soc.* **2001**, *123*, 1519−1520. (e) Lo, K.-H.; Tseng, W.-H.; Ho, R.-M. *Macromolecules* **2007**, *40*, 2621−2624. (f) Lo, K.-H.; Chen, M.-C.; Ho, R.-M.; Sung, H.-W. *ACS Nano* **2009**, *3*, 2660−2666.

(8) (a) Tseng, W.-H.; Chen, C.-K.; Chiang, Y.-W.; Ho, R.-M.; Akasaka, S.; Hasegawa, H. *J. Am. Chem. Soc.* **2009**, *131*, 1356−1357. (b) Hsueh, H.-Y.; Chen, H.-Y.; She, M.-S.; Chen, C.-K.; Ho, R.-M.; Gwo, S.; Hasegawa, H.; Thomas, E. L. *Nano Lett.* **2010**, *10*, 4994−5000.

(9) (a) Arkles, B. *Chem. Tech.* **1983**, *13*, 542−555. (b) Noll, W. *Chemistry and Technology of Silicones*: Academic Press: New York, 1968. (c) Tomanek, A. *Silicones and Industry*: Hanser (Wacker Chemie): Munich, Germany, 1991. (d) Beevers, M. S. *Dielectric Properties of Siloxanes, In Siloxane Polymers*, Clarson, S. J.; Semlyen, J. A.; Eds.; Prentice Hall: Englewood Cliffs, NJ, 1993. (e) Baker, E. B.; Barry, A. J.; Hunter, M. *J. Ind. Eng. Chem.* **1946**, *38*, 1117−1120. (f) Warrick, E. L.; Hunter, M. J.; Barry, A. *J. Ind. Eng. Chem.* **1952**, *44*, 2196−2202. (g) Young, O. B.; Dickerman, C. E. *Ind. Eng. Chem.* **1954**, *46*, 364−365. (h) ÅKerlöf, G. *J. Am. Chem. Soc.* **1932**, *54*, 4125−4139. (i) Chang, P.-S.; Buese, M. A. *J. Am. Chem. Soc.* **1993**, *115*, 11475−11484. (j) Thomas, D. R. *Crosslinking of Silicones, In Siloxane Polymers*; Clarson, S. J., Semlyen, J. A., Eds.; Prentice Hall: Englewood Cliffs, NJ, 1993. (k) Plate, N. A.; Durgarjan, S. G.; Khotimskii, V. S.; Teplyakov, V. V.; Yampolskii, Y. P. *J. Membrane Sci.* **1990**, *52*, 289−304. (l) Wang, C.; Wang, J.; Park, C. B.; Kim, Y.-W. *J. Mater. Sci.* **2004**, *39*, 4913−4915. (m) Hewitt, D. G.; Jing, L. *J. Polym. Sci., Part A: Polym. Chem.* **1998**, *36*, 1093−1106.

(10) Bita, I.; Yang, J. K. W.; Jung, Y. S.; Ross, C. A.; Thomas, E. L.; Berggren, K. K. *Science* **2008**, *321*, 939−943. (b) Lammertink, R. G. H.; Hempenius, M. A.; van den Enk, J. E.; Chan, V. Z.-H.; Thomas, E. L.; Vancso, G. J. *Adv. Mater.* **2000**, *12*, 98−103. (c) Park, C.; Yoon, J.; Thomas, E. L. *Polymer* **2003**, *44*, 6725−6760. (d) Guo, L. J. *Adv. Mater.* **2007**, *19*, 495−513. (e) Chemg, J. Y.; Ross, C. A.; Chan, V. Z. H.; Thomas, E. L.; Lammertink, R. G. H.; Vancso, G. J. *Adv. Mater.* **2001**, *13*, 1174−1178. (f) Choi, P.; Fu, P.-F.; Guo, L. J. *Adv. Funct. Mater.* **2007**, *17*, 65−70. (g) Chao, C.-C.; Ho, R.-M.; Georgopanos, P.; Avgeropoulos, A.; Thomas, E. L. *Soft Matter* **2010**, *6*, 3582−3587. (h) Chao, C.-C.; Ho, R.-M.; Georgopanos, P.; Avgeropoulos, A.; Thomas, E. L. *ACS Nano* **2010**, *4*, 2088−2094.

(11) (a) Gilroy, J. B.; Gädt, T.; Whittell, G. R.; Chabanne, L.; Mitchels, J. M.; Richardson, R. M.; Winnik, M. A.; Manners, I. *Nat. Chem.* **2010**, *2*, 566−570. (b) Massey, J. A.; Temple, K.; Cao, L.; Rharbi, Y.; Raez, J.; Winnik, M. A.; Manners, I. *J. Am. Chem. Soc.* **2000**, *122*, 11577−11584. (c) Ni, Y.; Rulkens, R.; Manners, I. *J. Am. Chem. Soc.* **1996**, *118*, 4102−4114. (d) Elio, J. C.; Rider, D. A.; Wang, J. Y.; Russell, T. P.; Manners, I. *Macromolecules* **2008**, *41*, 9474−9479. (e) Soto, A. P.; Manners, I. *Macromolecules* **2009**, *42*, 40−42. (f) He, F.; Gädt, T.; Jones, M.; Scholes, G. D.; Manners, I.; Winnik, M. A. *Macromolecules* **2009**, *42*, 7953−7960. (g) Chen, H.; Wu, X.; Duan, H.; Wang, Y. A.; Wang, L.; Zhang, M.; Mao, H. *ACS Appl. Mater. Interfaces* **2009**, *1*, 2134−2140. (h) Raez, J.; Manners, I.; Winnik, M. A. *J. Am. Chem. Soc.* **2002**, *124*, 10381−10395. (i) Wang, X. S.; Winnik, M. A.; Manner, I. *Macromolecules* **2002**, *35*, 9146−9150. (j) Cao, L.; Manners, I.; Winnik, M. A. *Macromolecules* **2002**, *35*, 8258−8260. (k) Massey, J. A.; Power, K. N.; Manners, I.; Winnik, M. A. *Adv. Mater.* **1998**, *10*, 1559−1562.

(12) (a) Hani, R.; Lenz, R. W. *Silicon-based Polymer science: a comprehensive resource*; Zeigler, J. M., Fearon, F. W. G., Eds.; Advances in Chemistry Series 224; American Chemical Society: Washington, DC, 1989. (b) Senshu, K.; Furuzono, T.; Koshizaki, N. *Macromolecules* **1997**, *30*, 4421−4428. (d) Nguyen, P.; Gómez-Elipe, P.; Manners, I. *Chem. Rev.* **1999**, *99*, 1515−1548. (e) Manners, I. *Angew. Chem., Intl. Ed. Engl* **1996**, *35*, 1602−1621. (f) Prange, R.; Allcock, H. R. *Macromolecules* **1999**, *32*, 6390−6392.

(13) (a) Tzeng, F.-Y.; Lin, M.-C.; Wu, J.-Y.; Kuo, J.-C.; Tsai, J.-C.; Hsiao, M.-S.; Chen, H.-L.; Cheng, S. Z. D. *Macromolecules* **2009**, *42*, 3073−3085. (b) Kuo, J.-C.; Lin, W.-F.; Yu, C.-H.; Tsai, J.-C.; Wang, T.-C.; Chung, T.-M.; Ho, R.-M. *Macromolecules* **2008**, *41*, 7967−7977. (c) Tsai, J.-C.; Kuo, J.-C.; Ho, R.-M.; Chung, T.-M. *Macromolecules* **2006**, *39*, 7520−7526. (d) Hsiao, T.-J.; Lee, J.-Y.; Mao, Y.-C.; Chen, Y.-C.; Tsai, J.-C.; Lin, S.-C.; Ho., R.-M. *Macromolecules* **2011**, *44*, 286−298. (e) Ho, R.-M.; Chung, T.-M.; Tsai, J.-C.; Kuo, J.-C.; Hsiao, B. S.; Sics, I. *Macromol. Rapid Commun.* **2005**, *26*, 107−111. (f) Lin, W.-F.; Hsiao, T.-J.; Tsai, J.-C.; Chung, T.-M.; Ho, R.-M. *J. Polym. Sci., Part A: Polym. Chem.* **2008**, *46*, 4843−4856. (g) Lee, J.-Y.; Tsai, J.-C. *J. Polym. Sci., Part A: Polym. Chem.* **2011**, *49*, 3739−3750.

(14) (a) Wolf, F. K.; Hofmann, A. M.; Frey, H. *Macromolecules* **2010**, *43*, 3314−3324. (b) Fu, J.; Luan, B.; Yu, X.; Cong, Y.; Li, J.; Pan, C. Y.; Han, Y. C.; Yang, Y. M.; Li, B. Y. *Macromolecules* **2004**, *37*, 976−986.

(15) (a) Ho, R.-M.; Chen, C.-K.; Chiang, Y.-W. *Macromol. Rapid Commun.* **2009**, *30*, 1439−1456. (b) Tseng, W.-H.; Chen, C.-K.; Chiang, Y.-W.; Ho, R. M.; Akasaka, S.; Hasegawa, H. *J. Am. Chem. Soc.* **2009**, *131*, 1356−1357. (c) Chiang, Y.-W.; Ho., R.-M.; Thomas, E. L.; Burger, C.; Hsiao, B. S. *Adv. Funct. Mater.* **2009**, *19*, 448−459. (d) Chung, T.-M.; Ho, R.-M.; Kuo, J.-C.; Tsai, J.-C.; Hsiao, B. S.; Sics, I. *Macromolecules* **2006**, *39*, 2739−2742.

(16) Natta, G.; Mazzanti, G.; Longi, P.; Bernardini, F. *J. Polym. Sci.* **1958**, *31*, 181−183.

(17) (a) Zeigler, R.; Resconi, L.; Balbontin, G.; Guerra, G.; Venditto, V.; Rose, C. D. *Polymer* **1994**, *35*, 4648−4655. (b) Habaue, S.; Baraki, H.; Okamoto, Y. *Macromol. Chem. Phys.* **1998**, *199*, 2211−2215.

(18) (a) Yasuda, H.; Ihara, E. *Macromol. Chem. Phys.* **1995**, *196*, 2417−2441. (b) Desurmont, G.; Li, Y.; Yasuda, H.; Maruo, T.; Kanehisa, N.; Kai, Y. *Organometallics* **2000**, *19*, 1811−1813. (c) Kawabe, M.; Murata, M. *Macromol. Chem. Phys.* **2001**, *202*, 1799−1805. (d) Kawabe, M.; Murata, M. *Macromol. Chem. Phys.* **2002**, *203*, 24−30. (e) Kaita, S.; Hou, Z.; Wakatsuki, Y. *Macromolecules* **2001**, *34*, 1539−1541. (f) Cai, Z.; Shinzawa, M.; Nakayama, Y.; Shiono, T. *Macromolecules* **2009**, *42*, 7642−7643. (g) Ban, H. T.; Kase, T.; Kawabe, M.; Miyazawa, A.; Ishihara, T.; Hagihara, H.; Tsunogae, Y.; Murata, M.; Shiono, T. *Macromolecules* **2006**, *39*, 171−176. (h) Mason, A. F.; Coates, G. W. *J. Am. Chem. Soc.* **2004**, *126*, 16326−16327. (i) Ruokolainen, J.; Mezzenga, R.; Fredrickson, G. H.; Kramer, E. J. *Macromolecules* **2005**,

38, 851−860. (j) Frauenrath, H.; Balk, S.; Keul, H.; Höcker., H. *Macromol. Rapid Commun.* **2001**, *22*, 1147−1151. (k) Chen, E. Y.-X. *Chem. Rev.* **2009**, *109*, 5157−5214.
(19) (a) Satoh, K.; Kamigaito, M. *Chem. Rev.* **2009**, *109*, 5120−5156. (b) Lutz, J. F.; Jakubowski, W.; Matyjaszewski, K. *Macromol. Rapid Commun.* **2004**, *25*, 486−492. (c) Kamigaito, M.; Satoh, K. *Macromolecules* **2008**, *41*, 269−276.
(20) (a) Chung, T. C. *Prog. Polym. Sci.* **2002**, *27*, 39−85. (b) Atiqullah, M.; Tinkl, M.; Pfaendner, R.; Akhtar, M. N.; Hussain, I. *Polym. Rev.* **2010**, *50*, 178−230.
(21) (a) Razavi, A.; Ferrara, J. *J. Organomet. Chem.* **1992**, *435*, 299−310. (b) Resconi, L.; Piemontesi, F.; Gamurati, I.; Sudmeijer, O.; Nifant'ev, I. E.; Ivchenko, P. V.; Kuz'mina, L. G. *J. Am. Chem. Soc.* **1998**, *120*, 2308−2321.
(22) Patsidis, K.; Alt, G. H.; Milius, W.; Palackal, S. J. *J. Organomet. Chem.* **1996**, *509*, 63−71.
(23) Bochmann, M.; Lancaster, S. J. *Organometallics* **1993**, *12*, 633−640.
(24) Cheng, G.-L.; Hu, C.-P.; Ying, S. K. *Macromol. Rapid Commun.* **1999**, *20*, 303−307.
(25) (a) Amin, S. B.; Marks, T. J. *J. Am. Chem. Soc.* **2007**, *129*, 2938−2953. (b) Carvill, A.; Tritto, I.; Locatelli, P.; Sacchi, M. C. *Macromolecules* **1997**, *30*, 7056−7062. (c) Carvill, A.; Zetta, L.; Zannoni, G.; Sacchi, M. C. *Macromolecules* **1998**, *31*, 3783−3789. (d) Lieber, S.; Brintzinger, H. H. *Macromolecules* **2000**, *33*, 9192−9199. (e) Tynys, A.; Eilertsen, J. L.; Seppala, J. V.; Rytter, E. *J. Polym. Sci., Part A: Polym. Chem.* **2007**, *45*, 1364−1376. (f) Kim, I.; Zhou, J. M. *J. Polym. Sci., Part A: Polym. Chem.* **1999**, *37*, 1071−1082. (g) Kim, I.; Choi, C. S. *J. Polym. Sci., Part A: Polym. Chem.* **1999**, *37*, 1523−1539. (h) Kawahara, N.; Kojoh, S.; Matsuo, S.; Kaneko, H.; Matsugi, T.; Toda, Y.; Mizuna, A.; Kashiwa, N. *Polymer* **2004**, *45*, 2883−2888. (i) Naga, N.; Mizunuma, K. *Polymer* **1998**, *39*, 5059−5067. (h) Naga, N.; Mizunuma, K. *Polymer* **1998**, *39*, 5059−5067. (j) Franceschini, F. C.; Tavares, T. T.; dos Santos, J. H. Z.; Ferreira, M. L.; Soares, J. B.P. *Macromol. Mater. Eng.* **2006**, *291*, 279−287. (k) Franceschini, F. C.; Tavares, T. T.; Greco, P. P.; Galland, G. B.; dos Santos, J. H. Z.; Soares, J. B.P. *J. Appl. Polym. Sci.* **2005**, *95*, 1050−1055.
(26) Han, C. J.; Lee, M. S.; Byun, D. J.; Kim, S. Y. *Macromolecules* **2002**, *35*, 8923−8925.
(27) (a) Resconi, L.; Piemontesi, F.; Franciscono, G.; Abis, L.; Fiorani, T. *J. Am. Chem. Soc.* **1992**, *114*, 1025−1032. (b) Liu, Z.; Somsook, E.; White, C. B.; Rosaaen, K. A.; Landis, C. R. *J. Am. Chem. Soc.* **2001**, *123*, 11193−11207.
(28) (a) Lynd, N. A.; Hillmyer, M. A. *Macromolecules* **2005**, *38*, 8803−8810. (b) Lynd, N. A.; Hillmyer, M. A. *Macromolecules* **2007**, *40*, 8050−8055. (c) Lynd, N. A.; Meuler, A. J.; Hillmyer, M. A. *Prog. Polym. Sci.* **2008**, *33*, 875−893.
(29) Hu, Y.; Krejchi, M. T.; Shah, C. D.; Myers, C. L.; Waymouth, R. M. *Macromolecules* **1998**, *31*, 6908−6916.

Macromolecules

Article

pubs.acs.org/Macromolecules

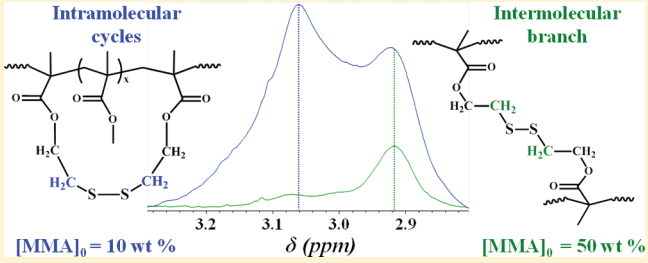
Quantification of Intramolecular Cyclization in Branched Copolymers by ^{1}H NMR Spectroscopy

Julien Rosselgong and Steven P. Armes*

Department of Chemistry, Dainton Building, University of Sheffield, Sheffield, South Yorkshire S3 7HF, U.K.

Supporting Information

ABSTRACT: Statistical copolymerization of a monovinyl with a divinyl monomer leads to macroscopic gels, microgels, or soluble branched copolymers, depending on the precise reaction conditions. This approach is widely used for the manufacture of soft contact lenses and also to prepare various biomedical hydrogels for the separation and purification of proteins, DNA, etc. According to Flory–Stockmayer theory, gelation should occur in such copolymerizations if there is more than 0.50 fully reacted divinyl comonomer per primary chain. However, many experimental studies indicate significant deviations from this classical theory, which are generally believed to be due to wastage of the divinyl comonomer via intramolecular cyclization. Unfortunately, experimental verification of this side reaction has proven elusive for the past seven decades. In the present study, we use a disulfide-based cleavable bifunctional comonomer to undertake the first experimental quantification of the extent of intramolecular cyclization in nonlinear methacrylic copolymers using ^{1}H NMR spectroscopy.



INTRODUCTION

It is well-known that the statistical copolymerization of a monovinyl monomer with a divinyl comonomer can lead to either cross-linked gels,[1] microgels,[2] or highly branched soluble copolymers[3,4] depending on the precise experimental conditions. This approach has been widely used for the manufacture of soft contact lenses,[5] for the synthesis of macroporous styrene–divinylbenzene beads for chromatography applications,[6] to prepare various biomedical hydrogels for the separation and purification of proteins or DNA,[7,8] to act as rheological modifiers,[9] and recently for the development of so-called "engineered emulsions".[10−13] Over the past two decades, the emergence of controlled radical polymerization techniques such as nitroxide-mediated polymerization,[14] atom transfer radical polymerization,[15,16] and reversible addition–fragmentation chain transfer polymerization (RAFT)[17] have led to many new studies of well-defined vinyl branched copolymers, including two recent review articles.[4,18] Potential applications include peptide-degradable biocompatible fibers,[19] thermoresponsive fluorescent copolymers for bacterial detection,[20] biodegradable DNA-binding copolymers,[21] and model nonlinear glycopolymers.[22] Flory developed a so-called "mean field" theory,[23,24] later extended by Stockmayer,[25] for an idealized formulation whereby a divinyl cross-linker reacts statistically with the monovinyl monomer to link up perfectly monodisperse primary chains. This analysis, which ignores intramolecular cyclization, predicts that a minimum of 0.50 fully reacted divinyl comonomers per primary chain is required to form an insoluble polymer network.[4,18] However, many experimental studies indicate significant deviations from this theory, which are generally believed to be due to participation of the divinyl comonomer in a side reaction known as intramolecular cyclization.[26−43] When a monovinyl monomer is copolymerized with a divinyl comonomer, reaction of the first double bond of the latter species creates a pendent vinyl group. If the remaining double bond of this bifunctional comonomer undergoes subsequent reaction, there are two possibilities: it can either react intermolecularly with another growing primary chain to create two branch points or it can react intramolecularly to make a cycle (or loop) within the same primary chain. This second event represents wastage of the divinyl comonomer in the branched copolymer synthesis.

Unfortunately, direct experimental quantification of the extent of intramolecular cyclization has proven elusive for the past seven decades, so this explanation for the failure of classical gelation theory has never been verified. In the present study, which involves the ^{1}H NMR analysis of methacrylic branched copolymers prepared by living radical copolymerization, we report the first direct quantification of the relative amounts of intermolecular branching and intramolecular cyclization in *any* nonlinear polymer system.

Recently, we conducted a series of statistical copolymerizations of methyl methacrylate (MMA) with a disulfide-based dimethacrylate (DSDMA) branching comonomer using reversible addition–fragmentation chain transfer (RAFT) polymerization.[35,36] Control experiments involving the RAFT homopolymerization of MMA in the absence of any DSDMA branching comonomer indicated chain transfer agent efficien-

Received: February 7, 2012
Revised: February 28, 2012
Published: March 13, 2012

ACS Publications © 2012 American Chemical Society

dx.doi.org/10.1021/ma3002609 | *Macromolecules* 2012, 45, 2731−2737

cies of between 80 and 90% [higher efficiencies (≈ 90%) were obtained for polymerizations conducted at $[MMA]_0$ = 50 wt % compared to $[MMA]_0$ = 10 wt %] for the cumyl dithiobenzoate (CDB), as judged by both ^{1}H NMR spectroscopy and gel permeation chromatography (GPC) analyses.[22] Monomer conversions of 96−99% were achieved within 30−96 h at 90 °C, with approximately first-order kinetics with respect to monomer, linear evolution of molecular weight with conversion, and relatively low final polydispersities ($1.19 < M_w/M_n < 1.29$) being observed.[35] Thus, the MMA homopolymerization shows pseudoliving character, which means that the primary chains in the corresponding branched copolymer syntheses should have a relatively narrow molecular weight distribution. Indeed, this was confirmed by GPC analyses of the branched copolymers after selective reductive cleavage of the disulfide bonds in the DSDMA units using tributylphosphine.[35] Moreover, monomer depletion studies using HPLC confirmed that the RAFT copolymerization of MMA and DSDMA is almost purely statistical at $[MMA]_0$ = 50 wt %.[35]

According to our previous work,[35,36] and also that of others,[18,32,37−42] it was expected that intramolecular cyclization should become much more prevalent at lower monomer concentrations. In order to examine this hypothesis, the initial monomer concentration was systematically varied from 10 to 50 wt % in order to control the relative proportions of intramolecular cyclization and intermolecular branching occurring in these branched copolymer syntheses (see Figure 1).

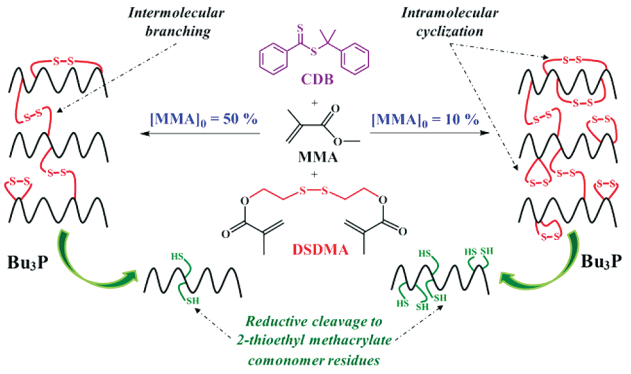


Figure 1. Schematic representation of the microstructure of methacrylic branched copolymers prepared using reversible addition−fragmentation chain transfer (RAFT) chemistry for the statistical copolymerization of methyl methacrylate (MMA) with a disulfide-based dimethacrylate (DSDMA) using cumyl dithiobenzoate (CDB) chain transfer agent and 1,1′-azobiscyclohexanecarbonitrile (ACCN) as initiator in toluene at 90 °C. The subsequent reductive cleavage of these branched $PMMA_n$−$DSDMA_x$ copolymers using tributylphosphine (Bu_3P) afforded the corresponding $PMMA_n$−$TEMA_x$ linear primary chains (where TEMA denotes 2-thioethyl methacrylate).

To a zeroth-order approximation, the primary chains are generated first, with most of the branching being confined to the latter stages of the reaction.[35] Thus, the branching efficiency is strongly influenced by the solution concentration of the linear primary chains. Below the critical overlap concentration (c^*), intramolecular cyclization becomes favored because the individual polymer coils are effectively isolated from each other. On the other hand, at concentrations well above c^*, intermolecular branching becomes favored, since the chains can interpenetrate. This situation has been confirmed by our recent study of a model system, whereby near-monodisperse homopolymer chains were cross-linked via quaternization chemistry at various concentrations both above and below c^*.[41] In the present system, we calculate the c^* for $PMMA_{55}$ homopolymer chains to be ∼11 vol % (or ∼14.6 wt %).[35] If the copolymerization of MMA with DSDMA is conducted at 50 wt %, this is well above c^* and should hence lead to the relatively efficient production of branched copolymer, whereas the same copolymerization performed at 10 wt % would be expected to suffer from very inefficient branching (and hence contain substantial amounts of intramolecular cycles). These scenarios have been verified for the first time in the present study, in which ^{1}H NMR spectroscopy has been utilized to distinguish between the fully reacted DSDMA units involved in intermolecular branches and intramolecular cycles, respectively.

RESULTS AND DISCUSSION

Figure 2 shows the ^{1}H NMR spectra recorded for five PMMA−DSDMA branched copolymers synthesized at $[MMA]_0$ = 10, 30, and 50 wt % (spectra A and B were recorded for copolymers synthesized at 50 and 30 wt %, respectively, while spectra C−E were recorded for copolymers prepared at 10 wt % in the presence of increasing amounts of DSDMA per primary chain) under conditions that were very close to the experimental gel point, as demonstrated by the high molecular weights reported by GPC (see Table 1). Also shown in the same Figure are the corresponding ^{1}H NMR spectra obtained after selective reductive cleavage of the disulfide bonds in the DSDMA units to afford the linear, near-monodisperse thiol-functionalized primary chains.[35,36] The most compelling evidence for our NMR peak assignments comes from recent work by Hawker's group, who reported the synthesis of a novel disulfide-based cyclic monomer, followed by its ring-opening polymerization to produce a linear polyester (see Figure S1).[45,46] The S−S−CH_2 (thiamethylene) protons in the cyclic monomer appear as a triplet at approximately δ 3.0, but this signal is shifted to approximately δ 2.9 in the polyester. These observations mirror almost perfectly what is observed in the ^{1}H NMR spectra of our branched vinyl copolymers (see Figure 2), which contain a range of overlapping signals at or above δ 3.00 due to various intramolecular cycles and a relatively well-defined signal at δ 2.92 due to intermolecular branches. Moreover, our assignments are supported by selective reductive cleavage of the disulfide bonds in the DSDMA units using excess tributylphosphine, since all the intra/intermolecular thiamethylene proton signals are shifted to a new singlet at δ 2.8, which is assigned to the HS−CH_2 signals of 2-thioethyl methacrylate (TEMA) residues. Similar subtle differences are also observed for the O−CH_2 (oxymethylene) protons of the copolymerized DSDMA units, but these signals are somewhat broader and harder to interpret since these atoms are closer to the methacrylic polymer backbone and hence less mobile. Presumably, the well-known gauche effect, whereby the dihedral angle for the disulfide bond is almost 90°,[44] also causes the adjacent methylene protons of the copolymerized DSDMA units to become particularly sensitive to their specific conformation (i.e., whether present as an intramolecular cycle or as a linear intermolecular branch). ^{1}H NMR spectrum A (see Figure 2) was recorded for the branched copolymer obtained at $[MMA]_0$ = 50 wt % (allowing for the CTA efficiency of 90%, the copolymer composition was $PMMA_{53}$−$DSDMA_{0.95}$ when $PMMA_{50}$−$DSDMA_{0.90}$ was targeted, see entry 1 in Table 1). This system has two signals due to O−CH_2 and S−S−CH_2 protons at δ 4.22 and δ 2.92 which are assigned to the

dx.doi.org/10.1021/ma3002609 | Macromolecules 2012, 45, 2731−2737

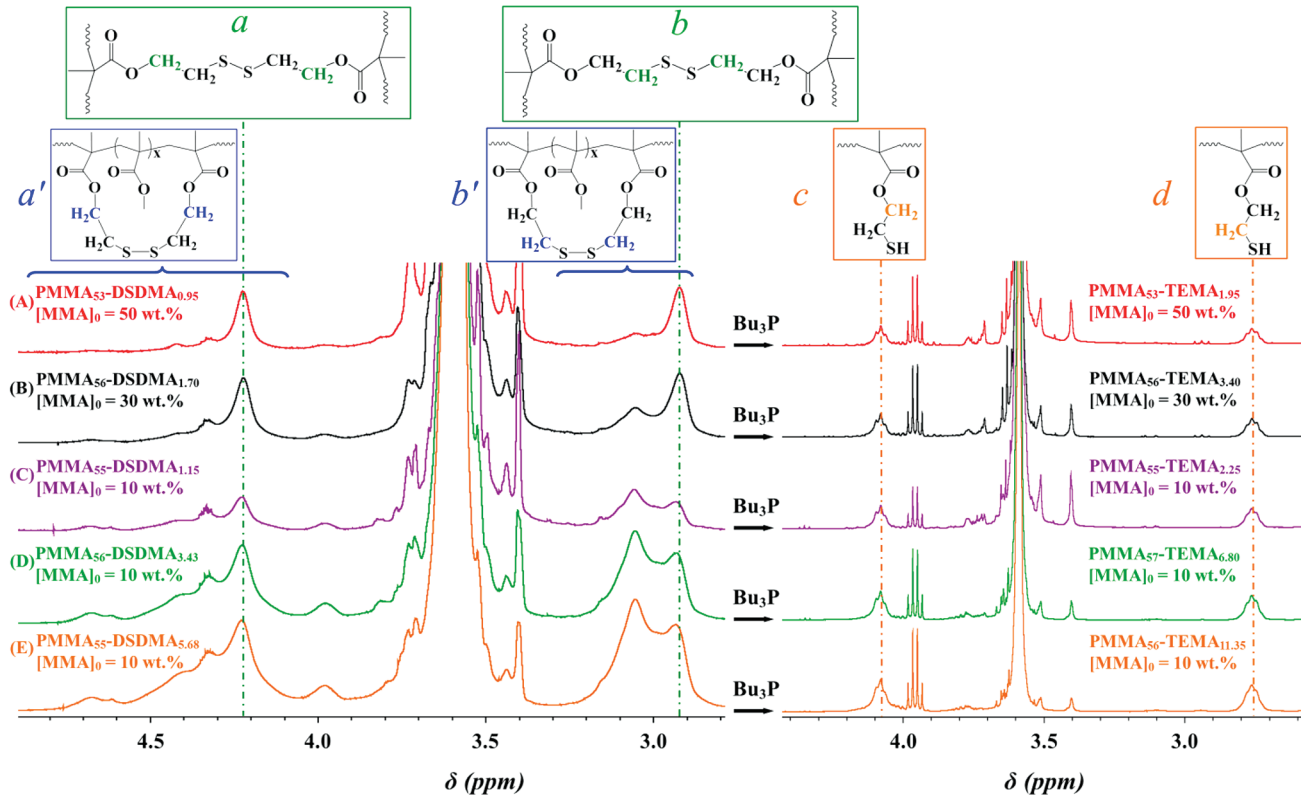


Figure 2. ^{1}H NMR spectra recorded for RAFT-synthesized PMMA$_n$–DSDMA$_x$ branched copolymers prepared at [MMA]$_0$ = 50, 30, and 10 wt %, both before (left) and after (right) selective cleavage of all disulfide bonds in the DSDMA comonomer residues using excess tributylphosphine. This chemical degradation affords PMMA$_n$–TEMA$_x$ linear primary chains (where TEMA denotes 2-thioethyl methacrylate residues).

Table 1. Summary of the Targeted and Actual Compositions (Calculated by ^{1}H NMR) for a Series of Soluble Branched Copolymers Prepared by RAFT at Various [MMA]$_0$ Using Increasing Amounts of DSDMA[a]

[MMA]$_0$ (wt %)	targeted composition	^{1}H NMR calculated composition	M_w (kg mol^{-1})	M_w/M_n	inter (%)	intra (%)
50	PMMA$_{50}$-DSDMA$_{0.90}$	PMMA$_{53}$-DSDMA$_{0.95}$	3325	36.1	61 ± 4	39 ± 4
30	PMMA$_{50}$-DSDMA$_{1.50}$	PMMA$_{56}$-DSDMA$_{1.70}$	4509	21.6	36 ± 6	64 ± 6
10	PMMA$_{50}$-DSDMA$_{1.00}$	PMMA$_{55}$-DSDMA$_{1.15}$	17	1.7	8 ± 3	92 ± 3
10	PMMA$_{50}$-DSDMA$_{3.00}$	PMMA$_{56}$-DSDMA$_{3.43}$	70	3.7	8 ± 2	92 ± 2
10	PMMA$_{50}$-DSDMA$_{5.00}$	PMMA$_{55}$-DSDMA$_{5.68}$	609	13.9	10 ± 5	90 ± 5

[a]The percentage degree of intermolecular branching and hence intramolecular cyclization (denoted inter and intra, respectively) was determined by peak deconvolution of the thiamethylene signal at δ 2.92 in the ^{1}H NMR spectra of the original branched copolymers (see also Figure 4). Molecular weight data were obtained by THF GPC using a triple detection system comprising refractive index, viscosity, and light scattering (15° and 90°) detectors. Final comonomer conversions in these branched copolymer syntheses ranged between 96% and 99%.[36]

intermolecular branch form of the DSDMA in the copolymer structure: these structures are labeled a and b, respectively, in Figure 2.

These initial assignments were confirmed by comparison with ^{1}H NMR spectra recorded for both the DSDMA comonomer (see spectrum D in Figure 3) and also the soluble fraction extracted from a DSDMA *homopolymerization* by RAFT that had been quenched at low conversion (see spectrum C in Figure 3).

Similarly, ^{1}H NMR spectrum B in Figure 2 was recorded for the branched copolymer prepared at [MMA]$_0$ = 30 wt % (PMMA$_{56}$–DSDMA$_{1.70}$, see entry 2 in Table 1). This spectrum also has two signals due to O–CH_2 and S–S–CH_2 protons at δ 4.22 and δ 2.92, respectively (see signals labeled a and b). However, there is clearly some complexity in these features, as indicated by the additional signals a′ and b′. Integration of signals c and d observed after disulfide cleavage (see spectrum B after Bu_3P treatment) and normalizing with respect to the larger O–CH_3 signal at δ 3.6 confirmed that these two signals are equivalent to ∼1.70 DSDMA units per primary chain. Moreover, the additional complexity (see signals a′ and b′) in the ^{1}H NMR spectrum of this branched copolymer correspond to around 66% of the integrated intensity of signals a and b. This suggests that there are ∼0.50 DSDMA units per primary chain in the form of an intermolecular branch and a further 1.2 DSDMA units per primary chain present as intramolecular cycles. Finally, inspection of ^{1}H NMR spectra C, D, and E recorded for the branched copolymers (see entries 3–5 in Table 1) synthesized at [MMA]$_0$ = 10 wt % confirmed substantial complexity and line broadening for the O–CH_2 and S–S–CH_2 signals at δ 4.1–4.5 (labeled a, a′) and δ 2.9–3.2 (labeled b, b′). Comparing these two features with that of the O–CH_3 signal at δ 3.6 indicated that up to 5.68 DSDMA units can be incorporated per primary chain without causing gelation, as shown in spectrum E.

dx.doi.org/10.1021/ma3002609 | *Macromolecules* 2012, 45, 2731–2737

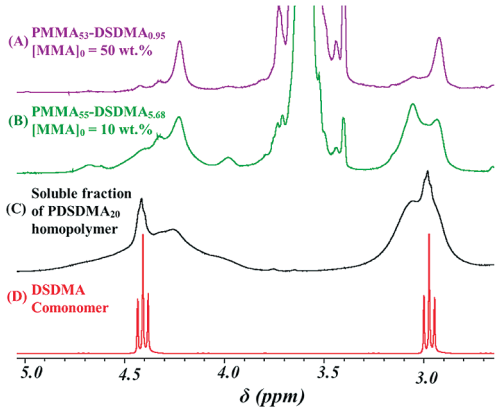


Figure 3. ^{1}H NMR spectra recorded in $CDCl_3$ for (A, B) RAFT-synthesized $PMMA_n$–$DSDMA_x$ branched copolymers prepared at $[MMA]_0$ = 50 and 10 wt %, respectively, (C) the soluble fraction extracted from the RAFT homopolymerization of DSDMA, and (D) the DSDMA comonomer alone.

Based on these spectroscopic observations and our previous results reported for this formulation,[35,36] our initial hypothesis was that the DSDMA branching comonomer was incorporated *exclusively in the form of intermolecular branches* under the stated synthesis conditions, with negligible intramolecular cyclization occurring at $[MMA]_0$ = 50 wt % (i.e., spectrum A in Figure 2). However, this did not prove to be the case. In fact, using peak deconvolution (see Figure 4), we estimate that ~61 ± 4% of the DSDMA units react to form intermolecular branches in this case, while the remaining DSDMA units are present as intramolecular cycles (see Table 1). This experimental observation is thus reasonably consistent with Flory–Stockmayer theory, which predicts 50% intermolecular branching and ignores the possibility of any intramolecular cyclization. Experimentally, many research groups have reported that up to approximately one fully reacted divinyl comonomer can be incorporated per primary chain without inducing macroscopic gelation.[4,27,35,36,38–41,48,49] This empirical observation seems to be true regardless of whether conventional free radical or living radical polymerization chemistry is utilized, provided that the solution polymerization concentration is well above the critical overlap concentration (c^*). Thus, the extent of intramolecular cyclization revealed by ^{1}H NMR spectroscopy in the present work allows the apparent discrepancy between theory and experiment to be reconciled: approximately one fully reacted DSDMA comonomer per primary chain does indeed correspond to the onset of gelation, but only ~61% of these branching/cross-linking units are actually present in the form of intermolecular branches, with the remaining units forming various types of intramolecular cycles. Peak deconvolution of the complex features based on the known line shapes of signals a and b shown in spectra C, D, and E suggest that more than 90% of the DSDMA units per primary chain are incorporated as intramolecular cycles within the $PMMA_{55}$–$DSDMA_{5.68}$

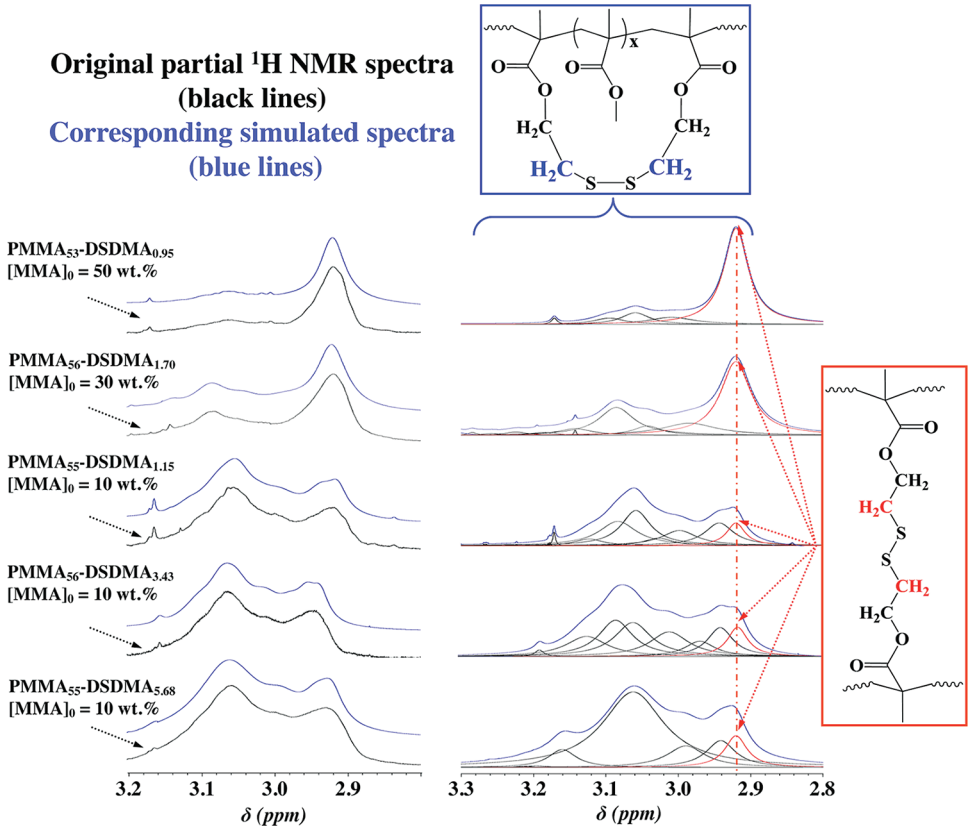


Figure 4. Partial ^{1}H NMR spectra recorded in $CDCl_3$ at 55 °C show the thiamethylene signals of the copolymerized DSDMA residues for soluble $PMMA_n$–$DSDMA_x$ branched copolymers prepared at $[MMA]_0$ = 50, 30, and 10 wt % using RAFT chemistry. The stacked spectra shown on the left correspond to the original partial ^{1}H NMR spectra (black lines) and the corresponding simulated spectra (blue lines; arbitrarily offset vertically above the real spectra) generated from peak-fitting. The stacked simulated ^{1}H NMR spectra shown on the right illustrate the various subpeaks used in each fitting procedure. In each spectrum, the red subpeak is assigned to the intermolecular branched structure, which is significantly reduced relative to the various subpeaks assigned to intramolecular cycles when branching copolymerizations are conducted at lower $[MMA]_0$.

dx.doi.org/10.1021/ma3002609 | *Macromolecules* 2012, 45, 2731–2737

branched copolymer synthesized at $[MMA]_0$ = 10 wt %. Thus, only 0.57 fully reacted DSDMA units per primary chain are actually present in the form of intermolecular branches when such branched copolymer syntheses are conducted in dilute solution. This explains the relatively low molecular weight obtained for this branched copolymer (see entry 5 in Table 1) compared to those prepared at 50 or 30 wt % monomer concentration (see entries 1 and 2 in Table 1).

In principle, the intramolecular cycles formed by fully reacted DSDMA comonomer can range from a 13-membered cycle (where the pendent vinyl group reacts immediately with the chain end; (i.e., x = 0 in Figure 5) up to relatively large cycles.

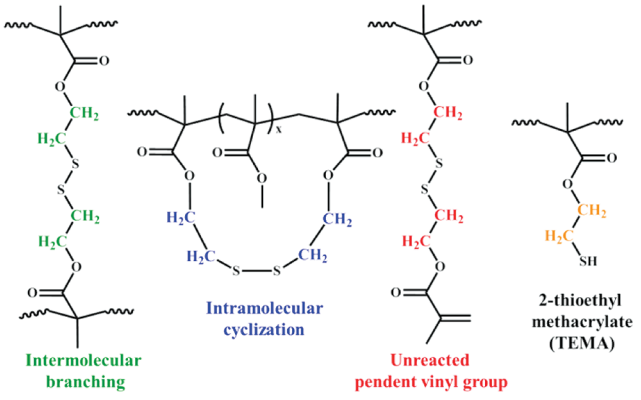


Figure 5. From left to right: (i) fully reacted DSDMA forming an intermolecular branch; (ii) fully reacted DSDMA forming an intramolecular cycle; (iii) a semireacted DSDMA with a pendent vinyl group. Far right: the pendent 2-thioethyl methacrylate (TEMA) residues that are formed after selective cleavage of all the disulfide bonds originally present in the branched copolymer as either intermolecular branches or intramolecular cycles using excess tributylphosphine.

In the latter case, the upper limit ring size corresponds to the mean length of the primary chains (~55 MMA residues). This rather wide range in ring size explains the complexity of the $-O-CH_2$ and $S-S-CH_2$ NMR signals that are observed in Figure 2. We suspect that our method is relatively insensitive to very large cycles, since these are likely to be spectroscopically indistinguishable from intermolecular branches. Thus, our ^{1}H NMR analysis may only provide a *lower limit* for the extent of intramolecular cyclization. Although we have focused on RAFT-synthesized branched copolymers in this paper, we have also made similar observations for the equivalent branched copolymers prepared using an ATRP formulation under comparable conditions.[50] Moreover, preliminary analysis of our RAFT-synthesized PMMA–DSDMA branched copolymers using quantitative ^{13}C NMR spectroscopy[50] indicates similar levels of intramolecular cyclization in each case. Since a delay time of 20 s is required between each scan to ensure full relaxation of the nuclear spins, recording such spectra requires rather long accumulation times (up to 60 h) to achieve sufficiently good signal-to-noise ratios. Nevertheless, the successful demonstration of ^{13}C NMR spectroscopy in this context is important, since in principle this technique offers much better resolution (and hence fewer overlapping signals) than ^{1}H NMR spectroscopy. These additional results will be reported elsewhere in due course.

Several research teams have described soluble branched copolymers prepared by such living radical polymerization chemistry as "hyperbranched".[28,33] Based on the results described herein, this term appears to be inappropriate, since essentially all of the "additional" fully reacted DSDMA units in the copolymer chains prepared at lower monomer concentrations are merely present in the form of intramolecular cycles, which make no contribution at all to the degree of branching. Thus, we recommend that the term "hyperbranched" is best avoided when describing such branched vinyl copolymers, unless supported by compelling additional experimental evidence.

In retrospect, the choice of MMA as a model monovinyl monomer in our studies was somewhat fortuitous. Almost any other alkyl methacrylate monomer would have had an additional $O-CH_2$ proton signal, which would have likely obscured the relatively weak $O-CH_2$ signal due to the DSDMA comonomer; such overlapping signals would have made our initial ^{1}H NMR peak assignments problematic. Moreover, the unusual sensitivity of the disulfide bond in the DSDMA comonomer to its local environment also played a key role,[44] as did the unexpected availability of almost ideal model cyclic compounds in the literature.[45,46]

CONCLUSIONS

In summary, we have shown for the first time that ^{1}H NMR spectroscopy can be used to distinguish between intramolecular cyclization and intermolecular branching in methacrylic branched copolymers. As expected, intramolecular cyclization becomes much more prevalent for branched copolymers synthesized in dilute solution, with up to 92% of the branching comonomer being consumed in this side reaction. The proportion of intermolecular branching that is observed for copolymer syntheses conducted in more concentrated solution is ~61 ± 4%, which allows the long-standing *apparent* discrepancy between theory and experiment to be reconciled. This work is expected to have broad implications for the synthesis of both microgels and gels as well as the growing literature on branched vinyl copolymers. Since intramolecular cyclization can now be explicitly quantified experimentally, our work should also inspire more sophisticated theoretical studies of gelation.

EXPERIMENTAL SECTION

The synthesis of all the branched copolymers and homopolymer reference materials described in this article has been recently reported elsewhere.[35] The ACCN initiator was used in conjunction with the CDB chain transfer agent for the RAFT polymerization of MMA at 90 °C since these reaction conditions had been previously shown[35] to give high conversions (which are essential for high degrees of branching) and relatively high RAFT agent efficiencies. All ^{1}H NMR spectra were recorded using a 500 MHz spectrometer in $CDCl_3$ at 328 K, and subpeak line shapes were fitted using Topspin 2.1 software (Bruker Biospin). This approach allows deconvolution of the selected area of the spectrum by fitting a Lorentzian function to every subpeak so as to determine their respective areas, their chemical shifts, and widths (in ppm). Our peak deconvolution strategy was as follows. We fitted the relatively well-resolved $S-S-CH_2$ signal at δ 2.92 (see spectrum A in Figure 2) due to intermolecularly reacted DSDMA units first and then used this characteristic Lorentzian peak shape and peak width when fitting the more complex $S-S-CH_2$ signals observed for the various branched copolymers prepared at higher dilution (see spectra B–E in Figure 2). Peak-fitting was conducted so as to reconstruct the original complex spectral envelope using the minimum possible number of subpeaks, with one of these subpeaks always designated as corresponding to the intermolecularly reacted DSDMA units. The envelope shape and the deconvoluted peaks are presented

dx.doi.org/10.1021/ma3002609 | *Macromolecules* 2012, 45, 2731–2737

in Figure 4; the peaks attributed to the intermolecular branch form of the DSDMA (δ 2.92 for the S−S−CH_2 signal) are shown in red. We did not attempt to assign any of the various intramolecular cycles but simply focused on estimating the relative proportions of intermolecular branching and intramolecular cyclization. We estimate that this rather conservative approach introduces an experimental uncertainty of approximately 2−6% in the extent of intermolecular branching presented in Table 1.

■ ASSOCIATED CONTENT

Supporting Information

^{1}H NMR spectra ($CDCl_3$) recorded for the cyclic 3-methylidene-1,9-dioxa-5,12,13-trithiacyclopentadecane-2,8-dione monomer and its copolymer with methyl methacrylate after RAFT ring-opening copolymerization, as reported by Paulusse et al.[45,46] This material is available free of charge via the Internet at http://pubs.acs.org.

■ AUTHOR INFORMATION

Corresponding Author

*E-mail: S.P.Armes@sheffield.ac.uk.

Notes

The authors declare no competing financial interest.

■ ACKNOWLEDGMENTS

The Lubrizol Corporation (Hazelwood, UK) is thanked for funding a PhD studentship for J.R. and for permission to publish this research. Mrs. S. Bradshaw, Dr. B. Taylor (U. Sheffield), and Dr. I. Prokes (U. Warwick) are thanked for performing the ^{1}H NMR experiments and for fruitful discussions. Prof. C. J. Hawker and Dr. J. Paulusse are thanked for allowing us to reproduce the ^{1}H NMR spectra of their cyclic disulfide monomer and also the corresponding linear copolymer (see Figure S1 in the Supporting Information). Dr. J. Craven, Dr. A. Hounslow, and Dr. P. Portius (U. Sheffield) are also thanked for fruitful technical discussions.

■ REFERENCES

(1) Walling, C. *J. Am. Chem. Soc.* **1945**, *67*, 441−447.
(2) Pelton, R. H.; Chibante, P. *Colloids Surf.* **1986**, *20*, 247−256.
(3) O'Brien, N.; McKee, A.; Sherrington, D. C.; Slark, A. T.; Titterton, A. *Polymer* **2000**, *41*, 6027−6031.
(4) Gao, H. F.; Matyjaszewski, K. *Prog. Polym. Sci.* **2009**, *34*, 317−350.
(5) Wichterle, O.; Lim, D. *Nature* **1960**, *185*, 117−118.
(6) Sherrington, D. C. *Chem. Commun.* **1998**, *21*, 2275−2286.
(7) Reisfeld, R. A.; Lewis, U. J.; Williams, D. E. *Nature* **1962**, *195*, 281−283.
(8) Dong, L.; Agarwal, A. K.; Beebe, D. J.; Jiang, H. R. *Nature* **2006**, *442*, 551−554.
(9) Chisholm., M.; Hudson., N.; Kirtley, N.; Vilela, F.; Sherrington, D. C. *Macromolecules* **2009**, *42*, 7745−7752.
(10) Weaver, J. V. M.; Rannard, S. P.; Cooper, A. I. *Angew. Chem.* **2009**, *48*, 2131−2134.
(11) Woodward, R. T.; Chen, L.; Adams, D. J.; Weaver, J. V. M. *J. Mater. Chem.* **2010**, *20*, 5228−5234.
(12) Woodward, R. T.; Weaver, J. V. M. *Polym. Chem.* **2011**, *2*, 403−410.
(13) Woodward, R. T.; Olariu, C. I.; Hasan, E. A.; Yiu, H. H. P.; Rosseinsky, M. J.; Weaver, J. V. M. *Soft Matter* **2011**, *7*, 4335−4340.
(14) Georges, M. K.; Veregin, P. N.; Richard, P. N.; Kazmaier, P. M.; Hamer, G. K. *Macromolecules* **1993**, *26*, 2987−2988.
(15) Kato, M.; Kamigaito, M.; Sawamoto, M.; Higashimura, T. *Macromolecules* **1995**, *28*, 1721−1723.
(16) Wang, J. S.; Matyjaszewski, K. *J. Am. Chem. Soc.* **1995**, *117*, 5614−5615.
(17) Chiefari, J.; Chong, Y. K.; Ercole, F.; Krstina, J.; Jeffery, J.; Le, T. P. T.; Mayadunne, R. T. A.; Meijs, G. F.; Moad, C. L.; Moad, G.; Rizzardo, E.; Thang, S. H. *Macromolecules* **1998**, *31*, 5559−5562.
(18) Poly, J.; Wilson, D. J.; Destarac, M.; Taton, D. *J. Polym. Sci., Part A: Polym. Chem.* **2009**, *47*, 5313−5327.
(19) Wang, L.; Li, C.; Ryan, A. J.; Armes, S. P. *Adv. Mater.* **2006**, *18*, 1566−1570.
(20) Shepherd, J.; Sarker, P.; Swindells, K.; Douglas, I.; MacNeil, S.; Swanson, L.; Rimmer, S. *J. Am. Chem. Soc.* **2010**, *132*, 1736−1737.
(21) Tao, L.; Liu, J.; Tan, B. H.; Davis, T. P. *Macromolecules* **2009**, *42*, 4960−4962.
(22) Semsarilar, M.; Ladmiral, V.; Perrier, S. *Macromolecules* **2010**, *43*, 1438−1443.
(23) Flory, P. J. *J. Am. Chem. Soc.* **1941**, *63*, 3096−3100.
(24) Flory, P. J. *Principles of Polymer Chemistry*; Cornell University Press: Ithaca, NY, 1953; pp 347−398.
(25) Stockmayer, W. H. *J. Chem. Phys.* **1944**, *12*, 125−131.
(26) Bütün, V.; Bannister, I.; Billingham, N. C.; Sherrington, D, C.; Armes, S. P. *Macromolecules* **2005**, *38*, 4977−4982.
(27) Li, Y.; Armes, S. P. *Macromolecules* **2005**, *38*, 5002−5009.
(28) Liu, B. L.; Kazlauciunas, A.; Guthrie, J. T.; Perrier, S. *Macromolecules* **2005**, *38*, 2131−2136.
(29) Vo, C. D.; Rosselgong, J.; Armes, S. P.; Billingham, N. C. *Macromolecules* **2007**, *40*, 7119−7125.
(30) Landin, D. T.; Macosko, C. W. *Macromolecules* **1988**, *21*, 846−851.
(31) Dotson, N. A.; Diekmann, T.; Macosko, C. W.; Tirrell, M. *Macromolecules* **1992**, *25*, 4490−4500.
(32) Dusek, K.; Spevacek, J. *Polymer* **1980**, *21*, 750−756.
(33) Wang, W.; Zheng, Y.; Roberts, E.; Duxbury, C. J.; Ding, L.; Irvine, D. J.; Howdle, S. M. *Macromolecules* **2007**, *40*, 7184−7194.
(34) Poly, J.; Wilson, D. J.; Destarac, M.; Taton, D. *Macromol. Rapid Commun.* **2008**, *29*, 1965−1972.
(35) Rosselgong, J.; Armes, S. P.; Barton, W.; Price, D. *Macromolecules* **2010**, *43*, 2145−2156.
(36) Rosselgong, J.; Armes, S. P.; Barton, W.; Price, D. *Macromolecules* **2009**, *42*, 5919−5924.
(37) Gao, H. F.; Polanowski, P.; Matyjaszewski, K. *Macromolecules* **2009**, *42*, 5925−5932.
(38) Gao, H. F.; Li, W.; Matyjaszewski, K. *Macromolecules* **2008**, *41*, 2335−2340.
(39) Gao, H.; Min, K.; Matyjaszewski, K. *Macromolecules* **2007**, *40*, 7763−7770.
(40) Wang, W. J.; Wang, D.; Li, B. G.; Zhu, S. *Macromolecules* **2010**, *43*, 4062−4069.
(41) Wang, R.; Luo, Y.; Li, B. G.; Zhu, S. *Macromolecules* **2009**, *42*, 85−94.
(42) Li, Y.; Ryan, A. J.; Armes, S, P. *Macromolecules* **2008**, *41*, 5577−5581.
(43) Gray, T. F. Jr.; Butler, G. B. *J. Macromol. Sci., Chem.* **1975**, *9*, 45−82.
(44) Kirby, A. J. *Stereoelectronic Effects*; Oxford University Press: Oxford, UK, 1996.
(45) Paulusse, J. M. J.; Amir, R. J.; Evans, R. A.; Hawker, C. J. *J. Am. Chem. Soc.* **2009**, *131*, 9805−9812.
(46) Paulusse, J. M. J.; Amir, R. J.; Evans, R. A.; Hawker, C. J. *J. Am. Chem. Soc.* **2010**, *132*, 16725.
(47) Casey, J. P.; Martin, R. B. *J. Am. Chem. Soc.* **1972**, *94*, 6141−6151.
(48) Bannister, I.; Billingham, N. C.; Armes, S. P.; Findlay, P.; Rannard, S. P. *Macromolecules* **2006**, *39*, 7483−7492.
(49) Isaure, F.; Cormack, P. A. G.; Sherrington, D. C. *Macromolecules* **2004**, *37*, 2096−2105.
(50) Rosselgong, J. Synthesis and Characterisation of Branched Methacrylic Copolymers by Living Radical Polymerisation. PhD Thesis, University of Sheffield, UK, 2010.

NOTE ADDED AFTER ASAP PUBLICATION

This article published ASAP on March 13, 2012. Reference 34 has been revised. The correct version posted on March 16, 2012.

dx.doi.org/10.1021/ma3002609 | *Macromolecules* 2012, 45, 2731−2737

Macromolecules

Article

pubs.acs.org/Macromolecules

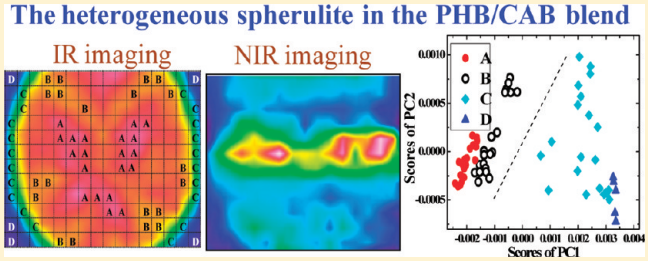
Effects of Hydrogen Bond Intermolecular Interactions on the Crystal Spherulite of Poly(3-hydroxybutyrate) and Cellulose Acetate Butyrate Blends: Studied by FT-IR and FT-NIR Imaging Spectroscopy

Nattaporn Suttiwijitpukdee, Harumi Sato, Miriam Unger, and Yukihiro Ozaki*

Department of Chemistry, School of Science and Technology and Research Center for Environment Friendly Polymers, Kwansei-Gakuin University, Sanda 669-1337, Japan

Supporting Information

ABSTRACT: The crystal melting behaviors of poly(3-hydroxybutyrate) (PHB) and cellulose acetate butyrate (CAB) blends were studied using infrared (IR) and near-infrared (NIR) imaging, which provided information about spherulite growth in dynamic blend systems. By analyzing the changes in the IR and NIR imaging spectra in the regions of the first and second overtones of the C═O stretching vibrations of PHB and CAB, the evolution of heterogeneous spherulite during the time-resolved isothermal crystallization process was explored. Time-resolved IR and NIR imaging and polarized microscopic studies detected the PHB domains are able to separate from the PHB/CAB blends early in the process. Principal component analysis (PCA) was used to classify the distribution of the different morphologies of spherulite. The first principal component suggests that the discrimination of the imaging spectra relies largely upon the crystallinity, while the second principal component indicates the variations in the amorphous portion of PHB, the CAB contents, and the intermolecular hydrogen bonding of PHB and CAB. The PC1−PC2 scores of different parts of the spherulite suggest that the areas of low crystallinity in the blend spherulite contain both PHB and CAB.



1. INTRODUCTION

Bacterial polymers, i.e., polyhydroxyalkanoates (PHAs), are biodegradable thermoplastics that have attracted significant attention for many years.[1−3] Among the PHA family, poly(3-hydroxybutyrate) (PHB) is exceedingly appealing because of its biodegradability, biocompatibility, and possible synthesis from renewable resources.[3−6] However, its rigidity, brittleness, and high melting point significantly block its commercial and practical applications.[7,8] The crystal structure of PHB was reported to be an orthorhombic system, i.e., $P2_12_12_1(D^4_2)$, with a = 5.76 Å, b = 13.20 Å, and c = 5.96 Å.[9] Our previous IR,[10−15] X-ray diffraction,[12,13] and differential scanning calorimetry (DSC)[13] investigations of the crystal structure and crystallization behavior of PHB suggest that PHB has weak C−H···O═C hydrogen bonds along the a-axis between the C═O groups in one helix and the CH_3 moieties of another helix structure. The C−H···O═C hydrogen bonds may be a key factor in stabilizing chain folding in the lamellar structure of PHB.[11−14] It is very likely that the high crystallinity of PHB is partly derived from the C−H···O═C hydrogen bonding.

It has been challenging to improve the properties of PHB for practical applications and industrial processability. One method is to prepare copolymers of PHB. For example, polyhydroxybutyrate-*co*-hydroxyvalerate (PHB-*co*-PHV)[16] and poly(3-hydroxybutyrate-*co*-3-hydroxyhexanoate) (PHB-*co*-HHx)[17] copolymers have been successfully synthesized. A blending process is also a frequently used technique to improve the properties of PHB. Thus, PHB polymer blends such as poly(ethylene glycol) (PEG),[18] poly(ethylene oxide) (PEO),[19] and poly(vinyl acetate) (PVAc)[20] have been intensively studied.

We have studied the crystal structures and crystallization behaviors of several kinds of PHB blends such as PHB/poly(L-lactide) (PLLA),[21] PHB/poly(*p*-vinylphenol) (PVPh),[22] PHB/poly(vinyl alcohol) (PVA),[23] and PHB/cellulose acetate butyrate (CAB) using IR spectroscopy, DSC, and X-ray crystallography.[24,25] For actual applications, CAB is ideal to blend with PHB since it is an abundant natural polymer derivative with environmentally friendly properties such as biodegradability and biocompatibility.[26,27] Moreover, PHB/CAB polymer blends have shown good properties with respect to elongation and toughness.[27,28] So far, this polymer system has undergone extensive investigations of its miscibility,[29−33] crystallization,[30−32] and orientation behavior.[33] For example, El-Shafee et al.[32] reported their investigations of miscible blends in the melt state. Furthermore, the effect of the equilibrium melting point depression of PHB crystals with increasing CAB content was described.[32] Moreover, small-angle X-ray scattering (SAXS) of PHB/CAB blends revealed that CAB exists in the interlamellar amorphous regions and

Received: July 13, 2011
Revised: February 28, 2012
Published: March 8, 2012

 © 2012 American Chemical Society

becomes a major component before the PHB domains crystallize.[32,33]

The process of crystallization from melt can be separated into three stages as primary nucleation, crystal growth, and secondary crystallization. In the primary nucleation process, a nucleus can be formed homogeneously by the statistic fluctuation in the melt phase or heterogeneously, when catalyzed by heterogeneity.[34] The theoretical models of crystallization were proposed a long time ago.[35−39] Hoffman and Lauritzen[36,37] developed the kinetic theory for the formation of fold chain crystal and the growth of lamellar spherulite based on surface energy concepts, which provides an understanding of how lamellar structures from the solution and melts. In the cases of miscible polymer blends, the addition of a miscible noncrystallizable polymer mostly causes a depression of spherulite growth rate of the crystallizable component. For partially miscible blends, spherulite growth may be further complicated by possible competition with heterogeneous or homogeneous melt nuclei. The crystallization of phase-separated blends occurs in the presence of noncrystallizable segregated domain. During forming of crystal lamellar, the dispersed particle is rejected and/or occluded by the growing spherulite.[34] The PHB/CAB blends were reported as the miscible blend in the melt state. Therefore, the miscibility and the interactions within the remaining amorphous phase should affect the crystallization process at the crystallization temperature.

For further understanding of this promising blend, we recently systemically explored the crystal structure, thermal behavior, and crystallization of PHB/CAB blends; it was found that the intermolecular hydrogen bonds between the C═O groups of PHB and the O−H groups of CAB (−C═O···H−O−) form physical cross-links in the blends.[24,25] These interactions lead to a reduction of the crystallization rate and crystallinity of PHB. Moreover, these interactions play a significant role in suppressing mobility and intramolecular hydrogen bonding (−C═O···H−C−) in the PHB crystal.[24,25]

Near-infrared (NIR) spectroscopy has been extensively utilized in the polymer field[40,41] since it is a nondestructive analysis method that is suitable for samples with longer optical path lengths such as films, granulates, fibers, and textiles.[41] It is also very useful for investigating structural details such as hydrogen bonding[42] and intra- and intermolecular interactions in polymers.[42,43]

Recently, IR imaging spectroscopy has attracted widespread interest in polymer science and technology and has frequently been used to investigate the phase separation, miscibility, and morphology of polymer blends.[44−52] With this technique, researchers can easily obtain information about the distributions of different components or different morphologies in blends. Additionally, it is possible to explore dynamic processes such as polymer dissolution and crystallization.[44] For example, in previous studies,[43−50] FT-IR imaging spectroscopy has been applied to study the miscibility of PHB/PLLA blends as a function of the blend compositions. From these investigations, the concentration dependence of phase separation at room temperature was determined.[48,49] Also, Gupper and Kazarian[50] examined solvent diffusion and solvent-induced crystallization in syndiotactic polystyrene using IR imaging spectroscopy.

In comparison with IR imaging spectroscopy, NIR imaging is a relatively new analytical technique in the polymer field. Because of the much smaller molar absorption in the NIR region, NIR radiation can penetrate much farther into a sample than IR radiation.[51] Moreover, since NIR bands arise mainly from overtones and combinations,[51−53] NIR imaging can readily be used to distinguish the spectra of different substances. NIR imaging is also very useful for probing bulk materials with little or no sample preparation even when the sample contains a lot of water. On the other hand, IR imaging spectra present a high signal-to-noise ratio.[52] Analysis of IR imaging spectra is frequently performed by measuring the well-defined peak heights or peak areas.

Furukawa et al.[21] combined NIR imaging with partial least-squares (PLS) regression to evaluate the homogeneity of binary blends of PHB and PLLA. The score images directly showed that the blends were highly homogeneous, and the standard deviations (STDs) of the histograms, which indicate the distribution of the score values, were small. These results qualitatively and quantitatively revealed the high level of homogeneity of PHB/PLLA blends.[21] Shinzawa et al.[54] explored the incipient effects of grinding cellulose at the molecular level by NIR imaging.

IR and NIR spectroscopic imaging as a combination of IR and NIR spectroscopy with digital image processing provides a three-dimensional data set, i.e., a spectral hypercube with the *X*- and *Y*-axes representing spatial information and the *Z*-axis representing spectral information.[51−53] Based on different imaging colors, the spatial distribution of the components that comprise a sample can possibly be visualized via IR and NIR spectroscopic imaging. Moreover, with array-based spectral sensing, the quantitative information about a trace sample can be obtained by parallel collection of the spectral records.[55] IR and NIR imaging techniques yield an ideal approach for the exploration of the spatial distribution of chemical species and the study of minute crystallization behavior in spatial directions.

In this work, we investigated the crystallization of PHB in the melt isothermal crystallization of PHB/CAB blends using both IR and NIR imaging spectroscopy. We obtained a conformational evaluation of the PHB crystals and revealed the spatial conformation changes of the formed spherulite in the blend systems. As discussed above, IR and NIR imaging spectroscopy have different advantages; therefore, a comparison of IR and NIR imaging and their spectra was carried out. In the present study, we discuss the following novel points regarding PHB/CAB blends: (1) The dynamics of the time-resolved crystallization process were explored by comparing NIR images of the PHB/CAB spherulite in the blends with the corresponding IR images. (2) Through spectroscopic investigations on the time-resolved crystallization process of PHB and polarized optical microscopic observations, it was found that the initiation of the spherulite-forming process in the PHB/CAB blend occurs due to conformational changes of the PHB chains. However, the intermolecular interactions in the blend systems in the spherulite are affected during crystal growth. (3) The calculations of the distribution of PHB and CAB with PCA revealed that the PHB crystal shows local differences in its conformation in the spherulite.

2. EXPERIMENTAL SECTION

2.1. Materials and Sample Preparation. PHB (number-average molecular weight, M_n, 2.9×10^5) and CAB (number-average molecular weight, M_n, 1.2×10^4) were purchased from Sigma-Aldrich Chemical Co., Ltd., and were used without any further treatment. The weight fractions of each substitution group, i.e., hydroxyl, acetyl, and butyryl

groups, in the CAB sample with respect to the total weight of CAB were 7.7, 43.7, and 48.6 mol %, respectively.

Samples of the PHB/CAB blends were prepared by weighing the prescribed amount of each powder and dissolving them in hot chloroform at 80 °C. The blend films were prepared by evaporating the solutions in Petri dishes at room temperature. The dishes were placed under vacuum at 60 °C for 16 h to completely remove the residual solvent after the films formed. The thickness of the sample films was controlled to be 50 μm using a hot press. Finally, a small piece of the film was mounted on a CaF_2 plate to prepare the sample for spectroscopic imaging and microscopy measurements.

2.2. IR and NIR Spectroscopic Imaging Measurements. IR and NIR spectroscopic imaging measurements were carried out using a Perkin-Elmer (Waltham, MA) imaging system consisting of a Spectrum One FT-NIR spectrometer coupled with a Spectrum Spotlight 300 NIR microscope. This integrated instrument is equipped with a 16 × 1 element (400 × 25 μm^2) MCT array detector and a single point 100 × 100 μm^2 MCT detector in the same Dewar flask. The symmetrically arranged objective and condenser provide image magnification of 6× at 1:1 imaging and have a numerical aperture of 0.58. Specifically designed optics permit 1:1 or 4:1 imaging of the sample area on the detector elements resulting in 25 × 25 μm^2 pixel sizes.

The temperature of the as-prepared samples was controlled using a high THC-15 unit (Yokohama, Japan). Prior to the imaging measurements, the PHB and PHB/CAB (80:20 wt %) blend films were first melted at 185 °C, which was maintained for 3 min to destroy any thermal history, and then cooled to the isothermal crystallization temperature, T_c, of 125 °C at a cooling rate of 30 °C/min. Throughout this experiment, the time, t, of 0 min was defined as the time when the sample temperature reached 125 °C. Imaging data were measured in normal transmission mode for an area of 400 × 300 μm^2 with a pixel size of 25 × 25 μm^2, and the IR and NIR spectra were collected by coadding 16 scans at a resolution of 8 cm^{-1}. The images were recorded *in situ* at 6 min intervals during the isothermal crystallization process. The resulting spectra and imaging data were analyzed using the Perkin-Elmer Spectrum IMAGE R 1.6.5 software package.

2.3. Polarized Optical Microscopy. After the spectroscopic imaging measurements, the crystalline morphology of neat PHB and a PHB/CAB blend (80:20 wt %) were observed at room temperature using an optical microscope (Olympus BX51, Japan) equipped with a crossed polarizer. In order to maintain the developed crystal constant during the transfer and microscopic preparation, the neat PHB and blend were immediately quenched to 0 °C and maintained for 5 min to freeze the crystals after the spectroscopic imaging measurements were complete. As a result, no further spherulite developed during the microscopic observations.

2.4. Principal Component Analysis. The image spectral data of each area (25 × 25 μm^2) were extracted from the NIR image with the Perkin-Elmer Spectrum IMAGE R1.6.5 software package and transferred into Unscrambler (Version 9.2: CAMO AS, Trondheim, Norway) software to undergo principal component analysis (PCA). The imaging spectra from a highly crystalline region, low crystalline regions in the spherulite, the edge of the spherulite, and the outside of spherulite were identified, separated, and designated as group A, B, C, and D, respectively. For groups A–C, 20 spectra points were selected for each one, whereas only five points were selected for group D due to the limited area. The original selected spectra in the region of 5500–3300 cm^{-1} were subjected to linear baseline correction and the second derivative using Savitzky-Golay (left and right 6 points, 2 orders) before the PCA calculation. The PCA calculation was carried out using a full cross-validation method.

3. RESULTS AND DISCUSSION

3.1. Composition-Dependent Imaging Spectral Variations in the Bands Associated with the C═O and OH Groups of the PHB/CAB Blends. Figures 1a and 1b show imaging spectra at 25 °C in the regions of 3750–3300 and 5600–4000 cm^{-1}, respectively, for neat PHB, neat CAB, and

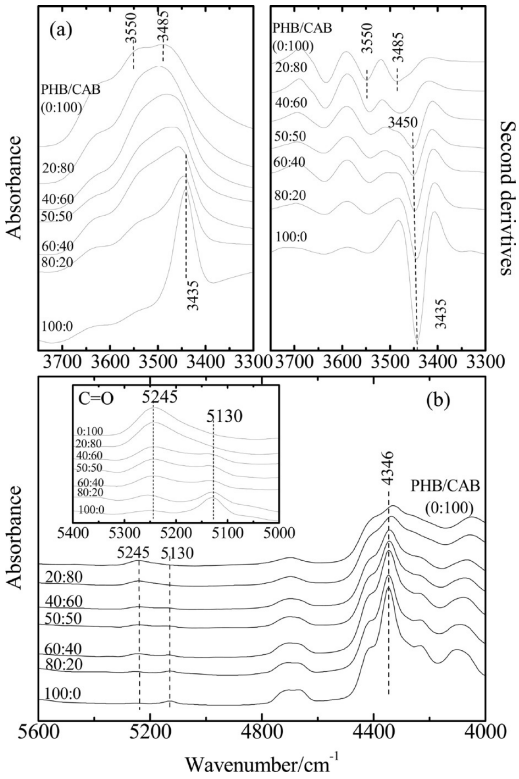


Figure 1. (a) IR imaging spectra in the region of 3750–3300 cm^{-1} and its second derivative spectra. (b) NIR imaging spectra in the region of 5600–4000 cm^{-1} of neat PHB, neat CAB, and PHB/CAB blends with various ratios measured at 25 °C.

PHB/CAB blends at various blending ratios. As described in the Experimental Section, the imaging data are recorded by measuring the sample in the area of 400 × 300 μm^2 using a MCT detector with spatial resolution of 25 × 25 μm^2. Therefore, the spectra as shown in Figure 1 should be the averaged data of the measured imaging area. In Figure 1, it is evident that the spectral peaks associated with the vibrations of the OH and C═O groups change with increasing PHB/CAB blending ratio. In the 3750–3300 cm^{-1} region, one strong peak at ~3435 cm^{-1} assigned to the first overtone of the stretching mode of the C═O groups involved in the intramolecular hydrogen bonding (PHB–C–H···O═C–PHB) of crystal PHB clearly appears in the neat PHB spectrum,[10] while the peak at 3465 cm^{-1} due to the amorphous part of PHB does not clearly show up, compared to our previous result for the casted thin film.[24,42,56] One reasonable cause is that the sample thickness in the present study is very large, about 50 μm, and therefore, the crystalline conformation of PHB may partially overlap between different layers in the lamellar structure and, then, the relative intensity of the peak at 3435 cm^{-1} is enhanced.

Moreover, after the blending ratio of PHB/CAB is up to 50:50, the peak at ~3435 cm^{-1} clearly shifts to ~3450 cm^{-1} as indicated in the second derivative spectra in Figure 1a. One possible cause for this shift is that the intramolecular interactions of PHB–C–H···O═C–PHB[10−14] are interrupted by the introduction of weak intermolecular interactions between the C═O groups in PHB and the OH groups in CAB, i.e., CAB–O–H···O═C–PHB interactions formed in the blend system. Therefore, during the crystallization process, the small fraction of OH groups in CAB, about 7.7 mol %, gives sufficiently large number of OH groups to form physically

dx.doi.org/10.1021/ma201598s | Macromolecules 2012, 45, 2738–2748

cross-linking networks between PHB and CAB in the blends. The cross-linking points formed in the blends may gradually confine the crystalline conformation and aggregation of PHB with increasing the CAB content in the blends which potentially results in the shift of the peak at 3435 cm^{-1}. Additionally, the peaks at 3485 and ~3550 cm^{-1} due to the hydrogen-bonded O−H stretching in interchain and intrachain interactions of CAB−CAB as reported in our previous studies.[24]

Figure 1b presents the imaging spectra in the region of 5600−4000 cm^{-1} with an enlargement of the 5400−5000 cm^{-1} region in the inset. The band at ~5130 cm^{-1}, which is assigned to the intramolecular hydrogen bonding between the C═O group and the H−C bond of the CH_3 group,[42] i.e., C═O···H−C, in the crystal of PHB quickly decreases with increasing CAB content in the blends and seemingly disappears at a PHB/CAB ratio of 20:80. However, the second overtone peak at ~5165 cm^{-1} for the amorphous C═O group in PHB cannot be observed in the blended system.[42] The asymmetric broad peak due to neat CAB at 5245 cm^{-1} indicates a combination peak of at least two bands, but it could not be separated even in the second derivative spectra because of its broad profile and the various C═O groups in CAB;[24] therefore, details of the bands contained within this broad peak are not shown in this work. The assignments for the characteristic bands of the PHB/CAB blends are listed in Table 1.

Table 1. Band Assignments for the IR and NIR Spectra of PHB/CAB Blends[a]

Peak No.	Wavenumber /cm^{-1}	Assignments
1	3435-3445	1st overtone, *intra* C=O, PHB (crystal)
2	3450	1st overtone, less-ordered, or intermediate state C=O, PHB (amorphous)
3	3465	1st overtone, *free* C=O, PHB (amorphous)
4	3485	*inter* OH,O-H•••O=C, CAB-CAB
5	~3550	*intra* CAB-CAB { -OH•••-O- (ether), CAB-CAB; -OH•••O=C, CAB-CAB
6	4346	C-H stretching and C-H deformation (crystal)
7	5130	2nd overtone, *intra* C=O, PHB (crystal)
8	5140	2nd overtone, less-ordered, or intermediate state C=O, PHB (amorphous)
9	5165	2nd overtone, *free* C=O, PHB (amorphous)
10	5245	2nd overtone, *free* C=O, CAB (amorphous)

[a]Abbreviations: inter = intermolecular hydrogen bonding interaction; intra = intramolecular hydrogen bonding interaction.

3.2. Time-Resolved Isothermal Crystallization of PHB/CAB Blends. Parts a, b, and c of Figure 2a present visual, NIR, and IR images of PHB/CAB (80/20 wt %) at 18, 36, and 66 min, respectively. It can be seen from these figures that spherulite is already evident at t = ~18 min, and the lamellar morphology of the spherulites can be observed from the visible images, since the crystalline and amorphous peaks appear at 5130 and 5160 cm^{-1}, respectively.[42] Therefore, the NIR images (Figure 2b) were calculated from the area ratios of the second overtone of the C═O stretching mode of the crystal structure (5140−5090 cm^{-1}) and that of the amorphous phase (5200−5150 cm^{-1}). The IR images (Figure 2c) were calculated from the area ratio of the corresponding first overtone band of the crystalline part (3445−3390 cm^{-1}) and that of the amorphous part (3480−3450 cm^{-1}) which cover the crystal peak at 3445 cm^{-1} and amorphous peak at 3465 cm^{-1}, respectively,[24] to avoid the influence of the peak at 3485 cm^{-1} assigned to the hydrogen-bonded O−H groups of CAB content.[24] Therefore, the selected range of this amorphous area is narrower than other regions. The calculated regions are shown in Figure 3. The area ratio was developed for two reasons: (1) to eliminate the influence of changes in the film thickness that could happen due to temperature and time in the crystallization process;[57] (2) to make some changes in the crystallinity visible. The images based on the crystal/amorphous band area ratios display the high crystallinity of the spherulite (shown in red) and the amorphous part, which is represented by the darker color in the images. The spherulite and the crystal growth behavior can be observed from the NIR and IR images. The NIR images show the high crystallinity in the middle part. The area ratio of the crystal/amorphous absorption bands could be observed in the middle part along the horizontal line (designated as the X-axis), which has a higher crystallinity than that along the vertical line (designated as the Y-axis) of the spherulite during the entire isothermal crystallization process. In the case of the IR images, the area ratios of the crystal/amorphous bands more obviously monitor the surface of spherulite morphology than the NIR images. The differences in the band ratios of the NIR and IR images may be caused by two effects. One is the effect of peak intensity; since the first overtone of the C═O stretching modes of PHB is much stronger than the second overtone, the composed images in the IR region depict the spherulite morphology more clearly than the NIR images. The second reason is that the first overtone of the C═O stretching vibration the IR region overlaps with some parts of the OH stretching band, and the spherulite is affected by the intermolecular C═O hydrogen bonding, as will be explained in the next part.

To investigate the growth of the lamellar in the isothermal crystallization process in three dimensions, we monitored the spherulite diameter as a function of the crystallization time in the X- and Y-axes. For the Z direction, we referred to the change in the crystalline peak intensity at 3445 cm^{-1} with time by comparing the changes at two points, $Z1$ and $Z2$. The first and second points were observed along the X-axis ($Z1$) and the Y-axis ($Z2$), respectively; both points were about 50 μm from the center point. Figure 4 illustrates the time-dependent changes (bottom) and second derivative imaging spectra (upper part) at $Z1$ in the regions of 5250−5050 and 3600−3350 cm^{-1}. Clear separation of the peak positions can be seen in the second derivative spectra. Even though the peak intensities in the NIR region are much weaker than those in the IR region, the crystal and amorphous absorption bands at 5130 and 5165 cm^{-1}, respectively, are more obviously separate than the corresponding peaks in the IR region. Additionally, the amorphous C═O peak at 5165 cm^{-1} shifts to a higher wavenumber (5180 cm^{-1}). It was also found that the peak at 5140 cm^{-1} occurs in the intermediate position between the crystalline peak at 5130 cm^{-1} and the amorphous peak at 5165 cm^{-1}; this peak exists only at t = 12 min, which is before the appearance of the spherulite. In the IR region of 3600−3350

dx.doi.org/10.1021/ma201598s | Macromolecules 2012, 45, 2738−2748

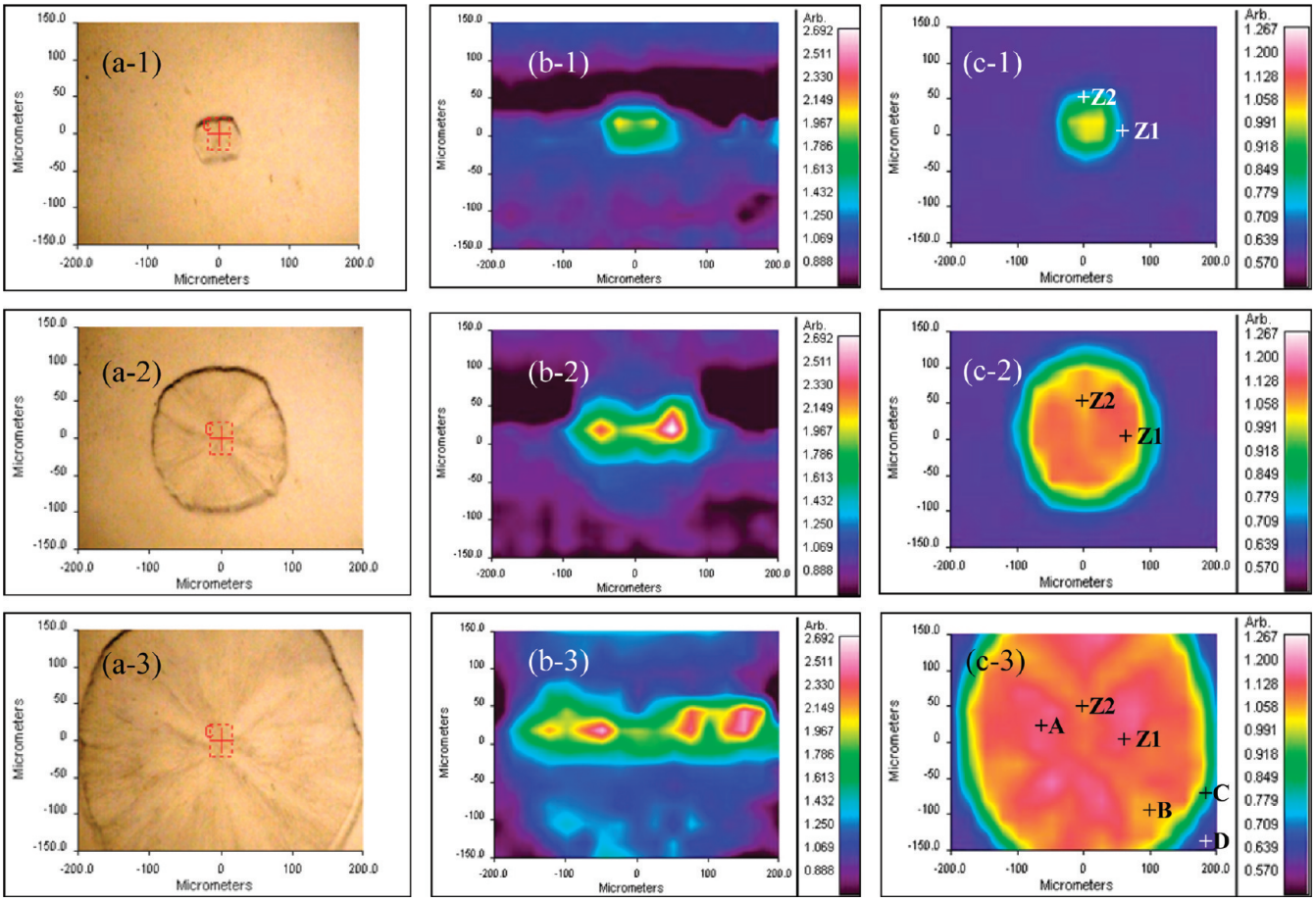


Figure 2. (a) Visual images, (b) NIR images, and (c) IR images of the PHB/CAB blend (80:20 wt %) during isothermal crystallization at 125 °C at around 18 min (a-1, b-1, c-1), 36 min (a-2, b-2, c-2), and 66 min (a-3, b-3, c-3).

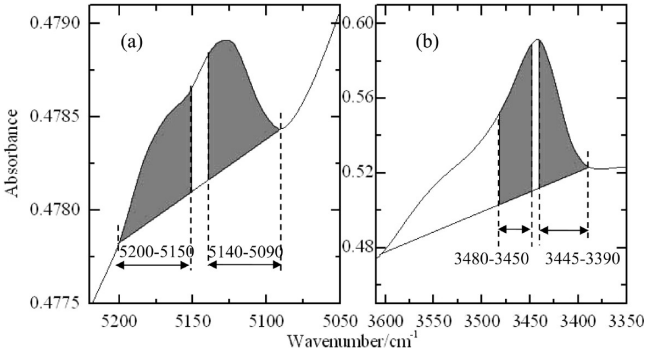


Figure 3. (a) NIR and (b) IR imaging spectra of the PHB/CAB (80:20) blend film.

cm^{-1}, a band at 3450 cm^{-1} also clearly emerges at the same time (12 min) as the peak at 5140 cm^{-1}. Therefore, these two peaks (5140 and 3450 cm^{-1}) can be reasonably assigned to the less ordered or the intermediate state of the crystalline part, which corresponds to the band at 1732 cm^{-1} that was detected during the crystallization process.[15] Although the IR spectra in the first overtone region (Figure 4b) were of stronger intensity than the NIR spectra in the second overtone, the peaks in the former overlap with each other more severely than in the latter (Figure 4a). Therefore, the 3600−3350 cm^{-1} IR region was used to probe the crystal growth along the *Z*-axis. At t = 0 min, the original and second derivative spectra show two peaks at 3465 and 3550 cm^{-1}, which are associated with the amorphous C═O groups of PHB and the O−H groups of CAB, respectively. The intensity of the amorphous peak at 3465 cm^{-1} decreased and that of the crystal peak at 3445 cm^{-1} increased as a function of time. On the other hand, the broad feature at 3550 cm^{-1} remains almost unchanged during the crystallization process. Therefore, monitoring the intensity change at peak 3445 cm^{-1} reveals the growth of the crystalline parts in the direction perpendicular to the substrate (designated as the *Z*-axis). As we know the crystal structure of PHB spherulite, the *a*-axis is the radial direction of the spherulite and the *b*- and *c*-axes rotate about the *a*-axis.[58] Therefore, the increase in the intensity of the peak at 3445 cm^{-1} refers to the increasing lamellar stacking in the *Z* direction, which can be ascribed to the increased conformational ordering in the spherulite.

Figure 5 compares the evolution of the crystal structure in the *X*, *Y*, and *Z* directions. The intensity change at *Z*1 occurs earlier than that at *Z*2. However, the crystallization rates at the two points are similar to each other, as can be seen in the parallel intensity changes of the peak at 3445 cm^{-1}. From the visible images, we can see that spherulite is elliptical rather than circular with the length in the direction of the *X*-axis being slightly longer than that in the direction of the *Y*-axis at the beginning (t = 18 min). Therefore, we examined the changes of the spherulite diameter along the *X* and *Y* directions. At first, the crystal lamellar changed faster in the direction of the *X*-axis than in the direction of the *Y*-axis after which the rate of change became equal for both axes directions, leading to a circular

dx.doi.org/10.1021/ma201598s | *Macromolecules* 2012, 45, 2738−2748

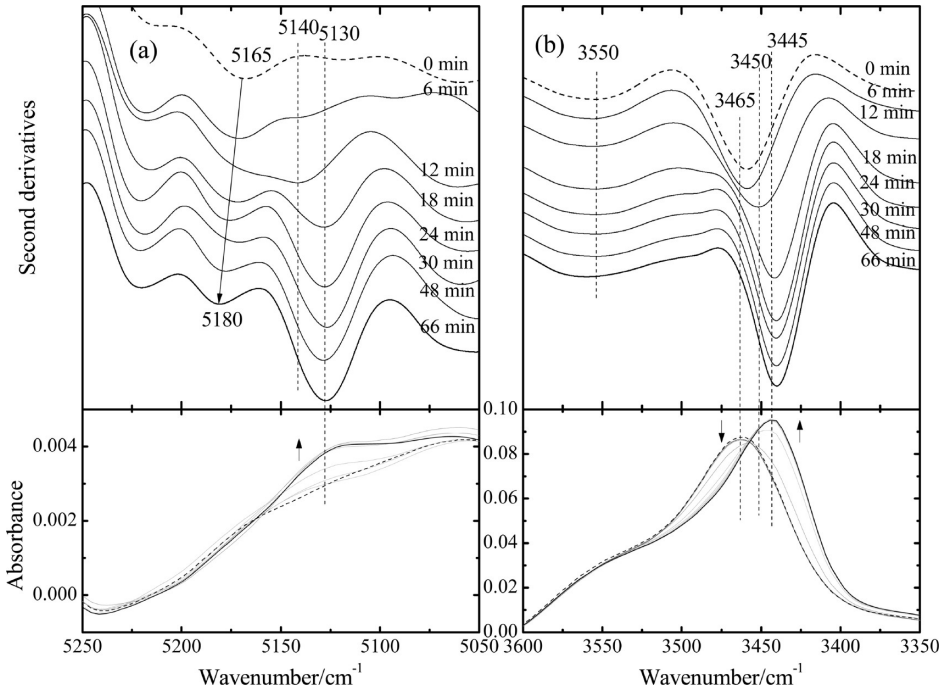


Figure 4. Time-resolved imaging spectra (bottom part) and their second derivatives (upper part) in the regions of (a) 5250−5050 cm^{-1} and (b) 3600−3350 cm^{-1} of the PHB/CAB blend (80:20 wt %) collected during the isothermal crystallization process at 125 °C.

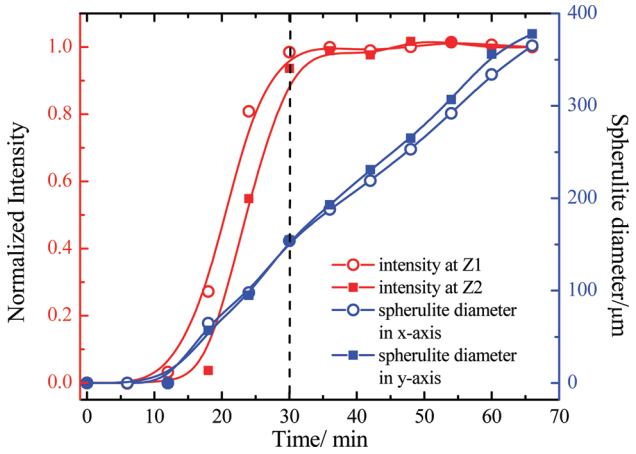


Figure 5. Normalized difference spectral intensity of the crystalline band at 3445 cm^{-1} and the spherulite dimensional growth in the directions of the *X*- and *Y*-axes as a function of crystallization time for the PHB/CAB blend (80:20 wt %) at 125 °C.

shape of the spherulite at around t = 30 min. However, the spherulite grew linearly in both directions, which is in good agreement with the previous report by Pizzoli et al.[30] The results of the analysis of the spherulite growth suggest that, from the starting time to t = 30 min, the crystal grew in three spatial directions and then developed in only the *X* and *Y* directions.

Figures 6a and 6b illustrate a visible image and an IR image, respectively, obtained from the area ratio of two regions of the crystalline section (3445−3390 cm^{-1}) and the amorphous section (3480−3450 cm^{-1}) of neat PHB measured at 125 °C during the isothermal crystallization process at t = 24 min. From the visible image, the banding of spherulite morphology is evident; however, it is difficult to find it on the IR image based on the specific area ratio. Comparing PHB/CAB and neat PHB, one highly possible cause for the differences may be stated as follows: the band texture morphology of PHB does not affect the area ratio image, but rather the effect is caused by the CAB contents in the blend, which contain the low

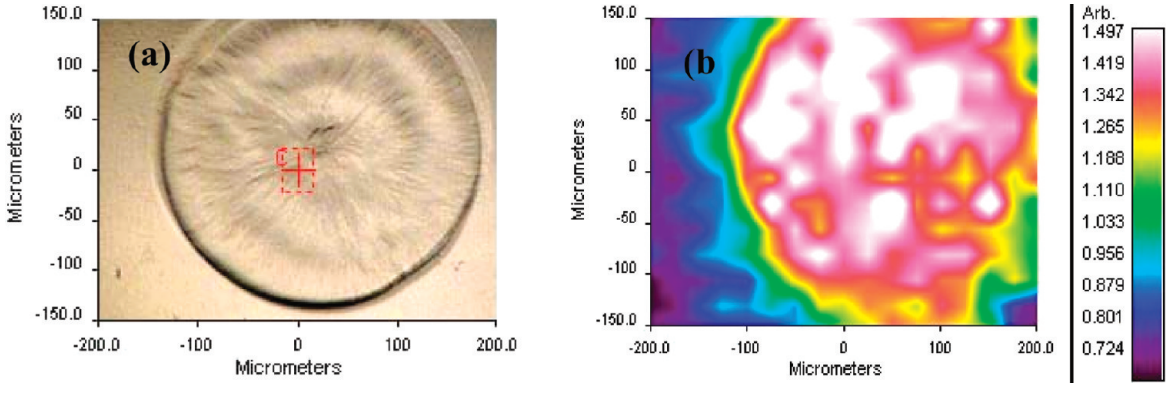


Figure 6. (a) A visual image and (b) an NIR image of PHB measured at 125 °C at t = 24 min.

dx.doi.org/10.1021/ma201598s | *Macromolecules* 2012, 45, 2738−2748

crystallinity part of the spherulite. Nevertheless, in the neat PHB system, there are some small differences between the visible and IR images because the increase in size of the PHB spherulite occurs very quickly at t = 24 min compared with scanning time of about 3 min.

3.3. Heterogeneous Spherulite Morphologies of the Isothermally Crystallized PHB/CAB Blends. Figures 7a and 7b show the crystalline spherulitic morphologies observed in the cross-polarized optical micrographs of the quenched samples of neat PHB and PHB/CAB blends (80:20), respectively, after the isothermal crystallization process is complete. In PHB spherulites, it is well-known that the lamellar crystals grow radially with stacking.[58−60] The chain folding of lamellar crystal and growth of spherulite theory were purposed by Hoffman and Lauritzen.[36,37] Because of the twisting of the PHB lamellar crystal, the spherulite exhibits a banded texture with a Maltese-cross-type pattern.[61,62] In the case of the blend, the bands are rough and not clear. However, we can see that some parts of spherulite have irregular morphology in the spherulite (Figure 7b). The band spacing in the X-axis at the starting time (shown by the arrow) is significantly different from that in the other parts of the spherulite. The morphology supports the visible image phenomena as the growth of spherulite in the X-axis direction is quicker at t = ∼18 min than that in the Y-axis. As is well-known, the crystallization behavior of a binary blend of crystalline and amorphous polymers results from competition between the segregation and crystallization processes. The crystalline component segregates from the amorphous part[30] and then migrates ahead of the growing front of the lamellae. In the PHB/CAB blend, the intermolecular hydrogen-bonding interactions between PHB and CAB form the physical cross-links of its amorphous parts, as we reported in a previous article.[24,25] Also, the spherulitic crystallization requires the polycrystalline aggregates as primary nuclei to initiate the crystal growth.[63] Thus, the fronts of the spherulites should be initially formed and would not incorporate into the spherulites during the growth process. For the crystal growth process, it is very likely that the initial state of spherulite is composed of PHB, which can easily segregate from the blends and form nuclei. However, the molecular weight of CAB is very small (M_n = 1.2 × 10^4) compared with that of PHB (M_n = 2.9 × 10^5). Thus, the spherulite crystal of the blend may contain also some CAB that is unable to completely segregate from the PHB in the later state. Therefore, the crystallinity of the spherulite is not completely homogeneous.

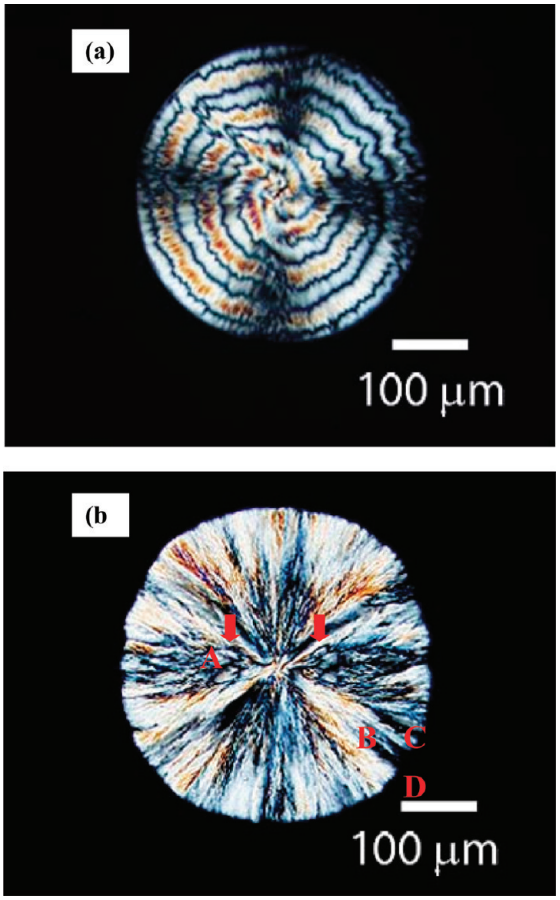


Figure 7. Polarized optical micrographs of quenched sample films of (a) PHB and (b) PHB/CAB blend (80:20 wt %).

By comparing the polarized microscope morphology of the blend (Figure 7b) with the spectra (Figures 2C and 3), we extracted the spectra at four different points (A, B, C, and D in Figures 2C and 3 and Figure 7b) of the spherulite. The first point, A, was selected along the X-axis, and the second one, B, shows bandless phenomena. The third point, C, was chosen at the edge of the spherulite, and the last point, D, was selected at the outside of the crystalline spherulite. Figure 8a shows the absorbance (bottom part) and second derivative spectra (upper part) in the second overtone C═O vibration region for the four points.

For point A, the second derivative spectrum shows two important peaks at 5130 and 5184 cm^{-1}, which are due to the second overtone of the stretching mode of the C═O group involved in the C═O···H−C intramolecular hydrogen bonding in the PHB crystal and to the amorphous C═O band, respectively, as described above.[42] At point B, the intensity of the peak at 5130 cm^{-1}, which is associated with the intramolecular hydrogen bonding of the crystal structure, decreases and the amorphous band shifts to a lower wavenumber. From our previous work, the decrease in the intramolecular hydrogen bonding in PHB crystal was determined to be responsible for the changes in the interactions from intramolecular hydrogen bonding to intermolecular hydrogen bonding between PHB and CAB in the blend.[24,25] Therefore, it is possible to deduce that the growth of the spherulite in the latter state contains some small fraction of CAB. At the edge of the spherulite, which is indicated by point C (shown as the green part in the IR image), the intensity of the crystallinity band at 5130 cm^{-1} is less than that at points A and B. This phenomenon is expected because it is at the interface region between the crystal and amorphous part. Finally, for point D, two peaks appear at ∼5165 and ∼5140 cm^{-1}. These peaks may be ascribed to the amorphous and the less-ordered structure or intermediate state, which moves to the front of the spherulite to expand the spherulite structure.

3.4. Classification of the Imaging Spectra in the Spherulite of PHB/CAB Blends by Principal Component Analysis (PCA). PCA was used to classify the differences in the spectra for each local area spectrum of the spherulite. PCA is the most widely used method for classifying and grouping spectra by compressing multivariate images into a number of factorials (i.e., principal components, PCs, or scores). Moreover, the yielded PCs which are orthogonal and independent to each other after PCA calculations present all of the information in the spectral channels for the large size image, and the

dx.doi.org/10.1021/ma201598s | Macromolecules 2012, 45, 2738−2748

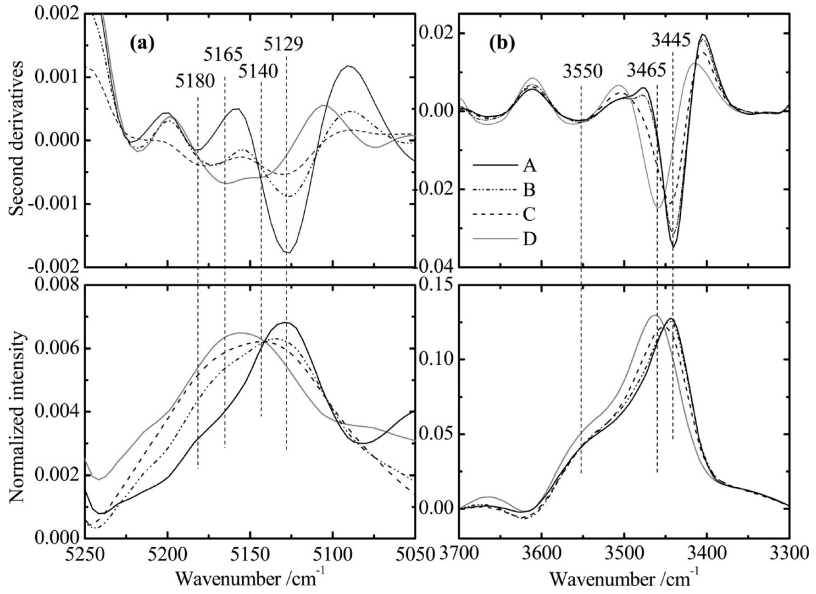


Figure 8. (a) NIR imaging spectra in the 5250−5050 cm^{-1} region and (b) IR imaging spectra in the 3700−3300 cm^{-1} region (bottom part) and their second derivatives (upper part) measured at points A, B, C, and D at t = 66 min.

obtained loadings indicate the contributions for the corresponding PC in spectral channels.[55,64,65] Exploiting the advantages of spectroscopy imaging, we may be able to extract each spectrum from the local areas (25 × 25 μm^2), which provides information about the structure at the local points presented in Figure 9. We classified the areas similarly to the

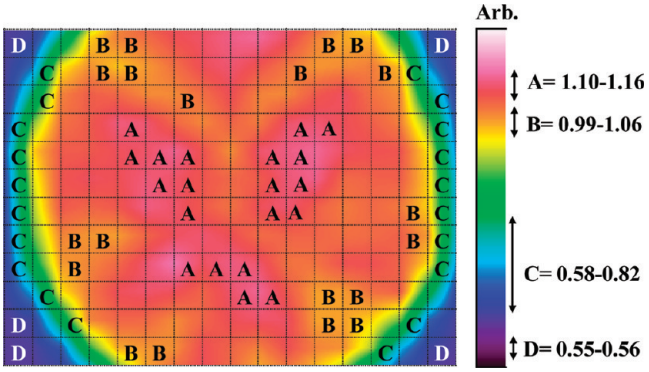


Figure 9. An IR image of the PHB/CAB (80:20) blend at t = 66 min during the isothermal crystallization process at 125 °C.

groupings presented in the above section: Group A is the highly crystalline area in the spherulite, which showed in the red color region. Group B is the low crystalline area, which showed in the orange color region. Group C is the interface of the spherulitic edge, and group D is the amorphous region outside the spherulite.

Twenty single spectra were extracted from 20 points of groups A−C; for group D, only five spectra were obtained since the amorphous area is limited, as shown in Figure 9. All the spectra in the region of 5500−3300 cm^{-1} were subjected to linear baseline correction and second derivative pretreatment to highlight subtle differences in the spectral features among the spectra before the PCA calculations.

Figure 10a illustrates the PCA scores plot of the first principal component (PC1) versus the second principle component (PC2) of each group in order to compare their variations. This plot clearly discriminates between groups A and B and groups C and D. Further classification between group A and group B is shown in the score plot in Figure 10b. Interestingly, the spectral points of group A are projected nearer to each other than the spectral points of group B. In other words, the variations in the score plot of group B are higher than those in group A. This indicates that group B contains heterogeneity within the group, while the spectra of group A are similar to each other. The differences between group A and group B may indicate that group B probably compose of a combination of PHB and a small fraction of CAB, while group A is highly crystallized and may only contain PHB content.

Figure 10c presents the loading plot of PC1 (solid line) and PC2 (broken line), which account for 95 and 4% of the total spectral variance, respectively, of the results shown in Figures 10a of the total 65 spectra points. It is evident in the loading plot of PC1 that the influent loadings are related to the first overtones of the C═O stretching modes at 3424, 3440, and 3470 cm^{-1}. Both the crystalline part represented by the peaks at 3424 and 3440 cm^{-1} and the amorphous part indicated by the peak at 3470 cm^{-1} significantly affect PC1; the crystalline peak at 3440 cm^{-1} contributes the highest loading value to this latent component. In addition, the region of the combination of the C−H stretching and C−H bending vibrations (4600−4200 cm^{-1}) affects this latent component. In particular, the peak at ∼4346 cm^{-1} is related to the crystal behavior, as described in a previous report.[36] However, judging from the peaks at 3460, 3610, 4350, and 4400 cm^{-1} in the PC2 loading plot (broken line), PC2 also imparts important information about the intermolecular interactions even though it accounts for only 4% of the total variance. The highest loading value of PC2 is strongly related to the peak at 3460 cm^{-1}, which corresponds to the intermolecular hydrogen bonding between CAB and PHB, as reported in our previous studies.[24] Furthermore, a weak loading value corresponds to the peak at ∼3610 cm^{-1}, which may be related to the O−H stretching vibration of the CAB in the blends.[66] In addition, the peak at ∼4350 cm^{-1} corresponds to the second overtone of C−H bending, and the peak at 4400

dx.doi.org/10.1021/ma201598s | Macromolecules 2012, 45, 2738−2748

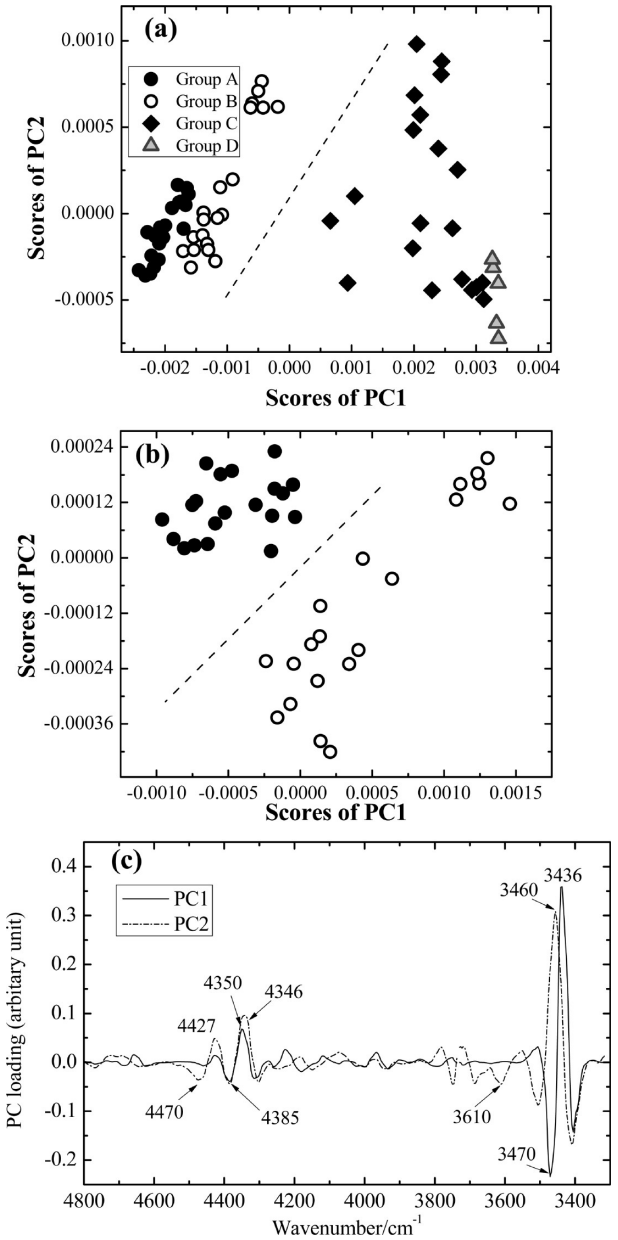


Figure 10. Score plots of PCA factor 1 vs factor 2 for (a) the 65 spectra of groups A, B, C, and D and for (b) the 40 spectra of groups A and B in the 5500−3300 cm^{-1} region. (c) PCA loadings plots of factor 1 and factor 2 of the results shown in (a) of 65 spectra points.

cm^{-1} is associated with the combination of the O−H stretching and C−O stretching modes of the glucose structure.[58] Therefore, this indicates that PC2 is influenced by the amorphous parts of PHB, CAB, and the intermolecular hydrogen bonds between PHB and CAB.

4. CONCLUSIONS

The crystallization behavior of PHB in its blend with CAB was explored using time-resolved IR and NIR imaging spectroscopy during the isothermal crystallization process at 125 °C. It was found that IR and NIR imaging are very useful for investigating changes in the molecular structure during the crystallization process. Thus, these methods provide information about spectral changes during the crystallization process and the distributions of different parts in heterogeneous spherulite systems. The following important conclusions were reached in the present study:

(1) From the IR and NIR imaging investigations, the structural changes and dynamic growth of spherulite in the blending system in three directions can be readily observed. The initial state of spherulite morphology is determined by the crystallizable PHB which shows earlier changes in crystallinity in the *X*-axis direction. The spherulite changes in the three directions until being limited in the *Z*-axis direction. After that, the spherulite enlarges only along the *X*- and *Y*-axes.

(2) Through the combination of spectroscopic imaging with polarized microscopic observation, the crystal behavior and growth of heterogeneous spherulite of PHB in the PHB/CAB melt isothermal crystallization were investigated. At the initial stage of crystallization, the amorphous PHB attempts to segregate from CAB and break the intermolecular hydrogen bonding (−O−H···O═C−), which acts as physical cross-links in the amorphous parts of the blends. As the crystallization process continues, the segregated PHB forms a lamellar structure similar to that of neat PHB. However, CAB that was not completely separated from the PHB will remain in the amorphous part of the spherulite.

(3) PCA has been proven to be able to clearly discriminate the imaging spectra from different parts of the spherulite. The loading plot of PC1 can be explained by introducing the crystallinity of PHB to the blend system, while the loading plot of PC2 indicates the contributions of the amorphous parts of PHB and CAB and the intermolecular hydrogen bonds of PHB and CAB. Thus, the large variations in PC1−PC2 scores plot derived from different parts of the spherulite may suggest that the low crystallinity regions in the blend spherulite contain both PHB and CAB.

(4) IR imaging is very useful for investigations of molecular structure changes in thin polymer films because of the strong intensity of the peaks in the IR region. On the other hand, NIR imaging is suitable for thick polymer samples, which benefits actual applications. In the present study, time-resolved crystallization images of the PHB/CAB blend were calculated from the area ratios of the crystal and amorphous peaks, and then the quantitative calculations of the crystalline peak intensity in the IR vibration region were more accurately compared to those in the NIR region. However, the absorption bands in the NIR imaging spectra are more obviously separated than the ones in the IR imaging spectra.

■ ASSOCIATED CONTENT

Supporting Information

Figures IS1−IS6. This material is available free of charge via the Internet at http://pubs.acs.org.

■ AUTHOR INFORMATION

Corresponding Author

*E-mail: ozaki@kwansei.ac.jp.

Notes

The authors declare no competing financial interest.

■ ACKNOWLEDGMENTS

The authors thank Dr. Nicolas Spegazzini (Kwansei Gakuin University) for valuable discussion particularly on the data analysis. This work was supported by Grant-in-Aid for Scientific Research (C) from MEXT (No. 20550026, No. 20550197), Grant-in-Aid for Scientific Research on Innovative Areas from MEXT (No. 21106521), and Shiseido Female Researcher Science Grant 2009. This works was supported also by Kwansei-Gakuin University "Special Research" project 2009–2014.

■ REFERENCES

(1) Lemoigne, M. *Ann. Inst. Past.* **1925**, *34*, 144–173.
(2) Doi, Y. In *Microbial Polyesters*; VCH Publishers: New York, 1990.
(3) Hocking, P. J.; Marchessault, R. H. Polyhydroxyalkanoates. In *Biopolymers from Renewable Resources*; Kaplan, D. L., Ed.; Springer-Verlag: Berlin, 1998; p 220.
(4) Iwata, T.; Doi, Y. *Macromol. Chem. Phys.* **1999**, *200*, 2429–2442.
(5) Yoshie, N.; Oike, Y.; Kasuya, K.; Doi, Y.; Inoue, Y. *Biomacromolecules* **2002**, *3*, 1320–1326.
(6) Akiyama, M.; Tsuge, T.; Doi, Y. *Polym. Degrad. Stab.* **2003**, *80*, 183–194.
(7) Kobayashi, G.; Shiotani, T.; Shima, Y.; Doi, Y. In *Biodegradable Plastics and Polymers*; Doi, Y., Fukuda, K., Eds.; Elsevier: Amsterdam, 1994; p 410.
(8) Marchessault, R. H.; Yu, G. *Polyesters II. Properties and Chemical Synthesis*. In *Biopolymers*; Doi, Y., Steinbüchel, A., Eds.; Wiley-VCH: Weinheim, 2003; Vol. *3b*, p 163.
(9) Yokouchi, M.; Chatani, Y.; Tadokoro, H.; Tani, H. *Polymer* **1973**, *14*, 267–272.
(10) Sato, H.; Murakami, R.; Padermshoke, A.; Hirose, F.; Senda, K.; Noda, I.; Ozaki, Y. *Macromolecules* **2004**, *37*, 7203–7213.
(11) Sato, H.; Dybal, J.; Murakami, R.; Noda, I.; Ozaki, Y. *J. Mol. Struct.* **2005**, *35*, 744–747.
(12) Sato, H.; Mori, K.; Murakami, R.; Ando, Y.; Takahashi, I.; Zhang, J.; Terauchi, H.; Hirose, F.; Senda, K.; Tashiro, K.; Noda, I.; Ozaki, Y. *Macromolecules* **2006**, *39*, 1525–1531.
(13) Sato, H.; Ando, Y.; Dybal, J.; Iwata, T.; Noda, I.; Ozaki, Y. *Macromolecules* **2008**, *41*, 4305–4312.
(14) Sato, H.; Nakamura, M.; Padermshoke, A.; Yamaguchi, H.; Terauchi, H.; Ekgasit, S.; Noda, I.; Ozaki, Y. *Macromolecules* **2004**, *37*, 3763–3769.
(15) Zhang, J.; Sato, H.; Noda, I.; Ozaki, Y. *Macromolecules* **2005**, *38*, 4274–4281.
(16) Doi, Y.; Kunioka, M.; Nakamura, Y.; Soga, K. *Macromolecules* **1986**, *19*, 2860–2864.
(17) Doi, Y.; Kitamura, S.; Abe, H. *Macromolecules* **1995**, *28*, 4822–4828.
(18) Rodrigues, J. A. F. R.; Parra, D. F.; Lugão, A. B. *J. Therm. Anal. Calorim.* **2005**, *79*, 379–381.
(19) Avella, M.; Martuscelli, E.; Greco, P. *Polymer* **1991**, *32*, 1647–1653.
(20) Chiu, H. J.; Chen, H. L.; Lin, T. L.; Lin, J. S. *Macromolecules* **1999**, *32*, 4969–4974.
(21) Furukawa, T.; Sato, H.; Shinzawa, H.; Noda, I.; Ochiai, S. *Anal. Sci.* **2007**, *23*, 871–876.
(22) Guo, L.; Sato, H.; Hashimoto, T.; Ozaki, Y. *Macromolecules* **2010**, *43*, 3897–3902.
(23) Huang, H.; Yun, H.; Zhang, J.; Sato, H.; Zhang, H.; Noda, I.; Ozaki, Y. *J. Phys. Chem. B* **2005**, *109*, 19175–19183.
(24) Suttiwijitpukdee, N.; Sato, H.; Zhang, J.; Hashimoto, T.; Ozaki, Y. *Polymer* **2011**, *52*, 461–471.
(25) Suttiwijitpukdee, N.; Sato, H.; Zhang, J.; Hashimoto, T. *Macromolecules* **2011**, *44*, 3467–3477.
(26) Yu, L.; Dean, K.; Li, L. *Prog. Polym. Sci.* **2006**, *31*, 576–602.
(27) Nishio, Y.; Matsuda, K.; Miyashita, Y.; Kimura, N.; Suzuki, H. *Cellulose* **1997**, *4*, 131–145.
(28) Wang, T.; Cheng, G.; Ma, S.; Cai, Z.; Zhang, L. *J. Appl. Polym. Sci.* **2003**, *89*, 2116–2122.
(29) Ceccorulli, G.; Pizzoli, M.; Scandola, M. *Macromolecules* **1993**, *26*, 6722–6726.
(30) Pizzoli, M.; Scandola, M.; Ceccorulli, G. *Macromolecules* **1994**, *27*, 4755–4761.
(31) Scandola, M.; Ceccorulli, G.; Pizzoli, M. *Macromolecules* **1992**, *25*, 6441–6446.
(32) El-Shafee, E.; Saad, G. R.; Fahmy, S. M. *Eur. Polym. J.* **2001**, *37*, 2091–2104.
(33) Park, J. W.; Tanaka, T.; Doi, Y.; Iwata, T. *Macromol. Biosci.* **2005**, *5*, 840–852.
(34) Di Lorenzo, M. L. *Prog. Polym. Sci.* **2003**, *28*, 663–689.
(35) Keith, H. D.; Padden, J. F. Jr. *J. Appl. Phys.* **1964**, *35*, 1270–1285.
(36) Hoffman, J. D.; Lauritzen, J. I. *J. Res. Natl. Bur. Stand., Sect. A* **1961**, *65*, 297–336.
(37) Lauritzen, J. I.; Hoffman, J. D. *J. Res. Natl. Bur. Stand., Sect. A* **1960**, *64*, 73–102.
(38) Hoffman, J. D. *Polym. Eng. Sci.* **1964**, *4*, 315–362.
(39) Price, F. P. *J. Polym. Sci., Part C: Polym. Symp.* **1963**, *3*, 117–119.
(40) Ozaki, Y., McClure, W. F., Christy, A. A., Eds. *Near-Infrared Spectroscopy in Food Science and Technology*; John Wiley & Sons, Inc.: Hoboken, NJ, 2007.
(41) Siesler, H. W., Ozaki, Y., Kawata, S., Heise, H. M., Eds. *Near-Infrared Spectroscopy; Principles, Instruments, Applications*; Wiley-VCH: Weinheim, 2002; p 213.
(42) Hu, Y.; Zhang, J.; Sato, H.; Futami, Y.; Noda, I.; Ozaki, Y. *Macromolecules* **2006**, *39*, 3841–3847.
(43) Sato, H.; Ozaki, Y.; Jiang, J.; Yu, R. Q.; Shinzawa, H. In *Raman, Infrared and Near-Infrared Chemical Imaging*; Šašić, S., Ozaki, Y., Eds.; John Wiley & Sons, Inc.: Hoboken, NJ, 2010; p 263.
(44) Kazarian, S. G.; Chan, K. L. A. *Macromolecules* **2004**, *37*, 579–584.
(45) Oh, S. J.; Koenig, J. L. *Anal. Chem.* **1998**, *70*, 1768–1772.
(46) Bhargava, R.; Wall, B. G.; Koenig, J. L. *Appl. Spectrosc.* **2000**, *54*, 470–479.
(47) Wessel, E.; Vogel, C.; Kolomiets, O.; Hoffmann, U.; Siesler, H. W. In *Infrared and Raman Spectroscopic Imaging*; Salzer, R., Siesler, H. W., Eds.; Wiley-VCH: Weinheim, 2009; p 297.
(48) Vogel, C.; Wessel, E.; Siesler, H. W. *Biomacromolecules* **2008**, *9*, 523–527.
(49) Vogel, C.; Wessel, E.; Siesler, H. W. *Macromolecules* **2008**, *41*, 2975–2977.
(50) Gupper, A.; Kazarian, S. G. *Macromolecule* **2005**, *38*, 2327–2332.
(51) Šašić, S., Ozaki, Y., Eds. *Raman, Infrared and Near-Infrared Chemical Imaging*; John Wiley & Sons, Inc.: Hoboken, NJ, 2010.
(52) Salzer, R., Siesler, H. W., Eds. *Infrared and Raman Spectroscopic Imaging*; Wiley-VCH: Weinheim, 2009.
(53) Reich, G. *Adv. Drug Delivery Rev.* **2005**, *57*, 1109–1143.
(54) Shinzawa, H.; Awa, K.; Ozaki, Y.; Sato, H. *Appl. Spectrosc.* **2009**, *63*, 974–977.
(55) Juan, A.; Maeder, M.; Hancewicz, T.; Duponchel, L.; Tauler, R. In *Infrared and Raman Spectroscopy Imaging*; Salzer, R., Siesler, H. W., Eds.; Wiley-VCH: Weinheim, 2009; pp 65–109.
(56) Murakami, R.; Sato, H.; Dybal, J.; Iwata, T.; Ozaki, Y. *Polymer* **2007**, *48*, 2672–2680.
(57) Bhargava, R.; Levin, I. W. *Spectrochemical Analysis Using Infrared Multichannel Detectors*; Blackwell Publishing: Chennai, 2005; p 122.
(58) Barham, P. J.; Keller, A.; Otun, E. L.; Holmes, P. A. *J. Mater. Sci.* **1984**, *19*, 2781–2794.
(59) Keith, H. D.; Padden, F. J. Jr. *Macromolecules* **1996**, *29*, 7776–7786.
(60) Owen, A. J. *Polymer* **1997**, *38*, 3705–3708.
(61) Singfield, K. L.; Hobbs, J. K.; Keller, A. *J. Cryst. Growth* **1998**, *183*, 683–689.
(62) Hobbs, J. K.; Binger, D. R.; Keller, A.; Barham, P. J. *J. Polym. Sci., Part B: Polym. Phys.* **2000**, *38*, 1575–1583.

(63) Keith, H. D.; Padden, F. J. Jr. *J. Appl. Phys.* **1964**, *35*, 1270−1285.
(64) Geladi, P.; Grahn, H. *Multivariate Image Analysis in Chemistry and Related Areas: Chemometric Image Analysis*; John Wiley & Sons: Chichester, 1996.
(65) Geladi, P.; Grahn, H.; Manley, M. Data Analysis and Chemometrics for Hyperspectral Imaging. In *Raman, Infrared, and Near-Infrared Chemical Imaging*; Šašić, S., Ozaki, Y., Eds.; John Wiley & Sons, Inc.: Hoboken, NJ, 2010; pp 93−107.
(66) Workman, J., Jr.; Weyer, L. *Practical Guide to Interpretive Near-Infrared Spectroscopy*; CRC Press/Taylor & Francis Group: New York, 2008.

Macromolecules

Article

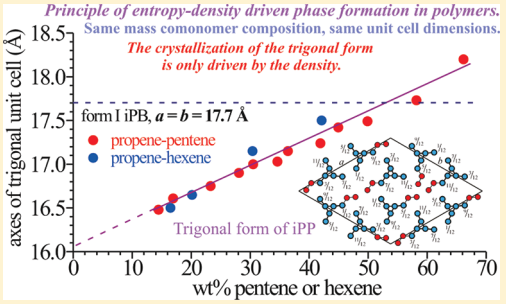
pubs.acs.org/Macromolecules

Crystal Structure of the Trigonal Form of Isotactic Propylene–Pentene Copolymers: An Example of the Principle of Entropy–Density Driven Phase Formation in Polymers

Claudio De Rosa, Odda Ruiz de Ballesteros,* Finizia Auriemma, and Maria Rosaria Di Caprio

Dipartimento di Chimica "Paolo Corradini", Università di Napoli "Federico II", Complesso di Monte S. Angelo, via Cintia, I-80126 Napoli, Italy

ABSTRACT: The crystal structure of the trigonal form of isotactic polypropylene in propylene–pentene random copolymers is presented. These copolymers crystallize in the α form of iPP for concentrations of pentene lower than 7–8 mol % and in the trigonal form for higher pentene concentration. The trigonal form does not crystallize by cooling from the melt but crystallizes from the amorphous by cold-crystallization or for samples with high pentene concentration by aging the amorphous samples at room temperature. The pentene units are included in the crystals of trigonal form and, at low concentration, also in the crystals of α form, producing increase of the unit cell dimension. The change of crystallization habit from monoclinic into trigonal occurring for concentrations higher than 10 mol % allows incorporation of higher amounts of pentene units in the crystals of the trigonal form than in the α form. The crystal structure of the trigonal form has been studied by analysis of the X-ray fiber and powder diffraction patterns and electron diffraction of single crystals of propylene–pentene copolymers having concentrations of pentene units in the range 20–54 mol %. Chains of propylene–pentene copolymers in the 3-fold helical chain conformation are packed in a trigonal unit cell according to the space group $R3c$ or $R\bar{3}c$. The dimension of the unit cell axes depends on the amounts of pentene units included in the crystal lattice, and when pentene concentration approaches 50 mol %, the value of $a = b$ axes becomes practically equal to that of the unit cell of the stable form I of isotactic polybutene.



INTRODUCTION

The crystallization of the trigonal form of isotactic polypropylene (iPP) in random propylene–hexene (iPPHe) and propylene–pentene (iPPe) copolymers, prepared with metallocene catalysts, has been recently described.[1−6] Both iPPHe and iPPe copolymers crystallize in the α form of iPP for comonomer concentrations lower than about 10 mol %, whereas they crystallize in the new trigonal form for higher hexene and pentene concentrations.[1−6] In these copolymers the increase of crystalline density due to the inclusion of comonomeric units in the crystals of iPP is the driving force that induces the crystallization of the trigonal form.[3−5] In fact, it has been demonstrated that accommodation of high concentrations of hexene or pentene units in the crystals of iPP induces a suitable increase of density that allows the crystallization of the 3-fold helical chains in a trigonal unit cell, according to the space groups $R3c$ or $R\bar{3}c$, where the helical symmetry of the chains is maintained in the crystal lattice,[3−5] as predicted by the principles of polymer crystallography.[7] According to the basic principles of crystallography, indeed, macromolecules in the crystal tend to achieve the closest distance between nonbonded neighboring atoms, corresponding to the minima of internal energy and of specific volume surface (principle of close packing). The mode of packing of polymer molecules is also guided by entropy: a molecule in a crystal tends to maintain part of its symmetry elements, provided that this does not cause a serious loss of density. In fact, in a more symmetric position a molecule has a greater freedom of vibration; that is, the structure corresponds to a wider energy minimum.[7]

The crystal structure of the α form of iPP has been considered for long time an exception of these principles because it does not comply with the possible rule of maintaining the 3-fold helical symmetry of the chains in the crystal lattice. In fact, chains of iPP assume the stable 3/1 helical conformation, but they are not packed in trigonal unit cells, maintaining the crystallographic 3-fold symmetry, because this would produce a crystal lattice with very low density.[7] However, if polypropylene macromolecules are modified for instance by incorporating bulky comonomeric units, like pentene or hexene, the inclusion of the comonomeric units in the crystals produces increase of density and the random copolymers crystallize in the trigonal form where the 3-fold helical symmetry of the chains is maintained in the crystal lattice. This occurs because the crystal density becomes as high as that of crystals of form I of isotactic polybutene (iPB)[8] due to the inclusion of the bulky comonomer. The resulting structure of the trigonal form of iPP found in iPPHe and iPPe

Received: August 12, 2011
Revised: February 14, 2012
Published: March 12, 2012

ACS Publications © 2012 American Chemical Society

copolymers is, therefore, very similar to that of form I of iPB[8] and has never been observed in iPP homopolymer because, in the absence of bulky side groups, it would have a too low density.[3−5] Therefore, the structure of the trigonal form of iPP in iPPHe and iPPe copolymers represents the fulfillment of the principles of polymer crystallography and indicates that the packing of polymer molecules is mainly driven by density (principle of entropy−density driven phase formation in polymers).[3]

The trigonal form of iPP has been recently found also in random propylene−butene copolymers (iPPBu).[9] The iPPBu copolymers are crystalline in the whole range of composition up to 100% of butene due to the cocrystallization of propene and butene units in the crystals of iPP and iPB at any composition.[9−11] In the case of iPPBu copolymers, however, even for concentration of butene as high as 50 mol %, the inclusion of butene units in the crystals of α form of iPP and the corresponding increase of density are not sufficient to promote the crystallization of the trigonal form in the bulk samples, as instead occurs in iPPe and iPPHe copolymers for lower concentrations of comonomeric units (about 10 mol %).[9,10] The trigonal form has been instead obtained in oriented fibers of iPPBu copolymers with butene concentrations of 40−60 mol %. In these samples crystals of α form present in the melt-crystallized compression-molded films transform by stretching at high deformations in the trigonal form.[9] This stress-induced transformation of the α form into the trigonal form occurs also in iPPHe copolymers having hexene content of 9−10 mol %[4,12] and indicates that in stretched fibers of iPPBu and iPPHe copolymers the trigonal form of iPP is more stable than the α form.[4,9] This confirms the principle of density−entropy driven phase formation in polymers, which establishes that the packing of polymer molecules is mainly driven by density and the chains symmetry tends to be preserved in the crystal lattice.[3−5,9]

A detailed model of the crystal structure of the trigonal form has been proposed for iPPHe[3,4] through analysis of both X-ray powder and fiber diffraction patterns. A preliminary model has been reported for iPPe copolymers based only on the X-ray powder diffraction profiles.[5] Chains in 3-fold helical conformation are packed in a trigonal unit cell with values of a and b axes that increase with increasing hexene or pentene concentration.[3−5] For instance, values of $a = b = 17.5$ Å and $c = 6.5$ Å have been found for the iPPHe sample with 26 mol % of hexene,[3,4] whereas values of axes $a = b = 17.1$ Å and $c = 6.5$ Å have been found for iPPe copolymers with 30 mol % of pentene.[5] The value of $a = b$ axes approaches the value of the unit cell of iPB ($a = b = 17.7$ Å)[8] for higher pentene concentrations (50−55 mol %), when the average composition of iPPe copolymers approaches that of iPB.[5] Therefore, when propene and pentene or hexene units are randomly distributed along the same macromolecules and the average overall composition of the two comonomers approaches that of 1-butene (≈50% C_3H_6 + ≈50% C_5H_{10} = C_4H_8), copolymer chains behave as poly(butene) macromolecules and crystallize into the stable form I of iPB.[5]

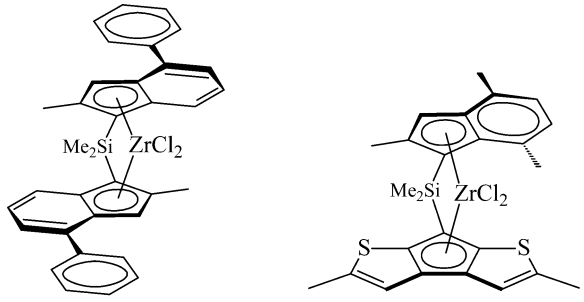
Detailed analyses of stretched fibers, crystal morphology, mechanical properties, and thermal and crystallization properties have been reported mainly for iPPHe copolymers.[1,4,10e,12,13d] In the case of iPPe copolymers, a study of the melting and crystallization behavior and of the morphology of samples with 1-pentene contents up to 50 mol % has been reported.[6] The wide-angle and small-angle X-ray diffraction data have suggested that, notwithstanding the intrinsic intrachain structural disorder, thin and wide lamellae characterize the morphology of the trigonal form in iPPe copolymers.[6] The thickness of the lamellae keeps constant, at around 4 nm, over the whole range of compositions in which the trigonal form develops, consistent with the composition-independent melting temperature of the trigonal form.[6] However, structural characterizations of iPPe copolymers in stretched fibers and single crystals have not been reported yet.

In this paper, we report the complete resolution of the crystal structure of the trigonal form of iPPe copolymers performed through the analysis of both X-ray powder and fiber diffraction patterns and electron diffraction of single crystals. The inclusion of the pentene units in the crystals of both α and trigonal form of iPP is analyzed on the basis of variations of the Bragg distances of reflections observed in the X-ray diffraction patterns and measurements of crystal density.

EXPERIMENTAL SECTION

Two sets of samples of random propylene−pentene copolymers with concentration of pentene comprised in the range 3−54 mol % have been prepared using two different metallocene catalysts, shown in Chart 1, activated with methylaluminoxane (MAO). The C_2-symmetric metallocene catalyst dimethylsilyl(2,2′-dimethyl-4,4′-diphenylindenyl)$ZrCl_2$ (**A** of Chart 1)[14] is highly isospecific but not completely regioselective and produces highly isotactic homopolymer sample and iPPe copolymers, containing no detectable *rr* triad stereodefects and only very small amount (about 0.2 mol %) of regiodefects due to the presence of secondary 2,1 propene units. The C_1-symmetric metallocene catalyst dimethylsilyl(2,4,7-trimethylindenyl)-(dithienocyclopentadienyl)$ZrCl_2$ (**B** of Chart 1)[15] is fully regioselective but not perfectly isoselective and produces iPP homopolymer and iPPe copolymers containing only stereo-errors, due to the presence of *rr* triad defects in concentration, for the homopolymer sample, of about 3.5 mol %.[15]

Chart 1. Structures of the Metallocene Catalyst Precursors Used in This Study



A **B**

The copolymerizations were run at 25 °C (with catalyst **A**) or 60 °C (with catalyst **B**) following the experimental procedure described in ref 5. A list of the analyzed samples is reported in Table 1.

The composition of the iPPe copolymers was determined by analysis of the resonances of CH_2 and CH in the ^{13}C NMR spectra, as suggested in ref 16. The NMR analysis also showed that all the copolymers present a random distribution of comonomers ($r_1 \times r_2 \approx 1$). Here in the following these copolymers will be addressed with symbols iPPeAn e iPPeBn, with **A** and **B** indicating the complex of Chart 1 used as catalyst for their preparation and n a sequential number. For each sample the pentene concentration (mol %) in the chain is specified in explicit.

dx.doi.org/10.1021/ma201849w | Macromolecules 2012, 45, 2749−2763

Table 1. Polymerization Temperature (T_p), Volume of Pentene in the Feed, Composition (wt % and mol % of Pentene Comonomeric Units), Intrinsic Viscosities ([η]), Viscosity-Average Molecular Masses (M_v), and Melting Temperatures of As-Prepared Samples (T_m) of Propylene−Pentene Copolymers Prepared with the Metallocene Catalysts of Chart 1

sample[a]	catalyst	T_p	mL pentene (feed)	wt % pentene	mol % pentene	[η] (dL/g)	$M_v \times 10^{-5}$	T_m (°C)[f]
iPPeA1	**A**	25	1	5.23	3.2	2.19[b]	4.00[d]	127.3
iPPeA2	**A**	25	2	8.61	5.3	1.87[b]	3.22[d]	104.7
iPPeA3	**A**	25	3	13.91	8.8	1.6[b]	2.60[d]	87.9
iPPeA4	**A**	25	4	16.62	10.7	1.75[b]	2.93[d]	72.1
iPPeA5	**A**	25	8	30.49	20.8	1.56[b]	2.51[d]	64.8
iPPeA6	**A**	25	12	36.39	25.6	1.48[b]	2.33[d]	65.3
iPPeA7	**A**	25	16	44.92	32.9	1.01[c]	1.06[e]	59.1
iPPeA8	**A**	25	22	54.52	45.5	1.02[c]	1.07[e]	48.1
iPPeB1[f]	**B**	60	1	6.02	3.7	0.476[c]	0.384[e]	113.1
iPPeB2	**B**	60	2	11.90	7.5	0.368[c]	0.271[e]	89.0
iPPeB3	**B**	60	2.5	14.45	9.2	0.501[c]	0.411[e]	75.0
iPPeB4	**B**	60	3	16.94	10.9	0.252[c]	0.162[e]	69.2
iPPeB5	**B**	60	4	23.28	15.4	0.251[c]	0.161[e]	65.2
iPPeB6	**B**	60	10	28.11	19.0	1.07[c]	1.15[e]	65.0
iPPeB7	**B**	60	7	34.61	24.1	0.244[c]	0.156[e]	63.4
iPPeB8	**B**	60	9.6	41.90	30.2	0.24[c]	0.153[e]	60.6
iPPeB9	**B**	60	15	49.89	37.4	0.191[c]	0.112[e]	59.0
iPPeB10	**B**	60	20	66.18	54.0	0.163[c]	0.09[e]	44.0

[a]The samples iPPeB1−iPPeB10 correspond to the samples reported in our previous preliminary paper (ref 5), but the pentene concentrations have been recalculated by analysis of high-resolution ^{13}C NMR spectra. In particular, the sample iPPeB2 with 7.5 mol % of pentene corresponds to the sample iPPe2 of ref 5, the one with a comonomer content of 4 mol % (the correct pentene concentration of this sample is 7.5 mol %). [b]From GPC in 1,2,4-trichlorobenzene (TCB) at 150 °C. [c]Measured in tetrahydronaphthalene (THN) at 135 °C with an Ubbelohde viscometer. [d]From the intrinsic viscosity values measured in TCB at 150 °C according to $[\eta] = K(M_v)^\alpha$, with $K = 1.9 \times 10^{-4}$ dL/g and $\alpha = 0.725$.[17a] [e]From the intrinsic viscosity values measured in THN at 135 °C according to $[\eta] = K(M_v)^\alpha$ with $K = 1.93 \times 10^{-4}$ dL/g and $\alpha = 0.74$.[17b] [f]Determined by DSC curves recorded at heating rate of 10 °C/min of as-prepared samples aged at room temperature up to complete crystallization of the samples with high pentene concentration.

The samples of iPPe copolymers prepared with the catalyst **A** show molecular masses (M_v in the range 1.1×10^5−4.0×10^5) higher than those of samples prepared with catalyst **B** (M_v in the range 1.0×10^4−4.0×10^4, with only the sample iPPeB6 showing $M_v = 1.1 \times 10^5$). The two sets of samples have been prepared to analyze the influence of the molecular mass on the crystallization of the trigonal form.

The viscosity-average molecular masses ($\bar{M}_v$) were obtained from the values of the intrinsic viscosities [η]. For the samples iPPeAn of higher molecular mass prepared with the catalyst **A**, the intrinsic viscosity was measured in 1,2,4-trichlorobenzene at 150 °C. The corresponding average molecular masses were obtained from the intrinsic viscosity values according to $[\eta] = K(\bar{M}_v)^\alpha$, with $K = 1.9 \times 10^{-4}$ and $\alpha = 0.725$.[17a] For the samples iPPeBn of lower molecular mass, prepared with the catalyst **B**, the intrinsic viscosity was measured in tetrahydronaphthalene at 135 °C using standard Ubbelohde viscosimeter. The corresponding average molecular masses were obtained according to $[\eta] = K(\bar{M}_v)^\alpha$, with $K = 1.93 \times 10^{-4}$ and $\alpha = 0.74$.[17b]

The SEC curves of all samples show narrow molecular weight distributions, with M_w/M_n around 2.0, typical of single-center metallocene catalysts.

The melting temperatures were determined with a differential scanning calorimeter (DSC) Mettler DSC-822 performing scans in flowing N_2 atmosphere and at a heating rate of 10 °C/min.

Oriented fibers of the sample iPPeA5 with 20.8 mol % of pentene were obtained by stretching compression-molded films at room temperature up to 600% deformation. Compression-molded films were prepared by heating the as-polymerized samples at temperatures 20−30 °C higher than the melting temperatures under a press at low pressure to avoid preferred orientations in the sample and by slow cooling to room temperature.

X-ray diffraction patterns were obtained with Ni filtered Cu Kα radiation. The powder profiles were obtained by an automatic Philips diffractometer, whereas the fiber diffraction patterns were recorded on a BAS-MS imaging plate (FUJIFILM) using a cylindrical camera and digitized with a digital imaging reader (Perkin-Elmer Cyclone Plus).

The crystallinity degree (x_c) were determined from the powder diffraction profiles by the ratio between the crystalline diffraction area (A_c) and the area of the whole diffraction profiles (A_t), $x_c = (A_c/A_t) \times 100$. The area of the crystalline diffraction A_c was evaluated by subtracting the area of the amorphous halo from the area of the whole diffraction profiles A_t. The diffraction profiles of the amorphous phase of samples iPPeB8−iPPeB10 and iPPeA8 with pentene concentration higher than 30 mol % were obtained from the X-ray diffraction profiles of the amorphous samples obtained by compression molding. In fact, these samples do not crystallize by cooling the melt to room temperature and amorphous films are obtained by compression molding. The amorphous samples then slowly crystallize by aging at room temperature. For the iPPe copolymer samples with pentene concentration in the range 3−30 mol %, the diffraction profiles of the amorphous phase were obtained from the X-ray diffraction profiles of the molten samples, by recording the diffraction profiles of the iPPe copolymers at different temperatures higher than the melting temperature. For each sample the 2θ position of the maximum of the amorphous halo at room temperature was obtained by extrapolation at 25 °C of the 2θ values of the maxima of the diffraction profiles of the molten samples recorded at various temperatures.

The diffraction profiles of the amorphous phases of each sample so obtained was then scaled and subtracted to the diffraction profiles of the semicrystalline samples.

Densities of the copolymer samples were evaluated by flotation at 25 °C of compression-molded films in solutions of water and ethyl alcohol. Values of the density of crystals (ρ_c) were calculated from the values of the experimental density (ρ_{sp}), the X-ray degree of crystallinity (x_c), and the values of density of amorphous phase (ρ_a) from the equation $1/\rho_{sp} = x_c/\rho_c + (1 - x_c)/\rho_a$.

Single crystals of the sample iPPeB7 with 24.1 mol % of pentene have been obtained from dilute amyl acetate solution. Single crystals

dx.doi.org/10.1021/ma201849w | Macromolecules 2012, 45, 2749−2763

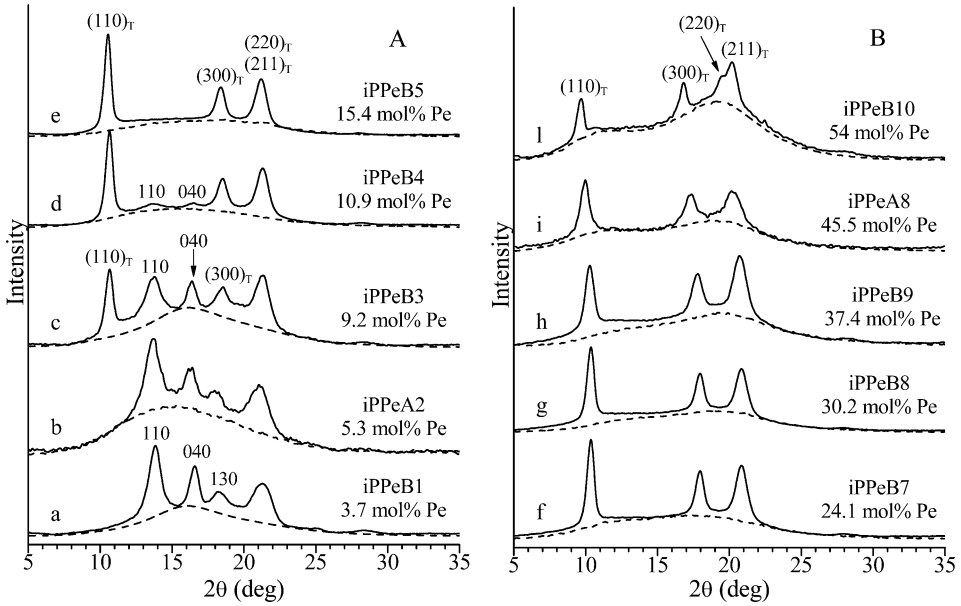


Figure 1. X-ray powder diffraction profiles of as-prepared and aged samples of iPPe copolymers. The 110, 040, and 130 reflections of the α form and the $(110)_T$, $(300)_T$, $(220)_T$, and $(211)_T$ reflections of the trigonal form of iPP are indicated. The diffraction profiles of the amorphous phase of each sample are reported as dashed lines. For the samples a–f the amorphous dashed lines correspond to profiles of molten samples after horizontal shift toward the extrapolated 2θ position at 25 °C of the maximum, whereas for samples g–l they are relative to the diffraction profiles recorded at room temperature of amorphous samples obtained by compression molding.

were analyzed by transmission electron microscope (TEM), in bright field and in selected area diffraction (50 μm diameter aperture) modes. A Philips transmission electron microscope, operating at 120 kV, was used.

Calculations of packing energy were performed with the software package[18] CERIUS2, using the force field PCFF.[19]

Calculated structure factors were obtained as $F_c = (\sum|F_{hkl}|^2 M_{hkl})^{1/2}$, where F_{hkl} is the structure factor of the hkl reflection, M_{hkl} is the multiplicity factor for powder diffraction, and the summation is taken over all reflections included in the 2θ range of the corresponding reflection peak observed in the X-ray powder diffraction profile. For the sake of simplicity, an isotropic thermal factor B = 9 Å^2 was assumed for all atoms whereas the atomic scattering factors as in ref 20 were used.

The observed structure factors (F_0) were evaluated from the intensities of the reflections observed in the X-ray powder diffraction profile, $F_0 = (I_0/LP)^{1/2}$, where LP is the Lorentz polarization factor for X-ray powder diffraction: $LP = (1 + \cos^2 2\theta)/(\sin^2 \theta \cos \theta)$. The experimental intensities (I_0) were evaluated by measuring the areas of the peaks in the X-ray powder diffraction profile, after subtraction of the amorphous halo.

Calculated X-ray powder diffraction profiles were obtained using the software package[18] CERIUS2, using the thermal factor B = 9 Å^2 and profile functions having half-height width regulated by the average crystallite size along a, b, and c axes (L_a, L_b, and L_c). In the calculations $L_a = L_b = L_c$ have been set equal to 100 Å, and the values were chosen to give the best agreement with the half-height width of the experimental peaks in the powder diffraction profiles. This value corresponds to a coherence length along a, b, and c and is not a true crystallite size.

The intensities of the reflections in the X-ray fiber diffraction pattern were quantitatively compared with calculated square modulus of structure factors. The observed intensities I_0 were evaluated by measuring the intensity of reflection spots recorded on the imaging plate after subtraction of background intensity, determined for each reflection by measuring the intensity of the closest region to the spot. The observed structure factors (F_0) were determined from the observed intensities (I_0) as $F_0 = (I_0/LP)^{1/2}$, where LP is the Lorentz and polarization factor for fiber diffraction $LP = (1 + \cos^2 2\theta)/[2(\sin^2 2\theta - \zeta^2)^{1/2}]$, with $\zeta = \lambda l/c$, l, and c being the order of the layer line and the chain axis periodicity, respectively. The calculated structure factors (F_c) were obtained as $F_c = (|F_{hkl}|^2 M_{hkl})^{1/2}$, where F_{hkl} is the structure factor of the hkl reflection and M_{hkl} is the multiplicity factor for fiber diffraction. An isotropic thermal factor B = 9 Å^2 and the atomic scattering factors of ref 20 have been assumed.

RESULTS AND DISCUSSION

Structural and Thermal Analyses. The X-ray powder diffraction profiles of as-prepared samples of iPPe copolymers are reported in Figure 1. As-prepared samples with pentene concentration higher than 30 mol % are initially amorphous and crystallize upon aging at room temperature. The corresponding diffraction profiles (curves g–l of Figure 1) have been recorded after at least 2 months aging at room temperature, up to achieve almost complete crystallization. We have verified that further aging at room temperature does not induce any change in the diffraction profiles and in the values of crystallinity degree.

The copolymer samples with low pentene concentration, up to 7–8 mol %, are crystallized in the α form of iPP, as evident by the presence of the 110, 040, and 130 reflections of the α form at $2\theta \approx 14°$, 17°, and 18°, respectively, in the diffraction profiles a and b of Figure 1. Samples with pentene content around 9 mol % crystallize as mixture of α form and trigonal form, as indicated by the contemporary presence of the 110, 040, and 130 reflections of the α form and of the $(110)_T$ and $(300)_T$ reflections at $2\theta \approx 10°$ and 18°, respectively, of the trigonal form,[3,4] in the diffraction profile c of Figure 1. For concentrations of pentene higher than 15 mol %, iPPe copolymers crystallize in the pure trigonal form of iPP, as shown by the presence of only the $(110)_T$, $(300)_T$, and $(211)_T$ + $(220)_T$ reflections at $2\theta \approx 10°$, 18°, and 21°, respectively, of the trigonal form, in the diffraction profiles e–l of Figure 1.

It is apparent from the diffraction profiles of Figure 1 that the values of diffraction angles of the 110 and 040 reflections of the α form for the iPPe copolymers with pentene concentration up

dx.doi.org/10.1021/ma201849w | Macromolecules 2012, 45, 2749–2763

to about 10 mol %, and those of the $(110)_T$ reflection of the trigonal form for the iPPe copolymers with higher pentene concentration, decrease with increasing the comonomer content. This indicates increase of unit cell dimensions of the monoclinic α form and of the trigonal form with increasing pentene concentration, and the inclusion of pentene units in the crystals of the trigonal form and possibly also into those of α form, at least for low concentrations. The values of a, b, and c axes and the values of β of the monoclinic unit cell of the α form and the values of $a = b$ axes of the unit cell of the trigonal form for the iPPe copolymers have been calculated from the Bragg distances of the reflections observed in the powder profiles of Figure 1. For the monoclinic α form, the values of the axes a, b, and c and the angle β have been optimized fixing the symmetry of the space group to $P2_1/c$ and the indices of the reflections observed in the experimental X-ray diffraction profiles. The result of this analysis gives values of c axis and of the angle β almost constant with composition at the value found in the α form of iPP,[21] that is, $c = 6.5 \pm 0.2$ Å and $\beta = 99.3 \pm 0.5°$. The values of unit cell axes are reported in Table 2 and in Figures 2A and 2B for the α form and the trigonal form, respectively, as a function of comonomer concentration.

Table 2. Values of *a*, *b*, and *c* Axes of the Monoclinic Unit Cell of *α* Form and Values of *a* = *b* Axes of the Unit Cell of the Trigonal Form That Crystallize in Samples of iPPe Copolymers

		α form (β = 99.3°)			trigonal form (γ = 120°, c = 6.5 Å)
sample	mol % pentene	a (Å)	b (Å)	c (Å)	a = b (Å)
iPP	0	6.65	20.96	6.50	
iPPeA1	3.2	6.74	21.33	6.54	
iPPeB1	3.7	6.76	21.35	6.54	
iPPeA2	5.3	6.83	21.56	6.44	
iPPeB2	7.5	6.81	21.62	6.46	
iPPeA3	8.8	6.84	21.63	6.46	
iPPeB3	9.2	6.84	21.64	6.58	16.48
iPPeB4	10.9	6.86	21.56	6.50	16.61
iPPeB5	15.4				16.75
iPPeB6	19.0				16.90
iPPeA5	20.8				17.00
iPPeB7	24.1				17.03
iPPeA6	25.6				17.15
iPPeB8	30.2				17.24
iPPeA7	32.9				17.42
iPPeB9	37.4				17.49
iPPeA8	45.5				17.73
iPPeB10	54.0				18.20

The unit cell dimensions of the α and trigonal forms that crystallize in isotactic propene−hexene copolymers, evaluated in refs 3 and 4 assuming the constant values of the chain axis c = 6.5 Å and of $\beta = 99.3°$ of the monoclinic unit cell of the α form of iPP,[21] are also reported in Figures 2A and 2B for comparison.[3,4]

For both propene−pentene and propene−hexene copolymers the values of a and b axes of the α form increase with increasing the comonomer concentration up to nearly 4 mol %, and then they remain almost constant for further increase of comonomer content (Figure 2A). This probably indicates that pentene units, as well as hexene units, are included (at least in part) in the crystals of α form up to nearly 4 mol % and for higher concentrations induce the formation of the trigonal form (Figure 1). The pentene and hexene units are also included in the crystals of the trigonal form, as indicated in Figure 2B by the increase of the a axis of the unit cell of the trigonal form with increasing the comonomer concentration. High concentrations of pentene and hexene are better tolerated in the crystals of the new trigonal form than in the α form, and the change of the crystallization habit at comonomer contents higher than 10 mol % allows a nearly complete accommodation of pentene and hexene units in the crystal lattice.

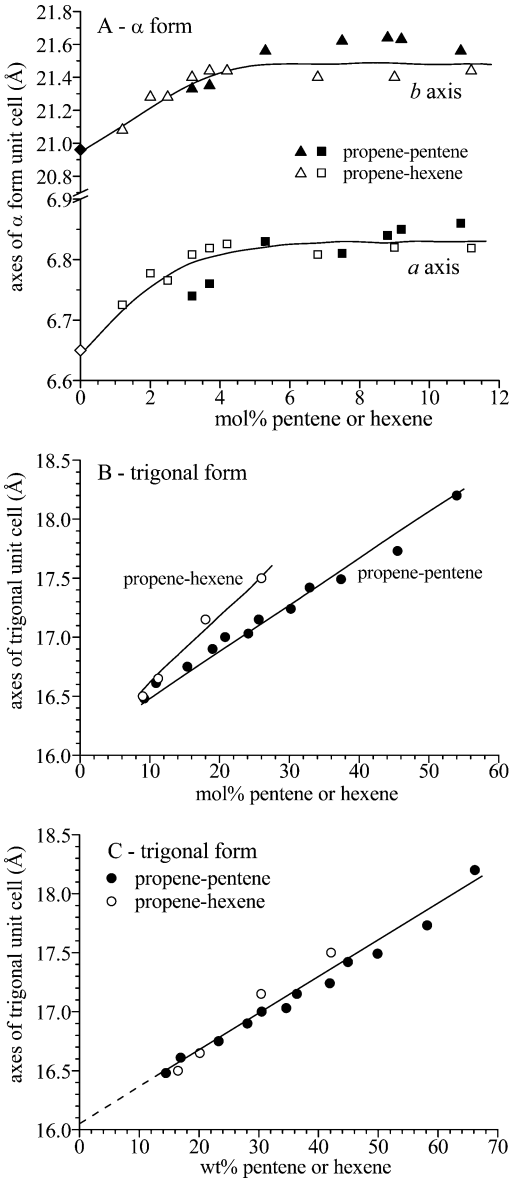


Figure 2. Values of a (■, □) and b (▲, △) axes of the monoclinic unit cell of the α form (A) and values of $a = b$ axes (●, ○) of the unit cell of the trigonal form (B) observed in as-prepared samples of iPPe (full symbols) and iPPHe (empty symbols)[3,4] copolymers, as a function of mol % (A, B) and wt % (C) of comonomeric units. The values of a and b axes (◊, ♦) of the unit cell of the α form of the iPP homopolymer[21] are also reported. In (C) the extrapolation of the straight line to zero comonomer composition (dashed line) gives the values of the axes of the unit cell of the hypothetical trigonal form of the iPP homopolymer ($a = b = 16.05$ Å).

dx.doi.org/10.1021/ma201849w | Macromolecules 2012, 45, 2749−2763

As also already reported in ref 6, the data of Figure 2B seem to indicate that the extent of lattice expansion depends on the size of the substituent. In fact, at a given molar composition the values of $a = b$ axes of the trigonal unit cell are larger for the iPPHe copolymers than for those of iPPe copolymers (Figure 2B), according to the hypothesis of inclusion of comonomeric units into the crystal lattice. However, the values of unit cell axes of the trigonal form of iPPHe and iPPe copolymers are almost fitted by a single master line if the data are reported as a function of comonomer concentration expressed as wt % of hexene or pentene units (Figure 2C). Therefore, at the same mass comonomer composition the dimensions of the trigonal unit cell are the same for pentene or hexene comonomers. This still indicates that the crystallization of the trigonal form and the unit cell dimensions are only driven by the density.[3,4] When the crystal density is sufficiently high (ca. 0.89 g/cm^3), at around 10 mol % of hexene or pentene, the trigonal form can crystallize.

The extrapolation of the master line to zero comonomer composition (dashed line in Figure 2C) gives the values of the axes of the unit cell of the hypothetical trigonal form of the iPP homopolymer $a = b = 16.05$ Å. These values would correspond to a theoretical density of crystals of the trigonal form of iPP of 0.865 g/cm^3, which is too low to allow crystallization of the trigonal form for the iPP homopolymer and is definitely lower than the crystalline density of 0.936 g/cm^3 of the monoclinic crystals of α form,[21] in agreement with the arguments of ref 7 concerning the lack of fulfillment of crystallography rules in the case of iPP homopolymer.

The value of $a = b$ axes of the trigonal form approaches the value of the unit cell of iPB[8] ($a = b = 17.7$ Å) for pentene concentrations of about 50 mol % (for instance, for the iPPeA8 sample containing 45.5 mol % of pentene values of $a = b = 17.73$ Å have been found (Figure 2B and Table 2)) and for hexene concentration of 25−30 mol % (for instance, values of $a = b = 17.5$ Å have been found for a iPPHe sample containing 26 mol % of hexene, Figure 2B).[4] In other words, when propene and pentene units are randomly blended along the same macromolecules and the average composition of the two comonomers approaches that of 1-butene (≈50% C_3H_6 + ≈50% C_5H_{10} = C_4H_8), copolymer chains behave as poly(butene) macromolecules and crystallize into the stable form I of iPB.[3−5]

It is worth noting that the lattice expansion is not necessarily an indication of inclusion of pentene unit in the crystals, but it could also be caused by strains at interface of thin crystallites due to segregation of comonomeric units in this region.[22] However, data of crystal density reported below are not in contrast with the hypothesis of inclusion (at least in part) of pentene in the crystals of both α and trigonal form.

The X-ray diffraction profiles of melt-crystallized compression-molded samples of some iPPe copolymers obtained by cooling from the melt to room temperature are reported in Figure 3. The diffraction profiles have been recorded soon after the preparation of the samples, without aging at room temperature. It is apparent that the copolymers with concentration of pentene up to 10 mol % crystallize in the α form of iPP as indicated by the presence of 110, 040, and 130 reflections of α form in the diffraction profiles a−c of Figure 3. The iPPe copolymers with pentene concentrations in the range 10−25 mol % seem to crystallize from the melt directly in the trigonal form (profiles d−f of Figure 3) and iPPe copolymers with concentrations of pentene higher than 25 mol % do not

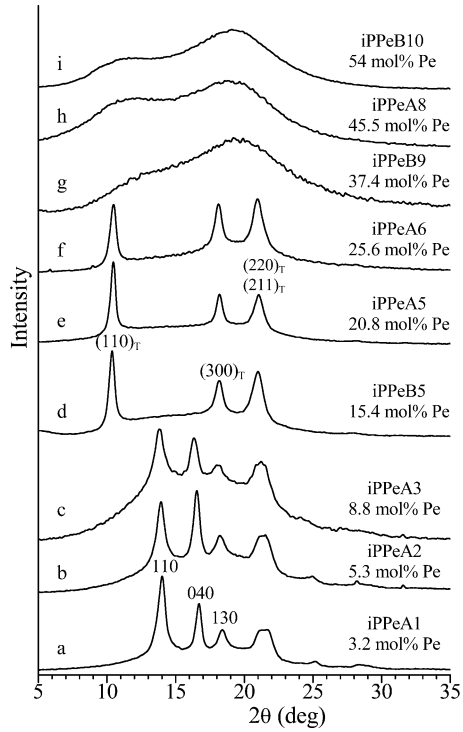


Figure 3. X-ray diffraction profiles of melt-crystallized samples of iPPe copolymers obtained by compression molding and cooling the melt to room temperature. The patterns have been recorded soon after the preparation of the samples, without aging at room temperature. The 110, 040, and 130 reflections of the α form of iPP and the $(110)_T$, $(300)_T$, and $(220)_T + (211)_T$ reflections of the trigonal form of iPP are indicated.

crystallize and amorphous samples are obtained by cooling the melt to room temperature (profiles g−i of Figure 3). These samples slowly crystallize in the trigonal form of iPP upon aging at room temperature, and the aging time necessary to allow complete crystallization of the sample increases with increasing the pentene concentration, from a few hours for the sample iPPeB9 with 37.4 mol % of pentene to several days for the sample iPPeB10 with the highest pentene concentration (54 mol %).

The X-ray diffraction profiles of the samples iPPeB9 and iPPeA8, with 37.4 and 45.5 mol % concentration of pentene, respectively, obtained by cooling from the melt and aged at room temperature for different times are reported in Figure 4, as an example. The degrees of crystallinity of the samples iPPeB9 and iPPeA8 are reported as a function of the aging time at room temperature in Figure 5.

It is apparent that for these samples the crystallization of the trigonal form at room temperature starts after 2−3 h (Figure 5). The aging time at room temperature necessary for allowing the complete crystallization of the sample in the trigonal form increases and the maximum achieved crystallinity decreases with increasing the pentene concentration (Figure 5).

The DSC thermograms recorded at the scanning rate of 10 °C/min of the as-polymerized and aged samples of some iPPe copolymers, composed of the first heating scans (curves a), the cooling scans from the melt (curves b), and the successive heating scans (curves c), are reported in Figure 6.

The samples with pentene content up to nearly 10 mol % show exothermic peaks in the cooling scans due to the crystallization from the melt of the α form of iPP (see curves b

dx.doi.org/10.1021/ma201849w | Macromolecules 2012, 45, 2749−2763

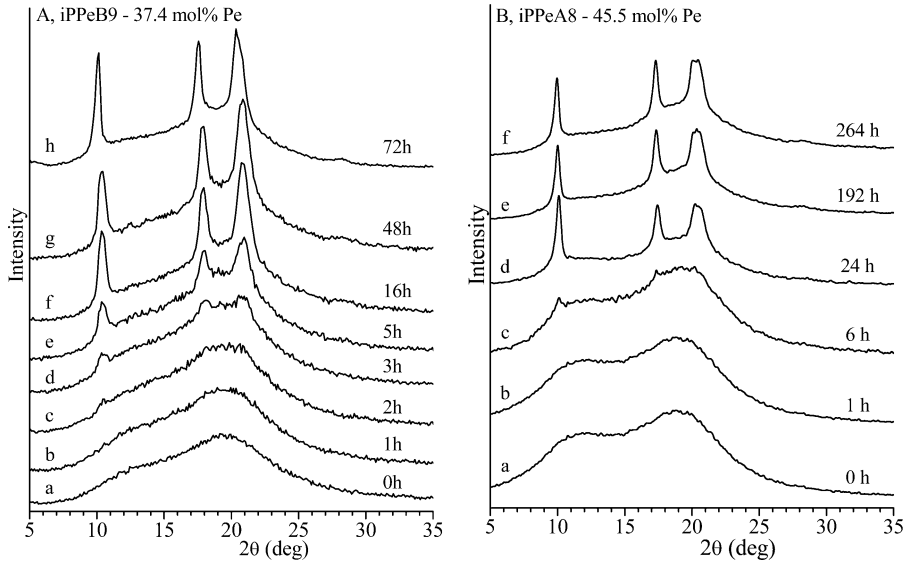


Figure 4. X-ray diffraction profiles of the samples iPPeB9 with 37.4 mol % of pentene (A) and iPPeA8 with 45.5 mol % of pentene (B) obtained by compression molding and cooling the melt to room temperature and aged at room temperature for the indicated times.

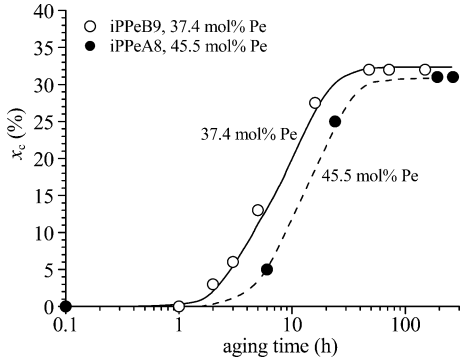


Figure 5. Degree of crystallinity of the samples iPPeB9 with 37.4 mol % of pentene (○) and iPPeA8 with 45.5 mol % of pentene (●) cooled from the melt to room temperature and aged at room temperature as a function of aging time.

of Figure 6A,B and curves a−c of Figure 3). For the iPPe copolymer samples with pentene content in the range 10−25 mol %, while the data of Figure 3 suggest a direct crystallization of the trigonal form from the melt (profiles d−f of Figure 3), the DSC of Figure 6C−E of the samples iPPeB4, iPPeA5, and iPPeA6 with 10.9, 20.8, and 25.6 mol % of pentene, respectively, clearly indicate that these sample do not crystallize during the cooling from the melt at 10 °C/min (curves b of Figure 6C−E), but they crystallize from the amorphous by cold-crystallization at 11−30 °C during the successive heating (curves c of Figure 6C−E), directly in the trigonal form (curves d−f of Figure 3). The cold-crystallization temperature increases with increasing pentene concentrations (Figure 6C−E).

The iPPe copolymer samples with pentene concentrations higher than 25 mol % do not crystallize by cooling from the melt, and no cold-crystallization of the amorphous occurs during the successive heating, at least at a scanning rate of 10 °C/min (see curves b and c of Figure 6F and curves g−i of Figure 3). These samples slowly crystallize in the trigonal form of iPP by aging at room temperature for several hours (Figures 4 and 5).

The data of Figures 3−6 indicate that in iPPe copolymers the new trigonal form does not crystallize by cooling from the melt (at least at a cooling rate of 10 °C/min) but crystallizes from the amorphous samples at room temperature and the crystallization rate decreases with increasing pentene concentration. This result is in agreement with data of ref 6, which showed that the copolymers with only trigonal form can be isothermally crystallized from the melt at around room temperature, although the crystallization rate is rather slow and decreases with increasing the pentene content.

The DSC data of Figure 6B−F also show a glass transition temperature for the iPPe copolymers of nearly −20 °C.

It is worth recalling that also in the case of iPPHe copolymers with hexene content higher than 10 mol % the trigonal form does not crystallize from the melt but slowly crystallizes by aging amorphous samples at room temperature for about 24 h.[4]

The values of melting temperature, corresponding to the endothermic peaks of the DSC curves a and c of Figure 6, and of degree of crystallinity, evaluated from the X-ray diffraction profiles of Figures 1 and 3, of as-prepared and aged samples and of melt crystallized samples of iPPe copolymers, are reported in Figure 7 as a function of pentene concentration. In the case of the copolymers iPPeB8−iPPeB10 and iPPeA8, which are amorphous after cooling from the melt to room temperature (Figure 3), the degrees of crystallinity of melt-crystallized samples have been determined on samples aged at room temperature up to complete crystallization.

It is worth noting that the samples having pentene content around 9 mol %, which are crystallized in mixtures of the α and trigonal forms (Figure 1) show broad melting endotherm with multiple peaks in the first heating curves of the as-prepared samples, due probably to the melting of crystals of the two forms (see for instance curve a of Figure 6B). However, for these compositions the melting temperature of crystals of α form is low and approaches that of the trigonal form (60−70 °C). Therefore, the melting of the crystals of the two modifications occurs quite simultaneously or belongs to the same broad endotherm. For these copolymers only the value of temperature corresponding to the most intense endothermic peak is reported in Figure7 and in Table 1.

dx.doi.org/10.1021/ma201849w | *Macromolecules* 2012, 45, 2749−2763

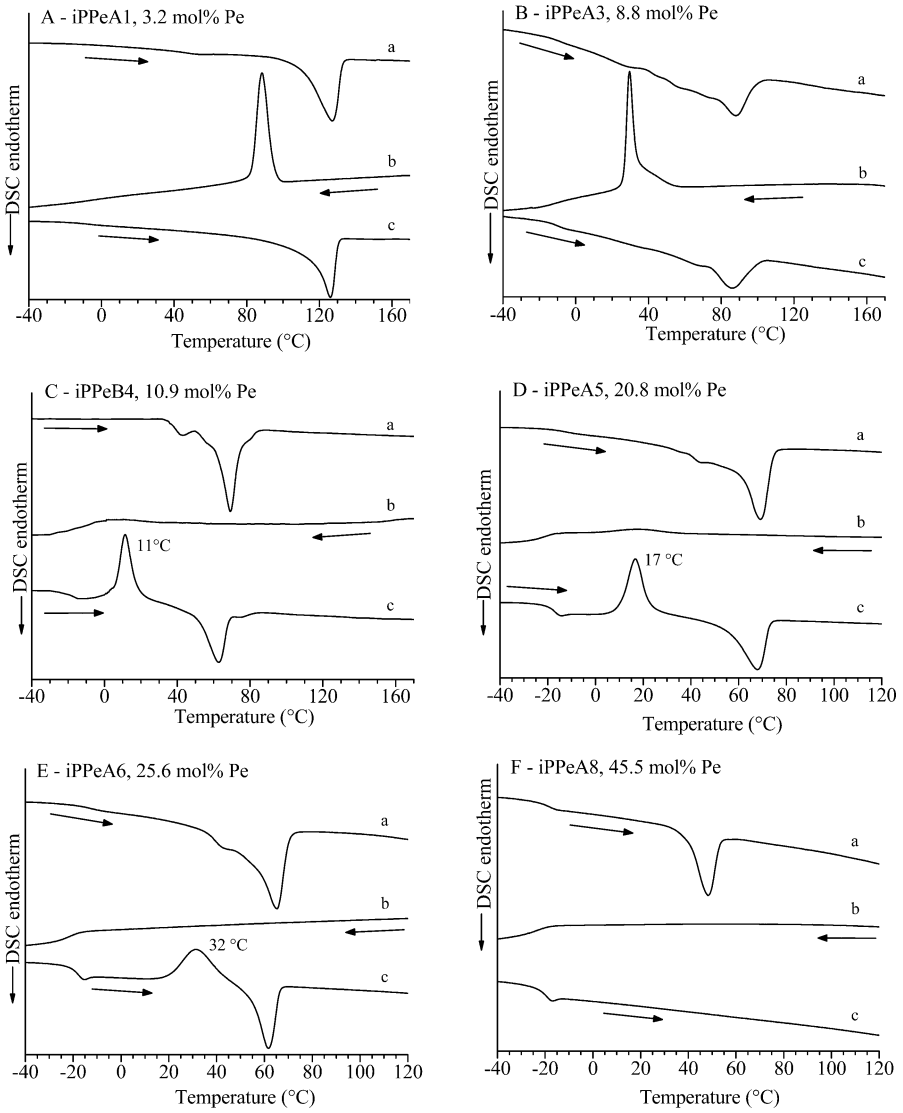


Figure 6. DSC thermograms of samples of iPPe copolymers of the indicated pentene concentrations recorded at scanning rate of 10 °C/min: (a) first heating curves of as prepared and aged samples, (b) cooling curves from the melt, and (c) successive heating curves.

It is apparent that the melting temperature and the crystallinity decrease with increasing the pentene concentration. In particular, the decrease of melting temperature and of crystallinity is fast up to nearly 10 mol % of pentene for the iPPe copolymers that crystallize in the α form and then becomes slower for copolymers with higher pentene concentration that crystallize in the trigonal form (Figure 7). This crossover reflects the fact that at low pentene concentrations pentene units are not easily included in the crystals of α form since they act as a lattice defect, producing large disturbance of the crystalline lattice and a consequent fast decrease of melting and crystallization temperature and crystallinity (Figure 7). For concentrations higher than 10 mol %, a larger number of pentene units are more easily accommodated in the crystalline lattice of the trigonal form, producing a lower decrease of crystallinity and melting temperature (Figure 7).

The possible inclusion/exclusion of pentene units in the crystals of α and trigonal form of iPP has been also analyzed by measurements of density, determined by flotation on melt-crystallized compression molded films of the iPPe copolymers, aged at room temperature up to complete crystallization. The experimental values of density (ρ_{sp}) of iPPe samples are reported in Figure 8A as a function of pentene concentration. The density decreases with increasing pentene concentration, according to the decrease of crystallinity (Figure 7B). A fast decrease is observed for pentene concentrations lower than 10 mol %, whereas for pentene contents higher than 10 mol %, when the trigonal form crystallizes, the density increases and keeps basically constant in the range of 10−45 mol % of pentene and then, finally, slightly decreases for higher pentene concentration.

The values of density of the crystalline phase of the iPPe copolymers (ρ_c), determined from the values of experimental density (ρ_{sp}), the degree of crystallinity and the values of density of amorphous phase (ρ_a), are reported in Figure 8B. The density of the amorphous phase of the iPPe samples with pentene content lower than 10 mol %, which crystallize in the α form of iPP (Figure 3), has been assumed equal to the density of amorphous iPP[23] (ρ_a = 0.854 g/cm^3). The density of the amorphous phase of the iPPe copolymers with higher pentene concentration, which crystallize in the trigonal form of iPP (Figures 3 and 4), instead, has been assumed equal to that of

dx.doi.org/10.1021/ma201849w | *Macromolecules* 2012, 45, 2749−2763

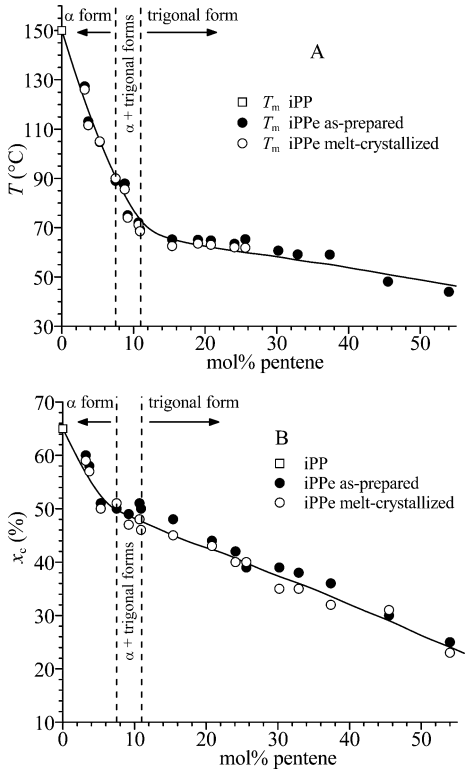


Figure 7. Melting temperatures (A) and degree of crystallinity (B) of as prepared (●) and melt crystallized (○) samples of iPPe copolymers. The melting temperature and the degree of crystallinity of the iPP homopolymer sample obtained with the same catalyst is also reported (□). In (B) the degrees of crystallinity of melt-crystallized samples correspond to those of compression-molded films. For the copolymers iPPeB8−iPPeB10 and iPPeA8 with pentene concentration higher than 30 mol %, which are amorphous after cooling from the melt to room temperature, the degrees of crystallinity of melt-crystallized samples correspond to those of samples aged at room temperature up to complete crystallization.

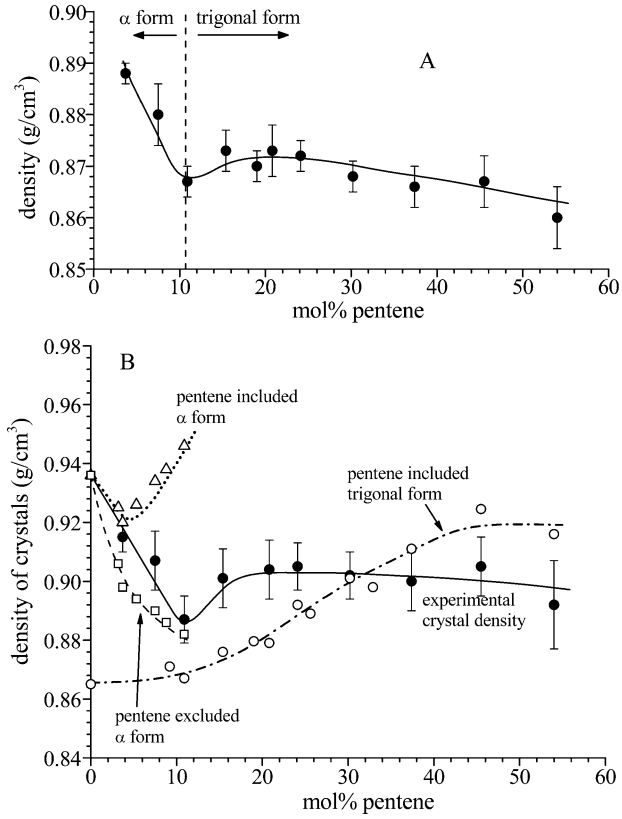


Figure 8. Values of experimental density (●, A) and density of the crystalline phase (●, B) of the iPPe copolymers as a function of pentene concentration. In (B) the experimental densities of crystals of iPPe copolymers (●) are compared with the theoretical densities of crystals of the α form calculated assuming complete inclusion of pentene units in the crystals (△, dotted line), or complete exclusion of pentene units from the crystals (□, dashed line), and volumes of the unit cell calculated from the unit cell parameters of Table 2. The experimental crystalline densities are also compared with the theoretical densities of crystals of the trigonal form (○, dotted-dashed line) calculated assuming complete inclusion of pentene units in the crystals and volumes of the unit cell calculated from the unit cell parameters of Table 2. Error bars in the values of crystalline density in (B) account for the errors in the experimental values of density, crystallinity, and density of amorphous phase.

the amorphous phase of the sample iPPeA8 with pentene content of 45.5 mol % (ρ_a = 0.851 g/cm^3). This latter value has been determined by flotation of amorphous compression-molded film of the sample iPPeA8, before the crystallization of the sample by aging at room temperature.

The trend of the values of the density of crystals of iPPe copolymers is similar to that of the experimental density of the semicrystalline samples. For copolymers with pentene content up to nearly 10 mol % that crystallize in the α form of iPP, the experimental density of the crystals of α form decreases with increasing pentene concentration (Figure 8B). This indicates that for this range of pentene content, in the hypothesis of inclusion of pentene units in the crystals of α form, the expansion of unit cell volume, due to this inclusion, is not compensated by increase of mass because pentene units are excluded or not completely included in the crystals of α form. This is confirmed in Figure 8B by comparing the experimental crystalline density with the theoretical density of α form crystals, calculated assuming complete inclusion of pentene units in the crystals and values of unit cell volume calculated from the experimental values of axes of unit cells of Table 2. It is apparent that for samples with pentene contents higher than 3−4 mol % and lower than 10 mol % the values of the calculated crystalline density are higher than the experimental ones, indicating that for these samples the pentene units are either excluded from crystals or included in the crystals of α form only in part. Only for pentene content lower than 2 mol %, the calculated and experimental crystalline densities are similar, indicating that at these low concentrations inclusion of pentene in the crystals of α form is feasible (Figure 8B).

On the other hand, as discussed above, the lattice expansion is not necessarily an indication of inclusion of pentene unit in the crystals, but it could also be caused by strains at interface of thin crystallites due to segregation of comonomeric units in this region.[22] In the hypothesis that the expansion of the unit cell axes observed in iPPe copolymers is not due to inclusion of the comonomer units in the crystals, the density of α form crystals calculated assuming exclusion of pentene units from the crystals would be not constant with composition at the value ρ_c = 0.936 g/cm^3, corresponding to the density of crystals of α form of iPP. The values of the theoretical density of α form crystals, calculated assuming exclusion of pentene units from the crystals and values of unit cell volume calculated from the experimental values of axes of unit cells of Table 2, are reported in Figure 8B. It is apparent that these values are always lower than the

dx.doi.org/10.1021/ma201849w | Macromolecules 2012, 45, 2749−2763

experimental values of crystalline density, indicating that the expansion of the unit cell volume is a result of inclusion, at least in part, of the pentene units in the crystals of α form.

For iPPe samples with pentene concentrations higher than 10 mol % that crystallize in the trigonal form, the experimental crystalline density increases and remains constant up to pentene concentration of 50 mol %. The values of theoretical density of crystals of the trigonal form, calculated from the experimental values of axes of the trigonal unit cell of Table 2 and assuming complete inclusion of pentene units in the crystals of the trigonal form, are very similar to the experimental values of crystalline density. However, for samples that crystallize basically into the trigonal form, the calculated densities are ≈2−3% lower than the experimental ones for copolymers with pentene contents in the range 10−30 mol %; they closely match the experimental values for pentene content around 30 mol % and become ≈2−3% higher for pentene concentrations in the range 40−55 mol %. This discrepancy may be due either to small uncertainty in the experimental values of density and/or unit cell parameters and crystallinity or also to nonuniform inclusion of pentene units in the crystals and amorphous phase. For example, in the case of the sample iPPeB5 with 15.4 mol % of pentene content, inclusion of 15.4 mol % of pentene units inside the crystals of the trigonal form produces a theoretical crystal density of 0.876 g/cm^3, which is ≈3% lower than the experimental value of 0.901 g/cm^3 of the crystalline density. This experimental value could be explained by assuming inclusion of higher amount of pentene units inside the crystals, that is, about 20 mol %. In this hypothesis the content of pentene units in the constitutional sequences able to crystallize into the trigonal form of iPP would be slightly higher than the average composition of the copolymer, whereas the constitutional sequences with pentene content lower than 20 mol % would be rejected into the amorphous phase. In any case the density data indicate that the crystallization of the new form allows much higher incorporation of pentene units in the crystals, and a density of crystals as high as 0.91 g/cm^3 is achieved for high pentene concentration. This is the key for the crystallization of the trigonal form and demonstrates the principle of density-driven phase formation in polymers.[3]

Fibers, Single Crystals, and Crystal Structure of the Trigonal Form. A preliminary model of the crystal structure of the trigonal form of iPP that crystallizes in iPPe copolymers, based only on data of X-ray powder diffraction profiles, has been proposed in ref 5. Here we report additional diffraction data from oriented fibers and electron diffraction of single crystals.

Oriented fibers of the trigonal form have been obtained by stretching at room temperature a compression-molded film of the sample iPPeA5 with 20.8 mol % of pentene concentration, which crystallizes in as-prepared and melt-crystallized samples in the trigonal form (Figures 1 and 3). The X-ray fiber diffraction pattern and the corresponding profile read along the equator of a fiber of the sample iPPeA5 stretched at 600% of deformation and annealed at 70 °C for 30 min are reported in Figure 9. The result that annealing improves the crystals and the corresponding diffraction pattern of the trigonal form, and no transformation into the α form is observed, indicates that the trigonal form is more stable than the α form in the stretched fibers of iPPe copolymers with high pentene concentration.

The fiber diffraction pattern of Figure 9A shows three strong reflections at 2θ = 10.4°, 17.9°, and 20.64° on the equatorial

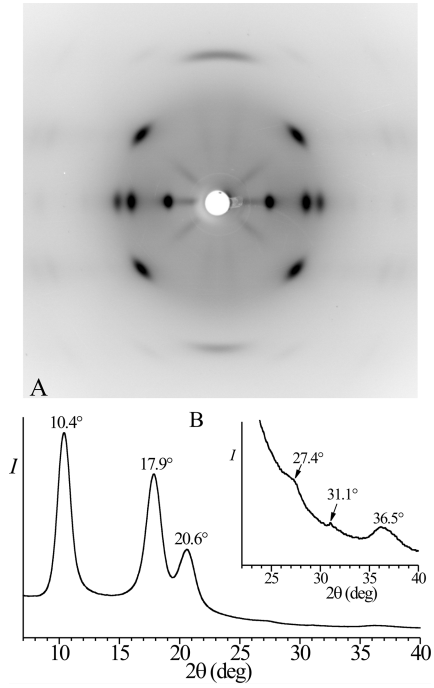


Figure 9. X-ray fiber diffraction pattern (A) and the corresponding intensity profile read along the equator (B) of an oriented fiber of the sample iPPeA5 with 20.8 mol % of pentene units stretched at room temperature up to 600% deformation and annealed at 70 °C for 30 min.

line (Figure 9B) and a strong reflection on the first layer line at 2θ = 20.8°. These reflections correspond to the $(110)_T$, $(300)_T$, and $(220)_T$ + $(211)_T$ reflections of the trigonal form observed at 2θ = 10.4°, 18.1°, and 21° in the powder diffraction profile of the compression-molded film (profile e of Figure 3). The chain axis periodicity evaluated from the X-ray fiber diffraction pattern of Figure 9A is c = 6.5 Å, indicating that the copolymer chains preserve the stable 3_1 helical conformation typical of the crystalline forms of iPP.

The experimental diffraction angles (2θ), Bragg distances (d_0), and intensities (I_0) of the reflections observed in the X-ray fiber diffraction pattern of Figure 9A of the sample iPPeA5 are listed in Table 3. It is apparent that, compared to the powder diffraction profile (profile e of Figure 3), in the fiber pattern a much higher number of reflections can be observed. This allows finding a more reliable model of the crystal structure of the trigonal form.

All reflections observed in the pattern of Figure 9A are accounted for by a trigonal unit cell with axes a = b = 17.0 Å and c = 6.5 Å, in agreement with the data obtained from the powder diffraction profiles of Table 2. The unit cell contains six copolymer chains in the 3_1 helical conformation packed according to a rhombohedral symmetry, according to the space group $R3c$. Assuming that all the pentene units of the iPPeA5 copolymer are included in the unit cell, the theoretical density of crystals of the trigonal form is 0.88 g/cm^3, in agreement with the experimental density of the crystalline phase of 0.90 g/cm^3 of the sample iPPeA5 with 20.8 mol % of pentene (Figure 8B).

Single crystals of pseudohexagonal shape of the trigonal form have been obtained from dilute solution of the sample iPPeB7 with 24.1 mol % of pentene. The selected area electron diffraction pattern of these single crystals of the trigonal form is

Table 3. Diffraction Angles (2θ), Bragg Distances (d_0), and Intensities (I_0) of the Reflections Observed in the X-ray Fiber Diffraction Pattern of Figure 9A of the Sample iPPeA5 Containing 20.8 mol % of Pentene and in the Electron Diffraction Pattern of Figure 10 of Single Crystals of the Sample iPPeB7 with 24.1 mol % of Pentene

X-ray fiber diffraction sample iPPeA5, 20.8 mol % Pe				electron diffraction of single crystals sample iPPeB7, 24.1 mol % Pe		
hkl[a]	2θ (deg)	d_0 (Å)	I_0	hkl[a]	2θ (deg)	d_0 (Å)
110	10.40	8.50	434	110	10.37	8.53
300	17.90	4.95	488	300	17.96	4.94
220	20.64	4.30	202	220	20.56	4.32
410	27.39	3.25	9			
330	31.10	2.87	4			
600	36.46	2.46	13			
211	20.88	4.25	460			
$31\bar{1}$	25.60	3.48	3			
321	29.61	3.02	5			
511	36.33	2.47	15			
431	39.26	2.30	7			
$10\bar{2}$	28.16	3.17	n.e.[b]			
$21\bar{2}$	31.70	2.82	4			
502	41.34	2.18	1			

[a]For the fiber pattern of the sample iPPeA5 with 20.8 mol % of pentene, the Miller indices hkl of the reflections are based on the trigonal unit cell with axes $a = b = 17.0$ Å and $c = 6.5$ Å, whereas for the electron diffraction of the sample iPPeB7 with 24.1 mol % of pentene the observed Bragg distances are consistent with a unit cell with axes $a = b = 17.06$ Å, $c = 6.5$ Å, in agreement with the data obtained from the powder diffraction profiles of Table 2. [b]The intensity of the $10\bar{2}$ nearly meridional reflection has not been evaluated (n.e.).

shown in Figure 10 and clearly indicates a hexagonal symmetry of the a^*b^* reciprocal lattice with a rhombohedral unit cell.

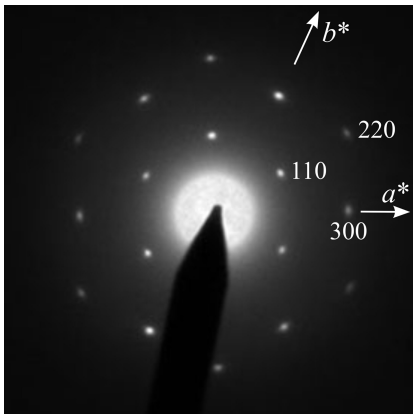


Figure 10. Selected area electron diffraction pattern of single crystals of the trigonal form of the sample iPPeB7 with 24.1 mol % of pentene.

The equatorial reflections observed in the electron diffraction pattern of Figure 10 and the corresponding Bragg distances are reported in Table 3.

The electron diffraction pattern gives a direct image of the a^*b^* reciprocal lattice of the trigonal form and confirms the trigonal unit cell already proposed for iPPHe copolymers in refs 3 and 4 and also found for iPPe copolymers. The equatorial 110, 300 and 220 reflections at Bragg distances of 8.53, 4.94, and 4.32 Å, respectively, in the electron diffraction pattern of Figure 10 (Table 3) are accounted for by the trigonal unit cell with axes $a = b = 17.06$ Å for the sample iPPeB7 with 24.1 mol % of pentene, in agreement with the values of Table 2 and Figure 2 obtained from the X-ray powder diffraction profiles. In the assumption that all the pentene units of the sample iPPeB7 are included in the unit cell with $a = b = 17.06$ Å, the theoretical density of crystals of the trigonal form for the sample iPPeB7 is 0.89 g/cm^3, in agreement with the density of the crystalline phase of 0.90 g/cm^3 (Figure 8B).

A model of packing for the crystal structure of the trigonal form of the iPPe copolymer according to the space group $R3c$ is shown in Figure 11. The 3_1 helical symmetry of the chains is

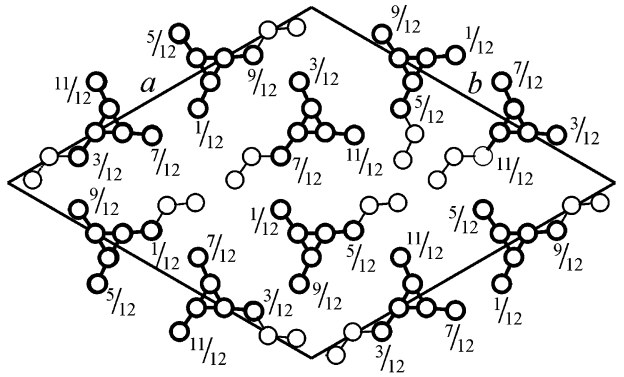


Figure 11. Model of the crystal structure of the trigonal form of iPP in the space groups $R3c$ for iPPe copolymers. Chains of iPPe copolymer with 20.8 mol % of pentene units in 3/1 helical conformation are packed in the trigonal unit cell with $a = b = 17.0$ Å and $c = 6.5$ Å. The atoms of final ethyl residue in the pentene branch, randomly distributed along each iPP chain, are shown as thin lines. The height of the propylene methyl groups are indicated in $c/12$ units ($c = 6.5$ Å).

maintained in the lattice, and the chain axes coincide with the crystallographic 3-fold axes. The structure contains high degree of disorder due to the constitutional disorder of the random copolymers chains that produces disorder in the positioning of the ethyl lateral groups in the unit cell.

The orientations of the chains around the 3-fold axes have been found by packing energy calculations and by comparison between calculated and experimental diffraction patterns. Because of the disorder in the positioning of pentene units inside the unit cell, a disorder in the orientation of chains around the chain axes may also be present. In fact, each chain containing 20 mol % of pentene units randomly distributed along the chain bears on average one pentene unit in a turn of the helix included in the chain axis (as in the model of Figure 11). Therefore, the lowest energy packing is probably achieved for slightly different orientations of the six chains included in the unit cell. In the model of Figure 11 only one of the possible low-energy positions of the final ethyl pendant groups of the pentene units is shown. We have checked that the azimuthal setting of the chains around the chain axes and the position of the pendant side groups of pentene units shown in Figure 11 comply with acceptable interatomic distances, which are higher than the sum of van der Waals radii of interacting species.

A good agreement between calculated structure factors and experimental intensities of reflections observed in the fiber diffraction pattern has been obtained introducing slight rotational disorder, corresponding to rotations of the chains of about ±12° around the chain axes with respect to the

dx.doi.org/10.1021/ma201849w | Macromolecules 2012, 45, 2749–2763

Table 4. Comparison between Observed Structure Factors (F_o) Determined from the Intensities Observed in the X-ray Diffraction Fiber Diffraction Pattern of the sample iPPeA5 with 20.8 mol % of Pentene of Figure 9 and Calculated Structure Factors (F_c) for the Model of Packing of the Trigonal Form of Figure 11 in the Space Group *R*3*c*, for the Same Model in the Presence of Disorder in the Orientation of the Chains around the Chain Axes (Corresponding to Slight Rotation of about ±12° with Respect to the Model of Figure 11) and for the Limit Disordered Model of Figure 12 in the Statistical Space Group $R\bar{3}c$[a]

						$F_c = (\|F_{hkl}\|^2 M_{hkl})^{1/2}$		
hkl	$2\theta_o$ (deg)	$2\theta_c$ (deg)	d_0 (Å)	d_c (Å)	F_0	*R*3*c*	*R*3*c* (rot. disorder)	$R\bar{3}c$ (rot. and up/down disorder)
110	10.40	10.41	8.50	8.500	146	136	147	147
300	17.90	18.08	4.95	4.907	204	216	202	197
220	20.64	20.90	4.30	4.250	142	138	133	133
410	27.39	27.77	3.25	3.212	34	21	32	16
330	31.10	31.58	2.87	2.833	24	47	50	50
600	36.46[b]	36.62	2.46[b]	2.454	50	55	43	38
520		38.17		2.357		85	67	64
211	20.88	21.02	4.25	4.227	188	153	143	111
$31\bar{1}$	25.60	25.77	3.48	3.458	18	70	64	20
321	29.61	29.81	3.02	2.997	26	40	52	36
$42\bar{1}$		35.08		2.56		19	32	13
511	36.33	36.69	2.47	2.449	51	113	92	10
431	39.26	39.74	2.30	2.268	25	7	10	10
$10\bar{2}$	28.16	28.12	3.17	3.174	n.e.[c]	78	75	74
202		30.06		2.973		32	31	10
$21\bar{2}$	31.70	31.89	2.82	2.806	17	35	36	28
312		35.30		2.543		12	4	-
$40\bar{2}$		36.90		2.436		30	20	20
$32\bar{2}$		38.44		2.342		5	4	4
502	41.34	41.38	2.18	2.182	13	41	32	31

[a]The Bragg angles and Bragg distances ($2\theta_o$ and d_0) observed in the X-ray fiber diffraction pattern of the sample iPPeA5 of Figure 9 and those calculated ($2\theta_c$ and d_c) for the trigonal unit cell with axes $a = b = 17.0$ Å and $c = 6.5$ Å are reported. [b]This reflection is very broad and spans from $2\theta = 35.7°$ to $2\theta = 37.2°$. [c]The intensity of the near meridional reflection $10\bar{2}$ has not been evaluated (n.e.).

average positions of chains shown in the model of Figure 11. We have checked that these small rotations do not produce too short interatomic distances, provided that the positions of the long side groups of pentene units of first neighboring chain do not overlap. A comparison between observed structure factors, evaluated form the intensities observed in the X-ray fiber diffraction pattern of the sample iPPeA5 containing 20.8 mol % of pentene units of Figure 9 (Table 3) and the structure factors calculated for the model of Figure 11 with axes $a = b = 17.0$ Å and $c = 6.5$ Å, in the space group *R*3*c*, and for a disordered model containing a slight disorder in the orientation of chains around the chain axes, corresponding to rotations of ±12° around the chain axes with respect to the average position of the model of Figure 11, is reported in Table 4.

It is apparent that the introduction of rotational disorder gives a better agreement between observed and calculated structure factors. In fact, the structure factor of the 110 reflection increases, whereas those of the 300, 600, 520, $31\bar{1}$, and 511 decrease by introducing rotational disorder in agreement with the experimental structure factors (Table 4). However, the calculated structure factors of the $31\bar{1}$, 321, $42\bar{1}$, 511, 202, and $21\bar{2}$ reflections are still too high with respect to the experimental ones (Table 4). The agreement between observed and calculated structure factors can be slightly improved by introducing another kind of disorder in addition to the rotational disorder, consisting in disorder in the up/down position of the helical chains. This means that up or down chains having the same chirality can be found with the same probability in each site of the lattice. It is worth noting that this kind of disorder, which normally affects the crystal structure of isotactic polymers and, in particular iPB in the form I,[8] would be at low or no cost of packing energy, provided that isomorphic, anticlined helices of iPPe copolymers substituting each other in the same site of the lattice maintain the same steric interactions with neighboring chains. A limit disordered model containing statistical up/down disorder that can be represented by the statistical space group $R\bar{3}c$ is shown in Figure 12. The calculated structure factors for the limit disordered model of Figure 12 with axes $a = b = 17.0$ Å and $c = 6.5$ Å, in the space group $R\bar{3}c$, containing both rotational

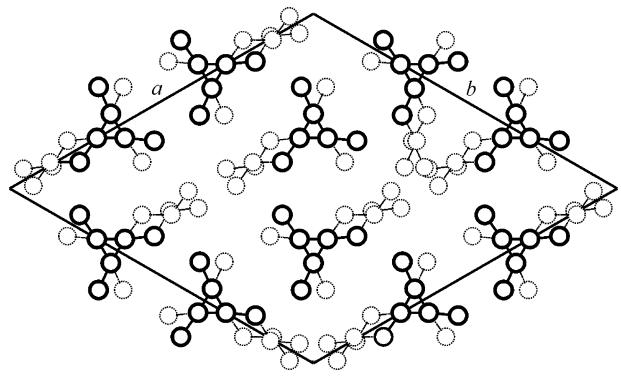


Figure 12. Limit disordered model of the crystal structure of the trigonal form of iPP for iPPe copolymers in the statistical space group $R\bar{3}c$. The structure contains disorder in the positioning of up and down chains in each site of the lattice. Two anticlined chains (up and down) having the same chirality that occupy the same lattice site are indicated with thick and thin dotted lines. The atoms of final ethyl residue in the pentene branch, randomly distributed along each iPP chain, are shown as thin-dotted lines.

dx.doi.org/10.1021/ma201849w | *Macromolecules* 2012, 45, 2749–2763

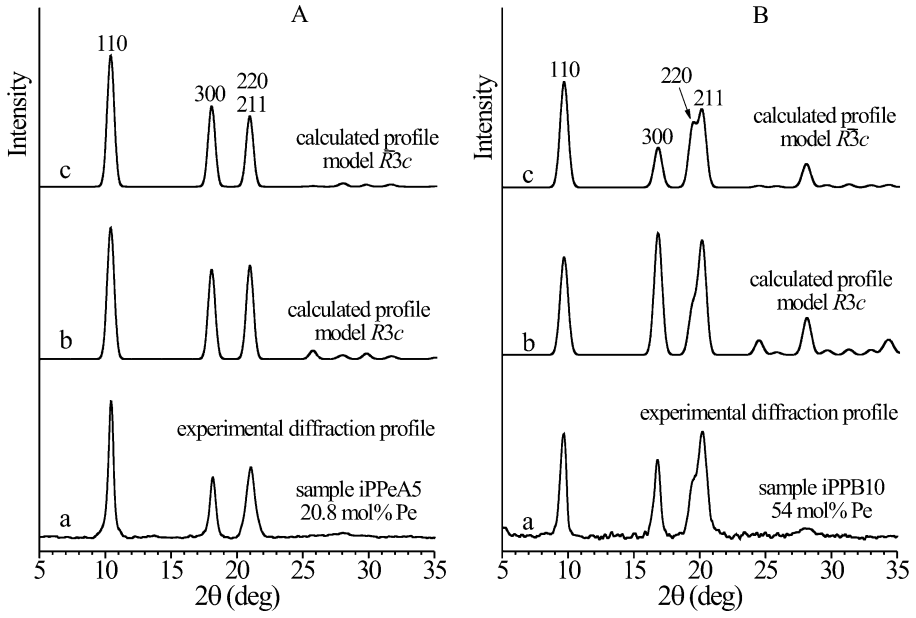


Figure 13. Comparison between the experimental X-ray powder diffraction profiles of the samples iPPeA5 with 20.8 mol % of pentene (A) and iPPeB10 with 54 mol % of pentene (B), after subtraction of the amorphous halo (curves a) and the calculated X-ray powder diffraction profiles for the model of crystal structure of Figure 11 in the space group *R*3*c* (curves b), and for the limit disordered model of Figure 12 containing up−down disorder corresponding to the statistical space group $R\bar{3}c$ (curves c). The dimensions of the axes of the trigonal unit cell vary according to the concentrations of pentene units included in the crystals and have been assumed as those reported in Table 2. Both models *R*3*c* and $R\bar{3}c$ present disorder in the orientation of the chains around the chain axes corresponding to rotations of chains of ±12° (A) and ±20° (B) with respect to the average position of the chains shown in the model of Figure 11.

and up/down disorder of the chains are compared with the experimental structure factors in Table 4. It is apparent from the data of Table 4 that the calculated structure factors of $31\bar{1}$, 321, $42\bar{1}$, 511, 202, and $21\bar{2}$ reflections decrease for the limit disordered model of Figure 12 in the space group $R\bar{3}c$, and a slight better agreement with the experimental structure factors is achieved.

A comparison between the experimental X-ray powder diffraction profiles of the trigonal form of the iPPeA5 sample with 20.8 mol % of pentene, after subtraction of the amorphous halo, and the powder profiles calculated for the model of Figure 11 in the space group *R*3*c* (unit cell axes $a = b = 17.0$ Å and $c = 6.5$ Å) containing rotational disorder (corresponding to rotations of the chains of ±12° around their axes with respect to the average positions of the chains in the model of Figure 11), and for the limit disordered model of Figure 12 in the space group $R\bar{3}c$ containing rotational and statistical up/down disorder is shown in Figure 13A. A fairly good agreement is obtained for the statistical model $R\bar{3}c$, in particular for the high values of the Bragg angles.

A similar comparison between the experimental powder diffraction profile of the sample iPPeB10 having the highest concentration of pentene (54 mol %) and the diffraction profiles calculated for the models of Figures 11 and 12 in the presence of rotational disorder is also reported in Figure 13B. The trigonal form of the sample iPPeB10 with 54 mol % of pentene is characterized by a bigger trigonal unit cell with axes $a = b = 18.20$ Å and $c = 6.5$ Å (Figure 2B and Table 2) due to the larger amount of pentene units included in the crystals with respect that of the sample iPPeA5 containing 20.8 mol % of pentene. Assuming a complete inclusion of pentene units in the crystals, the theoretical density of crystals of the trigonal form for the sample iPPeB10 is 0.91 g/cm^3, in agreement with the density of the crystalline phase of 0.89 g/cm^3 (Figure 8B). A quite good agreement has been obtained for a model containing rotational disorder, corresponding to rotations of about ±20° of the chains around their axes with respect to the average positions of the chains in the model of Figure 11 (curve b of Figure 13B). Statistical disorder in the up/down position of the chains, corresponding to the limit disordered space group $R\bar{3}c$ of Figure 12, may be also present (curve c of Figure 13B).

The fractional coordinates of the asymmetric unit in the model of Figure 12 proposed for the crystal structure of the trigonal form of iPPe copolymers, in the statistical space group $R\bar{3}c$ and with unit cell parameters $a = b = 17.0$ Å, $c = 6.5$ Å, are reported in Table 5. The coordinates correspond to the average position of the chains as that shown in the model of Figure 12, and the occupancy factors of the C4 and C5 atoms belonging to the final ethyl group of pentene unit have been set according to the concentration of pentene included in the cell (20.8 mol % for the sample iPPeA5). The coordinates used in the

Table 5. Fractional Coordinates of the Carbon Atoms of the Asymmetric Unit in the Model of Figure 12 of the Crystal Structure of the Trigonal Form of iPPe Copolymers in the Statistical Space Group $R\bar{3}c$ and with Unit Cell Parameters $a = b = 17.0$ Å, $c = 6.5$ Å[a]

atom	*x*/*c*	*y*/*c*	*z*/*c*	occupancy factor
C1	0.289	0.289	−0.065	0.5
C2	0.289	0.289	0.170	0.5
C3	0.231	0.190	0.250	0.5
C4	0.132	0.139	0.170	0.104
C5	0.076	0.043	0.251	0.104

[a]The atoms C4−C5 correspond to the lateral ethyl group of the pentene unit included in the cell with a concentration of 20.8 mol %.

dx.doi.org/10.1021/ma201849w | *Macromolecules* 2012, 45, 2749−2763

calculations of Table 4 and Figure 13A corresponding to the disordered models that give the best agreement with the experimental data can be obtained by introducing disorder in the rotation of the chains of ±12° with respect to the average position of the chains in the model of Figure 12.

The data of Table 4 and Figure 13 indicate that the structure of the trigonal form obtained in iPPe copolymers present disorder in the orientation of the chains around their axes and also statistical disorder in the up/down position of the chains. The disorder originates by the constitutional disorder due to the presence of large amounts (20−54 mol %) of pentene units randomly distributed along the chains that produces disorder in the positioning of the lateral ethyl group in the unit cell. The comparison between the experimental and calculated X-ray powder diffraction profiles of Figure 13 indicates, indeed, that with increasing the content of pentene units included in the trigonal unit cell a larger amount of rotational disorder in the orientation of the chains is present in the structure. The real structure is probably intermediate between the model of Figure 11 in the space group $R3c$, containing rotational disorder, and the limit disordered model of Figure 12 in the statistical space group $R\bar{3}c$, containing also disorder in the up/down position of the chains. In fact, it is apparent from the data of Table 4 that the introduction of this kind of disorder reduces the calculated structure factors of $31\bar{1}$, 321, $42\bar{1}$, 202, and $21\bar{2}$ reflections, improving the agreement with the experimental structure factors, but the structure factors of the 410, 211, and 511 reflections calculated for the statistical limit disordered model $R\bar{3}c$ are too low with respect to the experimental ones. This is also evident from the comparison of Figure 13B which indicates that upon introduction of statistical up/down disorder the calculated intensities of the 300 and 211 reflections decrease with respect to those calculated for the model $R3c$, containing only rotational disorder, but are too low with respect to experimental intensities (Figure 13B).

■ CONCLUDING REMARKS

The structure of the trigonal form of iPP that crystallizes in random copolymers of iPP with pentene has been described. iPPe copolymers crystallize in the monoclinic α form of iPP for concentrations of pentene lower than 7−8 mol %. The crystallization of the trigonal form occurs when the concentration of pentene units approaches 10−11 mol %.

X-ray diffraction analysis and density measurements have demonstrated that pentene units are included in the crystals of the trigonal form, and at low concentration, up to ≈2 mol % also in the crystals of α form. The crystallization of the trigonal form at pentene concentration higher that 10−11 mol % allows inclusion of larger amount of pentene in the crystals than that included in the crystals of the α form. The dimensions of unit cell axes of the trigonal form increase in the whole range of composition considered up to 54 mol % of pentene, indicating that large amounts of pentene units are well incorporated in the crystals of the new trigonal form. A comparison between the unit cell dimensions of the trigonal form found in propene−hexene and propene−pentene copolymers has shown that at a given molar composition the values of $a = b$ axes of the trigonal unit cell are larger for the iPPHe copolymers than for those of iPPe copolymers according to the hypothesis of inclusion of comonomeric units into the crystal lattice. However, the values of unit cell axes of the trigonal form are fitted by a single master line if the data are reported as a function of wt % of hexene or pentene units. Therefore, at the same mass comonomer composition the dimensions of the trigonal unit cell are the same for pentene or hexene comonomers. This confirms that the crystallization of the trigonal form and the unit cell dimensions are only driven by the density. When the crystal density is sufficiently high (ca. 0.89 g/cm^3), at around 10 mol % of hexene or pentene, the trigonal form can crystallize.

The melting temperature and crystallinity of iPPe copolymers rapidly decrease with increasing the pentene concentration up to nearly 10−11 mol %. For pentene concentrations higher than 10−11 mol %, larger amount of pentene units are more easily accommodated in the crystalline lattice of the trigonal form, producing a lower decrease of crystallinity and melting temperature.

The thermal analysis has also shown that the trigonal form of the iPPe copolymers does not crystallize by cooling from the melt but crystallizes from the amorphous by cold-crystallization or for samples with high pentene concentration by aging the amorphous samples at room temperature.

The crystal structure of the trigonal form of iPPe copolymers has been also studied, through the analysis of the X-ray powder and fiber diffraction patterns and electron diffraction of single crystals of iPPe samples with pentene concentrations of 20−54 mol %, and calculations of structure factors for various structural models. The chains of iPPe copolymers preserve the 3-fold helical conformation and are packed in a trigonal unit cell according the space group $R3c$ or $R\bar{3}c$. The dimensions of the axes of the trigonal unit cell increase with increasing the concentration of pentene units in the copolymer. For instance, values of $a = b = 17.0$ Å and $c = 6.5$ Å for the iPPe copolymer with 20.8 mol % of pentene up to values of $a = b = 18.20$ Å and $c = 6.5$ Å for the iPPe copolymer with 54 mol % of pentene have been found. The structure contains a high degree of disorder, due to the constitutional disorder of the random copolymer chains that produces disorder in the positioning of the ethyl lateral groups in the unit cell. Rotational disorder in the orientation of the chains around the chain axes, whose amount increases with increasing the pentene content, as well as statistical disorder in the up/down positioning of the chains are also present. Of course, the kinds of disorder that we have considered in explicit are probably not the only ones, but other kinds of disorder may be also included in the crystals of the trigonal form of iPPe copolymers, the most relevant one being disorder in conformation of the lateral side groups of pentene units probably coupled with small distortions of the chain backbone from the perfect 3/1 helical conformation.

The structure of the trigonal form found in the iPPe copolymers, as well as that found in the iPPHe copolymers, is similar to the structure of form I of iPB and demonstrates that the packing of polymer molecules is mainly driven by the crystallographic principles of the maximum entropy and density. The iPPe copolymers in which the less bulky ethyl lateral group allows a larger incorporation of pentene units in the crystals of the trigonal form represent the best example of the principle of density−entropy driven phase formation in polymers. In fact, iPPe copolymers having about 50 mol % of pentene with an average overall composition of propene and pentene approaching that of poly(1-butene) behave as iPB and crystallize into the same trigonal form.

■ AUTHOR INFORMATION

Corresponding Author

*Tel +39 081 674 448, fax +39 081 674 090, e-mail odda.ruizdeballesteros@unina.it.

Notes

The authors declare no competing financial interest.

■ ACKNOWLEDGMENTS

Financial support from Basell Polyolefins, Ferrara (Italy) is gratefully acknowledged. We thank Prof. Giovanni Talarico for the synthesis of the samples and Dr. Annette Thierry of CNRS of Strasbourg for her help in the TEM analysis.

■ REFERENCES

(1) Poon, B.; Rogunova, M.; Hiltner, A.; Baer, E.; Chum, S. P.; Galeski, A.; Piorkowska, E. *Macromolecules* **2005**, *38*, 1232.
(2) Lotz, B.; Ruan, J.; Thierry, A.; Alfonso, G. C.; Hiltner, A.; Baer, E.; Piorkowska, E.; Galeski, A. *Macromolecules* **2006**, *39*, 5777.
(3) De Rosa, C.; Auriemma, F.; Corradini, P.; Tarallo, O.; Dello Iacono, S.; Ciaccia, E.; Resconi, L. *J. Am. Chem. Soc.* **2006**, *128*, 80.
(4) De Rosa, C.; Dello Iacono, S.; Auriemma, F.; Ciaccia, E.; Resconi, L. *Macromolecules* **2006**, *39*, 6098.
(5) De Rosa, C.; Auriemma, F.; Talarico, G.; Ruiz de Ballesteros, O. *Macromolecules* **2007**, *40*, 8531.
(6) Stagnaro, P.; Boragno, L.; Canetti, M.; Forlini, F.; Azzurri, F.; Alfonso, G. C. *Polymer* **2009**, *50*, 5242.
(7) (a) Natta, G.; Corradini, P. *Nuovo Cimento, Suppl.* **1960**, *15*, 9. (b) Natta, G.; Corradini, P. *J. Polym. Sci., Polym. Phys. Ed.* **1959**, *29*, 29. (c) De Rosa, C. *Top. Stereochem.* **2003**, *24*, 71.
(8) Natta, G.; Corradini, P.; Bassi, I. W. *Nuovo Cimento, Suppl.* **1960**, *15*, 52.
(9) De Rosa, C.; Auriemma, F.; Vollaro, P.; Resconi, L.; Guidotti, S.; Camurati, I. *Macromolecules* **2011**, *44*, 540.
(10) (a) Arnold, M.; Henschke, O.; Knorr, J. *Macromol. Chem. Phys.* **1996**, *197*, 563. (b) Arnold, M.; Bornemann, S.; Köller, F.; Menke, T. J.; Kressler, J. *Macromol. Chem. Phys.* **1998**, *199*, 2647. (c) Abiru, T.; Mizuno, A.; Weigand, F. *J. Appl. Polym. Sci.* **1998**, *68*, 1493. (d) Alamo, R. G.; VanderHart, D. L.; Nyden, M. R.; Mandelkern, L. *Macromolecules* **2000**, *33*, 6094. (e) Hosoda, S.; Hori, H.; Yada, K.; Tsuji, M.; Nakahara, S. *Polymer* **2002**, *43*, 7451.
(11) (a) De Rosa, C.; Auriemma, F.; Ruiz de Ballesteros, O.; Resconi, L.; Camurati, I. *Macromolecules* **2007**, *40*, 6600. (b) De Rosa, C.; Auriemma, F.; Ruiz de Ballesteros, O.; Resconi, L.; Camurati, I. *Chem. Mater.* **2007**, *19*, 5122.
(12) De Rosa, C.; Auriemma, F.; Ruiz de Ballesteros, O.; De Luca, D.; Resconi, L. *Macromolecules* **2008**, *41*, 2172. De Rosa, C.; Auriemma, F.; Ruiz de Ballesteros, O.; Dello Iacono, S.; De Luca, D.; Resconi, L. *Cryst. Growth Des.* **2009**, *9*, 165.
(13) (a) Costa, G.; Stagnaro, P.; Trefiletti, V.; Sacchi, M. C.; Forlini, F.; Alfonso, G. C.; Tincul, I.; Wahner, U. M. *Macromol. Chem. Phys.* **2004**, *205*, 383. (b) Sacchi, M. C.; Forlini, F.; Tritto, I.; Stagnaro, P. *Macromol. Chem. Phys.* **2004**, *205*, 1804. (c) Sacchi, M. C.; Forlini, Losio, S.; Tritto, I.; Costa, G.; Stagnaro, P.; Tincul, I.; Wahner, U. M. *Macromol. Symp.* **2004**, *213*, 57. (d) Stagnaro, P.; Costa, G.; Trefiletti, V.; Canetti, M.; Forlini, F.; Alfonso, G. C. *Macromol. Chem. Phys.* **2006**, *207*, 2128.
(14) Spaleck, W.; Kuber, F.; Winter, A.; Rohrmann, J.; Bachmann, B.; Antberg, M.; Dolle, V.; Paulus, E. *Organometallics* **1994**, *13*, 954.
(15) (a) Resconi, L.; Guidotti, S.; Camurati, I.; Frabetti, R.; Focante, F.; Nifant'ev, I. E.; Laishevtsev, I. P. *Macromol. Chem. Phys.* **2005**, *206*, 1405. (b) Resconi, L.; Camurati, I.; Malizia, F. *Macromol. Chem. Phys.* **2006**, *207*, 2257.
(16) (a) Kissin, Y. V.; Brandolini, A. J. *Macromolecules* **1991**, *24*, 2632. (b) Sacchi, M. C.; Forlini, F.; Losio, S.; Tritto, I.; Wahner, U. M.; Tincul, I.; Joubert, D. J.; Sadiku, E. R. *Macromol. Chem. Phys.* **2003**, *204*, 1643. (c) Wahner, U. M.; Tincul, I.; Joubert, D. J.; Sadiku, E. R.; Forlini, F.; Losio, S.; Tritto, I.; Sacchi, M. C. *Macromol. Chem. Phys.* **2003**, *204*, 1738.
(17) (a) Scholte, T. G.; Meijerink, N. L.; Schoffeleers, H. M.; Brands, A. M. G. *J. Appl. Polym. Sci.* **1984**, *29*, 3763. (b) Moraglio, G.; Gianotti, G.; Bonicelli, U. *Eur. Polym. J.* **1973**, *9*, 623.
(18) *Cerius*^{2} *Modeling Environment*; Molecular Simulations Inc.: San Diego, CA, 1999.
(19) (a) Dinur, U.; Hagler, A. T.; New Approaches to Empirical Force Fields In *Review of Computational Chemistry*; **1991**; Chapter 4. (b) Maple, J. R.; Dinur, U.; Hagler, A. T. *Proc. Natl. Acad. Sci. U. S. A.* **1998**, *85*, 5350. (c) Sun, H.; Mumby, S. J.; Maple, J. R.; Hagler, A. T. *J. Am. Chem. Soc.* **1994**, *116*, 2978. (d) Sun, H. *Macromolecules* **1994**, *26*, 5942. (e) Sun, H. *Macromolecules* **1995**, *28*, 701.
(20) Cromer, D. T.; Mann, J. B. *Acta Crystallogr.* **1968**, *A24*, 321.
(21) Natta, G.; Corradini, P. *Nuovo Cimento, Suppl.* **1960**, *15*, 40.
(22) Alamo, R.; Domszy, R.; Mandelkern, L. *J. Phys. Chem.* **1984**, *88*, 6587.
(23) Brandrup, J.; Immergut, E. H.; Grulke, E. A. In *Polymer Handbook*; John Wiley: New York, 1999.

Macromolecules

Article

pubs.acs.org/Macromolecules

Stretch-Induced Crystal−Crystal Transition of Polybutene-1: An in Situ Synchrotron Radiation Wide-Angle X-ray Scattering Study

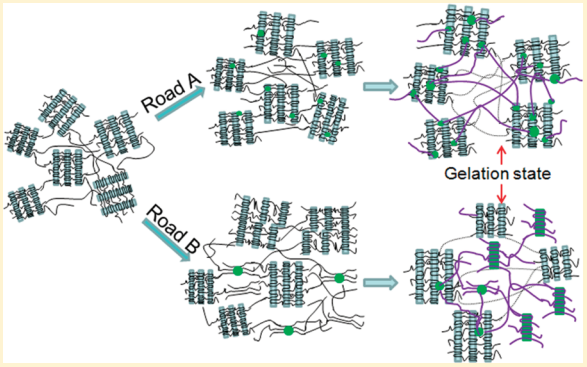
Yanping Liu,[†] Kunpeng Cui,[†] Nan Tian,[†] Weiqing Zhou,[†] Lingpu Meng,[†] Liangbin Li,*[,†] Zhe Ma,[‡] and Xiaolin Wang[§]

[†]National Synchrotron Radiation Lab and College of Nuclear Science and Technology, CAS Key Laboratory of Soft Matter Chemistry, University of Science and Technology of China, Hefei, China

[‡]Materials Technology, Eindhoven University of Technology, Eindhoven, The Netherlands

[§]Chinese Academy of Engineering Physics, Mianyang, China

ABSTRACT: Deformation induced crystal−crystal transition of polybutene-1 (PB-1) from forms II to I at different temperatures is studied with in situ synchrotron radiation wide-angle X-ray scattering (WAXS). Analyses on the evolution of crystallinity and orientations of forms II and I during tensile deformation show that stretch accelerates the transformation from forms II to I, which is interpreted based on either a direct crystal−crystal transition or an indirect approach via an intermediate state of melt, namely a melting recrystallization process. A three-stage mechanical deformation including linear deformation, stress plateau, and strain hardening is observed in the engineering stress−strain curves, which corresponds to a process of incubation, nucleation, and gelation of form I crystals. It establishes a nice correlation between phase transition and mechanical behavior in this study.



INTRODUCTION

The structure−mechanical property relationship of semicrystalline polymer materials is a long-standing challenge in polymer academic and industrial communities. For semicrystalline polymers composed of multiscale structures from monomer composition, lamellar crystal to spherulite, it is formidably difficult to correlate macroscopic mechanical property with microstructures at different length scales. Additionally, during tensile or other mechanical deformation, external force may induce complicated structural and morphological changes like solid−solid and liquid−solid transitions, which will lead to a feedback on the mechanical property and leave their signatures on the stress−strain curves.[1−5] During deformation, the structural evolution and mechanical property are dynamically coupled with each other, and in situ measurements combining structure and property characterizing techniques become essential on understanding structure and mechanical property relations of those materials. Indeed combining an in situ tensile tester with synchrotron radiation X-ray scattering techniques provides rich structure−property information for many semicrystalline polymers.[6−9] New phases were reported during deformation of polymers, like the mesophase of poly(ethylene terephthalate),[6,10−12] the conformation disordered hexagonal crystal in polyethylene (PE),[13] and the transient α'' phase found in polyamide.[14,15] Solid−solid phase transition may even lead to unique mechanical property, like the superelasticity of syndiotactic polypropylene (sPP) which is attributed to deformation-induced martensitic-like crystal−crystal transition.[16,17] Moreover, in the case of isotactic polypropylene (iPP), the transformation from α or γ crystals into the mesophase may bring various degree of mechanical properties ranging between stiff and elastomeric.[18−21]

Polybutene-1(PB-1) is a commercially interesting polyolefin because of its wide applications, like hot water pipes, pressurized tanks and tubes. However, applications of PB-1 are limited comparing with other polyolefins like polypropylene and polyethylene. In addition to slightly higher cost of the raw material, the complication of crystal−crystal transition is also an important consideration. The solid phase transition may bring undesirable effect, such as shrinkage of the molded objects caused by densification.[22,23] PB-1 exhibits multiphases depending on the crystallization condition: form I, twined hexagonal with a 3_1 helix; form I′, untwined hexagonal with a 3_1 helix; form II, tetragonal with an 11_3 helix; form II′, tetragonal structure; form III, orthorhombic with a 4_1 helix.[24−27] Form II is a metastable structure which forms when the polymer crystallizes from melt at atmospheric pressure, and which transforms into the thermodynamically stable form I when held at room temperature. Depending on the environmental condition, the transformation may take several weeks to finish, during which the material properties are changed profoundly.[22,28] With the help of tensile deformation, the

Received: December 7, 2011
Revised: March 8, 2012
Published: March 15, 2012

 © 2012 American Chemical Society dx.doi.org/10.1021/ma2026513 | *Macromolecules* 2012, 45, 2764−2772

transformation process will be accelerated.[29] After the transformation, the melting point increases to 135 °C of form I from 117 °C of form II. Besides that, the material will become rigid and display higher strength.[30−33] In order to shorten the transition time, recent work have been tried to obtain form I crystal directly under peculiar condition, like ultrathin film,[34] self-seeding[35] and different concentration of stereodefects.[36] Form III and form I′ have been found to form in solution crystallization, depending on the solvent, concentration and the crystallization temperature.[37−39] At higher temperature, both forms III and I′ first transform into form II by the aid of drawing, and then into form I.[40]

Because of the industrial and academic interests, the transformation from forms II to I has been extensively studied in the past decades.[41−48] It has been reported that this transformation is a nucleation-controlled process with nuclei localized at lamellar distortion points or the crystal surfaces or corners.[39] Based on X-ray and electron diffraction studies, Fujiwara et al.[49] and Kopp et al.[50] suggest that the (110) plane of form II tetragonal crystal becomes the same plane of form I hexagonal crystal. In this way, the helix displacement is minimized and the energetically unrealistic change of helix chirality is avoided. The transition kinetics is strongly dependent on the initial crystallization temperature and circumstance. High pressure[28,51] or pressured CO_2,[52,53] deformation[54−56] and additives like plasticizers or nucleating agents[57] are reported to accelerate the transition kinetics. Deformation assisted forms II to I transition of PB-1 has been studied since 1960s.[58] A strong effect of strain on the transformation was reported by Goldbach et al.,[59] where the importance of strain on the amorphous chains was emphasized as amorphous relaxation counteracted the accelerating effect. During stretch induced transition from forms II to I of PB-1, an unusual two-stage strain hardening was observed by Yang et al..[60] Though the accelerating effect of deformation on crystal−crystal transition from forms II to I is well recognized, no direct correlation between structure and mechanical property is established yet.

For the purpose of correlating the phase transformation with mechanical properties of PB-1, the phase transition of commercial grade sample during uniaxial tensile deformation is studied with in situ synchrotron radiation wide-angle X-ray scattering. Two transition points are observed on the engineering stress−strain curves, which correspond to nucleation of form I crystal and gelation of form I mechanical network, respectively. The transition from forms II to I follows two different routes, namely a direct crystal−crystal transition and a melting recrystallization process.

EXPERIMENTAL SECTION

The tensile test was carried out on a homemade miniature mechanical tester, which was equipped with a temperature controlled oven with nitrogen purge. Error of the force sensor of the apparatus was less than 1 N. The uniaxial tensile tests were performed at several designated temperatures (25, 50, and 80 °C) and the drawing speed was fixed at 3.15 mm/min. After the dumbbell shaped sample was mounted between two clamps of the tester with an initial length of 10 mm, temperature was increased to the designated temperature in 5 min. When the temperature was stabilized for 5 min, stretch was imposed on the sample. The change of sample width was followed with a high precision CCD camera.

In-situ WAXS measurements were carried out on synchrotron radiation X-ray scattering station with a radiation wavelength of 0.154 nm and Mar 345 image plate as a detector in National Synchrotron Radiation Laboratory (NSRL), Hefei, China. The sample-to-detector distance for WAXS was 323 mm. Fit2D software package was used to analyze the two-dimensional (2D) WAXS patterns. Air background was subtracted in the 2D scattering patterns.

PB-1 granules are kindly supplied by LyondellBasell Industries with a trade name of PB0110M, which has with a molecular weight M_w = 711000 g/mol and M_w/M_n= 3.1. The melting point and glass transition temperature are about 117 and −20 °C, respectively. The PB-1 plates with a thickness of 1 mm were first made through compression molding. For tensile testing, the plates were further cut into dumbbell shaped samples, with length and width of 29 and 4 mm, respectively. The samples were heated to 170 °C and held for 5 min to erase the processing history, then cooled to the crystallization temperatures 85, 95, 105 °C at a cooling rate of 9 °C/min. At the crystallization temperature of 85 and 95 °C, the samples were held isothermally for more than 40 min to crystallize completely. Because of the slow crystallization rate at 105 °C, the samples were held for more than 3 h. After complete crystallization, the samples were quickly mounted on the tester to carry out tensile experiments. No diffraction signal of form I was detected before uniaxial drawing.

RESULTS

According to the crystallization condition adopted in the sample preparation, the crystal phase in the PB-1 samples before tensile test is the metastable form II, which is also verified by the WAXS patterns. The three main diffraction peaks are observed at 2θ of about 11.8, 16.9, and 18.4°, which correspond to crystallographic planes (200), (220), and (213) of form II crystal, respectively.

Figure 1a depicts the engineering stress−strain curve (ESSC) of PB-1 during tensile test at room temperature (25 °C controlled by air condition), which was initially crystallized at 95 °C. Several selected two-dimensional (2D) WAXS patterns at various strain levels are inserted. The tensile deformation is

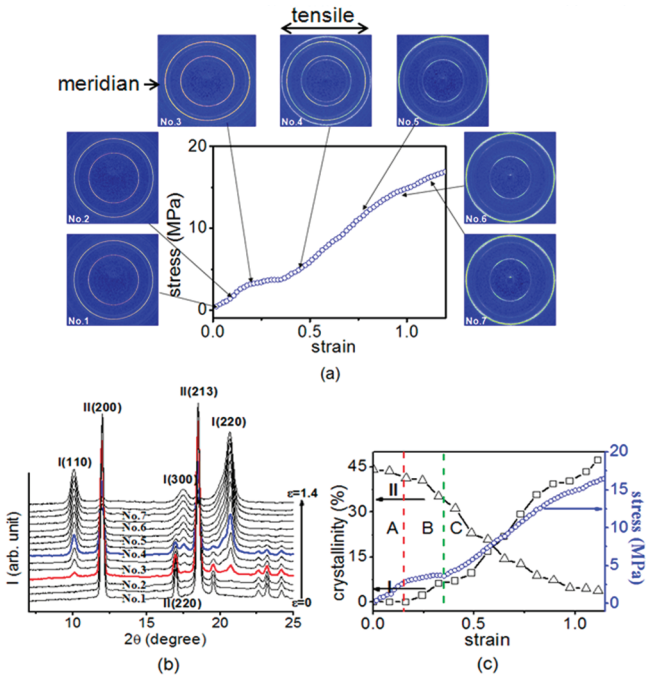


Figure 1. (a) Engineering stress−strain curve and the selected WAXS patterns during uniaxial tensile deformation at room temperature. (b) Corresponding one-dimensional WAXS curves. (c) Crystallinity of forms I and II calculated from part b in conjunction with the corresponding engineering stress−strain curve. The crystallization temperature (T_c) for this sample is 95 °C.

dx.doi.org/10.1021/ma2026513 | Macromolecules 2012, 45, 2764−2772

along horizontal direction. Before stretching, the diffraction peaks with relatively strong intensity of crystal planes (200), (220) and (213) of form II crystal are clearly viewed in the 2D WAXS patterns. Upon increasing strain to the yield point, deformation-induced orientation of crystals can be easily visualized in 2D WAXS patterns, while the appearance of more diffraction peaks indicates the formation of new crystal structure.

To present detailed evolution of phase transformation, the integrated one-dimensional (1D) WAXS curves during the tensile test are shown in Figure 1b. Three new diffraction peaks appear on 1D WAXS curves clearly when the engineering strain reaches about 0.2 (indicated by red line), which correspond to the crystallographic planes (110), (300), (220) of form I. These peak intensities of form I increase with strain, while that of form II decrease and finally die away. A quantitative analysis on the deformation induced crystal−crystal transition of forms II to I is presented in Figure 1c, where we plot the crystallinity of forms I and II during deformation. The corresponding ESSC is also plotted in Figure 1c for a direct correlation between structure and mechanical property. The evolution of the phase transition can be divided into three stages, which are separated by the red and green dash lines in Figure 1c. In stage A, no diffraction signal from form I can be detected, indicating that the transformation from forms II to I does not start yet. Stage A matches well with the linear deformation region as indicated by ESSC. Following the linear region, the ESSC enters into a stress plateau-like region, which is defined as stage B. Coincidently, form I appears exactly at the beginning of the stress plateau. The onset of the engineering stress plateau is essentially a mechanical yield, which suggests that the beginning of transition from forms II to I, or nucleation of form I corresponds to the yield of form II crystals. In stage B, the crystallinity of form I keeps at a low level though it still increases continuously. At the end of the engineering stress plateau region, the crystallinity reaches about 6%. Analogue to isothermal crystallization, if we define stage A as the induction period of crystallization, stage B is rather similar to the nucleation period. Stage C starts at the end of the stress plateau and the stress increases nearly linearly with strain again, which is a strain hardening region. Here the transition from forms II to I is accelerated, which may correspond to the growth stage of form I.

It is interesting to note that a slowdown of the transformation seems to exist at the beginning of stage C though the overall increase of the crystallinity of form I is rapid in this stage. In order to have a better view, we plot the crystallinity of form I in the true stress-true strain diagram during tensile deformation in Figure 2. Indeed a slowdown of the transformation rate from forms II to I accompanies with the stress level-up or strain hardening after the plateau region. Evidently

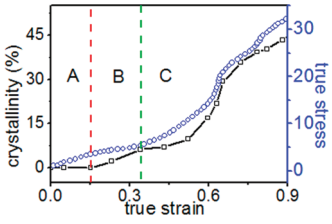


Figure 2. Crystallinity evolution of form I combining with the corresponding true stress−strain curve.

the strain hardening in stage C is due to the formation of a new mechanical network constructed by form I. The formation of the new mechanical network may take major share of stress, which releases form II from stress partially and consequently slows down the transformation. This will be discussed in more detail in the Discussion.

Deformation-induced orientation of forms II and I during tensile test is analyzed through the azimuthal intensity distribution of (200) crystal plane of form II and (110) of form I, which are plotted in Figure 3, parts a and b, respectively. As mentioned above, in stage A, only form II crystals exist, which remains isotropic as indicated by the azimuthal intensity distribution of (200) plane of form II. When the deformation enters into stage B, the orientation of (200) planes of form II starts to shift into the 45° direction which may be the shear band.[61−63] The coincidence between mechanical yield and crystal rotation is a general phenomenon in semicrystalline polymers.[1,64] At the beginning of stage B, scattering intensity of form I crystal emerges, with the crystal plane (110) polarized on the equator, in other words with chain axis tending to be parallel to the tensile direction. The different orientation of forms I and II in stage B indicates that nucleation of form I and rotation of form II are two uncorrelated events, though both correlate with the mechanical yield during tensile deformation at room temperature. Further increasing tensile strain, the orientation of form I (110) shifts to 45° in stage C, which is same as that of form II (200). Here it is more like that the growth of form I consumes form II crystals that already oriented in this direction.

The same tensile experiments with in situ synchrotron radiation WAXS to follow structure evolution were further carried out on samples crystallized at 85 and 105 °C, respectively. For conciseness, we present the crystallinity evolution of forms II and I and the engineering stress−strain curves during tensile test in Figure 4, parts a and b, respectively. The ESSC and the crystallinity evolution of forms II and I for samples crystallized at 85 °C (Figure 4a) and 105 °C (Figure 4b) are essentially same as that crystallized at 95 °C, which confirms that the three-stage transformation process from forms II to I is a general feature of PB-1. Comparing with the samples crystallized at lower temperatures (85 and 95 °C), stage B for the sample crystallized at 105 °C seems to be shorter, which is possibly due to different crystallite forms when crystallized at different temperatures. It is reported that at low supercooling PB-1 crystallized into hendritic structure, while at high supercooling spherulite is formed.[47] At the transition point between stages B and C, the crystallinity of form I always keeps at a relatively low level, which is less than 6% for both samples crystallized 85 and 105 °C. In general, within the temperature range we studied, initial crystallization temperature seems to play a weak role in the deformation induced crystal−crystal transition.

We further studied the effect of tensile deformation temperature on the crystal−crystal transition. Below the melting temperature of PB-1, in situ tensile deformation experiments on the sample crystallized at 95 °C were performed at 50 and 80 °C, respectively. As the overall trend of the engineering stress−strain curve and the evolution of forms II to I crystal−crystal transition at 50 °C is rather similar to that at room temperature, we only present data of 80 °C in Figure 5a. The ESSC can be divided into three regions which are same as that at low temperatures (separated by the red and green dash lines), but the specific structure evolution is

dx.doi.org/10.1021/ma2026513 | Macromolecules 2012, 45, 2764−2772

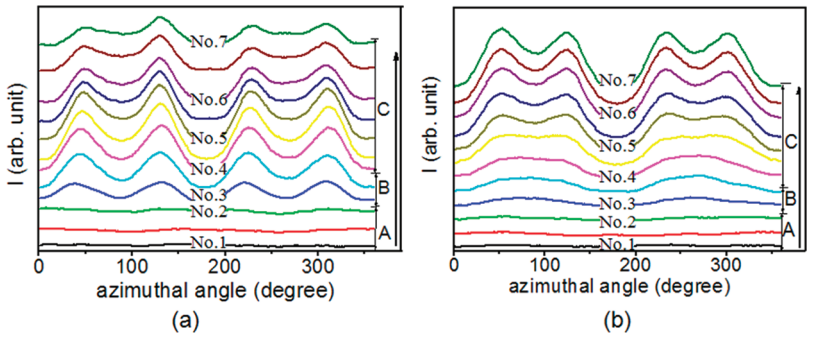


Figure 3. One-dimensional azimuthal intensity curves of (200) plane of form II (a) and (110) of form I (b) during deformation at room temperature with tensile direction in 0−180° (horizontal direction).

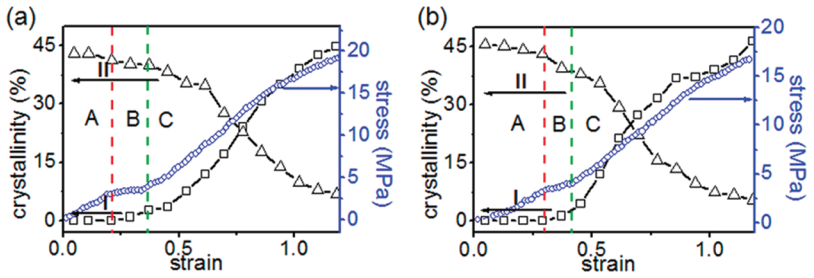


Figure 4. Crystallinity evolution of forms I and II in conjunction with the corresponding engineering stress−strain curves during deformation at 25 °C for the sample crystallized at temperatures of 85 °C (a) and 105 °C (b), respectively.

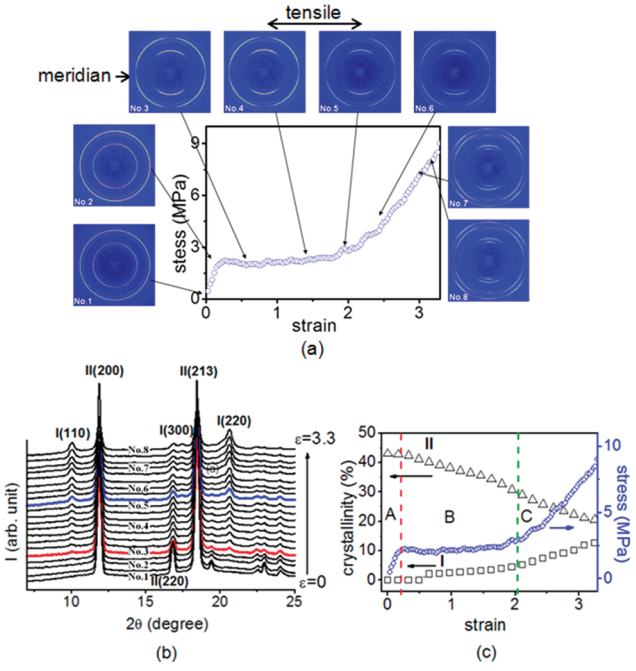


Figure 5. (a) Engineering stress−strain curve and the selected WAXS patterns during tensile deformation at 80 °C with T_c = 95 °C. (b) Corresponding one-dimensional WAXS curves. (c) Crystallinity evolution of forms I and II calculated from part b and the corresponding engineering stress−strain curve.

different from that at low temperatures. At 80 °C, form I does not appear at the first turning point (yield point) on the ESSC where the engineering strain is 0.2, but emerges in the middle of the plateau region with a strain of 0.6. Note that the plateau (stage B) covers a broader strain range from 0.2 to 2.1. Figure 5b shows the integrated one-dimensional WAXS curves during tensile deformation at 80 °C. The red curve corresponds to the first appearance of form I at the strain of 0.6, while the blue one corresponds to the second turning point or the onset of strain hardening. The diffraction intensity of form I is weaker than that of form II during the whole tensile deformation process as shown in Figure 5b. The crystallinity of both forms II and I are plotted versus engineering strain in Figure 5c, where the ESSC is also added for the convenience of correlating. In the stress plateau region (stage B), the crystal−crystal transformation from forms II to I is very slow and only 2% crystallinity of form I is generated at the end of the plateau region (Figure 5c). Interestingly, the crystallinity of form II declines obviously faster than the increase of that of form I, which suggests that the overall crystallinity of forms II and I in the sample decreases during the tensile deformation at 80 °C. In other words, part of form II melts rather than transforms to form I directly under stress at high temperature.

Parts a and b of Figures 6 show the azimuthal intensity distributions of the representative planes, crystal plane (200) of form II and (110) of form I, during tensile deformation at 80 °C for the whole process, respectively. In the linear deformation region (stage A), no obvious orientation of form II is observed (Figure 6a). As soon as the deformation enters into the stress plateau region (stage B), the (200) plane of form II starts to orient in about 50° direction. Further increasing strain, the azimuthal intensity of form II (200) shifts its maximum to about 68° at the strain of 0.6, where form I emerges. From the strain of 0.6 to the end of stage B (at strain of 2.1), the azimuthal intensity distribution of form II (200) keeps its peak position unchanged at 68°. In the strain hardening region (stage C) the orientation of form II (200) plane further shifts to meridian direction. On the other hand, the orientation of the crystallographic plane (110) of form I is along meridian direction from its first appearance at the strain

dx.doi.org/10.1021/ma2026513 | Macromolecules 2012, 45, 2764−2772

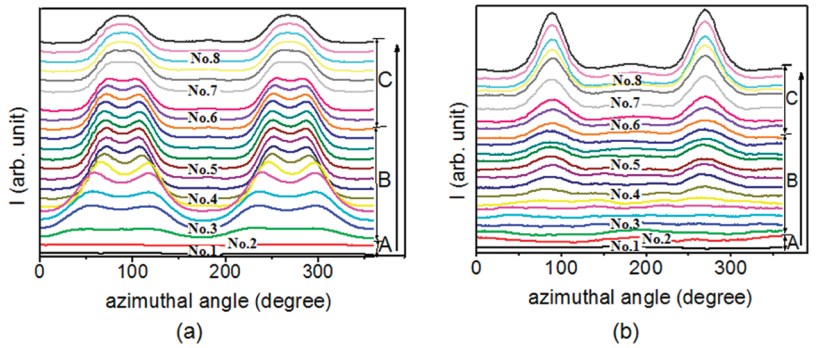


Figure 6. One-dimensional azimuthal intensity curves of (a) (200) plane of form II and (b) (110) plane of form I during uniaxial deformation at 80 °C with T_c = 95 °C. The tensile axis lies along the 0−180° direction, while 0° and 90° are meridian and equator, respectively.

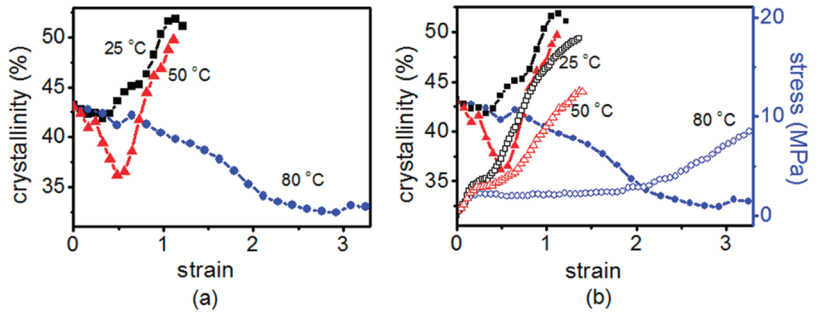


Figure 7. (a) Sum of the crystallinity (X_{II+I}) of forms II and I (solid symbol) (b) and the corresponding ESSC for different experimental temperatures 25, 50, and 80 °C (open symbol).

of 0.6, which keeps unchanged during the whole tensile deformation process.

Tensile deformation temperature does show significant influence on the phase transition. Instead of plotting crystallinity of forms II and I separately, here we plot the sum of their crystallinity during tensile deformation at different temperatures in Figure 7a, which is denoted as X_{II+I} for the convenience of description. As diffraction intensity is determined by many factors like structural factor, multiplicity factor, etc., Figure 7 only gives a semiquantitative trend of the overall mass or volume crystallinity. Note that the mass correction due to different densities of forms II and I does not affect the trends. In order to correlate the volume fractions of all solid crystals with the mechanical behaviors, the sum of crystallinity X_{II+I} are replotted together with the corresponding ESSCs in Figure 7b. At 25 °C, the sum of crystallinity X_{II+I} does not vary obviously in stages A and B, which levels up as entering the strain hardening region or stage C (see Figure 7b) and reaches a value of about 52%. On the contrary, tensile deformation at high temperature of 80 °C leads to a continuous decline of X_{II+I}, which reaches a low level of about 32%. At an intermediate temperature 50 °C, the evolution of X_{II+I} follows a nonmonotonic behavior, which first decreases in stages A and B to about 36%, and then increases back to about 50%. These three different evolution behaviors of X_{II+I} indicate that stress may induce form II crystal to melt at temperature below its melting point, while those molten amorphous part will crystallize into form I under further stretch, especially at intermediate temperatures as demonstrated at 50 °C. The evolution trends of the X_{II+I} correlate rather well with their corresponding ESSCs. The leveling up points of X_{II+I} at 25 and 50 °C locate exactly at the onset of stage C (strain hardening region). Though X_{II+I} does not show a leveling up at 80 °C, the onset of strain hardening corresponds to a flatting of the decrease trend of X_{II+I}, which may have the same physical mechanism as the leveling up at lower temperatures.

DISCUSSION

On the basis of in situ WAXS measurements during tensile deformation of PB-1, several interesting findings can be extracted. (i) The transformation from forms II to I is accelerated by uniaxial tensile deformation, which is suppressed with the increase of deformation temperature. (ii) During tensile deformation process, the sums of crystallinity X_{II+I} follow nearly monotonic increase and decrease with strain at 25 and 80 °C, respectively, while a nonmonotonic trend with first decrease and then increase process is observed at the intermediate temperature of 50 °C, which suggests that two different routes may exist in the transition from forms II to I. One is a direct transformation from the metastable form II to the stable form I at low temperature of 25 °C, which is similar to the phase transition at quiescent condition. The second occurs at high temperature of 80 °C, which is a process of deformation induced melting and recrystallization. (iii) Two interesting turning points have been found on the engineering stress−strain curves, which correspond to the specific structural transformations, respectively. At low temperature the transition from forms II to I begins at the first turning point (yield point). The second turning point indicates the onset of strain hardening, where a critical concentration of form I is generated to form a new mechanical network. Thus, this is a gelation point of the newly formed mechanical network with form I acting as the physical cross-link. Focusing on these points above, we will give some discussions in the following paragraphs.

dx.doi.org/10.1021/ma2026513 | *Macromolecules* 2012, 45, 2764−2772

The transformation from the metastable form II to the stable form I is accelerated largely by tensile deformation. In our experiments, the degree of phase transformation Φ reaches about 80% in 40 min at room temperature (Figure 1c and Figure 4, parts a and b). Here, the degree of phase transformation is defined as $\Phi = X_{It} / X_{II0}$, where X_{It} is the crystallinity of form I at time t, and X_{II0} is the crystallinity of form II before tensile deformation. However, it has been reported the transformation from forms II to I may take several weeks to finish under quiescent condition at room temperature.[44] When deformation is applied, the volumetric free energy difference between forms II and I is raised as $\Delta G = \Delta G_q + \Delta G_f$, where ΔG_q is the thermodynamic driving force at quiescent condition and ΔG_f is the driving force coming from external field like the stress in this work. Stress increases the free energy of form II and decreases the nucleation barrier of form I, which leads to an acceleration of the transformation from forms II to I. According to the transformation mechanism proposed by Fujiwara[49] and Lotz,[50] the (110) planes exist as an "invariant plane" (Figure 8a). Direct transition from tetragonal form II with 11_3 helix to trigonal form I with 3_1 helix gives a near-matching (−4%) of interhelical distance and preserves the chirality of helical planes, which seems to be an easy approach without large rearrangement of molecular units. In the normal direction of these planes, main part of the contraction takes place. Averagely, the interplanar distance is reduced by nearly 20% (see Figure 8a). The transformation is accelerated under tensile deformation via promoting the contraction. For example, in the vertical zone of Figure 8b, chains in the lamellae are parallel to the tensile direction. When the tensile stress σ_1 is applied on form II crystal, the stress σ_2 and σ_3 in the two directions perpendicular to σ_1 will assist the contraction of interhelix and interplanar distance of (110) planes respectively (see Figure 8b). Oppositely, in the horizontal zone, the stress parallel to the normal of (110) plane may play a negative role in contracting. This analysis is also consistent with the initial orientation of form I whose chain axis is along tensile direction.

The transition from forms II to I is delayed with the increase of temperature. Comparing with the result at lower temperatures, the transformation is much slower at 80 °C, where the transition degree Φ reaches less than 20% in 40 min (much less than 80% at room temperature). It has been reported that the phase transformation of PB-1 is a nucleation controlled process.[65] The nucleus of form I at quiescent condition is thought to be created mainly by thermal stresses, due to different thermal expansion coefficients of crystal and amorphous component. This thermal stress is prone to occur at regions with irregular stack of lamella, local variation of lamellar thickness, and bending of lamellae. At low temperature, tensile deformation amplifies local thermal stress and creates more sites for form I to nucleate, which behaves as a fast transition rate from forms II to I. On the other hand, higher temperature leads to faster relaxation of the thermal stress, which counteracts the acceleration effect of tensile deformation on the transition. Comparing with the several weeks needed for phase transition under quiescent condition, the transition rate is much faster by the aid of deformation, no matter what the temperature is. That is because the effect of deformation on the transformation is so large that the impact of temperature is minimized. In addition to the transition rate, different transition routes may occur at low and high temperatures, which also affects the transition rate at different temperatures and will be discussed below.

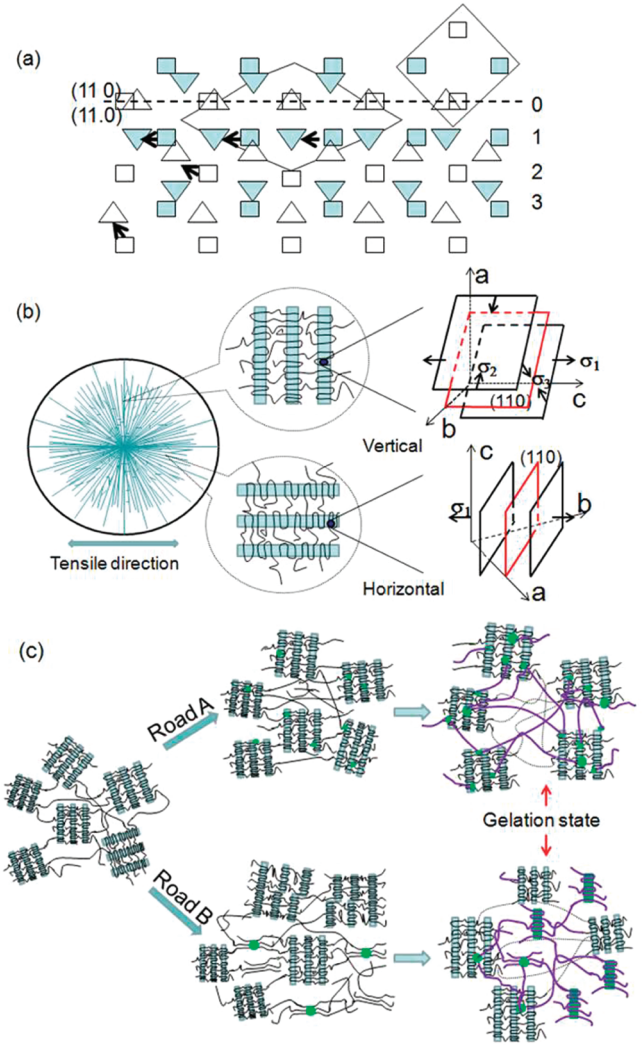


Figure 8. (a) Transformation scheme from forms II to I on the molecular level concerning with the "invariant plane" (110).[49] □ and △ represent 11_3 and 3_1 helices of forms II and I respectively. The different helical hands are shown as light and shaded. (b) Force condition of the planes (110) under uniaxial deformation in different zones of form II crystal. (c) Schematic diagrams for the gelation process of the form I mechanical network during the phase transition. A and B are the direct transformation from forms II to I and melting recrystallization process with melt as transient state, respectively. The blue and green blocks represent forms II and I crystal, respectively.

The evolution of the total crystallinity X_{II+I} at different temperatures suggests that two different routes may be followed by the transition from forms II to I, as illustrated in Figure 8c. One is the direct transition from forms II to I, which takes place at quiescent condition and under tensile deformation at room temperature. Naturally another way is indirect transition from forms II to I with amorphous phase as the intermediate state. This indirect approach is rather plausible as evidenced by the evolution of crystallinity at high temperatures during tensile deformation. As shown in Figure 7a, the sum of crystallinity X_{II+I} increases monotonically from about 43% to 52% at 25 °C. Here the increase of X_{II+I} has two possible interpretations. (i) The remaining amorphous part in the initial samples crystallizes into form I directly under tensile deformation. (ii) The increase of X_{II+I} may be due to larger crystalline diffraction intensities of form I than those of form II

dx.doi.org/10.1021/ma2026513 | Macromolecules 2012, 45, 2764−2772

with the same volume. If we take the first interpretation, the indirect transition approach from forms II to I with amorphous as the intermediate state can stand with further supports from the nonmonotonic evolution of X_{II+I} at 50 °C, which can be interpreted as a melting and recrystallization process. Now we take the second interpretation which means the crystalline diffractions of form I is much stronger than those of form II, so it can be assumed that the mass crystallinity is preserved during the transition from forms II to I at room temperature. With this scheme, the decrease of X_{II+I} in the first two stages (stage A and B) at 50 °C has to be attributed to melting of form II, while the increase of crystallinity in stage C is a recrystallization process, which confirms that the destruction of the original lamellae and recrystallization into new crystalline form occurs at the critical point C.[3] The X_{II+I} at 80 °C follows a monotonic decrease, which also supports the idea of tensile deformation induced melting and recrystallization process. Thus, both direct and indirect transition approaches take place during tensile deformation induced transition from forms II to I, where the direct transition process may prefer at room temperature and the indirect one takes more shares at high temperature. These two approaches are in line with the two debated mechanisms on interpreting yield and orientation of crystalline polymers during tensile test. The direct transition from forms II to I mirrors Young and others' crystalline slip model, while the indirect transition with melting and recrystallization falls in the Flory–Yoon[66] approach, which, however, recrystallizes into stable form I instead of the initial metastable form II. Under continuous deformation, it is difficult to recrystallize into form II, because amorphous chains tend to orient in the tensile direction, while form II is reported to crystallize only from random chain conformation.[40] The structural evolution during tensile deformation shows clearly fingerprints on mechanical properties, which gives a nice demonstration on the correlation between phase transition and mechanical properties. At 25 and 50 °C, the appearance of form I exactly follows the yield point, where form II cannot sustain the tensile stress and coarse slip of lamellar crystal starts. In other words, yield point announces the aging of the parent phase form II, which is also the right point for the daughter phase form I to generate. At 80 °C, yield corresponds to tensile deformation induced melting of form II, which does not transform into form I immediately. Thus, for PB-1 samples with form II as the parent phase, the yield point corresponds to the starting point of phase transitions either from forms II to I at low temperature or from form II to melt at temperature close to melting point. Obviously, it coincides with a generalized view that the mechanism governing the process of tensile deformation of semicrystalline polymers at low and moderate deformations seems to be strain controlled. According to this model, block slips determine the yield points (point A and B),[3] where nucleation of form I or melting of form II start. The second turning point in the engineering stress–strain curves leads to a strain hardening region, which takes place at relatively small strains (about 0.4) (Figure 1c and Figure 4, parts a and b). In the study of mechanical properties of other polyolefins, like polypropylene, polyethylene, polystyrene, etc. the strain hardening appears at larger strains (above 2).[67,68] In semicrystalline polymer without the complication of phase transition, the molecular network plays an important role in the strain hardening, where crystal blocks start to destruct. In current case, strain hardening appears at relative small strain, which should not be attributed to stretched network. As the transition from forms II to I is the major structural change in the stress plateau region before strain hardening, the stress level-up should be attributed to the formation of form I. Though the crystallinity of form I keeps relatively low (~5%) at the onset point of strain hardening, this is sufficient to establish a new mechanical network with form I crystals as physical cross-link if we compare the current system with physical gels. Indeed it is found that gelation of iPP melt during crystallization requires crystallinity of only 2% or less.[69] Though form I of PB-1 nucleates from a heterogeneous semicrystalline complex, the physical picture to construct the mechanical network should be similar to that in crystallization from melt. The difference here is that the initial network with form II as physical cross-link still exists though it can only sustain weak stress with a maximum of the plateau stress in the engineering stress–strain curves (see Figure 1c and Figure 4, parts a and b). In the stress plateau region, though form I crystals already appear, the concentration is low and they are dispersed in the heterogeneous matrix like suspensions without interaction among each other. Further increasing strain, the concentration of form I crystals increases, which finally reaches the gelation point with a crystallinity of about 5% (see Figure 8c). The formation of the new mechanical network contributes its role on sustaining stress, which reflects as strain hardening in the stress–strain curves.

■ CONCLUSIONS

Uniaxial tensile deformation induced the phase transition of PB-1 from forms II to I at different temperatures is investigated with in situ WAXS. The crystallinity evolution and orientation distribution of forms II and I show that the phase transformation is accelerated largely under tensile deformation. On the basis of the transition mechanism suggested by Fujiwara, the accelerating mechanism is deduced on the molecular level, as stretch could assist the interhelix and interplanar shrinkage of the "invariant plane" (110). Two phase transition routes are indicated in our experiment. The direct way from forms II to I may be dominant at low temperature, while the indirect one seems to be a process of deformation induced melting and recrystallization at high temperature. In the latter route, the metastable form II transforms into amorphous state due to uniaxial stretching at high temperature, which crystallizes into form I at large strain. The strain hardening takes place at a relatively small strain in uniaxial tensile deformation of PB-1, which is attributed to the mechanical network with form I crystal as the physical cross-link. A nice correlation between phase transition and mechanical property is established. The three stages of phase transformation, namely incubation, nucleation and gelation of form I, leave their signatures on the engineering stress–strain curve at different strain levels, respectively, reflecting as a three-stage mechanical behavior with linear deformation, stress plateau, and strain hardening.

■ AUTHOR INFORMATION

Corresponding Author

*E-mail: lbli@ustc.edu.cn.

Notes

The authors declare no competing financial interest.

■ ACKNOWLEDGMENTS

We would like to thank Prof. Wim H. de Jeu (Amherst), Prof. Bernard Lotz, and Dr. Bing Miao for helpful discussion, Prof. Guoqiang Pan and Dr. Zeming Qi for the assistance on WAXS

experiments, and Mr. Xiao Wang for the help on tensile tester. This work is supported by the National Natural Science Foundation of China (51033004, 50973103, 51120135002, 20904050), the Fund for One Hundred Talent Scientist of CAS, 973 program of MOST (2010CB934504), and the Doctoral Fund of MOE (200803580011). The research is also in part supported by the Opening Project of the State Key Laboratory of Polymer Materials Engineering (Sichuan University KF201001) and the State Key Laboratory of Polymer Physic and Chemistry (Changchun Institute of Applied Chemistry, CAS). We also would like to thank LyondellBasell Industries for providing PB-1 materials.

REFERENCES

(1) Galeski, A. *Prog. Polym. Sci.* **2003**, *28*, 1643−1699.
(2) Meijer, H. E. H.; Govaert, L. E. *Prog. Polym. Sci.* **2005**, *30*, 915−938.
(3) Men, Y. F.; Rieger, J.; Strobl, G. *Phys. Rev. Lett.* **2003**, *91*, 095502/1−4.
(4) Peterlin, A. *J. Mater. Sci.* **1971**, *6*, 490−508.
(5) Lin, L.; Agron, A. *J. Mater. Sci.* **1994**, *29*, 294−323.
(6) Samon, J. M.; Schultz, J. M.; Wu, J.; Hsiao, B. S.; Yeh, F.; Kolb, R. *J. Polym. Sci., Part B: Polym. Phys.* **1999**, *37*, 1277−1287.
(7) Kawakami, D.; Ran, S. F.; Burger, C.; Avila-Orta, C.; Sics, I.; Chu, B.; Hsiao, B. S.; Kikutani, T. *Macromolecules* **2006**, *39*, 2909−2920.
(8) Jiang, Z. Y.; Tang, Y. J.; Men, Y. F.; Enderle, H.; Lilge, D.; Roth, S. V.; Gehrke, R.; Rieger, J. *Macromolecules* **2007**, *40*, 7263−7269.
(9) Men, Y. F.; Rieger, J.; Lindner, P.; Enderle, H. F.; Lilge, D.; Kristen, M. O.; Mihan, S.; Jiang, S. C. *J. Phys. Chem. B* **2005**, *109*, 16650−16657.
(10) Kawakami, D.; Hsiao, B. S.; Ran, S. F.; Burger, C.; Fu, B.; Sics, I.; Chu, B.; Kikutani, T. *Polymer* **2004**, *45*, 905−918.
(11) Kawakami, D.; Ran, S. F.; Christian, B.; Fu, B.; Sics, I.; Chu, B.; Hsiao, B. S. *Macromolecules* **2003**, *36*, 9275−9280.
(12) Kawakami, D.; Christian, B.; Ran, S. F.; Avila-Orta, C.; Sics, I.; Chu, B.; Chiao, S. M.; Hsiao, B. S.; Kikutani, T. *Macromolecules* **2008**, *41*, 2859−2867.
(13) Kakiage, M.; Yamanobe, T.; Komoto, T.; Murakami, S.; Uehara, H. *Polymer* **2006**, *47*, 8053−8060.
(14) Wang, D. L.; Shao, C. G.; Zhao, B. J.; Bai, L. G.; Wang, X.; Yan, T. Z.; Li, J. J.; Pan, G. Q.; Li, L. B. *Macromolecules* **2010**, *43*, 2406−2412.
(15) Bai, L. G.; Hong, Z. H.; Wang, D. L.; Li, J. J.; Wang, X.; Pan, G. Q.; Li, L. B.; Li., X. H. *Polymer* **2010**, *51*, 5604−5611.
(16) Auriemma, F.; De Rosa, C. *Macromolecules* **2003**, *36*, 9396−9410.
(17) Auriemma, F.; De Rosa, C.; Esposito, S.; Mitchell, G. R. *Angew. Chem., Int. Ed.* **2007**, *46*, 4325−4328.
(18) Auriemma, F.; De Rosa, C. *J. Am. Chem. Soc.* **2006**, *46*, 11024−11025.
(19) De Rosa, C.; Auriemma, F.; Di Capua, A.; Resconi, L.; Guidotti, S.; Gamurati, I.; Nifant'ev, I. E.; Laishevtsev, I. P. *J. Am. Chem. Soc.* **2004**, *126*, 17040−17049.
(20) De Rosa, C.; Auriemma, F.; de Ballesteros, O. R.; Iacono, S. D.; De Luca, D.; Resconi, L. *Cryst. Growth Des.* **2009**, *9*, 165−176.
(21) De Rosa, C.; Auriemma, F. *Lect. Notes Phys.* **2007**, *714*, 345−371.
(22) Luciani, L.; Seppälä, J.; Löfgren, B. *Prog. Polym. Sci.* **1988**, *13*, 37−62.
(23) De Rosa, C.; Auriemma, F.; Resconi, L. *Angew. Chem., Int. Ed.* **2009**, *48*, 9871−9874.
(24) Luciani, L.; Seppälä, J.; Löfgren, B. *Prog. Polym. Sci.* **1988**, *13*, 37−62.
(25) Natta, G.; Corradini, P.; Bassi, I. *Nuovo Cimento Suppl.* **1960**, *1*, 52−67.
(26) Holland, V. F.; Miller, R. T. *J. Appl. Phys.* **1964**, *35*, 3241−3248.
(27) Goldbach, G.; Peitscher, G. *Polym. Lett.* **1968**, *6*, 783−788.
(28) Nakafuku, C.; Miyaki, T. *Polymer* **1983**, *24*, 141−148.
(29) Turner-Jones, A. *Polymer* **1966**, *7*, 23−59.
(30) Boor, J. Jr; Mitchell, J. C. *J. Polym. Sci.: Part A* **1963**, *1*, 59−84.
(31) Danusso, F.; Gianotti, G. *Makromol. Chem.* **1963**, *61*, 139−156.
(32) Azzurri, F.; Flores, A.; Alfonso, G. C.; Baltá Calleja, F. J. *Macromolecules* **2002**, *35*, 9069−9073.
(33) Azzurri, F.; Flores, A.; Alfonso, G. C.; Sics, I.; Hsiao, B. S.; Baltá Calleja, F. J. *Polymer* **2003**, *44*, 1641−1645.
(34) Zhang, B.; Yang, D.; Yan, S. *J. Polym. Sci., Part B: Polym. Phys.* **2002**, *40*, 2641−2645.
(35) Yamashita, M.; Ueno, S. *Cryst. Res. Technol.* **2007**, *42*, 1222−1227.
(36) De Rosa, C. D.; Auriemma, F.; Ballesteros, O. R.; Esposito, F.; Laguzza, D.; Girolamo, R. D.; Resconi, L. *Macromolecules* **2009**, *42*, 8286−8297.
(37) Jiang, Z. Y.; Sun, Y. Y.; Tang, Y. J.; Lai, Y. Q.; Funari, S. S.; Gehrke, R.; Men, Y. F. *J. Phys. Chem. B* **2010**, *114*, 6001−6005.
(38) Miyoshi, T.; Hayashi, S.; Imashiro, F.; Kaito, A. *Macromolecules* **2002**, *35*, 2624−2632.
(39) Lotz, B.; Thierry, A. *Macromolecules* **2003**, *36*, 286−290.
(40) Nakamura, K.; Aoike, T.; Usaka, K.; Kanamoto, T. *Macromolecules* **1999**, *32*, 4975−4982.
(41) Maruyama, M.; Sakamoto, Y.; Nozaki, K.; Yamamoto, T.; Kajioka, H.; Toda, A.; Yamada, K. *Polymer* **2010**, *51*, 5532−5538.
(42) Acierno, S.; Grizzuzi, N.; Winter, H. H. *Macromolecules* **2002**, *35*, 5043−5048.
(43) Fu, Q.; Heck, B.; Strobl, G.; Thomann, Y. *Macromolecules* **2001**, *34*, 2502−2511.
(44) Men, Y. F.; Rieger, J.; Homeyer, J. *Macromolecules* **2004**, *37*, 9481−9488.
(45) Chau, K. W.; Yang, Y. C.; Geil, P. H. *J. Mater. Sci.* **1986**, *21*, 3002−3014.
(46) Al-Hussein, M.; Strobl, G. *Macromol. Symp.* **2004**, *214*, 231−240.
(47) Jiang, S. D.; Duan, Y. X.; Li, L.; Yan, D. D.; Chen, E. Q.; Yan, S. K. *Polymer* **2004**, *45*, 6365−6374.
(48) Marigo, A.; Marega, C.; Cecchin, G.; Collina, G.; Ferrara, G. *Eur. Polym. J.* **2000**, *36*, 131−136.
(49) Fujiwara, Y. *Polym. Bull.* **1985**, *13*, 253−258.
(50) Kopp, S.; Wittmann, J. C.; Lotz, B. *J. Mater. Sci.* **1994**, *29*, 6159−6166.
(51) Armeniades, C. D.; Baer, E. *J. Macromol. Sci., Part B* **1967**, *1*, 309−334.
(52) Li, L.; Liu, T.; Zhao, L.; Yuan, W. K. *Macromolecules* **2009**, *42*, 2286−2290.
(53) Shi, J. Y.; Wu, P. Y.; Li, L.; Liu, T.; Zhao, L. *Polymer* **2009**, *50*, 5598−5604.
(54) Tanaka, A.; Sugimoto, N.; Asada, T.; Onogi, S. *Polym. J.* **1975**, *7*, 529−537.
(55) Sawai, D.; Anyashiki, T.; Nakamura, K.; Hisada, N.; Ono, T.; Kanamoto, T. *Polymer* **2007**, *48*, 363−370.
(56) Samon, J. M.; Schultz, J. M.; Hsiao, B. S.; Wu, J.; Khot, S. *J. Polym. Sci., Part B: Polym. Phys.* **2000**, *38*, 1872−1882.
(57) Kaszonyiova, M.; Rybnikar, F.; Geil, P. H. *J. Macromol. Sci., Phys.* **2004**, *B43*, 1095−1114.
(58) Schaffhauser, R. J. *J. Polym. Sci., Part B: Polym. Lett.* **1967**, *5*, 839−841.
(59) Goldbach, G. *Angew. Makromol. Chem.* **1973**, *29*, 213−227.
(60) Yang, Y. C.; Geil, P. H. *Makromol. Chem.* **1985**, *186*, 1961−1978.
(61) Bowden, P. B.; Jukes, J. A. *J. Mater. Sci.* **1972**, *7*, 52−63.
(62) Wu, J. B. C.; Li, J. C. M. *J. Mater. Sci.* **1972**, *11*, 434−444.
(63) Bowden, P. B.; Young, R. J. *J. Mater. Sci.* **1974**, *9*, 2034−2051.
(64) Bartczak, Z.; Argon, A. S.; Cohen, R. E. *Macromolecules* **1992**, *25*, 5036−5053.
(65) Gohil, R. M.; Miles, M. J.; Petermann, J. *J. Macromol. Sci. Phys.* **1982**, *B21*, 189−201.
(66) Flory, P. J.; Yoon, D. Y. *Nature* **1978**, *272*, 226−229.
(67) Kennedy, M. A.; Peacock, A. J.; Mandelkern, L. *Macromolecules* **1994**, *27*, 5297−5310.

(68) Nitta, K.; Ishiburo, T. *J. Polym. Sci., Part B: Polym. Phys.* **2002**, *40*, 2018−2026.
(69) Pogodina, N. V.; Winter, H. H. *Macromolecules* **1998**, *31*, 8164−8172.

Macromolecules

Article

pubs.acs.org/Macromolecules

Primitive Chain Network Simulation of Elongational Flows of Entangled Linear Chains: Stretch/Orientation-induced Reduction of Monomeric Friction

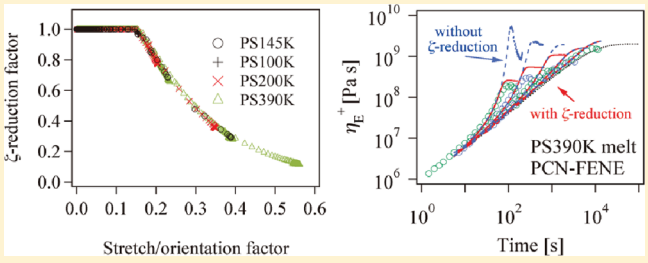
Takatoshi Yaoita,[†,‡,⊥] Takeharu Isaki,[‡] Yuichi Masubuchi,[†] Hiroshi Watanabe,[†,*] Giovanni Ianniruberto,[§] and Giuseppe Marrucci[§]

[†]Institute for Chemical Research, Kyoto University, Kyoto 611-0011, Japan

[‡]Material Science Laboratory, Mitsui Chemicals Inc., Chiba 299-0265, Japan

[§]Dipartimento di Ingegneria Chimica, Università "Federico II", P. le Tecchio 80, 80125 Napoli, Italy

ABSTRACT: Well-entangled monodisperse linear polystyrene melts exhibit monotonic thinning of the steady state elongational viscosity with increasing the strain rate $\dot{\varepsilon}$ even beyond the Rouse relaxation frequency, τ_R^{-1}. This behavior is quite different from the thinning followed by hardening at $\dot{\varepsilon} > \tau_R^{-1}$ observed for entangled semidilute solutions. We attempt to elucidate the molecular origin of this difference by focusing on the concept of stretch/orientation-dependent monomeric friction ζ recently proposed by Ianniruberto and co-workers. Specifically, literature data of the stress relaxation after cessation of transient elongational flow, reported for both PS melts and solutions, are analyzed to evaluate the stretch/orientation-dependent decrease of ζ. In our working hypothesis, ζ is expressed as a function of the factor $F_{so} = \tilde{\lambda}^2\overline{S}$, where $\tilde{\lambda}$ is the normalized stretch ratio of entangled subchains defined with respect to the fully stretched state, and $\overline{S}$ is an average orientational anisotropy of the components (polymer plus solvent if any) in the system. The factor F_{so} was estimated from the stress decay data after flow cessation. The resulting functional form of $\zeta(F_{so})$ was then used in the primitive chain network (PCN) simulation including finite extensible nonlinear elasticity (FENE) to examine the elongational behavior of melts and solutions. For melts the simulation indicates that ζ decreases significantly under fast elongation because the entangled subchains are short and approach the fully stretched (and fully oriented) limit rather easily. Hence, the steady elongational viscosity η_E follows this decrease of ζ to exhibit the monotonic thinning even at $\dot{\varepsilon} > \tau_R^{-1}$. In contrast, for solutions, the simulated η_E exhibits thickening at $\dot{\varepsilon} > \tau_R^{-1}$ because the average anisotropy $\overline{S}$ is governed by the solvent and remains small, thus overwhelming the increase of the subchain stretch $\tilde{\lambda}$. The simulated results proved to be in satisfactory agreement with the experiments.



1. INTRODUCTION

The molecular mechanisms responsible for the viscoelastic behavior of entangled polymeric liquids under fast uniaxial extensional flow have not been fully elucidated yet. For example, the strain-rate ($\dot{\varepsilon}$) dependence of the steady state uniaxial elongational viscosity η_E is quite different for melts[1−3] and solutions:[4−6] η_E of polystyrene (PS) solutions[4−6] decreases with increasing $\dot{\varepsilon}$ up to the equilibrium Rouse relaxation frequency τ_R^{-1} and then increases at higher $\dot{\varepsilon}$ when the entangled subchains begin to be stretched. In contrast, for PS melts,[1−3] η_E keeps decreasing monotonically even at $\dot{\varepsilon} > \tau_R^{-1}$.

The behavior of the semidilute solutions, thinning followed by hardening, is reasonably described by the tube model[4,5] that includes the mechanisms of chain stretch and convective constraint release[7] (CCR). However, this version of the tube model cannot describe the monotonic thinning seen for PS melts. Marrucci and Ianniruberto[8] proposed the interchain tube pressure effect (ICP) that for $\dot{\varepsilon} < \tau_R^{-1}$ predicted the −1/2 power law observed in the η_E vs $\dot{\varepsilon}$ curve of PS melts. Wagner et al.[9−11] incorporated the ICP mechanism into the version of tube model called molecular stress function (MSF) model showing that the model did not predict any upturn at $\dot{\varepsilon} > \tau_R^{-1}$ and could therefore satisfactorily describe the η_E data of PS melts. However, the tube relaxation time τ_a included in the MSF-ICP model was not deduced from a clear molecular basis and needed to be adjusted rather arbitrarily (to a value exceeding the terminal relaxation time for the case of low molecular weight PS melts.) In addition, combination of ICP with CCR, the latter being a basic mechanism in the tube model, leads to a failure in describing the η_E data.[12] Furthermore, it is not apparent why the ICP mechanism should be included in the tube model only for the case of entangled melts and not also for entangled solutions.

Considering the above uncertainty in the molecular understanding of the elongational behavior of entangled polymers, we recently conducted 3D multichain slip link simulations based

Received: November 17, 2011
Revised: February 20, 2012
Published: March 6, 2012

 © 2012 American Chemical Society dx.doi.org/10.1021/ma202525v | *Macromolecules* 2012, 45, 2773−2782

on the primitive chain network (PCN) model.[13] This model takes into account all known relaxation mechanisms, i.e., reptation,[14] thermal constraint release,[15] CCR, force balance at the entanglements, and finite extensibility (FENE), but no ICP. The simulated η_E exhibited thinning followed by thickening at $\dot{\varepsilon} > \tau_R^{-1}$, which is in quantitative agreement with the data for solutions but not for melts. Kushwaha and Shaqfeh[16] reported that their multichain slip link simulation also resulted in thickening at high strain rates under planar extensional flow.

It so appears that further improvement is necessary for the PCN-FENE simulation to describe the elongational behavior of both solutions and melts in a consistent way. In this study, we focus on the stretch/orientation-induced reduction of the monomeric (actually Kuhn-segment's) friction ζ proposed by Ianniruberto et al.[17] and incorporate this mechanism in the PCN-FENE simulation. The molecular basis of the proposed mechanism is the notion that elongated objects show a reduced (anisotropic) friction when roughly parallel to one another with respect to the randomly oriented state. Indeed, Uneyama et al.[18] analyzed the anisotropic reduction of ζ of a dumbbell model under fast shear flow to show that the viscoelastic relaxation accelerates in fast shear due to friction reduction but the end-to-end vector fluctuation time remains constant, in agreement with the dielectric response. Hua and Yang[19] also considered a decrease of ζ in fast flows, though induced in their case by a reduction of the entanglement density due to CCR. However, the prediction of the hardening of η_E at $\dot{\varepsilon} > \tau_R^{-1}$ remained unaltered.

In our approach, we assume as a working hypothesis that ζ is not affected by the entanglement density but depends only on a stretch/orientation parameter, $F_{so} = \tilde{\lambda}^2\overline{S}$, where $\tilde{\lambda}$ $(= \lambda/\lambda_{max})$ is a reduced stretch ratio of the entangled subchain defined with respect to the fully stretched limit of λ approaching λ_{max}, and $\overline{S}$ is an average orientational anisotropy of the components (polymer plus solvent) in the system. The flow-induced anisotropic decrease of the friction could result in a tensorial form of the friction coefficient,[17,18] but in this study we approximate this coefficient by a scalar quantity, ζ. In order to deduce the dependence of ζ on F_{so}, we analyze the tensile stress data of PS melts[20] and solutions[5] after cessation of transient uniaxial elongational flow, and evaluate this dependence from the data[5,20] of *initial* stress decay. Such a decay reflects the Rouse-like chain retraction with the (possibly reduced) monomeric friction $\zeta(F_{so})$, where F_{so} is the stretch/orientation parameter reached during the elongational start up just before the flow cessation.

The function $\zeta(F_{so})$ is then used in the PCN-FENE simulation to examine the elongational behavior of PS melts and solutions. It will be shown that the simulated η_E of PS melts exhibits monotonic thinning because the entangled subchains in PS melts are short, and approach the fully stretched and fully oriented limit rather easily. For this case, the reduction of ζ overwhelms the increase of the subchain tension, giving rise to a monotonic thinning of η_E. In contrast, for the semidilute solutions, the simulated η_E exhibits thinning followed by thickening at high $\dot{\varepsilon}$ because the average orientational anisotropy is governed by the solvent and remains small. This effect overwhelms the increase in chain stretch and maintains a small value of the stretch/orientation parameter F_{so}, thus keeping the friction coefficient close to the equilibrium value.

Before closing the paper we will also report on PCN-FENE simulation for PS melts under shear flow in order to show that ζ remains constant, i.e., that the friction reduction has no effect on the shear viscosity at experimentally accessible conditions.

2. RESULTS AND DISCUSSION

2.1. Working Hypothesis of Stretch/Orientation-Induced Reduction of Friction. The frictional interaction in a melt should weaken when the entangled subchains are stretched and oriented, and overlapping between Kuhn segments is effectively reduced. Conversely, in polymer solutions, since the solvent molecules relax almost instantaneously, the solvent−polymer frictional interaction is expected to be weakly affected by the subchain stretch and orientation, as discussed by Ianniruberto et al.[17] For the assumed decrease of the monomeric friction ζ, we may naturally choose the fully stretched and fully oriented state of the whole system (polymer plus solvent if any) as the reference state, where the friction attains the minimum value. Thus, as a working hypothesis, we take ζ to be a function of a stretch/orientation parameter F_{so} defined with respect to this reference state:

$$\zeta = \zeta(F_{so}) \quad \text{with} \quad F_{so} = \tilde{\lambda}^2\overline{S} \quad \text{and} \quad \tilde{\lambda} = \lambda/\lambda_{max} \qquad (1)$$

Here, λ is the (average) subchain stretch ratio defined with respect to the equilibrium state, $\tilde{\lambda}$ is the reduced stretch ratio normalized to the fully stretched state ($\lambda = \lambda_{max}$), and $\overline{S}$ is a weighted average orientational anisotropy of the components (polymer and solvent) in the system. Since the solvent stays isotropic under all conditions of our interest, $\overline{S}$ is assumed to be related to the anisotropy of the polymer, S_P, as

$$\overline{S} = \phi_P S_P \qquad (2)$$

where ϕ_P is the polymer volume fraction, and the polymer order parameter S_P representing the anisotropy of the subchain orientation vector $\boldsymbol{u}$ is obtained from the eigenvalues of the orientation tensor $\langle \boldsymbol{uu} \rangle$ (with $\langle ... \rangle$ indicating the ensemble average). More specifically, for uniaxial elongational flows S_P is given by $S_P = \langle u_x^2 \rangle - \langle u_y^2 \rangle$, where u_x, u_y are components parallel and perpendicular to the stretching direction, respectively. In shear flows, S_p is obtained from the eigenvalues associated with the two eigenvectors in the shear plane (see later).

The choice of $\tilde{\lambda}^2\overline{S}$ as the stretch/orientation parameter is suggested by the fact that $\tilde{\lambda}^2\overline{S}$ somehow measures the "monomer" orientation in the elongation direction, where by monomers we mean both the Kuhn segments of the polymer and the solvent molecules. Indeed, the subchain stretch $\tilde{\lambda}$ becomes unity when all Kuhn segments within the subchains are fully aligned to the subchain orientation $\boldsymbol{u}$, and the order parameter S_P of the polymer subchains becomes unity when the subchains themselves are fully oriented to the elongation direction. Of course, in the case of solutions $\overline{S}$ is never unity.

2.2. Overview of Stress Data after Cessation of Elongational Flow. The possible decrease of ζ due to chain stretch can be most clearly detected from data of the tensile stress σ_E^- after cessation of fast uniaxial elongational flow. The initial decay of σ_E^- due to Rouse-like chain retraction reflects relaxation of the stretched/oriented conformation of the entangled subchains reached *just before* the flow cessation, and it can then be used to verify whether or not ζ has been affected by the flow-induced stretch/orientation of the subchains. Furthermore, the stretch/orientation parameter F_{so} on which ζ has been assumed to depend is reflected in the σ_E^- data just before the flow cessation. On the basis of these

dx.doi.org/10.1021/ma202525v | Macromolecules 2012, 45, 2773−2782

arguments, we now examine literature data of stress before and after cessation of fast elongational flows.

Figure 1 shows the σ_E^- data of monodisperse linear PS melt (M = 1.45 × 10^5; PS145K) at 120 °C reported by Nielsen et al.[20] These data were measured after cessation of elongational flow in the transient hardening regime at strain rates $\dot{\varepsilon}$ = 0.001, 0.003, 0.01, and 0.03 s^{-1}; the flow time was chosen to achieve the same macroscopic Hencky strain for all rates, i.e., ε_{flow} = 3.0 (elongation ratio =20.1). The Rouse relaxation time of the chain is $\tau_R \cong 1.0 \times 10^3$ s,[20] and the Weissenberg number based on τ_R is $Wi_R \cong$ 1, 3, 10, and 30 for those $\dot{\varepsilon}$ values. In the experiments, the σ_E^- value immediately after the flow cessation is not completely free from artifacts such as the shock (vibration) of the stretching device as well as inertia. Thus, in Figure 1, the $\sigma_E^-(t)$ data are normalized by the data at short time (but still long enough to erase the effect of those artifacts), namely 1 s ($\ll \tau_R$), and plotted against the time t after the flow cessation. These $\sigma_E^-(t)/\sigma_E^-(1)$ data unequivocally allow us to examine the effect on the stress decay behavior of the elongational rate $\dot{\varepsilon}$ that existed before flow cessation.

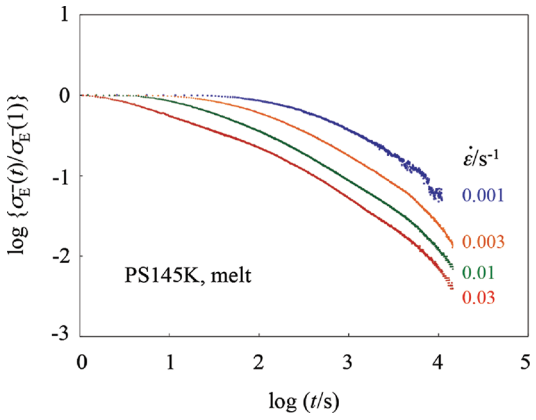


Figure 1. Stress decay data of PS145K melt[20] at 120 °C after cessation of elongational flow (up to ε_{flow} = 3). Numbers indicate the strain rate.

Figure 1 clearly demonstrates that the increase of $\dot{\varepsilon}$ (>1/ τ_R) results in an acceleration of the decay of the $\sigma_E^-(t)/\sigma_E^-(1)$ ratio, particularly at short times. For the highest $\dot{\varepsilon}$ (= 0.03 s^{-1}), an appreciable decay not seen at low $\dot{\varepsilon}$ starts at a very short time ($t \cong$ 2 s). These results already lend qualitative support to the mechanism of stretch/orientation-induced ζ-reduction. However, the finite extensibility (that leads to strain-hardening of the subchains) also contributes to this rapid decay at large $\dot{\varepsilon}$. Thus, a quantitative evaluation of the magnitude of the ζ-reduction requires a detailed analysis of the $\sigma_E^-(t)/\sigma_E^-(1)$ data, as discussed in the following.

To begin with, the terminal relaxation attributable to reptation typically observed in linear viscoelasticity should also dominate the nonlinear $\sigma_E^-(t)/\sigma_E^-(1)$ data at long times. This can indeed be observed in Figure 1 where all curves become roughly parallel to one another at long t. Figure 2 confirms that the terminal relaxation process, occurring well after the Rouse-like chain retraction process, is insensitive to the pre-elongational rate $\dot{\varepsilon}$. Indeed, Figure 2 shows that the normalized ratio $h_E^{-1}\{\sigma_E^-(t)/\sigma_E^-(0)\}$ for various $\dot{\varepsilon}$ can be superposed at long times with an adequate choice of the damping function h_E (with the data for $\dot{\varepsilon}$ = 0.001 s^{-1} being used as the reference). This time-rate separability is analogous to the time-strain separability[14] under step strains.

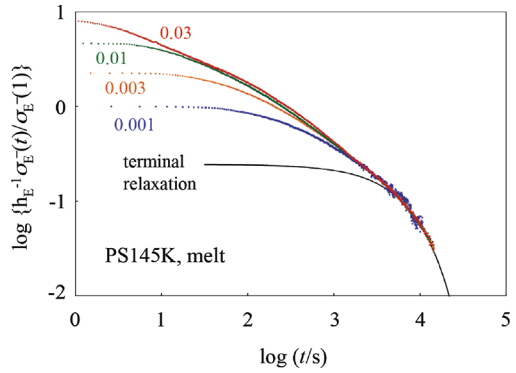


Figure 2. Test of time-rate factorability at long t for the stress decay data reported in Figure 1. Numbers indicate the strain rate.

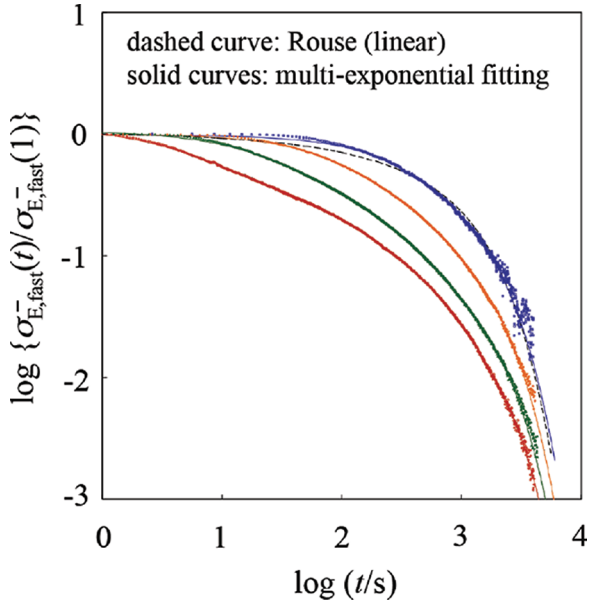


Figure 3. Same data as in Figure 1 but after subtraction of the terminal relaxation. Solid curves are the result of fitting with a sum of exponential relaxation modes (see Table 1). Dashed curve is the Rouse relaxation curve of linear viscoelasticity, eq 3 with t_{flow} = 3 × 10^3 s.

Data at long times in Figure 2 are well fitted by the single exponential $\{\sigma_E^-(t)/\sigma_E^-(1)\}_{terminal}$ = 0.245exp($-t/\tau_d$) with τ_d = 6.8 × 10^3 s. As can be noted from Figure 2, the terminal relaxation process somewhat contributes to the $\sigma_E^-(t)/\sigma_E^-(1)$ data even at short t, in particular for the case of the smallest $\dot{\varepsilon}$ = 0.001 s^{-1}. We need to subtract this contribution from the $\sigma_E^-(t)/\sigma_E^-(1)$ data for accurate examination of the fast relaxation process (Rouse-like chain retraction). The $\sigma_{E,fast}^-(t)/\sigma_{E,fast}^-(1)$ ratio for the *fast* relaxation process obtained after this subtraction is shown in Figure 3 together with the Rouse relaxation curve of *linear viscoelasticity* after flow cessation (dashed curve), the latter being straightforwardly obtained from the constitutive equation of the Rouse model[14] as:

$$\frac{\sigma_{Rouse}^-(t)}{\sigma_{Rouse}^-(1)} = Q\sum_{p=1}^{N} g_p^R \exp\left(-\frac{p^2 t}{\tau_R}\right) \quad \text{with}$$

$$g_p^R = \frac{1}{p^2}\left\{1 - \exp\left(-\frac{p^2 t_{flow}}{\tau_R}\right)\right\} \qquad (3)$$

dx.doi.org/10.1021/ma202525v | Macromolecules 2012, 45, 2773−2782

Equation 3 has been used for comparison with the data at the slowest rate, $\dot{\varepsilon} = 0.001\ s^{-1}$, for which the flow duration is $t_{flow} = 3 \times 10^3$ s.[20] In eq 3, we have used $\tau_R = 10^3$ s,[20] while Q is a normalization factor ensuring that the ratio $\bar{\sigma}_{Rouse}(t)/\bar{\sigma}_{Rouse}(1)$ is unity at $t = 1$. The number of Rouse segments per chain, N, was evaluated from the molar mass of this segment (= 850 for PS[21]). Figure 3 shows that the data for $\dot{\varepsilon} = 0.001\ s^{-1}$ are very close to the dashed curve, suggesting that no effect on the friction coefficient is present in such a slow elongational flow. It also shows that the approximation of the terminal relaxation to a single exponential (as used in the subtraction) is indeed acceptable even at short times.

As seen in Figure 3, the initial decay of the $\bar{\sigma}_{E,fast}(t)/\bar{\sigma}_{E,fast}(1)$ ratio due to chain retraction is considerably accelerated for all $\dot{\varepsilon}$ values larger than $0.001\ s^{-1}$, again lending support to the mechanism of stretch/orientation-induced ζ-reduction. Before reporting on a quantitative estimate of such a reduction (see next subsection), we here briefly consider solution data.

Stress decay data after cessation of elongational flow in the transient hardening regime have been reported also for two entangled semidilute PS solutions at room temperature.[5] The molecular weight M, concentration c, and solvent, for the two solutions respectively, are as follows: $M = 10.2 \times 10^6$ (PS10.2M), $c = 6$ wt %, dibutyl phthalate, and $M = 3.9 \times 10^6$ (PS3.9M), $c = 10$ wt %, diethyl phthalate.[5] The PS10.2M solution was elongated at the rate $\dot{\varepsilon} = 1.0\ s^{-1}$ ($Wi_R = 3.0$) up to three values of the Hencky strain $\varepsilon_{flow} = 2.0$, 2.5, and 4.0, whereas the PS3.9M solution had $\dot{\varepsilon} = 11.7\ s^{-1}$ ($Wi_R = 3.3$), and $\varepsilon_{flow} = 3.3$, 4.0, and 4.6. We analyze these data in the same way as for the PS145K melt to evaluate the tensile stress due to the fast relaxation (chain retraction) process. As before, the $\bar{\sigma}_{E,fast}(t)$ data were normalized by the stress value at a suitably short time t^* (but still long enough to erase possible artifacts): t^*=0.1s and t^*=0.05s for the PS10.2M and PS3.9M solutions, respectively. The $\bar{\sigma}_{E,fast}(t)/\bar{\sigma}_{E,fast}(t^*)$ ratios thus obtained are shown in Figures 4 and 5, respectively, together with the Rouse relaxation curve (after cessation of steady elongational flow, eq 3 with $g_p^R = 1/p^2$) properly normalized at $t = t^*$. We note that the data for the solutions are insensitive to ε_{flow} and virtually

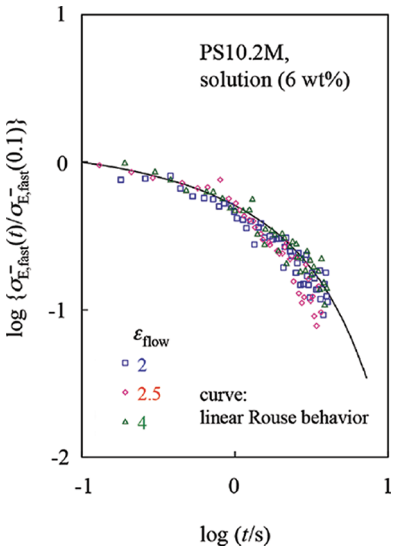


Figure 4. Stress decay during the fast relaxation process of the PS10.2M solution after cessation of elongational flow at $\dot{\varepsilon} = 1.0\ s^{-1}$. The curve is eq 3 with $g_p^R = 1/p^2$.

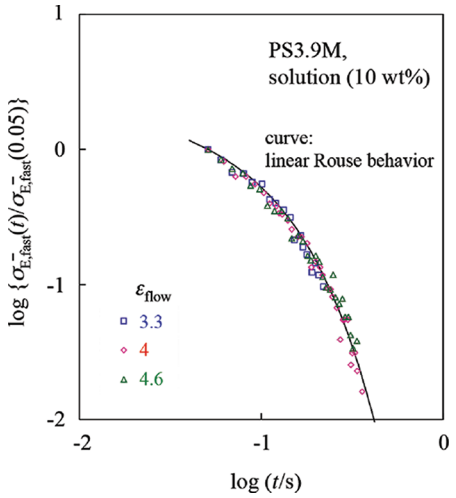


Figure 5. Stress decay during the fast relaxation process of the PS3.9M solution after cessation of elongational flow at $\dot{\varepsilon} = 11.7\ s^{-1}$. The curve is eq 3 with $g_p^R = 1/p^2$.

superpose to the Rouse curve. It so appears that the fast relaxation process of the solutions does not exhibit the nonlinear acceleration observed for the melt, despite the fact that the data for solutions and melts covered similar values of Wi_R (~3) and ε_{flow} (~3). This result implies that the stretch/orientation-induced ζ-reduction is negligible for solutions under the experimental conditions examined.

2.3. Evaluation of the Stretch/Orientation-Induced Reduction of the Friction Coefficient. Going back to the PS145K melt case, we observe that the fast relaxation data reported in Figure 3 for different $\dot{\varepsilon}$'s also appear to lie parallel to one another at long times. The time-rate separability is then examined in Figure 6a, where those data are reduced by a suitable damping function $h_{E,fast}$ and semilogarithmically plotted against time. All data sets show unambiguously the same "terminal" relaxation time τ_1 (reciprocal of the slope in the semilogarithmic plot at long times), and hence satisfy the separability. In addition, τ_1 (=1.1×10^3 s) agrees well with the Rouse time of PS145K, $\tau_R \cong 1.0 \times 10^3$ s, reported by Nielsen et al.[20] This result reveals that at times of the order of τ_R the friction coefficient is the same as at equilibrium, which indeed is reasonable because any possible effect of chain stretch has relaxed over that time scale. It now remains to analyze the behavior at shorter times where time-rate separability does not hold, as shown in Figure 6a and even more clearly in Figure 3.

At first sight, one may be tempted to evaluate the magnitude of the acceleration due to decrease of the friction coefficient from the initial stress decay rate. However, this evaluation method is not adequate because of the multimode nature of the relaxation at short times. The initial stress decay rate changes even for Rouse relaxation in the linear range: Indeed, although the mode relaxation times τ_R/p^2 are fixed quantities in such a case, the mode intensities g_p^R change with t_{flow} (see eq 3).

We therefore need a multimode analysis of the curves in Figures 3 or 6a. We perform such analysis by fitting the data with a sum of exponentially decaying modes, $\Sigma_p g_p \exp(-t/\tau_p)$, where the slowest one has the relaxation time τ_1 (=1.1×10^3 s as determined in Figure 6a for all $\dot{\varepsilon}$ values), and the fastest one has the smallest relaxation time τ_p experimentally resolved for each $\dot{\varepsilon}$ value. In particular, we have applied the procedure X suggested long time ago by Sobue et al.[22] The fitting parameters (times τ and magnitudes g) are reported in Table

dx.doi.org/10.1021/ma202525v | Macromolecules 2012, 45, 2773–2782

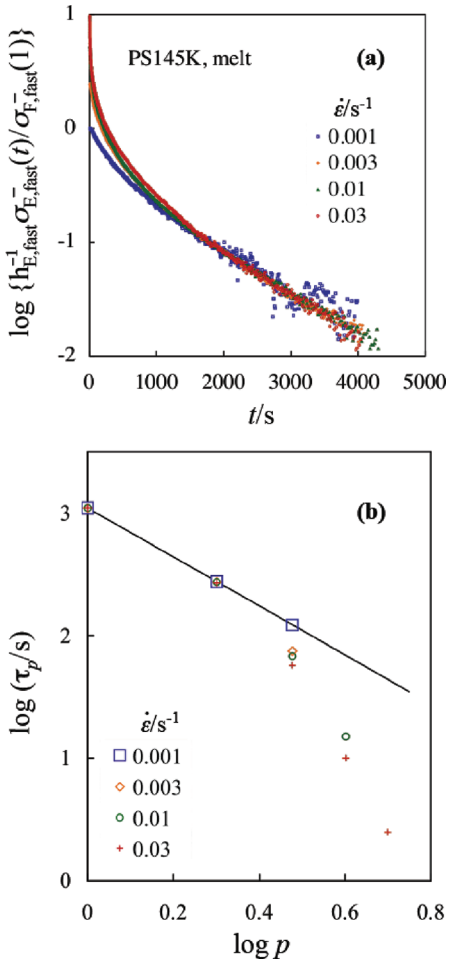


Figure 6. (a) Same data as in Figure 3 vertically shifted to test time-rate separability at long times. (b) Characteristic times of the multiexponential fit of the data in Figure 3. The straight line is eq 4.

1, and the resulting curves are drawn in Figure 3, showing an excellent fit.

The τ_p thus determined are double−logarithmically plotted against p in Figure 6b. For the smallest $\dot{\varepsilon} = 0.001$ s^{-1}, τ_p is well described by the Rouse relationship shown as a solid line in Figure 6b;

$$\tau_p = \frac{1.1 \times 10^3}{p^2} \quad \text{(in s)} \tag{4}$$

This result is in harmony with the close coincidence between the Rouse curve and the $\bar{\sigma}_{E,fast}(t)/\bar{\sigma}_{E,fast}(1)$ data for this $\dot{\varepsilon}$ shown in Figure 3. However, Figure 6b also demonstrates that τ_p for the higher order modes (with $p \geq 3$) at larger $\dot{\varepsilon}$ deviates downward from the Rouse scaling of eq 4. This deviation gives the acceleration of the higher mode relaxation due to the ζ reduction, which in turn enables us to evaluate the magnitude of this reduction, as explained later in more detail.

In Figure 6b, we also note that the τ_p's for the lower order modes remain proportional to p^{-2} and thus the relaxation of those modes is not accelerated even at large $\dot{\varepsilon}$. This result suggests that the relaxation is accelerated only when the entangled subchains are highly stretched. The stretch relaxes significantly through the higher order modes so that the acceleration vanishes in the time scale of lower order modes. This argument allows us to attribute the accelerated relaxation of the higher order modes to the stretch/orientation-induced reduction of the monomeric friction coefficient ζ (as well as to the FENE effect, as discussed below).

In particular, since all relaxation times at time t are proportional to the friction coefficient existing at the same time t, the friction coefficient just before flow cessation can be estimated from the *highest order mode resolved experimentally in the subsequent relaxation*. "Highest order mode" because all other modes become relevant only at longer times when the stretch/orientation parameter F_{so} (defined by eq 1) has at least partly relaxed toward zero. We therefore link the $\zeta(F_{so})/\zeta(0)$ ratio existing just before flow cessation to the $\tau_p(\dot{\varepsilon})/\tau_p(0)$ ratio for the highest order mode resolved experimentally (p = 3, 4, and 5 for $\dot{\varepsilon}$ = 0.003, 0.01, and 0.03 s^{-1}; cf. Figure 6b). The $\tau_p(\dot{\varepsilon})/\tau_p(0)$ ratio is represented in Figure 6b by the vertical distance between the data point and the Rouse straight line; i.e., it is the ratio between the smallest τ_p in Table 1 to the corresponding value from eq 4.

Recalling that relaxation times represent the ratio of friction coefficient to spring constant of subchains, we note that $\tau_p(\dot{\varepsilon})$ decreases not only due to the ζ reduction but also because of the FENE effect (increase of the spring constant of the subchain). Hence, the $\zeta(F_{so})/\zeta(0)$ ratio can be expressed in terms of the $\tau_p(\dot{\varepsilon})/\tau_p(0)$ ratio and the FENE factor f_{FENE} as

$$\frac{\tau_p(\dot{\varepsilon})}{\tau_p(0)} = \frac{1}{f_{FENE}} \frac{\zeta(F_{so})}{\zeta(0)} \tag{5a}$$

with

$$f_{FENE} = \frac{1}{1 - \tilde{\lambda}^2} \tag{5b}$$

where, from eq 1, $\tilde{\lambda} = \lambda/\lambda_{max}$, and λ_{max} is the maximum stretch ratio that is related to the number n of Kuhn segments between consecutive entanglements, *i.e.*:

$$\lambda_{max} = \sqrt{n} \tag{5c}$$

Notice that, because of flow, n is generally different from the equilibrium value n_0 since the number of subchains (sliplinks) decreases due to CCR.[16,23]

On the other hand, the elongational stress $\sigma_E(\dot{\varepsilon})$ just before the flow cessation is related to the stretch/orientation parameter F_{so} ($=\tilde{\lambda}^2\bar{S}$) that determines the $\zeta(F_{so})/\zeta(0)$ ratio.

Table 1. Parameters of the Multi-Exponential Relaxation

$\dot{\varepsilon}$/s^{-1}	τ_1/s	τ_2/s	τ_3/s	τ_4/s	τ_5/s	g_1	g_2	g_3	g_4	g_5
0.001	1100	275	122			0.485	0.50	0.05		
0.003	1100	275	75			0.210	0.37	0.42		
0.01	1100	273	68	15		0.096	0.23	0.36	0.37	
0.03	1100	270	57	10	2.5	0.055	0.16	0.215	0.41	0.30

dx.doi.org/10.1021/ma202525v | *Macromolecules* 2012, 45, 2773−2782

Specifically, with the decoupling approximation, σ_E can be expressed as

$$\sigma_E = 3\nu k_B T f_{FENE} \lambda^2 S_P = 3\nu_0 \frac{n_0}{n} k_B T f_{FENE} \tilde{\lambda}^2 \lambda_{max}^2 \frac{\bar{S}}{\phi_P} = \frac{3G_e n_0}{\phi_P} f_{FENE} F_{so} \quad (6)$$

Here, ν is the number density of entangled subchains and ν_0 its equilibrium value (linked by the relationship $\nu = \nu_0 n_0/n$), k_B and T are the Boltzmann constant and absolute temperature, respectively, and $G_e = \nu_0 k_B T$ is the plateau modulus in the linear viscoelastic regime. In deriving eq 6, use has been made of eqs 1, 2, and 5c.

As the f_{FENE} factor appearing in eqs 5a and 6 cannot be directly evaluated from the elongational $\sigma_E(\dot{\varepsilon})$ data, we will consider the plot of the $\tau_p(\dot{\varepsilon})/\tau_p(0)$ data (=$\{\zeta(F_{so})/\zeta(0)\}/f_{FENE}$) against reduced stress data, $\sigma_E\phi_P/(3G_e n_0)$ (=$F_{so}f_{FENE}$), by utilizing the stress value $\sigma_E(\dot{\varepsilon})$ at flow cessation and the known values of G_e, ϕ_P, and n_0. Concerning the latter quantity, for the melt n_0 is obtained from the ratio $M_e/M_{Kuhn} = 1.1 \times 10^4/720 \approx 15$,[23] while for solutions we adopt the scaling $n_0 = 15\phi_P^{-1.3}$. This plot for the PS melt[20] and the two solutions[5] is shown in Figure 7. Clearly, the ζ reduction is observed in the

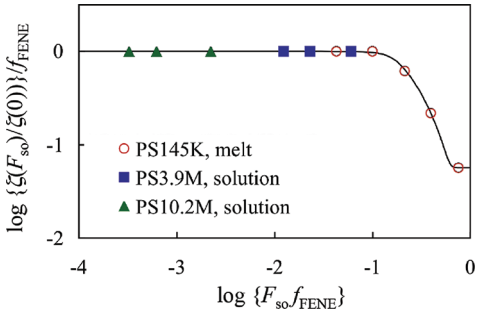


Figure 7. Plot of $\{\zeta(F_{so})/\zeta(0)\}/f_{FENE}$ (=$\tau_p(\dot{\varepsilon})/\tau_p(0)$ for the highest p available in Figure 6b for the melt, and =1 for solutions) against $F_{so}f_{FENE}$ (=$\sigma_E\phi_P/3G_e n_0$). The fitting curve is eq 7.

melt case but not for solutions under the experimental conditions examined.

In Figure 7, the solid curve shows the following purely empirical equation that fits the data:

$$\frac{\zeta(F_{so})}{\zeta(0)}\frac{1}{f_{FENE}} = \frac{1}{(1+\beta)^\gamma}\left\{\beta + \frac{1-\tanh\alpha(F'_{so} - F'^*_{so})}{2}\right\}^\gamma \quad (7a)$$

where $F'_{so} \equiv F_{so}f_{FENE}$ can be calculated from experimental quantities as

$$F'_{so} = \sigma_E\phi_p/(3G_e no) = \sigma_E\phi_p M_{Kuhn}/(3\rho RT) \quad (7b)$$

In eq 7a, F'^*_{so} (=0.14) is the threshold value for the onset of the stretch/orientation-induced reduction of ζ, while α (=20) and γ (=0.15) specify how rapidly ζ decreases with increasing F_{so}. The remaining parameter, β (=5.0×10^{-9}), specifies the asymptotic value of $\{\zeta(F_{so})/\zeta(0)\}/f_{FENE}$ (=$\{\beta/(1+\beta)\}^\gamma$ for large F_{so}).

Although eq 7 does not directly relate $\zeta(F_{so})/\zeta(0)$ to F_{so} because the f_{FENE} factor cannot be determined from the experimental data, in the PCN-FENE simulations to be considered in the next subsections both f_{FENE} and F_{so} are easily calculated at each time, thus allowing direct use of eq 7 to calculate (and then use) the friction reduction ratio $\zeta(F_{so})/\zeta(0)$.

A final comment on the empirical eq 7. In Figure 7, the data points are available only for $F_{so}f_{FENE}$ smaller than 0.75 and exhibit no leveling-off behavior. Thus, the above β value is obviously highly uncertain. However, the $F_{so}f_{FENE}$ factor never exceeded 0.8 in our simulations, and hence the uncertainty on β hardly affects the simulation results to be discussed next.

2.4. PCN-FENE Simulation of Elongational Flows. This section tests the hypothesis of the stretch/orientation-induced reduction of friction against literature data with the aid of the primitive chain network (PCN)[13] simulation. The simulation code is identical to that used in our previous companion paper[23] except for the treatment of the local friction. Polymer chains are described by a sequence of subchains having a molar mass comparable to the entanglement molecular weight M_e. The polymer chains are bound through sliplinks to form a network. Dynamics of the system is described by: 3D motion of the sliplinks, 1D monomer transport through the sliplinks, destruction of sliplinks occurring when chain ends pass sliplinks, and creation of new sliplinks when a large number of monomers (=$1.5n_0$)[23] slides out of a terminal slip link.

The kinetic equations for the 3D motion of the sliplinks and the 1D monomer transport through the sliplinks take the form

$$(\zeta_{s1} + \zeta_{s2})(\dot{\mathbf{R}} - \boldsymbol{\kappa}\bullet\mathbf{R}) = \sum_i^4 \mathbf{F}_i + \mathbf{F}_f + \mathbf{F}_B \quad (8)$$

$$\frac{\zeta_s}{\rho}\dot{n} = (F_i - F_{i-1}) + f_f + f_B \quad (9)$$

where, differently from the previous paper,[23] the subchain friction coefficient $\zeta_s = n\zeta$ accounts for changes of monomer number n in the subchains due to fluctuations in the number of entanglements, especially important in fast flows because of CCR. (In eq 8 ζ_{s1} and ζ_{s2} each refer to one of the two subchains forming the binary entanglement.) In this way, for a constant value of the monomeric friction coefficient ζ, the overall chain friction coefficient stays constant as it should (and different from the previous paper[23]). Hence, we first tested the effects of this correction and found that for a constant ζ the results of the present code are numerically close to those obtained in the previous companion paper. The important novelty here is the fact that we also allow for the monomeric friction coefficient ζ (and consequently also for the subchain friction ζ_s) to change as a consequence of the flow-induced chain orientation/stretch, as discussed in the previous sections.

The other symbols in eqs 8 and 9 have the usual meaning, i.e., $\mathbf{R}$ and $\dot{\mathbf{R}}$ are the slip link position and its time derivative, respectively, $\boldsymbol{\kappa}$ is the strain rate tensor, $\mathbf{F}_i$ the subchain elastic force (including the FENE effect at high stretch), $\mathbf{F}_f$ the osmotic force, and $\mathbf{F}_B$ the Brownian random force. In eq 9, $\dot{n}$ is the rate of change of n_i due to sliding of monomers from the (i-1)-th to the i-th subchain, ρ the local linear monomer density, F_i the subchain tension, f_f the osmotic force and f_B the random force. The Brownian forces are related to ζ_s through the

dx.doi.org/10.1021/ma202525v | Macromolecules 2012, 45, 2773−2782

Table 2. Parameters of PS samples

sample	ref	M	Z_0	n_0	T [°C]	G_0 [Pa]	τ_0 [s]	τ_R [s]
PS3.9M 10 wt % sol.	5	3.9×10^6	33	160	21	2.0×10^3	7.0×10^{-3}	3.9×10^{-1}
PS100K	3	1.0×10^5	9	15	130	2.9×10^5	5.6	2.3×10
PS200K	1	2.0×10^5	18	15	130	2.9×10^5	5.6	9.1×10
PS390K	1	3.9×10^5	35	15	130	2.9×10^5	5.6	3.5×10^2
PS200K−S	24	2.0×10^5	18	15	175	3.3×10^5	5.6×10^{-3}	9.2×10^{-2}
PS145K	20	1.45×10^5	13	15	120	2.9×10^5	140	1.2×10^3

fluctuation−dissipation theorem, i.e.,$\langle \mathbf{F}_B(t)\mathbf{F}_B(t')\rangle = 2(\zeta_{s1}+\zeta_{s2})k_BT\delta(t-t')\mathbf{I}$ ($\mathbf{I}$ = unit tensor) and $\langle f_B(t)f_B(t')\rangle = 2\zeta_s k_BT\delta(t-t')$.

In the PCN-FENE simulation the above eqs 8 and 9 are made nondimensional by using the equilibrium distance a between consecutive entanglements as the unit length, and the subchain equilibrium relaxation time $\tau_0 = \zeta_s(0)a^2/6k_BT$ as the unit time. These equations are integrated numerically using a simple Euler-type integration scheme. The variable friction coefficient $\zeta_s = n\zeta(F_{so})$ (appearing in the nondimensional equations through the ratio $n\zeta(F_{so})/n_0\zeta(0)$) is updated at intervals of unit time (i.e., every τ_0), and kept constant in between. (Notice that, although eqs 8 and 9 are integrated with a time step value much smaller than τ_0 for obvious numerical reasons, results are significant only every subchain characteristic time τ_0 in view of the coarse graining of the PCN model, which is at the level of the distance a between consecutive entanglements.) The friction ratio $\zeta(F_{so})/\zeta(0)$ is calculated through eq 7a after evaluating the stretch orientation parameter F_{so} ($=F'_{SO}/f_{FENE}$) from eq 7b. In both equations f_{FENE} is calculated from eq 5b, while the stress appearing in eq 7b is obtained from the simulation as

$$\frac{\sigma}{3G_e n_0} = \frac{Z}{Z_0} f_{FENE}\left(\frac{\mathbf{rr}}{n}\right) \tag{10}$$

where Z/Z_0 is the ratio of the current (average) subchain number per chain to its equilibrium value, and $\mathbf{r}$ is the nondimensional subchain end-to-end vector.

Except for the friction reduction extracted from relaxation data in the nonlinear range, and described by eq 7, all other basic parameters of the PS systems used in this work for the simulation and for comparison with experiments were evaluated with the method described in our previous paper,[23] i.e., through a comparison between PCN simulation results and *linear* viscoelastic data. These parameters are summarized in Table 2 together with the values of M and T. The Rouse relaxation time of the chains, τ_R, also reported in Table 2, is linked to τ_0 through: $\tau_R = (Z_0^2/2\pi^2)\tau_0$.[14] Further details of the simulation can be found in our previous work.[23]

Figure 8 compares the simulation results with the elongational stress growth and relaxation data reported for the PS145K melt[20] and for the PS3.9M 10 wt % solution.[5] (The relaxation data were used in previous sections to examine friction reduction effects.) The dashed and solid curves respectively indicate the results of the PCN-FENE simulation without and with the orientation/stretch-induced reduction of ζ. Here we omit the data for $\dot{\varepsilon} > 1/\tau_0$.

For the PS145K melt (left panel of Figure 8), the simulation with a *constant* ζ (dashed curves) clearly overestimates the viscosity data. Furthermore, the simulated viscosity at flow cessation, $\eta_E^{cessation}$, increases with increasing $\dot{\varepsilon}$, whereas the experiments show the opposite trend. This overestimation has been observed also in our previous work[23] for the steady

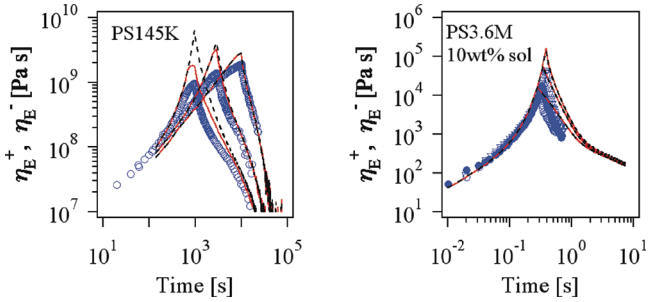


Figure 8. Viscosity growth and relaxation on start-up and cessation of uniaxial elongational flow for PS145K melt at 120 °C (left) and PS3.6M 10 wt % solution at 21 °C (right). Strain rates for PS145K are 0.001, 0.003, and 0.0003 s^{-1} from left to right and the maximum strain at the flow cessation is 3.0. Strain rate for PS3.6M solution is 11.7 s^{-1} and the maximum strains at the flow cessation are 3.3, 4.0, and 4.6 from left to right. Dashed and solid (red) curves, respectively, indicate the results of PCN-FENE simulation without and with the stretch/orientation-induced reduction of friction. Experimental data taken from ref 20 (for PS145K melt) and ref 5 (for PS3.6M solution) are shown with symbols.

elongational viscosity at $\dot{\varepsilon} > 1/\tau_R$. In contrast, the simulation results with the stretch/orientation-induced reduction of ζ (solid curves) are much closer to the data and reproduce the decrease of $\eta_E^{cessation}$ with increasing $\dot{\varepsilon}$ (for $\dot{\varepsilon} > 1/\tau_R$), which lends some support to the hypothesis of the ζ reduction.

For the PS3.9M 10 wt % solution (right panel of Figure 8), the simulation results come out insensitive to the ζ reduction mechanism because, due to a low polymer concentration, the average orientation $\bar{S} = \phi_P S_P$ is small and, at the same time, the maximum stretch ratio λ_{max} is large (so that $\tilde{\lambda}$ does not become large enough, see eq 1). The simulation results well mimic the data in this case.

Figure 9 shows the elongational viscosity growth function $\eta_E^+(t,\dot{\varepsilon})$ (up to the steady state) for PS100K, PS200K, and PS390K melts. The PCN-FENE simulation without the stretch/orientation-induced reduction of ζ (dashed curves) again overestimates the $\eta_E^+(t,\dot{\varepsilon})$ data[1,3] (symbols) at high $\dot{\varepsilon}$ ($\gg 1/\tau_R$) and for times such that the Hencky strain ε exceeds the critical value $\varepsilon_c \sim 2$, as already noted in our previous paper.[23] Incorporation of the ζ reduction in the simulation (solid curves) significantly improves agreement with data. This improvement is most clearly noticeable for the PS390K melt (bottom panel).

Figure 10 compares the simulated steady state viscosity $\eta_E(\dot{\varepsilon})$ with the data for PS100K, PS200K and PS390K melts. Since the applicable range of the simulation is limited as $\dot{\varepsilon} < 1/\tau_0$, the predictions are not available in high $\dot{\varepsilon}$ region. The viscosity obtained from the PCN simulation without FENE and ζ reduction (thin dotted curves) diverges at Wi_R ($=\dot{\varepsilon}\tau_R$) > 1, as noted in our previous paper.[23] Incorporation of FENE in the simulation (thick dashed curves) suppresses this divergence but

dx.doi.org/10.1021/ma202525v | *Macromolecules* 2012, 45, 2773−2782

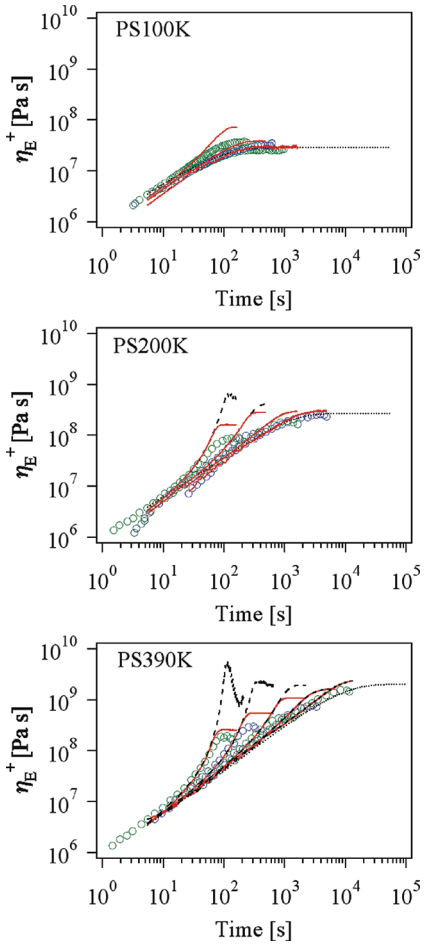


Figure 9. Uniaxial viscosity growth for PS100K, PS200K and PS390K melts at 130 °C. The strain rates are 0.003, 0.01, and 0.03 s^{-1} for PS100K, 0.001, 0.003, 0.01, and 0.03 s^{-1} for PS200K and 0.0003, 0.001, 0.003, 0.01, and 0.03 s^{-1} for PS390K. Experimental data (from refs 1 and 3) are shown with symbols. Dashed and solid (red) curves, respectively, indicate the PCN-FENE simulation results without and with the stretch/orientation-induced reduction of friction. Dotted curve is the linear viscosity growth function.

still leads to thickening of $\eta_E(\dot{\epsilon})$ at $Wi_R > 1$ where the melt data exhibit monotonic thinning. However, the PCN-FENE simulation with the stretch/orientation-induced reduction of ζ (thick solid curves) well mimics the monotonic thinning of the $\eta_E(\dot{\epsilon})$ data.

Fair agreement of simulation results with data (Figures 8−10) lends support to the molecular mechanism of orientation/stretch-induced reduction of the local friction. The data for PS melts and solutions are consistently described by this idea. However, we also note a nontrivial deviation from the data, for example, for the PS145K melt (left panel of Figure 8) and for the PS100K melt (top panels of Figures 9 and 10). These deviations may be partly attributable to the numerical integration scheme in our simulation that somewhat delays the ζ reduction with respect to the actual orientation/stretch of the subchains, and hence overestimates the transient viscosity. It is also possible that the empirical procedure adopted to determine eq 7a lacks sufficient precision. It should finally be mentioned that, of course, the starting hypothesis whereby ζ is dependent only on the parameter $F_{so} = \tilde{\lambda}^2\overline{S}$ (cf. eq 1) is open to possible revision. Indeed, ζ could be dependent on the stretch $\tilde{\lambda}$ and the orientation $\overline{S}$ separately, or on a different combination of them.

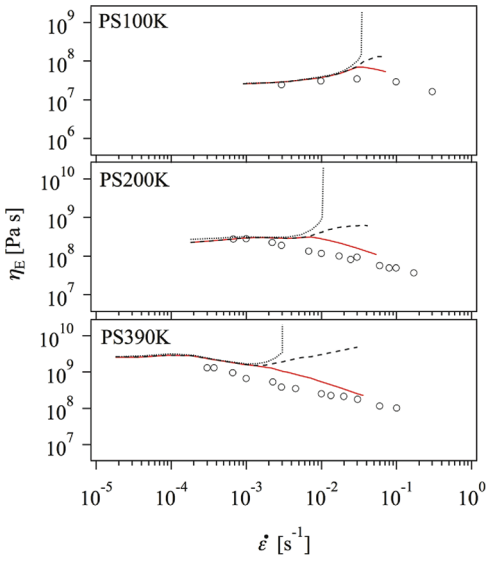


Figure 10. Steady elongational viscosity for PS100K (top), PS200K (middle) and PS390K (bottom) at 130 °C plotted against strain rate. The PCN simulation results without FENE and ζ reduction are shown with thin dotted curves. The PCN-FENE results without and with the stretch/orientation-induced reduction of friction are indicated with thick dashed and solid (red) curves, respectively. Experimental data from ref 3 are shown with unfilled circles.

Moreover ζ should be taken of tensorial form, as mentioned earlier. Modification along these lines might improve agreement between simulation and data. Nevertheless, the simple idea of a reduction of the scalar ζ due to subchain stretch/orientation led to a remarkable overall agreement between the PCN-FENE simulation and the data (Figures 8−10).

Before concluding on the extensional flows examined so far, it is informative to examine the relationship between the $\zeta(F_{so})/\zeta(0)$ ratio and the stretch/orientation parameter, $F_{so} = \tilde{\lambda}^2\overline{S}$. This relationship, underlying the plot shown in Figure 7, could not be specified on a purely experimental basis, as explained earlier. However, the PCN-FENE simulations reported in Figures 8−10 were based on evaluation of $\tilde{\lambda}$ and $\overline{S}$ at each simulation step and thus allow us to make a plot of the $\zeta(F_{so})/\zeta(0)$ ratio against F_{so} that corresponds to the plot in Figure 7. This $\zeta(F_{so})/\zeta(0)$ *vs* F_{so} plot is shown in Figure 11 for various melt systems. The results collapse on a master curve, which suggests that the $\zeta(F_{so})/\zeta(0)$ ratio is essentially (though perhaps not rigorously) a function of the single parameter F_{so}. We also note that the $\zeta(F_{so})/\zeta(0)$ ratio sharply decreases on increasing F_{so} above a threshold value ($\cong$ 0.15). This relationship between $\zeta(F_{so})/\zeta(0)$ and F_{so} is qualitatively similar to the empirical relationship between $\{\zeta(F_{so})/\zeta(0)\}/f_{FENE}$ and $F_{so}f_{FENE}$ shown in Figure 7.

It is also informative to quantify the effect of the ζ reduction on various quantities entering the PCN-FENE simulation. For this purpose, Figure 12 summarizes the viscosity reduction $\eta_E/\eta_{E,0}$, the subchain reduced square stretch $\tilde{\lambda}^2$, the average orientation $\overline{S}$, the FENE factor f_{FENE}, the entanglement density reduction Z/Z_0 (appearing in eq 10), and the $\zeta(F_{so})/\zeta(0)$ ratio, all obtained from the simulation of the PS390K melt in the steady state. These quantities are plotted against the τ_R-based Weissenberg number, Wi_R. The solid and dashed curves indicate the results with and without the ζ reduction. The $\zeta(F_{so})/\zeta(0)$ ratio starts decreasing with increasing Wi_R above unity (cf. bottom panel). This ζ reduction affects $\overline{S}$ and f_{FENE}

dx.doi.org/10.1021/ma202525v | *Macromolecules* 2012, 45, 2773−2782

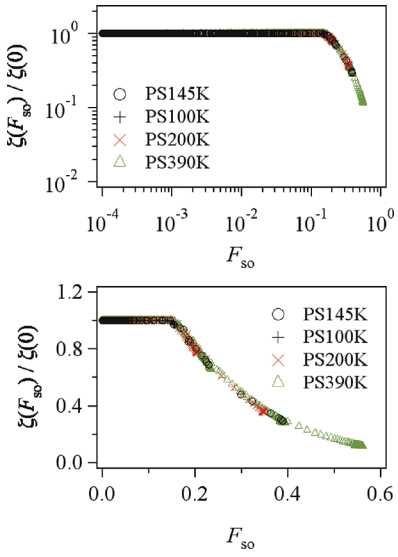


Figure 11. Reduction factor of the monomeric friction coefficient ζ plotted against the stretch/orientation parameter F_{so} obtained from the PCN-FENE simulations reported in Figures 8–10. Scales are logarithmic in the top panel and linear in the bottom panel. Different symbols indicate different PS systems.

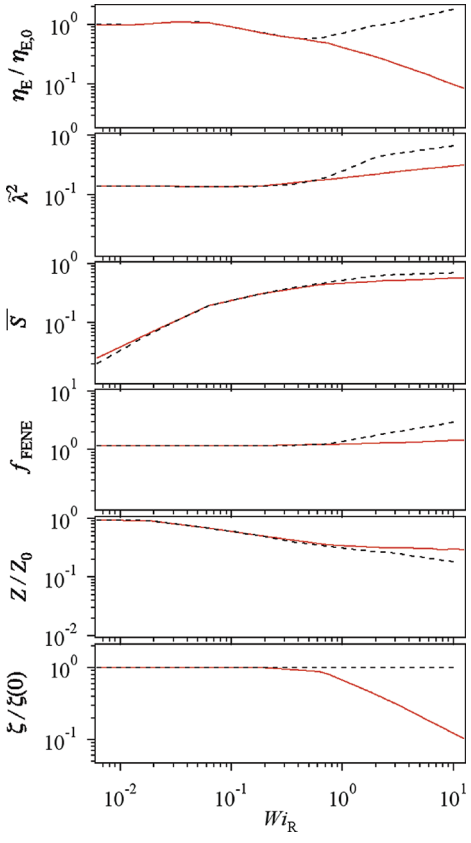


Figure 12. Factors representing the viscosity reduction $\eta_E/\eta_{E,0}$, the reduced chain stretch squared $\tilde{\lambda}^2$, the average orientation $\bar{S}$, the FENE factor f_{FENE}, and the local friction reduction $\zeta/\zeta(0)$ obtained from the PCN-FENE simulation for PS390K in the steady state. These factors are plotted against τ_R-based Weissenberg number Wi_R. The simulation results with and without the stretch/orientation-induced reduction of friction are indicated with the solid and dashed curves, respectively.

just moderately, but considerably suppresses the subchain stretch (compare the solid and dashed curves in the second top panel). The monotonic thinning of η_E results from a delicate combination of all these effects. (Note that f_{FENE} is slightly larger than unity even in the low Wi_R region because of the small n_0 value for PS melts, see Table 2.)

2.5. PCN-FENE Simulation of Shear Flows. It appears important to verify whether or not the friction reduction effect so far examined for elongational flows is also important for shear flows. In the shear case S_P is defined as the positive difference between the two eigenvalues of the orientation tensor $\langle \boldsymbol{uu} \rangle$ that correspond to the eigenvectors in the shear plane. Hence:

$$S_P = \sqrt{\{\langle u_x^2 \rangle - \langle u_y^2 \rangle\}^2 + 4\langle u_x u_y \rangle^2} \tag{11}$$

where x and y are the shear and gradient directions, respectively. All other equations to be used in the simulation remain the same as for the elongational flow case.

Figure 13 compares the PCN-FENE simulation results with and without ζ reduction (solid curves and plus symbols,

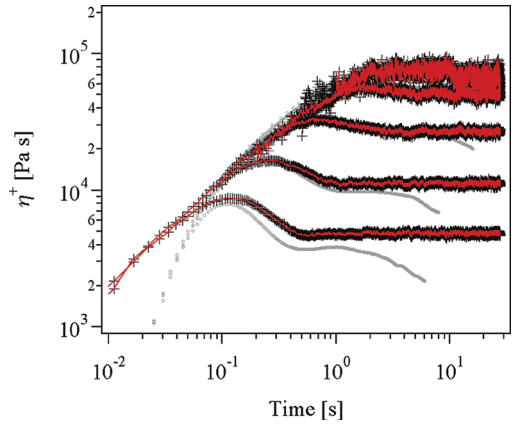


Figure 13. Shear viscosity growth function for PS200K–S. The PCN-FENE simulation results with and without the local friction reduction are shown with the solid curves (red) and the plus symbols, respectively. Data from ref 24 are shown by (gray) unfilled circles. Shear rates are 30, 10, 3, 1, and 0.3 s^{-1} from bottom to top.

respectively) to the PS200K–S melt data for the shear viscosity growth function $\eta^+(t,\dot{\gamma})$.[24] Simulations were made with the parameter values shown in Table 1, and cover the whole experimental range of Wi_R that extends up to 3.4. At such large Wi_R, ζ decreases in uniaxial elongational flow, and reduces the elongational viscosity (cf. middle panels of Figures 9 and 10). Conversely, under shear flow conditions, the simulated results with and without ζ reduction are indistinguishable, and in close agreement with the data (see Figure 13). In fact, in shear flow the stretch/orientation parameter F_{so} remains below the critical value ($\cong$ 0.15; cf. Figure 11) and thus the ζ reduction mechanism incorporated in the simulation is essentially ineffective for Wi_R up to 3.4. This result shows that the magnitude of ζ reduction is not a function of Wi_R only, but is also dependent on the type of flow. This result also shows that the previous PCN-FENE simulations for shear flow[25] conducted without accounting for the ζ reduction remain valid even after considering this new effect.

dx.doi.org/10.1021/ma202525v | Macromolecules 2012, 45, 2773–2782

3. CONCLUSIONS

We have attempted to elucidate the molecular origin of the different behavior in elongational flow between PS melts and solutions by focusing on a concept of stretch/orientation-induced decrease of the local friction ζ, as proposed by Ianniruberto and co-workers.[17] Specifically, literature data of the stress relaxation after cessation of transient elongational flow, reported for both a PS melt[20] and two PS solutions,[5] were analyzed to evaluate the magnitude of ζ reduction due to flow. In our working hypothesis, ζ was expressed as a function of an orientation/stretch factor $F_{so} = \tilde{\lambda}^2\overline{S}$, where $\tilde{\lambda}$ is the normalized stretch ratio of the entangled subchains (defined with respect to the fully stretched state), and $\overline{S}$ is an average orientational anisotropy of the components (polymer plus solvent, if any) in the system.

From the initial stress decay data on cessation of elongational flow, the $\zeta(F_{so})/\zeta(0)$ ratio was obtained as an implicit function of F_{so}. This function, showing a significant decrease of $\zeta(F_{so})$ upon increasing F_{so} (>0.15), was utilized in the primitive chain network (PCN) simulation, inclusive of the finite extensible nonlinear elasticity (FENE), to examine the elongational behavior of melts and solutions. For melts, the simulation indicated that ζ decreases significantly under fast elongational flow because the entangled subchains are short in PS melts, and therefore approach the fully stretched and fully oriented limit rather easily. As a consequence, the steady elongational viscosity η_E follows this decrease of ζ to exhibit a monotonic thinning even at $\dot{\varepsilon} > \tau_R^{-1}$. In contrast, for solutions, the simulated η_E exhibits thinning followed by thickening at $\dot{\varepsilon} > \tau_R^{-1}$ because the average anisotropy $\overline{S}$ is governed by the solvent and remains small, thereby overwhelming the increase of the subchain stretch $\tilde{\lambda}$ and limiting the increase of F_{so}, which remains smaller than 0.15. The simulated results are in satisfactory agreement with the experiments, thus suggesting that the different behavior of η_E in PS melts and solutions reflects the difference of the local orientational field (largely damped by the solvent in semidilute solutions).

Further tests for the change of local friction are clearly required, also to examine several other aspects, such as the influence of the molecular weight distribution, of branching, of a different chemistry, etc. For instance, uniaxial elongational experiments on entangled solutions of various polymer concentrations are critical for confirming the 0.15 threshold value of the F_{so} factor marking the onset of the ζ reduction effect. We are continuing our research along these directions and the results will be reported elsewhere.

AUTHOR INFORMATION

Corresponding Author

*E-mail: hiroshi@scl.kyoto-u.ac.jp.

Present Address

[⊥]Fabricated Products Development Division, Mitsui Chemicals Inc., Chiba 299−0265, Japan

Notes

The authors declare no competing financial interest.

ACKNOWLEDGMENTS

We are grateful to Dr. H. K. Rasmussen and to Dr. T. Schweizer for providing us with the extensional flow relaxation data of PS145K and the start-up shear data of PS200K−S, respectively. We are also grateful to the anonymous referees for their useful comments on the basis of which the paper has been improved.

REFERENCES

(1) Bach, A.; Almdal, K.; Rasmussen, H. K.; Hassager, O. *Macromolecules* **2003**, *36*, 5174.
(2) Luap, C.; Müller, C.; Schweizer, T.; Venerus, D. C. *Rheol. Acta* **2005**, *45*, 83.
(3) Nielsen, J. K.; Rasmussen, H. K.; Hassager, O.; McKinley, G. H. *J. Rheol.* **2006**, *50*, 453.
(4) Bhattacharjee, P. K.; Oberhauser, J. P.; McKinley, G. H.; Leal, L. J.; Sridhar, T. *Macromolecules* **2002**, *35*, 10131.
(5) Bhattacharjee, P. K.; Nguyen, D. A.; McKinley, G. H.; Sridhar, T. *J. Rheol.* **2003**, *47*, 269.
(6) Ye, X.; Larson, R. G.; Pattamaprom, C.; Sridhar, T. *J. Rheol.* **2003**, *47*, 443.
(7) Marrucci, G. *J. Non-Newtonian Fluid Mech.* **1996**, *62*, 279.
(8) Marrucci, G.; Ianniruberto, G. *Macromolecules* **2004**, *37*, 3934.
(9) Wagner, M. H.; Schaeffer, J. *J. Rheol.* **1992**, *36*, 1.
(10) Wagner, M. H.; Kheirandish, S.; Hassager, O. *J. Rheol.* **2005**, *49*, 1317.
(11) Wagner, M. H.; Rolón-Garrido, V. H. *Korea Austr. Rheol. J.* **2009**, *21*, 203.
(12) Dhole, S.; Leygue, S.; Bailly, C.; Keunings, R. *J. Non-Newtonian Fluid Mech.* **2009**, *161*, 10.
(13) Masubuchi, Y.; Takimoto, J.-I.; Koyama, K.; Ianniruberto, G.; Greco, F.; Marrucci, G. *J. Chem. Phys.* **2001**, *115*, 4387.
(14) Doi, M.; Edwards, S. *The Theory of Polymer Dynamics*: Oxford University Press: Oxford, U.K., 1986.
(15) Graessley, W. W. *Adv. Polym. Sci.* **1982**, *47*, 67.
(16) Kushwaha, A.; Shaqfeh, E. S. G. *J. Rheol.* **2011**, *55*, 463.
(17) Ianniruberto, G.; Brasiello, A.; Marrucci, G. *Proc. 7th Annu. Eur. Rheol. Conf.* **2011**, 61.
(18) Uneyama, T.; Horio, K.; Watanabe, H. *Phys. Rev. E* **2011**, *83*, 001800.
(19) Hua, C. C.; Yang, C. Y. *J. Polym. Res.* **2002**, *9*, 79.
(20) Nielsen, J. K.; Rasmussen, H. K.; Hassager, O. *J. Rheol.* **2008**, *52*, 885.
(21) Inoue, T.; Osaki, K. *Macromolecules* **1996**, *29*, 1595.
(22) Sobue, H.; Murakami, K. *Kogyo Kagaku Zasshi* **1961**, *64*, 2005.
(23) Yaoita, T.; Isaki, T.; Masubuchi, Y.; Watanabe, H.; Ianniruberto, G.; Marrucci, G. *Macromolecules* **2011**, *44*, 9675.
(24) Schweizer, T.; van Meerveld, J.; Ottinger, H. C. *J. Rheol.* **2004**, *48*, 1345.
(25) Masubuchi, Y.; Furuichi, F.; Horio, K.; Uneyama, T.; Watanabe, H.; Ianniruberto, G.; Greco, F.; Marrucci, G. *J. Chem. Phys.* **2009**, *131*, 114906.

Macromolecules

Article

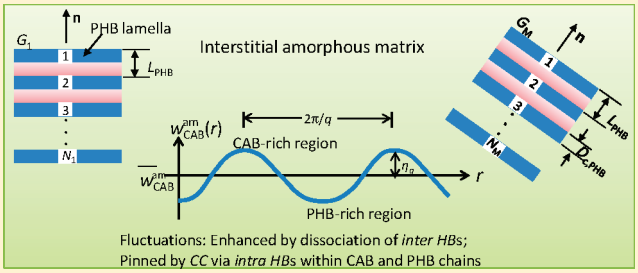
pubs.acs.org/Macromolecules

Simultaneous Synchrotron SAXS/WAXD Study of Composition Fluctuations, Cold-Crystallization, and Melting in Biodegradable Polymer Blends of Cellulose Acetate Butyrate and Poly(3-hydroxybutyrate)

Harumi Sato,* Nattaporn Suttiwijitpukdee, Takeji Hashimoto,† and Yukihiro Ozaki

Department of Chemistry, School of Science and Technology and Research Center of Environmental Friendly Polymer, Kwansei-Gakuin University, Gakuen 2-1, Sanda, Hyogo 669-1545, Japan

ABSTRACT: Self-assembly of poly(3-hydroxybutyrate) (PHB) and cellulose acetate butyrate (CAB) blends prepared by solvent casting was investigated by simultaneous synchrotron small-angle X-ray scattering (SAXS) and wide-angle X-ray diffraction as a function of temperature in a heating process of the blends. The results revealed different elemental processes occurring in three characteristic temperature regions: (1) low-T region, where cold crystallization (CC) of PHB into one-dimensional (1D) assemblies of PHB lamellar crystals occurs in the temperature (T) range $T_{cc,PHB} \leq T \leq T_{cc,CAB}$, where $T_{cc,PHB}$ and $T_{cc,CAB}$ are the onset temperature for CC in PHB and CAB, respectively; (2) crossover-T region, where partial melting/recrystallization of PHB occurs concurrently with CC of CAB in the interstitial amorphous matrix among the 1D PHB lamellar assemblies at $T_{cc,CAB} < T \leq T^*$, where T^* is a characteristic temperature close to the T at the higher melting endothermic peak of differential scanning calorimetry (DSC), $T_{m,DSC}$; and (3) high-T region, where PHB crystals melt and CAB partially melts/recrystallizes at $T > T^*$. The study also elucidated for the first time in this blend systems, to our best knowledge, the following points: (a) the existence of two glass transition temperatures (T_g's) in the amorphous matrix, with a lower T_g ($T_{g,l}$) determined by DSC and a higher T_g ($T_{g,h}$) determined from the SAXS intensity at low q (magnitude of the scattering vector) values as a function of T; (b) the evolution of the large length-scale composition fluctuations in the amorphous matrix of the blend at $T_{g,h} \leq T \leq T_{cc,CAB}$; (c) crystallization of CAB at $T > T_{cc,CAB}$ and a melting temperature for CAB crystals higher than 183 °C. The roles of intermolecular hydrogen bondings (HBs) between PHB and CAB, intramolecular HBs within PHB, and those within CAB as well as roles of the exchanges of those HBs on the self-assembling process, the composition fluctuations, and the miscibility of the blends in the amorphous phase were also clarified in the text.



1. INTRODUCTION

In this work, we aim to investigate self-assembly (including self-assembling processes, mechanisms, and structures as a whole) of poly(3-hydroxybutyrate) (PHB) and cellulose acetate butyrate (CAB) blends as a model polymer blend system in which *intra*- and *inter*-molecular hydrogen bondings (HBs) play significant roles on the self-assembly. The work concerned with the self-assembly at the mesoscopic length scale focuses on (1) cold crystallization (CC) of PHB and CAB into respective one-dimensional (1D) assemblies of crystallites which are randomly oriented in three-dimensional (3D) space, (2) large length-scale composition fluctuations built up in their amorphous phase, (3) composition-fluctuation-enhanced crystallization of PHB and CAB, and (4) crystallization-induced pinning of growth of the composition fluctuations into macroscopic phase-separation. We aim to explore also the roles of various HBs and their exchanges on the self-assembly concerned with items 1 to 4 described above.

PHB (Figure 1a) is a well-known microbially produced, biodegradable aliphatic polyester with thermoplasticity and mechanical properties similar to those of conventional synthetic polymers.[1−10] Because of its potential in environmental

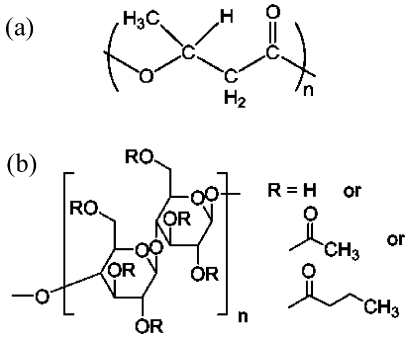


Figure 1. Chemical structures of the repeating units in (a) poly(3-hydroxybutyrate) (PHB) and (b) cellulose acetate butyrate (CAB).

Received: November 30, 2011
Revised: February 13, 2012
Published: March 8, 2012

 © 2012 American Chemical Society dx.doi.org/10.1021/ma202606y | *Macromolecules* 2012, 45, 2783−2795

conservation, many research groups have been involved in developing materials based on PHB as replacements for conventional, nonbiodegradable polymers. However, there is still a large technical barrier to realizing practical applications of PHB-based materials: PHB is rigid and brittle due to its high crystallinity. Moreover, it has a high melting point close to the temperature range where it is thermally unstable, which affects melt processability or processability around its melting temperature. Improved toughness and processability at least are thought to be crucial for practical applications of the PHB-based materials as advanced materials. Some works reported along this line will be given below.

There are several approaches to improve the physical properties of PHB-based materials, such as copolymerization and blending. Indeed, many polymers have been studied for their use as components to be blended with PHB in PHB blends, such as poly(ethylene glycol) (PEG),[11,12] poly(vinyl acetate) (PVAc),[13,14] poly(4-vinylphenol) (PVPh),[15,16] poly(vinyl alcohol) (PVA),[17] polylactide (PLLA),[18] and cellulose esters (CE).[19−24] Further numerous efforts have been made to enhance the miscibility of these blends and reduce the propensity for phase separation by using compatibilizers or introducing reactive groups to covalently link different polymer components in the blends.[25,26] The use of attractive intermolecular interactions to improve miscibility is particularly appealing, because it enables enhanced mixing of the component polymers at the molecular level.[27−29]

To further gain new insights into physical properties of PHB and its blends, we have been investigating their crystal structure, crystallization processes, and thermal behavior by means of infrared (IR) spectroscopy, differential scanning calorimetry (DSC), and wide-angle X-ray diffraction (WAXD).[30−41] We previously reported that in PHB lamellar crystals, the $-CH_3$ and $-C{=}O$ groups form a chain of $-C-H\cdots O{=}C-$ hydrogen bonds (HBs), (designated hereafter *intra* HBs of PHB) in between the two parallel helical chains.[30] Moreover, from the results of temperature-dependent IR and WAXD measurements, we concluded that the *intra* HBs stabilize the chain-folded lamellae and promote high crystallinity in PHB.[32] In addition, we recently studied the intermolecular HBs (designated hereafter *inter* HBs) of $-C-H\cdots O{=}C-$ between the $-C{=}O$ groups of PHB and the $-OH$ groups of PVPh in PHB/PVPh blends and their effect on cold crystallization (CC) and melting of PHB in the blends by using Fourier-transform IR (FTIR) spectroscopy, DSC, and WAXD.[41] We found a remarkable exchange between *inter* and *intra* HBs with increasing the PVPh content greater than the critical composition of ∼50 wt % or with decreasing crystallinity as determined by WAXD (X_c) and FTIR (f_{intra}) smaller than 30 and 20 wt %, respectively.[37]

In our previous work,[39] cellulose acetate butyrate (CAB) was selected as a hydroxyl-group-containing counter polymer for blending with PHB (Figure 1b). When CAB was blended, the crystallinity of PHB decreased; the PHB spherulites became small and imperfect.[39,40] Therefore, it is thought that the mechanical properties of PHB such as the elongation at break and toughness can be improved by blending with CAB as described in the introduction of our previous paper.[39] In addition, PHB is thermally unstable in molten state, thereby having a narrow temperature range for the melt processing. Compared with pure PHB, the lower crystallinity[39] and equilibrium melting temperature of PHB[22] in PHB/CAB blends are thought to improve the processability. Thus, the blending of PHB with CAB can offer opportunities to improve the mechanical properties and the processability. Since PHB contains $-C{=}O$ groups, and CAB contains both $-C{=}O$ and $-OH$ groups, PHB/CAB blends can have various kinds of HBs, as summarized in Table 2 in our previous report.[39] These HBs include not only *intra* HBs within PHB and *inter* HBs between PHB and CAB, as already pointed, but also *intra* HBs within CAB (including *intra* HBs between $-OH$ groups and $-O-$ (ether) groups and those between $-OH$ groups and $-C{=}O$ group within CAB). We concluded that the miscibility and the self-assembly of the blends generally depend on the relative strengths of these *intra* and *inter* HBs and exchanges among these HBs in response to external variables such as temperature and composition.[39] We also concluded that PHB/CAB and PHB/PVPh blends provide good model systems to generally study the fundamental physical science on the influence of HBs on the self-assembly of the blends.[37,39−41]

The previous study[39] explored self-assembly in PHB/CAB blends as a function of temperature in a heating process by FTIR, which directly elucidated the *intra* and *inter* HBs and their exchanges as a function of temperature (T) and weight fraction of CAB (w_{CAB}). It also indirectly elucidated the roles of the HBs and their exchanges on CC and melting of PHB via the characteristic crystalline band of PHB around 1723 cm^{-1} in the $-C{=}O$ stretching vibrational region. However, FTIR alone is not sufficient to explore the self-assembly of the blends, especially at the mesoscopic scale, although FTIR is a powerful microscopic-scale probe in directly studying the HBs.

By contrast, small-angle X-ray scattering (SAXS) directly probes the self-assembly of the blends at the mesoscopic scale, while WAXD directly probes the evolution of crystal structures and crystallinity in the blends. We anticipate that a combined SAXS/WAXD and FTIR method on the same blends specimens would directly provide fundamental information on the roles of HBs and their exchanges on the self-assembly of PHB/CAB blends.

Thus, in the present work, we studied the self-assembly of PHB/CAB blends at the mesoscopic scale by using a simultaneous synchrotron WAXD and SAXS method for the same blends as those used in the FTIR method.[39] In this paper, we report the following series of physical processes found in the order of increasing T in a heating process of the blends: (1) CC of PHB into a randomly oriented 1D assembly of PHB lamellar crystals; (2) large length-scale composition fluctuations which are built up in the amorphous matrix between the PHB lamellar assemblies; and (3) partial melting and recrystallization of PHB concurrently occurring with CC of CAB. Moreover the T-dependence of the SAXS intensities at low q's, where q is the magnitude of scattering vector $\mathbf{q}$ to be defined later in section 2.3, revealed (4) the existence of $T_{g,h}$, a glass transition temperature (T_g) higher than that observed by DSC ($T_{g,DSC}$ or $T_{g,l}$). The two T_g's, $T_{g,h}$, and $T_{g,l}$, may be essentially related to the local composition heterogeneities in the single-phase blend, which arises from large differences in the self-concentration[42,43] of the PHB and CAB segments, which in turn is attributed to the large difference in rigidity between the two kinds of segments. We would like to stress that to the best of our knowledge, findings 2−4 are reported here for the first time, which due to use of the strong incident X-ray intensity from the synchrotron undulator beamline (FSBL03XU) at SPring-8, Japan.

Table 1 lists important abbreviations used throughout the paper.

Table 1. List of Important Abbreviations

PHB: poly(3-hydroxybutyrate)

CAB: cellulose acetate butyrate

CC: cold crystallization

$T_{cc,PHB}$, $T_{cc,CAB}$: onset temperature for CC of PHB and CAB

$T_{g,h}$, $T_{g,h,SAXS}$: higher glass transition temperature of the blends measured by SAXS

$T_{g,l}$, $T_{g,DSC}$: lower glass transition temperature of the blends measured by DSC

HBs: hydrogen bondings

intra HBs: intramolecular HBs within CAB or within PHB

inter HBs: intermolecular HBs between CAB and PHB

w_{CAB}: weight fraction of CAB in the blend of PHB/CAB

"low-T region," "crossover-T region," and "high-T region": defined in section 3.2 and discussed in section 4.3.

$q_{m,PHB}$ or $q_{m,CAB}$: the magnitude of the scattering vector $\boldsymbol{q}$ at the SAXS maximum due to the long spacing of the PHB lamellae or the CAB crystallites, respectively.

L_K and $D_{c,K}$ (K = PHB or CAB): long spacing and crystallite thickness of the K-th component.

$T_{m,PHB,DSC}$: melting temperature of PHB crystals as determined by the temperature at the peak of the highest melting endotherm in DSC.

2. EXPERIMENTAL METHODS

2.1. Materials and Sample Preparation. Bacterially synthesized PHB, with number-averaged molecular weight $M_n = 2.9 \times 10^5$, and CAB, with number-averaged molecular weight $M_n = 6.5 \times 10^4$, were provided by Aldrich Chemical Corp. Inc. (St. Louis, MO). As shown in Figure 1b, CAB consists of hydroxyl groups, acetyl groups, and butyryl groups with the weight fraction of each group being 0.0089, 0.293, and 0.18 with respect to the total weight of CAB, respectively. Thus, the number of these groups per single CAB chain is $6.5 \times 10^4 \times 0.89 \times 10^{-2}/17.0 = 34.0$ for hydroxyl groups, $6.5 \times 10^4 \times 0.293/43.04 = 442$ for acetyl groups, and $6.5 \times 10^4 \times 0.18/71.1 = 165$ for butyryl groups.[39] The CAB sample used in this study was the same as that used in our previous report,[39] but different from that used in ref 40. It is important to note that these two CABs are different in the number of hydroxyl groups, acetyl groups, and butyryl groups per single CAB chain.

Pure PHB, pure CAB, and PHB/CAB blends were prepared by dissolving the prescribed amounts of powdered polymers in chloroform. The homogeneous solutions thus prepared were cast into films of about 5 mg in weight in an aluminum pan for DSC measurements. The same solutions were cast into films. The films were then stacked into films of ~0.5 mm thick in a sample cell which was sealed between two Kapton films for the simultaneous SAXS/WAXD measurements. All the prepared blend films, pure PHB films, and pure CAB films used for the DSC measurements and for the SAXS/WAXD measurements were dried at room temperature for solvent evaporation. Then all the films were put in a vacuum oven with N_2 purge at 130 °C for 9 h to completely remove residual solvent. Subsequently the PHB/CAB blends and pure CAB films were heated up to 145 °C for 1 min to remove air bubbles, and finally quenched rapidly in liquid nitrogen. On the other hand, the pure PHB films were heated up to 180 °C (above the melting temperature of PHB, 176 °C) for 1 min and quenched rapidly in liquid nitrogen. The blend film specimens, pure PHB, and pure CAB film specimens thus prepared are designated hereafter as "as-prepared films." The thermal history encountered by the as-prepared films may have caused crystallization of PHB to some extent in the as-prepared blends having w_{CAB} from 0.1 to 0.7, though the as-prepared blends films having $w_{CAB} > 0.7$ did not show any crystallinity of PHB. The as-prepared pure PHB films also showed some crystallinity, though the as-prepared pure CAB films were amorphous.

The difference in the thermal history encountered by the as-prepared PHB/CAB blend films and the as-prepared pure PHB films will give different initial states for these as-prepared films. Moreover, the difference in the sample thickness used for the DSC measurements and the SAXS/WAXD measurements also causes the difference in the thermal history, which in turn causes the difference in the initial states between the blend samples used for the DSC measurements and the SAXS/WAXD measurements and between the pure PHB samples used for the DSC measurements and the SAXS/WAXD measurements. These differences in the initial state should be taken into account, when their thermal behaviors are compared, in such a case as we compare the results shown in Figure 10 and those shown in Figure 11. All the as-prepared samples were kept below the $T_{g,l}$ before they were subjected to the DSC and SAXS/WAXD measurements.

2.2. DSC. DSC measurements were performed with a Perkin-Elmer Pyris6 DSC system (Waltham, MA) by sealing the as-prepared films in an aluminum pan, and pure indium was used as a standard material for temperature calibration of the calorimeter. The DSC thermograms were obtained in the first heating run of the as-prepared sample from −40 to +185 °C at a rate of 20 °C/min under N_2 purge. The melting temperature ($T_{m,PHB,DSC}$) of PHB was determined from the maximum of the endothermic peak in the first heating run. The T_g was measured as described in our previous report.[39]

2.3. Simultaneous SAXS and WAXD. The simultaneous SAXS and WAXD measurements were performed in the FSBL03XU undulator beamline (wavelength $\lambda = 1.0$ Å) at SPring-8, Japan. The sample-to-detector distances for the SAXS and WAXD measurements were set to 1693 and 75 mm, respectively. Dried chicken leg tendon collagen and cerium oxide powder were used as the standard references for the sample-to-detector distance corrections for SAXS and WAXD, respectively. Two-dimensional (2D) SAXS and WAXD patterns were recorded with a charge-coupled device (CCD) camera system comprising an image intensifier and a CCD detector (II+CCD; Hamamatsu Photonics, Hamamatsu, Japan) and with flat panel detector (FPD; Hamamatsu Photonics, C9728DK-10, Hamamatsu, Japan), respectively. The 2D SAXS and WAXD patterns were recorded simultaneously once every 2 s with exposure times of 0.8 and 1 s, respectively. We obtained the SAXS and WAXD profiles by circularly averaging their 2D patterns as a function of q, where $q = (4\pi/\lambda) \sin\theta$, 2θ is the scattering angle and Bragg diffraction angle for SAXS and WAXD, respectively, and λ is wavelength of the incident X-ray beam. The SAXS intensity profiles, $I_{obs}(q)$, after corrections for the absorption and empty-cell scattering, were further corrected for thermal diffuse scattering (TDS)[44,45] by assuming

$$I_{obs}(q) = Kq^{-4} + B \quad (1)$$

where B is the TDS, which is approximately independent of q over the narrow q-range covered in this experiment. The corrected scattering profile $I_c(q)$ was defined by

$$I_c(q) \equiv I_{obs}(q) - B \quad (2)$$

The value B was measured from the plot of $q^4 I_{obs}(q)$ vs q^4.

3. RESULTS

The 2D SAXS and WAXD patterns were independent of the azimuthal angle, indicating that the density fluctuations and the crystallites developed in the blends are randomly oriented in three-dimensional (3D) space. Hence, we shall present only circularly averaged SAXS and WAXD profiles in this work, as the necessary and sufficient information.

3.1. SAXS and WAXD Profiles of CAB. The WAXD profiles (Figure 2b) indicate that pure CAB is amorphous at 153 °C and crystalline at 182 °C, where the diffraction peaks at around $2\theta = 5.1°$, 6.5°, 10.0°, 11.5°, and 13.0° are ascribed to the CAB crystal structure, though the crystal structure is unidentified so far. However, its crystallinity seems to be obviously very low. CC starts to occur at $T \geq 157$ °C, as seen in the inset to Figure 2b. The small crystallinity developed could not be easily discerned with a conventional X-ray diffractometer in our laboratory and hence was carelessly overlooked in our previous work.[39] The SAXS profile at 182 °C shows a peak at around $q = 0.3$ nm^{-1}, which reflects the long spacing of the

dx.doi.org/10.1021/ma202606y | Macromolecules 2012, 45, 2783−2795

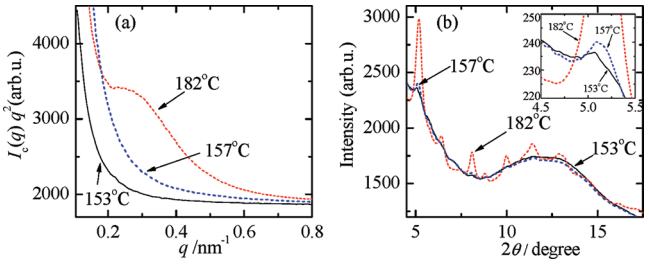


Figure 2. (a) SAXS and (b) WAXD profiles of pure CAB at 153, 157, and 182 °C.

CAB crystalline structure, while that at 157 °C shows only an excess scattering without the peak relative to that at 153 °C (see Figure 2a). The excess scattering may arise from the density fluctuations[46] developed prior to the CAB crystallization. The SAXS peak at $q \cong 0.3$ nm^{-1} and the WAXD peak at $2\theta \cong 5.1°$ will be used as markers for the CAB crystallization in the blends in the following analysis. To the best of our knowledge, this is the first report of the fact that the CAB can be crystallized above 157 °C, the presentation of which was made possible by the use of the strong incident beam from the undulator beamline at SPing-8.

3.2. Temperature Dependence of the SAXS Profiles of PHB/CAB (50/50) Blend. As shown in Figure 3a, the overall

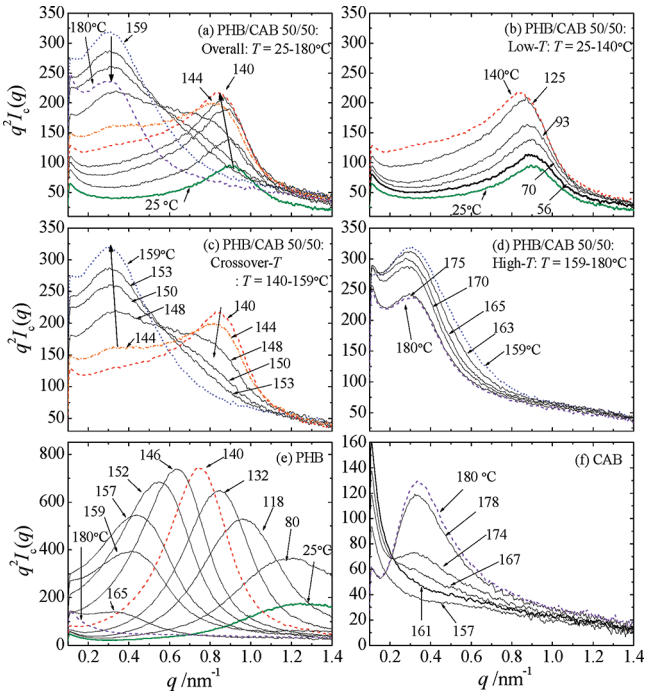


Figure 3. SAXS profiles of the PHB/CAB (50/50) blend at representative temperatures in the heating process from 25 to 180 °C: (a) overall trend, (b) trend in the low-T region from 25 to 140 °C, (c) trend in the crossover-T region from 140 to 159 °C, and (d) trend in the high-T region from 159 to 180 °C. Panels (e) and (f) show temperature dependence of SAXS profiles for pure PHB and pure CAB, respectively, as references for the blend.

SAXS profiles (corrected for the Lorentz factor, $q^2I_c(q)$) shows a T dependence that can be divided into three different regions: (b) a low temperature region from 25 to 140 °C (designated hereafter as "low-T region"), (c) a crossover region from 140 to 159 °C (designated hereafter as "crossover-T region"), and (d) a high temperature region from 159 to 180 °C (designated hereafter as "high-T region"), respectively. The overall trend is rather complex: With increasing T, the peak intensity at $q \sim 0.9$ nm^{-1} first increases in the low-T region; the peak intensity at $q \sim 0.9$ nm^{-1} decreases and disappears but, on the contrary, the peak intensity at $q \sim 0.3$ nm^{-1} appears and increases in the crossover-T region; the peak intensity at $q \sim 0.3$ decreases in the high-T region.

Comparisons of the observed profiles between pure CAB (Figure 3f) and the blend (Figure 3b–d) reveal that the peak at $q \sim 0.3$ nm^{-1} in the blend (Figure 3c,d) is primarily assigned to the long spacing of the CAB crystals developed through the CC of CAB from the amorphous CAB chains in the blend. Similar comparisons between pure PHB (Figure 3e) and the blend (Figure 3b,c) reveal that the peak at $q \sim 0.9$ nm^{-1} is due to the long spacing of the PHB lamellar crystals.

In the low-T region (Figure 3b), the peak intensity increases and the peak shifts to lower q values, which indicates (1) growth of the PHB lamellar assemblies in terms of the number of assemblies (or grains) G_M and the numbers of the lamellae N_l and N_M within the grains G_l and G_M, respectively, and (2) increase in interlamellar spacing L_{PHB}, respectively (see Figure 8 to be discussed in detail later).

In the crossover-T region (Figure 3c), the peak intensity at $q \cong 0.9$ nm^{-1} decreases and the q value at the peak ($q_{m,PHB}$) also decreases with T, suggesting partial melting (and possibly recrystallization) of the PHB lamellae and lamellar thickening with increasing T. In addition, the peak intensity at $q \cong 0.3$ nm^{-1} increases, indicating that CC of CAB results in the growth of assemblies of CAB crystals with respect to an increasing number of the CAB assemblies G_{CAB} and the CAB crystals N_{CAB} within a given CAB assembly, and a slight increase in its long spacing L_{CAB}, as indicated by the slight decrease in the q value at the peak ($q_{m,CAB}$) (see Figure 12, to be discussed in detail later). It is important to note that the peak intensity at $q \cong 0.3$ nm^{-1} for the blend start to increase with T at lower T (~148 °C) than that for the pure CAB (~167 °C). This indicates that the CAB in the blend can be crystallized at a lower T than the pure CAB.

In the high-T region (Figure 3d), the peak intensity at $q_{m,CAB}$ decreases with T, while $q_{m,CAB}$ hardly changes with T. We shall discuss origin of the decrease of the peak intensity later in section 4.3. It is important to note that the SAXS from the PHB assemblies significantly contribute to the net SAXS from the blend at the low q values around 0.2 nm^{-1}, both in crossover-T and high-T regions. The contribution of the PHB to the net scattering intensity I (q = 0.2 nm^{-1}) will be closely highlighted in Figure 10c and will be discussed in detail in the last paragraph of section 4.3.

3.3. Temperature Dependence of WAXD Profiles of PHB/CAB (50/50) Blend. In Figure 4, the peaks at $2\theta \cong 8.8°$ and 11.0° are due to the (020) and (110) diffractions from the PHB crystals in the blend, while the peaks at $2\theta \cong 5.1°$, 6.5°, 8.1°, 10.0°, 11.5° are assigned to the CAB crystals in the blend. The overall T-dependence of the profiles around 2θ = 5° and 11° shown in the insets (a) and (b), respectively, will be classified into low-T, crossover-T, and high-T regions, as presented in Figure 5 in the same way as in the case of the SAXS shown in Figure 3.

In the low-T region (Figure 5a), the (110) diffraction peak intensity at $2\theta \cong 10.5°–11.0°$ from the PHB crystals increases, and the Bragg angle at the peak shifts toward smaller 2θ with T,

dx.doi.org/10.1021/ma202606y | Macromolecules 2012, 45, 2783–2795

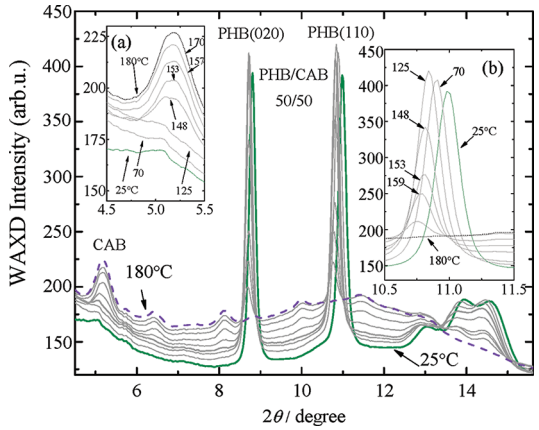


Figure 4. Temperature dependence of of the WAXD profiles for the PHB/CAB (50/50) blend in the heating process from 25 to 180 °C. The insets (a and b) highlight the detailed temperature dependence of the diffraction profiles at $2\theta \cong 5.1°$ for the CAB and diffraction profiles from the (110) lattice planes at $2\theta \cong 10.8–11.0°$ for the PHB.

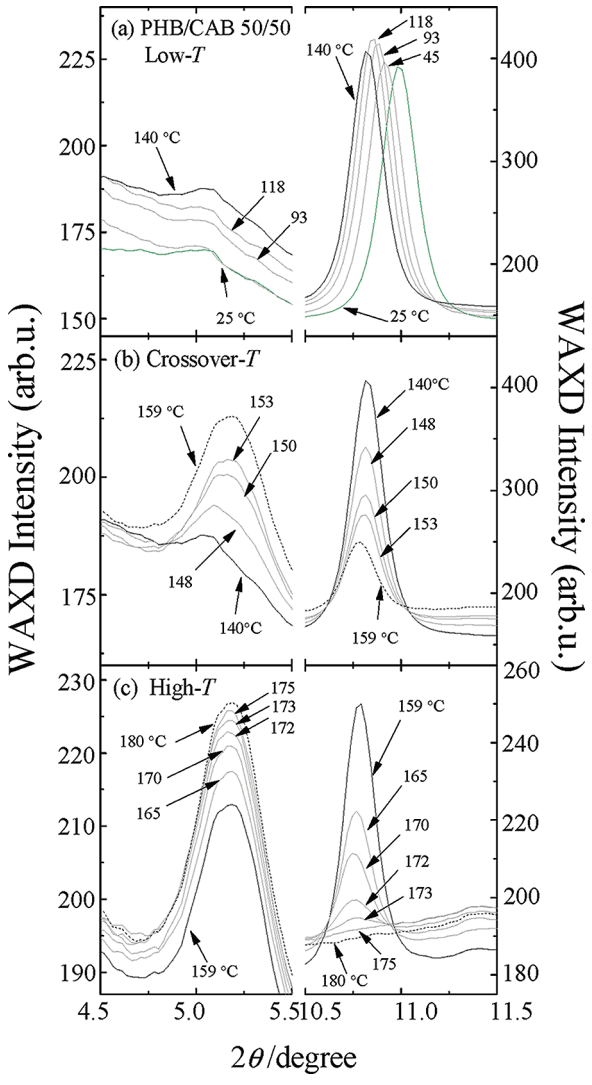


Figure 5. Temperature dependence of WAXD profiles for the PHB/CAB (50/50) blend at $2\theta \cong 5.1°$ from the CAB crystals and at $2\theta \cong 10.8–11.0°$ from the (110) lattice plane for the PHB crystals in (a) the low-T region, (b) the crossover-T region, and (c) the high-T region. The left and right ordinates refer to the relative diffraction intensity for CAB and PHB, respectively.

indicating that CC of PHB proceeds and the PHB crystals undergo thermal expansion with T, respectively. However, CAB still remains amorphous, as evidenced by the diffraction profiles at $2\theta \cong 5.1°$. In the crossover-T region, partial melting of PHB and recrystallization into more perfect crystals occur with increasing T, as evidenced by the decreasing diffraction intensity from the (110) lattice plane of PHB and almost no shift in the diffraction peak position: The latter seems to be a consequence of a counterbalance between the thermal expansion of the lattice and the lattice contraction due to the increasing perfection of the crystals. It should be noted that the melting and recrystallization of PHB will be recognized also in the SAXS profiles shown in Figure 3. Further, CC of CAB starts to develop, so that the peak intensity and width of the diffraction at $2\theta \cong 5.1°$ increases and narrows, respectively, at T higher than ~148 °C. The onset temperature for CC of CAB in the blend is lower than that for pure CAB ($\gtrsim$157 °C), which is consistent with the trend observed in SAXS. In the high-T region, the PHB crystals continue to melt up to ~173 °C and eventually transform into a complete melt, as evidenced by the decrease in the diffraction peak intensity from the (110) lattice plane with a peak shift toward smaller 2θ. CC of CAB continues to develop up to 180 °C at least, as evidenced by the increasing diffraction peak intensity at $2\theta \cong 5.1°$.

It is important to note some differences in the T-dependence of the WAXD and SAXS profiles in the high-T region: (1) the SAXS peak intensity at $q \cong 0.3$ nm^{-1}, apparently reflecting the long spacing of the CAB crystals, decreases with T, whereas the WAXD peak intensity at $2\theta \cong 5.1°$ keeps increasing, and hence CC of CAB continues to progress; (2) the SAXS peak at $q \cong 0.9$ nm^{-1}, reflecting the long spacing of PHB lamellar crystals, cannot be obviously observed, though the PHB crystals still exist. These apparent discrepancies will be clarified later in section 4.3.

3.4. Temperature Dependence of SAXS Intensities at $q \cong 0.2$ and 0.9 nm^{-1} in PHB/CAB (50/50) Blend. Figure 6 shows the temperature dependence of typical SAXS intensities at (a) $q = 0.9$ nm^{-1}, relevant to the PHB long period in the blend, and (b) $q = 0.2$ nm^{-1}, relevant to the CAB long period in the blend, both of which were obtained in the heating process for pure PHB, PHB/CAB (20/80, 25/75, 30/70, 50/50, and 60/40) blends, and pure CAB. The temperature where $[\partial I_c (q = 0.2 \text{ or } 0.9 \text{ nm}^{-1})/\partial T]$ vs T discontinuously changes is shown by the arrow with each specified temperature. These points shown in Figure 6a are assigned to the onset temperature $T_{cc,PHB}$ for CC of PHB. These points in Figure 6b are less clear, so that Figure 6b are enlarged in Figure 6, parts c (100–120 °C) and d (130–150 °C). The points at the lower temperatures shown in Figure 6b and 6c by the arrows with each specified temperature are assigned to the $T_{g,h}$ defined in section 1 (which is also referred to as $T_{g,h,SAXS}$ in order to show that the value was assessed by SAXS). The onset temperature for CC of CAB ($T_{cc,CAB}$) was estimated from the points at the higher temperatures in Figure 6b and 6d (shown by the red arrows with each specified temperature). Moreover, the $T_{cc,PHB}$ and $T_{cc,CAB}$ values were determined also from T-dependence of the WAXD peak intensities of the (110) and (020) lattice planes of the PHB crystals and at $2\theta \cong 5.1°$ for the CAB crystals, respectively, as will be shown later in conjunction with Figure 10b in section 4.3.

4. DISCUSSION

4.1. Scaling Analysis of SAXS Profiles in the Low-T Region. It is reasonable to assume that CC of PHB in the

dx.doi.org/10.1021/ma202606y | Macromolecules 2012, 45, 2783–2795

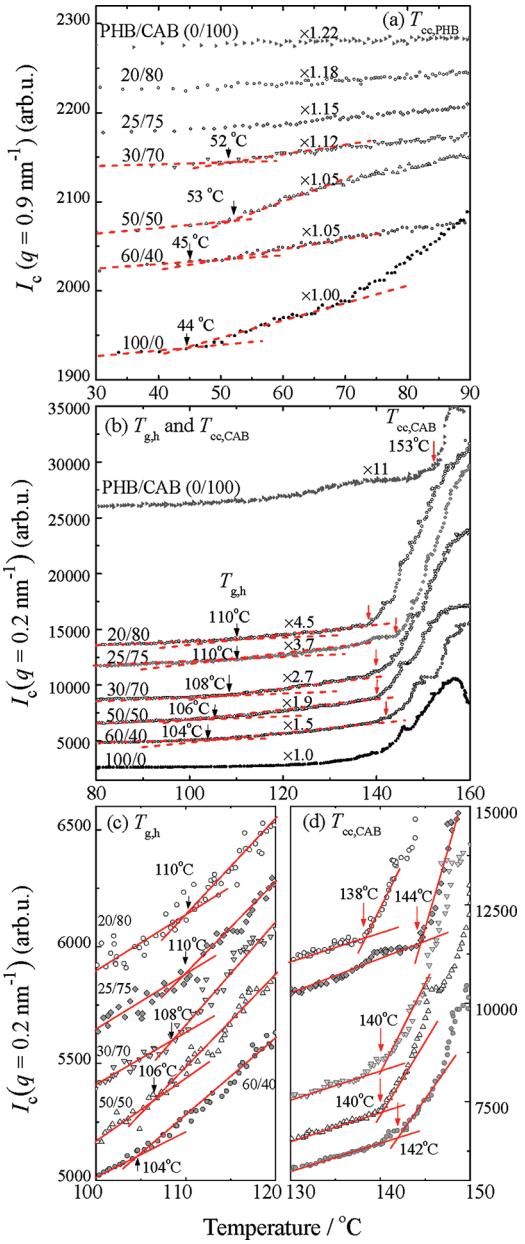


Figure 6. Temperature dependence of the SAXS intensities I from the PHB/CAB blends (a) at q = 0.9 nm^{-1} over the temperature range from 25 to 90 °C and (b) at 0.2 nm^{-1} from 80 to 160 °C, respectively. Panels c and d represent enlarged views of part b in the temperature range from 100 to 120 °C and from 130 to 150 °C, respectively, to clearly indentify the characteristic temperatures. The intensity for each blend, pure CAB and PHB was multiplied by the factor shown in parts a and b. The plots of the intensity vs temperature are vertically shifted to avoid an overlap of them.

low-T region, as evidenced in Figures 3b and 5a, involves growth of 1D assemblies of PHB lamellae that are randomly oriented in 3D space. The scattering from a randomly oriented 1D assembly, in which mass centers of scattering particles are oriented in the paracrystalline lattice, $I_{theor}(q)$, is given by[47−49]

$$I_{theor}(q)q^2 \sim [\langle |f(q)|^2 \rangle - |\langle f(q) \rangle|^2] + (1/\bar{v}) |\langle f(q) \rangle|^2 Z(q) * |S(q)|^2 \quad (3)$$

where $|\langle f(q) \rangle|^2$ is the form factor of the particle (lamella of thickness $D_{c,PHB}$ in our case) in the assembly; $Z(q)$ and $|S(q)|^2$ are the paracrystalline lattice factor and the shape factor of the assembly as a whole, respectively; the symbol * designates the convolution product; $\bar{v}$ is average volume per lattice; $\langle\ \rangle$ designates the average of $|f(q)^2|$ or $f(q)$ with respect to the polydispersity in the particle size and orientation fluctuations of the particles within the assembly.

For a qualitative analysis of $I_c(q)$ with $I_{theor}(q)$, we can neglect the diffuse scattering term [the first term of the right-hand side (rhs) of eq 3] due to the polydispersity of the particle size and the orientation fluctuations of the particle. Moreover, $|S(q)|^2$ is assumed to be given by the delta function in the case when the zeroth-order scattering from the assemblies as a whole is assumed not to have significant effects on $I_c(q)$ over the q-range covered in this work. In this case, eq 3 is simplified as

$$I_{theor}(q)q^2 \sim (1/\bar{v})|\langle f(q) \rangle|^2 Z(q) \quad (4)$$

Noting that $\bar{v} \propto L_{PHB}$ (the long spacing of the PHB lamellae in our case) and neglecting the polydispersity and the orientation fluctuations, $|\langle f(q) \rangle|^2 = |f(q)|^2$ which is given by

$$|f(q)|^2 \sim \Delta\rho^2 D_{(c,PHB)}{}^2 \frac{\sin^2(qD_{(c,PHB)}/2}{(qD_{(c,PHB)}/2)^2} \quad (5)$$

where $D_{c,PHB}$ is the PHB lamellar thickness, we can rewrite eq 4 as

$$I_{theor}(q)q^2 \sim \Delta\rho^2 \phi_{(L,PHB)}{}^2 q_m{}^{-1} \frac{\sin^2(\pi\phi_{L,PHB}x)}{(\pi\phi_{L,PHB}x)^2} Z(q) \quad (6)$$

Here $\Delta\rho$ is the electron density difference between PHB lamellae and their matrix, $\phi_{L,PHB}$ is the average volume fraction of the PHB lamellae in the assembly given by $\phi_{L,PHB} = D_{c,PHB}/L_{PHB}$, and

$$q_m \equiv 2\pi/L_{PHB}; \quad x \equiv q/q_m \quad (7)$$

Then from eqs 6 and 7, one obtains

$$I_{theor}(x)x^2 q_m \sim \Delta\rho^2 \phi_{L,PHB}{}^2 F(x) \quad (8)$$

with

$$F(x) \sim \frac{\sin^2(\pi\phi_{L,PHB}x)}{(\pi\phi_{L,PHB}x)^2} Z(x) \quad (9)$$

Consequently, if $\phi_{L,PHB}$ (the local crystallinity within the 1D assembly), $\Delta\rho^2$, and the paracrystalline distortion parameter are [and, thus, the paracrystalline lattice factor $Z(x)$] kept unchanged with T in the low-T region, the scaled structure factor $F(x)$ becomes universal with T, and hence the scaled scattering function $I_{theor}(x)\ x^2 q_m$ also becomes universal with T. $F(x)$ gives the scaling function for the structure factor from the self-similarly grown 1D assembly of lamellae with T. This $F(x)$ predicts the characteristic shape (or morphology) of the 1D self-assembly of PHB lamellar crystallites that is universal with T. It should be noted that the above equation is derived for the scattering from a single assembly. If there are many assemblies or grains, the rhs of eq 8 should be multiplied by the number of the assemblies (or grains) G_M.

Self-Similar Growth of 1D Assembly of PHB Lamellae. We examined the experimental scaled scattering function $I_c(x)\ x^2 q_m(T)$ against x in the low-T region, as shown in Figure 7,

dx.doi.org/10.1021/ma202606y | Macromolecules 2012, 45, 2783−2795

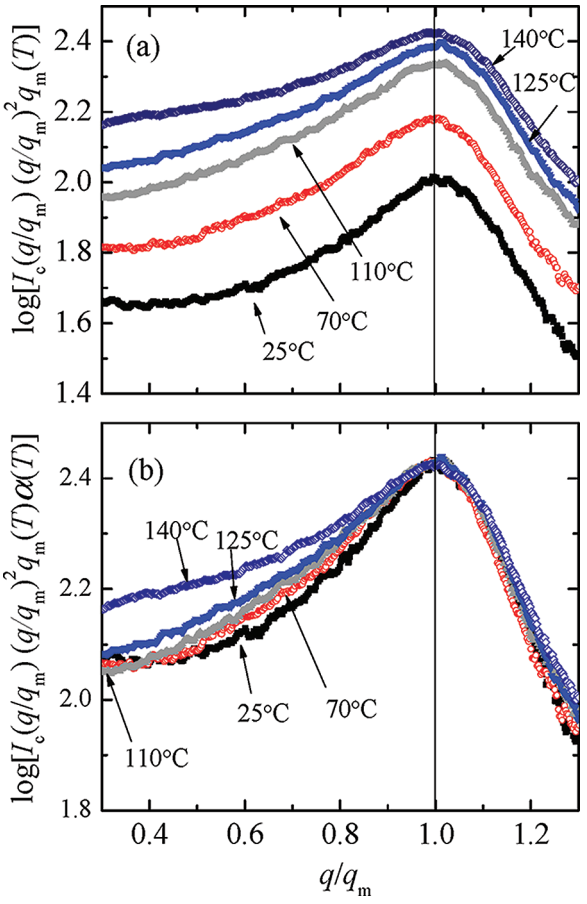


Figure 7. Scaling plots for SAXS profiles from PHB/CAB (50/50) blend in the low-T regions: (a) log $[I_c(q/q_m)(q/q_m)^2q_m]$ vs q/q_m and (b) log $[I_c(q/q_m)(q/q_m)^2q_m\alpha(T)]$ vs q/q_m, where $\alpha(T)$ is the vertical shift factor as defined by eq 10 in the text.

using the value $q_m(T)$ obtained from Figure 3b, which is discussed later in Figure 10d. In Figure 7a, the peak intensity of the scaled scattering function increases with T, which is due to the increase in the prefactor $\Delta\rho^2\phi_{L,PHB}{}^2G_M$ with T. We think that an increase in G_M, and hence an increase in the total number of PHB lamellae, is more likely responsible for the increase in the prefactor than an increase in $\Delta\rho^2\phi_L{}^2$ in the data shown in Figure 7a. In Figure 7b, the experimental scaled scattering functions are vertically shifted in the double logarithmic scale so that the function at the peak position of $x = (q/q_m) = 1$ at a given T becomes identical to that at 140 °C. The vertical shift is mathematically equivalent to multiplying the temperature dependent shift factor $\alpha(T)$ with the scaled scattering function $I_c(x)\ x^2q_m(T)$ at T, where $\alpha(T)$ is defined by

$$\alpha(T) \equiv [I_c(x=1)q_m]_{T=140°C}/[I_c(x=1)q_m]_T \qquad (10)$$

where from eq 8, $\alpha(T) = G_M(T = 140\ °C)\Delta\rho^2(T = 140\ °C)\phi_{L,PHB}{}^2(T = 140\ °C)/G_M(T)\Delta\rho^2(T)\phi_{L,PHB}{}^2(T)$. Thus, it generally depends on $G_M(T)$, $\Delta\rho(T)$, and $\phi_{L,PHB}(T)$. The vertically shifted scaled scattering functions facilitate a comparison of the shape of the functions at various T.

As shown in Figure 7b, the shape of the scaled scattering function is almost universal with T for 25 °C $\leq T \lesssim T_{g,h} \cong$ 110 °C. Thus, in this temperature range, the 1D assemblies of PHB lamellae grow self-similarly with T, as schematically illustrated in Figure 8a.

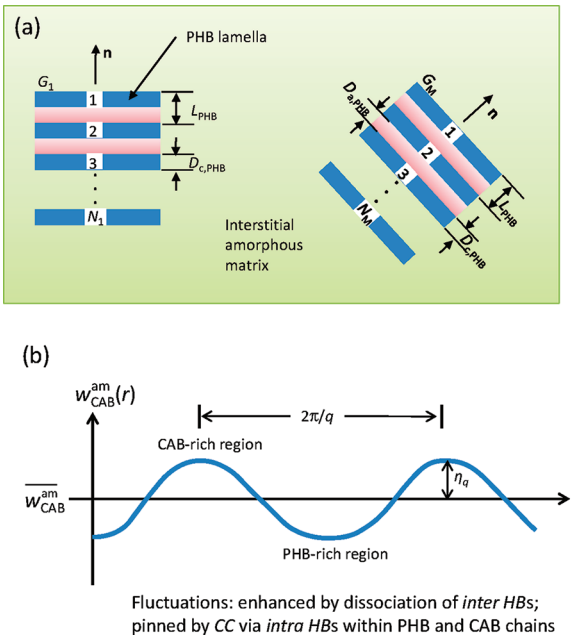


Figure 8. (a) Growth of one-dimensional assembly of PHB lamellar crystals in the amorphous matrix of the PHB/CAB mixture in the low-T region. The number of the assemblies G_M, the number of the lamellae N_M in the G_Mth assembly, the lamellar spacing L_{PHB}, and the lamellar thickness $D_{c,PHB}$ increase with T. $D_{a,PHB}$ is the thickness of the interlamellar amorphous region within the PHB lamellar assembly. (b) Fourier mode of the large length-scale composition fluctuations with wave number q which is built up in the interstitial amorphous matrix at $T_{g,h} < T < T_{cc,CAB}$.

Large Length-Scale Composition Fluctuations. The deviation of the scaled structure factor from the universal function seems to become remarkable at $T \gtrsim T_{g,h}$ (≅110 °C) in the small q-range at $q/q_m < 1$: The smaller the q-value, the larger is the deviation. Moreover the deviation becomes increasingly remarkable with T. We think that the deviation is caused by an evolution of the new scattering function such as the one given by eq 11 later, which tends to increase with decreasing q at q values smaller than q_m, in excess to the scattering from the 1D assemblies of the PHB lamellae. It is quite important to recall here that in the low-T region, CAB remains amorphous and only PHB is crystallized, and that the crystallinity in the blend is smaller than 0.28.[39] The evolution of the excess scattering at the small q-range reveals itself to be the evolution of the electron density fluctuations at a length scale r much larger than $2\pi/q_m \cong 7.0$ nm, the lamellar spacing. It is due to the evolution of the *large length-scale composition fluctuations* between PHB and CAB in the interstitial amorphous matrix between the PHB lamellar assemblies, as illustrated in Figure 8b.

Figure 8a schematically presents 1D assemblies of PHB lamellae crystals G_1 to G_M formed in the low-T region with the long spacing L_{PHB}, lamellar thickness $D_{c,PHB}$, interlamellar amorphous layer thickness $D_{a,PHB}$, and total number of the assemblies G_M. The unit vector **n** showing the assembly axis is randomly oriented in 3D space. Figure 8b presents a Fourier mode of the composition fluctuations with wave number q in the large length-scale composition fluctuations evolved at $T \gtrsim T_{g,h}$ in the low-T region in the interstitial amorphous matrix of the blend among the 1D assemblies of the PHB crystals. $w^{am}_{CAB}(r)$ represents the q-Fourier mode of the local composition

dx.doi.org/10.1021/ma202606y | *Macromolecules* 2012, 45, 2783–2795

of variation CAB in the amorphous matrix of the blend, whereas $\overline{w_{CAB}^{am}}$ is the bulk (average) composition of CAB in the amorphous phase. The spatial composition fluctuations are basically predicted by Ginzburg–Landau[50] and Cahn–Hilliard theory[51] or more generally by random phase approximation:[52] These basic theories predict the free energy and amplitude of the q-Fourier mode of the fluctuations as a function of the wavenumber q and the scattering function, $I_{fluct}(q)$, as given by

$$I_{fluct}(q) = I_{fluct}(q = 0)/(1 + q^2\xi^2) \quad (11)$$

where ξ is the correlation length of the thermal composition fluctuations.

4.2. Existence of Two T_g's in Amorphous Matrix of the Blends. As summarized in Figure 9, various characteristic temperatures were evaluated in this work as a function of the blend composition w_{CAB}, including not only (i) the melting temperature of PHB crystals as evaluated by the temperature at the peak of the highest melting endotherm in DSC[53] ($T_{m,PHB,DSC}$), (ii) T_g's as observed by DSC thermograms ($T_{g,DSC}$), but also (iii) $T_{cc,PHB}$, (iv) $T_{g,h,SAXS}$, and (v) $T_{cc,CAB}$, which were determined from the results shown in Figure 6 (see section 3.4).

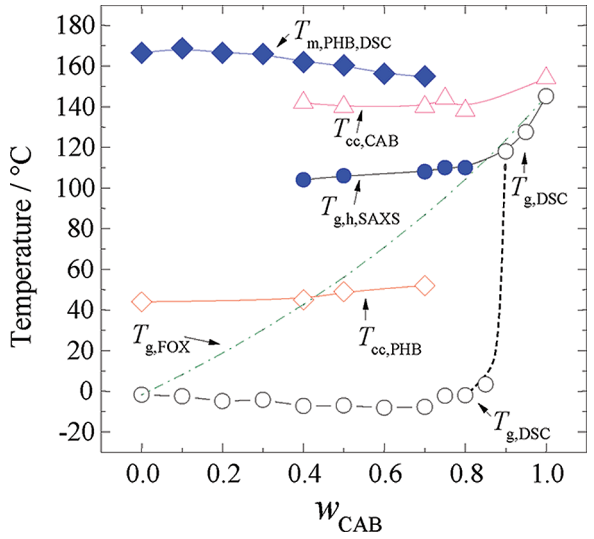


Figure 9. Various characteristic temperatures characterizing the PHB/CAB blends as a function of the blend composition w_{CAB}. The solid, broken, and dash-dot lines are visual guides.

Let us discuss first why $T_{g,DSC}$ shows a peculiar but intriguing w_{CAB} dependence: $T_{g,DSC}$ hardly depends on w_{CAB} in the range $0 \leq w_{CAB} \lesssim 0.85$, increases stepwise with w_{CAB} from 0.85 to 0.90 as indicated by the dotted line, and gradually increases with a further increase in w_{CAB} up to 1.0. The dash-dot line shows the T_g value predicted by Fox law[54] ($T_{g,Fox}$) for binary blends having uniform mixing of chain segments:

$$\frac{1}{T_{g,Fox}} = \frac{1 - w_{CAB}}{T_{g,PHB}} + \frac{w_{CAB}}{T_{g,CAB}} \quad (12)$$

where $T_{g,PHB}$ and $T_{g,CAB}$ are the T_g values for pure PHB (271 K) and pure CAB (418 K). The predicted T_g, which smoothly increases with w_{CAB} from $T_{g,PHB}$ to $T_{g,CAB}$, does not fit at all with $T_{g,DSC}$. The discrepancy suggests that the PHB and CAB segments are not uniformly mixed. We would like to discuss this peculiarity in the $T_{g,DSC}$ vs w_{CAB} plot in conjunction with the question regarding the physical meaning of $T_{g,h,SAXS}$ determined from the T dependence of the SAXS intensity I_c at low q (= 0.2 nm^{-1}).

As already clarified in section 4.1, the intensity $I_c(q = 0.2$ nm$^{-1})$ is sensitive to the large length-scale composition fluctuations of the PHB and CAB segments in the amorphous matrix which exist between the 1D assemblies of PHB lamellar crystals, as illustrated in Figure 8a. The stepwise increase in $\partial I_c(q = 0.2$ nm$^{-1})/\partial T$ with T at $T_{g,h,SAXS}$ suggests that the segmental motions in the intervening amorphous matrix are enhanced with T across $T_{g,h,SAXS}$, and thereby $T_{g,h,SAXS}$ is considered to reflect the value of T_g of the intervening amorphous matrix.

Then why was the signal for $T_{g,h,SAXS}$ not found by DSC? We think that the fact that CC of PHB occurs over a wide range between $T_{cc,PHB}$ and $T_{cc,CAB}$ in the low-T region obscures the signal for $T_{g,h,SAXS}$ in the DSC thermogram. If this is the case, we anticipate that more sophisticated and precise conventional or temperature-modulated DSC measurements (see for example ref 43) will find two T_g's in a blend of noncrystallizable PHB with CAB. This confirmation deserves future work.

Thus, we propose that for the blends with w_{CAB} between ~0.4 and ~0.8, there are two T_g's: $T_{g,h,SAXS} = T_{g,h}$ (a high T_g) and $T_{g,DSC} = T_{g,l}$ (a low T_g). We expect that the data on $T_{g,h}$ can be observed for the blends with w_{CAB} between 0 and 0.4 as well. These data are missing in Figure 9, simply because we did not measure SAXS for these blends. A possible origin of the two T_g's was already pointed out in the last paragraph of the section 1, and hence, it will not be repeated here. Since the thermal composition fluctuations shown in Figure 8b are insignificant at temperatures below $T_{g,h}$, the concept concerning the two T_g's seems valid. However we would like to note the fact that the effective blend composition in the amorphous matrix between the assemblies of PHB lamellar crystals ($\overline{w_{CAB}^{am}}$) is biased by the bulk (or net) blend composition w_{CAB} due to the crystallization of PHB. For example, for the blend with w_{CAB} = 0.5, crystallinity X_c assessed by DSC was 0.28.[39] If we assume that CAB is distributed uniformly outside the PHB lamellar crystals,$\overline{w_{CAB}^{am}}$ can attain a maximum value of 0.69.[55] If CAB exists more in the interlamellar space of thickness $D_{a,PHB}$ between the assemblies of PHB lamellae than in the interstitial region among the assemblies, then $\overline{w_{CAB}^{am}} < 0.69$.

It is intriguing to note that CC of PHB occurs even at $T < T_{g,h,SAXS}$ or $T_{g,h}$, so that $T_{cc,PHB} < T_{g,h}$. This fact may suggest that CC of the soft component of the blend (PHB) occurs dominantly through regions having $T_{g,l}$ via a diffusion-limited crystallization at least in the beginning, followed by large length-scale molecular rearrangements in the as-formed crystallites. By contrast, CC of the hard component (CAB) occurs only at $T > T_{g,h}$ so that $T_{cc,CAB} > T_{g,h}$. Thus, the hard component can undergo CC only above $T_{g,h}$. It is important to note the following facts in Figure 9: PHB cannot be crystallized in the blends having $w_{CAB} > 0.7$; CAB cannot be crystallized in the blends having $w_{CAB} < 0.4$. These facts will be discussed later in section 4.4.

4.3. Self-Assembling Mechanism During Heating. In this section we will focus on the particular blend with w_{CAB} = 0.5 and summarize its self-assembly mechanism and process in the heating process on the basis of systematic investigations of all the various physical quantities measured as a function of T in this work. Figure 10 presents (a) the DSC thermogram and the T dependence of (b) the peak intensity of the WAXD from

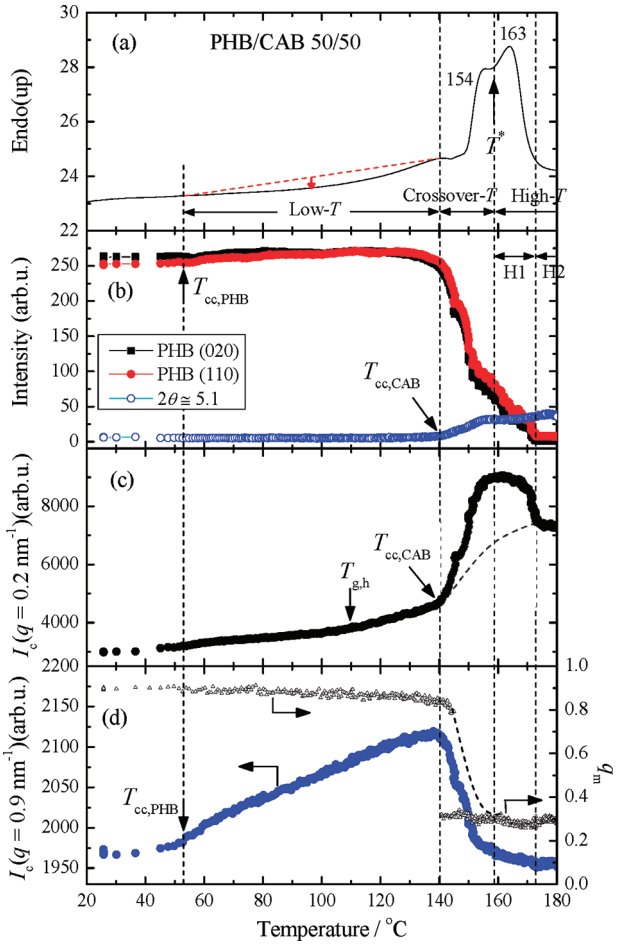


Figure 10. (a) DSC thermogram, and temperature dependence of (b) WAXD peak intensities from the (020) and (110) lattice planes of PHB crystals and at $2\theta \cong 5.1°$ from CAB crystals, and SAXS intensities I (q = 0.2 nm^{-1}) (c) and I (q = 0.9 nm^{-1}) (d). Panel d shows q_m also, which is the q value at the SAXS peak. The broken lines in parts (a), (c), and (d) are visual guides.

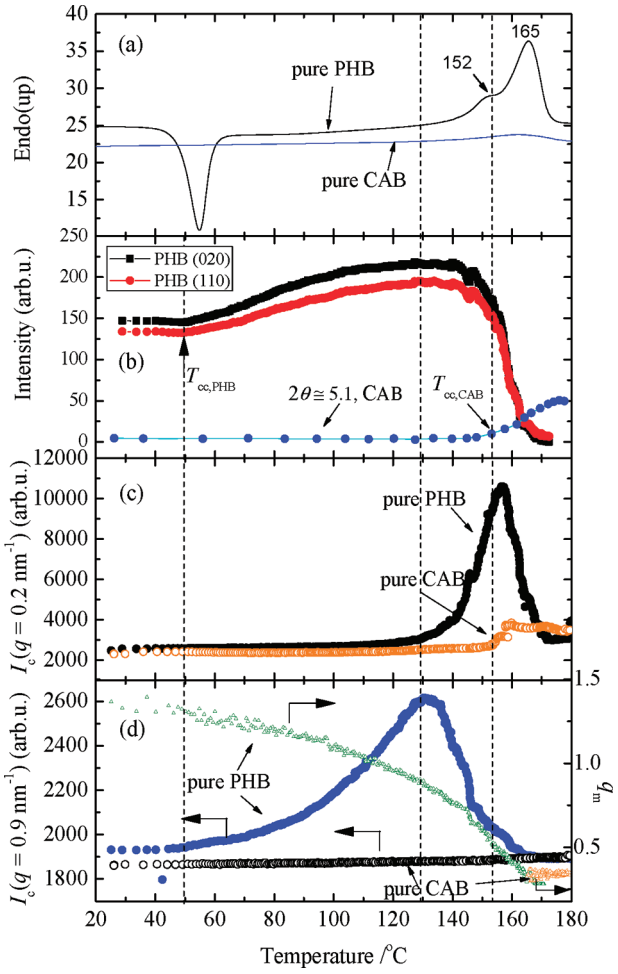


Figure 11. (a) DSC thermogram, and temperature dependence of (b) WAXD peak intensities from the (020) and (110) lattice planes of PHB crystals and at $2\theta \cong 5.1°$ from CAB crystals, and SAXS intensities I (q = 0.2 nm^{-1}) (c) and I (q = 0.9 nm^{-1}) (d) from pure PHB and pure CAB. The value q_m refers to the q-value at the SAXS peak from pure PHB (green) and pure CAB (orange).

(020) and (110) lattice planes of the PHB crystals and at $2\theta \cong 5.1°$ from the CAB crystals, (c) the SAXS intensity I (q = 0.2 nm^{-1}), and (d) the SAXS intensity I (q = 0.9 nm^{-1}) and the q value(s), q_m, at the SAXS intensity maximum (maxima). Figure 11 displays the corresponding physical quantities for pure PHB and CAB as references for the blend.[56]

As shown in Figure 10, all the physical quantities consistently indicate that the whole self-assembly process can be classified into the three T regions: low-T, crossover-T, and high-T regions, as described earlier in sections 3.2 and 3.3 in conjunction with Figures 3 and 5, respectively. The three T regions are characterized by the characteristic temperatures $T_{cc,PHB}$, $T_{cc,CAB}$, and T^*, as indicated by vertical dotted lines in Figure 10, where T^* is a characteristic temperature close to $T_{m,PHB,DSC} \cong 163$ °C.

Low-T Region. CC of PHB in the blend occurs at T sufficiently higher than $T_{g,l}$ but lower than $T_{cc,CAB}$ as discussed in section 4.2. This is elucidated by the increase in the WAXD peak intensities from the (020) and (110) lattice planes of PHB crystals at $T \geq T_{cc,PHB}$ (53 °C) > $T_{g,l} = T_{g,DSC}$ (−7.1 °C), as shown in Figures 9 and 10b. In this region, CAB still remains amorphous, as evidenced by the fact that the WAXD intensity at $2\theta \cong 5.1°$ from the CAB crystals remains almost zero, as shown in Figure 10b. The SAXS intensity I (q = 0.9 nm^{-1}) increases with T, and q_m accordingly decreases from 0.9 to 0.85, as shown in Figure 10d, as a consequence of growth of the 1D assemblies of PHB lamellar crystals in the amorphous matrix and thickening of the average lamellar spacing L_{PHB} from 7.0 to 7.4 nm, respectively (see Figure 8a).

The SAXS intensity I (q = 0.2 nm^{-1}) shows a relatively small increase with T compared with the increase in I (q = 0.9 nm^{-1}) with T, revealing the increase of the large length-scale composition fluctuations in the amorphous matrix of the blend with T as a consequence of the thermal expansion and increased free volume at $T > T_{g,l}$. At $T > T_{g,h}$, the mobility of the CAB and PHB segments further increases, which in turn increases $\partial I_c(q = 0.2\ nm^{-1})/\partial T$, as shown in Figures 6c and 10c, and produces the large length-scale composition fluctuations as illustrated in Figure 8b. The DSC thermogram shows the broad exothermic peak, as illustrated by the downward drift of the DSC thermogram (shown by the red arrow) from the baseline (shown by the red broken line) in Figure 10a, as a consequence of CC of PHB.

Comparisons of the results in Figures 10b and 11b reveal the following: (i) $T_{cc,PHB}$ for the blend (~55 °C) is higher than $T_{cc,PHB}$ for pure PHB (~50 °C); (ii) CC of PHB in the blend occurs to less extent than that of pure PHB, as evidenced by the

dx.doi.org/10.1021/ma202606y | Macromolecules 2012, 45, 2783−2795

fact that the WAXD diffraction peak intensity from the (020) and (110) crystal planes of PHB for the blend increase with T less than those for the pure PHB. The first finding is due to the incorporation of the hard CAB component, which has a high T_g in the blend, while the second finding is due to the difference in thermal histories of the as-prepared specimens between the blend and pure PHB, as pointed out in section 2.1. The latter also causes a considerable difference in q_m vs T between the blend and pure PHB, as shown in Figures 10d and 11d. As inferred from in Figures 11a and 11b, the crystallinity of pure CAB is much less than that of pure PHB under the given thermal treatments.

Crossover-T Region. In this region, partial melting and recrystallization of PHB occurs concurrently with CC of CAB with increasing T. This is evidenced not only by the decrease in the WAXD peak intensities from the (020) and (110) lattice planes of PHB crystals and the increase in the WAXD peak intensity at $2\theta \cong 5.1°$ from CAB crystals with T, as shown in Figures 5b and 10b, but also by the decrease and increase in SAXS intensity I at $q = 0.9$ and 0.2 nm^{-1} with T, respectively, as shown in Figures 10, parts d and c, respectively. This involves the apparent change in the SAXS peak position q_m also as indicated in Figures 10d with the broken line and Figure 3c. The trend in the q_m vs T plot in this region will be discussed more deeply later in conjunction with the trend in the high-T region.

Partial melting and recrystallization of PHB in the 1D assemblies of lamellar crystals causes the assemblies of the PHB lamellae G_1–G_M shown in Figure 8a to change into G_1'–G_M' shown in Figure 12, where the number of assemblies changes

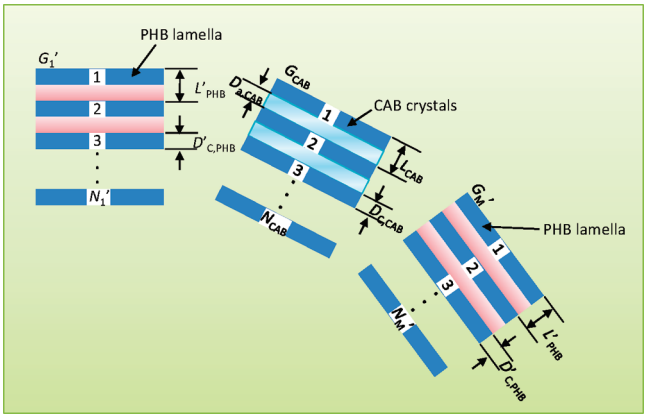


Figure 12. One-dimensional assemblies of PHB lamellae G_1' to G_M' and those of CAB crystallites G_{CAB} developed in the crossover T-region. N_1' and N_M' are the number of PHB lamellar crystals in the G_1'-th and G_M'-th assembly of PHB lamellae, while N_{CAB} is the number of CAB crystallites in the G_{CAB}-th assembly with the long period L_{CAB}, crystallite thickness $D_{c,CAB}$, and amorphous layer thickness of $D_{a,CAB}$.

from G_M to G_M', the number of lamellae in the assemblies changes from N_1 and N_M to N_1' and N_M', the set of the characteristic lengths of the assemblies changes from (L_{PHB}, $D_{c,PHB}$) to (L'_{PHB}, $D'_{c,PHB}$). CC of CAB occurs in the interstitial amorphous matrix, as illustrated in Figure 8a. More specifically it may occur in the regions rich in CAB, as illustrated in Figure 8b, because the crystallization of CAB is expected intuitively to be enhanced in the regions rich in CAB. We can call this intriguing but general phenomenon in blends composed of crystallizable polymers as *composition-fluctuation-enhanced crystallization*. CC of CAB gives rise to assemblies of CAB crystallites with long spacing L_{CAB} and crystal thickness $D_{c,CAB}$ in the interstitial amorphous matrix (shown in Figure 8a), as illustrated in Figure 12. The composition-fluctuation-enhanced crystallization occurs for PHB also in the regions rich in PHB, as shown in Figure 8b at $T_{g,h} < T < T_{cc,CAB}$ (low-T region). The DSC thermogram in the crossover-T region having the characteristic endothermic peak at $T \cong 154$ °C must reflect such the elemental self-assembly as elucidated by the simultaneous WAXD/SAXS study.

Comparisons between Figures 10 and 11[56] reveal that the partial melting and recrystallization of PHB in the blend occurs at T (from 140 to ∼160 °C), slightly higher than that for pure PHB (from 130 to 155 °C). This is considered to be due to the hardening of the medium brought about by the incorporation of the low-mobility CAB component. However, $T_{cc,CAB}$ is lower for the blend than for pure CAB, which is explained by the plasticizer effect of PHB as the soft component of the blend.

High-T Region. The melting of PHB crystals concurrently occurs with the partial melting and recrystallization of CAB. This is evidenced not only by the changes in the WAXD intensities from the PHB and CAB crystals with T, as shown in Figure 10b, but also by the changes in the SAXS intensities I at $q = 0.2$ nm^{-1} and 0.9 nm^{-1} with T, as shown in Figure 10, parts c and d, respectively. The melting process of the PHB crystals gives rise to the characteristic endothermic peak at ∼163 °C in the DSC thermogram. The WAXD peaks from the (020) and (110) crystal planes of PHB completely disappear in the higher T region (defined as H2) of the high-T region, while that at $2\theta \cong 5.1°$ from the CAB crystals show broad peaks at ∼159 and ∼178 °C with T which are superposed each other. The double peak in WAXD peak at $2\theta \cong 5.1°$ vs T might be associated with the melting and recrystallization of the CAB crystal.

The SAXS intensity I at $q = 0.2$ nm^{-1} shows a complex T dependence: It keeps nearly the constant maximum intensity level in lower T region of the high-T region, defined as H1, and drops to the lower constant intensity level in H2. This is in contrast to the constant or slightly increasing the WAXD intensity at $2\theta \cong 5.1°$ from CAB crystals throughout the H1 and H2 regions. We believe that the complex T dependence of I at $q = 0.2$ nm^{-1} is due to the overlap of two kinds of SAXS peaks: one reflecting the long spacing within the assemblies of CAB crystals and the other from that of PHB crystals, as visualized from the model illustrated in Figure 12. The SAXS peak from the assemblies of CAB crystals is expected to increase with T, as shown by the broken line in Figure 10c, judging from the increasing WAXD peak intensity at $2\theta \cong 5.1°$. However, as evidenced in Figure 3c and expected from Figure 3e, the SAXS peak intensity from the assemblies of PHB lamellae in the crossover-T region shifts toward smaller q values (see the broken line drawn for q_m in Figure 10d), though the peak intensity decreases. This effect of the low-q shift of the peak from PHB lamellae is expected to increase its contribution to the net SAXS intensity in the low-q tail intensity at $q = 0.2$ nm^{-1}. Upon further increase in T in the high-T region, the SAXS peak intensity from the PHB assemblies rapidly drops down due to further melting of PHB crystals, which decreases its contribution to I ($q = 0.2$ nm^{-1}). Therefore, the net intensity I ($q = 0.2$ nm^{-1}) decreases with T at $T \gtrsim 165$ °C.[57]

4.4. Further Insights into Self-Assembly Given by FTIR Studies. Let us first discuss the further insights into the self-assembly of the blend in the heating process. Our previous

dx.doi.org/10.1021/ma202606y | *Macromolecules* 2012, 45, 2783–2795

FTIR studies[39] on the same blend specimens used in this work elucidated the roles of *inter* HBs, *intra* HBs within CAB, *intra* HBs within PHB, and their exchanges on CC, melting of PHB in the blends, and miscibility (see Table 2 and section 3.5 of ref 39). Upon increasing T in the low-T region, *inter* HBs, which act as physical cross-links between PHB chains and CAB chains in the amorphous matrix, become weak and some of them are dissociated. The dissociation enhanced with T increasingly promotes PHB chains to undergo CC with T at $T \geq T_{cc,PHB}$. The PHB crystals formed are stabilized by the *intra* HBs within PHB, and hence CC involves the exchanges of HBs between *inter* HBs and *intra* HBs with respect to PHB. CC occurs even at $T_{g,l} < T < T_{g,h}$ through regions having $T_{g,l}$, where PHB segments are mobile, even though the PHB segments are still immobile in some other regions having $T_{g,h}$. Thus, $T_{cc,PHB}$ seems to be controlled by the dissociation of *inter* HBs rather than T_g. We note here that the *inter* HBs are found to effectively slow down the rate of the isothermal crystallization of PHB in the blend from its melt (see Tables 2 and 3 and Scheme 1 in ref 40).

Upon a further increase in T above $T_{g,h}$ in the low-T region, the dissociation of *inter* HBs further progresses, giving rise to the large length-scale composition fluctuations and hence resulting in the formation of CAB-rich regions and PHB-rich regions, as illustrated in Figure 8b, in the interstitial amorphous regions shown in Figure 8a. The fluctuations eventually bring about the phase separation between PHB-rich and CAB-rich phases, if they grow without a limitation. However the enhanced fluctuations driven by the dissociation of *inter* HBs will be suppressed by the association of *intra* HBs within CAB chains, which is effectively built up in the CAB-rich regions, and which promotes CC of CAB. It should be noted that *intra* HBs within CAB enhances first the composition fluctuations but later promotes CC of CAB, the later effect of which hinders and pins a further growth of the composition fluctuations. Thus, in this sense the *intra* CAB HBs act as a counterbalancing physical factor against the enhanced fluctuations driven by the dissociation of *inter* HBs. Here, the exchange from *inter* HBs to *intra* HBs within CAB occurs in the amorphous matrix, which triggers CC of CAB at $T > T_{cc,CAB}$ in the crossover-T region and thereby prevents phase separation of PHB and CAB in the amorphous matrix at a macroscopic scale. This factor is expected to keep the amorphous phase as a "trapped single phase." The PHB-rich regions also undergo the "composition-fluctuation-enhanced CC" of PHB which also prevents the macrophase separation. Moreover, the HB exchange between *inter* HBs and *intra* HBs within PHB occurs in this region.

In the high-T region, especially in the H2 region where the PHB crystals completely melt, the FTIR spectra in the OH stretching vibration region showed that the *inter* HBs are reformed.[39] This reformation provides a physical basis for miscible blends in the H2 region.

Let us next consider further insights into the composition dependence of the self-assembling process. It is interesting to note in Figure 9 that PHB cannot be crystallized in the blend with $w_{CAB} > 0.7$. Those blends remain in a single-phase and amorphous state below $T_{cc,CAB}$, thereby having a property as an optically transparent melt or glass below $T_{cc,CAB}$. These findings evidently reflect the fact that the number of *inter* HBs per single PHB chain increases with w_{CAB}, so that PHB chains are effectively trapped by the physical cross-links between PHB and CAB segments mediated by *inter* HBs and thereby unable to be either crystallized or phase-separated. Here again the *inter* HBs play a significant role in the self-assembly and miscibility of the blends. It is interesting to note also the fact that CAB does not crystallize at $w_{CAB} < 0.4$. This can be explained by an interpretation similar to that given above. Those insights obtained above will give further implications as follows. For the blends with $w_{CAB} > 0.7$, once CAB is crystallized by the heat-treatment above $T_{cc,CAB}$, then the small degree of CAB crystallinity developed will act as physical cross-links and give rise to a soft-elastomeric property between $T_{g,h}$ and $T_{cc,CAB}$ and a harder elastomeric property between $T_{g,DSC}$ and $T_{g,h}$. For the blends with $w_{CAB} < 0.4$, CAB is miscible with PHB in the amorphous phase[19] and melt. The equilibrium melting temperature of PHB in the blends decreases with CAB,[22] and the degree of crystallinity of PHB decreases,[39,58] which will lead to the improved mechanical properties such as the elongation at break and toughness[24] and the improved processability.

5. CONCLUSIONS

We elucidated the self-assembly of PHB/CAB blends during heating by simultaneous SAXS/WAXD investigations with a synchrotron undulator beamline. We identified the independent cold-crystallization (CC) processes of PHB and CAB in the blends into the one-dimensional assemblies of PHB crystals and those of CAB crystals in the different temperature ranges, as illustrated in Figures 8 and 12 and discussed in sections 4.1 and 4.3, respectively. The very strong incident beam intensity from the undulator beamline facilitated the detection of the crystallization of CAB with very small crystallinity for the first time.

The SAXS intensity at the low q measured as a function of temperature (T) in the low-T region elucidated the existence of a higher glass transition temperature $T_{g,h}$ in the interstitial amorphous matrix between the PHB lamellar assemblies as shown in Figure 8: This $T_{g,h}$ is higher than the T_g measured from the DSC thermogram,[39] defined as $T_{g,DSC}$ or $T_{g,l}$, a lower temperature T_g. The two T_g's, $T_{g,l}$ and $T_{g,h}$, were found in the amorphous matrix in the composition range of the blend specified by $0.4 \leq w_{CAB} \leq 0.8$, as shown in Figure 9. The origin of the two T_g's are presented in the text (sections 1 and 4.2).

At $T \geq T_{g,h}$, large length-scale thermal composition fluctuations between PHB and CAB evolved in the interstitial amorphous matrix as illustrated in Figure 8b, which is clarified by the scaling analysis of the SAXS scattering functions in the low-T region, as shown in Figure 7. Although the thermal fluctuations increase with T, their growth was found to be pinned due to the onset of CC of CAB at $T \geq T_{cc,CAB}$, the onset temperature for CC of CAB. Even below $T_{cc,CAB}$ ($T_{g,h} < T < T_{cc,CAB}$), growth of the fluctuations with time will be pinned due to CC of PHB, which will be induced in the regions rich in PHB, and thereby the interstitial amorphous matrix is kept in the single phase: This point deserves further investigation.

The concept of *composition-fluctuation-enhanced crystallization*, which is well anticipated from scientific intuition and which was actually verified in this work, is thought to be an important one applicable to other crystallizable blends having the interplay between crystallization and phase separation: In the case of PHB/CAB blends, it can happen in the crossover-T regions. Moreover, this concept has another important consequence: the fluctuation-enhanced crystallization suppresses and pins the development of the composition fluctuations into full macroscopic phase separation.

Comparisons of the present results accomplished by using SAXS/WAXD, as mesoscopic probes, with our previous FTIR results,[39] as a microscopic probe, for the same blend specimens elucidated the important roles of various *intra-* and *inter-*molecular hydrogen bonds and their exchanges with *T* on the self-assembly and miscibility of the blends as summarized in section 4.4. Thus, we would like to propose that PHB/CAB blends are useful and intriguing model systems to generally explore the fundamental physics concerning the roles of hydrogen bonds on the self-assembly of soft matters.

AUTHOR INFORMATION

Corresponding Author

*E-mail: hsato@kwansei.ac.jp.

Notes

The authors declare no competing financial interest.

[†]Professor Emeritus, Kyoto University, Kyoto 606-8501, Japan, and Honorary Chair Professor, National Tsing Hua University, Hsinchu 30013, Taiwan

ACKNOWLEDGMENTS

This work was supported by Grants-in-Aid for Scientific Research (C) from MEXT (No. 20550026, No. 20550197), a Grant-in-Aid for Scientific Research on Innovative Areas from MEXT (No. 21106521), and the Shiseido Female Researcher Science Grant 2009. This work was also supported also by a Kwansei-Gakuin University "Special Research" project 2009–2014. The synchrotron radiation experiments were performed at the FSBL03XU of SPring-8 with the approval of the Japan Synchrotron Radiation Research Institute (JASRI) (Proposal No. 2010B7253).

REFERENCES

(1) Lemoigne, M. *Bull. Soc. Chim. Biol.* **1926**, *8*, 770.
(2) Doi, Y. *Microbial Polyesters*; VCH Publishers: New York, 1990.
(3) Kobayashi, G.; Shiotani, T.; Shima, Y.; Doi, Y. In *Biodegradable Plastics and Polymers*; Doi, Y., Fukuda, K., Eds.; Elsevier: Amsterdam, 1994; p 410.
(4) Doi, Y.; Kitamura, S.; Abe, H. *Macromolecules* **1995**, *28*, 4822.
(5) Satkowski, M. M.; Melik, D. H.; Autran, J.-P.; Green, P. R.; Noda, I.; Schechtman, L. A. In *Biopolymers*; Steinbüchel, A., Doi, Y., Eds.; Wiley-VCH: Weinheim, Germany, 2001; p 231.
(6) Chiellini, E.; Solaro, R. *Recent Advances in Biodegradable Polymers and Plastics*; Wiley-VCH: Weinheim, Germany, 2003.
(7) Doi, Y. *ICBP 2003 First IUPAC International Conference on Bio-Based Polymers; Macromolecular Bioscience*, Vol.4, Issue 3; Wiley-VCH: Weinheim, Germany, 2004.
(8) Iwata, T.; Aoyagi, Y.; Fujita, M.; Yamane, H.; Doi, Y.; Suzuki, Y.; Takeuchi, A.; Uesugi, K. *Macromol. Rapid Commun.* **2004**, *25*, 1100.
(9) Vert, M. *Biomacromolecules* **2005**, *6*, 538.
(10) Bastioli, C. *Handbook of Biodegradable Polymers*; Rapra Technology Limited: U.K., 2005.
(11) Avella, M.; Martusscelli, E.; Greco, P. *Polymer* **1991**, *32*, 1647.
(12) Rodrigues, J. A. F. R.; Parra, D. F.; Lugao, A. B. *J. Therm. Anal. Cal.* **2005**, *79*, 379.
(13) Chiu, H. J.; Chen, H. L.; Lin, T. L.; Lin, J. S. *Macromolecules* **1999**, *32*, 4969.
(14) Chiu, H. J. *J. Appl. Polym. Sci.* **2006**, *100*, 980.
(15) Iriondo, P.; Iruin, J. J.; Fernandez-Berridi, M. J. *Macromolecules* **1996**, *29*, 5605.
(16) Xing, P.; Dong, L.; An, Y.; Feng, Z.; Avella, M.; Martuscelli, E. *Macromolecules* **1997**, *30*, 2726.
(17) Huang, H.; Hu, Y.; Zhang, J.; Sato, H.; Zhang, J.; Noda, I.; Ozaki, Y. *J. Phys. Chem. B* **2005**, *109*, 19175.
(18) Zhang, J.; Sato, H.; Furukawa, T.; Tsuji, H.; Noda, I.; Ozaki, Y. *J. Phys. Chem. B* **2006**, *110* (48), 24463.
(19) Scandola, M.; Ceccorulli, G.; Pizzoli, M. *Macromolecules* **1992**, *25* (24), 6441.
(20) Ceccoruli, G.; Pizzoli, M.; Scandola, M. *Macromolecules* **1993**, *26* (25), 6722.
(21) Pizzoli, M.; Scandola, M.; Ceccorulli, G. *Macromolecules* **1994**, *27* (17), 4755.
(22) El-Shafee, E.; Saad, G. R.; Fahmy, S. M. *Eur. Polym. J.* **2001**, *37*, 2091.
(23) Park, J. W.; Tanaka, T.; Doi, Y.; Iwata, T. *Macromol. Biosci.* **2005**, *5*, 840.
(24) Yu, L.; Dean, K.; Li, L. *Prog. Polym. Sci.* **2006**, *31*, 576.
(25) Ryan, A. J. *Nat. Mater.* **2002**, *1*, 8.
(26) Pernot, H.; Baumert, M.; Court, F.; Leibler, L. *Nat. Mater.* **2002**, *1*, 54.
(27) Kim, H. Y.; Ryu, D. Y.; Jeong, U.; Kho, D. H.; Kim, J. K. *Macromol. Rapid Commun.* **2005**, *26*, 1428.
(28) Asari, T.; Matsuo, S.; Takano, A.; Matsushita, Y. *Macromolecules* **2005**, *38*, 8811.
(29) Kushner, A. M.; Vossler, J. D.; Williams, G. A.; Guan, Z. *J. Am. Chem. Soc.* **2009**, *131*, 8766.
(30) Sato, H.; Nakamura, M.; Padermshoke, A.; Yamaguchi, H.; Terauchi, H.; Ekgasit, S.; Noda, I.; Ozaki, Y. *Macromolecules* **2004**, *37*, 3763.
(31) Sato, H.; Murakami, R.; Padermshoke, A.; Hirose, F.; Senda, K.; Noda, I.; Ozaki, Y. *Macromolecules* **2004**, *37*, 7203.
(32) Sato, H.; Dybal, J.; Murakami, R.; Noda, I.; Ozaki, Y. *J. Mol. Struct.* **2005**, *744–747*, 35.
(33) Zhang, J.; Sato, H.; Tsuji, H.; Noda, I.; Ozaki, Y. *J. Mol. Struct.* **2005**, *735–736*, 249.
(34) Sato, H.; Mori, K.; Murakami, R.; Ando, Y.; Takahashi, I.; Zhang, J.; Terauchi, H.; Hirose, F.; Senda, K.; Tashiro, K.; Noda, I.; Ozaki, Y. *Macromolecules* **2006**, *39*, 1525.
(35) Hu, Y.; Zhang, J.; Sato, H.; Futami, Y.; Noda, I.; Ozaki, Y. *Macromolecules* **2006**, *39*, 3841.
(36) Sato, H.; Ando, Y.; Dybal, J.; Iwata, T.; Noda, I.; Ozaki, Y. *Macromolecules* **2008**, *41*, 4305.
(37) Guo, L.; Sato, H.; Hashimoto, T.; Ozaki, Y. *Macromolecules* **2010**, *43*, 3897.
(38) Sato, H.; Ando, Y.; Mitomo, H.; Ozaki, Y. *Macromolecules* **2011**, *44*, 2829.
(39) Suttiwijitpukdee, N.; Sato, H.; Zhang, J.; Hashimoto, T.; Ozaki, Y. *Polymer* **2011**, *52*, 461.
(40) Suttiwijitpukdee, N.; Sato, H.; Zhang, J.; Hashimoto, T. *Macromolecules* **2011**, *44*, 3467.
(41) Guo, L.; Sato, H.; Hashimoto, T.; Ozaki, Y. *Macromolecules* **2011**, *44*, 2229.
(42) Lodge, T. P.; McLeish, T. C. B. *Macromolecules* **2000**, *33*, 5278.
(43) Zhao, J.; Ediger, M. D.; Sun, Y.; Yu, L. *Macromolecules* **2009**, *42*, 6777.
(44) Vonk, C. G. *J. Appl. Crystallogr.* **1973**, *6*, 81.
(45) Rathje, J.; Ruland, W. *Colloid Polym. Sci.* **1976**, *254*, 358.
(46) Guo, L.; Spegazzini, N.; Sato, H.; Hashimoto, T.; Masunaga, H.; Sasaki, S.; Takata, M.; Ozaki, Y. *Macromolecules* **2012**, *45*, 313.
(47) Hosemann, R.; Bagchi, S. N. *Direct Analysis of Diffraction by Matter*: North-Holland: Amsterdam, 1962.
(48) Hashimoto, T.; Todo, A.; Kawai, H. *Polym. J.* **1978**, *10*, 521.
(49) Hashimoto, T.; Ebisu, S.; Kawai, H. *J. Polym. Sci., Polym. Phys. Ed.* **1981**, *19*, 59.
(50) Landau, L. D.; Lifshitz, E. M. *Statistical Physics*; Pergamon: New York, 1964.
(51) Cahn, J. W.; Hilliard, J. E. *J. Chem. Phys.* **1958**, *29*, 258.
(52) de Gennes, P. G. *Scaling Concepts in Polymer Physics*; Cornell University Press: Ithaca, NY, 1979.
(53) If there is more than one peak, we take the highest melting peak.
(54) Fox, T. G. *Bull. Am. Phys. Soc* **1953**, *1*, 123.
(55) $w_{CABa\bar{m}} = ((0.5)/([0.5 + (0.5 - X_{c,PHB})]) = ((0.5)/((1 - 0.28))) = 0.69$.

(56) In order to compare the thermal behavior of the various physical quantities shown in Figures 10 and 11, it is important to note the difference in the initial states attained in the as-prepared films of the PHB/CAB blends and those of the pure PHB and CAB as well as those attained in the as-prepared films for the DSC measurements and for the SAXS/WAXD measurement as described earlier in section 2.1. Generally, the quenching of the specimens from the specified heat-treatment temperatures to the liquid nitrogen temperature is more effective for thin films used for the DSC measurements than for the thick films used for the SAXS/WAXD measurements. This will make the initial crystallinity of PHB in the as-prepared SAXS/WAXD samples larger than that in the as-prepared DSC samples.

(57) The difference between the observed intensity I (q = 0.2 nm^{-1}) shown by the filled symbols and the intensity drawn by the broken line in Figure 10c is expected to stem from the scattering by the PHB assemblies.

(58) The crystallinity of the as-prepared films for PHB/CAB blends measured by DSC and WAXD decreased with the increase in the CAB concentration. Qualitatively, the degree of crystallinity obtained by DSC and WAXD shows the same tendency (see Figure 7 and Table 1 of ref 39).

dx.doi.org/10.1021/ma202606y | *Macromolecules* 2012, 45, 2783−2795

Macromolecules

Article

pubs.acs.org/Macromolecules

Local Conformation and Cocrystallization Phenomena in Renewable Diaminoisoidide-Based Polyamides Studied by FT-IR, Solid State NMR, and WAXD

Lidia Jasinska-Walc,[†,‡,§] Maurizio Villani,[∥] Dmytro Dudenko,[⊥] Otto van Asselen, Enno Klop,[#] Sanjay Rastogi,[∥,#] Michael Ryan Hansen,[⊥] and Cor E. Koning*[,†,‡,&]

[†]Laboratory of Polymer Chemistry, Eindhoven University of Technology, Den Dolech 2, P.O. Box 513, 5600 MB Eindhoven, The Netherlands

[‡]Dutch Polymer Institute (DPI), PO Box 902, 5600 AX Eindhoven, The Netherlands

[§]Department of Polymer Technology, Chemical Faculty, Gdansk University of Technology, G. Narutowicza Str. 11/12, 80-952 Gdansk, Poland

[∥]Laboratory of Polymer Technology, Eindhoven University of Technology, P.O. Box 513, 5600MB Eindhoven, The Netherlands

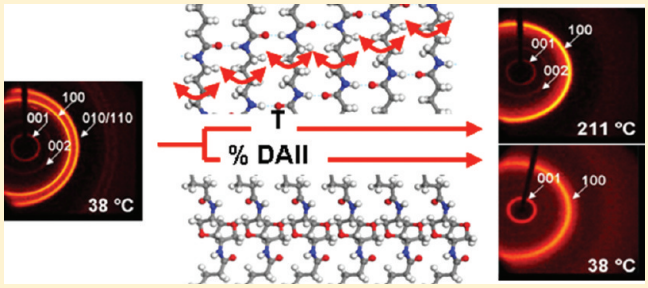
[⊥]Max Planck Institute for Polymer Research, Ackermannweg 10, 55128 Mainz, Germany

[#]Teijin Aramid BV, Research Institute, P.O. Box 5153, 6802 ED Arnhem, The Netherlands

[&]DSM Coating Resins, Ceintuurbaan 5, Zwolle, The Netherlands

Supporting Information

ABSTRACT: Biobased polyamides synthesized from diaminoisoidide (DAII), 1,4-diaminobutane, and sebacic acid are investigated by FT-IR, $^{13}C\{^{1}H\}$ magic-angle spinning/cross-polarization (CP/MAS) NMR spectroscopy, and WAXD. Their molecular conformation and mobility undergo distinct changes as a function of temperature and diaminoisoidide content in the compositions. The presence of randomly distributed diaminoisoidide (DAII) in the polyamides reduces their hydrogen bond density and affects the *trans/gauche* conformer population. FT-IR and $^{13}C\{^{1}H\}$ CP/MAS NMR were successfully employed to prove the incorporation of DAII both in the crystalline and amorphous phase of these materials. Changes in the position and intensities of the diaminoisoidide-assigned FT-IR and NMR signals prove that the DAII monomer causes a conformational disorder of the polyamides and thus influences the crystal structure of these materials, as also shown by WAXD experiments. Extensive *ab initio* calculations using a combination of DFT and MP2 methods reveal a number of stable conformers of DAII and thus an unexpectedly high flexibility of the isohexide unit.



INTRODUCTION

Isohexides have been recently regarded as one of the most promising alternatives for petrochemical monomers. The possible use of starch-based 1,4;3,6-dianhydrohexitols (isosorbide, isomannide, and isoidide) or their diamino derivatives with D-manno or L-ido conformation in the synthesis of poly(ester−amides) (PEAs) or polyamides (PAs) provides partially or entirely biobased materials and consequently demonstrates their multiple applications.[1−8] These bicyclic compounds are of natural origin, and their degradation products are nontoxic; Kricheldorf et al.[4] and Okada et al.[7] proved that isohexitol-based polymers can be successfully used as bioanalogous or biodegradable materials. Furthermore, a new approach toward poly(ester−amides) from isosorbide was proposed by Philip and Sreekumar.[8] These authors obtained optically active materials with high T_g's, which can be applied as electro-optic devices. Hitherto, isohexides are usually used as T_g-enhancing agents. However, our recent investigations revealed that diaminoisoidide (DAII), the exoexo diamine derivative of dianhydrohexitols, incorporated into the PA 4.10 backbone reduces the hydrogen bond density and thus the melting point of the polyamides.[9] This aspect in turn is especially important in view of their practical applications, since this allows tailoring hydrogen bonding which is required for some applications where melting temperature is not of critical importance.

Regardless of the chemical composition, polyamides exhibit a characteristic semicrystalline structure consisting of chain-folded, hydrogen-bonded sheets held together by van der Waals forces.[10,11] As reported previously, depending on the

Received: January 18, 2012
Revised: March 5, 2012
Published: March 13, 2012

 © 2012 American Chemical Society

distance between recurring amide groups, the sheets can stack together either with a progressive shear, yielding the so-called α-phase, or with an alternating shear, yielding the so-called β-phase.[12−20] The X-ray diffraction profiles of such polyamides display a typical diffraction peak indexed as 100 related to the interchain distance, as well as a 010/110 diffraction peak, related to the intersheet distance. Generally, for the known and commercially available PAs the formation of a pseudohexagonal phase is observed upon a solid state crystal to crystal transition upon heating (Brill transition).[13,21,22] The transformation of the triclinic structure with different interchain/intersheet distances into the pseudohexagonal form can be associated with the formation of hydrogen bonds between chains lying in adjacent sheets of the polyamides.[23] However, more recently it was proposed that no intersheet H-bonding occurs at the Brill transition temperature and that the intersheet and interchain distances become equal by a kind of cylindrical rotation of the methylene units between the H-bonded amide groups.[24] As it is well-known, the Brill transition observed using temperature-dependent WAXD experiments occurs as the merging of two X-ray diffraction peaks corresponding to the interchain and intersheet distances into a single diffraction peak. These changes, depending on the chemical structure and length of the repeat unit of the polyamides, can usually be observed either somewhat below or at the melting point of the polymers. Nonetheless, our recent XRD study carried out at room temperature for the copolyamides based on diaminoisoidide, 1,4-diaminobutane (DAB), and sebacic acid[9] showed that with increasing diaminoisoidide content in the copolyamides the typical structure with different interchain and intersheet distance was preserved for the products with DAII contents lower than around 40 mol %, while for the materials with higher DAII contents the structure changed into a close to hexagonal packing of polymer chains.

To follow the conformational changes of nylons, several spectroscopic techniques have been employed successfully. One of the commonly used methods for the analysis of polyamide chain motions is FT-IR spectroscopy. As reported earlier, a detailed insight into the position and intensity of FT-IR signals allowed to establish that during the Brill transition marked conformational changes occur in the methylene sequences of the polyamides, which reveal an enhanced mobility upon heating.[25−28] The conformational reorganization together with the weakening of the hydrogen bonding of the polymers can also be observed by $^{13}C\{^1H\}$ cross-polarization NMR spectroscopy (CP/MAS NMR).[29−32] More interesting, however, is that $^{13}C\{^1H\}$ CP/MAS NMR analysis can provide information regarding the coexistence of various crystalline polymorphs in the polymers and the differences in the conformational freedom of polymer chains within crystalline and noncrystalline regions.[33,34]

In our previous work we reported the synthetic route and the structural and thermal characterization of novel, fully renewable homo- and copolyamides from diaminoisoidide (synthesized from isomannide), 1,4-diaminobutane (in nature known as putrescine), and sebacic acid (derived from castor oil) (see Figure 1).[9] The X-ray analysis of the polyamides revealed that the presence of the DAII units in the polyamides affects their crystal structure. The present study focuses on the conformational changes and local chain dynamics of diaminoisoidide-based polyamides upon heating. $^{13}C\{^1H\}$ CP/MAS NMR and FT-IR spectroscopy were used as powerful techniques for the analysis of the structural behavior and mobility of the

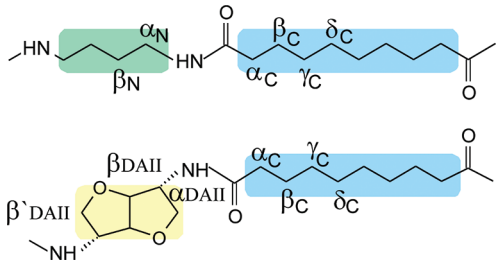


Figure 1. Sebacic acid (SA)/1,4-diaminobutane (DAB) and sebacic acid (SA)/diaminoisoidide (DAII) repeat units in the polyamides. Blue, green, and yellow areas depict PA chain fragments between the amide groups. Carbon labels, presented also in Table 2, were used for solid state NMR analysis.

polyamides as a function of the temperature. Particular attention was given to phase separation and the presence of diaminoisoidide in the crystal structure of the biobased materials. These techniques in combination with WAXD analysis were used to investigate cocrystallization of the comonomers.

EXPERIMENTAL SECTION

Materials. The homopolyamides and copolyamides based on diaminoisoidide (DAII), 1,4-diaminobutane (DAB), and sebacic acid (SA) (Figure 1) were synthesized via bulk polycondensation followed by solid state polymerization (SSP) or by interfacial polycondensation, as described in our previous work.[9] In this article the characterization of the polyamides including solution state NMR experiments, SEC, FT-IR, TGA, DSC, and room temperature WAXD analysis was presented. Temperature-dependent FT-IR, solid state NMR, and WAXD studies were carried out on the homopolymers based on 1,4-diaminobutane and sebacic acid (PA1) or diaminoisoidide and sebacic acid (PA2) as well as on the copolymers containing 20 and 43 mol % of diaminoisoidide (coPA3 and coPA4), respectively. For an overview of the molecular characterization and thermal properties of these polyamides see Table 1.

Table 1. Built-in Composition, Molecular Weight, Melting, and Crystallization Temperatures and Enthalpy of the Transitions Analyzed from the Second DSC Heating and Cooling Runs of the Homo- and Copolyamides

symbol	built-in composition (DAB/DAII)[a]	M_n (g/mol)	T_m (°C)	ΔH_m (J/g)	T_c (°C)	ΔH_c (J/g)
PA1	1.0/0	21900	246	67.3	221	75.4
PA2	0/1.0	4200	152	15.1	96	11.4
coPA3	0.80/0.20	20400	232	40.9	198	45.3
coPA4	0.57/0.43	3900	179, 198	32.8	156	39.3

[a]Molar ratio determined by NMR, T_m = melting point, T_c = crystallization temperature, and ΔH = enthalpy of the transition during melting (m) or crystallization (c).

FT-IR. Fourier transform infrared spectra (FT-IR) were obtained using a Varian 610-IR spectrometer equipped with an FT-IR microscope. The spectra were recorded in a transmission mode with a resolution of 2 cm^{-1}. PA films obtained from 1,1,1,3,3,3-hexafluoroisopropanol were analyzed on a zinc selenium disk and heated from 30 °C to slightly above melting points of the polyamides. For the purpose a Linkam TMS94 hotstage and controller were used. The samples were cooled in 10 °C steps and reheated with the same heating steps. For the study the spectra from the second heating run were collected. Varian Resolution Pro software version 4.0.5.009 was used for the analysis of the spectra.

dx.doi.org/10.1021/ma300133d | Macromolecules 2012, 45, 2796−2808

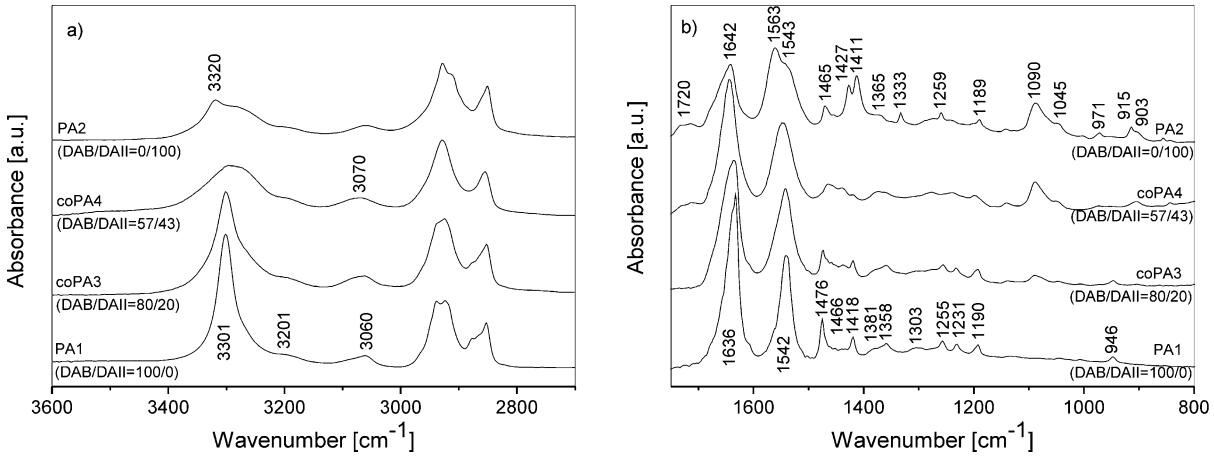


Figure 2. FT-IR spectra of homopolyamides PA1, PA2 and copolyamides coPA3, coPA4 recorded at 30 °C. The spectra show frequency ranges from 3600 to 2700 cm^{-1} (a) and 1750−800 cm^{-1} (b).

DSC. DSC measurements were carried out using DSC Q100 from TA Instruments. The analyses were performed in a nitrogen atmosphere with a heating rate of 10 °C/min. The events were analyzed from the second heating and cooling curve.

Solid State NMR. Variable-temperature (VT) $^{13}C\{^1H\}$ magic-angle spinning/cross-polarization (CP/MAS) NMR experiments were carried out on a Bruker ASX-500 spectrometer employing a double-resonance probe for rotors with 4.0 mm outside diameter. These experiments used 10.0 kHz MAS and a 4 μs $\pi/2$ pulse for ^1H. All VT $^{13}C\{^1H\}$ CP/MAS NMR spectra were recorded using a CP contact time of 3.0 ms and TPPM decoupling[35] during acquisition. The temperature was controlled using a Bruker temperature control unit in the range from 30 to 210 °C. The VT $^{13}C\{^1H\}$ CP/MAS NMR spectra were recorded under isothermal conditions at intervals of 10 °C, employing a heating rate of 2 °C/min between temperatures. Reported temperatures are corrected for friction induced heating due to spinning using ^{207}Pb MAS NMR of $Pb(NO_3)_2$ as a NMR thermometer.[36] The 2D $^1H-^1H$ double-quantum single-quantum (DQ-SQ) correlation and $^{13}C\{^1H\}$ frequency-switched Lee−Goldburg heteronuclear correlation (FSLG-HETCOR) experiments[37,38] were performed on a Bruker AVANCE-III 850 spectrometer using a double-resonance probe for rotors with 2.5 mm outside diameter. These experiments used spinning frequencies of 25.0 and 15.0 kHz, respectively. DQ excitation was performed using the BaBa sequence and the FSLG-HETCOR experiment used a CP time of 3.0 ms. Chemical shifts for ^1H and ^{13}C MAS NMR are reported relative to TMS using solid adamantane as an external reference.[39] CP conditions were optimized using L-alanine. All samples were annealed just below their melting temperature for 5 min under a flow of nitrogen gas before NMR analysis to remove precipitation-induced structural conformations.

Geometry Optimization and NMR Chemical Shift Calculations. All calculations were performed with a Gaussian03 program package (see ref 6 in Supporting Information). The geometries of 21 possible conformations obtained from the 1D potential energy surface (1D-PES) scanning procedure (Figure S1) were further fully optimized at the MP2/6-31G*, MP2/6-311G**, and the computationally less demanding B97-1/6-311G** level of theory. Harmonic vibrational frequencies and the Gibbs free energy differences were evaluated at the MP2/6-31G* and B97-1/6-311G** levels of theory. The most favorable conformers by energy (for both DFT and MP2 methods) have been proceeded for further NMR chemical shifts calculations at the B97-1/6-311G** level of theory. Further details about the 1D-PES procedure and the NMR chemical shift calculations are given in the Supporting Information.

WAXD. X-ray diffraction patterns were obtained employing a Bruker AXS HI-STAR area detector installed on a P4 diffractometer, using graphite-monochromated Cu Kα radiation (λ = 1.5418 Å) and a 0.5 mm collimator. The data were collected on SSP-synthesized powder contained in glass capillaries during heating at 10 °C/min from around 40 °C to melt and cooling from the melt to 40 °C with acquisition times of 5 min, using a Linkam TMS94 hotstage. Successively, the values of the temperatures reported here for heating/cooling cycles have been obtained by correcting the displayed temperature observed using the modified Linkam hotstage (see Supporting Information). This correction was made using a calibration curve with well-known melting temperature standards. The 2D data were corrected for detector nonuniformity and spatial distortion, subsequently background-corrected, and transformed into 1D profiles via integration.

RESULTS AND DISCUSSION

Spectroscopic techniques are very valuable to elucidate the conformational changes and chain motions of the polymers. For the analysis of polymer chain organization, the combination of Fourier transformed infrared (FT-IR) and solid state NMR spectroscopy is particularly suitable for obtaining complementary results. We employed FT-IR and $^{13}C\{^1H\}$ CP/MAS NMR spectroscopy for probing local conformations and cocrystallization of the comonomers in the crystal lattice of diaminoisoidide-based copolyamides. WAXD analysis was used to confirm the influence of local conformation on the chain packing of diaminoisoidide-based copolyamides.

Infrared Analysis of the Polyamides. FT-IR spectra of the homopolyamides PA1, PA2 and copolyamides coPA3, coPA4 (see Table 1) recorded at 30 °C are presented in Figure 2a,b. The figure shows spectra normalized according to the area under the symmetric and asymmetric methylene bands (2800−3000 cm^{-1}) in two spectral ranges, viz. 2700−3600 and 800−1750 cm^{-1}. By comparison of the bands at 3301−3320 and 3060−3070 cm^{-1}, which are assigned to the NH stretch and NH stretch with amide II overtone vibrations, significant changes in intensity can be observed. As reported by Schroeder et al.[40] and Skrovanek et al.,[41,42] the broadness and decrease in the intensity of the N−H stretching mode at 3300−3320 cm^{-1} upon heating of the linear polyamides are caused by a decrease in the absorptivity coefficient reflecting hydrogen bond diminishes and transformation of the hydrogen-bonded N−H groups into "free" and non-hydrogen-bonded N−H groups. Furthermore, the FT-IR studies employed by authors of even- and odd-type nylons revealed that the frequency of such bands reflects the average strength of the hydrogen-bonded N−H groups.[42] Following these observations and comparing the N−H stretching mode of the DAII-based polyamides, one can

dx.doi.org/10.1021/ma300133d | Macromolecules 2012, 45, 2796−2808

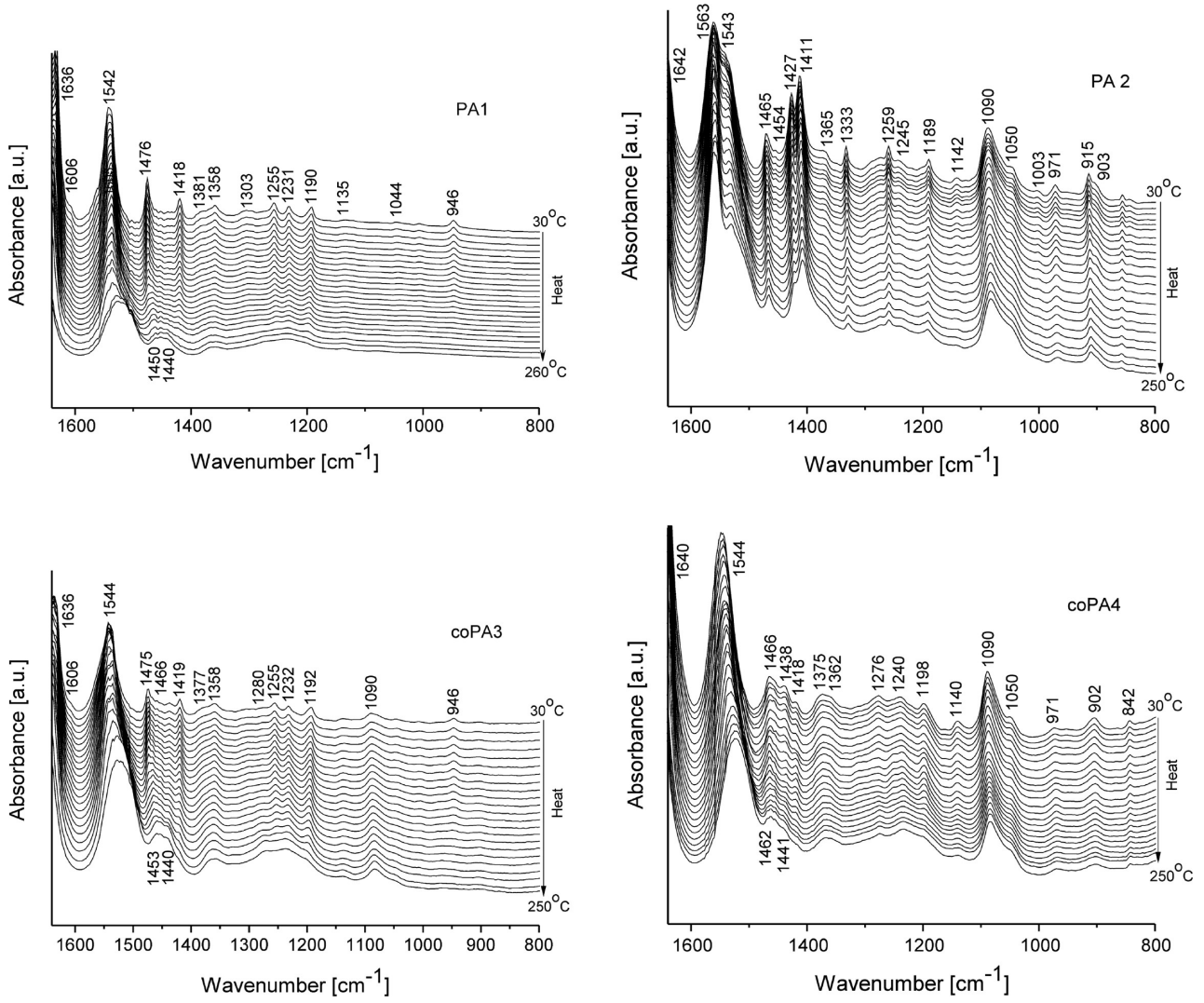


Figure 3. FT-IR spectra recorded on heating from 30 °C to above the melting point of the homopolyamides PA1, PA2 and copolyamides coPA3, coPA4 containing 23 and 48 wt % of diaminoisoidide, respectively.

conclude that the decrease and broadening of these signals, observed with increasing DAII content in the polyamides, are attributed to the change of their crystalline order and different strength of the hydrogen bonds in these materials. In the spectra recorded at 30 °C non-hydrogen-bonded N−H bands, usually observed at 3440−3450 cm^{-1}, were not detected as a result of their relatively low intensity and/or broadening of the hydrogen-bonded N−H mode. However, the FT-IR analysis supported by the 2D $^{13}C\{^{1}H\}$ FSLG-HETCOR results discussed below indicates that the incorporation of DAII units affects the hydrogen bond density and formation of non-hydrogen-bonded N−H groups in the synthesized polyamides. On this basis, the band visible at 1720 cm^{-1} and more pronounced for DAII-rich compositions can be assigned to non-hydrogen-bonded carbonyl groups. These signals for linear polyamides are usually visible around 1670−1690 cm^{-1}; however, the presence of isohexide units in the backbone of the polyamides might affect the shift in frequency of non-hydrogen-bonded amide I bands. Moreover, C−O−C groups of isohexide can contribute in the formation of the hydrogen bonds influencing the amount of carbonyl group that do not participate in hydrogen bonding. Simultaneously, in the region 800−1750 cm^{-1} (Figure 2b) several differences between the recorded spectra can be observed. For the copolymers and the homopolymer PA2 based on diaminoisoidide, new signals at 1333 cm^{-1} were found which are attributed to the amide III vibrations.[25,28] The presence of diaminoisoidide in the structure of the polymers was also proven by the development of the bands in the vicinity of 1080−1100 cm^{-1}. These signals are characteristic for the asymmetric COC stretching mode in ethers,[43] and the bands increase in intensity with increasing diaminoisoidide content of the PAs. An increased absorbance is also observed at 971, 911−915, and at 903 cm^{-1}. These bands are assigned to CH_2 rocking vibrations and to the C−CO stretching vibration in the crystalline phase.[44] Interesting information is also provided by bands at 1563 and 1411 cm^{-1}, found for PA2 synthesized via interfacial polycondensation and assigned to asymmetric and symmetric COO^{-} stretch vibrations, respectively.[43] These bands are characteristic for carboxylic acid ammonium salt and imply the presence of polyamide salt residuals formed as a byproduct during the synthesis.

In Figure 3, FT-IR spectra recorded upon heating of the homopolymers PA1, PA2 and the copolymers containing 20 and 43 mol % of DAII (coPA3, coPA4) are presented. The spectra of PA1 and coPA3 show broadening and weakening of

dx.doi.org/10.1021/ma300133d | Macromolecules 2012, 45, 2796−2808

the bands at 1476 and 1418 cm^{-1}, which are considered as CH_2 scissoring next to NH moieties with trans conformation and CH_2 scissoring next to CO moieties with trans conformation, respectively.[27,28] As reported by Yoshioka et al.,[27] the conformational changes of methylene segments attached to NH and CO moieties are related to the Brill transition of polyamides. Because of the lower energy barrier of the torsion around CH_2−NH, the thermal motion of these chain fragments is more pronounced as compared to the CH_2−CO fragments. These results are in agreement with our observations, since along with the decrease of hydrogen bond density the vibrations of the bands assigned to CH_2−NH at around 190 °C show a significantly reduced intensity, consistent with the hexagonal packing of PA1 chains above the Brill temperature. Simultaneously, when the trans conformation is lost upon heating, the signals around 1450 and 1440 cm^{-1} assigned to the CH scissor vibrations of gauche conformers become more visible. On the other hand, the signals at 1381, 1303, 1255, 1231, and 1044 cm^{-1} originating from CH_2 wagging or twisting and skeletal C−C stretch vibrations show broadening and weakening with increasing temperature.[25,26,28,45] Since the bands at 1381, 1303, and 1044 cm^{-1} almost disappear above 190 °C, they can be considered as Brill bands. The amide II and amide III coupled with hydrocarbon skeleton bands at 1542, 1358, and 1190 cm^{-1} also become broader and weaker; however, their presence is visible up to the melting point of the polyamide.[28] The copolymer containing 20 mol % of DAII (coPA3) undergoes similar conformational changes as PA1. However, as demonstrated previously,[9] diaminoisoidide-rich coPA4 and PA2 show a different behavior and crystallize into a close to hexagonal packing of the polymer chains. In agreement with this, the characteristic Brill bands visible for PA1 and coPA3 and the band at 1476 cm^{-1}, related to CH_2 scissoring next to NH moieties with trans conformation, are not observed for these polyamides (Figure 3). On the other hand, several new peaks assigned to the amorphous or crystalline phase of the polyamides were recognized. The bands observed above the melting point at 1080−1090, 1333, 1259, and 915 cm^{-1} in the spectra of the PA2 are related to the amorphous phase. Simultaneously, as discussed above, the presence of amide stretching vibration bands at 902−903 cm^{-1} in the spectra of PA2 and coPA4 and the vanishing of these bands at around 150−180 °C can be considered as further proof that DAII is present in the crystal phase of the PAs. This is in agreement with DSC measurements ($T_{m,PA2}$ = 152 °C, $T_{m1,coPA4}$ = 179 °C, see Table 1) and ^{13}C MAS NMR analysis of these polyamides (see below). Similar behavior, depicted by broadening and finally disappearance, shows the bands assigned to the C−CO stretch "crystalline band" at 946 cm^{-1} in the spectra of PA1 and coPA3; i.e., they become broader and weaker until disappearing when the melting temperature has been reached.[28]

Variable-Temperature Solid-State NMR Study. In our previous study we applied 2D solution-state NMR experiments (^1H−^1H COSY and ^1H−^{13}C gHMBC) to investigate the partial substitution of the linear 1,4-diaminobutane (DAB) in polyamide 4.10 by diaminoisoidide (DAII).[9] The examination revealed the presence of both DAB and DAII residues bonded to sebacic acid with almost expected compositions. In the solid state of these polymers, however, the packing will be governed by the hydrogen-bonding efficiency of the amide groups between the neighboring polymer chains as well as the flexibility of the DAII unit. Such complex packing behavior may lead to the presence of DAB and DAII residues in both crystalline and amorphous regions in the polymer samples. To reveal this kind of information, we used in the present work $^{13}C\{^1H\}$ CP/MAS NMR spectroscopy as a powerful technique for the analysis of the structural behavior of chain parts of the polyamides and their mobility upon heating. Furthermore, the experiments were performed as a function of temperature to characterize the different chain conformations and their populations in the samples. Particular attention was given to investigate phase separation and the presence of DAII in the crystal structure of the biobased materials. For the overall picture of the sample compositions with respect to crystalline and noncrystalline domains, the temperature-dependent $^{13}C\{^1H\}$ CP/MAS NMR experiments will give comparable results to those that can be obtained using T_1- or $T_{1\rho}$-filtering of ^{13}C.[34,46] This is due to interference effects that occur during the CP transfer step leading to a signal loss if the rate of molecular dynamics is on the time scale of the applied MAS or radio-frequency spin-lock fields. A recent example where this strategy has been utilized to determine phase compositions includes the characterization of block copolymers based on polypeptides.[47] For $^{13}C\{^1H\}$ CP/MAS NMR experiments the homopolyamides from DAB/DAII and SA (PA1 and PA2) were chosen as well as the copolyamide coPA4 with a DAB/DAII mole ratio of 0.57/0.43. The results presented in Figures 4−7, using the labeling scheme shown in Figure 1 and Table 2, summarize the isotropic ^{13}C chemical shifts for the α-, β-, γ-, and δ-methylene signals of the synthesized polyamides.

For PA1 several signals in the aliphatic region 25−45 ppm can be observed at 41.0 °C (Figure 4). These signals, together

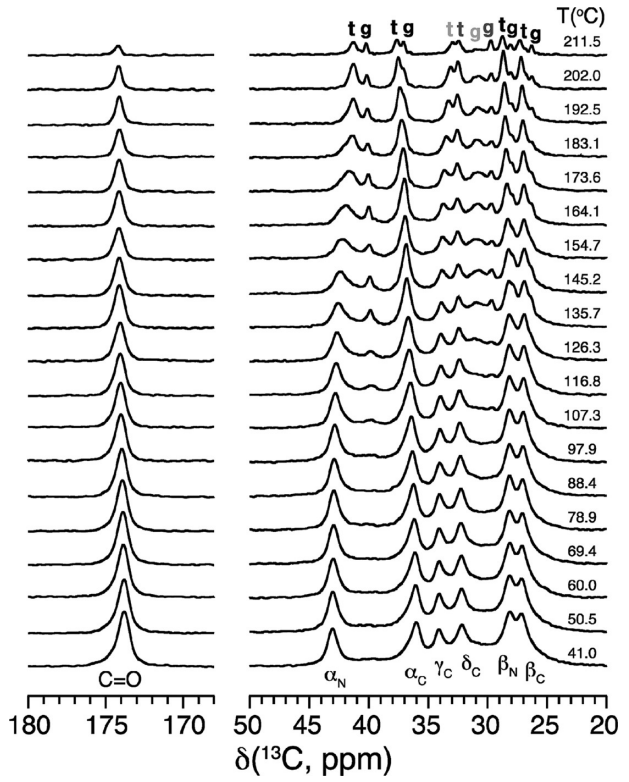


Figure 4. Variable-temperature solid-state $^{13}C\{^1H\}$ CP/MAS NMR spectra of the homopolyamide PA1 (commercially known as PA 4.10) recorded at 11.75 T (500 MHz for ^1H). Letters above the spectra indicate the positions of trans (t) and gauche (g) conformers while the assignment below employs the scheme shown in Figure 1.

dx.doi.org/10.1021/ma300133d | Macromolecules 2012, 45, 2796−2808

Table 2. ^{13}C Chemical Shifts for the Homopolyamides PA1, PA2 and Copolyamide coPA4 at 41.0 °C and Close to the Melting Point (211.5 or 164.1 °C)

	^{13}C chemical shift (ppm)									
	C=O	α_N	α_C	γ_C	δ_C	β_N	β_C	α_{DAII}	β_{DAII}	β'_{DAII}
PA1										
41.0 °C	173.9	43.1	36.1	34.2	32.2	28.1	27.3			
211.5 °C	174.2	41.3	37.6	33.0	32.7	28.7	27.2			
PA2										
41.0 °C	173.9		39.4	33.5−29.9	33.5−29.9		26.7	57.5	87.2	70.2
	179.8		37.4					55.0		
164.1 °C	179.3		39.9	33.2−29.5	33.2−29.5		26.3	57.8	88.1	73.0
			37.0							
coPA4										
41.0 °C	174.0	43.2	40.8	36.5	34.0−21.0	34.0−21.0	34.0−21.0	57.5	89.0	70.2
164.1 °C	174.5	42.4	40.3	37.3	34.0−25.0	34.0−25.0	34.0−25.0	58.2	88.4	73.3

with the single carbonyl at 173.9 ppm, appear relatively broad as a result of sample heterogeneity, conformational distributions, and local susceptibility present in the solid state of the polymer.[31,48] A careful examination of the ^{13}C aliphatic region allows the assignment of both sets of α- and β-methylene carbons related to the SA and DAB parts (see Figure 1 and Table 2). Moreover, the resonances originating from the γ_C- and δ_C-methylene groups can also be assigned. Upon heating, additional signals for PA1 are observed. Changes in their chemical shift position and intensity indicate a dynamic balance in statistics and populations of trans and gauche conformers.[49−51] The two different conformers are related to crystalline and noncrystalline parts of the sample, respectively, where the latter is a result of increased local chain mobility. For example, the gauche conformers for the α_N signal of PA1 are visible at a relatively low temperature of ∼110 °C, whereas these conformers for α_C become clearly visible at ∼190 °C only. Similar trends can be observed for the β_C and β_N resonances where the gauche conformers for both signals are visible at ∼115 °C. These observations suggest that the increased local molecular dynamics of the methylene units between hydrogen-bonded amide motifs, holding the polymer chains together in a sheetlike structure, first induces gauche conformations in the DAB part, while the SA part is affected at higher temperatures. Moreover, the ^{13}C chemical shift position of the α_C signal closely follows that of the carbonyl, supporting the idea that the increase in dynamics of the methylene motif is first propagated toward the DAB part. For the inner methylene groups of the SA part, γ_C and δ_C, the increase in mobility and appearance of gauche conformers are already visible at ∼120 °C. These observations show that the increase in dynamics of the amide motifs by out-of-plane wagging lead to a gradual reduction in hydrogen-bonding strength, causing displacement of the carbonyl and α_C to low field (higher ppm values). In addition to this dynamic process, the γ_C and δ_C methylene groups of the SA part also display increased mobility even at lower temperatures. For all resonances the gradual appearance of more gauche conformers causes a visible reduction in the fraction of trans conformers, although the performed $^{13}C\{^1H\}$ CP/MAS experiments are not quantitative; i.e., the CP transfer step mediated through the dipole−dipole coupling between ^{13}C and ^1H is reduced by mobility. Nevertheless, this observation is in line with the FT-IR analysis of PA1 (Figure 3, PA1), where above 190 °C the signals related to CH_2 scissoring vibration next to NH moieties with trans conformation and CH_2 scissoring vibration next to CO moieties with trans conformation at 1476 and 1418 cm^{-1}, respectively, become broader and then almost vanish. This finally leads to the Brill transition for PA1 (see WAXD analysis below).

For the homopolymer PA2 based on SA and DAII (Figure 1), the temperature-induced structural changes by increased molecular dynamics of the amide and methylene groups are less pronounced due to a broad overlap of the resonances in the region 20−45 ppm (Figure 5a). However, the PA2 sample includes two different carbonyl signals at 179.8 and 173.9 ppm, indicating two different chemical environments for PA2. Considering the low molecular weight of PA2 (see Table 1) and the difference in ^{13}C chemical shifts, it is possible to assign the signal at 173.9 ppm to SA bonded to DAII in the polymer chains, forming amide groups, and the signal at 179.8 ppm to nonpolymerized SA end groups, i.e., carboxylic acid groups. The presence of two different carbonyl environments also influences the DAII units found in the region 50−90 ppm. Here, the α_{DAII} resonances at ∼55 ppm and are split into two distinct signals, while the resonance for β_{DAII} and β'_{DAII} at ∼85 and ∼70 ppm, respectively, display broad multiple overlapping signals. These spectral features show that the DAII groups are quite flexible and can adopt a range of conformations (see below). Interestingly, the carbonyl signal at 173.9 ppm decreases on increasing temperature, whereas the signal at 179.8 ppm does not. Likewise, the decrease in signal intensity on going to higher temperatures can also be seen for the DAII units where only one of the signals from the α_{DAII} and β_{DAII} resonances, right- and leftmost, respectively, follow this trend. Thus, the carbonyl signal at 173.9 ppm and the signals following its decrease arise from amide groups in the polymer chains, which suggests that these signals originate from the crystalline part of the sample. The disappearance of the amide carbonyl signal at 173.9 ppm above 145 °C illustrate that the hydrogen bonds formed between the polymer chains in PA2 are somewhat weaker than those formed in PA1, resulting in the lower melting point for PA2. In contrast, the resonances associated with the carboxyl groups at 179.8 ppm represent the amorphous regions, which were further supported by the chemical shift position of these signals in the molten state of PA2 (top spectrum in Figure 5a). Surprisingly, the amorphous regions give a stronger CP signal than the corresponding signals from the crystalline domains. This could be related to the dimer formation of the carboxyl end groups or trapping caused by entanglement.[52] To further characterize the hydrogen bonding and molecular packing of PA2, the 2D $^{13}C\{^1H\}$ FSLG-HETCOR and $^1H-^1H$ DQ-SQ correlation spectra shown in

dx.doi.org/10.1021/ma300133d | Macromolecules 2012, 45, 2796−2808

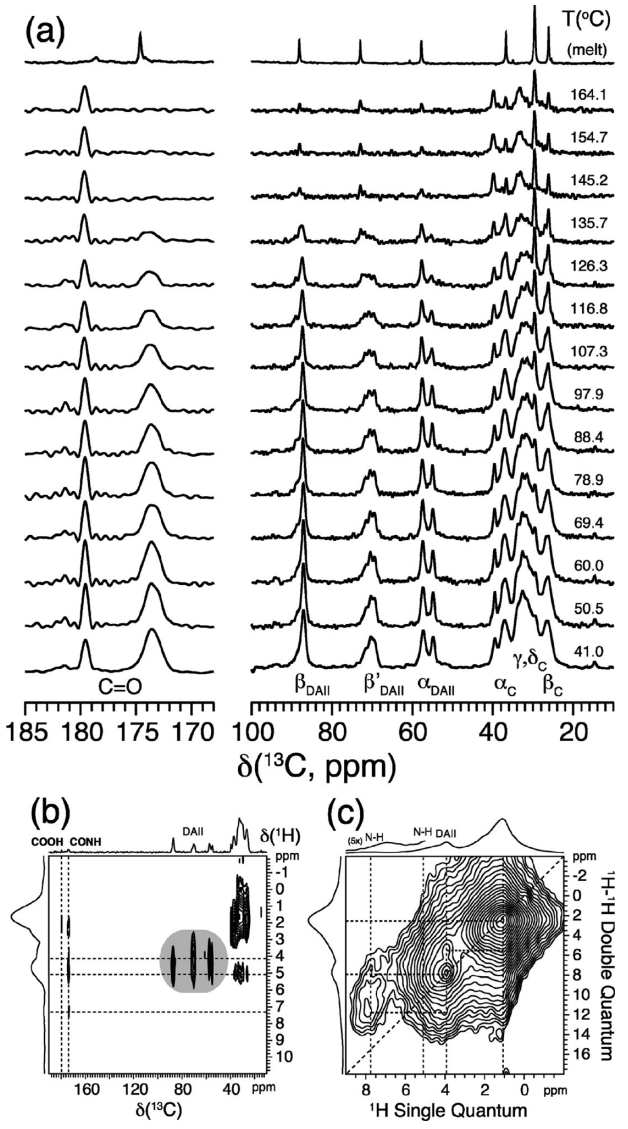


Figure 5. (a) Variable-temperature solid-state $^{13}C\{^1H\}$ CP/MAS NMR spectra of the homopolyamide PA2 recorded at 11.75 T (500 MHz for ^1H). (b) 2D $^{13}C\{^1H\}$ FSLG-HETCOR spectrum acquired using a 3.0 ms CP step and five FLSG blocks per t_1 increment to improve the ^1H resolution. (c) 2D $^1H-^1H$ double-quantum single-quantum (DQ-SQ) spectrum recorded using 80.0 μs of BaBa recoupling time. Both 2D spectra were recorded at 20.0 T, corresponding to 850.27 MHz for ^1H. The dashed lines in (b) and (c) identify selected cross-peaks and autocorrelation peaks.

Figures 5b and 5c have been recorded. From these spectra it is apparent that the amide groups give rise to two distinct ^1H signals centered at 5.0 and 7.3 ppm with quite different intensities (Figure 5b). The signals are not in close spatial proximity since no clear autocorrelation or off-diagonal cross-peaks between them is observed in the 2D $^1H-^1H$ DQ-SQ correlation spectrum (Figure 5c). Based on the ^1H chemical shifts, their intensities, and the values expected for hydrogen bonding of polyamides around 8 ppm,[53] the signals at 5.0 and 7.3 ppm can be assigned to DAII residues for which no hydrogen bonding occurs and to DAII groups with weak hydrogen bonding to the SA part, respectively. Combining the above results for PA2 suggests that the DAII units can be incorporated in both crystalline and noncrystalline regions of the sample. The crystalline regions are characterized by a pseudohexagonal structure where weak hydrogen bonds between the polymer chains are formed. The amorphous regions are, on the other hand, less structured and appear to be more stable with respect to temperature than the crystalline part, which most likely is caused by trapping of the carboxyl groups due to entanglement formation of polymer chains and/or dimer formation between them.

Figure 6 displays the VT $^{13}C\{^1H\}$ CP/MAS NMR results for the copolymer coPA4 with a DAB/DAII molar ratio of 0.57/0.43. From these spectra it is clear that all DAII-based fragments are fully incorporated into the copolymer due to the fact that only a single, albeit broad amide carbonyl resonance with a shoulder to high frequency is observed (cf. Figure 6a). At 41 °C, the main signal is located at 174.0 ppm and the shoulder

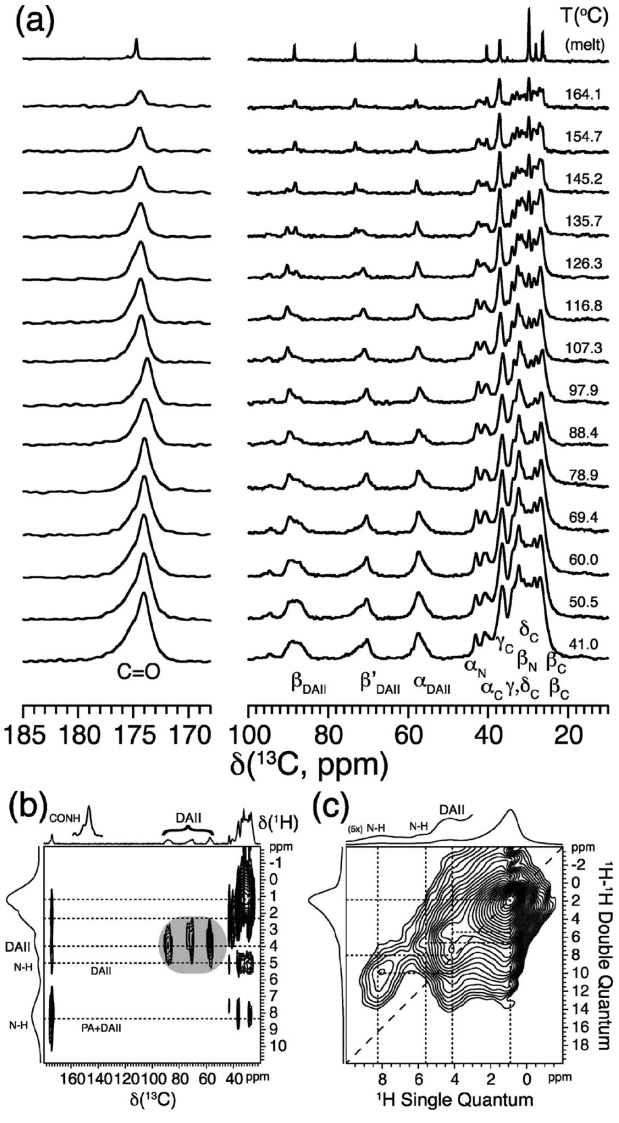


Figure 6. (a) Variable-temperature solid-state $^{13}C\{^1H\}$ CP/MAS NMR spectra of the copolymer coPA4 recorded at 11.75 T (500 MHz for ^1H). (b) 2D $^{13}C\{^1H\}$ FSLG-HETCOR spectrum acquired using a 3.0 ms CP step and five FLSG blocks per t_1 increment to improve the ^1H resolution. (c) 2D $^1H-^1H$ double-quantum single-quantum (DQ-SQ) spectrum recorded using 80.0 μs of BaBa recoupling time. Both 2D spectra were recorded at 20.0 T, corresponding to 850.27 MHz for ^1H. The dashed lines in (b) and (c) identify selected cross-peaks and autocorrelation peaks.

at 175.0 ppm. Upon increasing the temperature the shoulder gradually disappears, while the main signal shifts to higher frequency as a result of the increased mobility of the amide groups and weakening of the hydrogen bonds between the polymer chains (cf. Figure 4). Moreover, the presence of two different carbonyl resonances suggests that coPA4 includes two or more hydrogen bond environments. The larger number of methylene groups present in both the SA and DAB residues with very similar ^{13}C chemical shifts makes the region from 20 to 45 ppm crowded and difficult to interpret. However, some hints of the increased molecular dynamics as a function of temperature are visible on the high-frequency side, where the signals from the α_N and α_C groups related to the DAB and SA residues, respectively, are located. The α_N DAB signal at 43.2 ppm displays a slow decrease on increasing temperature accompanied by a shift to lower frequency, leading to a broadening of the α_C resonances. A similar dependence on temperature for this resonance was observed in PA1 (Figure 4), which led to the introduction of gauche conformers (see above). The temperature at which these conformers start to appear is similar for both PA2 and coPA4, suggesting that the SA- and DAB-based domains of the copolymer behave like in PA1 and that the lower melting point is mainly caused by the presence of DAII residues in the copolymer. The structural changes as a result of increased temperature are also visible for the DAII residues in the region 50−90 ppm. At 41 °C all resonances, α_{DAII}, β_{DAII}, and β'_{DAII}, appear quite broad where the resonances from α_{DAII} and β'_{DAII} have shoulders to low and high frequency, respectively. Compared to PA2, where distinct resonances from α_{DAII} are observed, the larger spread of these resonances indicates that the DAII fragments built into the polymer chains in coPA4 are quite flexible and can adopt a number of different conformations. The DAII resonances show even more pronounced conformational changes as compared to those in PA2 upon increasing the temperature. For α_{DAII} a gradual change of the low-frequency shoulder into a single resonance at higher frequency occurs, as also observed for PA2 (Figure 5a). Interestingly, the resonances for both β_{DAII} and β'_{DAII} show coexisting sharp signals of their high- and low-frequency parts in the temperature range 110−150 °C. Information about the local organization of polymer chains in coPA4 can be achieved from the 2D correlation spectra shown in Figures 6b and 6c. From the 2D $^{13}C\{^1H\}$ FSLG-HETCOR spectrum the presence of two different hydrogen bond environments can clearly be identified since the carbonyl signal is split into two signals with different intensities centered at 173.8 and 174.9 ppm. These signals show intense and broad correlations to the amide proton at 8.4 ppm and the aliphatic moieties, indicating stronger hydrogen bonding between the polymer chains in coPA4 as compared to PA2. The presence of two carbonyl signals also demonstrates that hydrogen bonds are formed between PA 4.10-PA 4.10, PA DAII.10-PA DAII.10, and PA 4.10- PA DAII.10 fragments, which, based on the experiments performed for PA1 and PA2 above, allow the assignment of the two former hydrogen bonds to the carbonyl at 173.8 ppm and the new DAII-based PAs hydrogen bond to the carbonyl at 174.9 ppm. As for PA2, the DAII units in coPA4 also include a signal at 5.0 ppm in the 2D $^{13}C\{^1H\}$ FSLG-HETCOR spectrum originating from DAII residues that do not participate in the hydrogen bonding. Further, the amide protons involved in hydrogen bonding are not in close spatial proximity, since no clear autocorrelation or off-diagonal cross peaks are observed in the 2D $^1H-^1H$ DQ-SQ correlation spectrum (Figure 6c). The above analysis shows that introduction of flexible DAII segments into the structure of PA 4.10 gives rise to an additional type of hydrogen bond, which appears to be compatible with a chain-folded structure as found in other PAs. Because of the unexpected flexible nature of the DAII units, a fraction of these do not participate in hydrogen bonding, which can lead to less ordered domains.

DAII Conformers from *ab Initio* Calculations. To characterize the flexibility and possible conformers for the DAII fragment and relate these to the experimentally observed ^{13}C chemical shifts found above for PA2 and coPA4, we have employed *ab initio* calculations using a combination of DFT and MP2 methods. Since such calculations are quite expensive and we do not know the specific polymer chain organization in either of the investigated samples, the calculations were performed for the gas phase on a simplified DAII fragment with propanoic acid side chains attached to both of its sides. Further details about the computations and the strategy for obtaining the conformational profiles are given in the Supporting Information.

The DAII fragments in both PA2 and coPA4 display broad ^{13}C resonances with hints of multiple signals from all of its three different carbon moieties. This fact might be attributed either to a coexistence of several conformers as reported by Liu et al.[54] and Wu et al.,[55] who carried out X-ray and *ab initio* studies on different isohexide derivatives or to the coexistence of several slightly different DAII domains with the same conformer. From the 1D potential energy surface-scanning procedure (see Figure S1), 21 possible conformations were obtained. These were further optimized at different levels of theory, revealing that a number of the 21 possible conformations are not stable and consequently interconvert as summarized in Table S1. This leaves nine conformers where the three most abundant ones according to their Boltzmann probabilities are labeled (i), (ii), and (iii) and shown in Figure 7a. We note that all nine conformers are within an energy difference of about 1−4 kcal, illustrating that the DAII fragment is indeed quite flexible (see Table S1). The NMR calculations performed for all nine conformers are graphically summarized in Figure 7b as an isotropic ^{13}C NMR spectrum, assuming a narrow line width of 0.25 ppm for each resonance. From this theoretical spectrum it is clear that all nine conformers give rise to quite large spreads of isotropic ^{13}C chemical shifts with averages centered at 92, 76, and 63 ppm for β_{DAII}, β'_{DAII}, and α_{DAII}, respectively. The average ^{13}C chemical shifts for β_{DAII} and β'_{DAII} are in reasonable agreement with the isotropic ^{13}C chemical shifts observed in this work (Figures 5 and 6), whereas the shift for α_{DAII} shows a larger discrepancy. This discrepancy is most likely reflecting our simplified model with two short propanoic acid fragments attached at the α_{DAII}-position of the DAII unit as compared to two long polymer chains. Furthermore, the ^{13}C chemical shifts calculated for the most abundant conformer (i) are in a very good agreement with our previous liquid-state NMR measurements using HMBC (see Figure S2). The populations of the DAII conformers calculated in the gas phase can obviously change when going to a solid packing of the polymer chains; i.e., spatial and/or steric effects may favor other conformers than (i), taking into account the low-energy barrier between them. Conformers with less effective volume, and thus less entropy demands, can in this way be favored, while in the gas phase they may not be the most abundant. The compatibility of the DAII fragments with the crystalline and the noncrystalline domains

dx.doi.org/10.1021/ma300133d | *Macromolecules* 2012, 45, 2796−2808

will obviously depend on their hydrogen bond formation possibilities and thereby on the orientation of the amide groups attached at the α_{DAII}-position. Assuming that all DAII conformers determined for the gas phase are equally possible in the solid, the superimposed spectra of all found conformers in Figure 7 illustrate a continuous spread of ^{13}C signals in the range from 50 to 90 ppm. The largest spread observed for β'_{DAII} is in agreement with the experimental solid-state $^{13}C\{^1H\}$ CP/MAS NMR spectra recorded for PA2 and coPA4 (Figures 5 and 6). A clear trend between DAII conformations (Figure S3) and the ^{13}C chemical shift for the α_{DAII}-position (Table S2) is difficult to derive. However, the two distinct ^{13}C resonances for α_{DAII} in PA2 compared to the spread of ^{13}C chemical shifts in Figure 7b suggest that these signals are related to two different domains. The ^{13}C chemical shift difference of ~2 ppm for the two signals, which is in the order of what we estimate for hydrogen bond formation between DAII fragments, could indicate that the two conformers are the same, with and without hydrogen bonding. This assumption is supported by the smooth decrease of the signal related to the crystalline domains on increasing temperature, which happens independently, whereas the signal from the amorphous phase displays almost no decrease. Comparison of PA2 and coPA4 (Figures 5 and 6) shows that the DAII fragments in coPA4 give rise to a much larger spread of ^{13}C chemical shifts, however, comparable to the spread observed for all nine conformers in Figure 7b. This suggests that the DAII fragments have more conformational freedom in coPA4 than PA2. The conformers related to the α_{DAII}-position in coPA4 start to show traces of the two conformers present in PA2 on increasing temperature. On the basis of this observation, we conclude that the DAII units in coPA4 are capable of linking polymer strands via hydrogen bonds to both PA4.10 and DAII-based fragments, leading to a range of DAII conformations at low temperatures. At higher temperatures, the hydrogen-bonded networks of DAII conformers in both PA2 and coPA4 undergo significant molecular dynamics. This results in complete averaging of the ^{13}C chemical shifts for the DAII units with almost identical ^{13}C chemical shifts in the melt for both polymers.

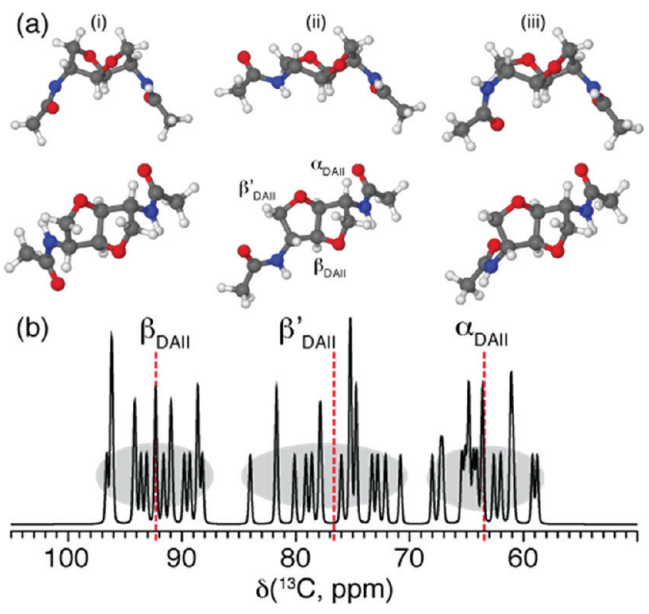


Figure 7. (a) Top and side views of the three most stable conformers found via gas phase MP2/6-31G* level of theory (see Supporting Information for details). For clarity, only methyl groups are shown while calculations were performed on propyl-substituted DAII fragments. (b) Graphical representation of the calculated ^{13}C chemical shifts for all found conformers (see Table S2). Vertical red dashed lines indicate the mean ^{13}C chemical shifts corresponding to 92.3 ± 2.8, 76.7 ± 3.6, and 63.5 ± 2.7 ppm for β_{DAII}, β'_{DAII}, and α_{DAII}, respectively.

WAXD. In our previous paper reporting XRD analysis of DAII-, DAB-, and SA-based copolyamides we showed that these biobased materials are semicrystalline over the whole range of compositions. It was also shown that the typical polyamide structure with different interchain and intersheet distances is preserved for samples with DAII contents lower than 50 mol %.[9] Samples having a higher DAII content crystallize into a close to hexagonal packing of polymer chains. In order to investigate how the DAII-based polyamide units are built into the crystal structure of PA 4.10 and which conformational modifications this entails, temperature-dependent X-ray diffraction measurements were performed on materials with a comparable and well-defined thermal history.

All samples were subjected to a first heating−cooling cycle at 10 °C/min, starting from about 40 °C and reaching a temperature well above their respective melting temperatures. During this cycle 2D X-ray diffraction patterns were collected with increasing temperature. After the first cycle, 2D X-ray diffraction patterns were collected for all the samples during a second heating/cooling cycle with the same rate and using the same temperature step.

In Figure 8a, X-ray diffraction profiles of the PA1 are shown. The profiles are reported as a function of temperature and represent the first heating cycle applied on the as-synthesized sample PA1. The PA1 crystallizes into the typical α and/or β form of the polyamide, displaying the four diffraction peaks in the range of 3−7° (2θ), 10−12° (2θ), and 18−25° (2θ), indexed as 001, 002, 100, and 010/110 (Table 3). The 100 diffraction peak corresponds to the interchain distance, which represents the distance between two chains lying within the same hydrogen-bonded sheet, while the 010 peak corresponds to the intersheet distance, i.e., the distance between two adjacent hydrogen-bonded sheets. The 001 and 002 diffraction peaks give information on the length of the chemical repeat unit. The 001 and 002 diffraction peaks shown in Figure 8a remain constant up to melting (~225 °C), while the interchain 100 and intersheet 010/110 diffraction peaks tend to merge with increasing temperature. The latter behavior is typically called the Brill transition in polyamides, and the temperature at which it occurs is the Brill transition temperature. The Brill transition for sample PA1, crystallized under the conditions described above, occurs at 196 °C. To follow the merging phenomena associated with the Brill transition, the *d*-spacing values of all the samples are reported in Figures 9a and 9b as a function of temperature for the first and the second heating runs, respectively. The *d*-spacing values have been calculated via Bragg's law. The analysis of WAXD profiles of PA1 shows that melting of this polyamide starts around 225−230 °C (Figure 8a) where an amorphous halo tends to strengthen in intensity. The observed temperature is consistent with the melting temperature of PA1 measured by DSC (reported in Table 1). Similar phenomena are observed for PA1 during the second heating run (Figure 8a′). The Brill transition occurs at 196 °C and the polymer melts completely around 225 °C. On cooling from the melt reverse behavior is observed, and further relevant data are available in the Supporting Information.

dx.doi.org/10.1021/ma300133d | *Macromolecules* 2012, 45, 2796−2808

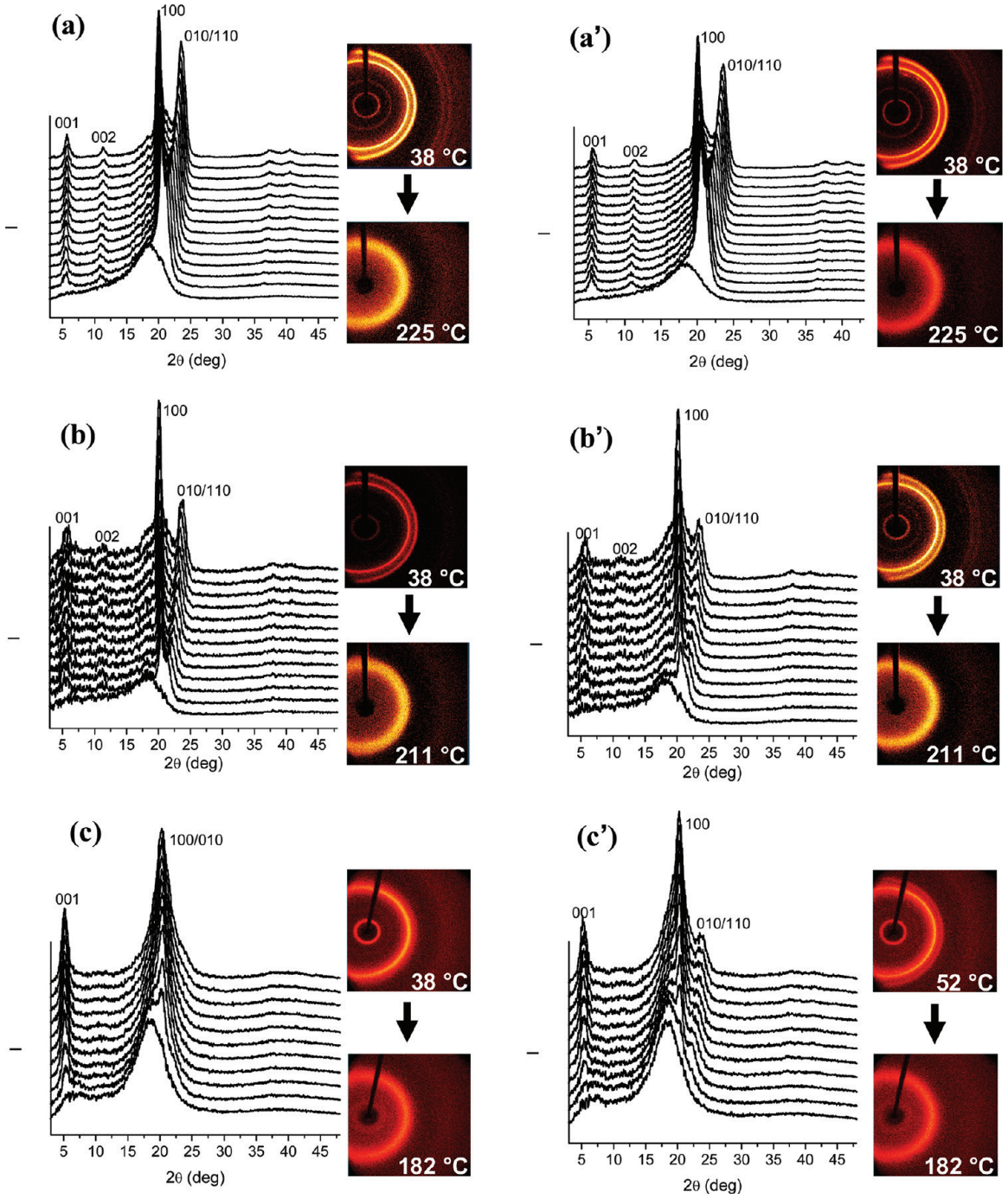


Figure 8. X-ray powder diffraction profiles of as-prepared homopolyamide PA1 (a, a′) and copolyamides coPA3 (b, b′) and coPA4 (c, c′) collected from around 40 °C until the melting temperature. The 1D integrated profiles are reported as a function of the temperature and correspond to the two heating runs applied for each sample (I heating run (a), (b), (c)); II heating run (a′), (b′), (c′)). The indices correspond to the packing mode of the α-phase and the β-phase of common polyamides. The temperatures of the recorded profiles are reported in the Supporting Information, and they are listed in Table 4.

Table 3. X-ray Diffraction Spacings of As-Prepared Co- and Homopolyamides with Different Contents of Diaminoisoidide Measured at Room Temperature

	X-ray diffraction (nm)				2θ (deg)			
symbol	001	002	100	010/110	001	002	100	010/110
PA1	1.561	0.776	0.442	0.379	5.66	11.38	20.00	23.46
coPA3	1.555	0.775	0.442	0.380	5.68	11.40	20.00	23.44
coPA4	1.686		0.442		5.24		20.00	
PA2	1.624		0.442		5.44		20.00	

dx.doi.org/10.1021/ma300133d | *Macromolecules* 2012, 45, 2796−2808

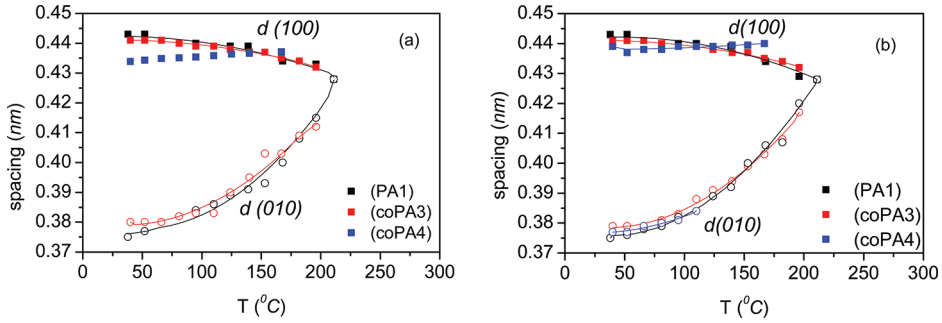


Figure 9. Temperature-dependent variations of 100, 010/110 spacing values calculated via Bragg's law considering the collected profiles (Figure 8) during the first heating run (a) and the second heating run (b).

In Table 4, crystallinity indexes calculated using the following formula are reported for each profile:

Table 4. Crystallinity Indexes Calculated for Each Profile Reported in Figure 8

	X_c (%)					
	PA1		coPA3		coPA4	
T (°C)	I heating	II heating	I heating	II heating	I heating	II heating
38	50	43	36	32	25	29
52	49	39	33	27	23	27
66	47	36	30	26	21	26
81	44	32	26	25	18	22
95	41	31	24	24	17	19
110	39	30	22	23	13	17
124	37	28	20	22	12	15
139	35	27	19	21	10	10
153	33	26	18	19	5	8
168	31	25	16	15	2	5
182	30	24	16	14		
196	29	23	15	13		
211	28	23				
225						

$$X_c = \frac{A_c}{A_c + A_a} \times 100$$

where A_c and A_a are the integrated intensities from the amorphous and crystalline phases, respectively. The integrated intensities were extracted from the experimental XRD patterns by a fitting procedure using the XRD profile of the material after melting, as explained in the Supporting Information. From the calculated X_c values one can conclude that the degree of crystallinity decreases as a function of temperature.

The coPA3 with DAB/DAII mole ratio 0.80/0.20 crystallizes into a crystal structure similar to that of PA1. The same four diffraction peaks typical for polyamides are displayed in the range of 3−7° (2θ), 10−12° (2θ), and 18−25° (2θ), indexed as 001, 002, 100, and 010/110 (Figure 8b). Their corresponding d-spacing values obtained from the pattern collected at room temperature are reported in Table 3. On comparing the d-spacing values of the four diffraction peaks for the two mentioned samples PA1 and coPA3, no significant differences were observed. However, a decrease of the 002 diffraction peak intensity is observed upon increasing the DAII content in the synthesized materials. In fact, the 002 diffraction peak decreases in intensity for coPA3 and totally disappears for coPA4 as a consequence of the crystal disorder caused by the increased DAII content in the copolymers. Simultaneously, the degree of crystallinity is lower than that of PA1, as presented in Table 4. Upon heating of the coPA3 sample, the 001 and 002 diffraction peaks remain constant up to melting (around 211 °C), while similar merging phenomena are observed for the interchain 100 and intersheet 010/110 diffraction peaks as compared to PA1. The Brill transition, however, is not observed for this sample. Clearly, this is due to the lower value of the melting temperature observed from WAXD measurements which decreases from 221 °C for PA1 to 211 °C for coPA3. Moreover, the crystallinity values for coPA3 presented as a function of temperature are lower than the respective values for PA1. Similar trends of the degree of crystallinity are also observed for these two samples during the second heating/cooling cycle.

The coPA4 crystallizes into a close to hexagonal cell similar to that of PA2.[9] The XRD pattern displays two strong diffraction peaks in the range of 3−7° (2θ) and 15−25° (2θ), indexed as 001 and 100. The 001 diffraction peak shifts to lower values of 2θ compared to the same diffraction peak of the other polyamides (Figure 8c and Table 3).[9] This indicates that the projection on the c-axis of the DAII monomer residue is somewhat longer than that of the DAB monomer residue, and it shows that the comonomers cocrystallize in the same crystal lattice. The different electronic density of the DAII fragments compared to the DAB fragments influences the intensity of the 001 diffraction peak, which is more intense for diaminoisoidide-rich coPA4 than the same diffraction peak observed for the other polyamides. Clearly, the as-synthesized coPA4 does not show a Brill transition. Only decreasing of the crystallinity index as a function of temperature is observed. CoPA4 presents a different diffraction profile after the first heating/cooling cycle (Figure 8c′). Considering that the crystallization occurs approximately with a rate of 10 °C/min, it could be concluded that the different crystallization conditions give rise to the coexistence of the two observed crystal structures. However, α and/or β phase can be considered to be less abundant compared to pseudohexagonal phase. In fact, the diffraction peak 010/110 is less intense compared to the corresponding diffraction peak of PA1 at low temperature. Upon increasing the temperature, only a decrease of the degree of crystallinity is observed. Moreover, no meaningful differences have been observed on comparing the temperature-dependent FTIR spectra collected for coPA4 during the two heating runs. Melting also occurs for the sample subjected to a second heating run around 182 °C. Similar behavior is observed on cooling from the melt, but the diffraction peak 010/110 is now only present as a shoulder with a low intensity (see Supporting

dx.doi.org/10.1021/ma300133d | Macromolecules 2012, 45, 2796−2808

Information). This seems to confirm our conclusion on the influence of crystallization conditions for the coPA4.

CONCLUSIONS

The conformation and flexibility of diaminoisoidide-, 1,4-diaminobutane-, and sebacic acid-based polyamide fragments and their influence on the chain organization in the crystalline and amorphous phases were investigated by FT-IR, solid-state NMR, and WAXD. This combined approach provided detailed information concerning nanophase separation and allowed identification of the specific differences between rigid and more flexible motifs in these semicrystalline polyamides. The spectroscopic analysis of the diaminoisoidide-based polyamides is particularly important for the investigation of their crystal structure stability. Simultaneously, the combination of the experimental techniques with *ab initio* calulations provides more insight into the flexibility of isohexide unit which in this case affects the hydrogen bonding and chain conformation of the polyamides. FT-IR measurements revealed that the incorporation of diaminoisoidide into the structure of PA1 (commercially known as PA 4.10) affects the hydrogen-bond density, causing conformational disorder of the chain fragments of the polymer. Upon heating of polyamide 4.10 and copolyamide coPA3, containing 20 mol % of diaminoisoidide, the FT-IR signals at 1475−1476 and 1418−1419 cm^{-1}, assigned to CH_2 scissoring with trans conformation, become less visible. This comes as a result of an increased number of gauche conformers, which leads to a hexagonal packing of the polymer chains. The dynamic balance between trans and gauche conformers of the polyamides was demonstrated by VT $^{13}C\{^1H\}$ CP/MAS NMR experiments. Besides, on combining spectroscopic techniques with *ab initio* calculations, viz. DFT and MP2 methods, the most abundant conformers of DAII were defined. The calculations showed a number of possible DAII conformers with the low-energy barrier between them and therefore relatively high flexibility of the isohexide unit.

Wide-angle X-ray scattering revealed that PA1 and coPA3 crystallize into α and/or β forms with different interchain and intersheet distances. Upon heating, PA1 undergoes a Brill transition, while the more diaminoisoidide-rich compositions greatly facilitate the formation of a pseudohexagonal phase, which was even observed at room temperature.

Of particular interest was the analysis of diaminoisoidide distribution in the crystalline and noncrystalline phases of the polyamides. The crystalline regions, containing hydrogen-bonded DAII residues, were identified by FT-IR C−CO stretching vibrations at 903 cm^{-1} together with ^{13}C resonances in the vicinity of 50−90 ppm. The decrease of the FT-IR signal intensities close to the melting point of the polyamides suggests that DAII comonomer is indeed incorporated into the crystalline phase of these materials. Moreover, relatively broad ^{13}C resonances of isohexide fragments suggested the coexistence of different DAII conformers in the crystalline and noncrystalline/amorphous domains, which was especially pronounced for the copolymer coPA4 based on SA, DAB, and DAII. The cocrystallization of DAB and DAII fragments followed by WAXD measurements revealed a shift of the 001 diffraction peak for the DAII-rich polyamides to lower 2θ values in comparison to PA 4.10. Further analysis of the X-ray data showed that the projection onto the *c*-axis of the DAII residue is longer than the DAB residue and that the comonomers cocrystallize. With an increasing content of DAII in the PAs, the crystal disorder increased, and thus, the degree of crystallinity was lower than that of the SA\DAB-based polyamide 4.10.

ASSOCIATED CONTENT

Supporting Information

An extensive quantum-chemical DFT and MP2 conformational analysis and WAXD study. This material is available free of charge via the Internet at http://pubs.acs.org.

AUTHOR INFORMATION

Corresponding Author

*E-mail: c.e.koning@tue.nl; Ph: +31-40-2475353; Fax: +31-40-2463966.

Notes

The authors declare no competing financial interest.

ACKNOWLEDGMENTS

The authors acknowledge Prof. H. W. Spiess for helpful discussions and continuing support. This work forms part of the research program of Dutch Polymer Institute (DPI, project # 656, #587, and #685). The financial support from DPI is gratefully acknowledged.

REFERENCES

(1) Fenouillot, F.; Rousseau, A.; Colomines, G.; Saint-Loup, R.; Pascault, J. P. *Prog. Polym. Sci.* **2010**, *35*, 578.
(2) Thiem, J.; Bachmann, F. *Makromol. Chem.* **1991**, *192*, 2163.
(3) Stoss, P.; Hemmer, R.; Derek, H. *Adv. Carbohydr. Chem. Biochem.* **1991**, *49*, 93.
(4) Gomurashvili, Z.; Kricheldorf, H. R.; Katsarava, R. *J. Macromol. Sci., Pure Appl. Chem.* **2000**, *A37*, 215.
(5) Caouthar, A. A.; Loupy, A.; Bortolussi, M.; Blais, J.; Dubreucq, L.; Meddour, A. *J. Polym. Sci., Part A: Polym. Chem.* **2005**, *43*, 2480.
(6) Caouthar, A.; Roger, P.; Tessier, M.; Chatti, S.; Blais, J. C.; Bortolussi, M. *Eur. Polym. J.* **2007**, *43*, 220.
(7) Okada, M.; Yamada, M.; Yokoe, M.; Aoi, K. *J. Appl. Polym. Sci.* **2001**, *81*, 2721.
(8) Philip, B.; Sreekumar, K. *Polym. Int.* **2001**, *50*, 1318.
(9) Jasinska, L.; Villani, M.; Wu, J.; van Es, D.; Klop, E.; Rastogi, S.; Koning, C. E. *Macromolecules* **2011**, *44*, 3458.
(10) Dreyfuss, P.; Keller, A. *J. Macromol. Sci., Part B: Phys.* **1970**, *B4*, 812.
(11) Atkins, E. D. T.; Hill, M. J.; Hong, S. K.; Keller, A.; Organ, S. *Macromolecules* **1992**, *25*, 917.
(12) Bunn, C.; Garner, E. V. *Philos. Trans. R. Soc., A* **1947**, *189*, 39.
(13) Jones, N. A.; Atkins, E. D. T.; Hill, M. J.; Cooper, S. J.; Franco, L. *Polymer* **1997**, *38*, 2689.
(14) Franco, L.; Cooper, S. J.; Atkins, E. D. T.; Hill, M. J.; Jones, N. A. *J. Polym. Sci., Part B: Polym. Phys.* **1998**, *36*, 1153.
(15) Cooper, S. J.; Atkins, E. D. T.; Hill, M. J. *Polymer* **2002**, *43*, 891.
(16) Hill, M. J.; Atkins, E. D. T. *Macromolecules* **1995**, *28*, 604.
(17) Jones, N. A.; Atkins, E. D. T.; Hill, M. J.; Cooper, S. J.; Franco, L. *Macromolecules* **1996**, *29*, 6011.
(18) Atkins, E. D. T.; Hill, M. J.; Jones, N. A.; Cooper, S. J. *J. Polym. Sci., Part B: Polym. Phys.* **1998**, *36*, 2401.
(19) Bermúdez, M.; León, S.; Alemán, C.; Muñoz-Guerra, S. *J. Polym. Sci., Part B: Polym. Phys.* **2000**, *38*, 41.
(20) Bermúdez, M.; León, S.; Alemán, C.; Muñoz-Guerra, S. *Polymer* **2000**, *41*, 8961.
(21) Brill, R. *J. Prakt. Chem.* **1942**, *161*, 49.
(22) Brill, R. *Macromol. Chem.* **1956**, *18/19*, 294.
(23) Colclough, M. L.; Baker, R. J. *J. Mater. Sci.* **1978**, *13*, 2531.
(24) Wendoloski, J. J.; Gardner, K. H.; Hirschinger, J.; Miura, H.; English, A. D. *Science* **1990**, *247*, 431.
(25) Vinken, E.; Terry, A. E.; Hoffmann, S.; Vanhaecht, B.; Koning, C. E.; Rastogi, S. *Macromolecules* **2006**, *39*, 2546.

(26) Vasanthan, N.; Murthy, N. S.; Bray, R. G. *Macromolecules* **1998**, *31*, 8433.
(27) Yoshioka, Y.; Tashiro, K. *Polymer* **2003**, *44*, 7007.
(28) Cooper, S. J.; Coogan, M.; Everall, N.; Priestnall, I. *Polymer* **2001**, *42*, 10119.
(29) Ando, I.; Asakura, T. *Solid State NMR Polym.* **1998**, *84*, xxxx.
(30) Hirschinger, J.; Miura, H.; Gardner, K. H.; English, A. D. *Macromolecules* **1990**, *23*, 2153.
(31) Harings, J. A. W.; Yao, Y.; Graf, R.; van Asselen, O.; Broos, R.; Rastogi, S. *Langmuir* **2009**, *25*, 7652.
(32) Yao, Y. F.; Graf, R.; Spiess, H. W.; Rastogi, S. *Macromolecules* **2008**, *41*, 2514.
(33) Holstein, P.; Spevaceck, J.; Geschke, D.; Thiele, V. *Prog. Colloid Polym. Sci.* **1991**, *85*, 60.
(34) Schreiber, R.; Veeman, W. S.; Gabrielse, W.; Arnauts, J. *Macromolecules* **1999**, *32*, 4647.
(35) Bennett, A. E.; Rienstra, C. M.; Auger, C. M.; Lakshmi, K. V.; Griffin, R. G. *J. Chem. Phys.* **1995**, *103*, 6951.
(36) Bielecki, A.; Burum, D. P. *J. Magn. Reson., Ser. A* **1995**, *116*, 215.
(37) van Rossum, B.; Forster, H.; de Groot, H. *J. Magn. Reson.* **1997**, *124*, 516.
(38) Feike, M.; Demco, D.; Graf, R.; Gottwald, J.; Hafner, S.; Spiess, H. W. *J. Magn. Reson., Ser. A* **1996**, *122*, 214.
(39) Marcombe, C.; Zilm, K. *J. Magn. Reson.* **2003**, *162*, 479.
(40) Schroeder, L. R.; Cooper, S. L. *J. Appl. Phys.* **1976**, *47*, 4310.
(41) Skrovanek, D. J.; Stephen, E. H.; Painter, P. C.; Coleman, M. M. *Macromolecules* **1985**, *18*, 1676.
(42) Skrovanek, D. J.; Painter, P. C.; Coleman, M. M. *Macromolecules* **1986**, *19*, 699.
(43) Silverstein, R. M.; Webster, F. X. *Spectrometric Identification of Organic Compounds*; John Wiley & Sons, Inc.: New York, 1998.
(44) Vasanthan, N.; Salem, D. R. *J. Polym. Sci., Part B: Polym. Phys.* **2000**, *38*, 516.
(45) Li, W.; Huang, Y.; Zhang, G.; Yan, D. *Polym. Int.* **2003**, *52*, 1905.
(46) Vanderhart, D. L.; Earl, W.; Garroway, A. *J. Magn. Reson.* **1981**, *44*, 361.
(47) Gitsas, A.; Floudas, G.; Mondeshki, M.; Lieberwirth, I.; Spiess, H. W.; Iatrou, H.; Hadjichristidis, N.; Hirao, A. *Macromolecules* **2010**, *43*, 1874.
(48) Vasanthan, N.; Willem, R.; Biesemans, M.; Goderis, B.; Basiura, M.; Magusin, P. C. M. M.; Bolbnya, I.; Koning, C. E. *Macromolecules* **2004**, *37*, 421.
(49) Vanderhart, D. L. *J. Magn. Reson.* **1981**, *44*, 117.
(50) Earl, W.; Vanderhart, D. L. *J. Magn. Reson.* **1982**, *48*, 35.
(51) Ando, I.; Asakura, T. *Solid State NMR of Polymers*; Elsevier: Amsterdam, 1998; Vol. *84*.
(52) Bohle, A.; Brunklaus, G.; Hansen, M. R.; Schleuss, T. W.; Kilbinger, A. F. M.; Seltmann, J.; Spiess, H. W. *Macromolecules* **2010**, *43*, 4978.
(53) Vinken, E.; Terry, A. E.; van Asselen, O.; Spoelstra, A. B.; Graf, R.; Rastogi, S. *Langmuir* **2008**, *24*, 6313.
(54) Liu, F. W.; Yan, L.; Zhang, J. Y.; Liu, H. M. *Carbohydr. Res.* **2006**, *341*, 332.
(55) Wu, J.; Eduard, P.; Thiyagarajan, S.; van Haveren, J.; van Es, D.; Koning, C. E.; Lutz, M.; Fonseca Guerra, C. *ChemSusChem* **2011**, *4*, 599.

Macromolecules

Article

pubs.acs.org/Macromolecules

Dielectric Behavior of Guest *cis*-Polyisoprene Confined in Spherical Microdomain of Triblock Copolymer.

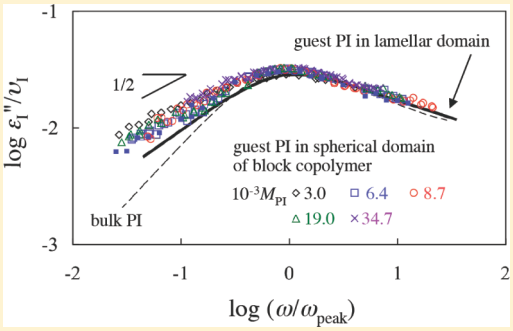
Quan Chen, Yumi Matsumiya, Tatsuya Iwamoto, Koji Nishida, Toshiji Kanaya, and Hiroshi Watanabe*

Institute for Chemical Research, Kyoto University, Uji, Kyoto 611-0011, Japan

Atsushi Takano, Kohei Matsuoka, and Yushu Matsushita

Department of Applied Chemistry, Graduate School of Engineering, Nagoya University, Furo-cho, Chikusa-ku, Nagoya 464-8603, Japan

ABSTRACT: Dielectric behavior was examined for ternary blends of guest *cis*-polyisoprene (PI) chains, coguest PS chains, and host PS−PI−PS triblock copolymers. The guest PI chains had the molecular weight $M_{g\text{-PI}}$ well below $M_{b\text{-PI}}$ of the PI blocks and were mixed in the spherical PI domains formed in the copolymers. PI has the type-A dipoles parallel along the chain backbone and its end-to-end vector fluctuation activates dielectric relaxation. The dielectric test was conducted at temperatures well below the glass transition temperature of the PS blocks, so that the PI blocks had their ends fixed on the glassy PS matrix and exhibited no end-to-end vector fluctuation. Thus, the slow dielectric response of the systems exclusively detected the global motion of the guest PI chains confined in the spherical PI domain. The dielectric mode distribution of the guest PI chains thus observed was broader than that of the same chains in bulk systems, reflecting the osmotic and spatial constraints on the chain dynamics in the spherical domains. The guest PI chains of different $M_{g\text{-PI}}$ exhibited nearly the same extent of mode broadening, despite their average coil size approached the domain size with increasing $M_{g\text{-PI}}$. This result suggested that the osmotic constraint was the primary factor affecting (broadening and retarding) the guest chain dynamics. The osmotic constraint appeared to be stronger in the spherical domain than in the lamellar domain, the latter being examined in literature.



1. INTRODUCTION

Block copolymers exhibit microphase separated domain structures, and the thermodynamic driving force for this structure formation is rather well understood:[1,2] Namely, the covalently connected but chemically different blocks segregate in space as much as they can, while satisfying the thermodynamic requirements of randomizing the location of the block junctions, randomizing the block conformation, and *uniformly* filling the domains with the constituent segments. These requirements, in particular the last two, are contradicting to each other because the uniform domain-filling requires neighboring blocks to have correlated (and not fully randomized) conformations, and compromise of those requirements determines the size and shape of the microdomains.[1−3]

The requirements explained above result in conformational correlation of the blocks in the microdomain and should affect (retard) the large-scale dynamics of the blocks. Dielectric measurements for copolymers consisting of *cis*-polyisoprene (PI) and polystyrene (PS) blocks have been proven to be very useful for examination of this effect(s). PI has the so-called type-A dipole parallel along the chain backbone, while PS does not.[4,5] Thus, the slow dielectric responses experimentally detected for the copolymer can be exclusively related to the end-to-end vector fluctuation of the PI block (having no inversion of type-A dipoles), in particular at low temperatures (T) well below the glass transition temperature $T_{g,PS}$ of the PS blocks where the PS segmental motion is quenched (undetectably slow).

For monodisperse linear PI, extensive studies[5−7] revealed that the dielectric mode distribution in bulk systems hardly changes with the molecular weight M (although slight mode narrowing is observed for high-M PI[8]) and that the mode distribution narrows moderately in semidilute and dilute solutions. For all these cases, the linear PI chains exhibit narrow distribution of the terminal dielectric relaxation modes characterized by a sharp peak of the dielectric loss ε'' immediately followed by a low-frequency (low-ω) part exhibiting the proportionality, $\varepsilon'' \propto \omega$. In contrast, in bulk PS−PI diblock copolymer forming lamellar domains, the PI block does not exhibit this low-ω proportionality but shows the mode distribution much broader compared to linear PI chains of the same M,[9] which indicates that the terminal dielectric relaxation time $\langle\tau\rangle_w$ (=second-moment average relaxation time defined in terms of the relaxation spectrum[5,6]) is much longer for the PI block than for the linear PI chains. This enormous retardation/broadening of the PI block dynamics can be

Received: January 22, 2012
Revised: March 3, 2012
Published: March 16, 2012

 © 2012 American Chemical Society dx.doi.org/10.1021/ma3001687 | *Macromolecules* 2012, 45, 2809−2819

related to constraints for the PI block dynamics,[5] the so-called *spatial* constraint due to conformational restriction within the microdomain (that reduces possible dynamic paths for conformational changes) and the *osmotic* constraint due to the very strong requirement of *uniform* domain-filling (that forces the blocks to move cooperatively). Although the spatial constraint has some effect on the mode broadening,[10−12] the osmotic constraint appears to dominate the retardation/broadening, as suggested from experimental observation that the mode distribution of PS−PI copolymers narrows on moderate dilution with a PI-selective solvent[13] and that the mode distribution is narrower for guest PI chains in the lamellar domain than for the PI block therein.[5,9]

The osmotic and spatial constraints, affecting the chain dynamics in the block copolymer domain, would change their magnitudes with the domain shape: These constraints are expected to affect the chain dynamics significantly in the discrete, spherical domain than in the continuous, lamellar domain. We may attempt to examine this expectation through dielectric tests. Specifically, we can focus on PS−PI−PS triblock copolymers having guest PI chains in the PI domain thereby distinguishing the effects of the two constraints on the chain dynamics: At low T ($<T_{g,PS}$), the middle PI block has its ends anchored on the glassy PS matrix and exhibits no dielectric relaxation (no end-to-end vector fluctuation), so that the dielectric signal from the guest PI chain in the PI domain can be most clearly observed. Those guest chains serve as a probe for the osmotic and spatial constraints. On an increase of the guest PI molecular weight $M_{g\text{-PI}}$ (that is still kept lower than the PI block molecular weight $M_{b\text{-PI}}$ so as to ensure mixing of the guest PI in the PI domain), the effect of the spatial constraint on the guest dynamics should be enhanced more significantly compared to the effect of the osmotic constraint. Thus, comparison of the dielectric responses of the guest chains having different $M_{g\text{-PI}}$ ($<M_{b\text{-PI}}$) should allow us to examine the relative importance of the two constraints in the spherical domain.

Following the above strategy, we conducted dielectric tests for ternary blends of PS−PI−PS copolymers forming spherical PI domains and containing the guest PI and coguest PS chains. (The coguest PS was utilized to increase the total PS volume fraction thereby ensuring formation of the spherical PI domains.) The dielectric response from the guest PI chains was clearly observed, and their broad dielectric mode distribution was found to hardly change with $M_{g\text{-PI}}$, suggesting that the osmotic constraint dominates the chain dynamics in the spherical domains. Furthermore, comparison of the responses of guest PI in the spherical and lamellar domains (the latter reported in literature[9]) suggested that the osmotic constraint is stronger in the spherical domain, as expected. Details of these results are presented in this paper.

2. EXPERIMENTAL SECTION

2.1. Materials. Two (almost) symmetric PS−PI−PS triblock copolymer samples were synthesized with sequential living anionic polymerization in high vacuum utilizing *s*-butyllithium and benzene as the initiator and the polymerization solvent, respectively. Small amounts of the reaction product were recovered after completion of the first and second steps of polymerization, and were characterized with SEC (Co-8020 and DP8020, Tosoh) equipped with a refractive index (RI) monitor and a ultraviolet (UV) adsorption monitor (LS-8000 and UV-8020, Tosoh) connected in series. The SEC elution solvent was tetrahydrofuran.

The molecular weight $M_{PS(1)}$ of the first PS precursor (first PS block) was determined from the elution volume calibration utilizing commercially available monodisperse PS standards (TSK's, Tosoh). The molecular weight M_{PI} of the PI block in the second PS−PI precursor was evaluated from $M_{PS(1)}$ of the first PS block with aid of the RI and UV intensity calibration utilizing those PS standards and monodisperse PI standards synthesize in the previous studies:[14,15] $M_{PI} = M_{PS(1)}\{w_{PI}/(1-w_{PI})\}$ with w_{PI} being the PI weight fraction in the PS−PI precursor determined from the RI/UV signal ratio of this precursor. Finally, the molecular weight $M_{PS(2)}$ of the last PS block in the PS−PI−PS copolymer sample was obtained from $M_{PS(1)}$, M_{PI}, and the weight fraction $w_{PS(2)}$ of the last PS block in the copolymer evaluated from the RI/UV signal ratio of the copolymer: $M_{PS(2)} = \{M_{PS(1)} + M_{PI}\}\{w_{PS(2)}/(1-w_{PS(2)})\}$. The characteristics thus determined for the two copolymer samples are summarized in Table 1, with the code number showing $10^{-3}M_{PS(1)}$-$10^{-3}M_{PI}$-$10^{-3}M_{PS(2)}$. The elution volume calibration with the PS and PI standards indicated that the polydispersity index was small (≤1.05) for all precursors and the two copolymer samples.

Table 1. Characteristics of PS−PI−PS Triblock Copolymer Samples[a]

code	$10^{-3}M_{PS(1)}-10^{-3}M_{PI}-10^{-3}M_{PS(2)}$ [b]	w_{PI} [c]
SIS 35−13−36	35.1−13.1−36.3	0.16
SIS 131−57−133	131−56.5−133	0.18

[a] Polydispersity index was small (≤1.05) for all precursors and the two copolymer samples. [b] M indicates the weight-average molecular weight (determined with uncertainty less than 10%). [c] w_{PI} indicates the weight fraction of PI block in the copolymer.

Five linear PI samples were utilized as the guest PI mixed in the PI domains of the PS−PI−PS copolymers. The molecular characteristics of those PI samples are summarized in Table 2. The highest-M sample was synthesized/characterized in the previous study,[15] and the remaining four samples were living-anionically synthesized in this study. Those four samples were characterized with the SEC elution volume calibration utilizing the monodisperse PI standards.[14,15]

Table 2. Characteristics of Linear PI and PS samples

code[a]	$10^{-3}M_w$	M_w/M_n
Linear *cis*-Polyisoprene (Guest)		
I-3	3.0	1.07
I-6	6.4	1.07
I-9	8.7	1.06
I-19	19.0	1.07
I-35[b]	34.7	1.05
Linear Polystyrene (Coguest)		
S-11[c]	10.5	1.08

[a] Code number indicates $10^{-3}M_w$ [b] Synthesized/characterized previously.[15] [c] Supplied from Tosoh Co. Ltd.

The materials subjected to the dielectric tests and the domain observation (TEM and SAXS) were the ternary blends of the PS−PI−PS copolymer, the guest PI, and the coguest PS. The neat PS−PI−PS copolymers were also examined for comparison. The coguest PS (with the characteristics shown in Table 2) was added to the ternary blends so as to keep the total PI volume fraction $\phi_{total\text{-PI}}$ small thereby allowing the PI block and guest PI chains to form spherical PI domains, as explained later in more detail. For the ternary blends, the guest PI molecular weight $M_{g\text{-PI}}$ was chosen to be well below the PI block molecular weight $M_{b\text{-PI}}$ to ensure the mixing of the guest PI into the domain of the PI block. (The coguest PS molecular weight M_{cg-PS} was much smaller than the PS block molecular weight, and thus the coguest PS was mixed in the PS block phase.) In fact, no macroscopic phase separation occurred for the ternary blends, as explained later for Figures 1 and 2.

In all ternary blends examined, the total (guest + block) PI weight fraction was set at $w_{total\text{-PI}} = 0.10$ (total volume fraction $\phi_{total\text{-PI}} = 0.11_2$)

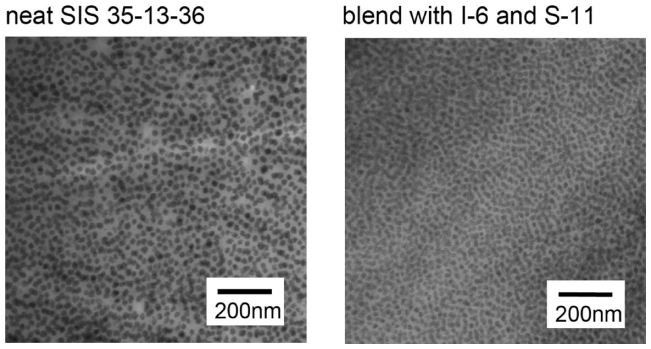


Figure 1. TEM images of neat SIS 35−13−36 copolymer and its ternary blend with the guest I-6 and coguest S-11. In the blend, the total volume fraction of the PI components is $\phi_{\text{total-PI}} = 0.11_2$, and the volume fraction of the guest PI is $\phi_{\text{g-PI}} = 0.056$.

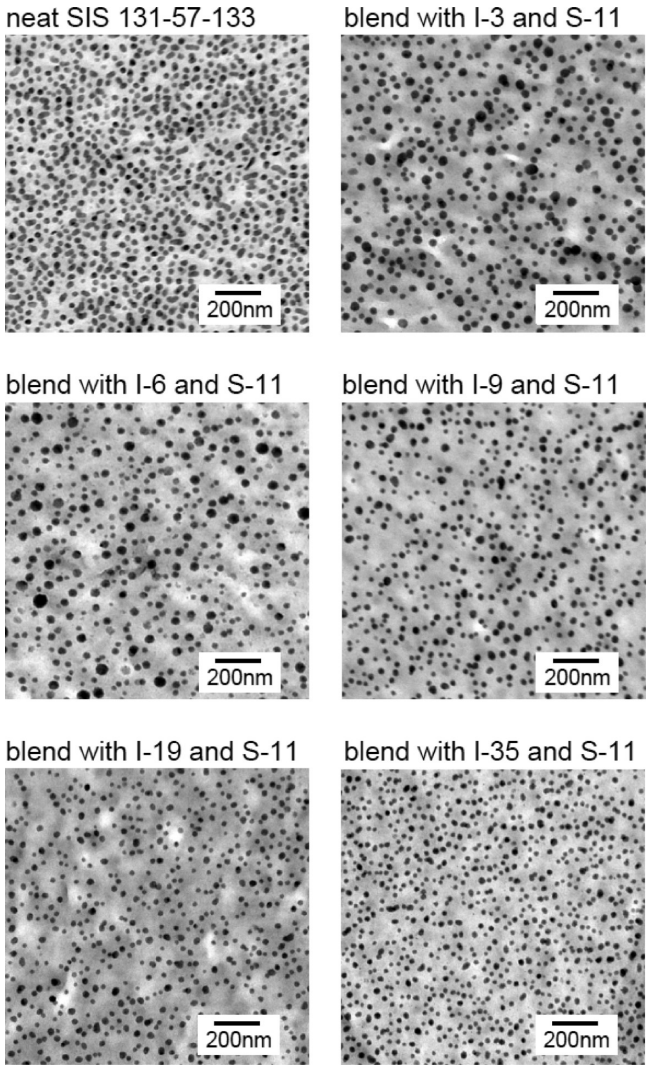


Figure 2. TEM images of neat SIS 131−57−133 copolymer and its ternary blends with the guest PI and coguest S-11. All blends have the same total volume fraction of the PI components, $\phi_{\text{total-PI}} = 0.11_2$, same volume fraction of the guest PI, $\phi_{\text{g-PI}} = 0.056$, and the same molecular weight of coguest S11, $M_{\text{cg-PS}} = 10.5 \times 10^3$. The guest PI molecular weight $M_{\text{g-PI}}$ in the blends is varied from 3.0×10^3 to 34.7×10^3.

and the guest PI weight fraction, at $w_{\text{g-PI}} = 0.050$ (guest PI volume fraction $\phi_{\text{g-PI}} = 0.056$). The weight fraction of the coguest PS in those blends, $w_{\text{cg-PS}}$, was chosen according to these $w_{\text{total-PI}}$ and $w_{\text{g-PI}}$ values: $w_{\text{cg-PS}} = 0.9-0.05(1-w_{\text{PI}})/w_{\text{PI}}$ with w_{PI} being the PI block weight fraction in the copolymer shown in Table 1.

The ternary blends were prepared by first dissolving prescribed masses of the copolymer, guest PI, and coguest PS in a 4/1 (w/w) mixed solvent of benzene (Bz) and methyl ethyl ketone (MEK) at a total polymer concentration of ≅10 wt %, Then, this solution was slowly cast onto a Teflon dish for a week at room temperature. (A half-closed desiccator was utilized for this solvent casting.) The cast film of the ternary blend was taken out from the Teflon dish and fully dried in vacuum at 150 °C on an electrode for the dielectric tests. Since Bz is a common good solvent for PS and PI whereas MEK is highly selective to PS, the casting from the mixed solvent enhances segregation of the PI components in an early stage of casting[16,17] to help formation of spherical PI domain. Because of this early segregation and also of the small $\phi_{\text{total-PI}}$ value (=0.11_2), the spherical PI domains containing the PI block and guest PI were formed in the ternary blends, as explained later for Figures 1 and 2. The neat PS−PI−PS copolymers, also cast from the mixed solvent, indeed formed spherical PI domains, despite ϕ_{PI} of the copolymers were considerably larger than $\phi_{\text{total-PI}}$ in the ternary blends.

2.2. Measurements. For the ternary PI/PS−PI−PS/PS blends and neat PS−PI−PS copolymers cast and fully dried as above, dielectric measurements were conducted with an impedance analyzer/dielectric interface system (1260 and 1296, Solartron) and a homemade dielectric cell composed of a guarded main electrode, a counter electrode, and a separate shielding jacket (on which these electrodes were tightly screwed for the measurements). The samples were annealed at 150 °C on the counter electrode in Ar atmosphere for 3 h in prior to the measurements, slowly pressed by the main electrode to be filled in the gap (= 0.3 mm) between the two electrodes, and then slowly cooled to room temperature. The measurements were conducted in Ar atmosphere at temperatures $T \leq 60$ °C ($<T_{\text{g,PS}}$), mostly at 0 °C.

For comparison, the dielectric measurements were conducted also for bulk PI samples (cf. Table 2) utilized as the guest PI in the ternary blends. The samples were charged in the dielectric cell at room temperature and subjected to the measurements in Ar atmosphere at the same temperatures as for the blends. (No annealing operation at 150 °C was necessary for the bulk PI samples, because these samples were liquids even at low $T \sim 0$ °C)

After the dielectric measurements for the ternary blends and neat copolymers, the electrodes were released (off-screwed) from the shielding jacket and the sample films having experienced the measurements were recovered from the gap between the electrodes. These films were subjected to small-angle X-ray scattering (SAXS) measurement and transmission electron microscope (TEM) observation. Those SAXS data and TEM images detected most faithfully the microdomain structure that corresponded to the dielectric data.

The SAXS measurements were conducted at room temperature with a laboratory goniometer (RINT-2000, Rigaku). The wavelength of X-ray was $\lambda = 0.154$ nm (Cu Kα line). The sample films were charged in a cell having a mica window, and the scattering intensity $I(q)$ was measured as a function of the magnitude of scattering vector, $q = \{4\pi/\lambda\}\sin(\theta/2)$ with θ = scattering angle. No desmearing correction was made for the $I(q)$ data.

For the TEM observation, the sample films were first stained with 3 wt % OsO_4 (aq) solution for 6 h at 60 °C, and then embedded in epoxy resin and sliced into ultrathin sections of 60−90 nm thickness with an ultramicrotome (Ultracut UCT; LEICA). These ultrathin sections, sliced at ambient temperature, were further stained with a vapor from 3 wt % OsO_4 (aq) solution for 1 h at 70 °C, and then subjected to TEM observation with a laboratory TEM system (JEM-1400, JEOL) at ambient temperature. The observation voltage was 120 kV.

3. RESULTS AND DISCUSSION

3.1. Microdomain Structure. Figures 1 and 2, respectively, show the TEM images for the neat SIS 35−13−36 and SIS 131−57−133 copolymers and their ternary blends with the guest PI and coguest PS. Figure 3 shows the SAXS intensity

dx.doi.org/10.1021/ma3001687 | Macromolecules 2012, 45, 2809−2819

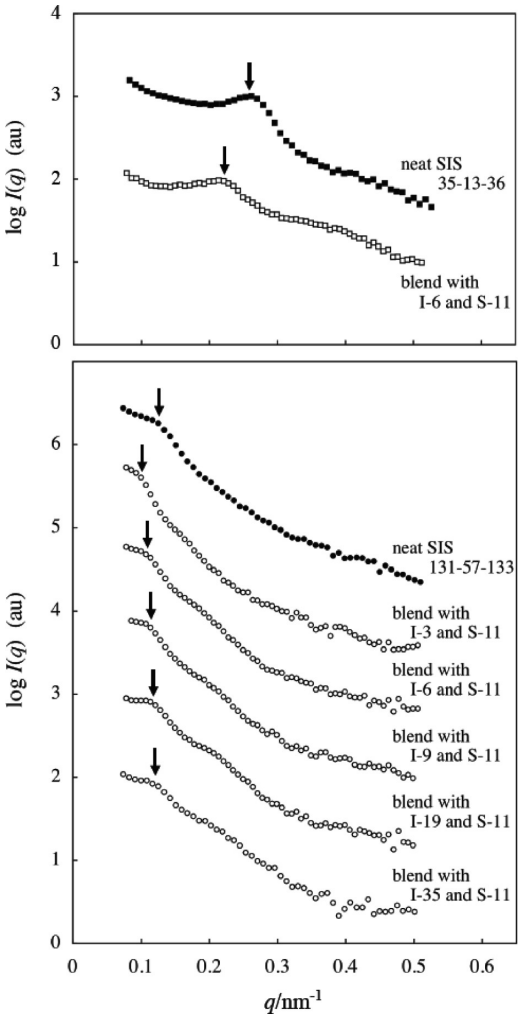


Figure 3. SAXS profiles of neat SIS 131−57−133 and SIS 35−13−36 copolymers and their ternary blends with the guest PI and coguest S-11 examined in Figures 1 and 2. The profiles are vertically shifted to avoid heavy overlapping of the data points. The arrows indicate the magnitude of the scattering vector for the first peak/shoulder, q_1.

$I(q)$ of these materials. All blends have the same total volume fraction of the PI components, $\phi_{\text{total-PI}} = 0.11_2$, the same volume fraction of the guest PI, $\phi_{\text{g-PI}} = 0.056$ ($=\phi_{\text{total-PI}}/2$), and the same molecular weight of the coguest PS, $M_{\text{cg-PS}} = 10.5 \times 10^3$, but different molecular weights $M_{\text{g-PI}}$ of the guest PI. (The coguest PS weight fraction is $w_{\text{cg-PS}} = 0.63$ and 0.67 in the blends with SIS 35−13−36 and SIS 131−57−133, respectively.)

For the ternary blends, the TEM images show that the spherical PI domains (dark domains) were formed without macroscopic phase separation between the copolymer and the guest PI; see Figures 1 and 2. The macroscopic phase separation did not occur because of the choice of $M_{\text{g-PI}}$ of the guest PI ($M_{\text{g-PI}} \leq M_{\text{block-PI}}/2$), and the spherical PI domains were formed thanks to the small $\phi_{\text{total-PI}}$ value ($= 0.11_2$) and also to the use of the mixed Bz/MEK casting solvent as explained earlier.

It should be noted that the spherical PI domains were formed also in the neat copolymers, although their ϕ_{PI} values (=0.18 and 0.20 for SIS 35−13−36 and SIS 131−57−133, respectively) were not small enough to guarantee the spherical domain formation at equilibrium.[1,2] The spherical domain was formed in the copolymers due to the use of the mixed casting solvent that enhanced the segregation of PI in an early stage of casting.[16,17] (The annealing temperature prior to the measurements, 150 °C, was still below the order−disorder transition temperatures of the copolymer thereby allowing the spherical domains formed during the casting process to survive.)

The SAXS profile (Figure 3) shows the first order scattering peak/shoulder and the higher order shoulder due to the interference between the spherical PI domains. The profiles are very broad, which is in harmony with the highly disordered spatial distribution of those domains noted in the TEM images (Figures 1 and 2). For the neat SIS copolymers, the disordered distribution of the domain location can be mostly attributable to the nonequilibrium feature in the sample preparation. Namely, the S blocks should have been vitrified in the late stage of the solvent casting thereby not allowing the PI domains to be aligned on an ordered lattice. (It is also known that the spherical domains cannot easily have the equilibrium size because of the barrier for transferring the copolymer chains from one domain to the other spatially separated domain.[18]) In addition, in the PI/SIS/PS ternary blends, the concentration gradient in the PS matrix phase during the solvent casting should have been compensated by the low-M coguest PS chains so that the S blocks anchored on the PI domains could have taken randomized conformation rather easily without violating the osmotic requirement of reducing the concentration gradient. Then, the thermodynamic driving force for the lattice formation of the PI domains should be significantly weakened to result in the disordered spatial distribution of those domains, as similar to the situation for block copolymer micelles dispersed in homopolymers chemically identical to the corona blocks.[19,20]

3.2. Change of Magnitude of Spatial Constraint for Guest PI Chains with $M_{\text{g-PI}}$. For examination of the magnitude of spatial confinement for guest PI chains in the spherical PI domains in the PI/SIS/PS blends, we attempted to evaluate the average diameter d_{PI} of those domains from the TEM images and SAXS data. For TEM, we directly measured the diameter of the domain images in Figures 1 and 2 and evaluated the average diameter, d^{app}. This d^{app} does not agree with d_{PI} because the domains in the ultrathin TEM specimen are not always sliced at their equator. Thus, we assumed random location of the domain slicing for which d_{PI} and the apparent d^{app} are related as $d^{\text{app}} = 2\{\int_0^{d_{\text{PI}}/2} \rho(h)\, dh\}/\{\int_0^{d_{\text{PI}}/2} dh\} = \{\pi/4\}d_{\text{PI}}$, where h is the height of the slicing plane measured from the equator and $\rho(h)$ ($=\{(d_{\text{PI}}/2)^2 - h^2\}^{1/2}$) is the radius of the domain section in this slicing plane. In Figure 4a, d_{PI} ($=4d^{\text{app}}/\pi$) thus evaluated from the TEM images for the PI/SIS/PS blends are plotted against the guest-PI molecular weight, $M_{\text{g-PI}}$; see circles. For comparison, d_{PI} evaluated from the TEM images for the neat SIS copolymers are shown with the horizontal dotted arrows.

The SAXS profiles for the blends (Figure 3) are very broad, as explained earlier. Thus, we cannot accurately utilize a relationship between d_{PI} and the magnitude of the scattering vector q_1 at the first order peak known for regular lattices of spherical domains. In fact, Hashimoto and co-workers[21] found a moderately discontinuous decrease of q_1 on disordering of the lattice of PS domains (micellar cores) in solutions of a styrene−butadiene (SB) copolymer in a B-selective solvent (*n*-tetradecane). This discontinuity is indicative of the failure of the lattice relationship between d_{PI} and q_1 for the randomly dispersed domains, and the origin of this failure has been analyzed in relation to the scattering from a simple liquid composed of spherical particles.[21] At the same time, Hashimoto and

dx.doi.org/10.1021/ma3001687 | Macromolecules 2012, 45, 2809−2819

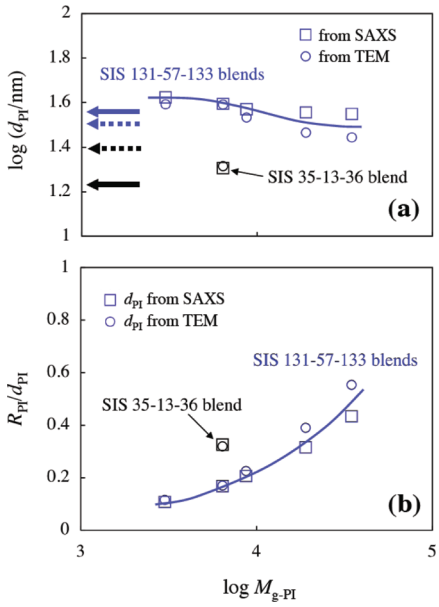


Figure 4. (a) Average diameter d_{PI} of spherical PI domain in PI/SIS/PS blends evaluated from SAXS data and TEM images. Horizontal solid and dotted arrows indicate the domain diameter in neat SIS copolymer evaluated from SAXS data and TEM image, respectively. The d_{PI} data are double-logarithmically plotted against the guest PI molecular weight $M_{g\text{-}PI}$. (b) Changes of a ratio of guest-PI chain size R_{PI} to the domain diameter d_{PI} with $M_{g\text{-}PI}$.

co-workers[21] also showed an empirical plot that specifies the magnitude of the discontinuity of q_1 on the lattice disordering as a function of the copolymer volume fraction Φ (see Figure 9 of ref 21). This plot can be cast in an empirical equation,

$$\log\left(\frac{q^*}{q_1}\right) = -0.062 \log \Phi - 0.027 \quad (\Phi < 0.4) \tag{1}$$

where q_1 is the data for the randomly dispersed spherical micelles and q^* is a hypothetical scattering vector that is observed *if* those micelles are arranged on a simple cubic lattice without changing their size. (Note that the discontinuity represented by the q^*/q_1 ratio is less than 10% for $\Phi > 0.1$ and becomes negligible for large $\Phi > 0.4$.[21]) The micellar core diameter d_{core} is related to q^* as

$$\phi_{core}\left(\frac{2\pi}{q^*}\right)^3 = \frac{4\pi}{3}\left(\frac{d_{core}}{2}\right)^3 \tag{2}$$

where ϕ_{core} is the volume fraction of the core.

Since the spatial distribution of the PI domains in our PI/SIS/PS blends is highly disordered (cf. Figures 1 and 2), we utilized eq 2 to estimate d_{PI} ($=d_{core}$ in eq 2) from the q_1 data (Figure 3) and the known volume fraction Φ of the SIS copolymer plus guest-PI after the minor correction with eq 1. (The guest PI is included in the PI domains thereby contributing to Φ.) The d_{PI} in the blends thus estimated from the SAXS data is shown with the squares in Figure 4a. For comparison, d_{PI} estimated from the SAXS data for the neat copolymers are shown with the horizontal solid arrows. (For the neat copolymer, the q^*/q_1 ratio was set to be unity because $\Phi = 1$.)

As seen in Figure 4a, the estimates of d_{PI} obtained from the TEM images and SAXS data are in reasonable agreement within experimental uncertainties. These d_{PI} values decrease gradually with increasing $M_{g\text{-}PI}$, which corresponds to a decrease of the mass $m_{g\text{-}PI}$ of the guest PI per PI domain. (This decrease of $m_{g\text{-}PI}$ possibly reflects a stronger penalty of a spatial confinement for the guest PI chain having larger $M_{g\text{-}PI}$.)

A ratio of the unperturbed end-to-end distance R_{PI} of the guest PI chains to the PI domain diameter d_{PI} can be utilized as a *measure* for the magnitude of the spatial constraint for those guest chains. We utilized an empirical equation,[22] $R_{PI} = 8.24 \times 10^{-2} M^{1/2}$ (nm), to evaluate the R_{PI}/d_{PI} ratio. In Figure 4b, this ratio is plotted against $M_{g\text{-}PI}$ of the guest PI chains. Some high-M guest PI chains have the R_{PI}/d_{PI} ratio $\geq$0.4, and those chains should be subjected to a considerable spatial constraint, as discussed below on a semiquantitative basis. (At the same time, we should also note that this constraint is not strong enough to force the guest chains to exhibit the macroscopic phase separation; cf. Figures 1 and 2.)

In the bulk state, the conformation of the guest PI chain is satisfactorily approximated to be Gaussian, and the distribution of its end-to-end distance r can be described by

$$P(r) = Kr^2 \exp\left(-\frac{3r^2}{2R_{PI}^2}\right) \quad \text{with} \quad K = \frac{4(3/2)^{3/2}}{\pi^{1/2} R_{PI}^3} \tag{3}$$

where R_{PI} ($=\langle r^2\rangle_{eq}^{1/2}$) is the average end-to-end distance at equilibrium and K is the normalization constant ensuring $\int_0^\infty P(r)\, dr = 1$. In Figure 5, the reduced distribution function

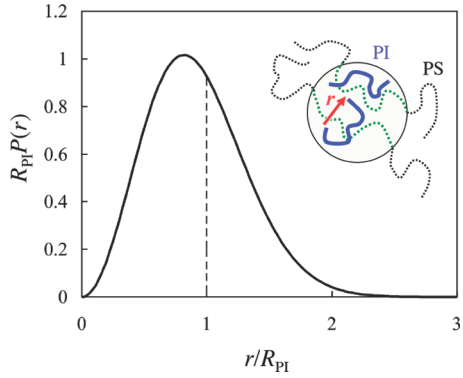


Figure 5. Gaussian distribution function of the end-to-end distance r of the guest PI chain having the unperturbed average, $R_{PI} = \langle r^2\rangle_{eq}^{1/2}$. The inset illustrates conformation of the guest PI chain (solid curves) and host copolymer chain (dotted curves).

$R_{PI}P(r)$ is plotted against a reduced end-to-end distance, r/R_{PI}. The inset illustrates the conformation of the guest PI chains (solid curves) and the host copolymer chains (dotted curves). As can be noted for the $R_{PI}P(r)$ curve, a considerable fraction (~40%) of the conformation of the guest chain cannot be realized and thus the chain should feel a rather strong spatial constraint if a hard wall is placed at a distance ~ R_{PI} from the chain end.

For the high-M guest PI chains having the R_{PI}/d_{PI} ratio $\geq$0.4 (cf. Figure 4b), the location of the center of gravity is highly limited if both ends of the chains are to be located at a distance > R_{PI} from the surface of the spherical PI domain (boundary to the glassy PS matrix), suggesting that a large fraction of those chains are spatially constrained. In contrast, for low-M guest PI chains having the R_{PI}/d_{PI} ratio as small as 0.1, this constraint would be very weak.

dx.doi.org/10.1021/ma3001687 | *Macromolecules* 2012, 45, 2809–2819

Thus, in summary, the spatial constraint for the guest PI chains examined in this study should be considerably enhanced on an increase of $M_{g\text{-}PI}$ that results in an increase of the R_{PI}/d_{PI} ratio from 0.1 to 0.4 (and more; see Figure 4b). If the spatial constraint is the main factor governing the global dynamics of the guest PI chains, their dielectric relaxation should be more significantly broadened and retarded (compared to the relaxation in the bulk state) with increasing $M_{g\text{-}PI}$. We keep this point in our mind to examine the dielectric behavior of the guest PI chains in the next section.

3.3.1. Dielectric Behavior. *Overview.* Figure 6 shows the dynamic dielectric constant $\varepsilon'(\omega)$ and dielectric loss $\varepsilon''(\omega)$

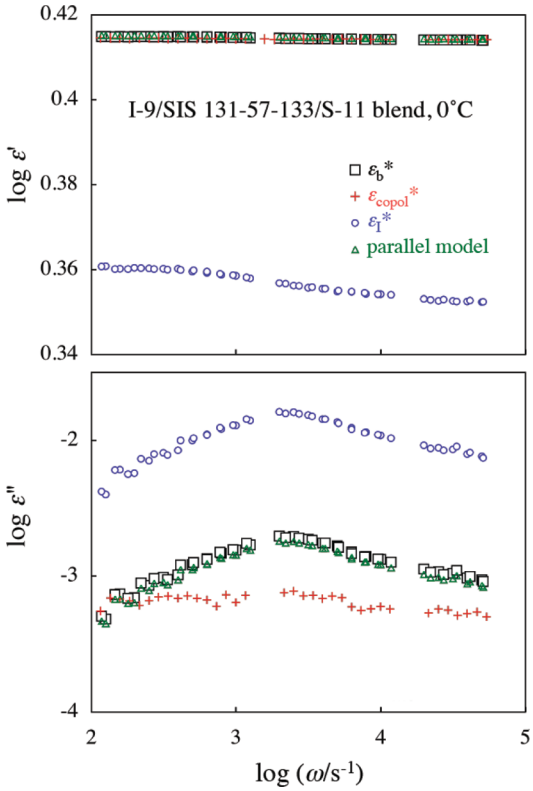


Figure 6. Dielectric data of I-9/SIS 131−57−133/S-11 blends (square) and neat SIS 131−57−133 copolymer (plus symbol) measured at 0 °C. The ε_I^* of the spherical PI domain obtained from the Maxwell−Wagner analysis are shown with the circles. For further details, see text.

measured for the I-9/SIS 131−57−133/S-11 ternary blend at 0 °C (squares). These data are double−logarithmically plotted against the angular frequency ω (squares). For comparison, the data obtained for the neat SIS 131−57−133 copolymer are also shown (plus symbols). This neat copolymer exhibits negligibly small ε'' and ω-insensitive ε', which reflects the microdomain structure illustrated in Figure 5: Namely, the S blocks and coguest PS chains are in the glassy state at 0 °C to exhibit no dielectric (segmental) relaxation. In contrast, the I block is in the rubbery state at 0 °C and exhibits active thermal motion (at a length scale smaller than the end-to-end distance). However, both ends of the I block are fixed at the boundary to the glassy PS matrix, so that the dielectric relaxation due to the non-inverted type-A dipoles (being activated only when the end-to-end vector fluctuates) is quenched.[23] In addition, the segmental relaxation of the I blocks occurs at high ω (>10^7 s^{-1} at 0 °C[4]) not covered in our experimental window. For these reasons, the neat copolymer exhibits negligible dielectric relaxation in the experimental window examined in Figure 6.

In contrast, the blend clearly exhibits slow dielectric relaxation as noted from the ε'' data shown with squares in Figure 6b, although its ε' data (Figure 6a) are close to the data for the neat copolymer (because the majority component in the blend and copolymer is the dielectrically inert PS). This relaxation, observed for all ternary blends examined, is exclusively attributable to the end-to-end vector fluctuation of the guest PI chains having the type-A dipoles and moving in the spherical PI domain. These guest chains have just a small volume fraction in the blend, $\phi_{g\text{-}PI}$ = 0.056, but their dielectric loss can be clearly resolved because of the lack of the loss of the S blocks/coguest PS chains and the I blocks.

Here, we attempt to examine the dielectric behavior of the PI chains (I block and guest PI) in the spherical PI domain. For this purpose, we can utilize the Maxwell−Wagner (MW) equation[24,25] for the complex dielectric permittivity $\varepsilon^*(\omega)$ $(= \varepsilon'(\omega) - i\varepsilon''(\omega))$ of dilute dispersions of spheres,

$$\varepsilon^*(\omega) = \varepsilon^*_m(\omega)\frac{\{2 - 2\phi\}\varepsilon^*_m(\omega) + \{1 + 2\phi\}\varepsilon^*_d(\omega)}{\{2 + \phi\}\varepsilon^*_m(\omega) + \{1 - \phi\}\varepsilon^*_d(\omega)}$$

$$\text{for small } \phi\ (\leq 0.1) \qquad (4)$$

where $\varepsilon_m^*(\omega)$ and $\varepsilon_d^*(\omega)$, respectively, indicate the permittivity of the medium and dispersed spheres at the angular frequency ω. For our blends, $\varepsilon^*(\omega)$, $\varepsilon_d^*(\omega)$, and $\varepsilon_m^*(\omega)$ are equivalent to $\varepsilon_b^*(\omega)$ of the blend as a whole, $\varepsilon_I^*(\omega)$ of the PI components in the spherical domain, and $\varepsilon_S^*(\omega)$ $(=\varepsilon_{glassy\text{-}S}' = 2.64)$ of the glassy S chains in the matrix, respectively, and $\phi = \phi_{total\text{-}PI} = 0.11_2$. Thus, eq 4 allowed us to evaluate $\varepsilon_I^*(\omega)$ from the $\varepsilon_b^*(\omega)$ and $\varepsilon_{glassy\text{-}S}'$ data. The results are shown in Figure 6 with the circles. (We also utilized the Hanai equation[26] for concentrated dispersions, but the results were very close to those shown in Figure 6 because our blend had just small $\phi_{total\text{-}PI}$.)

For the ε_b^* data shown in Figure 6, one might assume, instead of the MW equation (eq 4), a simple blending law for the parallel model:

$$\varepsilon_b'(\omega) = \phi_{total\text{-}PI}\varepsilon_I'(\omega) + (1 - \phi_{total\text{-}PI})\varepsilon_{glassy\text{-}S}' \qquad (5a)$$

$$\varepsilon_b''(\omega) = \phi_{total\text{-}PI}\varepsilon_I''(\omega) \quad (\varepsilon_{glassy\text{-}S}'' = 0) \qquad (5b)$$

We calculated ε_b^* from eq 5, with $\varepsilon_I'(\omega)$ and $\varepsilon_I''(\omega)$ therein being obtained from eq 4 (circles in Figure 6). The calculated ε_b^*, shown in Figure 6 with the triangles, are close to the ε_b^* data (squares), indicating an approximate but satisfactory validity of the simple parallel model for our blends. In fact, eq 5 can describe ε_b^* within acceptably small errors for copolymers systems having either spherical or nonspherical PI domains, *given that* the PS phase is glassy and exhibits no dielectric loss. Nevertheless, at high T where the PS matrix exhibits considerable dielectric loss due to the segmental relaxation, we confirmed that eqs 4 and 5 give considerably different ε_b^* values for the same set of ε_I^* and ε_S^*. Thus, in general, the use of eq 4 is desired for evaluation of $\varepsilon_I^*(\omega)$ of the PI components in the spherical domain. For this reason, we utilized eq 4 to evaluate $\varepsilon_I^*(\omega)$ for all blends examined. Those $\varepsilon_I^*(\omega)$ data are examined below to discuss the guest chain dynamics in the spherical PI domains.

dx.doi.org/10.1021/ma3001687 | Macromolecules 2012, 45, 2809−2819

3.3.2. Guest PI Dynamics in Spherical PI Domain. The top panel of Figure 7 compares the $\varepsilon_I''(\omega)$ data obtained for all ternary blends (containing various guest PI chains; cf. Table 2)

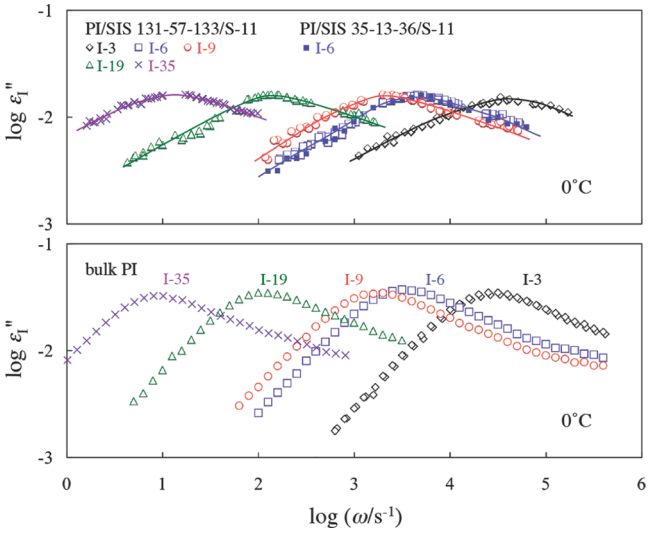


Figure 7. Top panel: ε_I'' data of the guest PI chains in spherical PI domains in the blends as indicated. Bottom panel: ε_I'' data of the guest PI chains in respective bulk state.

with the aid of eq 4. These $\varepsilon_I''(\omega)$ data are exclusively attributed to the end-to-end vector fluctuation of the guest chains, because the I block having the fixed ends exhibits no dielectric relaxation, as explained earlier. As a reference, the $\varepsilon_I''(\omega)$ data of the guest PI chains in respective bulk state are shown in the bottom panel. The data were measured and compared at 0 °C, except for the two high-M guest chains; the data in the blend and bulk for I-19 and I-35 were measured at T_{exp} = 40 and 60 °C, respectively, and compared at 0 °C after the time-frequency shift from those T_{exp} to 0 °C: The ω-shift factor a_T evaluated for the guest PI chains in bulk was applied also to those chains in the PI domain. The $\varepsilon_I''(\omega)$ data of those high-M guest PI chains were also subjected to a minor correction for the relaxation intensity ($\propto 1/T$ with T being the absolute temperature).

Figure 7 clearly indicates that the dielectric relaxation of the guest PI chain, either in the spherical PI domain or in bulk, becomes slower with increasing $M_{g\text{-PI}}$ because the relaxation reflects the global motion at the end-to-end length scale. We also note that the angular frequency ω_{peak} at the ε_I''-peak of each guest PI is a little higher in the spherical domain than in bulk. From this small difference of ω_{peak}, one might consider that the *global* motion of the guest PI chain is slightly accelerated in the spherical domain. However, this is not the case at all: All PI chains in bulk clearly exhibit the proportionality between ε_I'' and ω at low ω that characterizes the full relaxation in our experimental window, whereas this proportionality is observed for *none* of those chains in the spherical domain. Thus, the *global motion* of the guest PI chains is highly retarded (and its mode distribution is broadened) in the spherical domains compared to respective bulk systems, as explained in more detail in Appendix A in relation to the general, phenomenological framework of dielectric relaxation: For example, the I-3 chain has the second-moment average relaxation time (terminal relaxation time) $\langle\tau\rangle_w = 4.0 \times 10^{-5}$ s and $\langle\tau\rangle_w > 10^{-3}$ s in the bulk state and blend, respectively, and thus its relaxation is much slower in the blend; see Appendix A.

In the spherical domain, the guest PI chains are subjected to a very strong requirement of keeping the constant segmental density in the domain. This osmotic requirement forces the guest PI chains to move *cooperatively* with the PI blocks therein, which leads to the retardation/broadening of the dielectric relaxation of the guest PI chains explained above.[5,9,10] In addition, the guest PI chains are not allowed to escape the spherical domain, and this spatial constraint could also affect the relaxation of the guest PI chains.[5,10] Effects of these osmotic and spatial constraints on the guest PI motion/dielectric relaxation are further examine below.

Since the guest PI chains have the volume fraction $\upsilon_I = \phi_{g\text{-PI}}/\phi_{total\text{-PI}} = 0.5$ in the spherical domain, the dielectric loss of those chains normalized to unit volume is given by $\varepsilon_I''/\upsilon_I$. In Figure 8,

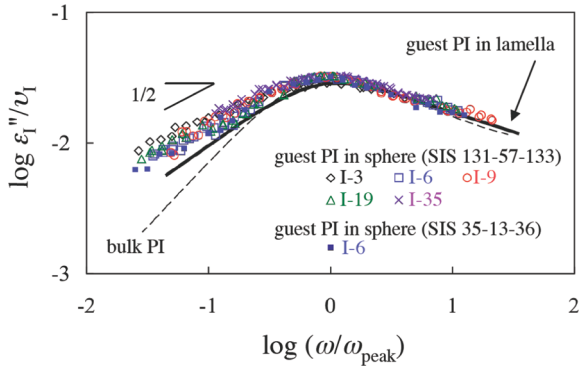


Figure 8. Comparison of dielectric mode distribution for guest PI chains in spherical domains in PI/SIS/S-11 blends, guest PI chains in a lamellar domain, and bulk PI.

the $\varepsilon_I''/\upsilon_I$ data of the guest PI chains in the spherical domains are double−logarithmically plotted against a frequency reduced at the ε_I'' peak, ω/ω_{peak}; see symbols. Those plots are indistinguishable for the guest PI chains having various $M_{g\text{-PI}}$ (and being subjected to the spatial constraint of various magnitudes, as explained earlier). For comparison, the plots are shown also for those chains in respective bulk state (where $\upsilon_I = 1$); see the dashed curve. These bulk chains have quite M-insensitive dielectric mode distribution, as explained in more detail in Appendix B. In literature,[9] the $\varepsilon_I''/\upsilon_I$ data at 0 °C are available for guest PI chains (with $10^{-3}M_{g\text{-PI}} = 4.5$ and 9.8) confined in lamellar polybutadiene (B) domains formed by a styrene−butadiene (SB) copolymer having $10^{-3}M_S = 8.6$ and $10^{-3}M_B = 8.5$, with M_B being comparable to $M_{g\text{-PI}}$. Those $\varepsilon_I''/\upsilon_I$ data, insensitive to $M_{g\text{-PI}}$ and $\phi_{g\text{-PI}}$ (in the range of $\phi_{g\text{-PI}} \leq 0.1$), are also shown in Figure 8; see the thick solid curve.

In Figure 8, we first confirm that the slow dielectric relaxation of the guest PI chains is much broader in the spherical domain than in bulk and no terminal proportionality ($\varepsilon'' \propto \omega$) is observed in the spherical domain. This broad mode distribution is characterized with an empirical fractional power-law, $\varepsilon'' \propto \omega^{\alpha}$ with $\alpha \cong {}^1/_2$, seen at $\omega < \omega_{peak}$. We also note that the dielectric mode distribution of the guest PI in the spherical domains is insensitive to $M_{g\text{-PI}}$. (This $M_{g\text{-PI}}$-insensitivity is noted also in lamellar domains examined in the previous study.[9]) Since the spatial constraint for those chains should be enhanced considerably on an increase of $M_{g\text{-PI}}$ (i.e., on an increase of the chain/domain size ratio, R_{PI}/d_{PI}, from 0.1 to 0.4 and more, as discussed for Figure 4b), the $M_{g\text{-PI}}$-insensitive mode distribution suggests that the global motion of the guest PI chains is dominantly affected by the osmotic constraint and the

dx.doi.org/10.1021/ma3001687 | Macromolecules 2012, 45, 2809−2819

spatial constraint has just a secondary effect (at least in the range of R_{PI}/d_{PI} examined).

In relation to this osmotic constraint, it should be noted that even the lowest-M and highest-M guest chains, I-3 and I-35, exhibit similarly broad dielectric mode distribution: Since the I-3 molecular weight ($= 3.0 \times 10^3$) is well below the entanglement molecular weight ($M_e \cong 5.0 \times 10^3$ for PI[22]), the I-3 chains in the bulk state essentially obey the Rouse dynamics[6] free from the entanglement effect. In contrast, the I-35 chains are rather well entangled to exhibit the reptation-like dynamics[6] in the bulk state. Thus, the coincidence of the broad dielectric mode distribution for the I-3 and I-35 (and all other) chains, characterized with the power-law type behavior ($\varepsilon'' \propto \omega^{\alpha}$ with $\alpha \cong {}^1/_2$) at low ω, suggests that the osmotic constraint in the spherical domain affects the motion of the guest chains at a length scale ξ well below the entanglement length a (=5.8 nm for PI[22]) and this effect is accumulated in a self-similar way (irrespective of the entanglement) up to the chain size R_{PI}. Detail of this accumulation is an interesting subject of future work.

Finally, we note that the dielectric mode distribution at high $\omega > \omega_{peak}$ is nearly the same for the guest PI chains confined in the spherical and lamellar domains (and for the chains in bulk), but the distribution at low $\omega < \omega_{peak}$ is a little broader in the spherical domain; compare the symbols and thick solid curve Figure 8. This result suggests that the osmotic constraint is stronger in the spherical domain than in the lamellar domain, possibly because the lamellar domain is continuous and has no wall (domain boundary) perpendicular to the lamellar surface. This lack of the wall would allow the guest PI chain to move and transfer its segments over a large length scale in the direction parallel to the lamellar surface without feeling a strong osmotic constraint. Furthermore, this segment transfer should help adjustment of the local segment density on motion of the other guest chains in the direction normal to the lamellar surface, thereby possibly reducing the osmotic constraint for the motion also in the normal direction. In contrast, in the spherical domains, the guest chain feels the wall in all directions at a distance within the domain diameter, and the segment transfer is always subjected to the strong osmotic constraint. This difference between the lamellar and spherical domains could have resulted in the observed difference of the slow dielectric mode distribution of the guest chains in these domains.

As explained above, we may naturally explain the difference of the guest dynamics in the lamellar and spherical domains in relation to the continuity of the domain. However, this explanation is just qualitative, and no quantitative analysis of the difference has been made. This quantitative analysis deserves further studies.

4. CONCLUDING REMARKS

For ternary blends of PS−PI−PS triblock copolymer, guest PI chains, and coguest PS chains, we have examined the dielectric behavior at low T ($<T_{g,PS}$). At such low T, no slow dielectric relaxation was activated by the glassy S blocks/coguest PS chains and by the I blocks having the ends anchored on the glassy PS matrix. Thus, the slow relaxation observed for the ternary blends was exclusively attributed to the global motion (end-to-end vector fluctuation) of the guest PI chains confined in the spherical PI microdomains formed by the copolymer. This relaxation in the spherical domains was found to be much slower and broader than that in bulk PI systems. Furthermore, the guest PI chains exhibited similarly broad relaxation in the spherical domain irrespective of their molecular weights $M_{g\text{-}PI}$. These results suggest that the global motion of the guest PI chains in the spherical domains is dominantly affected by the osmotic constraint (requiring uniform filling of the domain with the segments) so that the guest chains are forced to move highly cooperatively with the I blocks: The spatial confinement of the guest chains in the spherical domain gives just a secondary effect for the guest chain dynamics.

Furthermore, comparison of the dielectric mode distribution of the guest chains in the spherical and lamellar domains suggested that the osmotic constraint is stronger in the spherical domain: In the lamellar domain, the guest PI chain would move rather freely over a large length scale in the direction parallel to the lamellar surface, and this motion results in adjustment of the local segment density on motion of the other guest chains in the direction normal to the lamellar surface, thereby possibly reducing the osmotic constraint for the motion also in the normal direction. The lack of this mechanisms in the discontinuous spherical domain possibly led to the stronger constraint and the broader dielectric mode distribution.

APPENDIX A. PHENOMENOLOGICAL FRAMEWORK OF DIELECTRIC RELAXATION

A reviewer for this paper suspected that the dielectric relaxation of the guest PI chains is not significantly retarded in the spherical I domain because the angular frequency of the ε'' peak, ω_{peak}, is not very different for the PI chains in those domains and in bulk state. However, we can unequivocally conclude the significant retardation on the basis of the general, phenomenological framework of dielectric relaxation (in the linear stimulus-response regime), as explained below.

It is well-known that the decrease of dynamic dielectric constant from its static value, $\Delta\varepsilon'(\omega) \equiv \varepsilon'(0) - \varepsilon'(\omega)$, and the dielectric loss, $\varepsilon''(\omega)$, are related to the normalized dielectric relaxation function $\Phi(t)$ (=1 at time $t = 0$) and the dielectric relaxation intensity $\Delta\varepsilon$ as[5−7]

$$\Delta\varepsilon'(\omega) = \omega\Delta\varepsilon \int_0^\infty \Phi(t) \sin \omega t \, dt \tag{A1}$$

$$\varepsilon''(\omega) = \omega\Delta\varepsilon \int_0^\infty \Phi(t) \cos \omega t \, dt \tag{A2}$$

For the slow dielectric relaxation of the guest PI chains having noninverted type-A dipoles, $\Phi(t)$ is expressed as the auto-correlation function of the end-to-end vector $\mathbf{R}$:[5−7]

$$\Phi(t) = \frac{\langle \mathbf{R}(t)\cdot\mathbf{R}(0)\rangle_{eq}}{\langle \{\mathbf{R}(0)\}^2\rangle_{eq}} \tag{A3}$$

where $\langle\cdots\rangle_{eq}$ indicates the ensemble average at equilibrium. Because the PI chains are flexible, their $\Phi(t)$ unequivocally has the mode distribution that is expressed in a general form[5−7]

$$\Phi(t) = \sum_{p\geq 1} g_p \exp\left(-\frac{t}{\tau_p}\right) \quad \text{with } \tau_1 > \tau_2 > \tau_3 \ldots \tag{A4}$$

Here, g_p and τ_p are the intensity and relaxation time of pth relaxation mode, with the first (slowest) mode corresponding to the motion of the backbone of the chain as a whole. (g_p satisfies a relationship, $\sum_{p\geq 1} g_p = 1$, which corresponds to the initial condition, $\Phi(0) = 1$.)

dx.doi.org/10.1021/ma3001687 | Macromolecules 2012, 45, 2809−2819

As clearly noted from eqs A1, A2, and A4, $\Delta\varepsilon'(\omega)$ and $\varepsilon''(\omega)$ are expressed in terms of the relaxation times and intensities of the modes:

$$\Delta\varepsilon'(\omega) = \Delta\varepsilon \sum_{p\geq 1} g_p \frac{\omega^2 {\tau_p}^2}{1+\omega^2 {\tau_p}^2},$$
$$\varepsilon''(\omega) = \Delta\varepsilon \sum_{p\geq 1} g_p \frac{\omega\tau_p}{1+\omega^2 {\tau_p}^2} \quad \text{(A5)}$$

This expression is formally identical to the expression of the storage and loss moduli, G' and G'', in terms of the viscoelastic mode intensities and relaxation times.[5,6] Thus, all relationships established for the moduli are applicable to $\Delta\varepsilon'(\omega)$ and $\varepsilon''(\omega)$. Specifically, completion of the relaxation is characterized by the relationships that hold only at low ω well below $1/\tau_1$ (with τ_1 being the longest relaxation time):

$$\Delta\varepsilon'(\omega) = \Delta\varepsilon\omega^2 \sum_{p\geq 1} g_p {\tau_p}^2 \propto \omega^2,$$
$$\varepsilon''(\omega) = \Delta\varepsilon\omega \sum_{p\geq 1} g_p\tau_p \propto \omega \quad \text{(A6)}$$

(These relationships are analogous to the relationships well-known for the moduli, $G' \propto \omega^2$ and $G'' \propto \omega$ at low ω where the relaxation is completed.) Consequently, we can unequivocally conclude that the relaxation is *not* completed in a range of ω where the proportionality between $\varepsilon''(\omega)$ and ω (and between $\Delta\varepsilon'(\omega)$ and ω^2) is not observed. This is the case for the guest PI chains in the spherical I domains, as noted in Figures 7 and 8. Namely, in those domains, the slowest mode of end-to-end fluctuation of the guest PI chains has not completed in the range of ω examined. In contrast, the proportionality between $\varepsilon''(\omega)$ and ω is clearly observed for the same PI chains in respective bulk sate; see Figure 7. Thus, the end-to-end fluctuation of the PI chains is significantly retarded in the spherical domain compared to the bulk system.

We can also utilize an average relaxation time to quantitatively compare the PI dynamics in the spherical domains and in bulk systems. The first- and second-moment average relaxation times $\langle\tau\rangle_n$ and $\langle\tau\rangle_w$, being defined in terms of the mode relaxation times τ_p and intensities g_p, can be directly evaluated from the dielectric data at low ω (cf. eq A6).[5,6]

$$\langle\tau\rangle_n \equiv \frac{\sum_{p\geq 1} g_p\tau_p}{\sum_{p\geq 1} g_p} = \frac{1}{\Delta\varepsilon}\left[\frac{\varepsilon''(\omega)}{\omega}\right]_{\omega\to 0},$$
$$\langle\tau\rangle_w \equiv \frac{\sum_{p\geq 1} g_p {\tau_p}^2}{\sum_{p\geq 1} g_p\tau_p} = \left[\frac{\Delta\varepsilon'(\omega)}{\omega\varepsilon''(\omega)}\right]_{\omega\to 0} \quad \text{(A7)}$$

(These $\langle\tau\rangle_n$ and $\langle\tau\rangle_w$ are analogous to the well-known viscoelastic relaxation times,[28,29] η_0/G_∞' and $J_e\eta_0$ with η_0, G_∞', and J_e being the zero-shear viscosity, high-frequency storage modulus, and the steady-state recoverable compliance, respectively.) $\langle\tau\rangle_w$ is longer than $\langle\tau\rangle_n$ for any relaxation mode distribution, except for the case of single Maxwellian relaxation for which $\langle\tau\rangle_w = \langle\tau\rangle_n$. It should be noted that $\langle\tau\rangle_w$ heavily weighs on slow relaxation modes and can be utilize as the terminal dielectric relaxation time,[5,6] which is analogous to the use of $J_e\eta_0$ as the viscoelastic terminal relaxation time.[28,29]

Monodisperse linear PI chains in bulk state have a narrow distribution of the relaxation modes (cf. Appendix B), so that their dielectric $\langle\tau\rangle_n$ and $\langle\tau\rangle_w$ are rather close to each other ($\langle\tau\rangle_w \cong 2\langle\tau\rangle_n$) and a relaxation time defined in terms of the ε''-peak frequency, $\tau_{peak} = 1/\omega_{peak}$, has a value between the $\langle\tau\rangle_n$ and $\langle\tau\rangle_w$ values.[5−7] Thus, for the PI chains utilized in this study, we may safely utilize τ_{peak} evaluated in Figure 7 (instead of $\langle\tau\rangle_w$) as the dielectric terminal relaxation time in the bulk state. In contrast, for the guest PI chains confined in the spherical domains, the terminal proportionality, $\varepsilon''(\omega) \propto \omega$ (eq A6), is not observed in our experimental window. This fact enables us to conclude a relationship for the chains in those domains, $\langle\tau\rangle_w > \langle\tau\rangle_n > 1/\omega_{lowest}$ with ω_{lowest} being the lowest angular frequency examined in Figure 7. (The $\varepsilon''(\omega)/\omega$ ratio increases with decreasing ω and thus $[\varepsilon''(\omega)/\omega]_{\omega\to 0} > \varepsilon''(\omega_{lowest})/\omega_{lowest}$, which allows us to deduce this relationship.) Thus, the dielectric terminal relaxation time of the PI chains is significantly longer in the spherical domains than in the bulk state: For example, $\langle\tau\rangle_w > \langle\tau\rangle_n > 1/\omega_{lowest} = 10^{-3}$ s for I-3 in the spherical domain and $\langle\tau\rangle_w \cong \tau_{peak} = 4.0 \times 10^{-5}$ s for bulk I-3; see Figure 7.

In relation to the above argument, a comment needs to be made for τ_{peak} for a relaxation process with a broad mode distribution. Since the phenomenological framework is the same for G'' and ε'', we here focus on G'' of Rouse chains (bead−spring chains) as a well-known example of loss factor associated with the broad mode distribution. For the Rouse chain composed of $N + 1$ beads and N springs, $G''(\omega)$ is expressed as[29]

$$G''(\omega) = \nu k_B T \sum_{p=1}^{N} \frac{\omega\tau_p^{[R,G]}}{1+\omega^2\{\tau_p^{[R,G]}\}^2} \quad \text{(A8)}$$

where ν, k_B, and T denote the number density of the chain, Boltzmann constant, and absolute temperature, respectively, and $\tau_p^{[R,G]}$ is the viscoelastic relaxation time of pth Rouse mode:

$$\tau_p^{[R,G]} = \frac{\zeta b^2}{24 k_B T} \sin^{-2}\left\{\frac{p\pi}{2(N+1)}\right\} \quad \text{(A9)}$$

In eq A9, ζ and b represent the friction coefficient and step length of the Rouse segment. The intensity factor appearing in eq A8, $\nu k_B T$, is common for all Rouse modes. The first- and second-moment average viscoelastic Rouse relaxation times, $\langle\tau\rangle_n^{[R,G]}$ and $\langle\tau\rangle_w^{[R,G]}$, are given by[30]

$$\langle\tau\rangle_n^{[R,G]} \equiv \frac{\sum_{p=1}^{N} \nu k_B T \tau_p^{[R,G]}}{\sum_{p=1}^{N} \nu k_B T} = \frac{\zeta b^2}{36 k_B T}(N+2)$$
$$(\propto N \text{ for large } N) \quad \text{(A10)}$$

$$\langle\tau\rangle_w^{[R,G]} \equiv \frac{\sum_{p=1}^{N} \nu k_B T \{\tau_p^{[R,G]}\}^2}{\sum_{p=1}^{N} \nu k_B T \tau_p^{[R,G]}} = \frac{\zeta b^2}{180 k_B T}(2N^2+4N+9)$$
$$(\propto N^2 \text{ for large } N) \quad \text{(A11)}$$

Obviously, these $\langle\tau\rangle_n^{[R,G]}$ and $\langle\tau\rangle_w^{[R,G]}$ are longer than $\tau_N^{[R,G]}$ for the fastest (Nth) Rouse mode.

For several values of N, Figure 9 shows plots of a reduced loss modulus $G''(\omega)/\nu N k_B T$ against a reduced frequency $\omega\tau_N^{[R,G]}$.

dx.doi.org/10.1021/ma3001687 | Macromolecules 2012, 45, 2809−2819

The arrows indicate the relaxation frequency of the slowest Rouse mode, $1/\tau_1^{[R,G]}$, and the thin dotted curve indicates a modulus contribution from the fastest mode (with $p = N$) for the case of $N = 5$. In Figure 9, one *might* attempt to utilize the peak relaxation time τ_{peak} ($= 1/\omega_{peak}$) as an average relaxation time. However, this τ_{peak} is insensitive to N and much shorter than $\tau_1^{[R,G]}$ (cf. arrow), $\langle\tau\rangle_n^{[R,G]}$, and $\langle\tau\rangle_w^{[R,G]}$. This fact demonstrates that τ_{peak} *cannot* be utilized for discussion of the slow dynamics of the chain *given that* the chain exhibits a broad mode distribution and its loss peak is not immediately followed by the low-ω proportionality between the loss factor and ω. This conclusion is not limited to the Rouse modulus but applies to *any* broad relaxation process, *i.e.*, to the broad dielectric relaxation process of the guest PI chains in the spherical domains (seen in Figures 7 and 8).

Finally, it is informative to compare the modulus contribution from the fastest Rouse mode for $N = 5$ (thin dotted curve shown in Figure 9) and the modulus curve (plots for $N = 5$).

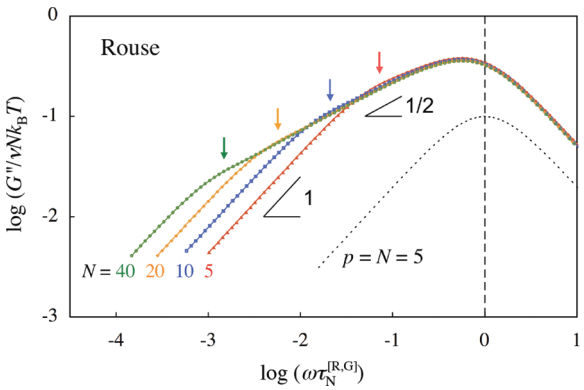


Figure 9. Plots of reduced viscoelastic loss modulus of Rouse chains composed of $N + 1$ beads and N springs ($N = 5$, 10, 20, and 40) against reduced frequency. The thin dotted curve indicates a contribution to the modulus from the fastest mode for the case of $N = 5$.

The peak for this fastest mode contribution emerges at $\omega\tau_N^{[R,G]} = 1$, whereas the peak for the modulus is observed at $\omega\tau_N^{[R,G]} \cong 0.6$. The contributions from the second and third fastest modes have the peaks at $\omega\tau_N^{[R,G]} = 0.804$ and 0.536, respectively (cf. eq A9). Thus, none of these modes exhibits the peak at $\omega\tau_N^{[R,G]} \cong 0.6$ observed for the modulus.[31] This fact demonstrates that a peak of G'' data (and of ε'' data) does not always correspond to a particular mode of molecular relaxation: For the broad mode distribution, the peak frequency ω_{peak} has, at best, just a semiquantitative meaning as an average relaxation frequency for a group of relaxation modes having large intensities. This fact also suggests that τ_{peak} of the broad ε'' data of the guest PI chains in the spherical domains cannot be utilized for discussion of the global motion of those chains.

APPENDIX B: DIELECTRIC BEHAVIOR OF BULK PI

The dielectric mode distribution is characterized with the ω dependence of the dielectric loss, $\varepsilon''(\omega)$, and the decrease of the dynamic dielectric constant, $\Delta\varepsilon'(\omega) \equiv \varepsilon'(0) - \varepsilon'(\omega)$,[5−7,27] as explained in Appendix A. In Figure 10, the $\varepsilon''(\omega)$ and $\Delta\varepsilon'(\omega)$ data measured for the guest PI chains in respective bulk systems are plotted against the reduced frequency ω/ω_{peak} (with ω_{peak} =ε''-peak frequency). The data at low ω(<l00ω_{peak}) are well superposed with each other, confirming that the slow, terminal dielectric mode

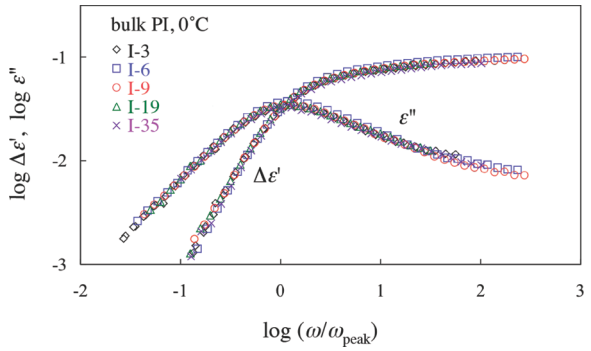


Figure 10. Comparison of dielectric mode distribution of bulk PI chains of various molecular weights.

distribution of the PI chains is insensitive to M in the nonentangled and moderately entangled regimes ($M_e < M < 10M_e$).[5−7,27] These M-insensitive plots of $\varepsilon''(\omega)$ against ω/ω_{peak} are shown in Figure 8 with the dashed curve.

In relation to the above feature of the nonentangled to moderately entangled PI chains, we note that highly entangled PI chains ($M > 20M_e$) exhibit a slightly narrower terminal mode distribution characterized with $\omega^{-1/2}$ dependence of ε'' at ω just above ω_{peak}.[8] However, in the plots of ε'' against ω/ω_{peak}, this narrowing for highly entangled PI corresponds to just a moderate decrease of ε'' at $\omega \gg \omega_{peak}$, by a factor of 20−30%, compared to ε'' of moderately entangled PI. Thus, in the entire range of M, the terminal dielectric mode distribution of bulk PI is essentially insensitive to M, unless we focus on the $\omega^{-1/2}$ dependence of ε'' of high-M PI at ω just above ω_{peak}. This M-insensitivity of the dielectric mode distribution differs from a considerable M-dependence seen for the terminal viscoelastic mode distribution.[6−8] This difference reflects a difference of the relationships between the chain conformation and the measured quantities, the orientational correlation at two separate times reflected in the dielectric quantity and the isochronal orientational anisotropy, in the viscoelastic quantity.[5−7,27]

AUTHOR INFORMATION

Notes

The authors declare no competing financial interest.

ACKNOWLEDGMENTS

This work was supported by the Grant-in-Aid for Scientific Research (B) (Grant No. 21350063), by Grant-in-Aid for Young Scientists (B) from MEXT (Grant No. 22750204), and partly by the Collaborative Research Program of Institute for Chemical Research, Kyoto University (Grant No. 2012-35).

REFERENCES

(1) Bates, F. S.; Fredrickson, G. H. *Annu. Rev. Phys. Chem.* **1990**, *41*, 525.
(2) Hamley, I. W. *The Physics of Block Copolymers*: Oxford Press: Oxford, U.K., 1998.
(3) Matsushita, Y. *Macromolecules* **2007**, *40*, 771.
(4) Adachi, K.; Kotaka, T. *Prog. Polym. Sci.* **1993**, *18*, 585.
(5) Watanabe, H. *Macromol. Rapid Commun.* **2001**, *22*, 127.
(6) Watanabe, H. *Prog. Polym. Sci.* **1999**, *24*, 1253.
(7) Watanabe, H. *Polym. J.* **2009**, *41*, 929.
(8) Glomann, T.; Schneider, G. J.; Bras, A. R.; Pyckhout-Hintzen, W.; Wischnewski, A.; Zorn, R.; Allgaier, A.; Richter, D. *Macromolecules* **2011**, *44*, 7430.

(9) Yao, M.-L.; Watanabe, H.; Adachi, K.; Kotaka, T. *Macromolecules* **1991**, *24*, 2955.
(10) Watanabe, H.; Sato, T.; Osaki, K.; Matsumiya, Y.; Anastasiadis, S. H. *Nihon Reoroji Gakkaishi (J. Soc. Rheol. Jpn.)* **1999**, *27*, 173.
(11) Karatasos, K.; Anastasiadis, S. H.; Pakula, T.; Watanabe, H. *Macromolecules* **2000**, *33*, 523.
(12) Floudas, G.; Paraskeva, S.; Hadjichristidis, N.; Fytas, G.; Chu, B.; Semenov, A. N. *J. Chem. Phys.* **1997**, *107*, 5502.
(13) Yao, M.-L.; Watanabe, H.; Adachi, K.; Kotaka, T. *Macromolecules* **1991**, *24*, 6175.
(14) Sawada, T.; Qiao, X.; Watanabe, H. *Nihon Reoroji Gakkaishi (J. Soc. Rheol. Jpn.)* **2007**, *35*, 11.
(15) Watanabe, H.; Urakawa, O.; Kotaka, T. *Macromolecules* **1993**, *26*, 5073.
(16) Inoue, T.; Soen, T.; Hashimoto, T.; Kawai, H. *J. Polym. Sci., Part A-2* **1969**, *7*, 1283.
(17) Arai, K.; UedaMshima, C.; Kotaka, T.; Yoshimura, K.; Murayama, K. *Polymer* **1984**, *25*, 230.
(18) Hashimoto, T.; Fujimura, M.; Kawai, H. *Macromolecules* **1980**, *13*, 1660.
(19) Watanabe, H.; Kotaka, T. *J. Rheol.* **1983**, *27*, 223.
(20) Watanabe, H. *Acta Polym.* **1997**, *48*, 215.
(21) Hashimoto, T.; Shibayama, M.; Kawai, H.; Watanabe, H.; Kotaka, T. *Macromolecules* **1983**, *16*, 361.
(22) Fetters, L. J.; Lohse, D. J.; Colby, R. H. *Chain Dimensions and Entanglement Spacings*, in *Physical Properties of Polymers Handbook*, 2nd ed.; Mark, J. E., Ed.; Springer: New York, 2007; Chapter 25.
(23) At 0 °C, the thermal motion of the I block is not quenched even if it has a fixed end-to-end vector **R**. For discussion of this motion, we may divide the I block into N subchains and focus on the end-to-end vector of nth subchain at time t, $\mathbf{u}(n,t)$ with n = 1, 2, ..., N. This subchain vector can be expressed as $\mathbf{u}(n,t) = \mathbf{R}/N + \mathbf{v}(n,t)$,[6] where $\mathbf{v}(n,t)$ is a randomly fluctuating vector satisfying a relationship, $\sum_n \mathbf{v}(n,t) = \mathbf{0}$ at any t. The orientational memory function of respective subchains, $\phi_{nn}(t) \equiv \langle \mathbf{u}(n,t)\cdot\mathbf{u}(n,0)\rangle$, decays from $\langle\{\mathbf{u}(n,0)\}^2\rangle$ ($=\langle \mathbf{R}^2\rangle/N$ *if* the I block has the Gaussian conformational distribution) to $\langle \mathbf{R}^2\rangle/N^2$ on an increase of time t from 0 to ∞. However, this reorientational motion of individual subchains does *not* activate the dielectric relaxation, because the subchain dipole is proportional to $\mathbf{u}(n,t)$ (for the I block having noninverted type-A dipoles) and thus the dielectric relaxation function of the I block is expressed as $\Phi(t) = \langle\{\sum_n \mathbf{u}(n,t)\}\cdot\{\sum_m \mathbf{u}(m,0)\}\rangle/\langle\{\sum_m \mathbf{u}(m,0)\}^2\rangle = 1$ (note that $\sum_n \mathbf{v}(n,t) = \mathbf{0}$ at any time t). This lack of the decay of $\Phi(t)$ reflects the growth of the orientational cross-correlation $\phi_{nm}(t) \equiv <\mathbf{u}(n,t)\cdot\mathbf{u}(m,0)>_{n\neq m}$: Namely, the decay of $\phi_{nn}(t)$ is exactly canceled by the growth of $\sum_{m\ (\neq n)} \phi_{nm}(t)$ to give the constant Φ ($=\sum_n \{\phi_{nn}(t) + \sum_{m\ (\neq n)} \phi_{nm}(t)\}/\sum_n \{\phi_{nn}(0)+\sum_{m\ (\neq n)} \phi_{nm}(0)\} = 1$).
(24) Wagner, K. W. *Arch. Elektrotech.* **1914**, *2*, 371.
(25) Steeman, P. A. M.; van Turnhout, J. *Dielectric Properties of Inhomogeneous Media*, in *Broadband Dielectric Spectroscopy*, Kremer, F., Schönhals, A., Eds.; Springer: Berlin, 2003; Chapter 13.
(26) Hanai, T. *Kolloid Z.* **1960**, *17*, 23.
(27) Matsumiya, Y. *Nihon Reoroji Gakkaishi (J. Soc. Rheol. Jpn.)* **2011**, *39*, 197.
(28) Ferry, J. D. *Viscoelastic Properties of Polymers*, 3rd ed.; Wiley: New York, 1980.
(29) Graessley, W. W. *Adv. Polym. Sci.* **1974**, *16*, 1.
(30) The summation in eqs A10 and A11 is made analytically by utilizing polygamma function, as pointed out by Dr. Takashi Uneyama at Institute for Chemical Research, Kyoto University.
(31) We can easily find, from numerical calculation, that two single Maxwellian modes of same relaxation intensity and different relaxation times, τ and τ' ($>\tau$), are summed to give just a broad single peak of the loss factor (G'' and/or ε'') at ω between $1/\tau$ and $1/\tau'$, i.e., at ω *not* corresponding to the relaxation frequencies of the two modes, given that the τ'/τ ratio is smaller than 5.8.

Macromolecules

Article

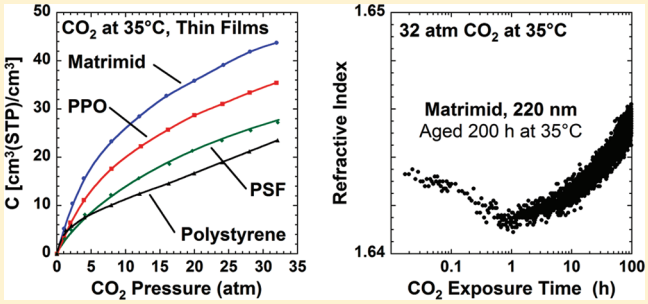
pubs.acs.org/Macromolecules

Carbon Dioxide Sorption and Plasticization of Thin Glassy Polymer Films Tracked by Optical Methods

Norman R. Horn and D. R. Paul*

Department of Chemical Engineering and Texas Materials Institute, The University of Texas at Austin, Austin, Texas 78712, United States

ABSTRACT: Our previous publications have demonstrated that thin glassy polymer films respond to highly sorbing penetrants, such as CO_2, quite differently than thick films. These studies focused on CO_2 permeation behavior and revealed that, for thin films, CO_2 permeability at constant CO_2 pressure goes through a maximum followed by a continual decrease in permeability owing to physical aging. So far, thick and thin glassy polymer films have been compared in the context of permeability, but lack of substantial means of obtaining thin film sorption data has prevented adequate comparison of thick and thin films in the context of gas solubility. In this paper, spectroscopic ellipsometry is used to obtain simultaneously the film thickness and CO_2 sorption capacity for thin glassy polymer films. This allows a more comprehensive look at CO_2 permeability, sorption, and diffusivity as a function of both CO_2 pressure and exposure time. The evidence reported here suggests that thin film sorption behavior is substantially different than that of thick film counterparts. Partial molar volume is determined from sorption-induced swelling data. Fractional free volume and diffusivity are calculated as a function of CO_2 pressure. Dual sorption model parameters are presented for Matrimid thin films for different aging times. Dynamic ellipsometry experiments show that refractive index minima, fractional free volume maxima, and CO_2 diffusivity maxima correlate well with observed CO_2 permeability maxima observed for thin Matrimid films. The results support the claim that plasticization and physical aging are competing processes but that aging dominates over long time scales. The CO_2 diffusivity behavior over time is most affected by the competing effects of plasticization and aging, and the evolution of CO_2 diffusivity is shown to be the main contributing factor to changes in CO_2 permeability at constant pressure.



1. INTRODUCTION

Polymers below their glass transition temperature, T_g, are nonequilibrium materials, and their properties, such as dielectric constant, density, and gas permeability, change with time by a process known as physical aging. For bulk polymers, i.e., thick films (l > several micrometers), this process occurs very slowly, but thin glassy polymer films (l < 1 μm) tend to age more quickly, and the reason for this behavior is not currently well-understood.[1−6] In general, gases with relatively low solubility in glassy polymers, such as O_2 or N_2, do not perturb the aging process significantly, and over reasonable time periods the effects of sorption are reversible. However, higher concentrations of more soluble penetrants, such as CO_2, cause plasticization, which is thought to increase free volume and facilitate molecular motions. Changes due to plasticization are not immediately reversible, and glassy polymers exhibit these "conditioning" effects even after all CO_2 is removed. While CO_2 plasticization of thick films has been studied extensively, plasticization studies involving thin films have been relatively rare until recently.[7,8] Since practical membrane systems require very thin films (~100 nm) to obtain high productivity, understanding how thin films respond to plasticizers is important for the development of robust membrane separation technology.

Gas transport in polymers follows the solution-diffusion model, whereby a gas first dissolves into the polymer and then diffuses through the thickness of the polymer. The gas permeability of any polymer film, defined as the gas flux normalized by the film thickness and the pressure driving force, consists of a solubility component, which is thermodynamic in nature, and a diffusivity component, which is kinetic in nature. They are related by the well-known equation $P = D \times S$. If two of the terms can be directly measured, then the third can be simply calculated.

Gas permeability can be measured in a number of ways, most notably with constant volume systems.[9] Solubility can be measured by gravimetric methods, such as magnetic suspension balance[10] or Cahn microbalance,[11−14] or by measuring pressure decay in a well-sealed constant volume system.[15,16] Diffusivity can be calculated for transient experiments from the time lag and the well-known equation $D = l^2/6t_{lag}$. For bulk polymer films, these methods have been widely used and are well-understood.

Gas sorption in thin polymer films, though, is not often investigated for two reasons. First, the time scale of diffusion is very short for thin films, and thus, it is impossible to estimate sorption from a combination of permeability and time lag

Received: January 23, 2012
Revised: February 27, 2012
Published: March 6, 2012

 © 2012 American Chemical Society

experiments. Second, the typical experimental methods for directly measuring sorption in thick films cannot be used with thin films. Pressure decay, magnetic suspension balance, and Cahn microbalance instruments require relatively large quantities of sample so thin films cannot be used in these devices. Quartz crystal microbalances have seen some use for measuring gas sorption in thin polymer films,[17−20] but a number of issues have limited its use.

Since the aforementioned methods are not useful for measuring sorption in thin films directly, the effect of thickness on gas sorption of both plasticizing and nonplasticizing gases in glassy polymers has not been explored to any significant extent. Thickness effects have been observed in physical aging[1−3,5,6] and plasticization studies,[7,8] though, and those results suggest that gas sorption in glassy polymers may also be dependent upon thickness. Tan et al. used X-ray reflectivity to study water sorption in thin polyimide films (l < 100 nm) and observed thickness-dependent swelling.[21] A survey of the literature[13,14,22−26] indicates that the extent of CO_2 sorption for Matrimid varies widely from one report to another, as seen in Figure 1. Some of

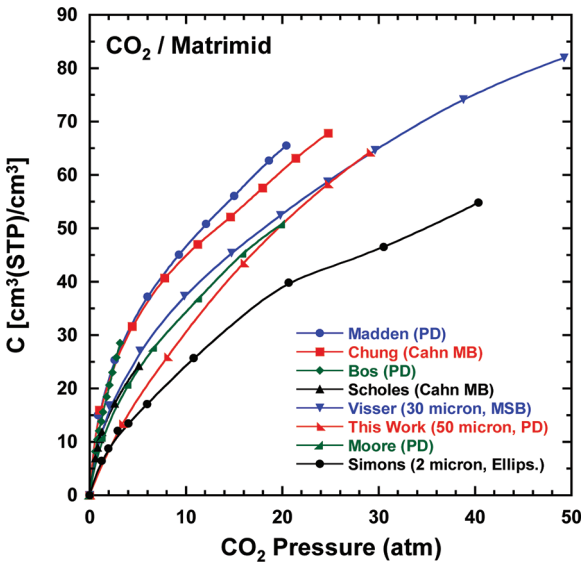


Figure 1. Literature data for Matrimid CO_2 sorption isotherms obtained from various methods and thicknesses. PD = pressure decay, MSB = magnetic suspension balance, MB = microbalance.[13,14,22−26]

these differences might be attributable to different sample histories, sample preparation procedures, experimental techniques, etc., but it appears film thickness may also be a factor.

A small number of papers have reported sorption data for thin polymer films using spectroscopic ellipsometry. Ellipsometry is a powerful method for characterizing thin polymer films, but the technique has been underutilized as a tool for obtaining sorption data. Sirard et al. investigated swelling and sorption in thin PDMS films with supercritical CO_2, showing that at high CO_2 pressures (>50 atm) thin PDMS films swell nearly 10% more than bulk PDMS films.[27] Wind et al. observed some differences in the thin film values of dual-sorption model parameters for CO_2 relative to thick films in 6FDA-DAM:DABA and its cyclohexanedimethanol monoester and substantially different CO_2 sorption at constant pressure for longer exposure times.[28,29] They attributed this difference primarily to the effect of thermal treatments on the films rather than to the effect of thickness itself. Wind noted, though, that the possibility of a fundamental difference between bulk films and thin films could not be ruled out and suggested studying the effect of thickness as an avenue of future research. Finally, Wind hypothesized that the assumptions of the optical model, such as constant specific refraction, might be too simplistic to capture the subtleties of CO_2 sorption behavior. In contrast, Rowe et al. used ellipsometry to track the effect of relative humidity upon thin films, and their results suggested that a polymer's specific refraction is indeed independent of density and temperature.[30] Even so, Rowe's approach assumed that the equilibrium sorption in thick and thin films was the same when compared at the same density or refractive index and thus did not conclude that sorption behavior differed in thick and thin films. Most recently, Simons et al. found that CO_2 sorption behavior for films ∼2−3 μm, measured via ellipsometry, only differed from bulk films in the Langmuir capacity (C'_H) parameter of the dual-sorption model; the Henry's law constant (k_d) and Langmuir affinity parameter (b) showed no thickness dependence.[23]

Even though there is some evidence in the literature that CO_2 sorption behavior differs between thick and thin glassy polymer films, no systematic study has been done to solidify this conclusion. In this paper, we present a method for measuring gas sorption with spectroscopic ellipsometry and investigate thickness-dependent CO_2 sorption of glassy polymer films. The sorption data are correlated with our previous work, demonstrating the effect of thickness on CO_2 permeation of thin glassy polymer films[7] to give a more complete picture of how plasticization proceeds for these materials. To our knowledge, this is the first time that CO_2 plasticization has been described in terms of independently obtained permeability and sorption data for thin films, with similar thicknesses and thermal histories, in order to describe CO_2 permeability, sorption, and diffusivity as a function of both pressure and exposure time.

2. THEORY

Ellipsometry involves reflecting plane-polarized light off a planar surface and detecting changes in the polarization state due to the sample. The data are then fitted to known optical models to give thickness and optical parameters. A major advantage of using ellipsometry for measuring sorption is that the film thickness and refractive index are determined independently of each other; thickness is decoupled from other optical data. A polymer's refractive index can be calculated from the well-known Cauchy dispersion equation:

$$n(\lambda) = A + B/\lambda^2 + C/\lambda^4 \tag{1}$$

where A, B, and C are constants fitted from optical data and λ is the wavelength. The Lorentz−Lorenz parameter can be calculated from the refractive index and is related to the mass density of the material by

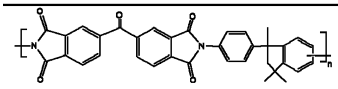
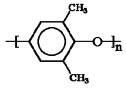
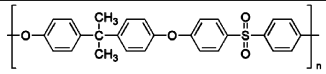
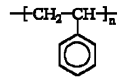
$$L = \frac{n^2 - 1}{n^2 + 2} = q\rho \tag{2}$$

where q is the specific refraction of the material, a constant which can be obtained from bulk values of refractive index and density. For mixed systems of j components, the Lorentz−Lorenz equation becomes

$$\frac{n^2 - 1}{n^2 + 2} = \sum q_j \rho_j \tag{3}$$

dx.doi.org/10.1021/ma300177k | Macromolecules 2012, 45, 2820−2834

Table 1. Polymer Structures and Bulk Properties

Polymer	ρ (gm/cm^3)	T_g (°C)	Refractive Index	V_{vdw} (cm^3/gm)	$\rho_{0°K}$ (gm/cm^3)
 Matrimid® 5218	1.20	310	1.648	0.532[a]	--
 Poly(2,6, dimethyl-1,4-phenylene) oxide (PPO)	1.069	210	1.573	0.588[a]	1.393[c]
 Polysulfone (PSF)	1.24	186	1.633	0.531[a]	1.503[c]
 Polystyrene (Styron 685d)	1.05	105	1.586	0.604[b]	1.225[c]

[a]Huang et al.[4] [b]Van Krevelen.[39] [c]Sanchez and Cho.[40]

This is sometimes called the Clausius−Mosotti equation.[31] For a two-component system of CO_2 and polymer this becomes

$$\frac{\langle n\rangle^2 - 1}{\langle n\rangle^2 + 2} = q_{CO_2}\rho_{CO_2} + q_p\rho_p \tag{4}$$

where $\langle n\rangle$ is an averaged refractive index for a particular wavelength range. In this study, the wavelength range selected was 450−750 nm. For the polymer, q is calculated from known bulk values of density and refractive index. For CO_2, the Virial equation is used to calculate the density,[32] and the refractive index, which is pressure dependent, is determined from literature values.[33]

A mass balance on the polymer film relates the polymer mass concentration of the swollen film to the thickness change due to swelling (assuming constant area due to adhesion).

$$\rho_p = \rho_p\frac{h_0}{h} \tag{5}$$

where ρ_p and h_0 are the density and thickness of the polymer before exposure to CO_2, respectively, and h is the thickness of the swollen film. The mass concentration of CO_2 in a polymer film can be estimated with knowledge of h_0, h, CO_2 pressure, and $\langle n\rangle$ by rearranging eq 4:

$$\rho_{CO_2} = \frac{1}{q_{CO_2}}\left(\frac{\langle n\rangle^2 - 1}{\langle n\rangle^2 + 2} - q_p\rho_p\frac{h_0}{h}\right) \tag{6}$$

The mass concentration can be converted to molar units by dividing by the molecular weight. All figures following will be reported in units of cm^3 (STP)/cm^3 (polymer), as is conventional in the literature. A plot of the change in film thickness versus the molar concentration of CO_2, denoted C_{CO_2}, can be used to calculate the partial molar volume of CO_2 in the polymer.[23]

$$v_{CO_2} = 22400\frac{\partial(\Delta h/h_0)}{\partial C_{CO_2}} \tag{7}$$

Time-dependent experiments require the use of an "apparent molar volume" instead of the partial molar volume.[29] While partial molar volume describes the differential volume change upon further sorption of gas, apparent molar volume refers to the average volume occupied by the gas on a molar basis.

$$\phi_{v_{CO_2}} = 22400\left[\frac{\Delta h/h_0}{C_{CO_2}}\right]_{T,P} \tag{8}$$

The fractional free volume of a polymer can be calculated as

$$f = \frac{V - V_0}{V} = 1 - \rho V_0 \tag{9}$$

where $V = 1/\rho$ is the specific volume and V_0 is the occupied volume of the polymer (or mixed system). Maeda[34,35] and Lee,[36] following Bondi,[37,38] indicate that the occupied volume is closely related to the van der Waals volume, V_{vdw}:

$$V_0 = (1/\rho^*)V_{vdw} \tag{10}$$

where ρ^* is the unitless packing fraction at absolute zero. Van Krevelen[39] estimated that the reciprocal of the packing fraction, $1/\rho^*$, was 1.3, assuming all polymers have the same packing fraction, 1/1.3 = 0.77, at absolute zero. Sanchez and Cho[40] suggested that a more appropriate measure of V_0 was the specific volume at absolute zero, i.e., $V_0 = v_{0\,K} = 1/\rho_{0\,K}$. The characteristic mass density, $\rho_{0\,K}$, can be obtained by extrapolating zero pressure densities to absolute zero. Van Krevelen's approximation should only be used in the absence of known values of packing fraction or characteristic mass density. Values of V_{vdw} and $\rho_{0\,K}$ for the polymers of interest in this study are given in Table 1. The packing fraction of CO_2 is 0.76,[38] and the van der Waals volume of CO_2 will be discussed further in section 4.4.

For a mixed system, the occupied volume includes contributions from each component:

$$V_{0,mix} = \sum w_j V_{0,j} = w_{CO_2}V_{0,CO_2} + (1 - w_{CO_2})V_{0,p} \tag{11}$$

dx.doi.org/10.1021/ma300177k | Macromolecules 2012, 45, 2820−2834

where w_j is the weight fraction, calculated from the mass concentrations of polymer and CO_2 as shown previously:

$$w_{CO_2} = \frac{\rho_{CO_2}}{\rho_{CO_2} + \rho_p} = \frac{\rho_{CO_2}}{\rho_{CO_2} + \rho_p \frac{h_0}{h}} \quad (12)$$

The denominator of eq 12 is also the density used to calculate the free volume of the mixed system. Making the appropriate substitutions in eq 9:

$$f = 1 - \left(\rho_{CO_2} + \rho_p \frac{h_0}{h}\right)[w_{CO_2} V_{0,CO_2} + (1 - w_{CO_2}) V_{0,p}] \quad (13)$$

3. EXPERIMENTAL SECTION

3.1. Materials. Four polymer systems were investigated in this research: the commercial polyimide Matrimid 5218, a polysulfone made from bisphenol A (PSF), poly(2,6-dimethyl-1,4-phenylene oxide) (PPO), and a commercial polystyrene designated as Styron 685d. The first three polymers are of particular interest as industrial separation membrane materials, and polystyrene was included for further comparison of fundamentally different polymer types. Polystyrene also has a lower T_g than the other polymers. The bulk properties of the polymers are presented in Table 1. Matrimid, PPO, and PSF have been compared before in the context of physical aging[41] and plasticization.[8]

3.2. Film Formation. Single-layer thin films were prepared by spin-casting polymer solutions onto precut, 1 cm ×1 cm silicon wafers; two to three drops of solution sufficiently covered the wafer without overflowing. It is recommended to measure the SiO_2 thickness of the silicon wafer before spin-casting the sample to ensure accuracy. Thickness of the polymer layer was controlled by varying the concentration of polymer from 2 to 3 wt % and the spin speed from 1200 to 2100 rpm for 90 s. Solvents used were cyclohexanone for Matrimid and PSF, chlorobenzene for PPO, and toluene for polystyrene. Following the spin-coating, the initial thickness was measured with a variable angle spectroscopic ellipsometer, which will be described in more detail later in this section. Samples were dried in a vacuum oven near 100 °C overnight to remove any residual solvent and water.

All glassy materials retain a thermal history derived from the film formation process and storage conditions up until testing. Each film was annealed on the silicon substrate at 15 °C above its T_g for 10 min and then rapidly quenched to room temperature to standardize the prior history. Samples were stored at 35 °C prior to testing. While these protocols do allow for reasonable comparison of the materials under the varying conditions of CO_2 exposure, it must be noted that annealing on a substrate is different than annealing in the freestanding state. Physical aging for a constrained film such as this may not proceed in exactly the same manner as a freestanding film because the substrate eliminates one of the film's "free surfaces".[42] Huang observed via ellipsometry that freestanding films tend to decrease in thickness by ~0.8% and increase in density slightly over 6000 h of aging at 35 °C.[1] For films annealed on a wafer, however, surface forces will affect this behavior. We observed slight increases in density with experimentally insignificant changes in thickness over 400 h of aging at 35 °C.

3.3. Ellipsometer Setup. A spectroscopic ellipsometer made by J.A. Woollam Co. (model 2000D) was used in this research. The CO_2 experiments were conducted with a high-pressure ellipsometry cell made of steel, containing two fused silica windows (Technical Glass Products) at an angle normal to the incident light. A diagram of the cell is presented in Figure 2. The windows were sealed with Buna-90 and Teflon O-rings (Buna O-rings were coated with a very thin layer of vacuum grease to improve the seal). The cell was connected to a transducer to monitor the pressure, a CO_2 cylinder with >99.99% purity (Praxair), and a house vacuum line. Pressure was controlled with the gas regulator connected to the cylinder. Temperature was controlled at 35 °C using four cartridge heaters (0.25 in diameter, 3 in. long, Omega) and a PID controller (Omega) to within 1 °C. The cell was always allowed to equilibrate at 35 °C for at least 15 min before calibration and testing. The ellipsometer angle and wavelength range were set to 70° and at least 450−900 nm, respectively. This wavelength range was selected to maximize the amount of data for calculating the optical parameters while avoiding wavelengths where absorbance is known to occur (<450 nm).

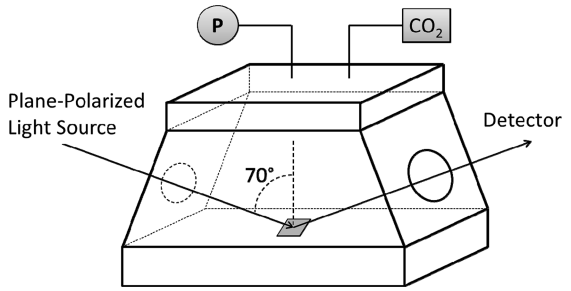


Figure 2. Schematic of high-pressure ellipsometry cell.

3.4. Calibration Procedures. A significant part of conducting high-pressure ellipsometry experiments is compensating for the birefringence of the windows that seal the cell. Even nonbirefringent windows can become birefringent owing to strain induced by the high pressure of gas inside the cell. Without accounting for window effects, large errors of as much as 30% can be introduced into refractive index measurements.[43] The WVASE32 software included with the ellipsometer was used to characterize both the "in-plane" and "out-of-plane" window effects. The "out-of-plane" corrections were determined independently with the ellipsometer calibration algorithm. The "in-plane" window effects cause offsets in the Δ ellipsometric angle and must either be measured separately or be included as adjustable parameters in the ellipsometer model. This procedure has been used previously by Sirard et al.[27]

3.5. Sorption Isotherm Experimental Procedure. Samples were tested before exposure to CO_2 at room temperature and ambient conditions to establish a baseline for the measurements. Following cell temperature equilibration, the sample was placed in the cell and the calibration algorithm was run at 35 °C and atmospheric air to check the "in-plane" window effects before CO_2 exposure. The sample was scanned again to estimate initial values for the delta offsets at ~1 atm and to observe any difference in the film's properties due to the temperature increase. These differences were generally small, but this additional scan helps determine the best initial conditions possible for maximum accuracy in the data analysis. Following this scan at 35 °C, the vacuum line was opened for 3−5 min to remove as much air as possible.

Upon initial exposure to CO_2, the vacuum line was left open for 15 s to purge any remaining air. The pressurization scheme included 1, 2, and 4 atm of CO_2 and then proceeded in increments of 4 atm up to 32 atm of CO_2. The film equilibrates very quickly owing to its short time scale of diffusion, but pressure fluctuations typically require additional equilibration time before acquiring data (about 1 min). At each pressure, the calibration algorithm was run (with the sample still in the cell) to account for the "in-plane" window effects, and then a spectroscopic scan of the sample was performed. This procedure follows, in general, that of Sirard et al.[27] After scanning at the maximum pressure, the pressure was then decremented to 24, 16, 8, and 2 atm to observe any CO_2 sorption hysteresis for the film. A final spectroscopic scan outside the cell at room temperature and atmospheric pressure was performed following the exposure to CO_2.

The optical data were fitted with a four-layer optical model as diagrammed in Figure 3. The model contained a silicon substrate layer, native oxide layer, a polymer/CO_2 layer, and an "ambient" CO_2 layer. Setting the topmost layer to "ambient" in the model options instructs the analysis program to treat the layer as the ambient CO_2 surroundings

dx.doi.org/10.1021/ma300177k | Macromolecules 2012, 45, 2820−2834

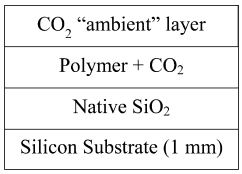


Figure 3. Four-layer optical model used by WVASE32 ellipsometer program to analyze optical data.

of the polymer layer rather than as an additional solid layer. The refractive index of CO_2 was determined by interpolating from literature data[33] and was assumed to be constant over the wavelength range at a given temperature and pressure. The polymer/CO_2 layer was modeled with the Cauchy dispersion equation. The fit parameters included the film thickness, Cauchy parameters *A*, *B*, and *C*, and delta offsets.

3.6. Constant Pressure Experimental Procedure. With a well-controlled high-pressure ellipsometry cell, one can construct a sorption isotherm with a variety of pressure points in a relatively short time. However, the effect of CO_2 on glassy polymers is known to be time-dependent, and a simple procedure was designed to obtain dynamic ellipsometric data for longer exposure times. In short, the ellipsometer is programmed to probe the polymer film every minute over the course of 100 h with constant CO_2 exposure.

As in the sorption isotherm procedure, samples were tested before exposure to CO_2 at room temperature and ambient conditions. To calibrate the ellipsometer, a standard silicon wafer with a ~50 nm SiO_2 thermal oxide layer was placed in the cell at 35 °C, and the cell was evacuated for 5 min. Next, the cell was pressurized with CO_2 at the pressure of interest, and the calibration algorithm was run to determine the "in-plane" window effects at that pressure. Initial delta offset values were obtained from an additional spectroscopic scan on the silicon wafer following the calibration algorithm. The cylinder was then closed and the standard silicon wafer replaced with the sample film wafer. After evacuating the cell for 3−5 min, the cylinder was opened and the system purged for 15 s. The opening of the cylinder is considered to be time zero for CO_2 exposure. Data collection always began within 1 min of opening the cylinder. Since plasticization is best understood on a logarithmic time scale, spectroscopic scans were taken every 10 s for the first 6−10 min using the ellipsometer's dynamic scanning mode. Then, the ellipsometer was set to scan the film once every minute for the next 100 h.

The dynamic ellipsometric data were analyzed with the same four-layer model described in section 3.5, with the initial conditions for the film and delta offsets determined from the scans before the dynamic experiment. The "point-by-point" analysis routine included with WVASE32 would fit the model to the data taken for the first time slice and then use those results as the initial guess values for the next time slice. Upon completion of the program, values for the film thickness, optical constants, and delta offsets were catalogued for each time the ellipsometer had scanned the sample.

Over the course of 100 h of CO_2 exposure, there is invariably some variation in pressure within the cell that cannot be controlled due to imperfect sealing. However, these fluctuations are typically within ±0.1 atm, and thus we assume in the analysis protocol that the pressure is constant over the duration of the experiment so that the molar density and refractive index of CO_2 can be considered constant in the calculations of the optical model. While this simplifying assumption is not strictly valid, the errors associated with it are relatively low (<0.01% for CO_2 refractive index, <1% for CO_2 molar density, and <0.1% for CO_2 concentration in the polymer film), so we believe it is justifiable.

4. RESULTS FROM SORPTION ISOTHERM EXPERIMENTS

An example of the data produced by the sorption isotherm procedure described in section 3.5 is presented in Figure 4 and includes the Ψ and Δ ellipsometric angles, sorption-induced swelling, and concentration of CO_2 for a 312 nm Matrimid film aged 1 day at 35 °C. As pressure is increased, the features of the ellipsometric angle curves shift to the right toward greater wavelengths, which frequently indicates a change in thickness. Similar shifts to the right are observed for prolonged CO_2 exposure times during constant pressure experiments as well. Though the shifts in the features appear small, they represent significant changes induced by plasticization. For instance, this film swells over 4% over the pressure range tested, sorbing up to 44 cm^3 (STP) of CO_2 per cm^3 of polymer.

Sorption isotherms are frequently presented in the literature with pressurization and depressurization steps, typically demonstrating hysteresis owing to the long relaxation times of the glassy state. In Figure 4, a small amount of hysteresis was observed during the depressurization step. The film thickness and CO_2 concentration decreased as pressure was decreased, but these measurements were still greater than those measured during the pressurization step. This behavior reflects the shorter relaxation times of thin films relative to thick films and the importance of exposure time to CO_2 plasticization. We observed similar hysteresis in other thin film sorption isotherm experiments, but here we do not present any further depressurization curves to preserve figure clarity.

4.1. Effect of Thickness on CO_2 Sorption. Figure 1 shows literature data for CO_2 sorption in Matrimid using a variety of methods. In most cases, the thickness of the sample used to generate the data was not given. In Figure 5, select data from Figure 1, where thicknesses were known, are presented alongside thin film CO_2 sorption isotherms measured via ellipsometry. Thick film (~50 μm) data in this work were obtained with pressure decay instruments to check against the literature. It should be noted that Simons et al. measured sorption of a 2 μm Matrimid with an ellipsometer but used a different instrument than in our work. J.A. Woolam Co. generally recommends that only polymer samples with thicknesses <1.5 μm be tested with the M-2000 ellipsometer to ensure accuracy; however, the results of Simons et al. are somewhat similar to those measured here.

The difference between thin and thick films is apparent; as thickness is decreased, the CO_2 sorption capacity tends to decrease as well. For example, CO_2 sorption at 20 atm decreases by over a factor of 2 as thickness is reduced to less than 100 nm. Below 2 μm, the changes appear to become less pronounced.

Figure 6 presents CO_2 sorption isotherms of multiple polymers in both the bulk state and thin film form. Bulk data were obtained from the literature,[22,34,44,45] and butyl rubber is included for comparison to a rubbery material.[46,47] Thin film data were obtained via ellipsometry with the procedure explained above; each film was aged 1 day at 35 °C before testing. In both plots, CO_2 sorption proceeds in the order of increasing T_g, i.e., polystyrene < PSF < PPO < Matrimid. Thickness apparently does not change the relationship between T_g and sorption capacity. However, each thin film exhibited significantly less CO_2 sorption than its bulk film counterpart, supporting the growing body of evidence suggesting that thick and thin films respond differently to gas sorption and permeation, especially when plasticization is significant. The greatest effect of thickness was observed with Matrimid; the bulk and thin films differed by 30%. The thin polystyrene film, however, showed the least departure from the bulk isotherm. This could be related to the relatively low T_g of polystyrene. It is possible that thickness effects upon sorption are not as pronounced

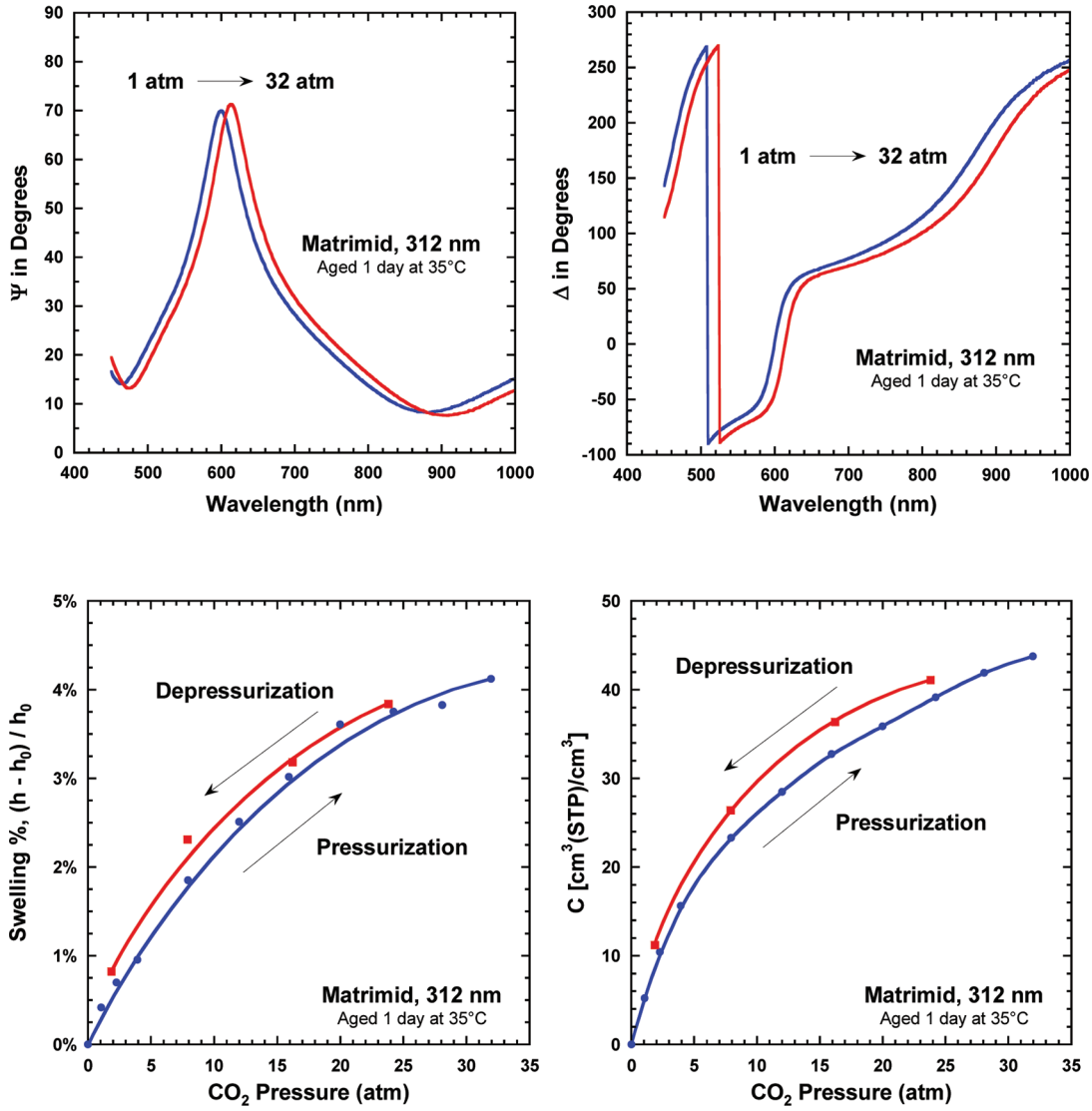


Figure 4. Example data for psi, delta, swelling, and concentration for a CO_2 sorption isotherm at 35 °C obtained via ellipsometry (312 nm Matrimid film, aged 1 day at 35 °C).

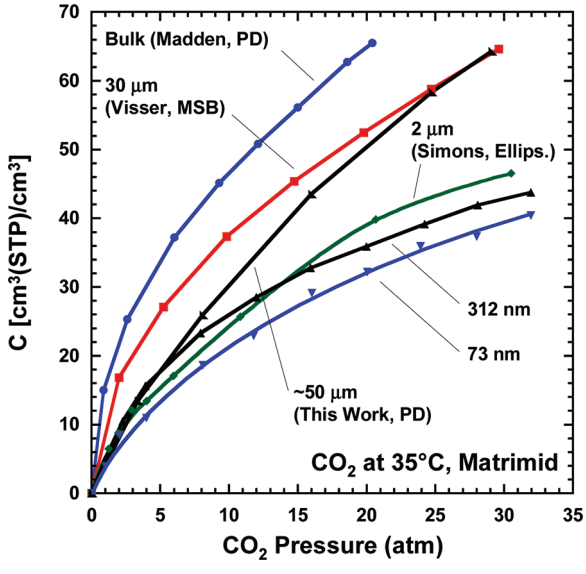


Figure 5. Effect of thickness on CO_2 sorption in Matrimid.

when the difference between the experimental temperature and T_g is small, but not enough data are available to be conclusive.

4.2. Effect of Aging Time on Thin Film CO_2 Sorption. Our previous work has demonstrated that aging time plays a significant role in CO_2 permeation behavior;[7] thus, it seems reasonable that CO_2 sorption would be affected by aging time as well. Figure 7 depicts sorption isotherms at multiple aging times for the four polymers of interest. Polystyrene, PPO, and PSF include aging times at 1 day and 1 month at 35 °C; these aging times were arbitrarily selected and have no particular significance other than to show this effect. For Matrimid, though, aging times of 1, 100, and 500 h at 35 °C were chosen deliberately to coincide with aging times from our previous work with Matrimid.

The polymers generally behaved as expected, with Matrimid, PSF, and polystyrene exhibiting decreased CO_2 sorption at longer aging times. It is notable that the thin film aged for only 1 h still exhibited considerably less sorption than any thick films shown in Figure 5. These data, along with other thin film data collected at different aging times, suggest that the thickness

dx.doi.org/10.1021/ma300177k | Macromolecules 2012, 45, 2820−2834

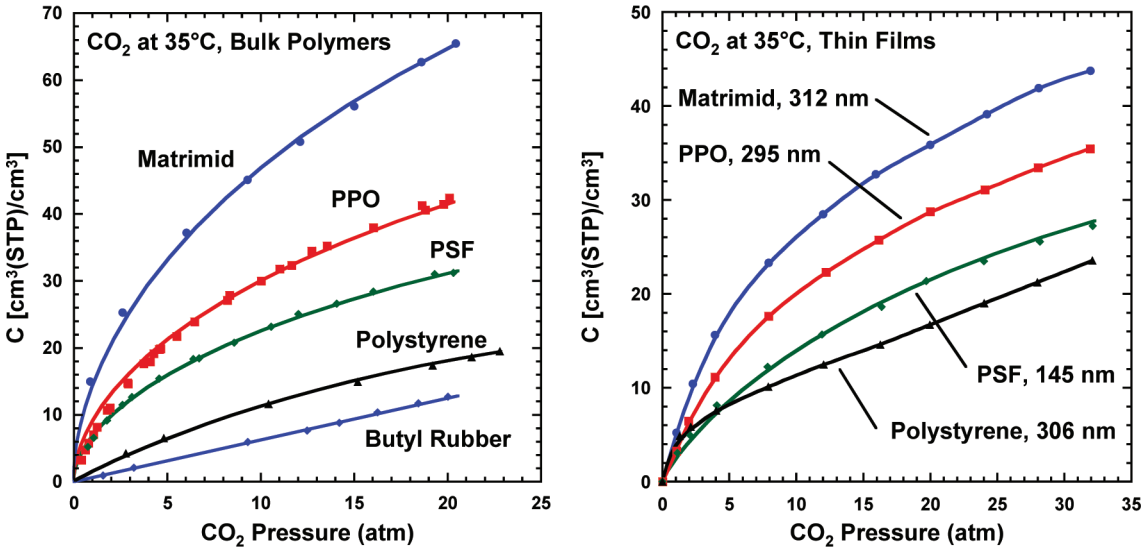


Figure 6. Sorption isotherms for various polymers. Bulk polymer data taken from the literature.[22,34,44−47] All thin films were aged for 1 day at 35 °C.

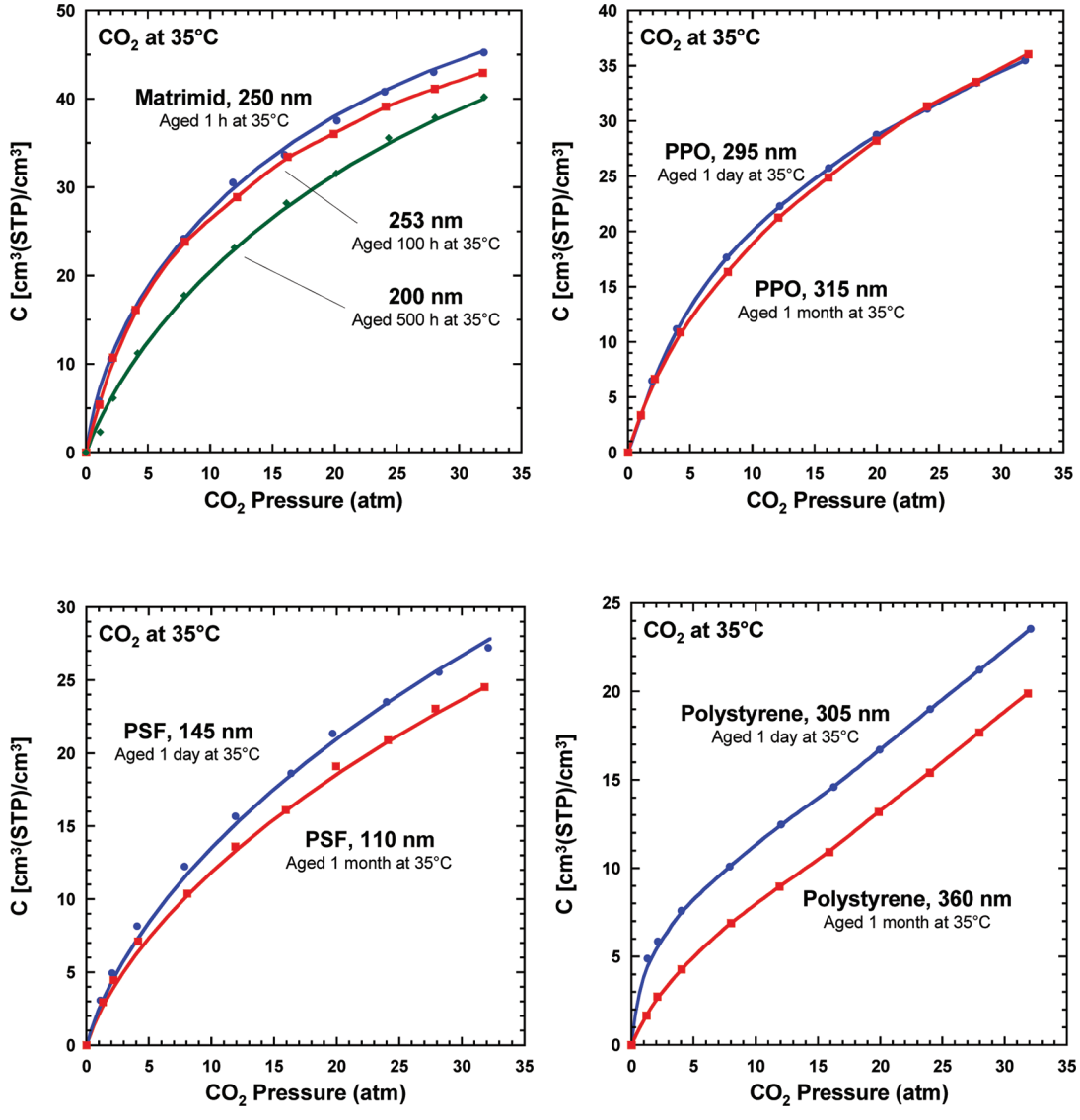


Figure 7. Effect of aging time on CO_2 sorption in thin films.

dx.doi.org/10.1021/ma300177k | *Macromolecules* 2012, 45, 2820−2834

effect upon sorption cannot be attributed merely to the accelerated aging characteristic of thin glassy polymer films. Interestingly, although Matrimid was most affected by a change in thickness, it was relatively less affected by aging time than PSF and polystyrene. Admittedly, the Matrimid film was aged only for ~500 h (~21 days), whereas the PSF and polystyrene films were aged for 1 month. Polystyrene changed the most due to aging; at 32 atm of CO_2 the film aged for 1 month sorbed nearly 20% less CO_2 than the film aged for 1 day. PPO, however, showed very little effect of aging time on sorption. We have suggested in a previous paper that the unusual response of PPO to CO_2 may be related to kinetic concerns that our experiments cannot fully ascertain.[8] Nonetheless, the data reported here indicate generally that aging time does affect CO_2 sorption significantly, but not as dramatically as thickness.

4.3. Partial Molar Volume. Plots of swelling as a function of CO_2 concentration are presented in Figure 8 for the films

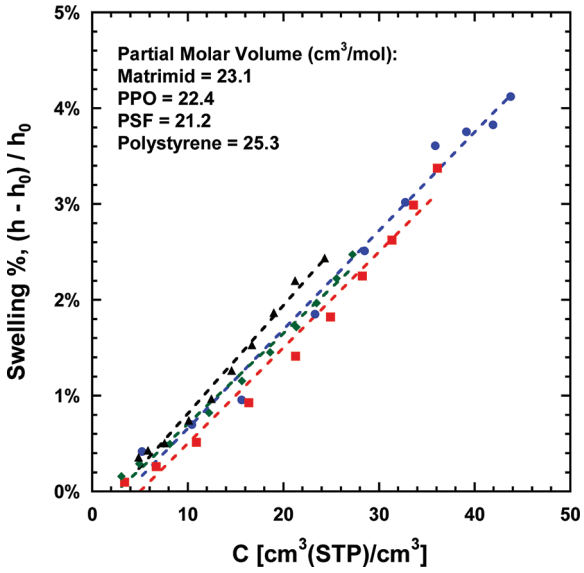


Figure 8. Swelling of thin films as a function of the CO_2 concentration at 35 °C. Each film was aged for 1 day at 35 °C prior to CO_2 exposure. Slopes of the lines represent CO_2 partial molar volume for (●) Matrimid, (■) PPO, (◆) PSF, and (▲) polystyrene, and the values are listed in cm^3/mol.

aged for 1 day. The slopes for each data set represent the partial molar volume of CO_2 in the polymer. The data generally fit well to a linear relationship, suggesting that molar volume of CO_2 in the polymer is independent of concentration, with a small offset in the low pressure range. Simons et al. noticed a similar offset in their work as well,[23] attributing it to an artifact of their ellipsometer technique. The similarity of these offsets suggests that this may be more than an artifact; it could be that at low partial pressures CO_2 swells the polymer very little. Although they did not report partial molar volumes for each polymer separately, they reported an average value of 25.3 cm^3/mol. The partial molar volumes calculated in this work are listed in Figure 8 and have an average value of 23.0 cm^3/mol. Like Simons et al., we found no distinct correlation between partial molar volume and the polymer glass transition temperature.

Additionally, the partial molar volumes calculated in this work and in Simons et al. are lower than those found by Wind et al., who proposed that the onset of plasticization occurred at a threshold CO_2 partial molar volume of 29 cm^3/mol. Bos et al. previously suggested in a similar manner that a critical CO_2 concentration of 37 ± 7 cm^3 STP/cm^3 indicated the onset of plasticization.[48] However, our results (and those of Simons et al.) indicate that neither of these conditions holds for thin films, which show significant plasticization at significantly different values of partial molar volume and pressure (or concentration). However, these data we present are for rather short exposure times (<1 h), and both CO_2 concentration and sorption-induced swelling would be expected to increase over longer exposure times. Although both quantities may tend to increase in tandem, such changes could potentially result in different partial molar volume calculations.

4.4. Fractional Free Volume as a Function of Pressure. When a polymer is plasticized, the polymer's permeability to gases increases for a time, which implies that the fractional free volume increases as well. One would expect that fractional free volume would generally increase as a function of CO_2 pressure because plasticization tends to increase as CO_2 is sorbed by the polymer. Hong et al.[49] and Chen et al.[50] observed such behavior via positron annihilation lifetime spectroscopy (PALS) for 1 mm thick samples of polycarbonate and polystyrene, respectively, plasticized by CO_2. Results from this work differed from those of prior researchers, but some further background is required to explain how these results were obtained.

Calculating the fractional free volume of a polymer typically requires knowing the density and occupied volume of the polymer alone. However, a mixed system requires accounting for the occupied volume of sorbed gas with a simple mixing rule (refer to eq 11). Determining the van der Waals volume of a sorbed species such as CO_2, though, is a nontrivial task, and the value chosen affects the calculations to a great extent. An upper bound for the occupied volume of CO_2 can be set by considering that the density of a CO_2 crystal at −78.5 °C is 1.562 g/cm^3, and thus the specific volume is 0.64 cm^3/g. Since any sorbed CO_2 would by necessity include more space between molecules than the crystal, one can reasonably say that any value for the occupied volume of CO_2 in a polymer system will be less than 0.64 cm^3/g. The "occupied volume" obtained from the van der Waals equation of state, 0.9739 cm^3/g,[32] can then be ruled out immediately. Theoretically determined values for the van der Waals volume of CO_2 vary in the literature. Bondi,[37] Ronova et al.,[51] and Wong[52] report values of 0.448, 0.422, and 0.311 cm^3/g, respectively.

In Figure 9, Wong's suggested value for the van der Waals volume, 0.311 cm^3/g, was used to calculate the fractional free volume as a function of pressure for each thin film from Figure 6. Upon inspection, one can see that the polymers do not behave exactly as expected. Instead of fractional free volume increasing as a function of pressure, it decreases from the initial value for each polymer before CO_2 exposure. This decrease is followed by a minimum and a slight recovery as CO_2 pressure is increased. The bowl-shaped curves are somewhat similar to plots of CO_2 permeability versus pressure for glassy polymers and suggest a similar interpretation. The decrease in fractional free volume with CO_2 pressure can be interpreted as "hole filling" within the polymer, similar to the initial decrease in CO_2 permeability at low pressures. As pressure is increased and the holes become fully filled, the continued swelling is responsible for the slight increase in free volume. The order of the polymers in the left plot of Figure 9 is notable as well. Instead of following in order of increasing CO_2 solubility, the polymers generally follow in order of increasing CO_2 permeability. This appears consistent with the general understanding that permeability is closely related to free volume.

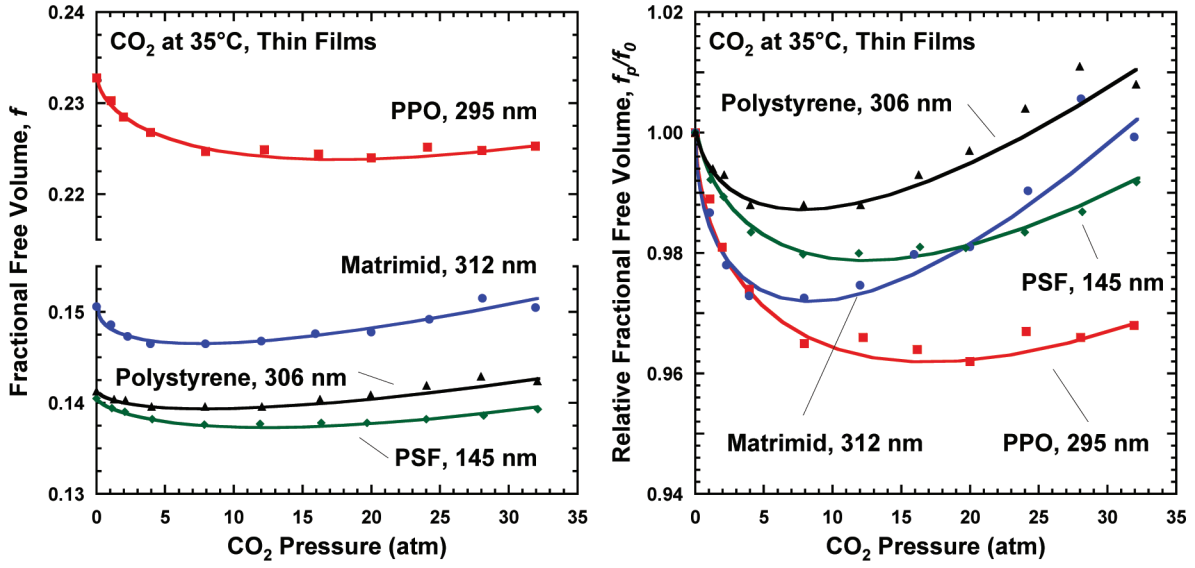


Figure 9. Fractional free volume of thin films as a function of CO_2 pressure, calculated from eq 9. Data at zero pressure indicate fractional free volume calculated before CO_2 exposure.

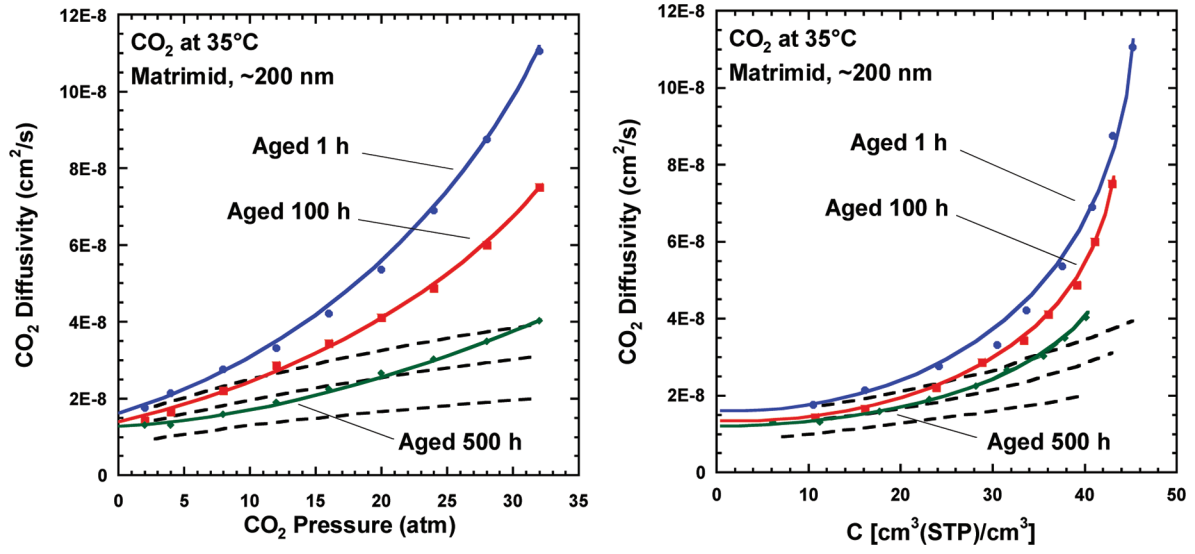


Figure 10. Apparent CO_2 diffusivity for Matrimid at different aging times, calculated from permeability measurements made previously[7] and sorption data obtained via ellipsometry. Dashed lines represent predictions from the dual-sorption model.

Again, these results are largely dependent upon the value of V_{vdw,CO_2} chosen for the calculations. For this set of data, a value of the van der Waals volume of CO_2 significantly greater than ~0.3 cm^3/g will cause the fractional free volume to decrease continuously as a function of pressure. To check this observation, we considered again the results of Rowe et al.,[30] using their data to calculate the fractional free volume of Matrimid and polysulfone as a function of the activity of water, also known to plasticize polymers. Two values of the van der Waals volume of water, ~0.385 and ~0.535 cm^3/g, were obtained from the literature.[53,54] Similar to the CO_2 experiments reported here, fractional free volume decreased with increased water uptake.[55]

One must keep in mind that there are multiple time scales at work during plasticization experiments, and the choices made during the execution of this work were rather arbitrary. The time scale for gas sorption to achieve a pseudo-steady state in a thin film is quite short, on the order of seconds, and holding pressure constant for a few minutes is sufficient to obtain useful ellipsometric measurements. Plasticization, though, occurs over a period of time much longer than the total time scale of these particular experiments (~1 h). Leaving the film at each pressure for a significantly longer time would have certainly resulted in higher fractional free volumes due to continued plasticization. As will be seen in section 5.1, fractional free volume increases as a function of CO_2 exposure time at constant CO_2 pressure. Indeed, even during the depressurization steps free volume clearly increased from the earlier measurements at the same pressures. The "hole-filling" process is dependent upon time, and thus understanding the effect of one's experimental methodology is critical to interpreting properly.

4.5. Estimating Dual Sorption Model Parameters and CO_2 Diffusivity as a Function of Pressure for Thin Matrimid Films. As mentioned previously, if accurate values of gas sorption and permeability are obtained under similar conditions, then diffusivity can be calculated from $D = P/S$. In Figure 10, CO_2 diffusion coefficients as a function of pressure

for Matrimid thin films have been estimated using sorption data from this study (Figure 7) and permeability data from our previous work (see Figure 5 from ref7). Although we have attempted to conduct comparable experiments with the different techniques by matching as many conditions as possible, some differences still exist between the two data sets and should be noted. First, the film thicknesses are not exactly the same in the two studies. The films in Figure 7 are ∼250 nm, whereas those from the previous study are ∼180 nm. Second, the CO_2 pressures and exposure times are somewhat different in the procedures of the two studies. Since the sorption experiments were performed with films attached to substrates, the aging history may also make a difference. The error due to these differences is not expected to be significant.

The dashed lines in Figure 10 represent the apparent CO_2 diffusivity predicted from the dual sorption, dual mobility model that do not take plasticization into account:

$$S = C/p = k_d + \frac{C'_H b}{1 + bp} \tag{14}$$

$$P = \left(k_d + \frac{FC'_H b}{1 + bp}\right) D_D \tag{15}$$

The model parameters k_d, C'_H, and b for the thin films were obtained via nonlinear least-squares regression analysis of the sorption data in Figure 7. The partial immobilization factor F was taken to be 0.1, following the suggestion of Aitken et al.[56] Next, the diffusion coefficient D_D was calculated from the experimentally determined permeability at 2 atm of CO_2. The predicted apparent CO_2 diffusivity at each pressure was then calculated from the theoretically determined permeability and solubility. The regressed parameters are presented in Table 2

Table 2. Dual-Sorption Model Parameters for Matrimid

	k_d ((cm³ STP)/(cm³ atm))	C'_H ((cm³ STP)/cm³)	b (1/atm)	D_D (cm²/s)
Moore–Koros[25]	1.44	25.5	0.367	
Chung et al.[14]	1.416	35.0	0.702	
thin films (this work)				
aged 1 h	0.554	32.5	0.204	13.9×10^{-8}
aged 100 h	0.490	32.4	0.202	11.9×10^{-8}
aged 500 h	0.489	27.3	0.174	6.52×10^{-8}

alongside literature values for comparison. Similar to Simons et al., the C'_H values for thin films differed significantly from bulk films, but values for k_d and b also exhibited thickness dependence. All model parameters show some dependence on aging time as well.

At low pressures, the estimated diffusivity of the thin films generally agrees with prior observations. The diffusivity of CO_2 in thick Matrimid films at 2 atm and 35 °C is $\sim 1.8 \times 10^{-8}$ cm²/s,[8] and the estimated diffusivity of the thin film aged for 1 h was 1.76×10^{-8} cm²/s. We believe this affirms the usefulness of our approach. The CO_2 diffusivity increases with CO_2 pressure (or concentration) as predicted by the dual sorption model,[9,57] but the values obtained from measurement of P and S depart from the model predictions as pressure increases. This effect upon diffusivity, which is over and beyond the dependence on concentration expected from the dual sorption model, is understood to be the result of plasticization. Also, CO_2 diffusivity is significantly greater for shorter aging times at all pressures, reflecting that free volume is greater at shorter aging times. At 2 atm, CO_2 diffusivity differs 30% between the films aged 1 and 500 h. At 32 atm, the difference is greater than 50%. Since plots of CO_2 diffusivity versus concentration do not collapse into a single curve, we can conclude that diffusion of plasticizing gases in glassy polymers is dependent on more variables than the gas concentration in the film alone. Aging and other effects of prior history must also play a role.

5. RESULTS FROM CONSTANT PRESSURE EXPERIMENTS

5.1. General Observations. Figures 11–13 show results from three separate constant pressure experiments with Matrimid thin films. Each film was 200–220 nm thick and had been aged for ∼200 h at 35 °C. Constant CO_2 pressure was maintained for ∼100 h at 35 °C. The thicknesses, aging time, and CO_2 pressures (8, 16, and 32 atm) correspond with our previous long-time CO_2 exposure studies with the same material. These conditions were originally selected to study the effect of pressure on CO_2 permeation behavior over exposure periods ranging from 500 to 1000 h and included pressures both above and below the so-called "plasticization pressure" of Matrimid (12–14 atm of CO_2). There was significant scatter in the data at 8 atm, and moving averages of refractive index and fractional free volume were plotted instead of the raw data. The scatter was likely due to the instrument being more sensitive to instrument fluctuations at lower pressures than at higher pressures, but the trends are still reasonably sound.

The films swelled noticeably even within 1 min of CO_2 exposure, and the initial swelling is directly related to the CO_2 pressure. Evidently, the greatest change in thickness occurs over a very short time period as the film responds to the sudden exposure to high-pressure gas. The films continued to swell over the course of 100 h and showed no signs of approaching a plateau within the time scale of this procedure. Correspondingly, the CO_2 concentration within the films followed a similar path. The initial sorption of CO_2 within the first minute of exposure was nominally greater than the additional sorption for the remainder of the experiment, and the initial sorption agrees with the sorption isotherms reasonably well. The film exposed to 32 atm of CO_2 showed the greatest increase in CO_2 concentration over 100 h, as expected. Like the swelling plots, there is no sign of approaching a plateau.

Plasticization is thought to increase free volume and decrease the density of the gas–polymer mixture. Since the refractive index is directly related to the density (see eq 2), continued exposure to CO_2 should cause the refractive index to decrease with time. However, plasticization and physical aging are simultaneous, competitive processes, and physical aging tends to increase density. Previous observations have shown that CO_2 permeability goes through a maximum during constant exposure to CO_2 over long time periods, suggesting that physical aging eventually dominates any further plasticization over time.[7,8] The high-pressure ellipsometry results mirror these CO_2 permeation studies. In each experiment, the refractive index initially decreased, then passed through a minimum, and proceeded to increase for the duration of the experiment. This indicates an initial decrease in density due to plasticization, but a trend toward densification for longer exposure times. The refractive index minima (1 h at 32 atm, 10–20 h at 16 atm, and 50–60 h at 8 atm) show remarkable agreement with the CO_2 permeability maxima from our previous work.[7] This clearly

dx.doi.org/10.1021/ma300177k | Macromolecules 2012, 45, 2820–2834

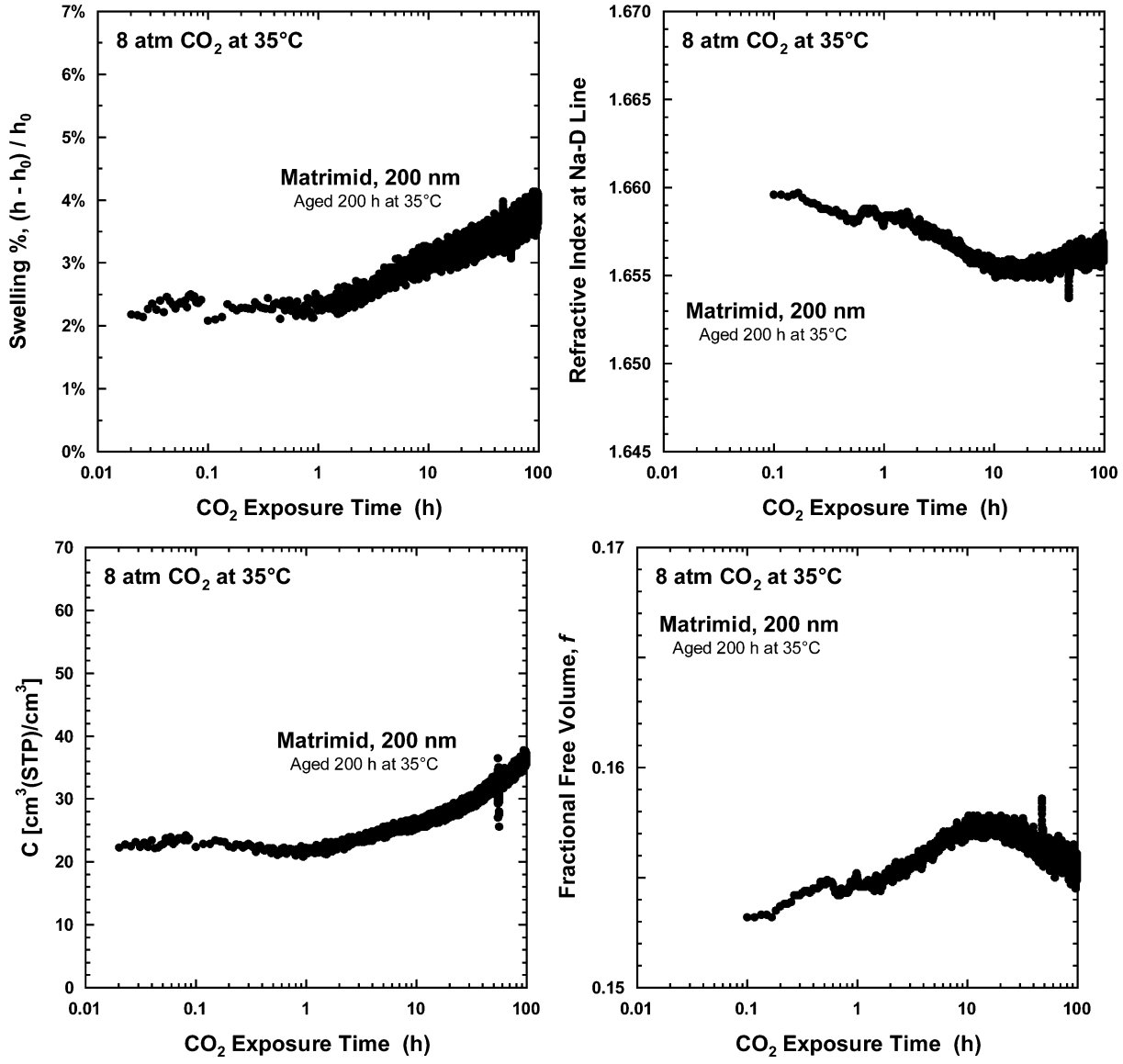


Figure 11. Results for a constant pressure experiment for a 200 nm Matrimid film, aged for 200 h at 35 °C and exposed to 8 atm of CO_2 at 35 °C for 100 h.

supports the interpretation that physical aging dominates plasticization for long exposure times and that CO_2 pressure governs the dynamics of the behavior. This behavior is particularly interesting given that the polymers evidently show continued swelling and CO_2 uptake long after the refractive index minima.

In section 4.4, fractional free volume initially decreased with CO_2 pressure and then, following a minimum, exhibited a slight increase. Fractional free volume at constant CO_2 pressure as a function of time behaved somewhat differently. (Note that the same value of V_{vdw,CO_2} was used for these calculations as before.) Comparing the fractional free volume plots in Figures 11−13, one can ascertain that fractional free volume exhibits a different dependence on pressure than seen in Figure 9. Instead of remaining relatively flat, fractional free volume increases with pressure and the trend is maintained throughout the experiment. This dependence upon pressure appears consistent with the work of Hong, Chen, and their co-workers mentioned previously,[49,50] who also performed their experiments under constant pressure conditions for long periods of time. More importantly, the evolution of fractional free volume over time mirrors the evolution of CO_2 permeability from our prior work. Like the refractive index minima, the fractional free volume maxima agree quite well with the CO_2 permeability maxima.

The nature of the time-dependent data only permits the calculation of apparent molar volume instead of partial molar volume; these data are presented in Figure 14. Because of the large amount of scatter for these calculations, moving averages of 10 values were plotted at each time instead of nominal values to emphasize the long-term trend. As a result, our comments here will be limited to a few qualitative assessments. First, the initial values increase with pressure, but the quantitative change in the apparent molar volume seems unrelated to pressure at all. Second, the local maxima appear to correspond broadly with the permeability maxima and refractive index minima, although it appears that the 8 atm CO_2 experiment has shifted to the left somewhat. Finally, the convergence of the curves for 8 and 16 atm leads one to ask if the 32 atm curve will also converge under continued CO_2 exposure.

dx.doi.org/10.1021/ma300177k | Macromolecules 2012, 45, 2820−2834

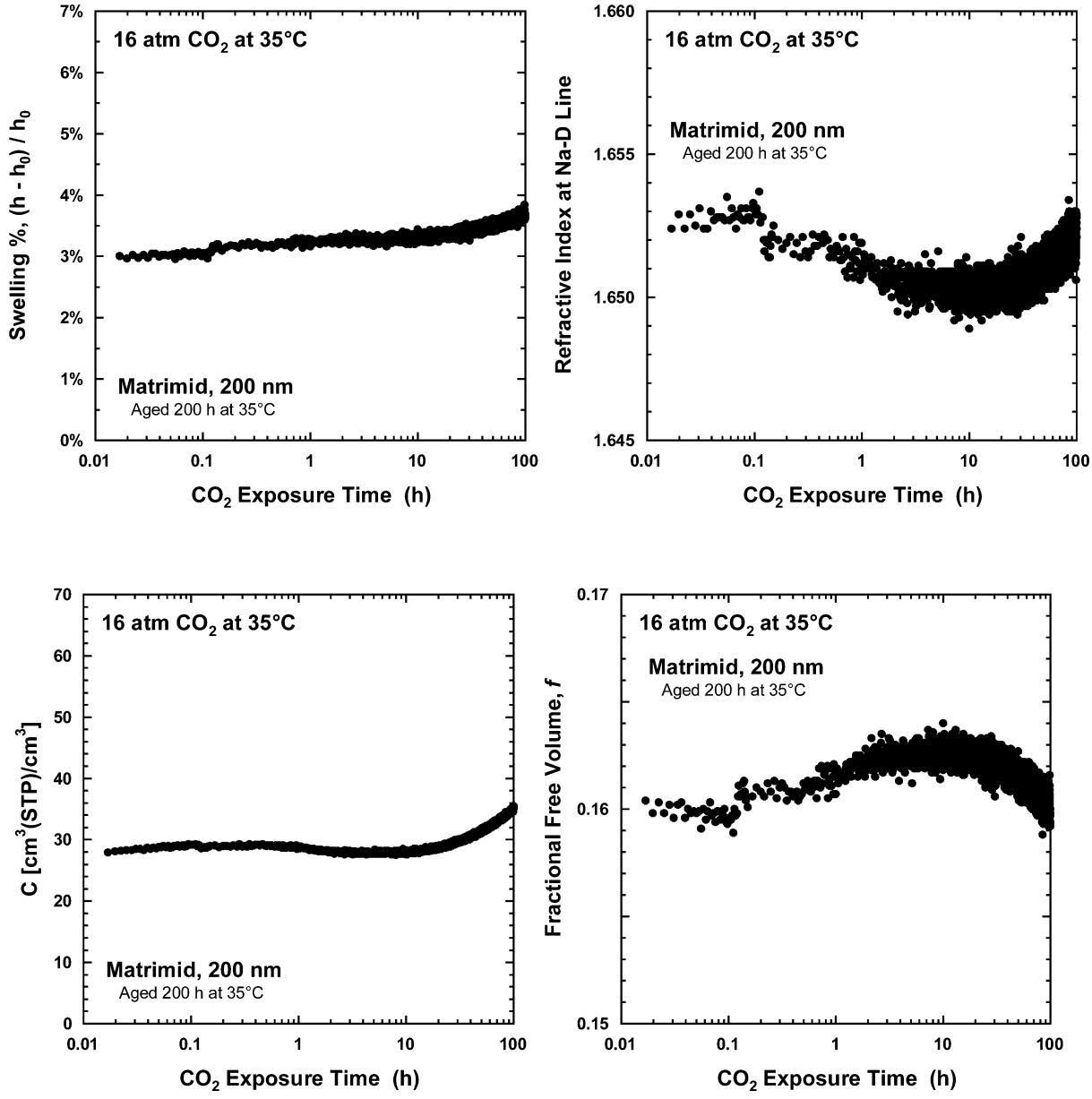


Figure 12. Results for a constant pressure experiment for a 200 nm Matrimid film, aged for 200 h at 35 °C and exposed to 16 atm of CO_2 at 35 °C for 100 h.

5.2. Estimating CO_2 Diffusivity as a Function of Time for Thin Matrimid Films. The CO_2 sorption data versus time at constant pressure can be correlated with permeability from our previous work to estimate diffusivity as a function of time. Selected exposure times from the concentration data were matched to the exposure times from the permeability data. Before calculating diffusivity, the concentration at each of those times was averaged over 10 min to smooth out variation in the data. The differences in the experimental conditions, namely freestanding versus mounted films, probably affect the quantitative results to some extent, but the results presented in Figure 15 are still instructive. As expected, a maximum in diffusivity occurs in the 32 and 16 atm CO_2 data, generally correlating with the permeability maximum and refractive index minimum. However, the CO_2 diffusivity at 8 atm changes little for much of the first 100 h of CO_2 exposure, although it eventually shows a significant decrease at later times.

These trends further emphasize the complexity of combined plasticization and physical aging phenomena. Clearly, CO_2 diffusivity changes with continued CO_2 exposure. However, the effect is more pronounced at greater pressures. Figure 15 suggests that permeability changes at lower pressures are initially driven by the change in solubility, i.e., the continued uptake of CO_2. The change in diffusivity is slower, and it is also affected by the progress of physical aging. Eventually, aging causes the diffusivity to decline at a relatively faster rate than that of the increasing CO_2 solubility, resulting in decreasing permeability with continued CO_2 exposure. At higher pressures, diffusivity changes more rapidly. Although continued CO_2 sorption does affect the permeability, the change in diffusivity with time plays a significantly greater role throughout the experiment. Besides illustrating again the importance of physical aging to diffusivity (as in Figure 10), the long-term trends strengthen our claim in section 4.2 that although physical aging

dx.doi.org/10.1021/ma300177k | Macromolecules 2012, 45, 2820−2834

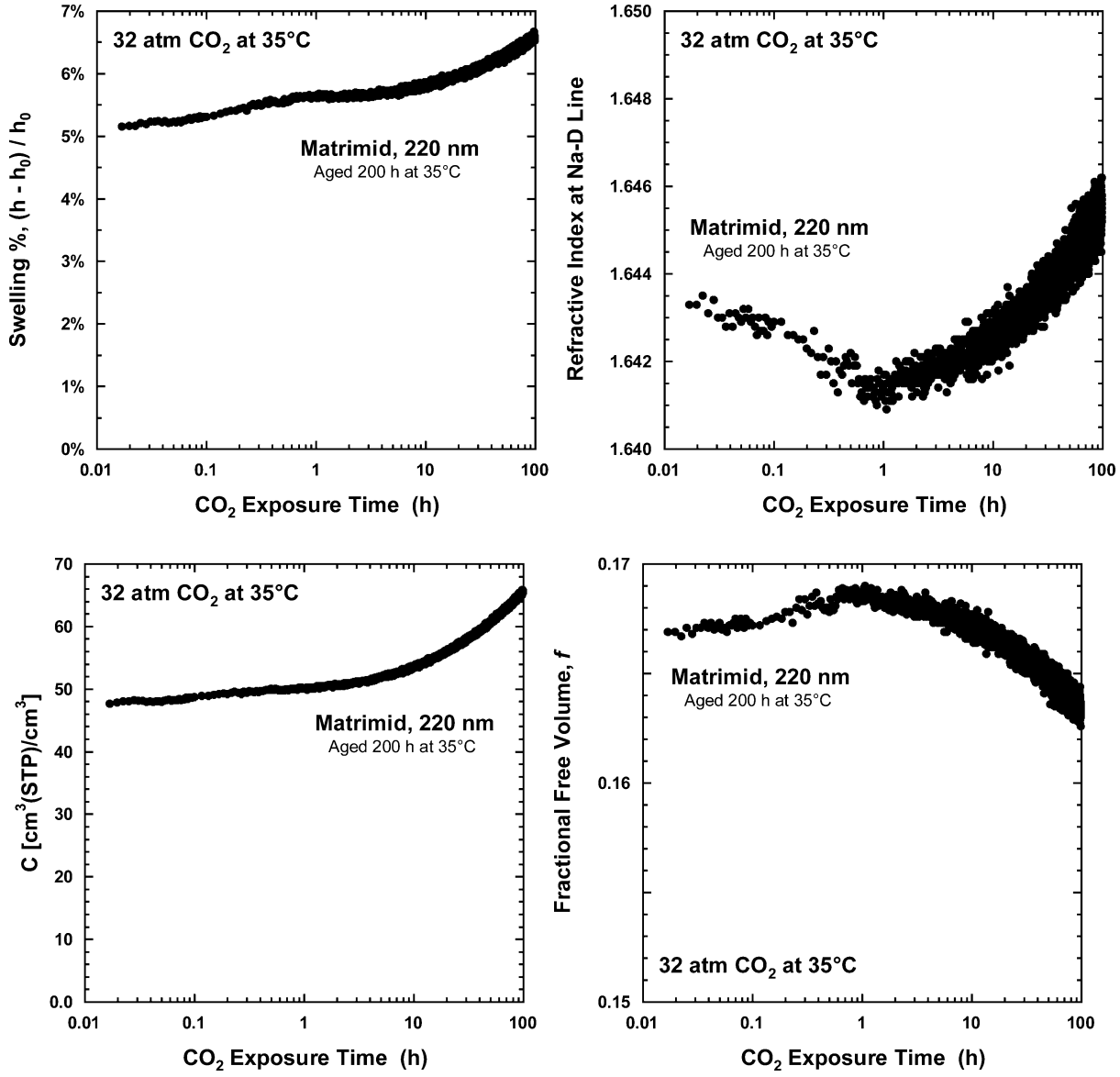


Figure 13. Results for a constant pressure experiment for a 220 nm Matrimid film, aged for 200 h at 35 °C and exposed to 32 atm of CO_2 at 35 °C for 100 h.

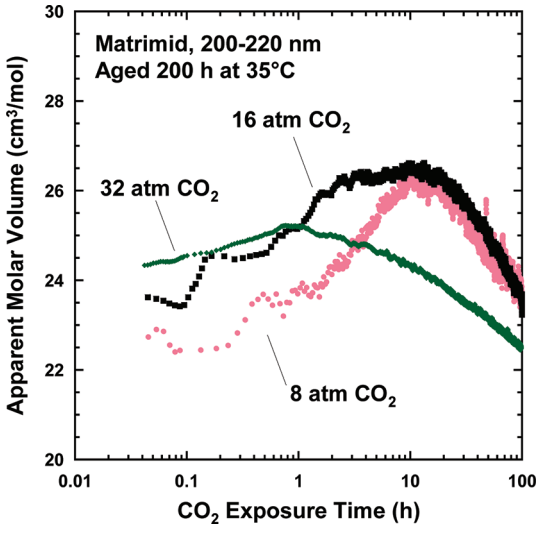


Figure 14. Apparent molar volume of CO_2 in Matrimid for constant pressure experiments at 35 °C.

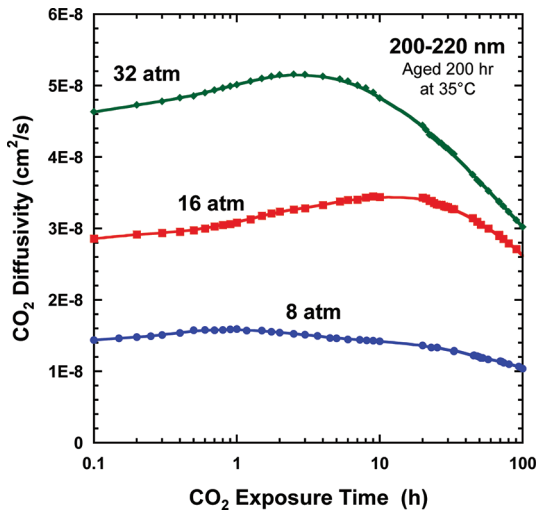


Figure 15. Apparent CO_2 diffusivity for Matrimid as a function of time, calculated from permeability measurements made previously[7] and sorption data obtained via ellipsometry.

dx.doi.org/10.1021/ma300177k | *Macromolecules* 2012, 45, 2820−2834

does affect CO_2 sorption, the results are not quite as dramatic as other factors.

6. CONCLUSIONS

Ellipsometry has been used to characterize CO_2 sorption in a series of thin glassy polymer films, providing further evidence that the consequences of plasticization are dependent on film thickness for glassy polymers. In general, thin films sorb significantly less CO_2 than most bulk films, and the magnitude of this difference may be connected to the glass transition temperature. Physical aging affects sorption behavior as well, but not as dramatically as thickness. The partial molar volume of CO_2 in thin films showed no obvious relationship with the polymer type or T_g, and the data suggest that previous claims regarding critical values of partial molar volume or concentration to induce plasticization may be oversimplifications. Fractional free volume as a function of CO_2 pressure showed an analogous behavior to CO_2 permeability as a function of pressure. While this result was somewhat surprising, it is relatively dependent on the particular methodology used in the experiments. Changing the time spent at a given pressure will generally change one's results to some extent. Diffusivity as a function of pressure was estimated for Matrimid from previously obtained permeability data at different aging times, and the results showed that aging and CO_2 sorption affect diffusivity strongly.

Dynamic ellipsometry experiments at constant CO_2 pressure demonstrated analogous behavior to previous permeability measurements as a function of time at constant pressure. The polymers exhibited continual sorption-induced swelling and CO_2 uptake throughout the experiment, and no approach toward a plateau could be determined within the experimental time scale. The times to reach refractive index minima and fractional free volume maxima corresponded well with previously observed times to reach permeability maxima, further demonstrating that physical aging dominates CO_2 plasticization for long exposure times. Fractional free volume did seem to exhibit a dependence upon CO_2 pressure when comparing the trends of the different constant pressure experiments.

Similar to the sorption isotherm experiments, CO_2 diffusivity was estimated by matching sorption measurements with permeability data at corresponding experimental times. The results show that CO_2 solubility is the driving factor of changes in CO_2 permeability at lower pressures due to diffusivity changing relatively slower. At higher pressures, changes in diffusivity, driven by physical aging, clearly have the greatest effect on CO_2 permeability even at short exposure times. In both cases, diffusivity is the primary component affected by physical aging that leads to the reduction in permeability seen in previous experiments.

An important part of this research and our previous work[7,8] has been to emphasize the complex behavior of physical aging and CO_2 plasticization in competition and to show how thin glassy polymer films differ from bulk films. Previously, knowledge of gas sorption behavior in thin films has been rather limited by the lack of adequate equipment able to measure film thickness and sorption capacity simultaneously, but ellipsometry overcomes these limitations and can be used to enhance our knowledge of gas transport behavior for both plasticizing and nonplasticizing gases. Understanding long-term property changes due to plasticization and physical aging is crucial toward the development of robust membrane separation modules, and this study provides a clearer picture of the dynamic relationship between CO_2 permeability, sorption, and diffusivity during plasticization over long time periods.

AUTHOR INFORMATION

Corresponding Author

*Tel +1 512 471 5392; fax +1 512 471 0542; e-mail drp@che.utexas.edu.

Notes

The authors declare no competing financial interest.

ACKNOWLEDGMENTS

The authors thank Stephen Sirard for his helpful comments, Prof. Keith Johnston for providing the high-pressure ellipsometry cell, Zachary Smith for his help obtaining thick film sorption analysis, Katrina Czenkusch for her assistance with Matlab, Brandon Rowe for the use of his data from previous work, the University of Texas at Austin Center for Nano- and Molecular Technology for the use of their facilities, and the J.A. Woolam Company (especially Ping He) for advice regarding dynamic data analysis. The authors gratefully acknowledge the U.S. Department of Energy for the generous funding of this project.

REFERENCES

(1) Huang, Y.; Paul, D. R. *Macromolecules* **2006**, *39*, 1554−1559.
(2) Huang, Y.; Paul, D. R. *Ind. Eng. Chem. Res.* **2007**, *46*, 2342−2347.
(3) Huang, Y.; Paul, D. R. *J. Membr. Sci.* **2004**, *244*, 167−178.
(4) Huang, Y.; Wang, X.; Paul, D. R. *J. Membr. Sci.* **2006**, *277*, 219−229.
(5) McCaig, M. S.; Paul, D. R. *Polymer* **2000**, *41*, 629−637.
(6) McCaig, M. S.; Paul, D. R.; Barlow, J. W. *Polymer.* **2000**, *41*, 639−648.
(7) Horn, N. R.; Paul, D. R. *Polymer* **2011**, *52*, 1619−1627.
(8) Horn, N. R.; Paul, D. R. *Polymer* **2011**, *52*, 5587−5594.
(9) Koros, W. J.; Paul, D. R.; Rocha, A. A. *J. Polym. Sci., Part B: Polym. Phys.* **1976**, *14*, 687−702.
(10) Weireld, G. D.; Frère, M.; Jadot, R. *Meas. Sci. Technol.* **1999**, *10*, 117−126.
(11) Berens, A. R. *Polym. Eng. Sci.* **1980**, *20*, 95−101.
(12) Scholes, C. A.; Chen, G. Q.; Stevens, G. W.; Kentish, S. E. *J. Membr. Sci.* **2010**, *346*, 208−214.
(13) Scholes, C. A.; Tao, W. X.; Stevens, G. W.; Kentish, S. E. *J. Appl. Polym. Sci.* **2010**, *117*, 2284−2289.
(14) Chung, T.-S.; Chan, S. S.; Wang, R.; Lu, Z.; He, C. *J. Membr. Sci.* **2003**, *211*, 91−99.
(15) Koros, W. J.; Paul, D. R. *Polym. Eng. Sci.* **1980**, *20*, 14−19.
(16) Koros, W. J.; Paul, D. R.; Fujii, M.; Hopfenberg, H. B.; Stannett, V. *J. Appl. Polym. Sci* **1977**, *21*, 2899−2904.
(17) Miura, K.-i.; Otake, K.; Kurosawa, S.; Sako, T.; Sugeta, T.; Nakane, T.; Sato, M.; Tsuji, T.; Hiaki, T.; Hongo, M. *Fluid Phase Equilib.* **1998**, *144*, 181−189.
(18) Aubert, J. H. *J. Supercrit. Fluids* **1998**, *11*, 163−172.
(19) Zhang, C.; Cappleman, B. P.; Defibaugh-Chavez, M.; Weinkauf, D. H. *J. Polym. Sci., Part B: Polym. Phys.* **2003**, *41*, 2109−2118.
(20) Pantoula, M.; Panayiotou, C. *J. Supercrit. Fluids* **2006**, *37*, 254−262.
(21) Tan, N. C. B.; Wu, W. L.; Wallace, W. E.; Davis, G. T. *J. Polym. Sci., Part B: Polym. Phys.* **1998**, *36*, 155−162.
(22) Madden, W. C.; Punsalan, D.; Koros, W. J. *Polymer* **2005**, *46*, 5433−5436.
(23) Simons, K.; Nijmeijer, K.; Sala, J. G.; van der Werf, H.; Benes, N. E.; Dingemans, T. J.; Wessling, M. *Polymer* **2010**, *51*, 3907−3917.
(24) Bos, A.; Pünt, I.; Strathmann, H.; Wessling, M. *AIChE J.* **2001**, *47*, 1088−1093.
(25) Moore, T. T.; Koros, W. J. *J. Appl. Polym. Sci.* **2007**, *104*, 4053−4059.

(26) Visser, T.; Wessling, M. *Macromolecules* **2007**, *40*, 4992−5000.
(27) Sirard, S. M.; Green, P. F.; Johnston, K. P. *J. Phys. Chem. B* **2001**, *105*, 766−772.
(28) Wind, J. D.; Sirard, S. M.; Paul, D. R.; Green, P. F.; Johnston, K. P.; Koros, W. J. *Macromolecules* **2003**, *36*, 6433−6441.
(29) Wind, J. D.; Sirard, S. M.; Paul, D. R.; Green, P. F.; Johnston, K. P.; Koros, W. J. *Macromolecules* **2003**, *36*, 6442−6448.
(30) Rowe, B. W.; Freeman, B. D.; Paul, D. R. *Macromolecules* **2007**, *40*, 2806−2813.
(31) Feynman, R. P.; Leighton, R. B.; Sands, M. *The Feynman Lectures on Physics*; Addison-Wesley Publishing Company, Inc.: Reading, MA, 1963.
(32) Lide, D. R. *CRC Handbook of Chemistry and Physics*, 78th ed.;Lide, D. R., Ed.; CRC Press: New York, 1997.
(33) Michels, A.; Hamers, J. *Physica* **1937**, *4*, 995−1006.
(34) Maeda, Y. Ph.D. Dissertation, University of Texas at Austin, 1985; p 413.
(35) Maeda, Y.; Paul, D. R. *J. Polym. Sci., Part B: Polym. Phys.* **1987**, *25*, 1005−1016.
(36) Lee, W. M. *Polym. Eng. Sci.* **1980**, *20*, 65−69.
(37) Bondi, A. *J. Phys. Chem.* **1964**, *68*, 441−451.
(38) Bondi, A. *Physical Properties of Molecular Crystals, Liquids, and Glasses*; John Wiley & Sons: New York, 1968.
(39) Van Krevelen, D. W. *Properties of Polymers*, 3rd ed.; Elsevier: New York, 1990; p 875.
(40) Sanchez, I. C.; Cho, J. *Polymer* **1995**, *36*, 2929−2939.
(41) Huang, Y.; Paul, D. R. *Polymer* **2004**, *45*, 8377−8393.
(42) Rowe, B. W.; Pas, S. J.; Hill, A. J.; Suzuki, R.; Freeman, B. D.; Paul, D. R. *Polymer* **2009**, *50*, 6149−6156.
(43) Stagg, B. J.; Charalampopoulos, T. T. *J. Phys. D: Appl. Phys.* **1993**, *26*, 2028−35.
(44) Maeda, Y.; Paul, D. R. *J. Polym. Sci., Part B: Polym. Phys.* **1987**, *25*, 981−1003.
(45) Morel, G.; Paul, D. R. *J. Membr. Sci.* **1982**, *10*, 273−282.
(46) Paul, D. R. In *Comprehensive Membrane Science and Technology*; Drioli, E., Giorno, L., Eds.; Academic Press: Oxford, 2010; Vol. *1*, pp 75−90.
(47) Koros, W. J. Personal communication, 1978.
(48) Bos, A.; Pünt, I. G. M.; Wessling, M.; Strathmann, H. *J. Membr. Sci.* **1999**, *155*, 67−78.
(49) Hong, X.; Jean, Y.; Yang, H.; Jordan, S.; Koros, W. J. *Macromolecules* **1996**, *29*, 7859−7864.
(50) Chen, H.; Cheng, M. L.; Jean, Y.; Lee, L. J.; Yang, J. *J. Polym. Sci., Part B: Polym. Phys.* **2008**, *46*, 388−405.
(51) Ronova, I. a.; Rozhkov, E. M.; Alentiev, A. Y.; Yampolskii, Y. P. *Macromol. Theory Simul.* **2003**, *12*, 425−439.
(52) Wong, J. M. Ph.D. Dissertation, University of Texas at Austin, 1986.
(53) Stone, M. T.; In'T Veld, P. J.; Lu, Y.; Sanchez, I. C. *Mol. Phys.* **2002**, *100*, 2773−2792.
(54) Scherer, J. R. *Proc. Natl. Acad. Sci. U. S. A.* **1987**, *84*, 7938−42.
(55) Horn, N. R. Ph.D. Dissertation, University of Texas at Austin, 2012.
(56) Aitken, C. L.; Koros, W. J.; Paul, D. R. *Macromolecules* **1992**, *25*, 3651−58.
(57) Stern, S. A.; Saxena, V. *J. Membr. Sci.* **1980**, *7*, 47−59.

Macromolecules

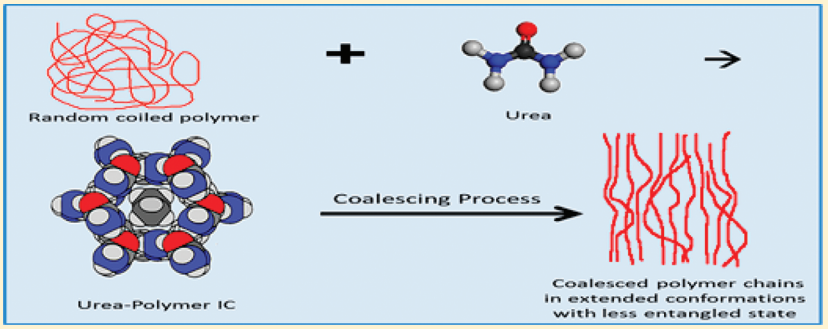
Article

pubs.acs.org/Macromolecules

Behavior of Poly(ε-caprolactone)s (PCLs) Coalesced from Their Stoichiometric Urea Inclusion Compounds and Their Use as Nucleants for Crystallizing PCL Melts: Dependence on PCL Molecular Weights

Alper Gurarslan, Jialong Shen, and Alan E. Tonelli*

Fiber & Polymer Science Program, Department of Textile Engineering, Chemistry, and Science, North Carolina State University, College of Textiles, Campus Box 8301, Raleigh, North Carolina 27695-8301, United States



ABSTRACT: We have formed noncovalent inclusion compounds (ICs) between guest poly(ε-caprolactone) (PCL) chains, with molecular weights ranging from ∼2000 to 80 000 g/mol, and host urea (U). Upon careful removal of the U host, each of the guest PCL chains were coalesced from their U-IC crystals to produce coalesced samples (c-PCLs). As previously observed for PCL and other polymer guests when coalesced from their ICs formed with host cyclodextrins (CDs), upon cooling from their melts, PCLs coalesced from their U-ICs also show enhanced abilities to crystallize, regardless of their molecular weight. Also consistent with polymer guests, including PCL, that were coalesced from their CD-ICs, c-PCLs obtained from their U-ICs retain their enhanced abilities to crystallize even after spending long times (weeks or more) in the melt. Because, unlike CD hosts, U does not thread over guest polymer chains in their ICs, we conclude that the enhanced ability of c-PCLs to crystallize from their melts upon removal of either host from their ICs is solely a consequence of their coalesced conformations/structures/morphologies, which are stable to prolonged melt-annealing. Furthermore, because c-PCLs with chain lengths well below and well above those corresponding to the entanglement molecular weight of PCL behave similarly, we conclude that their enhanced ability to crystallize from the melt is likely an exclusive consequence of the extended and unentangled arrangement of their coalesced chains. In addition, c-PCLs obtained from their U-ICs are observed to effectively act as self-nucleants, when added in small amounts to as-received PCLs, to produce nuc-PCLs, which like neat c-PCLs exhibit an enhanced ability to melt-crystallize.

INTRODUCTION

Recently,[1−5] we have observed that the bulk behaviors of polymers can be significantly altered from those normally processed from their solutions and melts. This is achieved by first forming noncovalent inclusion compounds (ICs) between guest polymers and certain small molecule hosts like cyclodextrins (CDs), where the guest polymer chains are confined to narrow channels (∼0.5−1.0 nm in diameter) and so are necessarily highly extended and separated from each other, as illustrated in Figure 1. Careful removal of the host crystalline lattice results in a coalesced polymer sample, as depicted there, where the coalesced guest polymer chains are suggested to be reorganized in a highly extended and unentangled manner carried over from their isolation and extension in their crystalline ICs.

This manner of nanoprocessing polymers has been shown to significantly alter their behaviors. Prior to the present study, we have coalesced polymers exclusively from their CD-ICs. Here we extend this approach to samples of poly(ε-caprolactone) (PCL) coalesced from ICs formed with the host urea (U) (see Figure 2) to learn if their behaviors are similar to or distinct from PCLs coalesced from CD-ICs, where the guest PCL chains are threaded through the cyclic host CDs. In addition, we examine the potential effect(s) of chain length/molecular weight on the behaviors of PCL samples coalesced from their U-ICs.

PCL is a biodegradable/bioabsorbable polyester first synthesized in the 1930s by ring-opening polymerization of ε-caprolactone. Today, PCL is well established in the biomedical field, often acting as the main component for

Received: February 8, 2012
Revised: March 8, 2012
Published: March 19, 2012

ACS Publications © 2012 American Chemical Society

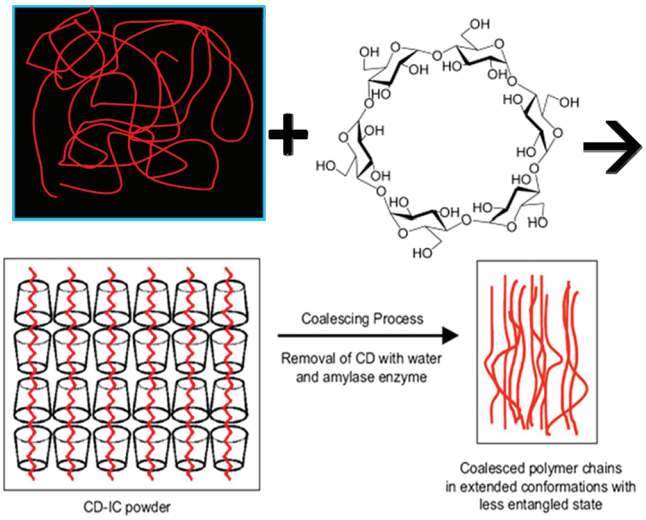


Figure 1. Formation of and coalescence of a polymer sample from its crystalline cyclodextrin inclusion complex.

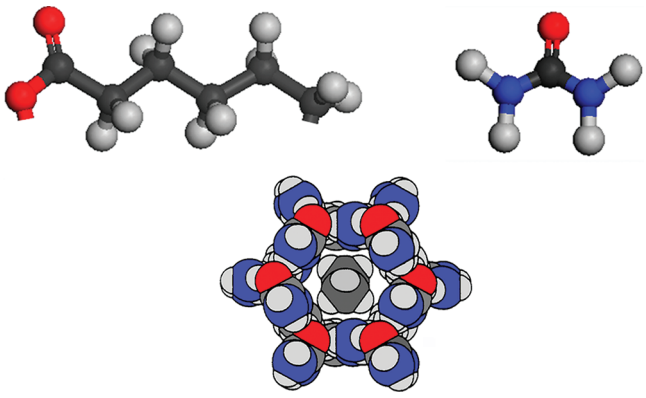


Figure 2. Poly(ε-caprolactone) repeat unit (top left) and urea (top right), where carbons are gray, hydrogens white, oxygens red, and nitrogens blue. Space-filling drawing of a channel in the polyethylene-U-IC, which is isomorphic with that of the PCL-U-IC (bottom).[6]

bone and cartilage tissue scaffolding. Because of its relatively low melting temperature, PCL can be melt processed using very simple techniques and is often strengthened upon addition of fillers, such as fibers or particulates.[7] Often times, PCL is used in combination with another biodegradable polyester, poly(L-lactic acid), and their blends have been shown to have good gas barrier properties.[8]

Despite PCL's many unique properties, it is not a very strong material. Because of its low softening temperature ($T_m \sim 59-64$ °C and glass-transition temperature $T_g \sim -60$ °C)[9] and comparatively poor room temperature physical properties (tensile strength of 20–42 MPa and a tensile modulus of 0.2–0.44 GPa),[10] PCL has not made great headway as a load bearing implantable material. If PCL could be strengthened in some fashion, then it might gain new biomedical applications, in particular for load-bearing implantables with superior compressive strengths. For example, if nucleating agents are used in the melt-crystallization of PCL to increase the homogeneity of its semicrystalline morphology and resultant strength, they must also be bioabsorbable and nontoxic for use as implantable materials. This was previously suggested for PCL coalesced from its α-CD-IC (c-PCL),[3] where, in addition, a variety of its behaviors and properties as films were examined and found to be improved over those of films formed from as-received PCL. Here we examine the effectiveness of PCLs coalesced from their U-ICs to also act as effective self-nucleants.

EXPERIMENTAL SECTION

Materials. Four types of poly(ε-caprolactone) having number-average molecular weights of 80 000, 42 500, 10 000, and 2000 g/mol (asr-PCL-80, -40, -10, and -2) (see Table 1) were obtained from Sigma-Aldrich, as were acetone, methanol, chloroform, dimethyl sulfoxide, and urea. It should be noted that each PCL contains a centrally located $-(CH_2-CH_2-O-CH_2-CH_2-)-$ unit, as shown below. As a consequence, the two connected PCL chains run in opposite directions.

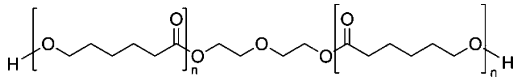


Table 1. PCL Samples

sample ID	commercial name	M_n[a] (g/mol)	n
PCL-2	polycaprolactone diol 189421	2000	8
PCL-10	polycaprolactone 440752	10000	43
PCL-40	polycaprolactone 181609	42500	186
PCL-80	polycaprolactone 440744	70–90000	350

[a]Provided by the manufacturer.

Methods. *Formation of PCL-U-ICs.* 1 g of PCL was dissolved in 100 mL of acetone at 50 °C, and 32.5 g of urea (U) was dissolved in 200 mL of methanol also at 50 °C, and the U solution was slowly added to the PCL solution in a dropwise manner. The temperature was lowered after mixing was complete, but stirring continued at room temperature for an additional 30 min. A further 2 days was allowed for inclusion complex formation, after which the resulting precipitate was filtered and vacuum-dried.

Coalescence of PCL from Its U IC. U can be removed from the PCL-U-IC by two techniques. Stirring 1 g of PCL-U-IC in 50 mL of methanol can completely remove the U. In a second route, 1 g of PCL-U-IC was stirred in excess water for 1 day and then filtered and dried. Then the resulting material was stirred in 35 mL of methanol to completely remove the U and obtain coalesced PCL. Though the second route takes longer, it requires less methanol. Finally, in both cases the coalesced PCL samples were vacuum-dried for 1 day.

PCL Films. Solvent cast PCL films were obtained by dissolving 1 g of PCL in 100 mL of acetone and then evaporating all the solvent. PCL films nucleated with c-PCL were obtained by solvent casting of 2.5% c-PCL with 97.5% as-received (asr)-PCL from acetone, which did not dissolve the c-PCL nucleant. All solvent cast films were vacuum-dried before further characterization. Melt-pressed films of asr and c-PCL-10 were prepared for polarized microscopy.

FTIR. A Nicolet 510P FTIR spectrometer was employed in the range 4000–400 cm^{-1}, with a resolution of 4 cm^{-1}. FTIR data were analyzed by using Omnic software. 64 scans were collected for each spectrum.

DSC. Differential scanning calorimetric (DSC) thermal scans were performed with a Perkin-Elmer Diamond DSC-7 instrument. Heating scans were started at 0 °C, and each sample was heated to 75 °C. After holding each sample in the melt for 5 min, they were cooled to 0 °C at the same rate they were previously heated (20 °C/min). Nitrogen was used as the purge gas. DSC data were analyzed with Pyris software, and melting and crystallization temperatures and enthalpies were calculated automatically by the software from the areas of their endothermic and exothermic peaks.

Polarized Microscopy. Polarized optical microscopic observations of asr and c-PCL-10 thin films were performed on a Nikon Eclipse 50i POL optical microscope equipped with a CCID-IRIS/RGB color video camera made by Sony Corp. Photographs was taken by using crossed polarizers and a 1/4 λ plate.

dx.doi.org/10.1021/ma300270g | Macromolecules 2012, 45, 2835–2840

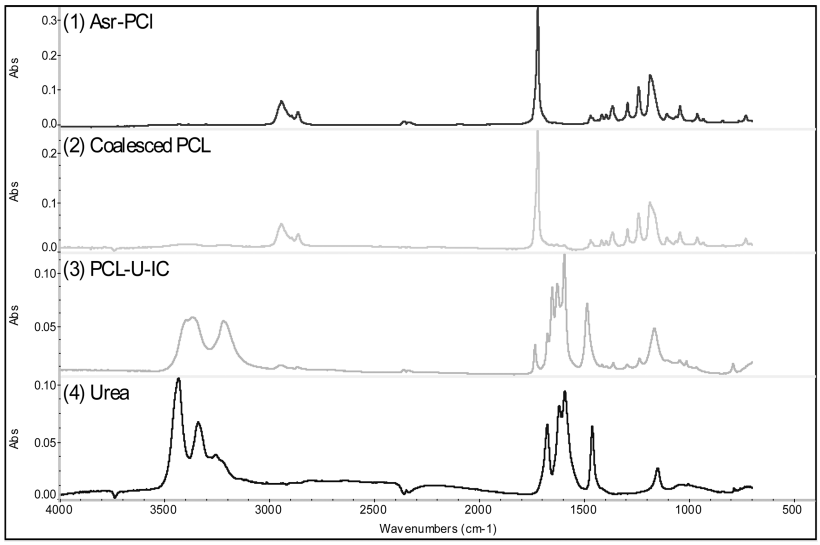


Figure 3. FTIR spectra of asr-PCL (1), c-PCL (2), PCL-U-IC (3), and U (4).

NMR. Dilute solutions of c-PCL and a mixture of 10 wt % urea and 90 wt % asr-PCL were prepared in 1:2 d_6-DMSO:$CDCl_3$ mixtures, and their ^{1}H NMR spectra were recorded on a Bruker 700 MHz spectrometer equipped with 5 mm i.d. CPTCI (^{1}H/^{13}C/^{15}N/D) *Z*-axis gradient cryoprobe. NMR data were analyzed with Topspin 2.1 software.

RESULTS AND DISCUSSION

IC formation was confirmed with FTIR and DSC. FTIR spectra of PCL-U-ICs exhibit peaks characteristic of both PCL and U, as seen in Figure 3. However, this is insufficient to distinguish PCL-U-IC from a physical mixture of PCL and U, but in conjunction with DSC observations they can be distinguished. As seen in Figure 4, the first heating scan of PCL-U-IC does not show a melting peak for PCL. Instead, melting peaks for free U and PCL-U-IC are observed at 134 and 142 °C, since excess U was employed in forming the PCL-U-IC. After melting of the PCL-U-IC, in the second heating scan we see melting peaks for free PCL and U as well as that of the partially re-formed PCL-U-IC.[6] All four U-IC's formed using PCLs with different molecular weights were confirmed this way. For comparison, the melting temperatures of c- and asr-PCL-80 were 55 and 61 °C, respectively.

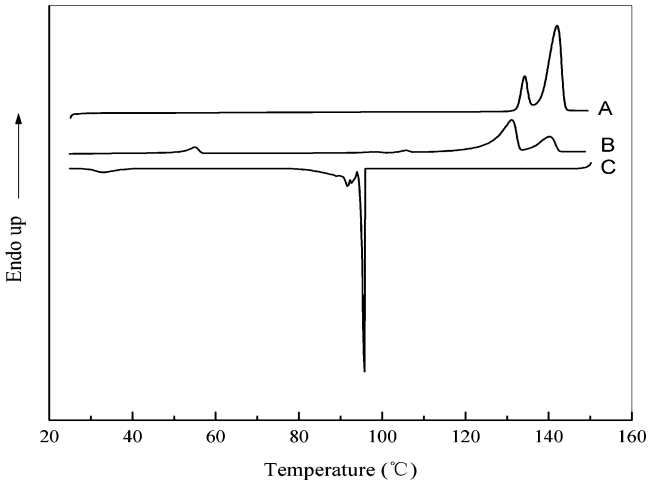


Figure 4. DSC thermograms of PCL-80-U-IC: first heating (A), second heating (B), first cooling (C).

Coalesced PCLs were obtained from their U-ICs after removing all of the host U. As seen in the FTIR spectra presented in Figure 3-(1),(2), it appears that very little if any U remains after coalescence. More sensitive ^{1}H NMR observations also confirm the virtual absence of remnant host U, as demonstrated in Figure 5 by the absence of the urea proton peak at ~5.35 ppm in the spectrum of c-PCL.

Table 2 summarizes the melt-crystallization of as-received (asr-) and c-PCL samples. It is clear that all c-PCL melts crystallize at significantly higher temperatures than their corresponding asr-melts, with the difference between them increasing with their molecular weights. It is also apparent that

Table 2. Crystallization Temperatures of Different Molecular Weight asr- and c-PCLs

	T_c (°C)		
sample	asr-PCLs	c-PCLs	T_c increments
PCL-2	17.0	26.5	9.5
PCL-10	16.8	32.5	15.7
PCL-40	18.8	35.0	16.2
PCL-80	11.7	33.3[a]	21.6

[a]For comparison, PCL-80 coalesced from its IC formed with host *α*-CD crystallized at T_c = 36.8 °C from the melt upon cooling at −20.0 °C/min.

Table 3. Crystallization Temperatures of c-PCLs before and after Annealing 2 and 4 weeks at 80 °C[a]

	T_c (°C)		
sample	initial	after annealing 2 weeks at 80 °C	after annealing 4 weeks at 80 °C
c-PCL-2	26.5	26.0	26.4
c-PCL-10	32.5	30.9	31.7
c-PCL-40	35.0	34.1	33.8
c-PCL-80	33.3	30.1	31.1

[a]Because flow times observed in a Cannon-Ubbelhode viscometer for 1 g/dL $CHCl_3$ solutions of asr- and c-PCLs, the latter both before and after annealing, were closely similar, long-term melt-annealing at 80 °C did not thermally degrade our PCL samples.

dx.doi.org/10.1021/ma300270g | *Macromolecules* 2012, 45, 2835−2840

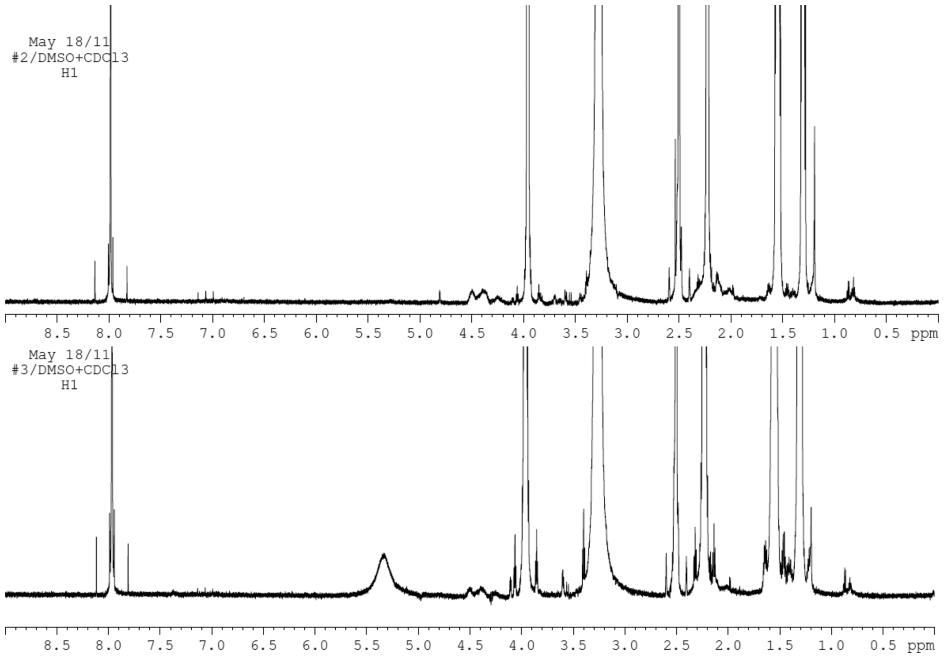


Figure 5. The 700 MHz ^{1}H NMR spectra of asr-PCL with 10 wt % of U (bottom) and c-PCL (top), which have been equally expanded.

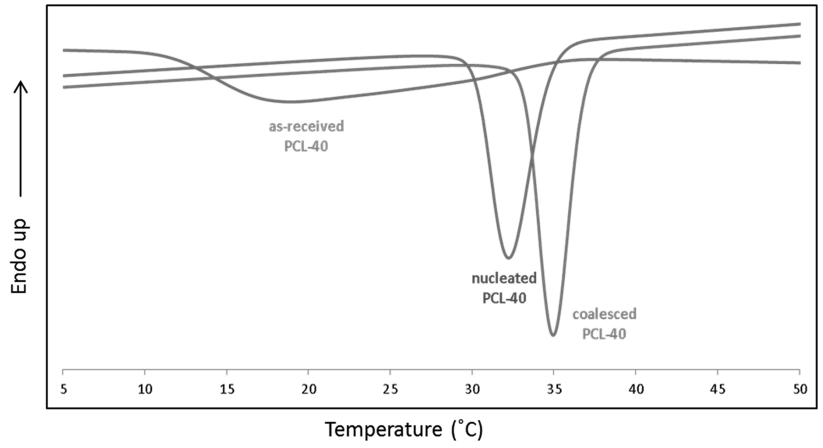


Figure 6. First cooling DSC scans from the melts of neat asr-PCL-40, self-nucleated nuc-PCL-40 (2.5 wt % c-PCL-40 + 97.5 wt % asr-PCL-40), and c-PCL-40.

Table 4. Crystallization Temperatures of Different Molecular Weight asr-, nuc-PCLs, and PCLs Nucleated with c-PCL-10

	T_c (°C)			
sample	PCL-2	PCL-10	PCL-40	PCL-80
as-received	17.0	16.8	18.8	11.7
coalesced	26.5	32.5	35	33.3
self-nucleated	18.8	27.9	32.3	29.6
nucleated with c-PLC-10	21.3	27.9	29.5	28.1

the T_c of the highest molecular weight asr-sample (PCL-80) is significantly lower than the T_cs of the others, which are very similar. This may be due to the presumably highly entangled nature of the high molecular weight asr-PCL-80 melt.

Most important is the similarity in the melt-crystallization temperatures of all the c-PCL samples, despite the vast differences in their molecular weights. This is consistent with the assumed extended, unentangled natures of their constituent PCL chains (see Figure 1).

The distinction between the T_cs of asr- and c-PCLs is maintained even after prolonged melt annealing of their c-melts at 80 °C, as can be seen in Table 3. This behavior suggested that c-PCLs would make excellent nucleation agents for enhancing the melt-crystallization of asr-PCLs.

In Figure 6, the first cooling DSC scans of neat asr-, c-, and nuc-PCL-40 (97.5 wt % asr-PCL-40 self-nucleated with 2.5 wt % c-PCL-40) reveal that the resulting nuc-PCL-40 and neat c-PCL-40 crystallize more readily than asr-PCL-40. The crystallization exotherms of c- and nuc-PCL-40 are much narrower/sharper, with crystallization ranges of ~9−10 °C compared with ~30 °C for asr-PCL-40, and occur at significantly higher temperatures (35 and 32.3 °C, respectively) compared with the crystallization exotherm of asr-PCL-40 (18.8 °C).

Table 4 presents a comparison of melt-crystallization temperatures for asr-, c-, and nuc-samples of all four PCLs.

dx.doi.org/10.1021/ma300270g | *Macromolecules* 2012, 45, 2835−2840

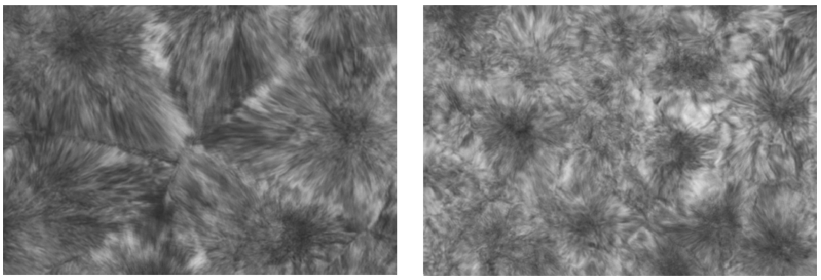


Figure 7. Optical microscopy images (500×, crossed polarizers, 1/4 λ plate) of melt-pressed asr-PCL-10 (left) and c-PCL-10 (right) films.

In addition to the self-nucleated samples, the T_cs of asr-PCL-2, -40, and -80 nucleated with c-PCL-10 are also given there, and they are seen to differ only minimally from the T_cs of their self-nucleated films. We can also see that the crystallization of nuc-PCL-2 is very similar to and not enhanced compared with asr-PCL-2, independent of whether it is self-nucleated or nucleated with c-PCL-10. This is likely a result of its very low molecular weight, corresponding to just 8 repeat units (see Table 1), but not to the absence of entanglements, because all of the c-PCL melts are believed to crystallize from unentangled melts. C-PCL-2 crystallizes less than 10 °C higher than asr-PCL-2, while the higher molecular weight c-PCLs crystallize from 16 to 22 °C higher in temperature than their asr-samples. The −20 °C/min cooling rate employed may not allow time sufficient for the asr-PCL chains to fully crystallize even though the nucleating c-PCL chains already have.

Crystallinities calculated from second heating DSC scans, assuming ΔH_m° = 135 J/g, are as follows: asr-, c-, and nuc-PCL80s are ∼34 ± 2% crystalline. If they have been melt pressed into film and are held at RT for a long time, all their crystallinities increase to ∼50%. PCL40: asr- and nuc- ∼ 49% crystallinities, PCL10: asr- and nuc- ∼ 47% crystallinities, and PCL2: asr- and nuc- have ∼60% crystallinities.

To briefly summarize our observations, we can say that all four PCLs, with molecular weights ranging from well below to well above the reported[11] entanglement molecular weight of PCL, ∼15 000 g/mol, when coalesced from their U-ICs are reorganized in a manner that significantly increases their melt-crystallization temperatures above those of their asr-samples. The difference in their thermal behaviors, and presumably their structures, is retained in their melts for extensive periods of time (see Table 3). In Figure 7, the optical microscope images of asr- and c-PCL-10 films observed under crossed polarizers are presented. There it is clear that the c-PCL-10 film has a finer scale, more homogeneous semicrystalline morphology (more uniform distribution of crystalline and amorphous regions), which apparently remains distinct from that of asr-PCL-10 even after extensive melt annealing.[12]

CONCLUSIONS

As previously observed for PCL and other polymer guests when coalesced from their ICs formed with host CDs,[1−5] upon cooling from their melts, PCLs coalesced from their U-ICs also show enhanced abilities to crystallize, regardless of their molecular weight. Also consistent were retention of the enhanced abilities of PCLs coalesced from their U-ICs to crystallize even after spending long times (weeks or more) in the melt. Because, unlike CD hosts, U does not thread over guest polymer chains when forming their ICs, we conclude that their enhanced ability to crystallize from their melts upon removal of the host U molecules is solely a consequence of their coalesced conformations/structures/morphologies, which are stable to prolonged melt-annealing. Furthermore, because c-PCLs with chain lengths well below and well above those corresponding to the entanglement molecular weight of PCL behave similarly, we conclude that their enhanced ability to crystallize from the melt is likely a consequence of the extended and unentangled arrangement of their coalesced chains.

PCL coalesced from its U-IC, while chemically identical to asr-PCL, shows a significantly improved melt-crystallizability because of its extended and unentangled coalesced structure. Small amounts of c-PCL can be used as a nucleant for the melt-processing of asr-PCL. As a consequence, c-PCL may eventually be useable as a fully compatible "stealth" nucleant in the formation of biodegradable/bioabsorbable, load-bearing, implantable medical devices made from PCL.[14]

AUTHOR INFORMATION

Corresponding Author

*E-mail: alan_tonelli@ncsu.edu.

Notes

The authors declare no competing financial interest.

ACKNOWLEDGMENTS

We are grateful to Dr. Hanna Gracz for recording the ^{1}H NMR spectra of asr- and c-PCLs and to the National Textile Center (US Commerce Department) and the TECS Department in the College of Textiles at NC-State University for partially supporting this work.

REFERENCES

(1) Tonelli, A. E. *Adv. Polym. Sci.* **2009**, *222*, 115.
(2) Tonelli, A. E. *J. Polym. Sci., Part A2: Polym. Phys. Ed.* **2009**, 1543.
(3) Williamson, B. R.; Krishnaswamay, R.; Tonelli, A. E. *Polymer* **2011**, *52*, 4517.
(4) Mohan, A.; Gurarslan, A.; Joyner, X.; Child, R.; Tonelli, A. E. *Polymer* **2011**, *52* (4), 1055−1062.
(5) Gurarslan, A.; Tonelli, A. E. *Macromolecules* **2011**, *44* (10), 3851.
(6) Choi, C.; Davis, D. D.; Tonelli, A. E. *Macromolecules* **1993**, *26*, 1468.
(7) Liu, H.; Han, C.; Dong, L. *Polym. Compos.* **2010**, *31* (9), 1653.
(8) Chiellini, E. *Environmentally Compatible Food Packaging*; Woodhead Publishing in Food Science, Technology and Nutrition; CRC: Boca Raton, FL, 2008.
(9) Middleton, J. C.; Tipton, A. J. *Biomaterials* **2000**, *21*, 2335.
(10) Mano, J. F.; Sousa, R. A.; Boesel, L. F.; Neves, N. M.; Reis, R. L. *Compos. Sci. Technol.* **2004**, *64*, 789.
(11) Grosvenor, M. P.; Staniforth, J. N. *Int. J. Pharm.* **1996**, *135*, 103.
(12) We have recently addressed the issue of why the organization/structure/morphologies/behaviors of polymers coalesced from their noncovalently bonded ICs, formed with both cyclodextrin and urea hosts, differ from those obtained by solution and melt processing.[13] What do we know: (A) They behave differently. (i) They crystallize

more readily, with higher T_cs, over a narrower temperature range, sometimes in unusual polymorphs, and apparently without chain folding. (ii) They have elevated T_gs. (iii) Their blends are intimately mixed. (iv) Their amorphous regions are more dense. (v) Their melts have much lower zero shear viscosities. (vi) They produce stronger, less extensible films and fibers. (vii) They are less permeable to gases (CO_2). (B) All the above behaviors remain, even after extensive periods (weeks) spent in their melts, and are independent of their molecular weights and their IC host (CD or U). (C) Because polymer-ICs are generally obtained as crystalline powders, we anticipate that upon coalescence from them the resulting coalesced polymer samples will consist of small unoriented regions (smaller than the sizes of their IC crystals) of extended and unentangled chains (see Figure 1). [Please note that, though the guest polymer chains in each crystal of the CD-IC powder are expected to be coalesced somewhat as indicated in Figure 1, we do not mean to imply that this results in the initial overall macroscopic orientation of all extended and unentangled chains. Rather, we suggest that the initial macroscopic organization of polymer chains in the melt might resemble something like a collection of small "nematic-like" regions randomly arranged without a preferred orientation of their directors. (See: Beers, D. E.; Ramirez, J. E. *J. Text. Inst.* **1990**, *81*, 561 for a discussion of Vectra, a liquid-crystalline ester/arylate copolymer, that evidences a macroscopically anisotropic melt, much like that suggested above locally for coalesced polymers).] (D) This anticipated structure(s) is consistent with their behaviors noted in (A), but we have not yet connected them to the long-time, high-temperature stability noted in (B). Thus our challenge, which is also offered to the reader, is: how can we directly observe the structure(s)/organization of coalesced polymers in their melts?

(13) Gurarslan, A.; Joijode, A. S.; Tonelli, A. E. *J. Polym. Sci., Part-A2: Polym. Phys. Ed.* **2012**.

(14) Gurarslan, A.; Tonelli, A. E. Self-Reinforcement of Polymer Composites, ACS National Meeting, Anaheim, *52*, 1, 186, March 2011.

Macromolecules

Article

pubs.acs.org/Macromolecules

A MWCNT/Polyisoprene Composite Reinforced by an Effective Load Transfer Reflected in the Extent of Polymer Coating

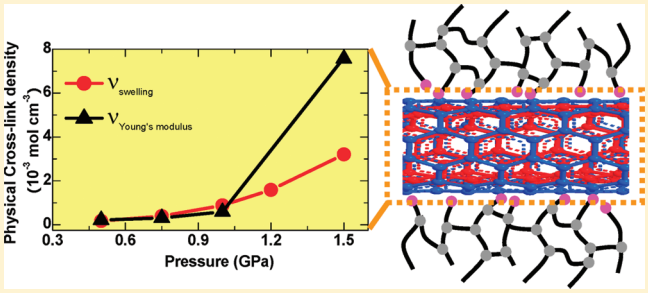
Junchun Yu,[†] Bounphanh Tonpheng,[†] Gerhard Gröbner,[‡] and Ove Andersson*,[†]

[†]Department of Physics, Umeå University, 901 87 Umeå, Sweden

[‡]Department of Chemistry, Umeå University, 90187 Umeå, Sweden

Supporting Information

ABSTRACT: Tensile and microstructural properties of multiwall carbon nanotube (MWCNT)/polyisoprene (PI) composites have been investigated after cross-linking achieved purely by simultaneous high-pressure high-temperature treatment. The method enables gradual increase of the cross-link density without interference of vulcanization chemicals, and the results suggest a link between an interfacial PI layer wrapped/coated on the MWCNTs and reinforcement in carbon nanotube (CNT)/PI composites. The interfacial layer, which is augmented by high-pressure treatment, was detected indirectly in swelling experiments and also reflected in results of atomic force microscopy. The results imply more efficient load transfer and mechanical reinforcement by CNTs with improved interfacial layer and that changes in the layer can be probed by swelling measurements.



INTRODUCTION

The filler/polymer composite materials of today have a long history of development.[1,2] Various fillers such as carbon black, carbon fibers, silica, and clays, etc.,[3] have been tested and proven favorable for mechanical and thermal reinforcement of polymers. But the recent discovery of new nanostructured materials and their extraordinary properties have raised expectations of major further improvements.[4] In particular, carbon nanotubes (CNTs)[5,6] and graphene[7] have mechanical and structural properties which are superior to those of the most commonly used fillers.[8] For example, assuming that CNTs in the perimeter of a bundle carried all the load, Yu et al.[9] obtained a tensile strength (σ_{UTS}) and a Young's modulus (E) of ∼22 and ∼1050 GPa, respectively, for a single-wall carbon nanotube (SWCNT) in a 19 nm bundle. Moreover, a 13 nm in diameter multiwall carbon nanotube (MWCNT) shows σ_{UTS} of 28 GPa and E in the range from ∼270 to 950 GPa,[10] or an E average of 1.8 TPa, as reported by Treacy et al.[11] In general, theoretical calculations for SWCNTs and MWCNT indicate even higher strength and typically show σ_{UTS} and E values of order of ∼1 TPa.[8,12] Besides the excellent mechanical properties, the unique structure with high aspect ratio (∼10^3) and low density make CNTs particularly interesting for the purpose of fabricating lightweight composites with high strength and stiffness.[1,13]

In order to obtain CNT-based polymer composites with much improved mechanical performance, it is essential that the microstructure provides an efficient load transfer between the polymer matrix and the CNTs.[14] Covalent functionalization of CNTs is one method that opens the possibility of strong bonding between the otherwise essentially inert CNTs and a polymer matrix. The capability of this method is shown by Moniruzzaman et al.'s[15] results of more than 2 times higher σ_{UTS} for fibers made of nylon-6, 10, and 1 wt % alkyl acid chloride group functionalized SWCNTs (SWCNT-$(CH_2)_n$-COCl) than fibers of nylon-6, 10, and 1 wt % nonfunctionalized SWCNTs, which implies increased reinforcement due to covalent bonds between the nylon matrix and the functionalized CNTs. Another method to obtain good load transfer is to use a cross-linkable polymer that can form a rigid matrix with good polymer−CNT interfacial contact between the entangled CNTs and the cross-linked polymer matrix. In fact, such a matrix even reinforce a fiber made of only CNTs and thus gives higher σ_{UTS} for the composite fiber than for the neat CNT fiber.[16] For example, SWCNT/poly(vinyl alcohol) and SWCNT/epoxy composite fibers showed σ_{UTS} of ca. 1.0 and 1.25 GPa, respectively, which are 40% and 80% stronger than neat SWCNT fibers (0.7 GPa).

In general, film or bulk composites show less improvement of mechanical properties than those in the form of fibers. The difference between these is well demonstrated by Sui and Wagner's[17] study of poly(methyl metacrylate) (PMMA) based SWCNT and MWCNT composites. A 1.5 wt % MWCNT/PMMA composite in the form of fibers showed 160% higher σ_{UTS} and 220% higher E than pure PMMA fibers, whereas the strength of thin film samples remained largely unchanged by MWCNTs. The difference was attributed to, e.g., the different sizes of the samples (fiber diameters of 500 nm and film thicknesses of 100 μm) and the alignment of the CNTs and polymer chains in the fibers. This is corroborated by a study of Young et al.,[18] which

Received: November 30, 2011
Revised: February 19, 2012
Published: March 13, 2012

 © 2012 American Chemical Society

showed that the strength of SWCNT/poly(vinyl alcohol) fibers increased strongly with decreasing fiber diameter. It thus appears that most previous successful reinforcements by CNTs concern composites in the form of fibers and/or rather hard matrixes such as PMMA, nylon, epoxy, etc.[19] Considering instead soft matrixes, then a 8.3 wt % MWCNT/nature rubber composite film showed ~60% higher σ_{UTS} and ~900% higher E than the pure polymer.[20] Although the relative improvement is good and better than those shown in many other studies of rubbery or soft materials, the highest σ_{UTS} and E only reached 7 and 10 MPa, respectively, which means that the composite still remained relatively weak and soft. However, we have shown that this can be changed by high-pressure high-temperature (HP&HT) treatment, which induces cross-links in the polymer matrix, polyisoprene PI, without the use of vulcanization chemicals.[21] In particular, a composite with 5 wt % SWCNT synthesized at 1.5 GPa, 513 K showed 115% higher σ_{UTS} (17 MPa), 137% higher E (220 MPa), and longer extension at break than PI processed at identical conditions (σ_{UTS} = 7.9 MPa and E = 93 MPa). An intriguing effect of the SWCNTs was an increased cross-link density as measured by the swelling method and shown concomitantly as the composites' strength increased.[21] The origin of this effect and its apparent relation with the reinforcement remained uncertain.

In this work, we have studied the mechanical and microstructural properties of MWCNT−polymer composites in elastic states ranging from relatively soft to hard, which were obtained by tuning the cross-link density via HP&HT treatment. We find that a MWCNT/PI composite synthesized at the highest pressure of 1.5 GPa not only show better mechanical properties than low-pressure counterparts but that this also correlates with much higher cross-link densities as measured by the swelling method. As nuclear magnetic resonance (NMR) results instead show fewer chemical cross-links in the composites than in pure PI suggests that the reduced swelling (high cross-link density) observed for PI with MWCNTs is due to an interface layer of strongly bound PI. The layer, which is also reflected in AFM results, is augmented by HP&HT treatment and may act as an active bridge for load transfer.

EXPERIMENTAL SECTION

Materials. Liquid *cis*-1,4-polyisoprene (PI) made from natural rubber, with a number-average relative molecular mass of 38 000, was purchased from Sigma-Aldrich. Solid high molecular weight (800 000, 97% cis) polyisoprene (LPI) was purchased from Scientific Polymer Products, Inc. MWCNTs produced by catalytic chemical vapor deposition were purchased from Nanocyl (3150 and 3151). Nanocyl 3150 (P-MWCNT: nonfunctionalized MWCNT) and Nanocyl 3151 (F-MWCNT: functionalized with less than 4% of −COOH) have a stated diameter of 10 nm, carbon purity of >95%, and a metal oxide content of <5%. Transmission electron microscopy (TEM) images show that the P-MWCNT has a diameter of ca. 10 nm and a length of ca. 1 μm, whereas F-MWCNT shows identical diameter but an average length of ~0.5 μm. All the materials were used without further purification.

Synthesis of MWCNT/PI Composite. The MWCNTs were dispersed in PI by solvent mixing. Briefly, for a typical 9.1 wt % MWCNT/PI sample, 400 mg of MWCNTs and 40 mL of toluene mixture (approximately 10 mg MWCNT:1 mL toluene) were sonicated with an ultrasonic pin (VCX130, Sonics & Materials, Inc.) at 75% power for 60 min (pulse 20 s on and 10 s off). Subsequently, 4 g of PI was added, and sonication was continued at 50% power for 120 min (pulse 20 s on and 20 s off). The solvent was thereafter removed in dynamic vacuum at 50 °C until the weight of the mixture remained constant (~7 days).

HP&HT Treatment of PI and Composite Samples. The highly viscous pastelike sample was loaded in a cylindrically shaped, custom-made, Teflon cell containing a type K thermocouple. The cell was mounted into a piston cylinder apparatus and the assembly transferred to a press, as described in more detail previously.[22,23] The pressure was generated by a hydraulic press and calculated from load/area with an empirical correction for friction, which had been established using the pressure dependence of a Manganin wire. The pressure inaccuracy was estimated as ±40 MPa at 1 GPa. The MWCNT/PI mixtures, and pure PI samples, were treated for 4 h at 513 K and a pressure in the range 0.25−1.5 GPa. The pressure and temperature were controlled using two proportional-integral-derivative (PID) controllers, which kept the pressure and temperature constant to within ±1 MPa and ±1 K during the 4 h HP&HT treatments.

Tensile Measurement. The HP&HT treated samples were removed from the Teflon cell as circular plates with thicknesses between 1 and 2 mm. A custom-made dog-bone-shaped die (16 mm in length and 7 mm in width) was used to cut the synthesized samples into dog bones for tensile testing. The exact dimensions of the samples were measured by means of a Nikon workshop microscope, and these values were used in the calculations of σ_{UTS} and E (in the range 1−5% strain). Tensile testing was performed at room temperature with a testing speed of 10 mm/min using an Instron 3343 tensile tester equipped a 500 N (or 1000 N) load cell. To enable the best comparison, the measurement procedure and analysis, e.g. testing speed and calculation of E, were the same as used previously.[21] To ensure accuracy and repeatability, at least two and occasionally three test pieces from the same sample were tested. (The preparation and analysis of one batch of a PI composite took about 7 days, which precluded a more extensive sample production.) The results of the different sample pieces normally differed less than 15%, as also found previously,[21] and occasional larger difference could be attributed to cracks in the sample plate. The stated σ_{UTS} and E are for the strongest dog-bone piece, which typically was the one cut from the center of the sample plate.

Nuclear Magnetic Resonance (NMR). The grinded solid (or highly viscous liquid) material was densely packed into a zirconia MAS rotor with Macor inserts free of carbon. Measurements were carried out at room temperature on a 400 MHz Infinity spectrometer (Chemagnetics) with a 4 mm double resonance cross-polarization magic angle spinning (CP MAS) probe. ^{13}C CP MAS NMR experiments under proton decoupling were acquired by using a contact time of 5 ms duration and a repetition delay of 3 s at a MAS speed of 6 kHz; direct polarization ^{13}C MAS NMR experiments under proton decoupling were performed at a MAS speed of 6 kHz. All ^{13}C NMR spectra were assigned using adamantane as an external reference. ^{1}H MAS NMR experiments were acquired by using a standard Hahn-echo pulse ($\pi/2-\tau-\pi-\tau-$acquisition) of 50 μs for each τ spacing and a repetition delay of 3 s at a magic angle spinning speed of 10 kHz.[24] Spectra were recorded with 120 transients and referenced by setting the =CH signal of PI to 5.2 ppm.[25] The intensity of the echo signal relative to the initial signal could be described by $\exp(-2\tau/T_2)$, where τ was varied between x and y, with T_2 describing the spin−spin relaxation time.[24]

Characterization of Cross-Link Density. Cross-link density was determined using the swelling method (υ_{swell}), E measurements (υ_E), and NMR measurements (υ_{NMR}).

In the swelling method, the samples were swelled in *n*-heptane or toluene at room temperature for 48 h.[21] A composite with 9.1 wt % P-MWCNT was also swelled further for 48 h with an additional weight increase of less than 1%, which confirms that 48 h swelling time is enough to reach near-equilibrium. The υ_{swell} was estimated by the Flory−Rehner equation (see Supporting Information).[21,26,27]

Results for E were used to calculate cross-link density (υ_E) or molecular weight between cross-links (M_c) from[27,28]

$$M_c = 3\rho RT/E \quad (1)$$

$$\upsilon_E = \rho/(2M_c) \quad (2)$$

where R and T are the gas constant and temperature, respectively; ρ is the polymer density. (In the calculations here, we have used the density of the polymer or the composites as measured by Archimedes'

principle by quickly immersing in water at 25 °C; see Supporting Information, Figure S1.) E was calculated from values for tensile stress versus strain in the 1−5% strain range. (In an ideal tetrafunctional network there are two chains per cross-link site, thus the factor of 2 in eq 2.)

NMR results were used to calculate cross-link density (υ_{NMR}) through the number of broken double bonds (C═C) during the HP&HT treatments. One broken double bond was assumed to result in one cross-link, and the consumption of double bonds was estimated from the area of the NMR signal before and after the HP&HT treatment, as obtained by integration of the relevant NMR peaks. With these assumptions, we find

$$\upsilon_{NMR} = \frac{D_{before} - D_{after}}{D_{before}} \frac{\rho}{68} \quad (3)$$

where D_{before} and D_{after} are the ratios of the double bonds peak area against total peak area in the NMR spectra before and after HP&HT treatment, respectively; 68 is the molecular weight of one repeat unit of PI containing one double bond, and ρ is the polymer density. We have used the density of the polymer or the composites as measured by Archimedes' principle. (An equation for calculation of cross-link density based on the peak areas depends on the cross-linking mechanism. Cross-linking can, e.g., occur without broken double bonds, which should still affect the ratio of the peak areas, but to a much lesser extent than if double bonds are consumed. Although the details of the cross-linking mechanism are not known with certainty, the method used here should still show the effect of pressure and CNT content on the cross-link density unless also the cross-linking mechanism is affected by these factors.)

To test the assumption of an interphase fraction that limits the swelling in a solvent, eq S1 of the Flory−Rehner equation was modified by assuming that an interphase layer of 10 nm does not swell at all after cross-linking and therefore behaves as an inert filler. The volume fraction of the network polymer in the swollen sample ϕ, which is used in analysis of the cross-link density, is then given by

$$\phi = [(m_d - m_f - m_i)/\rho]/[(m_d - m_f - m_i)/\rho + (m_s - m_d)/\rho_s] \quad (4)$$

where m_d, m_f, m_s, and m_i are respectively the masses of the sample dried after swelling, the filler, the swollen sample, and the interphase layer; ρ is the density of the polymer (0.92 g cm^{-3} for PI), and ρ_s is the density of the solvent (0.682 and 0.865 g cm^{-3} for n-heptane and toluene, respectively). The mass of the interphase layer was estimated from the dissolution data, which indicate that 1 wt % of MWCNTs can prevent 3.8 wt % of PI from dissolving in an approximately linear dependence of MWCNT content.

Atomic Force Microscopy (AFM) and High-Resolution Transmission Electron Microscopy (HRTEM). AFM analysis of the MWCNT/PI composite using tapping mode was carried out on a MultiMode AFM (Nanoscope IV Controller, Veeco Metrology) equipped with a LTESP probe (Veeco probe). The probe, which has a tip radius of ca. 8 nm and force constant of 48 N/m, operated at a resonant frequency of 190 kHz. AFM samples were cut by a Leica Reichert Ultracuts ultramicrotome equipped with diamond knife and subsequently placed on a silicon wafer (500 nm thick, 1.5 GPa treated PI) or the sample surface polished by a Leica EM FC 7 cryo-ultramicrotome equipped with diamond knife (1.0 and 0.5 GPa treated PI). HRTEM (Philips, TECNAI G2) equipped with a camera (Gatan 894 Carmera System) was used for imaging ultrathin sections (~50 nm by ultramicrotome, diamond knife) of samples. As shown in Figure 1, a HRTEM image of the HP&HT treated PIMW5 sample indicates good dispersion of MWCNTs in the composite. The tubular curved features are mostly single MWCNTs with a typical diameter of ~14 nm.

RESULTS AND DISCUSSION

Tensile stress−strain curves of high-pressure high-temperature (HP&HT) synthesized MWCNT/PI composites: 2.9, 4.8, and 9.1 wt % P-MWCNT filled PI composite (denoted as PIMW3, PIMW5, and PIMW9, respectively) and 9.1 and 16.7 wt % F-MWCNT filled PI composite (PIFMW9 and PIFMW17, respectively) are shown in Figure 2a. The samples were produced by first pressurizing to 1.5 GPa at room temperature, subsequently heating to 513 K, and finally annealing for 4 h before the samples were recovered (see Experimental Section). Control samples of pure PI were prepared by identical treatments. In addition, both composite and pure PI samples were also synthesized by the same procedure at lower pressures from 0.25 to 1.2 GPa. The tensile results of the 1.5 GPa treated samples (Figure 2a) show that the ultimate tensile strength (σ_{UTS}) and the Young's modulus (E) increased with increasing MWCNT content, but the ultimate strain at break (ε_B) was essentially unaffected. Except for PIFMW17, which showed ε_B of only ~10%, the composites and PI exhibited similar ε_B in the range 20−30%. The σ_{UTS} of PIMW3, PIMW5, and PIMW9 were 16.9, 20.2, and 24.1 MPa, respectively, or 114, 156, and 205% larger than that of PI treated under identical conditions (7.9 MPa).[21] The values of E were 207, 204, and 283 MPa, respectively, or 123, 119, and 204% larger than E of PI (93 MPa).[21] The F-MWCNT filled composites showed a similar tendency. The σ_{UTS} of PIFMW9 and PIFMW17 were 20.0 and 29.9 MPa, respectively (153 and 278% larger than PI), and the values of E were 223 and 400 MPa, respectively (140 and 330% larger than PI). Thus, the fractional increases of σ_{UTS} and E were about the same and the plot of σ_{UTS} against E is roughly linear (Figure 2b). Considering the CNT content, then PIMW3 shows the best reinforcement with a 2 times increase of σ_{UTS} by the addition of 3 wt % MWCNTs. A comparison with theoretical models (Support information) for CNT filled polymer composite (Figure 4b)[1] shows that the experimental values of E are slightly higher than values predicted for a composite with randomly distributed CNTs but lower than those of a composite with CNTs aligned along the stretching direction, which gives the highest possible E.

The HP&HT treatment changes the originally liquid mixtures to elastomers, i.e., cross-linked states.[29,30] The cross-linked structure is formed by a process in which either (i) polymer radicals, produced by e.g. scissoring, combine, or (ii) C═C double bonds are consumed, which may leave a polymer radical available for further cross-linking in a process similar to peroxide cross-linking of PI.[31] To study the change in microstructure, we have here

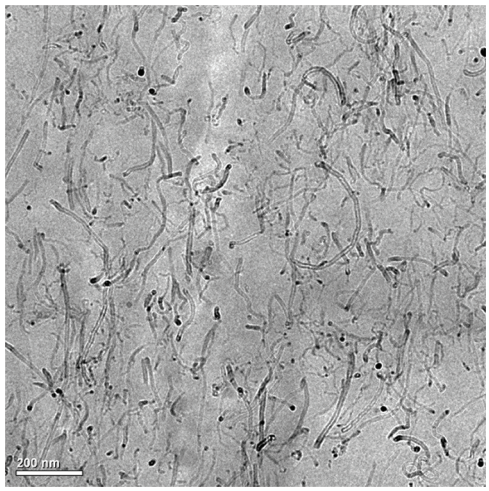


Figure 1. HRTEM of HP&HT treated PIMW5 composite. The scale bar is 200 nm.

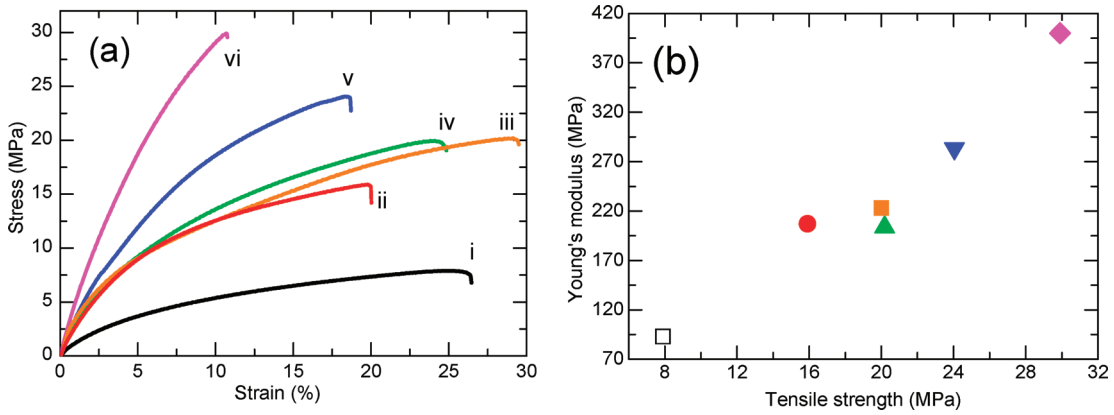


Figure 2. Stress–strain curves of PI and MWCNT/PI composites synthesized at 1.5 GPa. (a) Stress–strain curves of (i) PI, (ii) PIMW3, (iii) PIFMW9, (iv) PIMW5, (v) PIMW9, and (vi) PIFMW17 as indicated in the figure. (b) Young's modulus plotted against tensile strength for (□) PI, (●) PIMW3, (▲) PIMW5, (▼) PIMW9, (■) PIFMW9, and (◆) PIFMW17.

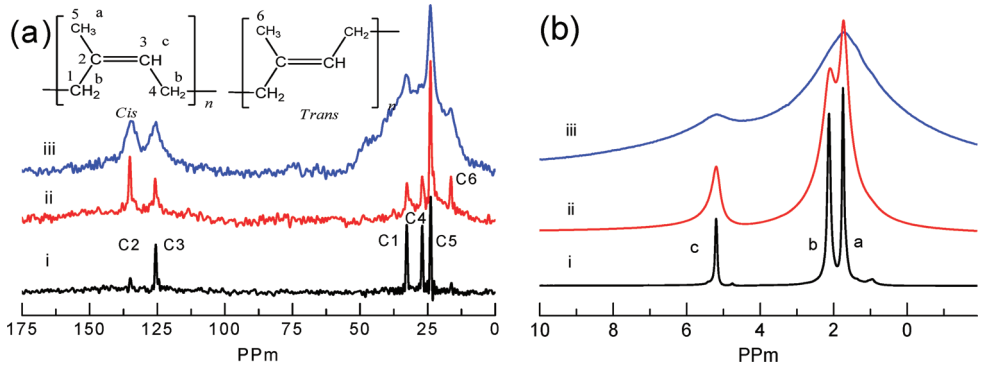


Figure 3. (a) Solid-state ^{13}C CP MAS NMR spectra of PI samples at 6 kHz sample spinning speed at room temperature (RT): (i) untreated, (ii) 1.0 GPa treated, and (iii) 1.5 GPa treated. Peak labels refer to the inset. (b) Solid-state ^{1}H MAS NMR at 10 kHz, RT: (i) untreated, (ii) 1.0 GPa treated, and (iii) 1.5 GPa treated. Peak labels refer to the inset in (a).

employed advanced high-resolution solid-state MAS NMR techniques.[30] As depicted in Figure 3a, the NMR spectrum of untreated PI shows resonances (peaks) at chemical shifts of 134.9, 125.5, 32.8, 27.0, and 23.9 ppm, which are assigned as indicated in the figure. This assignment is consistent with Buzaré et al.'s results of high cis PI.[32] After treatment at 1.0 GPa, the peak widths in the NMR spectra generally increased and the intensities of the C1 and C4 peaks were significantly reduced in comparison with the C5 peak. The C5 peak appears almost unaffected after the 1.0 GPa treatment, which implies that the methyl groups (C5) did not take part in the cross-linking process. A new pronounced NMR resonance appeared at 16.4 ppm, which is consistent with a resonance from trans PI,[32] suggesting a cis-to-trans conversion or that the extended chains form a trans configuration during HP&HT treatment. We note that cis-to-trans conversion has been found also during irradiation of PI, which concurrently consumed double bonds via two suggested mechanisms: cyclization and cross-linking.[33] Moreover, the intensity of the C2 peak at 134.9 ppm increased to about the same size as the C3 peak at 125.5 ppm, which indicates an enriched proton environment near C2 as a result of the cross-linking process. NMR spectra after 1.5 GPa treatments show similar, but even more pronounced, changes. The NMR peaks were significantly broadened; e.g., C1 and C5 appear superimposed on a broad peak in the 8–55 ppm range, and C2 and C3 have partly merged because of shorter spin–spin relaxation times T_2 and inhomogeneities caused by the cross-links. The broadness of the peaks precludes a complete assignment of new chemical configurations and, thus, detailed conclusions about the cross-linking mechanism. However, as discussed further below, the results can be used to estimate the effect of treatment pressure and CNT content on cross-link density.

The contribution of T_2 is determined by ^{1}H solid-state NMR (Hahn-echo pulse, 10 kHz, Figure 3b), which is also indicative of intramolecular and intermolecular dynamics. The NMR resonances at 1.8, 2.1, and 5.2 ppm were assigned to methyl ($-CH_3$), methylene ($-CH_2$), and methine group (=CH), respectively, in accordance with previously reported values.[25] T_2 was determined by fitting a function of the type exp $(-2\tau/T_2)$, in which the average of T_2 for the three resonances systematically decreased from 2.8×10^{-3} s in the untreated sample to 1.1×10^{-3} s after 1.0 GPa treatment and further down to 3.8×10^{-4} s for the 1.5 GPa treated sample (see Supporting Information, Figure S2). The decrease of T_2 is associated with a reduced molecular mobility, in agreement with a high degree of chemical cross-links. Thus, the T_2 results imply an increasing cross-link density υ with increasing treatment pressure, which gives a progressively stiffer structure due to shorter distances between network junctions.[34] Complementary swelling measurements (υ_{swell}) using toluene show that υ_{swell} increased from 4.3×10^{-4} mol cm^{-3} in the 1.0 GPa treated PI to 2.5×10^{-3} mol cm^{-3} in the 1.5 GPa treated PI. These results are in qualitative agreement with those derived from the Young's modulus (υ_E) using eqs 1 and 2 (see Experimental Section), which yielded $\upsilon_E = 3.0 \times 10^{-4}$ mol cm^{-3}

dx.doi.org/10.1021/ma202604d | Macromolecules 2012, 45, 2841–2849

at 1.0 GPa and 6.4×10^{-3} mol cm^{-3} at 1.5 GPa. Moreover, under the assumption that each cross-link has consumed one double bond, the cross-link density derived from NMR data (υ_{NMR}) using eq 3 (see Experimental Section) increases from 1.1×10^{-4} mol cm^{-3} at 1.0 GPa to 3.0×10^{-3} mol cm^{-3} at 1.5 GPa. The value at 1.0 GPa is uncertain because of the relatively small changes in the NMR resonances, but the result at 1.5 GPa indicates that the assumption provides a fair estimate of the cross-link density at high densities.

All three methods to calculate the cross-link density show that it increases strongly simultaneously as σ_{UTS} increases from ca. 1 to 7.9 MPa and E from ca. 3.3 to 93 MPa for a change of treatment pressure from 1 to 1.5 GPa. Since an increase of cross-link density typically improves σ_{UTS} and E,[35] we can conclude that this explains the reinforcement of pure PI.

Turning to the MWCNT/PI composites, Figure 4 (panels a and b) shows that both σ_{UTS} and E increase systematically with

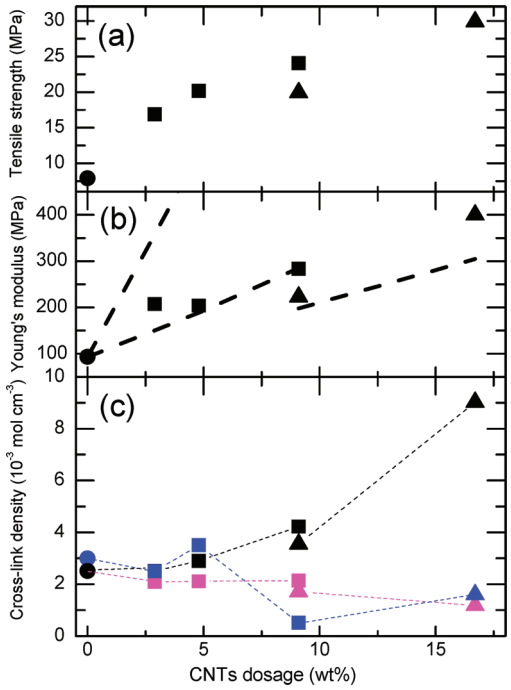


Figure 4. (a) Tensile strength, (b) Young's modulus, and (c) cross-link densities plotted against CNT content for 1.5 GPa HP&HT treated: (●) PI, (■) P-MWCNT filled, and (▲) F-MWCNT filled PI, respectively. The black dashed lines in (b) (from top to bottom) represent the Young's modulus predicted for composites with CNTs aligned in the stretching direction and randomly oriented in three dimensions, respectively (see Supporting Information). In (c), (●, ■, ▲, in black) represent υ_{swell} (toluene, eq S2), (■, ▲, in magenta) eq 4, and (●, ■, ▲, in blue) υ_{NMR} (eq 3). The dotted lines are only to guide the eye.

MWCNT content concurrently as the cross-link densities extracted from swelling experiments increase (Figure 4c, as well as Figure S3 in Supporting Information). As discussed in the previous paragraphs, there is a direct link between the (chemical) cross-link density of pure PI and its mechanical properties. It is therefore tempting to assume that the same correlation is valid for MWCNT filled PI and attribute the improved mechanical properties of the composites primarily or partly to an enhanced cross-linking rate in the presence of MWCNTs. However, results of the swelling method reflect both chemical cross-links and (trapped) entanglements or physical constraints. In HP&HT treated (low molecular weight) pure PI, chemical cross-links should be the paramount cause of reduced swelling, but this is not necessarily the case in the composites. We have previously found that HP&HT treated SWCNT/PI composites show a more significantly reduced swelling compared to pure PI treated under the same conditions.[21] Concurrently, SWCNTs seem to promote an effect similar to crazing, i.e., the bridging of microcracks by polymer fibrils when cracks develops in a polymer sample under tension. This effect was attributed to a disruption of the chemical cross-links due to the SWCNTs. To reconcile this result with the swelling results of higher cross-link density for SWCNT/PI composites than for pure PI, we conjectured that SWCNTs cause physical cross-links/constraints in the composites.[21] Since σ_{UTS} and E of the SWCNT/PI composites showed the same strong dependence on the measured cross-link density as pure PI, the total cross-link density in the composites, i.e., both chemical and physical cross-links/constraints, appears to reflect also the reinforcement of the samples. NMR was therefore applied to investigate the conjecture that extensive physical cross-links/constraints associated with the CNTs also arise during the HP&HT treatment and that these limit the swelling of the composites.

As shown in Figure 5a, ^{13}C CP-MAS spectra of 1.5 GPa treated MWCNT/PI composites and PI are similar; i.e., the MWCNTs do not cause significant changes. However, after treatment at 1.5 GPa, the ratio of the double-bond peak area to total peak area (D, Table S1, Supporting Information) had decreased from 29% to 23%, 24%, 22%, 28%, and 26% for PI, PIMW3, PIMW5, PIMW9, and PIFMW17, respectively. Thus, after the cross-linking process, which appears to consume double bonds, D of the high MWCNT content composites (9.1 and 16.7 wt %) was slightly larger than that of pure PI despite identical treatments. These results suggest that slightly fewer double bonds were consumed in the composites during HP&HT treatment, i.e., that the cross-linking process was weakly obstructed by the MWCNTs. We can conclude that the NMR results corroborate the hypothesis that CNTs in PI disrupt a continuous network of chemical cross-links and that this may explain the effect similar to crazing observed in HP&HT treated SWCNT/PI but not in HP&HT treated pure PI.[21] The results also supports Putz et al.'s[36] conjecture that MWCNT fillers disrupts the cross-linked network in epoxy and in particular at high cross-linking densities.

The slightly lower cross-link density in MWCNT/PI composite than PI, as measured by NMR, means that the higher cross-link density of the composites obtained from υ_{swell} and υ_{E} cannot be due to more chemical cross-links. We have attributed it to physical cross-links/constraints,[21] and the results of strongly reduced swelling indicate a surprisingly strong interaction between the CNTs and the polymer which is also reflected in the tensile results. The origin of this interaction is unknown but polymer wrapping and/or coating of the CNTs is one possibility,[37] and after the HP&HT treatment or perhaps after the strong sonication used to mix the CNTs, free radicals in the polymer chains may provide an additional source of interaction.[38] Moreover, cross-linking under highly densified conditions gives an irreversible densification that promote interfacial interaction between the CNTs and PI. The effect seems similar to that shown by rubber with carbon black fillers, which is referred to as bound rubber.[37] We may visualize this by a simplified two-layer model as described schematically in Figure 5b,c. The polymer matrix is here divided into an interfacial layer, or interphase, and a more distant layer. The former has properties affected by the

dx.doi.org/10.1021/ma202604d | Macromolecules 2012, 45, 2841−2849

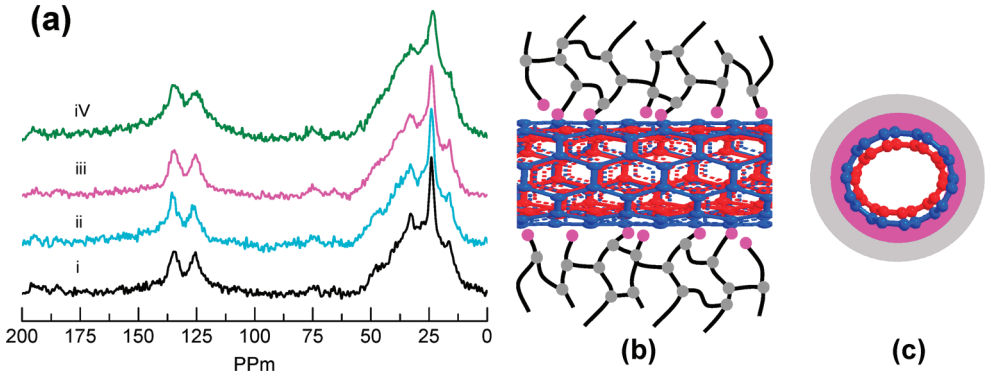


Figure 5. (a) Solid-state ^{13}C CP MAS NMR spectra obtained at 6 kHz spinning speed and at RT of (i) 1.5 GPa treated PI, (ii) 1.5 GPa treated PIMW3, (iii) 1.5 GPa treated PIMW5, and (iv) 1.5 GPa treated PIFMW17. (b, c) Schematic views of HP&HT cross-linked MWCNT/PI composite: (b) CNT side view and (c) CNT cross-sectional view. The gray dots indicate cross-links (shared electrons) after HP&HT treatment, and the magenta dots indicate radicals which are unable to form cross-links with other PI chains because of MWCNT hindrance. The magenta region represents an interphase layer with strong interfacial interaction and the gray region a more loosely connected layer in the bulk of the polymer.

interfacial interaction between the chains and the CNTs whereas the latter has properties similar to bulk PI.

In order to probe the possible existence of an interphase layer coated on the CNTs,[39] solid samples of (untreated) high molecular weight PI (LPI, M_W: 800 000, 97% cis, SP^2) and 4.8 and 9.1 wt % P-MWCNT filled LPI (LPIMW5, LPIMW9) were immersed in toluene and *n*-heptane. The solid LPI dissolved completely in both solvents, but this was not the case for LPIMW5 and LPIMW9, despite that the composites were kept in the solvent for more than 48 h. The composites remained in a swollen gel-like state, which indicate the presence of chemical and/or trapped physical cross-links, which were not present in LPI. The gel-like composites were extracted from the solvent, dried until the weight remained constant, and then weighed. The results showed that about 24% (LPIMW5) and 42% (LPIMW9) of the original weight remained. Since the solvents did not show signs of dissolved MWCNTs, the loss of weight must be mainly due to dissolved LPI. This indicates that there is a fraction of LPI which is more strongly attached to the MWCNTs, i.e., an interphase layer of LPI wrapped or coated around MWCNTs like bound rubber in composites with carbon black.[37] Assuming that all the MWCNTs remained in the gel fraction and, thus, were extracted, the weight percentage of MWCNTs increased to 20% and 22% in the extracted fractions of LPIMW5 and LPIMW9, respectively. The almost equal concentration of MWCNTs suggests that a surface related interaction between the MWCNTs and LPI prevents dissolution of the composites. The ca. 21 wt % of MWCNT in both samples corresponds roughly to a 10 nm polymer coating layer on the MWCNTs.

It seems reasonable to assume that the high cross-link densities calculated from the swelling results are due to a fraction of PI in which swelling is strongly limited by the PI–MWCNT interaction and presumably an interphase layer like that visualized in Figure 5c. We may test this assumption by subtracting a conjectured interphase fraction in the equation used for the analysis of the swelling experiments (eq S2). We here assume that an interphase layer of 10 nm, i.e., the same thickness as deduced in the dissolution experiment, does not swell at all after cross-linking and therefore behaves as an inert filler.

The cross-link densities calculated based on these assumptions (eq 4) are plotted against MWCNT content in Figure 4c, magenta symbols. The decreasing cross-link density with increasing MWCNT content is now in agreement with the NMR results, which indicates that the MWCNTs disrupt the chemical cross-linking process. This disruption near the CNT–PI interface should make the chemical cross-link density spatially inhomogeneous with a slightly lower density in the interphase layer than further away. It should also cause free radicals, or unpaired free electrons, to accumulate near the CNT–PI interface, as illustrated schematically in Figure 5b.

The pressure dependence of υ_{swell} for PIMW5 and PI derived from eq S1, i.e., without subtraction of an interfacial layer, is plotted in Figure 6b. The υ_{swell} of the composite is significantly higher than that of pure PI, which we attribute to physical

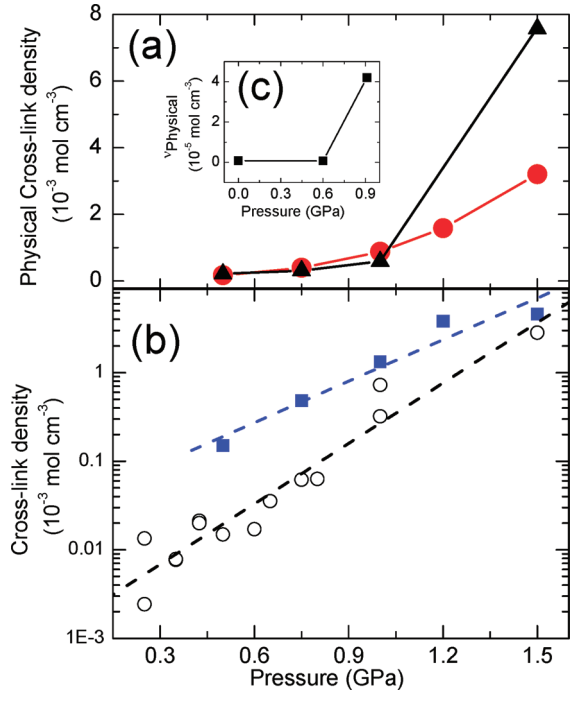


Figure 6. (a) Physical cross-link density (see text) of PIMW5 plotted versus treatment pressure as obtained from (●, in red) υ_{swell} (*n*-heptane, eq S1) and (▲) υ_E. (b) The υ_{swell} (*n*-heptane, eq S1) plotted versus treatment pressure for (○) PI and (■, in blue) PIMW5. (c) Physical cross-link density (*n*-heptane, eq S1) of LPIMW5 (■) plotted versus pressure for a sample annealed slightly above the glass transition temperature.

dx.doi.org/10.1021/ma202604d | *Macromolecules* 2012, 45, 2841–2849

cross-links/constraints induced by the MWCNTs. However, if these were only associated with the presence of the CNTs, then the conditions of the cross-linking process, i.e., the HP&HT treatment, would be irrelevant and the number, or the effect, of such cross-links would be constant. To study this, we may calculate a number for the "physical cross-link density" by assuming that the chemical cross-link density in the composites is identical to that in the similarly treated pure PI. (Our NMR data indicate that it is slightly less.) The difference must be due to cross-links/constraints induced by the presence of the CNTs, which restrain PI from swelling. In principle, these could be single chain entanglements but are more likely associated with mesoscopic PI domains, like thin layers on the CNTs, that do not swell and are therefore not locally confined as much as chemical cross-links. However, the calculated density should reflect the number of homogeneously distributed and locally confined (physical) cross-links that can cause the observed reduction of swelling.

We have calculated the physical cross-link density, as defined by the difference between υ_{swell} of PIMW5 and that of pure PI, i.e., $\upsilon_{swell,composite} - \upsilon_{swell,PI}$, as a function of treatment pressure. The results are depicted in Figure 6a and show that the physical cross-links/constraints increases with increasing pressure. A similar calculation using the tensile results ($\upsilon_{E,composite} - \upsilon_{E,PI}$) shows qualitatively the same behavior (Figure 6a). It thus seems as a higher treatment pressure augment the effect of physical cross-links/constraints. In terms of an interphase layer with highly constrained, or bound, PI the results imply an increase of its thickness with increasing treatment pressure.

The indication of pressure-induced enhancement of entanglements/physical constrains was further investigated by a study of LPIMW5 composites (Figure 6c) and LPI. The samples were treated at 0.60 GPa and 320 K or at 0.91 GPa and 380 K for 4 h. These conditions were chosen to study the effect of pressure on the CNT−PI interfacial contact by treatment above the glass transition temperature under pressure,[40] but still at a sufficiently low temperature to avoid chemical cross-linking. Absence of chemical cross-links was also verified as both the 0.60 and the 0.91 GPa treated LPI samples dissolved in toluene after stirring at 300 K. (But we note that the treatment increases PI entanglements because the LPI treated at 0.91 GPa needed significantly longer time to dissolve than untreated samples and the 0.60 GPa treated sample.) The physical cross-link density of LPIMW5, obtained by swelling in *n*-heptane for 48 h, increased from 8.5×10^{-7} mol cm^{-3} for the untreated sample to 4.2×10^{-5} mol cm^{-3} after treatment at 0.91 GPa. (The corresponding cross-link densities of pure LPI were 0 and 2.2×10^{-6} mol cm^{-3}, respectively.) These results support that the CNT−PI interfacial interaction increase with increasing treatment pressure.

Apparently, the enhancement of the composites' tensile properties with increasing treatment pressure could be partly or predominantly due to an augmented interfacial layer, which is reflected in the rise of physical cross-links/constraints. An augmented layer can provide such an effect via better load transfer between the three domains: bulk PI−interface layer−MWCNT and/or better distribution of stresses. Crack initiation in CNT composites is likely to occur near CNT tips due to high local stresses and distribution of stresses in the bulk PI can be mediated by an interfacial layer.

Further indications of a PI layer on the MWCNTs surface are provided by microscopy images. As discussed above, swelling of untreated LPIMW5 and LPIMW9 indicated entanglement or some other surface interaction between the MWCNTs and LPI, which resulted in a network that prevented dissolution. To study a similar effect in PI, the untreated PIMW5 composite was redispersed in toluene again,[41] whereas the HP&HT treated PIMW5 was cut by an ultramicrotome and examined by AFM and HRTEM.

As shown in Figure 7b, an image of untreated PIMW5 indicates polymer coating near the tip of one single tube (position 1). The lack of coating at position 2 shows that it is a single MWCNT, which is particularly obvious in the comparison of the height profiles (Figure 7d). The corresponding amplitude image shown in Figure 7c supports the existence of a polymer layer on the MWCNT. We find it noteworthy that there is no significant amount of visible PI deposited on the substrate without a

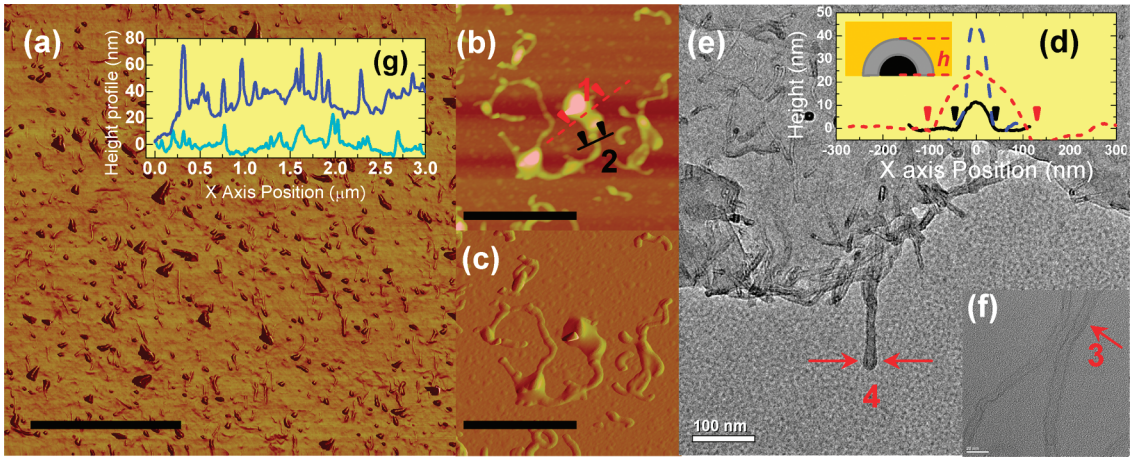


Figure 7. AFM images of (a) 1.5 GPa treated PIMW5 (phase image, *z* range = 50°), (b) untreated PIMW5 (height image), (c) untreated PIMW5 (amplitude image); the scale bars in (a), (b), and (c) are 1 μm. (d) Height profile of treated and untreated PIMW5 measured along the lines in (b) and the corresponding height image of (a). The markers in (d) show the corresponding positions of the markers shown in (b). The inset in (d) shows schematically that the measured height, *h*, may be the combined height of a MWCNT and an interphase layer, which adheres well to the CNTs. HRTEM images of (e) 1.5 GPa treated PIMW5 and (f) untreated PIMW5 composite; the scale bars in (e) and (f) are 100 and 20 nm, respectively. (g) Height profiles of PIMW5 sample treated at 1.0 GPa (bottom) and 1.5 GPa (top).

dx.doi.org/10.1021/ma202604d | *Macromolecules* 2012, 45, 2841−2849

MWCNT, which suggests an affinity between PI and MWCNTs giving PI coated/wrapped MWCNTs.

It is more difficult to find a corresponding feature in the sample by HRTEM. The HRTEM image shown in Figure 7f indicates only a thin coating by a slightly thicker diameter (~15 nm) near the arrows (position 3) than at other places (~12 nm). A reason for the lack of a visible coating layer can be that the carbon coating of the TEM grid reduces the contrast and/or that the coated polymer has low contrast compared to the MWCNTs.[41]

For the 1.5 GPa treated PIMW5 sample (Figure 7a), the height of a typical tubular feature was ca. 20−30 nm as measured by AFM (see the height profile in Figure 7g, top, where most of the peaks were linked to CNTs oriented parallel with the surface by direct comparison with the AFM surface image). The corresponding plot of the 1.0 GPa treated PIMW5 sample (Figure 7g, bottom) shows peaks with heights of ~15 nm, whereas only a few peaks of ~10 nm peak heights could be detected in a 0.5 GPa treated PIMW5 sample. Consequently, the results corroborate the existence of a strongly bound layer with a thickness that increases with increasing treatment pressure, from about 10 nm without pressure treatment up to about 30 nm after 1.5 GPa treatment, as depicted in Figure 7d. In HRTEM, a coating can be observed only on MWCNTs pulled out of the matrix. Only a few such MWCNTs were detected, and the MWCNT in Figure 7e (position 4) appears coated with a polymer layer, especially at the tip where the diameter is ~22 nm (see arrows). The noncoated MWCNT had a typical diameter of ca. 12 nm in the HRTEM images.

We note that only a few MWCNTs indicate pull-out of from the matrix and that some MWCNT tips, shown in Figure 7e, are close to the edges. This is in contrast with results of many composites synthesized at ambient conditions[42] as well as SWCNT/PI composites synthesized at 1.0 GPa,[21] which showed more signs of CNT pull-out. These results suggest that the main reason for failure change gradually with increasing treatment pressure from CNT pull-out at low pressures to crack initiation near the CNT tips for samples with the highest cross-link densities, which are produced at very high pressure.

The interphase polymer layer, as reflected in the AFM and HRTEM results and indicated by the swelling experiments, appears to be the CNT/rubber correspondence to "bound rubber" in carbon black/rubber composites and is referred to as "strong physical adsorption" in other CNT/polymer system.[38,43,44] Qu et al.[37] have recently studied this effect in a carbon black/rubber composite, and their results suggest the existence of an interface layer with 1 order of magnitude higher stiffness than that of the rubber matrix. Swelling measurements of carbon black filled PI composites also indicate a bound surface coating, but it is not as suggested here for CNT composites linked to tensile reinforcement.[21] This seems reasonable considering the difference in the filler geometry and strength between carbon black and CNT fillers. It also seems reasonable that the extent and the effects of an interfacial layer are more pronounced in CNT composites than carbon black composites because of larger specific surface area of CNTs. In the case of CNTs, the interfacial layer appears to be quantitatively described by swelling results, augmented by high-pressure treatment and correlated with the mechanical properties. The correlation between the cross-link density obtained from swelling results and the mechanical properties suggests that the interface or "bound" PI layer is linked to the degree of reinforcement.

Figure 8 shows results of σ_{UTS} and E of both MWCNT/PI and SWCNT/PI[21] composites plotted against υ_{swell} (for swelling in toluene, see Figure S4 in Supporting Information). The samples were treated in the 0.5−1.5 GPa range and include CNT contents in the 1−20 wt % range. As shown in the figure, the mechanical properties appear to be correlated with υ_{swell}, which reflects changes in both chemical cross-link density and interfacial or bound PI. The correlation holds roughly independent of CNT content, type of CNTs (MWCNTs or SWCNTs), and treatment pressure. We find two possibilities for a link between reinforcement and an augmented interfacial layer: (i) improved load transfer and (ii) reduced tendency of crack initiation/propagation. These effects, in parallel with changes in the chemical cross-link density, seem as the most likely explanation for the reinforcement observed with increasing treatment pressure. The observed correlation between υ_{swell} and reinforcement with increasing CNT content may reflect the increasing extent of load transfer through interfacial layers, which implies that poor reinforcement, e.g. due to agglomeration of CNTs, can be revealed by swelling measurements.

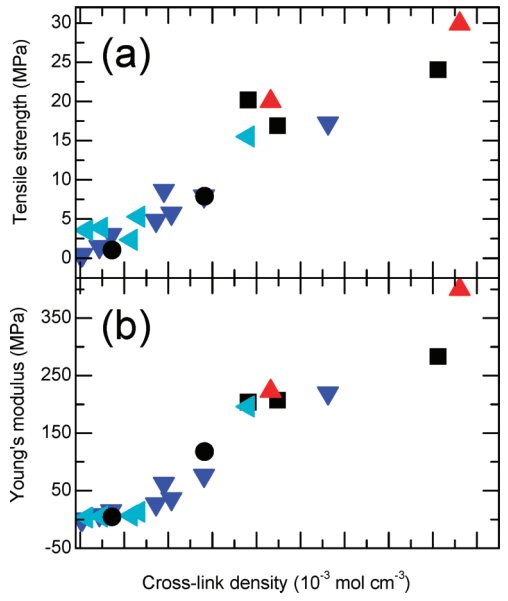


Figure 8. (a) Tensile strength and (b) Young's modulus plotted against υ_{swell} (*n*-heptane) for HP&HT treated (●) PI (at 1.0[21] and 1.5 GPa), (■) P-MWCNT filled (treated at 1.5 GPa), (▲, in red) F-MWCNT filled (treated at 1.5 GPa), (◀, in cyan) P-MWCNT filled (treated in the 0.5−1.2 GPa range), and (▼, in blue) SWCNT filled PI (treated in the 0.5−1.5 GPa range).

■ CONCLUSIONS

MWCNT/PI composites and pure PI have been cross-linked by high-pressure high-temperature treatment, which makes it possible to investigate the effects of a gradually increasing cross-link density without interference of vulcanization chemicals. The strongest composites were produced by treatment at 1.5 GPa, e.g., the tensile strength of PI increased 2 times by adding 3 wt % MWCNTs. Swelling experiments show that composites swell less than pure PI despite identical treatments, which implies higher cross-link densities in the composites. But NMR results and analysis of cracks after tensile testing[21] indicate that the number of chemical cross-links in the MWCNT filled PI are less than those in PI, which precludes that CNTs promote the

chemical cross-linking rate and rather obstruct cross-linking. Still, the mechanical properties of the composites increase with increasing cross-link densities, as obtained from swelling results, which suggests that the effect that restrain swelling in the composites also provides and/or reflects reinforcement. Results of AFM and solution experiments indicate that the restrained swelling is due to a tightly bound interfacial layer on the MWCNTs, which is augmented by cross-linking under high-pressure conditions. This explains the results of reduced swelling in a solvent and the concurrent increase of reinforcement. A similar reduction of swelling is detected with increasing CNT content, which also in this case reflects reinforcement and indicates a link between the amount of interfacial layer and the extent of (layer) mediated load transfer.

■ ASSOCIATED CONTENT

Supporting Information

Description of swelling experiments; theoretical calculation of E of a composite; results of T_2 of untreated PI, and 1.0 and 1.5 GPa treated PI; calculation of cross-link densities from NMR and tensile results, and complementary swelling result using *n*-heptane or toluene. This material is available free of charge via the Internet at http://pubs.acs.org.

■ AUTHOR INFORMATION

Corresponding Author

*E-mail: ove.andersson@physics.umu.se.

Notes

The authors declare no competing financial interest.

■ ACKNOWLEDGMENTS

We are grateful for financial support from Magn. Bergvalls Foundation, Kempe Foundation, and the Swedish Research Council. We thank Dr. Mingguang Yao, Jilin University, for help with TEM analysis, Lenore Johansson for the help with the cryo-ultramicrotome, and M. Azam for assistance with laboratory work.

■ REFERENCES

(1) Coleman, J. N.; Khan, U.; Blau, W. J.; Gun'ko, Y. K. *Carbon* **2006**, *44*, 1624−1652.
(2) Balazs, A. C.; Emrick, T.; Russell, T. P. *Science* **2006**, *314*, 1107−1110.
(3) Moniruzzaman, M.; Winey, K. I. *Macromolecules* **2006**, *39*, 5194−5205.
(4) Ajayan, P. M.; Tour, J. M. *Nature* **2007**, *447*, 1066−1068.
(5) Iijima, S. *Nature* **1991**, *354*, 56−58.
(6) Iijima, S.; Ichihashi, T. *Nature* **1993**, *363*, 603−605.
(7) Novoselov, K. S.; Geim, A. K.; Morozov, S. V.; Jiang, D.; Zhang, Y.; Dubonos, S. V.; Grigorieva, I. V.; Firsov, A. A. *Science* **2004**, *306*, 666−669.
(8) Chae, H. G.; Liu, J.; Kumar, S. *Carbon Nanotubes, Properties and Applications*; CRC Press: Boca Raton, FL, 2006; pp 214−252.
(9) Yu, M.-F.; Files, B. S.; Arepalli, S.; Ruoff, R. S. *Phys. Rev. Lett.* **2000**, *84*, 5552.
(10) Yu, M.-F.; Lourie, O.; Dyer, M. J.; Moloni, K.; Kelly, T. F.; Ruoff, R. S. *Science* **2000**, *287*, 637−640.
(11) Treacy, M. M. J.; Ebbesen, T. W.; Gibson, J. M. *Nature* **1996**, *381*, 678−680.
(12) Lu, J. P. *Phys. Rev. Lett.* **1997**, *79*, 1297.
(13) Baughman, R. H.; Zakhidov, A. A.; de Heer, W. A. *Science* **2002**, *297*, 787−792.
(14) Bose, S.; Khare, R. A.; Moldenaers, P. *Polymer* **2010**, *51*, 975−993.
(15) Moniruzzaman, M.; Chattopadhyay, J.; Billups, W. E.; Winey, K. I. *Nano Lett.* **2007**, *7*, 1178−1185.
(16) Ma, W.; Liu, L.; Zhang, Z.; Yang, R.; Liu, G.; Zhang, T.; An, X.; Yi, X.; Ren, Y.; Niu, Z.; Li, J.; Dong, H.; Zhou, W.; Ajayan, P. M.; Xie, S. *Nano Lett.* **2009**, *9*, 2855−2861.
(17) Sui, X.; Wagner, H. D. *Nano Lett.* **2009**, *9*, 1423−1426.
(18) Young, K.; Blighe, F. M.; Vilatela, J. J.; Windle, A. H.; Kinloch, I. A.; Deng, L.; Young, R. J.; Coleman, J. N. *ACS Nano* **2010**, *4*, 6989−6997.
(19) Zhang, X.; Liu, T.; Sreekumar, T. V.; Kumar, S.; Moore, V. C.; Hauge, R. H.; Smalley, R. E. *Nano Lett.* **2003**, *3*, 1285−1288.
(20) Bhattacharyya, S.; Sinturel, C.; Bahloul, O.; Saboungi, M.-L.; Thomas, S.; Salvetat, J.-P. *Carbon* **2008**, *46*, 1037−1045.
(21) Tonpheng, B.; Yu, J.; Andersson, B. M.; Andersson, O. *Macromolecules* **2010**, *43*, 7680−7688.
(22) Yu, J.; Tonpheng, B.; Gröbner, G.; Andersson, O. *Carbon* **2011**, *49*, 4858−4866.
(23) Yu, J.; Tonpheng, B.; Andersson, O. *Macromolecules* **2010**, *43*, 10512−10520.
(24) Lindström, F.; Williamson, P. T. F.; Gröbner, G. *J. Am. Chem. Soc.* **2005**, *127*, 6610−6616.
(25) Poliskie, G. M.; Gleason, K. K. *Polym. Compos.* **2005**, *26*, 799−805.
(26) Flory, P. J. *J. Chem. Phys.* **1950**, *18*, 108−111.
(27) Flory, P. J.; John Rehner, J. *J. Chem. Phys.* **1943**, *11*, 512−520.
(28) Gent, A. N.; Kaang, S. Y. *J. Polym. Sci., Part B: Polym. Phys.* **1989**, *27*, 893−911.
(29) Bellander, M.; Stenberg, B.; Persson, S. *J. Appl. Polym. Sci.* **1999**, *73*, 2799−2806.
(30) Yu, J.; Tonpheng, B.; Grobner, G.; Andersson, O. *J. Mater. Chem.* **2011**, *21*, 13672−13682.
(31) Oh, S. J.; Koenig, J. L. *J. Polym. Sci., Part B: Polym. Phys.* **2000**, *38*, 1417−1423.
(32) Buzaré, J.-Y.; Silly, G.; Emery, J.; Boccaccio, G.; Rouault, E. *J. Appl. Polym. Sci.* **2003**, *87*, 3−8.
(33) Golub, M. A.; Danon, J. *Can. J. Chem.* **1965**, *43*, 2772−2785.
(34) Orza, R. A.; Magusin, P. C. M. M.; Litvinov, V. M.; van Duin, M.; Michels, M. A. J. *Macromolecules* **2007**, *40*, 8999−9008.
(35) Nielsen, L. E.; Landel, R. F. *Mechanical Properties of Polymers and Composites*, 2nd ed.; Marcel Dekker: New York, 1994.
(36) Putz, K. W.; Palmeri, M. J.; Cohn, R. B.; Andrews, R.; Brinson, L. C. *Macromolecules* **2008**, *41*, 6752−6756.
(37) Qu, M.; Deng, F.; Kalkhoran, S. M.; Gouldstone, A.; Robisson, A.; Van Vliet, K. J. *Soft Matter* **2011**, *7*, 1066−1077.
(38) Verge, P.; Peeterbroeck, S.; Bonnaud, L.; Dubois, P. *Compos. Sci. Technol.* **2010**, *70*, 1453−1459.
(39) Donnet, J.-b.; Custodero, E. *Science and Technology of Rubber*, 3rd ed.; Elsevier Academic Press: Amsterdam, 2005; p 383.
(40) Pawlus, S.; Sokolov, A. P.; Paluch, M.; Mierzwa, M. *Macromolecules* **2010**, *43*, 5845−5850.
(41) A very small amount of the composite sample (less than 10 mg) was redispersed in ca. 20 mL of toluene by high-power sonication for 30 min (75% power, 20 s on 20 s off). Subsequently, the mixture was left for sedimentation for 30 min so that, if energetically favorable, the CNTs could become coated/wrapped by the polymer. A silicon wafer or carbon film coated TEM grid was quickly dipped in the solution and air-dried 24 h before microscopic examination.
(42) Qian, D.; Dickey, E. C.; Andrews, R.; Rantell, T. *Appl. Phys. Lett.* **2000**, *76*, 2868−2870.
(43) Nah, C.; Lim, J. Y.; Cho, B. H.; Hong, C. K.; Gent, A. N. *J. Appl. Polym. Sci.* **2010**, *118*, 1574−1581.
(44) Shim, B. S.; Zhu, J.; Jan, E.; Critchley, K.; Ho, S.; Podsiadlo, P.; Sun, K.; Kotov, N. A. *ACS Nano* **2009**, *3*, 1711−1722.

Macromolecules

Article

pubs.acs.org/Macromolecules

Side-Chain-Controlled Self-Assembly of Polystyrene–Polypeptide Miktoarm Star Copolymers

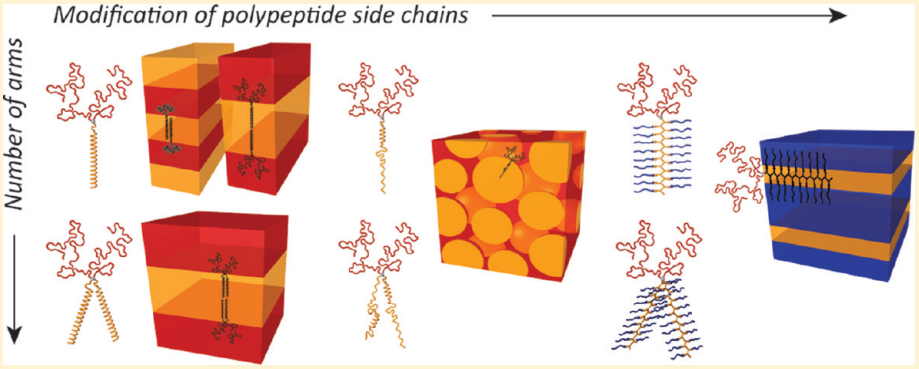
Susanna Junnila,[†] Nikolay Houbenov,[†] Anastasis Karatzas,[‡] Nikos Hadjichristidis,[‡,⊥] Akira Hirao,[§] Hermis Iatrou,*[,‡] and Olli Ikkala*[,†]

[†]Molecular Materials, Department of Applied Physics, Aalto University (previously Helsinki University of Technology), P.O. Box 15100, 00076 Aalto, Finland

[‡]Department of Chemistry, University of Athens, Panepistimiopolis, Zografou, 15771 Athens, Greece

[§]Polymeric and Organic Materials Department, Graduate School of Science and Engineering, Tokyo Institute of Technology, Tokyo 152-8552, Japan

Supporting Information



ABSTRACT: We show how the self-assembly of miktoarm star copolymers can be controlled by modifying the side chains of their polypeptide arms, using A_2B and A_2B_2 type polymer/polypeptide hybrids (macromolecular chimeras). Initially synthesized PS_2PBLL and PS_2PBLL_2 (PS, polystyrene; PBLL, poly(ε-*tert*-butyloxycarbonyl-L-lysine)) miktoarms were first deprotected to $PS_2PLLHCl$ and $PS_2PLLHCl_2$ miktoarms (PLLHCl, poly(L-lysine hydrochloride)) and then complexed ionically with sodium dodecyl sulfonate (DS) to give the supramolecular complexes $PS_2PLL(DS)$ and $PS_2(PLL(DS))_2$. The solid-state self-assemblies of these six miktoarm systems were studied by transmission electron microscopy (TEM), Fourier transform infrared spectroscopy (FTIR), and small- and wide-angle X-ray scattering (SAXS, WAXS). The side chains of the polypeptide arms were observed to have a large effect on the solubility, polypeptide conformation, and self-assembly of the miktoarms. Three main categories were observed: (i) lamellar self-assemblies at the block copolymer length scale with packed layers of α-helices in PS_2PBLL and PS_2PBLL_2; (ii) charge-clustered polypeptide micelles with less-defined conformations in a nonordered lattice within a PS matrix in $PS_2PLLHCl$ and $PS_2PLLHCl_2$; (iii) lamellar polypeptide–surfactant self-assemblies with β-sheet conformation in $PS_2PLL(DS)$ and $PS_2(PLL(DS))_2$ which dominate over the formation of block copolymer scale structures. Differences between the 3- and 4-arm systems illustrate how packing frustration between the coil-like PS arms and rigid polypeptide conformations can be relieved by the right number of arms, leading to differences in the extent of order.

INTRODUCTION

Nonlinear block copolymer architectures such as graft copolymers, star block copolymers, miktoarm star copolymers, and more complex architectures, including H-shaped and cyclic block copolymers, have recently gained much attention.[1−7] In addition to the total degree of polymerization (N), relative sizes of the blocks (f_i), and the interaction parameters (χ_{ij}) between the different monomer units, the molecular architecture also plays a significant role.

Miktoarm star copolymers are chemically asymmetric star-shaped polymers in which all blocks originate from a single branching point. In binary A_mB_n miktoarm systems composed of m blocks of polymer A and n blocks of polymer B, the minimization of interfacial tension and stretching free energy of the arms results in shifted phase boundaries compared to AB diblock copolymers.[8−10] This means that different linear and miktoarm architectures with the same volume fractions of A and B can present dissimilar self-assembled structures. The A_2B type miktoarm star copolymers are often referred to as "Y-shaped" block copolymers and can also be considered as the simplest graft copolymers.[11,12] Lamellar, cylindrical, and bicontinuous cubic morphologies have been observed for this

Received: December 20, 2011
Revised: February 22, 2012
Published: March 7, 2012

ACS Publications © 2012 American Chemical Society

architecture.[8,13,10] At large volume fractions of B, the two A arms are forced to the concave side of the interface, leading to disordered wormlike micelles[13] and spheres.[14] For A_2B_2 miktoarm star copolymers, classical block copolymer phases including lamellar, cylindrical, and spherical morphologies have been reported.[15] Interestingly, the architecturally symmetric A_nB_n systems, in general, show larger lamellar periodicities than the corresponding diblock copolymers due to chain crowding near the junction point, which leads to an increase in chain stretching.[16,17] This effect disappears with increasing arm length.[15]

Incorporation of rigid-rod-like blocks in block copolymers increases conformational asymmetry and introduces new interactions between the anisotropic rods, leading to self-assembly behavior different from all-coil block copolymers.[18] Polypeptide blocks which adopt the α-helical conformation have been extensively used as rigid rods in linear block copolymers[19] and have recently been employed in A_2B,[20] AB_2,[21] and ABC[22,23] miktoarm systems. In the solid state, the packing of the α-helical rods typically leads to lamellar self-assemblies regardless of the volume fractions of the components.[24−26] The α-helices are not necessarily ideal, fully extended rods,[27] as their folding has been observed to depend on the length of the blocks,[24] the exact chemical nature of these blocks,[24,28] and the hydrogen-bonding capability of the casting solvent.[29]

Supramolecular interactions, particularly complexation with surfactants, have been widely used to create new self-assembled materials from block copolymers[30,31] and homopolypeptides.[32−34] Moreover, miktoarm star copolymer complexes with oppositely charged homopolymers[35] and surfactants[36] have also been studied. In addition, intramolecular association of different arms has been employed to construct pH-responsive supramolecular self-assemblies.[37,38]

Our hypothesis is that the steric packing constraints, imposed by the miktoarm architecture, together with the polypeptide conformation and possible additional supramolecular interactions, will allow tunable self-assemblies if we learn to properly control the extent of frustration. This has encouraged us to continue our studies of ABC miktoarm chimera with one polypeptide and two coil-like arms[23] with a series of A_2B and A_2B_2 type miktoarm chimeras with two polystyrene and one or two polypeptide arms. The conformation and mutual interactions of the polypeptide blocks have been modified by electrostatics and complexation with surfactants, by using poly(L-lysine) chains with *N-tert*-butyloxycarbonyl (Boc) protecting groups, their deprotected hydrochloride salt forms, and supramolecular complexes of the latter with low molecular weight surfactant. We have studied the self-assemblies by transmission electron microscopy (TEM), Fourier transform infrared spectroscopy (FTIR), and small- and wide-angle X-ray scattering (SAXS, WAXS).

EXPERIMENTAL SECTION

Synthesis. The synthesis of PS_2PBLL and PS_2PBLL_2 miktoarms has been reported previously.[39] This includes the preparation of in-chain mono- and diamino-functionalized polymers, abbreviated as PS-NH_2-PS and PS-$(NH_2)_2$-PS, by anionic polymerization high-vacuum techniques and appropriate linking chemistry. After this, the amino groups are used for the ring-opening polymerization of *ε-tert*-butyloxycarbonyl-L-lysine *N*-carboxyanhydride. $PS_2PLLHCl$ and $PS_2PLLHCl_2$ miktoarms were prepared by deprotecting the corresponding PBLL miktoarms by dissolving the polymers in dichloromethane (CH_2Cl_2, about 20% w/v) and adding an equal volume of trifluoroacetic acid (TFA) at room temperature. The solution was stirred for 2 h, after which the solvents (TFA and CH_2Cl_2) were removed by distillation in vacuum. Depending on the solubility of the final polymers, the solid polymers were dissolved or suspended in water and purified by dialysis in Milli-Q water to remove low-molecular-weight species from deprotection. Completion of the deprotection was verified by NMR spectroscopy in DMSO-d_6.[40] The molecular characteristics of the miktoarms are collected in Table 1, and the synthesis and the molecular structures are shown in Scheme 1.

Table 1. Molecular Characteristics of the Miktoarm Star Copolymers

miktoarm	$M_n \times 10^{-3}$ (g/mol)	PS−peptide composition (wt %)	M_w/M_n[a]
PS_2PBLL	31.5[a]	60.5−39.5[b]	1.02
PS_2PBLL_2	41.2[a]	48.9−51.1[b]	1.21
$PS_2PLLHCl$	28.0[c]	68.0−32.0[c]	
$PS_2PLLHCl_2$	35.3[c]	57.0−43.0[c]	
$PS_2PLL(DS)$	39.7[c]	48.0−52.0[c]	
$PS_2(PLL(DS))_2$	55.1[c]	36.6−63.4[c]	

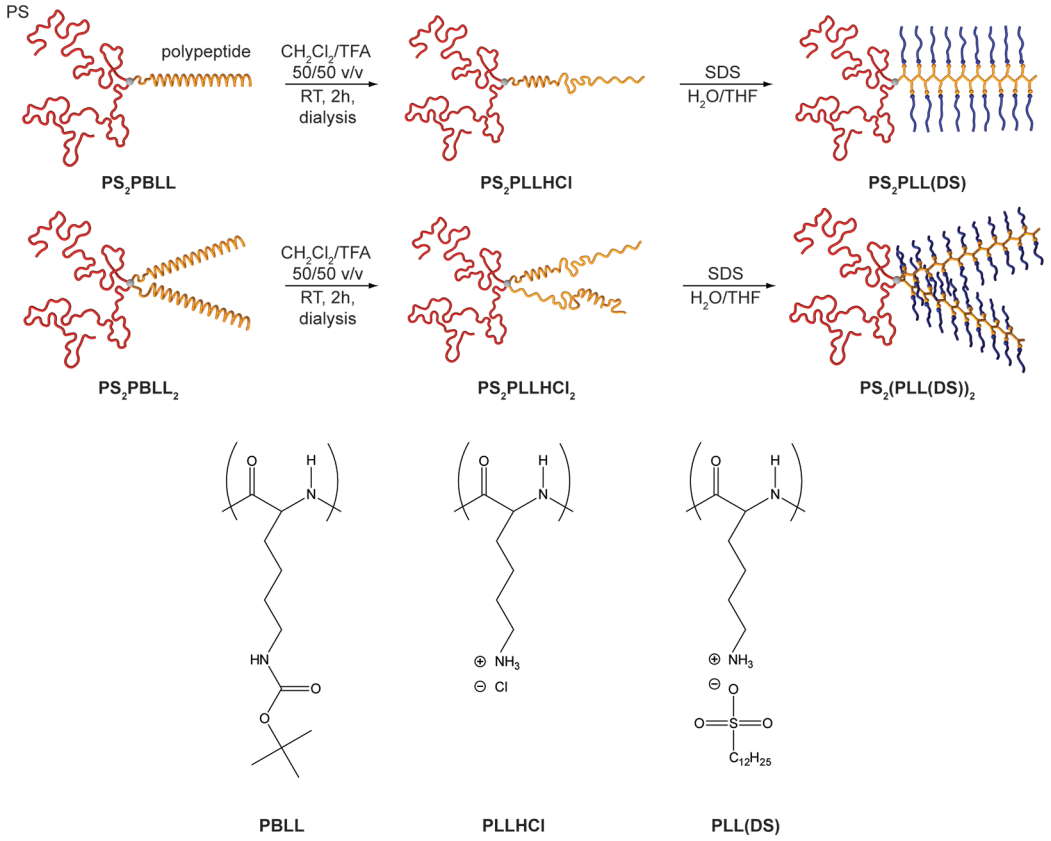
[a]By SEC-TALLS in DMF (0.1 N LiBr) at 60 °C.[39] [b]By UV−vis spectrometry.[39] [c]Calculated based on PS_2PBLL and PS_2PBLL_2 M_n and nominal compositions.

Sample Preparation and Complexation. Bulk samples of the PS_2PBLL and PS_2PBLL_2 miktoarms were prepared by dissolving each as 1 wt % solution in chloroform ($CHCl_3$, Sigma-Aldrich, ≥99.0%) and allowing slow evaporation of the solvent over the course of ∼2 weeks, followed by drying under vacuum ($p < 10^{-2}$ mbar). $PS_2PLLHCl$ and $PS_2PLLHCl_2$ miktoarms were dissolved as 1 wt % solutions in ultrapure Milli-Q water containing 11 and 6 wt % of tetrahydrofuran (THF, Sigma-Aldrich, ≥99.9%), respectively, and the solvent mixture was slowly evaporated over the course of ∼2 weeks, followed by drying under vacuum. $PS_2PLL(DS)$ and $PS_2(PLL(DS))_2$ supramolecular complexes were prepared by mixing solutions of the $PS_2PLLHCl$ and $PS_2PLLHCl_2$ miktoarms, respectively, in 1:1 molar ratio with sodium 1-dodecanesulfonate (SDS, Aldrich, ≥99%) which was dissolved as 0.9 wt % solution in water containing 11 wt % of THF. In both cases, the combination of the constituents immediately resulted in a white precipitate. The precipitates were washed with Milli-Q water, collected, allowed to dry in air, and vacuumed.

TEM Characterization. Bulk samples were cut to 70 nm sections at −40 °C using a Leica EM UC7 Ultramicrotome and a 35° Diatome diamond knife, transferred to Quantifoil R3.5/1 holey carbon support film grids, and stained at room temperature by exposing the grids to ruthenium tetroxide (RuO_4) vapors for 1 min. The structures of PS_2PBLL, PS_2PBLL_2, $PS_2PLLHCl$, and $PS_2PLLHCl_2$ were imaged in bright-field mode with a FEI Tecnai 12 transmission electron microscope operating at an accelerating voltage of 80 kV and recorded with a Gatan UltraScan 1000 CCD camera. Small-scale structures of $PS_2PLL(DS)$ and $PS_2(PLL(DS))_2$ were imaged in bright-field mode with a JEOL JEM-3200FSC field emission transmission electron microscope operating at an accelerating voltage of 100 kV and recorded with a Gatan Ultrascan 4000 CCD camera.

SAXS and WAXS Measurements. SAXS and WAXS measurements were performed with a rotating anode Bruker Microstar microfocus X-ray source (Cu Kα radiation, λ = 1.54 Å) with two beamlines. The SAXS beam is equipped with Montel parallel optics and further collimated with four sets of JJ X-ray four-blade slits, resulting in a beam area of approximately 1 mm × 1 mm at the sample position. The scattering intensities were measured using a Bruker AXS HI-STAR 2D area detector at a sample-to-detector distance of 159 cm. The WAXS beam is equipped with Montel focusing optics, resulting in a beam area of approximately 0.8 mm × 0.8 mm at the sample position. The scattering intensities were measured with a Bruker AXS Vantec 2D area detector at a sample-to-detector distance of 10 cm. For the measurements, nonoriented bulk samples were sealed between Mylar films. Diffraction data were integrated over the whole detector

Scheme 1. Synthetic Strategy and Molecular Structures of the Synthesized and Complexed Miktoarm Star Copolymers



area. Background was measured separately and reduced from the spectra. The magnitude of the scattering vector is given by $q = (4\pi/\lambda) \sin \theta$, where 2θ is the scattering angle. Positions of reflections have been obtained by fitting Gaussian peaks together with an appropriate background to data that has not been Lorentz corrected.

FTIR Measurements. Dry samples were mixed with KBr and pressed into pellets. Transmission spectra were recorded with a Nicolet 380 FT-IR spectrometer. 64 spectra were averaged with 2 cm^{-1} resolution.

RESULTS AND DISCUSSION

Bulk samples of the PS_2PBLL and PS_2PBLL_2 miktoarms were prepared by slow evaporation from $CHCl_3$ with the objective of achieving equilibrium or near-equilibrium morphologies. The samples were not additionally thermally annealed since elevated temperatures have been shown to lead to partial thermal deprotection of the Boc groups of PBLL.[23] Similarly, the $PS_2PLLHCl$ and $PS_2PLLHCl_2$ miktoarms were slowly evaporated from H_2O/THF solvent mixtures. In the preparation of the supramolecular complexes, the mixing of the constituents resulted in a white precipitate which was collected and dried. Complex formation was verified by elemental analysis (see Supporting Information) which showed that 95−101% of the PLL repeating units were complexed with DS surfactants. Therefore, the complexes are denoted as $PS_2PLL(DS)$ and $PS_2(PLL(DS))_2$ according to the nominal compositions. Our aim was to use the surfactants to force the polypeptide backbone into the β-sheet conformation, which could not be achieved by other means in this study. Therefore, the precipitated complexes were studied without further treatments, knowing that organic solvent treatment may completely change the conformation of the polypeptide as well as the resulting self-assembly.[34,41]

The solid-state morphologies of the miktoarms were visualized with TEM (Figure 1). The miktoarms PS_2PBLL and PS_2PBLL_2 with protected L-lysine arms form lamellar self-assemblies which are revealed upon staining the PS blocks with RuO_4 (i.e., PS appears dark in the images). However, the self-assemblies of the 3- and 4-arm systems are not identical, as both (i) the long-range order and (ii) the lamellar periodicity differ. PS_2PBLL_2 is evidently better organized with a higher overall order and a lamellar periodicity of 13−17 nm. This indicates that there is no excessive steric frustration of the 4-arm chimera to limit a space-filling lamellar assembly. By contrast, PS_2PBLL only shows limited lamellar stacks with no apparent order observed between them. The predominant lamellar periodicity is 21−26 nm (Figure 1a). However, also lamellar stacks with a smaller periodicity of 12−16 nm are observed (additional TEM micrographs shown in the Supporting Information). This suggests higher packing frustration in the 3-arm chimera, still having propensity for the lamellar assembly.

In the $PS_2PLLHCl$ and $PS_2PLLHCl_2$ stars containing hydrochloric acid salts, TEM reveals micelles where the PLLHCl cores are surrounded by PS chains (Figure 1c,d). In both cases, the diameter of the micelles is 17−25 nm according to TEM micrographs. Similar morphologies have been previously observed in block copolymer ionomers due to charge clustering, the aggregation number of the micelles ranging from tens to several hundreds depending on the counterion and block copolymer composition.[42] Finally, in the supramolecular complexes $PS_2PLL(DS)$ and $PS_2(PLL(DS))_2$, lamellar self-assemblies with periodicities of ca. 4 nm are found (Figure 1e,f). These lamellae are composed of the alternating polypeptide and surfactant layers of the PLL(DS) arms. As the complex

dx.doi.org/10.1021/ma202747h | Macromolecules 2012, 45, 2850−2856

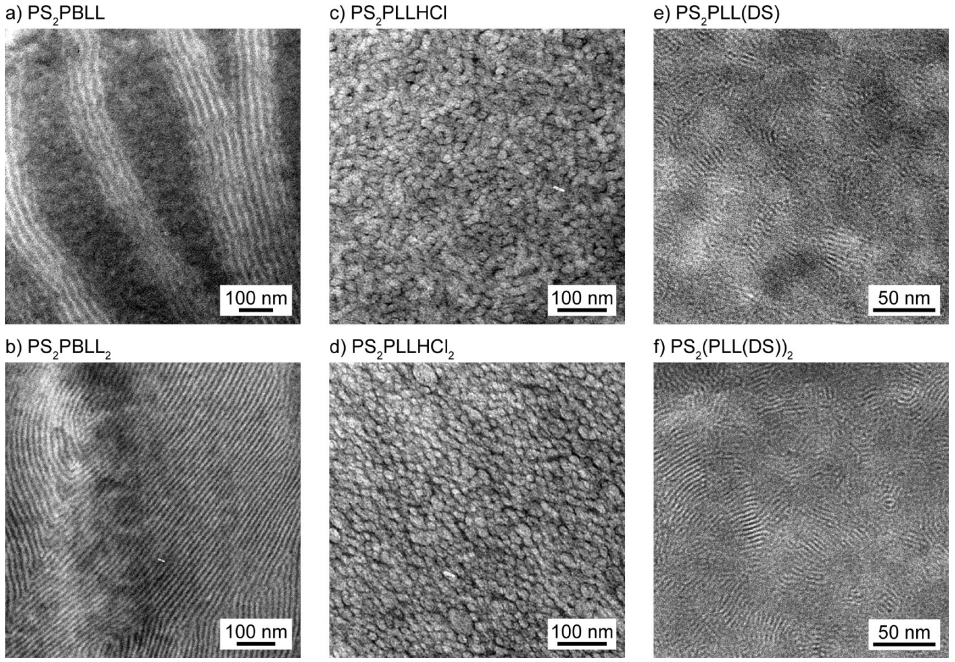


Figure 1. TEM micrographs of the miktoarm bulk samples, stained with RuO_4 (PS dark). Note the different scale in the organization of (a–d) compared to (e, f). Additional TEM micrographs of PS_2PBLL are shown in the Supporting Information.

lamellar areas are rather small and randomly oriented, the PS chains that surround the lamellae do not form any well-ordered phases on the block copolymer length scale; therefore, TEM does not reveal any clear structures on the block copolymer scale.

SAXS (Figure 2) was used to verify the block copolymer scale structures observed in TEM and to extract more exact

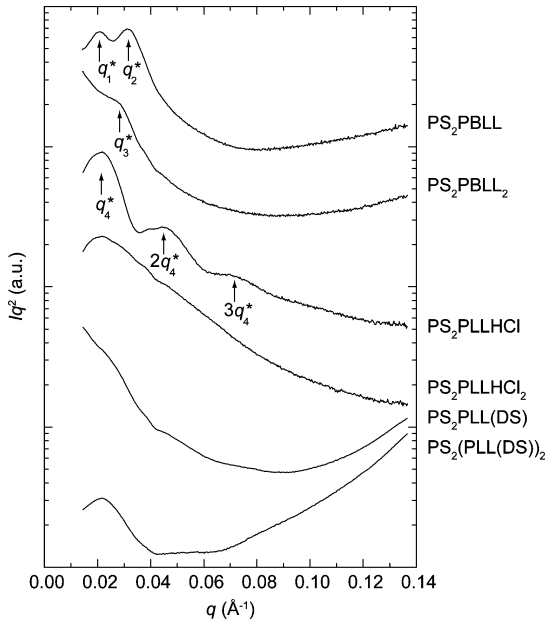


Figure 2. SAXS curves of the miktoarm star copolymers.

information about the structural sizes. For PS_2PBLL, two reflections are observed at $q_1^* = 0.020$ Å^{-1} and $q_2^* = 0.032$ Å^{-1}, corresponding to 31 and 20 nm structures, respectively. These reflections verify the coexistence of two different lamellar long periods, as observed in TEM (Figure 1a and Figure S1). PS_2PBLL_2 shows a single shoulder at $q_3^* = 0.028$ Å^{-1}, corresponding to a lamellar long period of 22 nm. A very similar scattering curve was observed previously in the lamellar self-assembly of an ABC miktoarm star chimera with a single polypeptide arm.[23] The micellar-forming $PS_2PLLHCl$ has three broad reflections at $q_4^* = 0.019$ Å^{-1}, $2q_4^*$, and $3q_4^*$ which correspond to a structural size of 33 nm. This reflects the average distance of the polypeptide micelles in the PS matrix, although they do not form a well-defined lattice. $PS_2PLLHCl_2$ shows a broad reflection at low q range, probably due to a similar structure as in $PS_2PLLHCl$, as suggested by TEM. It is hard to extract a structural size for this sample in a meaningful way from the SAXS data, as scattering intensity remains relatively high toward larger q values. The absence of well-defined micelle-to-micelle reflections could be an indication of higher polydispersity in the micellar size of $PS_2PLLHCl_2$. For the supramolecular complexes, no reflections are expected in SAXS, as no block copolymer scale organization was observed in TEM. However, $PS_2(PLL(DS))_2$ shows a broad reflection at 0.021 Å^{-1}, which corresponds to a structural size of 30 nm. This reflection is tentatively assigned to the average distance of neighboring polypeptide–surfactant domains.

The conformation of the polypeptide arms was studied by FTIR (Figure 3). PS_2PBLL and PS_2PBLL_2 show a sharp amide I band at 1651 cm^{-1}, originating mainly from the C=O stretching of peptide bonds participating in α-helical conformation.[43] Additionally, the Boc protecting groups give rise to the two broad bands at 1714 and 1686 cm^{-1}. The amide II region at 1560–1520 cm^{-1} shows multiple overlapping bands and is not therefore used to interpret the polypeptide conformation. The spectra of $PS_2PLLHCl$ and $PS_2PLLHCl_2$ display a number of different amide I bands at 1652 and 1618 cm^{-1} for $PS_2PLLHCl$ and at 1682, 1653, and 1626 cm^{-1} for $PS_2PLLHCl_2$. These multiple bands are evidence of a mixture of conformations for the PLLHCl arms, including α-helices and antiparallel β-sheets for $PS_2PLLHCl$, and, in addition, turns[44] observed near 1680 cm^{-1} for $PS_2PLLHCl_2$. Therefore, the

dx.doi.org/10.1021/ma202747h | Macromolecules 2012, 45, 2850–2856

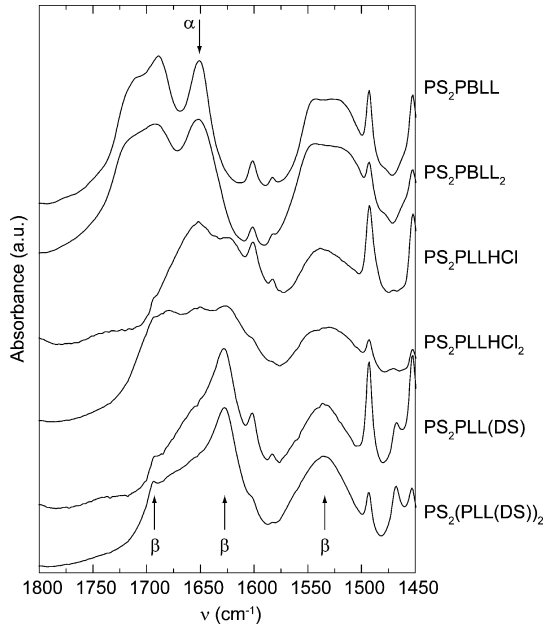


Figure 3. FTIR spectra of the miktoarm star copolymers.

conformation is not well-defined in these miktoarms. Also surfactant complexation of the polypeptide arms results in dramatic conformational changes: both $PS_2PLL(DS)$ and $PS_2(PLL(DS))_2$ show amide I bands at 1693−1692 and 1628 cm^{-1} corresponding to antiparallel β-sheets with small amounts of α-helical or random coil conformations at ∼1660 cm^{-1}. The amide II band can now also be used and its location at 1535 cm^{-1} supports this interpretation.

The differences in the morphologies and conformations of the miktoarms are also evident in WAXS (Figure 4). Packing of

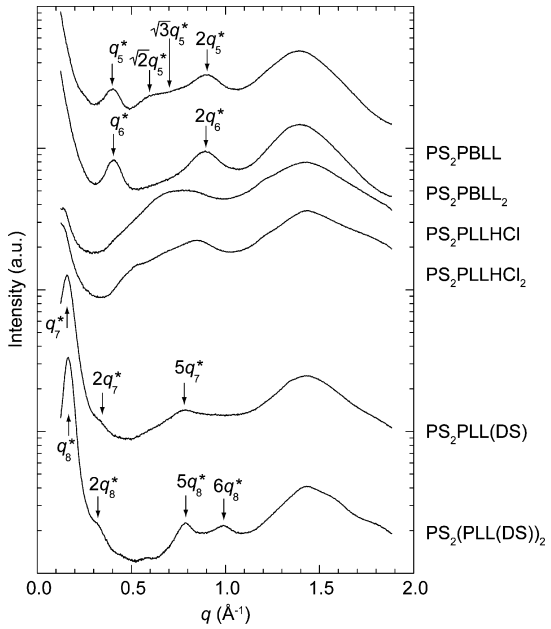


Figure 4. WAXS curves of the miktoarm star copolymers.

the relatively rod-like α-helices is observed for PS_2PBLL at q_5^* = 0.40 $Å^{-1}$, $\sqrt{2}q_5^*$, $\sqrt{3}q_5^*$, and $2q_5^*$ (see Supporting Information for detailed fitting) which strongly implies coexistence of both hexagonal and tetragonal local packing. The helix-to-helix distance is, based on the value of q_5^*, 1.6 and 1.8 nm in the tetragonal and hexagonal arrangements, respectively. Previously, hexagonal packing of α-helices have been reported in several polymer/polypeptide chimeras.[24,45,25] In our case, however, the added interfacial frustration of the miktoarm architecture might lead to a different kind of packing from the one typically favored by linear chimeras. For PS_2PBLL_2, distinct WAXS reflections q_6^* = 0.40 $Å^{-1}$ and $2q_6^*$ are observed, but the absence of $\sqrt{2}q_6^*$ or $\sqrt{3}q_6^*$ reflections prevents unambiguous assignment of the helical packing geometry.

In the direction perpendicular to the lamellae, the helices can either (i) stack to form bilayers, (ii) interdigitate, or (iii) fold back and forth as kinked rods.[21,24] Based on the molecular weights of the polypeptide arms and the well-known geometry of the α-helix, the length of a single ideal α-helical arm, L_{helix}, is 8.2 nm for the present PS_2PBLL and 6.9 nm for PS_2PBLL_2. Bilayer stacking of helices will then require a polypeptide layer thickness, $d_{peptide}$, of up to $\sim 2L_{helix}$ while interdigitation leads to $d_{peptide}$ which is $\sim L_{helix}$. Tilting can, in both cases, reduce the thickness of the polypeptide layer. Folding of the helices back and forth, on the other hand, always leads to $d_{peptide} < L_{helix}$.[24] Considering the overall periodicity as observed in SAXS, the weight fractions of the blocks, and the specific volumes of PBLL and PS, conclusions can be drawn from the probable packing of the PBLL α-helices (Table 2). The relatively small molecular weights[24] and casting from a weakly hydrogen-bonding solvent[29] support the formation of nearly ideal α-helices in the present study. Therefore, comparing $d_{peptide}$ to L_{helix} should give a direct measure of the packing of the helices. For the PS_2PBLL lamellar self-assembly with 20 nm periodicity, the value of 1.06 implies very perfect interdigitation of the helices in an approximately perpendicular direction to the block copolymer scale lamellae. Interdigitation has also previously been observed in a miktoarm chimera with two different coil-like arms and one polypeptide arm.[23] On the other hand, the larger PS_2PBLL periodicity of 31 nm cannot be explained by folding or tilting, since they would both reduce the thickness. The value of 1.64 for the relation of $d_{peptide}$ and L_{helix} must therefore represent a stacked bilayer of α-helices. A very similar figure is obtained for PS_2PBLL_2, also suggested to represent a stacked bilayer configuration. This is reasonable, as the addition of a second polypeptide arm should drive the balance between the interdigitated and stacked configurations, both observed in the 3-arm system, toward the stacked bilayer configuration for the 4-arm system. Previously, stacked bilayers have been reported for miktoarms with one coil-like arm and two polypeptide arms, regardless of the weight fractions of the components.[21] The structures are schematically illustrated in Figure 5.

For $PS_2PLLHCl$ and $PS_2PLLHCl_2$, WAXS (Figure 4) does not show distinct small-scale structures other than broad correlation reflections. This is not surprising, taking into account the mixed conformations of the PLLHCl arms discussed above. On the other hand, the polypeptide−surfactant organization of $PS_2PLL(DS)$ and $PS_2(PLL(DS))_2$ observed in TEM (Figure 1e,f) is clearly confirmed by WAXS. For $PS_2PLL(DS)$, reflections q_7^* = 0.16 $Å^{-1}$, $2q_7^*$, and $5q_7^*$ are observed, corresponding to a lamellar periodicity of 3.9 nm. This fits well with the thickness of a single PLL β-sheet (1.5 nm) surrounded on each side by C_{12} chains and also with previous reports on polymer−surfactant[46,47] and polypeptide−surfactant complexes[32,40] with C_{12} surfactants. No evidence of crystallization

dx.doi.org/10.1021/ma202747h | Macromolecules 2012, 45, 2850−2856

Table 2. Helix Packing Geometry in the PS_2PBLL and PS_2PBLL_2 Miktoarms

miktoarm	d_{SAXS}[a] (nm)	$d_{peptide}$[b] (nm)	d_{PS}[c] (nm)	L_{helix}[d] (nm)	$d_{peptide}/L_{helix}$	helix packing geometry
PS_2PBLL	31	13.4	17.6	8.2	1.64	bilayer
	20	8.7	11.3	8.2	1.06	interdigitation
PS_2PBLL_2	22	12.1	9.9	6.9	1.75	bilayer

[a] d_{SAXS}: lamellar long period from SAXS. [b] Thickness of polypeptide layer $d_{peptide} = d_{SAXS}(1 + w_{PS}\nu_{PS}/w_{PBLL}\nu_{PBLL})^{-1}$ where w is mass fraction and ν specific volume, $\nu_{PS} = 0.95$ and $\nu_{PBLL} = 1.11$ cm^3/g. [c] Thickness of PS layer $d_{PS} = d_{SAXS} - d_{peptide}$. [d] Length of an ideal α-helical PBLL arm, $L_{helix} = N_{PBLL} \times 0.15$ nm/n, where N_{PBLL} = degree of polymerization of PBLL and n = number of PBLL arms.

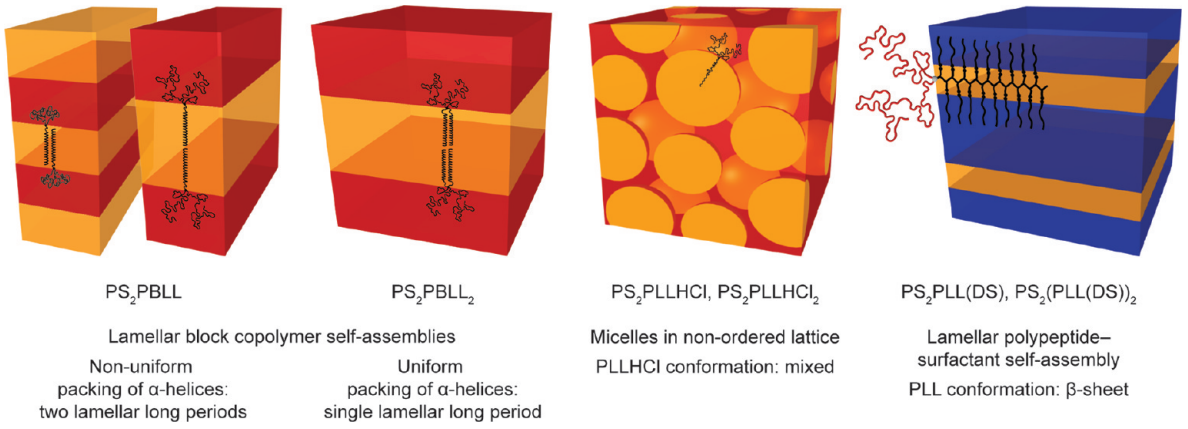


Figure 5. Schematic illustration of the packing of the miktoarm molecules in bulk (red, PS; yellow, polypeptide; blue, surfactant).

of the C_{12} chains[41] can be found in the WAXS curve, and hence they are expected to take up slightly less space than in the all-trans conformation (1.5 nm). The broad reflection located at 1.39−1.44 Å^{-1} in all of the miktoarms reflects average distances between the amorphous segments of the polymers[21] and is here overlapped with the amorphous halo from the surfactant tails. Slightly more intense reflections are observed for $PS_2(PLL(DS))_2$ at $q_8^* = 0.16$ Å^{-1}, $2q_8^*$, $5q_8^*$, and $6q_8^*$ which imply that the 4-arm system is structurally identical but to some extent better organized. The multiple reflections in WAXS demonstrate well-ordered packing of the PLL(DS) complex arms which overrides the block copolymer scale organization. On the other hand, the existence of the PS arms brings frustration into the systems and effectively limits the size of the PLL(DS) domains, as observed in TEM (Figure 1e,f). The fact that $PS_2(PLL(DS))_2$ is observed to form slightly larger self-assembled domains in TEM illustrates how the number of competing arms needs to be balanced to relieve interfacial frustration.

CONCLUSIONS

We have shown how modification of the polypeptide arms can be used to control the self-assemblies of A_2B and A_2B_2 type miktoarm star copolymer chimeras. The side chains of the polypeptide arms influence not only solubility but also conformation and, therefore, self-assembly of the systems in the solid state due to modified packing frustration. In PS_2PBLL and PS_2PBLL_2 miktoarms, the α-helical polypeptide conformation promotes lamellar self-assemblies. The frustration between the rod-like PBLL and the coil-like PS arms leads to a suppressed ability of PS_2PBLL to form an overall, space-filling lamellar order, and structures with two different packing mechanisms of the α-helical arms are observed. In PS_2PBLL_2, the frustration is better balanced, and a uniform lamellar self-assembly with bilayer stacking of the α-helices is observed. In the miktoarms with PLLHCl salts, polyelectrolytic charge clustering leads to polypeptide micelles which show relatively random polypeptide conformations and are located in a nonordered lattice within a PS matrix. Ionic complexation of the polypeptide arms with DS leads to particularly pronounced small-scale ordering of the polypeptide−surfactant complex arms which dominates over the formation of block copolymer scale structures. These findings pave the way for learning to balance frustration, supramolecular concepts, and tunable properties in new polymer materials.

ASSOCIATED CONTENT

Supporting Information

Elemental analysis of $PS_2PLL(DS)$ and $PS_2(PLL(DS))_2$, additional TEM micrographs of PS_2PBLL, and fitting of the WAXS curve of PS_2PBLL. This material is available free of charge via the Internet at http://pubs.acs.org.

AUTHOR INFORMATION

Corresponding Author

*E-mail: olli.ikkala@aalto.fi (O.I.), iatrou@chem.uoa.gr (H.I.).

Present Address

[⊥]4700 King Abdullah University of Science and Technology, Thuwal 23955-6900, Kingdom of Saudi Arabia.

Notes

The authors declare no competing financial interest.

ACKNOWLEDGMENTS

This work made use of the Aalto University Nanomicroscopy Center (Aalto-NMC) premises. Dr. Jani Seitsonen is thanked for the TEM imaging of the surfactant-scale structures and Panu Hiekkataipale for the assistance and discussions regarding SAXS/WAXS experiments. The Academy of Finland is gratefully acknowledged for financial support.

REFERENCES

(1) Pitsikalis, M.; Pispas, S.; Mays, J. W.; Hadjichristidis, N. *Adv. Polym. Sci.* **1998**, *135*, 1−137.
(2) Ishizu, K.; Uchida, S. *Prog. Polym. Sci.* **1999**, *24*, 1439−1480.
(3) Tezuka, Y.; Oike, H. *Prog. Polym. Sci.* **2002**, *27*, 1069−1122.
(4) Ge, Z. S.; Liu, S. Y. *Macromol. Rapid Commun.* **2009**, *30*, 1523−1532.
(5) Hirao, A.; Murano, K.; Oie, T.; Uematsu, M.; Goseki, R.; Matsuo, Y. *Polym. Chem.* **2011**, *2*, 1219−1233.
(6) Read, D. J.; Auhl, D.; Das, C.; den Doelder, J.; Kapnistos, M.; Vittorias, I.; McLeish, T. C. B. *Science* **2011**, *333*, 1871−1874.
(7) Ungar, G.; Tschierske, C.; Abetz, V.; Holyst, R.; Bates, M. A.; Liu, F.; Prehm, M.; Kieffer, R.; Zeng, X. B.; Walker, M.; Glettner, B.; Zywocinski, A. *Adv. Funct. Mater.* **2011**, *21*, 1296−1323.
(8) Hadjichristidis, N.; Iatrou, H.; Behal, S. K.; Chludzinski, J. J.; Disko, M. M.; Garner, R. T.; Liang, K. S.; Lohse, D. J.; Milner, S. T. *Macromolecules* **1993**, *26*, 5812−5815.
(9) Milner, S. T. *Macromolecules* **1994**, *27*, 2333−2335.
(10) Tselikas, Y.; Iatrou, H.; Hadjichristidis, N.; Liang, K. S.; Mohanty, K.; Lohse, D. J. *J. Chem. Phys.* **1996**, *105*, 2456−2462.
(11) Pennisi, R. W.; Fetters, L. J. *Macromolecules* **1988**, *21*, 1094−1099.
(12) Mays, J. W. *Polym. Bull.* **1990**, *23*, 247−250.
(13) Pochan, D. J.; Gido, S. P.; Pispas, S.; Mays, J. W.; Ryan, A. J.; Fairclough, J. P. A; Hamley, I. W.; Terrill, N. J. *Macromolecules* **1996**, *29*, 5091−5098.
(14) Mavroudis, A.; Avgeropoulos, A.; Hadjichristidis, N.; Thomas, E. L.; Lohse, D. J. *Chem. Mater.* **2003**, *15*, 1976−1983.
(15) Beyer, F. L.; Gido, S. P.; Uhrig, D.; Mays, J. W.; Tan, N. B.; Trevino, S. F. *J. Polym. Sci., Part B: Polym. Phys.* **1999**, *37*, 3392−3400.
(16) Turner, C. M.; Sheller, N. B.; Foster, M. D.; Lee, B.; Corona-Galvan, S.; Quirk, R. P.; Annis, B.; Lin, J. S. *Macromolecules* **1998**, *31*, 4372−4375.
(17) Zhu, Y. Q.; Gido, S. P.; Moshakou, M.; Iatrou, H.; Hadjichristidis, N.; Park, S.; Chang, T. *Macromolecules* **2003**, *36*, 5719−5724.
(18) Olsen, B. D.; Segalman, R. A. *Mater. Sci. Eng., R* **2008**, *62*, 37−66.
(19) Gallot, B. *Prog. Polym. Sci.* **1996**, *21*, 1035−1088.
(20) Sun, J.; Chen, X. S.; Guo, J. S.; Shi, Q.; Xie, Z. G.; Jing, X. B. *Polymer* **2009**, *50*, 455−461.
(21) Babin, J.; Taton, D.; Brinkmann, M.; Lecommandoux, S. *Macromolecules* **2008**, *41*, 1384−1392.
(22) Gitsas, A.; Floudas, G.; Mondeshki, M.; Lieberwirth, I.; Spiess, H. W.; Iatrou, H.; Hadjichristidis, N.; Hirao, A. *Macromolecules* **2010**, *43*, 1874−1881.
(23) Junnila, S.; Houbenov, N.; Hanski, S.; Iatrou, H.; Hirao, A.; Hadjichristidis, N.; Ikkala, O. *Macromolecules* **2010**, *43*, 9071−9076.
(24) Douy, A.; Gallot, B. *Polymer* **1982**, *23*, 1039−1044.
(25) Schlaad, H.; Kukula, H.; Smarsly, B.; Antonietti, M.; Pakula, T. *Polymer* **2002**, *43*, 5321−5328.
(26) Schlaad, H.; Smarsly, B.; Losik, M. *Macromolecules* **2004**, *37*, 2210−2214.
(27) Papadopoulos, P.; Floudas, G.; Klok, H. A.; Schnell, I.; Pakula, T. *Biomacromolecules* **2004**, *5*, 81−91.
(28) Losik, M.; Kubowicz, S.; Smarsly, B.; Schlaad, H. *Eur. Phys. J. E* **2004**, *15*, 407−411.
(29) Schlaad, H.; Smarsly, B.; Below, I. *Macromolecules* **2006**, *39*, 4631−4632.
(30) Ikkala, O.; ten Brinke, G. *Chem. Commun.* **2004**, *19*, 2131−2137.
(31) Hammond, M. R.; Mezzenga, R. *Soft Matter* **2008**, *4*, 952−961.
(32) Ponomarenko, E. A.; Tirrell, D. A.; MacKnight, W. J. *Macromolecules* **1996**, *29*, 8751−8758.
(33) Canilho, N.; Scholl, M.; Klok, H. A.; Mezzenga, R. *Macromolecules* **2007**, *40*, 8374−8383.
(34) Hanski, S.; Junnila, S.; Almasy, L.; Ruokolainen, J.; Ikkala, O. *Macromolecules* **2008**, *41*, 866−872.
(35) Li, J.; He, W. D.; He, N.; Han, S. C.; Sun, X. L.; Li, L. Y.; Zhang, B. Y. *J. Polym. Sci., Polym. Chem.* **2009**, *47*, 1450−1462.
(36) Hammond, M. R.; Li, C. X.; Tsitsilianis, C.; Mezzenga, R. *Soft Matter* **2009**, *5*, 2371−2377.
(37) Liu, H.; Li, C. H.; Liu, H. W.; Liu, S. Y. *Langmuir* **2009**, *25*, 4724−4734.
(38) Iatridi, Z.; Tsitsilianis, C. *Chem. Commun.* **2011**, *47*, 5560−5562.
(39) Karatzas, A.; Iatrou, H.; Hadjichristidis, N.; Inoue, K.; Sugiyama, K.; Hirao, A. *Biomacromolecules* **2008**, *9*, 2072−2080.
(40) Hanski, S.; Houbenov, N.; Ruokolainen, J.; Chondronicola, D.; Iatrou, H.; Hadjichristidis, N.; Ikkala, O. *Biomacromolecules* **2006**, *7*, 3379−3384.
(41) Junnila, S.; Hanski, S.; Oakley, R. J.; Nummelin, S.; Ruokolainen, J.; Faul, C. F. J.; Ikkala, O. *Biomacromolecules* **2009**, *10*, 2787−2794.
(42) Moffitt, M.; Eisenberg, A. *Macromolecules* **1997**, *30*, 4363−4373.
(43) Lee, N. H.; Frank, C. W. *Langmuir* **2003**, *19*, 1295−1303.
(44) Krimm, S.; Bandekar, J. *Adv. Protein Chem.* **1986**, *38*, 181−364.
(45) Klok, H. A.; Langenwalter, J. F.; Lecommandoux, S. *Macromolecules* **2000**, *33*, 7819−7826.
(46) Bergström, M.; Kjellin, U. R. M.; Claesson, P. M.; Pedersen, J. S.; Nielsen, M. M. *J. Phys. Chem. B* **2002**, *106*, 11412−11419.
(47) Starodubtsev, S. G.; Laptinskaya, T. V.; Yesakova, A. S.; Khokhlov, A. R.; Shtykova, E. V.; Dembo, K. A.; Volkov, V. V. *Polymer* **2010**, *51*, 122−128.

Macromolecules

Article

pubs.acs.org/Macromolecules

Force−Fluctuation Relation of a Single DNA Molecule

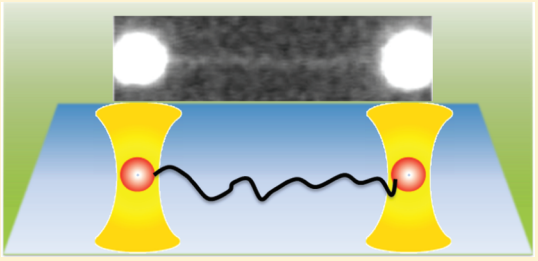
Takeshi Baba,[†] Takahiro Sakaue,[‡,§] and Yoshihiro Murayama*[,†]

[†]Department of Applied Physics, Tokyo University of Agriculture and Technology, Tokyo 184-8588, Japan

[‡]Department of Physics, Kyushu University, 33, Fukuoka 812-8581, Japan

[§]PRESTO, Japan Science and Technology Agency (JST), 4-1-8 Honcho Kawaguchi, Saitama 332-0012, Japan

ABSTRACT: We observed transverse fluctuations of single DNA molecules by fluorescence microscopy. The end-to-end distance of DNA molecules was varied by using dual trap optical tweezers, and the force−fluctuation relation was experimentally obtained in wide ranges of the force regime. In strong force regime, the theory of a stretched worm-like chain with fixed both ends explains the experimental results. On the other hand, in the low force regime, the fluctuations approach the value for an ideal ring polymer. We introduce an interpolate formula for the force−fluctuation relation by considering strong and low force limits, which captures the overall trend of experimental results. The proposed force−fluctuation relation will be useful for quantitative discussions in various sectors of polymer physics and biological processes which involve the conformation change of DNA and other biopolymers, where the loading and the fluctuation are relevant factors.



INTRODUCTION

Biopolymers such as nucleic acids and proteins are thermally fluctuating in aqueous solution. In some biological processes in living cells, the fluctuation has an important role. In gene expression or replication, the reactions are regulated by site-specific bindings of proteins such as a transcription factor which searches the specific site by Brownian motion. A weak nonspecific binding of the protein to DNA causes a 1-dimensional Brownian motion on fluctuating DNA,[1] and a thermally excited bending of DNA permit the protein to move from one site to another site.[2] Very recently, Hodge et al. has shown that a transient DNA loop formation can result in the physical basis regulation of transcription through nucleosomal DNA.[3]

A force−extension relation for a single DNA, suggested by Marko and Siggia,[4] is widely used for not only DNA but also proteins and other polymers. The relation is an approximate interpolation formula, indicating the entropic elasticity of the worm-like chain (WLC), which well explains the elastic responses obtained in experiments. Although transverse fluctuations[5,6] and loop formation[7] of single DNA molecules are both experimentally and theoretically investigated, the force−fluctuation relation has not been observed systematically and there is no equation for the force−fluctuation relation in wide regime from low force to strong force limit. If the force−fluctuation relation is established as well as the force−extension relation, it must be useful for considering the role of the fluctuation of polymers in physical and biological processes.

In this paper, we observed fluctuations of single DNA molecules by fluorescence microscopy, varying its extension (end-to-end distance) in wide range by using dual trap optical tweezers. Moreover, a practical formula for the force−fluctuation relation is proposed, which is obtained in the same manner as Marko-Siggia's force−extension relation.

MATERIALS AND METHODS

We used dual-trap optical tweezers to stretch a λ-phage DNA molecule with 2 μm diameter polystyrene beads attached to its ends via biotinylated oligo-nucleotides.[8] The DNA-beads complexes were diluted with buffer solution (10 mM Tris-HCl, 1 mM EDTA, pH 7.4), and the final nucleotide concentration of DNA was about 10 nM. For the fluorescence measurement of single DNA molecules 10 nM of YOYO-1 (Molecular Probes) and 0.1% p-phenylenediamine were added to the solution. The sample solution was introduced into a homemade chamber of a nitrile rubber O-ring (diameter 17.5 mm and thickness 1.5 mm) sandwiched between two glass coverslips.

Both beads images were captured by a CCD camera (IPX-VGA-210, IMPERX) at a frame rate of 25 frames per second (fps), and they were analyzed in real time on a PC with LabVIEW and Vision softwares (National Instruments). The distance between the two beads centers determines the extension of DNA and the displacement of one bead from the focus of the laser beam determines the force acting on DNA. After trapping the bead−DNA−bead complex, the force−extension curves were obtained in stretching and relaxing processes. The force−extension curves showed a worm-like behavior:[4]

$$\frac{fl_p}{k_BT} = \frac{l}{L} + \frac{1}{4(1 - l/L)^2} - \frac{1}{4} \quad (1)$$

where f is a force acting on DNA, l is an extension (end-to-end distance), L is a total contour length, l_p is a persistence length, k_B is Boltzmann's constant and T is absolute temperature. The contour length and the persistence length of λ-DNA (48 502 bp) in aqueous solution are 16.5 μm and about 50 nm, respectively. However, the

Received: January 4, 2012
Revised: March 3, 2012
Published: March 19, 2012

 © 2012 American Chemical Society dx.doi.org/10.1021/ma300019a | *Macromolecules* 2012, 45, 2857−2862

intercalation of YOYO-1 to DNA increases the contour length and the persistence length of DNA.[5] In our experiments, we chose DNA molecules which showed worm-like behavior with more than 18 μm in contour length. All experiments were performed at room temperature (T = 298 K).

In fluorescence measurements, a mercury lamp (100 W) with a excitation filter (472 ± 15 nm) was used as the excitation light source, and the fluorescence images through a dichroic filter and an emission filter (520 ± 17 nm) were captured by another CCD camera (WAT-120N, WATEC) at 7.5 fps; the frame rate corresponds to the exposure time of 0.13 s. The spatial resolution was 0.083 μm/pixel.

RESULTS AND DISCUSSIONS

Quantification of the Transverse Fluctuation of a Stretched DNA. In each measurement, first, we obtained a force−extension curve, and L was determined by fitting using eq 1; we fixed l_p to 65 nm for all results, considering the effect of YOYO-1 on l_p.[5] Then we obtained fluorescence images of the DNA for several extensions. Figure 1 shows fluorescence

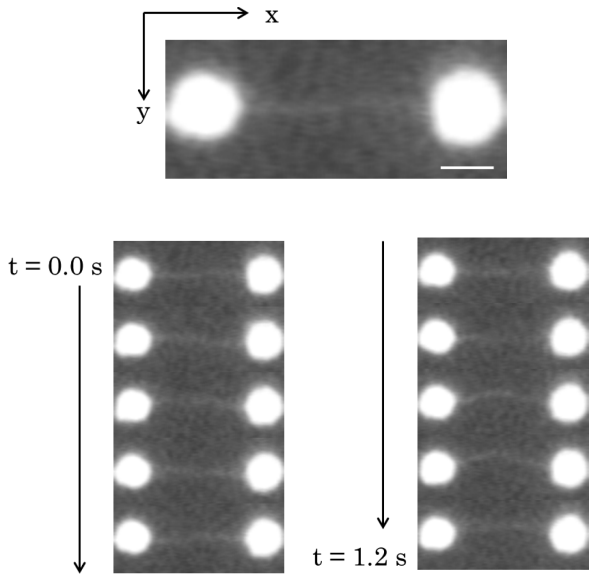


Figure 1. Fluorescence images of a single DNA molecule. Top: a snapshot of the fluorescence image of a stretched DNA. White scale bar is 2 μm. Bottom: the time series of fluorescence images during 1.2 s at a time interval of 0.13 s.

images of a single DNA molecule (L = 18.3 μm) stretched to l = 8.7 μm which corresponds to l/L = 0.47 and f = 0.07 pN, where f is not measured but calculated by eq 1 with l_p = 65 nm to avoid the measurement error. The large bright circles at both ends are beads trapped by optical tweezers, and the DNA is stretched to x direction in the top of Figure 1. We can see the transverse fluctuation of the DNA molecule in y direction in the bottom of Figure 1.

By analyzing each fluorescence image, we obtained the fluorescence intensity profile along y direction at each x. The profile showed a peak around the DNA segment. We obtained y_1 and y_2 where the intensity is 95% of the peak intensity. Since the peak is between y_1 and y_2, we determined the position of the DNA segment $y(x,t)$ by $y = (y_1 + y_2)/2$. Figure 2 shows the time average of y during 30 s (225 frames) at each x. The left-side end of the DNA is set to x = 0, and error bars are the standard deviations $\sigma_y(x)$. The time average $\langle y \rangle$ is almost 0 in 1.5 μm < x < 7.0 μm, while out of these positions, the beads at both DNA's ends affect the $\langle y \rangle$ which shows nonzero values.

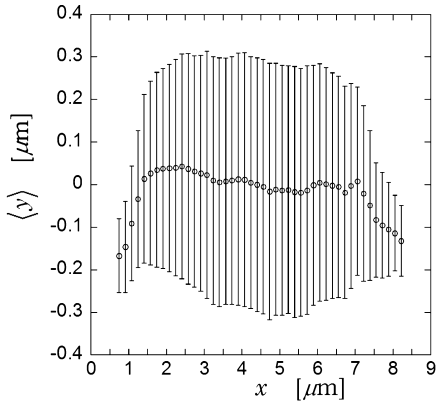


Figure 2. Time average of the transverse position of DNA segment $y(x,t)$ at the longitudinal coordinate x during 30 s (225 frames). The error bars represent its standard deviation.

We note that $\sigma_y(x)$ is large at the middle of the DNA and small at around the fixed ends. The dependence of the DNA fluctuation on the longitudinal coordinate x is shown in Figure 3. The variance $\sigma_y^2(x)$ is almost quadratic function of x, which

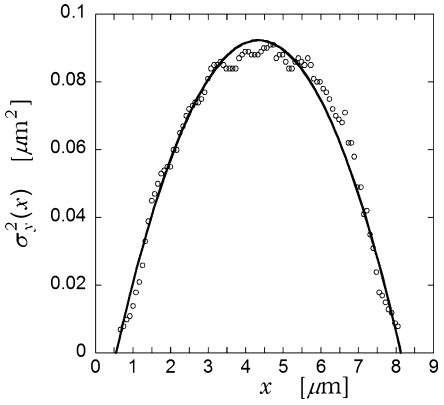


Figure 3. Transverse fluctuation of DNA at the longitudinal coordinate x. These data are identical to the data in Figure 2. The solid line is a quadratic function in eq 2 with l = 8.7 μm.

has a peak at the middle of the DNA. Then, we fit these results by

$$\sigma_y^2(x) = a\left(x - \frac{l}{2}\right)^2 + \sigma_{\max}^2 \qquad (2)$$

where a and $\sigma_{\max}^2$ are fitting parameters; we used two parameters for the fit to obtain the peak value as accurate as possible from experimental data. The solid line in Figure 3 is obtained with $\sigma_{\max}^2$ = 0.092 μm^2. The relation between $\sigma_{\max}^2$ and f is shown in Figure 4. We can see that $\sigma_{\max}^2$ decreases as f increases. These results in Figure 3 and Figure 4 are qualitatively reasonable, given the situation that the both ends of DNA are fixed to beads and it is stretched by optical tweezers. In the next paragraph, we shall analyze fundamental fluctuation properties of the stretched WLC to provide a quantitative understanding of these observations.

Fluctuation in a Stretched Worm-Like Chain (WLC). Let us consider a WLC with bending modulus $\kappa = l_p k_B T$ stretched along x direction.[4] Its conformation is parametrized

dx.doi.org/10.1021/ma300019a | Macromolecules 2012, 45, 2857−2862

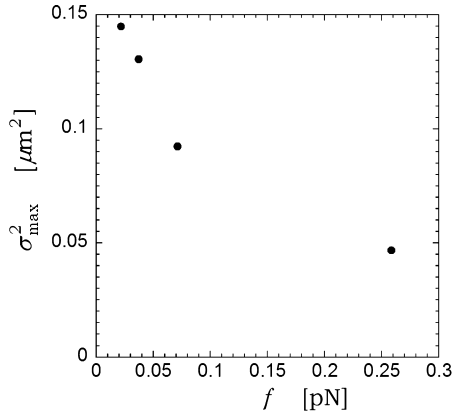


Figure 4. Relation between σ_{max}^2 and f. These four plots were obtained for identical DNA.

by a space curve $\boldsymbol{r}(s) = (r_x(s), r_y(s), r_z(s))$ of total contour length L, where s is arc length and $\boldsymbol{r}(0) = \vec{0}$. The free energy is

$$F = \int_0^L \frac{\kappa}{2}\left(\frac{\partial \boldsymbol{t}(s)}{\partial s}\right)^2 \mathrm{d}s - fl \tag{3}$$

where $\boldsymbol{t}(s) = (t_x(s), t_y(s), t_z(s))$ is a unit tangent vector, and the force f appears as a Lagrange multiplier to fix the end-to-end distance $l = r_x(s) - r_x(0)$. It is convenient to define a dimensionless quantity $\phi \equiv fl_p/(k_BT)$. In the strong force regime $\phi \gg 1$, the chain is substantially stretched along the x direction; the tangent $\boldsymbol{t}(s)$ almost directs the x direction, and only weakly fluctuates. In such a situation, the stored length due to thermal fluctuation becomes $L - l \simeq \int \mathrm{d}s\ |\boldsymbol{t}_\perp(s)|^2/2$ with $\boldsymbol{t}_\perp(s) = (t_y(s), t_z(s))$ being transverse components. In addition, from the constraint $|\boldsymbol{t}(s)| = 1$, the x component of the tangent vector can be written as $t_x = 1 - |\boldsymbol{t}_\perp|^2/2 + O(|\boldsymbol{t}_\perp|^4)$. To quadratic order, the relation $(\partial_s \boldsymbol{t}(s))^2 = (\partial_s \boldsymbol{t}_\perp(s))^2$ holds, so that the free energy can be written as

$$F = \frac{1}{2}\int_0^L \mathrm{d}s \left[\kappa\left(\frac{\partial \boldsymbol{t}_\perp}{\partial s}\right)^2 + f|\boldsymbol{t}_\perp|^2\right] - fL \tag{4}$$

Under our experimental conditions, both ends of the chain are fixed, so the transverse fluctuation should have a reversal symmetry with maximum at the midpoint, as shown in Figure 3. To implement the boundary conditions $\boldsymbol{r}_\perp(0) = \boldsymbol{r}_\perp(L) = \vec{0}$, where $\boldsymbol{r}_\perp(s) = (r_y(s), r_z(s)) = \int_0^s \mathrm{d}s'\, \boldsymbol{t}_\perp(s')$, we define the Fourier transform as

$$\boldsymbol{t}_\perp(s) = \frac{1}{L}\sum_{n=1}^{\infty} \hat{\boldsymbol{t}}_\perp(n) \cos\left(\frac{n\pi s}{L}\right) \tag{5}$$

Omitting a constant factor fL, the free energy eq 4 can be rewritten in Fourier space as

$$F = \frac{1}{2}\left(\frac{1}{2L}\right)\sum_{n=1}^{\infty} \hat{\boldsymbol{t}}_\perp(n)\hat{\boldsymbol{t}}_\perp(-n)[\kappa(\pi n/L)^2 + f] \tag{6}$$

Mode correlations follow from the equi-partition theorem as

$$\begin{aligned}\langle \hat{\boldsymbol{t}}_\perp(n_1)\cdot\hat{\boldsymbol{t}}_\perp(n_2)\rangle &= 2\frac{4Lk_BT}{\kappa(n_1\pi/L)^2 + f}\delta_{(n_1+n_2)0} \\ &= \frac{8L}{l_p((n_1\pi/L)^2 + l_f^{-2})}\delta_{(n_1+n_2)0}\end{aligned} \tag{7}$$

where the leading factor 2 in the first line takes account of the two independent components in $\boldsymbol{t}_\perp$, and $l_f = (\kappa/f)^{1/2} = l_p\phi^{-1/2}$ stands for a correlation length of $\boldsymbol{t}_\perp(s)$, which depends on f. The correlation function is then

$$\begin{aligned}\langle \boldsymbol{t}_\perp(s_1)\cdot\boldsymbol{t}_\perp(s_2)\rangle = 2\frac{L}{l_p\pi^2}\sum_{n_1=1}^{\infty}\frac{1}{n_1^2 + p^2}[&\cos(n_1(\tilde{s}_1 + \tilde{s}_2)) \\ &+ \cos(n_1(\tilde{s}_1 - \tilde{s}_2))]\end{aligned} \tag{8}$$

where variables $p = L/(\pi l_f)$ and $\tilde{s} = \pi s/L$ are introduced. Using a formula

$$\sum_{n=1}^{\infty}\frac{\cos(nx)}{n^2 + a^2} = \frac{\pi}{2a}\frac{\cosh(a(\pi - x))}{\sinh(a\pi)} - \frac{1}{2a^2} \quad [0 \le x \le 2\pi] \tag{9}$$

eq 8 becomes

$$\begin{aligned}\langle \boldsymbol{t}_\perp(s_1)\cdot\boldsymbol{t}_\perp(s_2)\rangle = \phi^{-1/2} \\ \times\left[\frac{\cosh\{p(\pi - (\tilde{s}_1 + \tilde{s}_2))\} + \cosh\{p(\pi - (|\tilde{s}_1 - \tilde{s}_2|))\}}{\sinh(p\pi)} - \frac{2}{\pi p}\right]\end{aligned} \tag{10}$$

This expression obtained through the Fourier cosine expansion analysis looks a bit awkward, but by calculating the contour integral of $\langle|\boldsymbol{t}_\perp(s)|^2\rangle$ for long WLCs $L \gg l_f$

$$\begin{aligned}\int_0^L \mathrm{d}s\langle(\boldsymbol{t}_\perp(s))^2\rangle &\simeq \phi^{-1/2}L\left[\frac{\cosh(p\pi)}{\sinh(p\pi)} - \frac{2}{p\pi}\right] \\ &\simeq \phi^{-1/2}L\end{aligned} \tag{11}$$

one can check the force−extension relation

$$l = L - \frac{1}{2}\int_0^L \mathrm{d}s\ \langle(\boldsymbol{t}_\perp(s))^2\rangle \simeq L\left(1 - \frac{\phi^{-1/2}}{2}\right) \tag{12}$$

for strongly stretched WLCs.[9]

dx.doi.org/10.1021/ma300019a | Macromolecules 2012, 45, 2857−2862

Using eq 10, the transverse fluctuation can be deduced as

$$\langle \boldsymbol{r}_\perp(s)^2\rangle = \int_0^s ds_1 \int_0^s ds_2 \,\langle \boldsymbol{t}_\perp(s_1)\cdot\boldsymbol{t}_\perp(s_2)\rangle$$
$$= \frac{Ll_f\phi^{-1/2}}{\pi}\left[\left\{2\tilde{s} + \frac{1}{p}\left(\frac{\cosh(p(\pi-2\tilde{s}))}{\sinh(p\pi)} - \frac{\cosh(p\pi)}{\sinh(p\pi)}\right)\right\} - \frac{(2\tilde{s})^2}{2\pi}\right]$$
$$= Ll_f\phi^{-1/2}\left[-2\left(\frac{s}{L}-\frac{1}{2}\right)^2 + \frac{1}{2} + \left(\frac{l_f}{L}\right)\frac{\cosh\{(L-2s)/l_f\} - \cosh\{L/l_f\}}{\sinh\{L/l_f\}}\right] \quad (13)$$

It is noted that this equation has a desired reversal symmetry $\langle \boldsymbol{r}_\perp(s)^2\rangle = \langle[\boldsymbol{r}_\perp(L-s)]^2\rangle$. The last term in the large bracket in eq 13 quickly approaches to a constant value $-l_f/L$ with the increase in $s(\geq l_f)$, which is negligible in the long WLC $L/l_f \gg 1$; the value of L/l_f is 10^2 to 10^3 in our experiments. Since $s/L = (\langle r_x(s)\rangle)/l = (x/l)(\equiv\hat{x})$, the transverse fluctuation in y direction at $\hat{x}$ can be described by the following equation:

$$\sigma_y^2(\hat{x}) = \frac{\langle|\boldsymbol{r}_\perp(\hat{x})|^2\rangle}{2} \simeq -Ll_p\phi^{-1}\left[\left(\hat{x}-\frac{1}{2}\right)^2 - \frac{1}{4}\right] \quad (14)$$

where the leading factor $^1/_2$ in the first equality is due to the projection on $x-y$ plane. We note that the transverse fluctuation of a strongly stretched DNA with fixed both ends is almost quadratic, showing the maximum $\sigma_{max}^2 \simeq Ll_p\phi^{-1}/4$ at the middle ($\hat{x} = {}^1/_2$). As eq 13 shows, however, a deviation from the quadratic function is expected to be apparent for very stiff polymers such as actin filaments and microtubules under the moderate tension ($L/l_f \sim 1$).

Comparison between Theory and Experiments. For a single DNA molecule of L = 18.3 μm, the transverse fluctuations obtained in both experiments and eq 14 are shown in Figure 5. In strong force regime (ϕ = 9.2), the experimental data is nearly described by eq 14. Note that there are no fitting parameters in eq 14, where l_p is fixed to 65 nm. In the lower force regimes (ϕ = 1.3), however, the deviation of the theoretical curves from the experimental results becomes apparent. At around both fixed ends, the brightness of the beads may suppress the actual DNA's fluctuations in the image analysis.

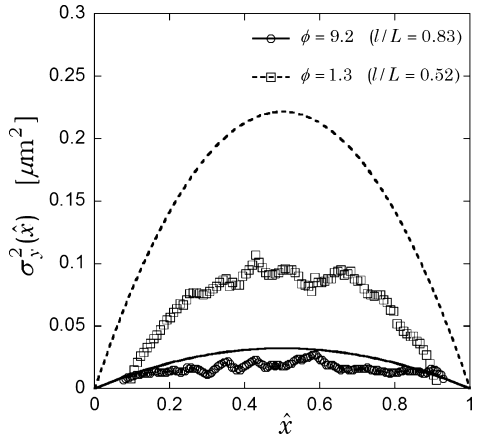


Figure 5. The transverse fluctuation $\sigma_y^2(\hat{x})$ in different force regimes ϕ = 9.2 and 1.3, where L = 18.3 μm and l_p = 65 nm.

To see the dependence of the transverse fluctuation on the tension of DNA, $\hat{\sigma}_{max}^2 \equiv \sigma_{max}^2/Ll_p$ is plotted with solid symbols as a function of ϕ^{-1} in Figure 6. It is found that all data

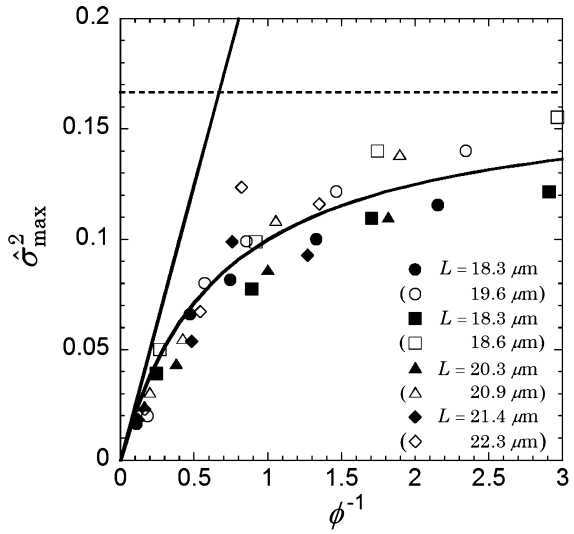


Figure 6. Dependence of $\hat{\sigma}_{max}^2$ on ϕ^{-1}. The data for four different DNA molecules are plotted. The difference of L might be caused by the binding ratio of YOYO-1 to DNA and/or the nonspecific binding of DNA to beads. The solid and dashed lines are $\hat{\sigma}_{max}^2 = \phi^{-1}/4$ and 1/6, respectively. The solid curve is eq 15. The solid and open symbols are results obtained by data analysis for each DNA using l_p = 65 and 50 nm, respectively. Note that the values of L slightly depend on the choice of l_p, since they were determined from the force–extension curve by fitting using eq 1 with fixed l_p.

in different L are almost collapsed to a single curve, which indicates that the relation between the fluctuation normalized by Ll_p is determined by the normalized force ϕ. In the strong force regime ($\phi^{-1} \ll 1$), we can see that the theory of a stretched WLC ($\hat{\sigma}_{max}^2 = \phi^{-1}/4$) well explain the experimental results. As ϕ^{-1} increases, however, the experimental results deviate from the theoretical values and approach to a constant value. The dashed black line in Figure 6 indicates $\hat{\sigma}_{max}^2 = {}^1/_6$ which corresponds to the square of the gyration radius of an ideal ring polymer.[10] Because the both ends of DNA are fixed in our experiments, the low force limit ($\phi^{-1} \to \infty$) is realized when the end-to-end distance is 0, in which the linear DNA should behave a ring polymer.[11] Thus, our results in both strong and low force limit in Figure 6 are reasonable.

The force–extension relation eq 1 was obtained by interpolating the low force linear response behavior and the high force regime close to full stretching. It turned out to be of great practical importance, and has been widely used for the elastic characterization of single polymers. Indeed, the normalized form of the force–extension relation in eq 1 means that we can treat polymers in any scales with the same way; both a single DNA in micrometer scale[12,13] and a single protein in nanometer scale[14−16] show identical force–extension curves when the force and the extension are normalized by

dx.doi.org/10.1021/ma300019a | Macromolecules 2012, 45, 2857−2862

k_BT/l_p and L, respectively. In the same spirit, we propose the following force−fluctuation relation

$$\hat{\sigma}_{max}{}^2 = \frac{\phi^{-1}}{4(1 + 3\phi^{-1}/2)} \quad (15)$$

where we interpolate strong and low force limiting behaviors to cover the entire force range. As demonstrated in Figure 6, the proposed formula eq 15 captures overall trend of experimental results. Once $\hat{\sigma}_{max}{}^2$ is obtained from eq 15, one can construct the full spatial fluctuation profile using eq 14 as

$$\sigma_y^2(\hat{x}) \simeq 4\sigma_{max}{}^2\hat{x}(1 - \hat{x}) \quad (16)$$

which is expected to be very accurate for strongly stretched long WLCs ($\phi \gg 1$, $L \gg l_f$). Moreover, the construction of the interpolation formula eq 15 guarantees that the above fluctuation profile in the weak force regime ($\phi \ll 1$) coincides with the exact result for ideal chains whose both ends are trapped in fixed positions.[11]

Close inspection reveals that the curve shows slightly larger values than experimental values. The difference may come from several reasons: e.g., the effect of beads, underestimation of the fluctuation in image analysis, overestimation of l_p, and the oversimplification in eq 15. Recent experiments have shown that YOYO-1 labeled DNA has a persistence length of 50 nm.[17] Accordingly, our experimental data were analyzed again using l_p = 50 nm, instead of 65 nm, and the results are plotted with open symbols in Figure 6. In the strong to intermediate force regime, the theoretical curve seems to fit the results of l_p =50 nm better than those of l_p =65 nm. Although several factors mentioned above should be clarified by future studies, the force−fluctuation relation in eq 15 may be practically useful for the quantitative estimation of the fluctuation of manipulated polymers.

Another interesting feature lies in the nature of fluctuation under the strong stretching. In this regime, the maximum fluctuation given by eq 14 and eq 16 can be transformed as

$$\sigma_{max}{}^2 \simeq \frac{Ll_p\phi^{-1}}{4} = \frac{Lk_BT}{4f} \quad (17)$$

which indicates that the fluctuation is independent of the persistence length. Physically, this arises from the combination of the following two factors $\phi^{-1/2}$ and l_f in eq 13. The first factor is the amplitude of the tangent correlation $\langle \boldsymbol{t}_\perp(s)\cdot\boldsymbol{t}_\perp(s)\rangle$, which decays as $l_p^{-1/2}$. On the other hand, the second one is the correlation length $l_f = l_p\phi^{-1/2}$, which grows as $l_p^{1/2}$, resulting in the cancellation with the first. Exploiting this unique property, one can extract the contour length of sample polymers from the fluctuation measurement. Since this involves only one parameter (L), it should allow an accurate determination of the contour length from the fitting.

Finally, we would like to point out the possible implication of our study to the behaviors of DNA confined in nanoscale slits. In narrow two-dimensional slit geometries, the slit spacing provides an additional length scale, decomposing the bond correlation length l_p into longitudinal $l_\parallel$ and transverse $l_\perp$ components, while in larger length scale, the DNA assumes the fluctuating two-dimensional coil conformation. Recently, Chen et al. investigated the conformational properties of DNA chains pulled at their ends in nanoslits, and proposed a force−extension relation by modifying the Marko−Siggia formula by including the dependence of $l_\parallel$ on the slit spacing.[18] In contrast to the force−extension relation, the force−fluctuation relation is free from the correlation length as manifested in eq 17. Therefore, we expect that the present result can be applied to the DNA in nanoslits, too.

CONCLUSIONS

In this paper, we observed transverse fluctuations of single DNA molecules whose both ends were fixed by optical tweezers. The end-to-end distance was widely changed, and the force−fluctuation relation was experimentally obtained. In the strong force regime, the theory for worm-like chain explains the force−fluctuation relation, while in the low force regime, the fluctuation approaches a value for an ideal ring polymer. We introduced an interpolate formula which describes the force−fluctuation relation in the entire force regime. The formula captures the overall trend in experiments, which will be practically useful for the quantitative discussion not only in polymer physics but also in biological processes in living cells.

AUTHOR INFORMATION

Corresponding Author

*E-mail: ymura@cc.tuat.ac.jp.

Notes

The authors declare no competing financial interest.

ACKNOWLEDGMENTS

We thank K. Okumura, H. Nakanishi, and J. Wakou for discussions. This work was supported by MEXT KAKENHI 18068005, the TUAT program "Interdisciplinary Research Unit in Photon-Nano Science", and in part, the JSPS Core-to-Core Program "International research network for non-equilibrium dynamics of soft matter".

REFERENCES

(1) Wang, Y. M.; Austin, R. H.; Cox, E. C. *Phys. Rev. Lett.* **2006**, *97*, 048302.
(2) Halford, S. E.; Marko, J. F. *Nucleic Acids Res.* **2004**, *32*, 3040−3052.
(3) Hodges, C.; Bintu, L.; Lubkowska, L.; Kashlev, M.; Bustamante, C. *Science* **2009**, *325*, 626−628.
(4) Marko, J. F.; Siggia, E. D. *Macromolecules* **1995**, *28*, 8759−8770.
(5) Quake, S. R.; Babcock, H.; Chu, S. *Nature* **1997**, *388*, 151−154.
(6) Crut, A.; Lasne, D.; Allemand, J.-F.; Dahan, M.; Desbiolles, P. *Phys. Rev. E* **2003**, *67*, 051910−1−6.
(7) Yan, J.; Kawamura, R.; Marko, J. F. *Phys. Rev. E* **2005**, *71*, 061905.
(8) Murayama, Y.; Wada, H.; Sano, M. *EPL* **2007**, *79*, 58001.
(9) Even if we apply the Fourier expansion in the form $\boldsymbol{t}_\perp(s) = (1/L)\sum_{n=-\infty}^{\infty}\hat{\boldsymbol{t}}_\perp(n)\, e^{2\pi ins/L}$ with the periodic boundary condition, we obtain the same force−extension relation as eq 12. The fluctuation profile also remains intact, expect for the boundary region $s \lesssim l_f$ and $L - s \lesssim l_f$. One can check that the only modification is required in the last term in the large bracket in eq 13, where the factor l_f should be replaced by $2l_f$.
(10) Grosberg, A. Y.; Khokhlov, A. R. *Statistical Physics of Macromolecules*; AIP Press: Melville, NY, 1994.
(11) Kawai, K.; Okumura, K. *Chem. Phys. Lett.* **2007**, *439*, 369−373.
(12) Smith, S. B.; Finzi, L.; Bustamante, C. *Science* **1992**, *258*, 1122−1126.
(13) Bustamante, C.; Marko, J. F.; Siggia, E. D.; Smith, S. *Science* **1994**, *265*, 1599−1600.
(14) Rief, M.; Gautel, M.; Oesterhelt, F.; Fernandez, J. M.; Gaub, H. E. *Science* **1997**, *276*, 1109−1112.
(15) Kellermayer, M. S. Z.; Smith, S. B.; Granzier, H. L.; Bustamante, C. *Science* **1997**, *276*, 1112−1116.

(16) Ishii, T.; Murayama, Y.; Katano, A.; Maki, K.; Kuwajima, K.; Sano, M. *Biochem. Biophys. Res. Commun.* **2008**, *375*, 586−591.
(17) Günther, K.; Mertig, M.; Seidel, R. *Nucleic Acids Res.* **2010**, *38*, 6526−6532.
(18) Chen, Y.-L.; Lin, P.-k.; Chou, C.-F. *Macromolecules* **2010**, *43*, 10204−10207.

Macromolecules

Article

pubs.acs.org/Macromolecules

pH-Responsive Hairy Particles Synthesized by Dispersion Polymerization with a Macroinitiator as an Inistab and Their Use as a Gas-Sensitive Liquid Marble Stabilizer

Syuji Fujii,[†,*] Kodai Aono,[†] Motomichi Suzaki,[†] Sho Hamasaki,[†] Shin-ichi Yusa,[‡] and Yoshinobu Nakamura[†,§]

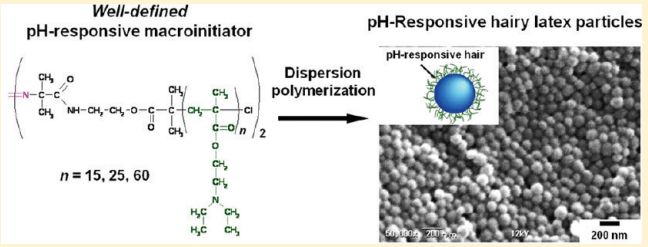
[†]Department of Applied Chemistry, Faculty of Engineering, Osaka Institute of Technology, 5-16-1 Ohmiya, Asahi-ku, Osaka 535-8585, Japan

[‡]Graduate School of Engineering, University of Hyogo, 2167 Shosha, Himeji, Hyogo 671-2280, Japan

[§]Nanomaterials Microdevices Research Center, Osaka Institute of Technology, Osaka, Japan

Supporting Information

ABSTRACT: We studied dispersion polymerization in detail using *well-defined* pH-responsive poly[2-(diethylamino)ethyl methacrylate]- (PDEA-) based macroinitiators as an inistab (*ini*tiator + *stab*ilizer). Colloidally stable polystyrene (PS) latex particles carrying pH-responsive PDEA hair (PDEA–PS particles) were successfully synthesized in polymerization media with solubility parameters ranging between 22.3 $(MPa)^{1/2}$ and 26.0 $(MPa)^{1/2}$. The number-average particle diameters were finely controlled between 90 and 460 nm. The PDEA–PS latex particles were dispersed in acidic aqueous media in which the PDEA hair was protonated and solvated, and were flocculated in basic aqueous media in which the PDEA hair was deprotonated and precipitated. The dried PDEA–PS particles served as an effective gas-responsive stabilizer for liquid marbles. The liquid marbles were stable in H_2O vapor for over 18 h, but disintegrated immediately (<2 s) upon exposure to HCl gas.



INTRODUCTION

Dispersion polymerization is widely used to synthesize near-monodisperse polymer latex particles with diameters ranging between submicrometer and micrometer.[1−14] During the polymerization, an initially homogeneous mixture of solvent, monomer, initiator and steric stabilizer nucleates and then grows into polymer particles. The solvent is selected to be a poor solvent for the polymers being formed, but a good solvent for the monomers and the stabilizers, which protects the particles from coalescence by steric stabilization.[7] For the steric stabilizer, polymers with various kinds of architecture have been used: homopolymers, block copolymers and graft copolymers.[1−10] As homopolymer stabilizers, poly(acrylic acid),[2,4] poly(*N*-vinylpyrrolidone),[3] hydroxypropyl cellulose,[4,6c] and poly(dimethylsiloxane) (PDMS),[8] have been successfully employed. Block[9] and graft[10] copolymers, which are generally designed to have medium-soluble blocks and anchoring blocks, have also been proven to work as effective steric stabilizers. In addition to the preprepared steric stabilizers mentioned above, macromonomers,[11] macro chain transfer agents[12] and macroinitiators,[13] which form block or graft copolymer-type steric stabilizers during the dispersion polymerization, have become of interest. Polymeric azoinitiators (macroazoinitiators) can generate block copolymers via free radical polymerization and the block copolymers can function as colloidal stabilizers in dispersion polymerization systems if their structures and chemistry are suitable. Kawaguchi and co-workers[13a] reported polymerization of methyl methacrylate (MMA) using a PDMS-based azoinitiator and demonstrated that colloidally stable polymer particles were obtained using polymerization media with suitable solubility parameters. Okubo and co-workers[13b] synthesized poly(methyl methacrylate) (PMMA) particles carrying PDMS hair by dispersion polymerization using the PDMS-based azoinitiator as an inistab (*ini*tiator + *stab*ilizer).[14] Kitano and co-workers[13c,d] conducted a series of synthetic studies of hairy polystyrene (PS) latex particles using tailor-made poly(*N*-isopropylacrylamide) and poly(methacryloyloxyethyl-*D*-glucopyranoside)-based macroazoinitiators. Tauer[13e] demonstrated the one-pot production of hairy PS latex particles using poly(ethylene glycol)-based macroazoinitiators. These macroinitiator-based dispersion polymerizations are versatile and facile routes toward hairy polymer latexes and are applicable to a wide range of monomers. In the majority of cases, colloidal stabilizers used in the dispersion polymerization are polydisperse and media-soluble stimuli-independent polymers, whereas dispersion polymerization using *well-defined stimuli-responsive* polymeric stabilizers has not been investigated in detail. Recently, we reported the

Received: January 6, 2012
Revised: March 3, 2012
Published: March 12, 2012

 © 2012 American Chemical Society

synthesis of pH-responsive poly[2-(diethylamino)ethyl methacrylate]- (PDEA-) based macroazoinitiators (PDEA$_n$−MAI) with a narrow molecular weight distribution and indicated their possible use as inistabs.[14] PDEA homopolymer is a weak polybase with a pK_a value of 7.3,[14,15] which is soluble in aqueous media below pH 7 due to protonation of the tertiary amine groups. At pH 8 or above, PDEA homopolymer has very low or zero charge density, and neutral PDEA chains precipitate in aqueous media.

Herein we describe dispersion polymerization using the *well-defined* PDEA-based inistab for the synthesis of PS latex particles carrying pH-responsive PDEA hair (PDEA$_n$−PS particles). The effects of the solubility parameter of the media, degree of polymerization of PDEA, and concentration of the inistab have been investigated in detail. To the best of our knowledge, this is the first systematic study on hairy latex particles synthesized by dispersion polymerization using an inistab with a narrow molecular weight distribution. The PS latex particles obtained were characterized in terms of their particle size, size distribution, morphology, chemical composition, and colloidal stability using the laser diffraction method, scanning electron microscopy (SEM), elemental microanalysis, ^{1}H nuclear magnetic resonance spectroscopy (^{1}H NMR), and aqueous electrophoresis measurements and turbidity measurements, respectively. Furthermore, one of these dried particles was shown to be an interesting gas-responsive particulate liquid marble stabilizer.

EXPERIMENTAL SECTION

Materials. 2-Bromoisobutyryl bromide (98%), triethylamine (99.5%), 2-(diethylamino)ethyl methacrylate (DEA, 99%), styrene, PS homopolymer (average MW 45 000), 2-propanol (IPA, purity 99%), copper(I) chloride [Cu(I)Cl, 99%], heptane (99%), cyclohexane (99%), toluene (99%), cyclohexanone (99%), ethanol (99.5%) and ethylene glycol (99%) were purchased from Sigma-Aldrich. 2,2′-Bipyridyl (bpy, 99+%), chloroform-*d* ($CDCl_3$, 99.8%), *n*-dodecane (99%), 1,4-dioxane (99%), *n*-amylalcohol (99%) and 1-butanol (99%) were purchased from Wako Chemicals. 2,2′-Azobis[2-methyl-*N*-(2-hydroxyethyl)propionamide] (VA-086) was kindly provided by Wako Chemicals. Styrene was purified by passage through a column of activated basic alumina (activated, basic, Brockmann 1, standard grade, ~150 mesh, 58 Å) prior to storage at −15 °C before use. Milli-Q water (Millipore Corp., MA) with a specific resistance of 18.2×10^6 Ω·cm was used. The silica gel used for removal of the atom transfer polymerization (ATRP) copper catalyst was 10180 grade (70−230 mesh, 40 Å) and was used as received from Sigma-Aldrich.

Preparation of PDEA−MAI by ATRP. 2,2′-Azobis{2-methyl-*N*-[2-(2-bromoisobutyryloxy)ethyl] propionamide} (AMBEP) was synthesized using VA-086 according to our previous report.[14] In a 30-mL round-bottomed flask, AMBEP (0.263 g, 0.449 mmol) and DEA (10 g, 54.0 mmol, target degree of polymerization, DP of 60) and IPA (10 mL) were mixed and degassed by nitrogen bubbling for 30 min and then Cu(I)Cl (0.0891 g, 0.900 mmol) and bpy (0.281 g, 1.80 mmol) were quickly added. The reaction mixture immediately turned dark brown and progressively became more viscous, indicating the onset of polymerization. The polymerization was quenched by exposing the reaction vessel to air. The resulting polymer was diluted with IPA and passed through a silica column to remove the spent ATRP catalyst. The final macroazoinitiator was dried under vacuum overnight to obtain an off-white product. A similar protocol was used for ATRP with other target DPs ranging between 15 and 60 (see Table 1). Hereafter, the target DP is shown as a subscript after PDEA.

Characterization of PDEA−MAI.

Gel Permeation Chromatography (GPC). GPC analysis was performed using a refractive index (RI) detector equipped with a Shodex Ohpak SB-G guard column and SB−804 HQ column (bead size =10 μm, exclusion limit: $M_n = 1.0 \times 10^6$, pullulan) working at 40 °C under a flow rate of 0.6 mL/min. An 0.3 M Na_2SO_4 aqueous solution containing 0.5 M acetic acid was used as an eluent. The molecular weight of the sample polymer was calibrated with standard poly(2-vinylpyridine) samples of six different molecular weights ranging from 5.70×10^3 to 3.16×10^5 g/mol.

^{1}H NMR Measurements. ^{1}H NMR spectra were recorded in $CDCl_3$ for all macroazoinitiators using a JEOL EX-270 NMR spectrometer.

Table 1. Reaction Conditions for the Atom Transfer Radical Polymerization of DEA Using AMBEP and Molecular Weight Data for PDEA−MAI

moiety	units	PDEA$_{15}$−MAI[a]	PDEA$_{25}$−MAI[b]	PDEA$_{60}$−MAI[b]
AMBEP[c]	g	0.79	0.31	0.26
DEA	g	7.5	5.0	10
2-propanol	mL	10	5.0	10
Cu^{1}Cl[c]	g	0.26	0.11	0.089
bpy[c]	g	0.84	0.33	0.28
M_n(cal)[d]		6100	9900	22 700
M_n(^{1}H NMR)[e]		6300	9300	23 300
M_w(GPC)[f]		13 300	17 700	17 800
M_w/M_n[g]		1.06	1.07	1.13
DP (^{1}H NMR)[h]		16	27	63

[a]35 °C, 6 h, N_2 [b]25 °C, 24 h, N_2 [c]AMBEP/Cu(I)Cl/bpy, 1/2/4 (molar ratio). [d]M_n(cal): Theoretical molecular weight. [e]M_n(^{1}H NMR): Number-average molecular weight determined using ^{1}H NMR spectroscopy. [f]M_w(GPC): Weight-average molecular weight determined using GPC. [g]M_w/M_n: Polydispersity determined using GPC. [h]DP: Degree of polymerization determined by ^{1}H NMR spectroscopy.

Dispersion Polymerization Using PDEA−MAI. PS latex particles were synthesized by the dispersion polymerization of styrene using PDEA−MAI as an inistab under various conditions as shown below (for reaction condition details, see Supporting Information). The latex particles obtained were purified by repeated centrifugation-redispersion cycles with IPA using a Beckman Coulter Allegra 64R centrifuge ALV03E06 with a Beckman F1202 rotor (typically 20 000 rpm for 10−30 min) or a Hitachi CF16RX type centrifuge with a Hitachi T15A36 rotor (typically 5000 rpm for 30 min).

Method 1: Polymerization Media. Dispersion polymerizations of styrene were conducted using the PDEA$_{60}$−MAI or PDEA$_{25}$−MAI in various media, namely heptane, *n*-dodecane, cyclohexane, toluene, cyclohexanone, 1,4-dioxane, *n*-amylalcohol, IPA, ethanol, ethylene glycol, and a mixture of IPA and water. The volume ratio of IPA/water was varied between 100/0 and 80/20. The PDEA$_{60}$−MAI (2.18 g; 1.0 mol % based on styrene) and styrene monomer (1.0 g) were added to the polymerization medium (10 mL) in a flat-bottomed 13.5-mL vial containing a magnetic stirrer bar. The reaction mixture was vigorously stirred at room temperature until the macroazoinitiator and monomer dissolved completely. The reaction mixture was then degassed using five alternating cycles of evacuation and pressurization with dry nitrogen (starting with evacuation). The polymerization was started by placing the reaction vessel in an oil bath (80 °C). The reaction was allowed to proceed for 48 h with continuous stirring at 500 rpm under a nitrogen atmosphere.

Method 2: Degree of Polymerization of PDEA$_n$−MAI. Dispersion polymerizations using PDEA$_n$−MAI with DPs of 15, 25, and 60 were conducted in IPA under similar conditions as those used in method 1 at an azo group concentration of 1.0 mol % based on styrene monomer. The polymerization was conducted at 80 °C under nitrogen atmosphere for 48 h.

Method 3: Combination of PDEA$_{60}$−MAI and Small Azoinitiator. PDEA$_{60}$−MAI (0.218 g; 0.1 mol % based on styrene), VA-086 (0.0249 g; 0.9 mol % based on styrene), and styrene monomer (1.0 g) were added to IPA (10 mL) in a flat-bottomed 13.5-mL vial containing a magnetic stirrer bar. The reaction mixture was vigorously stirred at

room temperature until the macroazoinitiator, VA-086 and monomer had dissolved completely. The reaction mixture was then degassed using five alternating cycles of evacuation and pressurization with dry nitrogen (starting with evacuation). The polymerization commenced by placing the reaction vessel in an oil bath (80 °C). The reaction was allowed to proceed for 1 week with continuous stirring at 500 rpm under a nitrogen atmosphere. A similar protocol was used for the dispersion polymerization using a mixture of $PDEA_{60}$–MAI and VA-086 at a constant azo group concentration of 1.0 mol % based on styrene monomer (the molar ratio of $PDEA_{60}$–MAI/VA-086 was varied between 100/0 and 0/100).

Characterization of $PDEA_n$–PS Latex Particles.

Aqueous Electrophoresis. ζ potentials were calculated from the measured electrophoretic mobilities using a Malvern Zetasizer Nano Nano-ZS ZEN3600 equipped with a He–Ne laser light source (4 mW at 632.8 nm). Measurements were obtained as a function of pH on diluted dispersions (0.01 wt %) by gradually adding NaOH, starting from an initial pH of approximately 3. The ζ potentials were averaged over 20 runs. The variance was typically within the size of the data points shown.

Scanning Electron Microscopy (SEM). The centrifugally washed latex dispersion droplets were dried on an aluminum stub and sputter-coated with gold using an Au coater (SC-701 Quick Coater, Elionix, Japan) in order to minimize sample-charging problems. The SEM studies were carried out using a Keyence VE-8800 SEM operated at 5 kV.

Fourier Transform Infrared (FT-IR) Spectroscopy. The compositions of the synthesized particles were studied by FT-IR measurement of samples dispersed in KBr discs using a Horiba Freexact-II FT-720 (20 scans per spectrum at 4 cm^{-1} resolution).

Chemical Composition. CHN elemental microanalyses were carried out using a CHN-Corder MT-5 (Yanaco, Japan). The PDEA loadings of the $PDEA_n$–PS particles were determined by comparing their nitrogen contents to that of the PDEA homopolymer prepared by free radical solution polymerization in toluene.

^{1}H NMR Spectroscopy. ^{1}H NMR spectra were recorded with a Varian Mercury 300 spectrometer for the PS particles solution in $CDCl_3$. The integrated intensity of the relatively weak signal at around 4.1 ppm due to the two oxymethylene protons adjacent to the ester group of the DEA residues (chosen because this peak is not obscured by overlapping PS signals) was compared to the integration of the three protons on the polymer backbone from the styrene residues at 1.2–2.3 ppm to estimate the weight ratio of PS and PDEA in the latex particles. The pH-responsive behavior of the $PDEA_n$–PS particles in water was investigated in D_2O/DCl or D_2O/NaOD.

Percentage Transmittance (% T) Measurement. % T values at 545 nm of the aqueous dispersion of the $PDEA_n$–PS latex particles were recorded on a Shimadzu UV-1600 spectrophotometer using a 1.0 cm path length quartz cell at various pHs. The measurements were conducted on the upper portion of the sample since the precipitated polymer in aqueous media settled down to the bottom of the quartz cell, which led to high % T values.

Particle Size Analysis by Laser Diffraction Method. A Malvern Mastersizer 2000 instrument equipped with a small volume Hydro 2000SM sample dispersion unit (approximately 150 mL including the flow cell and tubing), a HeNe laser operating at 633 nm and solid-state blue laser source operating at 466 nm were used to determine the size of the latex particles. The stirring rate was adjusted to 2,000 rpm. The mean particle diameter was taken to be the volume mean diameter (D_v), which is mathematically expressed as $D_v = \sum D_i^4 N_i / \sum D_i^3 N_i$ (D_i, the diameters of individual particles; N_i, the number of particles corresponding to the diameters).

Liquid Marble Preparation. An aqueous dispersion of the $PDEA_{60}$–PS particles (synthesized at a $PDEA_{60}$–MAI/VA-086 molar ratio of 10/90, see method 3) after centrifugal washing was freeze-dried overnight and stored under vacuum at 25 °C before use. Individual liquid marbles were prepared by rolling a 15 μL droplet of deionized water over the freeze-dried $PDEA_{60}$–PS particle powder. The dried particles immediately coated the water droplet and rendered it both hydrophobic and nonwetting.

Characterization of the Liquid Marbles.

Digital Photography. Digital images were captured using a Ricoh Caplio R7 camera operating in optical wide zoom mode.

High-Speed Camera. For observation of the motion of liquid marbles, a high speed camera (VW-6000, Keyence) equipped with a zoom lens (VH-Z20R, Keyence) and a free angle stand (VW-S200, Keyence) were used. The shutter speed was set at 2 ms and a frame rate of 497.723/s was utilized.

RESULTS AND DISCUSSION

PDEA–MAI. A combination of conventional free radical polymerization with ATRP using AMBEP was achieved. Because DEA can be polymerized in a controlled manner by ATRP at a relatively low temperature (25 °C) in protic media,[16,17] well-defined macroazoinitiators were prepared without significant loss of the azo functional group. The percentage of the decomposed difunctional initiator was calculated to be below 0.2%, considering the k_d value of the AMBEP at 25 °C (1.38×10^{-9} s^{-1}).[14] The synthetic details and characterization data for $PDEA_n$–MAI with various degrees of polymerization are summarized in Table 1. For the $PDEA_{15}$–MAI system, ATRP was conducted at 35 °C in order to start the polymerization from homogeneous solution: AMBEP did not dissolve in the medium at 25 °C because there was not enough DEA monomer which also served as a solvent for AMBEP. For the ATRP of DEA, Br-based initiator was used in combination with Cu^ICl catalyst and bpy ligand in order to obtain the macroinitiators with better controlled molecular weight: the mixed halogen system R–Br/CuCl should give faster initiation, slower propagation, and therefore better control of molecular weight.[18] The resulting $PDEA_n$–MAI should carry alkyl chlorides as an end group. It is clear that there is a relatively good agreement between the target number-average molecular weights (M_n) calculated from the monomer/initiator molar ratios and those determined experimentally from ^{1}H NMR studies. Since ATRP has a reasonably good living character, the molecular weight distributions (polydispersity, M_w/M_n) of these polymer chains are relatively narrow (below 1.13), which allows significantly better control than conventional radical polymerization.

PDEA–PS Latex Particles. Hairy particles are defined as particles that carry grafted linear polymer chains having high affinity with the dispersing media on their surface. Several methods for the synthesis of these hairy particles have been proposed: (i) "grafting-from" method,[19] (ii) "grafting-to" method,[20] and (iii) emulsion/dispersion polymerizations in the presence of reactive polymers, such as media-philic macromonomer[11] macro chain transfer agents[12] and macro-initiators,[13] which serve as colloidal stabilizers, and (iv) self-assembly of block copolymers.[21] In the present work, a PDEA macroazoinitiator was used for the synthesis of PS latex particles carrying pH-responsive hair by dispersion polymerization. There have been several reports on the use of cationic polymers for pigment dispersion,[22] but there is surprisingly little work on the use of *well-defined* cationic polymers as latex stabilizers. This omission is quite surprising, since cationic polymers and latexes are commonly used in cosmetic and personal care products.

Method 1. It has been reported that the diameter of the latex particles can be controlled using polymerization media with different solubility parameter (SP) values in dispersion polymerization systems.[6c] SP values of the media determined the critical chain length of the polymers formed during the

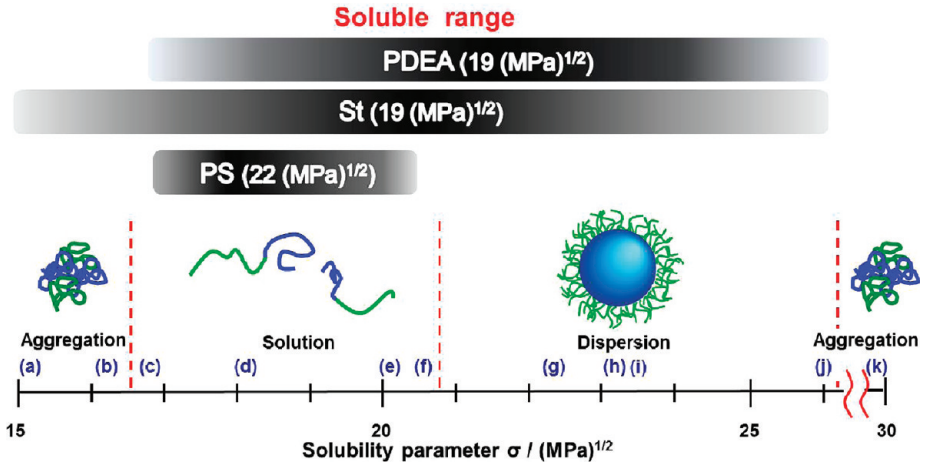


Figure 1. Relationship between SP values and morphologies of PDEA–PS products. SP values for solvents: (a) heptane [15.1 $(MPa)^{1/2}$], (b) *n*-dodecane [16.2 $(MPa)^{1/2}$], (c) cyclohexane [16.8 $(MPa)^{1/2}$], (d) toluene [18.2 $(MPa)^{1/2}$], (e) cyclohexanone [20.3 $(MPa)^{1/2}$], (f) 1,4-dioxane [20.5 $(MPa)^{1/2}$], (g) *n*-amylalcohol [22.3 $(MPa)^{1/2}$], (h) 1-butanol [23.3 $(MPa)^{1/2}$], (i) 2-propanol [23.5 $(MPa)^{1/2}$], (j) ethanol [26.0 $(MPa)^{1/2}$], and (k) ethylene glycol [29.9 $(MPa)^{1/2}$].

polymerization, which should affect latex diameters. In this study, the dispersion polymerizations were conducted in media with various SP values, namely heptane, *n*-dodecane, cyclohexane, toluene, cyclohexanone, 1,4-dioxane, *n*-amylalcohol, IPA, ethanol, ethylene glycol, and a mixture of IPA/water (Figure 1).

Before conducting the polymerizations, the relationship between SP values of the media and solubilities of PDEA, PS and styrene monomer in the media was investigated. Solubility check experiments were conducted at the same solute concentrations as the polymerization recipe. The SP value (δ) of styrene monomer, PDEA and PS homopolymers are calculated to be 18.9, 19.0, and 21.6 $(MPa)^{1/2}$, respectively, using the following Fedors equation,[23]

$$\delta = \left[\frac{\sum E_{coh}}{\sum V}\right]$$

where E_{coh} and V are atomic and group contributions for the energy of vaporization and molar volume, respectively.[24] SP values of the polymerization media were obtained from the Polymer Handbook.[24] PDEA homopolymer (M_n, 1.00×10^4 g/mol; M_w/M_n, 1.63: prepared by free radical solution polymerization in toluene) was dissolved in media with SP values ranging between 16.8 and 26.0 $(MPa)^{1/2}$, which are relatively close to that of PDEA [19.0 $(MPa)^{1/2}$]. In contrast, the PDEA homopolymer was not dissolved completely in media with SP values of 29.9 $(MPa)^{1/2}$ and at and below 16.2 $(MPa)^{1/2}$. Styrene monomer was completely dissolved in all media used in this study except for ethylene glycol. PS homopolymer was dissolved in media with SP values ranging between 16.8 and 20.5 $(MPa)^{1/2}$ and was swollen in media with SP values at and below 16.2 $(MPa)^{1/2}$, but was not dissolved in media with SP values at and above 22.3 $(MPa)^{1/2}$. Dispersion polymerizations could be accomplished in media with SP values between 22.3 $(MPa)^{1/2}$ and 26.0 $(MPa)^{1/2}$, where PDEA and styrene were dissolved and PS was not, as expected (Figure 1). The $PDEA_{60}$-*block*-PS copolymer solutions were produced in media with SP values ranging between 16.8 $(MPa)^{1/2}$ and 20.5 $(MPa)^{1/2}$, and aggregations were obtained above 26.0 $(MPa)^{1/2}$ and below 16.8 $(MPa)^{1/2}$. The formation of the PS latex particles consists of two stages: (1) the formation of PDEA-*block*-PS copolymers through the thermal decomposition of the azo group and free radical polymerization of styrene and (2) self-assembly of the PDEA-*block*-PS copolymers driven by the interaction between precipitated PS components in the media. Since the PDEA component is soluble in IPA, it should effectively operate as a colloidal protective hair layer to disperse the PS particles stably in the media of the dispersion polymerization system. As a control experiment, when AIBN was used as the initiator in place of the macroazoinitiators, the resulting polymers did not consist of particles, but coagulated. These results indicate that the macroinitiator had two functions as an initiator and a colloidal stabilizer in the dispersion polymerization.

SEM studies after centrifugal washing confirmed that spherical nanoparticles with relatively monodispersed diameters were synthesized (Figure S1, Supporting Information). The number-average diameters increased slightly from 85 to 103 nm with a decrease in SP value from 26.0 to 23.3 $(MPa)^{1/2}$. This result indicates that polymerization media with SP values close to that of PS gave longer critical precipitation chain lengths, which led to larger latex particles. A similar trend was also observed in the dispersion polymerization system by Tseug et al.[3]

SEM images and particle size distribution curves of $PDEA_{25}$–PS latex particles prepared using 1 mol % $PDEA_{25}$–MAI based on monomer in the polymerization media with IPA/water compositions of 100/0, 95/5 and 80/20 are shown in Figures S2 and S3, Supporting Information. Colloidally stable latex particles were obtained and the particles were spherical and reasonably monodisperse in all polymerization systems. It was expected that the addition of water to the media would cause a decrease in critical length of the diblock polymers needed for precipitation and thus affect the particle sizes. However, there was little effect of the composition of polymerization media on the diameters (volume-average diameters ranged between 118 and 121 nm).

Method 2. The macroinitiator concentration in the dispersion polymerization was determined as described below.[14] In general, for free radical polymerizations using a low molecular weight initiator, the concentration of the initiator was set at or below a few wt % based on monomers. The number of azo groups in a unit macroinitiator weight is very small compared to that in the low molecular weight initiator: 1

dx.doi.org/10.1021/ma300048m | *Macromolecules* 2012, 45, 2863–2873

Table 2. Diameter, Diameter Distribution, and Chemical Composition Data for the PDEA−PS Latex Particles Synthesized in This Study

	media	solubility parameter of media/(MPa)$^{1/2}$	D_n[a]/nm	D_v[b]/nm	D_w/D_n[c]	PDEA/% (^{1}H NMR)[d]	N/%[e]	PDEA/% (CHN%)[f]	PS/%[g]	PDEA-*b*-PS/PS homopolymer (w/w)[h]
$PDEA_{15}$−PS (100/0)[i]	IPA	23.5	103	100 ± 30	1.12	23	1.41	18.7	81.3	100/0
$PDEA_{25}$−PS (100/0)[i]	IPA	23.5	116	120 ± 40	1.16	18	1.02	13.1	86.9	100/0
$PDEA_{60}$−PS(100/0)[i]	IPA	23.5	126	130 ± 40	1.17	16	1.24	16.4	83.6	100/0
$PDEA_{60}$−PS (50/50)[i]	IPA	23.5	189	190 ± 110	1.17	8	0.58	7.7	92.3	46.0/54.0
$PDEA_{60}$−PS (30/70)[i]	IPA	23.5	298	300 ± 120	1.14	7	0.41	5.4	94.6	31.8/68.2
$PDEA_{60}$−PS (20/80)[i]	IPA	23.5	388	390 ± 170	1.15	4	0.23	3.1	96.9	17.4/82.6
$PDEA_{60}$−PS (10/90)[i]	IPA	23.5	392	400 ± 180	1.08	3	0.22	2.9	97.1	16.6/83.4
$PDEA_{60}$−PS (5/95)[i,j]	IPA	23.5	463	470 ± 220	1.18	2	0.15	2.0	98.0	11.2/88.8
$PDEA_{60}$−PS (100/0)[i]	*n*-amylalcohol	22.3	85	110 ± 36	1.05	18	1.64	21.7	78.3	100/0
$PDEA_{60}$−PS (100/0)[i]	1-butanol	23.3	84	107 ± 33	1.04	22	1.80	23.8	76.2	100/0
$PDEA_{60}$−PS (100/0)[i]	ethanol	26.0	103	126 ± 43	1.10	13	1.21	16.0	84.0	100/0
$PDEA_{25}$−PS (100/0)[i]	IPA/water (95/5)	24.7	106	120 ± 40	1.11	10	0.86	11.4	88.6	100/0
$PDEA_{25}$−PS (100/0)[i]	IPA/water (80/20)	21.2	103	120 ± 40	1.08	6	0.50	6.6	93.4	100/0
PS homopolymer						∼0		100		
PDEA homopolymer					100	7.55	100			

[a]Number-average diameter determined using SEM images (n = 200). [b]Volume-average diameter determined by laser diffraction method. [c]Polydispersity determined using SEM images (n = 200). [d]PDEA% determined using ^{1}H NMR spectroscopy. [e]Determined by elemental analysis. [f]Determined by comparing nitrogen content to that of the PDEA homopolymer. [g]100 − PDEA% (CHN%). [h]Calculated assuming that N % determined by microelemental analysis is all from the PDEA component and weight-ratio of PDEA and PS of the PDEA-*block*-PS copolymer is the same as that of $PDEA_{60}$−PS particles synthesized in IPA media ($PDEA_{60}$−MAI/VA-086, 100/0). [i]$PDEA_{60}$−MAI/VA-086 (molar ratio). [j]The sample contained coagulant, 21%. PDEA−PS latex (79%) was used for characterizations.

mol azo groups per 22,700 g $PDEA_{60}$−MAI vs 1 mol azo groups per 164.2 g of AIBN. In the dispersion polymerization using the macroinitiator, the concentration of the initiator should be calculated based on mol %, not on wt %. In this study, the free radical dispersion polymerization was conducted at a macroinitiator concentration of 1.0 mol % (218 wt % for the $PDEA_{60}$−MAI system) based on styrene monomer. In free radical polymerization, the initiation rate of polymerization, R_i, is given by $R_i = f\rho_i$, where f is the initiator efficiency and ρ_i is the generation rate of radicals. ρ_i is expressed as $\rho_i = 2k_d[I]$, where [I] is the initiator concentration. In general, free radical dispersion polymerizations are carried out in the R_i range of 10^{13}−10^{14} $mL^{-1}s^{-1}$.[6c,14,25] Assuming that the k_d value of the $PDEA_n$−MAI is equal to that of AMBEP (3.40×10^{-6} s^{-1} at 80 °C)[14] and the f value of the initiator is similar to that reported for other macroazoinitiators (0.3),[26] the initiator concentration giving a R_i of 1.2×10^{13} $mL^{-1}s^{-1}$ was determined in this study, and was found to be comparable to the general dispersion polymerizations. There are a limited number of reports in which the effects of colloidal stabilizer molecular weight on the latex size and its distribution have been studied using colloidal stabilizers with narrow molecular distributions. Thus, it is worth investigating the effects of molecular weight of $PDEA_n$−MAI on the colloidal stability, latex size and its distributions.

Dispersion polymerizations using $PDEA_n$−MAI with various degrees of polymerization were carried out in IPA at 80 °C for 48 h (Table 2). In all cases, polymerization led to colloidally stable milky IPA dispersions of PS particles and the conversion of the styrene was gravimetrically determined to be 95% for the $PDEA_{60}$−MAI system.

SEM images and laser diffraction particle size analysis indicated that an increase of polymerization degree of PDEA increased particle diameters from 100 to 130 nm (Figures S4 and S5, Supporting Information). This result is contrary to the tendency observed in the dispersion polymerization systems using homopolymer-type colloidal stabilizers.[27] Homopolymer-type colloidal stabilizers with larger degree of polymerization, which have stronger stabilization ability for latex particles, generally lead to latex particles with smaller diameters. On the other hand, in the case of inistab, it is expected that a longer PDEA chain length should lead to a longer critical chain length of the PDEA-*block*-PS copolymers with longer PS block needed to precipitate in the media. The longer PS block, which forms core of the particles, should result in polymer latex particles with larger diameters. It is worth emphasizing that colloidally stable latex particles were successfully synthesized even using $PDEA_{15}$−MAI with the shortest PDEA chain length. (Note: polymeric colloidal stabilizers with degrees of polymerization ranging between 90 and 2700 are usually used for dispersion

dx.doi.org/10.1021/ma300048m | Macromolecules 2012, 45, 2863−2873

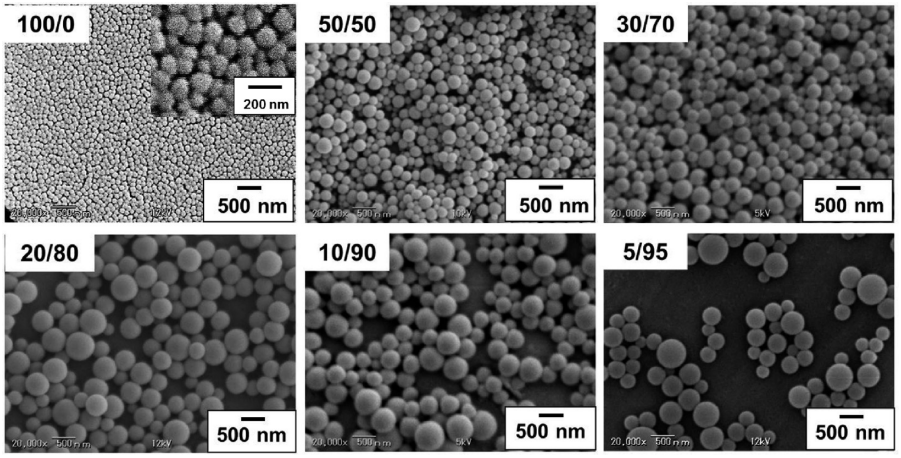


Figure 2. SEM images of $PDEA_{60}$–PS particles synthesized by the dispersion polymerization using $PDEA_{60}$–MAI in combination with VA-086 ($PDEA_{60}$–MAI/VA-086 molar ratio) in IPA. Inset shows a magnified image of $PDEA_{60}$–PS particles (100/0) synthesized using $PDEA_{60}$–MAI.

polymerization.)[27] Polymerization using $PDEA_{60}$–MAI at a concentration of 0.1 mol % (21.8 wt %) based on styrene (R_i = 1.2×10^{12} mL^{-1} s^{-1}) resulted in low conversion of monomer (30%) and a transparent polymer solution was obtained. This result again indicates that the concentration of initiator should be considered based on mol % and that a suitable amount of initiators is required to obtain latex.

Method 3. Table 2 shows the effect of varying the $PDEA_{60}$–MAI/VA-086 molar ratio on the particle diameter of a series of $PDEA_n$-PS latexes, each prepared at a constant azo group concentration of 1.0 mol % based on the monomer.

SEM, laser diffraction and dynamic light scattering studies indicated an increase of mean diameter with a decrease of $PDEA_{60}$–MAI/VA-086 molar ratio (Tables 2 and S3 (Supporting Information), and Figures 2 and 3). Near-spherical

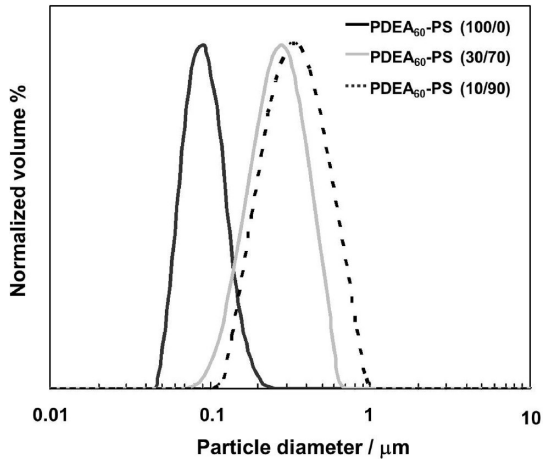


Figure 3. Laser diffraction particle size distribution curves obtained for $PDEA_{60}$–PS latex particles synthesized with a combination of $PDEA_{60}$–MAI and VA-086 ($PDEA_{60}$–MAI/VA-086 molar ratio).

latex particles were obtained and the number-average diameter (D_n) was controlled between 103 and 463 nm, which accorded well with the laser diffraction results. Hydrodynamic diameters in IPA measured by dynamic light scattering were larger than number-average diameters in dry state determined from SEM images: the difference should be due to solvated PDEA hair (Tables 2 and S3 (Supporting Information)). The polydispersities were almost constant (D_w/D_n, 1.08–1.18) and no coagulum was obtained in any of the polymerization systems except in the 5/95 molar ratio system. As the number of free radicals generated from $PDEA_{60}$–MAI (and hence the $PDEA_{60}$-*block*-PS copolymer which can serve as a colloidal stabilizer) increases, the nucleation stage becomes more extensive, which leads to a larger number of smaller final latex particles being formed. In the case of $PDEA_{60}$–MAI/VA-086 molar ratio of 5/95 system, the amount of $PDEA_{60}$–PS block copolymer generated was not enough to stabilize all the PS homopolymer nuclei/particles, which led to the formation of 21% coagulant. In order to synthesize monodisperse latex particles, it is important to separate nucleation and growing periods and to make the nucleation period short.[1] In the dispersion polymerization using inistab, the particle nucleation period is long because PDEA-*block*-PS copolymers, which form nuclei and work as colloidal stabilizer, are generated throughout the polymerization. This caused long nucleation period and overlap of nucleation and growing periods, which made difficult to synthesize highly monodisperse latex particles.

The FT-IR spectra of the $PDEA_{60}$–PS particles, PDEA and PS homopolymers are depicted in Figure S6. The spectrum of PS homopolymer shows the characteristic absorbances of a monosubstituted arene, with two other arenes at 761 and 701 cm^{-1} for the C═C–H out-of-plane bending. The FT-IR spectrum of the PDEA homopolymer shows a characteristic ester carbonyl band at 1728 cm^{-1}, which was assigned to the DEA residues. Characteristic bands due to both the PS and PDEA components were observed in the spectrum of the $PDEA_{60}$–PS latex particles, as expected. The $PDEA_{60}$–PS particles synthesized using only $PDEA_{60}$–MAI showed a stronger carbonyl absorbance (1728 cm^{-1}) compared with those synthesized using the $PDEA_{60}$–MAI/VA-086 mixture (10/90). This result indicates a higher PDEA loading amount in the $PDEA_{60}$–PS particles synthesized. The chemical compositions of $PDEA_{60}$–PS latexes were analyzed by ^1H NMR spectroscopy and elemental analysis.

Figure 4 shows the ^1H NMR spectra recorded for the $PDEA_{60}$–PS particles prepared at $PDEA_{60}$–MAI/VA-086 molar ratios of 10/90 and 100/0 in IPA medium. In the absence of a polymeric stabilizer, only PS signals were observed (data not shown). Latexes prepared using $PDEA_{60}$–MAI contained additional weak signals due to the DEA residues at approximately 4.0, 2.7, 2.5, and 1.1 ppm (see Figure 4).

dx.doi.org/10.1021/ma300048m | *Macromolecules* 2012, 45, 2863–2873

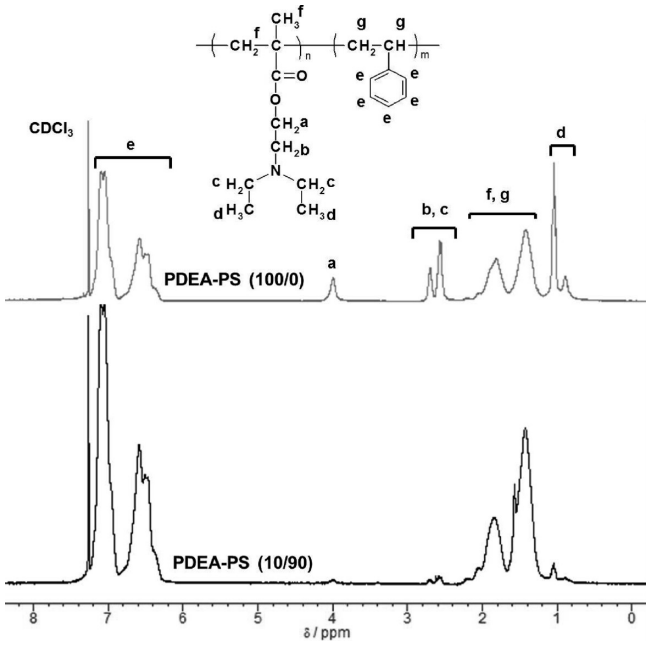


Figure 4. ^{1}H NMR spectra for $PDEA_{60}$–PS particles synthesized at $PDEA_{60}$–MAI/VA-086 molar ratios of 100/0 and 10/90, dissolved in $CDCl_3$ to allow the calculation of PDEA contents.

Increasing the $PDEA_{60}$–MAI/VA-086 molar ratio resulted in an increase of the PDEA loading amount in the particles due to the larger specific surface area.

PDEA chains occupied the molecular area of the particle surface and the square root of the occupied molecular area decreased with increasing $PDEA_{60}$–MAI/VA-086 molar ratio (Table 3). This result indicates PDEA hair grafted to the PS particle surface more densely at a higher $PDEA_{60}$–MAI/VA-086 molar ratio. Hydroxy groups bonded to the PS chain end, which originate from the VA-086 initiator and have affinity with IPA media, are expected to exist on the PS particle surface. The hydroxyl groups should serve as a colloidal costabilizer and the PDEA hair graft density decreases at higher VA-086 concentration. In all cases, the square root of the occupied PDEA molecular area was larger than the diameter of gyration of the $PDEA_{60}$ chain (D), which was calculated using the equation shown below,

$$D = 2\sqrt{\frac{na^2}{6}}$$

where n and a are bond number and bond length, respectively. This result suggests a random coil configuration of PDEA hair on the particle surface, although it is also possible for $PDEA_{60}$–PS block copolymers to form a PS and PDEA mixed surface layer and to have a brush-type configuration.[28]

The solvated PDEA hair nature of the $PDEA_{60}$–PS particles in acidic solution was indicated by ^{1}H NMR studies (see Supporting Information, Figure S7). At pH 3, a broad signal due to the protonated PDEA chains was observed at 1.0–1.7 ppm (due to the methyl protons of the diethyl amino group). In contrast, this signal was not observed at pH 10, since the PDEA chains are in their neutral, nonsolvated form at this pH. It is also worth noting that the atomic force microscopy studies indicated solvated PDEA hair in acidic solution.[28]

Transmission values (%T) for an aqueous dispersion of the $PDEA_{60}$–PS latex particles (0.1 wt %; synthesized at $PDEA_{60}$–MAI/VA-086, 10/90) were measured at various pH values, see Figure 5. % T values were less than 10% at and below pH 5.0. Thus, PDEA is soluble in acidic aqueous media and can serve as an effective steric stabilizer, which leads to a stable colloidal dispersion. Increasing the pH to approximately pH 7.0 led to a

Table 3. Comparison between Square Root of the Occupied Molecular Area and the Diameter of Gyration of PDEA Chains

	media	number of PDEA molecules per one PS particle $\times 10^{-3}$	PDEA chain occupied molecular area at the particle surface/nm^2	square root of the occupied molecular area/nm	diameter of gyration of PDEA chain/nm
$PDEA_{15}$–PS (100/0)[a]	IPA	7.7	4.33	2.08	0.69
$PDEA_{25}$–PS (100/0)[a]	IPA	7.2	5.87	2.42	0.89
$PDEA_{60}$–PS(100/0)[a]	IPA	12.0	4.15	2.04	1.38
$PDEA_{60}$–PS (50/50)[a]	IPA	17.2	6.50	2.55	1.38
$PDEA_{60}$–PS (30/70)[a]	IPA	46.2	6.03	2.46	1.38
$PDEA_{60}$–PS (20/80)[a]	IPA	57.2	8.26	2.87	1.38
$PDEA_{60}$–PS (10/90)[a]	IPA	55.1	8.76	2.96	1.38
$PDEA_{60}$–PS (5/95)[a,b]	IPA	62.0	10.8	3.29	1.38
$PDEA_{60}$–PS (100/0)[a]	*n*-amylalcohol	11.2	3.39	1.84	1.38
$PDEA_{60}$–PS (100/0)[a]	1-butanol	5.7	3.91	1.98	1.38
$PDEA_{60}$–PS (100/0)[a]	ethanol	11.6	4.28	2.07	1.38
$PDEA_{25}$–PS (100/0)[a]	IPA/water (95/5)	4.7	7.50	2.70	0.89
$PDEA_{25}$–PS (100/0)[a]	IPA/water (80/20)	2.4	14.1	3.75	0.89

[a] $PDEA_{60}$–MAI: VA-086 (molar ratio). [b] The sample contained coagulant, 21%. PDEA–PS latex (79%) was used for characterizations.

dx.doi.org/10.1021/ma300048m | *Macromolecules* 2012, 45, 2863–2873

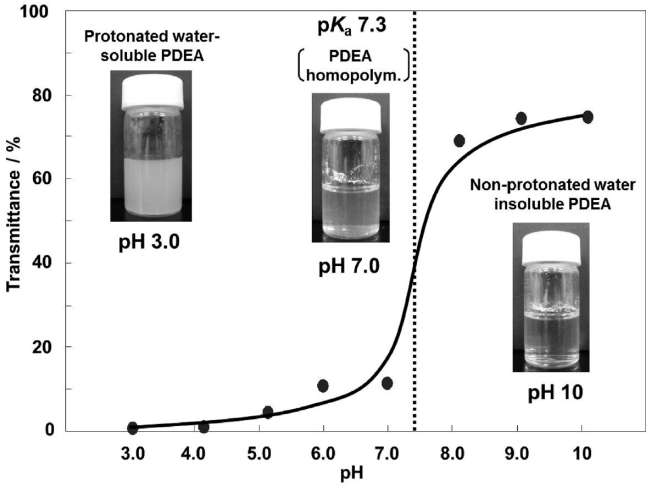


Figure 5. Percent transmittance (%T) at 545 nm for aqueous dispersion of the 392 nm-sized PDEA$_{60}$–PS particles (synthesized at the PDEA$_{60}$–MAI/VA-086 molar ratio of 10/90) at 0.1 wt % as a function of pH.

gradual increase in % *T* values. The PDEA has a pK_a value of 7.3 and the PDEA steric stabilizer should be around 1% and 10% deprotonated at pH 5.3 and 6.3, respectively. Therefore, we expect the PDEA$_{60}$–PS latex to lose stability gradually as the pH increased. Indeed, a rapid increase in %T was observed between pH 7.0 and 8.1, and above pH 8.1 a constant value of % *T* (approximately 80%) was observed. This is consistent with the aggregation and settling of the PDEA$_{60}$–PS latex, and this feature can be confirmed by direct visual inspection.

The particle sizes and their distributions obtained for dilute aqueous dispersions of the PDEA$_{60}$–PS latex particles at acidic and basic media using the laser diffraction method are shown in Figure 6. The particle size was measured to be 390 ± 150 nm at

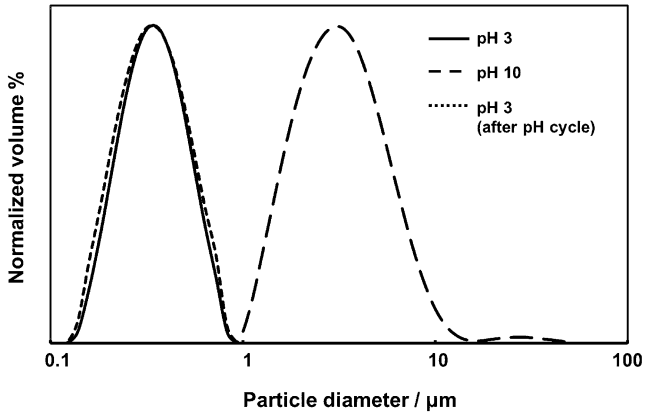


Figure 6. Laser diffraction particle size distribution curves obtained for 392 nm-sized PDEA$_{60}$–PS latex particles (synthesized at the PDEA$_{60}$–MAI/VA-086 molar ratio of 10/90) at pH 3 and pH 10.

pH 3 with relatively narrow particle size distributions, suggesting a high degree of dispersion of the PDEA$_{60}$–PS latex particles. On the other hand, at pH 10 the PS particles were obviously flocculated and showed particle sizes with a broad particle size distribution (4.18 ± 3.59 μm). Adjusting the pH back to 3 from 10 led to the redispersion of the PDEA$_{60}$–PS latex particles. The diameter was measured to be 390 ± 160 nm, which was almost the same value as that measured before addition of the base. This result indicates that PDEA hair on the surface of the particles was reprotonated and the particles regained colloidal stability.

The variations of ζ potential at various pHs for the PDEA$_{60}$–PS are shown in Figure 7. The PDEA$_{60}$–PS particles with

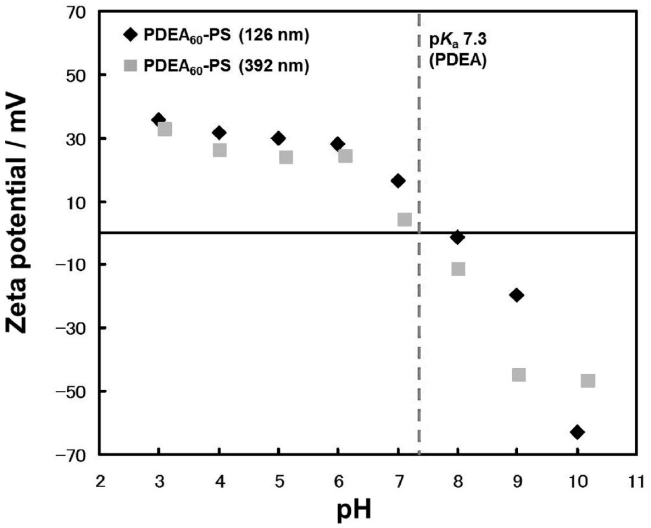


Figure 7. Variations of ζ potential at various pHs for PDEA$_{60}$–PS latex particles synthesized at PDEA$_{60}$–MAI/VA-086 molar ratios of 100/0 (126 nm) and 10/90 (392 nm).

number-average diameters of 126 and 392 nm had isoelectric points around pH 7.5–8.0. Since the pK_a of PDEA homopolymer is around pH 7.3,[14] the DEA residues are nearly 61.3–83.4% deprotonated at the isoelectric points. At a low pH, the DEA residues are protonated and positive ζ potentials of up to approximately +36 mV are obtained. The PS latex particles can be dispersed at a low pH (<about 7.3) because the PDEA hair is solvated and serves as an effective colloidal stabilizer in the media. Above pH 8.0, negative ζ potentials are obtained, since the neutral hair chains collapse onto the PS latex surface at this pH and the latex mobility should be determined by the hydroxide anions adsorbed on the latex surface.[14] The PS particles can be flocculated at a high pH (>about 7.3) where the PDEA hair was deprotonated, and the flocs were precipitated on the bottom of the vial or attached to the planar air–water surface and to the glass wall. The threshold pH value of this dispersion-flocculation is near the pK_a value of PDEA (7.3) and this dispersion-flocculation cycle was reversible. The particles could be subjected to at least five pH cycles (between pH 10 and pH 3) without causing salt induced flocculation. These results also indicate that the surfaces of the PS particles were occupied by the PDEA component.

The dispersion polymerization approach presented in this study can be applied to other vinyl monomers (Figures S8 and S9, Supporting Information); colloidally stable PMMA, poly(*p*-bromostyrene), and poly(4-fluorostyrene) particles can be successfully synthesized in protic media [ethanol for PMMA and IPA for poly(*p*-bromostyrene) and poly(4-fluorostyrene)].

Liquid Marbles Stabilized by the PS Particles Carrying PDEA Hair. Liquid marbles are liquid droplets stabilized with relatively hydrophobic particles[29] adsorbed at a gas–liquid interface such as surface-modified lycopodium powder,[30] hydrophobic silica particles,[31] carbon black,[32] and synthetic

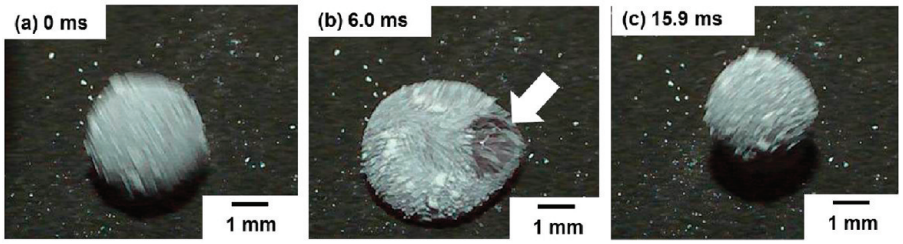


Figure 8. Elastic deformation of the liquid marble (15 μL) occurred on contact with PET film. The liquid marble stabilized with 392 nm-sized $PDEA_{60}$–PS particles was allowed to fall onto the PET film from a height of 2 cm. (a) 0 ms, (b) 6.0 ms, and (c) 15.9 ms after contact with the PET film. The arrow indicates the bare air–water interface formed upon deformation of the liquid marble.

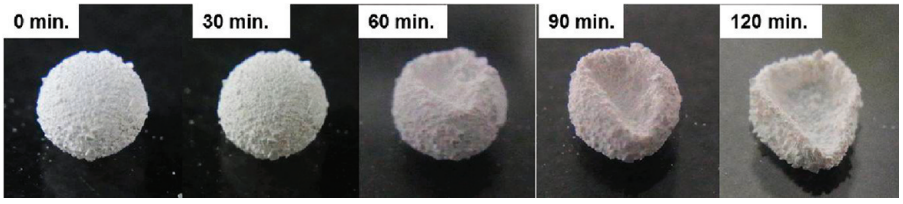


Figure 9. Digital photographs illustrating the effect of water evaporation on the gradual deformation and eventual collapse of a liquid marble (15 μL) stabilized with 392 nm-sized $PDEA_{60}$–PS particles after being placed on a glass slide at 25 °C.

polymer latexes.[33] They have attracted increasing attention in view of their potential applications in cosmetics, pharmaceuticals, and home and personal care products.[34] In principle, synthetic latexes should be particularly attractive for preparing liquid marbles, since they can be readily designed with specific surface chemistry. Recently, some of the present authors reported[33c,g] that PDEA–PS latexes can be used to prepare pH-responsive liquid marbles. It was demonstrated that a liquid marble floating on a water pool prepared in a Petri dish can be disintegrated by the addition of HCl aqueous solution into the water pool.

Herein, the application of the 392 nm-sized $PDEA_{60}$–PS particles as a "gas-responsive" liquid marble stabilizer was investigated. The 392 nm-sized $PDEA_{60}$–PS particles were obtained as a fine white powder after drying. An individual liquid marble was readily prepared by rolling a 15 μL droplet of deionized water over the dried $PDEA_{60}$–PS particles. The marble remained intact after transfer onto a glass slide and even onto the planar surface of water. These liquid marbles clearly have significant surface roughness, which suggests that they are coated with latex multilayers, rather than just a monolayer. When a fully coated liquid marble (15 μL) was allowed to fall onto a PET film from a height of 2 cm, it bounced and retained its original shape.

High-speed digital photography confirmed that elastic deformation of the liquid marble occurred upon contact with the PET film (see Figure 8). Interestingly, a bare air–water interface, which was not covered with the $PDEA_{60}$–PS particles, appeared on the surface of the deformed liquid marble (see arrow in Figure 8b: 6.0 ms after contact with the PET film), and disappeared upon reformation back to spherical morphology (Figure 8c: 15.9 ms after contact with the PET film). Upon deformation of the liquid marble from the spherical morphology, the air–water surface area increased and the bare air–water interface appeared.

Figure 9 shows the morphological changes of the liquid marble upon drying. The $PDEA_{60}$–PS particles were irreversibly adsorbed at the air–water interface and the total surface area of the liquid marble remained constant. Thus, the liquid marble adjusted its surface-to-volume ratio by undergoing deformation. The inner water completely evaporated after 120 min, which was confirmed gravimetrically.

Next, the effect of introducing HCl gas or aqueous vapor on the stability of individual liquid marbles placed on the slide glass was examined (see Figures 10). Here, the destabilization

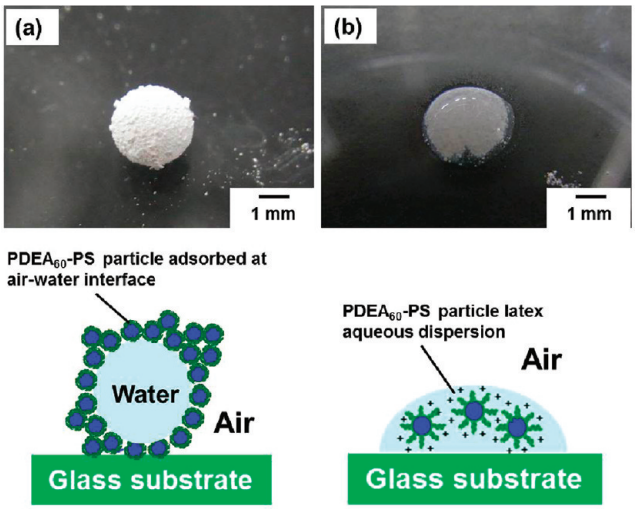


Figure 10. Gas-responsive behavior of a liquid marble: (a) before and (b) after exposure to HCl vapor. After exposure to HCl vapor, the $PDEA_{60}$–PS particles dispersed into the inner aqueous solution and the liquid marble burst.

times were defined as the times required for the liquid marbles to burst or to start shrinking after exposure to the gases. Enhanced stabilities (for at least 18 h) of the liquid marbles were achieved under saturated aqueous vapor, where the nonprotonated $PDEA_{60}$–PS particles were sufficiently hydrophobic to adsorb strongly at the air–water surface and evaporation of inner water was suppressed. These liquid marbles eventually shrank due to slow evaporation of water. However, the liquid marbles always burst under HCl atmosphere within a few seconds (approximately 2 s). This is because the PS particles carrying protonated PDEA chains have

dx.doi.org/10.1021/ma300048m | Macromolecules 2012, 45, 2863–2873

high wettability to the aqueous phase and hence disperse into the inner aqueous solution, which leads to destruction of the liquid marbles. These results indicate a possible use of $PDEA_{60}$–PS latex-stabilized liquid marbles as gas sensors and stimuli-responsive capsules.

In control experiments, no liquid marbles could be formed under any conditions using either charge stabilized PS latex or sterically stabilized PS latexes prepared using permanently hydrophilic stabilizers such as sodium dodecyl sulfate and monomethoxy-capped poly(ethylene glycol) methacrylate. These observations confirm the essential role played by the chemically grafted PDEA chains in promoting liquid marbles formation.

■ CONCLUSIONS

SP values of the polymerization media can significantly affect the nature of the resulting products: latex, solution, or aggregates. $PDEA_n$–PS latex particles were successfully synthesized by dispersion polymerization using *well-defined* PDEA–MAI in protic media, namely *n*-amylalcohol, IPA, and ethanol with SP values between 22.3 $(MPa)^{1/2}$ and 26.0 $(MPa)^{1/2}$, where PDEA and styrene monomer are soluble and PS is insoluble. Using $PDEA_n$–MAI with various DPs, the latex size could be finely controlled between 100 and 130 nm. The molar ratio of $PDEA_{60}$–MAI and VA-086 can significantly affect the latex size (between 130 and 470 nm). The colloidal stability of the PS latexes was strongly influenced by the nature of the PDEA hair chains. The latexes were colloidally stable at a low pH due to protonation of the tertiary amine groups in the DEA residues and flocculated at a high pH due to deprotonation. This is borne out by ζ potential vs pH measurements, which indicated isoelectric points between pH 7.5 and 8.0. This dispersion polymerization approach circumvents the need for surface pretreatment/modification of core particles, with grafting-from and grafting-to methods needed in many cases. Furthermore, the core component can be easily controlled by choosing monomers to be polymerized in the dispersion polymerization. One of these $PDEA_{60}$–PS particles was proven to behave as a gas-responsive liquid marble stabilizer. Liquid marbles (15 μL) of around 3 mm diameter, which were stable over 18 h in H_2O vapor, were readily formed and could be placed on a hydrophilic glass surface. The liquid marbles were rapidly disintegrated upon exposure to HCl gas (<a few seconds), presumably due to desorption of the latex particles from the surface of the liquid marbles. This gas-responsive liquid marble stabilizer application is the subject of further investigation in our laboratory.

■ ASSOCIATED CONTENT

Ⓢ Supporting Information

Dynamic light scattering procedures and results, scanning electron microscope (SEM) images, laser diffraction particle size distribution curves, FT-IR spectra, ^1H NMR spectra, and recipes for the dispersion polymerization of styrene. This material is available free of charge via the Internet at http://pubs.acs.org.

■ AUTHOR INFORMATION

Corresponding Author

*E-mail: s.fujii@chem.oit.ac.jp.

Notes

The authors declare no competing financial interest.

■ ACKNOWLEDGMENTS

We thank Wako Chemicals for the kind donation of the 2,2′-azobis[2-methyl-*N*-(2-hydroxyethyl)propionamide]. We thank Prof. M. Nawafune, Prof. K. Akamatsu and Dr. Tsuruoka for their assistance with the centrifuge experiments. We thank Mr. M. Inoue for his assistance with the dynamic light scattering experiments. This work was supported by a Grant-in-Aid for Scientific Research on Innovative Areas "Molecular Soft-Interface Science" from the Ministry of Education, Culture, Sports, Science and Technology of Japan.

■ REFERENCES

(1) (a) Lovell, P. A.; El-Aasser, M. S. *Emulsion Polymerization and Emulsion Polymers*; John Wiley and Sons: Chichester, U.K., 1997. (b) Kawaguchi, S.; Ito, K. *Adv. Polym. Sci.* **2005**, *175*, 299.
(2) Almog, Y.; Reich, S.; Levy, M. B. *Polym. J.* **1982**, *14*, 131.
(3) Tseng, C. M.; Lu, Y. Y.; E l -Aasser, M. S.; Vanderhoff, J. W. *J. Polym. Sci.: Polym. Chem. Ed.* **1986**, *24*, 2995.
(4) (a) Lok, K. P.; Ober, C. K. *Can. J. Chem.* **1985**, *63*, 209. (b) Ober, C. K.; Lok, K. P.; Hair, M. L. *J. Polym. Sci., Lett. Ed* **1985**, *23*, 103. (c) Lok, K. P.; Ober, C. K. *Macromolecules* **1987**, *20*, 268.
(5) Winnik, M. A.; Lukas, R.; Chen, W. F.; Furlong, P.; Croucher, M. D. *Macromol. Chem., Macromol. Symp.* **1987**, *10/11*, 483.
(6) (a) Paine, A. J. *J. Colloid Interface Sci.* **1990**, *138*, 157. (b) Paine, A. J. *Macromolecules* **1990**, *23*, 3104. (c) Paine, A. J. *J. Polym. Sci., Polym. Chem. Ed* **1990**, *18*, 2485.
(7) Napper, D. H. *J. Colloid Interface Sci.* **1997**, *58*, 390.
(8) (a) Pelton, R. H.; Osterroth, A.; Brook, M. A. *J. Colloid Interface Sci.* **1990**, *137* (1), 120. (b) Pelton, R. H.; Osterroth, A.; Brook, M. A. *J. Colloid Interface Sci.* **1991**, *147* (2), 523.
(9) (a) Dawkins, J. V.; Taylor, G. *Polymer* **1979**, *20*, 599. (b) Jialanella, G. L.; Firer, E. M.; Piirma, I. *J. Polym. Sci., Part A: Polym. Chem.* **1992**, *30*, 1925. (c) Windsor, C.; Marazek, Z.; Winnie, M. A.; Croucher, M. D.; Riess, G. *Eur. Polym. J.* **1994**, *31* (1), 121. (d) Canelas, D. A.; Betts, D. E.; DeSimone, J. M. *Macromolecules* **1996**, *29*, 2818. (e) Baines, F. L.; Dionisio, S.; Billingham, N. C.; Armes, S. P. *Macromolecules* **1996**, *29*, 3096.
(10) (a) Lepilleur, C.; Beckman, E. J. *Macromolecules* **1997**, *30*, 745. (b) Giles, M. R.; Griffiths, R. M. T.; Aguiar-Ricardo, A.; Silva, M. M. C. G.; Howdle, S. M. *Macromolecules* **2001**, *34*, 20.
(11) (a) Shaffer, K. A.; Jones, T. A.; Canelas, D. A.; DeSimone, J. M. *Macromolecules* **1996**, *29*, 2704. (b) Lacroix-Desmazes, P.; Guyot, A. *Macromolecules* **1996**, *29*, 4508. (c) Kawaguchi, S.; Winnik, M. A.; Ito, K. *Macromolecules* **1996**, *29*, 4465. (d) Chen, M.-Q.; Kishida, A.; Akashi, M. *J. Polym. Sci., Polym. Chem* **1996**, *34*, 2213. (e) Dupin, D.; Fujii, S.; Armes, S. P.; Reeve, P.; Baxter, S. M. *Langmuir* **2006**, *22*, 3381.
(12) Fujii, S.; Minami, H.; Okubo, M. *Colloid Polym. Sci.* **2004**, *282*, 569.
(13) (a) Nakamura, K.; Fujimoto, K.; Kawaguchi, H. *Colloids Surf. A: Physiochem. Eng. Aspects* **1999**, *153*, 195. (b) Okubo, M.; Fujii, S.; Maenaka, H.; Minami, H. *Colloid Polym. Sci.* **2002**, *280*, 183. (c) Kitano, H.; Kawabata, J. *Macromol. Chem. Phys.* **1996**, *197*, 1721. (d) Kitano, H.; Kawabata, J.; Muramoto, T. *Macromol. Chem. Phys.* **1996**, *197*, 3657. (e) Tauer, K. *Polym. Adv. Technol* **1995**, *6*, 435.
(14) Fujii, S.; Kakigi, Y.; Suzaki, M.; Yusa, S.; Muraoka, M.; Nakamura, Y. *J. Polym. Sci. Part A: Polym. Chem* **2009**, *47*, 3431.
(15) Bütün, V.; Armes, S. P.; Billingham, N. C. *Polymer* **2001**, *42*, 5993.
(16) Liu, S.; Weaver, J. V. M.; Tang, Y.; Billingham, N. C.; Armes, S. P. *Macromolecules* **2002**, *35*, 6121.
(17) Bories-Azeau, X.; Armes, S. P. *Macromolecules* **2002**, *35*, 10241.
(18) Matyjaszewski, K.; Shipp, D. A.; Wang, J.-L.; Grimaud, T.; Patten, T. E. *Macromolecules* **1998**, *31*, 6836.
(19) (a) Zhu, P. W.; Napper, D. H. *J. Colloid Interface Sci.* **1996**, *177*, 343. (b) Angot, S.; Ayres, N.; Bon, S. A. F.; Haddleton, D. M. *Macromolecules* **2001**, *34*, 768. (c) Zheng, G.; Stöver, H. D. H.

Macromolecules **2001**, *35*, 6828. (d) Ohno, K.; Morinaga, T.; Koh, K.; Tsujii, Y.; Fukuda, T. *Macromolecules* **2005**, *38*, 2137.
(20) Yasui, M.; Shiroya, T.; Fujimoto, K.; Kawaguchi, H. *Colloids Surf.* **1997**, *8*, 311.
(21) (a) Bütün, V.; Billingham, N. C.; Armes, S. P. *J. Am. Chem. Soc.* **1998**, *120*, 11818. (b) Harada, A.; Kataoka, K. *Science* **1999**, *283*, 65. (c) Weaver, J. V. M.; Tang, Y.; Liu, S.; Iddon, P. D.; Grigg, R.; Billingham, N. C.; Armes, S. P.; Hunter, R.; Rannard, S. P. *Angew. Chem., Int. Ed.* **2004**, No. 43, 1389.
(22) (a) Creutz, S.; Jerome, R. *Langmuir* **1999**, *15*, 7145. (b) Hoogeveen, N. G.; Cohen-Stuart, M.; Fleer, G. *J. Macromol. Chem. Phys.* **1994**, *98*, 161. (c) Amalvy, J. I.; Unali, G.-F.; Li, Y.; Granger-Bevan, S.; Armes, S. P.; Binks, B. P.; Rodrigues, J. A.; Whitby, C. P. *Langmuir* **2004**, *20*, 4345.
(23) Fedros, R. F. *Jet Propul. Lab. Q. Tech. Rev.* **1973**, *3*, 45.
(24) Brandrup, J.; Immergut, E. H.; Grulke, E. A. *Polymer Handbook*, 4th ed.; Wiley: New York, 1999.
(25) (a) Shen, S.; Sudol, E. D.; El-Aasser, M. S. *J. Polym. Sci., Part A: Polym. Chem.* **1993**, *31*, 1393. (b) Okubo, M.; Ikegami, K.; Yamamoto, Y. *Colloid Polym. Sci.* **1989**, *267*, 193.
(26) Walz, R.; Bömer, B.; Heitz, W. *Makromol. Chem* **1977**, *178*, 2527.
(27) Shen, S.; Sudol, E. D.; El-Aasser, M. S. *J. Polym. Sci., Polym. Chem* **1994**, *32*, 1087.
(28) Fujii, S.; Suzaki, M.; Nakamura, Y.; Sakai, K.; Ishida, N.; Biggs, S. *Polymer* **2010**, *51*, 6240.
(29) (a) Fujii, S.; Murakami, R. *KONA Powder Particle J* **2008**, *26*, 153. (b) Bormashenko, E. *Curr. Opin. Colloid Interface Sci.* **2011**, *16*, 266. (c) McHale, G.; Newton, M. I. *Soft Matter* **2011**, *12*, 7.
(30) (a) Aussilious, P.; Quéré, D. *Nature* **2001**, *411*, 924. (b) Aussilious, P.; Quéré, D. *Proc. R. Soc. A: Math. Phys. Eng. Sci* **2006**, *426*, 973.
(31) (a) Wang, W.; Bray, C. L.; Adams, D. J.; A. Cooper, I. *J. Am. Chem. Soc.* **2008**, *130*, 11608. (b) Dandan, M.; Erbil, H. Y. *Langmuir* **2009**, *25*, 8362. (c) Inoue, M.; Fujii, S.; Nakamura, Y.; Iwasaki, Y.; Yusa, S. *Polym. J.* **2011**, *43*, 778.
(32) Dandan, M.; Erbil, H. Y. *Langmuir* **2009**, *25*, 8362.
(33) (a) Bormashenko, E.; Stein, T.; Whyman, G.; Bormashenko, Y.; Pogreb, R. *Langmuir* **2006**, *22*, 9982. (b) Gao, L. C.; McCarthy, T. J. *Langmuir* **2007**, *23*, 10445. (c) Dupin, D.; Armes, S. P.; Fujii, S. *J. Am. Chem. Soc.* **2009**, *131*, 5386. (d) Bormashenko, E.; Pogreb, R.; Whyman, G.; Musin, A.; Bormashenko, Y.; Barkay, Z. *Langmuir* **2009**, *25*, 1893. (e) Matsukuma, D.; Watanabe, H.; Yamaguchi, H.; Takahara, A. *Langmuir* **2011**, *27* (4), 1269. (f) Fujii, S.; Kameyama, S.; Armes, S. P.; Dupin, D.; Suzaki, M.; Nakamura, Y. *Soft Matter* **2010**, *6*, 635. (g) Fujii, S.; Suzaki, M.; Armes, S. P.; Dupin, D.; Hamasaki, S.; Aono, K.; Nakamura, Y. *Langmuir* **2011**, *27*, 8067.
(34) (a) Dampeirou, C. WO Patent 034917, 2005. (b) Lahanas, K. M. U.S. Patent 6,290,941, 2001.

Macromolecules

Article

pubs.acs.org/Macromolecules

Characterization of Micelles of Small Triblock Copolymer by Small-Angle Scattering

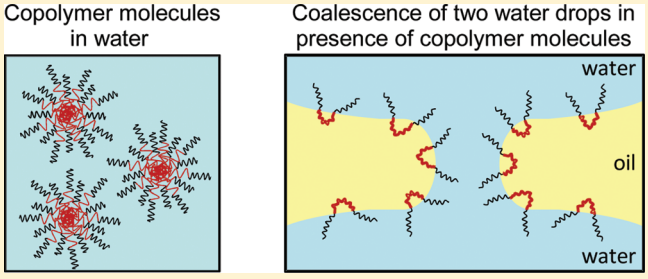
Amandine Forny-Le Follotec,*[,†,‡,⊥] Otto Glatter,[§] Isabelle Pezron,[†] Loïc Barré,[‡] Christine Noïk,[‡] Christine Dalmazzone,[‡] and Léa Metlas-Komunjer[†]

[†]Groupe Interfaces et Milieux Divisés, EA 4297 UTC/ESCOM Transformations Intégrées de la Matière Renouvelable, Université de Technologie de Compiègne, BP 20529, 60200 Compiègne Cedex, France

[‡]IFP Energies Nouvelles, 1&4 avenue de Bois-Préau, 92852 Rueil-Malmaison, France

[§]Department of Chemistry, University of Graz, A-8010 Graz, Austria

ABSTRACT: We investigated the structures formed in water by small triblock copolymers consisting of two poly(ethylene oxide) (PEO) side blocks and a central poly(dimethylsiloxane) (PDMS) block. Our objective was to identify a possible relation between the spontaneous curvature of copolymers and their efficiency in the demulsification of water-in-crude oil emulsions observed in earlier studies. Spherical micelles containing about 100 molecules, i.e., with a highly curved structure, were detected using concentrations of up to 20 wt % of copolymer in water at room temperature. At higher concentrations or at higher temperature, micelles changed to an elongated shape. SAXS data and analysis of electron density profile variation inside the scattering object revealed the inner structure of the micelle. Finally, the role of the high spontaneous curvature of the demulsifier copolymer is discussed in relation with the mechanism of coalescence of water droplets involved in the breaking of water-in-crude oil emulsions.



I. INTRODUCTION

During crude oil extraction, off-shore but also on-shore, water is present in abundance. The strong mechanical solicitations in pumps and valves often foster the formation of extremely stable emulsions of water-in-oil type. In order to diminish the transportation and refinery costs, water should be separated from crude oil. Classical physical treatments based on gravitational separation, optionally enhanced by electrocoalescence, or heating can be used to break these emulsions. However, these processes are time-consuming; therefore, chemical additives such as amines, copolymers of ethylene oxide, of propylene oxide, etc., in various solvents are used to accelerate the demulsification process.[1−3]

Unfortunately, the efficiency of such formulations is strongly dependent on the composition of the crude oil. In fact, some of the most important parameters are the content and ratio of surface-active constituents, namely asphaltenes and resins. To avoid expensive on-field tests, demulsifier molecules with high efficiency, and working independently of the origin of the crude oil, were actively searched for.[4] Laboratory studies and field tests showed that small triblock copolymers of poly(ethylene oxide) (PEO) and poly(dimethylsiloxane) (PDMS) type act as efficient demulsifiers regardless of the crude oil composition. The interfacial properties of such copolymers have been studied in detail;[5−7] however, no clear-cut relationship between chemical composition and demulsifying efficiency is established so far. The conformation of the demulsifier molecules at the oil−water interface was suggested to be of particular interest for the understanding of the demulsification process. In particular, the spontaneous curvature of interfaces formed in presence of surface-active molecules was shown to be related to the stabilizing (and destabilizing) ability of these molecules in emulsification processes.[8]

A detailed examination of self-assembled structures of the aforementioned molecules should provide useful information about their spatial configuration at interfaces. Therefore, we propose small-angle scattering as a method to determine the size and shape of self-assembled structures of efficient crude oil demulsifier and to consequently deduce the structural requirements for these compounds to successfully separate water from crude oil.

The interfacial behavior of triblock silicone copolymers has been studied by numerous authors. Kanellopopoulos and Owen measured the surface tension γ of aqueous solutions of a series of triblock silicone copolymers and determined the area occupied by each molecule via the Gibbs equation.[9] Surprisingly, they observed that the minimum area per molecule was 0.6 nm^2 for a central dimethylsiloxane segment length DMS > 23, while being 0.8−1.3 nm^2 for DMS < 23. As explanation, the authors proposed the looping of the central silicone segment when exceeding a certain length (DMS > 23). Measuring γ versus solution concentration also allowed to

Received: December 1, 2011
Revised: March 1, 2012
Published: March 12, 2012

 © 2012 American Chemical Society dx.doi.org/10.1021/ma202610n | *Macromolecules* 2012, 45, 2874−2881

determine the critical micelle concentrations (CMC) of the copolymers. Thus, a copolymer containing on average 12.5 dimethylsiloxane monomers (i.e., 950 g/mol) as central block and two polyether side blocks of 2200 g/mol, with each containing an equal number of randomly distributed poly(ethylene oxide)−poly(propylene oxide) (PEO−PPO) monomers, they found a CMC value of 0.126 g/L (24×10^{-6} mol/L). However, the properties of the formed micelles are not discussed.

Yang et al. established phase diagrams for PEO−PDMS−PEO polymers with different proportions of EO and DMS segments: 350−750−350, 550−750−550, 750−750−750, 750−1000−750, and 750−1300−750, which correspond to 48.3, 59.5, 66.7, 60, and 53.7 wt % of PEO.[10] The concentrations and lengths of the hydrophobic and hydrophilic blocks of these polymers cause the formation of either hexagonal or lamellar phases. At very low and very high polymer concentrations, the solution is said to be isotropic. Micelles are obviously present but not described in detail: only strong dependence of their size on temperature is mentioned.

Zhan et al. studied the behavior of aqueous solutions of small triblock copolymer EO_9−DMS_7−EO_9 with TEM. On the basis of the obtained images, the authors suggested a sphere-to-rod transition of the assemblies as the concentration of copolymer in the solution increases.[11]

Yan et al. observed 1 wt % of EO_{15}−DMS_{15}−EO_{15} in water by cryo-TEM and observed small unilamellar and large multilamellar vesicles as well as threadlike micelles.[12] Zou et al. published a phase diagram of the same copolymer in glycerol−water mixtures: lamellar phase and micelle formation depended on the polymer concentration.[13]

Hill et al. and Lin et al. observed vesicle formation, or lamellar phase dispersions, and micelles with EO_7−DMS_{15}−EO_7 and EO_{12}−DMS_{15}−EO_{12}.[14,15] They concluded that the coexistence of vesicles and micelles was due to the polydispersity of the copolymer sample. They also suggested that micelles are of spherical shape for longer hydrophilic chain.

Taken together, literature indicates that spherical micelles of PEO−PDMS−PEO triblock copolymers cannot be formed in water if the hydrophilic PEO chains are below a critical length. Comparing with classical surfactants, this corresponds to the situation where the area per polar headgroup is small and the critical packing parameter (cpp) exceeds 1/3; i.e., the structure is less curved. The cpp gives understanding about the spontaneous curvature a surface-active molecule will adopt. It takes into account the volume of the hydrophobic chain v, its fully stretched length l_c, and the effective area occupied by the polar head a_0: cpp = $v/(a_0 l_c)$.[16] It is not straightforward to estimate the cpp value of a triblock copolymer since the volume v should also take into account the hindrance of the whole molecule, i.e., the volume between the two hydrophobic chains, which depends on the conditions (e.g., bulk, plane or curved interfaces, curvature of the molecule, etc.).

To the best of our knowledge, the detailed quantitative study of the structures of PEO−PDMS−PEO block copolymer micelles in water is not proposed in the literature up to now.

In contrast, micelles of several poly(ethylene oxide)−poly(propylene oxide)−poly(ethylene oxide) copolymers have been fully described.[17−20]

One of the best-documented block copolymers of this type is P85 surfactant with formula EO_{25}−PO_{40}−EO_{25}. It was extensively studied by small-angle scattering. The molecules form spherical micelles in water whenever a phase line of critical micelle concentration and critical micelle temperature is crossed.

P85 has been studied in scattering vector q range of 0.2−5 nm^{-1} by both small-angle neutron and X-ray scattering (SANS and SAXS).[17] Pair distance distribution functions ($p(r)$) and excess scattering length density distributions gave information about the shape and the size of micelles. Spheres with an inner PPO core radius of 3 nm and an outer shell of PEO with a thickness of 5 nm have been detected. Pedersen also elucidated the particular q^{-2} behavior at large q as corresponding to a hazy interface due to dissolved flexible PEO chains in water. Mortensen and Pedersen already suggested similar structures in 1993[18] and in 1994 Glatter et al.[19] defined the P85 micelles as a star-shaped structure consisting of a compact PPO core and a soft PEO shell with starlike arms extending into the water phase. In such a model, the electron density of the shell, determined by deconvolution of the $p(r)$ function, decreases monotonically with distance because the interface is not sharp. Mortensen et al. also showed that by increasing temperature, the shape of micelles changes from spheres to ellipsoids.[18]

Orthaber et al. also used SAXS and SANS to study micelles of a similar PEO−PPO−PEO copolymer P94 with composition EO_{17}−PO_{42}−EO_{17}.[20] The electron density distribution from deconvolution of the $p(r)$ function revealed a lower electron density for the hydrophobic part, but a higher electron density of hydrophilic part with respect to the solvent. The zero crossing of the density can be used to estimate the radius of the hydrophobic part, which is about 2.5 nm, whereas the PEO shell thickness is 5.5 nm. In view of these results it seems reasonable to conclude that sufficient contrast between hydrophobic and hydrophilic parts makes small-angle scattering a powerful tool to study the structure of micelles of PEO−PPO−PEO triblock copolymers in detail.

In this study, we propose to investigate the structure formed by triblock copolymer EO_{12}−DMS_{13}−EO_{12} with concentrations up to 30 wt % in water by means of SAXS and SANS. The efficiency of this polymer in demulsifying water in crude oil emulsions has been demonstrated in a previous study.[21] Indeed, our objective is to relate its structural features with its demulsifying properties.

II. EXPERIMENTAL SECTION AND DATA TREATMENT

A. Sample. The demulsifier molecule purchased from Momentive Performance Materials, Meyrin, Switzerland, was used as received. It is a triblock copolymer consisting of two equal side blocks of PEO and a central block of PDMS. The stated composition is PEO_{12}−$PDMS_{13}$−PEO_{12} with a molecular weight of about 2100 Da: 550 Da for each of the PEO parts and 1000 Da for the PDMS part and a density of 1.049 g/cm^3. The critical micelle concentration determined in ultrapure water (18 MΩ cm^{-1}) at 20 °C is 0.0017 wt % or 8.1×10^{-6} mol/L. The area per molecule was 0.45 nm^2 as calculated from the slope of γ vs ln C curve.[5]

B. Dynamic Light Scattering (DLS). Dynamic light scattering measurements were performed at a scattering angle of 90° with a Zetasizer 3000HSA (Malvern Instruments) on three different samples of 1 wt % copolymer in water at room temperature (about 20 °C). The method consists in determining the hydrodynamic radius from the diffusion coefficient and the Brownian movement of nanosized colloids. A DLS experiment has been performed to check if this hydrodynamic radius was in accordance with SAXS and SANS results. Only low concentration (i.e., 1%) was used to avoid interaction between micelles. The angle of the beam was kept constant (90°), and the autocorrelation function was analyzed with the assumption of Brownian motion of noninteracting micelles.

dx.doi.org/10.1021/ma202610n | Macromolecules 2012, 45, 2874−2881

C. Small-Angle Neutron Scattering (SANS). SANS experiments were carried out on a small-angle PAXE spectrometer at the Laboratoire Léon Brillouin at CEA/Saclay, France. Three wavelength/sample-to-detector distance configurations, 10 Å/5 m, 6 Å/2 m and 5 Å/1.1 m, were used corresponding to a range of 0.08−3.9 nm^{-1} scattering vectors q, respectively. The polydispersity wavelength $\Delta\lambda/\lambda$ is close to 5%.[22] Solutions of 1, 2, 5, 10, 20, and 30 wt % of copolymer in deuterated water were studied in quartz cells (2 mm, Hellma) at room temperature (about 22 °C). The detected intensities were divided by the transmission and sample thickness, corrected for empty-cell scattering, and normalized to scattering from hydrogenated water. Absolute units (cm^{-1}) were obtained by measuring the incident flux.

D. Small-Angle X-ray Scattering (SAXS). SAXS measurements were performed at IFPEN, Rueil-Malmaison (France) on an in-house experimental setup. A copper rotating anode generator (Rigaku Micromax 007), operating at 0.8 kW, provides an X-ray beam, which is reflected on a parabolic multilayer mirror from Xenocs. The reflected monochromatic beam (λ = 0.154 nm) is collimated by two pairs of crossed slits whose parasitic scattering is removed by another pair of crossed guard slits located just before the sample. These measurements will be referred to as "pointlike beam" experiments. The 5 wt % solution of copolymer in distilled water was loaded in a cell closed by two thin-glued mica windows with 1 mm optical path. A 2D multiwire proportional position-sensitive detector from Rigaku collected the scattering intensity, which was found isotropic. The position of each pixel, relatively to the position of the direct beam, is converted into the magnitude of the scattering vector q (defined as $q = (4\pi/\lambda)\sin(\theta/2)$ for an angle θ) thanks to external standard (Ag behenate). The covered q range is 0.1−2.66 nm^{-1}. After normalization with respect to thickness, transmission, and measuring time, the water signal was subtracted from the sample signal and the raw intensities were converted to the scattering cross section $I(q)$ in absolute scale (cm^{-1}) thanks to measurement of toluene as secondary standard. The present experiments were conducted at various temperatures from 20 to 60 °C.

Another set of SAXS experiments were performed at the University of Graz, Austria at 25 °C (referred to as "linear beam" experiments). The SAXS equipment comprises a SAXSess camera (Anton-Paar, Graz, Austria), connected to an X-ray generator (Philips, PW1730/10) operating at 40 kV and 50 mA with a sealed-tube Cu anode. A Göbel mirror was used to convert the divergent polychromatic X-ray beam into a focused line-shaped beam of Cu Kα radiation (λ = 0.154 nm). The 2D scattering pattern was recorded by a PI-SCX fused fiber-optic taper charged-couple device (CCD) camera from Princeton Instruments, which is a division of Roper Scientific, Inc. (Trenton, NJ). Background subtraction was performed on the 2D image before integration into the one-dimensional scattering function $I(q)$. The temperature of the capillary and the metallic sample holder was controlled by a Peltier element. Samples were exposed to X-rays for 10 min, and measurements were performed in triplicate. After averaging, scattering curves were put on absolute scale using water as a secondary standard,[20] and the smeared data were corrected for instrumental broadening.

Ideally, a scattering experiment uses a pointlike primary beam, sample, and detector resolution and implies monochromatic radiation. However, most experiments do not meet all of the requirements, which leads to smearing effects. Moreover, instrumental broadening effects result in broader and shorter peaks in the intensity curve.

Figure 1 illustrates the smearing effects for the linear beam experiment in comparison to the pointlike beam experiment. The data shows that comparison between the two beams is only possible after desmearing data from the linear experiment.

The scattering length densities used for SAXS (ρ) and SANS (b) are presented in Table 1.

Smeared linear beam data (crosses) result in a curve with broader and less pronounced peaks. In contrast, peaks of the desmeared linear beam curve are similar to those of the pointlike beam curve and statistical noise is lower.

Data were treated and modeled with the PCG software, GIFT, from the Department of Chemistry, University of Graz, Austria. This

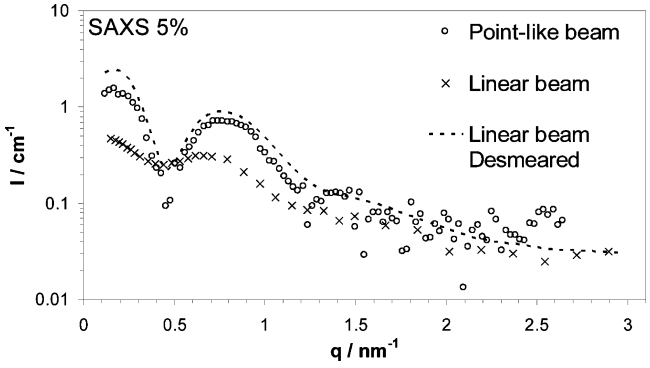


Figure 1. Scattering intensity for 5 wt % data (SAXS) with pointlike beam (20 °C) or linear beam (25 °C) setup. Pointlike beam data should be compared to desmeared linear beam data.

Table 1. Electron Densities and Scattering Length Densities[23]

	SAXS ρ (e^- Å^{-3})	SANS b (10^{10} cm^{-2})
DMS	0.316	0.06
EO	0.35	0.6
H_2O	0.334	−0.56
D_2O		6.38

method considers the intensity $I(q)$ on absolute scale [cm^{-1}] as the product of the particle density n [cm^{-3}], the form factor $P(q)$ being the scattering cross section per particle [cm^2] (not normalized) and the structure factor $S(q)$.

$$I(q) = nP(q)S(q)$$

Methods for the comprehensive analysis of small-angle scattering data, including least-squares methods, indirect Fourier transformation, square-root deconvolution, size distribution determinations, and modeling with corrections for instrumental smearing effects have been reviewed in detail by Pedersen.[17] He also described various models for form factors and structure factors for different geometries.

The desmeared scattering curve is the Fourier transform of the pair distance distribution function (PDDF or $p(r)$):

$$I(q) = 4\pi \int_0^\infty \frac{p(r)\,\sin(qr)}{qr}\,dr$$

If one wants to take into account the slit length and width effects and the wavelength effect, this desmeared curve has to be smeared. This smeared curve is called an "approximated curve" as it is calculated by a weighted least-squares fit to experimental data, the indirect Fourier transformation (IFT). The method works for dilute systems, where interparticle effects are negligible and, hence, the structure factor is constant ($S(q) = 1$). The intensity is only related to the form factor containing the intraparticle effects.

The generalized indirect Fourier transformation (GIFT) is the advanced version for interacting systems, taking into account the interparticle effects ($S(q) \neq 1$).

The convolution square root technique is then used to deconvolute the $p(r)$ function of micelles into the radial density profile $\rho(r)$ assuming spherical shape

$$p(r) = r^2\langle\tilde{\rho}^2(r)\rangle = \langle\int \rho(x)\rho(1-x)\,dx\rangle$$

where $\langle\ \rangle$ stands for the spherical average and $\tilde{\rho}^2(r)$ is the convolution square. For more details concerning the treatment the reader is referred to refs 24 and 25.

dx.doi.org/10.1021/ma202610n | Macromolecules 2012, 45, 2874−2881

III. RESULTS

Solutions containing 1 wt % of copolymer in water were analyzed by DLS. Figure 2 presents an example of the results

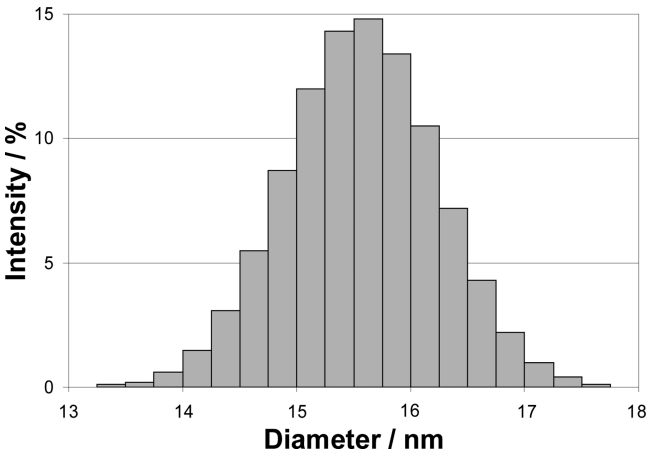


Figure 2. Intensity scattered by 1 wt % of copolymer in water from DLS measurement at 20 °C.

obtained from light scattering measurements. The micelle size distribution is monomodal and quite sharp, with a mean diameter of 15.5 nm. Measurements were performed on three different samples to investigate the reproducibility. All three samples gave very similar results, and only one of them is reported for clarity of the illustration.

To assess the structural details of the formed micelles, we performed SAXS and SANS measurements on samples containing between 1 and 30 wt % of copolymer in D_2O for SANS and H_2O for SAXS.

Characteristic scattered intensities I versus scattering vector q (scattering functions) are shown in Figure 3. The intensity is divided by the solution concentration: correction for monomer concentration was not necessary as the CMC is very low compared to the used concentrations.

The intensity curves at high q-values ($q > 0.5$ nm^{-1}) are superimposed for all examined concentrations, signifying that scattering curves only depend on the form factor $P(q)$ of the micelles. The shape of the curves in this high q-region indicates that micelles have a similar shape. The position of the minimum and the first side maximum in SAXS data (between 0.4 and 0.7 nm^{-1}) remained unchanged for each concentration; the size of the micelle can therefore be considered as constant.

For low q-values ($q < 0.5$ nm^{-1}), the scattering intensity decreases as the concentration increases, indicating beginning interactions between the micelles. This effect will be addressed below by means of variation of structure factor with the scattering vector.

The GIFT method is used to determine the PDDF or $p(r)$ function corresponding to the approximated curve with the best fit to the experimental data.[24,25] Figure 4 shows the example of the treatment of the 2 wt % solution data.

The $p(r)$ functions, corresponding to the approximated curves for all examined concentrations, are presented in Figure 5. The SANS curves present the bell shape ending at 15 nm for all concentrations. This indicates that the copolymer forms globular micelles with a maximum dimension of ~15 nm, in agreement with DLS data of Figure 2. For 30 wt % copolymer, the shape of the curve changes at large distances, indicating that micelles become elongated or that the polydispersity in the

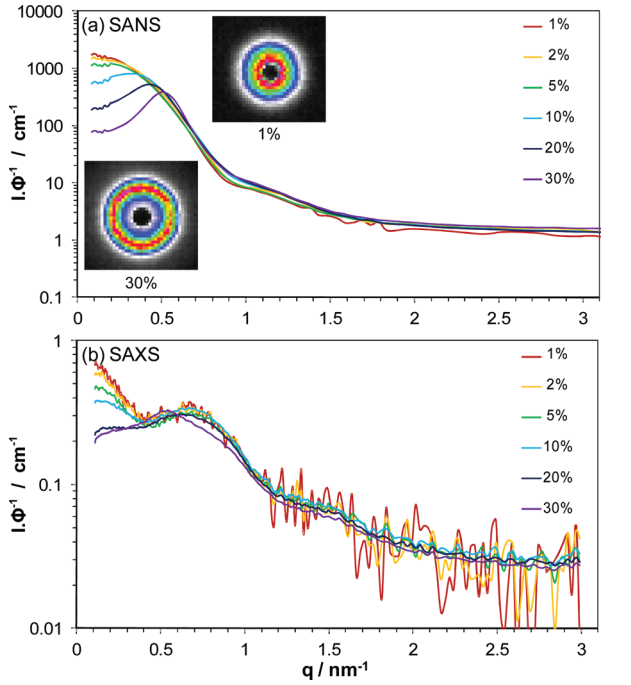


Figure 3. (a) SANS and (b) linear beam SAXS data of 1, 2, 5, 10, 20, and 30 wt % copolymer in D_2O and H_2O, respectively. Inset: SANS 2D representations of intensity obtained with 1 and 30% of copolymer in D_2O show isotropic scattering.

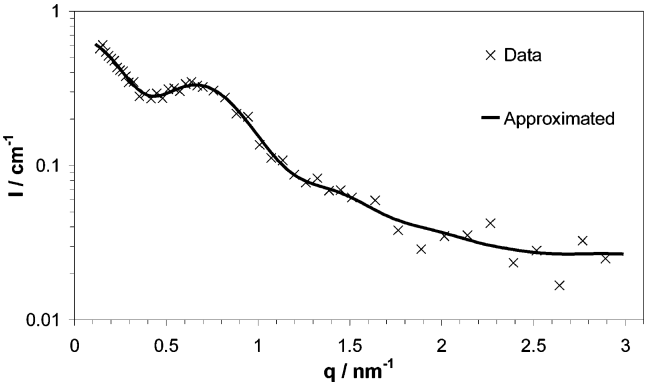


Figure 4. Scattering intensity (linear beam) for 2 wt % data (SAXS).

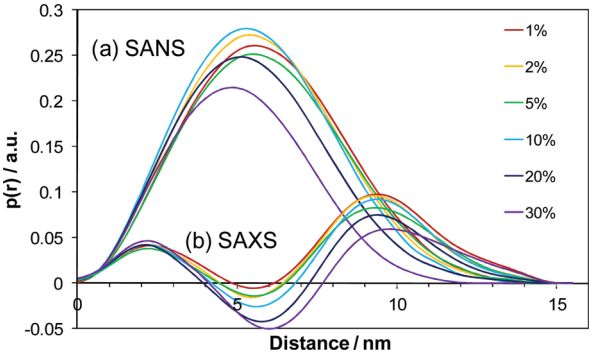


Figure 5. Pair distance distribution function at room temperature for (a) SANS and (b) SAXS data of 1, 2, 5, 10, 20, and 30 wt % of copolymer in D_2O and H_2O, respectively.

system increases. The shape of these curves confirms that the neutrons "see" a global homogeneous sphere because of the low

dx.doi.org/10.1021/ma202610n | Macromolecules 2012, 45, 2874–2881

contrast between the PDMS core and the PEO shell (0.06×10^{10} and 0.6×10^{10} cm^{-2}) compared with the deuterated water (6.38×10^{10} cm^{-2}).

According to the SAXS data, the difference in electron density induces negative contributions to the PDDF: the contrast of the silicone chain to water is negative ($\Delta\rho$ = −0.018 e$^-$ Å^{-3}) while it is positive for ethylene oxide chain to water ($\Delta\rho$ = 0.016 e$^-$ Å^{-3}). Thus, hydrophobic and hydrophilic parts of the assembly are distinguishable with X-rays. Moreover, SAXS data confirm the particle maximum dimension of about 15 nm, including the slight elongation (or the higher polydispersity) for the micelles in 30% solutions (quasi-linear part of the curve between 11 and 15 nm).

The scattering length and the electron density distribution of spheres can be obtained by deconvolution of the $p(r)$. The distribution from SANS data shown in Figure 6a confirms

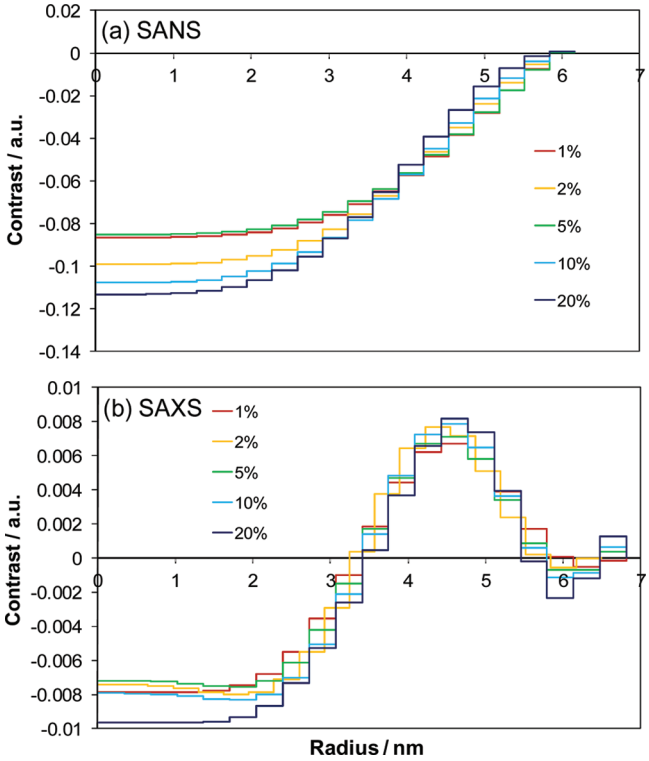


Figure 6. Density profile difference for 1, 2, 5, 10, and 20 wt % of copolymer in (a) D_2O and in (b) H_2O deduced from the SANS and SAXS data, respectively.

that the contrast between deuterated water and silicone or ethoxylated chain is of same sign, indicating that the core and the shell of the micelle are not distinguishable with this technique. In contrast, the constant negative contribution of the PDMS part for distances up to 2 nm from the center of the micelle is visible by SAXS (Figure 6b); it approaches zero at about 3.5 nm. The density difference equal to zero can be used as an estimation of the radius of the core (interfacial layer) equal to 3.5 nm, whereas the positive density difference corresponds to the hydrophilic shell. The electron density difference increases monotonically; i.e., the interface between the core and the shell is not sharp: the mobility of the polymer chains causes a gradual transition between the two parts. The decrease in the electron density from 4.5 to 5.5−6 nm indicates that the copolymer forms star-shaped micelles in water, with a compact PDMS core and a soft PEO shell with starlike arms extending into the water phase similarly to the micelles of PEO−PPO−PEO copolymers.[25]

Therefore, the micelle structure of triblock PEO−PDMS−PEO copolymer can be summarized as follows: a dense PDMS core, composed of hydrophobic chains, with a radius of about 2 nm, a transition region from 2 to 4.5 nm, where EO and DMS segments are mixed, and a shell with a thickness of ∼1 nm composed of hydrophilic PEO chains and water.

The density profile presented in Figure 6b indicates that zero contrast; i.e., transition between DMS core and EO shell is situated at about 3.5 nm. Therefrom, one can estimate the aggregation number of micelle, i.e., the number of triblock copolymer molecules in the micelle, as

$$N_{agg} = \frac{\text{total volume of PDMS}}{\text{volume of one PDMS chain}} = \frac{4\pi r_{PDMS}{}^3}{3v_{1PDMS}}$$

With a radius r of 3.5 nm per PDMS part and a volume v of 1.77 nm^3 per PDMS chain (deduced from the molecular weight and the density of bulk silicone chain, which is different from the density of a hydrated polymer), the aggregation number is ∼100 molecules per micelle. Fritz et al. showed that the density inside the core of a micelle is smaller than in the bulk.[26] In our calculation, variation in density was not taken into account, and the aggregation number of 100 is given as rough estimation only.

As the total volume for one molecule of triblock copolymer is 3.31 nm^3, 100 molecules should occupy about 330 nm^3. The total volume of the micelle, determined from the external radius of 5.5 nm, is around 700 nm^3. Therefore, the excess of water is about 370 nm^3, and the number of water molecules per copolymer is estimated to be ∼120, i.e., 5 molecules of water for 1 ethylene oxide group. The hydration number correlates with the high affinity of ethylene oxide chains for water.[27]

The GIFT treatment also provides information about the structure factor of the assemblies (Figure 7). As pointed out earlier, structure factor is close to 1 (strictly speaking, equal to 1 for infinite dilution) for low copolymer concentration. This is almost the case for the structure factor calculated from 1% SAXS data (Figure 7b), which remains nearly constant and equal to 1 for all values of scattering vector q.

As the structure factor describes the interference of interparticle scattering, interparticle interactions increase with the concentration and the distance between the micelles decreases. This effect is visible on the shape of structure factor calculated from both SANS and SAXS data: the $S(0)$ value decreases dramatically with concentration, while the interaction peak becomes sharper and moves to higher q-values, reflecting the increasing interparticle interactions due to the decrease of the mean distance between neighboring particles.

According to our observations, SAXS and SANS structure factors are comparable. This indicates that the only changing parameter between X-rays and neutrons is the form factor of the assemblies, corresponding to the different $p(r)$ functions.

The volume fractions corresponding to the structure factors are presented in Table 2. The estimated values from SAXS and SANS model are higher than the experimental values due to the presence of water in the micelle, similarly to what was reported by Lindner et al. for P94 copolymer.[28]

Another set of SAXS experiments was performed with the aim to examine the influence of temperature on the size and

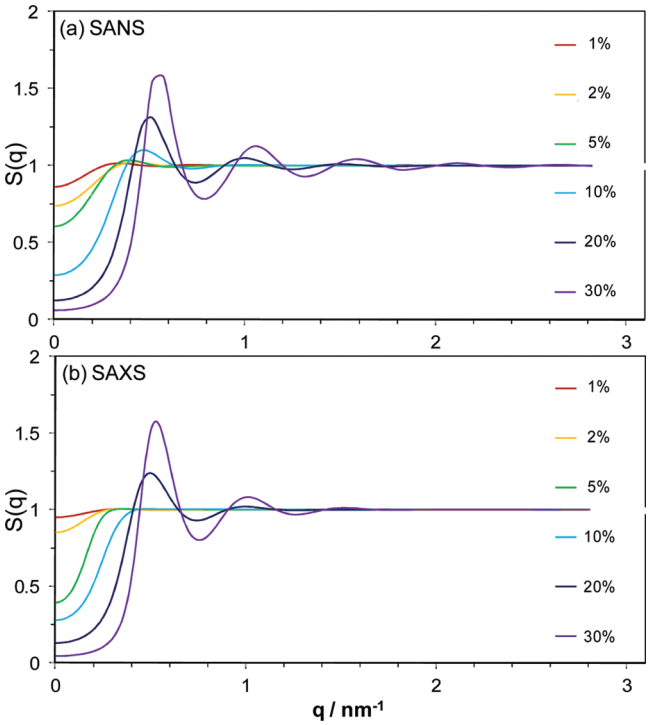


Figure 7. Structure factor deduced from (a) SANS and (b) SAXS data for 1, 2, 5, 10, 20, and 30 wt % of copolymer in D_2O and H_2O solutions, respectively.

Table 2. Volume Fractions: Experimental Data and Estimation from the Fitting Curves of $S(q)$ for SAXS and SANS Data

Φ_v(exp), %	Φ_v(SAXS), %	Φ_v(SANS), %
0.95	0.6	1.9
1.9	2.0	3.8
4.8	11.9	6.4
9.5	16.4	16
19.1	26.2	26.5
28.6	38.6	35.3

shape of the micellar structure. A pointlike beam was used for the experimental setup.

Figure 8 shows the scattering intensity I versus the scattering vector q for the 5 wt % copolymer solution in H_2O at

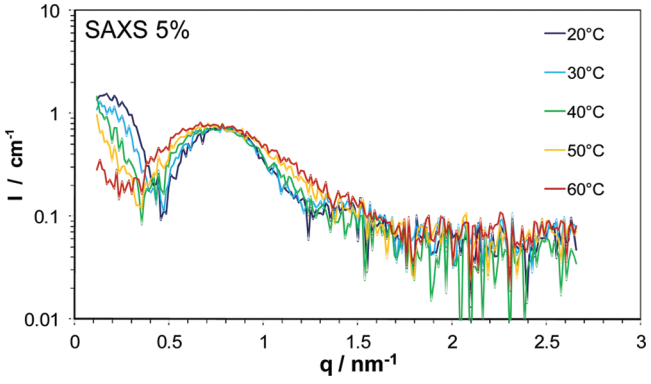


Figure 8. Scattering intensity for 5 wt % data (SAXS) with pointlike beam for different temperatures from 20 to 60 °C.

temperatures between 20 and 60 °C. As the temperature increases, the position of the first minimum changes from q = 0.47 to 0.35 nm^{-1}, already indicating an increase of the micelle size.

The increase of the size of the micelle is confirmed by the $p(r)$ function presented in Figure 9: the maximum dimension is

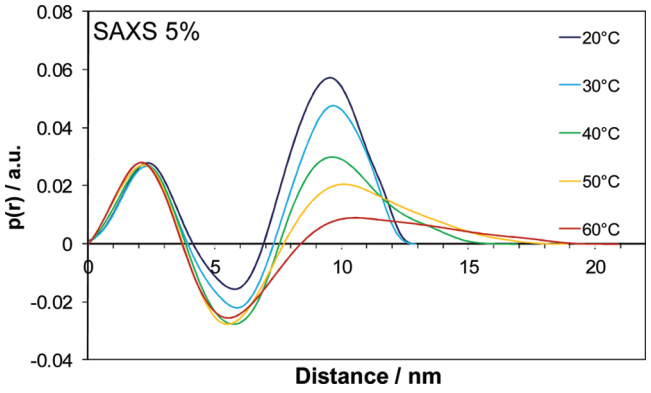


Figure 9. Pair distance distribution function $p(r)$ for SAXS of 5 wt % copolymer in H_2O at temperatures between 20 and 60 °C.

13 nm at 20 and 30 °C and increases to 17, 19, and 21 nm respectively for 40, 50, and 60 °C.

In addition, the bell-like shape of the $p(r)$ curves for temperatures of 20 and 30 °C indicates that micelles are of spherical shape. For higher temperatures, the shape of the $p(r)$ curve changes: at 60 °C it becomes almost linear at large distances, indicating that with increasing temperature the objects become rodlike and more elongated up to 21 nm. Similar effects have also been observed with PEO−PPO−PEO copolymers.[18]

IV. DISCUSSION AND CONCLUSION

The small-angle scattering data presented here indicate that in the presence of water EO_{12}−DMS_{13}−EO_{12} molecules preferentially self-assemble to form spherical micelles at concentrations up to 20 wt %. The micelles have a core of low electronic density and an outer shell with a high electronic density when compared to water. The core contains the silicone segments of polymer followed by a mix of hydrophobic and hydrophilic chains. The ethoxylated chains spread into surrounding water. The radius of the micelle is about 5.5 nm. The transition between the hydrophobic core and hydrophilic chain is situated at about 3.5 nm. Similarly to P85 micelles studied by Mortensen and Pedersen,[18] the micelles increase in size with increasing temperature (up to 21 nm). For temperatures over 40 °C, significant elongation can be observed.

The spherical shape of self-assembled structures corresponds to a low value of critical packing parameter of the molecule (cpp ≤1/3) and to a high spontaneous curvature.[16] This finding is is in agreement with our previous detailed study of five triblock PEO−PDMS−PEO copolymers with different proportions of hydrophilic PEO and hydrophobic PDMS parts,[21] where we show that efficient demulsifier copolymers stabilize oil-in-water emulsions while inefficient copolymers stabilize water-in-oil emulsions. This observation seems to be in line with the Bancroft rule and Langmuir Harkins "truncated" wedge theory predicting that surfactants with a dominant hydrophilic part favor water as continuous phase while surfactants with a prevailing hydrophobic part favor oil as continuous phase.[8] The effect of the surfactant is the opposite

dx.doi.org/10.1021/ma202610n | Macromolecules 2012, 45, 2874−2881

when considering the demulsification efficiency: a hydrophilic surfactant capable of stabilizing an oil-in-water emulsion favors breaking the water-in-oil emulsion. To test this hypothesis, the series of copolymers described above was studied at high concentration where liquid crystals form. Indeed, a poorly demulsifying copolymer formed inversed liquid crystal phases while highly efficient copolymers formed direct structures.[29] However, due to the presence of two bulky hydrophilic "heads", triblock copolymers should not be considered as classical surfactant molecules as one cannot calculate the so-called critical packing parameter (cpp) which provides an insight into the spontaneous curvature and hence the shape of the self-assembled structures. To the best of our knowledge, there is no analogous parameter adapted to amphiphilic triblock copolymers in the literature.

Coming back to the role of the demulsifier molecule in the process of separation of water from water-in-crude oil emulsions, a necessary condition is the coalescence of small water droplets. As shown in this study, the spontaneous curvature of the self-assembled copolymer molecules in water corresponds to the curvature of an oil droplet in water, with small hydrophobic parts oriented inside the oil drop. It is likely that the molecule adopts the same spontaneous curvature at the oil/water interface. A schematic representation of two water droplets approaching each other is given in Figure 10a.

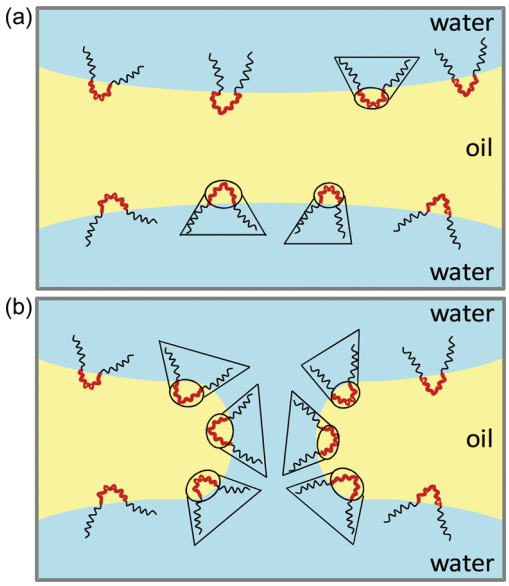


Figure 10. Schematic representation of the nucleation of a hole in the oil lamella between two water droplets: efficient polymers spontaneous curvature fits the oil/water curvature of the hole.

In order to break the oil lamella separating the two water drops, a hole must nucleate in the film (Figure 10b). The molecule fits to a highly positively curved interface, created by the channel formation when two droplets approach each other. As suggested by Kalbanov and Wennerstrom, the energy barrier associated with the nucleation process can be lowered and nucleation of a hole favored if the curvature of the molecules at the oil/water interface corresponds to the curvature of the nucleating hole.[8] As suggested in Figure 10b, the high local curvature of the nucleating hole may provoke regional accumulation of demulsifier molecules, thereby diminishing the energy barrier. However, the necessary condition for such action is the orientation of copolymer molecules at the oil–water interface. In the case of water drops dispersed in an oil phase, molecules with high curvature (or small ccp values) such as the one studied here may be appropriate. Good field performance of this copolymer agrees well with such analysis, as it has also been proven that molecules not forming spherical micelles in water, i.e., having higher cpp value, are less efficient demulsifiers.[29]

AUTHOR INFORMATION

Corresponding Author

*E-mail: amandine.forny@gmail.com.

Present Address

[⊥]University of Geneva, Pharmaceutical Sciences, CH-1211 Geneva 4, Switzerland.

Notes

The authors declare no competing financial interest.

ACKNOWLEDGMENTS

The authors thank J. JESTIN from the Laboratoire Léon Brillouin for all the SANS experiments performed in CEA Saclay, J. M'HAMDI for his help with SAXS measurements carried out in IFPEN, and the members of the Department of Chemistry for helping in SAXS measurements in the University of Graz as well as data interpretation.

REFERENCES

(1) Angle, C. W. In *Encyclopedic Handbook of Emulsion Technology*; Sjöblom, J., Ed.; Marcel Dekker: New York, 2001; p 541.

(2) Sjöblom, J.; Johnsen, E. E.; Westvik, A.; Ese, M. H.; Djuve, J.; Auflem, I. H.; Kallevik, H. In *Encyclopedic Handbook of Emulsion Technology*; Sjöblom, J., Ed.; Marcel Dekker: New York, 2001; p 595.

(3) Kim, Y. H.; Nikolov, A. D.; Wasan, D. T.; Diaz-Arauzo, H.; Shelly, C. S. Demulsification of water in crude oil emulsions: Effects of film tension, elasticity, diffusivity and interfacial activity of demulsifier individual components and their blends. *J. Dispersion Sci. Technol.* **1996**, *17*, 33–53.

(4) Dalmazzone, C.; Noik, C.; Komunjer, L. Mechanism of crude-oil/water interface destabilization by silicone demulsifiers. *SPE J.* **2005**, 44–53.

(5) Daniel-David, D.; Pezron, I.; Clausse, D.; Dalmazzone, C.; Noik, C.; Komunjer, L. Interfacial properties of a silicone copolymer demulsifier at the air/water interface. *Phys. Chem. Chem. Phys.* **2004**, *6*, 1570–1574.

(6) Daniel-David, D.; Pezron, I.; Dalmazzone, C.; Noik, C.; Clausse, D.; Komunjer, L. Elastic properties of crude oil/water interface in presence of polymeric emulsion breakers. *Colloids Surf., A* **2005**, *270–271*, 257–262.

(7) Daniel-David, D.; Le Follotec, A.; Pezron, I.; Dalmazzone, C.; Noik, C.; Barre, L.; Komunjer, L. Destabilisation of water-in-crude oil emulsions by silicone copolymer demulsifiers. *Oil Gas Sci. Technol.* **2008**, *63*, 165–173.

(8) Kalbanov, A.; Wennerstrom, H. Macroemulsion stability: The oriented wedge theory revisited. *Langmuir* **1996**, *12*, 276–292.

(9) Kanellopopoulos, A. G.; Owen, M. J. The adsorption of polydimethylsiloxane polyether ABA block copolymers at the water/air and water/silicone fluid interface. *J. Colloid Interface Sci.* **1971**, *35*, 120–125.

(10) Yang, J.; Wegner, G.; Koningsveld, R. Phase behavior of ethylene oxide-dimethylsiloxane PEO-PDMS-PEO triblock copolymers with water. *Colloid Polym. Sci.* **1992**, *270*, 1080–1084.

(11) Zhan, X. L.; Chen, B.; Zhang, Q. H.; Yi, L. M. Sphere-to-rod transition of short-chain PEO-b-PDMS-b-PEO in aqueous solution

induced by copolymer concentration. *Chin. Chem. Lett.* **2008**, *19*, 1363−1366.
(12) Yan, Y.; Hoffmann, H.; Makarsky, A.; Richter, W.; Talmon, Y. Swelling of L_α -phases by matching the refractive index of the water-glycerol mixed solvent and that of the bilayers in the block copolymer system of $(EO)_{15}-(PDMS)_{15}-(EO)_{15}$. *J. Phys. Chem. B* **2007**, *111*, 6374−6382.
(13) Zou, A.; Hoffmann, H.; Eastoe, J.; Glatter, O. Glycerol-induced swollen lamellar phases with siloxane copolymers. *J. Colloid Interface Sci.* **2007**, *316*, 723−729.
(14) Hill, R. M.; He, M.; Lin, Z.; Davis, H. T.; Scriven, L. E. Lyotropic liquid crystal phase behavior of polymeric siloxane surfactants. *Langmuir* **1993**, *9*, 2789−2798.
(15) Lin, Z.; Hill, R. M.; Davis, H. T.; Scriven, L. E.; Talmon, Y. Cryo Transmission Electron Microscopy study of vesicles and micelles in siloxane surfactant aqueous solutions. *Langmuir* **1994**, *10*, 1008−1011.
(16) Israelachvili, J. N. In *Intermolecular and Surface Forces*, 2nd ed.; Academic Press: New York, 1991.
(17) Pedersen, J. S. Analysis of small-angle scattering data from colloids and polymer solutions: modeling and least-squares fitting. *Adv. Colloid Interface Sci.* **1997**, *70*, 171−210.
(18) Mortensen, K.; Pedersen, J. S. Structural study on the micelle formation of poly(ethylene oxide)-poly(propylene oxide)-poly-(ethylene oxide) triblock copolymer in aqueous solution. *Macromolecules* **1993**, *26*, 805−812.
(19) Glatter, O.; Scherf, G.; Schillen, K.; Brown, W. Characterization of a poly(ethylene oxide)-poly(propylene oxide) triblock copolymer $(EO_{27}-PO_{39}-EO_{27})$ in aqueous solution. *Macromolecules* **1994**, *27*, 6046−6054.
(20) Orthaber, D.; Bergmann, A.; Glatter, O. SAXS experiments on absolute scale with Kratky systems using water as a secondary standard. *J. Appl. Crystallogr.* **2000**, *33*, 218−225.
(21) Le Follotec, A.; Pezron, I.; Noik, C.; Dalmazzone, C.; Metlas-Komunjer, L. Triblock copolymers as destabilizers of water-in-crude oil emulsions. *Colloids Surf., A* **2010**, *365*, 162−170.
(22) Lairez, D. Resolution of a small-angle neutron scattering spectrometer. *J. Phys. IV* **1999**, *9*, 67−81.
(23) Feigin, L. A.; Svergun, D. I. In *Structure Analysis by Small-Angle X-Ray and Neutron Scattering*; Plenum Press: New York, 1987.
(24) Glatter, O. In *Neutrons, X-Rays and Light: Scattering Methods Applied to Soft Condensed Matter*, 1st ed.; Lindner, P., Zemb, T. H., Eds.; North-Holland Delta Series: Amsterdam, 2002; Chapter 5, pp 103−124.
(25) Glatter, O.; Fritz, G.; Lindner, H.; Brunner-Popela, J.; Mittelbach, R.; Strey, R.; Egelhaaf, S. Nonionic micelles near the critical point: micellar growth and attractive interaction. *Langmuir* **2000**, *16*, 8692−9701.
(26) Fritz, G.; Scherf, G.; Glatter, O. Applications of Densiometry, Ultrasonic Speed Measurements, and Ultralow Shear Viscosimetry to Aqueous Fluids. *J. Phys. Chem. B* **2000**, *104*, 3463−3470.
(27) Branca, C.; Magazu, S.; Maisano, G.; Migliardo, F.; Migliardo, P.; Romeo, G. Hydration study of PEG/water mixtures by quasi elastic light scattering, acoustic and rheological measurements. *J. Phys. Chem. B* **2002**, *106*, 10272−10276.
(28) Lindner, H.; Scherf, G.; Glatter, O. Dynamic and static properties of the concentrated micellar solution and gel phase of a triblock copolymer in water. *Phys. Rev. E* **2003**, *67*, 061402.
(29) Forny-Le Follotec A.; Glatter O.; Pezron I.; Barré L.; Noïk C.; Dalmazzone C.; Metlas-Komunjer L. Characterization of Liquid Crystal Structures of Small Triblock Copolymer by Small Angle Scattering. Manuscript in preparation.

Macromolecules

Article

pubs.acs.org/Macromolecules

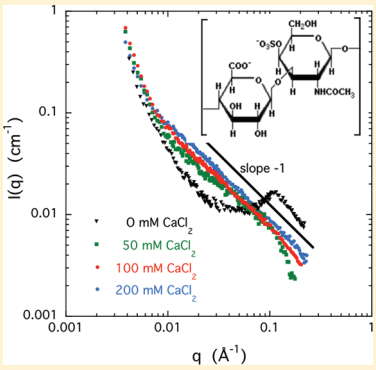
Chondroitin Sulfate in Solution: Effects of Mono- and Divalent Salts

Ferenc Horkay,*[,†] Peter J. Basser,[†] Anne-Marie Hecht,[‡] and Erik Geissler[‡]

[†]Section on Tissue Biophysics and Biomimetics, Program in Pediatric Imaging and Tissue Science, Eunice Kennedy Shriver National Institute of Child Health and Human Development, National Institutes of Health, 13 South Drive, Bethesda, Maryland 20892, United States

[‡]Laboratoire Interdisciplinaire de Physique CNRS UMR 5588, Université J. Fourier de Grenoble, B.P.87, 38402 St Martin d'Hères cedex, France

ABSTRACT: Chondroitin sulfate (CS) is a linear sulfated polysaccharide found in cartilage and other tissues in the body. Small-angle neutron scattering (SANS) and dynamic light scattering (DLS) measurements are made on semidilute CS solutions to determine ion-induced changes in the local order of the CS chains and in their dynamic properties. In salt-free CS solutions SANS detects the correlation peak due to local ordering between adjacent chains in which the characteristic interchain distance is $d \approx 57$ Å. In both monovalent and divalent salts (NaCl and $CaCl_2$) aligned linear regions are distinguishable, corresponding to distance scales ranging from the length of the monomer unit (8 Å) to about 1000 Å. With increasing calcium ion concentration, the scattering intensity increases. Even in the presence of 200 mM $CaCl_2$, however, neither phase separation nor cross-linking occurs. DLS in the CS solutions reveals two characteristic relaxation modes, the fast mode corresponding to the thermal concentration fluctuations. The collective diffusion coefficient D decreases with increasing calcium ion concentration and exhibits a power law function of the single variable c/J, where c is the CS concentration and J is the ionic strength of the salt in the solution. This result implies that the effect of the sodium and calcium ions on the dynamic properties of CS solutions is fully accounted for by the ionic strength.



INTRODUCTION

Chondroitin sulfate (CS), an important macromolecule prevalent in living organisms, is a sulfated glycosaminoglycan (GAG) composed of alternating sugars (*N*-acetylgalactosamine and glucuronic acid). A typical chondroitin chain may contain over 100 individual sugar units, each of which can be sulfated in variable positions and quantities. Despite the relative simplicity of its chemical structure, the CS molecule carries biological information and participates in many biological functions. CS interacts with a variety of molecules, such as growth factors, cytokines, chemokines, adhesion molecules, and lipoproteins, and also plays an important role in cancer biology.[1−5] CS is involved in cell growth, neuronal development, and spinal cord injury. It also possesses important biological properties for tissue integration, including anti-inflammatory activity, water, and nutrient absorption.

Figure 1 shows the chemical structure of the CS chain repeating unit, the molecular weight of which is 459 Da

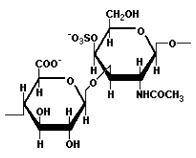


Figure 1. Chemical structure of the disaccharide repeating unit of the CS chain.

(excluding counterions). The hydrophilic polysaccharide backbone, combined with the electrostatic repulsion among the negatively charged molecules, ensures that solutions in water are stable over a wide range of pH and salt concentration. The average molecular weight of naturally occurring CS chains lies in the range 30−40 kDa. The distance between charges depends on the position of the sulfate and carboxyl groups and varies between about 3 and 5 Å.[6] CS is a naturally stiff polymer with a persistence length of roughly 80 Å.[7] In solution or in its biological milieu, changes in the local environment, due for example to hydration, salt concentration, or ionic composition, influence the interactions with neighboring CS molecules and other surrounding species.

CS is frequently attached to proteins as part of a proteoglycan. Chondroitin sulfate proteoglycans (CSPGs) are important components of the extracellular matrix (ECM). In the central nervous system (CNS) they play an essential role in controlling neuronal differentiation and development. They guide axonal growth,[10] inhibit neural crest cell migration,[11] and, in later stages of development as well as in adulthood, regulate neuronal plasticity by forming perineuronal nets around synapses.[12,13] In damaged nervous systems, they exhibit growth-inhibitory activities in the glial scar such as hindering axon regeneration or compensatory sprouting.[14−16]

The ability of sulfated polysaccharides to complex divalent cations, especially calcium ions, is an important biological

Received: December 12, 2011
Revised: February 16, 2012
Published: March 7, 2012

 © 2012 American Chemical Society

function of this class of polymer. For example, proteoglycans (and their constituent glycosaminoglycan chains) perform an important role in the regulation of endochondral ossification, since local degradation or disaggregation of proteoglycan initiates calcification of epiphyseal cartilages.[17−19] GAG components of the tendon (CS and dermatan sulfate) associate with collagen and are involved in the fibril assembly process during tendon development.

CS is the major structural component of the bottlebrush-shaped molecule aggrecan, a large aggregating proteoglycan in the cartilage ECM, which forms complexes with hyaluronan and provides compressive resistance under external load. These large aggrecan/hyaluronan complexes are enmeshed in a network of collagen, where the structural stability is enhanced by the ionic interactions between the negatively charged CS bristles and the positive charges on the collagen fibrils. In this context the interaction between the CS chains and different cations is of particular importance. Woodward and Davidson reported that bone calcification occurs through the release of calcium ions bound to proteoglycans in cartilage.[20,21] Previous studies also indicated that (i) the degree of calcium ion binding to chondroitin sulfate was larger than that of sodium ions and (ii) the association of calcium ions with the polymer cannot be ascribed solely to electrostatic forces. However, no significant differences were detectable in the degree of ion binding of different chondroitin sulfate isomers.[22]

The purpose of the present study is to advance our understanding of the physical−chemical properties and biological function of CS by exploration of the effect of ion concentration and valence on the structure and dynamics of CS solutions. We report a systematic investigation using complementary experimental techniques, small-angle neutron scattering (SANS), and dynamic light scattering (DLS). The ion concentration is varied in a wide concentration range around the physiological conditions and beyond.

The organization of this paper is as follows. First, the sample preparation is described, and the SANS and DLS techniques and experimental setups are briefly introduced. Then SANS results for CS solutions are presented as a function of the polymer concentration. SANS probes the structure over a broad range of length scales extending from ∼1 nm to macroscopic sizes. DLS is used to determine the effect of the ionic environment on the dynamic response over a similar range of ionic concentrations. A comparison is made between the effects of sodium chloride and calcium chloride on the organization and dynamic properties of the CS solutions. In the final section, we discuss some biological implications of the results.

EXPERIMENTAL SECTION

Sample Preparation. For the SANS measurements, solutions of the sodium salt of chondroitin sulfate (Sigma-Aldrich) were prepared in D_2O and in H_2O for those with DLS. The CS concentration ranged between 1% and 20% w/w. Concentrations of added sodium chloride and calcium chloride were varied between 0 and 500 mM and 0 and 200 mM, respectively. DLS measurements were made on CS solutions containing 100 mM NaCl, with concentrations of $CaCl_2$ between 0 and 200 mM.

In all samples the pH was 7, where CS is fully dissociated. The samples were allowed to homogenize for 2−3 days. Both SANS and DLS measurements were made at 25.0 ± 0.1 °C.

Small-Angle Neutron Scattering Measurements. The SANS measurements were made on the NG3 instrument at NIST, Gaithersburg, MD. Solutions were placed in sample cells of 1 mm optical path equipped with quartz windows. The wavelength of the incident radiation was λ = 8 Å, with wavelength spread $\Delta\lambda/\lambda$ = 0.10. The transfer wave vector range explored was 2.8×10^{-3} Å^{-1} < q < 0.3 Å^{-1}, where $q = (4\pi n/\lambda)\sin(\theta/2)$, with θ being the scattering angle and n the refractive index of the medium (in SANS experiments, n is close to unity). After azimuthal averaging, the spectra were corrected for detector response and cell window scattering. The incoherent background was subtracted following the procedure described previously.[23] Normalization was carried out using standard NIST samples. To convert to thermodynamic units, the value of the contrast factor $(\rho_p - \rho_{D_2O})^2$ of the dissociated monomer in D_2O was taken to be 1.56×10^{21} cm^{-4}.

Dynamic Light Scattering. DLS measurements were made with an ALV DLS/SLS 5022F goniometer (ALV Langen, Germany), with a HeNe laser working at 6328 Å and an ALV 5000E multitau correlator. Measurements were performed in the angular range 30°−150° with accumulation times of 200 s. Absolute intensities were obtained by normalizing with respect to toluene. Transmission measurements were made at 6328 Å with a Uvikon 810 spectrophotometer. The refractive index increment of the CS−water system was taken to be 0.17 cm^3/g.

RESULTS AND DISCUSSION

Small-Angle Neutron Scattering. SANS yields information on the organization of the CS molecules over a length scale range $2\pi/q$ that extends from 20 to 4000 Å. The SANS response for the CS solutions in D_2O with 100 mM NaCl is shown in Figure 2 at five different polymer concentrations c ranging from 1% to 20% w/w. Since the overlap concentration c^* (= $3M/4R_G^3$, where M is the mass and R_G the radius of gyration of the polymer), estimated from the geometry of the molecule, is ∼1%, all the solutions belong to the semidilute concentration regime.

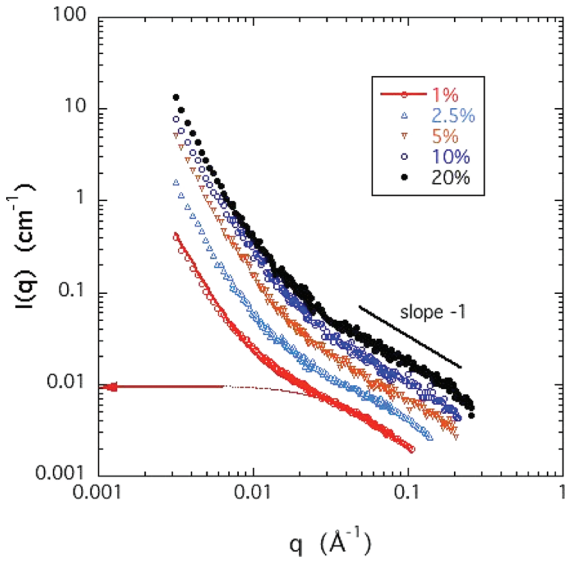


Figure 2. SANS curves of CS solutions at different concentrations in 100 mM NaCl. Horizontal arrow at left axis and dotted curve indicate the thermodynamic contribution of the intensity calculated from DLS for the 1% w/w CS sample (see Appendix A).

Each SANS curve displays two clearly distinguished power law regions. At high q (0.015 Å^{-1} ≤ q ≤ 0.25 Å^{-1}, corresponding to distances ranging from the size of the repeating unit to beyond the persistence length) the intensity varies as $1/q$, indicating that the scattering elements are linear, in conformity with the semirigid nature of the individual CS chains. In solutions of neutral polymers, this q-range would

dx.doi.org/10.1021/ma202693s | Macromolecules 2012, 45, 2882−2890

correspond to the single chain regime, where the intensity is proportional to the polymer concentration. In semidilute solutions, however, the molecules overlap to form a random mesh. The deviation from $1/q$ behavior at about 0.02 Å^{-1} is governed by the interchain distance (mesh size), which decreases with increasing concentration. At low q the curves in Figure 2 exhibit a different power law behavior of slope steeper than or equal to −3. Such behavior is a general feature in polyelectrolyte solutions and is attributed to surface scattering from large clusters.[24−27] The crossover point q_x between these two regimes yields a distance $L = 1/q_x$ over which linear behavior holds (see Appendix A). L thus possesses the attributes of a persistence length. The values of L, which is a decreasing function of polymer concentration, are listed in Table 1.

Table 1. Length of Apparent Linear Behavior from SANS in CS Solutions Containing 100 mM NaCl

c (w/w)	L (Å)	c (w/w)	L (Å)
0.01	127	0.1	71
0.025	93	0.2	71
0.05	74		

To describe these two regimes, the following expression is used:

$$I_{tot}(q) = I_{dyn}(q) + Aq^{-n} \quad (1)$$

where the first term is due to the thermal concentration fluctuations and the second describes the contribution from the large clusters. In eq 1, A and n are constants. The continuous curve through the 1% CS solution data in Figure 2 is the fit to eq 1, where the first term is expressed as (see Appendix A, eq A6)

$$I_{dyn}(q) = (\rho_p - \rho_{D_2O})^2 \frac{kTc^2}{\kappa} \frac{1}{(1 + (q\xi)^2)^{1/2}} \frac{1}{1 + (qr_c)^2} \quad (2)$$

In eq 2, $(\rho_p - \rho_{D_2O})^2 = 1.56 \times 10^{21}$ cm^{-4} is the value previously noted for the neutron scattering length contrast between CS and D_2O,[28] k is the Boltzmann constant, T the absolute temperature, $\kappa = 79.6$ kPa is the osmotic modulus of the 1% solution obtained by DLS (see Appendix B), r_c is the cross-sectional radius of the CS chain, and ξ is the correlation length of the thermal fluctuations of the linear chain section. The arrow on the left axis of Figure 2 shows the calculated intensity from eq 2 at $q = 0$. The fit to the SANS data yields $\xi = 34$ Å, with $r_c = 6.2$ Å. The value of r_c is in good agreement with that reported for CS by Tanaka.[22] In Appendix A, the value of ξ is compared with that determined from DLS for the same CS solution. According to Table 1, the length scale L determined from the crossover point q_x is much greater than the thermal correlation length ξ. This result implies that the concentration fluctuation modes in the solution are not isotropic but principally involve motions perpendicular to the chain axes.

The intensity of the SANS responses in Figure 2 is an increasing function of concentration. For neutral polymers in the high q region, where single chain behavior is expected, the scattering intensity is generally proportional to the polymer concentration, i.e., $I(q) \propto c$. In the high q region of the present CS solutions, however, the concentration dependence of the intensity is weaker than linear: over the whole concentration range $I(q) \propto c^m$, with $m = 0.7$. This finding implies that in solutions of this charged polymer, coupling between the chains is not negligible even at high resolution ($q\xi > 1$).

Figures 3a and 3b show the SANS response of a 4% w/w salt-free CS solution, together with that of solutions containing

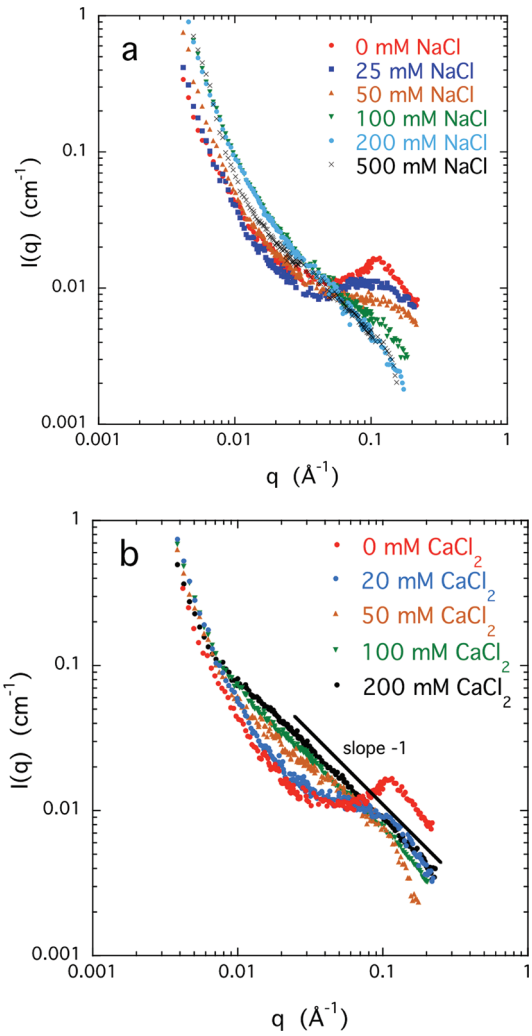


Figure 3. SANS response of 4% w/w CS solutions at different concentrations of (a) NaCl and (b) $CaCl_2$.

increasing concentrations of NaCl and $CaCl_2$, respectively. The salt-free solution displays a correlation peak at $q^* = 0.11$ Å^{-1}. In this condition where the Coulomb repulsion between adjacent chains is maximum, local ordering occurs, with a characteristic interchain separation distance $d = 2\pi/q^* \approx 57$ Å.[a] With increasing salt concentration the correlation peak becomes broader and weaker, gradually disappearing at about 100 mM NaCl or above 20 mM $CaCl_2$. Above these values of salt concentration the q^{-1} behavior is recovered. For both sodium and calcium ions the SANS responses exhibit an isoscattering point at $q \approx 0.06$ Å^{-1} where the scattering intensity is independent of the salt concentration.

A remarkable feature of Figure 3b is that all the curves in the region $q < 0.01$ Å^{-1} are practically identical. This is the length scale range in which the effects of cross-linking on the structure become visible in scattering measurements.[29,30] The observed invariance of the signal to $CaCl_2$ concentration implies that calcium ions do not form permanent cross-links.

dx.doi.org/10.1021/ma202693s | Macromolecules 2012, 45, 2882−2890

At high ionic concentration an appreciable difference becomes apparent between the responses to NaCl and to $CaCl_2$. Although the scattering response with both salts becomes practically independent of the salt concentration, the intensity of the calcium containing solution is significantly greater. In this system, the rod-like $1/q$ variation of the intensity extends to significantly lower values of q: with 200 mM $CaCl_2$ the value of L is ~170 Å. (We note that birefringence measurements reveal no evidence of liquid crystalline regions in these CS solutions.) In general, an increase in intensity is the signature of associations among polymer chains. The results imply that divalent calcium ion, unlike the monovalent sodium ion, significantly enhances interchain association between neighboring CS chains.

In summary, in the salt-free solution the electrostatic repulsion among the stiff negatively charged CS molecules results in local stacking with short-range order, as demonstrated by the correlation peak in the SANS measurements. With increasing salt concentration, for both sodium and calcium ions, local order decreases, and the behavior of the CS solution approaches that of neutral polymer solutions; i.e., the scattering response becomes independent of the salt concentration. The main effect of high salt concentrations is to reduce the Debye screening length, i.e., to reduce the repulsion among the negative charges on the polymer chains. SANS also reveals dynamic chain association, but not permanent cross-links, mediated by the divalent calcium ions. Phase separation does not occur, even in the presence of 200 mM $CaCl_2$.

Dynamic Light Scattering. The structural changes due to the presence of ions also affect the dynamic properties of CS solutions. DLS probes concentration fluctuations on the length scale of visible light. Figure 4 shows typical field correlation functions

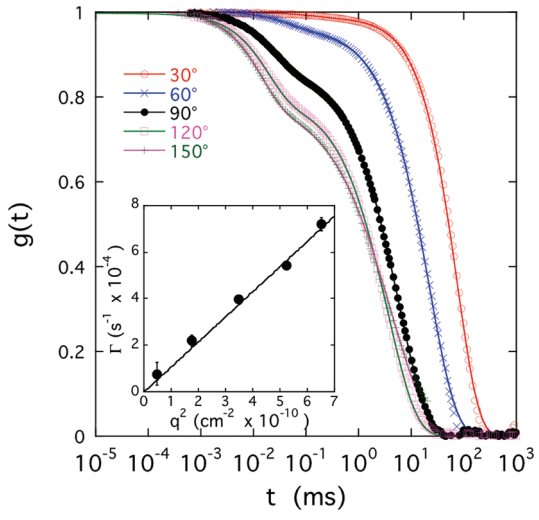


Figure 4. Angular dependence of the field correlation function $g(t)$ of light scattered by CS solution at c = 2% w/w in 100 mM NaCl at different scattering angles θ. Inset: variation of fast relaxation rate Γ with q^2.

measured in a 2% w/w CS solution containing 100 mM NaCl at five different scattering angles θ. Each curve displays a double relaxation process, the two relaxation rates being separated by two or more orders of magnitude, which, as detailed in Appendix B, can be described by

$$g(t) = a \exp(-\Gamma t) + (1 - a) \exp[-(\Gamma_s t))^{\mu}] \quad (3)$$

The amplitudes a and $(1 - a)$ are the relative intensities of the fast and slow relaxation modes, respectively, with Γ and Γ_s the corresponding relaxation rates. The fast relaxation rate Γ is diffusive and is proportional to q^2. This relationship is illustrated in the inset of Figure 4, where the values of Γ obtained by fitting eq 3 to the correlation function are plotted against q^2. Γ represents the relaxation of the thermal concentration fluctuations, which are governed by the collective diffusion coefficient D[31]

$$D = \Gamma/q^2 \quad (4)$$

It follows that the correlation length ξ describing the spatial range of the thermal concentration fluctuations is defined by the Stokes–Einstein relationship[31]

$$\xi = \frac{kT}{6\pi\eta D} \quad (5)$$

in which η is the viscosity of the solvent.

The slow relaxation component in eq 3 (second term) is due to the internal modes of large clusters. For such modes, where no unique correlation length is distinguishable, the relaxation process can be represented by a stretched exponential decay with an exponent $\mu \approx 2/3$. The trend in Figure 4 shows that the intensity of the slow component $(1 - a)$ increases with decreasing scattering angle θ, indicating that the clusters are very large. This finding is consistent with the large increase in intensity at small values of q in the SANS responses. The clusters have nonuniform internal organization; i.e., there is no well-defined mesh size. (The increase in intensity of the slow component may be appreciated by noting that the field correlation function $g(t)$ in Figure 4 is normalized to unity: the absolute value of the intensity scattered by the osmotic fluctuations is independent of θ.) While the Nernst–Hartley model provides some insight into the effect of ion mobility on the fast mode, it does not describe the phenomenology of the slow mode.[25,32] There has been much speculation in the literature about the origin of the slow component; however, a complete interpretation of this mode still remains elusive. It is important to note that aggregate formation has also been observed in dilute CS solutions by light scattering measurements.[33–35]

Figure 5 shows the DLS field correlation functions at fixed scattering angle θ = 150° in solutions of different CS

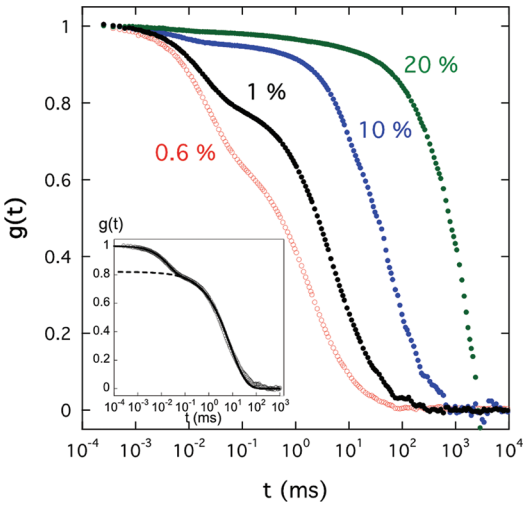


Figure 5. Field correlation functions $g(t)$ of light scattered at θ = 150° by CS solutions of different concentration c in 100 mM NaCl. Inset shows fit of eq 3 to the data from c = 1% w/w (continuous line); dashed line is the second term in the fit to this equation.

concentration with 100 mM NaCl. The curves exhibit the same double relaxation behavior as before and are accordingly

dx.doi.org/10.1021/ma202693s | Macromolecules 2012, 45, 2882–2890

decomposed using eq 3. The inset in the figure illustrates the decomposition for the 1% w/w sample. With increasing concentration, Γ_s becomes slower. The relative intensity $(1 - a)$ of this component also increases. Decrease of Γ_s with increasing polymer concentration has also been reported for semidilute solutions of flexible polyelectrolytes.[25]

The values of the diffusion coefficient obtained from the fast relaxation rate are plotted as a function of c in Figure 6. Over

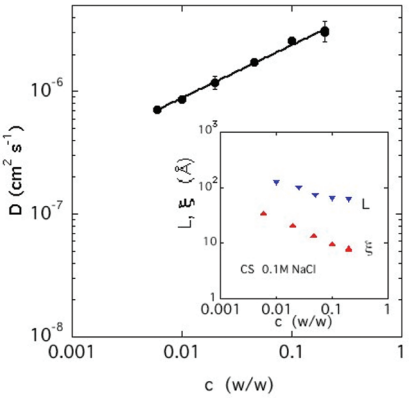


Figure 6. Dependence of D on CS concentration in solution with 100 mM NaCl. The slope of the power law fit is 0.43. Inset: characteristic linear range L from SANS and correlation length ξ from DLS.

the entire concentration range (0.6% w/w $\leq c \leq$ 20% w/w), D obeys a power law dependence of the form

$$D = D_0 c^m \tag{6}$$

with m = 0.43. The experimental exponent is lower than that predicted by de Gennes[31] for uncharged polymers of infinite molecular weight in good solvent conditions (m = 3/4). A similar low value for the exponent m has been observed in solutions of hyaluronic acid.[36] The deviation from the neutral polymer value may be related to long-range hydrodynamic interactions in polyelectrolyte systems.

The correlation length ξ calculated using eq 5 is displayed in the inset of the figure (lower curve). For solutions of uncharged flexible polymers ξ corresponds to the mesh size of the network. The dynamics of polyelectrolyte solutions is based on the same scaling assumption as that used in solutions of neutral polymers. It relies on the existence of the single length scale where both hydrodynamic and electrostatic interactions are screened. The screening of these interactions happens at distances comparable with the solution correlation length, as confirmed both by the effective medium calculations of Muthukumar[37−39] and by experiment.[40]

In the inset in Figure 6 the thermodynamic length scale ξ is compared with the length L of the linear chain sections observed in SANS. The latter is more than 5 times greater than ξ; i.e., the length of the linearly ordered structures substantially exceeds the range of the thermodynamic interactions. The concentration dependence of these two lengths is, however, closely similar.

The effect of calcium ions on the dynamics of CS solutions is illustrated in Figure 7, where the values of D measured in solutions containing 100 mM NaCl and 100 mM $CaCl_2$ are plotted as a function of CS concentration. The inclusion of the $CaCl_2$ decreases the value of D by a factor of almost 2. The power law fit through the data points is similar to that of eq 6 in which

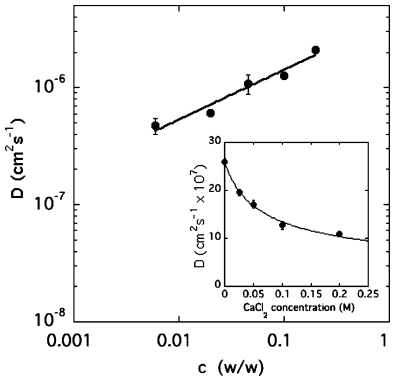


Figure 7. Variation of the collective diffusion coefficient D with concentration of CS solution in 100 mM NaCl + 100 mM $CaCl_2$. Inset: variation of D with $CaCl_2$ concentration for c = 10% w/w.

m = 0.42, i.e., within experimental error the same dependence as with NaCl alone. The inset in this figure shows the variation of D with $CaCl_2$ concentration for c = 10%. The continuous line is the fit to a power law with respect to the $CaCl_2$ concentration, c_{CaCl_2}, in which the exponent is −0.45. Thus

$$D \propto c_{CaCl_2}{}^{-0.45\pm0.03} \tag{7}$$

The exponents found for the power law dependence of D on the CS concentration and for the $CaCl_2$ concentration are, within experimental error, numerically identical and opposite in sign. This inverse relationship between c and c_{CaCl_2} suggests that D is a function of a single variable, c, normalized by the ion concentration. To accommodate for the different valences, the ion concentration of the solution must be expressed in terms of the ionic strength J ($=^1/_2\sum Z_i^2 c_i$, where Z_i is the valence of the ionic species i and c_i its molar concentration) of the added salt. In Figure 8, D is plotted as a function of the normalized variable c/J,

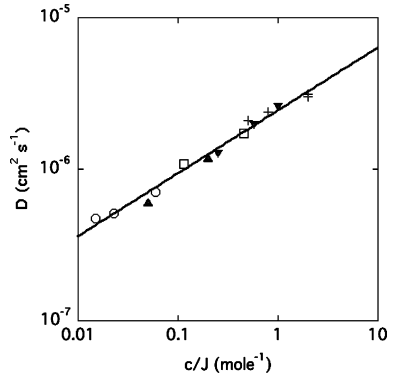


Figure 8. Dependence of D on the variable c/J, where c is expressed in mass fraction w/w and J is the ionic strength in moles. Symbols: ○, c = 0.006; ▲, c = 0.02; □, c = 0.046; ▼, c = 0.1; +, c = 0.2.

where J includes all the added ions. In this figure, each polymer concentration c is denoted by a different symbol. Within experimental error, all the data points fall on a master curve, defined by

$$D = 2.43 \times 10^{-6}(c/J)^{0.415}\ \text{cm}^2\ \text{s}^{-1} \tag{8}$$

where, for convenience, c is expressed in w/w and J in moles. It is notable that these measurements are in good agreement with those

dx.doi.org/10.1021/ma202693s | Macromolecules 2012, 45, 2882−2890

of Trivant et al. made on CS solutions in the low concentration regime.[33]

In summary, the DLS correlation functions of the CS solutions display two distinct relaxation modes. The fast component is diffusive and is governed by the thermal concentration fluctuations. The slow mode reflects the presence of large clusters that give rise to the strong excess scattering at low q in SANS. The collective diffusion coefficient D derived from the fast mode increases with CS concentration and decreases with increasing calcium ion content. Over the range of ion concentrations studied, D displays a power law dependence of the single variable c/J. This relationship, which is independent of the valence of the added ions, is evidence against specific binding effects between calcium ions and the anionic groups of the CS chain.

BIOLOGICAL IMPLICATIONS

In this section we show how the physical properties of CS solutions discussed in this paper are related to certain physiological roles of this molecule. Instead of providing a comprehensive list of potential biological implications of the results, we illustrate with a few specific examples the usefulness of the quantitative physical−chemical approach to address problems that cannot be resolved by other means.

The structural stability of CS solutions under high salt concentrations observed by SANS is a precondition for this molecule to form stable connections with different biological molecules. Owing to the high charge density of CS, most interactions between the target molecules and CS are ionic in character. CS binds extracellular matrix components together, mediating the binding of bone-like cells, such as osteoblasts and osteoclasts, to the matrix, and capturing soluble molecules such as growth factors into the matrix and at cell surfaces.[41,42]

Both the binding ability and the mobility of the CS molecule play an important part in wound repair. Together with other proteoglycans, e.g., dermatan sulfate, CS forms a homogeneous meshwork around the wound, sealing the injury site and preventing damage to surrounding healthy tissue. In this process the high mobility of the CS molecule, by virtue of its small size, is a significant advantage. In addition, its stability and extended configuration in the presence of calcium ions provides structural integrity and suitable mechanical strength.

In cartilage, two further physical properties are also of critical significance, namely rapid response to external stress and a high osmotic modulus to withstand compressive loading. Fast recovery after deformation requires a high collective diffusion coefficient D, which can be quantified by DLS. Figure 9 shows that for CS solutions in 100 mM NaCl D is almost 5 times greater than in a typical neutral polymer poly(vinyl alcohol) (PVA) solution in water.[43]

In the aggrecan bottlebrush, the load bearing capacity of cartilage depends strongly on the CS component, which varies with age of the tissue, the state of health or disease (e.g., osteoporosis, rheumatoidal arthritis), and the depth within the cartilage layer.[44−46] The measure of resistance to compressive loads is the osmotic modulus $\kappa = c\ \partial\Pi/\partial c$, where Π is the osmotic pressure in the solution. This quantity can be determined from DLS measurements. In this case, κ is inversely related to the intensity of light scattered by the thermal concentration fluctuations (see Appendix B).

Figure 10 shows the concentration dependence of the osmotic modulus of CS solutions in 100 mM NaCl. The value of κ in a 20% w/w CS solution with 100 mM NaCl is about

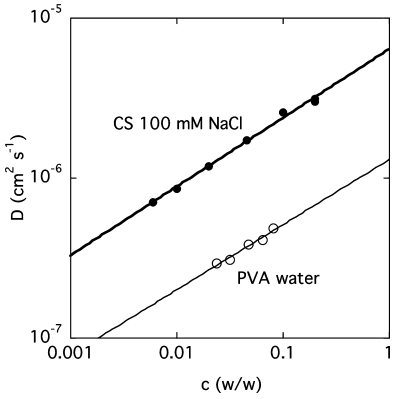


Figure 9. Comparison of $D(c)$ of CS in 100 mM NaCl with that of poly(vinyl alcohol) in water at 25 °C.

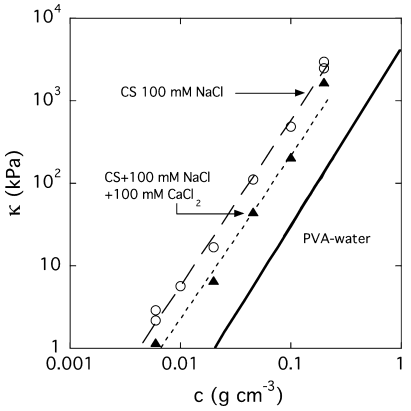


Figure 10. Concentration dependence of the osmotic modulus κ of CS solutions in 100 mM NaCl without (open symbols) and with (filled symbols) 100 mM $CaCl_2$. The continuous line is the corresponding data from the PVA−water system.[43]

3 MPa. Addition of 100 mM calcium chloride decreases κ by a factor of less than 3. The solid line in this figure shows the dependence of κ for a PVA−water solution at the same concentration.[43] The much higher value of κ in CS solutions, by more than an order of magnitude, makes this molecule exceptionally well suited as a structural material for compression resistance.

CONCLUSIONS

Chondroitin sulfate, a major component in biological tissues, participates in a variety of physiological functions. To comprehend its biological role and to develop effective strategies for tissue design and replacement, it is of particular importance to understand the effects of ions on its structure and dynamics.

Observations by SANS and DLS, made on CS solutions under different ionic conditions, close to and beyond the physiological range, reveal significant changes in the local order in the low ion concentration range. In the physiological range the structure of the CS solutions depends only weakly on the salt concentration. In both NaCl and $CaCl_2$ aligned linear regions are distinguishable corresponding to length scales ranging from the monomer length to about 150 Å. With increasing $CaCl_2$ concentration, the region of the SANS response in which linear behavior holds extends toward increasingly lower values of q. The scattering intensity also

dx.doi.org/10.1021/ma202693s | Macromolecules 2012, 45, 2882−2890

increases, indicating that calcium ions enhance the interchain attraction. The SANS responses, however, reveal no sign either of precipitation or of cross-linking due to calcium ions.

The DLS measurements of the CS solutions exhibit two distinct relaxation modes, the fast diffusive component of which corresponds to the thermal concentration fluctuations of collective diffusion. The collective diffusion coefficient D decreases with increasing calcium ion content. Over the range of concentrations studied, D displays a power law dependence on the single variable c/J, where c is the CS concentration and J is the ionic strength of the salt in the solution. The diffusion coefficient of CS in 100 mM NaCl is almost 5 times greater than in the solutions of typical neutral water-soluble polymers at the same concentration.

The measure of resistance of a biopolymer system to dehydration is the osmotic modulus κ. Within the aggrecan bottlebrush, which is the essential load bearing component in cartilage, the concentration of CS is ~20%. The present DLS results indicate that the osmotic modulus of a 20% CS solution with 100 mM NaCl attains the value 3 MPa.

APPENDIX A

Determination of Crossover Point q_x

Figure 11 shows the SANS data as Figure 2, with the straight line fits to the two power law regions in q of slope −3 and −1. The points of intersection q_x are listed in Table 1.

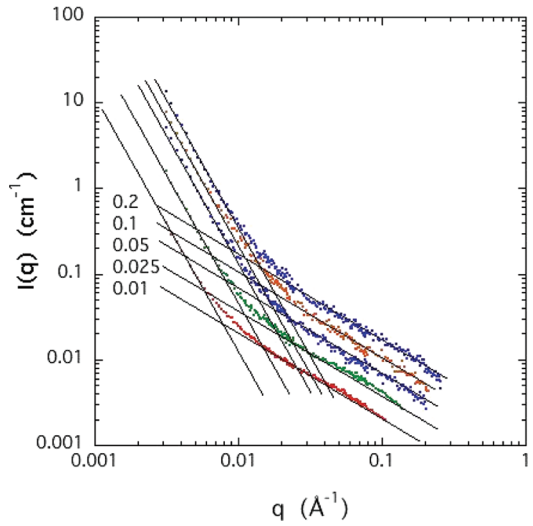


Figure 11. Power law fits to SANS spectra at different CS concentrations 100 mM NaCl.

SANS Structure Factor of CS Solutions

In neutral polymer systems containing large scale inhomogeneities (gels and semidilute solutions) the SANS response can be treated as the sum of two separable components

$$I_{tot}(q) = I_{dyn}(q) + I_{quasi\text{-}static}(q) \quad (A1)$$

In the q range $qR \gg 1$ where R is the characteristic size of the inhomogeneity, the second term can be replaced by a power law function, such that

$$I_{tot}(q) = I_{dyn}(q) + Aq^{-n} \quad (A2)$$

where A is a constant and n is generally greater than or equal to 3.

The intensity scattered by the thermal fluctuations, $I_{dyn}(q)$, is inversely proportional to the osmotic modulus $\kappa = c\,\partial\Pi/\partial c$, where Π is the osmotic pressure in the solution. In a SANS experiment, the intensity scattered by these concentration fluctuations in the thermodynamic limit $q \to 0$ is therefore

$$I_{dyn}(0) = (\rho_p - \rho_{D_2O})^2 \frac{kTc^2}{\kappa} \quad (A3)$$

where $(\rho_p - \rho_{D_2O})^2$ is the neutron scattering length contrast between CS and D_2O, k is Boltzmann's constant, and T is the absolute temperature. In solutions and gels of neutral flexible polymers, the intensity of the dynamic contribution can be described by

$$I_{dyn}(q) = I_{dyn}(0)S(q) \quad (A4)$$

where the structure factor $S(q)$ has the Ornstein−Zernike form

$$S(q) = \frac{1}{1 + q^2\xi^2} \quad (A5)$$

in which ξ is the correlation length of the concentration fluctuations. The validity of this decomposition has been verified for various neutral and charged gel systems.[26,43,47−49]

In the case of CS, owing to the semi-rigid character of the chain, it is necessary to replace eq A4 by an expression that takes into account its geometry, i.e., both the linear character of the chain segments and their cross-sectional radius r_c. To incorporate these features into the structure factor for the q range $qr_c \leq 1$, we employ the expression

$$S(q) = \frac{1}{(1 + q^2\xi^2)^{1/2}} \frac{1}{1 + q^2 r_c^2} \quad (A6)$$

in which square root in the first factor reproduces the linear nature of the fluctuating chain segments and the second factor accounts for the cylindrical shape of the polymer molecule. This yields for the intensity scattered by the thermodynamic fluctuations the expression

$$I_{dyn}(q) = (\rho_p - \rho_{D_2O})^2 \frac{kTc^2}{\kappa} \frac{1}{(1 + (q\xi)^2)^{1/2}} \frac{1}{1 + (qr_c)^2} \quad (A7)$$

The fit shown in Figure 2 yields for the 1% w/w CS solution in 100 mM NaCl, ξ = 34 Å, with r_c = 6.2 Å. The measured value of D from DLS for this sample is 8.55×10^{-7} cm^2 s^{-1}, which, according to eq 5, corresponds to ξ = 29 Å. In view of the completely independent nature of these measurements and the experimental error associated with each, this agreement is satisfactory.

APPENDIX B

Light Scattering Background

In polymer solutions, the spontaneous concentration fluctuations scatter radiation with an intensity that is inversely proportional to the osmotic modulus κ (= $c\,\partial\Pi/\partial c$, where Π is the osmotic pressure).[50] DLS measures the time-dependent

fluctuations of the scattered light intensity, $I(t)$, by constructing the intensity correlation function[51]

$$G(t) = \langle I(0)I(t)\rangle/\langle I(t)\rangle^2 = 1 + \beta|g(t)|^2 \quad \text{(B1)}$$

where β is the optical coherence factor of the apparatus, $g(t)$ is the field correlation function, and the brackets $\langle\ \rangle$ mean averages over the experimental accumulation time. For simple diffusion processes the field correlation function is

$$g(t) = \exp(-\Gamma t) \quad \text{(B2)}$$

where Γ is the relaxation rate of the concentration fluctuations. In semidilute polymer solutions and gels these fluctuations obey the relation

$$\Gamma = Dq^2 \quad \text{(B3)}$$

where D is the collective diffusion coefficient of the polymer chains.[31] According to simple scaling theory of neutral polymer solutions, D is related to a correlation length ξ through the Stokes−Einstein expression

$$D = \frac{kT}{6\pi\eta\xi} \quad \text{(B4)}$$

where η is the viscosity of the solvent.

If the polymer solution contains associations, e.g., large clusters of size R much greater than $1/q$, a slow contribution also appears in the correlation function. In the experimental range $qR \gg 1$, such objects possess no intrinsic characteristic size and display a broad range of decay rates, often represented by a stretched exponential decay. The normalized correlation function of the total field is thus

$$g(t) = a\exp(-\Gamma t) + (1-a)\exp[-(\Gamma_s t))^{\mu}] \quad \text{(B5)}$$

where a and Γ are the relative amplitude and relaxation rate of the fast process, while $(1-a)$ and Γ_s are the corresponding quantities for the clusters. The exponent μ is usually smaller than 1. Figure 5 shows that the intensity of the slow component $(1-a)$ increases with decreasing scattering angle θ. According to the inverse relationship between scattered intensity and osmotic modulus $\kappa = c\,\partial\Pi/\partial c$, where Π is the osmotic pressure, this implies that the contribution of the large quasistatic objects to the thermodynamic fluctuations is practically negligible and that the essential part of the osmotic pressure can be identified with the fast mode.

The intensity of light scattered by the osmotic fluctuations is given by the Rayleigh ratio R_θ

$$R_\theta = a\langle I(t)\rangle = \frac{KkTc^2}{\kappa} \quad \text{(B6)}$$

where $\langle I(t)\rangle$ is the total scattered intensity averaged over the experimental time. K [$= (2\pi n\ \mathrm{d}n/\mathrm{d}c)^2/\lambda^4$, with λ the wavelength of the incident light and $\mathrm{d}n/\mathrm{d}c$ the refractive index increment of the polymer solvent pair] is the optical contrast factor due to the difference in refractive index between solvent and polymer.

The fast mode defines the osmotic modulus κ of the system. Analysis of the intensity correlation function allows both the relative amplitude a and the relaxation rate Γ of this collective diffusion component to be determined for different scattering angles θ, and κ can be calculated from the Rayleigh ratio of the dynamically scattered light by eq B6.

AUTHOR INFORMATION

Corresponding Author

*E-mail: horkay@helix.nih.gov.

Notes

The authors declare no competing financial interest.

ACKNOWLEDGMENTS

This research was supported by the Intramural Research Program of the NICHD, NIH. We acknowledge the support of the National Institute of Standards and Technology, U.S. Department of Commerce, in providing the neutron research facilities used in this work. This work utilized facilities supported in part by the National Science Foundation under Agreement DMR-0944772. We gratefully acknowledge the help and consultation of Dr. Boualem Hammouda (NIST) with the SANS experiment.

ADDITIONAL NOTE

[a]The distinction of the factor 2π between the interchain distance $d = 2\pi/q^*$ and the length $L = 1/q_x$ describing the range of linear behavior relates to their different nature. The first is the repeat distance over which the phase of a scattered wave is reinforced in a regular array and corresponds to Bragg condition $qd = 2\pi$. The second defines the distance over which the wave is attenuated, as expressed by the function $\exp(-qL)$.

REFERENCES

(1) Prabhakar, V.; Sasisekharan, R. *Adv. Pharmacol.* **2006**, *53*, 69−115.
(2) Asimakopoulou, A. P.; Theocharis, A. D.; Tzanakakis, G. N.; Karamanos, N. K. *In Vivo* **2008**, *22*, 385−390.
(3) Karamanos, N. K.; Syrokou, A.; Vanky, P.; Nurminen, M.; Hjerpe, A. *Anal. Biochem.* **1994**, *221*, 189−199.
(4) Lamari, F. N.; Karamanos, N. K. *Adv. Pharmacol.* **2006**, *53*, 33−34.
(5) Theocharis, A. D.; Tsolakis, I.; Tzanakakis, G. N.; Karamanos, N. K. *Adv. Pharmacol.* **2006**, *53*, 281−295.
(6) J. Ruggiero, J.; Vieira, R. P.; Mourão, P. A. S. *Carbohydr. Res.* **1994**, *256*, 275−287.
(7) Bathe, M.; Rutledge, G. C.; Grodzinsky, A.; Tidor, B. *Biophys. J.* **2005**, *88*, 3870−3887.
(8) Gu, W.-L.; Fu, S.-L.; Wang, Y.-X.; Li, Y.; Lü, H.-Z.; Xu, X.-M.; Lu, P.-H. *BMC Neurosci.* **2009**, *128*, 1−15.
(9) Treloar, H. B.; Nurcombe, V.; Key, B. *J. Neurobiol.* **1996**, *31*, 41−55.
(10) Landolt, R,M.; Vaughan, L.; Winterhalter, K. H.; Zimmermann, D. R. *Development* **1995**, *121*, 2303−2312.
(11) Pizzorusso, T.; Medini, P.; Berardi, N.; Chierzi, S.; Fawcett, J. W.; Maffei, L. *Science* **2002**, *298*, 1248−1251.
(12) Brakebusch, C.; Seidenbecher, C. I.; Asztely, F.; Rauch, U.; Matthies, H.; Meyer, H. *Mol. Cell. Biol.* **2002**, *22*, 7417−7427.
(13) Bradbury, E. J.; Moon, L. D.; Popat, R. J.; King, V. R.; Bennett, G. S.; Patel, P. N. *Nature* **2002**, *416*, 636−640.
(14) Moon, L. D.; Asher, R. A.; Rhodes, K. E.; Fawcett, J. W. *Nat. Neurosci.* **2001**, *4*, 465−466.
(15) Barritt, A. W.; Davies, M.; Marchand, F.; Hartley, R.; Grist, J.; Yip, P. *J. Neurosci.* **2006**, *26*, 10856−10867.
(16) Carulli, D.; Pizzorusso, T.; Kwok, J. C. F.; Putignano, E.; Poli, A.; Forostyak, S.; Andrews, M. R.; Deepa, S. S.; Glant, T. T.; Fawcett, J. W. *Brain* **2010**, *133*, 2331−2347.
(17) Buckwalter, J. A. *Clin. Orthop. Relat. Res.* **1983**, *172*, 207−232.

(18) Hunter, G. K.; Wong, K. S.; Kim, J. J. *Arch. Biochem. Biophys.* **1988**, *260*, 161−167.
(19) Anderson, H. C.; Garimella, R.; Tague, S. E. *Front. Biosci.* **2005**, *10*, 822−837.
(20) Hascall, V. C.; Hascall, G. K. In *Cell Biology of Extracellular Matrix*; Hay, E. D., Ed.; Plenum: New York, 1981; pp 39−63.
(21) Woodward, C.; Davidson, E. A. *Proc. Natl. Acad. Sci. U. S. A.* **1998**, *60*, 201−205.
(22) Tanaka, K. *J. Biochem.* **1978**, *83*, 647−53.
(23) Horkay, F.; Hecht, A.-M.; Mallam, S.; Geissler, E.; Rennie, A. R. *Macromolecules* **1991**, *24*, 2896−2901.
(24) Borsali, R.; Nguyen, H.; Pecora, R. *Macromolecules* **1998**, *31*, 1548−1555.
(25) Zhang, Y.; Douglas, J. F.; Ermi, B. D.; Amis, E. *J. Chem. Phys.* **2001**, *114*, 3299−3313.
(26) Horkay, F.; Basser, P.; Hecht, A. M.; Geissler, E. *Macromolecules* **2000**, *33*, 8329−8333.
(27) Horkay, F.; Hecht, A. M.; Geissler, E. *J. Polym. Sci., Part B: Polym. Phys.* **2006**, *44*, 3679−3686.
(28) Sears, V. F. *Neutron News* **1992**, *3*, 26−37.
(29) Horkay, F.; Hecht, A. M.; Mallam, S.; Geissler, E.; Rennie, A. R. *Macromolecules* **1991**, *24*, 2896−2902.
(30) Horkay, F.; Hecht, A. M.; Geissler, E. *Macromolecules* **1994**, *27*, 1795−1798.
(31) de Gennes, P. G. *Scaling Concepts in Polymer Physics*; Cornell University Press: Ithaca, NY, 1979.
(32) Forster, S.; Schmidt, M. *Adv. Polym. Sci.* **1995**, *120*, 51−133.
(33) Tivant, P.; Turq, P.; Drifford, M.; Magdelenat, H.; Menez, R. *Biopolymers* **1983**, *22*, 643−662.
(34) Ghosh, S.; Peitzsch, R. M.; Reed, W. F. *Biopolymers* **1992**, *32*, 1105−1122.
(35) Peitzsch, R. M.; Burt, M. J.; Reed, W. F. *Macromolecules* **1992**, *25*, 806−815.
(36) Horkay, F.; Basser, P. J.; Londono, D. J.; Hecht, A.-M.; Geissler, E. *J. Chem. Phys.* **2009**, *131*, 184902.
(37) Muthukumar, M. *Polymer* **2001**, *42*, 5921−5923.
(38) Muthukumar, M. *J. Chem. Phys.* **1997**, *107*, 2619−2635.
(39) Dobrynin, A. V.; Rubinstein, M. *Prog. Polym. Sci.* **2005**, *30*, 1049−1118.
(40) Boris, D. C.; Colby, R. H. *Macromolecules* **1998**, *31*, 5746−5755.
(41) Schneiders, W.; Reinstorf, A.; Biewener, A.; Serra, A.; Grass, R.; Kinscher, M.; Heineck, J.; Rehberg, S.; Zwipp, H.; Rammelt, S. *J. Orthop. Res.* **2009**, *27*, 15−21.
(42) Dunham, J. In *Bone*; Hall, B. K., Ed.; CRC Press Inc.: Boca Raton, FL, 1992; Vol. *5*.
(43) Horkay, F.; Burchard, W.; Geissler, E.; Hecht, A. M. *Macromolecules* **1993**, *26*, 1296−1303.
(44) Roughley, P. J.; White, R. J. *J. Biol. Chem.* **1980**, *255*, 217−224.
(45) Lauder, R. M.; Huckerby, T. N.; Brown, G. M.; Bayliss, M. T.; Nieduszynski, I. A. *Biochem. J.* **2001**, *358*, 523−528.
(46) Schinagl, R. M.; Gurskis, D.; Chen, A. C.; Sah, R. L. *J. Orthop. Res.* **1997**, *15*, 499−506.
(47) Horkay, F.; Burchard, W.; Hecht, A. M.; Geissler, E. *Macromolecules* **1993**, *26*, 3375−3380.
(48) Geissler, E.; Horkay, F.; Hecht, A. M. *J. Chem. Phys.* **1994**, *100*, 8418−8424.
(49) Horkay, F.; Hecht, A. M.; Geissler, E. *Macromolecules* **1998**, *31*, 8851−8856.
(50) Landau, L. D.; Lifschitz, E. M. *Statistical Physics*, 2nd ed.; Pergamon Press: Oxford, 1969.
(51) Berne, R.; Pecora, R. *Dynamic Light Scattering*; Academic Press: London, 1976.

Macromolecules

Article

pubs.acs.org/Macromolecules

Unique Nonlinear Behavior of Nano-Filled Elastomers: From the Onset of Strain Softening to Large Amplitude Shear Deformations

Aurélie Papon,[†] Samy Merabia,*[,‡] Laurent Guy,[§] François Lequeux,[†] Hélène Montes,[†] Paul Sotta,[⊥] and Didier R. Long*[,⊥]

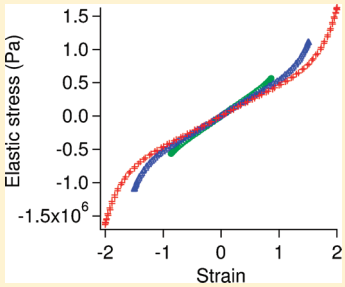
[†]Physico-Chimie des Polymères et Milieux Dispersés, ESPCI ParisTech, 10 rue Vauquelin, F-75231 Paris Cedex 5, France

[‡]Laboratoire de Physique de la Matière Condensée et Nanostructures, Université Lyon I/CNRS, 43 Boulevard du 11 Novembre 1918, 69622 Villeurbanne Cedex, France

[§]Rhodia Opérations, 15 rue Pierre Pays, BP 52, F-69660 Collonges-au-Mont-d'Or, France

[⊥]Laboratoire Polymères et Matériaux Avancés, CNRS/Rhodia, 85 avenue des Frères Perret, F-69192 Saint-Fons, France

ABSTRACT: Adding fillers in elastomers is known to increase the elastic modulus and the wear resistance of elastomers, but also to increase nonlinear dissipation, a phenomenon known as the Payne effect. Indeed, when submitted to deformations of the order of a few per cents or more, the elastic modulus can decrease down to values much smaller than the initial one. On the other hand, when submitted to large amplitude oscillatory shear at a frequency ω, frequency analysis shows that the contribution of higher harmonics 3ω, 5ω, ..., to the response is quite small. This might appear somehow as a paradox since the nonlinear behavior of filled elastomers can be strongly marked. We discuss here in detail a possible physical origin of these various features. We do it by comparing experimental results performed on model elastomers to the prediction of a model proposed recently, based on the presence of glassy bridges linking neighboring particles. We show that the kinetics of rupture and rebirth of these glassy bridges can explain these effects.



I. INTRODUCTION

Filled elastomers are systems of very great practical importance, due to their unique properties. Nonreinforced polymer matrices generally do not exhibit mechanical properties suitable for some practical purposes, being too soft and fragile.[1] On the contrary, elastomers filled with carbon black or silica particles have a shear modulus much (up to a few 100 times) higher than that of the pure elastomer, exhibit a high dissipative efficiency, and are extremely resistant to both fracture and abrasion, which makes them highly useful for damping materials, shock absorbers, or tires.[1−13]

When submitted to periodic deformations at a frequency ω of typical order of magnitude 1 Hz, and of amplitudes γ_0 of the order of a few per cents or more, the apparent elastic modulus $G'(\omega,\gamma_0)$ decreases down to values much smaller than the value in the linear regime; this is the so-called Payne effect. In some systems studied by Payne, the modulus dropped from a few 10^7 Pa down to a few 10^6 Pa.[8] Conversely, in an unfilled matrix, a roughly constant modulus is observed until 100% of strain.[6,8,9,12,14−18] After the system has been put at rest and during subsequent deformations, the elastic modulus in the linear regime is smaller than that of the initial system, but recovers progressively—at least partially—the initial value.[5,19] It is an issue of major importance to understand this unique behavior in order to be able to control and tune the properties of these systems. These effects cannot be simply explained by the trivial geometric role of the solid particles, but must involve the modification of the polymer dynamics near the solid interface, which leads for example to the Payne effect.[10,11,13]

We proposed recently that these effects are the consequence of the presence of a glassy layer around the fillers, which can build glassy bridges between neighboring fillers.[20−24] Indeed, it had long been proposed that the polymer matrix in the vicinity of the filler is glassy.[11,25−30] This picture is also consistent with experimental studies that demonstrated that the glass transition temperature T_g in thin polymer films in contact with a solid substrate differs from the one in the bulk, in a way that depends on the polymer−substrate interaction.[31−40] The link between glass transition in thin films and physical properties of nanocomposites has been emphasized by many other authors.[41−49] The model we propose, the glassy bridge reinforcement model (GBRM), has provided a unified picture to account for (1) reinforcement amplitudes, (2) the Payne effect, (3) recovery effects, and (4) specific features of the plastic properties of filled elastomers.[50−52]

As regards mechanical properties, it is often thought that a nonlinear behavior under periodic solicitations at frequency ω would result in contributions to the response at higher frequency harmonics 3ω, 5ω, ... In particular, this is the case when the stress σ is a nonlinear, nonretarded function of the deformation x with a constitutive relation of the type: $\sigma(x) = k^{(1)}x + k^{(3)}x^3 + k^{(5)}x^5 + ...$ On the other hand, regarding filled elastomers, it has

Received: October 12, 2011
Revised: February 23, 2012
Published: March 9, 2012

 © 2012 American Chemical Society

been reported that, whereas the storage modulus can be much smaller than the small amplitude linear modulus, the response is still quasi-harmonic: if the applied strain is a sine wave, the measured stress is also a quasi-sinusoidal wave with small higher harmonic components.[53−56] This might thus appear somehow as a paradox. In addition, some of us have recently shown[57] that a significant deviation from the quasi-harmonic behavior can be measured in model samples. It is therefore important to clarify this feature, and also to check whether the model we have proposed for explaining the reinforcement and the Payne effect can also explain this behavior.

For describing the response of filled elastomers, we have argued that a key feature is the dynamical state of the glassy bridges.[50,51] It is characterized by a relaxation time, or lifetime, which is assumed to depend on the distance between the fillers, the polymer/filler interactions, the local stress value and history. The presence of a local stress in between the fillers leads to a reduction of the local glass transition temperature and an acceleration of the local dynamics. When the stress is released after local plastic deformation, physical aging takes place. The lifetime of the glassy bridge increases again. These features result in a complex history dependence of the dynamical state of the glassy bridges. In a permanent regime of sinusoidal deformation, the storage and dissipative moduli depend on the distribution of the lifetimes of glassy bridges in the system. The purpose of this paper is to study in more detail some specific aspects of the nonlinear behavior regarding both the storage and the dissipative moduli, and also how the higher harmonic contributions depend on strain amplitude and temperature. To this aim, we compare experimental results to the predictions of the glassy bridge reinforcement model and show that they match qualitatively. It is important to stress that no modification has been implemented in the model as compared to our previous works[50,51] in which the reinforcement mechanisms, the Payne and Mullins effects and the plastic behavior as deduced from the model were studied in detail. Thus, everything that was put forward in these previous papers remains valid for the simulations considered here.

The paper is organized as follows. In section II, we define in a precise way the studied quantities. Section III is the experimental part of the paper. The experimental model systems are described and their nonlinear response to large amplitude oscillatory strain (LAOS) is discussed. Section IV is the theoretical part of the paper. The physical ingredients of the GBRM and its numerical resolution are recalled. In section V, we present the results of the simulations and we discuss and compare them to the experimental data in section VI.

II. DEFINITION OF THE NONLINEAR PROBLEM

Here we aim at quantifying in detail the nonlinear behavior of filled elastomers submitted to large amplitude sinusoidal deformations. Both the in-phase and out-of phase response need to be defined in the nonlinear regime. The method is briefly described starting from the linear case, and then generalized to the nonlinear case. Following Cho et al.,[58] as well as some other authors[54,55,59−64] (see also ref 65 for review), the stress is decomposed into an elastic and a viscous part. In the linear regime, the stress ensuing a sinusoidal strain $\gamma(t)$ can classically be written as

$$\sigma(t) = G'\gamma(t) + G''\dot{\gamma}(t)/\omega \tag{1}$$

It is the sum of two terms: one in-phase with the strain corresponding to the elastic response $\sigma' = G'\gamma$ and one in quadrature with the strain corresponding to the viscous response $\sigma'' = G''\dot{\gamma}/\omega$. Thus, for an applied strain $\gamma = \gamma_0 \sin(\omega t)$, the elastic stress σ' is a sine wave—odd part—and the viscous part σ'' a cosine—even part. Then, when σ' is plotted as a function of γ—respectively σ'' as a function of $\dot{\gamma}/\omega$—a straight line with a slope G'—respectively G'' is obtained.

If a large amplitude sinusoidal strain is applied, the measured stress can be non sinusoidal, but it is still periodic. It can be decomposed in a unique way into odd−σ' and even−σ'' parts:

$$\sigma(t) = \sigma'(t) + \sigma''(t) \tag{2}$$

with

$$\sigma'(t) = (\sigma(t) - \sigma(-t))/2 \tag{3}$$

$$\sigma''(t) = (\sigma(t) + \sigma(-t))/2 \tag{4}$$

An analysis may be performed in the frequency domain. For an applied deformation $\gamma(t) = \gamma_0 \sin(\omega t)$, the in-phase and out-of phase stress responses $\sigma'(t)$ and $\sigma''(t)$ are given respectively by

$$\sigma'(t) = \sum_{n=1}^{\infty} a_n(\omega, \gamma_0) \sin(n\omega t) \tag{5}$$

$$\sigma''(t) = \sum_{n=1}^{\infty} b_n(\omega, \gamma_0) \cos(n\omega t) \tag{6}$$

Because σ' and σ'' are odd functions of γ and $\dot{\gamma}$ respectively, a_n and b_n are nonzero only for odd values of n. The most straightforward way to expand σ' and σ'' as functions of the instantaneous strain and instantaneous strain rate, respectively, has been described recently by Ewoldt et al[61] and is

$$\sigma'(x) = \gamma_0 \sum_{n:\text{odd}}^{\infty} e_n(\omega, \gamma_0) T_n(x) \tag{7}$$

$$\sigma''(y) = \gamma_0\omega \sum_{n:\text{odd}}^{\infty} v_n(\omega, \gamma_0) T_n(y) \tag{8}$$

where $T_n(x)$ is the nth order Chebyshev polynomial of the first kind, with $x = \gamma/\gamma_0$ and $y = \dot{\gamma}/\dot{\gamma}_0$. These polynomials are defined by

$$T_n(\cos\theta) = \cos(n\theta) \tag{9}$$

and satisfy the relation $T_n(\sin\theta) = \sin(n\theta)(-1)^{(n-1)/2}$ (n: odd). Some more details are given in Appendix. With these notations, one has the following relations:

$$\begin{aligned} \gamma_0 e_n(\omega, \gamma_0) &= a_n(\omega, \gamma_0)(-1)^{(n-1)/2} \quad n\text{: odd} \\ \gamma_0\omega v_n(\omega, \gamma_0) &= b_n(\omega, \gamma_0) \quad n\text{: odd} \end{aligned} \tag{10}$$

The dissipated energy per period is

$$W = \int_0^T \sigma''(t)\dot{\gamma}\, dt = \gamma_0 b_1(\omega, \gamma_0)\pi \tag{11}$$

dx.doi.org/10.1021/ma202278e | Macromolecules 2012, 45, 2891−2904

where $T = 2\pi/\omega$ is the period. W depends only on $b_1(\gamma_0,\omega)$. In,[50,51] the nonlinear dependence of the first harmonics (which dominates the response) was computed by the GBRM:

$$G'(\omega,\gamma_0) = \frac{a_1(\omega,\gamma_0)}{\gamma_0} = e_1(\omega,\gamma_0)$$
$$G''(\omega,\gamma_0) = \frac{b_1(\gamma_0,\omega)}{\gamma_0} = \omega v_1(\omega,\gamma_0) \quad (12)$$

and was then discussed and compared to the results published by Payne. However, in experimental data obtained in,[57] other non linear terms clearly reveal a specific behavior of filled rubbers. Therefore, in this paper the whole nonlinear dependence of σ' and σ'' as a function of the deformation amplitude is considered and compared to experimental data. It is given by the expansion

$$\sigma'(t) = \gamma_0\left(e_1(\omega,\gamma_0)\frac{\gamma(t)}{\gamma_0} + e_3(\omega,\gamma_0)\left(4\left(\frac{\gamma(t)}{\gamma_0}\right)^3 - 3\frac{\gamma(t)}{\gamma_0}\right) + ...\right) \quad (13)$$

$$\sigma''(t) = \gamma_0\omega\left(v_1(\omega,\gamma_0)\frac{\dot\gamma(t)}{\gamma_0\omega} + v_3(\omega,\gamma_0)\left(4\left(\frac{\dot\gamma(t)}{\gamma_0\omega}\right)^3 - 3\frac{\dot\gamma(t)}{\gamma_0\omega}\right) + ...\right) \quad (14)$$

which we wrote up to third order. We made use of $T_1(x) = x$ and $T_3(x) = 4x^3 - 3x$. Larger order expansions within the Chebyshev representation can be obtained from the tabulated polynomials.[74]

III. EXPERIMENTS

A. Sample Preparation. We briefly describe the model samples used here, the synthesis and the properties of which have been extensively described elsewhere.[20−24] The model filled elastomers consist of grafted silica particles dispersed in a poly(ethyl acrylate) matrix. Two kinds of grafter have been used: TPM (3-(trimethoxysilyl)propyl methacrylate), which can react with the monomer and thus create a covalent bond with the matrix (covalently grafted samples, CG), and C8TES (*n*-octyltriethoxysilane) with which there are only hydrogen bonds between the residual OH groups on the silica surface and the polymer (non-covalently grafted samples, NCG). Two samples are presented here: T50 CG 30% (silica diameter = 42 nm, grafting density = 3.2 nm^{-2}, silica volume fraction = 0.22) and T30 NCG 25% (silica diameter = 26 nm, grafting density = 2 nm^{-2}, silica volume fraction = 0.15).

B. Mechanical Measurements. The mechanical measurements were performed on an Anton Paar MCR 501 rheometer in simple shear strain with a plate−plate geometry. The samples were cylinders of 8 mm in diameter and 2 mm thick and were glued on the rheometer plates with a cyanoacrylate glue (Loctite 406). The measurements were done at 0.1 Hz and between 30°C (=T_g + 40 °C) and 80°C (=T_g + 90 °C). The rheometer was interfaced with a computer so that the strain and stress signals could be directly recorded and analyzed.

Contrary to the linear case, the generalized moduli depend on the strain and shear rate. The curves obtained by plotting σ' vs γ and σ'' vs $\dot\gamma(t)/\omega$ are thus not straight lines anymore. As an example, the signal analysis is shown in Figure 1 for the sample T30 NCG 25%. As explained in,[57] the inhomogeneity of the strain field in the plate−plate geometry has been taken into account. Indeed a correction factor of 3/2 has been applied to the experimentally measured nonlinear terms $e_3(\omega,\gamma_0)$ and $v_3(\omega,\gamma_0)$. This correction is applied in all following experimental results.

In order to describe the nonlinear behavior of the elastic part, we choose to use the slopes p_0, p_1, and p_2 in the σ' vs γ curve, as described in Figure 2:

- p_0 is the slope of the curve at small strain amplitude in the linear regime, it corresponds to $e_1(\omega,\gamma_0 = 0) = G'(\omega)$, which is the linear storage modulus,
- p_1 is the slope at the origin,
- p_2 is the slope at large strain.

Using this analysis, the ratios p_1/p_0 and p_2/p_0 can be plotted as a function of the strain amplitude. At small strain amplitudes, we expect both ratios to tend to 1, since in the linear case $p_2 = p_1 \to p_0$. At higher strains, it is observed that p_1 decreases and that $p_2 \geq p_1$ (Figure 2). As temperature decreases, the Payne effect is expected to increase, which is indeed what is observed in Figures 3a and 4a. The strain-hardening phenomenon, probed by the variation of p_2/p_0, seems to be less sensitive to temperature (see Figures 3b and 4b). Thus, the temperature dependence indicates that the variation of p_2 cannot be attributed to the strain-softening of glassy bridges only. The elastic stress is plotted as a function of the strain in Figure 5, at different temperatures, for a strain amplitude of 100%. The main result here is that strain hardening is observed, and that it is more pronounced at low temperature. Thus, in these samples and at these temperatures, the strain hardening cannot be explained only by the finite extensibility of the chains. The viscous stress as a function of the strain rate $\dot\gamma$ is also plotted in Figure 5 for the same temperatures. The higher harmonic contributions to the elastic stress are plotted in Figure 5.(c). Note that higher harmonic amplitudes are indeed small. We observed that e_3 is positive, which is the signature of the strain hardening behavior (see eqs 13 and 14).

IV. DESCRIPTION OF THE MODEL

We briefly recall the principle of the GBR model.[51]

A. Shift of the Glass Transition Temperature T_g in the Vicinity of the Fillers. It was proposed that the reinforcement is the consequence of an increase of the glass transition temperature of the matrix in the vicinity of the fillers.[37,39] In the GBRM, the fillers are modeled by solid spheres that interact with their neighbors through elastic springs that mimic the mechanical behavior of a glassy polymer layer. Indeed, the modification of the glass transition of a polymer domain is given by[23,51]

$$T_g(z,\sigma) \approx T_g\left(1 + \left(\frac{\beta}{z}\right)^{1/\nu}\right) - \frac{\sigma}{K} \approx T_g\left(1 + \frac{\beta}{z}\right) - \frac{\sigma}{K} \quad (15)$$

where z is the distance from the nearest filler interface, T_g is the bulk glass transition temperature of the pure rubber and $\nu \approx 0.88$. The first term in the right-hand side of eq 15 is the effect of the interaction between the fillers and the matrix.

dx.doi.org/10.1021/ma202278e | Macromolecules 2012, 45, 2891−2904

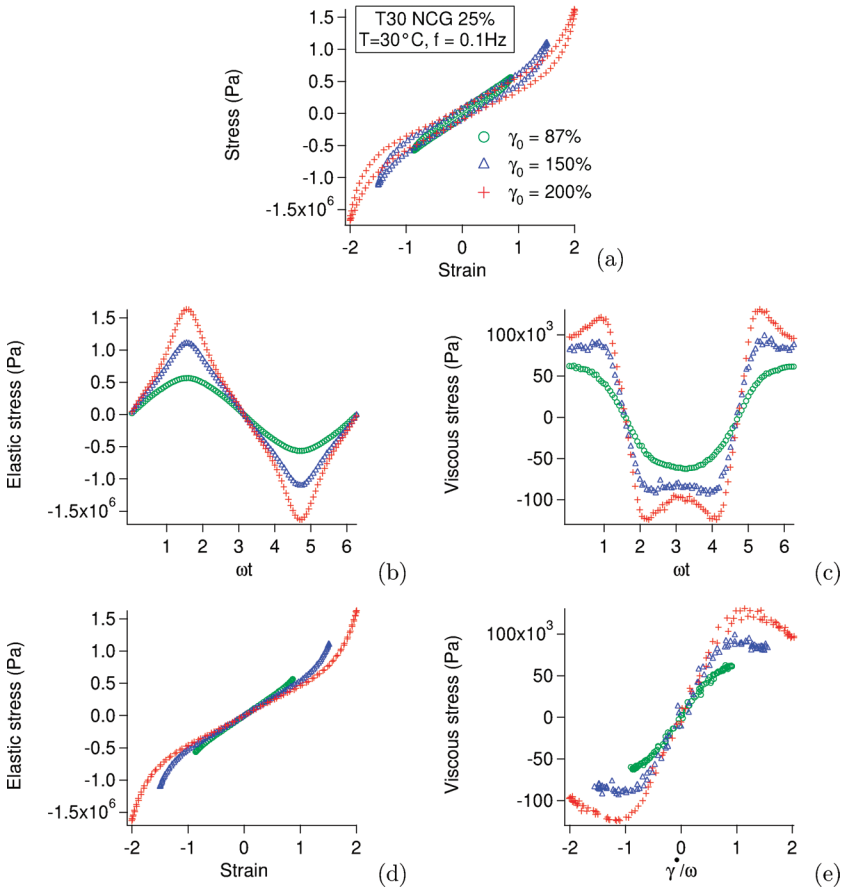


Figure 1. Signal analysis for the sample T30 NCG 25%. (a) Lissajous plot: stress vs strain. As the strain amplitude is increased, the Lissajous plot is more and more deviating from the elliptic shape obtained in the linear case. (b) Elastic stress (odd part of the total stress signal) vs time. (c) Viscous stress (even part of the total stress signal) vs time. (d) Elastic stress vs strain: the curve is not a straight line at large strain and shows a strain-hardening behavior. (e) Viscous stress vs $\dot{\gamma}(t)/\omega$: the nonlinearity is seen as a shear-thinning.

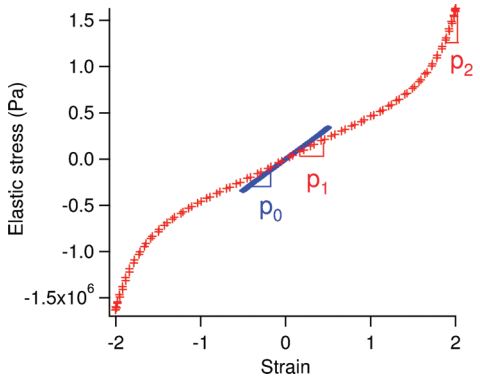


Figure 2. Elastic stress σ' as a function of the strain γ inside one strain cycle. p_0 is the slope of the curve at low strain amplitude, in the linear regime. p_1 and p_2 are the slopes in the nonlinear regime at small and large strain amplitudes, respectively.

The second term is the decrease of T_g due to the local stress σ, which is the plasticizing effect of an applied stress. K depends on the polymer. It relates the yield stress σ_y to the temperature T and the polymer glass transition temperature T_g by $\sigma_y = K(T_g - T)$. K is of the order of 10^6 Pa·K^{-1} typically.[66] β has dimension of a length, the precise value of which depends on the matrix–filler interaction. In the case of strong interactions, we argued in[51] that $\beta \sim 1$ nm.

B. Lifetime of Glassy Bridges: Aging. Glassy bridges are not permanent. Within a glassy bridge in between two neighboring particles, at equilibrium, we assume that the polymer locally has the dominant relaxation time τ_α given by the William–Landel–Ferry (WLF) law of the corresponding polymer,[67] modified by the T_g shift of eq 15 due to interfacial effects and the local stress σ. Hence under stress, glassy bridges may strain-soften when their local glass transition temperature decreases above the sample temperature. This temperature effect can also be expressed in term of time scale: we assume that the lifetimes (breaking times) of glassy bridges are comparable to the local dominant relaxation times τ_α of the glassy bridges. The breaking time is thus given by

$$\log\left(\frac{\tau_\alpha(z,\sigma)}{\tau_g}\right) = -\frac{C_1(T - T_g(z,\sigma))}{C_2 + (T - T_g(z,\sigma))} \quad (16)$$

where $T_g(z,\sigma)$ is given by eq 15 where z is taken to be half the distance between the surfaces of the neighboring particles, τ_g = 100 s (the relaxation time at T_g) and T is the temperature. C_1 and C_2 are the WLF parameters of the considered polymer.[67] Equation 16 gives *the equilibrium value of the breaking time*, which is obtained when the distance z, the local stress σ and the temperature T have been maintained fixed for a long time. In general, the breaking time depends on the history of the glassy bridge and is denoted by $\tau_\alpha(t)$. The corresponding evolution of glassy bridge is thus expected to follow the classical aging

dx.doi.org/10.1021/ma202278e | *Macromolecules* 2012, 45, 2891–2904

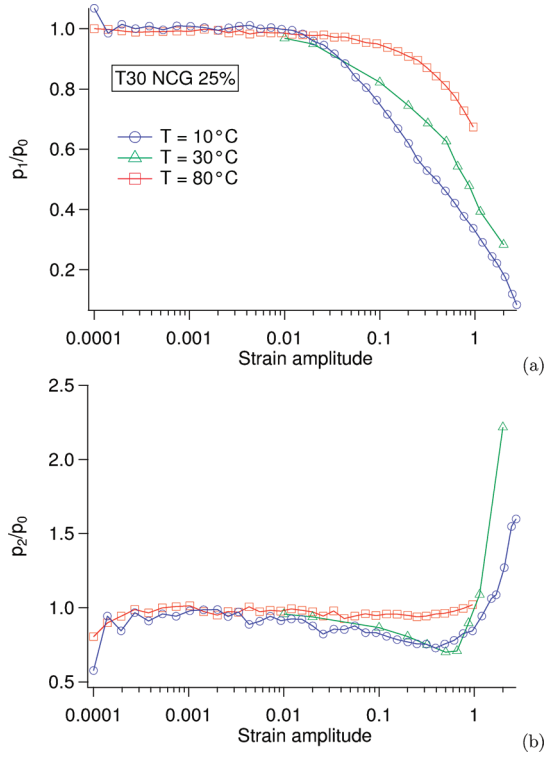


Figure 3. Ratios p_1/p_0 (a) and p_2/p_0 (b) vs strain amplitude at different temperatures (10, 30, and 80 °C) for the sample T30 NCG 25%. As temperature decreases, the Payne effect becomes larger so that p_1/p_0 decreases more abruptly. p_2/p_0 first follows this decrease and then increases due to the large strain-hardening.

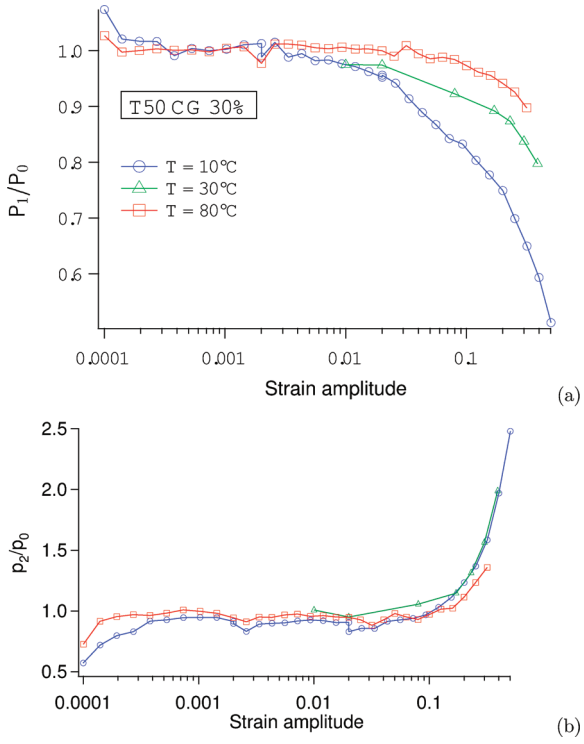


Figure 4. Ratios p_1/p_0 (a) and p_2/p_0 (b) vs strain amplitude at different temperatures (10, 30, and 80 °C) for the sample T50 CG 30%. Again the Payne effect is larger at lower temperature but it is smaller than for the T30 NCG 25% sample so that p_2/p_0 seems to be a monotonic increasing curve.

properites of glasses. $\tau_\alpha(t)$ evolves toward its equilibrium values linearly in time (see, e.g., ref 68).

It was shown that the kinetics of yield, birth and aging of glassy bridges is a key feature for explaining the dependence of $G'(\omega,\gamma_0)$ and $G''(\omega,\gamma_0)$ on the amplitude (Payne effect), and especially the presence of the peak of $G''(\omega,\gamma_0)$ at intermediate deformation amplitudes for strongly reinforced elastomers.[8,51] It is also essential for understanding the plastic behavior of filled elastomers.[50,52] As we shall see, this kinetics is also key for understanding the higher harmonic response of filled elastomers.

C. Modeling. The model described above needs to be solved numerically. The relevant degrees of freedom are the centers of mass of the fillers. The diameter d of the fillers sets the unit length scale. The dynamics is supposed to be non inertial. Each particle i interacts with $n = 10$ neighboring particles. The corresponding equation of motion for particle i is

$$\vec{F}_{\mathrm{el}}^{\,i} + \vec{F}_{\mathrm{hs}}^{\,i} + \vec{F}_{\mathrm{Hydro}}^{\,i} = \vec{0} \tag{17}$$

where $\vec{F}_{\mathrm{el}}$ is the elastic force between two neighboring particles and is the sum of the contributions of the glassy bridges and of the rubbery matrix. $\vec{F}_{\mathrm{hs}}$ is the hard core repulsion between fillers and $\vec{F}_{\mathrm{Hydro}}$ is the friction force between two neighboring particles. The elastic force is given by

$$\vec{F}_{\mathrm{el}}(\vec{r}) = -k_\infty(\vec{r} - l_0\vec{u}) - k_0(\vec{R}_{ij} - \vec{R}_{ij}^{\,ref}) \tag{18}$$

where l_0 is the equilibrium length of the rubbery springs, $\vec{r}$ is the vector joining the centers of the two particles, and $\vec{u}$ is the unit vector joining the two particles. To represent the effect of the rubbery matrix (of typical elastic modulus 1 MPa), we set $k_\infty = 1$. This spring constant sets the unit of modulus. All the results will therefore be expressed in units of MPa. The glassy modulus, 10^9 Pa, is typically 3 orders of magnitude larger than the rubbery modulus. The glassy spring constant is thus set to $k_0 \sim 10-100$. (Note that k_0 is much smaller than 1000 because geometrical aspects regarding glassy bridges have to be taken into account[51]). Finally, $\vec{R}_{ij} = \vec{R}_i - \vec{R}_j$, and $\vec{R}_i$ is the vector position of filler i. A viscous force between two neighboring particles in our simulations has to be added to stabilize the simulation, and is written as

$$\vec{F}_{\mathrm{Hydro}} = -\zeta\frac{\mathrm{d}\vec{R}_{ij}}{\mathrm{d}t} \tag{19}$$

The relaxation time of glassy bridges then follows a linear evolution in time toward its equilibrium value. More details regarding the implementation of the model into a numerical code are given in refs 69−71. In ref 51, we discussed in more detail how the physical parameters of the system can be translated into the parameters of the simulation. The length scales are made dimensionless thanks to the filler diameter which set the unit length scale. If we assume that their diameter is 20 nm, typical dimensionless values for β will be of order 0.05 (corresponding to $\beta = 1$ nm in physical units). The parameters and the corresponding values used in our simulations are summarized in Table 1.

V. SIMULATIONS: RESULTS

We have considered a system of 5000 particles with a volume fraction $\Phi = 40\%$. To describe the dynamics of the glassy springs, the WLF parameters of polyisoprene (PI),[72] for which $T_g = 213$ K, have been used. The parameter K, which describes

dx.doi.org/10.1021/ma202278e | Macromolecules 2012, 45, 2891−2904

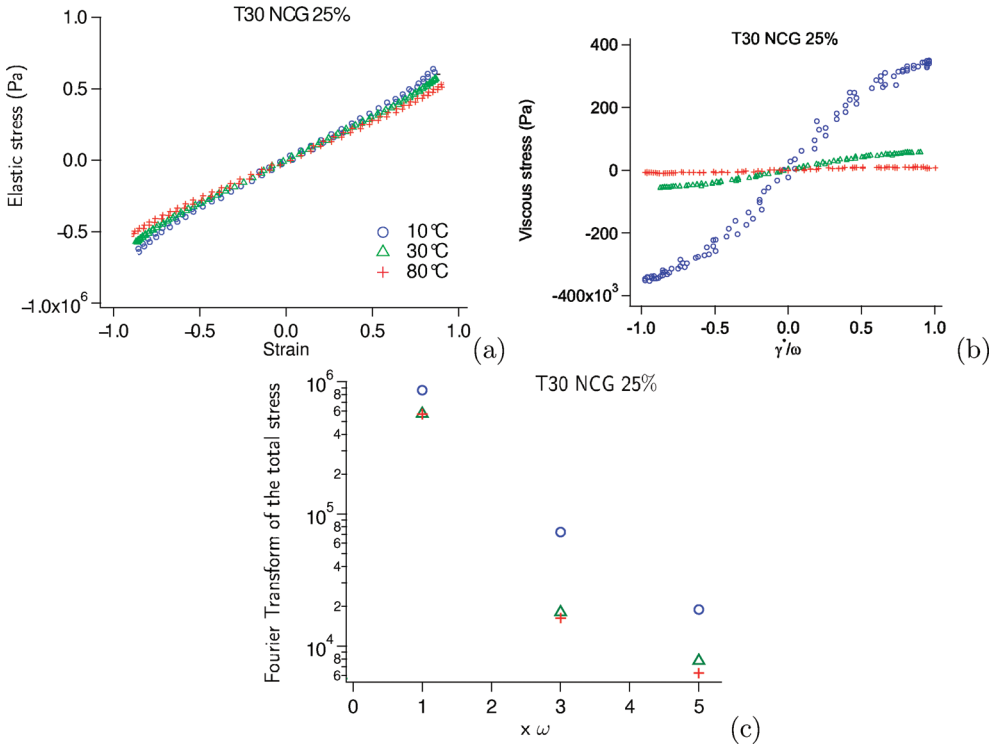


Figure 5. Signal analysis for the sample T30 NCG 25%. (a) Elastic stress (odd part of the total stress signal) vs strain $\gamma(t)$, for the same deformation amplitude γ_0 at three different temperatures. One observes significant strain hardening at low temperature. (b) Viscous stress (even part of the total stress signal) vs $\dot{\gamma}(t)/\omega$ for the same experiments. (c) Components $\gamma_0 e_n(\omega,\gamma_0)$ of the Chebyschev expansion of the total stress in the same experiments, up to the fifth harmonic. Though small, we can note that the stronger the reinforcement (i.e., the lower the temperature), the stronger the higher harmonic contribution.

Table 1. Parameters of the Model[a]

parameter	physical value	value in the simulation
number of particles		N = 5000
volume fraction	10−40%	40%
filler diameters	20 nm	d = 1.0
connectivity of springs		n = 10
rubbery modulus	5 × 10^5 Pa	k_∞ = 1
glassy modulus	10^9 Pa	k_0 = 10−100
glass transition temperature T_g of the pure rubber	213 K	T_g = 213 K
temperature of the experiment T	T	T = 263 K
typical deformation rate	1 s^{-1}	$\dot{\gamma}$ = 1 s^{-1}
dissipative modulus at large deformation amplitudes	10^6 Pa	ζ= 4 s
coefficient β	0.4−0.8 nm	0.02−0.04
coefficient K	10^6 Pa·K^{-1}	0.3
coefficient α	$\lesssim$1	0.4

[a]In addition to the glass transition temperature of the matrix, one needs the complete WLF law of the considered polymer.

the stress-softening in eq 15, has been taken to be 0.3 MPa·K^{-1}. The other parameters characterizing the network of soft springs and the hardcore interactions between particles are the same as in our previous studies and are fixed.[50,51] We have considered two values of the dimensionless parameter β, 0.04 and 0.02, and two values for the parameter k_0, 10 and 100. For each value of β and k_0, simulations have been performed at various temperatures, from T = 263 K = T_g + 50 K up to T = 323 K = T_g + 110 K. A sinusoidal deformation $\gamma(t) = \gamma_0 \sin(\omega t)$ with a fixed pulsation ω = 1 s^{-1} has been imposed. As the model system may be more dissipative than the experimental systems because of the large value of the friction ζ, the viscous contribution on the total stress $\sigma_{hydro}(t) = G''_{\text{high T}}\,\gamma_0 \cos(\omega t)$, where $G''_{\text{high T}} \simeq$ 3.86 MPa is the loss modulus measured at high temperature for the smallest value of β (T = 323 K, β = 0.02), has been subtracted from the stress. Note in particular that, for these parameter values, the apparent modulus is found to be independent of the strain amplitude (i.e., there is no Payne effect), and so that, in this regime, the viscous stress originates only from the friction coefficient ζ between particles.

The elastic response of a sample defined by the parameters β = 0.04 and T = 323 K is shown in Figure 6. Both the stress versus strain curves, the elastic and viscous stresses as a function of time and the elastic and viscous stresses as a function of strain and strain rate, respectively, are shown. A strain-hardening behavior is observed. The parameters chosen here correspond to a moderate reinforcement, and a relatively high temperature. The main features observed in the experiments (Figure 1) are reproduced qualitatively. In particular, the elastic curve shows strain-hardening at large amplitude, and the viscous stress depends nonmonotonously on the instantaneous strain rate.

The elastic stress at several temperatures and for two different values of β, 0.02 and 0.04, is plotted as a function of strain in Figure 7. The corresponding viscous stress (for β = 0.02 only) is plotted in Figure 8. A hardening of the elastic stress is observed at the extremities of the cycle. The stronger the reinforcement, and the lower the temperature, the larger the hardening effect. The observed behavior is also qualitatively similar to that observed experimentally in Figure 5 where strain hardening was found to be significant at low temperature. Regarding the viscous stress, a behavior qualitatively similar to

dx.doi.org/10.1021/ma202278e | Macromolecules 2012, 45, 2891−2904

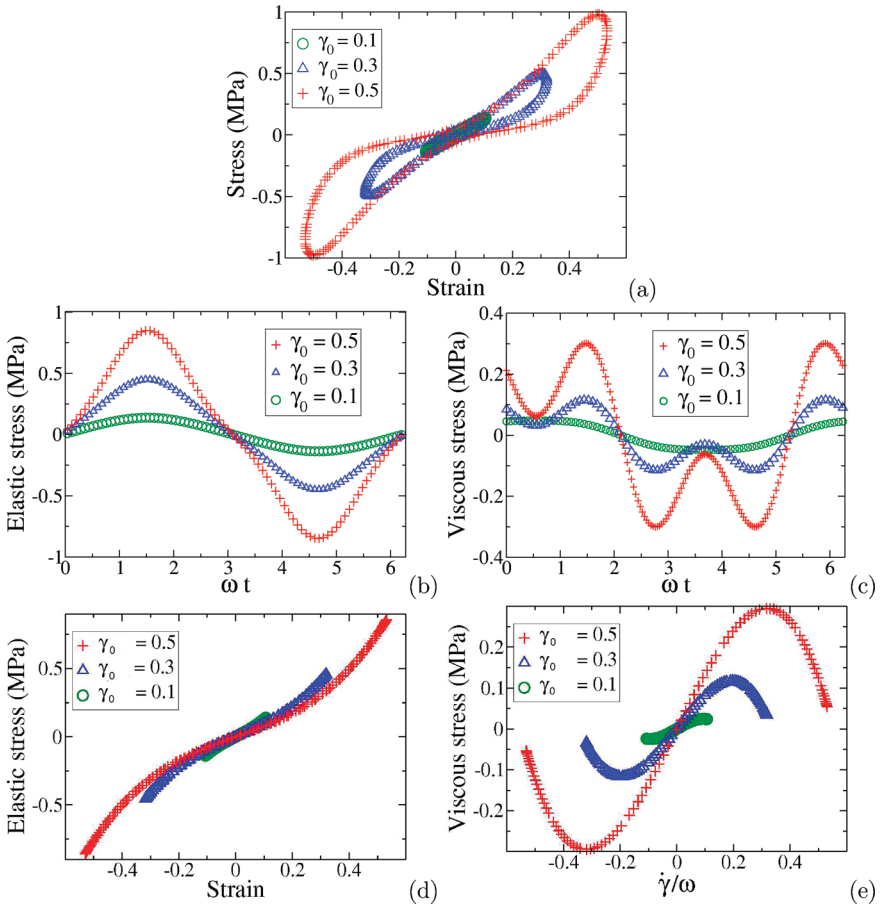


Figure 6. Stress curves simulated with the model with $\beta = 0.04$, $k_0 = 100$ and $T = 323$ K (using the WLF parameters of PI with $T_g = 213$ K). Other parameters are $\Phi = 40\%$; $K = 0.3$; $\zeta = 4$ s; pulsation $\omega = 1$ s^{-1}. The contribution to the stress due to the friction between particles has been subtracted as explained in the text. (a) Lissajous plot: stress vs strain. (b) Elastic stress vs time. (c) Viscous stress vs time. (d) Elastic stress vs strain: the curve at large amplitude shows strain-hardening. (e) Viscous stress vs $\dot{\gamma}(t)/\omega$: the nonlinearity is seen as a shear thinning. The observed behavior is qualitatively similar to the experimental results of Figure 1.

that of the experimental data, in which the viscous stress goes through a maximum at intermediate strain rates, is observed.

VI. DISCUSSION

A. Aging or Rebirth of Glassy Bridges within a Strain Cycle. First let us recall that the decrease of the elastic modulus can be interpreted as a strain softening of the glassy bridges as observed experimentally in ref 22 and in the frame of the GBRM.[51] Thus, the decrease, with the strain amplitude γ_0, of the slope of $\sigma'(\gamma)$ at zero strain from p_0 to p_1 can be interpreted as a decrease of the average number of glassy bridges in the systems with the average level of stress. We will show now that we can interpret the strain hardening as the consequence of the slowing down of the strain rate at the extremities of the cycle. We focus on the aging—or rebirth—of glassy bridges within a strain cycle. The slower the strain rate, the more glassy bridges can recover relatively long relaxation times. These recoveries occur most efficiently in the parts of the cycle where the strain rate is the smallest. As a consequence, these glassy bridges that rebuild during the slowest part of the strain cycle will contribute to the elastic response. This effect appears explicitly in the GBRM. Let us define the integrated distribution of relaxation times $P(\log \tau)$ as the number of glassy springs having a relaxation time larger than, or equal to τ. $P(\log \tau)$ is related to the distribution of relaxation times by the relation

$$P(\log \tau) = N_{tot} \int_{\tau}^{\infty} Q(\tau)\, d\tau \tag{20}$$

where $Q(\tau)$ is the normalized distribution of relaxation times, and N_{tot} is the total number of glassy springs. In our simulations, this total number is constant and equal to $N_{tot} \approx 25000$. This number corresponds to the fact that our system contains 5000 beads, which interact typically with 10 neighbors. Thus, the number of glassy bridges is fixed, only the relaxation time associated with each glassy bridge varies during the simulations. The integrated distribution is thus related also to the distribution by the relation $N_{tot}Q(\tau) = (-1/\tau)\ (dP(\log \tau))/(d[\log(\tau)])$. $P(\log \tau)$ is therefore a decreasing function of $\log\tau$, from N_{tot} down to zero at large values of $\log\tau$ as can be seen in Figures 9 and 10. Large values of the slope of P correspond to peaks in the distribution Q. Note that the sharp drop at $\log \tau \approx -2$ corresponds to the short time cutoff in our simulations which we set at 10^{-2} s and is thus an artifact of the simulation. We assume thus that the relaxation time of glassy bridges can never be shorter than 10^{-2} s, which is not important because the considered frequencies in the simulations are always much smaller than 100 Hz. In Figure 9, the integrated distribution $P(\log \tau)$ in systems undergoing a sinusoidal deformation of amplitude $\gamma_0 = 0.5$ is plotted at different instantaneous values of

dx.doi.org/10.1021/ma202278e | Macromolecules 2012, 45, 2891−2904

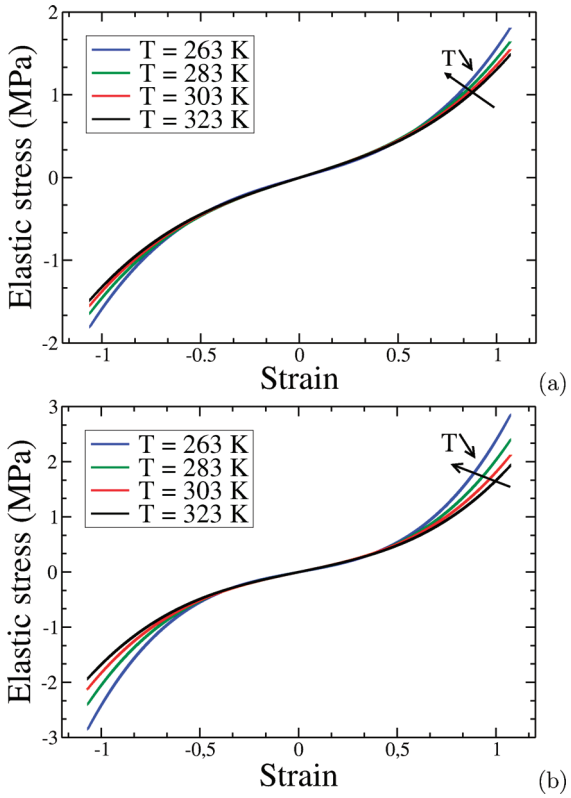


Figure 7. Simulations: elastic stress as a function of strain at different temperatures. The parameters are $\beta = 0.02$, $k_0 = 100$ (a) and $\beta = 0.04$, $k_0 = 100$ (b). A temperature dependent hardening is observed at the extremities of the cycle, due to a slowing down of the deformation rate. The stronger the reinforcement, and the lower the temperature, the larger the effect.

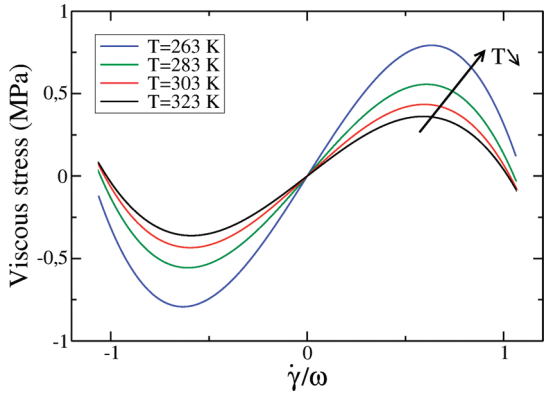


Figure 8. Simulations: viscous stress in a sample with $\beta = 0.02$, $k_0 = 100$, $\gamma_0 = 100\%$, at different temperatures.

the strain $\gamma(t)$. We consider a relatively strongly reinforced system ($\beta = 0.04$; $T = 263$ K), and the same system at higher temperature ($T = 323$ K). Indeed, one can see in Figure 9 that the number of glassy bridges with breaking times larger than typically 1 s—the solicitation period—is larger for values of $\gamma(t)$ close to the maximum $\gamma_0 = 0.5$. When the strain rate slows down, the relaxation time of the glassy bridges can increase, whereas at high values of the strain rate the glassy bridges break more frequently. This is the same mechanism as the one we discussed in ref 50 for accounting for the unique plastic properties of filled elastomers. Indeed, it was argued in ref 50

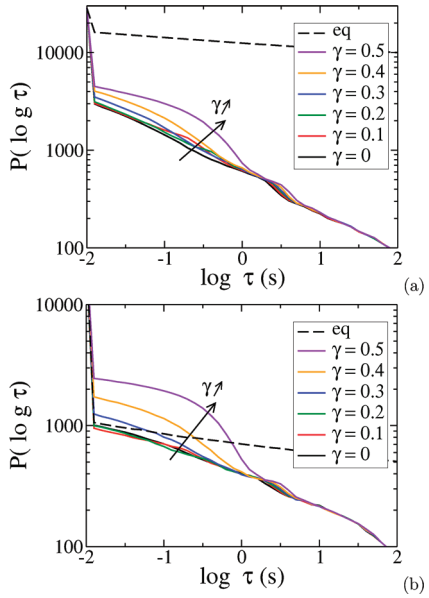


Figure 9. Integrated distributions of relaxation times of glassy bridges $P(\log\tau)$ of systems undergoing a sinusoidal deformation with an amplitude $\gamma_0 = 0.5$, plotted at different values of the instantaneous strain $\gamma(t)$:from bottom to top, $\gamma = 0$; 0.1; 0.2; 0.3; 0.4 and γ_{max}. $P(\log \tau)$ is the number of glassy springs having a relaxation time larger than τ. The total number of glassy bridges is ≃25000. (a) reinforced system ($\beta = 0.04$; $T = 263$ K), for which p_2 is smaller than p_0 (see Figure 11); (b) a moderately reinforced system ($\beta = 0.04$; $T = 323$ K) for which p_2 is larger than p_0 (see Figure 11). Other parameters are the same as in Figure 6. Dashed curves show the distributions prior to deformation. In the moderately reinforced system (b), the number of glassy springs having a lifetime comparable at least to the deformation period, $\tau \sim 1$ s, may be larger than at equilibrium. In this case, the slope p_2 is larger than p_0.

that when a static strain is applied and maintained constant for a long time, the glassy bridges recover long relaxation times in this new imposed deformation state, thus creating a new reference state corresponding to a plastic deformation with respect to the initial state at rest (before the static strain has been applied). The same mechanism is at work in the case of cyclic strain discussed in this paper. The observed hardening is a consequence of the aging of the glassy bridges at the extremities of the deformation cycles: thus this does not correspond to strain hardening *per se*, but to what we propose to call "slowing down hardening", a property which should be observed in self-healing systems in general.

The mechanisms at work are schematized in Figure 10, in order to make the interpretation we propose more precise. In Figure 10a, we represent the state of the sample before deformation are applied, and after a long aging time which has allowed the glassy bridges to age up to time scales comparable to 10^5 s. It corresponds to the integrated distribution of relaxation times in thick dashed line (Figure 10d). When a periodic deformation of relatively large amplitude γ_0—e.g., 50% or 100%—is applied, and after a few cycles when the permanent regime is reached, many glassy bridges of long relaxation times have melted (Figure 10b). The distribution of relaxation times is modified (thick black line in Figure 10d). Glassy bridges with very long relaxation times are still present in the system, but they form isolated clusters which are not submitted fully to the large deformation amplitude applied on a macroscopic scale. These clusters are separated by polymers which is in a rubbery state,

dx.doi.org/10.1021/ma202278e | *Macromolecules* 2012, 45, 2891–2904

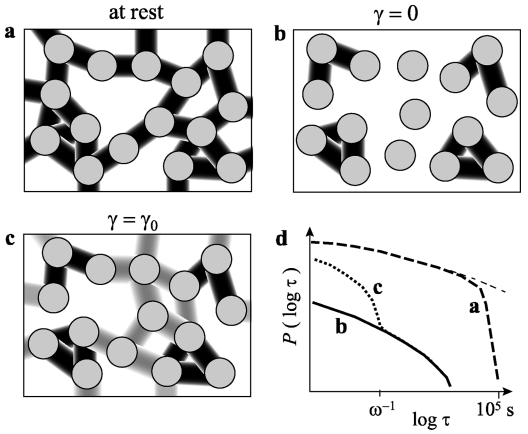


Figure 10. Schematics of the glassy bridges in a filled elastomer. In black, we represent the glassy bridges with very long relaxation times, i.e., much longer than the solicitation period ω^{-1}. In gray, these are glassy bridges with lifetimes comparable to the deformation period. In white, we represent either the rubbery matrix, or glassy bridges with lifetimes much shorter than ω^{-1}. See the text for comments. (a) Glassy bridges in an aged sample, e.g. with an aging time of order 10^5 s, before any deformation is applied. (b) Snapshot of the glassy bridges in the same sample when submitted to a periodic deformation of large amplitude. This snapshot is taken at a time which corresponds to a maximum of the shear rate, i.e., when the instantaneous value of the strain amplitude γ is zero. (c) Snapshot of the glassy bridges, as in part b, but taken at an extremity of the deformation cycle, i.e., at $\gamma = \gamma_0$. Because the strain rate slows down in the vicinity of an extremity of the cycle, glassy bridges with a slightly larger relaxation times have time to appear as compared to b). (d) Integrated distribution of relaxation times corresponding to cases a (dashed curve), b (full curve), and c (dotted curve). The thin dashed curve corresponds to the integrated distribution at equilibrium, which may not be reached in an accessible aging time.

or close to that state. Within one cycle, however, in the part of the cycle for which $\dot{\gamma}$ is small, the relaxation times of the glassy bridges linking such clusters increase, and come close to the value ω^{-1}. That corresponds to the glassy bridges in light gray in Figure 10.c. This is the origin of the slowing down hardening. During the permanent regime of the applied periodic solicitation, the distribution of relaxation time oscillate between the behavior described in Figure 10, parts b and Figure c, corresponding to the dotted line and the thick black line in Figure 10d, respectively.

B. Effect on the Elastic Stress. Let us focus now on the nonlinear elastic stress. The ratios p_1/p_0 and p_2/p_0 are plotted as a function of the strain amplitude in Figures 11 and 12, at different temperatures and for the same parameter values as in Figure 7. For the two interaction parameters β considered, the ratio p_1/p_0 decreases more abruptly, i.e., the Payne effect becomes larger, when temperature decreases. For the system with a weak polymer/filler interaction, Figure 12 shows that at high temperature, the Payne effect is modest and practically independent of temperature in the considered temperature range. For the relatively reinforced system $\beta = 0.04$, the ratio p_2/p_0 decreases with the strain amplitude at low temperature, while it increases at high temperature. On the other hand when $\beta = 0.02$, for all the temperatures considered, the ratio p_2/p_0 increases with the strain amplitude, following a curve that is nearly independent of temperature, except for the lowest considered temperature ($T = 263$ K).

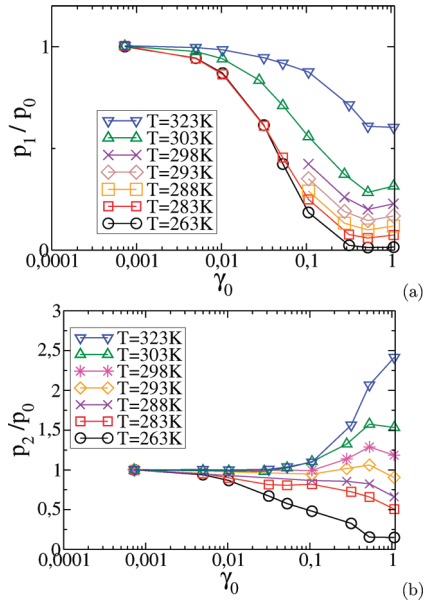


Figure 11. Simulation results: the ratios p_1/p_0 (a) and p_2/p_0 (b) vs strain amplitude γ_0 at different temperatures (T = 263 K, 283 K, 303 and 323 K) for $\beta = 0.04$ and $k_0 = 100$. As temperature decreases, the Payne effect becomes larger so that p_1/p_0 decreases more abruptly. p_2/p_0 decreases with the strain amplitude at low temperature, while it increases at high temperature. Other parameters are the same as in Figure 6. The results are to be compared to those of Figure 3.

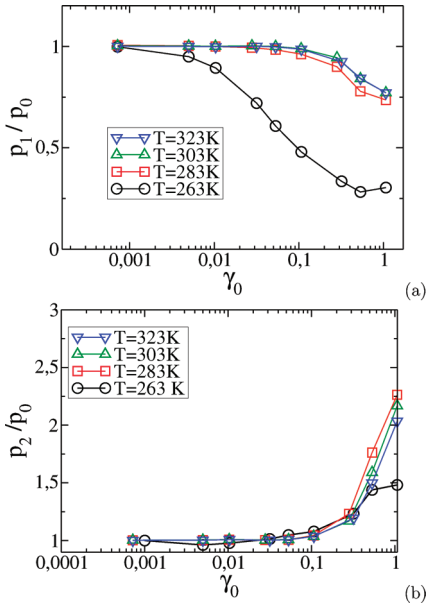


Figure 12. Simulation results: the ratios p_1/p_0 (a) and p_2/p_0 (b) vs strain amplitude at different temperatures (T = 263 K, 283 K, 303 and 323 K) for a small value of $\beta = 0.02$ and $k_0 = 100$. At high temperature, the Payne effect is modest and practically independent of temperature. At all considered temperatures, the ratio p_2/p_0 increases with the strain amplitude, following a curve which is nearly independent of temperature. Other parameters are the same as in Figure 6. The results are to be compared to those of Figure 4.

We have proposed above that the elastic modulus at the extremities of the strain cycle $\gamma(t) = \gamma_0$ can be larger than that at $\gamma(t) = 0$ (for a given deformation amplitude γ_0) because glassy bridges can build relatively long relaxation times around

dx.doi.org/10.1021/ma202278e | Macromolecules 2012, 45, 2891−2904

positions for which $\dot{\gamma} = 0$. On the other hand, one might expect that the elastic modulus should be smaller than p_0 there. This is the case for strongly reinforced systems, with large Payne effect: the "slowing down hardening" cannot compensate for the strong amplitude of the Payne effect, as can be seen in Figure 11 for a system with $\beta = 0.04$ at $T = 263$ K. On the other hand, for moderately reinforced systems (the system with $\beta = 0.04$ considered in Figure 11 at high temperature, i.e., T = 303 or 323 K, and the system with $\beta = 0.02$ in Figure 12 at any temperature), the slope p_2 is larger than p_0, as it is also the case experimentally (see Figures 3 and 4). We propose the following explanation: the applied deformation changes the distribution of distances between fillers, and can bring some of them closer together. This results in a shift of glassy bridge lifetimes toward longer times and thus possibly in a stiffening of the sample at large deformation amplitudes as compared to the undeformed state. This interpretation is consistent with Figure 13 which displays the distributions of distances $N(z)$ between the centers of mass of neighboring particles at different instantaneous values of the strain. The results for a relatively strongly reinforced sample ($\beta = 0.04$ and $T = 263$ K) are plotted in Figure 13a. No shift toward smaller distances is observed in this case.

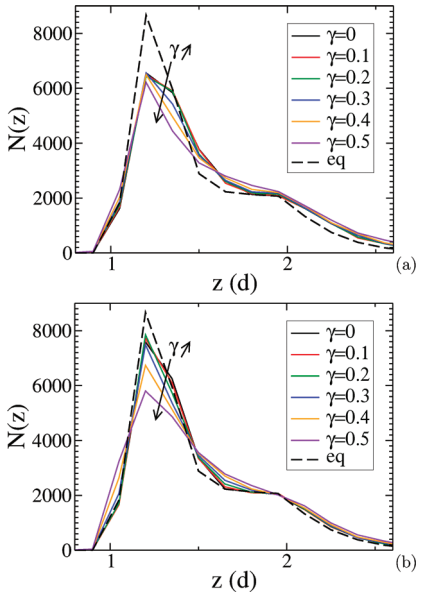


Figure 13. Distribution of distances $N(z)$ between the centers of mass of neighboring particles for systems undergoing a sinusoidal deformation of amplitude $\gamma_{max} = 0.5$, plotted at different values of the instantaneous strain: from top to bottom, $\gamma = 0$, 0.1, 0.2, 0.3, and 0.4 and γ_{max}. $N(z)$ is the number of pairs whose center of mass lies between z and $z + \Delta z$, with $\Delta z = 0.15d$. The total number of distinct pairs of particles is ≃25000. Key: (a) reinforced system ($\beta = 0.04$; $T = 263$ K); (b) a moderately reinforced system ($\beta = 0.04$; $T = 323$ K). Other parameters are the same as in Figure 6. Dashed curves show the equilibrium distributions prior to deformation. Note that at 323 K and at maximum strain, two neighboring particles may come very close to each other, consistently with the large value of p_2 compared to p_0.

In the case of a moderately reinforced system ($\beta = 0.04$ and $T = 323$ K, Figure 13b), it is observed that some fillers can come closer together under applied strain as compared to the equilibrium system, thus leading to a stiffening at large deformation amplitudes. The difference regarding the distribution of distances between the initial, nondeformed system, and the one at the maximum deformation amplitude might seem tiny. However, one must bear in mind that the reinforcement parameter β is not very large ($\beta = 0.04$), and that the temperature is relatively high ($T = 323$ K). The glassy layer thickness e_g, given by[21,22]

$$e_g = \beta \frac{T_g}{T - T_g} \tag{21}$$

is on the order of 0.09 in the dimensionless system of the simulations, which corresponds to about 2 nm in real samples. As a consequence, the polymer layers situated between fillers further apart than $z \approx 1.2$ are more than 60 K above their glass transition, and do not contribute to the building of glassy bridges. Only fillers closer than $z \approx 1.2-1.1$ contribute significantly to the reinforcement. We see thus that the elastic forces within the material can bring some fillers closer together as compared to the initial nondeformed sample, and lead to values of p_2 larger than p_0.

C. Effect on the Dissipative Stress. As discussed in ref 51, the dissipation in filled elastomers has three different origins. The most obvious is the one of the elastomer matrix, far from the polymer−filler interfaces. The second one is due to the transition region between the matrix and the glassy layer. The third one is due to the kinetics of rupture and rebirth of glassy bridges, which is of interest here. This third source of dissipation becomes efficient at intermediate deformation amplitudes γ_0. Indeed, at small γ_0, the lifetime distribution of the glassy bridges is not modified by the deformation and the second origin of viscous stress dominates. However, at intermediate to large values of γ_0 the kinetics of rupture and rebirth of glassy bridges may contribute significantly to the dissipation. More precisely, the peak observed both in the experiments and in the simulations (see Figures 1 and 6, respectively) may also be explained by the "slowing down hardening". Let us consider the behavior of the viscous stress as a function of $\dot{\gamma}$. At the point at which $\dot{\gamma} = 0$, the viscous stress is zero. Close to this point, the lifetimes of the glassy bridges are comparatively large, because of the "slowing down hardening" effect discussed above. Then, $\dot{\gamma}$ increases and $\sigma''(t)$ first increases linearly (as can be seen in Figures 1 and 6), because the distribution of glassy bridge lifetimes is not yet modified as compared to the situation at zero shear rate. As the strain rate, as well as the instantaneous strain, increase further, the distribution shifts to shorter times, as it is observed in Figure 9. The sample then becomes less dissipative, which corresponds to the peak of $\sigma''(t)$.

D. Nonlinearity and Nonharmonic Behavior. To further illustrate how the nonlinear behavior depends on the reinforcement parameters k_0, β and T, the stress/strain curve, the elastic stress as a function of the strain and the viscous stress as a function of the strain rate are shown for a system with $\beta = 0.04$ and $k_0 = 10$ at $T = 323$ K (Figure 14) and for a system with $\beta = 0.02$, $k_0 = 100$, $T = 263$ K (Figure 15). In this latter case, the cubic contribution to the viscous strain dominates at large strain rates. In some instances the viscous stress may show values of opposite sign to the strain rate for large values of the latter, as it is observed in Figure 8. The contributions of the harmonics ω, 3ω and 5ω to the elastic stress are plotted in Figure 16. It is observed that $\gamma_0 e_5(\omega,\gamma_0)$ is about one decade smaller than $\gamma_0 e_3(\omega,\gamma_0)$, which is itself one decade smaller than $\gamma_0 e_1(\omega,\gamma_0)$, as it is the case regarding experimental results (see Figure 5c). The stronger the reinforcement, i.e., the lower the temperature in Figure 16, the larger the amplitude of $e_3(\omega,\gamma_0)$ and $e_5(\omega,\gamma_0)$.

dx.doi.org/10.1021/ma202278e | Macromolecules 2012, 45, 2891−2904

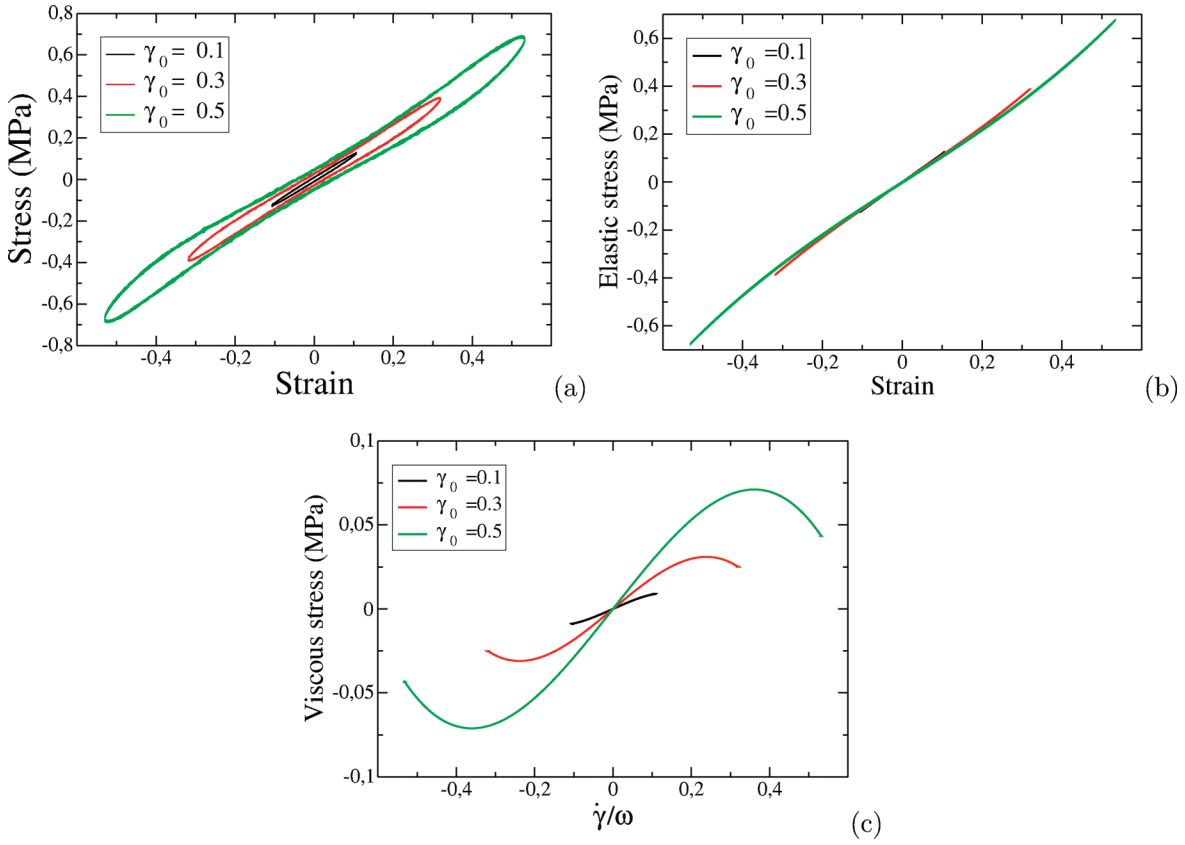


Figure 14. Simulations: stress/strain curve (a), elastic stress (b), and viscous stress (c) of a sample with β = 0.04, k = 10, and T = 323 K.

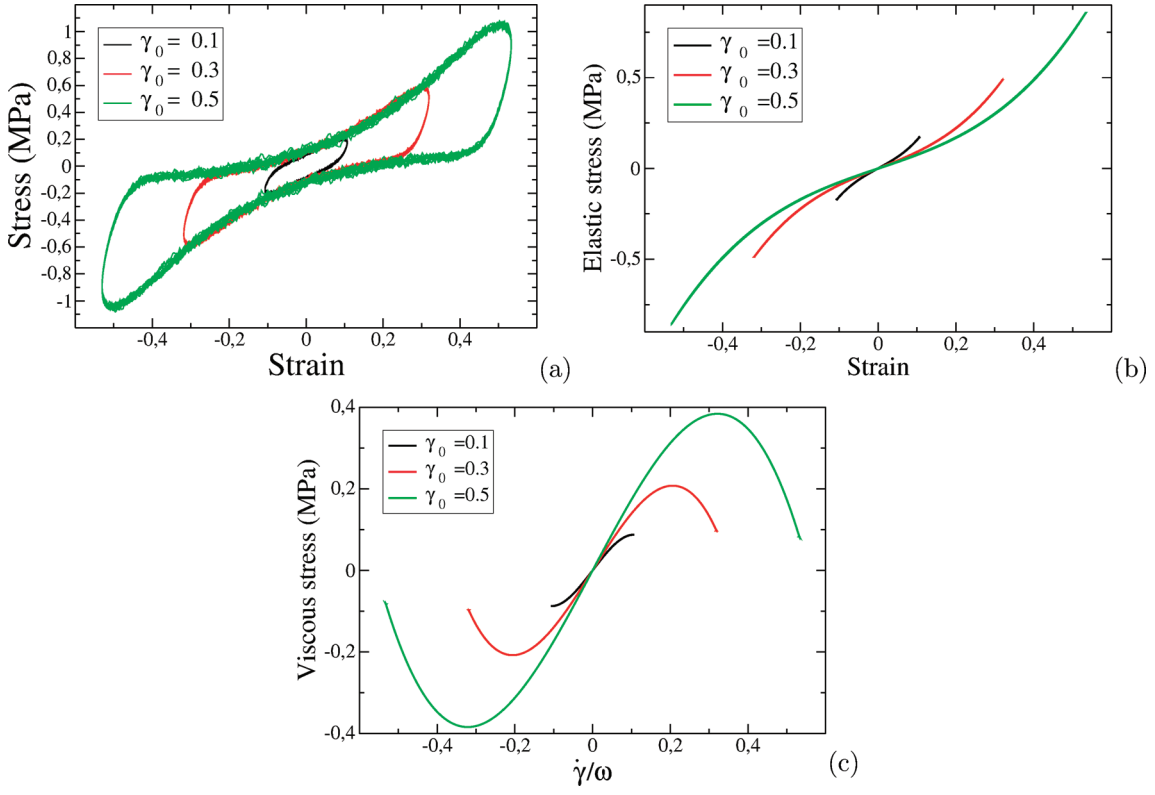


Figure 15. Simulations: stress/strain curve (a), elastic stress (b), and viscous stress (c) of a sample with β = 0.02, k = 100, and T = 263 K.

Thus, the "slowing down hardening" is mainly due to the contribution of the third harmonics. On the other hand, e_3 is quite small compared to the apparent "slowing down hardening" observed in Figure 5a. The hardening is defined by the slope

dx.doi.org/10.1021/ma202278e | *Macromolecules* 2012, 45, 2891–2904

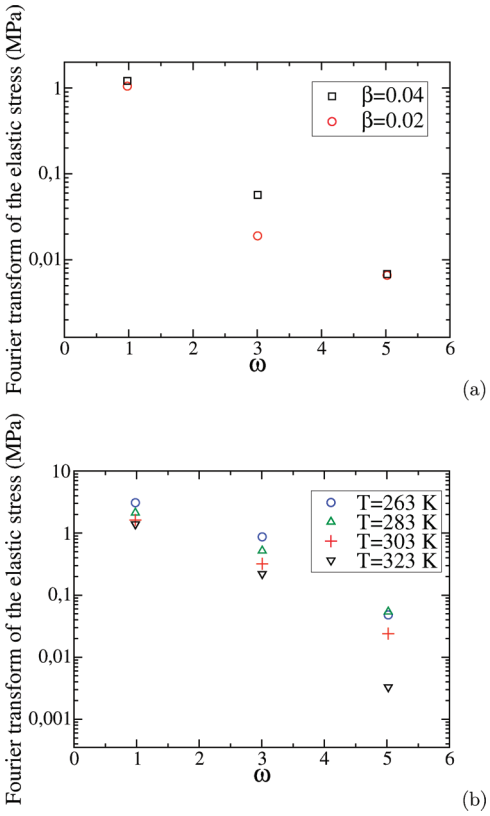


Figure 16. Components of the Chebyschev expansion of the total stress $\gamma_0 e_n(\omega,\gamma_0)$, up to the fifth order for systems deformed with an amplitude $\gamma_0 = 0.5$. (a) $k_0 = 100$, $T = 323$ K; (b) $k_0 = 10$, $\beta = 0.04$. The data in part a with $\beta = 0.02$ are qualitatively very similar to the experimental results displayed in Figure 5c, especially those at 80 °C. Note also that the stronger the reinforcement, the larger the amplitude of higher harmonics.

(or differential modulus, as it is often called[75]) at large strain $P_2 = ((d\sigma'(t))/(d\gamma))|_{\gamma=\gamma 0}$. According to eqs 7 and 9:[74,76]

$$p_2 = \frac{d\sigma'}{d\gamma}|_{\gamma=\gamma_0} = \sum_{n:\text{odd}}^{\infty} n^2 e_n \tag{22}$$

That is, up to third order

$$p_2 = \frac{d\sigma'}{d\gamma}|_{\gamma=\gamma_0} \approx e_1 + 9e_3 \tag{23}$$

which could be deduced directly from eq 13 as well. Thus, even if e_3 is small as compared to e_1, it can lead to a significant hardening because of the factor 9 in this equation, which was also noted in ref 61.

A last point that deserves to be discussed regards the specific features of the nonlinear behavior of filled elastomers. As mentioned in the introduction, it is often thought that a nonlinear behavior under periodic solicitations at frequency ω should necessarily result in the appearance of contributions to higher frequency harmonics 3ω, 5ω, ..., which is the case in particular when the stress is a nonlinear, nonretarded function of the deformation x with a constitutive relation of the type: $\sigma(x) = k^{(1)}x + k^{(3)}x^3 + k^{(5)}x^5 + ...$ Under these circumstances, large higher harmonic contributions are indeed associated with a strongly nonlinear behavior. On the contrary, as we have discussed, it is well-known that filled elastomers have a strong nonlinear behavior, in the sense that the elastic modulus $G'(\gamma_0,\omega) = e_1(\gamma_0,\omega)$ strongly depends on γ_0—which is the Payne effect—whereas higher harmonics are quite small, as we have seen both in experimental results and in simulations. Filled elastomers thus behave as nonlinear materials as regards their response to deformation of increasing amplitudes, but as almost linear materials under permanent oscillatory shear of fixed amplitude. The deformation amplitude γ_0 essentially modifies the lifetime distribution of glassy-bridges, and thus their contribution to the mechanical response. In particular, for deformation amplitudes larger than a few percent, or ten percents, depending on the systems, the difference between the initial distribution of relaxation times and the distribution during the experiment is huge (see Figure 9). On the other hand, the variation of the distribution of relaxation times in one strain cycle can be quite small as shown in the same figure. In a first approximation, the applied periodic deformation modifies the *average* distribution of relaxation times. If this distribution did remain constant—and thus equal to its average value—during the sinusoidal strain cycles, the response would be rigorously harmonic. However, as we have discussed, the lifetimes of glassy bridges evolve slightly during the deformation cycle, which results in small higher harmonic contributions.

VII. CONCLUSION

We have shown that the GBRM can account for the nonlinear behavior of filled elastomers submitted to large amplitude oscillatory shear experiments. Though they might be present in some experiments, and certainly at sufficiently large deformation amplitudes, the finite extensibility of the chains did not dominate the non sinusoidal response of the studied samples. Our point of view is that filled elastomers can be described by two elastic moduli: a rubbery one, and a glassy one, and the distribution of relaxation times associated with the glassy component. The applied strain does not change the elastic moduli, but modifies the lifetime distribution and thus, in particular, modifies the contribution of the glassy modulus. Thus, the main feature of the nonlinear response during periodic oscillations is the following: the amplitude of the deformation changes drastically the distribution of relaxation times as compared to the initial nondeformed system (Payne effect). The higher harmonic contributions are the results of fluctuations of the distribution of relaxation times during one period, and are a much smaller effect. The behavior of filled elastomers is at odds compared to systems which could be described by a nonlinear and nonretarded constitutive relation of the type $\sigma(x) = k^{(1)}x + k^{(3)}x^3 + k^{(5)}x^5 + ...$, for which there might be no possible distinction between the nonlinear behavior and the higher harmonics contributions. It appears thus that the glassy layer picture is able to explain various aspects of the mechanical behavior of filled elastomers: the reinforcement amplitudes; the Payne effect;[51] the recovery effects and specific features of the plastic properties of filled elastomers,[50,52] and the small—though not negligible—nonharmonic behavior of filled elastomers.

VIII. APPENDIX

The family of the Chebyshev polynomials of the first kind, T_n, form an Hilbertian basis of the $L^2[-1, +1]$ Hilbert space of

dx.doi.org/10.1021/ma202278e | Macromolecules 2012, 45, 2891−2904

squared integrable functions defined on [−1, +1], the corresponding scalar product being defined by:[73,74]

$$(f, g) = \int_{-1}^{+1} \frac{f(x)g(x)}{(1 - x^2)^{1/2}}\, dx \tag{24}$$

This means that (a) these polynomials satisfy to the orthogonal relations

$$(T_n, T_m) = \int_{-1}^{+1} \frac{T_n(x)T_m(x)}{(1 - x^2)^{1/2}}\, dx = \frac{\pi}{2}\delta_{n,m} \tag{25}$$

where $\delta_{n,m}$ is the Kronecker symbol which is one when $n = m$ and zero otherwise, (b) any function of $L^2[-1, +1]$ can be written in a unique way as an expansion

$$f(x) = \sum_{n=0}^{\infty} f_n T_n(x) \tag{26}$$

with

$$f_n = \frac{2}{\pi} \int_{-1}^{+1} \frac{T_n(x)f(x)}{(1 - x^2)^{1/2}}\, dx \tag{27}$$

The basic properties of these polynomials and their recursive relations, as well as the tabulation of the first of them are given in ref 74.

AUTHOR INFORMATION

Corresponding Author

*E-mail: samy.merabia@univ-lyon1.fr; didier.long-exterieur@eu.rhodia.com.

Notes

The authors declare no competing financial interest.

ACKNOWLEDGMENTS

The Ph.D. thesis of A.P. has been funded by Rhodia.

REFERENCES

(1) Nielsen, L. E.; Landel, R. F. *Mechanical Properties of Polymers and Composites*: Marcel Dekker: New York, 1994.
(2) Medalia, A. I. *Rubber Chem. Technol.* **1986**, *60*, 45−61.
(3) Edwards, D. C. *J. Mater. Sci.* **1990**, *25*, 4175−4185.
(4) Harwood, J. A. C.; Mullins, L.; Payne, A. R. *J. Appl. Polym. Sci.* **1965**, *9*, 3011−3021.
(5) Kraus, G. *Rubber Chem. Technol.* **1978**, *51*, 297−321.
(6) Kraus, G. *J. Appl. Polym. Sci. Appl. Polym. Symp.* **1984**, *39*, 75−92.
(7) Medalia, A. I. *Rubber Chem. Technol.* **1978**, *51*, 437−523.
(8) Payne, A. R. *J. Appl. Polym. Sci.* **1963**, *7*, 873.
(9) Payne, A. R. *J. Appl. Polym. Sci.* **1965**, *9*, 1073−1082.
(10) Heinrich, G.; Kluppel, M. *Adv. Polym. Sci.* **2002**, *160*, 1−44.
(11) Wang, M. J. *Rubber Chem. Technol.* **1998**, *71*, 520−589.
(12) Payne, A. R. *J. Appl. Polym. Sci.* **1962**, *21*, 368−372.
(13) Heinrich, G.; Kluppel, M.; Vilgis, T. A. *Reinf. Elastomers* **2002**, *6*, 195−203.
(14) Rendek, M.; Lion, A. *Zamm-Z. Angew. Math. Mech.* **2010**, *90*, 436−458.
(15) Rendek, M.; Lion, A. *KGK, Kautsch. Gummi Kunstst.* **2009**, *62*, 463−470.
(16) Lion, A.; Kardelky, C.; Haupt, P. *Rubber Chem. Technol.* **2003**, *76*, 533−547.
(17) Lion, A. *Continuum Mech. Thermodyn.* **1996**, *8*, 153−169.
(18) Hofer, P.; Lion, A. *J. Mech. Phys. Solids* **2009**, *57*, 500−520.
(19) Bueche, F. *J. Appl. Polym. Sci.* **1961**, *15*, 271−281.
(20) Berriot, J.; Lequeux, F.; Montès, H.; Monnerie, L.; Long, D.; Sotta, P. *J. Non-Cryst. Solids* **2002**, *307*, 719−724.
(21) Berriot, J.; Montes, H.; Lequeux, F.; Long, D.; Sotta, P. *Macromolecules* **2002**, *35*, 9756−9762.
(22) Berriot, J.; Montes, H.; Lequeux, F.; Long, D.; Sotta, P. *Europhys. Lett.* **2003**, *64*, 50−56.
(23) Montes, H.; Lequeux, F.; Berriot, J. *Macromolecules* **2003**, *36*, 8107−8118.
(24) Montes, H.; Chaussée, T.; Papon, A.; Lequeux, F.; Guy, L. *EPJE* **2010**, *31*, 263−268.
(25) Kaufmann, S.; Slichter, W. P.; Davis, D. D. *J. Polym. Sci., Part A2* **1971**, *9*, 829−839.
(26) Haidar, B.; Salah Deradji, H.; Vidal, A.; Papirer, E. *Macromol. Symp.* **1996**, *108*, 147−161.
(27) Tsagaropoulos, G.; Eisenberg, A. *Macromolecules* **1995**, *28*, 6067−6077.
(28) Tsagaropoulos, G.; Eisenberg, A. *Macromolecules* **1995**, *28*, 396−398.
(29) Tsagaropoulos, G.; Kim, J.-S.; Eisenberg, A. *Macromolecules* **1996**, *29*, 2222−2228.
(30) Struik, L. C. E. *Polymer* **1987**, *28*, 1521−1533.
(31) Wallace, W. E.; van Zanten, J. H.; Wu, W. L. *Phys. Rev. E.* **1995**, *52*, R3329.
(32) van Zanten, J. H.; Wallace, W. E.; Wu, W. L. *Phys. Rev. E.* **1996**, *53*, R2053.
(33) Grohens, Y.; Brogly, M.; Labbe, C.; David, M.-O.; Schultz, J. *Langmuir* **1998**, *14*, 2929−2932.
(34) Keddie, J. L.; Jones, R. A. L.; Cory, R. A. *Europhys. Lett.* **1994**, *27*, 59−64.
(35) Mattsson, J.; Forrest, J. A.; Borjesson, J. *Phys. Rev. E.* **2000**, *62*, 5187−5200.
(36) Hall, D. B.; Dhinojwala, A.; Torkelson, J. M. *Phys. Rev. Lett.* **1997**, *79*, 103−106.
(37) Long, D.; Lequeux, F. *EPJ E* **2001**, *4*, 371−387.
(38) Merabia, S.; Long, D. *EPJ E* **2002**, *9*, 195−207.
(39) Merabia, S.; Sotta, P.; Long, D. *EPJ E* **2004**, *15*, 189−210.
(40) Sotta, P.; Long, D. *EPJ E* **2003**, *11*, 375−388.
(41) Ellison, C. J.; Torkelson, J. M. *Nat. Mater.* **2003**, *2*, 695−700.
(42) Ciprari, D.; Jacob, K.; Tannenbaum, R. *Macromolecules* **2006**, *39*, 6565−6573.
(43) Putz, K.; Krishnamoorti, R.; Green, P. F. *Polymer* **2007**, *48*, 3540−3545.
(44) Kropka, J. M.; Putz, K. W.; Pryamitsyn, V.; Ganesan, V.; Green, P. F. *Macromolecules* **2007**, *40*, 5424−5432.
(45) Baeurle, S. A.; Usami, T.; Gusev, A. A. *Polymer* **2006**, *47*, 8604−8617.
(46) Rao, Y.-Q.; Pochan, J. M. *Macromolecules* **2007**, *40*, 290−296.
(47) Rittigstein, P.; Priestley, R. D.; Broadbelt, L. J.; Torkelson, J. M. *Nat. Mater.* **2007**, *6*, 278−282.
(48) Gusev, A. A. *Macromolecules* **2006**, *39*, 5960−5962.
(49) Kalfus, J.; Jancar, J. *Polymer* **2007**, *48*, 3935−3937.
(50) Merabia, S.; Sotta, P.; Long, D. R. *J. Polym. Sci., Part B: Polym. Phys.* **2010**, *48*, 1495−1508.
(51) Merabia, S.; Sotta, P.; Long, D. R. *Macromolecules* **2008**, *41*, 8252−8266.
(52) Chazeau, L.; Brown, J. D.; Yanyo, L. C.; Sternstein, S. S. *Polym. Compos.* **2000**, *21*, 202−222.
(53) Roland, C. M. *J. Rheol.* **1990**, *1*, 25−34.
(54) Leblanc, J. L. *Rubber Chem. Technol.* **2005**, *78*, 54−75.
(55) Leblanc, J. L. *J. Appl. Polym. Sci.* **2006**, *100*, 5102−5118.
(56) Wagner, M. H.; Rolon-Garrido, V. H.; Hyun, K.; Wilhelm, M. *J. Rheol.* **2011**, *55*, 495−516.
(57) Papon, A.; Montes, H.; Lequeux, F.; Guy, L. *J. Polym. Sci., Part B: Polym. Phys.* **2010**, *48*, 2490−2496.
(58) Cho, K. S.; Hyun, K.; Ahn, K. H.; Lee, S. J. *J. Rheol.* **2005**, *3*, 747−758.
(59) Leblanc, J. L. *Rubber Chem. Technol.* **2010**, *83*, 65−96.
(60) Klein, C. O.; Spiess, H. W.; Calin, A.; Balan, C.; Wilhem, M. *Macromolecules* **2007**, *40*, 4250−4259.
(61) Ewoldt, R. H.; Hosoi, A. E.; McKinley, G. H. *J. Rheol.* **2008**, *52*, 1427−1458.

(62) Ng, T. S. K.; McKinley, G. H. *J. Rheol.* **2011**, *55*, 627−654.
(63) Ewoldt, R. H.; Clasen, C.; Hosoi, A. E.; McKinley, G. H. *Soft Matter* **2007**, *3*, 634−643.
(64) Yu, W.; Wang, P.; Zhou, C. *J. Rheol.* **2009**, *53*, 215−238.
(65) Hyun, K.; Wilhelm, M.; Klein, C. O.; Cho, K. S.; Nam, J. G.; Ahn, K. H.; Lee, S. J.; Ewoldt, R. H.; McKinley, G. H. *Prog. Polym. Sci.* **2011**, *36*, 1697−1753.
(66) Wu, S. *Polym. Int.* **1992**, *29*, 229.
(67) Ferry, J. D. *Viscoelastic Properties of Polymers*: Wiley: New York, 1980.
(68) Merabia, S.; Long, D. *J. Chem. Phys.* **2006**, *125*, 234801.
(69) Long, D.; Sotta, P. *IMA Volume in Mathematics and its Applications: Modeling of Soft Matter*; Calderer, M.-C. T., Terentjev, E. M., Eds.; Springer Science+Business Media, Inc.: New York, 2005; Vol. *141*, pp 205−234.
(70) Long, D.; Sotta, P. *Macromolecules* **2006**, *39*, 6282−6297.
(71) Long, D.; Sotta, P. *Rheol. Acta* **2007**, *44*, 1029−1044.
(72) Mark, J. E. In *Physical Properties of Polymers Handbook*; American Institute of Physics: Melville, NY, 1996.
(73) Riesz, F.; Sz.-Nagy, B. *Functional Analysis*; Dover: New York, 1990.
(74) Abramowitz, M.; Stegun, I. A. *Handbook of Mathematical Functions*; Dover: New York, 1964.
(75) Gardel, M. L.; Shin, J. H.; MacKintosh, F. C.; Mahadevan, L.; Matsudaira, P.; Weitz, D. A. *Science* **2004**, *304*, 1301−1305.
(76) Ewoldt, R. H.; Hosoi, A. E.; McKinley, G. H. *Integr. Comp. Biol.* **2009**, *49*, 40−50.

Macromolecules

Article

pubs.acs.org/Macromolecules

Chebyshev Collocation in Polymer Field Theory: Application to Wetting Phenomena

Su-Mi Hur,[†,⊥] Carlos J. García-Cervera,[‡] and Glenn H. Fredrickson*[,†,§,⊥]

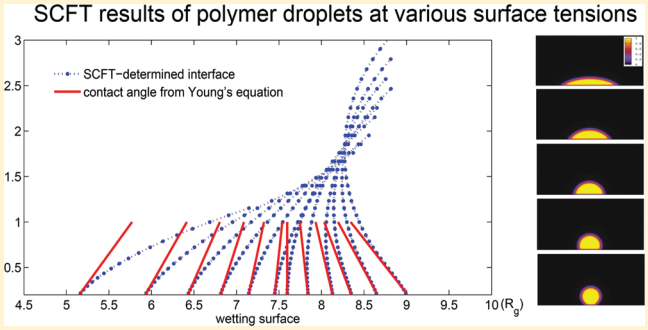
[†]Department of Chemical Engineering, University of California, Santa Barbara, California 93106, United States

[‡]Department of Mathematics, University of California, Santa Barbara, California 93106, United States

[§]Department of Materials, University of California, Santa Barbara, California 93106, United States

[⊥]Materials Research Laboratory, University of California, Santa Barbara, California 93106, United States

ABSTRACT: An efficient numerical self-consistent field theory (SCFT) algorithm is developed for polymer systems subject to nonperiodic boundary conditions. The method involves collocation with a Chebyshev polynomial basis in order to solve the modified diffusion equations of SCFT and relax the fields experienced by polymer segments to a consistent mean-field solution. For Dirichlet boundary conditions on a block copolymer film, we demonstrate that the Chebyshev scheme preserves spectral accuracy, unlike existing methods based on collocation with a Fourier sine basis or finite differences. This advantage is shown to translate into significant benefits for accuracy, computational cost, and memory requirements in high-resolution SCFT simulations of meso and nanostructured polymer thin films. As a nontrivial application of the new Chebyshev method, the static wetting behavior of a two-dimensional fluid polymer droplet on a solid surface was investigated via SCFT simulations. The interaction between the surface and polymer segments is modeled with a local contact Flory–Huggins parameter that can be mapped to a surface tension. Contact angles obtained from simulations with varying surface and interfacial tensions are shown to be consistent with Young's equation. The results demonstrate that Chebyshev-based SCFT is a viable and efficient technique for exploring complex morphologies and equilibrium phenomena in polymer thin films.



1. INTRODUCTION

Self-consistent field theory (SCFT) has proven to be an extraordinarily successful theory and has been widely used for predicting the equilibrium behavior of structured polymers, especially that of multicomponent blends and molten block copolymers.[1,2] The most expensive step in SCFT simulations involves the solution of a modified diffusion equation (MDE) for the chain propagator, which describes the spatial distribution of polymer segments in a prescribed potential field. Two efficient and widely used numerical approaches to solve MDEs are the spectral method introduced in 1994 by Matsen and Schick[3] and a pseudospectral, operator-splitting method introduced in 2002 by a group at Los Alamos.[4,5] In the former approach, the spatial part of the differential operator is projected onto a truncated basis function space (the Galerkin procedure) and the chain contour evolution is treated analytically, i.e. a semidiscrete type of approach. In contrast, the pseudospectral approach utilizes an operator splitting scheme for contour stepping that is second-order accurate in the contour variable s and imposes spectral collocation on the split spatially dependent operators. This so-called split step Fourier method was previously shown to be an excellent method for solving the time-dependent Schrödinger equation.[6−8]

In the polymer context, the spectral method is superior in computational efficiency to the pseudospectral method for high-accuracy SCFT calculations of free energies and phase boundaries of block copolymers[9] when the symmetries of all phases are known. The spectral method compensates for its poor M^3 scaling, where M is the number of spatial grid points or spectral components, by the fact that it can readily incorporate the symmetry of the morphology to reduce M and thus achieve comparable accuracy with fewer basis functions than the pseudospectral method; the latter only being efficiently implemented in parallelepiped computational cells. However, in many cases where advanced knowledge of the symmetry is not available, or where no symmetry is expected, the pseudospectral method is advantaged. Its lower computational cost of $O(M \log(M))$ further enables the efficient execution of large cell simulations in multidimensions. Studies related to defect formation and populations, screening of large parameter spaces to discover new or desirable types of self-assembly, and "field-theoretic simulations" (FTS) that go beyond the mean-field assumption in SCFT and incorporate field fluctuations are situations for which the pseudospectral approach is particularly well suited.

Received: November 2, 2011
Revised: February 22, 2012
Published: March 9, 2012

 © 2012 American Chemical Society

While the above SCFT approaches were initially developed for and widely applied to the study of bulk equilibrium properties of polymers, i.e. macroscopic properties far from any bounding surfaces, scientific and technological interest has grown considerably in recent years in *thin films* of block copolymers and other self-assembling polymer systems. In part, this has been driven by the microelectronics industry, which has been exploring self-assembling block copolymer thin films as an advanced lithography tool for patterning devices on 10 nm scales.[10−13] This emerging technological interest has prompted extensive modeling and SCFT simulations of polymeric systems in confined geometries.[14−19]

Unlike a bulk, unbounded fluid, where periodic boundary conditions are normally applied, SCFT or FTS simulations of a confined polymeric system require nonperiodic boundary conditions to be imposed on the chain propagator. To model a boundary that is impenetrable, such as a solid wall, a homogeneous Dirichlet boundary condition for the chain propagator in the MDE is a natural choice,[20] as this boundary condition on the propagator also implies that the average densities of all chain segments vanish at the solid boundary. However, in polymer solutions of high concentration or molten polymers, the total polymer segment density rises from zero to the uniform bulk concentration very rapidly away from the surface. To avoid the computational burden of resolving this sharp surface feature in a numerical simulation with a uniform mesh, effective boundary conditions have been employed. In the case of neutral surfaces with no preferential affinity, homogeneous Neumann (reflective) boundary conditions are appropriate.[14,21,22] However, reflective boundary conditions do not capture a variety of effects resulting from the ignored boundary layer, such as entropically driven surface phenomena, and most real surfaces exhibit some degree of preferential affinity when exposed to multiple fluid components. For such "selective" bounding surfaces that energetically favor certain polymer species, mixed or Robin type boundary conditions on the propagators are most appropriate.[23,24] Unfortunately, however, an incompressible model of multiple polymer components with Robin boundary conditions requires imposing additional nonlinear conditions among parameters that appear in the boundary conditions.[2] An added complication is that Fourier basis functions are not suitable for pseudospectral computations with Robin boundary conditions.

Matsen introduced a useful way of implementing an attractive interaction between a surface and a particular polymer component, while still preserving a vanishing total polymer segment density at the solid boundary.[15] Through this *masking method*, a generalized incompressibility condition is imposed that specifies a (total) polymer density function (a "mask") that vanishes outside the physical domain and rises smoothly away from the domain boundaries to the bulk polymer density inside the physical domain. The entropy loss that the polymer chains experience due to the surface is related to the shape of masking function and its width. Surface field terms in the model proportional to the product of the mask function and individual species densities control the strength of surface affinity. In such a masking approach, both periodic and nonperiodic boundary conditions can be applied. Periodic boundary conditions (PBCs) are most useful when the mask is used to produce a confined polymer domain of complex shape; the masked region is embedded in a larger domain that is a parallelepiped and is subject to PBCs. While this approach has the benefit of being adaptable to a wide range of confinement geometries,[18] it results in a loss of computational efficiency because it is necessary to resolve and compute thoughout the entire simulation domain, which extends outside of the physical domain. For simply shaped physical domains, such as a planar polymer thin film, imposing Neumann, Dirichlet, or Robin boundary conditions on the MDE, rather than PBCs, is evidently preferable.

Within the pseudospectral framework, the most straightforward way to solve problems where homogeneous Dirichlet or Neumann boundary conditions are imposed at opposing boundaries is to substitute a sine or cosine basis, respectively, for the plane wave basis used in pseudospectral treatments of a periodic system. Unfortunately, however, such Fourier sine (cosine) solutions impose more severe restrictions on an approximated function in order to achieve ideal "spectral" accuracy. Spectral accuracy refers to a situation where functional approximation errors decrease faster than any fixed negative power of the number of basis functions M. To achieve spectral accuracy with a truncated sine (cosine) representation of a function requires not only infinite smoothness within the domain, but all even (odd) derivatives of the function of second and higher order must vanish at both boundaries.[25] Unfortunately, these conditions are usually not met for most polymer field theory problems in confined geometries. Furthermore, Fourier series expansions cannot be used to impose Robin/mixed boundary conditions, which are appropriate for surfaces with preferential affinity. While the masking method can accommodate surface selectivity, the use of plane waves (and the *uniform* collocation grid necessary to enable fast Fourier transforms) demands a large number of basis functions in order to resolve the sharp rise in polymer segment density near a surface.

For all these reasons, an alternative to masking and sine and cosine spectral collocation for confined polymer problems with nonperiodic boundary conditions would be highly desirable. An ideal method would utilize irregular grids with more collocation points placed in the boundary regions, still enable the use of fast Fourier transforms (FFTs) for efficient $O(M \log M)$ computations, and exhibit spectral accuracy. To this end, and in place of trigonometric interpolants on equispaced points, we have adapted SCFT algorithms to use algebraic Chebyshev polynomials on irregular grids using Chebyshev points, which are clustered near boundaries. Chebyshev polynomials enable high accuracy spectral approximations without suffering boundary restrictions, and they still can be applied in tandem with the fast Fourier transform (FFT), which permits rapid transformations from a set of spectral coefficients to a set of collocated values of a function in the spatial domain.[25,26]

In this study, we introduce a pseudospectral algorithm for solving the MDE of SCFT that can handle nonperiodic boundary conditions efficiently while conserving spectral accuracy. Such a method is ideal for studying structured polymeric fluids under confinement. For reasons described below, we have chosen to retain an operator splitting algorithm in which the contour evolution operator is separated into a term involving just the potential field and a second term is $\sim\exp(\Delta s \nabla^2)$ corresponding to free diffusion. Unlike the case when Fourier basis functions are used, the Laplacian term is not diagonal in the transformed Chebyshev space. To overcome this, a Padé approximation is used to reexpress the operator in a form with consistent second order accuracy in the contour step Δs that can be applied as a series of two Helmholtz-type equations. A literature scheme using tau collocation (and a Chebyshev polynomial basis) provides an efficient $O(M)$ numerical algorithm for solving such Helmholtz equations.[27] In section 2, we summarize a set of SCFT model equations for an AB diblock copolymer melt and introduce the

detailed numerical methods. Subsequently in section 3, the performance of the new Chebyshev pseudospectral SCFT method and methods based on collocation with trigonometric sine and cosine functions are compared for a confined compressible AB diblock copolymer melt. Last, in section 4, we present a nontrivial application of the new algorithm by simulating the static wetting behavior of a two-dimensional polymer droplet on a flat surface and observing contact angle variations with surface energetics. We relate the Flory−Huggins interaction parameters in the model to surface tensions, and polymer droplets of various contact angles are simulated by modulating the Flory−Huggins parameters.

2. SCFT MODEL AND NUMERICAL ALGORITHM

In the following section we briefly describe the SCFT models and numerical methods used in this study. A detailed algorithm for the diffusion equation solver using operator splitting and Chebyshev polynomial basis functions is presented in section 2.2.

2.1. SCFT Model. To evaluate the performance of Chebyshev bases to solve SCFT equations, we have studied a standard model system comprising an AB diblock copolymer melt. The model equations for AB block copolymers in confinement is built on the standard Gaussian-chain model with a harmonic stretching energy. The interaction energy is modeled with a Flory-type local contact interaction between dissimilar A and B polymer segments, denoted by χ. In addition to the harmonic stretching energy of the Gaussian chains and the segmental interaction energy, a penalty for local density fluctuations away from the average segment density ρ_0 is modeled using the compressible Helfand model.[28] A homogeneous Dirichlet boundary condition is used to implement confinement.

We consider an nVT ensemble with n monodisperse AB diblock copolymer chains, each composed of N segments, of which the A block accounts for fN segments and the B-block for $(1-f)N$ segments, respectively. We assume equal statistical lengths for the two segment types and equal segment volumes $v_0 = 1/\rho_0$, such that the total volume of the melt is $V = nN/\rho_0$. The parameter f can thus be interpreted as the average volume fraction of type A segments in the melt. In the Helfand-type compressible model that we adopt, a quadratic energy penalty for total density variations is included in the partition function:

$$\exp[-\beta U_{comp}] = \exp\left[-\frac{\zeta}{2\rho_0}\int_V d\mathbf{r}\,(\sum_i \hat{\rho}_i(\mathbf{r}) - \rho_0)^2\right] \quad (1)$$

where the stiffness parameter ζ controls the strength of the penalty for local density fluctuations away from the average density ρ_0, and $\hat{\rho}_i(\mathbf{r})$ denotes the microscopic density of polymer segments of type i. β is the nondimensionalizing factor, $1/k_BT$, where k_B and T are the Boltzmann constant and temperature. The incompressible model is approached in the limit $\zeta \to \infty$. Throughout this study, we set $\zeta N = 100$, which is large enough to accurately reproduce the phases and phase boundaries observed in the incompressible model, while dramatically speeding up convergence of the SCFT field iterations.[29,30] In addition, use of the compressible model enables the polymer density to decay near the boundary, so there is no conflict with an imposed Dirichlet boundary condition. As ζN increases, the boundary layer in density at the surface becomes sharper and more spatial resolution is required to accurately resolve the propagators and fields.

The many-body problem inherent in a system of interacting polymer chains can be converted into a statistical field theory through a formally exact Hubbard-Stratonovich transformation.[2] For the present model, the field-theoretic representation of the canonical partition function can be expressed in normalized units as:

$$Z = \int \mathcal{D}W_+\mathcal{D}W_- \exp(-H[W_+, W_-]) \quad (2)$$

where a functional integral appears over two real fields, $iW_+(\mathbf{x})$ and $W_-(\mathbf{x})$, and the effective Hamiltonian for the diblock copolymer melt has the following form:

$$H[W_+, W_-]/C = \int_{\bar{V}} d\mathbf{x}\left[\frac{1}{\chi N}W_-^2(\mathbf{x}) - \frac{2\zeta N}{\chi N + 2\zeta N}iW_+(\mathbf{x}) - \frac{1}{\chi N + 2\zeta N}(iW_+(\mathbf{x}))^2\right] - \bar{V}\ln Q[W] \quad (3)$$

In this expression, $C = \rho_0 R_g^3/N$ is a dimensionless concentration of chains, and $\mathbf{x}$ $(=\mathbf{r}/R_g)$ and $\bar{V} = V/R_g^3$ are dimensionless positions and volumes reduced using the unperturbed radius of gyration R_g of a copolymer. The complex-valued auxiliary potential fields, W_A and W_B, that act on A and B segments, respectively, are defined as $W_A = iW_+ - W_-$ and $W_B = iW_+ + W_-$, where W_+ is a pressure-like field that couples to total (A + B) density variations and W_- is an exchange potential field conjugate to the difference between the A and B segment densities.

$Q[W]$ is the normalized single-chain partition function for a diblock copolymer defined by

$$Q = \frac{1}{\bar{V}}\int d\mathbf{x}\, q(\mathbf{x}, 1; [W]) \quad (4)$$

where the (forward) chain propagator $q(\mathbf{x},s;[W])$, which gives the statistical weight of observing the end of a polymer (subject to the fields $W_\pm(\mathbf{x})$) with contour length s at normalized position $\mathbf{x}$, satisfies

$$\frac{\partial}{\partial s}q(\mathbf{x}, s; [W]) = \nabla^2 q(\mathbf{x}, s; [W]) - W(\mathbf{x}, s)q(\mathbf{x}, s; [W]) \quad (5)$$

The field W appearing in this equation is defined by

$$W(\mathbf{x}, s) = \begin{cases} iW_+(\mathbf{x}) - W_-(\mathbf{x}), & 0 \le s \le f \\ iW_+(\mathbf{x}) + W_-(\mathbf{x}), & f < s \le 1 \end{cases} \quad (6)$$

and eq 5 is to be solved solved subject to the uniform "initial" condition $q(\mathbf{x},0)=1$. The physical content of this initial condition is that a polymer of zero length $s = 0$ is not influenced by the field.

Reduced segment density operators (volume fractions) for A and B segments of the block copolymer can be evaluated from the chain propagator $q(\mathbf{x},s;[W])$ and a corresponding complementary (backward) propagator $q_c(\mathbf{x},s;[W])$

$$\phi_A(\mathbf{x}) = \frac{\rho_A}{\rho_0} = \frac{1}{Q}\int_0^f ds\, q(\mathbf{x}, s; [W])q_c(\mathbf{x}, 1-s; [W]) \quad (7)$$

$$\phi_B(\mathbf{x}) = \frac{\rho_B}{\rho_0} = \frac{1}{Q}\int_f^1 ds\, q(\mathbf{x}, s; [W])q_c(\mathbf{x}, 1-s; [W]) \quad (8)$$

dx.doi.org/10.1021/ma202427n | Macromolecules 2012, 45, 2905−2919

The complementary propagator satisfies a diffusion equation very similar to eq 5, but it is propagated from a uniform initial condition backward from the B end of the diblock ($s = 1$).[2]

The above equations constitute a statistical field theory model of a diblock melt in formally exact correspondence with the starting molecular model. In the present work, we will invoke an approximation known as self-consistent field theory (SCFT), where the partition function and averages of observable operators are assumed to be dominated by a single "mean-field" configuration of the two fields $W^*_{\pm}(\mathbf{x})$. These mean fields are obtained by solving the saddle point equations given by:

$$\left.\frac{\delta H}{\delta i W_+}\right|_{W^*_{\pm}} = \phi_A(\mathbf{x}) + \phi_B(\mathbf{x}) - \frac{2\zeta N}{\chi N + 2\zeta N} - \frac{2iW^*_+(\mathbf{x})}{\chi N + 2\zeta N} = 0 \tag{9}$$

$$\left.\frac{\delta H}{\delta W_-}\right|_{W^*_{\pm}} = \frac{2}{\chi N} W^*_-(\mathbf{x}) - \phi_A(\mathbf{x}) + \phi_B(\mathbf{x}) = 0 \tag{10}$$

Since we work in the canonical ensemble, the Helmholtz free energy immediately follows from:

$$\beta A = -\ln Z \approx H[W^*_+, W^*_-] \tag{11}$$

The mean-field approximation inherent in SCFT proves to be asymptotically exact in the $C \to \infty$ limit and is accurate for block copolymer melts of high molecular weight, except very close to the order−disorder transition.[31] In situations where SCFT breaks down, the full field theory can be stochastically sampled using field-theoretic simulation (FTS) techniques,[2,32] although such methods will not be discussed here.

The numerical SCFT scheme utilized in this study amounts to the following steps:

1. Initialize the fields $W_{\pm}(\mathbf{x})$ with a random number generator.
2. Solve the modified diffusion equations for the chain propagators q and q_c using a pseudospectral method.
3. Calculate the normalize partition function Q and density operators based on the result of step 2.
4. Update the $W_{\pm}(\mathbf{x})$ fields using a relaxation method to obtain a solution $W^*_{\pm}(\mathbf{x})$ of eqs 9 and 10.
5. Repeat steps 2−4 until a convergence criterion has been satisfied.

In section 4, we report on studies of wetting/dewetting phenomena on a planar surface using a compressible blend of A and B homopolymers. The basic model equations and numerical SCFT scheme are the same as before, but there is an additional term for the interaction between a specified wall profile ($\phi_w(\mathbf{x})$) and the two species of polymer segments, so that the resulting Hamiltonian has the following form:

$$H[W_+, W_-]/C = \int_{\bar{V}} d\mathbf{x} \left[\frac{1}{\chi N} W^2_-(\mathbf{x}) - \frac{2\zeta N}{\chi N + 2\zeta N} iW_+(\mathbf{x}) - \frac{1}{\chi N + 2\zeta N} (iW_+(\mathbf{x}))^2 \right. \tag{12}$$

$$\left. + \frac{\chi_{wA}N - \chi_{wB}N}{\chi N} \phi_w(\mathbf{x}) W_-(\mathbf{x}) - \frac{\chi_{wA}N + \chi_{wB}N}{\chi N + 2\zeta N} \phi_w(\mathbf{x}) iW_+(\mathbf{x}) \right] \tag{13}$$

$$- \bar{V} v_A \ln Q_A[W_A] - \bar{V} v_B \ln Q_B[W_B] \tag{14}$$

where $Q_A[W_A]$ and $Q_B[W_B]$ are the single-chain partition functions for A and B homopolymers, respectively, and χ_{wA} and χ_{wB} are Flory parameters describing the strength of the interactions of the A and B segments with the surface. The wall profile is a smooth function that is unity at the surface and decays to zero into the interior of the fluid. A particular tanh form for ϕ_w is described in section 4.1. v_A and v_B are the volume fractions of A and B homopolymers, respectively, and ϕ_A and ϕ_B are evaluated from the chain propagators for A and B, $q_A(\mathbf{x},s;[W_A])$ and $q_B(\mathbf{x},s;[W_B])$

$$\phi_A(\mathbf{x}) = \frac{\rho_A}{\rho_0} = \frac{v_A}{Q_A} \int_0^1 ds\, q_A(\mathbf{x}, s; [W_A]) q_A(\mathbf{x}, 1-s; [W_A]) \tag{15}$$

$$\phi_B(\mathbf{x}) = \frac{\rho_B}{\rho_0} = \frac{v_B}{Q_B} \int_0^1 ds\, q_B(\mathbf{x}, s; [W_A]) q_B(\mathbf{x}, 1-s; [W_B]) \tag{16}$$

2.2. Chebyshev Pseudospectral Solution of the MDE.

In this section, we discuss a Chebyshev polynomial based pseudospectral method for the numerical solution of the modified diffusion equation (MDE) (eq 5). As mentioned in the introduction, the standard pseudospectral approach[4] for solving the MDE (eq 5) with Fourier bases relies on a Trotter-type operator splitting scheme for the evolution operator that is used to step the propagator forward in s from the initial condition:

$$q(s + \Delta s, \mathbf{x}; W) = e^{\Delta s \mathcal{L}} q(s, \mathbf{x}; W) \tag{17}$$

$$e^{\Delta s \mathcal{L}} = e^{-\Delta s W/2} e^{\Delta s \nabla^2} e^{-\Delta s W/2} + O(\Delta s^3) \tag{18}$$

In this propagation method, the operator $\exp(-\Delta s W/2)$ is applied locally on a collocation grid in real space, the operator $\exp(\Delta s \nabla^2)$ is applied locally in Fourier space, and a discrete Fourier transform (DFT) is used to affect the transformations between the two spaces. This approach for the case of PBCs has the benefit of unconditional stability, second order accuracy in s, a low computational cost dominated by the DFT (of order M log M operations), and spectral accuracy in space. For Dirichlet or Neumann boundary conditions, the same approach can be followed, but substituting plane wave collocation with sine and cosine based collocation and discrete sine (DST) and discrete cosine (DCT) transforms, respectively, for the DFT. For the latter two types of boundary conditions, the method generally suffers a loss of spectral accuracy, although the stability and efficiency benefits are preserved.

As we will compare the performance of our new Chebyshev pseudospectral algorithm for the case of Dirichlet boundary conditions against sine pseudospectral solutions, a few details are provided on the latter. We utilize a type I DST (DST-I) to transform between the collocated values of a function and its sine spectral coefficients. In DST-I, equally spaced collocation points indexed with $(1, ..., N_x - 1)$ are situated in the interior domain $(x \in (0,L))$ excluding the zero points at the boundaries at $x = 0$ and $x = L$. The operator $e^{\Delta s \nabla^2}$ is applied by performing a DST-I of $e^{-\Delta s W} q(s, x; W)$ evaluated on the collocation grid, appending a factor of $e^{-\Delta s \pi^2 j^2/L^2}$ to the jth sine coefficient of the result for $j = 1, 2, ..., N_x - 1$, and back-transforming via a DST-I to real space.

The loss of spectral accuracy intrinsic to the use of trigonometric bases for nonperiodic boundary conditions can be overcome by using bases constructed from Chebyshev polynomials, defined by $T_k(x) = T_k(\cos\theta) = \cos(k \arccos x)$ and with an appropriate choice of collocation grid.[25,26]

However, the diffusion operator needed for the splitting scheme, $e^{\Delta s \nabla^2}$, is no longer diagonal in the Chebyshev representation. One obvious option we considered was a backward differentiation formula (BDF) for the MDE that avoids the use of this operator, replacing it with the solution of a Helmholtz-type equation at each contour step. Unfortunately, both second and fourth-order BDF schemes generally do not perform well in SCFT as compared with operator splitting.[33] We have therefore sought ways of efficiently computing $e^{\Delta s \nabla^2}$ in the Chebyshev representation consistent with the second-order accurate update formula eq 18, and preserving stability and spectral accuracy in space. While the present work compares the performance of second-order accurate formulas in Δs, it should be noted that the accuracy of contour stepping can be readily improved either through a fourth-order splitting method[34] or Richardson extrapolation.[35]

In presenting the Chebyshev scheme, it is convenient to consider the simplest case of a one-dimensional domain $x \in [0,L]$ with homogeneous Dirichlet conditions imposed a both boundaries. A prerequisite step is to rescale x to a new independent variable $z = 2x/L - 1$ that varies over $-1 \le z \le 1$. The modified diffusion equation is rescaled accordingly

$$\frac{\partial q}{\partial s} = \frac{1}{K}\nabla_z^2 q - Wq \tag{19}$$

where $K = L^2/4$. Chebyshev collocation can be easily performed since Chebyshev polynomials are cosine functions after a change in the independent variable. In particular, the most convenient grid uses the minmax points of $T_{N_x}(z) = \cos(N_x\theta)$, namely

$$z_k = \cos\theta_k,$$
$$\theta_k = \frac{k\pi}{N_x} \quad (k = 0, 1, ..., N_x), \tag{20}$$

These Chebyshev points are equally spaced on the unit circle in θ, but are nonuniform in $z \in [-1,1]$ and concentrated near the two boundaries.

We consider "tau" approximations to functions $u(z)$ based on truncated Chebyshev polynomial expansions, i.e.

$$u(z) \approx \sum_{n=0}^{N_x} a_n T_n(z) \tag{21}$$

Collocation of this expression at the Chebyshev points z_k, thus produces a discrete cosine transform of type I (DCT-I):

$$u(z_k) = \sum_{n=0}^{N_x} a_n T_n(z_k) = \sum_{n=0}^{N_x}{}'' \gamma_n a_n T_n(z_k)$$
$$= \sum_{n=0}^{N_x}{}'' (\gamma_n a_n)\cos[\pi kn/(N_x)] = DCT\{\gamma_n a_n\}_k$$
$$(k = 0, 1, ..., N_x) \tag{22}$$

where

$$\gamma_n = \begin{cases} 2, & n = 0 \text{ or } N_x \\ 1, & 0 < n < N_x \end{cases} \tag{23}$$

and consistent with standard DCT-I convention, a double primed sum is defined as

$$\sum_{n=0}^{N_x}{}'' f_n \equiv \frac{1}{2}(f_0 + f_{N_x}) + \sum_{n=1}^{N_x - 1} f_n \tag{24}$$

The inverse transform to obtain the Chebyshev coefficients of a function is correspondingly

$$a_n = \frac{2}{\gamma_n N_x}\sum_{k=0}^{N_x}{}'' u(z_k)\cos[\pi kn/(N_x)] = \frac{DCT^{-1}\{u(z_k)\}_n}{\gamma_n}$$
$$(n = 0, 1, ..., N_x) \tag{25}$$

As discussed above, we follow a Trotter-type splitting approach in which the contour evolution operator of the rescaled MDE eq 19 is split into free potential and free diffusion parts. The problematic free diffusion operator is further approximated using a Padé approximation as follows

$$e^{\Delta s/K\nabla_z^2} = \frac{1}{1 - \frac{\Delta s}{K}\nabla_z^2 + \frac{1}{2}\left(\frac{\Delta s}{K}\nabla_z^2\right)^2} + O(\Delta s^3) \tag{26}$$

As the Padé approximation has second order accuracy, the truncation error in the overall contour stepping operator

$$e^{-\Delta s W/2}\left[\frac{1}{1 - \frac{\Delta s}{K}\nabla^2 + \frac{1}{2}\left(\frac{\Delta s}{K}\nabla^2\right)^2}\right]e^{-\Delta s W/2} \tag{27}$$

remains as $O(\Delta s^3)$. Equation 26 can be conveniently partitioned as

$$\frac{1}{1 - \frac{\Delta s}{K}\nabla_z^2 + \frac{1}{2}\left(\frac{\Delta s}{K}\nabla_z^2\right)^2}$$
$$= 2\left(\frac{K}{\Delta s}\right)^2 \frac{1}{\left[\nabla_z^2 - \frac{K}{\Delta s}(1+i)\right]}\frac{1}{\left[\nabla_z^2 - \frac{K}{\Delta s}(1-i)\right]} \tag{28}$$

Thus, the operator in eq 26 can be applied by two successive solutions of a Helmholtz-type equation to find $u(z)$ satisfying

$$[\nabla_z^2 - \lambda]u(z) = f(z) \tag{29}$$

for a prescribed $f(z)$, each solution using a different complex parameter $\lambda = K/\Delta s(1 \pm i)$.

To solve the 1-D Helmholtz equation, we use an existing efficient Chebyshev tau numerical algorithm whose derivation is outlined in a text by Canuto et al.[27] Specifically, the algorithm utilizes a recursion relation to express the equations for the Chebyshev coefficients a_n of the unknown function $u(z)$, i.e. $u(z) \approx \sum_{n=0}^{N_x} a_n T_n(z)$, in pentadiagonal form

$$-\frac{c_{n-2}\lambda}{4n(n-1)}a_{n-2} + \left(1 + \frac{\lambda\beta_n}{2(n^2-1)}\right)a_n$$
$$- \frac{\lambda\beta_{n+2}}{4n(n+1)}a_{n+2}$$
$$= \frac{c_{n-2}}{4n(n-1)}\hat{f}_{n-2} - \frac{\beta_n}{2(n^2-1)}\hat{f}_n$$
$$+ \frac{\beta_{n+2}}{4n(n+1)}\hat{f}_{n+2} \quad (n = 2, ..., N_x) \tag{30}$$

dx.doi.org/10.1021/ma202427n | Macromolecules 2012, 45, 2905−2919

where $\hat{f}_n$ denotes the Chebyshev coefficients of $f(z_k)$,

$$\beta_n = \begin{cases} 1, & 0 \le n \le N_x - 2 \\ 0, & n > N_x - 2 \end{cases} \tag{31}$$

and

$$c_k = \begin{cases} 2, & k = 0 \\ 1, & k \ge 1 \end{cases} \tag{32}$$

The Dirichlet boundary conditions

$$u(-1) = u(1) = 0 \tag{33}$$

can be written as

$$\sum_{n=0,even}^{N_x} a_n = 0, \qquad \sum_{n=0,odd}^{N_x} a_n = 0. \tag{34}$$

Since even and odd coefficients a_n are decoupled in both eqs 31 and 34, we can construct two separate linear matrix equations for the even and odd terms in the form $\mathbf{L}\vec{a} = \vec{g}$, where $\mathbf{L}$ in the two cases is a nearly tridiagonal matrix with a dense top row due to the boundary condition, i.e.

$$\begin{pmatrix} 1 & 1 & 1 & 1 & \dots & 1 \\ l_1 & d_1 & u_1 & 0 & \dots & 0 \\ 0 & l_2 & d_2 & u_2 & \dots & 0 \\ & & & \vdots & & \end{pmatrix} \begin{pmatrix} a_0 \\ a_2 \\ a_4 \\ \vdots \end{pmatrix} = \begin{pmatrix} 0 \\ g_2 \\ g_4 \\ \vdots \end{pmatrix} \tag{35}$$

$$\begin{pmatrix} 1 & 1 & 1 & 1 & \dots & 1 \\ l_1 & d_1 & u_1 & 0 & \dots & 0 \\ 0 & l_2 & d_2 & u_2 & \dots & 0 \\ & & & \vdots & & \end{pmatrix} \begin{pmatrix} a_1 \\ a_3 \\ a_5 \\ \vdots \end{pmatrix} = \begin{pmatrix} 0 \\ g_3 \\ g_5 \\ \vdots \end{pmatrix} \tag{36}$$

The vector $\vec{g}$ is defined by

$$g_n = \frac{c_{n-2}}{4n(n-1)}\hat{f}_{n-2} - \frac{\beta_n}{2(n^2-1)}\hat{f}_n + \frac{\beta_{n+2}}{4n(n+1)}\hat{f}_{n+2} \tag{37}$$

Both linear systems can be solved from the bottom up using Gaussian elimination with a computational cost of $O(N_x)$.

In summary, the Chebyshev-based contour stepping algorithm for the MDE is as follows:

1 Evaluate $f(z_k) = e^{-\Delta s W(z_k)/2} q(z_k, s; [W])$ for $k = 0,...,N_x$
2 Compute $\hat{f}_n$ by the inverse DCT-I transformation defined in eq 25
3 Construct the g_n vector from eq 37
4 Solve eqs 35 and 36 in the case of $\lambda = K/\Delta s(1 - i)$ using Gaussian elimination
5 Construct g_n in eq 37 with $\hat{f}_n$ replaced by a_n from the solutions of step 4
6 Solve eqs 35 and 36 for $\lambda = K/\Delta s(1 + i)$ using Gaussian elimination
7 Transform a_n back to real space to obtain $u(z_k)$ using the DCT-I transformation defined in eq 23
8 Evaluate $q(z_k s + \Delta s; [W]) = e^{-\Delta s W(z_k)/2} u(z_k)$ for $k = 0, ..., N_x$

Evidently this series of steps can be repeated $N_s = 1/\Delta s$ times to evolve a solution of $q(z,s;[W])$ from the initial condition $q(z,0) = 1$ to the opposing chain end at $s = 1$. The overall computational effort is dominated by the DCT-I operations, namely $O(N_s N_x \log N_x)$ floating point operations per solution of the MDE.

A system with homogeneous Neumann boundary conditions can be solved by the same method, but where the top rows of the matrixes in eqs 35 and 36 are replaced, respectively, by

$$[0, 2^2, 4^2 ... (N_x - 1)^2] \tag{38}$$

and

$$[1^2, 3^2, 5^2 ... N_x{}^2] \tag{39}$$

A significant advantage of the Chebyshev pseudospectral method is that it can also be applied to the case of mixed or Robin type boundary conditions, for which Fourier-based methods are inapplicable. In the Robin case, the even and odd coefficients are no longer decoupled and the full pentadiagonal system must be solved at steps 4 and 6 in the algorithm. Nonetheless, this can still be accomplished with $O(N_x)$ effort.

2.3. Quadrature Scheme. Computation of the single chain partition function, eq 4, and the free energy, eq 3, involve spatial integrals of the form

$$I = \int_0^L dx\, f(x) = \frac{L}{2}\int_{-1}^1 dz\, f(z) \equiv \frac{L}{2}\bar{I} \tag{40}$$

To retain spectral accuracy, one must apply a consistent quadrature scheme. A suitable choice in the present situation is Clenshaw–Curtis quadrature, which is a spectral method for numerical integration that utilizes Chebyshev points:[36]

$$\begin{aligned} \bar{I} &= \int_{-1}^1 dz\, f(z) = \int_0^\pi d\theta \sin\theta\, f(\cos(\theta)) \\ &\approx \int_0^\pi d\theta \sin\theta \sum_{k=0}^{N_x} a_k \cos k\theta \\ &= \sum_{k=0,even}^{N_x} a_k \frac{2}{1-k^2} = \sum_{n=0}^{N_x} f(z_n) w_n \end{aligned} \tag{41}$$

The last equality and the analytic form of the Clenshaw–Curtis "weights" w_n follows from the expression for a_k (eq 25):

$$w_n = \frac{4}{\gamma_n N_x} \sum_{k=0,even}^{N_x} \frac{1}{\gamma_k} \frac{\cos[\pi k n/(N_x)]}{1-k^2} \quad (n = 0, ..., N_x) \tag{42}$$

The end point weights $w_0 = w_{N_x}$ from this formula adopt the simple expressions $1/(N_x{}^2-1)$ and $1/N_x{}^2$ for even and odd N_x, respectively.

For sine basis calculations, the spatial integral can be evaluated similarly by means of the formula

$$\begin{aligned} I &= \int_0^L dx\, f(x) = \int_0^L dx \sum_{j=1}^{N_x} a_j \sin(\pi j x/L) \\ &= \frac{2L}{\pi} \sum_{j=1,odd}^{N_x} \frac{a_j}{j} \end{aligned} \tag{43}$$

dx.doi.org/10.1021/ma202427n | Macromolecules 2012, 45, 2905–2919

Replacing a_j with its definition in terms of DST-I, one can determine the weight coefficients w_l for the sine basis quadrature

$$I = \frac{2L}{\pi} \sum_{j=1,odd}^{N_x} \frac{1}{j}\left[\frac{2}{N_x+1}\sum_{l=1}^{N_x} \sin\left(\frac{\pi j l}{N_x+1}\right) f(x_l)\right] = L\sum_{l=1}^{N_x} w_l f(x_l) \quad (44)$$

which are precomputed at the beginning of the SCFT simulation.

There is an additional concern when evaluating the free energy in eq 3. Unlike the calculation of the partition function Q, which involves a spatial integral of the chain propagator, the integrand in the free energy equation contains the pressure field, $iW_+(x)$, and related terms that do not satisfy Dirichlet boundary conditions. However, from eq 9, we know iW^*_+ takes the value $-\zeta N$ at $x = 0,L$, so a simple shift of $iW_+(x)$ by ζN (which does not change the free energy) renders the above quadrature scheme applicable.

2.4. SCFT Field Relaxation. Still remaining is a description of the numerical scheme used to relax the $W_\pm$ fields to a mean-field solution. Here we employ a simple relaxation scheme based on the fictitious dynamics:

$$\partial_t iW_+ = \frac{\delta H}{\delta iW_+} \quad (45)$$

$$\partial_t W_- = -\frac{\delta H}{\delta W_-} \quad (46)$$

The opposing uphill and downhill relaxation of the pressure and exchange-like fields $W_\pm$ reflects the saddle point configuration that we seek. For both the pseudospectral sine and Chebyshev based methods, eqs 45 and 46 are integrated by the explicit forward Euler formula. The time step Δt is fixed to be the same for both methods and just below the stability limit. Better performing semi-implicit algorithms have been developed for integrating these equations in cases of Fourier bases[37] and other schemes such as Anderson mixing have proven effective in a more general SCFT context.[33,38] However, as none of these methods have yet to be explored or optimized for Chebyshev collocation, we have chosen simple Euler relaxation in order to compare the performance of sine and Chebyshev solutions on an equal footing.

3. PERFORMANCE OF CHEBYSHEV-BASED CALCULATIONS

In this section, we compare the accuracy, rate of convergence, and computation time of our new Chebyshev scheme against the sine pseudospectral method in SCFT calculations for an AB diblock copolymer system subject to Dirichlet boundary conditions. As a test problem, we chose a compressible diblock copolymer melt with $f = 0.7$, $\zeta N = 100$, and $\chi N = 17$ that is confined to a slit of $L = 10R_g$ in width. The block copolymer composition is assumed to be homogeneous in the directions transverse to x, so the MDE and SCFT equations are solved in one-dimension.

3.1. Convergence in N_s. First, we evaluate how the accuracy of the pseudospectral calculations is affected by the number of steps used along the chain contour, N_s, related to the step width as $\Delta s = 1/N_s$. For these tests, full SCFT simulations are not conducted; instead the MDE (eq 5) is solved once for the following prescribed smooth fields:

$$iW_+ = -110e^{-10(x-5)^2} - 110e^{-10(x+5)^2} + 10 \quad (47)$$

$$W_- = [-10\cos(2\pi x/3) + 5]\cos(2\pi x/20) \quad (48)$$

for $x \in [-5,5]$. The partition function Q in eq 4 is also calculated from the solution of MDE for each value of N_s considered. N_x is fixed at 1024 for all the calculations.

Figure 1 shows the error in the partition function Q as a function of N_s on a logarithmic scale. The reference ("exact") solution is obtained from a simulation with $N_s = 100000$. As expected, the error decreases as N_s^{-2} for both sine and Chebyshev pseudospectral schemes, showing that both are second order methods in Δs, as expected (a linear fit gives a slope of −2.0611 with norm of residuals =0.16905).

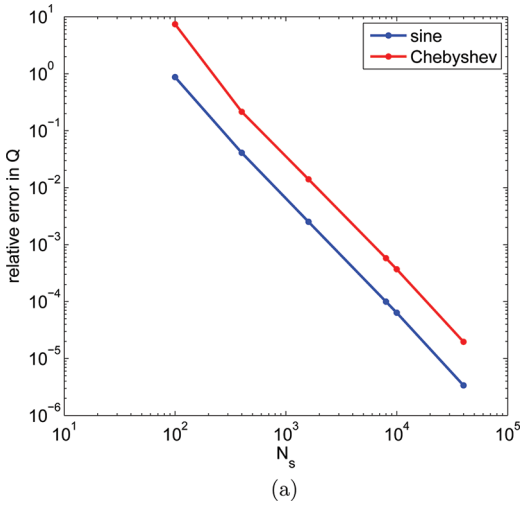
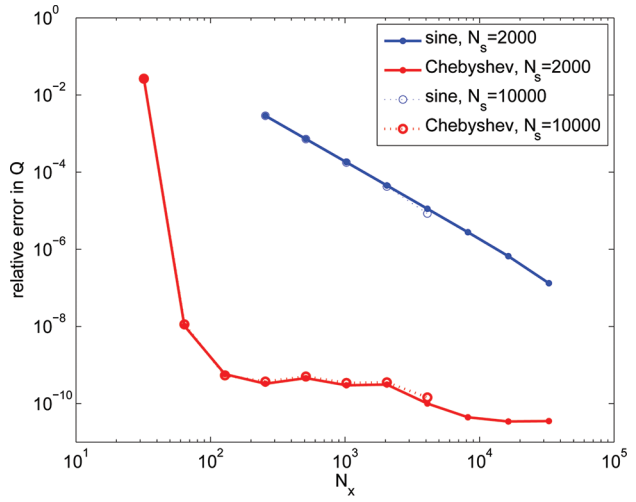


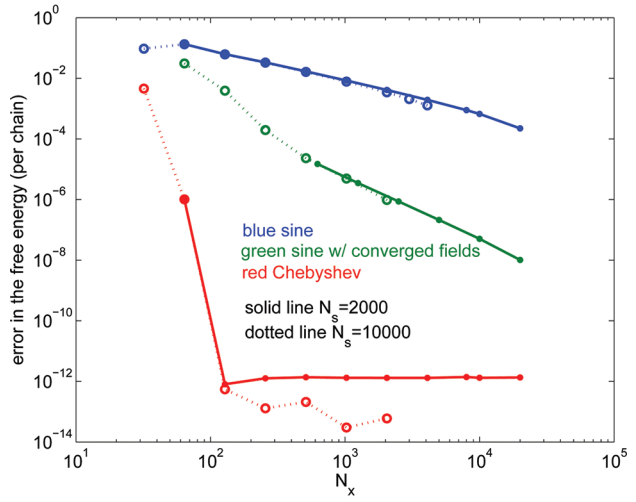
Figure 1. Error in the partition function Q for the Chebyshev and sine-based pseudospectral solutions of the MDE as a function of number of contour steps N_s. The propagator was calculated using specified smooth potential fields. The "exact" solution is obtained from a simulation with $N_s = 100000$. N_x is fixed at 1024.

3.2. Convergence in N_x. Next, the convergence rate with the number of grid points, N_x is examined. As mentioned in the Introduction, besides the infinite smoothness requirement for $q(x)$, all even derivatives of $q(x)$ of second and higher order must vanish at both boundaries for a truncated Fourier sine series to exhibit ideal spectral accuracy. In Figure 2a, the error in the partition function Q, which is evaluated from $q(x,1)$ by using eq 48 and the appropriate quadrature scheme, is plotted logarithmically as a function of N_x. We isolate the error due to the contour discretization by selecting two large values of N_s = 2000 and 10000. The results of simulations with (N_x = 65536, N_s = 2000) and (N_x = 32768, N_s = 10000) are used as "exact" reference values for the error calculations. While the error in the sine-based solutions decreases proportional to N_x^{-2} (a linear fit gives a slope of −2.0413 with norm of residuals =0.18879), the Chebyshev results show a much more rapid decrease in the error consistent with spectral accuracy. This implies that the requirements on even higher derivatives of $q(x)$ at the boundaries are not met for the problem, and the observed second order spatial accuracy for the sine pseudospectral solution indicates that the second order derivatives of the chain propagator at the boundaries do not vanish. The higher density of the Chebyshev

dx.doi.org/10.1021/ma202427n | Macromolecules 2012, 45, 2905−2919



(a)



(b)

Figure 2. (a) Error in the partition function for varying number of spatial grid points N_x for the pseudospectral methods with Chebyshev and sine bases. Propagators were calculated using specified smooth potential fields. The number of chain contour steps N_s was held fixed at 2000 and 10000. (b) Error in the free energy per chain of a confined compressible AB diblock copolymer vs N_x for the Chebyshev and sine bases in converged SCFT calculations. Each SCFT simulation was initiated from randomly distributed field configurations. System parameters are $\chi N = 17$, $\zeta N = 100$, $L = 10$, and $f = 0.7$.

collocation points at the boundaries also contributes to the improved performance of the Chebyshev results. With Chebyshev collocation, the polymer density depletion layer, which is ~0.5 R_g for the parameters used, can be resolved and the calculation starts being accurate with a fewer number of grid points N_x.

We also compared the relative performance of the two algorithms in a full SCFT calculation with $\chi N = 17$. Figure 2b shows the error in the free energy per chain calculated after the field relaxation converged. Each simulation was initiated with field configurations composed of random numbers uniformly distributed over $[-0.5, 0.5]$ and was terminated when the error, defined as the sum of the l_1 norms of the right-hand sides of eqs 9 and 10, drops below 10^{-13}. While the error in the free energy from the Chebyshev-based SCFT shows exponential decay with increasing N_x (consistent with spectral accuracy), the error in the sine basis SCFT decays much more slowly as the power law $\sim N_x^{-1.1}$. It is notable that the sine SCFT result shows even slower decay with N_x than the N_x^{-2} decay observed in Figure 2(a) for the partition function Q computed for prescribed $W_\pm$ fields. Evidently, errors in the computation of the chain propagators, which feed into both the value of Q and the normalized densities, are amplified in the final converged SCFT fields and densities. This is illuminated by the green curve in Figure 2b, which shows the error in the free energy per chain versus N_x for $W_\pm$ fixed at "exact" saddle point values obtained from a very large N_x simulation. The error in this case is localized in the ln Q term of the free energy and shows the expected second order N_x^{-2} behavior.

We have also examined the accuracy of the Chebyshev algorithm for full SCFT calculations of diblock copolymer melts subject to different boundary conditions. In Figure 3a, the error in the free energy per chain of an incompressible diblock copolymer ($f = 0.7$) melt with homogeneous *Neumann* boundary conditions at $x = 0$ and L is shown as a function of N_x. For comparison, we also show results obtained from a pseudospectral calculation with a cosine basis. Both the Chebyshev basis and cosine basis SCFT calculations show ideal spectral accuracy, which shows that this is a special case in which the solution has all odd derivatives equal to zero on the boundary. Since the Chebyshev algorithm requires more computational effort, as will be discussed in the next section, it is preferable to use the cosine pseudospectral algorithm for systems with purely reflecting boundary conditions. However, Neumann boundary conditions themselves are unable to capture a variety of phenomena in confined polymer systems that can emerge from either finite width interfaces or a preferential affinity of one component to the surface.[39] This can be resolved through an addition of a surface affinity delta function to the field, although this addition would adversely effect the convergence of the free energy. Fortunately, the relative free energy between different phases necessary for the construction of phase diagrams typically exhibits faster convergence. Matsen and Griffiths demonstrated that Neumann BCs with a surface affinity could be transformed into a Robin-type BC. Through this transformation, they observed much improved convergence with the spectral method.[40]

Finally, we consider a compressible diblock copolymer melt subject to the Robin boundary conditions:

$$\left[\frac{\partial}{\partial x} q(x, s; [W]) + \kappa(s) q(x, s; [W])\right]_{x=0,L} = 0 \tag{49}$$

where

$$\kappa(s) = \begin{cases} \kappa_A = 0.3, & 0 \le s \le f \\ \kappa_B = -0.7, & f < s \le 1 \end{cases} \tag{50}$$

The parameters κ_A and κ_B have units of inverse length and characterize the strengths of potentials that attract segments of type A and B, respectively, to the surface.[2] SCFT calculations conducted using the Chebyshev method and the same melt conditions and parameters used previously show spectral accuracy as illustrated in Figure 3b.

3.3. Computation Time. In this section, we compare the computational cost of the sine and Chebyshev based pseudospectral SCFT methods in view of their widely differing spatial accuracy. Both methods were implemented in

dx.doi.org/10.1021/ma202427n | Macromolecules 2012, 45, 2905–2919

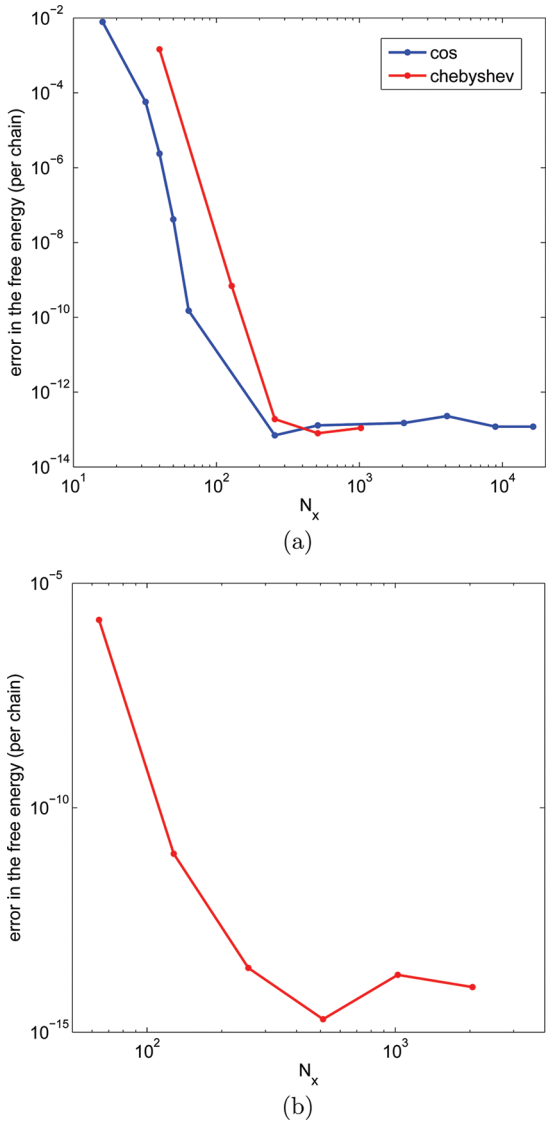


Figure 3. Error in the free energy per chain from SCFT simulations of a compressible AB diblock copolymer as a function of the number of spatial grid points N_x for (a) Chebyshev and cosine basis calculations for Neumann boundary conditions, and (b) Chebyshev basis calculations for mixed (Robin) boundary conditions. Each SCFT simulation was initiated from randomly distributed field configurations. System parameters are $\chi N = 17$, $L = 10$, and $f = 0.7$. $\zeta N = 100$ is used for mixed (Robin) boundary condition.

FORTRAN 90 on a 2.00 GHz Intel Xeon CPU and the profiling program Gprof was used to produce the timing results. For an initial comparison, 10 iterations of SCFT calculations with various N_x were conducted with N_s fixed at 1000. The total computation times, including initialization steps, solution of the modified diffusion equations, quadratures and density calculations, and field updates are plotted as a function of N_x in Figure 4. We also separated out the cost of performing in both cases the forward and backward fast Fourier transforms (FFTs) using the FFTW libraries.[41] In both the Chebyshev and sine based simulations, solving the modified diffusion equation is the most time-consuming step; this is particularly the case in the Chebyshev scheme. Since we only conducted 10 iterations, the initialization steps including generating weighting factors and FFT plans in the FFTW library accounts for a measurable

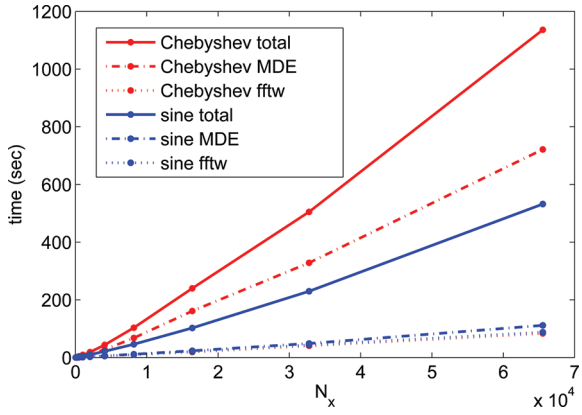


Figure 4. CPU time to perform 10 SCFT iterations with the Chebyshev and the sine basis pseudospectral algorithms. The contributions to the total CPU time from the FFT routine (FFTW) and the MDE solver are also included. System parameters are $\chi N = 17$, $\zeta N = 100$, $L = 10$, and $f = 0.7$. N_s is fixed at 1000.

fraction of the total computation time. The importance of these initialization steps diminishes considerably in a full SCFT calculation, where at least 1000 iterations are conducted. In such cases the fraction of run time contributed by the diffusion equation solvers is dominant.

To ensure the maximum efficiency and scaling of the FFT algorithm $O(N_x \log N_x)$, we only used values of N_x that are powers of 2. Both algorithms require one pair of real to real FFTs (forward and backward) per contour step of the diffusion equation solver. The CPU time used for the FFT is thus approximately the same for both methods as shown in Figure 4. The remaining calculations of the diffusion equation solver in the split-step sine basis algorithm involve only a few multiplications of $O(N_x)$, so the cost of the diffusion equation solver is dominated by FFTW. However, the Chebyshev basis calculation involves a number of additional algebraic operations including two steps of Gaussian elimination and two steps of filling the $\vec{g}$ vector. While these calculations are $O(N_x)$ in contrast to the FFT at $O(N_x \log N_x)$ flops, evidently a large prefactor multiplying the $O(N_x)$ term causes the algebraic calculations to dominate the diffusion equation solver in the Chebyshev case. Figure 4 shows that the Chebyshev basis calculations are almost twice as expensive as the sin basis algorithm at any number of grid points. However, one should keep in mind that the sine basis calculation requires a significantly larger number of grid points to reach a comparable accuracy in free energy.

A more practical assessment of the performance of the two algorithms compares the CPU time required to to achieve a particular specified error in the free energy. In Table 1, we

Table 1. CPU Time (s) and Error Levels Obtained for Varying N_x in Chebyshev and Sin-Based SCFT Simulations

	N_x	number of iterations	CPU time	error in the free energy
sin	$2^7 = 128$	2600	252.54	6.24e-02
	$2^{14} = 16\,384$	2300	37435.24	2.71e-04
Chebyshev	$2^6 = 64$	2200	242.32	2.40e-07
	$2^7 = 128$	2200	436.14	round off level $O(10^{-14})$
	$2^{13} = 8192$	2000	33175.99	round off level $O(10^{-14})$

dx.doi.org/10.1021/ma202427n | Macromolecules 2012, 45, 2905−2919

summarize the CPU time and error in the free energy observed in full SCFT simulations conducted with the same parameters as in section 3.2. As noted previously, we employ a simple forward Euler update scheme to integrate the field relaxation eqs 45 and 46; the time steps for the pressure field iW_+ and exchange field W_- were set to 3 and 4, respectively, in the present study. For the same field update constants (time steps), we observed a similar rate of convergence for the two algorithms. Thus, the difference in computation time between the methods is primarily determined by the efficiency of solving the MDE. Other update schemes are available[33,37] to accelerate convergence or increase stability, although we expect that such methods would impact both algorithms in a similar manner so that our comparison would be still valid. Because of the spectral accuracy of the Chebyshev basis pseudospectral method, Table 1 shows that round off error levels were achieved in the free energy with N_x = 128 and a CPU time of just below 500 s. In contrast, the sine basis calculation with N_x = 16384 has an error in the free energy of order 3×10^{-4} and requires nearly 100 times more CPU time! The remarkable spectral accuracy of the Chebyshev algorithm thus translates into very significant reductions in computation time, particularly for demanding high accuracy SCFT simulations.

The Chebyshev algorithm reduces not only the CPU time of an SCFT simulation, but also the amount of memory required. The memory requirements of pseudospectral methods are dominated by the need to store the chain propagator, which involves N_sN_x double precision numbers. While we have seen that the Chebyshev and sine basis algorithms have comparable variations in accuracy with N_s, the Chebyshev algorithm requires dramatically smaller N_x values for comparable error levels. The memory requirements of the Chebyshev algorithm are thus reduced proportionally by this reduction in N_x.

4. CHEBYSHEV-BASED SCFT STUDY OF POLYMER WETTING

Having demonstrated that our Chebyshev-based pseudospectral method significantly outperforms comparable sine-based algorithms for SCFT calculations on confined polymers, we now provide a nontrivial example of how the method can be fruitfully applied to the wetting behavior of a polymer droplet on a surface. In addition to the advantage of implementing Dirichlet boundary conditions efficiently and with spectral accuracy, the extra resolution provided by the clustering of Chebyshev points near the boundaries also contributes to the attractiveness of Chebyshev basis SCFT in studies of a wide range of systems including thin block copolymer films and mixed polymer brushes.

While there have been studies on wetting behavior of polymer melt droplets on surfaces using particle based simulations, the methods employed have had large computational requirements and are significantly limited in the molecular weights that can be investigated.[42−47] In contrast, SCFT models can be used to study polymer melts of arbitrary composition, architecture, and molecular weight, and at a computational cost that is independent of molecular weight. Most SCFT studies on polymer thin films to date have been focused on predicting the influence of surface energetics on the morphologies of the block copolymer in the interior of the film.[15−18] Here we demonstrate that the Chebyshev-based pseudospectral SCFT approach is an excellent choice for such thin films studies and related investigations of surface wetting properties. As a model system, we have chosen to investigate the wetting behavior of a homopolymer droplet, surrounded by a second immiscible homopolymer, on a flat substrate. Specifically, we consider a compressible A/B homopolymer blend, where the A homopolymer is the continuous surrounding fluid and the B homopolymer constitutes the polymer droplet. Related SCFT models of block copolymer droplets have been investigated in the literature,[48] but these did not utilize Chebyshev-based numerical methods and contact angle trends with surface energetics was not explored.

In our wetting model, we specify a wall profile $\phi_w(x)$ that is unity at the substrate surface and decays smoothly to zero into the fluid. The total polymer segment density (A + B) is thus constrained harmonically by the Helfand compressibility term to $1 - \phi_w(x)$ and vanishes at the surface, consistent with Dirichlet conditions on the polymer propagators. Flory−Huggins interaction parameters $\chi_{AB} = \chi$, χ_{wA}, and χ_{wB} are introduced to describe the strength of binary contact interactions between A and B segments, A segments and the surface, and B segments and the surface, respectively. In the following section, we explain how the map the Flory−Huggins parameters to values of the surface tension of the surrounding polymer A γ_A, the surface tension of the droplet polymer B γ_B, and the A-B interfacial tension σ, respectively. For consistency with thermodynamics, we expect Young's equation to apply on a macro-scale, relating the contact angle of the drop on the surface θ to the interfacial and surface tensions:

$$\sigma \cos(\theta) = \gamma_A - \gamma_B \tag{51}$$

By precomputing σ, γ_A and γ_B using one-dimensional SCFT simulations and then conducting two-dimensional SCFT simulations of a drop configuration and measuring the contact angle, we will be able to test whether macroscopic wetting phenomena can be extracted from SCFT simulations conducted on 1−1000 nm length scales.

4.1. Surface and interfacial tensions vs Flory−Huggins parameters. To calculate the interfacial tension between the A and B polymers, σ, we have conducted one-dimensional SCFT simulation of a symmetric A and B homopolymer blend in a periodic box. For $\chi_{AB}N > 2$, the system macrophase separates into coexisting A-rich and B-rich phases (α and β phases) with two interfaces across the domain. The interfacial tension of the two-component system is related to the surface excess free energy of the system computed by identifying a Gibbs dividing surface that eliminates the surface excess areal density of the two components. It follows that the surface tension in the blend is simply the surface excess Helmholtz free energy per unit area,

$$F^{(s)} = F^{(tot)} - F^{(\alpha)} - F^{(\beta)} = 2\sigma\mathcal{A} \tag{52}$$

where the factor of 2 arises from the two interfaces created by the use of periodic boundary conditions and $\mathcal{A}$ is the interfacial area of one such interface. $F^{(tot)}$ is the total free energy of the heterogeneous system, while $F^{(\alpha,\beta)}$ are the free energies of the homogeneous A- and B-rich phases. Since we have used a symmetric polymer blend with equal volume fractions, there is

no difference in the free energies of two phases. The homogeneous state free energy can be computed analytically as:

$$F^{(\alpha)} = \bar{V}^{(\alpha)}\left[\frac{1}{\chi N}(W^*_-)^2 - \frac{2\zeta N}{\chi N + 2\zeta N} iW^*_+ - \frac{1}{\chi N + 2\zeta N}(iW^*_+)^2 + \nu_A^{(\alpha)}(iW^*_+ - W^*_-) + \nu_B^{(\alpha)}(iW^*_+ + W^*_-) + \nu_A^{(\alpha)} \ln \nu_A^{(\alpha)} + \nu_B^{(\alpha)} \ln \nu_B^{(\alpha)}\right] \quad (53)$$

where

$$iW^*_+ = -\zeta N + \frac{\chi N + 2\zeta N}{2}(\phi_A^{(\alpha)} + \phi_B^{(\alpha)}) \quad (54)$$

$$W^*_- = \frac{\chi N}{2}(\phi_A^{(\alpha)} - \phi_B^{(\alpha)}) \quad (55)$$

$$\nu_{A(B)}^{(\alpha)} = \phi_{A(B)}^{(\alpha)}/(\phi_A^{(\alpha)} + \phi_B^{(\alpha)}) \quad (56)$$

and $\phi_A^{(\alpha)}$ and $\phi_B^{(\alpha)}$ are the volume fractions of A and B in the α phase. The last two terms in eq 53 are from the mixing entropy. The simulation box size was chosen to be $L = 160$, which was confirmed large enough to avoid finite size effects, and the compressibility parameter ζN was set to 100.

Following the above procedure, the interfacial tension for the binary homopolymer blend is shown in Figure 5a as a function of $\chi_{AB}N$. The tension has been nondimensionalized by a factor of $\beta R_g^2/\ C = \beta N/(\rho_0 R_g)$. As expected, the tension extrapolates to zero at the $\chi_{AB}N = 2$ critical point and is consistent with the asymptotic $\sim(\chi_{AB})^{1/2}$ relationship predicted by Helfand–Tagami at strong segregation.[49]

Next, we turn to estimating the surface tension between one of the polymers and the substrate from a one-dimensional Chebyshev-based SCFT calculation for a compressible ($\zeta N = 100$) pure homopolymer melt that is confined in a channel with Dirichlet boundary conditions at both boundaries. As the A- and B-type polymers are structurally identical, it is not necessary to distinguish whether the melt is of species A or B at this stage. Again, the surface tension is computed as an excess surface free energy per unit area, in this case associated with the presence of the two bounding walls, and is dictated by a combination of entropic and enthalpic factors. As discussed above, the wall density $\phi_w(x)$ is a specified smooth function that is unity at the boundaries where homogeneous Dirichlet boundary conditions are imposed on the polymer density. The particular choice adopted here is a simple tanh profile (for the wall at $x = 0$):

$$\phi_w(x) = 1 - \tanh(x/w) \quad (57)$$

where w is the width of the wall and is set to $0.2R_g$ in this study. The enthalpic interactions between polymer and wall were modeled by a Flory-type contact interaction of the form $\chi_w\phi_w(x)\phi(x)$, where $\phi(x)$ is the relevant normalized polymer segment density. The excess surface free energy has the form of:

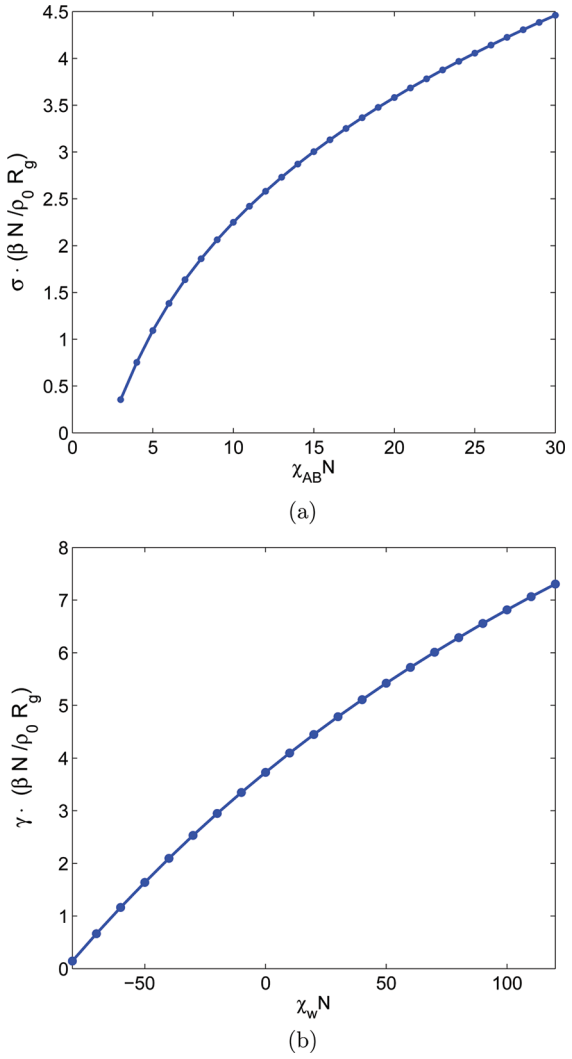


Figure 5. (a) Interfacial tension of a symmetric phase-separated A/B homopolymer blend as a function of the segregation strength $\chi_{AB}N$, and (b) surface tension of a homopolymer against a substrate as a function of the polymer–wall interaction parameter χ_wN.

$$\bar{\gamma} = \gamma(\beta N/\rho_0 R_g) = \int_0^L dx\left[-iW^*_+(x) - \frac{1}{2\zeta N}(iW^*_+(x))^2\right] - L \ln Q[iW^*_+ + \chi_w N\phi_w] \quad (58)$$

where

$$\left.\frac{\delta H}{\delta iW_+}\right|_{iW^*_+} = -\frac{iW^*_+(x)}{\zeta N} - 1 + \phi(x) = 0 \quad (59)$$

The simulation box size was chosen to be $L = 20$, and the compressibility parameter ζN was set to 100.

The surface tension of the homopolymer, $\bar{\gamma}$, nondimensionalized by a factor of $\beta R_g^2/C = \beta N/(\rho_0 R_g)$, is plotted as a function of χ_wN in Figure 5b. We observe an almost linear relationship between χ_wN and $\bar{\gamma}$. The slope in Figure 5b approximately corresponds to the integral of the product of the wall profile and the polymer density, $\int dx\ \phi_w(x)\phi(x)$, and the

dx.doi.org/10.1021/ma202427n | Macromolecules 2012, 45, 2905–2919

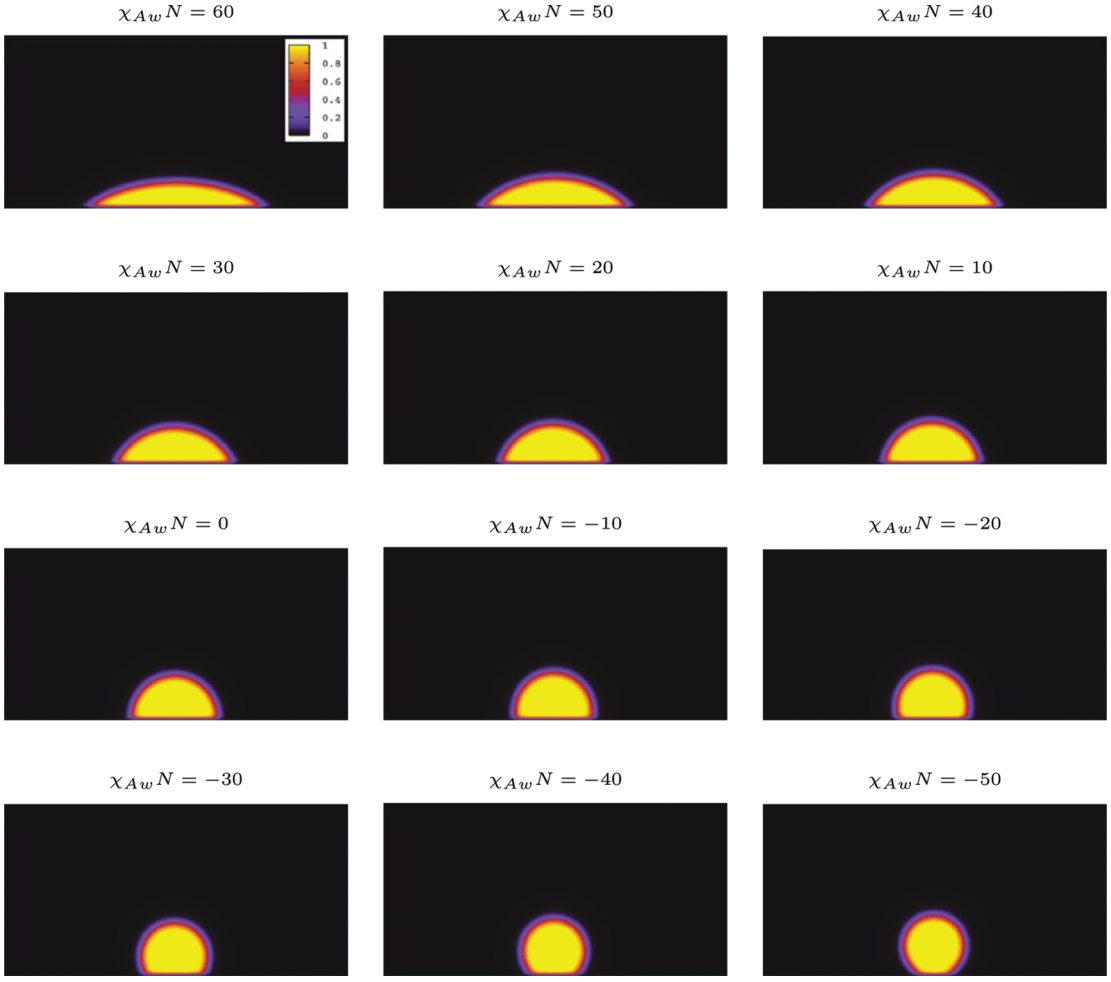


Figure 6. SCFT simulation results showing the density profile of B Homopolymer droplets on a substrate with varying Flory interaction parameters χ_{Aw} between the substrate (wall) and the majority fluid A polymer phase. The B-surface interaction parameter was set to $\chi_{Bw}N = 0$ and the A−B interactions were fixed at $\chi_{AB}N = 17$.

intercept at $\chi_w N = 0$, $\overline{\gamma} \approx 3.7288$ corresponds to the entropic contribution to the surface tension. Since the polymer density profile varies slightly from the expected $1 - \phi_w(x)$ by an amount that depends on $\chi_w N$ and ζN in a compressible model, there is a small deviation from linearity for larger magnitudes of $\chi_w N$. In a strictly incompressible model, where the polymer density is fixed at $1 - \phi_w(x)$, $\overline{\gamma}$ is strictly proportional to $\chi_w N$ with a slope of $\int dx\ \phi_w(x)\phi(x) = \int dx\ \phi_w(x)(1 - \phi_w(x))$ dependent only on the wall profile.

An approximate analytic form for the *entropic* contribution to γ in an incompressible model can be deduced from the ground state dominance approximation:[15]

$$\overline{\gamma} = \gamma(\beta N/\rho_0 R_g) \approx \frac{1}{4}\int dx\ \frac{[\phi'(x)]^2}{\phi(x)} \qquad (60)$$

although we have found that this expression is not quantitative. SCFT simulations conducted for an *incompressible* homopolymer confined by the wall profile of eq 57 yields an entropic contribution to $\overline{\gamma}$ of 6.458, which is significantly larger than the value of 1.875 predicted by eqs 57 and 60. Nonetheless, the slope of the SCFT-derived linear relationship between $\overline{\gamma}$ and $\chi_w N$ is *exactly* $\int dx\ \phi_w(x)(1-\phi_w(x)) = 0.061$.

4.2. SCFT Simulations of Droplet Contact Angle. As a showcase for our new Chebyshev pseudospectral method, we have conducted SCFT simulations of a compressible blend of A and B homopolymers, confined between opposing surfaces and with a B droplet configuration in contact with one of the surfaces. The simulations have been conducted in two dimensions, assuming homogeneity in the third dimension, since we are only interested in contact angle. However, the approach could be easily extended into a full three-dimensional calculation. We have used a simulation cell size that is $L_x = 10\ R_g$ between the opposing surfaces where Dirichlet conditions are applied, and $L_y = 20\ R_g$ in the transverse y direction where periodic boundary conditions are imposed. We have verified that this cell is large enough so that finite size effects are negligible on the droplet properties reported here. The box is discretized using Chebyshev and plane wave basis spectral collocation with $N_x = 256$ and $N_y = 128$ points in the x and y directions, respectively. $N_s = 200$ is used throughout the study and the volume fraction of the continuous phase A polymer is set to 0.95, and the B homopolymer droplet volume fraction is fixed at 0.05. The compressibility parameter was chosen as $\zeta N = 100$.

The Chebyshev algorithm is only slightly modified in the two-dimensional case. We retain the $O(\Delta s^2)$ accurate operator

dx.doi.org/10.1021/ma202427n | *Macromolecules* 2012, 45, 2905−2919

splitting formula of eq 18, but further decompose the x and y components of the free diffusion operator according to

$$e^{\Delta s \nabla^2} = e^{\Delta s \nabla_x^2} e^{\Delta s \nabla_y^2} \quad (61)$$

The y-dependent propagator is applied by an FFT in the y direction, followed by a local multiplication of the exponential operator in k_y reciprocal space and an inverse FFT. The x-dependent propagator is then handled by a Padé approximation as was described in the one-dimensional case.

Since only the surface tension difference between A and B influence the contact angle, we fix $\chi_{Bw}N = 0$ and sweep the tension difference by varying $\chi_{Aw}N$ from 60 to −50. The value of $\chi_{AB}N$ was fixed at 17. From the results of the last section encapsulated in parts a and b of Figure 5, these Flory interaction parameters can be translated uniquely into an A-B interfacial tension $\overline{\sigma} = \sigma(\beta N/\rho_0 R_g) = 3.2508$, the surface tension of the B polymer $\overline{\gamma}_B = 3.7288$, and a range of $\overline{\gamma}_A$ surface tensions ranging from 5.7211 to 1.6391. We present representative B-segment density profiles of the B-rich polymer droplets for the $\chi_{Aw}N$ sweep in Figure 6. All the runs were started with random field configurations, without any bias toward the droplet location, but the B droplet was consistently observed to be formed next to a wall where it can reduce the interfacial area between A and B at a comparable free energy cost in the surface layer. As drops were nucleated at random positions along the surfaces, we have shifted the fields to relocate the drops at the center of the bottom surface in each simulation cell. For positive $\chi_{Aw}N$, i.e., an A-repulsive surface, the B polymer droplet spreads into a thin layer over the surface, wetting the surface and thereby shielding the surface from component A. Conversely, a negative $\chi_{Aw}N$ causes the polymer to partially or completely dewet the surface. When $\chi_{wA}N$ is very large and negative, the energy gain from A wetting the surface exceeds the free energy cost of additional A/B interface forming, so the polymer droplet will completely dewet the surface. Similarly, for a very large positive $\chi_{wA}N$, the B droplet completely wets the surface. From Young's equation (eq 51), the surface tension values of these wetting and dewetting transitions can be estimated by setting the contact angle as 0 and 180°, respectively. Then from Figure 5b, the values of $\chi_{wA}N$ corresponding to the surface tension values of the wetting and dewetting transitions can be estimated approximately as +106.6 and −64.2.

It is of interest to analyze the SCFT results shown in Figure 6 in the context of Young's equation by comparing predicted and observed (SCFT) contact angle values. For each set of χ parameters, we have determined the surface and interfacial tensions by the procedures described in the previous section. The contact angle θ was then predicted using Young's eq 51. In Figure 7, we show the location of the SCFT A/B interface (blue curve) along with the predicted contact angle (red line) for each value of $\chi_{Aw}N$ simulated. The location of the A/B interface was determined as the locus of points in the x−y plane where the B polymer density corresponds to half of the maximum (bulk density of B inside the droplet). The close coincidence of the predicted contact angles with the limiting equilibrium shapes of the polymer drops is reassuring and suggests that macroscopic thermodynamics is operative even for the ∼$10R_g$ (50 nm) scale droplets that have been simulated.

For a more quantitative comparison, we have attempted to extract contact angles from the SCFT images. The discrete A/B interface location data is interpolated using cubic splines and

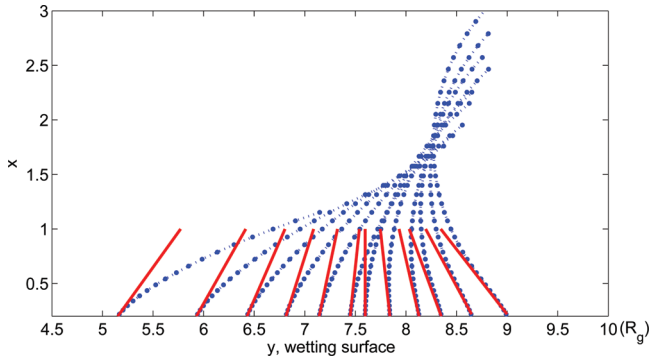


Figure 7. The interface curve (blue) for the images in Figure 6 along with lines (red) which have predicted contact angle from Young's equation for each cases.

the splines are differentiated to obtain an approximation for the local slope of the interface. Evaluating this slope at the substrate surface $x = 0$ was found to lead to erroneous results, due to the finite width of the wall region that defines the interface between the two polymers and the surface. For $\chi_{Aw}N \geq 0$, we have found that using the slope at an elevated "contact" height equal to the wall width, $x = w = 0.2$, leads to contact angles in close agreement with the Young predictions. For $\chi_{Aw}N < 0$, the optimal contact height shifts a bit further away from the wall as $\chi_{Aw}N$ gets smaller, the contact angle drops below 90°, and the A polymer invades more of the surface. We have arbitrarily chosen $x = 0.3$ as the contact height to analyze the data with negative values of $\chi_{Aw}N$, which is a reasonable compromise, but does not locate all the data on the curve predicted by Young's equation, as shown in Figure 8. We expect that this subtlety of

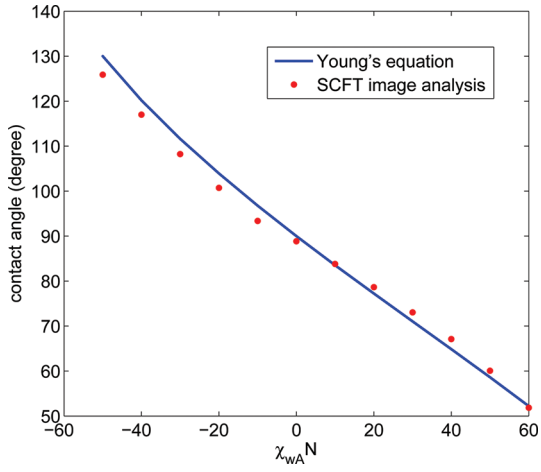


Figure 8. Measured contact angles from SCFT simulations compared with predicted contact angles from Young's equation for a range of A-attractive and A-repulsive surfaces.

identifying a macroscopic contact angle would be less pronounced in a strictly incompressible model, since slight density variations on top of composition variations in the wall region near the surface undoubtedly complicate interpretation of the contact angle trends with $\chi_{Aw}N$.

5. SUMMARY AND CONCLUSIONS

A highly efficient and accurate numerical self-consistent field theory (SCFT) algorithm has been introduced for polymer systems subject to nonperiodic boundary conditions. The new

pseudospectral method solves the modified diffusion equation (MDE) by a procedure similar to the split-step Fourier method, but Chebyshev polynomials are employed instead of the Fourier trigonometric basis functions. The contour evolution operator $e^{\Delta sL}$ is split with second-order accuracy in the contour step Δs into the product of operators $e^{-\Delta sW/2}e^{\Delta s\nabla^2}e^{-\Delta sW/2}$. The operator containing the potential field, W, is easily applied as a multiplication in real space, while the free diffusion operator involving the Laplacian is applied in Chebyshev space. Unlike the case of Fourier bases, the Laplacian operator is not diagonal when expressed in a Chebyshev basis, so we approximate the diffusion operator with a second-order accurate (in Δs) Padé approximation that allows the operator to be applied by solving two successive Helmholtz equations in the Chebyshev representation. The latter are solved by an efficient $Q(N_x)$ scaling numerical algorithm, where N_x is the number of spatial Chebyshev points used across the domain, and the overall operation count for a single solution of the MDE is $O(N_sN_x \log N_x)$, where N_s is the number of points used along the chain contour.

The performance of the new Chebyshev-based pseudospectral method was compared with trigonometric-based pseudospectral methods for a confined compressible AB diblock copolymer melt. It is confirmed that the Chebyshev algorithm preserves spectral accuracy in solutions of the MDE irrespective of boundary restrictions, while sine basis calculations for the case of Dirichlet boundary conditions exhibits much poorer second order accuracy in space. The accuracy of sine-based solutions in full SCFT calculations, which require multiple solutions of the MDE to iterate the fields to self-consistency, is even lower than second order, while spectral accuracy is preserved in the Chebyshev approach. Although the CPU time of the Chebyshev algorithm is roughly twice that of the sine pseudospectral algorithm for the same N_x and N_s values, the practical CPU time for an SCFT calculation with a specified accuracy can be orders of magnitude less with the Chebyshev algorithm, since the spectral accuracy permits the use of a much smaller number N_x of Chebyshev points than sine collocation points.

The Chebyshev algorithm was demonstrated by simulating the static wetting behavior of a homopolymer droplet, immersed in a continuous phase of a second polymer, on a solid surface. We first showed how to computationally map the Flory–Huggins interaction parameters between the two polymers and surface into surface and interfacial tensions. Then Chebyshev polynomial based SCFT simulations were conducted for systems of various polymer–substrate surface tensions by modulating the Flory interactions between the polymers and the surface. Contact angles of the polymer droplet were extracted from the density configurations of SCFT simulations and were found to agree well with predicted values from Young's equation and the computed surface and interfacial tensions.

More broadly, the Chebyshev technique should enable high accuracy and high efficiency SCFT simulations for a broad range of confined polymer systems, including block, graft, and random copolymer thin films, mixed polymer brushes, and laterally confined blends and copolymers. It is flexible enough to be able to impose a variety of selective and nonselective interactions at opposing boundaries and should thereby enable studies of a range of surface enrichment, structuring, wetting, and dewetting phenomena in polymer formulations of arbitrary complexity. Beyond mean-field theory, the algorithm can be adapted to full stochastic simulations of polymer field theory models, so-called "field-theoretic simulations,"[2,32] which could extend the accuracy and efficiency benefits to confined, strongly fluctuating systems such as solvated polymer systems and polyelectrolytes.

AUTHOR INFORMATION

Notes

The authors declare no competing financial interest.

ACKNOWLEDGMENTS

S.M.H., C.J.G.-C, and G.H.F. acknowledge partial support from the Focus Center Research Program (FCRP)-Center on Functional Engineered Nano Architectonics (FENA) and Award No. DMR-0904499 from the CMMT Program of the National Science Foundation. We also acknowledge use of the MRL/CNSI Computational Facilities at UCSB supported by the MRSEC Program of the National Science Foundation under Award No. DMR-1121053.

REFERENCES

(1) Matsen, M. W. *Soft Matter, Vol. 1: Polymer Melts and Mixtures*: Wiley-VCH Verlag GmbH & Co. KGaA: Weinheim, Germany, 2006; Chapter 2
(2) Fredrickson, G. H. *The Equilibrium Theory of Inhomogeneous Polymers*; Clarendon Press: Oxford, U.K., 2006.
(3) Matsen, M. W.; Schick, M. *Phys. Rev. Lett.* **1994**, *72*, 2660.
(4) Tzeremes, G.; Rasmussen, K. Ø.; Lookman, T.; Saxena, A. *Phys. Rev. E* **2002**, *65*, 041806.
(5) Rasmussen, K. Ø.; Kalosakas, G. *J. Polym. Sci., Part B: Polym. Phys.* **2002**, *40*, 1777–1783.
(6) Strang, G. *SIAM J. Numer. Anal.* **1968**, *5*, 506–517.
(7) Taha, T. R.; Ablowitz, M. I. *J. Comput. Phys.* **1984**, *55*, 203–230.
(8) Weideman, J. A. C.; Herbst, B. M. *SIAM J. Numer. Anal.* **1986**, *23*, 485–507.
(9) Matsen, M. W. *Eur. Phys. J. E* **2009**, *30*, 361–369.
(10) Hamley, I. W. *Nanotechnology* **2003**, *14*, R39–R54.
(11) Cheng, J. Y.; Mayes, A. M.; Ross, C. A. *Nat. Mater.* **2004**, *3*, 823–828.
(12) Segalman, R. A. *Mater. Sci. Eng. R: Rep.* **2005**, *48*, 191–226.
(13) Stoykovich, M. P.; Nealey, P. F. *Mater. Today* **2006**, *9*, 20–29.
(14) Fredrickson, G. H. *Macromolecules* **1987**, *20*, 2535–2542.
(15) Matsen, M. W. *J. Chem. Phys.* **1997**, *106*, 7781.
(16) Pickett, G. T.; Balazs, A. C. *Macromolecules* **1997**, *30*, 3097–3103.
(17) Yu, B.; Sun, P.; Chen, T.; Jin, Q.; Ding, D.; Li, B.; Shi, A. *Phys. Rev. Lett.* **2006**, *96*, 138306.
(18) Bosse, A. W.; Garca-Cervera, C. J.; Fredrickson, G. H. *Macromolecules* **2007**, *40*, 9570.
(19) Hur, S.; García-Cervera, C. J.; Kramer, E. J.; Fredrickson, G. H. *Macromolecules* **2009**, *42*, 5861–5872.
(20) Alexander-Katz, A.; Moreira, A. G.; Fredrickson, G. H. *J. Chem. Phys.* **2003**, *118*, 9030.
(21) Silberberg, A. *J. Colloid Interface Sci.* **1982**, *90*, 86–91.
(22) Milner, S. T.; Morse, D. C. *Phys. Rev. E* **1996**, *54*, 3793.
(23) de Gennes, P. G. *Scaling Concepts in Polymer Physics*, 1st ed.; Cornell University Press: Ithaca, NY, 1979.
(24) Wu, D. T.; Fredrickson, G. H.; Carton, J. *J. Chem. Phys.* **1996**, *104*, 6387.
(25) Boyd, J. P. *Chebyshev and Fourier Spectral Methods: Second Revised ed.*, 2nd ed.; Dover Publications: London, 2001.
(26) Gottlieb, D.; Orszag, S. A. *Numerical Analysis of Spectral Methods: Theory and Applications*; Society for Industrial Mathematics: Philadelphia, PA,1987.
(27) Canuto, C.; Hussaini, M.; Quarteroni, A.; Zang, T. A. J.; Canuto, C. *Spectral Methods in Fluid Dynamics*; Springer: Berlin, 1991.
(28) Helfand, E. *J. Chem. Phys.* **1975**, *62*, 999.

(29) Wang, Q. *J. Chem. Phys.* **2008**, *129*, 054904−054904−6.
(30) Chantawansri, T. L.; Hur, S.; García-Cervera, C. J.; Ceniceros, H. D.; Fredrickson, G. H. *J. Chem. Phys.* **2011**, *134*, 244905.
(31) Fredrickson, G. H.; Helfand, E. *J. Chem. Phys.* **1987**, *87*, 697.
(32) Fredrickson, G. H.; Ganesan, V.; Drolet, F. *Macromolecules* **2001**, *35*, 16−39.
(33) Stasiak, P.; Matsen, M. *Eur. Phys. J. E* **2011**, *34*, 110.
(34) McLachlan, R. *Numer. Math.* **1993**, *66*, 465−492.
(35) Ranjan, A.; Qin, J.; Morse, D. C. *Macromolecules* **2008**, *41*, 942−954.
(36) Clenshaw, C. W.; Curtis, A. R. *Numer. Math.* **1960**, *2*, 197−205.
(37) Ceniceros, H. D.; Fredrickson, G. H. *Multiscale Model. Simul.* **2004**, *2*, 452.
(38) Thompson, R. B.; Rasmussen, K. O.; Lookman, T. *J. Chem. Phys.* **2004**, *120*, 31.
(39) Mark, W, M. *Curr. Opin. Colloid Interface Sci.* **1998**, *3*, 40−47.
(40) Matsen, M. W.; Griffiths, G. H. *Eur. Phys. J. E* **2009**, *29*, 219−227.
(41) Frigo, M.; Johnson, S. G. *Proc. IEEE* **2005**, *93*, 216.
(42) Wagner, L. *Phys. Rev. E* **1995**, *51*, 499.
(43) Heine, D. R.; Grest, G. S.; Webb, E. B. *Phys. Rev. E* **2003**, *68*, 061603.
(44) Heine, D. R.; Grest, G. S.; Webb, E. B. *Phys. Rev. Lett.* **2005**, *95*, 107801.
(45) Milchev, A.; Binder, K. *J. Chem. Phys.* **2002**, *116*, 7691.
(46) Müller, M.; Binder, K. *Macromolecules* **1998**, *31*, 8323−8346.
(47) Müller, M.; MacDowell, L. G. l. *J. Phys.: Condens. Matter* **2003**, *15*, R609−R653.
(48) Kim, J. U.; Matsen, M. W. *Soft Matter* **2009**, *5*, 2889−2895.
(49) Helfand, E.; Tagami, Y. *J. Polym. Sci., Part B: Polym. Lett.* **1971**, *9*, 741−746.

Macromolecules

Article

pubs.acs.org/Macromolecules

Effects of Topology and Ionic Strength on Double-Stranded DNA Confined in Nanoslits

Po-keng Lin,[†] Chih-Chen Hsieh,[‡] Yeng-Long Chen,*[,†,§,⊥] and Chia-Fu Chou*[,†]

[†]Institute of Physics and Research Center for Applied Sciences, Academia Sinica, Nangang, Taipei, Taiwan

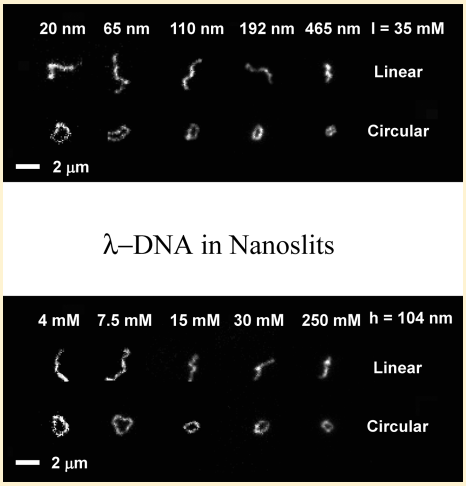
[‡]Department of Chemical Engineering, National Taiwan University, Taipei, Taiwan

[§]Department of Physics, National Taiwan University, Taipei, Taiwan

[⊥]Department of Chemical Engineering, National Tsing-Hua University, Hsinchu, Taiwan

Supporting Information

ABSTRACT: We investigate experimentally the effects of electrostatic interactions and topological constraints on DNA dynamics in nanoslit confinement by studying the equilibrium shape and dynamics of single linear and circular λ-DNA confined in a silicon/glass nanoslit. Having examined the dependence of chain radius of gyration $R_{\|}$, shape asphericity A, and relaxation time τ on chain topology, slit height h (20−782 nm), and solvent ionic strength I (8.2−268.8 mM), it is found that the chain shape becomes more aspherical as h and I decrease. Moreover, in strong sub-Kuhn length confinement, the DNA relaxation time increases with decreasing h in a smooth and broad transition. Our results provide experimental evidence to confirm that the scaling exponents of radius of gyration and of relaxation time are the same for linear and circular DNA and help resolve conflicting observations of the qualitative dependencies of chain radius of gyration and relaxation time in sub-Kuhn length slits.



I. INTRODUCTION

Topological constraints play an important role in DNA condensation and DNA packaging in viruses. Bacteriophage DNA packed in small capsids form highly supercoiled[1] and complicated knots.[2] The size of these DNA molecules is typically larger than 10 kbp, with radius of gyration R_{bulk} > 300 nm in free solution and much greater than the size of the capsid (≈50 nm). The strong packing severely restricts on the DNA conformation and dynamics. Recent studies have elucidated confinement effects on the DNA structure and dynamics.[3−9] In strong confinement, it is now known that restrictions on the chain conformational entropy result in an increase in the segmental correlation length.[10−13] In addition, it has been well-known that electrostatic interactions strongly affect DNA conformation and dynamics and that controlling the solvent ionic strength is a mechanism for manipulating DNA properties. It has been shown that the DNA persistence length can change by more than a factor 2 between high and low solvent ionic strength.[14−20] In strong confinement, such increase in the DNA segmental stiffness can significantly affect DNA dynamics.[21]

Classical polymer theories provide some insights into how confinement affects DNA properties. For DNA molecules with contour length (L) greater than a few hundred nanometers, one may consider double-strand DNA molecules as a wormlike polymer with a persistence length p, width w, and Kuhn length $L_K = 2p$. The polymer size is characterized by its radius of gyration R_g. For polymers in a good solvent, the power law dependence of R_g on polymer contour length $L = N_K L_K$ is given by $R_g = L_K N_K^{\nu}$, with ν = 3/4 and 3/5 in two (2D) and three (3D) dimensions, respectively.[22,23] Here N_K is the number of Kuhn length. For polymers in free solution (3D), the dependence of R_g on L for linear and circular DNA has been characterized through the measurement of the DNA diffusivity (D). By considering the Zimm model, $D \sim 1/R_g$, it is found that $\nu \approx 0.6$.[24] In 2D, recent experiments directly measured the radius of gyration of DNA adsorbed onto a surface and found that $\nu \approx 0.75$, and the scaling exponent are the same for linear and circular DNA, in agreement with the prediction for two-dimensional self-avoiding walk (SAW).[25]

The sizes and shapes of linear and circular polymers in two and three dimensions have also been well-studied by simulations via lattice model analysis,[26] Brownian dynamics simulations,[27] and Monte Carlo methods.[28] These studies found that the theoretical scaling exponents closely agree with the predictions of Flory,[23] and they are the same for linear and circular chains. For the shape of polymer, which can be characterized by its asphericity, exact

Received: September 1, 2011
Revised: February 22, 2012
Published: March 6, 2012

 © 2012 American Chemical Society dx.doi.org/10.1021/ma202695e | *Macromolecules* 2012, 45, 2920−2927

analytical calculation,[29,30] 1/d expansions method,[31] and Brownian dynamics simulation,[27,32] all found that a ring polymer undertakes an anisotropic shape on average. Furthermore, the shape of two-dimensional circular chains was examined over a wide range of chain stiffness, and it was found that the dependence on the chain stiffness is captured by theory.[33]

Although the physical properties of circular DNA in quasi-one-dimensional, 2D, and 3D environments have been extensively investigated, experimental studies of the conformation and dynamics of circular DNA in the transitional quasi-two-dimensional (Q2D) systems have been limited.[25,33−36] The Q2D geometry allows direct examination of how the rich behavior of confined polymers depends on the length scale of L, R_g, p, and w. For confined semiflexible polymers, two regimes of properties have been observed: the moderately confined ($L_k < h < R_g$) and the strongly confined ($h < L_k$). Simple steps of micro/nanofabrication can provide nanoslits with well-defined slit height h, which enable precise control of the confinement comparable to or even smaller than the persistence length p. These devices permit us to study the polymer physics of DNA in Q2D environment and investigate the transition of static and dynamic properties from 3D to 2D.

In the moderately confined regime ($L_k < h < R_g$), de Gennes's blob theory predicts the qualitative dependence of chain extension, diffusivity, and relaxation time on N_K and h. In this picture, a DNA molecule can be thought of as a string of blobs with diameter equal to h confined in nanoslit that follows 2D SAW statistics.[37] Within each blob, the chain conformation follows 3D SAW statistics. The radius of gyration of a SAW polymer in free solution is $R_F = (pw)^{1/5}(Na)^{3/5}$, where N is the number of polymer segments and a is the monomer size.[38] Thus, a blob with g segments has diameter $h \sim (pw)^{1/5}(ga)^{3/5}$. A confined chain consists of $N_{blob} = N/g$ blobs and its R_g can be expressed as

$$R_g \sim hN_{blob}^{3/4} \sim h\left(\frac{N}{g}\right)^{3/4} \sim \left(\frac{pw}{h}\right)^{1/4} L^{3/4} \tag{1}$$

The qualitative dependences of dynamic properties are also predicted by scaling theory.[37,39] Each blob is regarded as a nondraining sphere with friction coefficient $\zeta_{blob} = 6\pi\eta h$, where η is the solvent viscosity. In 2D, the interblob hydrodynamic interactions (HI) are considered to be negligible. However, the influence of HI in Q2D systems remains a topic of research. With and without HI in Q2D, the chain friction coefficient may be expressed as

$$\zeta_{chain}^{R} = \zeta_{blob}N_{blob} = \zeta_{blob}\left(\frac{N}{g}\right) = 6\pi\eta\left(\frac{pw}{h^2}\right)^{1/3} L \quad \text{(Rouse)} \tag{2a}$$

$$\zeta_{chain}^{Z} = 6\pi\eta R_g = 6\pi\eta\left(\frac{pw}{h}\right)^{1/4} L^{3/4} \quad \text{(Zimm)} \tag{2b}$$

The chain elastic relaxation time may be estimated from ζ_{chain} by considering the polymer as a spring with spring constant $k = k_BT/R^2$, where T is the absolute temperature. This gives

$$\tau^{R} \sim \zeta_{chain}^{FD}R^2 \sim \left(\frac{1}{h}\right)^{7/6}(pw)^{5/6}L^{5/2} \quad \text{(Rouse)} \tag{3a}$$

$$\tau^{Z} \sim \zeta_{chain}^{HI}R^2 \sim R^3 \sim \left(\frac{pw}{h}\right)^{3/4} L^{9/4} \quad \text{(Zimm)} \tag{3b}$$

Recent experiments[40,41] have suggested that intrachain hydrodynamic screening may not completely eliminate the influence of HI. By considering the dependence of τ_{relax} on N, we thus aim to verify the hydrodynamic screening effect in Q2D.

In very strong confinement ($h < L_K$), the chain backbone is deflected by the walls and the competition between chain elasticity and confinement entropy affect chain conformation and dynamics. Odijk and others have estimated the free energy of wormlike chain (WLC) confined in a capillary and a slit.[10−12] In this regime, the polymer exhibits the 2D pancake conformation and can be regard as a chain of rods, each with deflection length $\lambda \approx (h^2p)^{1/3}$ and diameter w. The free energy of a polymer confined in a slit is given by

$$\frac{F}{k_BT} \cong \frac{R^2}{pL} + \frac{N_\lambda{}^2E}{R^2h} \tag{4}$$

where the excluded volume per Odijk segments is $E \approx w\lambda^2$ and the number of rods in a chain is $N_\lambda = L/\lambda$. The first term in eq 4 captures the contributions from the entropic elasticity of polymer chain, and the second term arises from the excluded volume repulsion between deflection segments. Minimizing the free energy gives the equilibrium size R_g of polymer in strongly confined slits.

$$R_g \sim \left(\frac{pw}{h}\right)^{1/4} L^{3/4} \tag{5}$$

which is the same qualitative result obtained for moderate confinement.

In both regimes, the ionic strength of buffer can affect significantly affect the DNA elasticity and electrostatic repulsion between DNA segments.[42] The length scale of this electrostatic interaction between DNA segments in ionic solutions can be characterized by the Debye length

$$\kappa^{-1} = \sqrt{\frac{\varepsilon\varepsilon_0k_BT}{2Z_AZ_Be^2I}} \tag{6}$$

where ε is the dielectric constant of water, ε_0 is the permittivity of free space, k_B is the Boltzmann constant, Z_i is the valence of the ions, e is the electronic charge, and I is the ionic strength in units of number of molecules per liter. A very rough estimate of the effective width of a DNA molecules, accounting for electrostatic interaction, is to consider $w = 2\kappa^{-1}$. More accurate calculations by Stigter, who applied the Poisson−Boltzmann theory to calculate the rod−rod electrostatic repulsive interaction potential in monovalent salt solutions and mapping the effective width to that between neutral rods, gives the effective DNA width as

$$w = \frac{1}{\kappa}\left(0.7704 + \log\frac{2\pi\nu_{eff}{}^2}{\varepsilon\varepsilon_0k_BT\kappa}\right) \tag{7}$$

where ν_{eff} is the effective DNA line charge.[43,44]

The ionic strength dependence of the electrostatic persistence length for wormlike polyelectrolyte chains is analytically derived by Odijk[16] and Skolnick and Fixman[18] (OSF) using Poisson−Boltzmann theory. The total persistence

dx.doi.org/10.1021/ma202695e | Macromolecules 2012, 45, 2920−2927

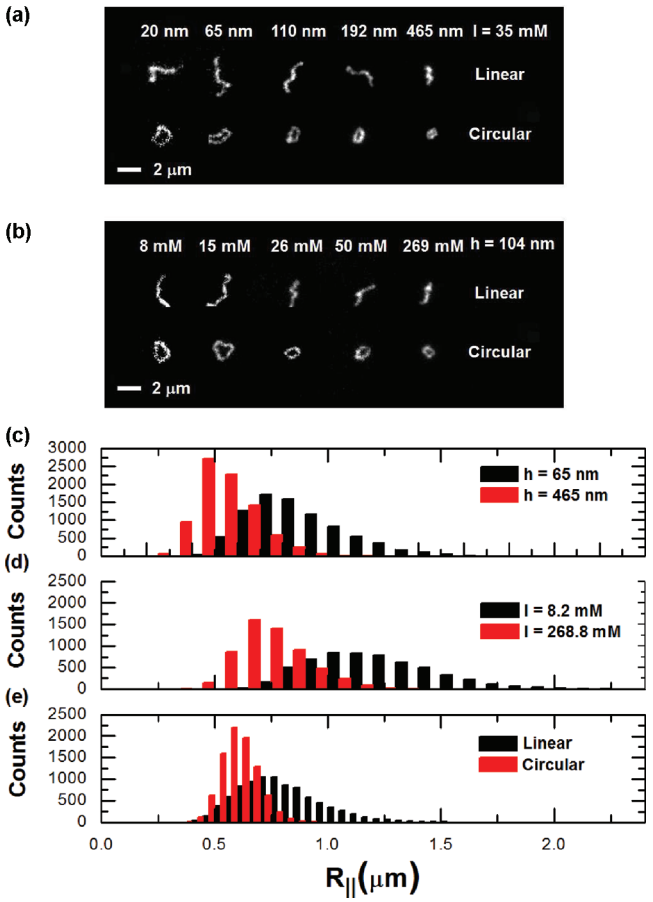


Figure 1. Fluorescence images of linear and circular λ-DNA in nanoslits at (a) h = 20 to 465 nm and (b) I = 8.2−268.8 mM. Histograms of R_g for (c) linear λ-DNA in h = 65 nm and h = 465 nm where I = 50.2 mM; (d) linear λ-DNA in I = 8.2 mM and I = 268.8 mM where h = 104 nm; and (e) linear and circular λ-DNA, where h = 110 nm and I = 50.2 mM.

length is the sum of the intrinsic persistence length (p_0) and the electrostatic persistence length (p_{el})

$$p = p_0 + p_{el} = p_0 + \frac{1}{4\kappa^2 l_B} = p_0 + \frac{0.0324[M]}{I} \quad [nm] \tag{8}$$

where p_0 is the intrinsic persistence length and l_B is the Bjerrum length. Another model developed by Dobrynin et al.[19] suggests

$$p = 46.1 + \frac{1.9195[M]}{\sqrt{I}} \quad [nm] \tag{9}$$

We will examine these dependences in our experiments.

Several recent experiments and simulations have characterized the dependence of the projected radius of gyration ($R_{||}$),[45−48] extension (R),[17,49−51] shape anisotropy (A),[49,52] diffusivity (D),[17,48,49,53−55] and relaxation time (τ_{relax})[40,46,48,49,52,56] on the slit height (h). However, some disagreements are reported. In the report by Bonthuis et al.,[45] it was found that the projected chain radius of gyration reaches a minimum at $h \approx R_{||,bulk}/2$. Additionally, the qualitative dependence of $R_{||}$ and τ_{relax} on h changes dramatically between moderate and strongly confined regimes. In contrast, recent work by Tang et al.[46] reported no qualitative change for either $R_{||}$ and τ_{relax} in h. In this work, we revisit these disagreements by

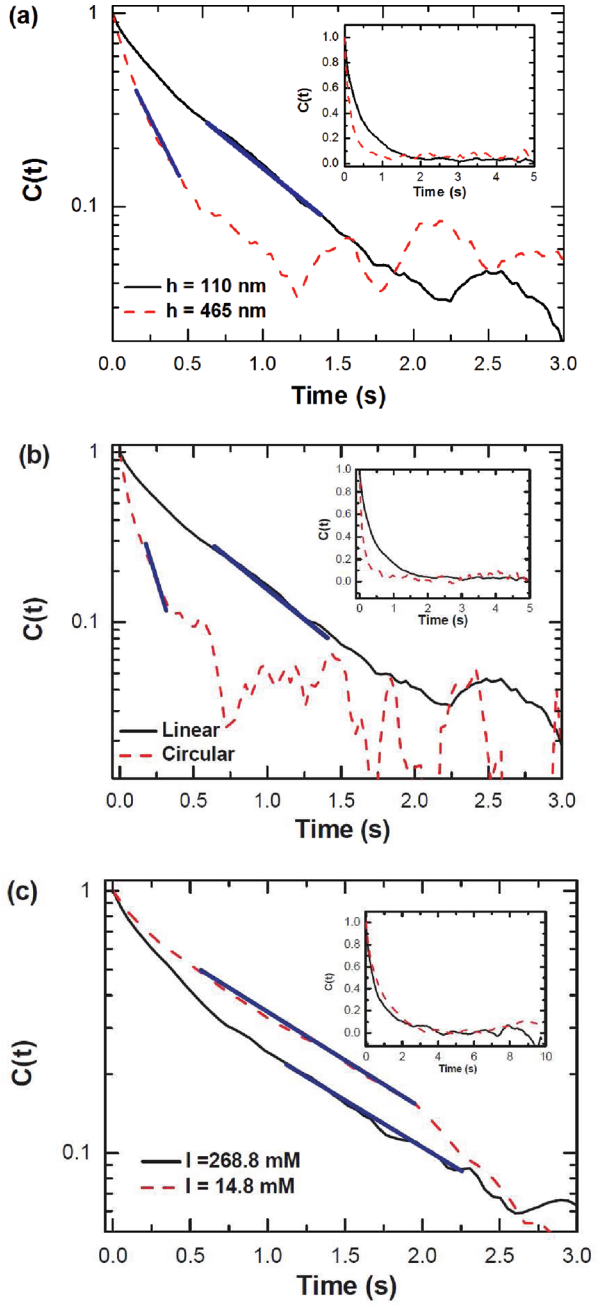


Figure 2. Autocorrelation function $C(t)$ (on a semilog scale) of (a) linear DNA for h = 110 nm and h = 465 nm slits, I = 50.2 mM; (b) linear and circular DNA in a h = 110 nm slit with I = 50.2 mM; and (c) linear DNA for I = 268.8 mM and I = 14.8 mM in a h = 104 nm slit. The blue solid lines show the exponential fits for obtaining the relaxation time. The inset shows $C(t)$ on the linear scale.

experimentally investigating the radius of gyration, shape asphericity, and relaxation time for both single linear and circular λ-DNA confined in nanoslit with varying slit height h (20−782 nm). The dependence of DNA properties on the solvent ionic strength I (8.2−268.8 mM) is also investigated.

II. METHODS

A. Device Fabrication. The nanoslit fluidic devices are made by first patterning silicon wafers with photolithography, followed by reactive ions etching (RIE) to the desired depth with a combination of CF_4 and O_2 gas, and finally anodic bonding to a 0.17 mm thick Pyrex

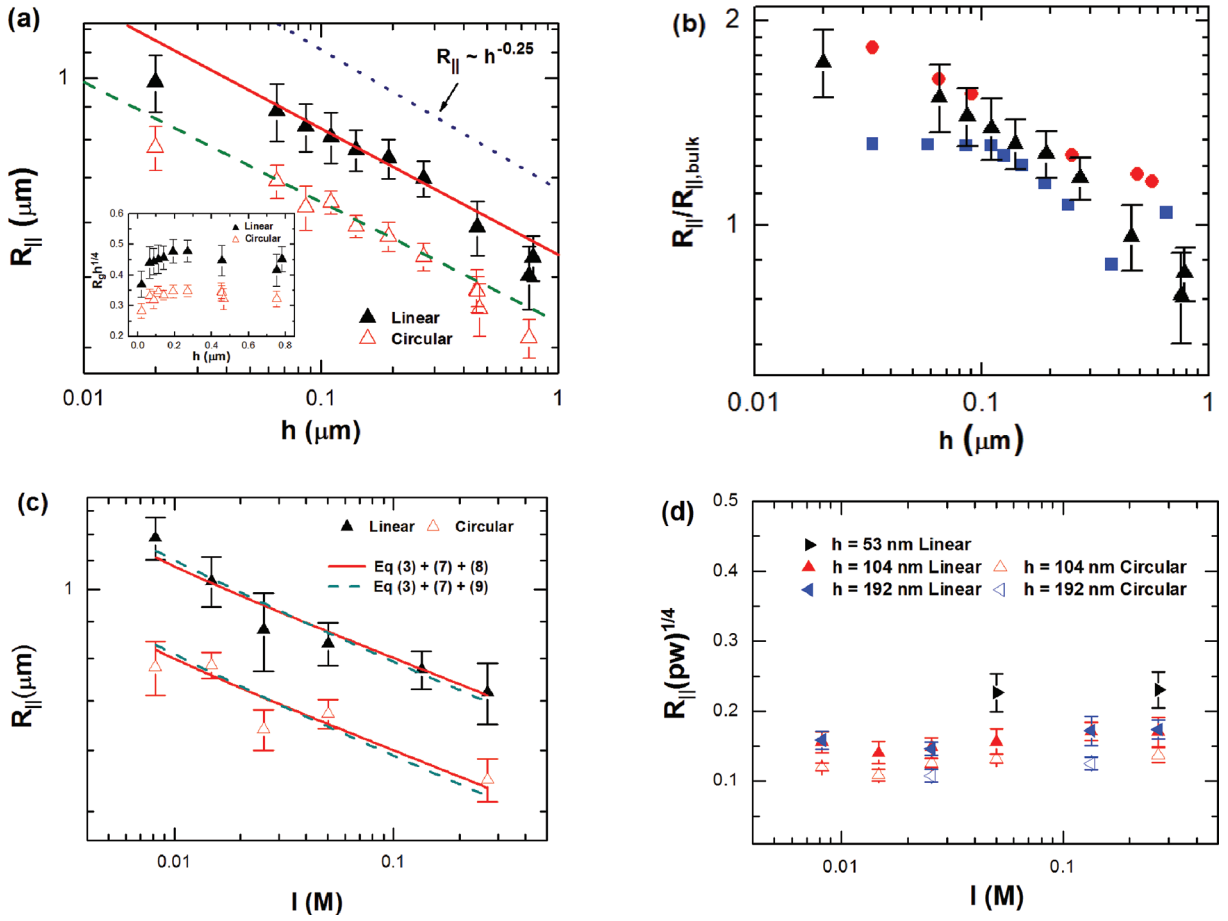


Figure 3. (a) The in-plane radius of gyration $R_{||}$ vs slit height h with ionic strength I = 50.2 mM. The solid (dashed) line is the best fit to linear (▲) and circular (△) λ-DNA for h = 65−465 nm and h = 65−270 nm, respectively. The dotted line is the scaling prediction of blob model with the slope −0.25. Comparison between measurements of $R_{||}h^{1/4}$ and scaling theory is shown in the inset. (b) Comparison of $R_{||}/R_{||,bulk}$ as a function of h for results of ref 45 (squares), ref 46 (circles), and this study (triangles). (c) The in-plane radius of gyration $R_{||}$ vs ionic strength I with h = 104 nm. The solid (dashed) line is the best fit for linear (▲) and circular (△) λ-DNA for I = 8.2−268.8 mM. (d) $R_{||}(pw)^{1/4}$ vs I for h = 53, 104, and 192 nm.

cover glass (Corning 7740) at 300 °C and 700 V. The nanoslits used in the experiments are 100 μm wide and 20−782 nm high. The height of the nanoslits is verified by KOSAKA ET4000A surface profiler before sealing and by scanning electron microscope after sealing.

B. DNA Preparation. The linear λ-DNA is purchased from New England BioLabs. λ-DNA has complementary single-stranded end overhangs (12 bases). Therefore, DNA can be ligated to form circles or multimers. The DNA concentration is diluted from 500 to 5 μg/mL and heated to 65 °C for 10 min to prevent the formation of DNA multimers. The DNA molecules are incubated to reanneal the sticky ends at room temperature for at least 7 days. The prepared sample contains 10% circular DNA, as determined by optical observation, and no condensed or supercoiled DNA conformation was observed. The DNA buffer solution contains 0.5X TBE (45 mM tris base, 45 mM boric acid, and 1 mM EDTA) with 10 mM sodium chloride (NaCl). The ionic strength I and Debye length κ^{-1} of the buffer solution are ≈50.2 mM[57,58] and ≈2 nm, respectively. DNA molecules are labeled with the fluorescent dye YOYO-1 (Molecular Probes) at a ratio of four base pairs per dye. Prior studies have found the contour length and the persistence length of YOYO-labeled λ-DNA are L = 22 μm and p = 67 nm.[11,59,60] However, several recent force spectroscopy experiments investigated the influence of YOYO-1 concentration on the DNA structure[61−63] and found L and p have strong dependences on the YOYO-1 concentration reduce the effective charge of the negatively charged DNA backbone, which has raised questions about the precise value of p. More detailed experiments in the future are needed to clarify the effects of YOYO-1 on DNA stiffness. The buffer solution contains 0.1% pop-6 (v/v) (Applied Biosystems), which can reduce the surface attraction to prevent the DNA sticking on surface, 3% 2-mercaptoethanol (v/v) (Sigma-Aldrich), 0.1% β-D-glucose (w/w) (Sigma-Aldrich), 10 μg/mL catalase (Roche), and 50 μg/mL glucose oxidase (Roche) in 0.5X TBE buffer with 10 mM NaCl. The viscosity η of the solution is 1.09 cP at 297 K as determined by capillary viscometry. The bulk radius of gyration of linear $R_{bulk,L}$ and circular $R_{bulk,C}$ form λ-DNA can be estimated indirectly from bulk diffusivity measurements with the relation $R_{bulk} = 0.203k_bT/(6\eta)^{1/2}D_{bulk}$.[42,64] In our experiments, $R_{bulk,L}$ and $R_{bulk,C}$ are found to be 693 and 438 nm, respectively.

C. Fluorescence Microscopy. DNA molecules are introduced into the nanoslit by capillary flow. After 1 h of equilibration, Brownian motion of DNA molecules is recorded. All experiments are performed at room temperature (≈25 °C). Fluorescence wide-field microscopy is performed with an Olympus IX70 microscope with a 100× (NA 1.35, resolution 0.4 μm) oil immersion objective, illuminated with an argon laser (488 nm, Coherent Innova 90). Images of over 30 DNA molecules at each slit height are captured by EM-CCD (Andor DV887DCS-BV) with 10 ms exposure time. The longest relaxation time of the DNA molecules is typically much larger than the exposure time, and the images are captured without rotational averaging. The total observation time is much greater than the measured stretch relaxation time of λ-DNA in a 32 nm slit (≈3 s).[46] Generally, 200 frames over a period of 20 s are recorded for each DNA. A shutter (LS3T2, Vincent Associates) is synchronized with CCD for uniform fluorescence images and to reduce photobleaching. Figure 1a,b shows the snapshot fluorescence images of individual linear and circular λ-DNA in a nanoslit from moderate (L_K < h < $R_{g,bulk}$) to strong

dx.doi.org/10.1021/ma202695e | Macromolecules 2012, 45, 2920−2927

confinement ($h < L_K$). The DNA molecules are optically tracked to ensure that the linear and circular topologies are clearly distinguished and are stable over the observation period, as shown in the Supporting Information video. The projected radius of gyration is extracted from image analysis, as described in the next subsection. Figure 1c–e shows the histograms of $R_{||}$ for different slit height, ionic strength, and chain topology. As expected, the distributions are shifted Gaussian for self-avoiding walks.

D. Image Acquisition and Analysis. Raw images of DNA molecules are processed by subtracting the background intensity. The background intensity is calculated from the average intensity of image with no DNA in the field. After subtracting the background intensity from the image, the total density of a single DNA molecule, $I(t)$, is calculated from the intensity distribution, $I(\mathbf{r},t)$. Here $\mathbf{r}$ is the position of each pixel and the zeroth moment

$$I(t) = \int I(r, t)\, \mathrm{d}r \tag{10}$$

accounts for the total intensity $I(t)$ of a single DNA molecule. The value of $I(t)$ is monitored to exclude possible DNA fragments and concatemers from the experiment ensemble. The decay of $I(t)$ as a function of time allows us to quantify the fluorescence bleaching effect, which is corrected for in our analysis. The molecular center of mass is given by

$$r_{\mathrm{cm}}(t) = \frac{1}{I(t)} \int \mathbf{r} I(\mathbf{r}, t)\, \mathrm{d}r \tag{11}$$

The shape and size of the DNA molecule are defined by calculating the radius of gyration tensor $\mathbf{G}$, given by

$$G_{ij}(t) = \frac{1}{I(t)} \int (r_i - r_{\mathrm{cm},i})(r_i - r_{\mathrm{cm},j}) I(r, t)\, \mathrm{d}\mathbf{r} \tag{12}$$

From the DNA image, which is projected onto two dimensions, the major and minor eigenvalues of $\mathbf{G}$ (λ_1 and λ_2) are calculated. The DNA image can be approximated by an ellipse with the major ($\mathbf{R}_M$) and minor ($\mathbf{R}_m$) principal axis, respectively.

$$R_M = 2\sqrt{\lambda_1}, \quad R_m = 2\sqrt{\lambda_2} \tag{13}$$

The shape are quantified by the in-plane radius of gyration $R_{||}$, which is given by

$$R_{||} = \frac{1}{2}\sqrt{R_M{}^2 + R_m{}^2} \tag{14}$$

The shape of the DNA molecule can be characterized by its asphericity A_2,[65,66] defined by

$$A_2 = \frac{(\lambda_1 - \lambda_2)^2}{(\lambda_1 + \lambda_2)^2} \tag{15}$$

A_2 ranges from 0 (spherical) to 1 (rod). The relaxation time τ is obtained from the radius-of-gyration autocorrelation function $C(t)$, given by

$$C(t) = \frac{\langle \delta R_{||}(t + t_0)\delta R_{||}(t_0))\rangle}{\langle \delta R_{||}{}^2(t_0)\rangle} = \frac{\langle (R_{||}(t + t_0) - \langle R_{||}(t)\rangle)(R_{||}(t_0) - \langle R_{||}(t)\rangle)\rangle}{\langle (R_{||}(t_0) - \langle R_{||}(t)\rangle)^2\rangle} \sim \mathrm{e}^{-t/\tau} \tag{16}$$

where $\langle R_{||}(t)\rangle$ is the ensemble averaged in-plane radius of gyration, determined by averaging statically uncorrelated DNA conformations. $\delta R_{||}(t) = R_{||}(t) - \langle R_{||}(t)\rangle$ is the fluctuation of $R_{||}$ around the mean value. As shown in Figure 2, $C(t)$ undergoes exponential decay, with typical chain relaxation time between 0.1 and 1 s.

III. RESULTS AND DISCUSSION

A. Static Scaling Analysis of Topological Dependence of DNA in Nanoslit. The dependence of $R_{||}$ of λ-DNA on h at moderate ionic strength (I = 50.2 mM) is first investigated. Figure 3a shows that $R_{||}$ of linear and circular λ-DNA monotonically increases with decreasing slit height. The ratio of $R_{||}$ between linear and circular λ-DNA can be used to compare the topological dependence of DNA for different confinement conditions. The mean value of the ratio $\langle R_{||,L}\rangle / \langle R_{||,C}\rangle$ with different slit heights is ≈1.34 ± 0.03, which is in good agreement with the modified Yu–Fujita model[23] that

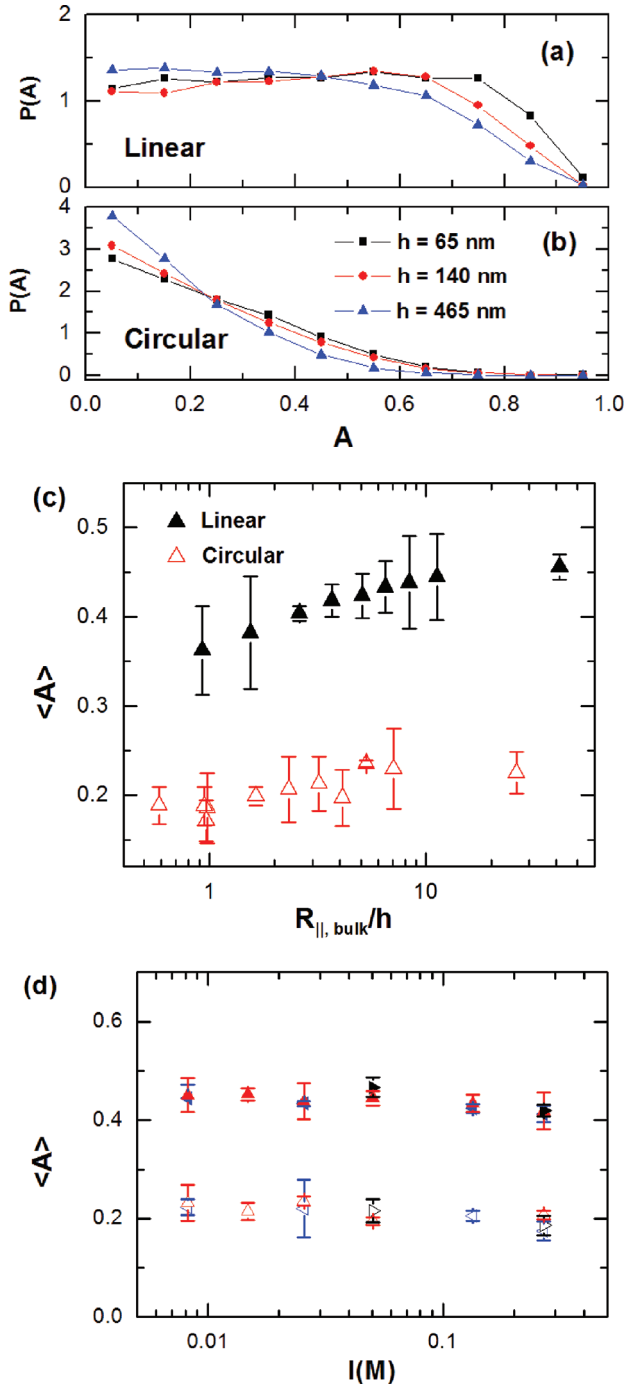


Figure 4. Probability density distribution of measured asphericity A of (a) linear and (b) circular λ-DNA for h = 465 nm (blue), 140 nm (red), and 65 nm (black). (c) The mean asphericity $\langle A\rangle$ vs $R_{||,\mathrm{bulk}}/h$ of linear (▲) and circular (Δ) λ-DNA. (d) Mean asphericity $\langle A\rangle$ as a function of I for linear (solid triangles) and circular (hollow triangles) λ-DNA for h = 53 nm (black), 104 nm (red), and 192 nm (blue).

dx.doi.org/10.1021/ma202695e | Macromolecules 2012, 45, 2920–2927

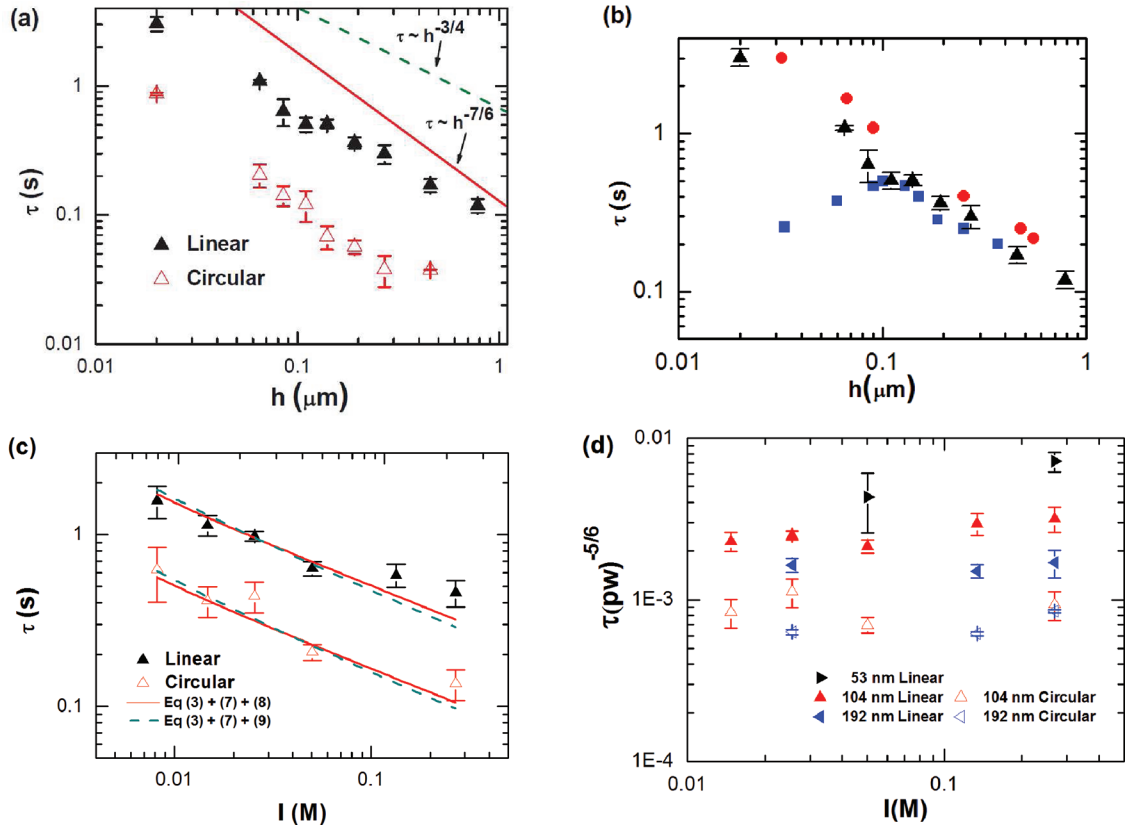


Figure 5. (a) Experimental results of relaxation time τ as a function of slit height h with ionic strength I = 50.2 mM. The solid (dashed) line is the scaling prediction of the blob model (freely draining) and blob model (full intrachain HI) with slope = −7/6 and −3/4, respectively. (b) τ vs h of ref 45 (squares), ref 46 (circles), and this study (triangles). (c) τ vs I with h = 104 nm. The solid (dashed) line is the best fit with $\tau = \beta(pw)^{5/6}$ to linear (▲) and circular (Δ) λ-DNA for I = 8.2−268.8 mM. (d) Rescaled relaxation time $\tau\ (pw)^{-5/6}$ vs I.

predicts the ratio to be 1.33 for 2D SAW. The scaling exponent $\nu_{\parallel}$ are found to be −0.22 ± 0.02 and −0.21 ± 0.02 for linear and circular DNA, respectively. It is observed that the $\nu_{\parallel}$ depends weakly on the chain topology, and it is slightly smaller than the theoretical predicted value of $\nu_{\parallel}$ = −0.25.[39] This appears to agree quantitatively with the measurements by other groups[46] for the moderate confinement regime. In this regime, these measurements also agree well with the theoretical prediction, as shown in the inset of Figure 3a. In the strong confinement regime, further comparison of $\langle R_{\parallel}\rangle/\langle R_{\parallel,\mathrm{bulk}}\rangle$ of linear λ-DNA between this work and previous studies found that $\langle R_{\parallel,\mathrm{L}}\rangle$ measured here qualitatively agrees with the measurements of ref 46 as shown in Figure 3b. The quantitative differences with ref 46 may be attributed to different estimates of $\langle R_{\parallel,\mathrm{bulk}}\rangle$. However, the current measurements of $\langle R_{\parallel}\rangle/\langle R_{\parallel,\mathrm{bulk}}\rangle$ increase monotonically, in disagreement with ref 45, which found that $\langle R_{\parallel}\rangle$ has a minimum at $h \approx \langle R_{\parallel,\mathrm{bulk}}\rangle/2$ and becomes constant for h < 100 nm.

At a lower solvent ionic strength, intrachain electrostatic repulsion leads to increased DNA persistence length and width. The effect on $\langle R_{\parallel}\rangle$ is shown for linear and circular DNA for I = 8.2−268.8 mM in Figure 3c. From eq 1, $R_{\parallel} = \alpha(pw)^{1/4}$ is fit to the experimental results with w (eq 7) and p determined via eqs 8 and 9, using α as a fitting parameter. The best fits capture the experimental data and yielding α_{L} = 0.110 ± 0.003 (eq 7 + eq 8), α'_{L} = 0.110 ± 0.004 (eq 7 + eq 9), α_{C} = 0.150 ± 0.004 (eq 7 + eq 8), and α'_{C} = 0.160 ± 0.003 (eq 7 + eq 9) for linear and circular λ-DNA, respectively. This fitting result suggests that the ionic effects on the radius of gyration of DNA can be captured by the blob model with ionic strength dependence of DNA persistence length and width. Figure 3d further shows $\langle R_{\parallel}\rangle(pw)^{1/4}$ vs I for h = 53, 104, and 192 nm. By accounting for the ionic strength dependence of p and w on I, it is found that $\langle R_{\parallel}\rangle(pw)^{1/4}$ is nearly independent of I. This verifies that electrostatic interactions affects DNA conformation mainly through p and w. However, these current experiments are unable to distinguish the validity of eqs 8 and 9, due to the limited range of the ionic strength studied. Future studies like those of ref 20 need to be performed to test the predictions of eqs 8 and 9.

The shapes of linear and circular DNA are known to be different in bulk. We have thus measured the asphericity for both linear (A_{L}) and circular (A_{C}) DNA with different nanoslit height h. Figures 4a and 4b show the probability distributions of A_{L} and A_{C} with h = 65, 140, and 465 nm, respectively. Both the distributions of A_{L} and A_{C} extend toward larger values of asphericity with decreasing h, indicating that the chain shapes become more rodlike. The probability distribution of A_{L} is very broad and even. In contrast, the distribution of A_{C} is centered at 0 and decays rapidly. This indicates that the shape of circular DNA is more circular-symmetric than linear DNA, as expected. Figure 4c shows the average A_{L} and A_{C} as a function of $R_{\parallel,\mathrm{bulk}}/h$. For all $R_{\parallel,\mathrm{bulk}}/h$, the values of $\langle A_{\mathrm{C}}\rangle$ are smaller than $\langle A_{\mathrm{L}}\rangle$, as expected. Both $\langle A_{\mathrm{L}}\rangle$ and $\langle A_{\mathrm{C}}\rangle$ increase with increasing $R_{\parallel,\mathrm{bulk}}/h$, which means that the larger principal axis of ellipsoid increases and the smaller principal axis decreases with increasing $R_{\parallel,\mathrm{bulk}}/h$. The values of $\langle A_{\mathrm{L}}\rangle$ and $\langle A_{\mathrm{C}}\rangle$ are between 0.36−0.46 and 0.19−0.23 for $R_{\parallel,\mathrm{bulk}}/h$ = 0.9−41, respectively. Previous simulation by

dx.doi.org/10.1021/ma202695e | Macromolecules 2012, 45, 2920−2927

Bishop et al.[67] found that $\langle A_L \rangle$ and $\langle A_C \rangle$ of 2D linear polymer and circular polymer are 0.53 and 0.20, respectively. The mean asphericity of circular DNA is consistent with the simulation result, but that of linear DNA is lower than the simulation result. The deviation of the measured $\langle A_L \rangle$ from simulation may be attributed to the microscope lateral resolution (≈350 nm). Because of this limitation, the observed R_2 is likely larger than the actual R_2, and the observed A_L would be smaller than the simulation results. Figure 4d shows the average A_L and A_C as a function of I (8.2−268.8 mM) with h = 53, 104, and 192 nm. The results show that the shape asphericity is nearly independent of the ionic strength with A_L and A_C around 0.44 and 0.21, respectively.

B. Relaxation Time of Linear and Circular DNA in Nanoslit. *Dependence on Slit Height.* In addition to examining the chain conformation, the effects of confinement and ionic strength on the chain relaxation time are also examined. Figure 5a shows the relaxation time τ as a function of the slit height for both linear and circular λ-DNA. The relaxation time is found to monotonically increase with decreasing slit height. This behavior is expected, as stronger confinement restricts chain relaxation and increases the relaxation time. From the moderate to strong confinement regime, $\tau \sim h^{-1}$ is found to capture the qualitative dependence, with the scaling exponent of linear ($\nu_{\tau,L}$) and circular ($\nu_{\tau,C}$) λ-DNA found to be −0.93 ± 0.04 and −0.99 ± 0.02, respectively. This shows that ν_τ is nearly invariant for linear and circular DNA. Furthermore, the observed scaling exponent falls between the predictions of τ with freely draining and full intrachain HI, suggesting that the hydrodynamic interactions between chain segments are partially screened.

The comparison of τ_L between the current study and those of refs 45 and 46 is shown in Figure 5b. In moderate confinement, the current measurements of rotational relaxation time τ_r agree quantitatively with those measured in refs 45 and 46, within the error bars. Small quantitative differences may be due to the differences in the buffer content. However, for h < 100 nm, ref 45 found that the τ_L has a maximum at h = 100 nm (≈2p) and τ_L sharply decreases with decreasing h. This unexpected result qualitatively contradicts the study of ref 46 and our measurements.

Dependence on Ionic Strength. The dependence of τ on I is shown in Figure 5c. For both linear and circular DNA, τ is found to increase nearly 4 times as I decrease from 268.8 to 8.2 mM. From eq 2), $\tau = \beta(pw)^{5/6}$ is fit to the experimental results with w and p determined from eqs 7 and 8, using β as a fitting parameter. The best fits capture the observation for I < 52.2 mM, yielding β_L = 0.0020 ± 0.0001 (eq 7 + eq 8), β'_L = 0.0008 ± 0.0001 (eq 7 + eq 9), β_C = 0.0030 ± 0.0002 (eq 7 + eq 8), and β'_C = 0.0009 ± 0.0001 (eq 7 + eq 9) for linear and circular λ-DNA, respectively. This fitting result suggests that the ionic effects on the relaxation time of DNA can be well characterized by the OSF model for ionic strength dependence of p and w.

IV. CONCLUSIONS

We have systematically investigated the topological dependences of the chain size, chain shape, and the chain relaxation time for both linear and circular λ-DNA in nanoslits by varying both the slit height and ionic strength. To our knowledge, our experiment is the first to investigate the transition from unconfined bulk to nanoslit confinement for circular DNA. We find no qualitative differences from the moderate to strongly confined regime for the chain conformation and chain relaxation time for both linear and circular λ-DNA. Our results confirm that the scaling exponents of radius of gyration and relaxation time are topologically invariant and close to the predicted values from scaling theories. For linear λ-DNA, our results agree qualitatively with the measurements of ref 46. The λ-DNA results of ref 45 for $R_{||}$ and τ_{relax} in the strongly confined regime have qualitative similarities with those properties found for quasi-1D confined DNA[68] and that may also be due to strong surface interactions with the confined DNA, leading to arrested dynamics for the DNA molecules. Understanding the properties of topological dependence of DNA in nanoslit can guide the investigation of DNA packing in confined environment using lab-on-a-chip technology.

■ ASSOCIATED CONTENT

Supporting Information

Video. This material is available free of charge via the Internet at http://pubs.acs.org.

■ AUTHOR INFORMATION

Corresponding Author

*E-mail: yenglong@phys.sinica.edu.tw (Y.-L.C.); cfchou@phys.sinica.edu.tw (C.-F.C.).

Notes

The authors declare no competing financial interest.

■ ACKNOWLEDGMENTS

This work was supported by Academia Sinica Program on Nanotechnology, Academia Sinica Career Development Award (to Y.L.C.), and by National Science Council (ROC) 98-2112-M-001-004-MY3 (to Y.L.C.), and 99-2112-M-001-027-MY3 (to C.F.C.). Work was performed in part at the Academia Sinica Nano Core Facilities.

■ REFERENCES

(1) Espejo, R. T.; Canelo, E. S.; Sinsheim, Rl. *Proc. Natl. Acad. Sci. U. S. A.* **1969**, *63*, 1164.
(2) Arsuaga, J.; et al. *Proc. Natl. Acad. Sci. U. S. A.* **2002**, *99*, 5373.
(3) Riemer, S. C.; Bloomfield, V. A. *Biopolymers* **1978**, *17*, 785.
(4) Smith, D. E.; et al. *Nature* **2001**, *413*, 748.
(5) Muthukumar, M. *Phys. Rev. Lett.* **2001**, *86*, 3188.
(6) Fuller, D. N.; et al. *Proc. Natl. Acad. Sci. U. S. A.* **2007**, *104*, 16868.
(7) Grayson, P.; et al. *Proc. Natl. Acad. Sci. U. S. A.* **2007**, *104*, 14652.
(8) Kim, Y.; et al. *Lab Chip* **2011**, *11*, 1721.
(9) Persson, F.; et al. *Nano Lett.* **2009**, *9*, 1382.
(10) Odijk, T. *Macromolecules* **1983**, *16*, 1340.
(11) Odijk, T. *J. Chem. Phys.* **2006**, *125*, 204904.
(12) Odijk, T. *Phys Rev E* **2008**, *77*, 060901(R).
(13) Chen, Y.-L.; Lin, P.-K.; Chou, C.-F. *Macromolecules* **2010**, *43*, 10204.
(14) Reisner, W.; et al. *Phys. Rev. Lett.* **2007**, *99*, 058302.
(15) Jo, K.; et al. *Proc. Natl. Acad. Sci. U. S. A.* **2007**, *104*, 2673.
(16) Odijk, T. *J. Polym. Sci., Part B: Polym. Phys.* **1977**, *15*, 477.
(17) Hsieh, C. C.; Balducci, A.; Doyle, P. S. *Nano Lett.* **2008**, *8*, 1683.
(18) Skolnick, J.; Fixman, M. *Macromolecules* **1977**, *10*, 944.
(19) Dobrynin, A. V. *Macromolecules* **2005**, *38*, 9304.
(20) Zhang, C.; et al. *J. Chem. Phys.* **2008**, *128*, 225109.
(21) Yeh, J. W. *Nano Lett.* **2012**, http://dx.doi.org/10.1021/nl2045292.
(22) de Gennes, P. G. *Scaling Concepts in Polymer Physics*; Cornell University Press: Ithaca, NY, 1979.
(23) Flory, P. *Statistical Mechanics of Chain Molecules*; Interscience Publishers: New York, 1969.

(24) Doi, M.; Edwards, S. F. *The Theory of Polymer Dynamics*; Oxford University Press: New York, 1986.
(25) Witz, G.; et al. *Phys. Rev. Lett.* **2008**, *101*, 148103.
(26) Privman, V.; Rudnick, J. *J. Phys. A: Math. Gen.* **1985**, *18*, L789.
(27) Bishop, M.; Michels, J. P. J *J. Chem. Phys.* **1986**, *85*, 1074.
(28) Reiter, J. *Macromolecules* **1990**, *23*, 3811.
(29) Gaspari, G.; Rudnick, J.; Beldjenna, A. *J. Phys. A: Math. Gen.* **1987**, *20*, 3393.
(30) Wei, G. Y. *Physica A* **1995**, *222*, 152.
(31) Rudnick, J.; Beldjenna, A.; Gaspari, G. *J. Phys. A: Math. Gen.* **1987**, *20*, 971.
(32) Bishop, M.; Michels, J. P. J *J. Chem. Phys.* **1985**, *83*, 4791.
(33) Drube, F.; et al. *Nano Lett.* **2010**, *10*, 1445.
(34) Witz, G.; et al. *Phys. Rev. Lett.* **2011**, 106.
(35) Robertson, R. M.; Laib, S.; Smith, D. E. *Proc. Natl. Acad. Sci. U. S. A.* **2006**, *103*, 7310−7314.
(36) Alim, K.; Frey, E. *Phys. Rev. Lett.* **2007**, 99.
(37) Daoud, M.; de Gennes, P. G. *J. Phys. (Paris)* **1977**, *38*, 85.
(38) Schaefer, D. W.; Joanny, J. F.; Pincus, P. *Macromolecules* **1980**, *13*, 1280.
(39) Brochard, F.; de Gennes, P. G. *J. Chem. Phys.* **1977**, *67*, 52.
(40) Hsieh, C. C.; Balducci, A.; Doyle, P. S. *Macromolecules* **2007**, *40*, 5196.
(41) Lin, P.-K.; et al. *Phys. Rev. E* **2011**, *84*, 031917.
(42) Odijk, T.; Houwaart, A. C. *J. Polym. Sci., Polym. Phys.* **1978**, *16*, 627.
(43) Stigter, D. *J. Colloid Interface Sci.* **1975**, *53*, 296.
(44) Schellman, J. A.; Stigter, D. *Biopolymers* **1977**, *16*, 1415.
(45) Bonthuis, D. J.; et al. *Phys. Rev. Lett.* **2008**, *101*, 108303.
(46) Tang, J.; et al. *Macromolecules* **2010**, *43*, 7368.
(47) Dai, L.; et al. *Soft Matter* **2012**, *8*, 2972.
(48) Jones, J. J.; van der Maarel, J. R. C.; Doyle, P. S. *Nano Lett.* **2011**, *11*, 5047−5053.
(49) Lin, P. K.; et al. *Phys Rev E* **2007**, *76*, 011806.
(50) Lin, P. K.; et al. *Macromolecules* **2009**, *42*, 1770.
(51) Tang, J.; Trahan, D. W.; Doyle, P. S. *Macromolecules* **2010**, *43*, 3081.
(52) Balducci, A.; Hsieh, C. C.; Doyle, P. S. *Phys. Rev. Lett.* **2007**, *99*, 238102.
(53) Balducci, A.; et al. *Macromolecules* **2006**, *39*, 6273.
(54) Strychalski, E. A.; Levy, S. L.; Craighead, H. G. *Macromolecules* **2008**, *41*, 7716.
(55) Chen, Y. L.; et al. *Phys Rev E* **2004**, *70*, 060901(R).
(56) Trahan, D. W.; Doyle, P. S. *Macromolecules* **2011**, *44*, 383−392.
(57) Li, A. Z.; et al. *Biopolymers* **1996**, *38*, 367.
(58) Perrin, D.; Dempsey, B. *Buffers for pH and Metal Ion Control*; Chapman and Hall: London, 1974.
(59) Makita, N.; Ullner, M.; Yoshikawa, K. *Macromolecules* **2006**, *39*, 6200.
(60) Baumann, C. G.; et al. *Proc. Natl. Acad. Sci. U. S. A.* **1997**, *94*, 6185.
(61) Sischka, A.; et al. *Biophys. J.* **2005**, *88*, 404−411.
(62) Murade, C. U.; et al. *Nucleic Acids Res.* **2010**, *38*, 3423−3431.
(63) Gunther, K.; Mertig, M.; Seidel, R. *Nucleic Acids Res.* **2010**, *38*, 6526−6532.
(64) Smith, D. E.; Perkins, T. T.; Chu, S. *Macromolecules* **1996**, *29*, 1372.
(65) Rudnick, J.; Gaspari, G. *Science* **1987**, *237*, 384.
(66) Aronovitz, J. A.; Nelson, D. R. *J. Phys. (Paris)* **1986**, *47*, 1445.
(67) Bishop, M.; Saltiel, C. J. *J. Chem. Phys.* **1988**, *88*, 3976.
(68) Reisner, W.; et al. *Phys. Rev. Lett.* **2005**, *94*, 196101.

Macromolecules

Article

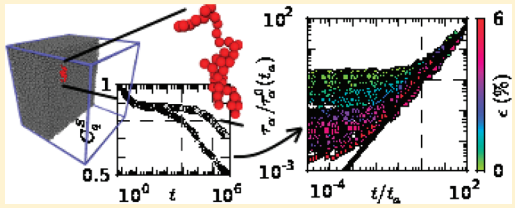
pubs.acs.org/Macromolecules

Recovery of Polymer Glasses from Mechanical Perturbation

Anton Smessaert* and Jörg Rottler

Department of Physics and Astronomy, The University of British Columbia, 6224 Agricultural Road, Vancouver, British Columbia, V6T 1Z1, Canada

ABSTRACT: Molecular dynamics simulations of a coarse-grained model of a polymer glass were used to study the recovery regime following deformation at constant stress or constant strain rate. We monitor dynamical as well as structural and energetic quantities to characterize the impact of deformation on the relaxation process. The α-relaxation times are reduced relative to an unperturbed sample immediately after deformation, and we observe a gradually increasing "erasure" of memory with increasing amount of deformation. Remarkably, the single deformation parameter that captures this continuous transition is the total strain at the end of deformation. For deformation up to of order the yield strain, the evolution of multiple measures of short-range order and the inherent structure energy closely track changes of the α-relaxation time, suggesting that the "rejuvenated" state is close to that of a younger glass. For larger strains accessible by constant strain rate deformation, however, plastic yield generates a distinctly different thermodynamic state.



INTRODUCTION

Amorphous solids are generally not in thermodynamic equilibrium but slowly change their properties over time. As the material relaxes or "ages", structural relaxation times increase due to small configurational changes that are assisted by thermal motion. Aging or structural recovery effects are particularly important in polymer glasses:[1] density, enthalpy and yield stress increase, but also the tendency for shear localization, which limits the lifetime to failure. Deformation and flow interact with the intrinsic relaxation dynamics in complicated ways. Numerous experimental observations[2−6] suggest that the history of a glass can be altered by mechanical perturbation in such a way that the material appears "younger". However, the nature and extent of this "mechanical rejuvenation" in aging glasses is far from understood and frequently debated.[7] While the often reported increase of the relaxation dynamics or molecular mobility during deformation in experiments[8,9] and simulations[10−12] may suggest that the "material clock" has indeed been turned back, the thermodynamic state reached by mechanical perturbation could still be very different from a glass that was rejuvenated through thermal cycling or other means.

Studies of "rejuvenation" tend to differentiate between the subyield regime of small stresses and the postyield regime where the material has undergone significant plastic deformation. In the subyield regime, the seminal work of Struik[2] showed based on creep experiments that stress can lead to an apparent reduction of relaxation times as determined from double−logarithmic shift factors. This effect has been qualitatively reproduced in molecular simulations of polymer glasses;[13] however, the material rapidly returned to the original aging trajectory once the deformation ceased.[14] It is therefore often suggested that subyield deformation only transiently perturbs the aging dynamics and that there is no direct connection to changes in material properties.[7,15,16] For postyield deformation, however, rejuvenation experiments on polystyrene[4] and polycarbonate[5,6] glasses demonstrate more convincingly thermal and yield stress properties akin to a much younger glass. Simulations that investigate the energy landscape of such strongly deformed glasses[17−19] make similar observations and report that the material has been taken to higher inherent structure energies. The deformation trajectory, however, does not appear to return the material to the exact same position on the landscape as a thermal quench but rather to a different state.

A recent series of experiments on PMMA glasses by Lee and Ediger provides very detailed insight into the interaction between physical aging and plastic deformation.[20,21] These authors employ a fluorescence microscopy technique that permits measurements of segmental relaxation times simultaneously with macroscopic mechanical response.[9] During creep deformation at constant stress, they report significantly increased molecular mobility, but true erasure of aging was only found in the flow regime.[20] A second study focused on the recovery behavior immediately following the deformation period, where again two different situations were identified: in the preflow regime only transient rejuvenation effects occurred and relaxation times rapidly returned to those of an unperturbed glass, while glasses that experienced postyield deformation displayed no memory effects and were found to age in the same way as a thermally quenched glass. On the basis of these observations, the authors suggest that mechanical rejuvenation does occur in the postyield regime.[21]

The present contribution aims to further elucidate the mechanisms and variables that control rejuvenation effects from the perspective of molecular simulations. Here we study model

Received: January 4, 2012
Revised: February 15, 2012
Published: March 7, 2012

 © 2012 American Chemical Society dx.doi.org/10.1021/ma3000253 | *Macromolecules* 2012, 45, 2928−2935

polymer glasses in the recovery regime after creep deformation in a protocol modeled closely after that of ref 21. By systematically varying the age, stress amplitude, and duration of the creep period, we are able to explore a wide range of deformation parameters. We also use a constant strain rate deformation protocol, which allows us to extend this study further into the regime of plastic flow. As in experiments, the relaxation times are reduced in the deformed samples and can reach those of a freshly quenched glass. We observe a continuous transition from the "transient rejuvenation" regime at small deformation to the full "erasure" of aging after plastic yield. Remarkably, the single parameter that controls the degree of rejuvenation is the strain amplitude at the end of the deformation period. On the basis of the simulation results, we establish several theoretical recovery scenarios and discuss their implications.

In order to help resolve the debate around the nature of the rejuvenated state, we complement our calculations of relaxation times with several measures for local short-range order in the glass and by probing the inherent structure energies. Although these change only logarithmically with time, we can still monitor their recovery trajectories and compare to unperturbed reference samples. These measures suggest that the structure of the rejuvenated state is close to that of a freshly quenched glass for small deformations. Larger strains, however, can take the glass to different configurations even though the material appears the same from a dynamical point of view.

METHODS

We simulate the time evolution of glassy polymers via the molecular dynamics technique. As a model we choose the well-known FENE bead−spring potential, which combines a 6−12 Lennard-Jones (LJ) bead with a stiff spring that inhibits chain-crossings.[22] This coarse-grained model has been studied extensively in the glass phase and shows the characteristic behavior expected for polymer glasses.[13,23−26] All results are given in the usual LJ-units, i.e., depth of the LJ energy-well u_0, bead diameter a, and mass m, as well as in the characteristic time scale $\tau_{LJ} = (ma^2/u_0)^{1/2}$, and we choose a time step of $\Delta t = 0.0075\tau_{LJ}$. To decrease the computational effort we truncate the LJ-potential at $1.5a$ and shift for continuity. Our simulations consist of 1000 chains of 50 beads each in an initially cubic simulation box with periodic boundary conditions. The box size is chosen so that the system is initially at a density of $1.005a^{-3}$, which yields a glass at close to zero pressure immediately after the quench. The simulations are performed with LAMMPS[27] and we employ a Langevin thermostat and Nosé-Hoover type barostat where applicable. The glass is generated in three steps:[13] first, we equilibrate the polymer melt at a temperature of $1.2u_0/k_B$ and constant volume using standard methods.[28] In the second step, the system is quenched in $1500\tau_{LJ}$ to the temperature $T = 0.2u_0/k_B$, which is well below the glass transition at $T_g \simeq 0.35u_0/k_B$.[25] In a final step, we switch to the NPT ensemble and quickly ramp the pressure to zero in $37.5\tau_{LJ}$.

This "new" glass is the actual starting point of our study. In accordance with isothermal uniaxial tensile creep experiments we apply mechanical stress in one direction following the protocol shown in Figure 1a. The simulations are performed at fixed pressure $P_{xx} = P_{yy} = 0$ and constant temperature $T = 0.2u_0/k_B$. In the first time interval t_w the glass ages at $P_{zz} = 0$. This is followed by a period of stress application t_s during which the pressure is held constant at $P_{zz} = -\sigma$. To avoid discontinuities, we quickly ramp the pressure to its new value in $37.5\tau_{LJ}$. In the final recovery period t_r the glass again ages at $P_{xx} = P_{yy} = P_{zz} = 0$. In this recovery regime we observe to which extent the mechanical perturbation has altered the polymer glass and its return to the aging dynamics.

In this study, we explore glasses in the quasi-adiabatic limit of negligible aging during deformation. Since the intrinsic time-dependence in the glass phase is logarithmic, we must restrict the deformation time to $t_s < t_w$. To reach larger strain magnitudes in the creep protocol described above, one either has to simulate very long wait times or has to increase the applied stress amplitude. The later leads to numerical instabilities in the barostat around the yield point, which effectively constrains the accessible strain to <6%. In order to reach deformations in the postyield regime, we apply an alternative protocol shown in Figure 1b. The glass is deformed in the z-direction at a constant strain rate $\dot{\epsilon}$ and the barostat only fixes the perpendicular pressure $P_{xx} = P_{yy} = 0$. This approach avoids the numerical problems and yields comparable deformation states that are then aged at zero pressure in the recovery regime.

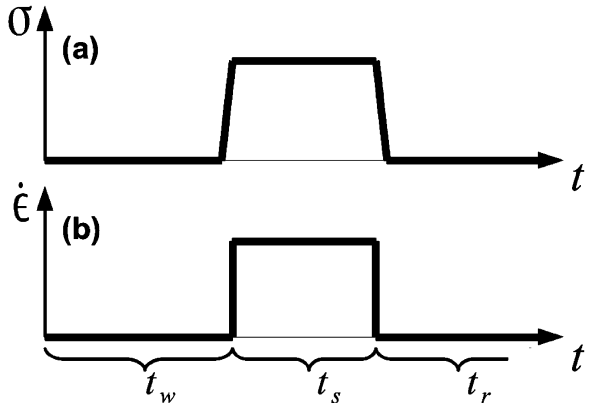


Figure 1. Schematic protocol of the (a) uniaxial tensile creep and (b) uniaxial fixed strain rate simulation and recovery with time parameters t_w, t_s, and t_r (see text).

RESULTS

Immediate impact of creep. When tensile stress is applied to a glass, the material reacts first with an elastic response followed by plastic deformation. In Figure 2a, we show the plastic part of the creep compliance of our glass for a range of imposed stress amplitudes:

$$J(t, t_w) = \frac{\varepsilon(t, t_w)}{\sigma}$$

The strain $\varepsilon = \Delta L/L$ is calculated along the z-direction and the values at $t_s = 15000\tau_{LJ}$ are given in the legend. It is clearly visible that larger stresses yield higher creep compliances, which indicates a nonlinear response. In Figure 2, we show results for a glass with age $t_w = 75000\tau_{LJ}$, and for increasing wait times we observe (not shown here) the well-known double logarithmic shift toward smaller compliance as discussed for instance in ref 13. In Figure 2b, we show the self-part of the intermediate scattering function which is a standard measure of relaxation times in aging glasses[29]

$$C_q^S(t, t_a, t_r) = \langle \exp(i\mathbf{q}\cdot[\mathbf{r}(t + t_a + t_r) - \mathbf{r}(t_a + t_r)]) \rangle$$

Here, the average is performed over all beads at a certain time, $\mathbf{r}(t)$ is the position of a bead at time t and the wavevector $\mathbf{q} = 2\pi\mathbf{e}_z$ corresponding to a displacement of a in the direction of the applied stress. The age of the glass after unloading is given by $t_a = t_w + t_s$. The main graph shows the dynamical behavior of glasses that were exposed to different stress amplitudes immediately after the release of the stress, i.e., $t_r = 0$. We can clearly identify three regimes: A ballistic regime at very small time scales where the beads can move without collisions is followed by a plateau at intermediate time scales. This indicates that the beads are unable to escape from their position

dx.doi.org/10.1021/ma3000253 | Macromolecules 2012, 45, 2928−2935

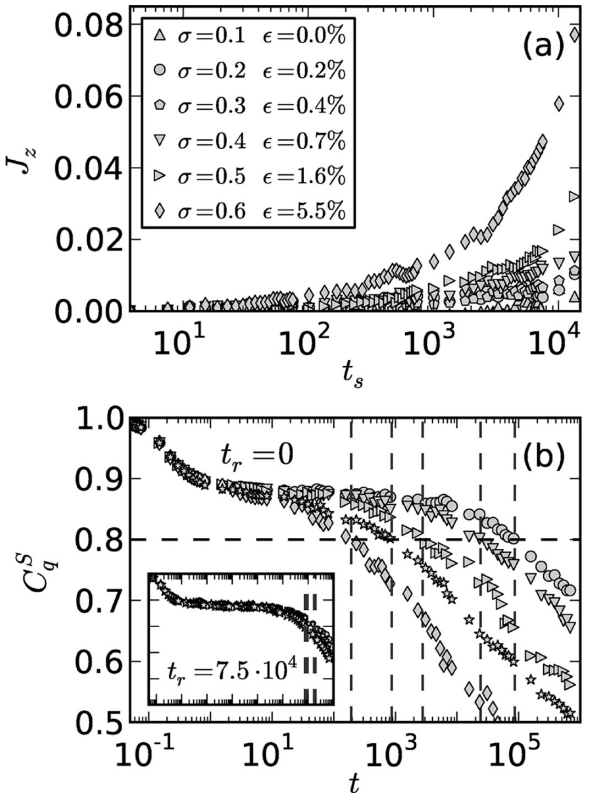


Figure 2. Panel a shows the creep compliances of a glass with age $t_w = 75000\tau_{LJ}$. The indicated strains are calculated at $t_s = 15000\tau_{LJ}$. Panel b shows the intermediate scattering function C_q^S of the perturbed glasses shown in part a with stress release at $t_s = 15000\tau_{LJ}$ and a just-quenched glass (★). The main graph shows C_q^S just after unloading ($t_r = 0$) and the inset is calculated at $t_r = 75000\tau_{LJ}$. The dashed lines define the α-relaxation time.

due to the crowded surroundings. Indeed the shell of neighbors is thought of as a cage to the central bead. The plateau is followed by a logarithmic decay of the intermediate scattering function indicating longer ranged diffusion. The end of the plateau, i.e., the mean time at which a cage-escape occurs is called α-relaxation time τ_α. Aging increases the intrinsic time scale of the glass, and the resulting lengthening of the plateau is visible in the inset of Figure 2b. In this study, we define τ_α as the time when $C_q^S(\tau_\alpha, t_a, t_r) = 0.8$, as indicated by the dashed lines. The shift behavior that we are interested in is insensitive to the precise value of the threshold. In the main graph of Figure 2b, we show that the mechanical perturbation yields a shift toward smaller times, which agrees with previous studies.[1,2,13] The relaxation curve for $\varepsilon = 5.5\%$ indicates that this glass relaxes even faster than the just-quenched glass. The reason for this is that the later already has an effective age of $\sim10^3\tau_{LJ}$, which it acquires during the quench. The inset shows that the differences in the relaxation behavior disappear after a long recovery period. In the following, we clarify whether the impact of mechanical perturbation is transient or permanent by studying the path of recovery.

Recovery of the Relaxation Time. The evolution of the α-relaxation time after unloading holds key information about the change in the aging dynamics. Lee and Ediger showed experimentally that τ_α measured in the recovery regime can be shifted onto the relaxation time of an unperturbed sample.[21] This behavior was associated with mechanical rejuvenation, and the shift time was found to depend on the applied stress. Furthermore, they repeated the experiment with a sample deeper in the glass phase and found merely transient changes. The relaxation time did not behave like that of a new glass, but rather returned to the original unperturbed evolution after a short time. In Figure 3, we show the relaxation time of an

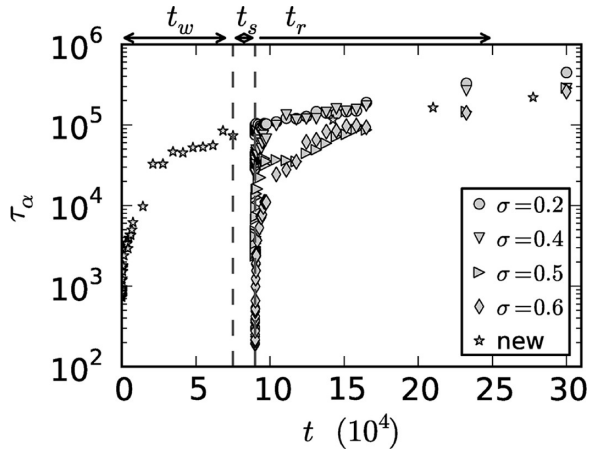


Figure 3. Evolution of α-relaxation time of a just-quenched "new" glass compared to those of mechanically perturbed glasses in the recovery regime. The glasses are identical in the initial aging regime $t_w = 75000\tau_{LJ}$, the creep time is $t_s = 15000\tau_{LJ}$, and the time regimes are indicated by the dashed lines. Other results from simulations with these parameters are shown in Figure 2.

unperturbed glass together with τ_α in the recovery regime after mechanical perturbation with several stress amplitudes. In all cases, we find that the relaxation time immediately after unloading decreases with increasing stress amplitude. For $\sigma < 0.5$, our results show a rapid return to the unperturbed evolution, which suggests a nonpermanent change of the aging dynamics. In qualitative agreement with ref 21, τ_α for larger stresses $\sigma \geq 0.5$ exhibits dynamics very similar to a just-quenched glass but shifted in time.

To illuminate this apparent transition from transient to permanent change, we compare the recovery paths of perturbed glasses in a wide parameter range to those of unperturbed control samples. To this end, we calculate the τ_α dynamics of a just-quenched glass by averaging results of multiple simulations. We find the well-known power law behavior with aging exponent $\mu \simeq 0.89$ and refer to it as the "generic" aging scenario $\tau_\alpha^0 \propto t_w^\mu$.[29,30] In Figure 4, the generic aging is indicated as continuous black line and in the inset we show the relaxation time of unperturbed glasses: The initial value depends on the wait time and the power law behavior is seen for $t > t_w$. In the main graph, we collapse this data by rescaling with the total age $t_a = t_w + t_s$ and τ_α^0 at this age. The dashed lines are guides to the eye and illustrate the ideal path of unperturbed glasses until the power law behavior is resumed at their intersection. Changes introduced by mechanical perturbation can therefore be seen as departure from this expected path. The applied rescaling allows us to compare glasses of all ages and with varying time intervals of stress application t_s.

In Figure 5, we show the evolution of the relaxation time of mechanically perturbed glasses in the recovery regime. The results were gathered from simulations with parameters $10^3\tau_{LJ} \leq t_w \leq 10^5\tau_{LJ}$ and $0.1u_0/a^3 \leq \sigma \leq 0.6u_0/a^3$. We find that the magnitude of change from the unperturbed behavior is best characterized by the total strain ε at the end of creep—not the

dx.doi.org/10.1021/ma3000253 | Macromolecules 2012, 45, 2928−2935

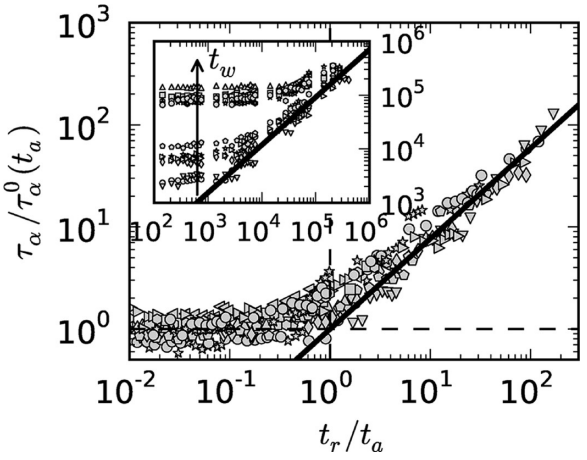


Figure 4. Relaxation time dynamics of unperturbed glasses with a range of wait times $10^3\tau_{LJ} \le t_w \le 10^5\tau_{LJ}$ in a double logarithmic plot. The continuous black line is the "generic" aging dynamics t_α^0 and in the inset (axes: τ_α over t_r) we show the shift of τ_α with increasing t_w. The main graph shows a data collapse with t_r measured in units of glass age $t_a = t_w$ and τ_α being rescaled by $t_\alpha^0(t_a)$. The dashed lines are guides to the eye.

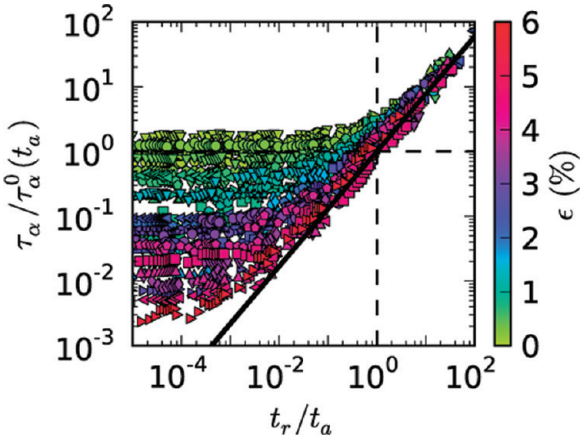


Figure 5. Relaxation time of mechanically perturbed glasses in the recovery regime. The coloring represents the total strain at time of unloading. The continuous line indicates the generic aging dynamics and the dashed lines are guides to the eye.

stress amplitude. Note that the further away τ_α is from the horizontal dashed line, the stronger the impact of the perturbation, and the larger the corresponding strain. Indeed, one can identify three recovery behaviors in Figure 5, which are indicated by coloring: The green curves ($\varepsilon \le 1\%$) are in close proximity to the dashed line and the relaxation time stays constant at time scales smaller than the glass age t_a. This means that creep with small total strain has little impact on the glass and the behavior essentially equals that of an unperturbed sample. At intermediate strains $1\% \le \varepsilon \le 3\%$ (blue curves) the initial τ_α is at a lower value but it begins to evolve *before* reaching the black line. The merger with the generic glass behavior, however, only takes place at the intersection of the dashed lines. This indicates time scales around the original glass age and the implications are discussed in the next paragraph. Finally, the red curves indicate that the largest strains $\varepsilon \ge 3\%$ yield the lowest τ_α. Remarkably, the relaxation times of these strongly perturbed glasses do not begin to evolve immediately but stay approximately constant until reaching the generic aging dynamics which is then followed. This is the behavior that we expect from a glass of a younger age, i.e., we observe apparent mechanical rejuvenation.

To better understand the recovery behavior observed in Figure 5, we show a sketch of idealized paths in Figure 6. As

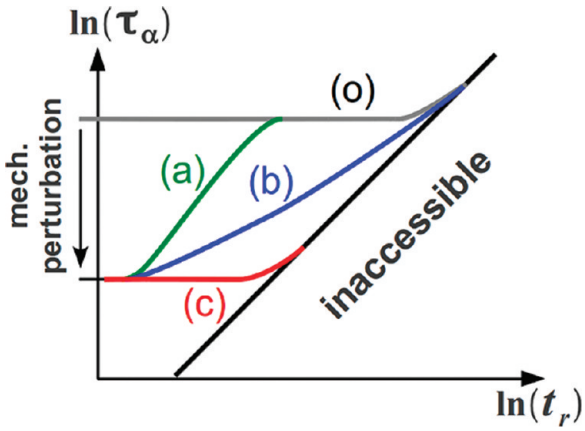


Figure 6. Sketch of possible recovery paths of the α-relaxation time. Line ○ is the path of an unperturbed glass and lines a−c are possible paths of glasses after mechanically perturbation. The diagonal black line indicates the generic aging dynamics.

before, the diagonal black line indicates the generic aging dynamics and path ○ would be followed by an unperturbed glass. We have shown that mechanical perturbation results in a shift toward lower τ_α, which is the starting point of possible recovery scenarios: path a is a fast rejoining of the original (unperturbed) aging trajectory, which is then followed. This is an example of a memory effect. The glass *remembers* its age and the appropriate relaxation time is recovered on time scales that are small compared to the aging dynamics. Path b, also exhibits dynamics on smaller time scales, but it merges with the original aging trajectory at a later time. Indeed the intersection is at times of the order of the glass age whereupon the power law behavior is resumed. This timing shows that the original age is still remembered by the perturbed glass. By comparing Figure 5 and Figure 6 it is easy to see that glasses with intermediate total strain (blue) follow this path. Similarly, the recovery from large strains (red) is found to follow the third idealized trajectory (c). The relaxation time essentially stays constant until the generic aging behavior is reached. The merger happens at times that are smaller than the original age, which apparently indicates a loss of memory, i.e., mechanical rejuvenation. However, it is important to realize that no curve in Figure 5 truly enters the region to the right of the black line. The reason for this lies in the nonequilibrium nature of glasses. The evolution of τ_α is driven by the relaxation toward equilibrium and a given value can only become stable when thermodynamic equilibrium is reached. Since for an ideal glass this state is never reached, the black line acts as an upper time limit for the impact of memory effects, which is the recovery of remembered age and corresponding τ_α. Furthermore, dynamics on very small time scales (ballistic regime) can not alter the relaxation time, because collective motion is required. This means that a lower initial τ_α gives the glass less time to act on its memory. As a result, a strongly perturbed glass that has a small initial relaxation time but that still remembers its original age behaves very similar to a truly rejuvenated glass when viewed only from this dynamical perspective.

dx.doi.org/10.1021/ma3000253 | *Macromolecules* 2012, 45, 2928−2935

Recovery of the Local Structure. Identifying structural quantities that are sensitive to aging has proven to be difficult, and it is still unknown how the age is encoded in the spatial configuration. To the best of our knowledge, no power-law behaviors similar to that of the α-relaxation time are known. We are, however, able to find measures of the local structure with logarithmic dependencies on the glass age. We calculate a variety of such quantities to better characterize the recovery path after deformation and the underlying thermodynamic state. Similar to the relaxation time analysis, we approximate the "generic" aging behavior (indicated via superscript 0) and compare this to the evolution after deformation. To perform a combined analysis for varying stress amplitudes and glass ages (see section for parameter ranges) we use the same rescaling approach as for τ_α. Note that in the case of logarithmic dependencies, the rescaling yields a change of the generic aging slope (continuous black line in Figure 7 and following). We can still use the approach, however, because the evolution during aging and therefore the change of the slope is small.

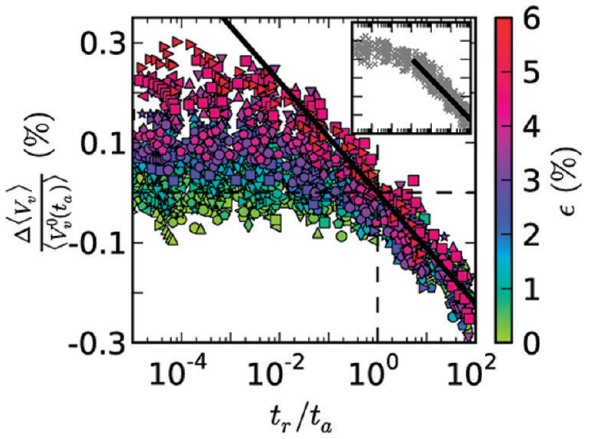


Figure 7. Percentage change of the rescaled average Voronoi cell volume with respect to the "generic" value $\Delta\langle V_v\rangle = \langle V_v(t)\rangle - \langle V_v^0(t_a)\rangle$ at glass age $t_a = t_w + t_s$. Shown in the main graph is the evolution of mechanically perturbed glasses in the recovery regime. The coloring represents the total strain at time of unloading. The continuous line indicates the generic aging dynamics and the dashed lines are guides to the eye. The inset shows the evolution of the average cell volume for just-quenched glasses and the black line is a logarithmic fit that yields the generic aging dynamics.

We first study the decrease of volume during aging in the NPT ensemble by performing a Voronoi tessellation on configuration snapshots and calculating the average cell volume $\langle V_v\rangle$.[31] In the main graph of Figure 7, we show the recovery paths after creep for the same simulations as in Figure 5. As before, the horizontal dashed line indicates the expected path of an unperturbed glass until the intersection with the continuous black line, which indicates the generic aging behavior. The calculation of the generic aging $\langle V_v^0\rangle$ is shown in the inset of Figure 7, and this is exemplary for all quantities with logarithmic dependency on the glass age: We combine the simulation data of six just-quenched glasses and fit for the slope of the emerging logarithmic behavior. In the main graph, the coloring again indicates the total strain at time of unloading. One can clearly see that the deviation from the unperturbed path increases with increasing strain, which agrees with our results from the dynamical perspective. We also observe the merger of red (large strains) recovery paths with the continuous line at time scales smaller than t_a, indicating erasure of memory.

In the absence of long-range order, which is the case for glasses, the local spatial order is important for the characterization of the thermodynamic state. We calculate three measures of the local structure that are sensitive to aging and their recovery paths are shown in Figure 8. Since we focus on mechanical rejuvenation and because the data is relatively noisy, only the results for strains $\varepsilon \geq 2.5\%$ are shown. In panel a, one can see the evolution of the average coordination number $\langle c_v\rangle$, i.e., the number of beads that form the nearest neighbor shell which we calculate using the Voronoi tessellation. We find that the number of participating beads is decreasing with increasing glass age and that an increase in strain leads to larger coordination numbers. In panel b, we show the recovery paths of the triangulated surface order parameter

$$S = \sum_q (6 - q)\nu_q$$

which is sensitive to short-range order and often used in the study of amorphous metals.[13,32] Here q is defined for each bead in the coordination shell as the number of nearest neighbors that are also part of the shell, and ν_q is the number of beads in the shell that have the same q. This order parameter decreases

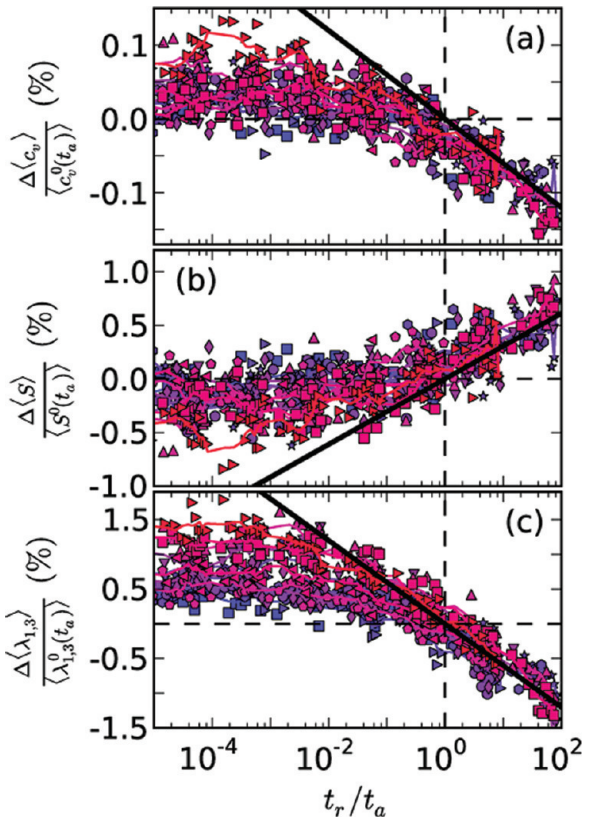


Figure 8. (a) Difference in the coordination number $\Delta\langle c_v\rangle = \langle c_v(t)\rangle - \langle c_v^0(t_a)\rangle$, (b) triangulated surface order parameter $\Delta\langle S\rangle = \langle S(t)\rangle - \langle S^0(t_a)\rangle$, and (c) evolution of the eigenvalue difference $\Delta\langle\lambda_{1,3}\rangle = \langle\lambda_{1,3}(t)\rangle - \langle\lambda_{1,3}^0(t_a)\rangle$. All three quantities are rescaled percentage changes with respect to the "generic" value at glass age $t_a = t_w + t_s$. The coloring represents the total strain at time of unloading (see, e.g., Figure 7). The thick black line indicates the generic aging dynamics and the dashed lines are guides to the eye. The continuous colored lines are running averages and also serve as guides to the eye.

dx.doi.org/10.1021/ma3000253 | Macromolecules 2012, 45, 2928−2935

during aging, which is a sign of increasing order and packing fraction. We find that $\langle S \rangle$ is larger after mechanical deformation and that the recovery path for large strains is similar to that of younger unperturbed glasses. The third structural quantity that we show is the averaged difference between the biggest and the smallest eigenvalue of the moment of inertia tensor of the cages $\langle \lambda_{1,3} \rangle = \langle \lambda_1 - \lambda_3 \rangle$. The Voronoi tessellation identifies the cage for each bead and after setting the origin of the coordinate system to the position of the central bead, we calculate the tensor using the positions of all beads that form the cage. We find that all eigenvalues decrease with glass age, and more importantly that all *differences* exhibit a logarithmic dependency as well. This means that the aging dynamics manifest in a change of the cages toward a more spherical shape. In Figure 8c, we only show the evolution of $\langle \lambda_{1,3} \rangle$ and the just discussed "generic" aging behavior is again indicated by the continuous black line. The observed paths resemble the expected behavior of younger unperturbed glasses, which indicates mechanical rejuvenation. All of these measures of local order show the now familiar dependence on strain, i.e., incease in strain yields further distance from the unperturbed aging path.

Recovery in the Potential Energy Landscape. The potential energy is another quantity that is sensitive to aging, and the depth of the occupied minima in the potential energy landscape has been the focus of previous studies.[17−19] We explore this third perspective on the recovery paths by investigating the evolution of the inherent structure energy $\langle u_{min} \rangle$ in the recovery regime. The calculations are performed using a gradient descent algorithm on spatial configuration snapshots, which yields results in agreement with the potential energy after a very fast quench to zero temperature. In analogy to the analysis of the local structure (see above section), we calculate the "generic" aging behavior $\langle u^0_{min} \rangle$ and rescale the recovery paths of simulations with varying stress amplitudes and glass ages to allow a direct comparison.

In Figure 9, we show the recovery of the inherent structure energy of mechanically perturbed glasses after unloading. As before, the horizontal dashed line marks the expected path of an unperturbed glass and the continuous black line is the generic aging behavior. The shown energies are calculated solely from contributions of nonbonded beads, since the stiff springs between bonded monomers do not age. We find that the depths of the minima decrease with increasing total strain, which is indicated by color code. The green curves ($\varepsilon \leq 1\%$) closely follow the horizontal dashed line and cross over to the generic behavior at times of the order of the glass age. This indicates that the mechanical perturbation was too weak to yield changes in the aging dynamics. For intermediate strains $1\% < \varepsilon < 5\%$ (blue and purple) we observe a decreased initial depth of the minima $\langle u_{min} \rangle$ and the onset of dynamics at times smaller than t_a. However, in agreement with the relaxation time dynamics and the evolution of the local structure, we find that the merger with the generic dynamics takes place at time scales similar to the glass age. The recovery paths at larger strains (red) resemble the expected paths of younger unperturbed glasses: An initially constant behavior is followed by the crossover to the generic aging at time scales *smaller* than the original age of the glass, suggesting mechanical rejuvenation.

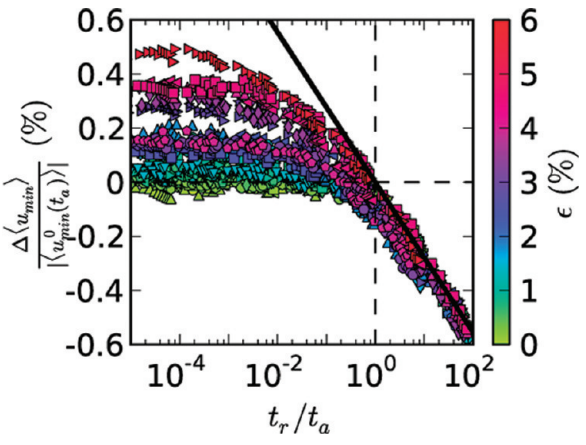


Figure 9. Percentage change of the difference between the minimized potential energy of a mechanically perturbed glass $\Delta\langle u_{min} \rangle = \langle u_{min}(t) \rangle - \langle u^0_{min}(t_a) \rangle$ and the "generic" behavior at glass age $t_a = t_w + t_s$. Shown is the evolution of the potential energy landscape in the recovery regime. The coloring represents the total strain at time of unloading. The continuous line indicates the generic aging dynamics and the dashed lines are guides to the eye.

Recovery after Constant Strain Rate Deformation. We extend the range of strains beyond those accessible with the creep protocol by deforming at constant strain rate, and results in the recovery regime are shown in Figure 10. In close analogy to Figure 5, the α-relaxation time in panel a decreases with increasing total strain. Although results for different strain rates and wait times again collapse for the same amount of strain, we note that the α-relaxation time (as defined here through the decay of the intermediate scattering function) begins to change noticeably only for strains greater than ∼2%. This observation points to some differences between the two deformation protocols that require further investigation. Focusing on the regime of strains larger than 6%, we can now see that the recovery paths saturate and cannot enter the region to the right of the generic aging curve (thick solid line) as explained before. In contrast, we show in panel b that the Voronoi volume can be driven beyond the range covered by unperturbed aging dynamics. This is clearly visible for strains $\varepsilon > 12\%$, as the recovery paths overshoot the generic aging curve. It signifies that we find cell volumes at time scales at which unperturbed aging would have relaxed them to smaller sizes. With regard to the parameters describing local order (see Figure 8), we find a similar overshoot in the recovery curves of the eigenvalue differences, but not for the coordination number and triangulated surface order parameter (not shown). We suspect that these quantities would also begin to show overshoots for even larger deformations. Finally, the inherent structure energy shown in panel c also exhibits a recovery path that enters the regime inaccessible to unperturbed aging. We find that strongly perturbed glasses ($\varepsilon > 12\%$) occupy minima in the potential energy landscape at time scales at which an unperturbed glass would already have relaxed to deeper minima. This implies that the underlying thermodynamic state after deformation is distinct from that of a younger glass.

CONCLUSIONS

We investigate the recovery of a simple polymer glass from uniaxial creep deformations via molecular dynamics simulations. By comparing the recovery paths to the behavior of unperturbed control samples, we are able to analyze the impact of mechanical perturbation on the aging dynamics. We monitor the evolution of multiple quantities sensitive to aging: the α-relaxation time, inherent structure energy and measures of local spatial order, as they give three different perspectives on

dx.doi.org/10.1021/ma3000253 | *Macromolecules* 2012, 45, 2928−2935

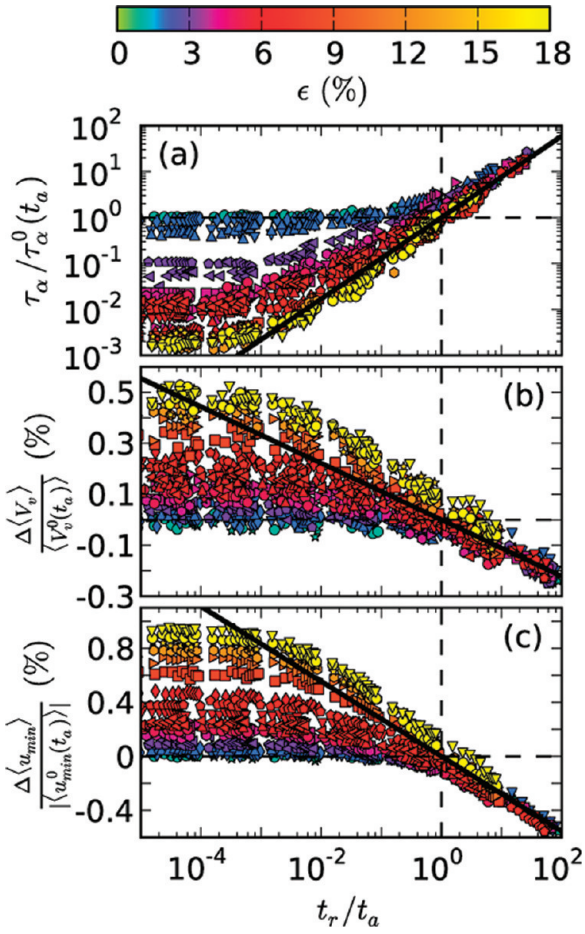


Figure 10. Evolution of (a) α-relaxation time, (b) Voronoi cell volume, and (c) inherent structure energy in the recovery regime after deformation with constant strain rates $\dot{\epsilon} = 10^{-5}\tau_{LJ}^{-1}$ and $10^{-6}\tau_{LJ}^{-1}$ and two waiting times. Parts b and c show percentage changes as defined in Figure 7 and Figure 9, and the coloring represents the total strain at time of unloading. The continuous lines indicate the generic aging dynamics and the dashed lines are guides to the eye.

perturbed glasses. Furthermore, we use a simple rescaling ansatz to allow a direct comparison of glasses with varying ages t_w, durations of the creep period t_s, and stress amplitudes. In the regime of negligible aging during deformation, all of the data suggests that the impact on the aging behavior is described solely by the total strain ϵ after unloading, i.e., an increase in strain yields a recovery path further away from the unperturbed control path. Indeed, one can find a clear progression from seemingly no impact at $\epsilon \leq 1\%$ to transient changes at $1\% \leq \epsilon \leq 3-5\%$ and finally permanent alterations of the glass history at larger strains. This transition from "transient rejuvenation" to full "erasure" of aging is *continuous* and the onset of permanent changes is around the yield strain.[25]

We propose to distinguish between transient and permanent changes of the glass memory by identifying the time scale at which a perturbed glass recovers the aging behavior known from unperturbed samples. If this time scale is around the full age $t_a = t_w + t_s$, then the glass has preserved its memory. On the other hand, if the time scale is smaller than t_a, then the glass history has been altered. We visualize this measure of memory effects in Figure 6.

The permanent erasure of history is often referred to as "mechanical rejuvenation", and it is still a matter of debate whether the underlying thermodynamic state is similar to that of a younger unperturbed glass. To get more information on this underlying state, we combine the observed logarithmic dependencies of local order and inherent structure energy on the glass age with the evolution of τ_α. By comparing the three perspectives on the recovery paths of the perturbed glasses, we can make two observations: For samples deformed via tensile creep to strains of 3−6%, all quantities indicate permanent rejuvenation as defined above. This agreement of dynamical, structural, and energetic criteria suggests that the underlying thermodynamic state is indeed similar to that of a younger glass. The simulations at constant strain rate that reach strains beyond the yield strain show, however, that mechanical deformation can push structural but not dynamical quantities beyond those of younger glasses. These results indicate a distinct thermodynamic state.

The creep deformation protocol used here closely follows that of recent experimental studies.[21] The results are in agreement with earlier studies insofar, as in observing transient changes of the aging dynamics in the subyield regime and permanent changes in the postyield regime. Additionally, we show that the transition toward permanent mechanical rejuvenation is continuous, and that its only control parameter is the total strain after unloading. This finding supports an earlier study that reports the importance of strain in describing accelerated dynamics during deformation.[33] Combining dynamical, structural, and energetic perspectives furthermore suggests that mechanical rejuvenation can lead to underlying thermodynamic states of younger glasses, but also to distinct states. It would be very interesting to compare in detail the present simulation results in the recovery regime to the theory of physical aging and mechanical rejuvenation in polymer glasses developed recently by Chen and Schweizer.[34] Their approach makes a rich array of predictions for the non-equilibrium mechanical response as a function of deformation parameters, but model calculations have so far only focused on steady state deformation.

AUTHOR INFORMATION

Corresponding Author

*E-mail: anton@physics.ubc.ca.

Notes

The authors declare no competing financial interest.

ACKNOWLEDGMENTS

We thank the Natural Sciences and Engineering Council of Canada (NSERC) for financial support. Computing time was provided by WestGrid.

REFERENCES

(1) Hutchinson, J. M. *Prog. Polym. Sci.* **1995**, *20*, 703−760.
(2) Struik, L. C. E. *Physical aging in amorphous polymers and other materials*; Elsevier Scientific Pub. Co.: Amsterdam, 1978.
(3) Struik, L. C. E. *Polymer* **1997**, *38*, 4053−4057.
(4) Hasan, O.; Boyce, M. *Polymer* **1993**, *34*, 5085−5092.
(5) Govaert, L.; van Melick, H.; Meijer, H. *Polymer* **2001**, *42*, 1271−1274.
(6) van Melick, H.; Govaert, L.; Raas, B.; Nauta, W.; Meijer, H. *Polymer* **2003**, *44*, 1171−1179.
(7) McKenna, G. B. *J. Phys.: Condens. Matter* **2003**, *15*, S737−S763.
(8) Loo, L. S.; Cohen, R. E.; Gleason, K. K. *Science* **2000**, *288*, 116−119.

(9) Lee, H.; Paeng, K.; Swallen, S. F.; Ediger, M. D. *Science* **2009**, *323*, 231−234.
(10) Capaldi, F. M.; Boyce, M. C.; Rutledge, G. C. *Phys. Rev. Lett.* **2002**, *89*, 175505.
(11) Riggleman, R. A.; Lee, H.; Ediger, M. D.; de Pablo, J. J. *Phys. Rev. Lett.* **2007**, *99*, 215501.
(12) Riggleman, R. A.; Schweizer, K. S.; Pablo, J. J. d. *Macromolecules* **2008**, *41*, 4969−4977.
(13) Warren, M.; Rottler, J. *Phys. Rev. E* **2007**, *76*, 031802.
(14) Warren, M.; Rottler, J. *Phys. Rev. E* **2008**, *78*, 041502.
(15) Lee, A.; McKenna, G. B. *Polymer* **1990**, *31*, 423−430.
(16) Santore, M. M.; Duran, R. S.; McKenna, G. B. *Polymer* **1991**, *32*, 2377−2381.
(17) Utz, M.; Debenedetti, P. G.; Stillinger, F. H. *Phys. Rev. Lett.* **2000**, *84*, 1471−1474.
(18) Lacks, D. J.; Osborne, M. J. *Phys. Rev. Lett.* **2004**, *93*, 255501.
(19) Lyulin, A. V.; Michels, M. A. J. *Phys. Rev. Lett.* **2007**, *99*, 085504.
(20) Lee, H.; Ediger, M. D. *J. Chem. Phys.* **2010**, *133*, 014901.
(21) Lee, H.; Ediger, M. D. *Macromolecules* **2010**, *43*, 5863−5873.
(22) Kremer, K.; Grest, G. S. *J. Chem. Phys.* **1990**, *92*, 5057.
(23) Bennemann, C.; Paul, W.; Binder, K.; DÃijnweg, B. *Phys. Rev. E* **1998**, *57*, 843−851.
(24) Varnik, F.; Baschnagel, J.; Binder, K. *Phys. Rev. E* **2002**, *65*, 021507.
(25) Rottler, J.; Robbins, M. O. *Phys. Rev. E* **2003**, *68*, 011507.
(26) Papakonstantopoulos, G. J.; Riggleman, R. A.; Barrat, J.; de Pablo, J. J. *Phys. Rev. E* **2008**, *77*, 041502.
(27) Plimpton, S. *J. Comput. Phys.* **1995**, *117*, 1−19.
(28) Auhl, R.; Everaers, R.; Grest, G. S.; Kremer, K.; Plimpton, S. J. *J. Chem. Phys.* **2003**, *119*, 12718.
(29) Kob, W.; Barrat, J. *Phys. Rev. Lett.* **1997**, *78*, 4581−4584.
(30) Chen, K.; Schweizer, K. S. *Phys. Rev. Lett.* **2007**, *98*, 167802.
(31) http://math.lbl.gov/voro++.
(32) Shi, Y.; Falk, M. L. *Phys. Rev. B* **2006**, *73*, 214201.
(33) Warren, M.; Rottler, J. *J. Chem. Phys.* **2010**, *133*, 164513.
(34) Chen, K.; Schweizer, K. S. *Phys. Rev. E* **2010**, *82*, 041804.